ENGINEERING BEHAVIOR OF TYPE I LIGHTWEIGHT CELLULAR CONCRETE AND THE EFFECTS OF PARTIAL SATURATION AND CONFINEMENT

by

Daniel DeSpain Barlow Seely

A dissertation submitted to the faculty of
The University of Utah
in partial fulfillment of the requirements for the degree of

Doctor of Philosophy

Department of Civil and Environmental Engineering

The University of Utah

August 2024

The University of Utah Graduate School

STATEMENT OF DISSERTATION APPROVAL

The dissertation of **Daniel DeSpain Barlow Seely**

has been approved by the following supervisory committee members:

Steven F. Bartlett	, Chair	**date approved** Date Approved
Pedro Romero-Zambrana	, Member	**date approved** Date Approved
Chris P. Pantelides	, Member	**date approved** Date Approved
Evert C. Lawton	, Member	**date approved** Date Approved
Jeffery Ralston Moore	, Member	**date approved** Date Approved

and by **Michael Ernest Barber**, Chair of

the Department of **Civil & Environmental Engineering**

and by Darryl P. Butt, Dean of The Graduate School.

ABSTRACT

Lightweight cellular concrete (LCC) is increasingly utilized in geotechnical applications; therefore, it is vital to understand the engineering behavior of LCC under partially saturated field conditions. This study advances this knowledge by quantifying the effects of partial saturation on the low and high-strain elastic moduli and the ultimate shear strength at low to moderate levels of specimen confinement commonly encountered in roadway and retaining systems.

Back-pressure saturated hydraulic conductivity tests were performed on specimens prepared with a bentonite treatment to prevent hydraulic by-pass along the sidewall. Micro-computed tomography (CT) scans were performed on some specimens over a range of saturation from 1.6% to 35%. The results from this process were used to estimate the void size and pore water distribution within the partially saturated LCC.

A unique test protocol was developed and interpreted using a non-linear regression model to evaluate the degree of saturation that may be expected in long-term field conditions. Uniaxial compression strength (UCS) testing was also conducted at various curing times. A non-linear regression model fitted to these data showed that the specimens gained almost all their long-term strength after 70 days. Therefore, standardizing our test protocol to 70+ days for subsequent testing allowed comparative testing by minimizing curing effects.

Subsequently, test specimens were subjected to five partial saturation treatments, resulting in a range of saturation from 2.8% to 20.4%. These partially saturated test specimens were utilized in a testing program that included non-destructive resilient modulus (RM) testing, followed by either UCS testing or drained triaxial compressive strength testing.

Simple linear and multiple linear regression models (SLR & MLR) were developed using the data produced from the five treatment sets. These regression models include the initial yield stress, peak yield stress, and Young's modulus for uniaxial and confined-drained axial compression. Also, an MRL model for the RM under varying stress conditions was developed. Lastly, we developed UCS and triaxial compression tests paired with RM testing to establish a "surrogate" estimate of the resilient modulus RM for engineering practice. The predictive models are suggested for preliminary engineering estimations and are limited to the ranges presented for this study.

TABLE OF CONTENTS

ABSTRACT iii

LIST OF FIGURES viii

LIST OF TABLES xiii

ACKNOWLEDGMENTS xv

CHAPTERS

1 INTRODUCTION 1

Literature Review and Previous Research 3
Geotechnical Engineering Applications 9
Knowledge Gaps 19
Problem Statement 21
Research Contributions and Goals 22
Research Tasks 24

2 LCC MATERIAL CHARACTERIZATION 27

Batch Design and Samples 27
Sample Preparation 29
Specific Gravity 30
Unit Weight and Phase Relationships 31
CT Scanning and VSD Estimation 33

3 PARTIALLY SATURATED STATES 50

Partial Saturation Treatment Protocol 50
Partial Saturation Treatment Statistics 52
Long-Term Saturation 57
CT Imaging of Partially Saturated LCC 62

4 HYDRAULIC CONDUCTIVITY 76

Methods 76

Results 80
Discussion 82

5 RESILIENT MODULUS 84

Methods 85
Results 88
Discussion 93

6 UNIAXIAL COMPRESSIVE STRENGTH 95

Methods 96
Results 99
Discussion 104

7 DRAINED TRIAXIAL COMPRESSIVE STRENGTH 108

Methods 109
Results 111
Discussion 118

8 LCC PREDICTIVE MODELS 121

Uniaxial Compressive Strength Models 123
Drained Triaxial Compressive Models 127
Resilient Modulus Models 131

9 CONCLUSIONS 137

10 IMPLEMENTATION AND FUTURE WORK 141

Limitations 141
Future Work 142
Industry Standards 143

APPENDICES

A PARTIALLY SATURATED STATISTICAL ANALYSIS 144

B CT IMAGES OF PARTIALLY SATURATED LCC 161

C RESILIENT MODULUS TEST RESULTS 186

D UNIAXIAL COMPRESSIVE STRENGTH TEST RESULTS 187

E TRIAXIAL COMPRESSION STRENGTH TEST RESULTS 188

REFERENCES 796

LIST OF FIGURES

Figure 1. Plot of the estimated uniaxial compressive strength as a function of porosity and time. 6

Figure 2. Excerpt of the mix design report from Aerix Industries..... 28

Figure 3. Plot of the dry unit weight for the LCC specimens as a function of time. 33

Figure 4. Photograph of the Zeiss Xradia 620 Versa. 35

Figure 5. Photograph of a test specimen prepared for CT scanning. 36

Figure 6. Initial view from the CT scan image reduction for sample B1-23. 37

Figure 7. Initial view from the CT scan image reduction for sample B1-24. 38

Figure 8. Initial view from the CT scan image reduction for sample B3-24. 39

Figure 9. Plot of the VSD estimations for Sample B1-23..... 45

Figure 10. Plot of the VSD estimations for Sample B1-23..... 46

Figure 11. Plot of the VSD estimations for Sample B1-23..... 47

Figure 12. Plot of the merged VSD estimations for Samples B1-23, B1-24, and B1-24. 48

Figure 13. Plot of the combined VSD estimations for all WipFrag analyses. 49

Figure 14. Histograms of the degrees of saturation resulting from each of the treatments. 53

Figure 15. Box plot of the degrees of saturation resulting from each of the treatments... 54

Figure 16. Plot of the t-distribution with the t-statistic and critical t-value identified..... 56

Figure 17. Plot of the saturation data as a function of time from the long-term saturation test. 58
Figure 18. Plot of the total unit weight data as a function of time from the long-term saturation test. 59
Figure 19. Plot of the long-term degree of saturation regression model (Equation 9) for B3-30, B3-31, and B3-32 with confidence and prediction bands. 61
Figure 20. CT scan image of specimen B1-23 after the AD treatment. 63
Figure 21. CT scan image of specimen B1-23 after the M5 treatment. 64
Figure 22. CT scan image of specimen B1-23 after the D1 treatment. 65
Figure 23. CT scan image of specimen B1-23 after the V8 treatment. 66
Figure 24. CT scan image of specimen B1-24 after the AD treatment. 67
Figure 25. CT scan image of specimen B1-24 after the M5 treatment. 68
Figure 26. CT scan image of specimen B1-24 after the D1 treatment. 69
Figure 27. CT scan image of specimen B1-24 after the V8 treatment. 70
Figure 28. CT scan image of specimen B3-24 after the AD treatment. 71
Figure 29. CT scan image of specimen B3-24 after the M5 treatment. 72
Figure 30. CT scan image of specimen B3-24 after the D1 treatment. 73
Figure 31. CT scan image of specimen B3-24 after the V8 treatment. 74
Figure 32. Photo of the LCC specimen with the bentonite gel sidewall treatment. 77
Figure 33. Photo of an LCC specimen in the hydraulic conductivity test cell. 78
Figure 34. Plot of the hydraulic conductivity over a range of effective confining stresses. 82
Figure 35. Photo of the resilient modulus testing apparatus. 87

Figure 36. Plot of the resilient modulus of the LCC specimens as a function of confining stress. 89
Figure 37. Plot of the resilient modulus of the LCC specimens as a function of the applied deviator stress. 90
Figure 38. Plot of the resilient modulus of the LCC specimens as a function of the dry unit weight. 91
Figure 39. Plot of the resilient modulus of the LCC specimens as a function of saturation. 92
Figure 40. Plot of the resilient modulus of the LCC specimens as a function of the height-to-diameter ratio. 93
Figure 41. Photo of the 7075-aluminum system compliance calibration disc. 97
Figure 42. Photo of a specimen prepared for UCS testing in the load frame without padded end caps. 98
Figure 43. Photo of a specimen prepared for UCS testing in the load frame with padded end caps. 99
Figure 44. Plot of the initial yield and the UCS of the air-dried LCC specimens as a function of time. 100
Figure 45. Plot of the initial yield and the UCS of the cured LCC specimens as a function dry unit weight. 101
Figure 46. Plot of the initial yield and the UCS of the LCC specimens as a function of saturation. 102
Figure 47. Plot of the Young's modulus of the LCC specimens as a function of dry unit weight. 103

Figure 48. Plot of the Young's modulus of the LCC specimens as a function of saturation. 104
Figure 49. Plot of the uniaxial compressive strength as a function of curing time and the regression model (Equation 20) with confidence and prediction bands. 106
Figure 50. Photo of the triaxial testing apparatus with a test specimen in the triaxial cell. 110
Figure 51. Plot of the triaxial Young's modulus of the LCC specimens as a function of saturation. 112
Figure 52. Plot of the triaxial Young's modulus of the LCC specimens as a function of the effective confining stress. 113
Figure 53. Plot of the triaxial Young's modulus of the LCC specimens as a function of the dry unit weight. 114
Figure 54. Plot of the yield stresses in triaxial compression of the LCC specimens as a function of the effective confining stress. 115
Figure 55. Plot of the yield stresses in triaxial compression of the LCC specimens as a function of saturation. 116
Figure 56. Plot of the Mohr's circles, K_f line, and Mohr-Coulomb failure envelope for the initial yield points for all triaxial tests. 117
Figure 57. Plot of the Mohr's circles, K_f line, and Mohr-Coulomb failure envelope for the peak stress points for all triaxial tests. 118
Figure 58. CT scan image of specimen B1-23 after the AD treatment, No. 0243..... 162
Figure 59. CT scan image of specimen B1-23 after the AD treatment, No. 0729..... 163
Figure 60. CT scan image of specimen B1-23 after the M5 treatment, No. 0243..... 164

Figure 61. CT scan image of specimen B1-23 after the M5 treatment, No. 0729..... 165

Figure 62. CT scan image of specimen B1-23 after the D1 treatment, No. 0243..... 166

Figure 63. CT scan image of specimen B1-23 after the D1 treatment, No. 0729..... 167

Figure 64. CT scan image of specimen B1-23 after the V8 treatment, No. 0243..... 168

Figure 65. CT scan image of specimen B1-23 after the V8 treatment, No. 0729..... 169

Figure 66. CT scan image of specimen B1-24 after the AD treatment, No. 0243..... 170

Figure 67. CT scan image of specimen B1-24 after the AD treatment, No. 0729..... 171

Figure 68. CT scan image of specimen B1-24 after the M5 treatment, No. 0243..... 172

Figure 69. CT scan image of specimen B1-24 after the M5 treatment, No. 0729..... 173

Figure 70. CT scan image of specimen B1-24 after the D1 treatment, No. 0243..... 174

Figure 71. CT scan image of specimen B1-24 after the D1 treatment, No. 0729..... 175

Figure 72. CT scan image of specimen B1-24 after the V8 treatment, No. 0243..... 176

Figure 73. CT scan image of specimen B1-24 after the V8 treatment, No. 0729..... 177

Figure 74. CT scan image of specimen B3-24 after the AD treatment, No. 0243..... 178

Figure 75. CT scan image of specimen B3-24 after the AD treatment, No. 0729..... 179

Figure 76. CT scan image of specimen B3-24 after the M5 treatment, No. 0243..... 180

Figure 77. CT scan image of specimen B3-24 after the M5 treatment, No. 0729..... 181

Figure 78. CT scan image of specimen B3-24 after the D1 treatment, No. 0243..... 182

Figure 79. CT scan image of specimen B3-24 after the D1 treatment, No. 0729..... 183

Figure 80. CT scan image of specimen B3-24 after the V8 treatment, No. 0243..... 184

Figure 81. CT scan image of specimen B3-24 after the V8 treatment, No. 0729..... 185

LIST OF TABLES

Table 1. General classification of LCC..... 4

Table 2. Summary of the specific gravity test results. 31

Table 3. Summary of the estimated VSD for sample B1-23. 41

Table 4. Summary of the estimated VSD for sample B1-24. 42

Table 5. Summary of the estimated VSD for sample B3-24. 43

Table 6. Summary of the combined estimated VSD for samples B1-23, B1-24, and B3-24..... 44

Table 7. Summary of the resulting degrees of saturation for each of the saturation treatments. 51

Table 8. Saturation sample mean and population standard deviation for the treatments. 52

Table 9. Summary of the nonlinear regression statistics for the long-term saturation model (Equation 9) for the data shown in Figure 19. 61

Table 10. Summary of the resulting degrees of saturation, in percent, of the specimens undergoing CT scans..... 62

Table 11. Summary of the hydraulic conductivity test results..... 81

Table 12. Resilient modulus testing sequence for base/subbase materials. 88

Table 13. Summary of the nonlinear regression statistics for the uniaxial compressive strength as a function of curing time (Equation 20). 106

Table 14. Summary of the regression results for Equation 27..... 124

Table 15. Regression statistics and ANOVA results of Equation 27. 124

Table 16. Summary of the regression results for Equation 28..... 125

Table 17. Regression statistics and ANOVA results of Equation 28. 126

Table 18. Summary of the regression results for Equation 29..... 127

Table 19. Regression statistics and ANOVA results of Equation 29. 127

Table 20. Summary of the regression results for Equation 30..... 128

Table 21. Regression statistics and ANOVA results of Equation 30. 128

Table 22. Summary of the regression results for Equation 31..... 129

Table 23. Regression statistics and ANOVA results of Equation 31. 130

Table 24. Summary of the regression results for Equation 32..... 130

Table 25. Regression statistics and ANOVA results of Equation 32. 130

Table 26. Summary of the regression results for Equation 33..... 132

Table 27. Regression statistics and ANOVA results of Equation 33. 132

Table 28. Summary of the regression results for Equation 34..... 133

Table 29. Regression statistics and ANOVA results of Equation 34. 133

Table 30. Summary of the regression results for Equation 35..... 134

Table 31. Regression statistics and ANOVA results of Equation 35. 135

Table 32. Summary of the regression results for Equation 36..... 136

Table 33. Regression statistics and ANOVA results of Equation 36. 136

ACKNOWLEDGMENTS

Aerix Industries graciously supplied the test specimens for this research project. Staff at Aerix Industries for whom I am thankful for their valuable advice for LCC testing and sample preparation included Joseph Feiler, Brian Masloff, Milton Gomez, Sami Safi, and Nico Sutmoller.

I would thank IGES, Inc. who provided support for me throughout my graduate studies and allowed unlimited access to their Geotechnical Laboratory for this research. I am appreciative of Jerry Flannery who was always willing to lend a helping hand with my research testing when needed.

I would like to express appreciation to my dissertation committee who challenged me where I needed it and were willing to give me their time and advice for my research. I and thankful to Dr. Lawton who taught me nearly everything I know about soil mechanics. Thank you to Dr. Bartlett who sought me out for this project and for his valuable guidance, advice, and wisdom throughout this research project – you've taught me more than you know.

Thank you to Ella who taught me how to work with the CT scan photos, to Syliva who helped with many specimen preparations, and to Henry who helped with the CT scans. Finally, thank you Amber for your patience and unconditional support throughout my graduate studies.

CHAPTER 1

INTRODUCTION

The ACI Committee 523 (2006) defines Lightweight Cellular Concrete (LCC) as a concrete product with an oven-dried unit weight of 50 pcf (800 kg/m3) or less and is made from hydraulic cement, water and preformed foam. Although not within the bounds set forth by the ACI, it is commonly accepted that LCC's unit weight ranges from 20 pcf to 120 pcf. LCC is also known as low-density cellular concrete (ACI Committee 523 2006), foamed concrete (Amran et al. 2015), lightweight foamed concrete (Kozłowski and Kadela 2018), low-density foam concrete (Song and Lange 2021), aerated concrete (Narayanan and Ramamurthy 2000), or simply cellular concrete (Hardy et al. 2004).

Lightweight concrete was employed in construction as early as Roman times, where vesicular volcanic aggregates were included in concrete construction. The modern technology of LCC was first developed in the early 1900s in Sweden (Sutmoller 2020) and used in Europe and the United States as part of flooring systems. Cellular concrete was initially patented in 1923 by Axel Eriksson and was known as Ytong (Chica and Alzate 2019). A Swiss patent in 1932 by Siporex included a vapor curing process developed by Eklund (Chica and Alzate 2019; Taylor and Halsted 2021). Foamed concrete was used in the Soviet Union by Kudriashoff starting in 1938, where it was

employed for non-structural construction elements (Chica and Alzate 2019). The use of LCC expanded through Europe and the rest of the world from the mid-1940s and began incorporating hydrolyzed protein-based foams, increasing the quality control of LCC production (Sutmoller 2020). The United Kingdom was introduced to LCC in the 1950s for load-bearing applications, including coal slag from thermoelectric plants (Chica and Alzate 2019). LCC technology was applied in oil wells and as fill for excavations around 1970 (Chica and Alzate 2019). In 1980, the Falkirk railway tunnel in Scotland utilized approximately 4,500 m^3 of LCC for the first large-scale project using LCC as fill (Chica and Alzate 2019). These introductions made advances in the production and quality of LCC of synthetic-based foam liquid concentrates in the early 1990s, which brought more stability to the foam air cells and the longevity of the LCC (Sutmoller 2020). Typical lightweight cellular concrete is considered a relatively impervious (i.e., impermeable) material but may also be classified as permeable using modern hybrid foam. These foams, consisting of protein-based and synthetic-based concentrates, were developed in the early 2000s, introducing permeable lightweight cellular concrete with a connecting open cell structure known as PLCC (Sutmoller 2020).

Many of the recent advancements in LCC technology involve the use of additives. These additives include fly ash, peroxide, slag, silica fume, sugarcane filter cake, laterite, palm oil fuel ash, waste clay brick, clay brick, soil, plastic waste (PE, PVC), recycled waste (glass, plastic), expanded polystyrene foam (EPS), latex, salt waste, polypropylene fibers, quick lime, poly-olefin, silica powders, sand, kaolin, bentonite food additives (methylcellulose, iota carrageenan gum), PVA fibers, cenospheres (Chica and Alzate 2019), vermiculite, perlite, water-reducing admixtures, set accelerators, high-reactivity

metakaolin (ACI Committee 523 2006). Many of the advances in additive constituents are driven by improvements for structural applications in Civil Engineering.

The primary advantages of LCC are (1) a significant reduction in weight, (2) thermal and acoustic insulation, (3) fire resistance, (4) relatively lower cost of production when compared with typical concrete, (5) ease of mixing and pumping, (6) omission of vibration during the placement as needed in typical concrete placement and (7) does not require compaction like typical fill soils (Chica and Alzate 2019).

LCC is increasingly utilized in highway projects as a lightweight fill for settlement mitigation applications. Approximately 65,000 cubic yards of LCC have recently been used for new highway construction on the West Davis Corridor in Davis County, UT, which opened to the public in January 2024. Applications for LCC on this project included rapid embankment construction, bridge approaches, MSE wall backfill, and backfill over sensitive utilities. A fundamental understanding of the geotechnical engineering properties of LCC is crucial to the success of construction projects and long-term performance throughout the design life in which LCC is employed.

Literature Review and Previous Research

Although its primary constituent is Portland cement, LCC does not necessarily behave as typical concrete. Most LCC projects do not incorporate steel reinforcement or aggregates typically used in structural and pavement concrete. Almost all the research and testing defining the engineering properties of LCC has taken a hybrid approach based on soil, rock, and concrete testing. However, LCC is not soil, rock, or conventional concrete. With this in mind, LCC should be considered an intermediate material from a

geotechnical and materials standpoint. Lastly, it is vital to consider the method of production, the LCC density and strength classification, the mix design, and other additives when evaluating data published in the literature.

LCC may be generally classified by its unit weight and compressive strength, as shown in Table 1 (Aerix Industries n.d.). Much of the laboratory characterization of LCC follows the typical concrete strength protocol, defined by the compressive strength (unconfined, uniaxial) as a function of curing time. Also, as customary, the 28-day compressive strength is the defining strength characterization for LCC. The compressive strength of LCC should be performed per ASTM C796 and C495 (ACI Committee 523 2006; ASTM C09 Committee 2012, 2019a).

The determination of the as-cast density of LCC is described in ASTM C796, while the sampling and testing of insulating LCC are to be performed per ASTM C513 (ASTM C09 Committee 2011a, 2019a). The coefficient of thermal expansion is typically 5.0 x 10^{-6} to 7.0 x 10^{-6}/°F but varies with density (ACI Committee 523 2006).

Table 1. General classification of LCC.
LCC classification is generally based on the density or unit weight and the minimum uniaxial compressive strength at 28 days.

Class	LCC unit weight (pcf)	Minimum compressive strength at 28 days (psi)
I	24-29	10
II	30-35	40
III	36-41	80
IV	42-49	120
V	50-79	160
VI	80-90	300

The determination of the thermal conductivity is performed per ASTM C177, C518, and C1363 (ASTM C16 Committee 2019a; b, 2021), while the fire resistance of LCC is controlled per ASTM E119 (ASTM E05 Committee 2020).

The permeability or, more appropriately, hydraulic conductivity of closed cell LCC is typically in the range of 10^{-5} cm/sec to 10^{-6} cm/sec. This property is generally performed per ASTM D2434 (ASTM D18 Committee 2019a), with freezing and thawing evaluated per ASTM C666 (ASTM C09 Committee 2015). LCC mixtures are assessed per ASTM C796 and C869 (ASTM C09 Committee 2011b, 2019a). Also, Kearsley and Wainwright (2001) have developed a methodology to optimize the fly ash content for strength.

René Féret was the first to develop a relationship for concrete strength in 1896, including the air volume as a variable.

$$f_c = K\left(\frac{c}{c+w+a}\right)^2 \quad (1)$$

where f_c (MPa) is the compressive strength of concrete, K is a constant, c is the volumetric proportion of cement, w is the volumetric proportion of water, and a is the volumetric proportion of air (Kearsley and Wainwright 2002). Additionally, Kearsley and Wainwright (2002) have determined experimentally that the compressive strength of LCC may be determined by

$$f_c = 39.6(\ln(t))^{1.174}(1-p)^{3.6} \quad (2)$$

where t is the time or age since casting in days and p is the mature porosity measured after one year. A plot of the compressive strength as a function of the porosity from Equation 2 is shown in Figure 1.

The vacuum saturation porosity (%), P, of LCC may be determined by

$$P = \frac{W_{sat} - W_{dry}}{W_{sat} - W_{wat}} \quad (3)$$

where W_{sat} is the weight in air of the saturated specimen, W_{wat} is the weight in water of the saturated sample, and W_{dry} is the weight of the oven-dried sample.

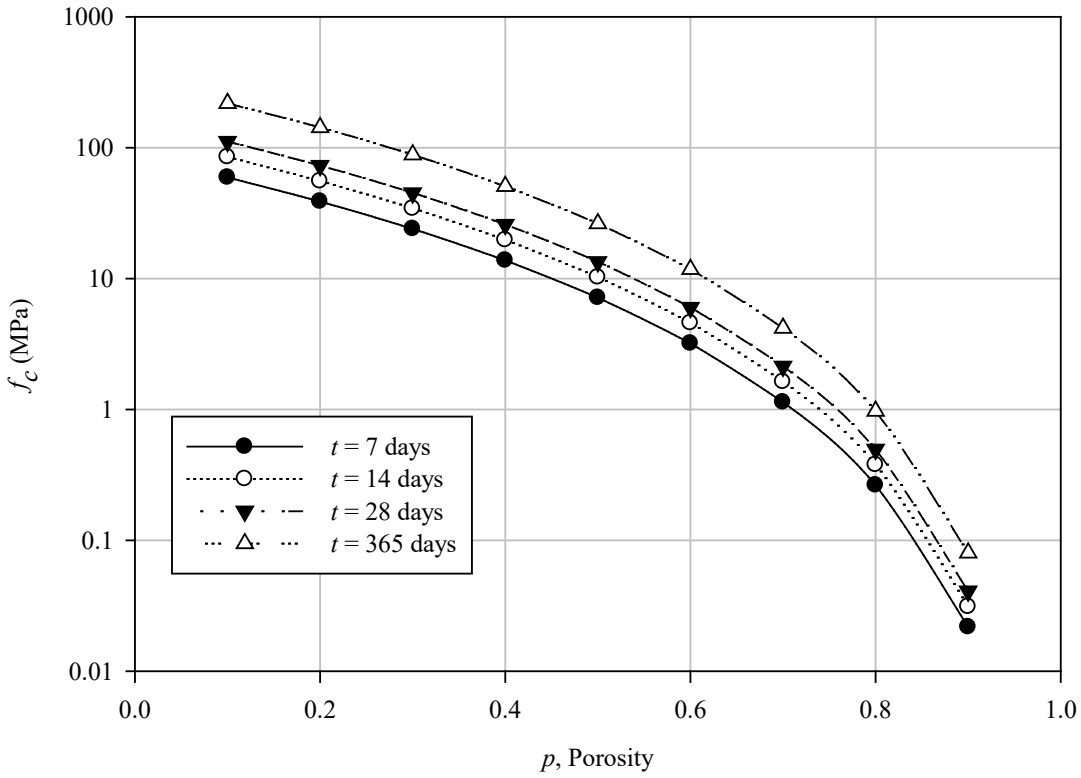

Figure 1. Plot of the estimated uniaxial compressive strength as a function of porosity and time.

Intuitively, the strength of LCC increases with a decrease in porosity and increases with time as the curing reaction progresses. The steady-state strength as a function of time, however, is not apparent.

For this relationship, the specimens were oven-dried to a constant weight, placed in a desiccator under vacuum for at least 3 hours, and then filled with de-aired distilled water (Cabrera and Lynsdale 1988).

Various alternative methods have been evaluated to determine LCC's porosity, including 1) freeze-drying, vacuum-drying, 2) oven-drying at 60°C, and 3) oven-drying at 105°C. The last method produces the highest porosity but perhaps overestimates the true porosity due to damage to the microstructure (Galle 2001). Galle (2001) also suggests that the most appropriate method of porosity determination is the freeze-drying method.

Tikalsky et al. (2004) have developed a modified freeze-thaw procedure that involves saturation of the LCC specimens before the freeze-thaw cycling. The study has shown that strength, depth of initial water penetration, absorption, and absorption rate all affect the freeze-thaw durability of LCC. These authors demonstrated that the density and permeability of the LCC are not significant variables in freeze-thaw durability. However, further research should be undertaken to generate a more extensive data set to characterize the freeze-thaw durability of LCC further and more completely.

A comprehensive experimental study was undertaken at the Sandia National Laboratories to determine the mechanical material properties of cellular concrete with controlled unit weights of 62.4 pcf and 87.4 pcf. This testing program included unconfined compression, triaxial compression, uniaxial strain, extension, and tension tests (Hardy et al. 2004). The Sandia study generated constitutive models based on the cap plasticity models (Sandler and Rubin 1979) for both unit weight classes.

Kearsley and Wainwright (2002) showed that the strength of LCC is dependent mainly on dry density and age but not necessarily affected by the ash type or ash content. In contrast, Jones and McCarthy (2005) have shown that using fly ash in foamed concrete significantly improves its properties (e.g., reducing the heat of hydration).

A contributing study was undertaken with LCC used as subgrade fill. This study found that adding fly ash contributed to strengthening the LCC. The strengthening effect was due to pozzolanic and hydration reactions, which aided the densification of the structural skeleton (Liu et al. 2020). Liu et al. (2020) recommend a fly ash content of 25 percent to optimize this admixture. Using fly ash as an admixture in LCC has also created a more uniform air void distribution and consistent air voids (Nambiar and Ramamurthy 2007). Nambiar and Ramamurthy (2007) have also shown that the air void shape in LCC does not necessarily significantly affect LCC properties. Narayanan and Ramamurthy (2000) and Ramamurthy et al. (2009) provide overviews of the data and relationships in the literature.

As LCC is used more in geotechnical applications, the performance of LCC during earthquakes has been an area of research interest. Tiwari et al. (2018) undertook a study to investigate the response of LCC under dynamic loading under cyclic simple shear testing. Specimens utilized in the study were Class II and Class IV LCC. Data sets and models were generated for dynamic backbone curves, maximum shear modulus curves, modulus reduction curves, and damping curves.

Song and Lange (2021) presented data on the dynamic Young's modulus measurement using the resonant column test per ASTM C215 (ASTM C09 Committee 2019b). Unit weights of the LCC considered in the study ranged from 25.5 pcf to 123.5

pcf. As expected, the dynamic Young's modulus exhibited a dependence on the unit weight of the LCC. This relation was expressed as an exponential increase in stiffness with an increase in unit weight.

To date, the studies of Hardy et al. (2004), Song and Lange (2021), and (Tiwari et al. 2017, 2018) show the most comprehensive material property evaluations applicable to the geotechnical implementation of LCC.

Geotechnical Engineering Applications

According to ACI Committee 523 (2006), geotechnical engineering applications of LCC includer embankments, roadway bases, pipeline and culvert backfills, void space and tank infills, and insulation and isolation fills. In most cases, LCC offers advantages over other earthen commonly used materials in geotechnical engineering. These advantages include low density, ease of excavation, relatively controllable strength, strength advantages over conventional compacted soil, high resistance to freeze-thaw, self-leveling and consolidation behavior, favorable energy dissipation and damping, inert and non-flammable properties, and construction with LCC requires less transportation costs. Teig and Anderson (2012) suggest the following benefits of the use of LCC: 1) lighter and stronger than conventional compacted soil, 2) small equipment used in construction leading to lower environmental impacts, 3) bridge abutments may experience significantly reduced lateral earth pressures and small live load surcharges. 4) block-like behavior (similar to geofoam) and reduced inertial effects in seismic conditions, 5) reduced imposed settlements compared to conventional compacted soil fill, and 6) up to 30% cost savings as compared to conventional cast-in-place concrete walls

with soil fills. Additionally, Taylor and Halsted (2021) listed the following alternate advantages: 1) LCC provides for aggregate conservations, 2) resistance to freeze-thaw, 3) self-leveling and consolidation, 4) energy dissipation and damping, 5) LCC is very excavatable, 6) LCC is considered inert and non-flammable, 7) materials may be locally sourced, 8) LCC is easily pumpable, 9) construction with LCC requires fewer transportation costs and reduces emissions, and finally, 10) LCC construction offers worker safety advantages.

Backfill

LCC has been placed adjacent to bridge abutments and retaining walls as a lightweight fill to reduce settlement, and due to its cementitious nature, it requires no compaction. According to ACI Committee 523 (2006), the general fill should comprise 30 pcf material. Still, the upper two to three feet of the fill should consist of 42 pcf material so that this material is less susceptible to frost damage and provides a solid base for pavement or approach slabs.

Several instances demonstrate that LCC may be used as mechanically stabilized earth wall (MSE) fill (Bartlett 2015; Pradel and Tiwari 2015; Sutmoller 2020; Teig and Anderson 2012; Tiwari et al. 2017, 2018).

Bartlett (2015) suggested using Rankine Theory for lateral earth pressures using the effective friction angle obtained from direct simple shear tests and a relatively low cohesion intercept. Tiwari et al. (2017) suggest using a stress-dependent effective friction angle and zero cohesion for MSE external stability calculations. Also, numerical

analyses of LCC used as MSE wall fill reinforced with geogrid behave as a semi-rigid body under cyclic conditions and perform well (Pradel and Tiwari 2015).

Teig and Anderson (2012) reported an embankment fill over the Colton railway flyover that utilized LCC due to settlement and right-of-way constraints imposed on the project. The project required a relatively high seismic design acceleration criterion. A numerical evaluation method was developed for this project based on previous work performed in similar geomaterials and applications by Bartlett et al. (2011) and Bartlett and Lawton (2008).

Roadways

LCC has been used in roadway construction as a base over soft soils. When used as such, LCC has been shown to span localized settlements up to 3.2 ft (ACI Committee 523 2006). Sutmoller (2020) and Taylor and Halsted (2021) have noted advantages when LCC has been used for subgrade modifications and improvements. Also, work was undertaken by Decký et al. (2016) to back-calculate the modulus of LCC by in-situ testing of a sand subgrade and LCC base material. The study was based on the theoretical 2-layer Sojuzdornii equivalent deformation model. Lastly, Averyanov (2018) undertook extensive research evaluating using LCC in soft soil conditions as a base material in a pavement section. The study showed many advantages to using LCC as a base material, particularly a reduction in the depth of over-excavation and the replacement of poor subgrade materials.

Inti et al. (2021) suggest the advantageous use of PLCC in pervious parking lot sections to replace the granular subbase. Testing indicated the PLCC demonstrated

sufficient strength and permeability with infiltration rates of about 700 in./hr. These authors found that the density of the PLCC is critical when considering the strength, infiltration rate, and water storage. Effluents from infiltration typically showed a higher pH and alkalinity than conventional granular permeable pavement sections.

Pipeline and Culvert Fills

Allen and Meade (1984) discuss an embankment fill on I-275 in Kentucky, where LCC was utilized as an embankment material spanning an existing box culvert. The vertical stresses caused by conventional fill (soil) would exceed the box culverts' structural capacity. Hence, LCC was a lightweight material for embankment construction that reached heights up to 47 feet. The dry unit weight of the LCC used for the project was 25 to 30 percent of conventional fill, but saturated LCC unit weights were about 60 to 70 percent of traditional embankment material. The report details construction methods, laboratory test results, and instrumentation. Class II test specimens were subjected to 20 cycles of temperature changes from 0 to 70 °F. Unfortunately, some specimens completely disintegrated under these test conditions. The instrumentation data seems inconclusive and merits more evaluation.

Void Fills

LCC is an effective material for large void fills where flowability is a factor and a reduction in dead load is desired. Examples of void fills are abandoned swimming pools, abandoned pipelines, excavations, annular spaces around pipelines, undemolished structures, tunnels, and underground fuel or oil tanks (ACI Committee 523 2006;

Sutmoller 2020). Federal regulations indicate that LCC is an inert substance for abandonment applications (ACI Committee 523 2006).

Insulation and Isolation Fills and Miscellaneous Applications and Void Fills

Regions that experience permafrost conditions have typically employed crushed-rock air convection embankment (ACE) technologies to prevent permafrost from thawing in road constructions. ACE is an insulator in summer and a convection cooler in winter conditions. Wu et al. (2020) undertook a study in which numerical simulations compared the performance of typical ACE embankments and the replacement of crushed rock with LCC. The study indicates that LCC has better thermal conductivity and heat capacity performance with a reduced cost. Advantages, as seen elsewhere, are the reduction of the environmental impact resulting from the installation. Additional insulation and isolation applications are possible for utility protection and geothermal utility insulation (Sutmoller 2020).

LCC has been used with EPS for a potential fault crossing. The LCC and EPS system was designed to absorb fault offset over a water pipeline in a rupture event (Taylor 2015).

Lastly, LCC blocks have been used as an energy dissipation system for runaway truck ramps, particularly for airplanes adopted by the FAA (Taylor and Halsted 2021). Other applications Taylor and Halsted (2021) presented include lightweight dam and levee structural fills, landslide repair, and slope stabilization.

Durability

The durability of LCC from a highway/roadway perspective is the ability of the material to last through the design life of the application under conditions of varying water content, chemical attack from both natural water sources and potential roadway surface contaminants, and resisting damage from repetitive traffic loading. LCC's degree of durability depends on the material's location within the pavement section as a direct function of the traffic loading, confinement, and strains. Also, the vertical position of the LCC in a pavement system may affect its freeze-thaw susceptibility. For example, if the LCC is placed sufficiently deep, where nightly temperature changes are insignificant, the performance of the LCC may not be adversely impacted by frost.

Lannen et al. (2018) characterized the strength of cellular grout and abrasion resistance. Abrasion testing protocols were per ASTM C1138M-19 Standard Test Method for Abrasion Resistance of Concrete (Underwater Method) (ASTM C09 Committee 2019c). Their study consisted of cellular grout samples with unit weights ranging from 90 pcf to 110 pcf, representing the high end of LCC unit weights. The general testing protocol outlined in ASTM C1138M-19 involves the agitation of a concrete specimen submerged underwater using a rotating agitator that moves a set of hardened chrome steel grinding balls of varying prescribed sizes. The testing results report the mass or volume loss due to the abrasion, which occurs after a specified duration of agitation. Lannen et al. (2018) also reported the average depth of abrasion.

Liu et al. (2019) studied a selection of factors influencing durability, which include wet density, compressive strength, filling aspect ratio, safety factor, slope rate of connecting surface, steel wire mesh setting, production equipment, agitation sufficient

degree, flow valve, single layer pouring thickness, single layer pouring time, interlayer pouring interval time, construction environment, curing time, vehicle load, drainage condition, chemical corrosion, and temperature change. Although the highlight of the paper is the application of fuzzy logic utilizing the Analytical Hierarchy Process (AHP) and Fuzzy Comprehensive Evaluation (FCE), the inputs to the study are of interest from a durability standpoint. Some areas of the study address project-specific durability concerns and are not likely to have significant research impacts concerning highway/roadway applications. Curing time is an important consideration when developing research or a testing program for durability. Any testing results will vary due to LCC's mechanical and chemical behavior being dependent on the rate of reaction cure time. Of most importance for applying LCC to highway and roadway durability conditions are items are the wet density, compressive strength, vehicle load, drainage condition, chemical corrosion, and temperature change, respectively.

The unit weight or density of the LCC will primarily be a function of the design and reflected in the project specifications. However, the in-place (i.e., wet) density will be influenced by natural wetting-induced changes in water content resulting from surface infiltration or subsurface unsaturated flow. Tiwari et al. (2017) state that LCC has a low water absorption ability, suggesting that some research has been undertaken to address absorption. The authors report LCC hydraulic conductivities from 10^{-3} cm/sec to 10^{-6} cm/sec, which supports the notion that water absorption may be relatively low. However, when coupled with LCC's open vesicular pore structure, this relatively low hydraulic conductivity suggests that water absorption may be controlled by diffusion rather than advective flow. Even though LCC's potential for water adsorption is a site/project-

specific factor, the range of its influence on the mechanical properties of LCC will be addressed in this research.

The literature has thoroughly demonstrated the correlation of LCC's unconfined compressive strength (UCS) as a function of the cast density. Thus, the in-situ UCS of LCC will always be important in project design and construction. Because of this, the UCS of test samples is often used as an "index" measure of the quality of the LCC mix. Kozłowski and Kadela (2018), Namsone et al. (2017), and Tiwari et al. (2017), among many others, have suggested relationships in the form of regression equations for the UCS as a function of the unit weight or density.

The durability of LCC as a function of temperature change is an important aspect to consider in the highway/roadway application. Tiwari et al. (2017) have suggested that LCC has a high freeze-thaw resistivity, but no confirmation data was given in their study. However, this subject has also been discussed in the research of Kozłowski and Kadela (2018).

In addition, a Latvian study on LCC durability was conducted and reported by Namsone et al. (2017). It included the durability aspects of strength, density, water absorption, carbonization, and frost resistance. One unique durability aspect explored by Namsone et al. (2017) is the tendency of LCC to exhibit shrinkage. The authors argue that shrinkage is due to cement hydration and water loss and that shrinkage causes strength reduction and increases thermal conductivity and susceptibility to freeze-thaw cycles. Carbonation, a process that transforms $Ca(OH)_2$ to $CaCO_3$, does not necessarily appear to affect compressive strength, but it does influence shrinkage. The results indicate that carbonation depth is typically less than six mm. These authors further

suggest that analyzing the experimental data shows a correlation between water absorption, carbonation depth, and compressive strength; however, they do not present any correlation plots. Independently, the frost resistance and carbonation were qualitatively observed. Nonetheless, additional research is needed to correlate durability factors with UCS values. This exploration would be of value to practicing engineers.

Like most research papers involving LCC, Kozłowski and Kadela (2018) have reported on testing to address the apparent density and compressive strength. Additionally, these authors investigated the modulus of elasticity, flexural strength, and LCC degradation under freeze-thaw cycles. The modulus of elasticity and flexural strength are important factors to consider when including LCC as a structural component in a pavement section. Still, these factors are not necessarily direct indicators of durability. The data and degradation analysis based on the number of freeze-thaw cycles was done by comparing the compressive strength after 25 freeze-thaw cycles. Kozłowski and Kadela (2018) have reported an approximately 15% reduction in strength after being subjected to the freeze-thaw cycles, a relatively modest decrease from a durability standpoint.

The most comprehensive study on LCC's mechanical properties was published by Tiwari et al. (2017). Their study includes laboratory testing on Class II and Class IV LCC specimens with a range of 19.7 pcf to 47.7 pcf unit weights. The test methods in the study include cast and cured unit weight, unconfined compressive strength, direct shear strength, direct simple shear strength, isotropically consolidated-drained and consolidated-undrained triaxial compressive strength, K_0 consolidation, hydraulic conductivity, and one-dimensional consolidation. The saturated direct simple shear

effective friction averaged 35° with an effective cohesion intercept of 750 psf. The effective friction angle obtained from the consolidated drained and undrained triaxial compression shearing mode of the saturated test specimens averaged 34° with an effective cohesion intercept of 1,630 psf.

The results from the K_0 consolidation testing showed a range from 0.2 to 0.5, corresponding to Poisson's ratio values from 0.2 to 0.3, respectively. Class II LCC exhibited significant deformation with vertical stresses higher than 6,250 psf, while Class IV LCC showed considerable deformation with vertical stresses higher than 14,600 psf. The data generated by the study seems to indicate that the strength and stiffness of the LCC generally decrease with 100% saturation. The hydraulic conductivity testing was performed using ASTM D5084 (ASTM D18 Committee 2016a), commonly known as the flexible-wall or back-pressure saturated permeability. The hydraulic conductivity results ranged from 1.7×10^{-4} cm/sec to 1.2×10^{-3} cm/sec, indicating no decrease in permeability with an increase in effective confining stress.

The test data presented mainly applies to the general geotechnical design aspects to be encountered in a project involving LCC, particularly for applying LCC backfill for MSE retaining walls. It was noted that the strain rate used in the unconfined compressive strength testing was 0.5%/hr, which is exceptionally low and would tend to underestimate the strength of the LCC cylinders significantly. Also noted was that the hydraulic conductivity test results showed no appreciable change when subjected to varying effective confining stresses. However, this result is contrary to intuition and experience. Admittedly, Tiwari et al. (2017) have identified hydraulic conductivity as an area that requires additional research. It is apparent that the durability information and

conclusions derived from the paper are interpretive. Also, the testing was stress-controlled and not strain-controlled, which limits the data value in use from a service-limit state perspective, the limit state most applicable to pavement design.

Knowledge Gaps

Previous research has been conducted on LCC, including a history and characterization of various engineering parameters. Geotechnical applications include backfill, roadways, pipelines, culvert backfill, void fills, insulation and isolation fills, and durability.

Because the data presented by Lannen et al. (2018) is very brief and specific to the high end of the LCC unit weight range, the findings do not apply to evaluating the durability of typical LCC as a potential base or subbase material or as a underlayment for bridge approach slabs. In these applications, the LCC will not be a wearing surface; hence, it will not be subjected to abrasion from traffic loading. Also, modeling suggests that pavement materials typically undergo induced tensile strains from 10^{-5} to 10^{-7} at the pavement-base interface. Hence, the high-strain abrasion action produced by the ASTM C1138M-19 test procedure does not represent the small-strain levels incurred at the pavement-LCC base interface; therefore, the test is too aggressive for the applications suggested above.

Another important topic absent in the current literature is defining the point in time when the mechanical and durability behavior of the LCC has reached a steady state. This research defines this point as when sufficient hydration reaction has occurred where no appreciable strength gain is demonstrated with additional curing time. Therefore,

strength and durability test data are only comparable when the hydration reaction is sufficiently complete. For example, from a construction standpoint, the LCC product will not be put into traffic service until a certain level of curing has occurred. From a design standpoint, the "steady state" properties are needed to evaluate the serviceability and ultimate limit states for various failure mechanics and live and dead-loading combinations.

Another aspect of durability that requires detailed evaluation is the effect of the degree of saturation or water content on the mechanical behavior of LCC. Data presented by Tiwari et al. (2017) suggest that saturating the LCC to 100% yields a decrease in compressive strength. However, this conclusion is not substantiated by the test data reported therein. Hence, the study does not provide a means of vetting the conclusion or exploring the effects of varying saturation states on the mechanical and durability properties.

A vital engineering property for the design of roadways is the stiffness or low-strain modulus of the pavement system materials. It is apparent in the literature that the modulus available is derived from the stress-strain data of testing using monotonic loading at moderate to high levels of strain. However, traffic loading impulses are relatively low-strain and time-dependent. In addition, the magnitude of the induced pressure depends on the various vehicle types' weight and wheel loading configurations. The pavement's modulus is typically dependent on the state of stress and the confinement of the pavement material. LCC's resilient modulus is an additional engineering property missing in research literature and engineering practice. This property is an essential input for mechanistic pavement design and can be performed in a triaxial cell used in

geotechnical soil testing. The resilient modulus testing protocol is performed per AASHTO Technical Subcommittee: 1a, Soil and Unbound Recycled Materials 2017). The axial load is applied to a cylindrical test specimen using a haversine-shaped load pulse, which simulates traffic loading. The confinement and load amplitude are varied throughout the test, producing a stress-dependent modulus of elasticity. Since the loading simulates traffic loading, it also addresses the long-term durability of LCC.

Problem Statement

The use of LCC for geotechnical applications is rapidly increasing in popularity, particularly in roadway projects. As discussed previously, LCC has many advantages over conventional compacted soils in roadway projects and is typically utilized for vertical stress reduction and the resulting settlement mitigation.

Except for one direct shear test, published laboratory test data has been generated on either fully saturated or "dry" test specimens; both states are rarely if ever, achieved in pavement applications. For example, partial saturation is inevitable as surface runoff infiltrates pavement sections through pathways from cracking, expansion joints, damage, etc. Projects with relatively high groundwater tables may partially saturate LCC as the matric suction increases saturation. Therefore, accounting for the degree of saturation as it changes with time and its effect on LCC's behavior and engineering properties is essential to advance the state of knowledge.

Because LCC is subject to a curing process driven by a hydration reaction, there is an elapsed time where testing may be undertaken to reasonably define the long-term

(i.e., steady state) properties for comparative purposes. The literature review has discovered a research gap addressing this phenomenon and concept.

Although the cyclic loading behavior of LCC has been briefly explored and published, the data applies to geotechnical earthquake engineering. Due to the advantages of using LCC for roadway applications, it is a natural progression to utilize LCC as a base or subbase material in constructing pavement sections and approach slabs. No data has been published on the pertinent engineering properties (i.e., resilient modulus), moisture effects, and durability of LCC undergoing repetitive, simulated traffic loadings.

Research Contributions and Goals

The primary research contributions and goals are as follows. 1) Because LCC is subject to curing, which changes the material behavior with time, suites of tests or comparisons of test results are complex or invalid when tests are performed at various curing stages. Thus, this research seeks to establish the elapsed time (i.e., the time for curing) before material testing or evaluation of the tests should commence. 2) The current literature presents test results for dry or "fully" saturated conditions. However, these water content states represent the endpoints of the saturation spectrum and are less likely to be encountered in field applications of LCC. Unfortunately, the effects of the degree of saturation on the material behavior of LCC remain primarily unknown and not discussed in the literature. Thus, an essential goal of this research is to generate representative geotechnical material properties (e.g., compressive strength, stiffness, low-strain moduli, durability, etc.) at varying degrees of saturation. This current study will

employ both uniaxial compressive strength, triaxial compressive strength, and resilient modulus testing to evaluate the effects of saturation on LCC's mechanical and durability properties. This research envisions that LCC will have relatively widespread application as a base or subbase replacement in pavement systems. Unfortunately, current research and engineering practice lack the critical material properties required for incorporating LCC into the design and construction of pavement sections. The most obvious example is that no resilient modulus data have been published to support mechanistic pavement design. Thus, this research will generate data on resilient moduli values at varying degrees of LCC saturation. This evaluation will allow the incorporation of LCC in mechanistic pavement design as a stronger and stiffer material than many compacted soils. 3) There is also little understanding regarding the effects of sample confinement on hydraulic conductivity. Thus, another research objective is to evaluate whether variations in the effective confinement pressure affect the hydraulic conductivity of LCC. 4) Also, because resilient modulus (RM) testing is relatively specialized and expensive, the data generated from the uniaxial and triaxial compression tests will be compared and correlated to develop models for estimating the RM for these standard tests. This new knowledge can also be used to support LCC mechanistic pavement design. 5) Lastly, empirical models will also be developed to appropriately evaluate the degree of saturation's effects on LCC's engineering behavior, focused primarily on the stiffness (i.e., initial modulus) of the LCC as measured by the RM tests.

We believe these evaluations are warranted and necessary to contribute to the state-of-the-art knowledge regarding LCC's mechanical behavior and properties. In addition, the anticipated widespread application of LCC for pavement and other roadway

systems requiring rapid construction techniques positions this study to become a significant contribution to engineering practice.

Research Tasks

The first task of the current research is to characterize the LCC samples cast from three batches: Batch 1 (B1), Batch 2 (B2), and Batch 3 (B3). These batches have corresponding average batch cast unit weights of 27.7 pcf, 28.2 pcf, and 28.6 pcf, respectively, averaging 28.2 pcf as a population. A total of 35 Styrofoam cylinder mold boxes, each containing four samples, were filled, totaling 140 samples. The initial phase of the test program revolved around the uniaxial or unconfined compressive strength (UCS) of the LCC cylinders as a function of time. The UCS tests were performed to a point where no appreciable gain in strength was observed with time, at which point the remaining testing program commenced. Due to the strength change with time, testing must either be performed simultaneously (impossible due to limited equipment availability) or when the strength increase is no longer significant. If so, the tests performed using this latter approach have comparable and implementable results.

Because the degree of saturation is not a direct measurement and is computed through phase relationships, the specific gravity of the solids in LCC must be determined. Four specific gravity determinations were performed on each of the three batches of LCC.

The saturated hydraulic conductivity were measured on three specimens from of each of the batches of LCC per ASTM D5084 (ASTM D18 Committee 2016a) in a staged fashion with the effective confining stresses of 2.5 psi, 5 psi, 7.5 psi, and 10 psi.

LCC samples (60 in total) were subjected to various treatments to produce specimens over a range of degrees of saturation. The samples will be subjected to an air-dried treatment (AD), exposure to a 100% humidity environment for one week (H100), submerged in water for 5 minutes, then exposed to a 100% humidity environment for one week (M5), submerged in water for one day, then exposed to a 100% humidity environment for one week (D1), and finally submerged in water for one week, then exposed to a 100% humidity environment for one week (W1).

A simple model based on regression analysis is developed to indicate the range of possible degrees of saturation of LCC due to burial in a high-humidity environment.

Once the saturation treatment for the individual specimens was complete, all specimens underwent a primary resilient modulus test per the base loading schedule from AASHTO T307 (AASHTO Technical Subcommittee: 1a, Soil and Unbound Recycled Materials 2017). Since the range of stresses in the resilient modulus tests is in the range of elastic deformation for LCC, subsequent secondary tests can be performed and provide a one-to-one compassion between the primary and secondary tests. As the resilient modulus is expressed and a culmination of all stress conditions, the results were initially evaluated using commonly accepted model forms as shown and discussed in Von Quintus and Killingsworth (1998).

Several test specimens were selected for uniaxial and triaxial compression tests in general accordance with ASTM C796 and C495 (ASTM C09 Committee 2012, 2019a) and ASTM D2166 (ASTM D18 Committee 2016b). We note that all compressive tests on the uniaxial and triaxial specimens were tested after the resilient modulus test sequence was performed. The subsequent compressive testing is valid because the

resilient modulus test is non-destructive, and its low-strain load cycling does not significantly affect the results for the high-strain, destructive compression tests. In addition, upon completion of the compressive testing and in quick succession, a water content determination was conducted following ASTM D2216 (ASTM D18 Committee 2016b) for these specimens.

Ultimately, correlative models based on regression analysis were developed from the secondary surrogate tests (uniaxial and triaxial compression) to estimate the resilient modulus from these standard geotechnical tests and to explore the effects of saturation on the engineering behavior of LCC.

Finally, an estimated strength for LCC is proposed in terms of the Mohr-Coulomb strength envelope derived from the triaxial compressive strength tests.

CHAPTER 2

LCC MATERIAL CHARACTERIZATION

Batch Design and Samples

The LCC cylinders utilized in this study, with a target density of 28 pcf, were batched on 5/26/2020 at and by Aerix Industries in Golden, CO. The sample cylinders, with an Aerix Sample ID of 20-600, were cast from three batches, Batch 1 (B1), Batch 2 (B2), and Batch 3 (B3), with corresponding cast unit weights of 27.7 pcf, 28.2 pcf, and 28.6 pcf, respectively. The cylinders had a nominal diameter of three-inches and a nominal length of six-inches. A total of 35 Styrofoam cylinder molds containing four samples were filled, totaling 140 samples. Aerix retained two molds (eight total samples) from Batch 1 for comparative uniaxial compression testing, two each at seven, 14, 28, and 56 days. An excerpt of the mix design report Aerix Industries is shown in Figure 2.

The samples were allowed to cure at the Aerix laboratory for one day, after which the Styrofoam cylinder molds were carefully packaged into three 45-gallon plastic storage bins and strapped onto two separate pallets for shipping. Reddaway picked up the pallets in the early evening of 5/28/2020. The pallets arrived at the Intermountain GeoEnvironmental Services, Inc. (IGES) geotechnical laboratory in South Salt Lake, UT, on the morning of 6/1/2020. The samples arrived in good condition with no signs of

damage. A total of 24 cylinders from B1, 76 cylinders from B2, and 32 cylinders from B3 were provided for the study.

Date: 26 May 2020
Sample ID: 20-600
Client: Dan Seely / University of Utah
Application: PhD Research for Impermeable LDCC and Permeable PLDCC
Target Density: 28 pcf (Actual = 27.7 pcf + 28.2 pcf + 28.6 pcf. **Avg. = 28.2 pcf**)
Target Strength: To Be Determined

Date	No.	Age	Density	load	Strength
02 Jun 2020	1	7 Days	23.1 pcf	756 lbs	107 pcf
	2	7 Days	23.1 pcf	747 lbs	106 pcf
				(Avg @ 7 days	= 106.5 pcf)
09 Jun 2020	3	14 Days	23.5 pcf	967 lbs	137 psi
	4	14 Days	23.7 pcf	1019 lbs	144 psi
				(Avg @ 14 days	= 140 psi)
23 Jun 2020	5	28 Days	22.8 pcf	1314 lbs	186 psi
	6	28 Days	22.7 pcf	1264 lbs	179 psi
				(Avg @ 28 days	= 182 psi)
21 Jul 2020	7	56 Days			
	8	56 Days			

Foam Density = 3.0 pcf ** Three batches were made and 35 Styrofoam molds, each with 4 cylinders, were filled.

	Log No.	Lab Batch Weight	Unit
Cement	Quikrete Type I/II	B1 = 25, B2 = 35 pcf, B3 = 30 **	Lbs
Fly ash	N/A	N/A	g.
Sand	N/A	N/A	g.
Water	0.50 w/c ratio	B1 = 12.5, B2 = 17.5, B3 = 15	Lbs.
Chemical	Mearlcrete	25	ml/L
Additive			
Base Density		114.5	pcf

Figure 2. Excerpt of the mix design report from Aerix Industries.

Mix design parameters and select strengths of the LCC cylinders retained by Aerix Industries.

Sample Preparation

The sample preparation started by removing the samples from their molds. This was done by systematically cutting the Styrofoam from the LCC cylinders into sections. The Styrofoam cutting was accomplished using a DemandTM Products, Inc. CutRite Hot Knife CRTM fitted with an eight-inch blade. The samples were placed on a wire rack to air-dry for one day before sample preparation and testing.

After the samples were allowed to air-dry for one day, the ends of the specimens were ground using a Kent USA SGS-608 surface grinder. The surface grinder was fitted with a trued diamond cup wheel and tooled with a hardened four-inch V-block on a magnetic chuck. The V-block was subsequently squared to within 0.0002" over about four-inches perpendicular to the grinding wheel. The specimens were indexed and placed on the V-block (lengthwise aligned with the V notch), and the end (cross-section) was surface ground until ~95% cleanup was achieved. The specimens were then rotated and indexed 180 degrees end-to-end, and grinding was repeated. The end parallelism of each specimen was checked with a Fowler C-16 comparator. Measurements showed 0.003", or less variation across the diameter of the specimens, which confirmed the quality of the grinding setup.

As testing progressed, it was observed that the bottom of the specimens exhibited a frothier texture than the rest of the sample (termed a "soft bottom"). The soft bottoms were, therefore, ground off from the specimens for subsequent testing by removing approximately one-quarter to 3/8 of an inch from the bottom of the specimen during the grinding process.

The dimensions of the test specimen were measured to within 0.001" using a calibrated digital caliper and digital height gauge. The length of each specimen was measured at three different locations at approximately 120 degrees from one another using the digital height gauge, with the specimen standing vertically on a clean granite surface plate. The diameter of each test specimen was determined with a digital caliper in three locations (top quarter, middle, and bottom quarter) and approximately 120 degrees from one another. The mass of each specimen was determined to the nearest 0.01 g using a calibrated AND FX-3000i digital scale. The representative specimen dimension was computed from the average measurement for each respective specimen.

Specific Gravity

The solids' specific gravity was determined per ASTM D854 (ASTM D18 Committee 2014). A total of 12 test specimens were prepared for specific gravity testing which were sampled from portions of destructed samples following completed uniaxial compressive strength tests. The specimens were prepared for specific gravity testing by pulverizing the sub-samples in a mortar and pestle. The results of the specific gravity tests are summarized in Table 2, yielding an average of 2.671 with a standard deviation of 0.036. This average specific gravity was used for all subsequent phase relationship computations.

Table 2. Summary of the specific gravity test results.
Specific gravity tests were performed on pulverized sub-samples of destructed test specimens used for uniaxial compressive strength testing.

Sample No.	Specific Gravity
B1-01	2.715
B1-05	2.687
B1-10	2.633
B1-15	2.625
B1-18	2.671
B2-04	2.667
B2-09	2.654
B2-14	2.630
B3-03	2.737
B3-08	2.717
B3-13	2.657
B3-17	2.663

Unit Weight and Phase Relationships

Standard geotechnical phase relationships were utilized to estimate the degree of saturation based on the unit weight determination, as described above, the specific gravity of the solids, and the water content. The water content was determined after previous destructive testing was performed per ASTM D2216 (ASTM D18 Committee 2019b). The water content, ω, is computed by,

$$\omega = \frac{m_w}{m_s} \tag{4}$$

where m_w is the mass of water loss upon drying and m_s is the mass of the dry solids. The total unit weight of the specimen, γ, is determined by,

$$\gamma = \frac{m \cdot g}{V} \tag{5}$$

where m is the specimen's total mass, g is gravity's acceleration, and V is the volume of the specimen. The dry unit weight, γ_d, is determined by,

$$\gamma_d = \frac{\gamma}{1 + \omega} \quad (6)$$

Finally, the degree of saturation, S, is calculated by,

$$S = \frac{\omega}{\left(\frac{\gamma_w}{\gamma_d}\right) - \left(\frac{1}{G_s}\right)} \quad (7)$$

where γ_w is the unit weight of water (62.43 pcf), and G_s is the specific gravity of the solids. The porosity, n, of the LCC is determined by,

$$n = 1 - \frac{\gamma_d}{G_s \cdot \gamma_w} \quad (8)$$

As the hydration curing reaction advanced with time, LCC's dry unit weight also increased, as shown in Figure 3. The cured dry unit of the LCC had an average of 19.66 pcf with a minimum of 18.93 pcf, a maximum of 20.81 pcf, and a standard deviation of 0.3871 pcf. The cured porosity of the LCC used in this study had an average of 88.21% with a minimum of 87.52%, a maximum of 88.65%, and a standard deviation of 0.2321%.

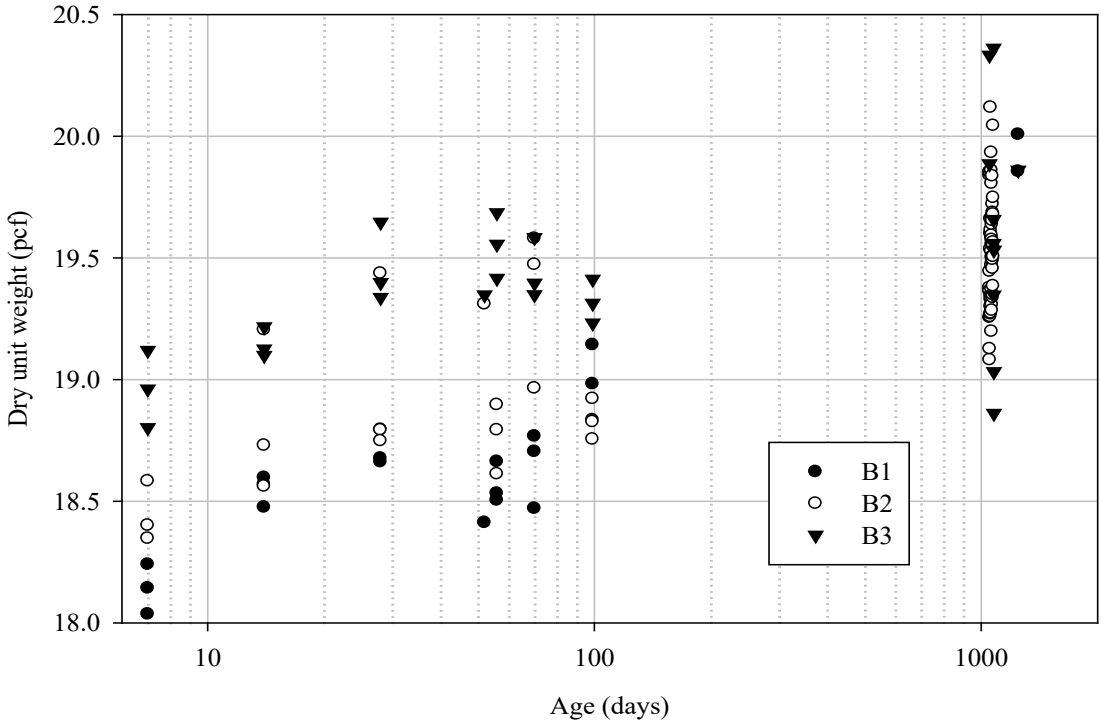

Figure 3. Plot of the dry unit weight for the LCC specimens as a function of time.

As the curing time and thus the hydration reaction of the LCC advances, the dry unit weight of the specimens increases. As shown in Chapter 6, the uniaxial compressive strength follows a similar trend.

CT Scanning and VSD Estimation

Three test specimens, B1-23, B1-24, and B3-24, with corresponding dry unit weights of 19.86 pcf, 20.01 pcf, and 19.86 pcf, respectively, were selected to undergo micro-computed tomography (CT) scans. The CT scans were performed to understand better the cellular void sizes, void-size distribution (VSD), and visual interpretation of the consistency of the samples. This scanning was also done to understand the distribution of pore water as a function of the degree of saturation. The CT scans were performed at the Surface Analysis Laboratory of the Utah Nanofab at the University of Utah. The

instrument used to conduct the CT scans was a Zeiss Xradia 620 Versa 3D X-Ray Microscope/Nano-CT Scanner, shown in Figure 4.

Because the CT scanning machine operates at an elevated temperature and preservation of the degree of saturation was paramount to the study, the specimens must be sealed to prevent any water loss due to evaporation during the scanning process. A unique set of end caps were machined from polyethylene using a Grizzly G0570G metal lathe. The end caps were cut square and machined with an O-ring groove around the circumference. The O-ring groove allowed for a 0.012" thick latex membrane to be stretched over the specimens and sealed to the end caps with a rubber O-ring for the duration of the CT scans. A recess was machined in the bottom platen to fit and index on the Zeiss Xradia 620 Versa specimen pedestal platen, as shown in Figure 5. After the CT scanning process was completed, the data were post-processed using Zeiss Reconstructor software by adjusting the center shift, beam hardening, and peak equalization across the specimen cross-section. Example images of the initial cross-sectional views of the CT scans are shown in Figure 6, Figure 7, and Figure 8. The post-processing resulted in cross-section image slices spaced about 0.003" lengthwise for a total length of about 3.106".

Images similar to those shown in Figure 6, Figure 7, and Figure 8 were selected for slices at the center of the specimens (image 0486) as well as 0.778" above and below the center of the specimens (i.e., images 0243 and 0729, respectively). The selected images were adjusted for contrast and inverted in preparation for further VSD analysis. The converted images were analyzed with WipFrag Fragmentation Analysis Software version 2.7.27, by WipWare.

Figure 4. Photograph of the Zeiss Xradia 620 Versa.

The Xradia 620 Versa micro-CT scanner was used to scan three select test specimens at four levels of saturation. The data generated from the CT scans were used to estimate the VSD of the LCC.

Figure 5. Photograph of a test specimen prepared for CT scanning.

The photo shows the test specimen sealed in a latex membrane and O-rings to prevent any changes to the degree of saturation during the CT scan.

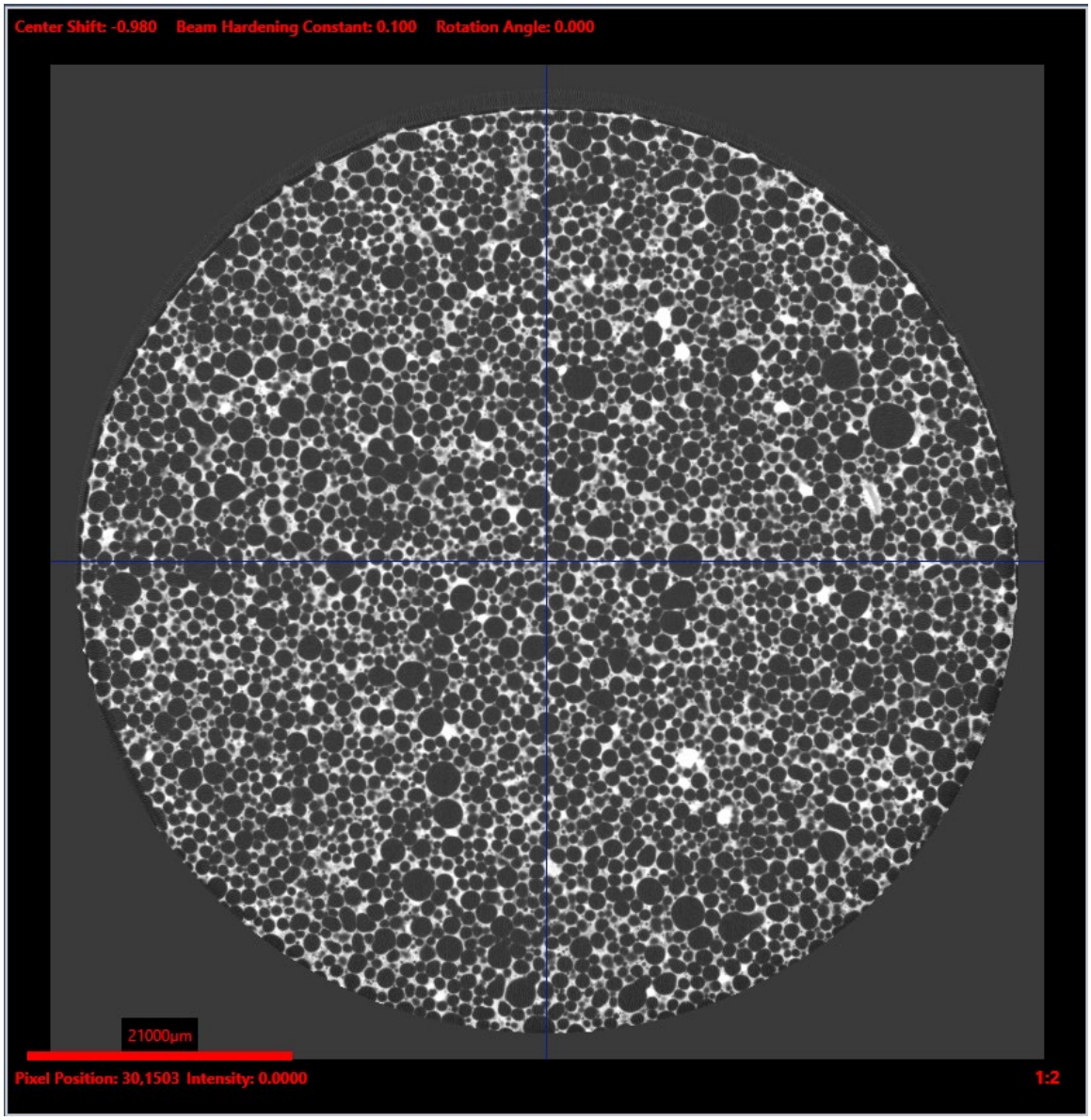

Figure 6. Initial view from the CT scan image reduction for sample B1-23.

Test specimen B1-32 CT image cross-section for the air-dried state. The dark spherical objects are the foamed air voids, and the light matrix is the concrete skeleton structure. The red scale bar in the lower left of the image is 21,000 µm.

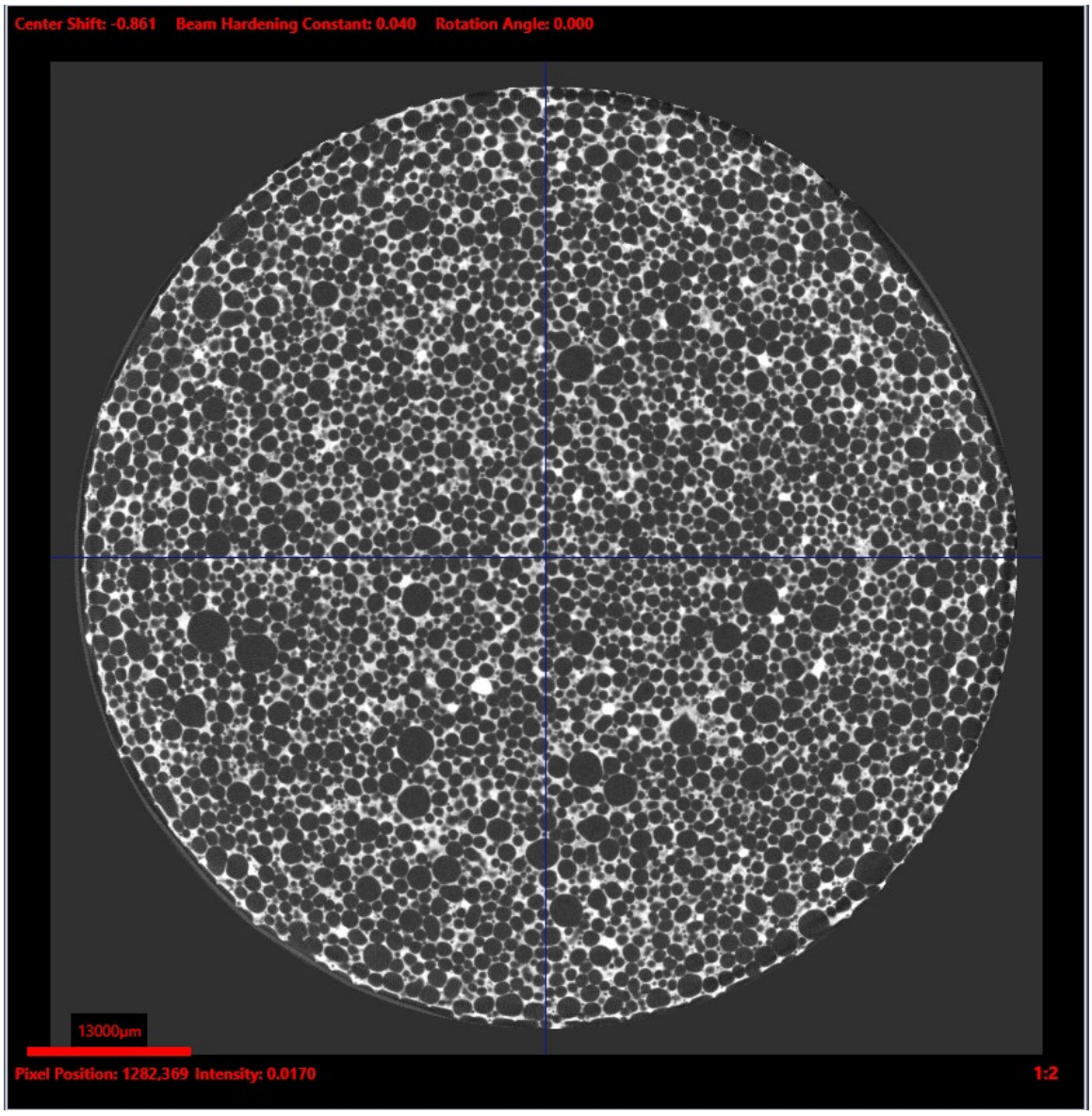

Figure 7. Initial view from the CT scan image reduction for sample B1-24.

Test specimen B1-34 CT image cross-section for the air-dried state. The dark spherical objects are the foamed air voids, and the light matrix is the concrete skeleton structure. The red scale bar in the lower left of the image is 13,000 µm.

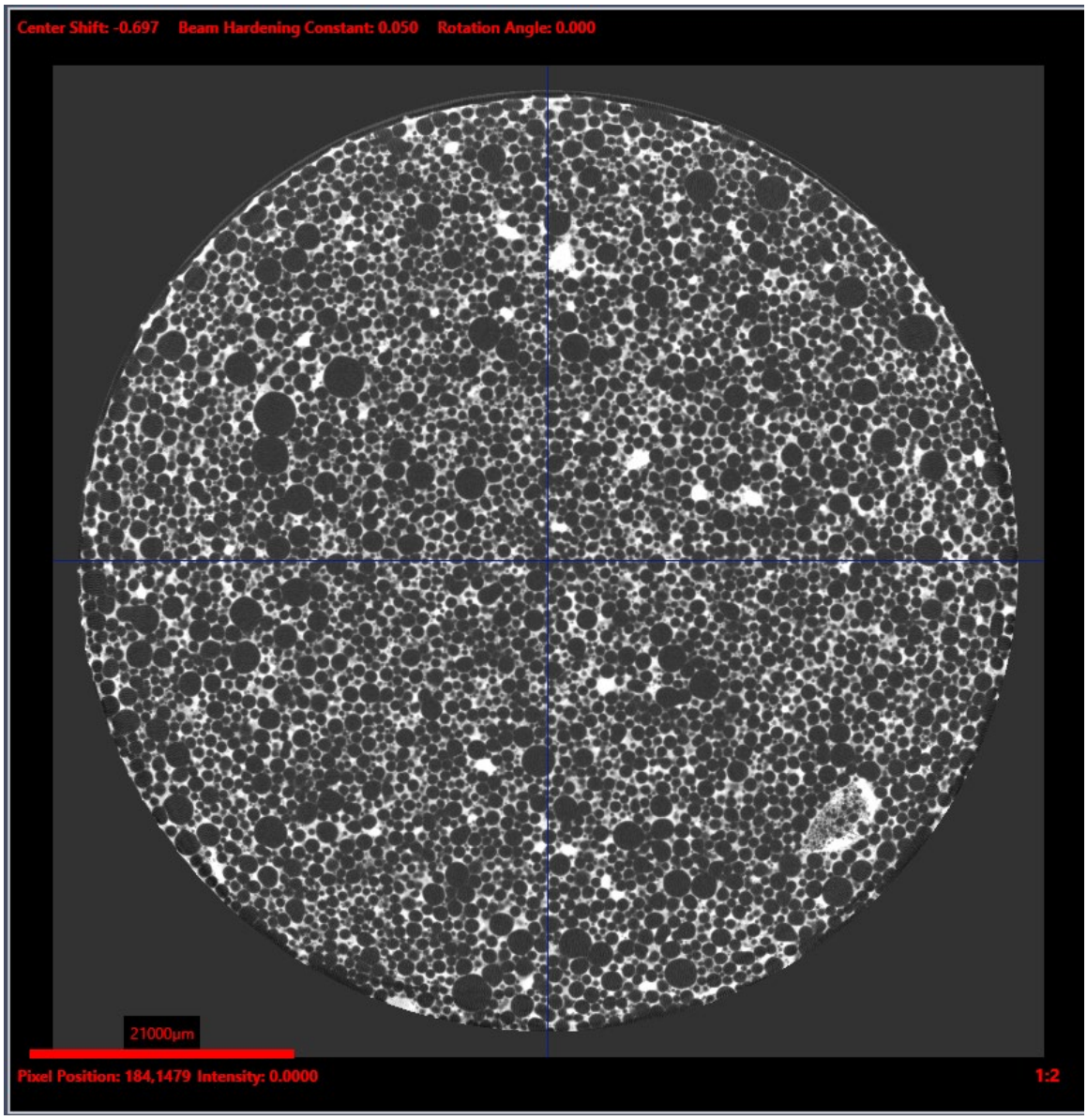

Figure 8. Initial view from the CT scan image reduction for sample B3-24.

Test specimen B3-24 CT image cross-section for the air-dried state. The dark spherical objects are the foamed air voids, and the light matrix is the concrete skeleton structure. The red scale bar in the lower left of the image is 21,000 µm.

The images were scaled and scanned with the WipFrag software, which typically identifies particles but, in this case, identifies voids in the image and computes and assigns a corresponding equivalent diameter of a sphere based on the 2-D cross-section. The void sizes were further analyzed resulting in a void size distribution, as summarized in Table 3, Table 4, and Table 5.

Table 6 summarizes a composite VSD that combines the results from the three analyses for each of the three specimens, providing an average estimated VSD of the LCC specimens. The VSD results are graphically displayed for intra-sample comparison in Figure 9, Figure 10, and Figure 11. Figure 12 shows the graphs of each merged plot for inter-sample comparison. Figure 13 illustrates the results for the average of nine VSDs for the LCC used in this study.

As shown in the VSD tables, the maximum void size observed in the LCC specimen was less than 6.75 mm in diameter. As the nominal minimum specimen dimension is three inches (the diameter), this yields a minimum specimen dimension to the maximum void size ratio of about 11. Standard geotechnical testing practices suggest this ratio, comparing the maximum particle size, however, should be at least six and up to 10. The ratio of 11 satisfies the accepted testing criteria and the assumption that the larges void sizes likely do not influence the test results.

Table 3. Summary of the estimated VSD for sample B1-23.
VSD estimations were accomplished with the use of WipFrag software. The merged slices estimation is a sum of all the voids from the slices 0243, 0486, and 0729 for an average VSD of the specimen.

Void size	Percent finer			
(mm)	Slice 0243	Slice 0486	Slice 0729	Merged slices
6.75	100.00	100.00	100.00	100.00
4.50	99.14	100.00	100.00	99.71
3.00	97.90	98.48	96.76	97.71
2.00	86.05	83.92	79.81	83.24
1.30	40.76	39.08	33.78	37.86
0.90	11.41	10.60	8.47	10.15
0.60	3.49	3.01	2.42	2.97
0.40	1.27	1.07	0.89	1.08
0.25	0.34	0.28	0.27	0.30
0.17	0.19	0.15	0.17	0.17
0.12	0.13	0.11	0.13	0.12
0.08	0.09	0.08	0.10	0.09
0.05	0.02	0.02	0.02	0.02
0.03	0.00	0.00	0.00	0.00

Table 4. Summary of the estimated VSD for sample B1-24.
VSD estimations were accomplished with the use of WipFrag software. The merged slices estimation is a sum of all the voids from the slices 0243, 0486, and 0729 for an average VSD of the specimen.

Void size	Percent finer			
(mm)	Slice 0243	Slice 0486	Slice 0729	Merged slices
6.75	100.00	100.00	100.00	100.00
4.50	100.00	100.00	99.55	99.85
3.00	96.45	98.26	96.24	96.98
2.00	82.91	86.10	79.27	82.76
1.30	39.79	42.42	37.34	39.85
0.90	10.57	11.83	9.92	10.77
0.60	3.21	3.61	3.00	3.27
0.40	1.11	1.27	1.02	1.13
0.25	0.30	0.32	0.26	0.30
0.17	0.16	0.16	0.14	0.15
0.12	0.11	0.10	0.10	0.10
0.08	0.08	0.07	0.08	0.07
0.05	0.02	0.02	0.02	0.02
0.03	0.00	0.00	0.00	0.00

Table 5. Summary of the estimated VSD for sample B3-24.
VSD estimations were accomplished with the use of WipFrag software. The merged slices estimation is a sum of all the voids from the slices 0243, 0486, and 0729 for an average VSD of the specimen.

Void size	Percent finer			
(mm)	Slice 0243	Slice 0486	Slice 0729	Merged slices
6.75	100.00	100.00	100.00	100.00
4.50	100.00	100.00	99.53	99.84
3.00	96.41	93.25	94.53	94.73
2.00	81.74	74.59	77.40	77.90
1.30	49.24	43.28	45.43	45.98
0.90	16.85	14.85	15.08	15.60
0.60	4.06	3.46	4.03	3.85
0.40	1.40	1.18	1.42	1.33
0.25	0.42	0.36	0.41	0.40
0.17	0.22	0.20	0.20	0.21
0.12	0.15	0.14	0.13	0.14
0.08	0.10	0.10	0.10	0.10
0.05	0.03	0.03	0.03	0.03
0.03	0.00	0.00	0.00	0.00

Table 6. Summary of the combined estimated VSD for samples B1-23, B1-24, and B3-24.
VSD estimations were accomplished with the use of WipFrag software. The estimation is a sum of all the voids from the slices 0243, 0486, and 0729 for each of the three specimens resulting in an average VSD of the specimens.

Void size (mm)	Percent finer
6.75	100.00
4.50	99.85
3.00	95.48
2.00	79.53
1.30	43.94
0.90	13.99
0.60	3.66
0.40	1.27
0.25	0.36
0.17	0.19
0.12	0.13
0.08	0.09
0.05	0.03
0.03	0.00

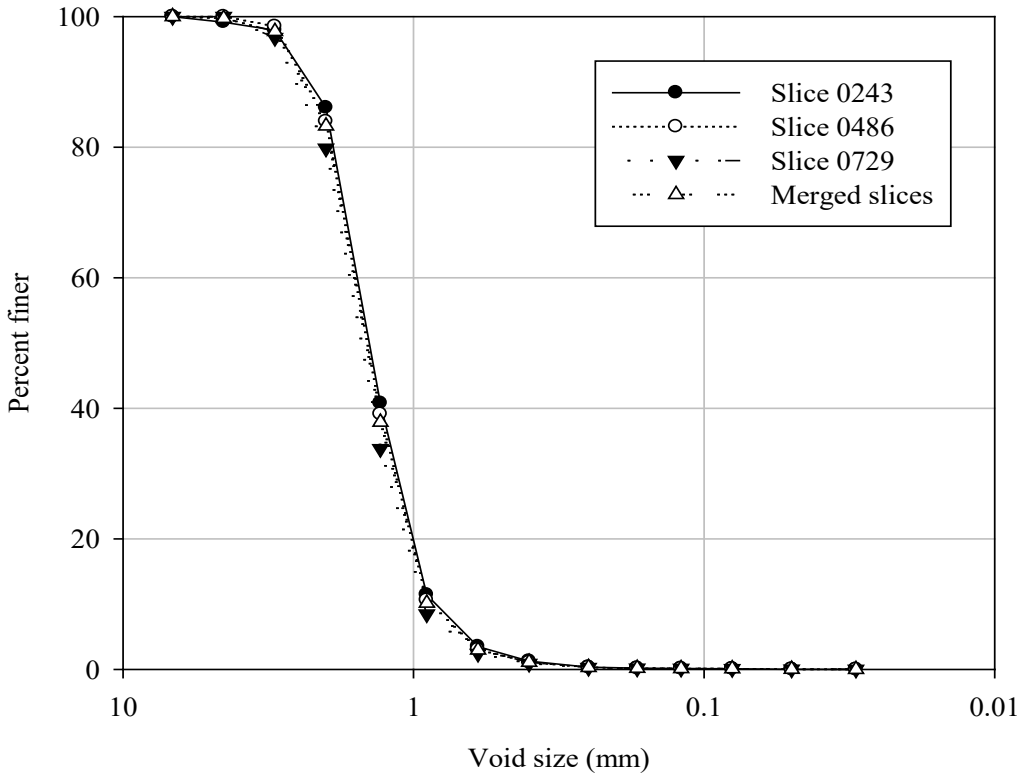

Figure 9. Plot of the VSD estimations for Sample B1-23.

A comparison of the plots for the data shown in Table 3 which indicates a relatively small variance of the VSD within the sample.

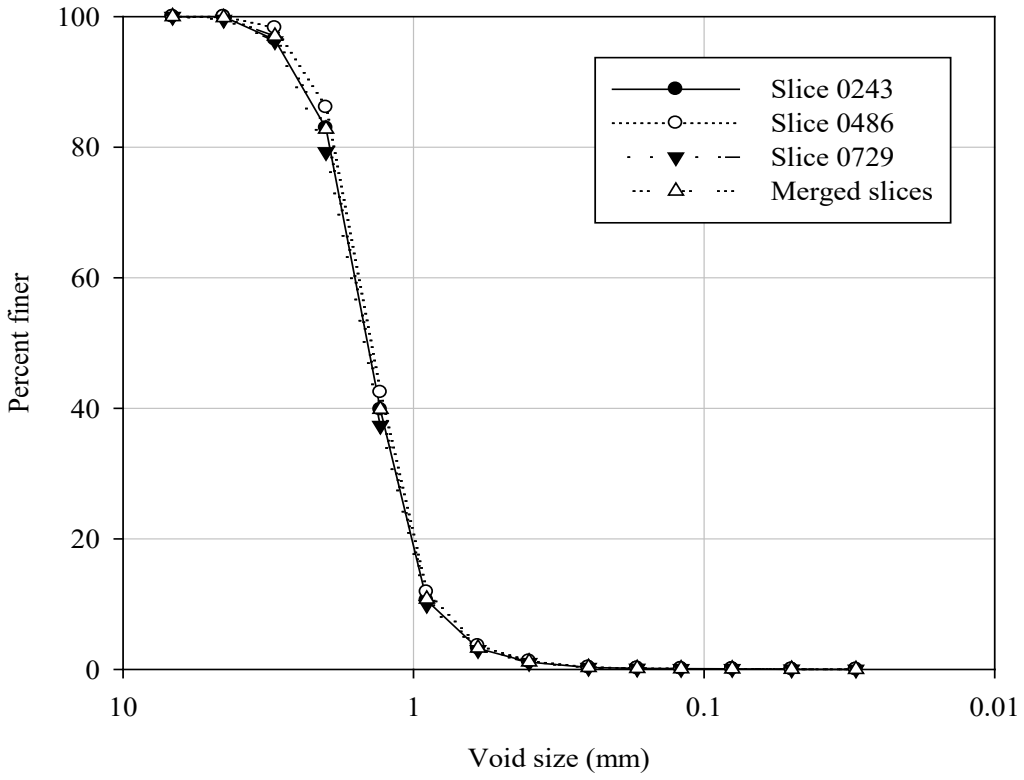

Figure 10. Plot of the VSD estimations for Sample B1-23.

Comparison of the plots for the data shown in Table 4 which indicates a relatively small variance of the VSD within the sample.

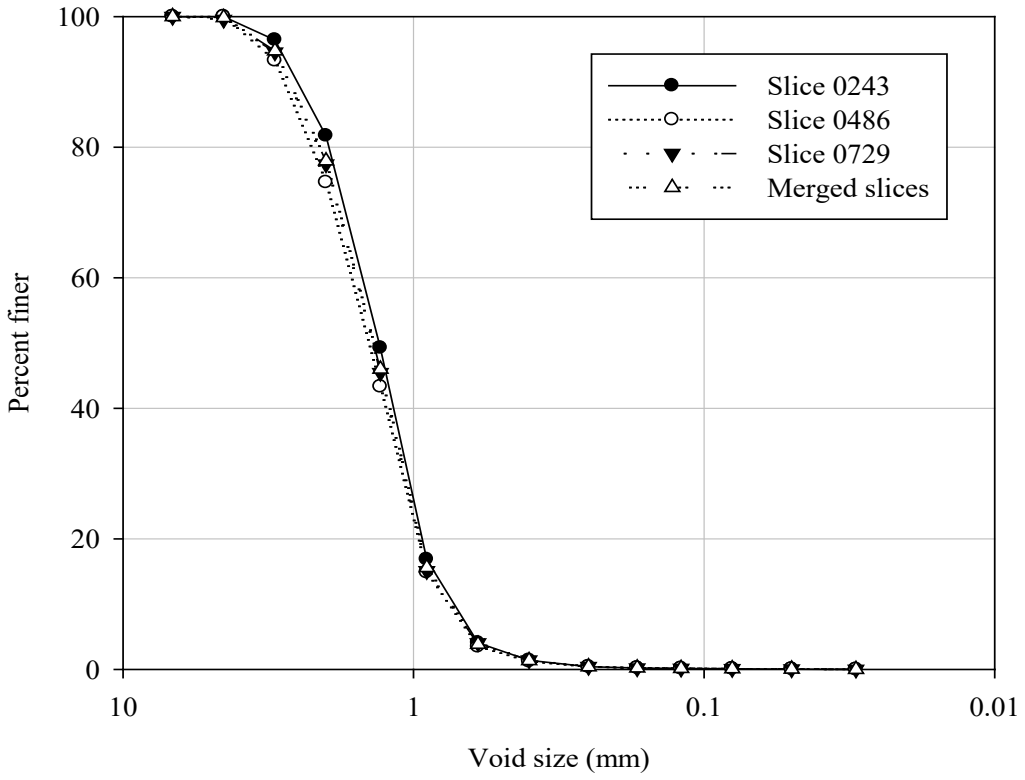

Figure 11. Plot of the VSD estimations for Sample B1-23.

Comparison of the plots for the data shown in Table 5 which indicates a relatively small variance of the VSD within the sample.

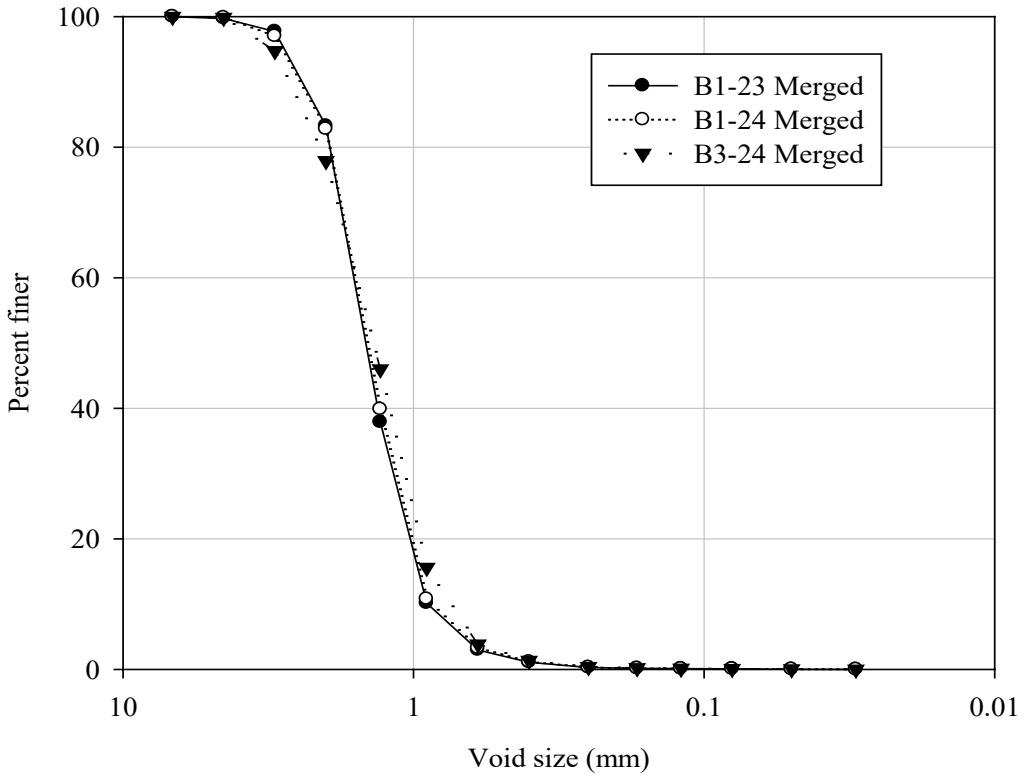

Figure 12. Plot of the merged VSD estimations for Samples B1-23, B1-24, and B1-24.

Comparison of the plots of each merged analysis from Table 3, Table 4, and Table 5 which indicates a slightly different VSD for sample B1-24.

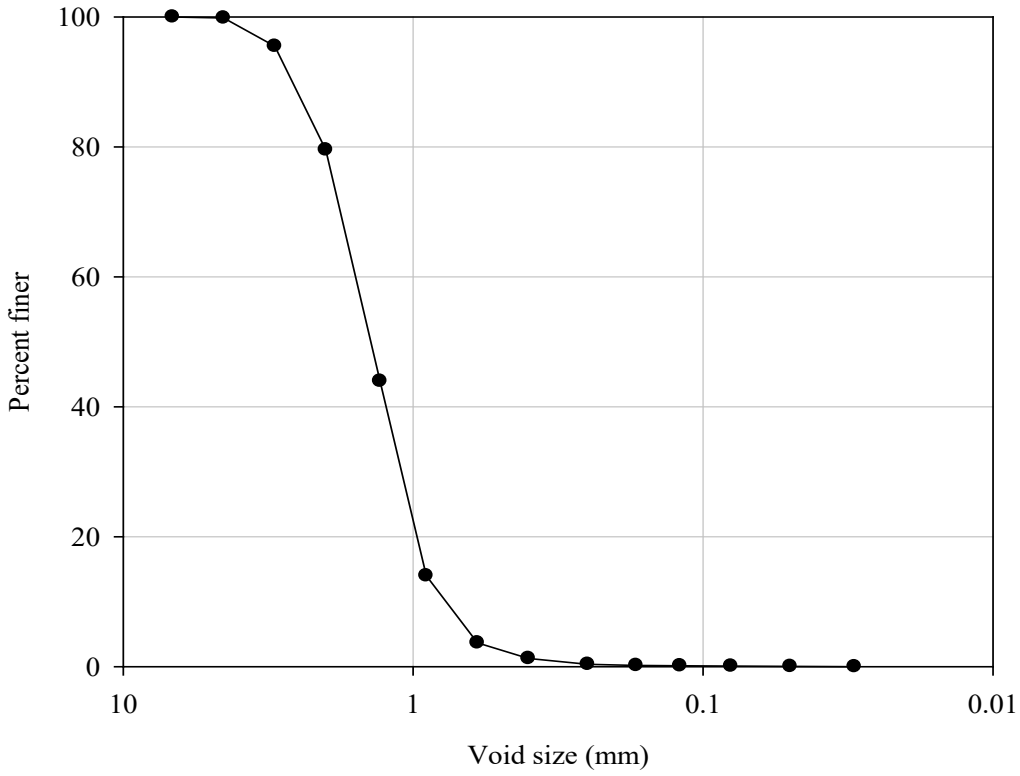

Figure 13. Plot of the combined VSD estimations for all WipFrag analyses.
Plot of the data shown in which is the average VSD representing the LCC used in this study.

CHAPTER 3

PARTIALLY SATURATED STATES

A program was devised to produce a range of partially saturated LCC states that may be encountered in-situ conditions. The program included five treatments (i.e., degrees of saturation, described below) for the LCC samples to investigate the effects of the saturation degree on LCC's engineering behavior. After completing the treatments, mechanical testing was done, including non-destructive resilient modulus testing, followed by either a uniaxial compressive strength or the consolidated-drained axial compression triaxial testing.

Partial Saturation Treatment Protocol

The treatments included groups identified as AD, H100, M5, D1, and W1, with each group having 12 specimens. All partially saturated treatment protocols were performed in a controlled laboratory environment, having an ambient temperature of about 72° F and an atmospheric pressure of about 12.6 psi. The AD (air-dried) treatment protocol exposed the samples to relatively low relative humidity (typically no more than 50%) for about 24 hours. The H100 treatment protocol exposed the samples to a 100% relative humidity environment for one week. The M5 treatment protocol started by submerging the samples in water for 5 minutes and then allowing them to equalize by

exposure to a 100% relative humidity environment for one week. The D1 treatment protocol consisted of submerging the samples in water for 24 hours and then allowing them to equalize by exposure to a 100% relative humidity environment for one week. Finally, the W1 treatment protocol consisted of submerging the samples in water for one week and allowing them to equalize by exposure to a 100% relative humidity environment for one week. A summary of the resulting degrees of saturation for each of the treatments is shown in Table 7. The data in the table are the degrees of saturation, in percent, achieved from each treatment protocol described above.

Table 7. Summary of the resulting degrees of saturation for each of the saturation treatments.

AD	H100	M5	D1	W1
2.955	4.449	11.907	15.986	17.531
3.091	4.441	9.783	15.504	18.374
3.067	4.275	10.281	15.480	20.368
3.122	4.227	9.679	15.802	19.438
3.620	4.981	10.444	17.123	18.652
3.716	4.647	10.055	17.533	16.078
3.541	4.967	9.884	15.493	15.842
3.455	4.996	9.860	15.764	17.084
3.449	5.033	9.889	17.973	18.536
3.329	5.100	9.389	15.708	18.283
4.014	5.288	9.142	15.832	17.781
3.825	5.112	9.293	17.547	18.503

Partial Saturation Treatment Statistics

The sample mean and population standard deviation for each treatment are shown in Table 8. Figure 14 shows histograms of the resulting saturations for each treatment, while Figure 15 shows a box plot of the saturation for each treatment. Several observations are noted from the results shown in these figures. The first observation is that the variance increases with the degree of saturation achieved for each treatment group. The second observation is that the AD, H100, and M5 treatments are easily distinguished as populations with differing saturation means. The third observation from Figure 14 is that it is not apparent that treatments D1 and W1 have different sample means and variances. The following sections will further explore these hypotheses, and the supporting statistical evaluation is presented in Appendix A.

Table 8. Saturation sample mean and population standard deviation for the treatments. The data listed in the table are the degrees of saturation, in percent, achieved from each of the treatment protocols described above.

Statistic	AD	H100	M5	D1	W1
Sample mean	3.432	4.793	9.967	16.312	18.039
Population standard deviation	0.317	0.349	0.069	0.900	1.235

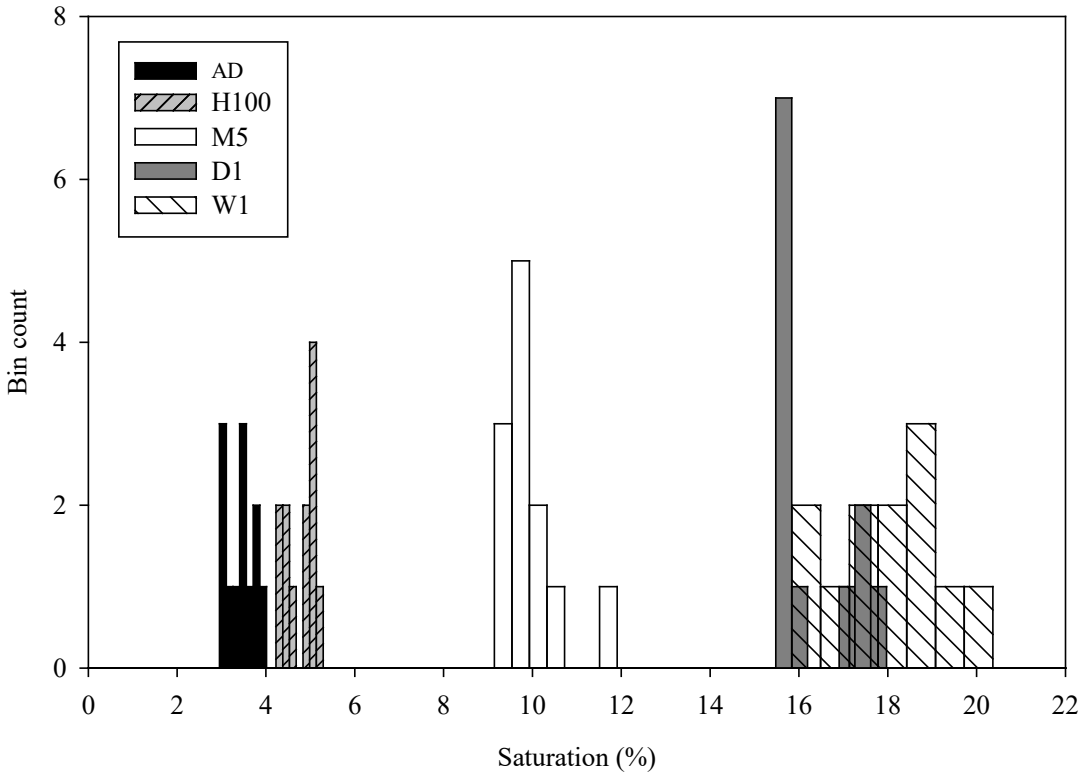

Figure 14. Histograms of the degrees of saturation resulting from each of the treatments.

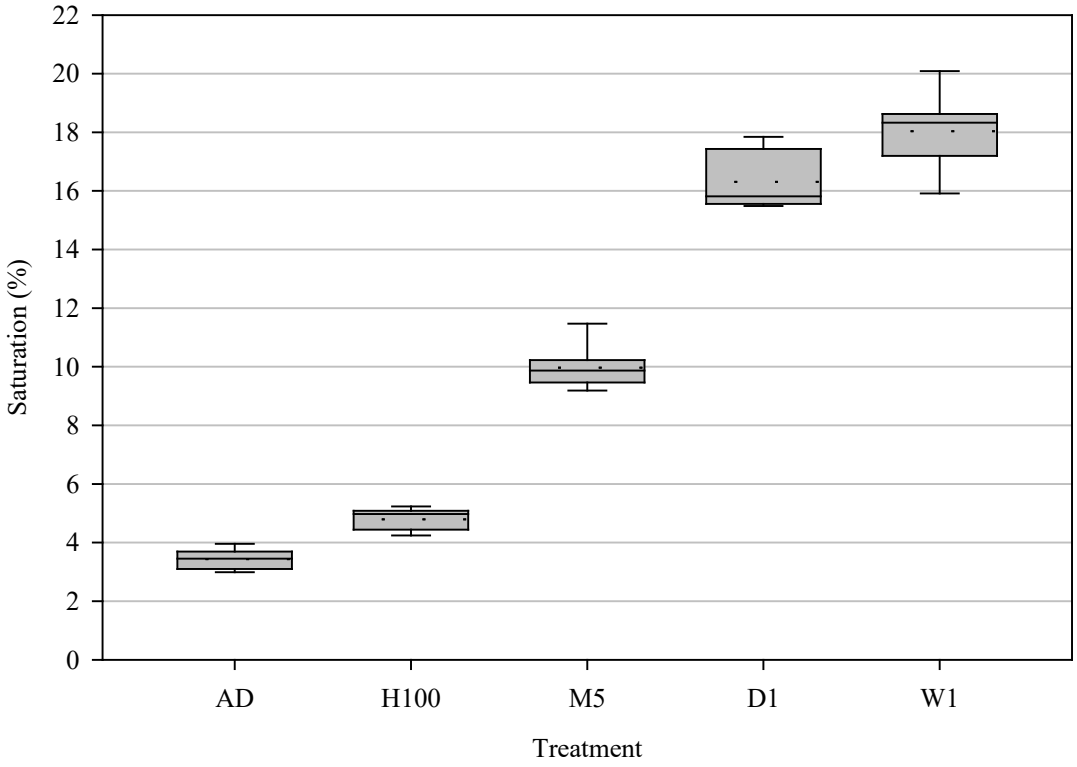

Figure 15. Box plot of the degrees of saturation resulting from each of the treatments.

The dashed line in each box represents the mean of the data set while the solid line within the box represents the median or 50th percentile of the data set. Treatments AD, H100, and M5 indicate an obvious difference between the means. It is not apparent, however, that there is a difference between the means for groups D1 and W1.

F-Test for Sample Variance

As shown in Figure 14 and Figure 15, it is evident that the variance increases with an increase in saturation resulting from the treatments. An initial F-test with a significance level, $\alpha = 0.05$, is warranted to test for equal or unequal variance in the two

data sets to decide to pursue a pooled-variance t-test or an independent variance t-test as appropriate. The null hypothesis for the F-test states there is no statistically significant difference between the variance of the two data sets. The alternative hypothesis for the F-test states that there is a statistically significant difference between the variance of the two data sets. The analysis resulted in an F-statistic for treatments in D1 and W1 are 1.885 and 0.308, respectively. The critical F-statistic was computed to be 2.818. Since the F-statistic for D1 is greater than the critical F-statistic, the null hypothesis is rejected, and the alternative hypothesis is accepted. Therefore, with 95% confidence, there is statistical evidence of a difference between the variance between the two data sets and an independent variance t-test is appropriate.

t-Test for Difference Between the Means

The widths of the histogram bars for each group in Figure 14 are scaled by bin size, which aids in comparing variance within the group. Treatments AD, H100, and M5 indicate a noticeable difference between the means. It is not apparent, however, that there is a difference between the means for groups D1 and W1.

A standard t-test with a significance level of $\alpha = 0.05$ was performed to evaluate if there is a "significant" difference between the means of the two data sets. The null hypothesis for the t-test states there is no statistically significant difference between the means of the two data sets. The alternative hypothesis is that there is a statistically significant difference between the means of the two data sets. In other words, the mean for W1 is statistically greater than D1, and the two means must be treated and evaluated separately. The analysis resulted in a computed t-value test statistic of 3.749 with a

weighted critical t-value of 2.201 for a single-tailed test (Figure 16). The null hypothesis is rejected because the test statistic t-value is greater than the critical t-value, and the alternative hypothesis is accepted (i.e., the means are statistically different). Therefore, with 95% confidence, there is statistical evidence that the mean of group W1 is greater than the mean of group D1. See also Appendix A.

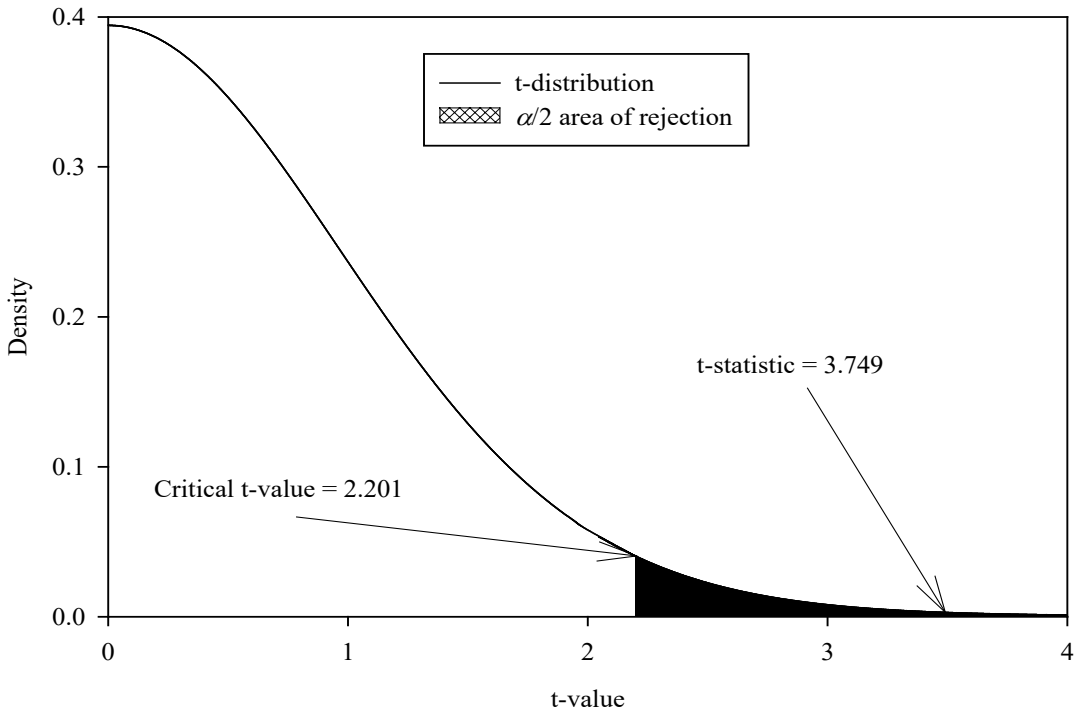

Figure 16. Plot of the t-distribution with the t-statistic and critical t-value identified.

Long-Term Saturation

Three test specimens, B3-30, B3-31, and B3-32, with corresponding dry unit weights of 19.03 pcf, 18.86 pcf, and 19.53 pcf, were selected for a long-term saturation test. The test aimed to understand the possible range of the degree of saturation that may be encountered in the field for LCC from ambient conditions below roadway grade. The LCC will likely absorb water after curing and then subsequently being buried. This absorption may be due to installation near the groundwater table, where it may be subject to capillary action, exposure to free water from surrounding earthen materials, or subject to surface water infiltration through pavement sections or embankment fills. Each of the above scenarios resides in a high-humidity environment, which has been shown to promote partially-saturated flow through advection and diffusion (Seely et al. 2014).

The samples were cured, oven-dried, and subsequently subjected to a 100% relative humidity environment for 321 days. The mass of each specimen was determined about every 7 days for the test duration. The resulting change in saturation as a function of time is shown in Figure 17, with the corresponding increase in total unit weight being shown in Figure 18.

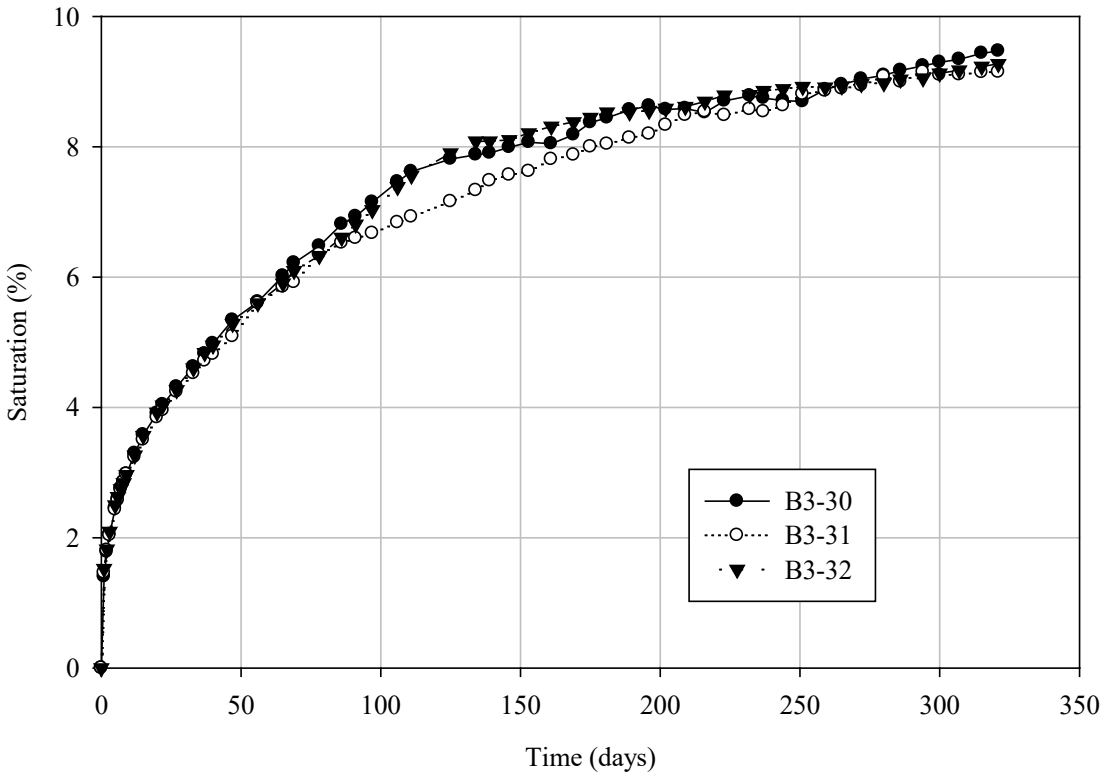

Figure 17. Plot of the saturation data as a function of time from the long-term saturation test.

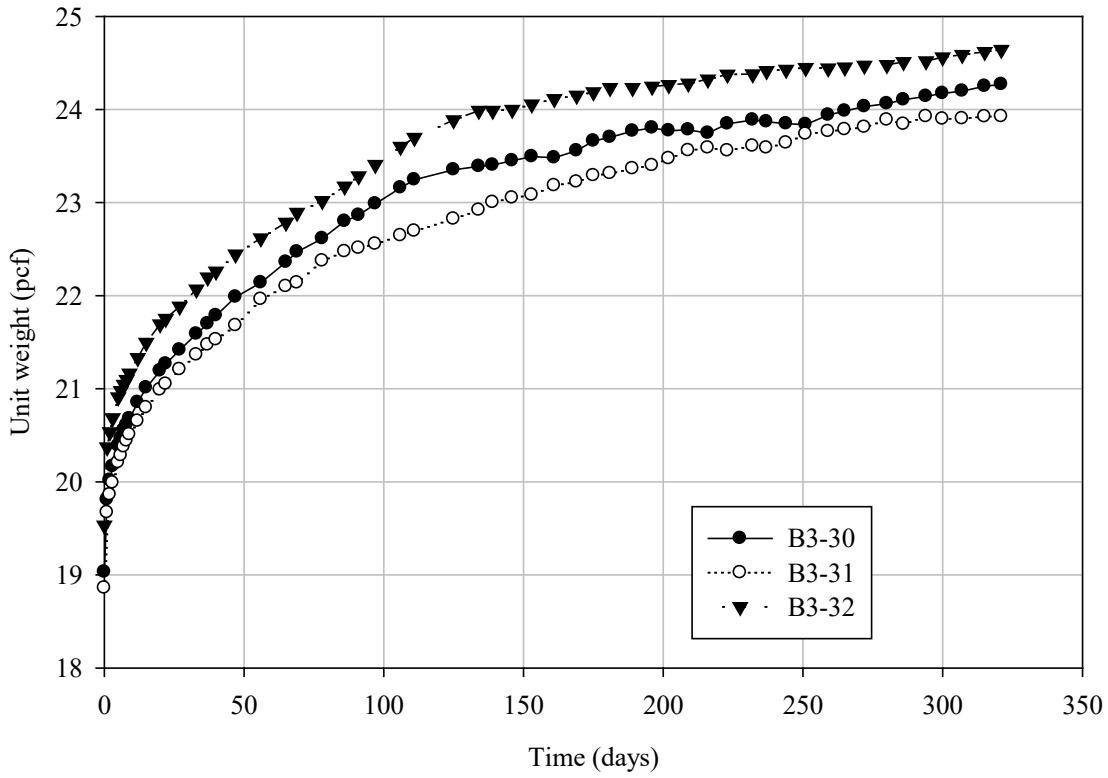

Figure 18. Plot of the total unit weight data as a function of time from the long-term saturation test.

Nonlinear Regression Model

As observed in Figure 17, the degree of saturation rapidly increases when exposed to the high humidity environment, then tapers to a gradual asymptote. The data resembles both hyperbolic and exponential curves, which were further explored.

Nonlinear regressions were performed using SigmaPlot version 11.0.0.77. The nonlinear regression method assumes the population is normally distributed about the mean regression function, the variance of the dependent variable is constant, and the resulting residuals are independent of each other (i.e., not correlated). Several hyperbolic and exponential forms were regressed through an iterative process with a 95% confidence interval $\alpha = 0.05$ that regression coefficients are statistically significant (i.e., are not zero). The form given in Equation 9 provided the best fit and has p-values. A *p*-value of 0.05 or greater signifies that the given regression coefficient has a 95% or greater probability of being non-zero.

$$S(\%) = a(1 - e^{-b \cdot x}) + c(1 - e^{-d \cdot x}) \qquad 9$$

Summaries of the regression results with the associated coefficients and *p*-values are found in Table 9. Plots of the fitted models from the regression for each test specimen are shown in Figure 19.

Based on the experimental data and reasonable extrapolation of the nonlinear regressions, we believe that under normal subsurface field conditions, LCC will have a minimum long-term degree of saturation of approximately 9%. Since LCC is often used as a lightweight fill for settlement mitigation, this total unit weight effect should be accounted for in the increase in total stress (i.e., $\Delta\sigma$ calculations) of the embankment fill.

Table 9. Summary of the nonlinear regression statistics for the long-term saturation model (Equation 9) for the data shown in Figure 19.

Model parameter	Regression value	*p*-value	*p*-value acceptance criterion
a	2.3739	<0.0001	$<\alpha$
b	0.6039	<0.0001	$<\alpha$
c	6.9349	<0.0001	$<\alpha$
d	0.0111	<0.0001	$<\alpha$
R^2	0.9978		
ANOVA		<0.0001	$<\alpha$
Normality		0.2188	$>\alpha$

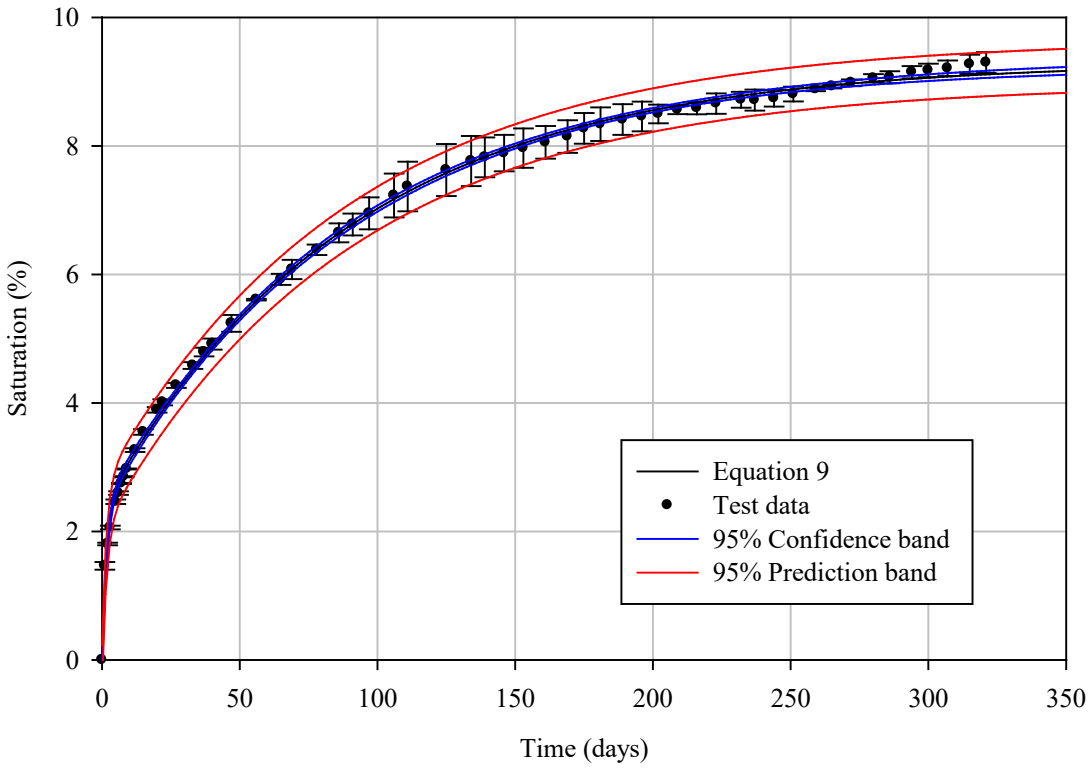

Figure 19. Plot of the long-term degree of saturation regression model (Equation 9) for B3-30, B3-31, and B3-32 with confidence and prediction bands.

CT Imaging of Partially Saturated LCC

As previously noted, computed tomography (CT) imaging was used to gain insight into pore water distribution at various degrees of saturation. The identical specimens discussed in Chapter 2, B1-23, B1-24, and B3-24, were subjected to the AD, M5, and D1 treatments and imaged with the Zeiss Xradia 620 Versa micro-CT scanner. The specimens were oven-dried after CT scanning before the subsequent saturation treatment was applied. One additional and final saturation treatment produced higher saturation than the W1 treatment. This extra treatment, V8, was performed by submerging the specimens in water with a high-vacuum applied for about 8 hours. This treatment produced the highest degree of saturation of all the treatments in the study, averaging 30.2% saturation. The resulting degrees of saturation for the CT scan test program are summarized in Table 10. The CT scan images for the center of specimen B1-23 are shown in Figure 20, Figure 21, Figure 22, and Figure 23. The CT scan images for the center of specimen B1-24 are shown in Figure 24, Figure 25, Figure 26, and Figure 27. Finally, the CT scan images for the center of specimen B3-24 are shown in Figure 28, Figure 29, Figure 30, and Figure 31. Additional images for each specimen located 0.778" above and below the center of the specimen (image 0243 and 0729, respectively) are shown in Appendix B.

Table 10. Summary of the resulting degrees of saturation, in percent, of the specimens undergoing CT scans.

Specimen	AD	M5	D1	V8
B1-23	1.609	10.05	16.86	35.37
B1-24	1.773	9.99	16.35	24.67
B3-24	1.675	10.80	16.43	30.61

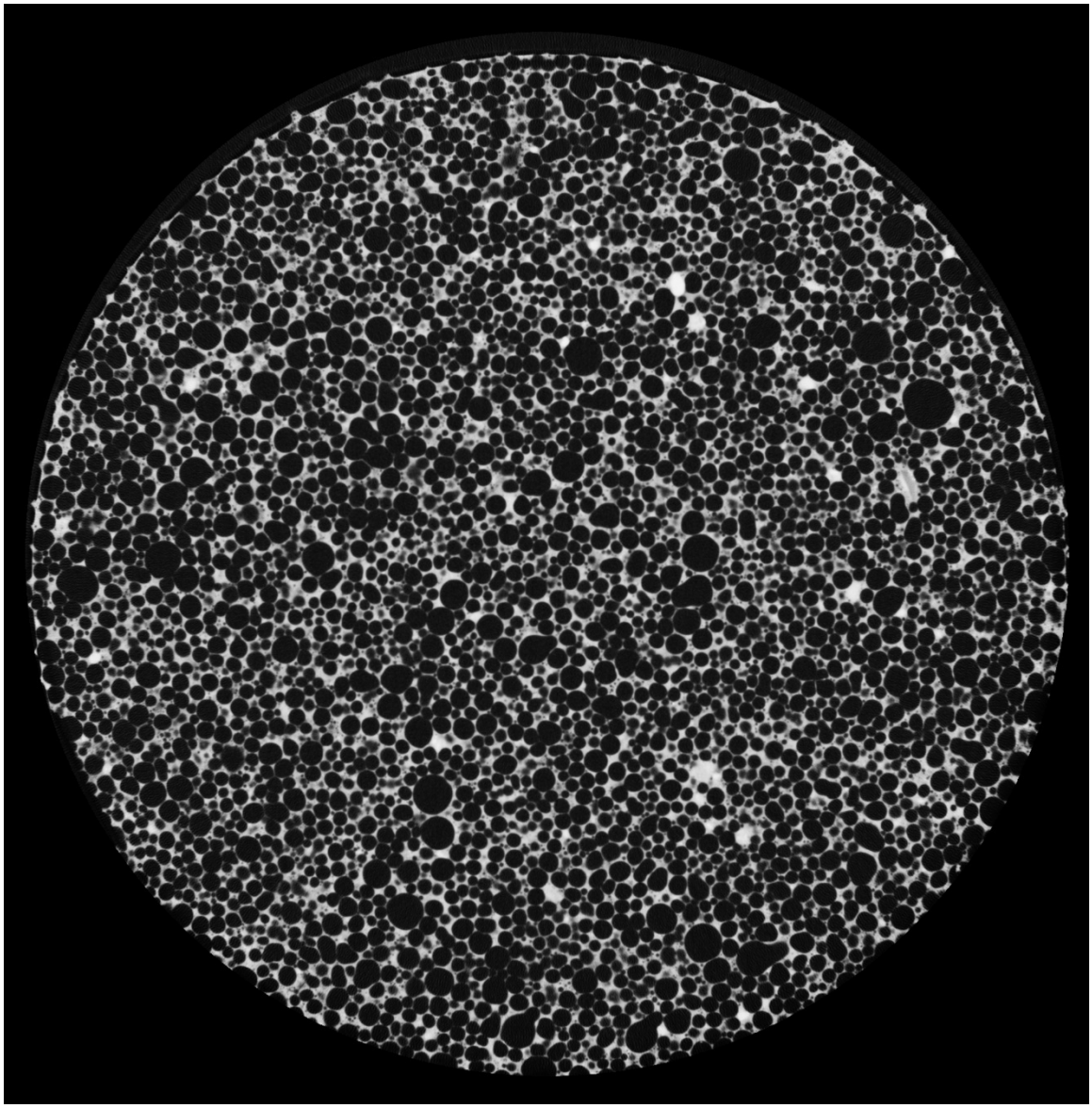

Figure 20. CT scan image of specimen B1-23 after the AD treatment.

B1-23 CT image cross-section for the air-dried state near the center of the specimen. The dark spherical objects are the foamed air voids with the light matrix being the concrete skeleton structure. The degree of saturation is 1.61%. No pore water is discernable from the image.

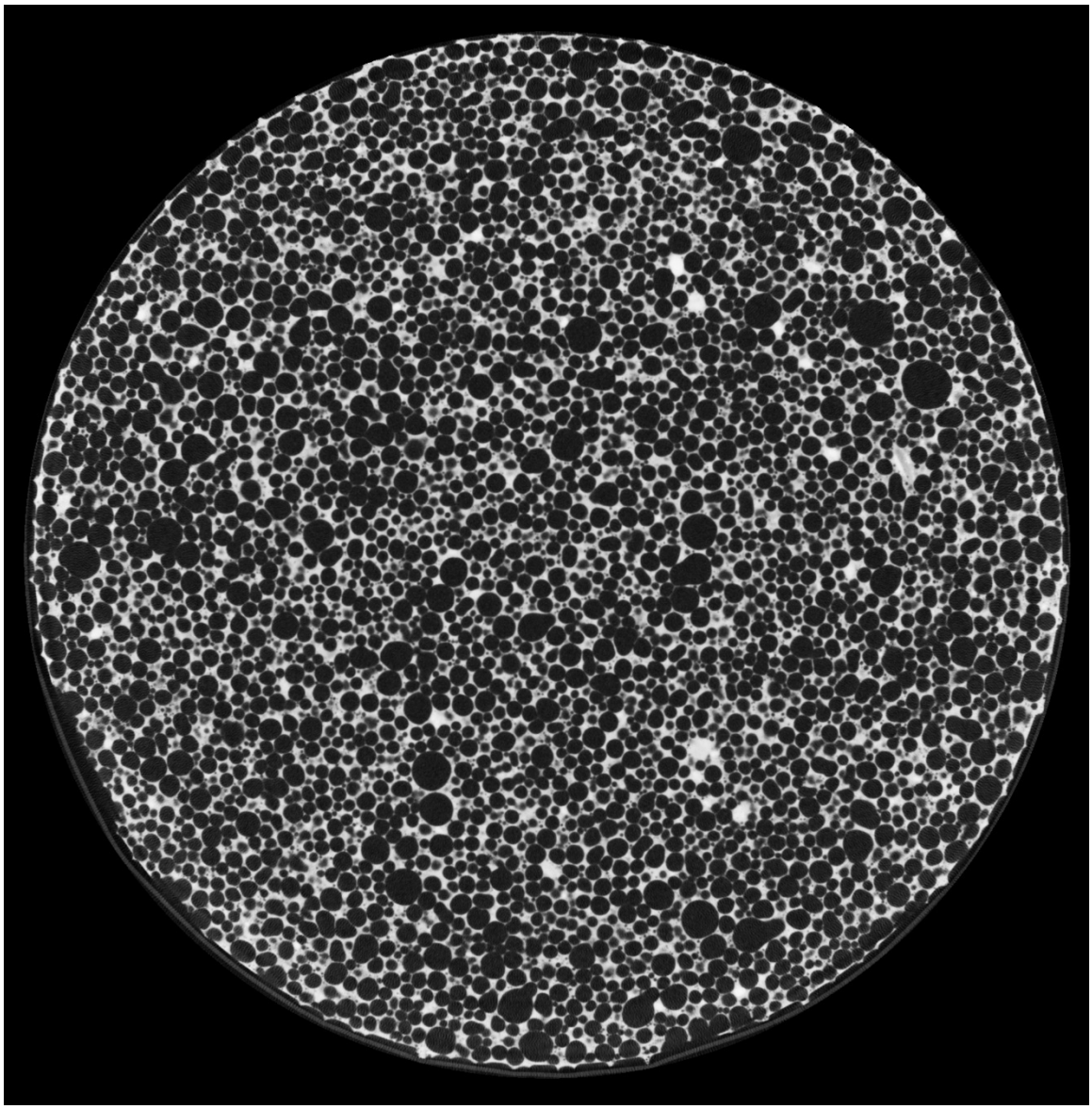

Figure 21. CT scan image of specimen B1-23 after the M5 treatment.

B1-23 CT image cross-section after the M5 treatment near the center of the specimen. The dark spherical objects are the foamed air voids with the light matrix being the concrete skeleton structure. The degree of saturation is 10.05%. No pore water is discernable from the image.

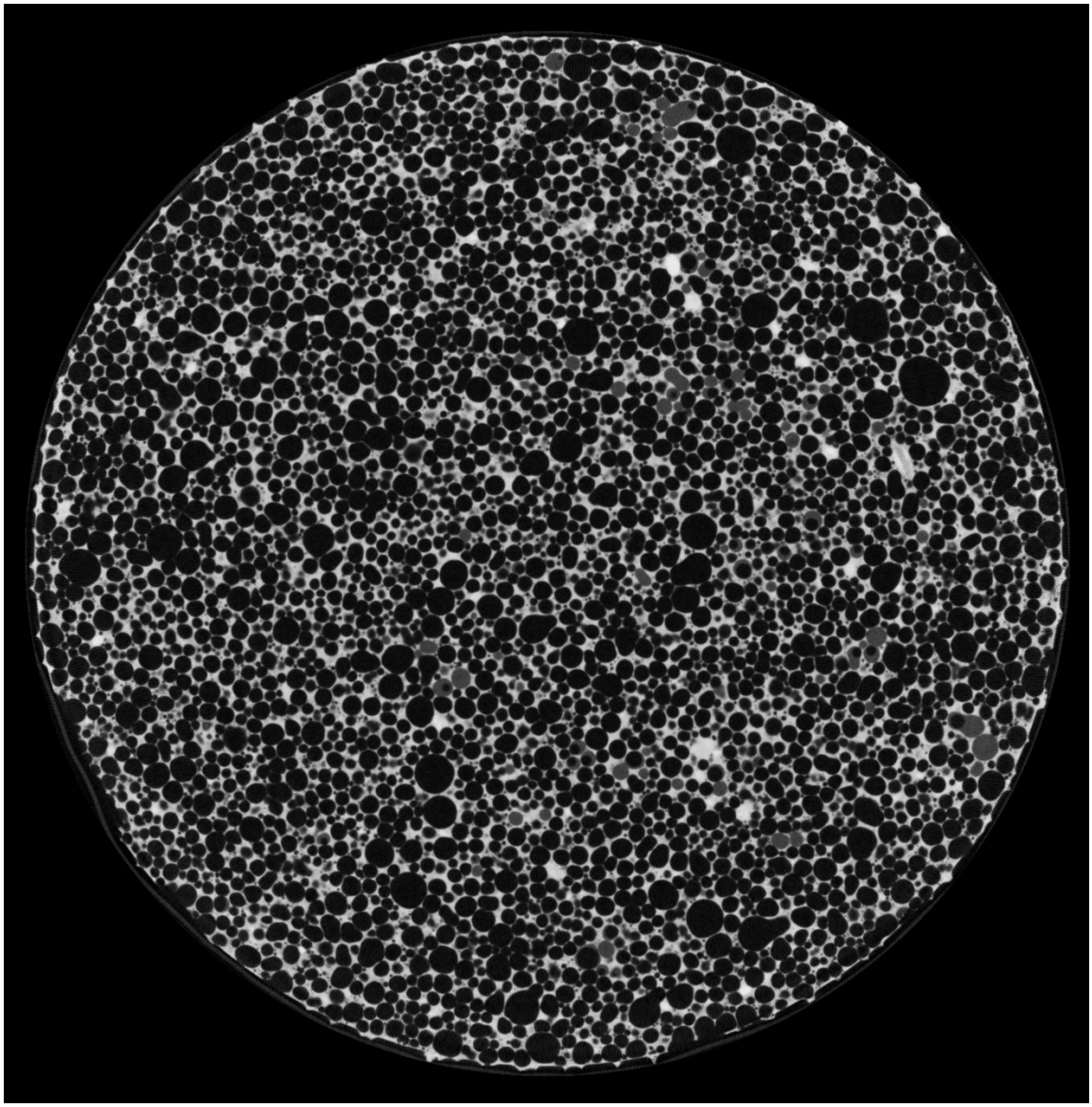

Figure 22. CT scan image of specimen B1-23 after the D1 treatment.

B1-23 CT image cross-section after the D1 treatment near the center of the specimen. The dark spherical objects are the foamed air voids with the light matrix being the concrete skeleton structure. The degree of saturation is 16.86%. Free pore water is visible in the image as grey spheres.

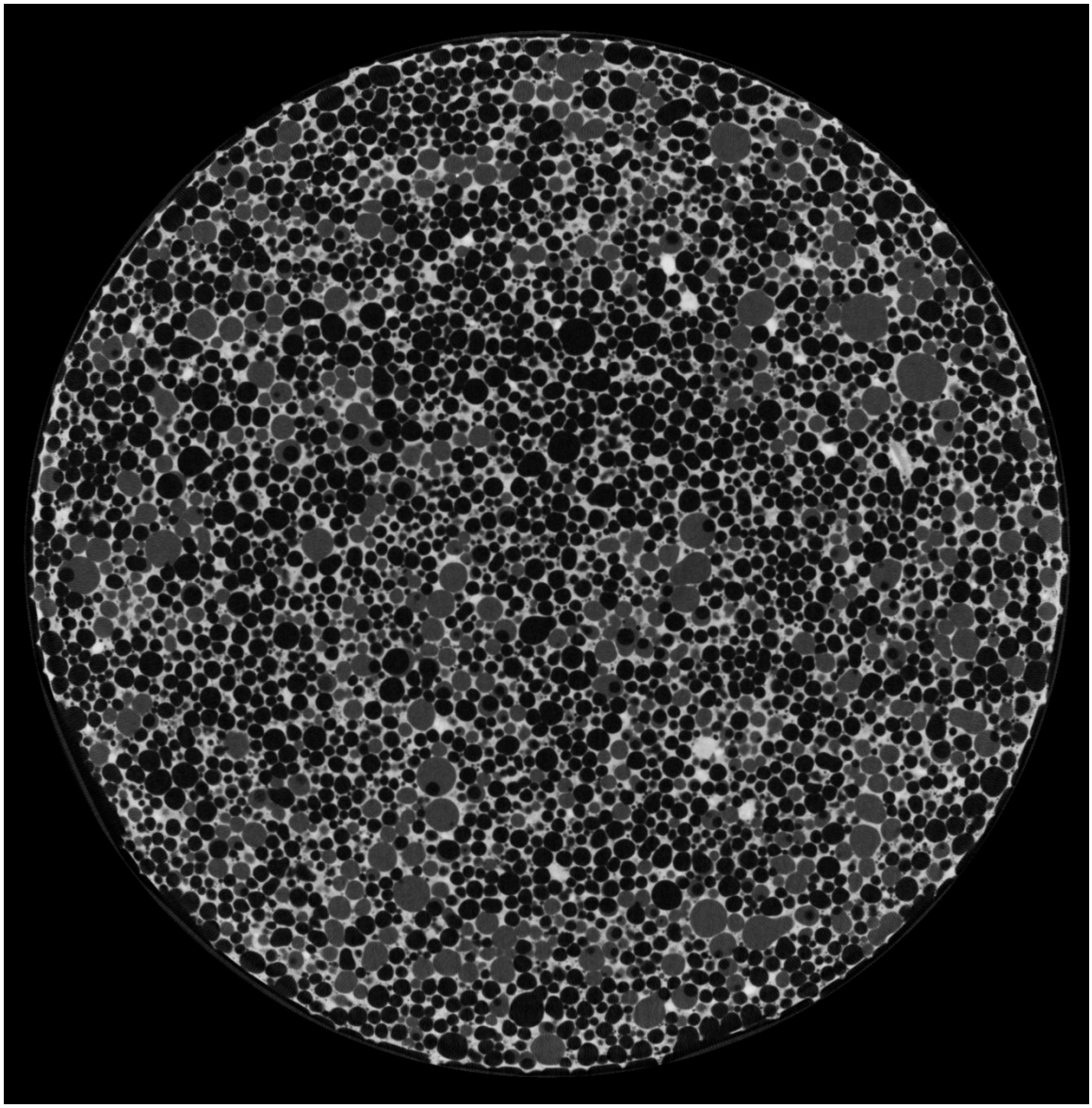

Figure 23. CT scan image of specimen B1-23 after the V8 treatment.

B1-23 CT image cross-section after the V8 treatment near the center of the specimen. The dark spherical objects are the foamed air voids with the light matrix being the concrete skeleton structure. The degree of saturation is 35.37%. Free pore water is visible in the image as grey spheres.

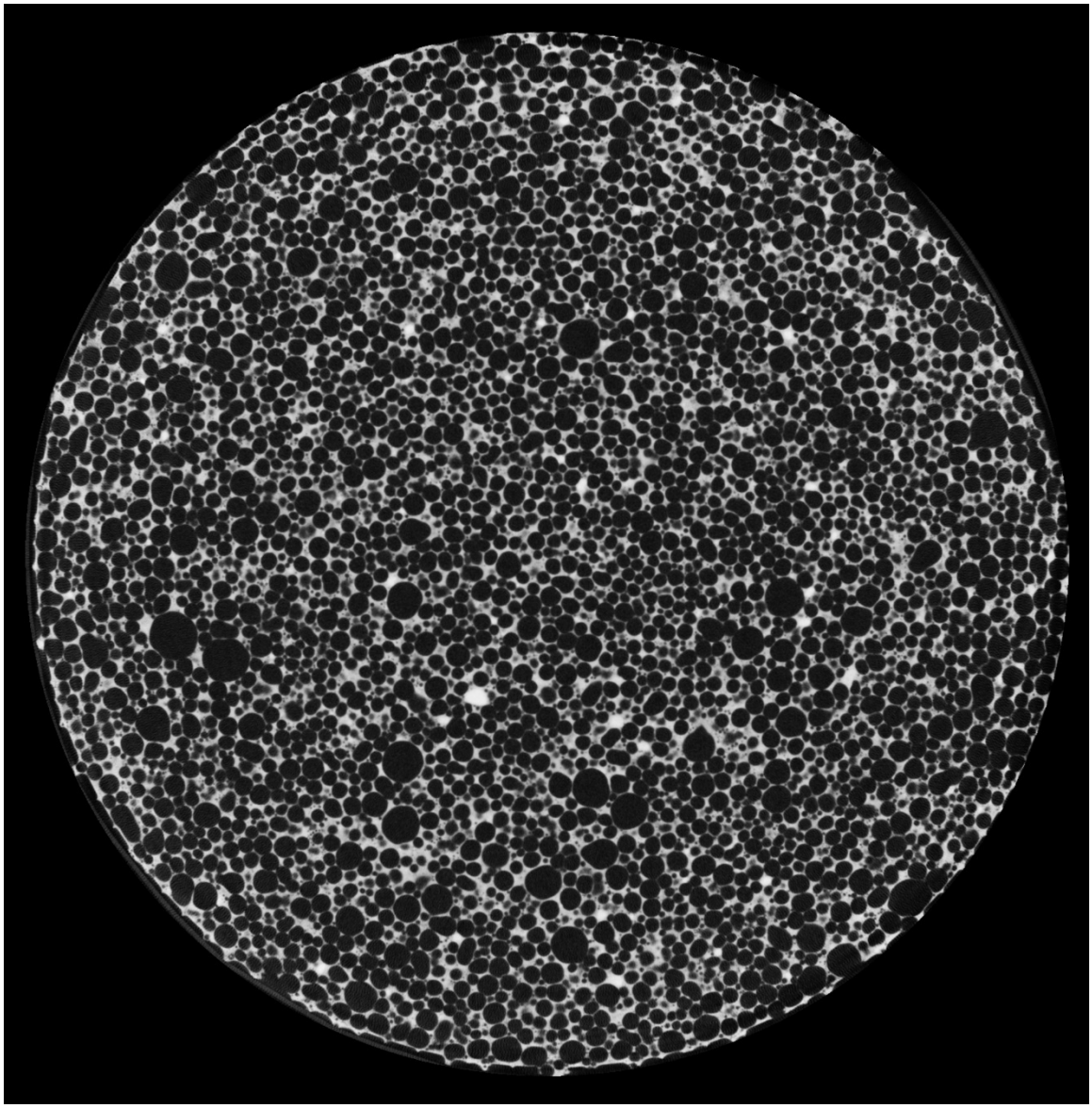

Figure 24. CT scan image of specimen B1-24 after the AD treatment.

B1-24 CT image cross-section for the air-dried state near the center of the specimen. The dark spherical objects are the foamed air voids with the light matrix being the concrete skeleton structure. The degree of saturation is 1.77%. No pore water is discernable from the image.

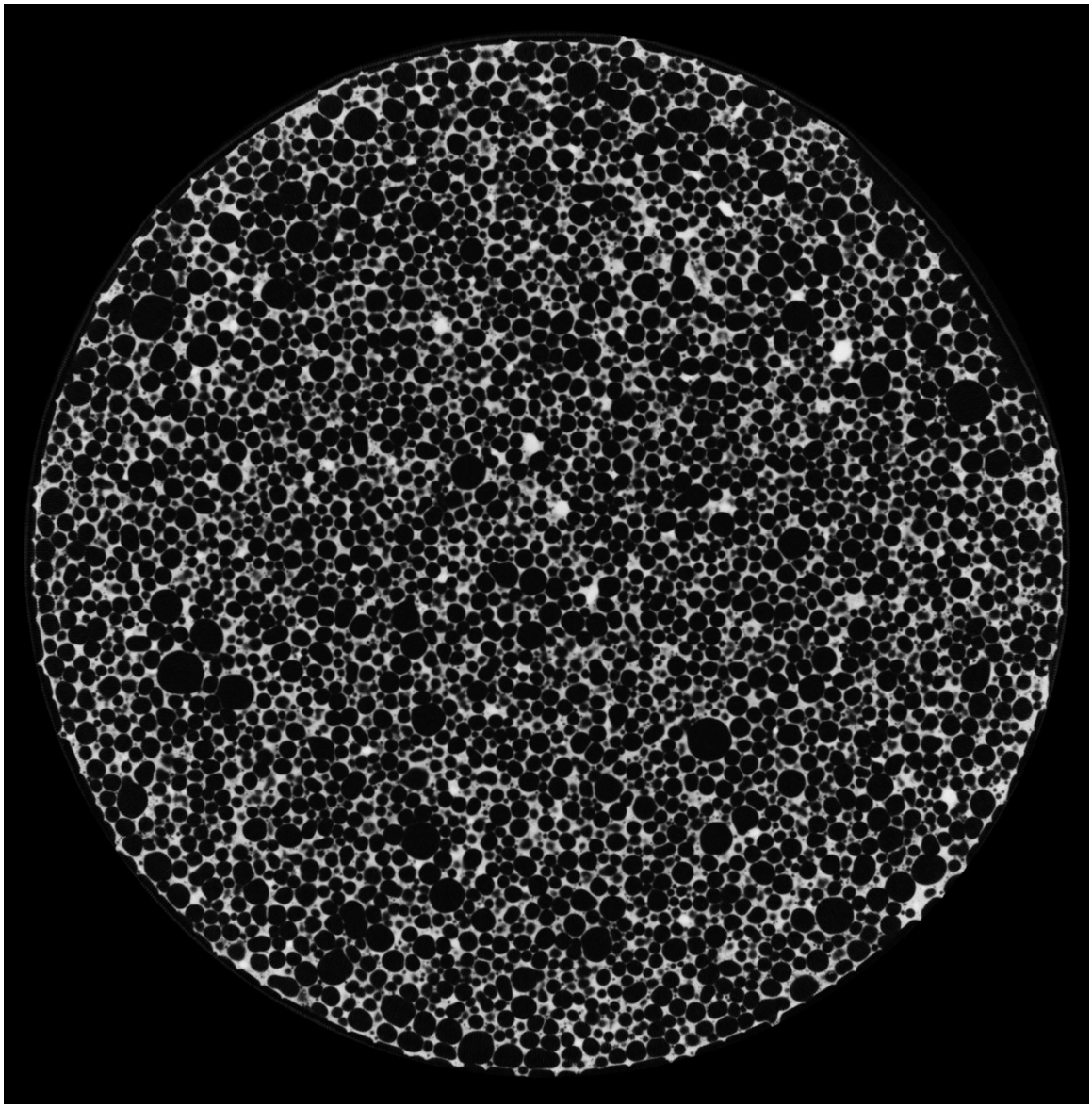

Figure 25. CT scan image of specimen B1-24 after the M5 treatment.

B1-24 CT image cross-section after the M5 treatment near the center of the specimen. The dark spherical objects are the foamed air voids with the light matrix being the concrete skeleton structure. The degree of saturation is 9.99%. No pore water is discernable from the image.

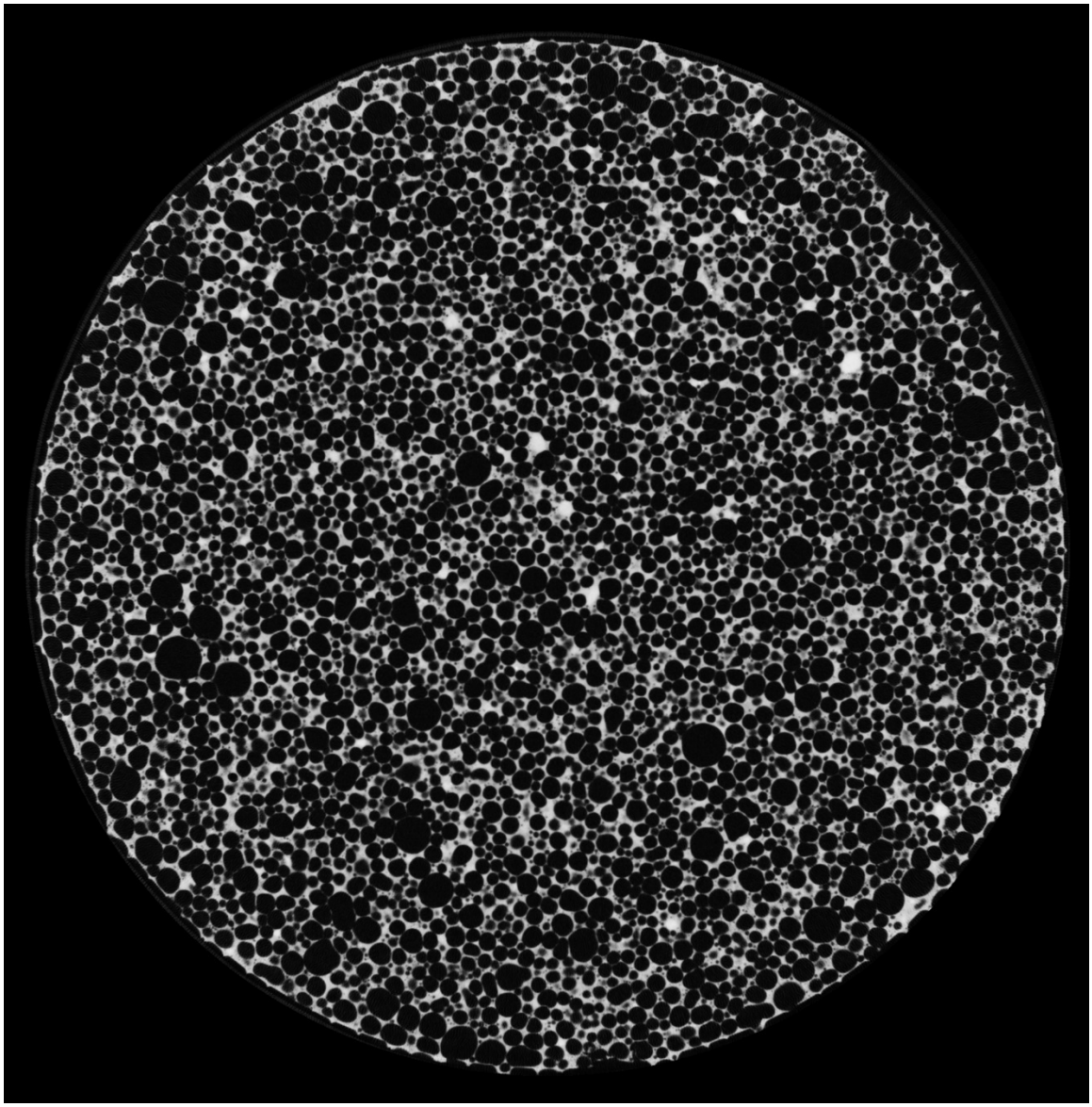

Figure 26. CT scan image of specimen B1-24 after the D1 treatment.

B1-24 CT image cross-section after the D1 treatment near the center of the specimen. The dark spherical objects are the foamed air voids with the light matrix being the concrete skeleton structure. The degree of saturation is 16.35%. No pore water is discernable from the image.

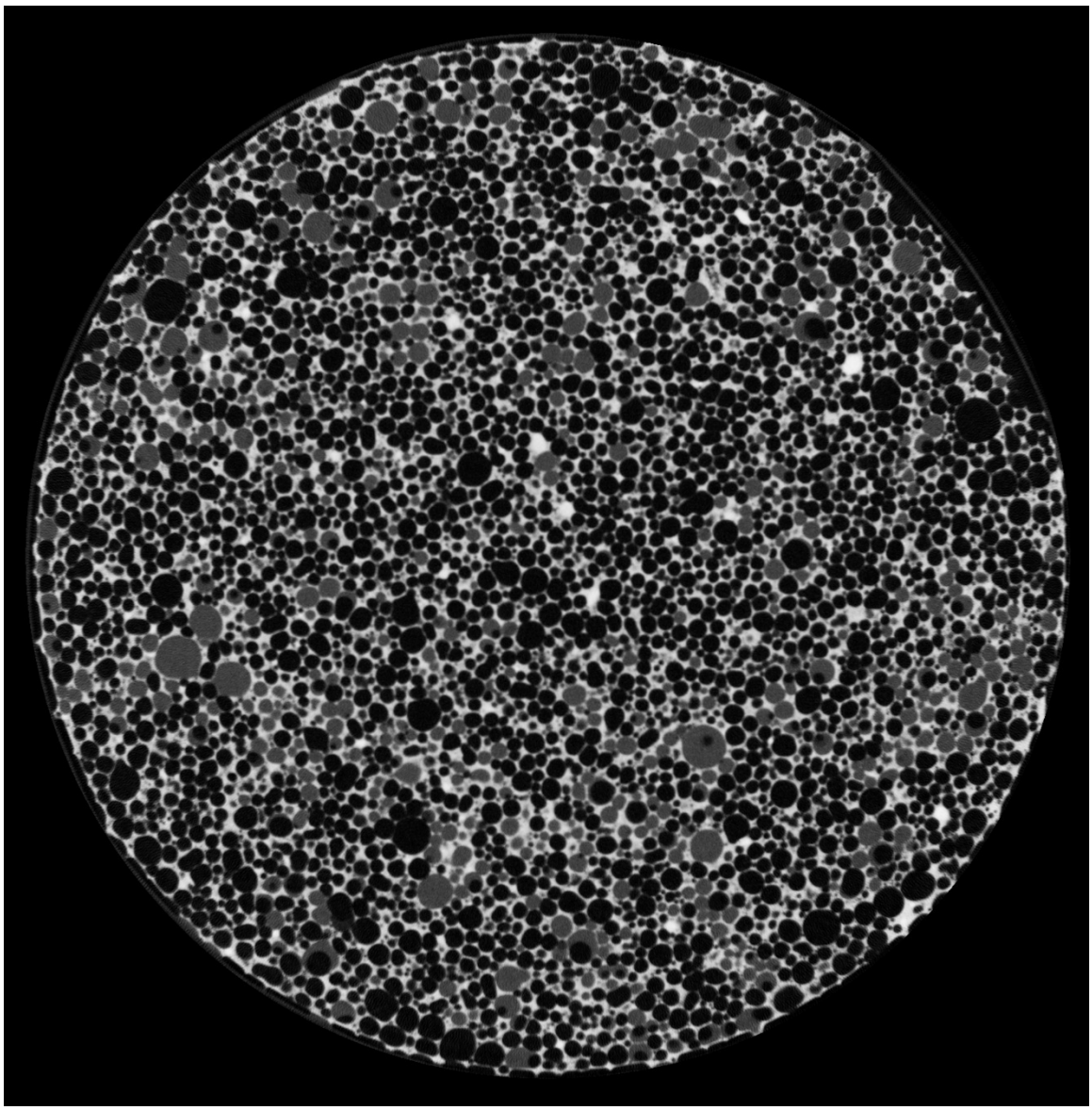

Figure 27. CT scan image of specimen B1-24 after the V8 treatment.

B1-24 CT image cross-section after the V8 treatment near the center of the specimen. The dark spherical objects are the foamed air voids with the light matrix being the concrete skeleton structure. The degree of saturation is 24.67%. Free pore water is visible in the image as grey spheres.

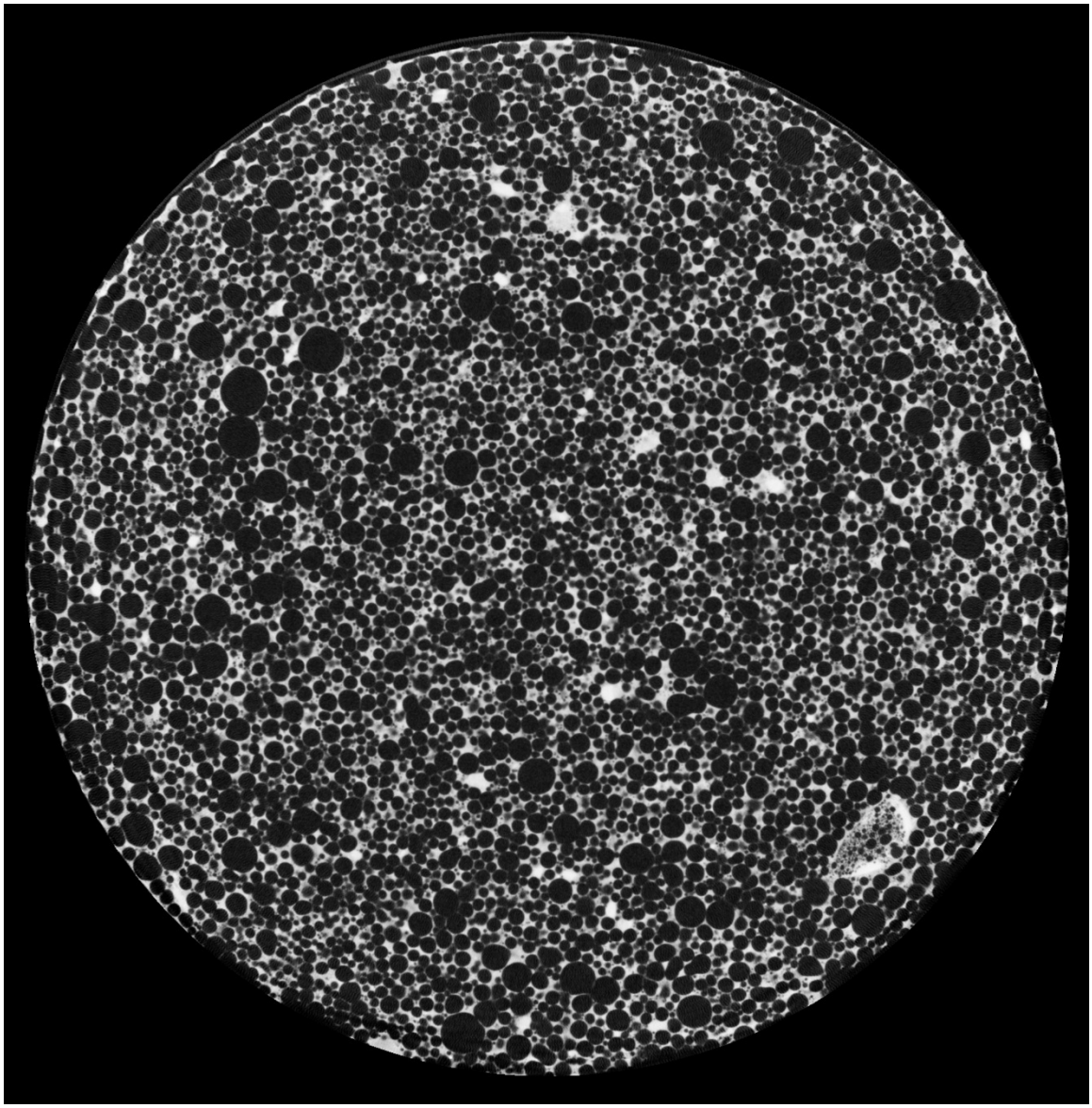

Figure 28. CT scan image of specimen B3-24 after the AD treatment.

B3-24 CT image cross-section for the air-dried state near the center of the specimen. The dark spherical objects are the foamed air voids with the light matrix being the concrete skeleton structure. The degree of saturation is 1.67%. No pore water is discernable from the image.

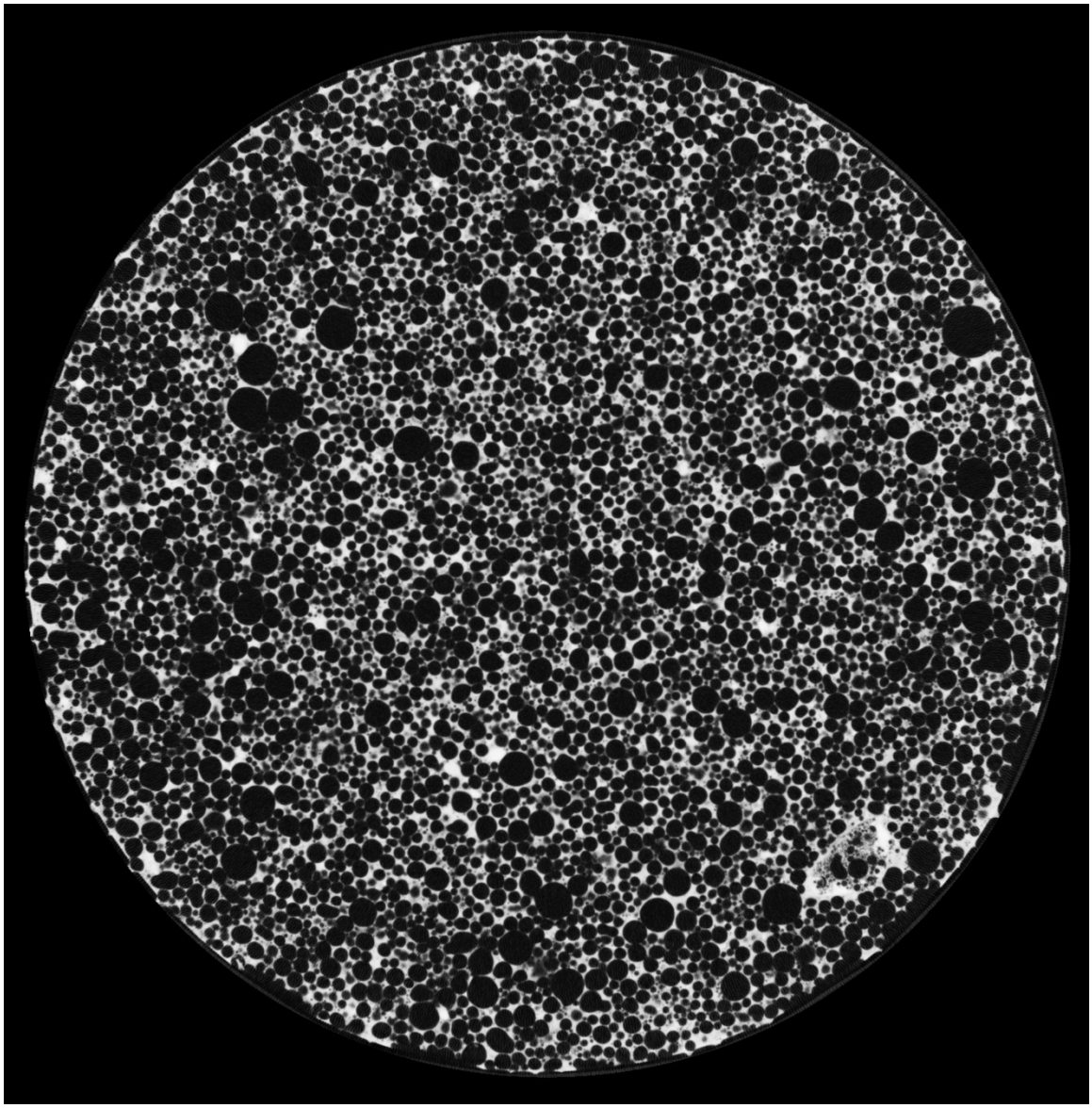

Figure 29. CT scan image of specimen B3-24 after the M5 treatment.

B3-24 CT image cross-section after the M5 treatment near the center of the specimen. The dark spherical objects are the foamed air voids with the light matrix being the concrete skeleton structure. The degree of saturation is 10.80%. No pore water is discernable from the image.

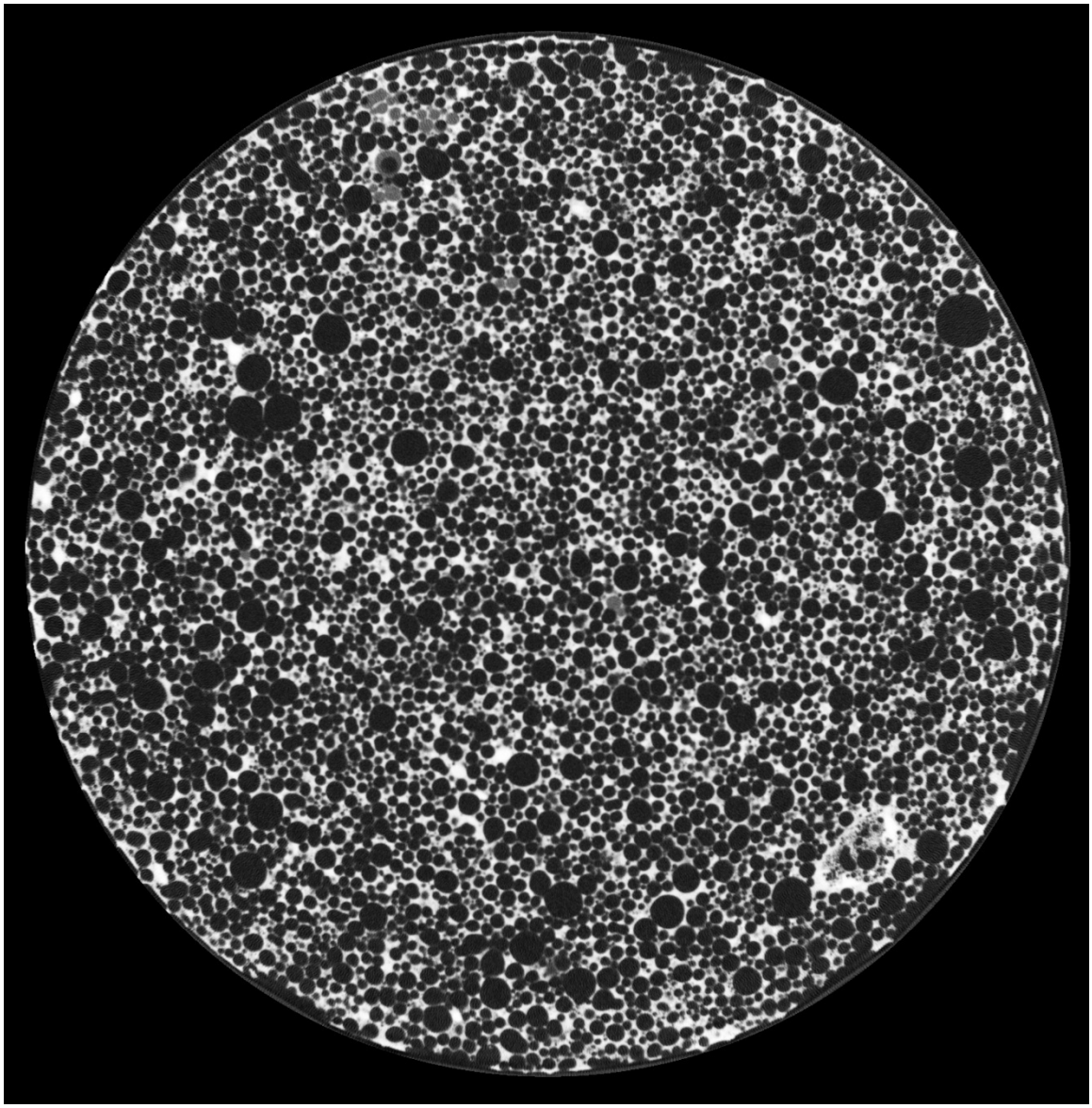

Figure 30. CT scan image of specimen B3-24 after the D1 treatment.

B3-24 CT image cross-section after the D1 treatment near the center of the specimen. The dark spherical objects are the foamed air voids with the light matrix being the concrete skeleton structure. The degree of saturation is 16.43%. Free pore water is visible in the image as grey spheres.

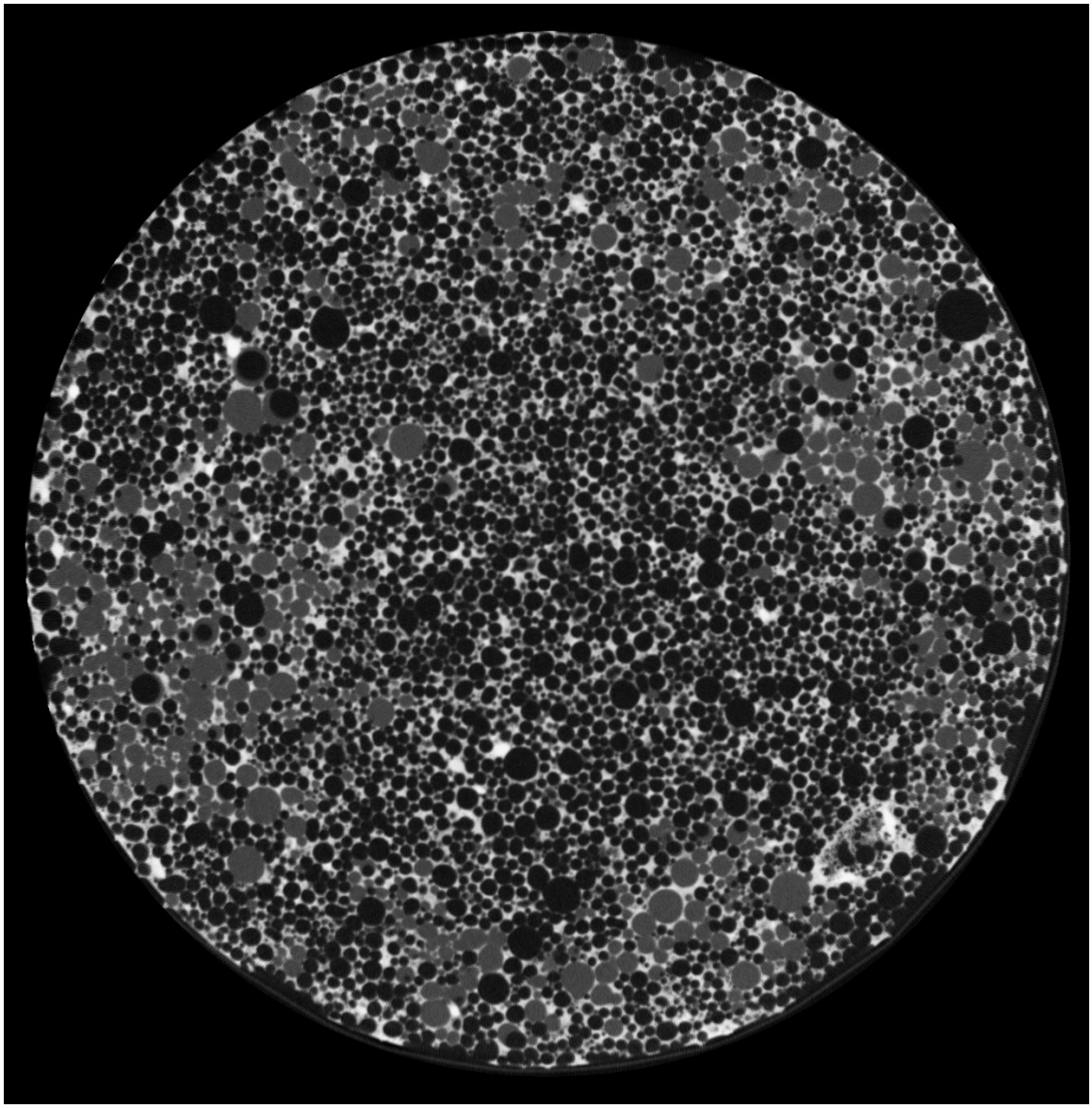

Figure 31. CT scan image of specimen B3-24 after the V8 treatment.

B3-24 CT image cross-section after the V8 treatment near the center of the specimen. The dark spherical objects are the foamed air voids with the light matrix being the concrete skeleton structure. The degree of saturation is 30.61%. Free pore water is visible in the image as grey spheres.

As seen in the images shown in Figure 20 through Figure 30, free water is not observable in the voids of the specimens for up to about 11% saturation. Free water was not observed in one specimen up to 16.4% while free water was observed in two of the specimens above 16.4% saturation. Free water was observed in all specimens above 25% saturation. We can conclude from these data that the pore water carrying capacity is exceeded in the matrix and micro-pores around 16.4% saturation. For partially saturated states below 16.4%, the pore water is distributed through the matrix and micro-pores and is likely transported through advective matric suction and diffusion.

Where free pore water is observable (above 16.4% saturation) the distribution of the water is observed to be randomly dispersed or clustered around large groups of voids. Viewing the CT slices in sequence allows one to gain insight into the pathways of the water in the specimen. The free water is rarely isolated and flow paths can be roughly traced from void to void. This observation gives visualization of the mechanisms of fluid flow in the highly saturated or fully saturated state.

CHAPTER 4

HYDRAULIC CONDUCTIVITY

As discussed by Tiwari et al. (2017), further study of the fluid flow behavior of LCC is warranted. Also addressed by Tiwari et al. (2017) is a lack of knowledge regarding the behavior of the saturated hydraulic conductivity when the LCC is subjected to varying levels of effective confinement. Therefore, a saturated hydraulic conductivity test program was undertaken to explore further and answer these posed research questions.

Methods

Saturated hydraulic conductivity tests are typically performed in general accordance with ASTM D5084 (ASTM D18 Committee 2016a). Three test specimens from batches B1, B2, and B3 were prepared by cutting and surface-grinding the ends to an approximately three-inch finished length.

Previous research has shown that fluid flow bypass may occur between the specimen and the latex membrane when test specimens have a rough or porous surface on the circumference (Seely et al. 2014). LCC exhibits a rough, circumferential surface and has the potential to have a porous structure depending on the amount of adhesion between the cement and the Styrofoam mold during the curing process. This previous experience

led to a sidewall treatment to minimize or preclude fluid flow bypass. The specimen sidewall was treated with a thin paste of hydrated CETCO Super Gel-X bentonite (Figure 32) before the specimen was placed in a latex membrane and in the triaxial cell for testing (Figure 33).

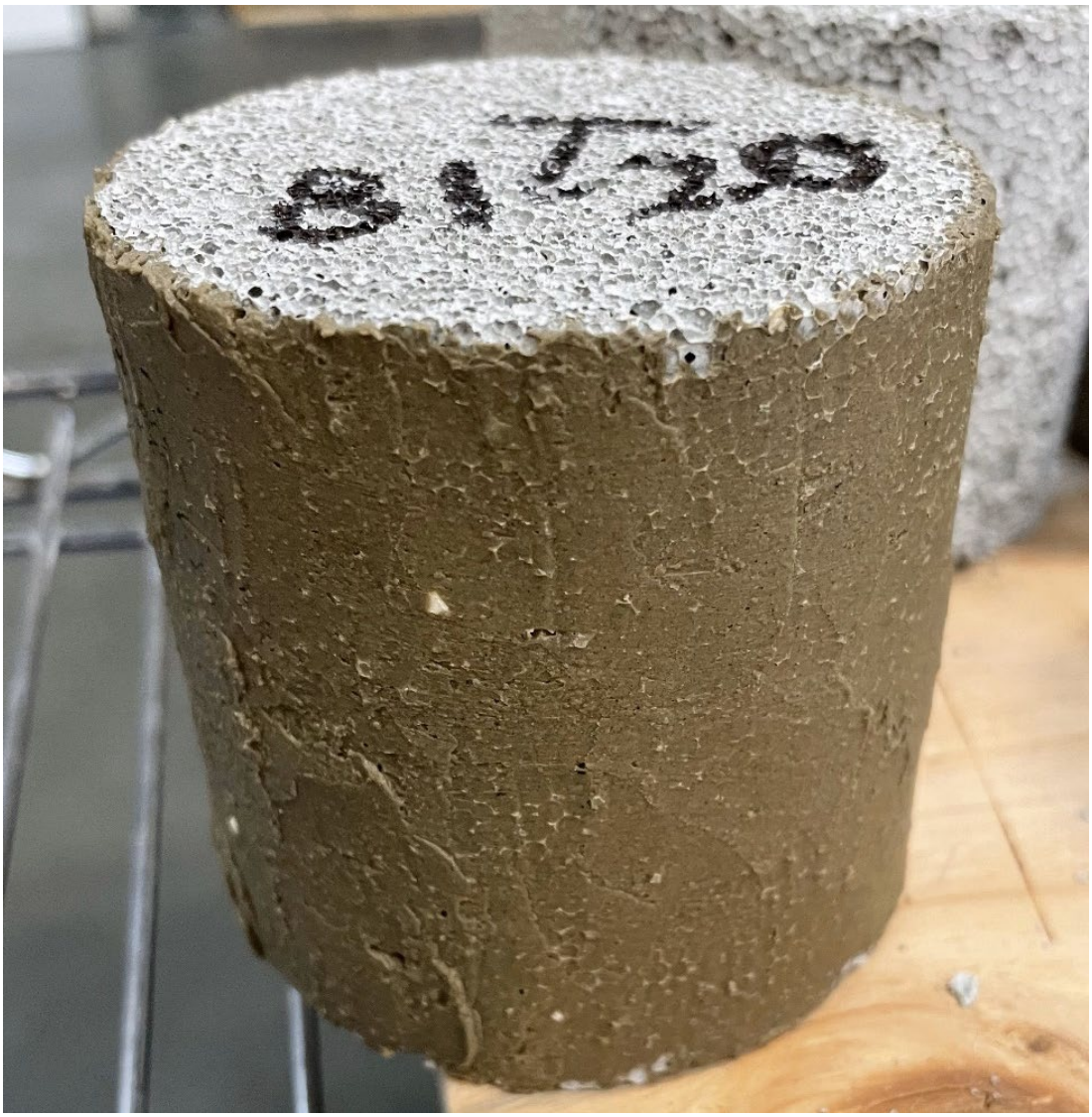

Figure 32. Photo of the LCC specimen with the bentonite gel sidewall treatment.

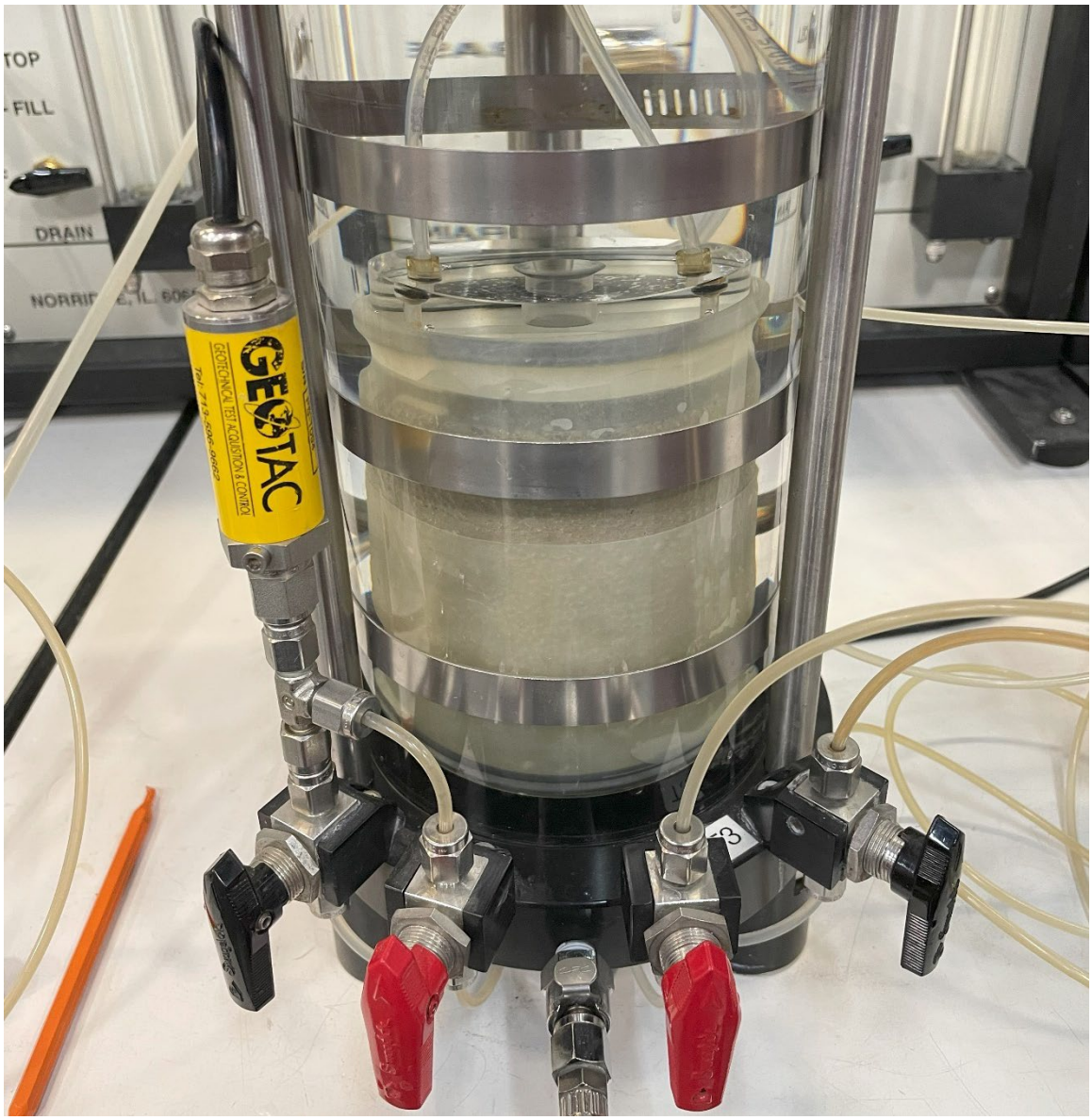

Figure 33. Photo of an LCC specimen in the hydraulic conductivity test cell.

After a curing age of 217 days, each test specimen was treated and placed in a latex membrane and then sealed on the top and bottom caps of the triaxial cell. The cell was filled with de-aired water, and a slight pressure head confinement was applied while monitoring for leaks. The specimen was then flooded with de-aired water from the bottom up until the water was seen percolating from the top of the specimen. A minor amount of effective confining stress was maintained while systematically increasing the pore pressure to saturate the test specimen. This method of saturation, typically termed back-pressure saturation, follows Boyle's law, which describes the relationship between the pressure and volume of a gas, ultimately pushing the gas within the specimen into solution of the pore water. As the pore pressure and confinement were incrementally increased, the Skempton's B-value was computed in an undrained condition,

$$B = \frac{\Delta u}{\Delta \sigma_3} \tag{10}$$

where Δu is the undrained change in pore pressure when subjected to $\Delta \sigma_3$ (i.e., the change in the minor principal stress or confining stress). A B-value of 0.95 is commonly accepted as a point at which the test specimen was considered saturated. Upon reaching a B-value of 0.95 or greater, the effective confining stress was increased to the desired level of confinement. The volume of the cell and test specimen was monitored with time until consolidation was complete, and no perceptible volume change was observed in the system. A hydraulic gradient, i, is applied to the test specimen by increasing the head, Δh, at the bottom of the specimen with respect to the top of the specimen,

$$i = \frac{\Delta h}{l} \tag{11}$$

where l is the length of the specimen. The flow rate, q, is measured and recorded and the hydraulic conductivity, k, is estimated following Darcy's law,

$$q = k \cdot i \cdot A \qquad 12$$

where A is the specimen cross-sectional area. Since the apparatus used in this study employed a set of burettes and an air-over water pressure system, the falling-head, rising-tailwater hydraulic conductivity is calculated by,

$$k = \frac{a \cdot l}{2 \cdot A \cdot \Delta t} \cdot \ln\left(\frac{\Delta h_1}{\Delta h_2}\right) \qquad 13$$

where a is the cross-section area of the burettes, Δt is the change in time, $t_2 - t_1$, and Δh_1 and Δh_2 are the head losses across the specimen at t_1 and t_2, respectively. The temperature of the test system was noted at the time of the test.

The effective confining stress was increased to the subsequent prescribed pressure after obtaining multiple steady-state readings, followed by consolidation and permeability steps. This method of repeated testing with increasing pressure is termed a staged test.

Results

A summary of the hydraulic conductivity, corrected for fluid density and viscosity to 20° C, is shown in Table 11. The average hydraulic conductivity from the tests was 4.9×10^{-5} cm/sec, with a maximum of 1.0×10^{-4} cm/sec and a minimum of 9.6×10^{-6} cm/sec. These values fall within a range typically obtained for silts, karst, and reef limestones (Schwartz and Zhang 2003). On average, the test specimens exhibited a 0.04 orders-of-magnitude decrease in hydraulic conductivity per psi of effective confinement increase from 2.5 to 10 psi. The lowest effect from confinement increase was about 0.01 of an

order of magnitude. The highest effect from confinement increase was about 0.08 orders-of-magnitude decrease per psi of effective confinement increase. The results are shown in Figure 34.

Table 11. Summary of the hydraulic conductivity test results.
The hydraulic conductivity values are in cm/sec. The values in the table are corrected to 20° C based on the permeant fluid density and viscosity at the time of the test.

Test Specimen	Effective confining stress (psi) 2.5	5.0	7.5	10.0
B1-20	2.24E-05	1.74E-05	1.53E-05	1.48E-05
B1-21	5.26E-05	4.38E-05	3.95E-05	2.31E-05
B1-22	5.81E-05	5.14E-05	5.09E-05	4.88E-05
B2-20	2.00E-05	1.68E-05	1.33E-05	9.58E-06
B2-21	9.67E-05	9.17E-05	7.26E-05	7.18E-05
B2-22	8.94E-05	7.73E-05	6.71E-05	6.54E-05
B3-20	5.81E-05	4.22E-05	3.56E-05	3.45E-05
B3-21	1.04E-04	5.05E-05	4.09E-05	2.68E-05
B3-22	1.01E-04	6.13E-05	4.19E-05	2.52E-05

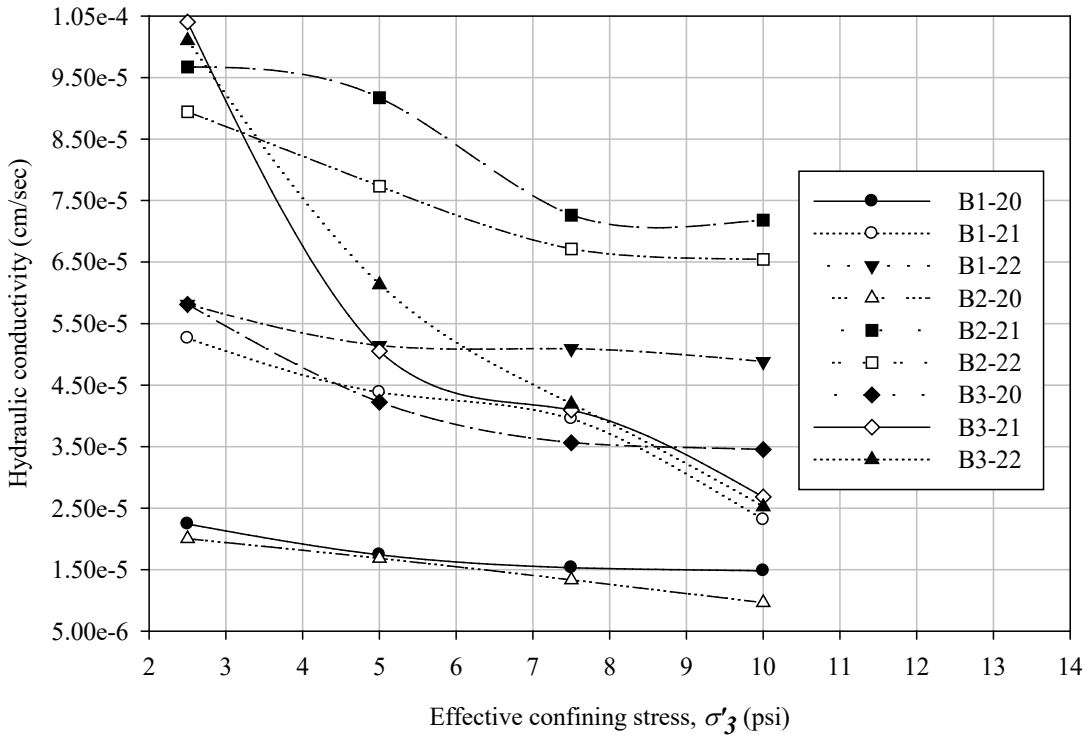

Figure 34. Plot of the hydraulic conductivity over a range of effective confining stresses.

Discussion

Although the hydraulic conductivity tests included Skempton's B-checks to confirm saturation, it does not guarantee 100% saturation during the test's permeability phase. As shown in Figure 23, Figure 27, and Figure 31, LCC exhibits occluded and continuous (interconnected) void spaces. The continuous void spaces that form upon casting or are later connected through microfractures formed through the curing process. Although the B-checks reflect near 100% saturation as pressure equilibrium likely occurs across the thin vesicle walls, the hydraulic conductivity is likely governed by advection flow through the interconnected void spaces and microfractures.

Tiwari et al. (2017) opine that the hydraulic conductivity of LCC is not affected by confinement, but this conclusion warrants further investigation. The data generated for this study indicates that confining pressure influences the hydraulic conductivity with an average of 0.04 orders-of-magnitude decrease in hydraulic conductivity per psi of effective confinement increase. In addition, we believe that the bentonite gel sidewall treatment employed aids in eliminating potential bypass flow and, therefore, potentially erroneous results. Also, increasing the confinement pressure likely affects the micro-fracture network within the LCC by decreasing the fracture openings and decreasing the effective hydraulic radii of some of the interconnected voids. Lastly, the hydraulic conductivity results reported by Tiwari et al. (2017) ranged from 1.7×10^{-4} cm/sec to 1.2×10^{-3} cm/sec, about an order of magnitude higher than values obtained by this study. It is presumed that sidewall bypass flow may explain this discrepancy. Because LCC is somewhat variable in its mechanical properties, some differences can be expected in test results. Nonetheless, we recommended that sidewall bypass treatment (bentonite gel, vacuum grease, or other) be employed when testing the hydraulic conductivity of LCC to reduce experimental variability.

CHAPTER 5

RESILIENT MODULUS

The resilient modulus (RM) estimates the modulus of elasticity of a material when subjected to rapid loading. The state of stress varies throughout the test and is designed to simulate the stress states when the pavement base and subbase materials experience traffic loads. The material's RM is used to estimate the structural layer coefficients or used directly in mechanistic-empirical pavement design. The test results of the resilient modulus, M_R, are typically fit to one or more of the following four equations (Von Quintus and Killingsworth 1998). (We note that the functional form of Equation 14 is a statistical fit of their data used for convenience and does not imply a mechanistic relationship.)

$$M_R = K_1 \cdot \sigma_B^{K_2} \tag{14}$$

$$M_R = K_3 \cdot \sigma_d^{K_4} \tag{15}$$

$$M_R = K_5 \cdot \sigma_d^{K_6} \cdot (1 + \sigma_3)^{K_7} \tag{16}$$

$$M_R = K_8 \cdot p_a \cdot \left(\frac{\sigma_B}{p_a}\right)^{K_9} \cdot \left(\frac{\sigma_d}{p_a}\right)^{K_{10}} \tag{17}$$

where K_1 through K_{10} are fitting parameters, σ_B is the bulk stress,

$$\sigma_B = (\sigma_d + \sigma_3) + 2 \cdot \sigma_3 \quad (18)$$

σ_d is the deviator stress,

$$\sigma_d = \sigma_1 - \sigma_3 \quad (19)$$

where p_a is one atmosphere, σ_1 is the major principal stress, and σ_3 is the major principal stress or confining stress.

A primary objective of this study was to estimate the possible range of values of the RM of LCC for engineering applications. To our knowledge, this information does not exist in the published literature. This information will improve the profession's understanding of LCC's long-term durability, contributing to its future implementation. Also, as part of this durability study, we will explore the possible effect(s) that water (as measured by saturation level) has on the RM.

A series of RM tests were performed to achieve these objectives. The series included test specimens treated with the saturation treatments discussed in Chapter 3 and aged in a humidified environment ranging from 1,051 to 1,077 days. This program included 12 specimens each from the AD, H100, M5, D1, and W1 saturation groups. Also, as discussed in Chapters 6 and 7, each specimen was tested without delay for uniaxial or triaxial compressive strength upon completing the RM testing. As such, this allowed a direct comparison of the test results measured in the low-strain, non-destructive RM tests and the high-strain, destructive compressive strength tests.

Methods

The RM test was performed per AASHTO T-307 (AASHTO Technical Subcommittee: 1a, Soil and Unbound Recycled Materials 2017). The tests were

performed on a calibrated GeoComp LoadTrac II load frame in conjunction with a three-phase stepper motor cyclic actuator and a Cyclic-RM Actuator Controller. The test specimen was placed in a triaxial cell and isolated with a latex rubber membrane, as described in Chapter 4, but without any sidewall treatment. The triaxial cell was placed and centered in a load frame, and the cell pressure was controlled by regulated compressed air through the Cyclic-RM Actuator Controller. The deviator stress was applied from the three-phase stepper motor cyclic actuator, which is also controlled by the Cyclic-RM Actuator Controller (see Figure 35). Displacement measurements are taken with two linear displacement transducers to compute the axial strain from the applied deviator stress. The deviator load is a haversine-shaped load pulse for 0.1 seconds followed by a 0.9-second rest period. The confining pressure and deviator stress was varied from an initial conditioning sequence, 0, followed by 15 additional test sequences, as summarized in Table 12. The test is performed in a drained condition with the sample valves vented to atmospheric pressure. The resilient modulus results, the applied cyclic stress divided by the axial strain, are reported as the average of the moduli resulting from the final five load pulses for each sequence 1 through 15.

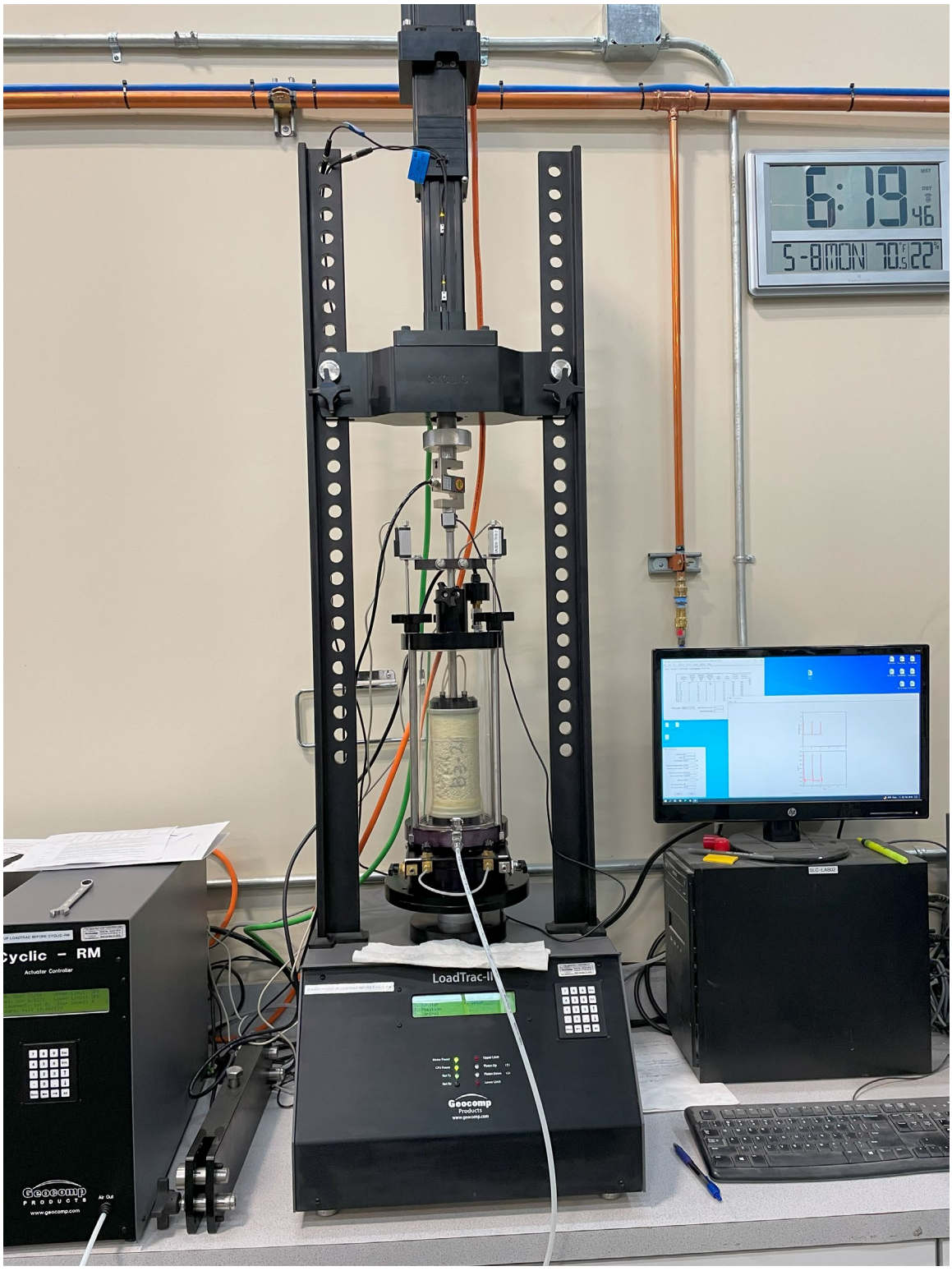

Figure 35. Photo of the resilient modulus testing apparatus.

Table 12. Resilient modulus testing sequence for base/subbase materials.

Sequence No.	Confining pressure (psi)	Max. axial stress (psi)	Cyclic stress (psi)	Constant stress (psi)	No. of load applications
0	15	15	13.5	1.5	500–1000
1	3	3	2.7	0.3	100
2	3	6	5.4	0.6	100
3	3	9	8.1	0.9	100
4	5	5	4.5	0.5	100
5	5	10	9.0	1.0	100
6	5	15	13.5	1.5	100
7	10	10	9.0	1.0	100
8	10	20	18.0	2.0	100
9	10	30	27.0	3.0	100
10	15	10	9.0	1.0	100
11	15	15	13.5	1.5	100
12	15	30	27.0	3.0	100
13	20	15	13.5	1.5	100
14	20	20	18.0	2.0	100
15	20	40	36.0	4.0	100

Results

The results from the RM of the LCC specimens as a function of the confining stress, as a function of the deviator stress as a function of the dry unit weight, as a function of the saturation, and as a function of the height-to-diameter ratio are shown in Figure 36, Figure 37, Figure 38, Figure 39, and Figure 40, respectively.

The average RM measured was 70,974 psi, with a maximum of 671,130 psi and a minimum of 19,123 psi. The complete test reports from each of the RM tests are attached in Appendix C, where the data for each test specimen is fit to Equation 14, Equation 15, Equation 16, and Equation 17.

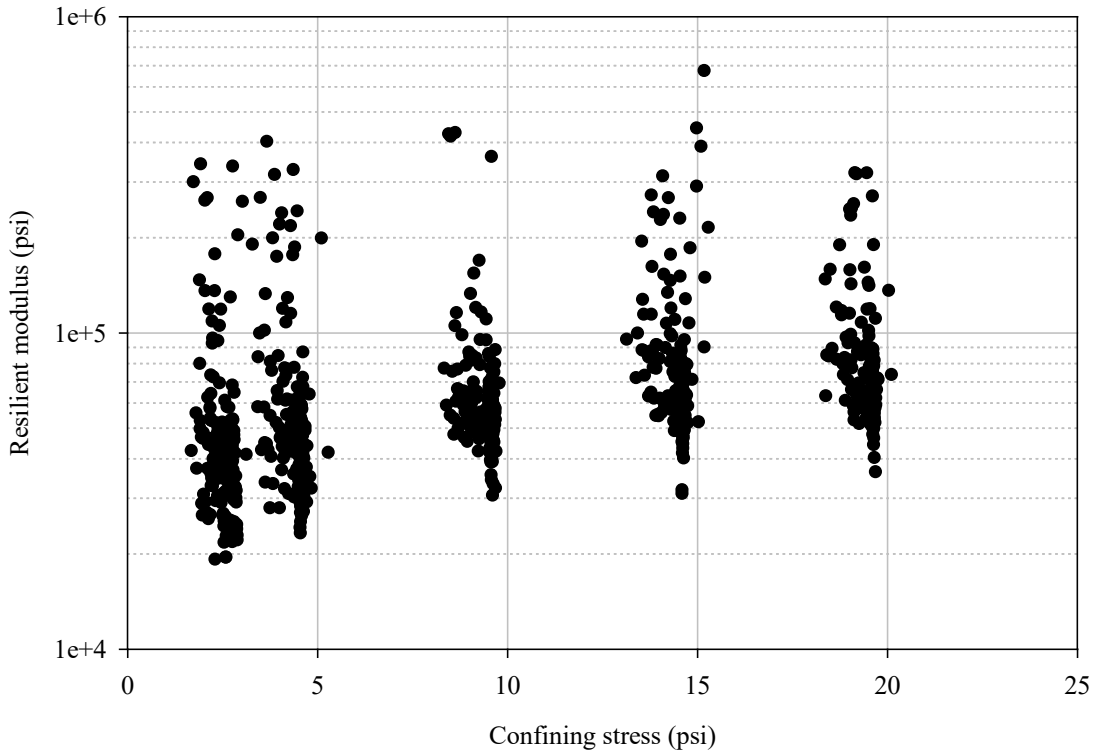

Figure 36. Plot of the resilient modulus of the LCC specimens as a function of confining stress.

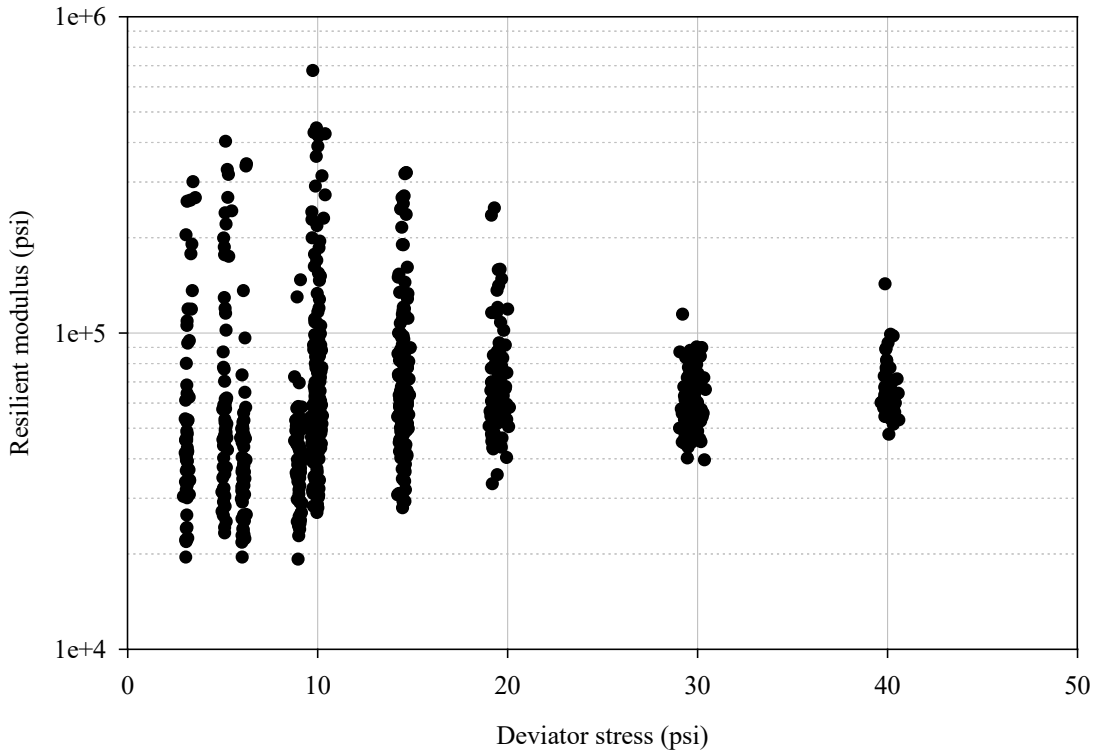

Figure 37. Plot of the resilient modulus of the LCC specimens as a function of the applied deviator stress.

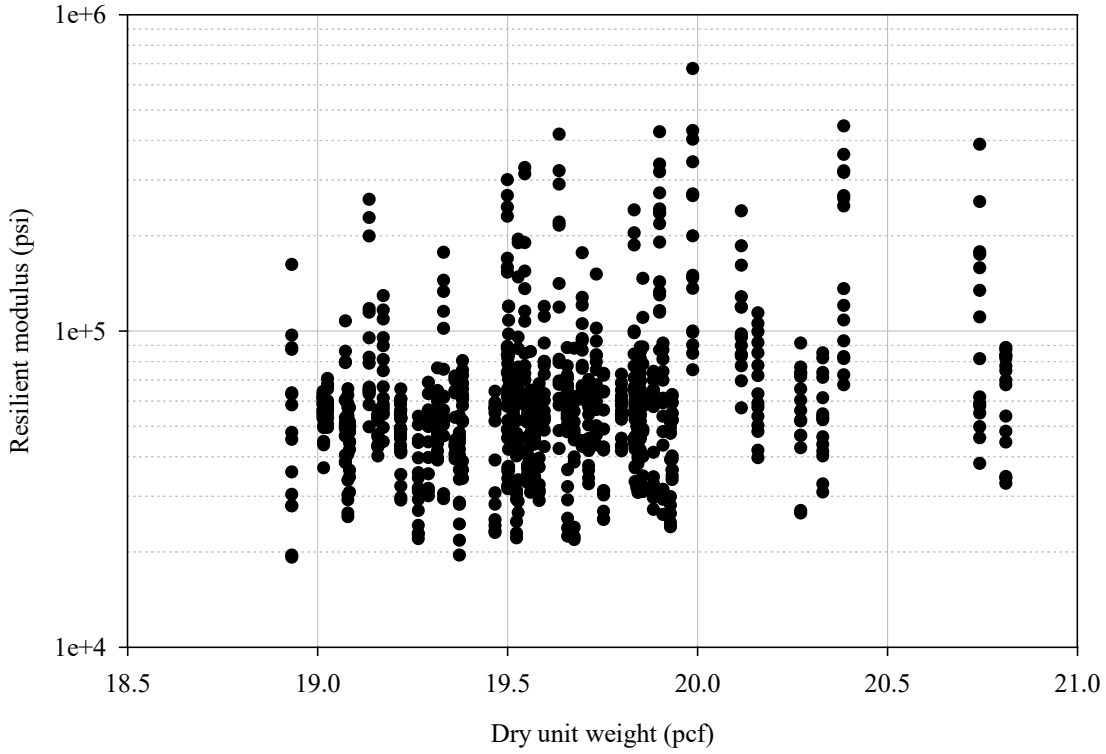

Figure 38. Plot of the resilient modulus of the LCC specimens as a function of the dry unit weight.

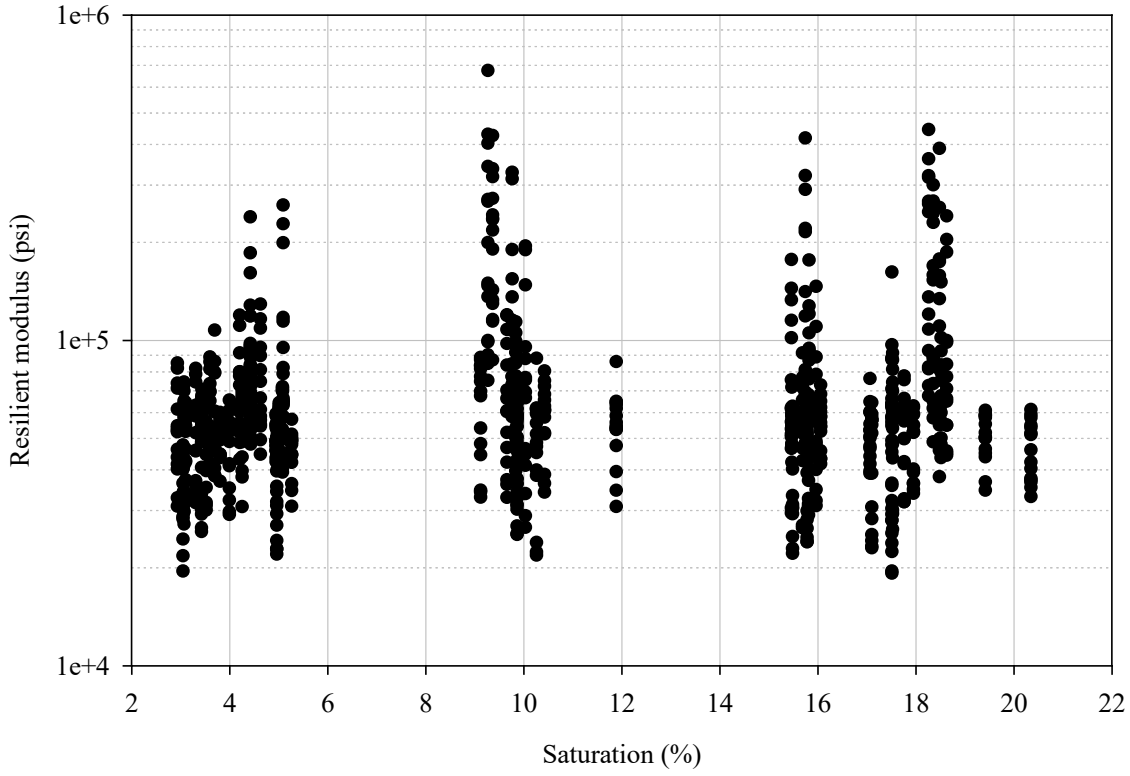

Figure 39. Plot of the resilient modulus of the LCC specimens as a function of saturation.

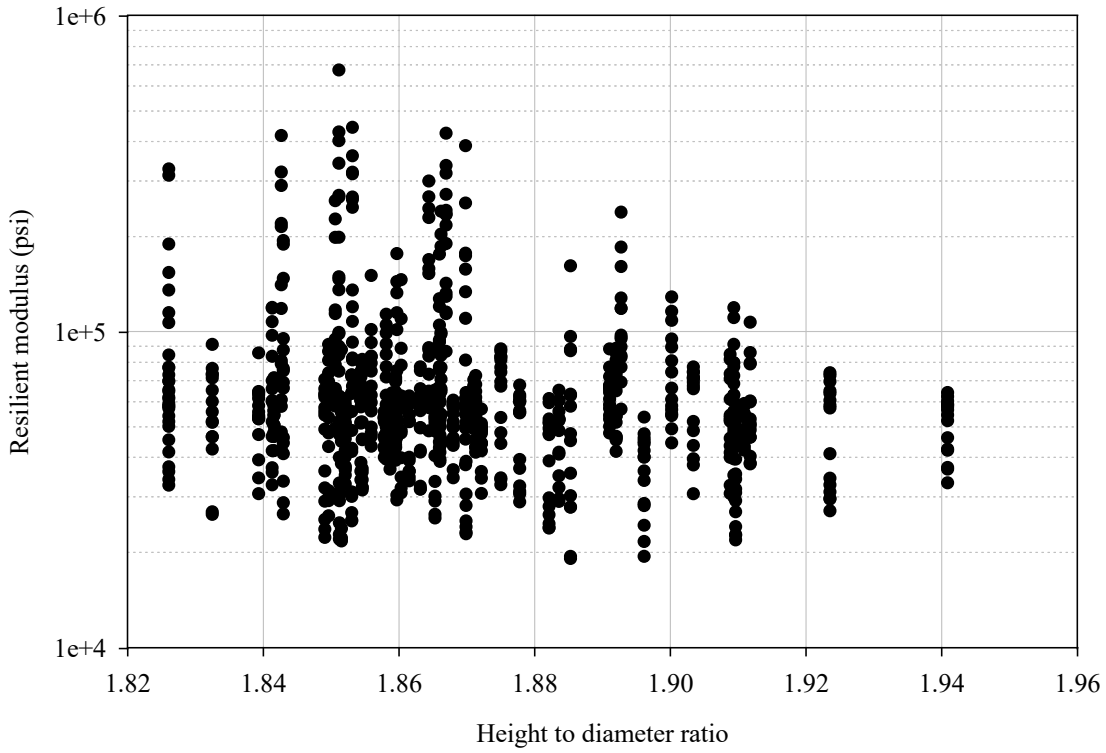

Figure 40. Plot of the resilient modulus of the LCC specimens as a function of the height-to-diameter ratio.

Discussion

The data shown in Figure 36 indicate an increase in measured RM with increased confining stress. This response is expected from a fundamental soil and rock mechanics perspective because confining stress increases the interparticle contact stress, thus increasing the material's stiffness.

The data shown in Figure 37 indicate an increase in RM with increasing deviator stress. Experience has shown that soils behave similarly when subjected to RM testing. Also, as expected, the data shown in Figure 38 indicate an increase in RM with an

increase in the dry unit weight. We conclude that an increase in dry unit weight provides more solids (cement) to the specimen's skeletal structure, improving its stiffness.

However, the data shown in Figure 39 does not provide a strong relationship between the degree of saturation and its possible influence on the stiffness of LCC under the loading schedule shown in Table 12. The data may indicate a slight increase in RM as the saturation increases. We believe that the inclusion of the water, whether absorbed or adsorbed in the skeletal matrix, behaves in an undrained condition due to the rapid loading of the RM test protocol. This effect may have a minor contribution to the stiffness of the LCC specimen due to the included water's relative incompressibility. However, this independent variable has a minor contribution to LCC's stiffness within the range of saturation treatments explored.

Lastly, the data shown in Figure 40 indicate a decrease in stiffness as the specimen's length decreases. However, this effect is an artifact of the specimen preparation and an uncontrolled variable in the study. This effect and its removal from the correlation evaluations are further addressed in Chapter 8.

In summary, the independent variables with the highest statistically significant correlations with RM are the confining stress, deviator stress, dry unit weight, and the specimen's height-to-diameter. Therefore, the data shown in Figure 36, Figure 37, Figure 38, Figure 39, and Figure 40 are used in model generation using multilinear regression presented in Chapter 8.

CHAPTER 6

UNIAXIAL COMPRESSIVE STRENGTH

The UCS test is relatively quick, inexpensive, and requires no specialized equipment beyond what is found in a typical material testing laboratory. Because of this, the current state of practice in engineering design primarily utilizes the UCS for LCC quality control testing.

One objective of this study was to determine the lapsed time when the mechanical behavior of LCC no longer has appreciable change from the curing reaction. It is likely that, in practice, equipment availability constraints are encountered, and tests will be performed sequentially and at different curing times. Therefore, it will be important when performing suites of tests (e.g., uniaxial and three-point triaxial test) and correlating the results with the results from other tests (e.g., resilient modulus test) that the effect of curing time is controlled or accounted for in the experimental design and interpretation of the results. Therefore, uniaxial compressive tests were performed on air-dried specimens throughout the curing process to understand LCC's strength gain with time. The test program included 57 UCS tests with curing ages ranging from seven days to 99 days. The series was subsequently supplemented with five additional UCS tests that extended beyond 1,050 days of curing.

Another primary objective of this study was to determine the effects of the degree of saturation on the UCS of LCC. A series of UCS tests were performed to achieve this objective. The series included test specimens with ages ranging from 1,051 to 1,075 days and at various saturation treatments, as discussed in Chapter 3. These treatments included five specimens each from the AD, H100, M5, D1, and W1 saturation groups, respectively. Also, all UCS tests in this series were performed promptly after the completion of resilient modulus testing so that the specimens' moisture content and curing time remained unchanged between the execution of the UCS and RM testing.

Methods

The specimens for UCS testing were prepared as described in Chapter 2. The tests were performed on a calibrated GeoComp LoadTrac II load frame. The system compliance was accounted for in all strain computations by measuring the system displacements as a function of force using a 7075-aluminum calibration disc (see Figure 41). The calibration disc was machined from 3-inch stock on a Grizzly G7075 metal lathe with an end parallelism of less than 0.001" across the diameter.

Testing in uniaxial compression was performed in general accordance with ASTM C495 and ASTM D2166 (ASTM C09 Committee 2012; ASTM D18 Committee 2016b). The initial 27 tests were performed on surface-ground-only test specimens against the end platens (Figure 42). Following conversations with Aerix Industries, the method was modified to utilize Forney end caps with 50-durometer pads. This capping treatment allowed a consistent comparison against industry methods (Figure 43). All tests were initiated by applying a seating load of 5 lbs. The loading strain rate varied

from 0.5%/min to 0.75%/min, where the most consistent results were found to be at 0.75%/min, with the specimens typically reaching failure within one minute. Initially, it was observed that the specimens tended to fail from the bottom up, indicating the weakest material is likely located at the bottom of the specimens. Subsequently, the test specimens were prepared by removing 1/8" to ¼" of the bottom of the samples before testing. After testing, the failed specimens were placed in a convection oven at 230° F for water content determinations.

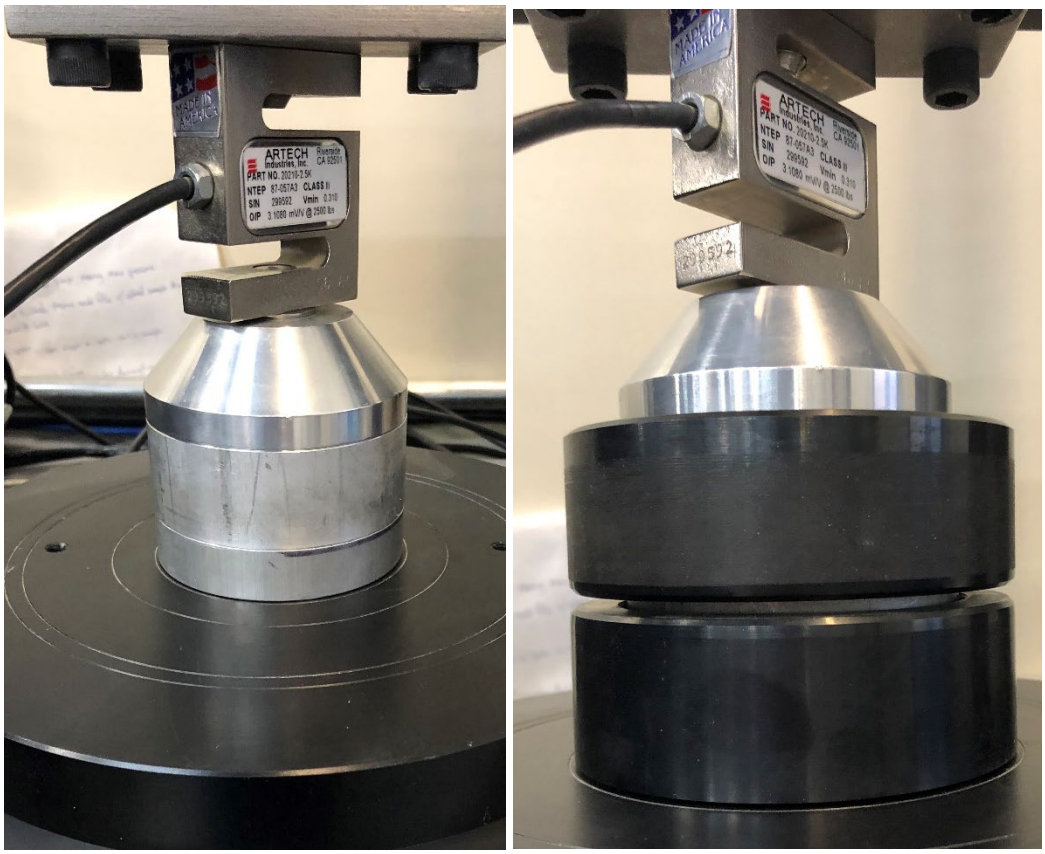

Figure 41. Photo of the 7075-aluminum system compliance calibration disc.

Figure 42. Photo of a specimen prepared for UCS testing in the load frame without padded end caps.

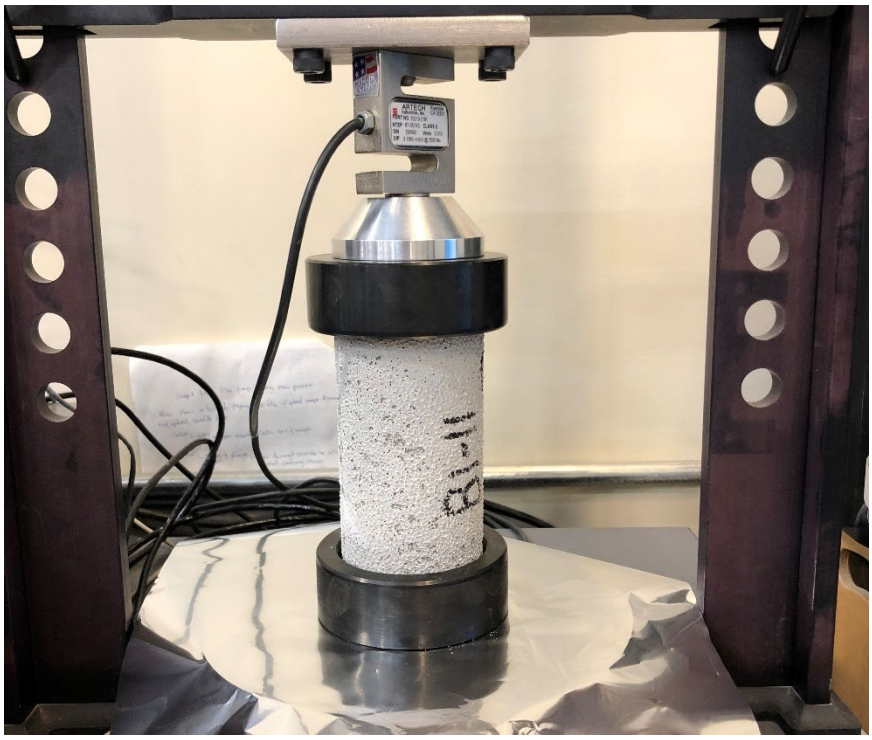

Figure 43. Photo of a specimen prepared for UCS testing in the load frame with padded end caps.

Results

The results from the initial UCS testing with the peak axial stress as a function of time are shown in Figure 44. Most of the test specimens exhibited either an initial reduction in strength before reaching the ultimate UCS stress or a substantial deviation from the initial straight-line portion of the stress-strain curve. This strength loss (i.e., deviation from Young's modulus line) was recorded as the initial yield. The initial yield of the test specimens as a function of time is also shown in Figure 44.

Figure 45 shows the results of the initial yield and UCS for the cured specimens (older than 10,50 days) as a function of the dry unit weight in pcf. The results of the initial yield and UCS as a function of saturation are shown in Figure 46. The results of the Young's modulus as a function of dry unit weight are shown in Figure 47. Finally,

Figure 48 displays a plot of the Young's modulus of the test specimens as a function of saturation. The complete test reports from each of the UCS tests are attached in Appendix D.

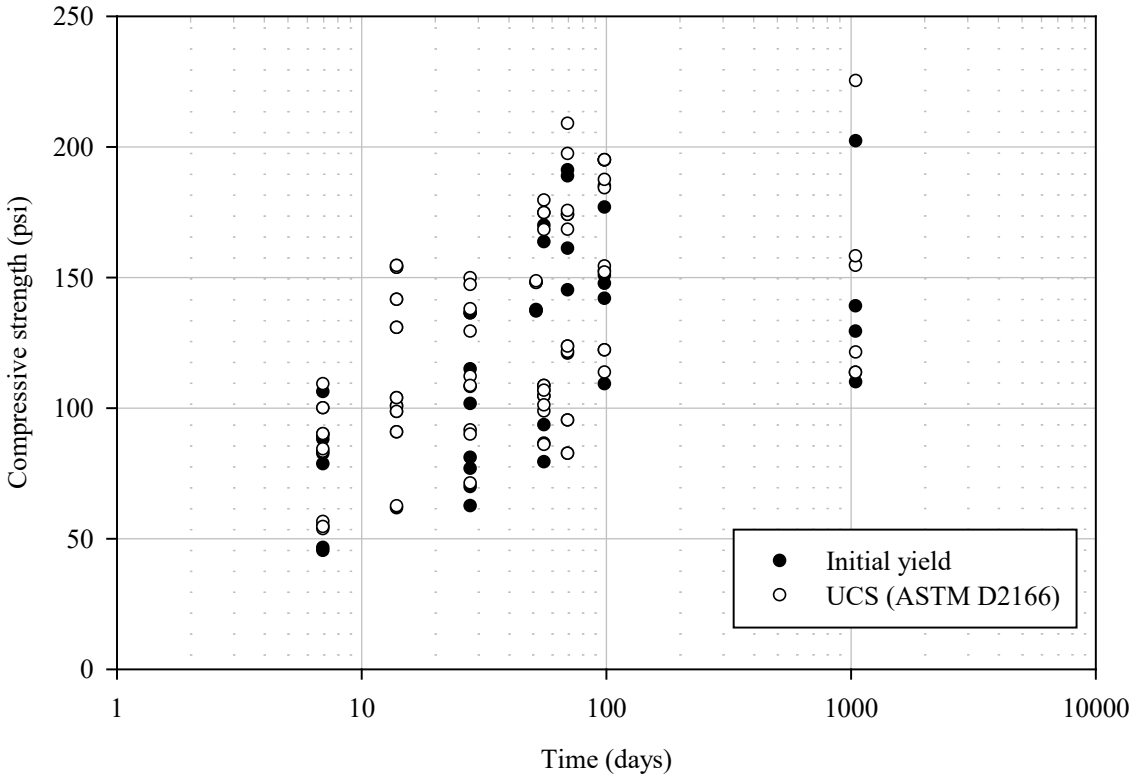

Figure 44. Plot of the initial yield and the UCS of the air-dried LCC specimens as a function of time.

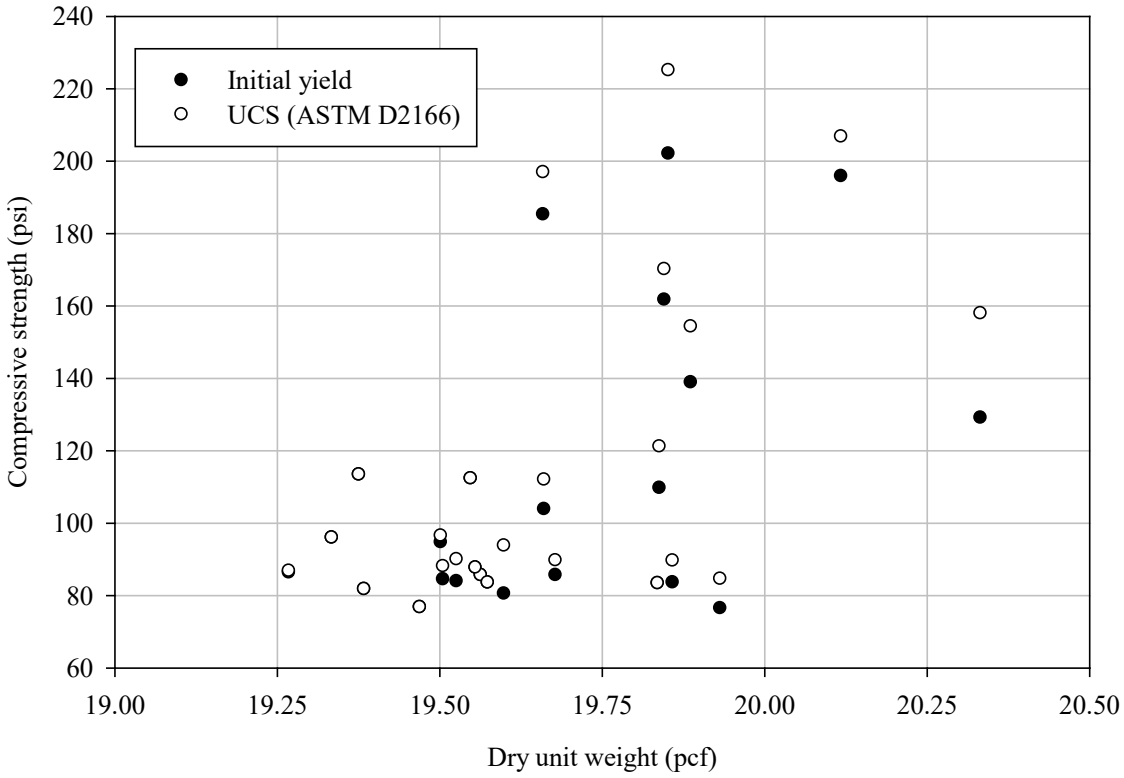

Figure 45. Plot of the initial yield and the UCS of the cured LCC specimens as a function dry unit weight.

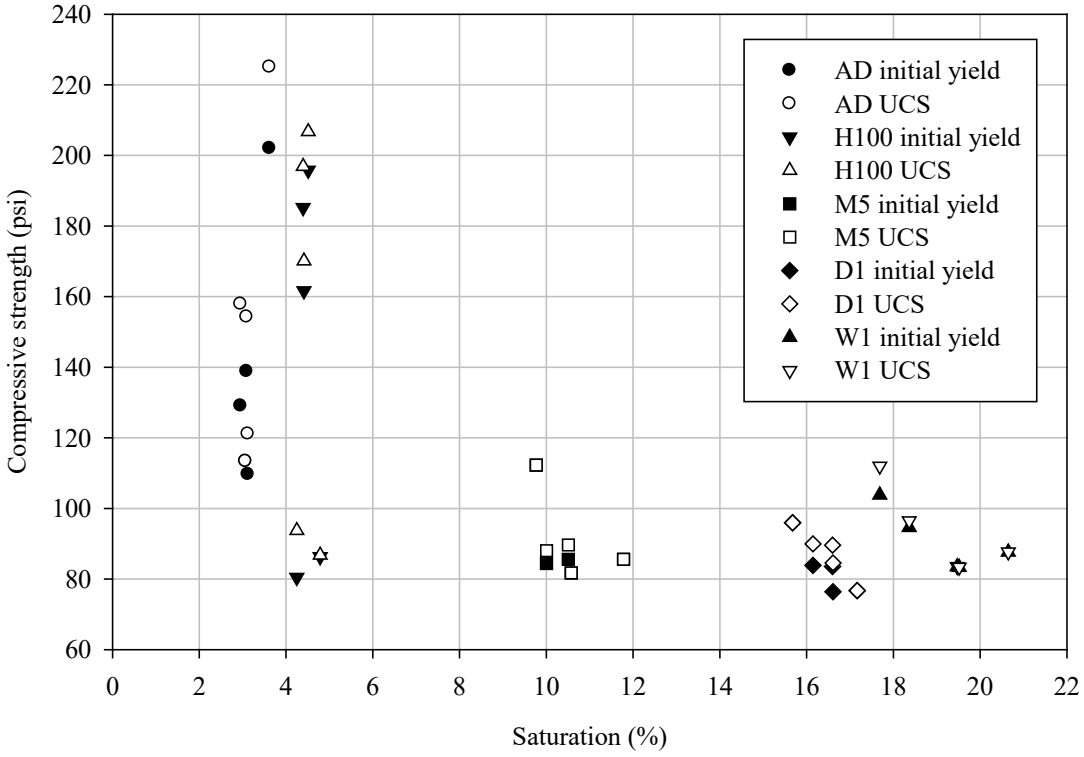

Figure 46. Plot of the initial yield and the UCS of the LCC specimens as a function of saturation.

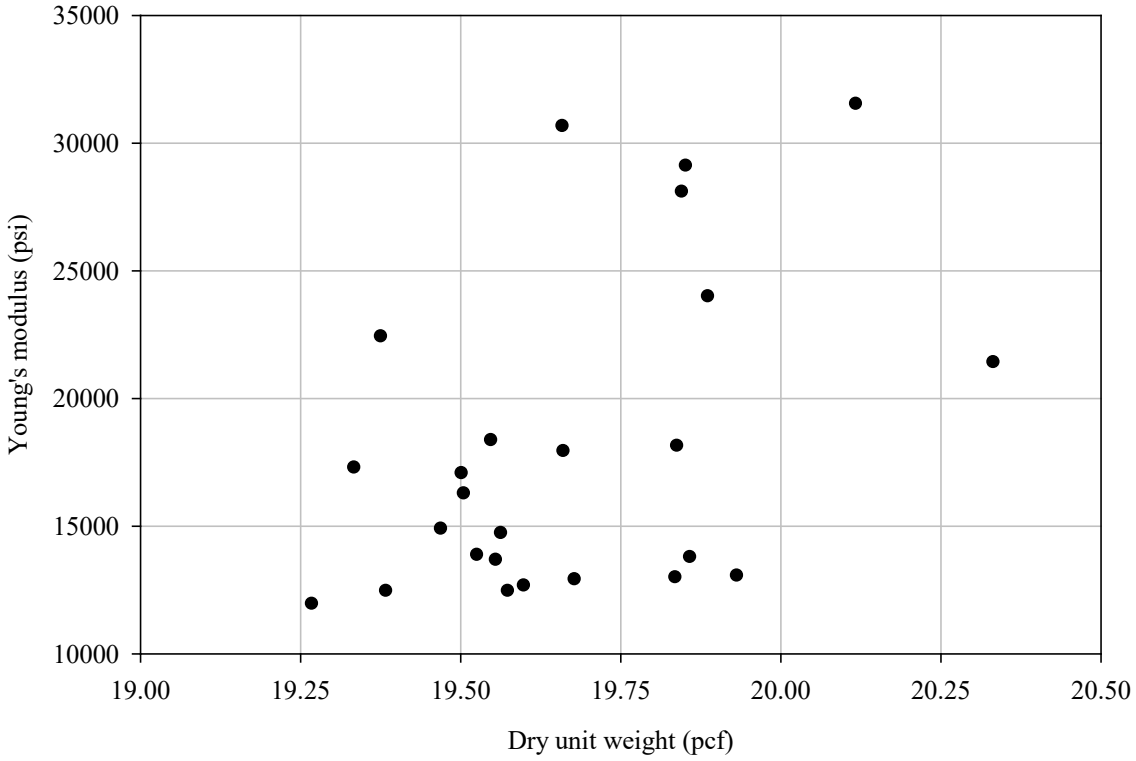

Figure 47. Plot of the Young's modulus of the LCC specimens as a function of dry unit weight.

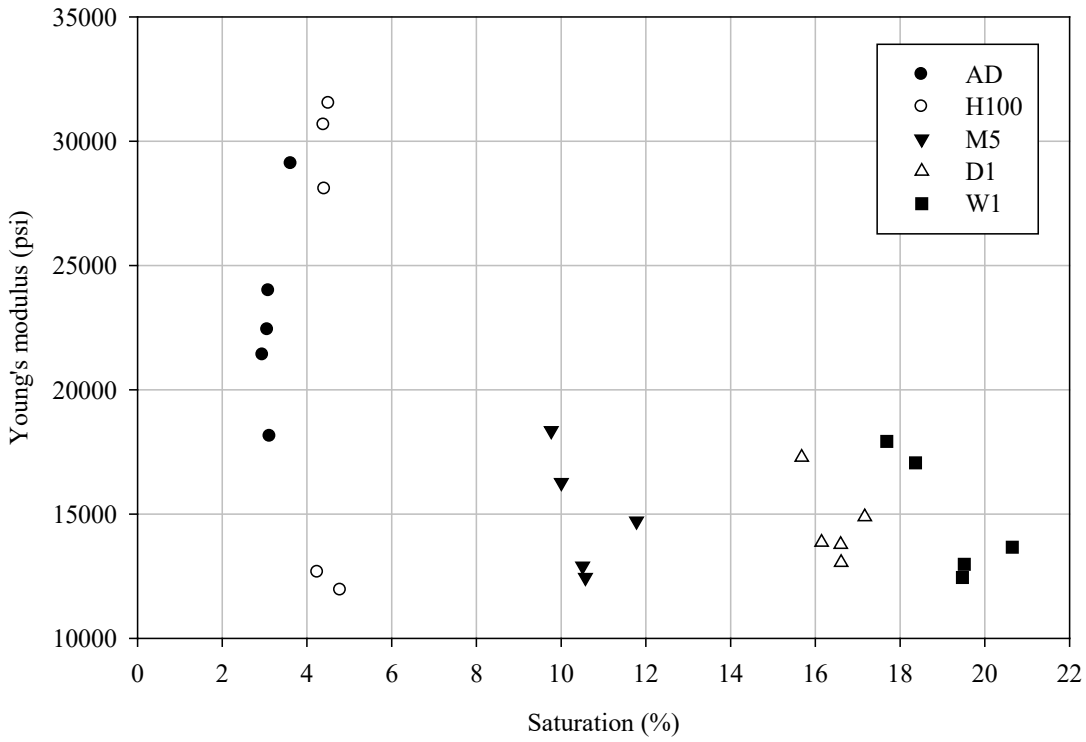

Figure 48. Plot of the Young's modulus of the LCC specimens as a function of saturation.

Discussion

The data from Figure 44 were used to estimate the time at which the engineering behavior of LCC no longer has appreciable effects from the curing reaction. This point in time was calculated by performing a nonlinear regression on the data and evaluating these results.

The nonlinear regressions were performed using SigmaPlot version 11.0.0.77 in the manner described in Chapter 2. Several hyperbolic and exponential forms were regressed through an iterative process with a best-fit mean line and a 95% confidence interval band (i.e., $\alpha = 0.05$). The functional form given in Equation 20 provided the best

fit with satisfactory p-values. Summaries of the regression statistics for each test specimen are presented in Table 10. A plot of the fitted model (Equation 20) from the regression is shown in Figure 49.

$$U = a(1 - e^{-b \cdot t}) \quad (20)$$

To estimate the time at which the engineering behavior of LCC no longer has appreciable effects from the curing reaction, we chose a 1% change in slope as a reasonable (i.e., non-zero) criterion. Calculating the first derivative of Equation 20 yields,

$$\frac{dU}{dt} = a \cdot b \cdot e^{-b \cdot t} \quad (21)$$

Solving for *t*, in Equation 21 gives,

$$t = \frac{-\ln\left(\frac{\frac{dU}{dt}}{a \cdot b}\right)}{b} \quad (22)$$

Given the one-percent slope criteria above and the nonlinear regression constants from Table 13, the UCS for the LCC reaches a point where negligible effects from the curing are reached after 70 days.

As expected, the data shown in Figure 45 and Figure 47 indicate an increase in compressive strength and Young's modulus with increasing dry unit weight. However, this study's data range for unit weight is relatively small because we sought to have cast specimens of the same unit weight. Nonetheless, the increase in dry unit results from more solids (i.e., cement) forming the specimen's skeletal structure, contributing to increases in strength and stiffness.

Table 13. Summary of the nonlinear regression statistics for the uniaxial compressive strength as a function of curing time (Equation 20).

Model parameter	Regression value	*p*-value	*p*-value acceptance criterion
a	143.6342	<0.0001	$<\alpha$
b	0.1043	<0.0001	$<\alpha$
R^2	0.3073		
ANOVA		<0.0001	$<\alpha$
Normality		0.4379	$>\alpha$

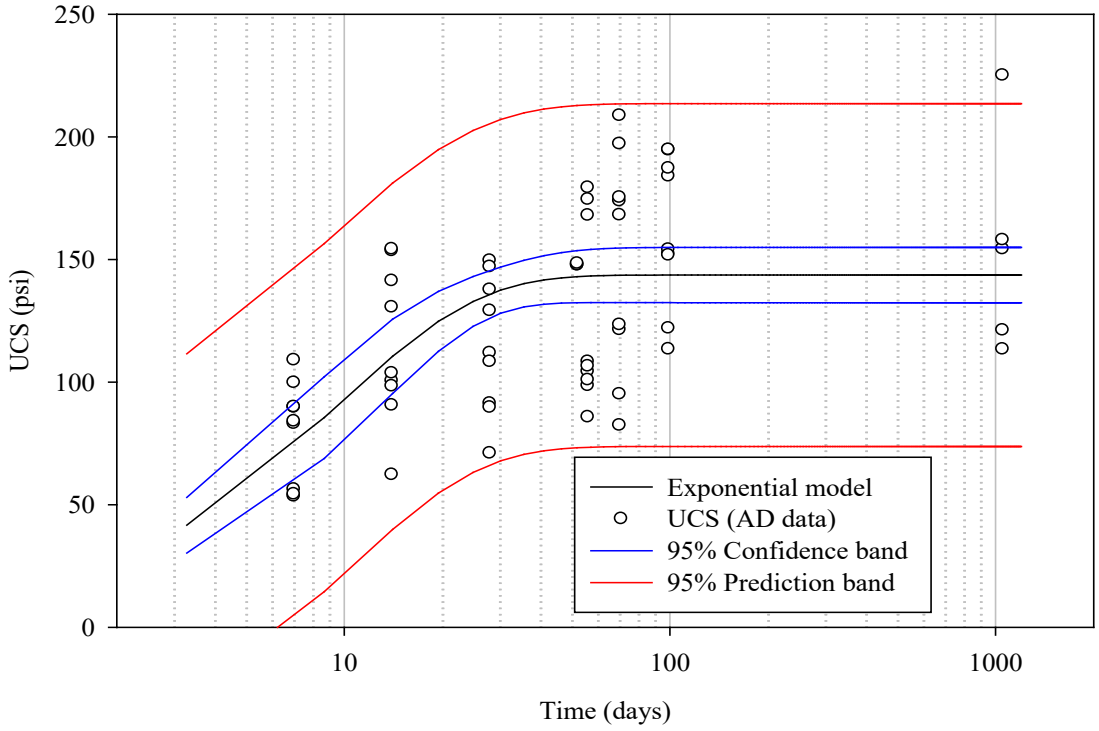

Figure 49. Plot of the uniaxial compressive strength as a function of curing time and the regression model (Equation 20) with confidence and prediction bands.

The data shown in Figure 46 and Figure 48 indicate a slight decrease in the compressive strength and stiffness as the saturation increases. The matric suction within the specimen is decreased as the degree of saturation increases by increasing the radii of the water-mineral interface menisci and reducing the water tensile forces. This decrease in matric suction contributes to decreased stiffness and strength measured in the LCC.

The independent variables with the highest correlations are the dry unit weight and the degree of saturation. Therefore, the data shown in Figure 45, Figure 46, and Figure 48 are used in model generation using multilinear regression, as discussed in Chapter 8.

CHAPTER 7

DRAINED TRIAXIAL COMPRESSIVE STRENGTH

Some advantages of the triaxial strength tests include that the test method allows for back-pressure saturation (as discussed in Chapter 4), consolidation of the test specimen, and both drained and undrained conditions during the shearing phase. The consolidation conditions can closely replicate field conditions and be in isotropic, anisotropic, or K_0 configurations. Shearing of the test specimen can mimic most field conditions encountered in engineering projects, such as axial compression, axial extension, lateral compression, or lateral extension. The equipment required to perform the tests is much less ubiquitous than the UCS test equipment but is relatively common in geotechnical testing laboratories. Proper test performance requires more advanced training and time than the UCS test and, therefore, is more costly.

One objective of this study was to estimate the strength of LCC in terms of the Mohr-Coulomb strength envelope derived from the isotropically consolidated triaxial compression tests (CIDTx). The triaxial data are also utilized to correlate to the resilient modulus as a surrogate test. Another objective of this study was to determine the effects of the degree of saturation on the triaxial compressive strength of LCC. A series of CIDTx were performed to achieve this objective. The series included test specimens with ages ranging from 1,052 to 1,077 days and at various saturation treatments, as discussed

in Chapter 3. This program included seven specimens from the AD, H100, M5, D1, and W1 saturation groups, respectively. The range of nominal effective confinement was three to 12 psi. All triaxial tests in this series were performed promptly after the completion of resilient modulus testing.

Methods

The specimens for triaxial testing were prepared as described in Chapter 2. The tests were performed on a calibrated GEOTAC triaxial system comprising a triaxial cell, a DigiFlow flow pump, and a Sigma-1 load frame, as shown in Figure 50. Consolidated-drained triaxial compression testing is performed in general accordance with ASTM D7181 (ASTM D18 Committee 2020). The test specimens were previously prepared in a triaxial cell for resilient modulus testing. The triaxial cell was filled with de-aired water and placed in the triaxial load frame. The typical saturation phase was omitted from the testing protocol, and the prescribed effective confining stress was applied. During consolidation, the volumetric and axial strain data are logged and plotted for a time-rate of strain analysis to determine an appropriate strain rate. Taylor and Casagrande's methods were used to analyze the time rate data. It was found that t_{90}, the time at which 90% of the consolidation occurred, was reached in less than two minutes for the consolidation phase. The strain rate, $\dot{\varepsilon}$, for the shearing phase of the tests was estimated at 0.2%/minute by:

$$\dot{\varepsilon} = \frac{4\%}{10 \cdot t_{90}} \qquad 23$$

The specimens were sheared in a drained condition with the specimen valves open to the atmosphere. Volumetric strain during shearing was determined by the axial

displacement, the known area of the loading piston, and the volume change in the cell. The specimens were sheared to 15% axial strain before termination of the test. Following testing, the failed specimens were placed in a convection oven at 230° F for water content determination.

Figure 50. Photo of the triaxial testing apparatus with a test specimen in the triaxial cell.

Results

The results from the triaxial Young's modulus of the LCC specimens as a function of saturation, as a function of the effective confining stress, and as a function of the dry unit weight are shown in Figure 51, Figure 52, and Figure 53, respectively.

Like the UCS tests results, most of the test specimens exhibited either an initial reduction in strength prior to the peak stress or a strong deviation from the initial straight-line portion of the stress-strain curve. At this initial yield stress, the mean Poisson's ratio for all test specimens was 0.231 with a standard deviation of 0.0412. The mean axial strain to reach the initial yield stress was 0.268% with a standard deviation of 0.0847%.

At the peak yield stress, which is beyond the elastic range and into the plastic deformation range, the mean ratio of the axial strain to the lateral strain (the pseudo-Poisson's ratio) for all test specimens was 0.0814 with a standard deviation of 0.0635. The mean axial strain to reach the peak yield stress was 4.27% with a standard deviation of 3.27%.

The results of the initial yield stress and peak yield stress in triaxial compression of the LCC specimens as a function of the effective confining stress and as a function of saturation are shown in Figure 54 and Figure 55, respectively.

The Mohr's circles for the initial yield and the peak stress are plotted in Figure 56 and Figure 57, respectively. The complete test reports from each of the triaxial tests are attached in Appendix E.

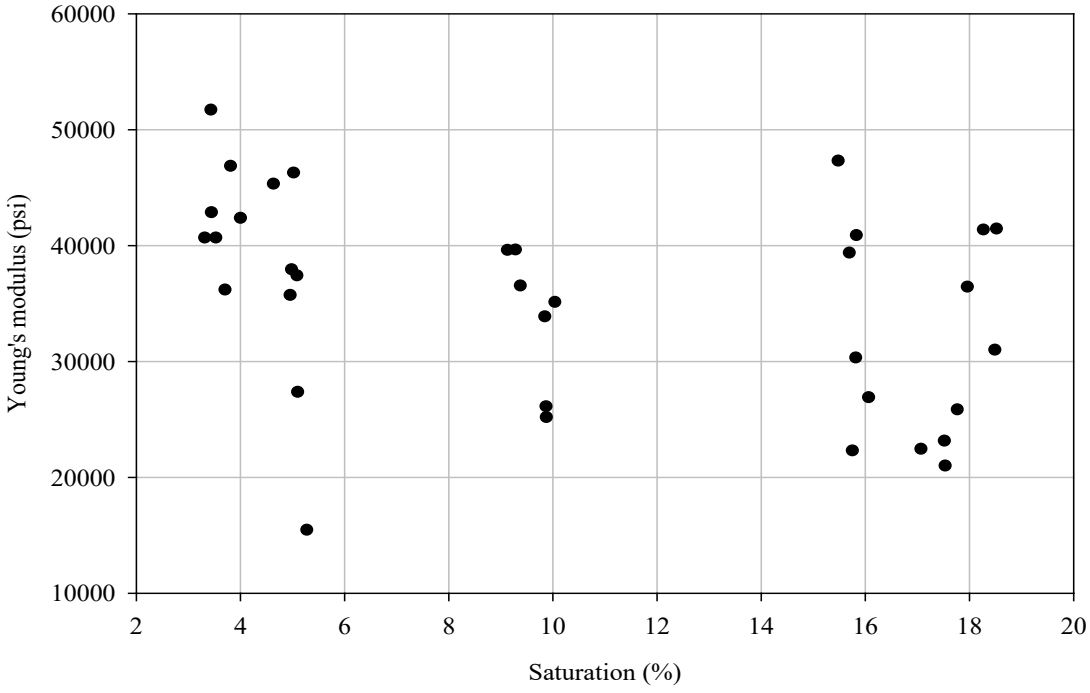

Figure 51. Plot of the triaxial Young's modulus of the LCC specimens as a function of saturation.

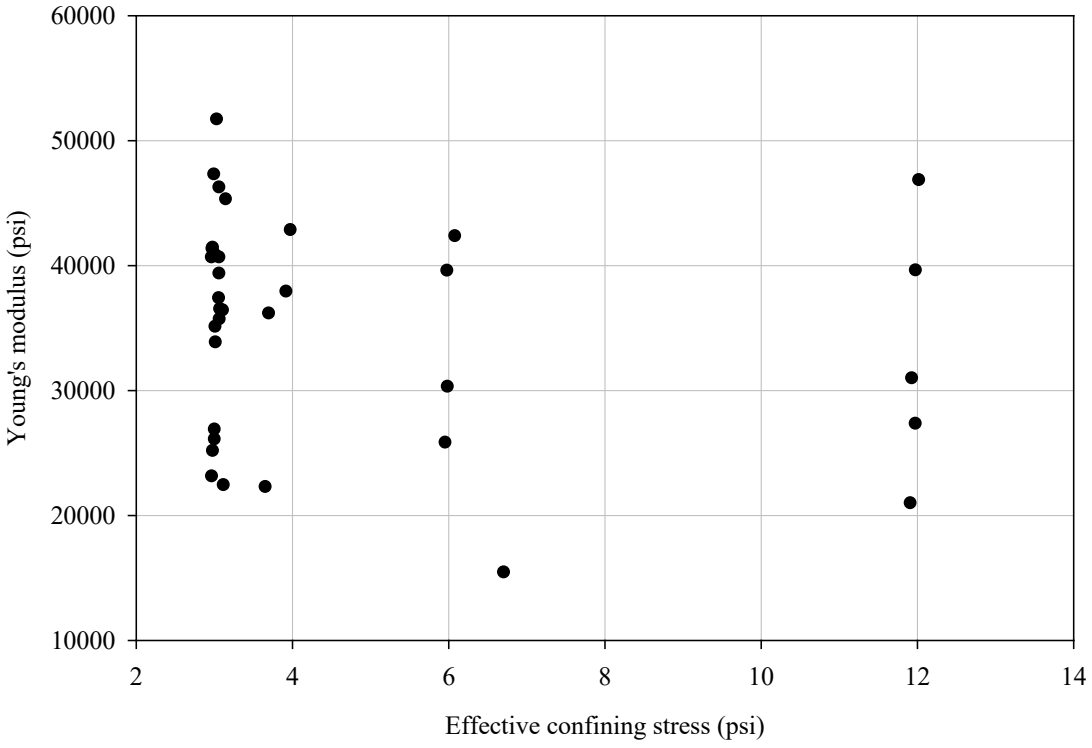

Figure 52. Plot of the triaxial Young's modulus of the LCC specimens as a function of the effective confining stress.

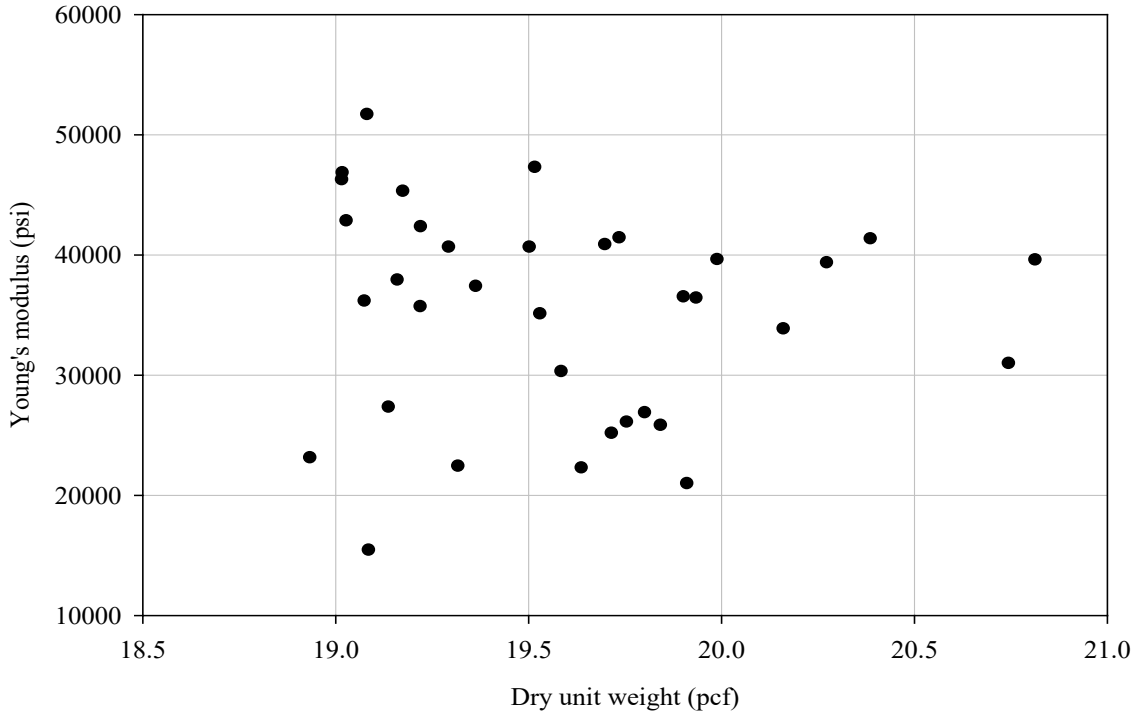

Figure 53. Plot of the triaxial Young's modulus of the LCC specimens as a function of the dry unit weight.

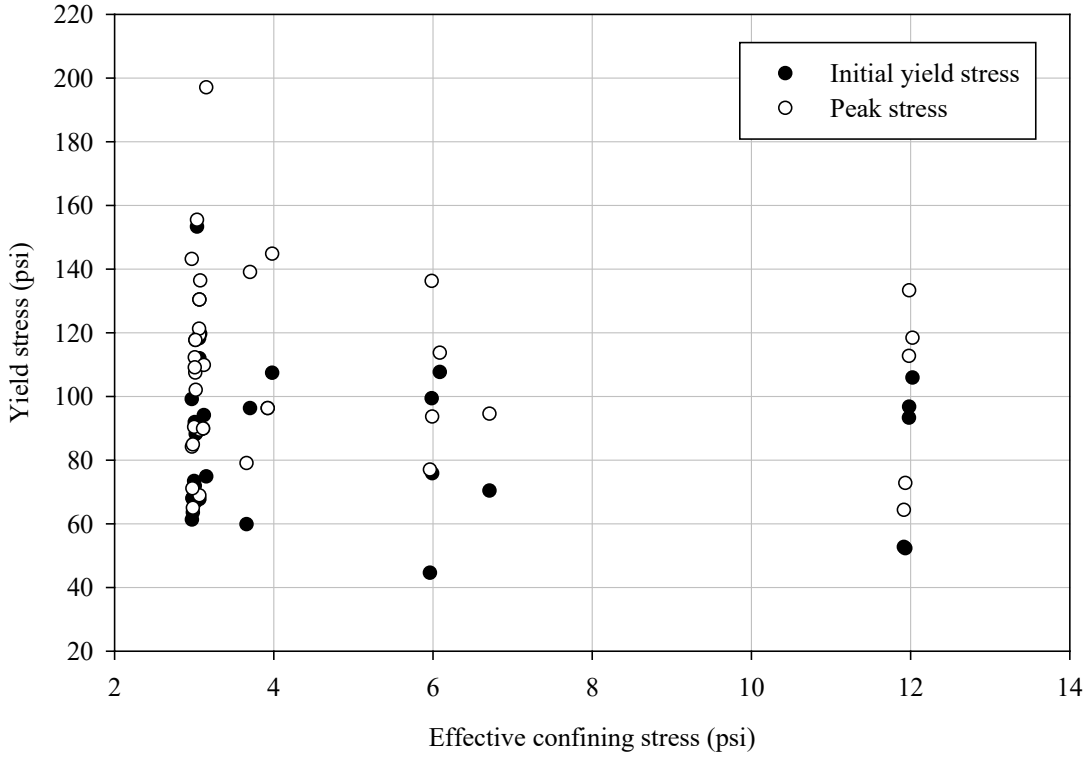

Figure 54. Plot of the yield stresses in triaxial compression of the LCC specimens as a function of the effective confining stress.

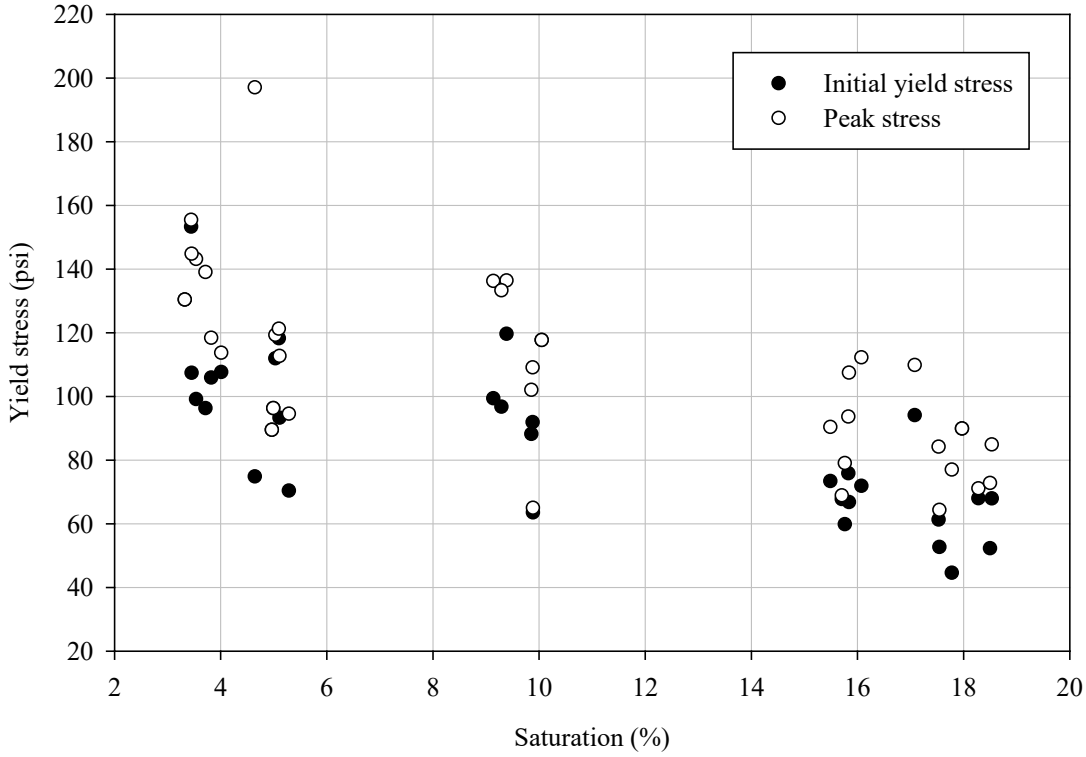

Figure 55. Plot of the yield stresses in triaxial compression of the LCC specimens as a function of saturation.

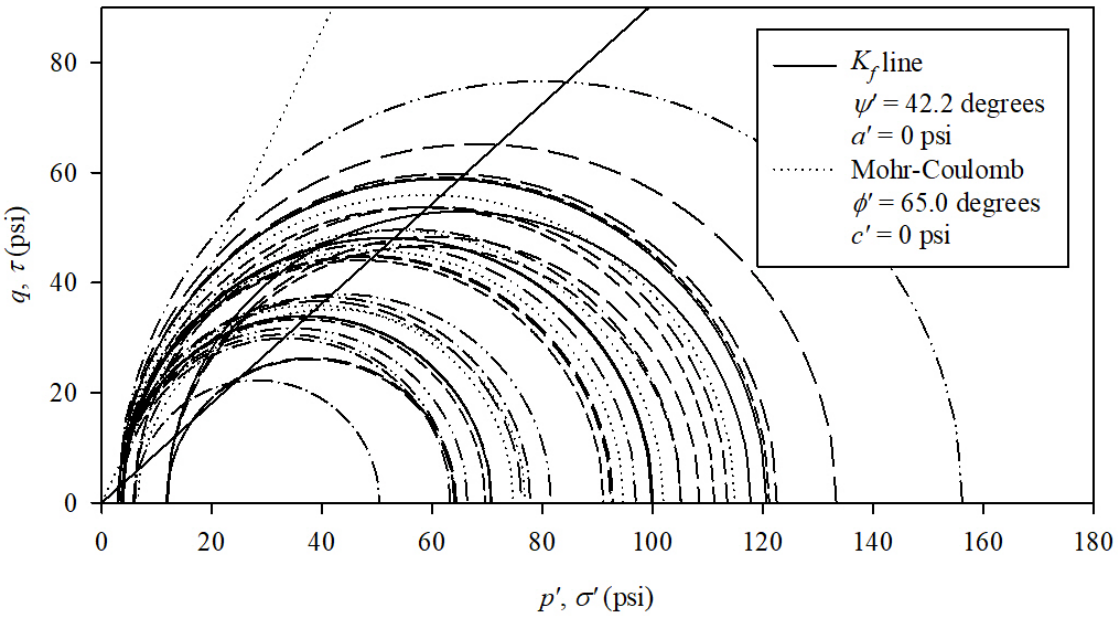

Figure 56. Plot of the Mohr's circles, K_f line, and Mohr-Coulomb failure envelope for the initial yield points for all triaxial tests.

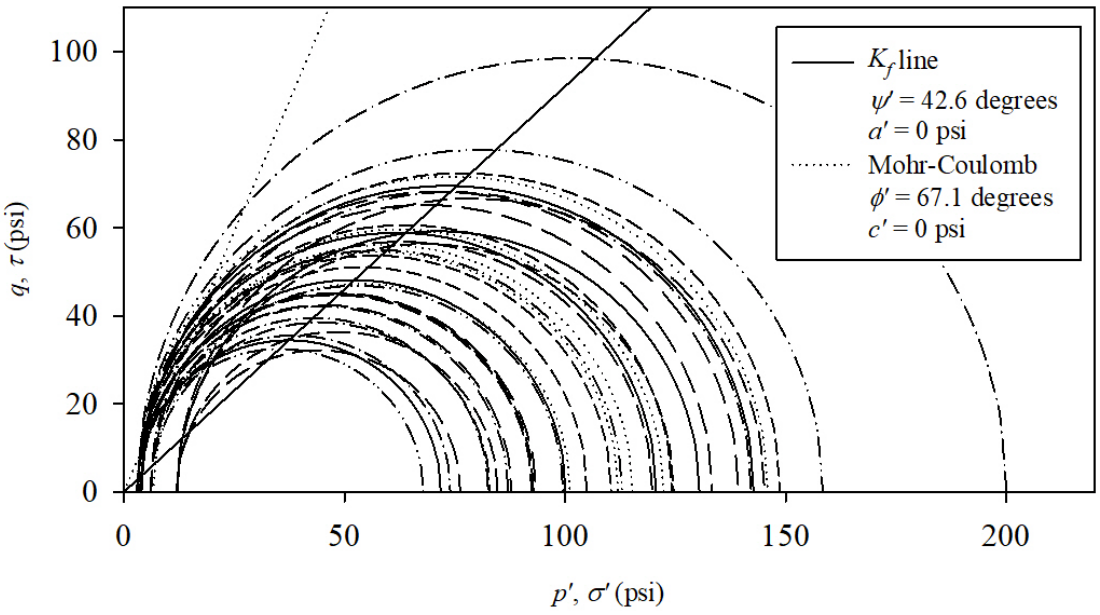

Figure 57. Plot of the Mohr's circles, K_f line, and Mohr-Coulomb failure envelope for the peak stress points for all triaxial tests.

Discussion

The Young's modulus in triaxial compression, as seen in Figure 51, Figure 52, and Figure 53, is affected by the saturation, the dry unit weight, and to a lesser affect, the effective confining stress. The data shown in these figures are used in model generation using multilinear regression and is discussed in Chapter 8.

The increase in modulus with an increase in dry unit weight is expected as previously discussed. The effect on the modulus from saturation indicates a greater influence than the minimal impact observed from the effective confining stress. This is partially explained by the effects on the matric suction within the specimen as the degree of saturation increases, as discussed in Chapter 6. This decrease in matric suction

contributes to the decrease in stiffness measured in the LCC by reducing internal tensile stresses. Also, due to the increased strain rate (compared to the RM testing), the large deformation (again, compared to the RM testing), and distortion of the fabric, there is likely an effect from the increase in pore water pressure in the occluded or tightly bound water filled voids. Although the test is performed in a drained condition during shearing, the localized excess pore water pressure is a result of a partially drained state, resulting in a complex distribution of effective stress during shearing.

The strength in triaxial compression, as seen in Figure 54 and Figure 55 has a minor affect from the effective confining stress and a more pronounced affect from the degree of saturation. The trends from these to independent variables follow those seen for the triaxial Young's modulus.

The effective friction angles, as shown in Figure 56 and Figure 57 are 65.0° and 67.1° for the initial yield stress state and the peak strength, respectively. The effective cohesion intercept for each case is zero. This indicates a purely frictional material in the range of stresses tested in this study, which are relatively low. Tiwari et al. (2017) have suggested a conservative value for the effective friction angle of 35° be used for saturated design purposes. The authors have also reported that the partially saturated friction angle of 40° was obtained through direct shear testing, but the degree of saturation for this test is unknown. The authors suggest that the effective friction angle for design may be increased to 40° for Class-II or Class-IV LCC when subjected to normal stresses less than 1,000 kPa (145 psi). Considering the range of effective confining stresses for this study (3 to 12 psi), and considering the findings from Tiwari et al. (2017), the use of the

effective friction angle of 65.0° is reasonable for partially saturated conditions in the low range of stresses used in this study.

The mean Poisson's ratio, ν, of 0.231 results in an at-rest lateral earth pressure, K_0, of 0.3 by the following relationship,

$$K_0 = \frac{\nu}{1-\nu} \qquad 24$$

CHAPTER 8

LCC PREDICTIVE MODELS

One objective of the current research was to develop predictive models for estimating the engineering behavior of LCC and the effects of the degree of saturation. In addition, MLR models were developed to assess the potential correlation of RM test results with those obtained from the UCS and triaxial compression tests. These latter models were correlated with the RM test results using paired UC and Triaxial tests performed on the same specimens. If successful, these correlations will enable the estimation of RM results using relatively straightforward, less expensive, and ready-available UCS and triaxial compression tests.

The data presented in the previous chapters were used to perform statistical analyses to evaluate the relationship between the independent variables (i.e., predictor variables) and the dependent variable (i.e., variable to be estimated) using multiple linear regression analysis (MLR). Regression analysis aims to develop a predictive best-fit statistical model that may be used to calculate the value of a dependent variable from one or more independent variables (Levine et al. 2001).

This chapter used two regression methods: simple linear regression (SLR) (i.e., regression using a single independent variable) and MLR (i.e., regression using multiple independent variables). The SLR and MLR regression analyses were performed using

Microsoft Excel with the Analysis ToolPak, which uses the least-square method to minimize the sum of the squares (i.e., variance) between the dependent and independent variables using linear relationships or relationships that can be linearized by transformation of the dependent or independent variables, or both. Closed-form matrix operations are used to solve for the best-fit coefficients of the system of linear equations. The general form of the SLR model is,

$$Y_i = \beta_0 + \beta_1 \cdot X_i + \varepsilon_i \quad (25)$$

where Y_i is the predictive value of the dependent variable, Y, for observation, i, β_0 is the Y-intercept parameter, β_1 is the slope parameter, and X_i represents the independent variables, X. The value of ε_i is the random error in Y for observation i (Levine et al. 2001). The general form of the MLR model is,

$$Y_i = \beta_0 + \beta_1 \cdot X_{1i} + \beta_2 \cdot X_{2i} + \beta_3 \cdot X_{3i} + \cdots + \beta_k \cdot X_{ki} + \varepsilon_i \quad (26)$$

where $\beta_1 \ldots \beta_k$ are the partial slopes (i.e., partial derivatives) for their respective X variables (Levine et al. 2001).

Three essential assumptions are needed for valid SLR and MLR regression analyses. The first assumption, normality of error, requires the error values to be normally distributed and centered around the best-fit regression line in n^{th} dimensional space. The second assumption, homoscedasticity, requires the variation about the best-fit line to be constant across all values of X_i. The final assumption, independence of errors, requires the errors to be independent (i.e., not correlated) with all values of X_i (Levine et al. 2001).

Residual error plots can be used to judge the validity of the above assumptions. The residual error is plotted by the difference from the best-fit Y values for each X_i value. This plotting is done separately plots for each independent variable. The overall quality of the regression model is generally judged by the magnitude of the coefficient of determination, $R^{2,}$ and the magnitude of the standard error, s_e, as well as an inspection of the analysis of variance (ANOVA) table. For example, an R^2 value of 1.00 means that the X_i values explain 100 percent of the variability in the Y value (i.e., a "perfect" fit).

Similarly, an R^2 value of 0.60 means that 60 percent of the variability is explained by the X_i values, etc. The value of s_e measures the standard deviation of the errors in a regression model. The model's standard error is a measure of the average deviation or dispersion of the points on the residual error scatter plot around the best-fit line. An ANOVA table is used to judge if the partial slopes ($\beta_1 \ldots \beta_k$) are statistically significant using the F-statistic and its corresponding p-value. For this test, the null hypothesis is that β_i is zero (i.e., not significant). For this research, an acceptance criterion of the alternative hypothesis that β_i is non-zero was a 95% confidence with a p-value < α = 0.05.

Uniaxial Compressive Strength Models

The data shown in Figure 45 and Figure 46 in Chapter 6 were used to generate the following model to estimate the UCS of LCC as a function of the dry unit weight, γ_d, in pcf, and the degree of saturation, S, in percent,

$$UCS = \frac{1}{\beta_0 + \beta_1 \cdot \gamma_d^2 + \beta_2 \cdot \ln(S)} \qquad 27$$

The range of use with statistical significance for γ_d and S in Equation 27 is limited to 18.9 pcf to 20.8 pcf and 2.9% to 20.5%, respectively. A summary of the regression results for Equation 27 are shown in Table 14. The regression statistics and ANOVA results for Equation 27 are shown in Table 15.

Table 14. Summary of the regression results for Equation 27.

Statistic	Regression coefficient	Standard Error	*t*-statistic	*p*-value
b_0	4.035E-02	1.438E-02	2.805	0.01032
b_1	-9.181E-05	3.609E-05	-2.544	0.01850
b_2	2.229E-03	4.997E-04	4.461	0.00020

Table 15. Regression statistics and ANOVA results of Equation 27.

Multiple R	0.8017
R square	0.6428
Adjusted R square	0.6103
Standard error	0.001643
Observations	25

Variation source	Degrees of freedom	Sum of squares	Mean square	*F*-statistic	*p*-value
Regression	2	1.07E-04	5.343E-05	19.79	1.209E-05
Residual	22	5.94E-05	2.700E-06		
Total	24	1.66E-04			

The data shown in Figure 45 and Figure 46 in Chapter 6 were used to generate the following model to estimate the initial yield for the UCS test, IY_{UCS}, of LCC as a function of γ_d in pcf, and S in percent,

$$IY_{UCS} = min\left(\begin{matrix}(\beta_3 + \beta_4 \cdot \ln(\gamma_d) + \beta_5 \cdot S)^2, \\ \frac{1}{\beta_0 + \beta_1 \cdot \gamma_d^2 + \beta_2 \cdot \ln(S)}\end{matrix}\right) \quad 28$$

As with Equation 27, the range of use with statistical significance for γ_d and S in Equation 28 is limited to the ranges of 19.3 pcf to 20.3 pcf and 2.9% to 20.5%, respectively. A summary of the regression results for Equation 28 are shown in Table 16. The regression statistics and ANOVA results for Equation 28 are shown in Table 17.

No statistically significant correlation was found for the UCS or IY_{UCS} with the height-to-diameter ratio, $R_{H:D}$, for the test specimens.

Table 16. Summary of the regression results for Equation 28.

Variable	Coefficient	Standard Error	*t*-statistic	*p*-value
b_3	-118.3	62.85	-1.882	0.0732
b_4	43.66	21.05	2.074	0.0499
b_5	-0.1419	0.04243	-3.345	0.002931

Table 17. Regression statistics and ANOVA results of Equation 28.

Multiple R	0.7017
R square	0.4924
Adjusted R square	0.4463
Standard error	1.258
Observations	25

Variation source	Degrees of freedom	Sum of squares	Mean square	*F*-statistic	*p*-value
Regression	2	33.79	16.90	10.67	5.760E-04
Residual	22	34.83	1.58		
Total	24	68.63			

The data shown in Figure 46 in Chapter 6 were used to generate the following model to estimate the modulus of elasticity, E_{UCS}, of LCC as a function of the degree of saturation, S, in percent,

$$E_{UCS} = \left(\beta_6 + \beta_7 \cdot \ln(S)\right)^2 \quad 29$$

The range of use with statistical significance for S in Equation 29 is limited to the range of 2.9% to 20.5%. A summary of the regression results for Equation 29 are shown in **Error! Not a valid bookmark self-reference.**. The regression statistics and ANOVA results for Equation 29 are shown in Table 19.

No statistically significant correlation was found for the E_{UCS} with γ_d or $R_{H:D}$ for the test specimens.

Table 18. Summary of the regression results for Equation 29.

Variable	Coefficient	Standard Error	*t*-statistic	*p*-value
b_6	173.8	10.91	15.93	6.412E-14
b_7	-19.150	4.843	-3.954	6.300E-04

Table 19. Regression statistics and ANOVA results of Equation 29.

Multiple R	0.6362
R square	0.4047
Adjusted R square	0.3788
Standard error	17.06
Observations	25

Variation source	Degrees of freedom	Sum of squares	Mean square	*F*-statistic	*p*-value
Regression	1	4549	4549	15.64	6.300E-04
Residual	23	6691	290.9		
Total	24	1.124E+04			

Drained Triaxial Compressive Models

The data shown in Figure 52 and Figure 53 in Chapter 7 were used to generate the following model to estimate the modulus of elasticity in triaxial compression, E_{TX}, of LCC as a function of the effective confining stress, σ'_3, in psi and γ_d, in pcf,

$$E_{TX} = e^{\frac{\beta_8 \cdot \sigma_3' + \beta_9 \cdot \sigma_3' \cdot \ln(S) + \beta_{10} + \beta_{11} \cdot \sigma_3' \cdot \sqrt{\gamma_d}}{\sigma_3'}} \quad (30)$$

The range of use with statistical significance for σ'_3 and γ_d, in Equation 30 is limited to 3.0 psi to 12.0 psi to 18.9 pcf to 20.8 pcf, respectively. A summary of the regression results for Equation 30 are shown in Table 20. The regression statistics and ANOVA results for Equation 30 are shown in Table 21.

No statistically significant correlation was found for the E_{TX} with S or $R_{H:D}$ for the test specimens.

Table 20. Summary of the regression results for Equation 30.

Variable	Coefficient	Standard Error	*t*-statistic	*p*-value
b_8	1.687	4.249	0.3969	6.941E-01
b_9	-0.2835	0.08385	-3.381	1.966E-03
b_{10}	0.9402	0.4511	2.084	4.549E-02
b_{11}	2.059	0.9798	2.102	4.381E-02

Table 21. Regression statistics and ANOVA results of Equation 30.

Multiple R	0.5568
R square	0.3100
Adjusted R square	0.2433
Standard error	0.24
Observations	35

Variation source	Degrees of freedom	Sum of squares	Mean square	*F*-statistic	*p*-value
Regression	3	0.8276	0.2759	4.643	8.557E-03
Residual	31	1.842	0.05942		
Total	34	2.670			

The data shown in Figure 54 and Figure 55 in Chapter 7 were used to generate the following models to estimate the initial yield of the deviator stress, $\sigma_{d.i}$, and the maximum deviator stress, $\sigma_{d.max}$ for the triaxial compression test, of LCC as a function of σ'_3 in psi and S in percent,

$$\sigma_{d.i} = e^{\frac{\beta_{12}\cdot\ln(\sigma'_3)+\beta_{13}\cdot\ln(\sigma'_3)\cdot\ln(S)+\beta_{14}}{\ln(\sigma'_3)}} \quad (31)$$

$$\sigma_{d.max} = \beta_{15} + \beta_{16}\cdot\frac{1}{\sigma_{d.i}} \quad (32)$$

where $\sigma_{d.i}$ in Equation 32 is the prediction obtained from Equation 31. The range of use with statistical significance for, σ'_3, and S, in Equation 31 and Equation 32 are limited to the ranges of 3.0 psi to 12.0 psi to 13.3% to 18.5%, respectively. A summary of the regression results for Equation 31 are shown in Table 22. The regression statistics and ANOVA results for Equation 31 are shown in Table 23. A summary of the regression results for Equation 32 are shown in Table 24. The regression statistics and ANOVA results for Equation 32 are shown in Table 25.

No statistically significant correlation was found for the $\sigma_{d.i}$ or $\sigma_{d.max}$ with γ_d or $R_{H:D}$ for the test specimens.

Table 22. Summary of the regression results for Equation 31.

Variable	Coefficient	Standard Error	*t*-statistic	*p*-value
b_{12}	4.860	0.1716	28.327	3.119E-24
b_{13}	-0.3204	0.05223	-6.135	7.348E-07
b_{14}	0.3563	0.1730	2.060	4.758E-02

Table 23. Regression statistics and ANOVA results of Equation 31.

Multiple R	0.7475
R square	0.5587
Adjusted R square	0.5311
Standard error	0.1947
Observations	35

Variation source	Degrees of freedom	Sum of squares	Mean square	*F*-statistic	*p*-value
Regression	2	1.536	0.7680	20.26	2.067E-06
Residual	32	1.213	0.03791		
Total	34	2.749			

Table 24. Summary of the regression results for Equation 32.

Variable	Coefficient	Standard Error	*t*-statistic	*p*-value
b_{15}	208.1	20.60	10.10	1.249E-11
b_{16}	-8498	1717	-4.948	2.151E-05

Table 25. Regression statistics and ANOVA results of Equation 32.

Multiple R	0.6526
R square	0.4259
Adjusted R square	0.4085
Standard error	22.61
Observations	35

Variation source	Degrees of freedom	Sum of squares	Mean square	*F*-statistic	*p*-value
Regression	1	1.251E+04	1.251E+04	24.48	2.151E-05
Residual	33	1.687E+04	511.2		
Total	34	2.938E+04			

Resilient Modulus Models

The residual plots from the regression process revealed a testing artifact in the data attributed to the test specimens' height-to-diameter ratio, $R_{H:D}$, which is also shown in Figure 40. Because the goal of the predictive model was to be used to estimate RM sans the test procedure, a decision was made to remove the effects from the testing artifact from the data for the standalone MR model.

Regression analysis can eliminate specific artifact effects from estimates of our independent variable by adjusting the *Y* values (Ostle and Malone 1988). In this case, a linear regression was performed with the independent variable in the desired transformation, 1/*MR*, and with the dependent variable, which is the source of the artifact effect, $R_{H:D}$. The regression is in the form of Equation 33, where b_1 is the slope of the line. The independent variable is adjusted as follows,

$$M_{R.adjusted} = \frac{1}{\frac{1}{M_{R.raw}} - \beta_{18}(R_{H:D} - \overline{R_{H:D}})} \quad 33$$

where $\overline{R_{H:D}}$ is the mean height-to-diameter ratio. A summary of the regression results for Equation 33 are shown in Table 20. The regression statistics and ANOVA results for Equation 33 are shown in Table 21.

Table 26. Summary of the regression results for Equation 33.

Variable	Coefficient	Standard Error	*t*-statistic	*p*-value
b_{17}	-6.449E-05	2.118E-05	-3.045	2.394E-03
b_{18}	4.459E-05	1.133E-05	3.937	8.889E-05

Table 27. Regression statistics and ANOVA results of Equation 33.

Multiple R	0.1303
R square	0.0170
Adjusted R square	0.0159
Standard error	0.00
Observations	900

Variation source	Degrees of freedom	Sum of squares	Mean square	*F*-statistic	*p*-value
Regression	1	1.089E-09	1.089E-09	15.50	8.889E-05
Residual	898	6.312E-08	7.029E-11		
Total	899	6.421E-08			

The data shown in Figure 36, Figure 37, and Figure 38 in Chapter 5 were used to generate the following model to estimate the resilient modulus, M_R, of LCC as a function of the confining stress, σ_3, in psi and γ_d, in pcf and deviator stress, σ_d, in psi,

$$M_R = \frac{1}{\beta_{19} + \beta_{20} \cdot \ln(\sigma_3) + \beta_{21} \cdot \gamma_d^2 + \beta_{22} \cdot \ln(\sigma_d)} \quad 34$$

The range of use with statistical significance for σ_3, γ_d, and σ_d in Equation 34 is limited to 1.7 psi to 20.1 psi, 18.9 pcf to 20.8 pcf, and 2.9 psi to 40.7 psi, respectively. A summary

of the regression results for Equation 34 are shown in Table 28. The regression statistics and ANOVA results for Equation 34 are shown in Table 29.

No statistically significant correlation was found between *MR* and *S* for the test specimens.

Table 28. Summary of the regression results for Equation 34.

Variable	Coefficient	Standard Error	*t*-statistic	*p*-value
b_{19}	6.718E-05	5.760E-06	11.66	2.316E-29
b_{10}	-6.565E-06	4.502E-07	-14.58	2.171E-43
b_{21}	-1.016E-07	1.476E-08	-6.886	1.077E-11
b_{22}	1.702E-06	5.119E-07	3.325	9.206E-04

Table 29. Regression statistics and ANOVA results of Equation 34.

Multiple R	0.5397
R square	0.2912
Adjusted R square	0.2889
Standard error	0.00
Observations	900

Variation source	Degrees of freedom	Sum of squares	Mean square	*F*-statistic	*p*-value
Regression	3	1.838E-08	6.127E-09	122.7	1.364E-66
Residual	896	4.473E-08	0.0		
Total	899	6.312E-08			

Surrogate Test Models

The UCS and triaxial compression tests were performed following the resilient modulus tests, providing a direct test comparison without introducing specimen effects.

The data from the resilient modulus tests and the subsequent UCS test were used to generate the following model to estimate the resilient modulus, M_R, of LCC as a function of the confining stress, σ_3, in psi and γ_d, in pcf, modulus of elasticity from the UCS test, E_{UCS}, in psi, and the degree of saturation, S, in percent,

$$M_R = \frac{1}{\beta_{23} + \beta_{24} \cdot \ln(\sigma_3) + \beta_{25} \cdot \gamma_d^2 + \beta_{26} \cdot E_{UCS}^2 + \beta_{27} \cdot \ln(S)} \quad 35$$

The range of use with statistical significance for σ_3, γ_d, E_{USC}, and S in Equation 35 is limited to the ranges of 1.7 psi to 20.1 psi, 19.3 pcf to 20.3 pcf, 11,940 psi to 31,520 psi, and 2.9% to 20.5%, respectively. A summary of the regression results for Equation 35 is shown in Table 30. The regression statistics and ANOVA results for Equation 35 are shown in Table 31.

Table 30. Summary of the regression results for Equation 35.

Variable	Coefficient	Standard Error	*t*-statistic	*p*-value
b_{23}	8.576E-05	1.711E-05	5.012	8.382E-07
b_{24}	-6.471E-06	5.005E-07	-12.93	8.208E-32
b_{25}	-1.097E-07	4.392E-08	-2.497	1.295E-02
b_{26}	-1.021E-14	1.984E-15	-5.145	4.343E-07
b_{27}	-2.894E-06	6.955E-07	-4.161	3.941E-05

Table 31. Regression statistics and ANOVA results of Equation 35.

Multiple R	0.6044
R square	0.3653
Adjusted R square	0.3584
Standard error	0.00
Observations	375

Variation source	Degrees of freedom	Sum of squares	Mean square	*F*-statistic	*p*-value
Regression	4	1.160E-08	2.899E-09	53.2	2.064E-35
Residual	370	2.015E-08	0.0		
Total	374	3.174E-08			

The data from the resilient modulus tests and the subsequent drained triaxial compression tests were used to generate the following model to estimate the resilient modulus, M_R, of LCC as a function of the confining stress, σ_3, in psi, modulus of elasticity from the UCS test, E_{TX}, in psi, the effective confining stress from the triaxial test, $\sigma'_{3.TX}$, in psi and γ_d, in pcf,

$$M_R = \frac{1}{\beta_{28} + \beta_{29} \cdot \ln(\sigma_3) + \beta_{30} \cdot \ln(E_{TX}) + \beta_{31} \cdot \ln(\sigma'_{3.TX}) + \beta_{32} \cdot \sqrt{\gamma_d}} \quad (36)$$

The range of use with statistical significance for σ_3, E_{TX}, $\sigma'_{3.TX}$, and γ_d, in Equation 36, is limited to 1.7 psi to 20.1 psi, 15,410 psi to 51,660 psi, 3.0 psi to 12.0 psi, 18.9 pcf to 20.8 pcf, respectively. A summary of the regression results for Equation 36 are shown in Table 32. The regression statistics and ANOVA results for Equation 36 are shown in Table 33.

.

Table 32. Summary of the regression results for Equation 36.

Variable	Coefficient	Standard Error	*t*-statistic	*p*-value
b_{28}	2.184E-04	2.870E-05	7.612	1.275E-13
b_{29}	-2.648E-06	4.721E-07	-5.609	3.309E-08
b_{30}	-3.885E-06	1.170E-06	-3.320	9.623E-04
b_{31}	-1.560E-06	6.631E-07	-2.352	1.905E-02
b_{32}	-3.411E-05	5.860E-06	-5.820	1.032E-08

Table 33. Regression statistics and ANOVA results of Equation 36.

Multiple R	0.3702
R square	0.1371
Adjusted R square	0.1304
Standard error	0.00
Observations	525

Variation source	Degrees of freedom	Sum of squares	Mean square	*F*-statistic	*p*-value
Regression	4	4.314E-09	1.079E-09	20.65	8.300E-16
Residual	520	2.716E-08	5.22E-11		
Total	524	3.148E-08			

CHAPTER 9

CONCLUSIONS

LCC is increasingly utilized in geotechnical applications, particularly in roadway projects. Typical LCC applications for these projects include use as flowable fill, retaining wall backfill, and vertical stress reduction as large inclusions in earthen embankments. The data presented in the literature for LCC is relatively sparse and is based mainly on the unconfined compression test in a dry state or, in some limited cases, a confined state and either dry or fully saturated. Observations from the dry vs. saturated test data indicate a transition from a brittle failure behavior in the dry state to an elastoplastic failure behavior at full saturation. Additionally, increasing confinement has shown (1) no conclusive effect on the hydraulic conductivity, and in some cases, a (2) decrease in the initial yield stress has been observed. In addition, no studies or data are presented in the literature on the use of LCC in pavement sections as a base or subbase material for roadways. LCC is typically deployed in a buried configuration in roadway and other applications where partial saturation is inevitable. Therefore, the in-situ LCC will experience partial saturation and significant differences in the principal stresses resulting from the applied live and dead loads.

This study's experimental findings and evaluations are based on a Type I LCC using an extensive laboratory testing program with various partial saturation treatments,

resulting in partial saturation degrees ranging from 2.8% to 20.4%. A high-humidity environment experiment yielded a minimum of 9% long-term saturation to represent field conditions above the water table.

We found that an initial curing period of approximately 70 days is required for the LCC to reach a reasonable steady state condition. This finding is based on a series of dry uniaxial compressive strength (UCS) tests carried out as a function of curing time. Normalizing our data to the 70-day strength allowed for reasonable comparisons, thus preventing erroneous comparisons and interpretations and providing a long-term strength value for design.

The resilient modulus (RM) tests were performed under a nominal range of confinement from three psi to 20 psi and a nominal deviatoric stress range from three psi to 40 psi, which are typical test ranges for base and subbase materials. The average resilient modulus was 71 ksi, comparable to the compacted granular materials results of Davich et al., (2004). We note that the RM results were somewhat affected by sample confinement but not significantly affected by increasing saturation. From these data, we developed an RM regression model for estimating the resilient modulus as a function of the confining, deviatoric stress, and the dry unit. Our favorable RM results suggest that LCC can be used as a base or subbase material over the range of saturation and stress conditions explored in this study.

The UCS results ranged from about 80 to 200 psi at or after the 70-day cure time. This relatively high variability was seen across all saturation ranges and cure times. We believe that the source of the UCS is complex and primarily results from a combination of chemical bonding of the cement particles achieved during cement hydration and curing

and a minor component from matric suction. The UCS test results show that the unconfined strength and its modulus are reduced by increasing the degree of saturation, but the effect is relatively minor. Nonetheless, we developed predictive models for estimating (1) the peak UCS, (2) initial yield stress, and (3) uniaxial Young's modulus for LCC as a function of the dry unit weight and the degree of saturation.

However, we found that the degree of saturation significantly influences the strength and modulus in drained triaxial compression more so than the confinement effect. Previous research suggests that LCC should be viewed as a cohesionless material with an effective friction angle of up to 40° for normal stresses up to 145 psi. However, our data suggest an effective friction angle of 65° for partially saturated conditions as a reasonable mean estimate for cases below 12 psi confinement. Further, we found a mean Poisson's ratio of 0.231 (i.e., at-rest lateral earth pressure coefficient of 0.3). These mean values are recommended for all degrees of saturation.

Predictive models were developed to estimate the confined-drained Young's modulus, initial yield, and peak deviatoric stresses. The confined Young's modulus for LCC is a function of the effective confining stress, the dry unit weight, and the degree of saturation. The yield stress models are a function of the effective confining stress and the degree of saturation.

We developed UCS and triaxial compression test data to make a "surrogate" estimate of the resilient modulus RM for engineering practice. This development incorporated a height-to-diameter ratio correction. The UCS-RM surrogate model is a function of confining stress, dry unit weight, uniaxial Young's modulus, and the degree of saturation. The drained triaxial compression surrogate model is a function of the

pavement confining stress, the confined Young's modulus, the triaxial effective confining stress, and the dry unit weight. The predictive models are suggested for preliminary engineering estimations and are limited to the ranges presented for this study. For the final design, we encourage RM testing, as applicable, due to the variability of the LCC material and the relative importance of the project.

CHAPTER 10

IMPLEMENTATION AND FUTURE WORK

Limitations

The data set generated for this study is limited to Type I (Table 1) LCC of a particular mix design using the foaming agent and specimens provided by Aerix Industries (Figure 2). The reported Poisson ratio was 0.231, and the resulting K_0 was 0.3. The recommended effective friction angle of 65° is a reasonable mean design estimate for confining pressures (i.e., σ'_3) at or below 12 psi. The drained friction angle and Poisson's ratio are essential for designing retaining walls, buried structures, culverts, tunnels, and slope stabilization projects.

Implementation and reliance on the MLR models presented for this study have limitations. The first and most narrow limitation is the cured dry unit of the LCC, which ranges from 18.9 pcf to 20.8 pcf. LCC mixes with higher densities have the potential to be stiffer and stronger, and our work may not produce representative design values for these mixes.

The second limitation of the MLR models is the degree of saturation, which ranges from 2.8% to 20.4%. However, we believe that short of the complete inundation of the LCC for an extended period, the range of saturation we tested will likely cover the partially saturated conditions encountered in many, if not most, roadway and field

applications. In addition, the RM testing was limited to the stress ranges shown in Table 12. The data from the drained triaxial compression tests are limited to nominal effective confining stress from 2.5 psi up to 12 psi. However, these stress ranges are typical for base/subbase materials and moderately high retaining systems and embankments.

Further details of the limitations of each model are presented in Chapter 8, but the guidelines above are a reasonable summary. Lastly, engineering judgment should be exercised when utilizing the models and extrapolating beyond these limitations or for other uses and applications of LCC.

Future Work

Although the data set generated for this study is comprehensive, future work should include expanding the data set based on the cured dry unit weight of the LCC to cover the spectrum of values presented in Table 1. Further investigation is also warranted to advance understanding of the role of excess pore pressure and matric suction for partially saturated LCC during monotonic and cyclic loading.

Regarding pavement systems, future work should include an instrumented field demonstration project for roadways or bridge approaches. Possible application(s) include LCC underneath a roadway pavement or a concrete bridge approach slab. Instrumentation of the project should consist of measurements of stress and strain and monitoring of permanent distress within the LCC and manifestations at the pavement surface. Since LCC is susceptible to freeze/thaw damage yet has good insulation properties, instrumentation should also include monitoring the temperature within the

LCC to estimate long-term freeze/thaw performance. Also, the field demonstration project could consist of sections that cover the full range of LCC types.

Industry Standards

As the use of LCC increases in geotechnical applications, a standardized testing program should be established for LCC design. This standardization should include test specimen preparation procedures and expansion beyond UCS testing of air-dried samples. This study contributes significantly to developing methods for evaluating the effects of partial saturation and confinement on LCC's low and high-strain stiffness and strength properties.

As mentioned in this study, cast test specimens for LCC typically exhibit a "soft bottom," which may significantly affect laboratory testing results. Complete removal of this material is imperative for reasonable test result comparison. The current standard Styrofoam molds create a three-inch diameter by six-inch long specimen, which must be trimmed and squared. As discussed previously, the $R_{H:D}$ may affect the results from laboratory tests. It is recommended that the LCC industry employ a longer cast length of seven inches, allowing for the complete removal of the "soft bottom" and yielding a test specimen with an $R_{H:D}$ of at least two.

APPENDIX A

PARTIALLY SATURATED STATISTICAL ANALYSIS

LCC sample treatment saturation statistical evaluation

Dan Seely
8/23/2023

Test sample saturation (%) sorted by treatments:

AD = Air-dried
H_{100} = High humidity environment for one week
M_5 = submerged in water for 5 minutes then high humidity environment for 1 week
D_1 = submerged in water 1 day then high humidity environment for 1 week
W_1 = submerged in water 1 week then high humidity environment for 1 week

AD	H_{100}	M_5	D_1	W_1
2.955	4.449	11.907	15.986	17.531
3.091	4.441	9.783	15.504	18.374
3.067	4.275	10.281	15.480	20.368
3.122	4.227	9.679	15.802	19.438
3.620	4.981	10.444	17.123	18.652
3.716	4.647	10.055	17.533	16.078
3.541	4.967	9.884	15.493	15.842
3.455	4.996	9.860	15.764	17.084
3.449	5.033	9.889	17.973	18.536
3.329	5.100	9.389	15.708	18.283
4.014	5.288	9.142	15.832	17.781
3.825	5.112	9.293	17.547	18.503

Sample means:

$\mu_{AD} := \text{mean}(AD) = 3.432$

$\mu_{H100} := \text{mean}(H_{100}) = 4.793$

$\mu_{M5} := \text{mean}(M_5) = 9.967$

$\mu_{D1} := \text{mean}(D_1) = 16.312$

$\mu_{W1} := \text{mean}(W_1) = 18.039$

Dan Seely
8/23/2023

Population standard deviations:

$\sigma_{AD} := \text{stdev}(AD) = 0.317$

$\sigma_{H100} := \text{stdev}(H_{100}) = 0.349$

$\sigma_{M5} := \text{stdev}(M_5) = 0.690$

$\sigma_{D1} := \text{stdev}(D_1) = 0.900$

$\sigma_{W1} := \text{stdev}(W_1) = 1.235$

Histogram data:

$n_{bins} := 7$

$5\ H_{AD\_}y$

$\text{dnorm}(x, \mu_{AD}, \sigma_{AD})$

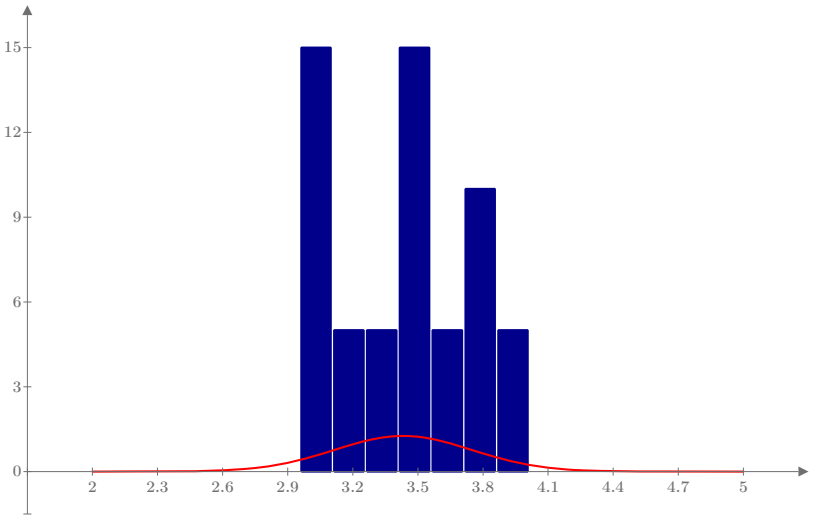

$H_{AD\_}x$

x

Figure 1. Histogram and normal probability distribution plot of saturation for data set AD.

Dan Seely
8/23/2023

$H_{H100\_}y$

$\text{dnorm}\left(x, \mu_{H100}, \sigma_{H100}\right)$

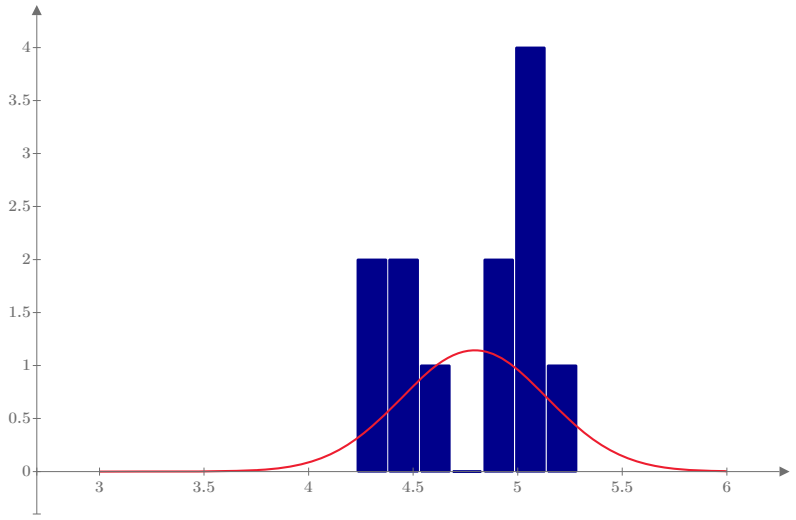

$H_{H100\_}x$

x

Figure 2. Histogram and normal probability distribution plot of saturation for data set H_{100}.

$H_{M5\_}y$

$\text{dnorm}\left(x, \mu_{M5}, \sigma_{M5}\right)$

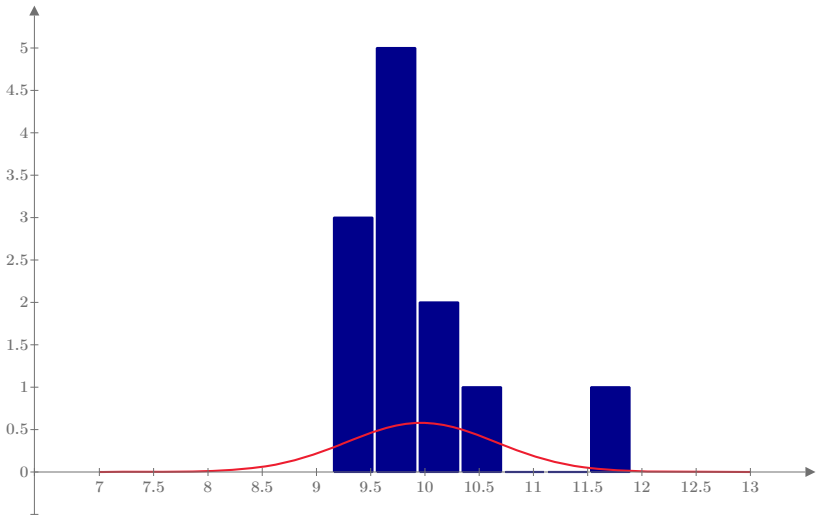

$H_{M5\_}x$

x

Figure 3. Histogram and normal probability distribution plot of saturation for data set M_5.

Dan Seely
8/23/2023

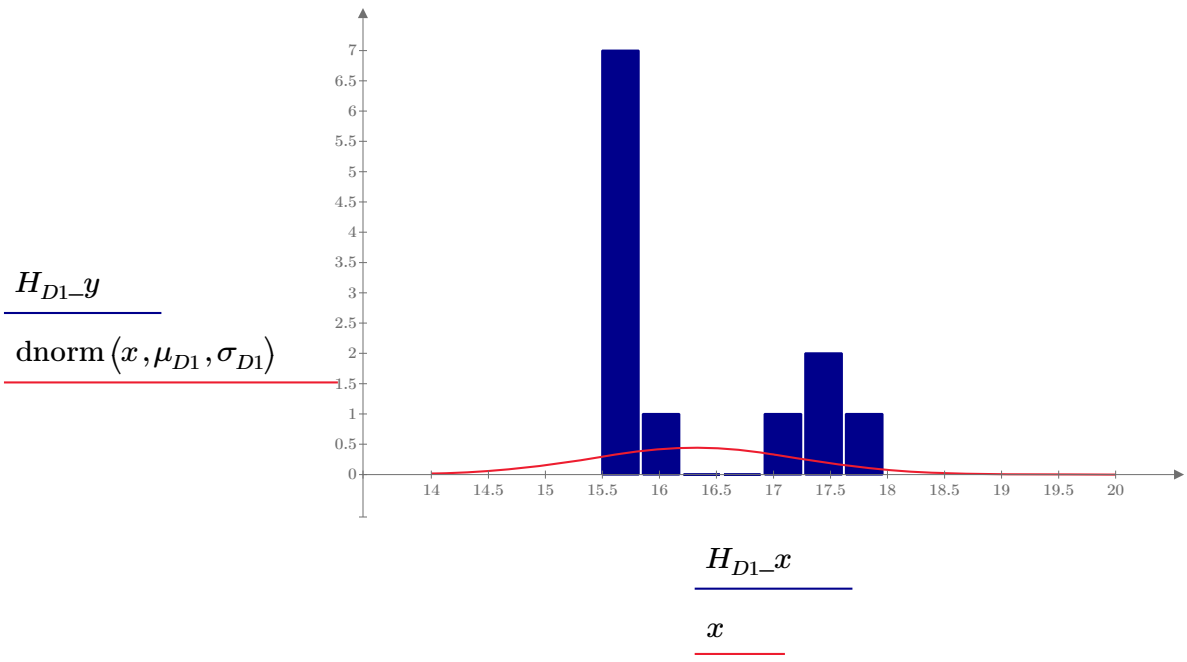

Figure 4. Histogram and normal probability distribution plot of saturation for data set D_1.

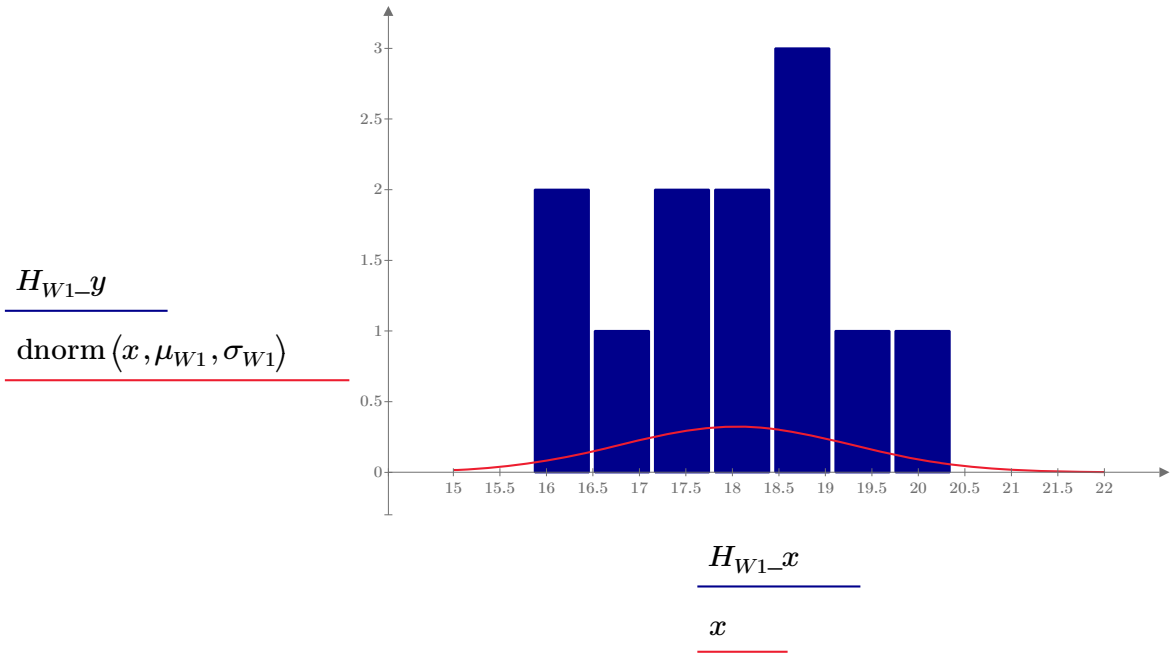

Figure 5. Histogram and normal probability distribution plot of saturation for data set W_1.

Dan Seely
8/23/2023

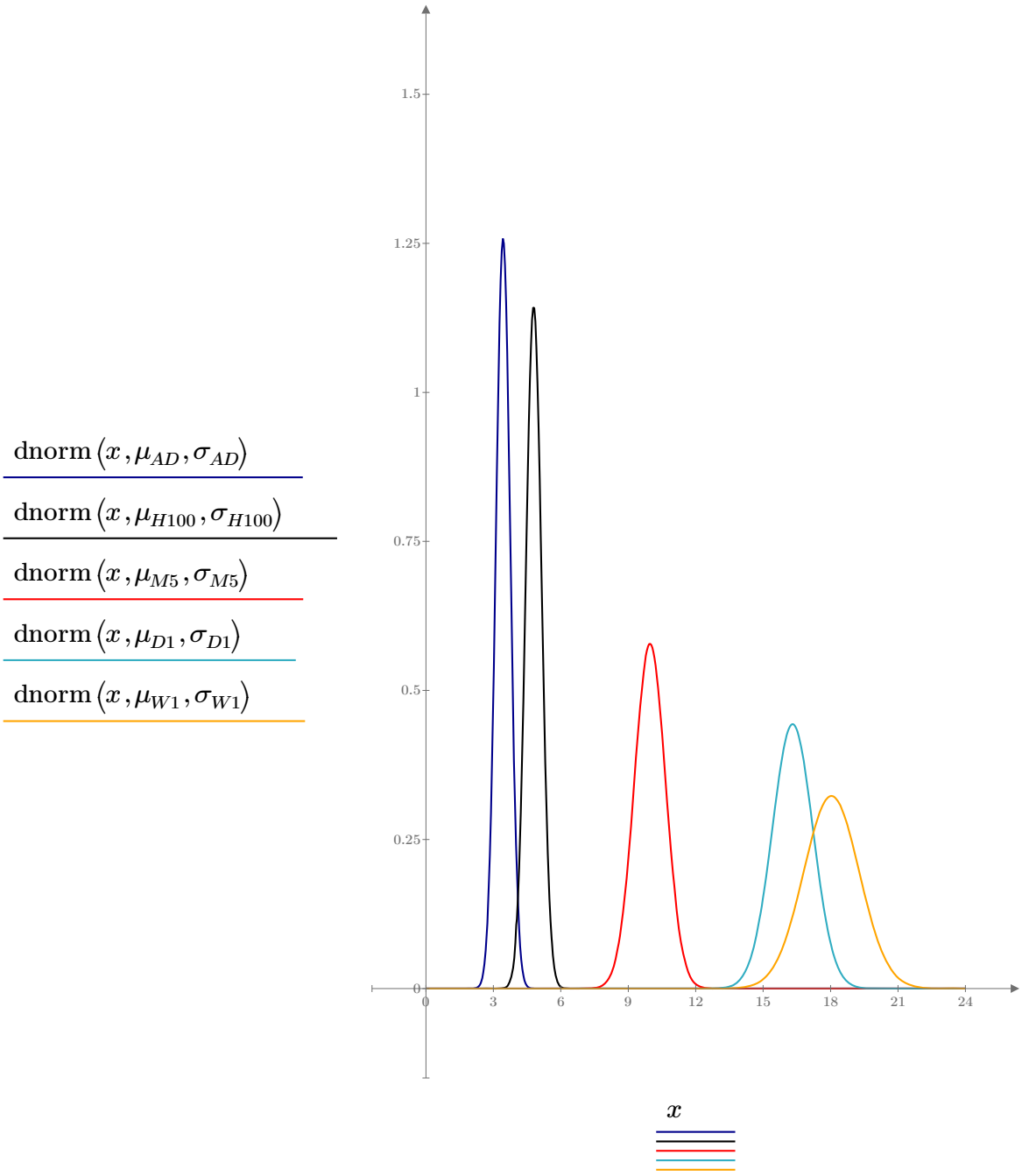

Figure 6. Composite normal probability distribution plots of saturation for all data sets. Note the variability increases with the degree of saturation.

Dan Seely
8/23/2023

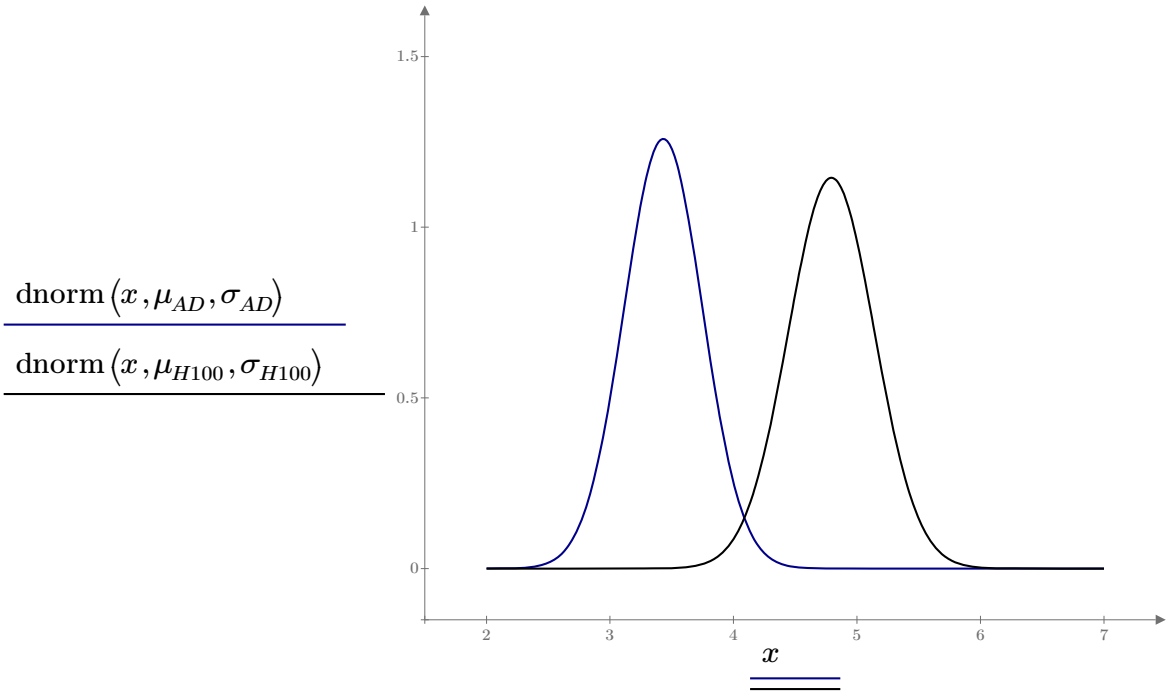

Figure 7. Comparison of the normal distribution plots of AD and H_{100}.

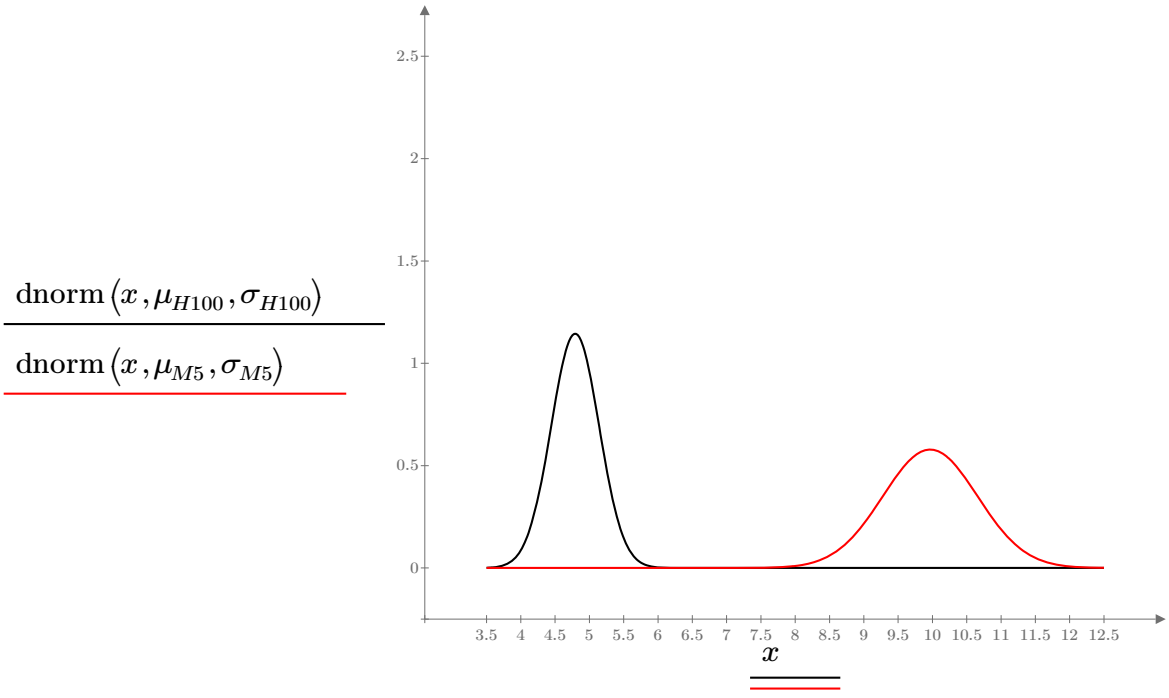

Figure 8. Comparison of the normal distribution plots of H_{100} and M_5.

Dan Seely
8/23/2023

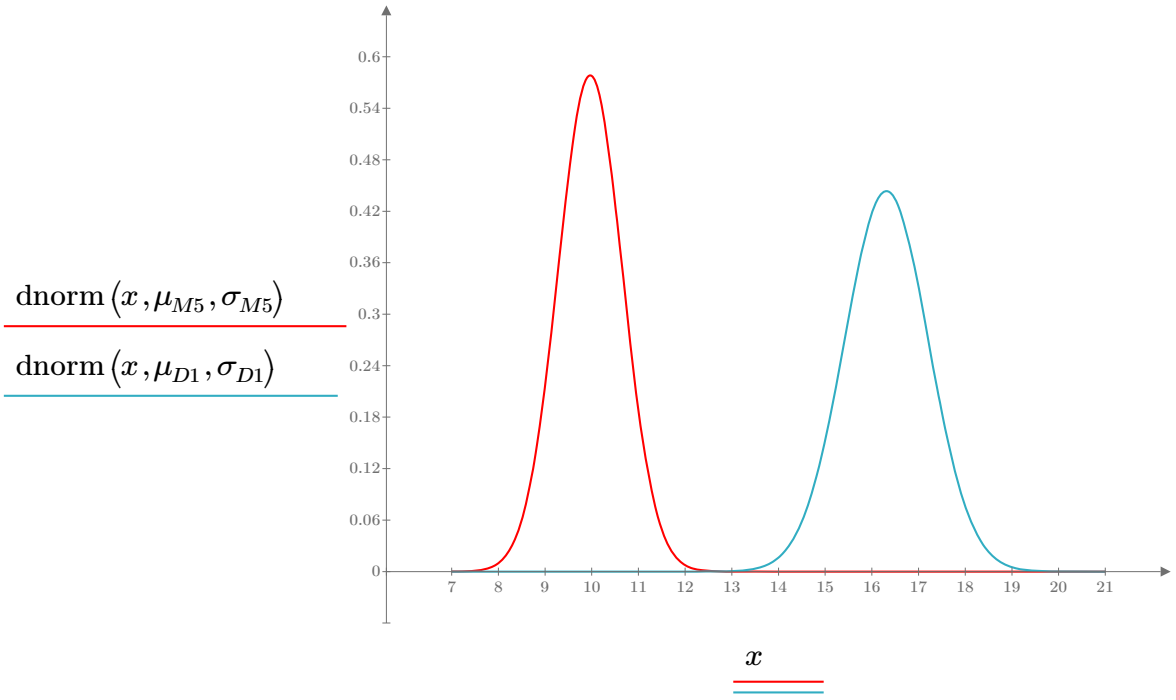

Figure 9. Comparison of the normal distribution plots of M_5 and D_1.

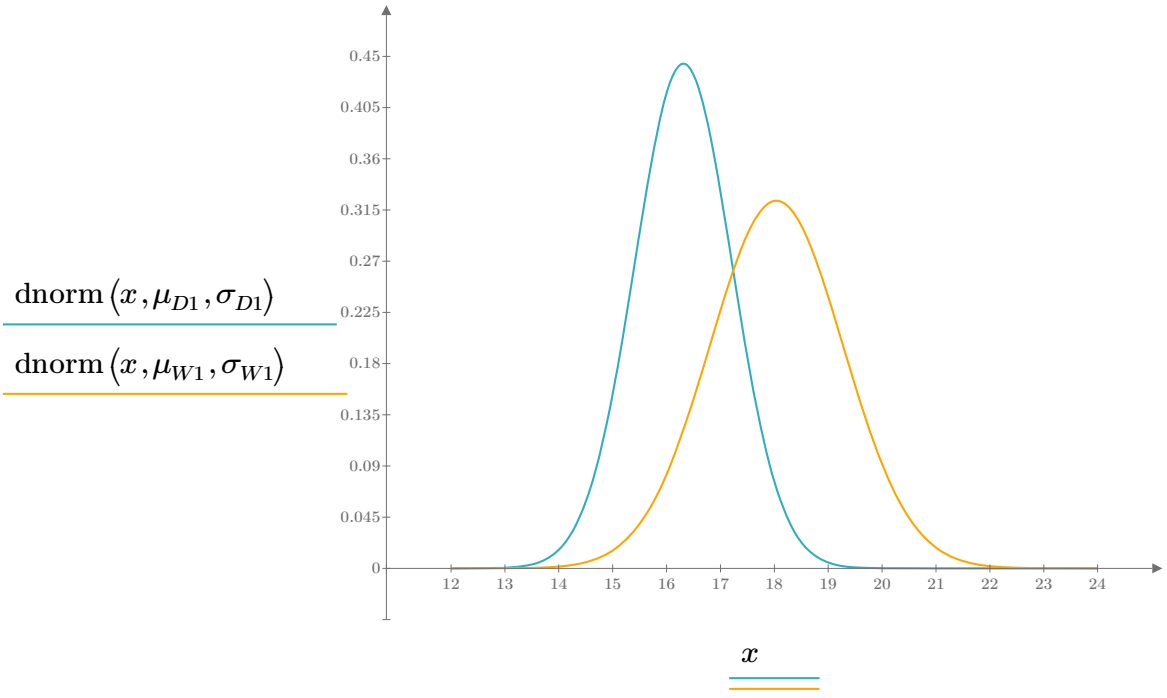

Figure 10. Comparison of the normal distribution plots of D_1 and W_1. Additional analysis is warranted to determine if there is a significant difference between the means of the two sets.

Dan Seely
8/23/2023

Box plot data:

$$BP_{AD} := \text{boxplot}(AD) = \begin{bmatrix} 3.099 \\ 3.452 \\ 3.692 \\ 2.955 \\ 4.014 \end{bmatrix}$$

25% quartile
50% quartile
75% quartile
Minimum of data set
Maximum of the data set

$$BP_{H100} := \text{boxplot}(H_{100}) = \begin{bmatrix} 4.443 \\ 4.974 \\ 5.083 \\ 4.227 \\ 5.288 \end{bmatrix}$$

$$BP_{M5} := \text{boxplot}(M_5) = \begin{bmatrix} 9.462 \\ 9.872 \\ 10.225 \\ 9.142 \\ 10.444 \\ 11.907 \end{bmatrix}$$

$$BP_{D1} := \text{boxplot}(D_1) = \begin{bmatrix} 15.555 \\ 15.817 \\ 17.431 \\ 15.48 \\ 17.973 \end{bmatrix}$$

$$BP_{W1} := \text{boxplot}(W_1) = \begin{bmatrix} 17.196 \\ 18.329 \\ 18.623 \\ 15.842 \\ 20.368 \end{bmatrix}$$

Dan Seely
8/23/2023

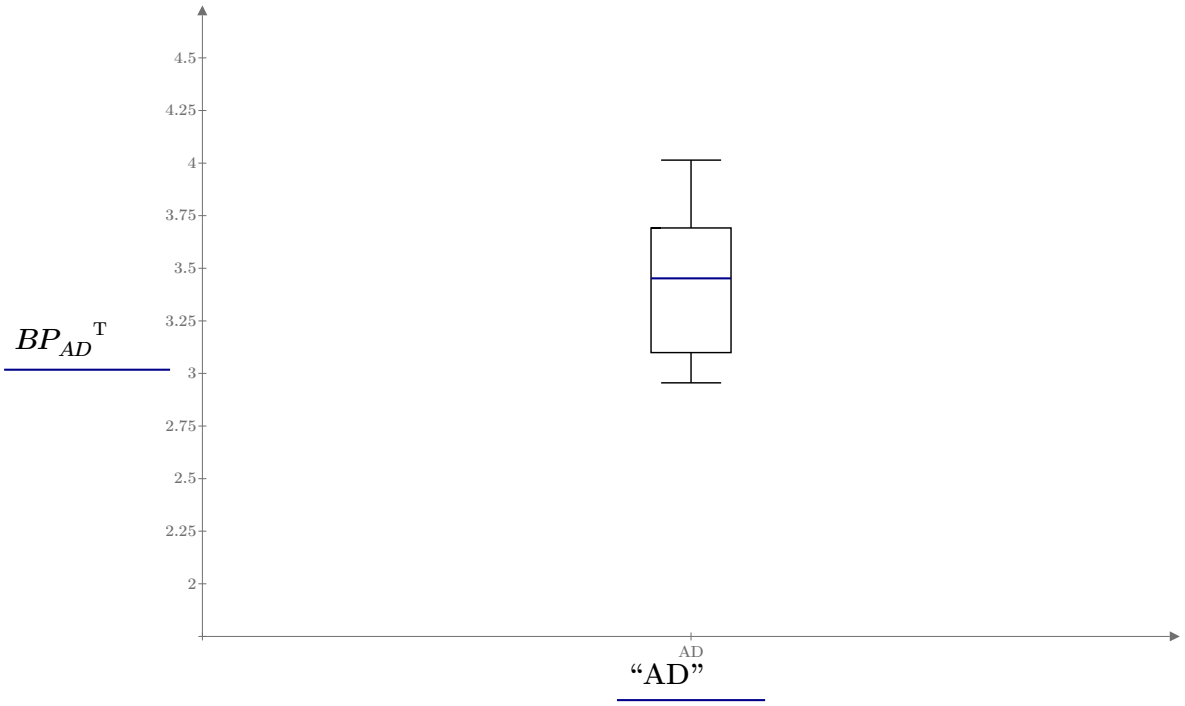

Figure 10. Box plot of the saturation for data set AD.

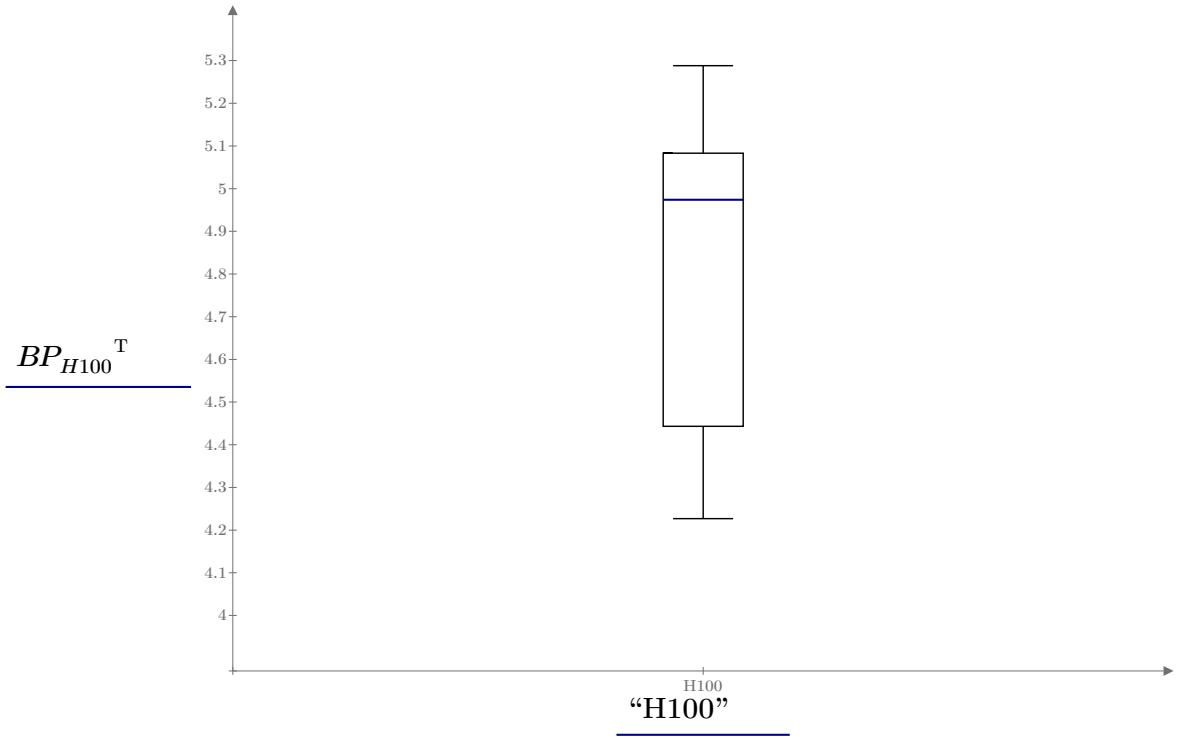

Figure 11. Box plot of the saturation for data set H_{100}.

Dan Seely
8/23/2023

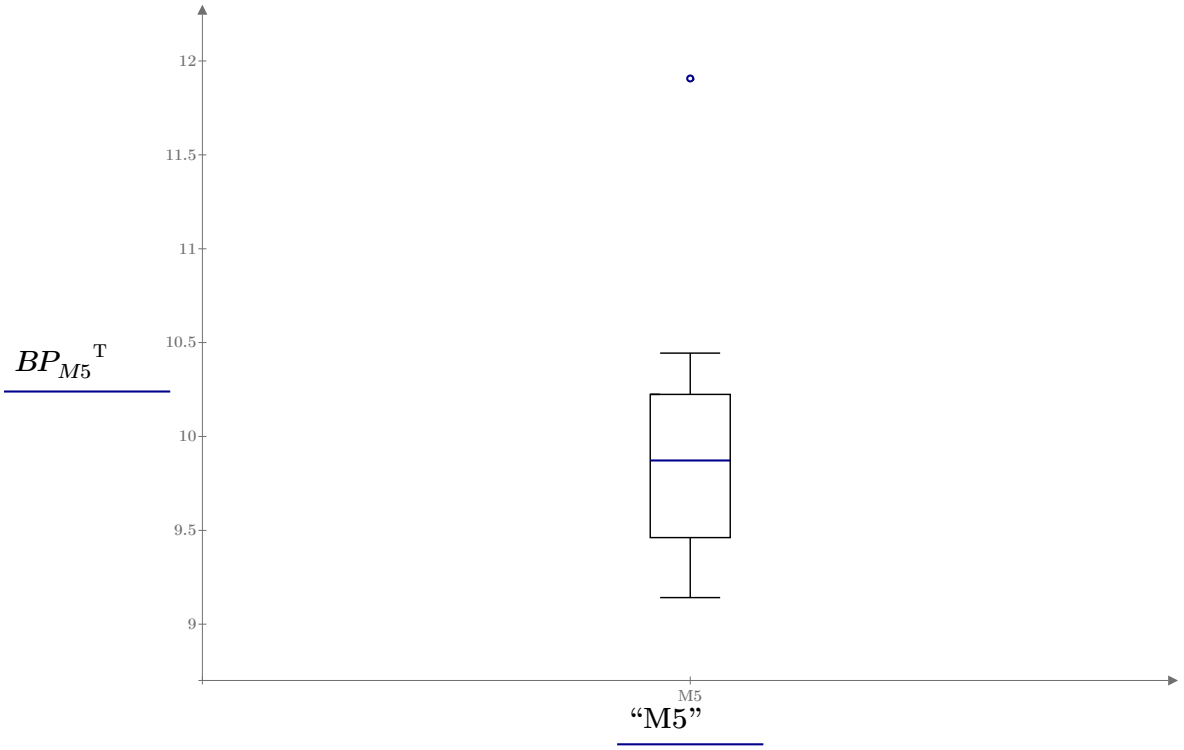

Figure 12. Box plot of the saturation for data set M_5.

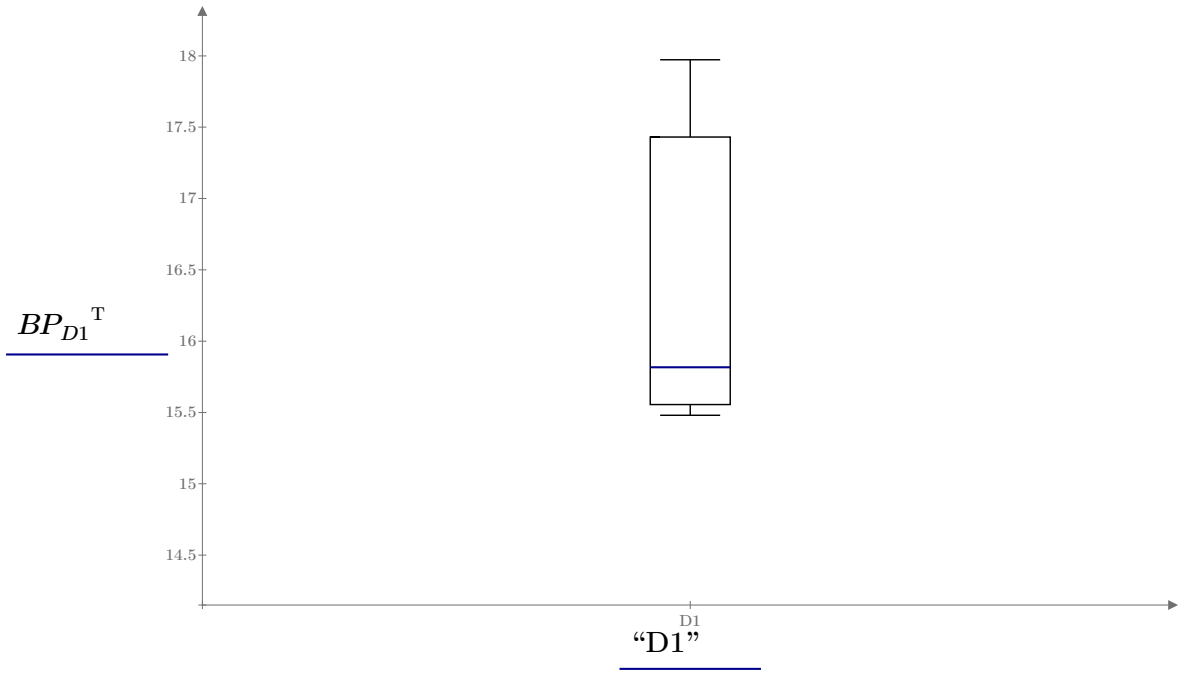

Figure 13. Box plot of the saturation for data set D_1.

Dan Seely
8/23/2023

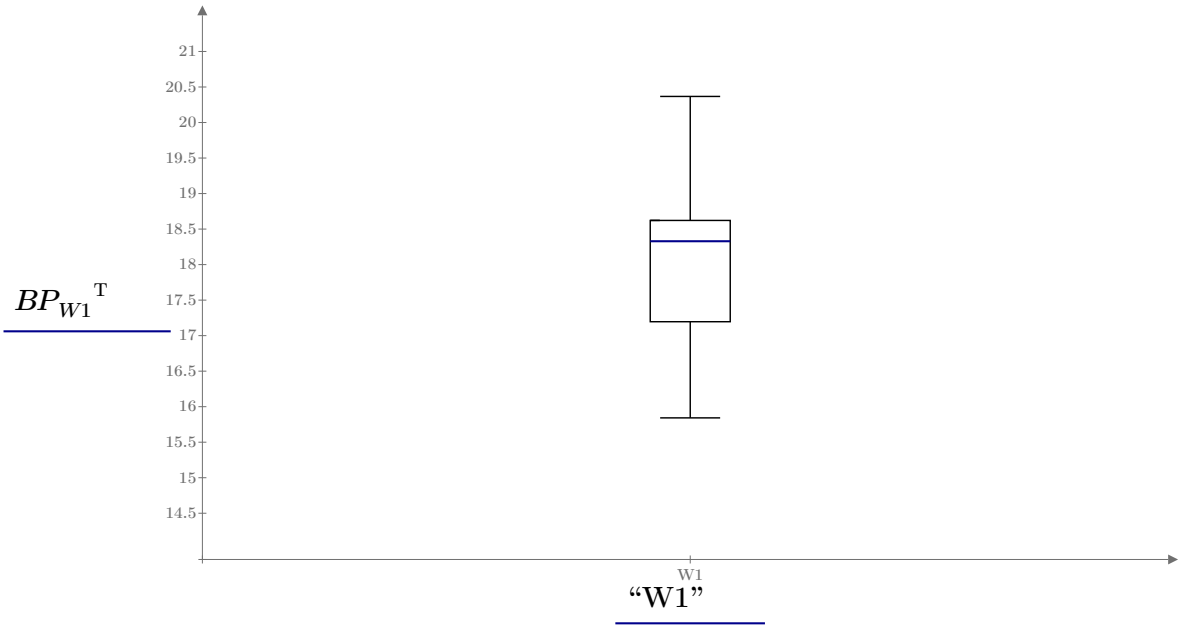

Figure 14. Box plot of the saturation for data set W_1.

Dan Seely
8/23/2023

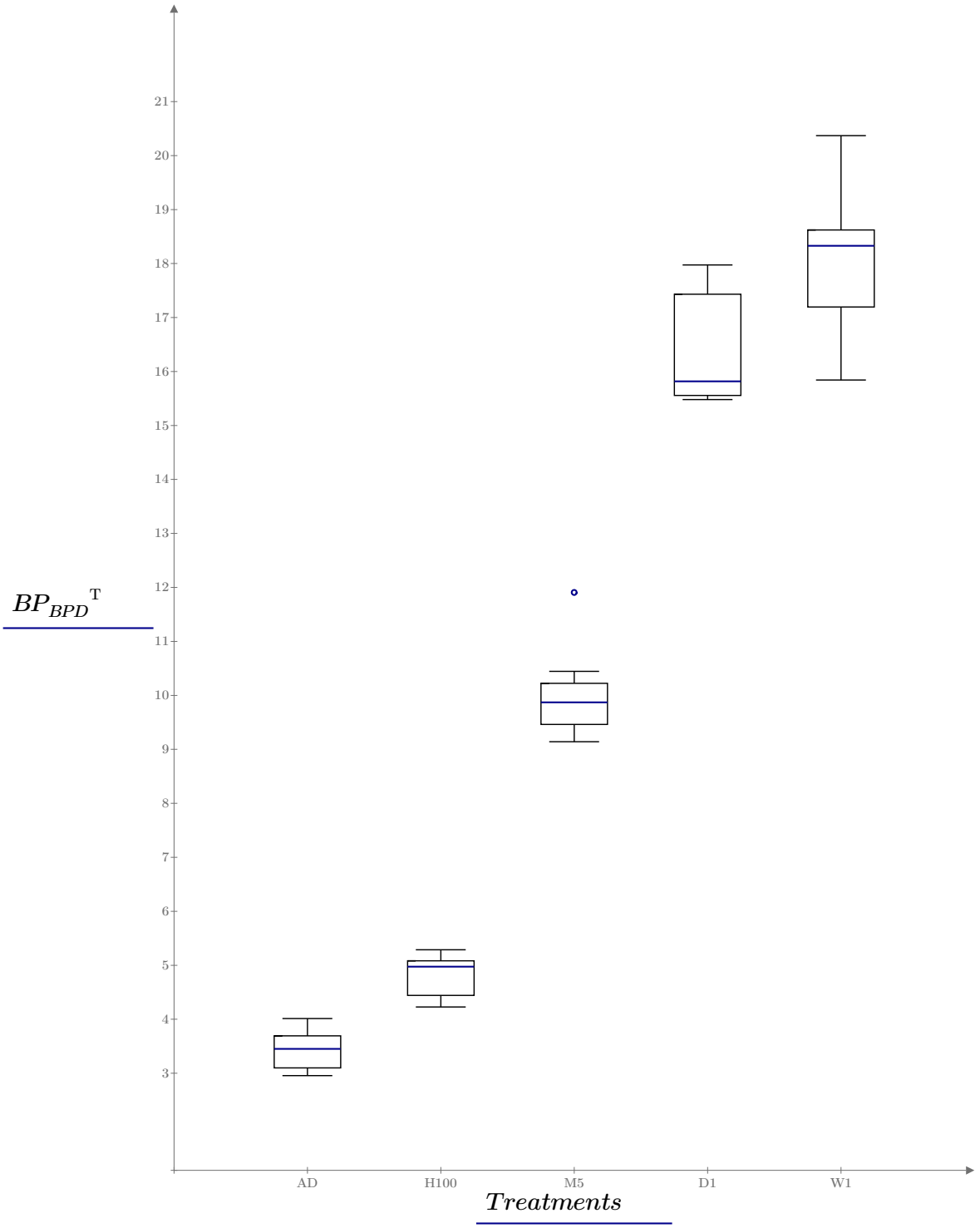

Figure 15. Comparison box plot of the saturation for all data sets.

Dan Seely
8/23/2023

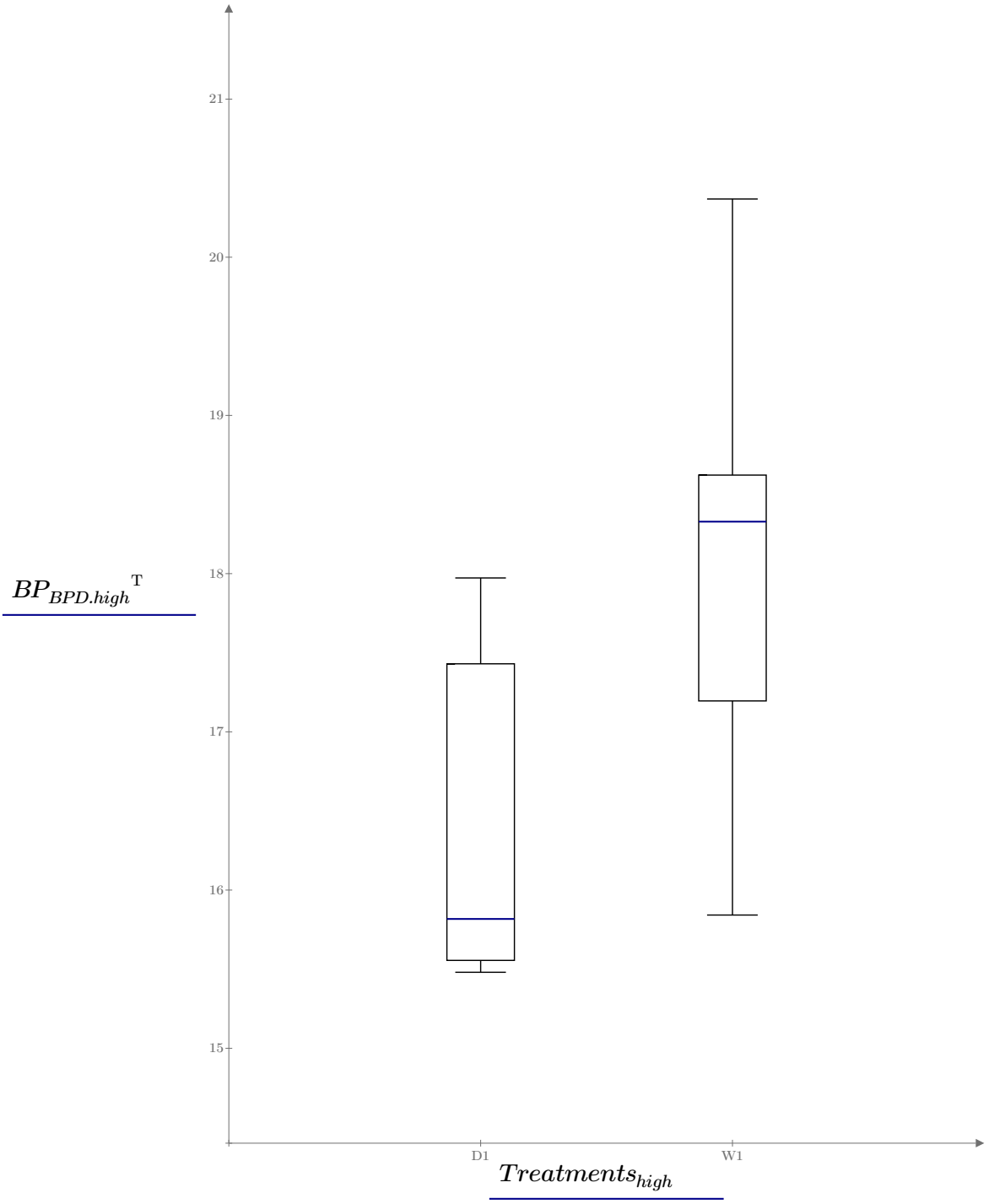

Figure 16. Comparison box plot of the saturation for data sets D_1 and W_1. Additional analysis is warranted to determine if there is a significant difference between the means of the two sets.

Dan Seely
8/23/2023

Upon inspection of the histograms, probability distribution curves and the box plots, further inspection is warranted to evaluate whether or not there is a difference between group D_1 and group W_1.

Hypothesis testing (F-test):

Since it is evident that the variance increases with an increase in saturation due to the treatments, an initial F-test is warranted to test for equal variance in the two data sets to decide on a pooled-variance t-test or an independent variance t-test is appropriate:

Null and alternate hypothesis:

H0: There is no statistically significant difference between the variance of the two data sets.
H1: There is a statistically significant difference between the variance of the two data sets.

$\alpha := 0.05$ Significance level

$DF_{D1} := \text{length}\left(D_1\right) - 1 = 11$ Degrees of freedom

$DF_{W1} := \text{length}\left(W_1\right) - 1 = 11$ Degrees of freedom

$\text{F} := \text{Ftest}\left(D_1, W_1\right) = \begin{bmatrix} 1.885 \\ 0.308 \end{bmatrix}$ F-test statistic
Probability the statistic is larger

$crit_F := \text{qF}\left(1 - \alpha, DF_{D1}, DF_{W1}\right) = 2.818$

$\text{F}_0 > crit_F = 0$ Hypothesis test, reject H0, accept H1

Since there is statistical evidence of a difference between the variance between the two data sets, an independent variance t-test is warranted.

Dan Seely
8/23/2023

Hypothesis testing (t-test, independent variance):

Null and alternate hypothesis:

H0: There is no significant difference between the two samples.
H1: m1 < m2 (means)

$n1 := \text{length}\left(D_1\right) = 12$

$n2 := \text{length}\left(W_1\right) = 12$

No. samples for each data set

$m1 := \text{mean}\left(D_1\right) = 16.312$

$m2 := \text{mean}\left(W_1\right) = 18.039$

Sample Means

$s1 := \text{stdev}\left(D_1\right) \cdot \sqrt{\frac{n1}{n1-1}} = 0.94$

$s2 := \text{stdev}\left(W_1\right) \cdot \sqrt{\frac{n1}{n1-1}} = 1.29$

Sample standard deviations

$\nu := n1 + n2 - 2 = 22$

Degrees of freedom

$w1 := \frac{s1^2}{n1} = 0.074$

Weight factor 1

$w2 := \frac{s2^2}{n2} = 0.139$

Weight factor 2

$t := \frac{|m1 - m2|}{\sqrt{\frac{s1^2}{n1} + \frac{s2^2}{n2}}} = 3.749$

Test statistic (t-value)

$crit_{D1} := \left|\text{qt}\left(\frac{\alpha}{2}, n1-1\right)\right| = 2.201$

Critical value, D_1

$crit_{W1} := \left|\text{qt}\left(\frac{\alpha}{2}, n2-1\right)\right| = 2.201$

Critical value, W_1

Dan Seely
8/23/2023

$$crit_t := \frac{w1 \cdot crit_{D1} + w2 \cdot crit_{W1}}{w1 + w2} = 2.201$$ Weighted critical value.

$t > crit_t = 1$ Hypothesis test, reject H0, accept H1

Since the t-value is greater than the critical value, we reject the null hypothesis, H0, and accept the alternate hypothesis, H1.

There *is* statistical evidence that m1 < m2.

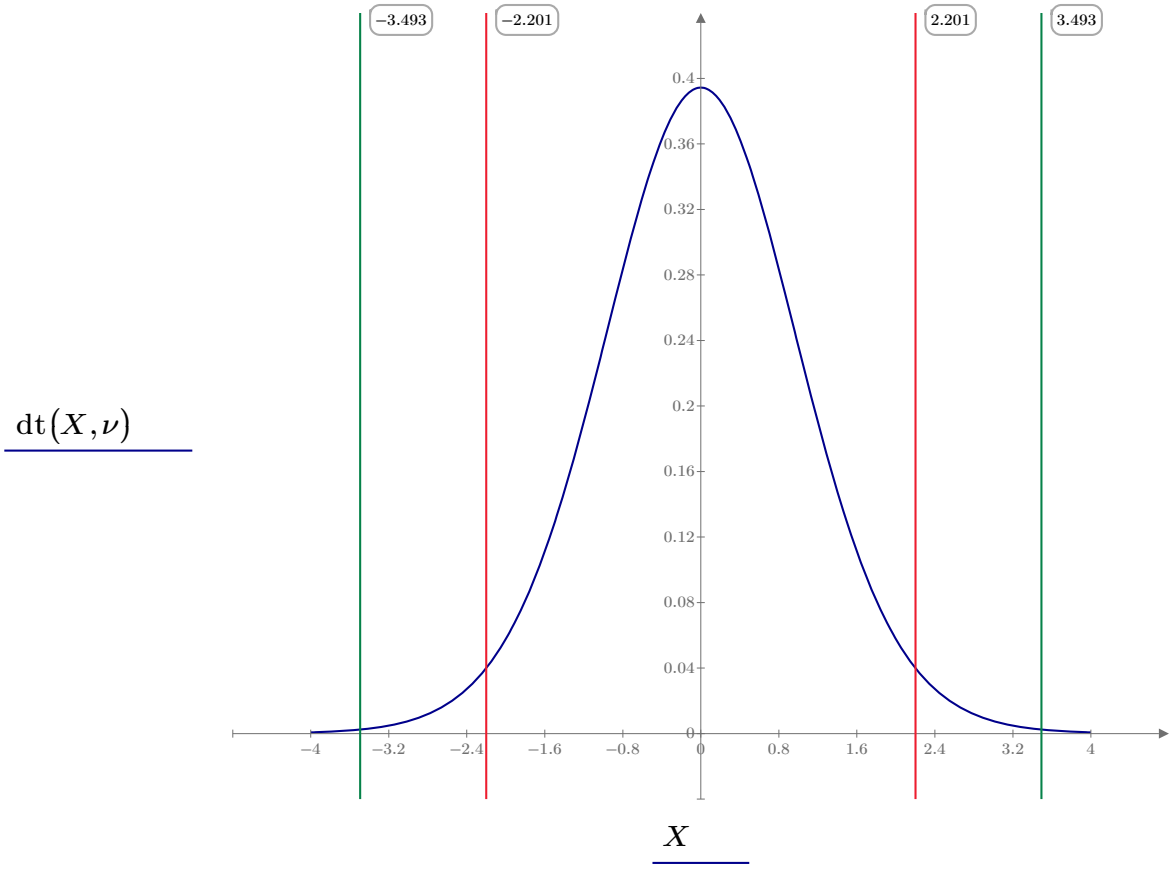

Figure 17. Plot of the critical values and t-statistic values for a t-distribution. Since the t-statistic falls outside of the 95% confidence area, Ho is rejected and H1 is accepted, therefore therefore there is statistical evidence that m1 < m2 and there is a difference in the means for D_1 and W_1 data sets.

APPENDIX B

CT IMAGES OF PARTIALLY SATURATED LCC

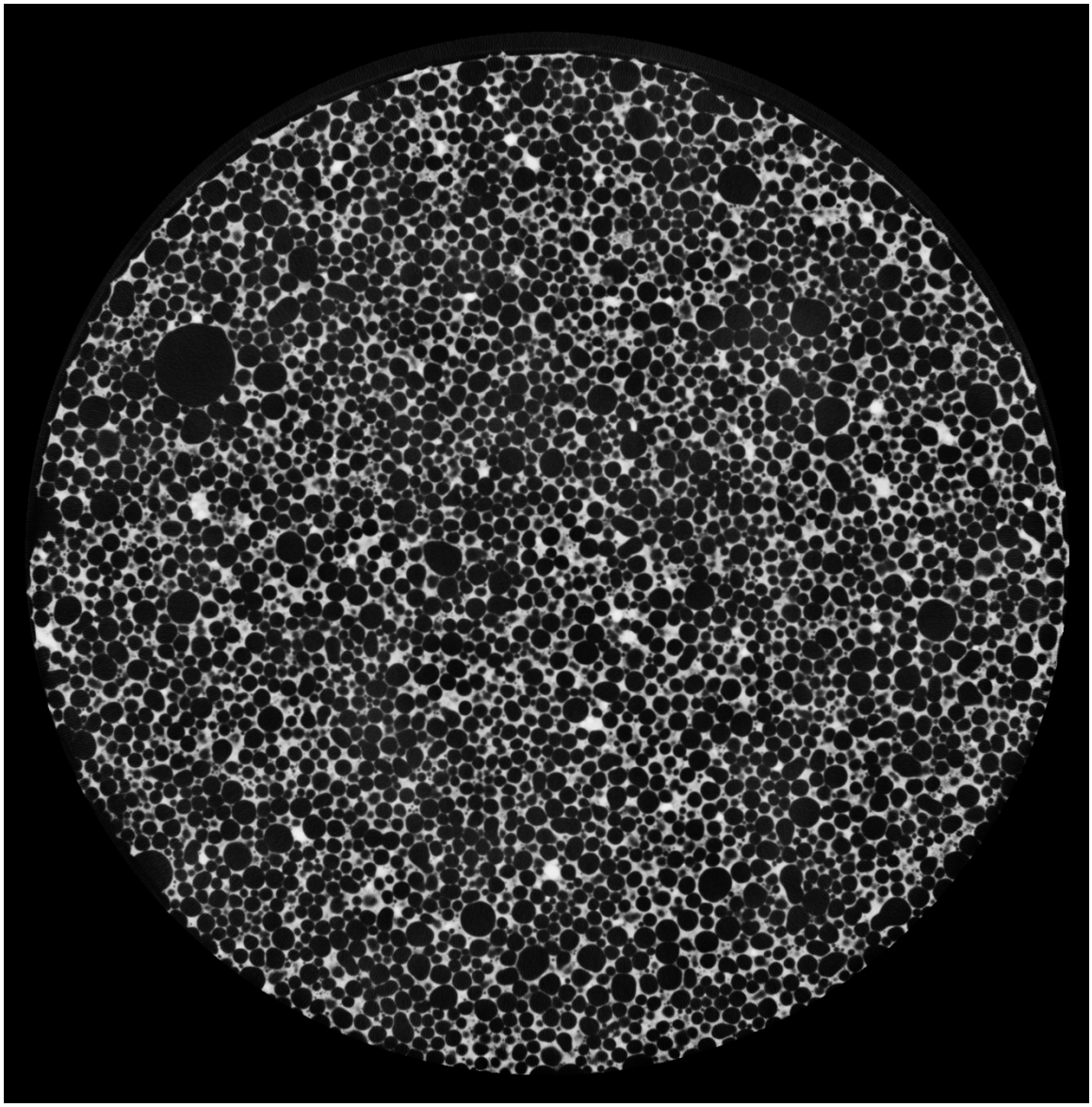

Figure 58. CT scan image of specimen B1-23 after the AD treatment, No. 0243.

The image cross-section is located 0.778” above the center of the specimen. The dark spherical objects are the foamed air voids, and the light matrix being the concrete skeleton structure. The degree of saturation is 1.61%. No free pore water is visible in the image.

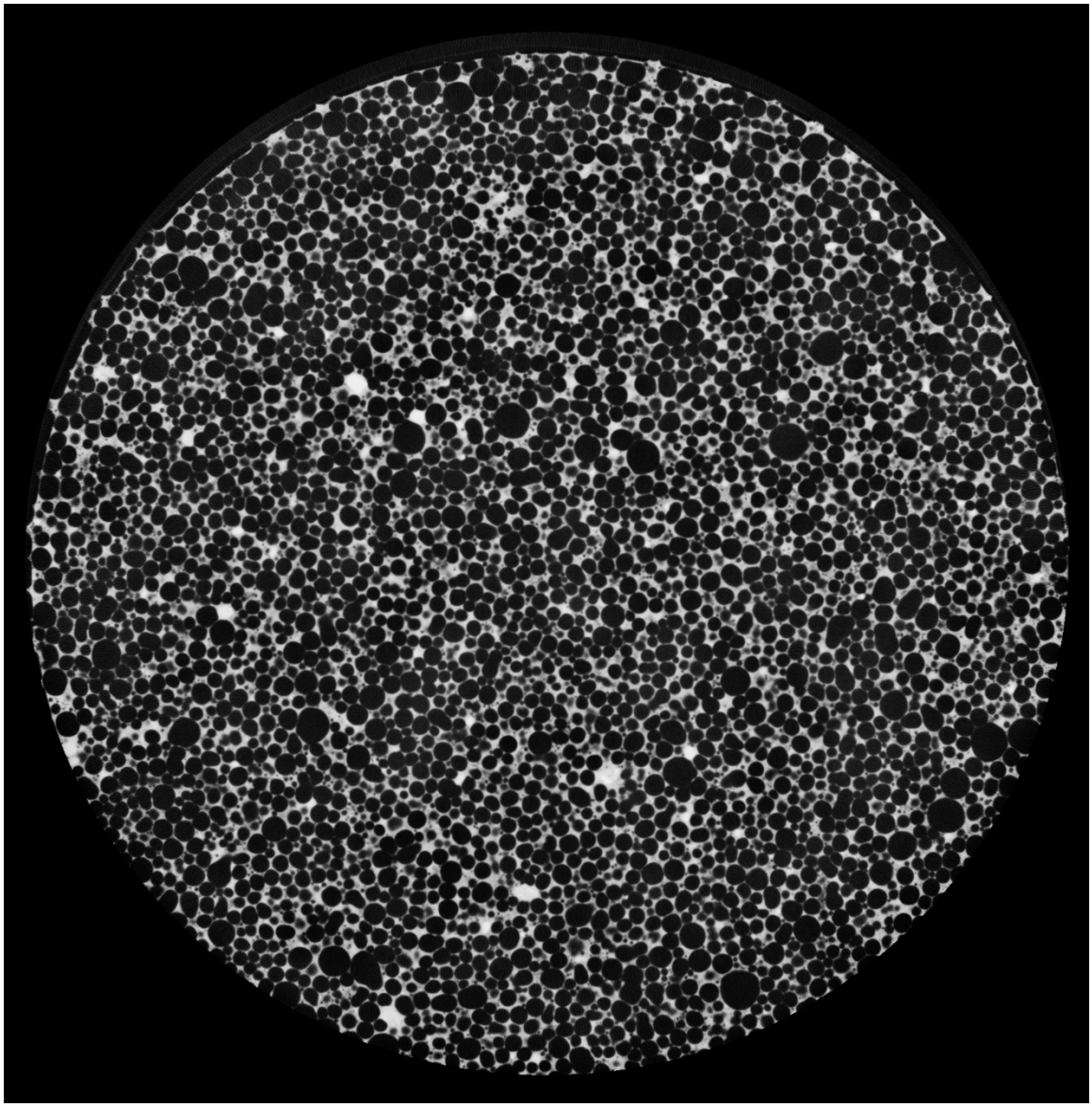

Figure 59. CT scan image of specimen B1-23 after the AD treatment, No. 0729.

The image cross-section is located 0.778” below the center of the specimen. The dark spherical objects are the foamed air voids, and the light matrix being the concrete skeleton structure. The degree of saturation is 1.61%. No free pore water is visible in the image.

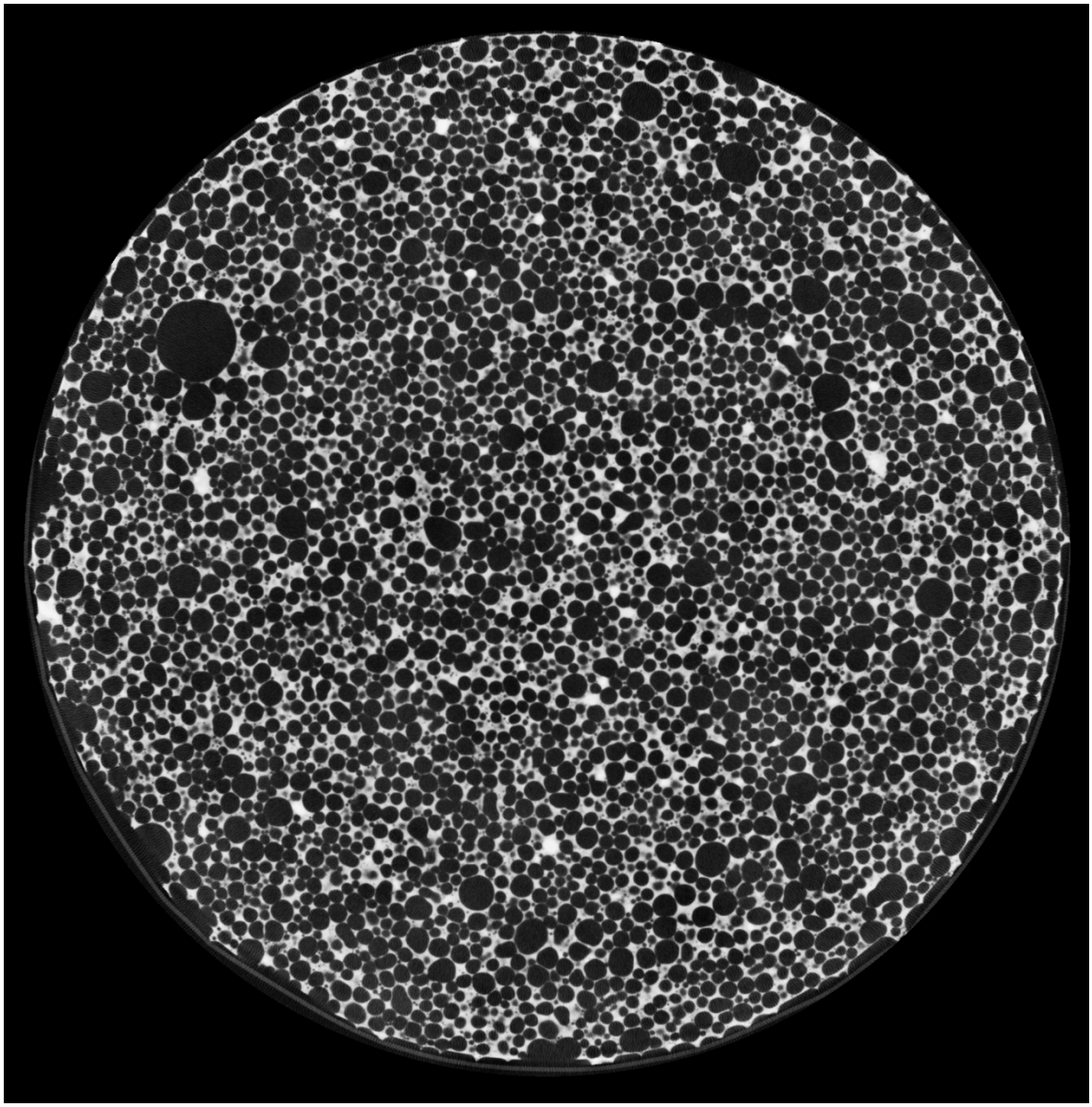

Figure 60. CT scan image of specimen B1-23 after the M5 treatment, No. 0243.

The image cross-section is located 0.778” above the center of the specimen. The dark spherical objects are the foamed air voids, and the light matrix being the concrete skeleton structure. The degree of saturation is 10.05%. No free pore water is visible in the image.

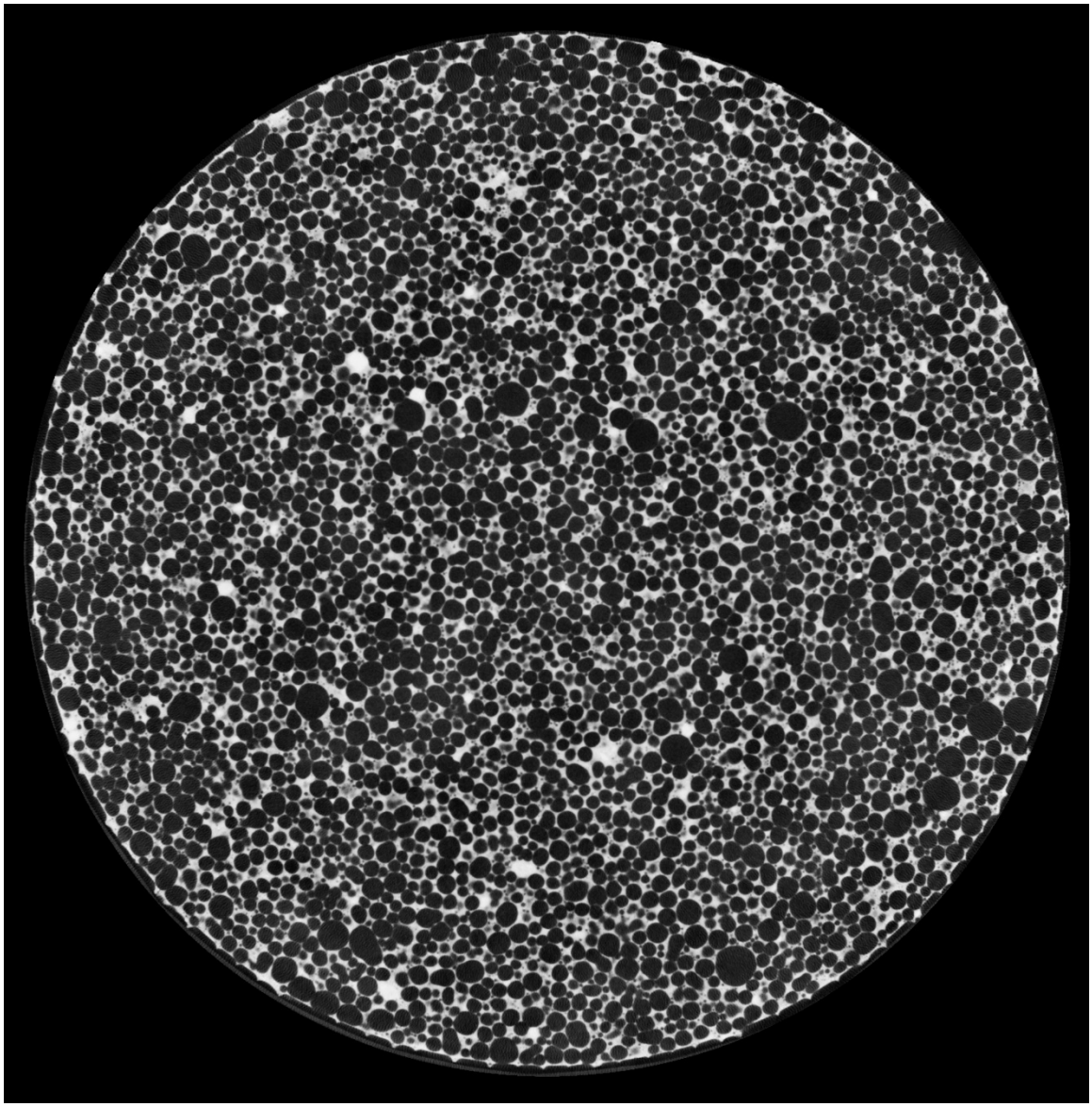

Figure 61. CT scan image of specimen B1-23 after the M5 treatment, No. 0729.

The image cross-section is located 0.778” below the center of the specimen. The dark spherical objects are the foamed air voids, and the light matrix being the concrete skeleton structure. The degree of saturation is 10.05%. No free pore water is visible in the image.

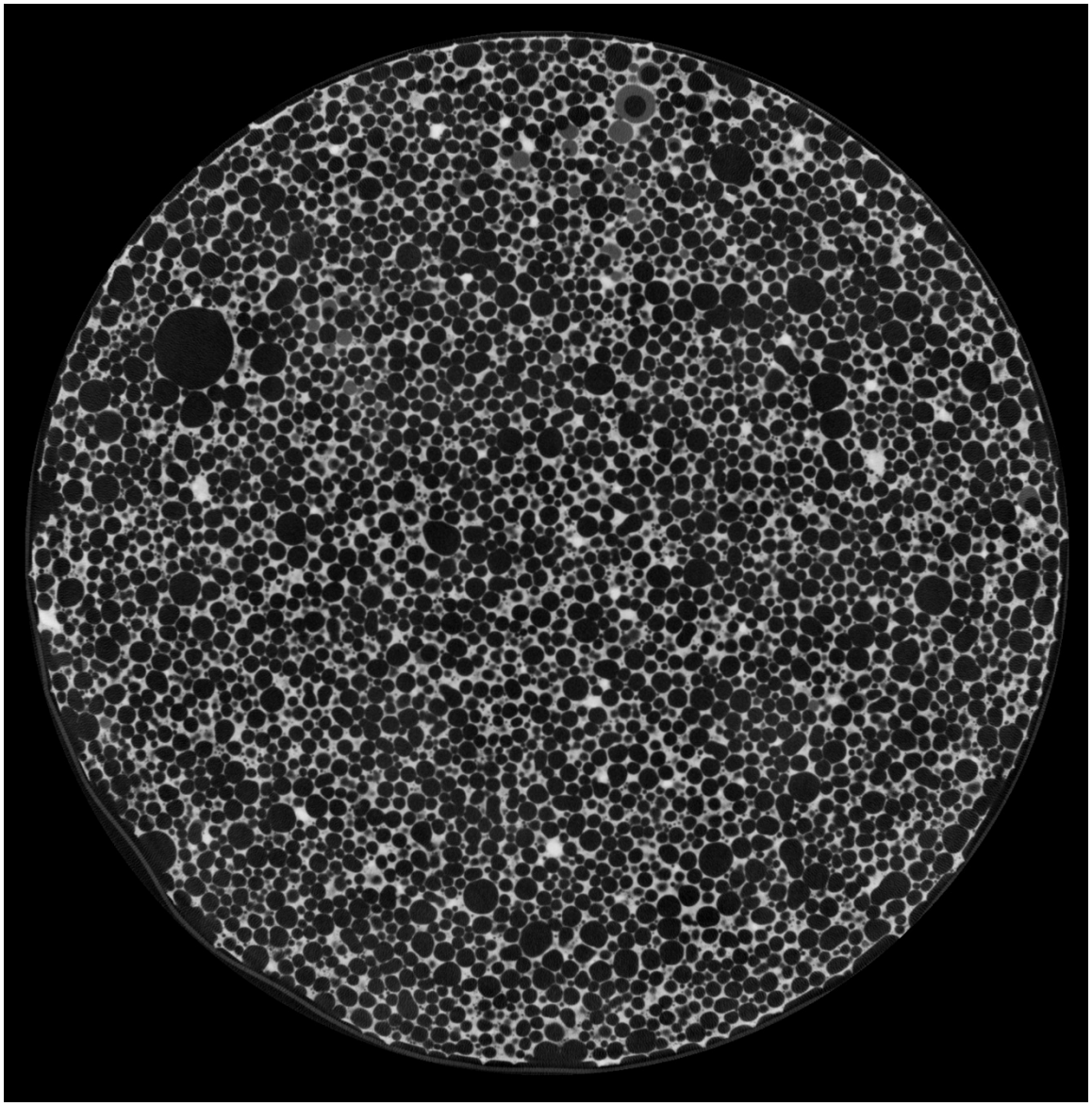

Figure 62. CT scan image of specimen B1-23 after the D1 treatment, No. 0243.

The image cross-section is located 0.778” above the center of the specimen. The dark spherical objects are the foamed air voids, and the light matrix being the concrete skeleton structure. The degree of saturation is 16.86%. Free pore water is visible in the image as grey spheres.

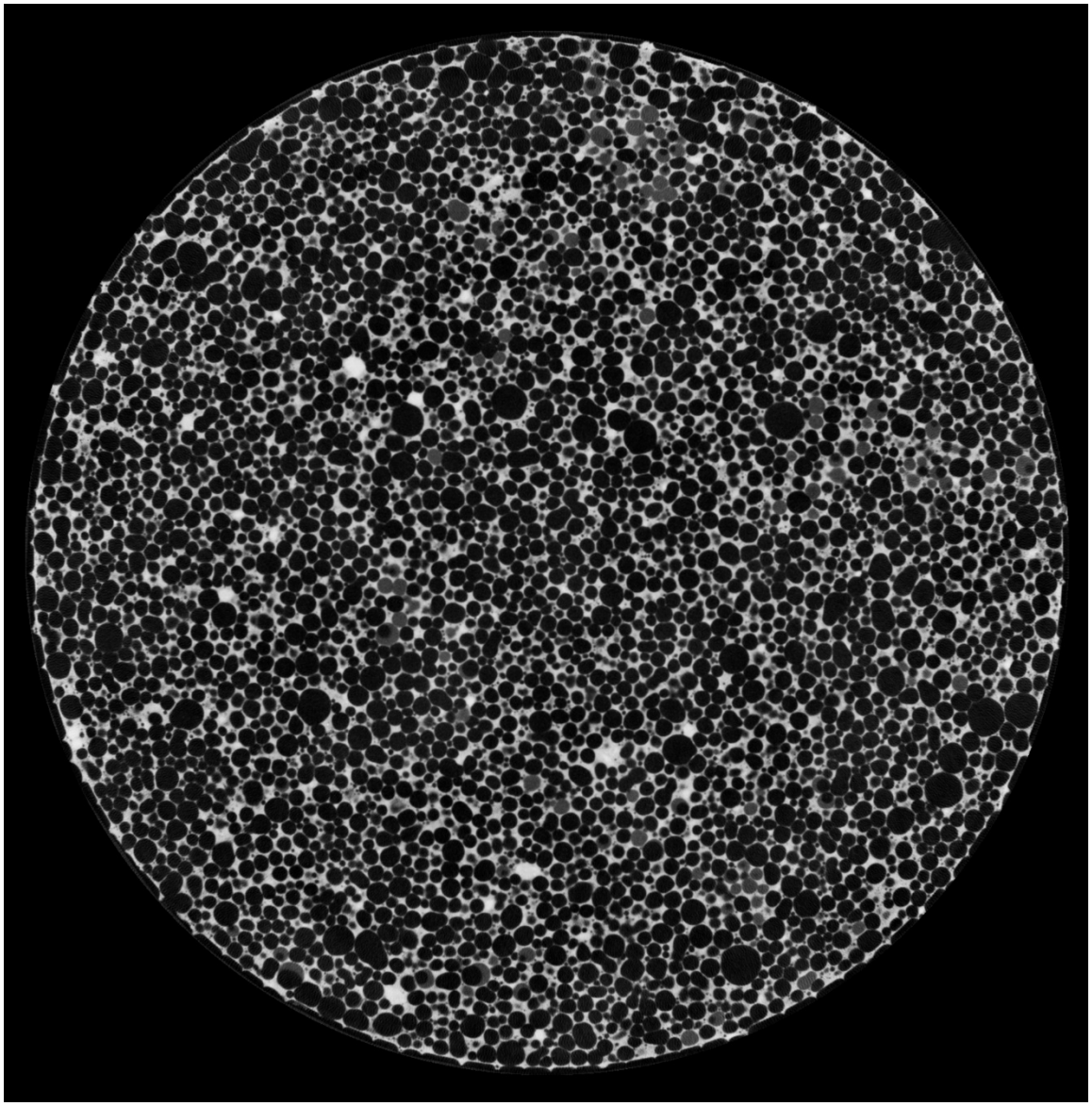

Figure 63. CT scan image of specimen B1-23 after the D1 treatment, No. 0729.

The image cross-section is located 0.778” below the center of the specimen. The dark spherical objects are the foamed air voids, and the light matrix being the concrete skeleton structure. The degree of saturation is 16.86%. Free pore water is visible in the image as grey spheres.

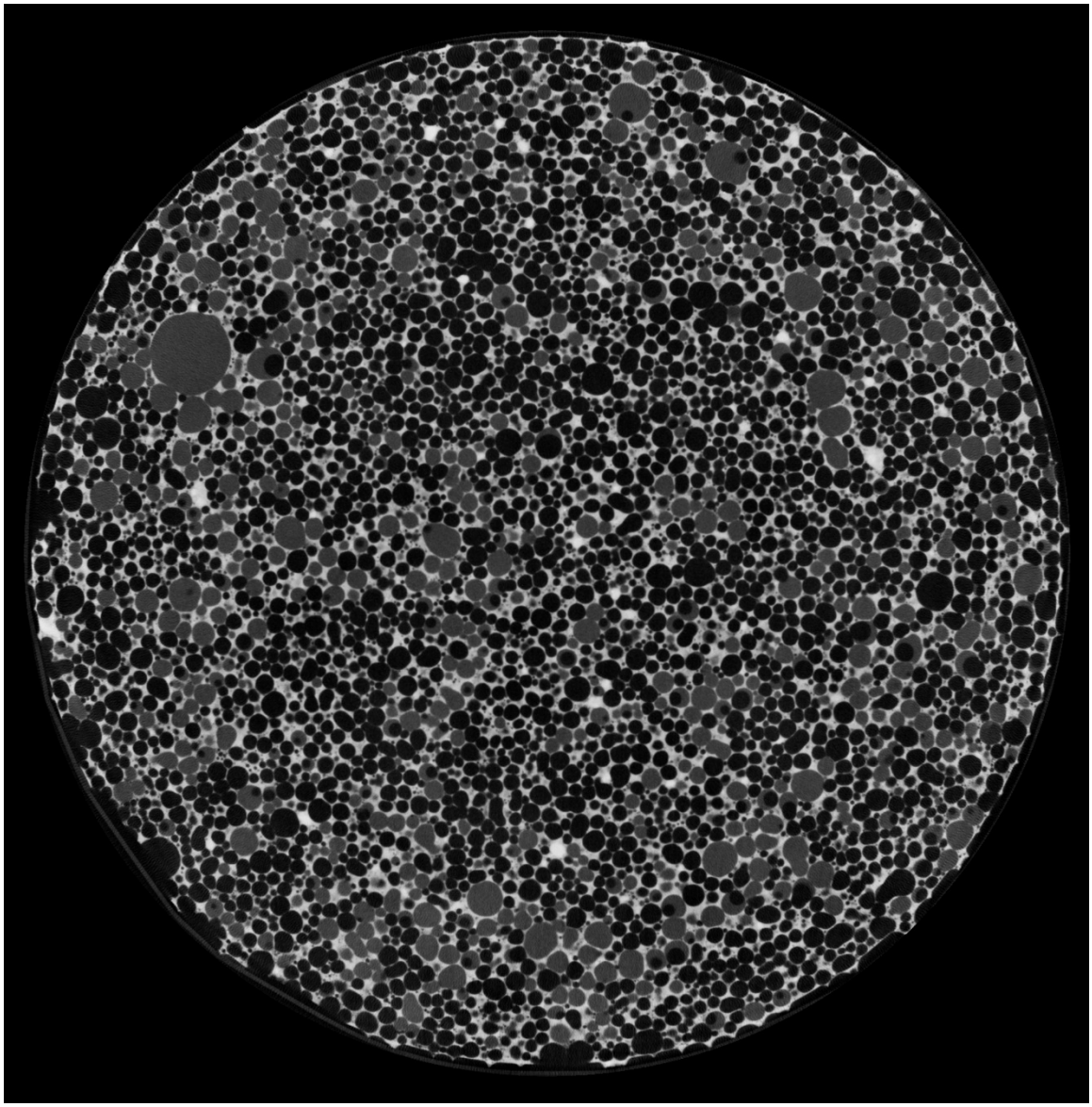

Figure 64. CT scan image of specimen B1-23 after the V8 treatment, No. 0243.

The image cross-section is located 0.778” above the center of the specimen. The dark spherical objects are the foamed air voids, and the light matrix being the concrete skeleton structure. The degree of saturation is 35.37%. Free pore water is visible in the image as grey spheres.

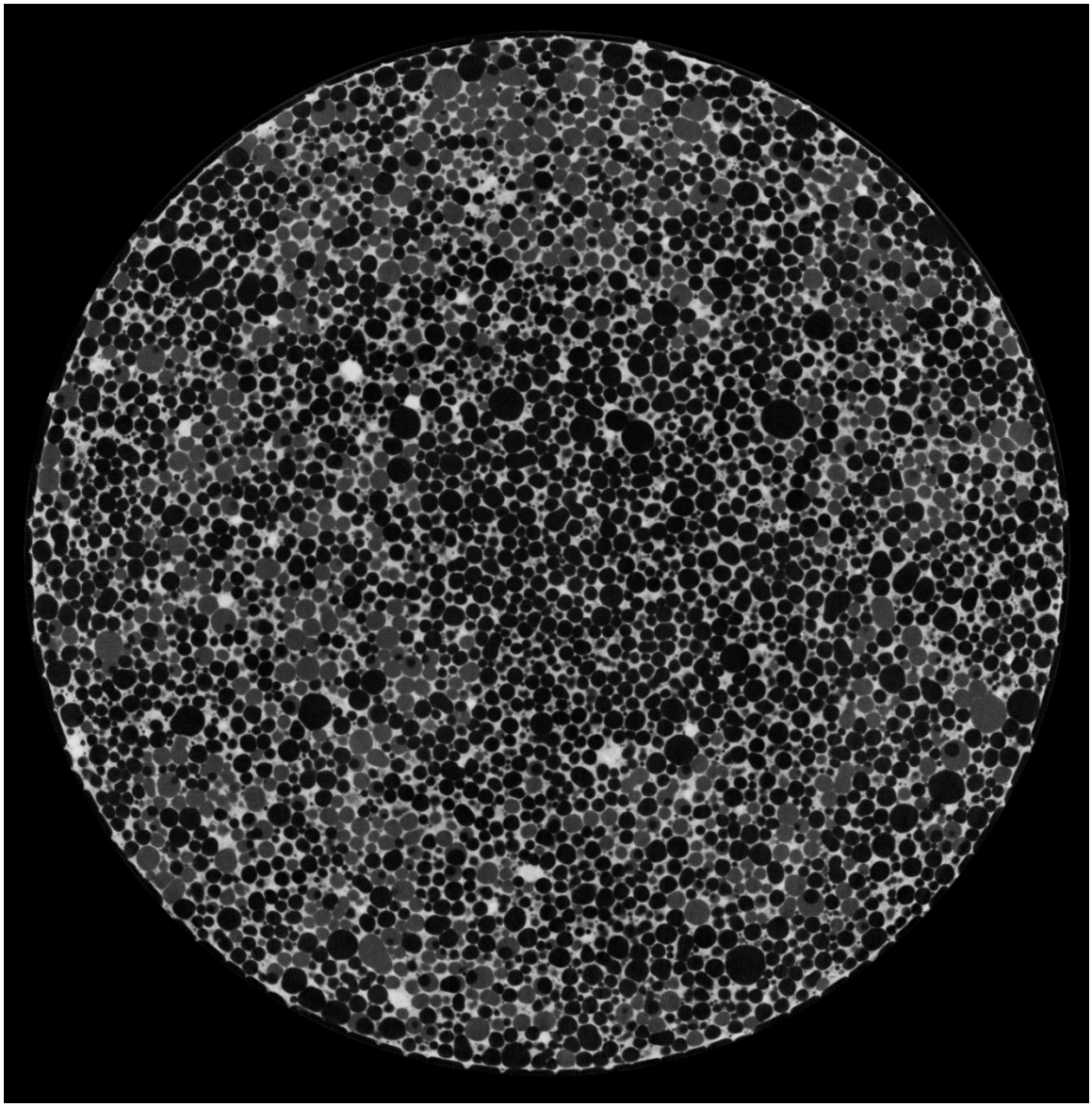

Figure 65. CT scan image of specimen B1-23 after the V8 treatment, No. 0729.

The image cross-section is located 0.778” below the center of the specimen. The dark spherical objects are the foamed air voids, and the light matrix being the concrete skeleton structure. The degree of saturation is 35.37%. Free pore water is visible in the image as grey spheres.

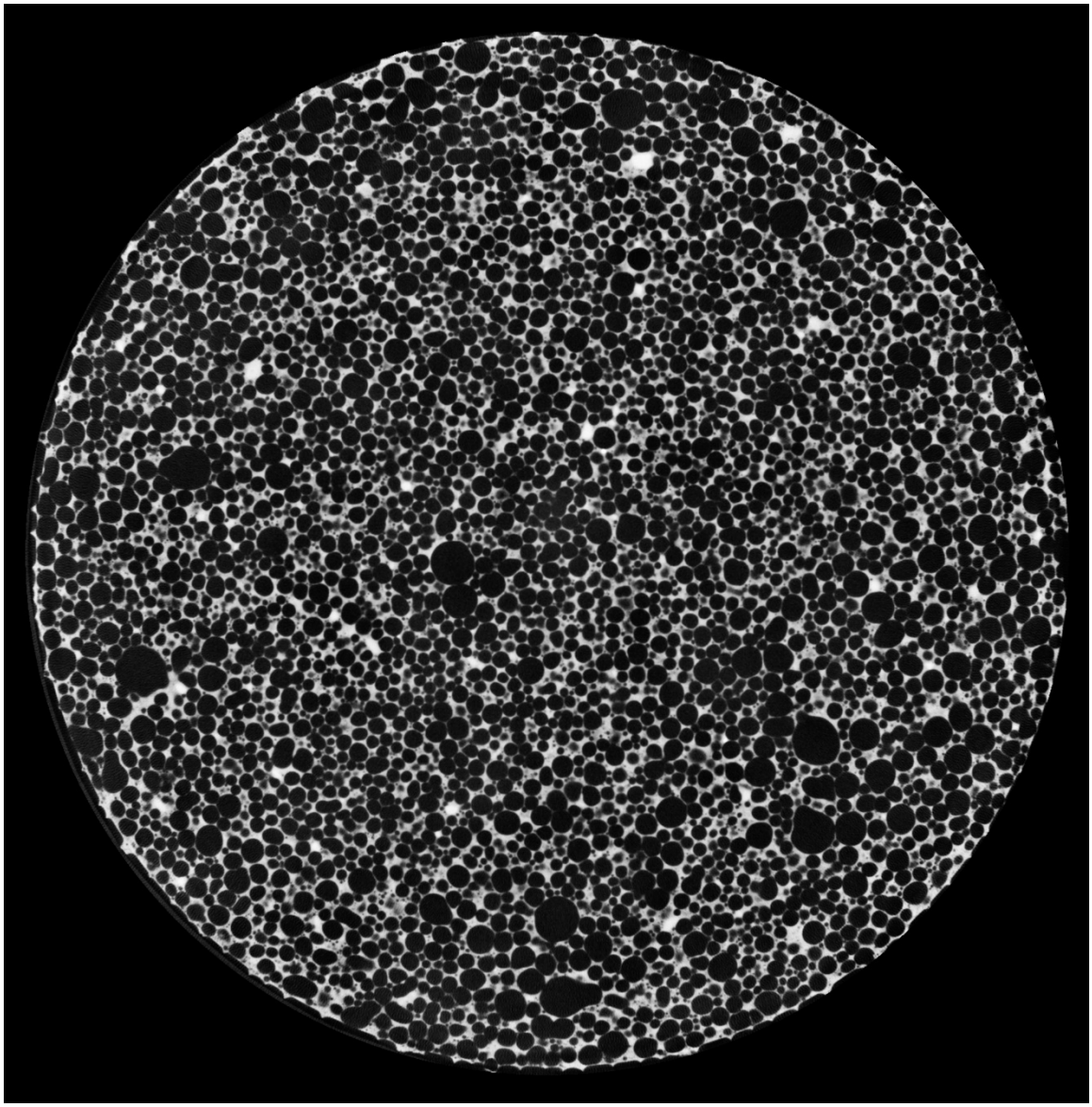

Figure 66. CT scan image of specimen B1-24 after the AD treatment, No. 0243.

The image cross-section is located 0.778” above the center of the specimen. The dark spherical objects are the foamed air voids, and the light matrix being the concrete skeleton structure. The degree of saturation is 1.77%. No free pore water is visible in the image.

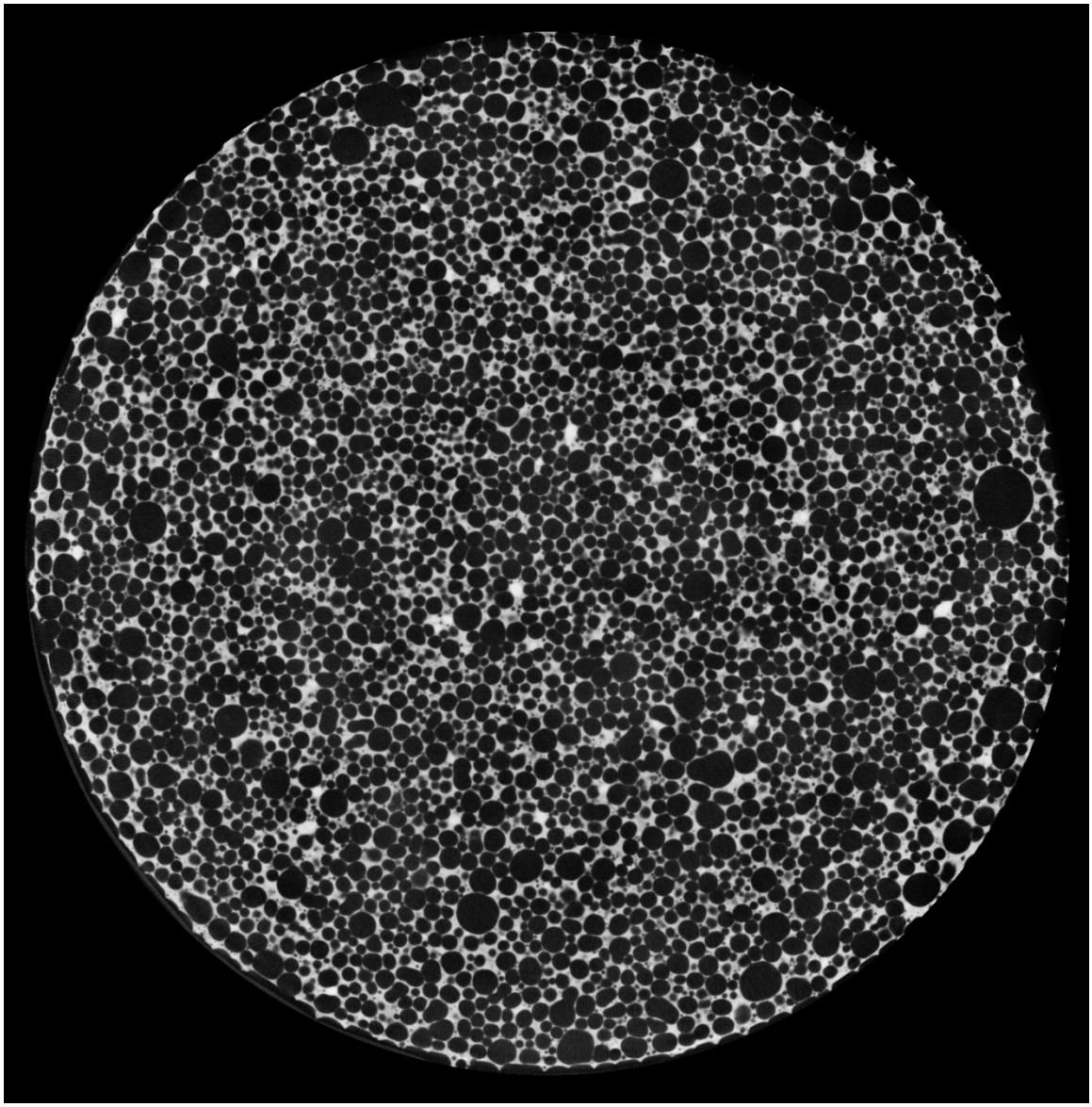

Figure 67. CT scan image of specimen B1-24 after the AD treatment, No. 0729.

The image cross-section is located 0.778” below the center of the specimen. The dark spherical objects are the foamed air voids, and the light matrix being the concrete skeleton structure. The degree of saturation is 1.77%. No free pore water is visible in the image.

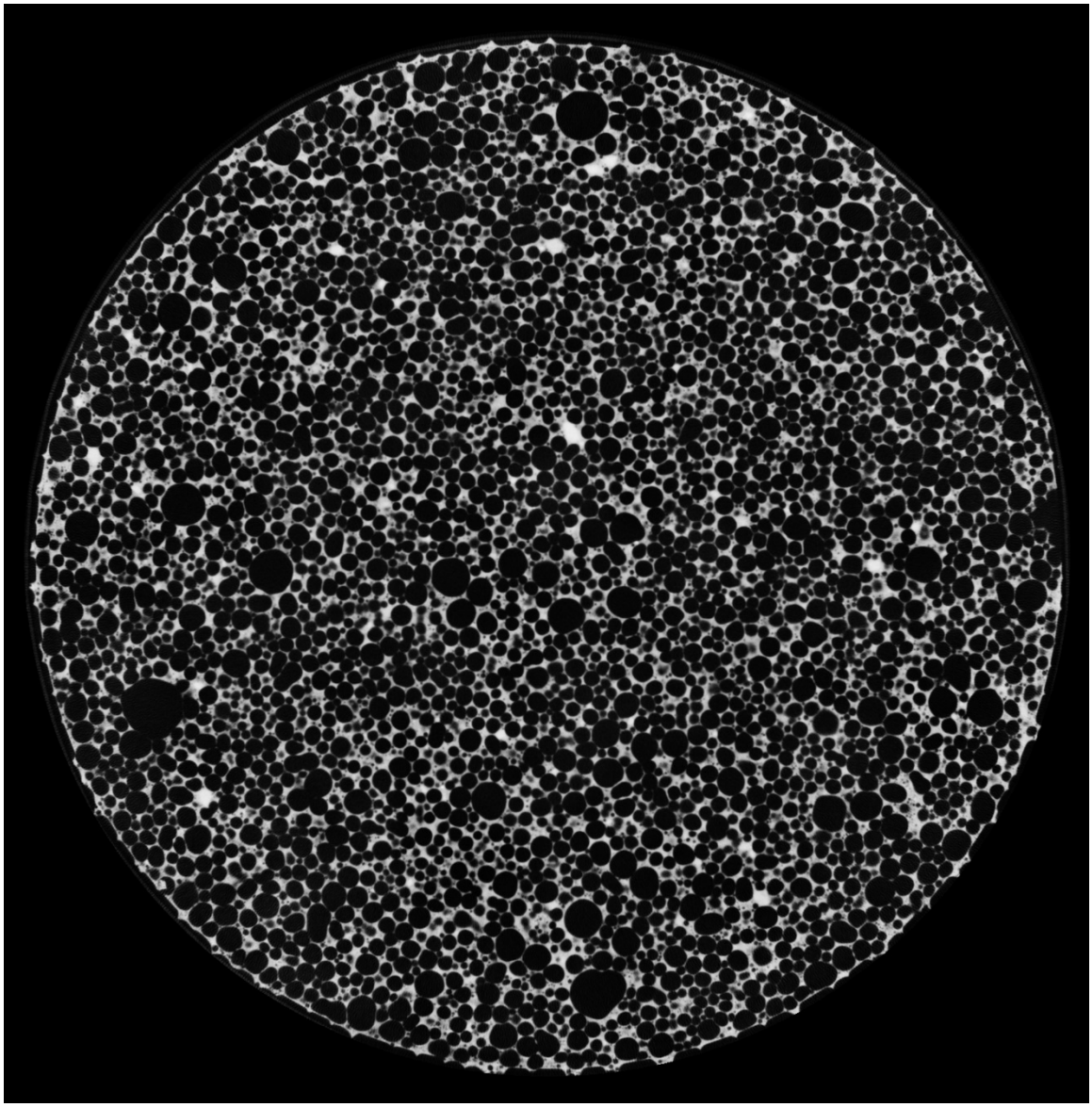

Figure 68. CT scan image of specimen B1-24 after the M5 treatment, No. 0243.

The image cross-section is located 0.778” above the center of the specimen. The dark spherical objects are the foamed air voids, and the light matrix being the concrete skeleton structure. The degree of saturation is 9.99%. No free pore water is visible in the image.

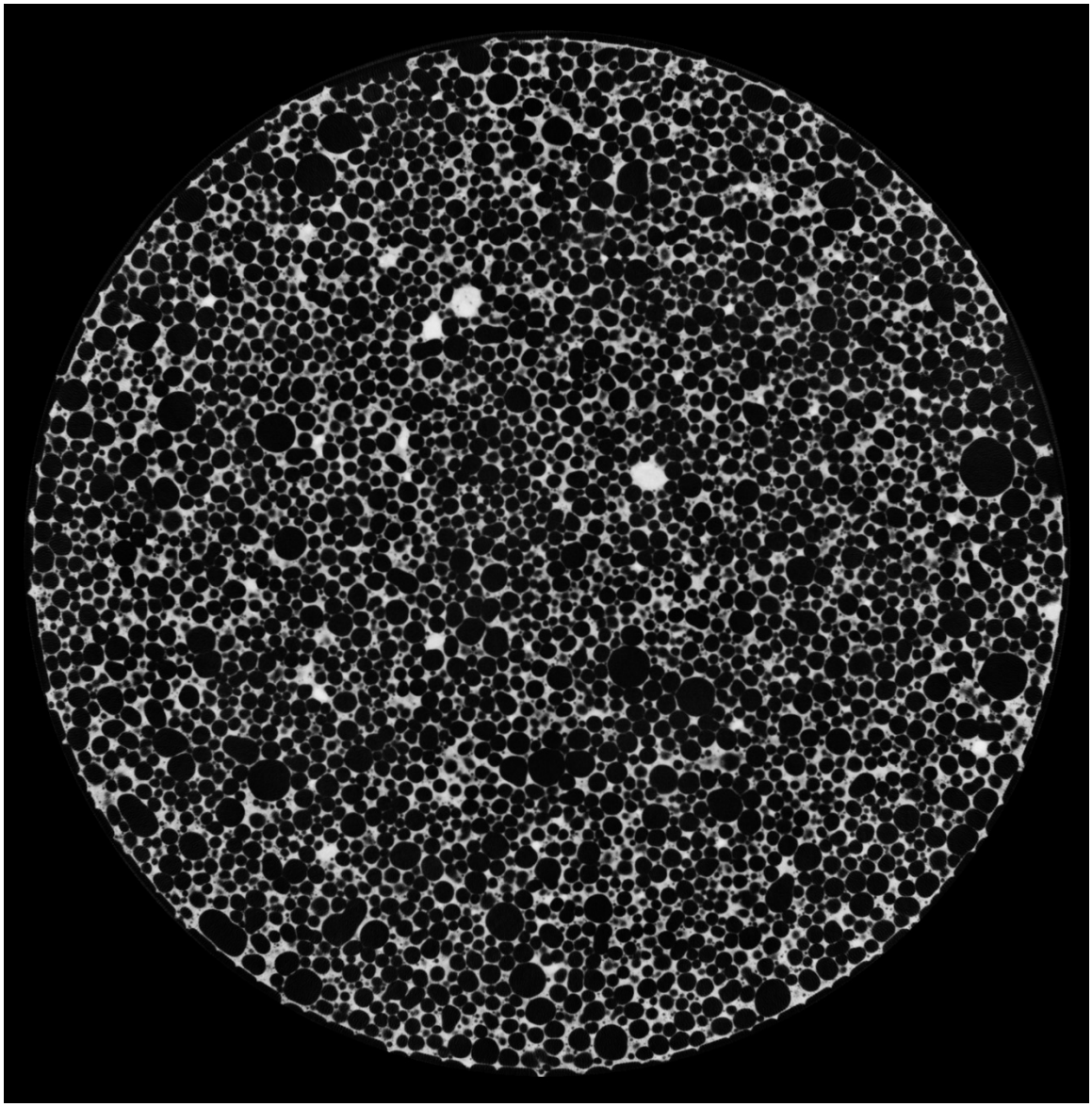

Figure 69. CT scan image of specimen B1-24 after the M5 treatment, No. 0729.

The image cross-section is located 0.778” below the center of the specimen. The dark spherical objects are the foamed air voids, and the light matrix being the concrete skeleton structure. The degree of saturation is 9.99%. No free pore water is visible in the image.

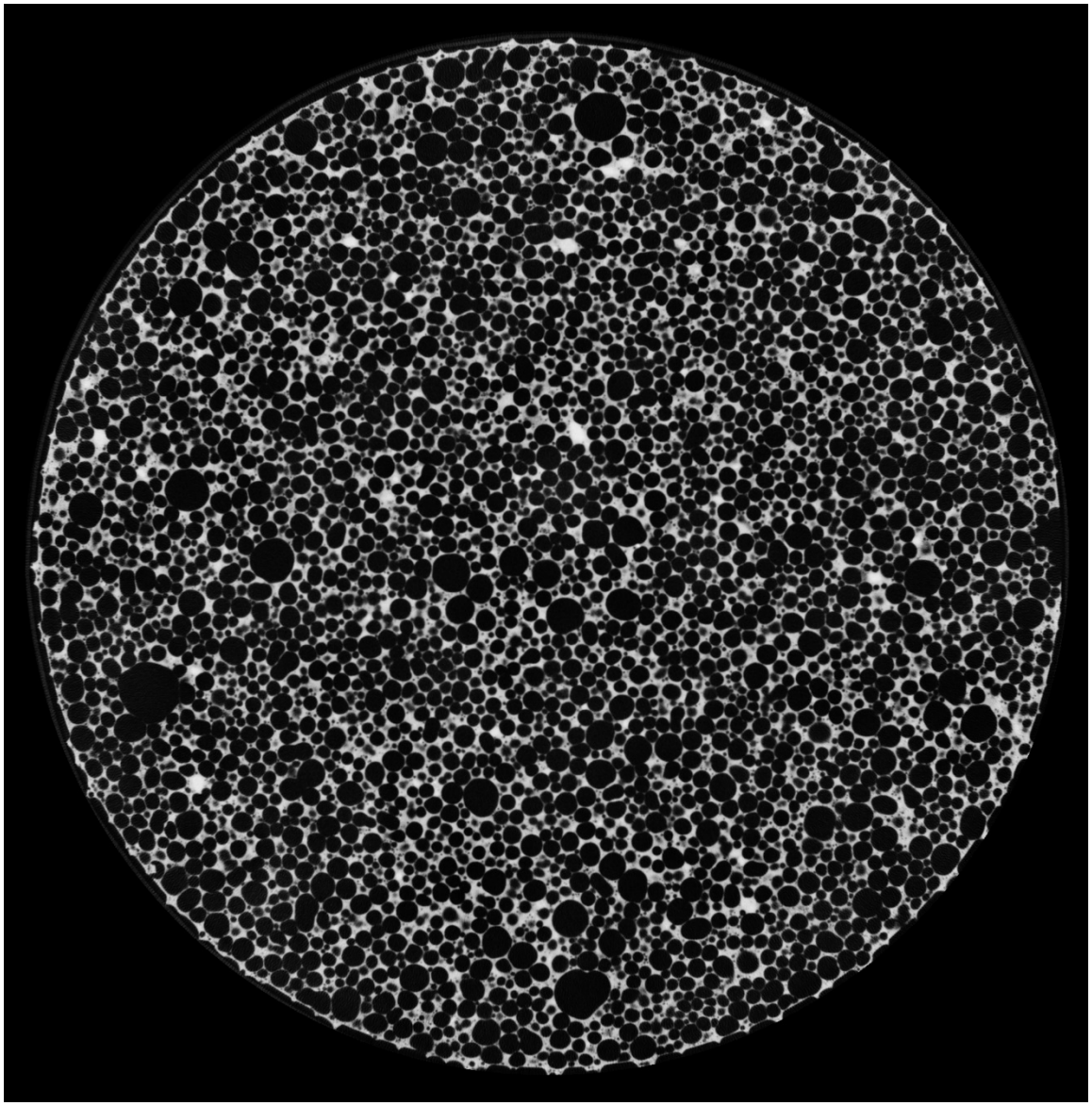

Figure 70. CT scan image of specimen B1-24 after the D1 treatment, No. 0243.

The image cross-section is located 0.778” above the center of the specimen. The dark spherical objects are the foamed air voids, and the light matrix being the concrete skeleton structure. The degree of saturation is 16.35%. No free pore water is visible in the image.

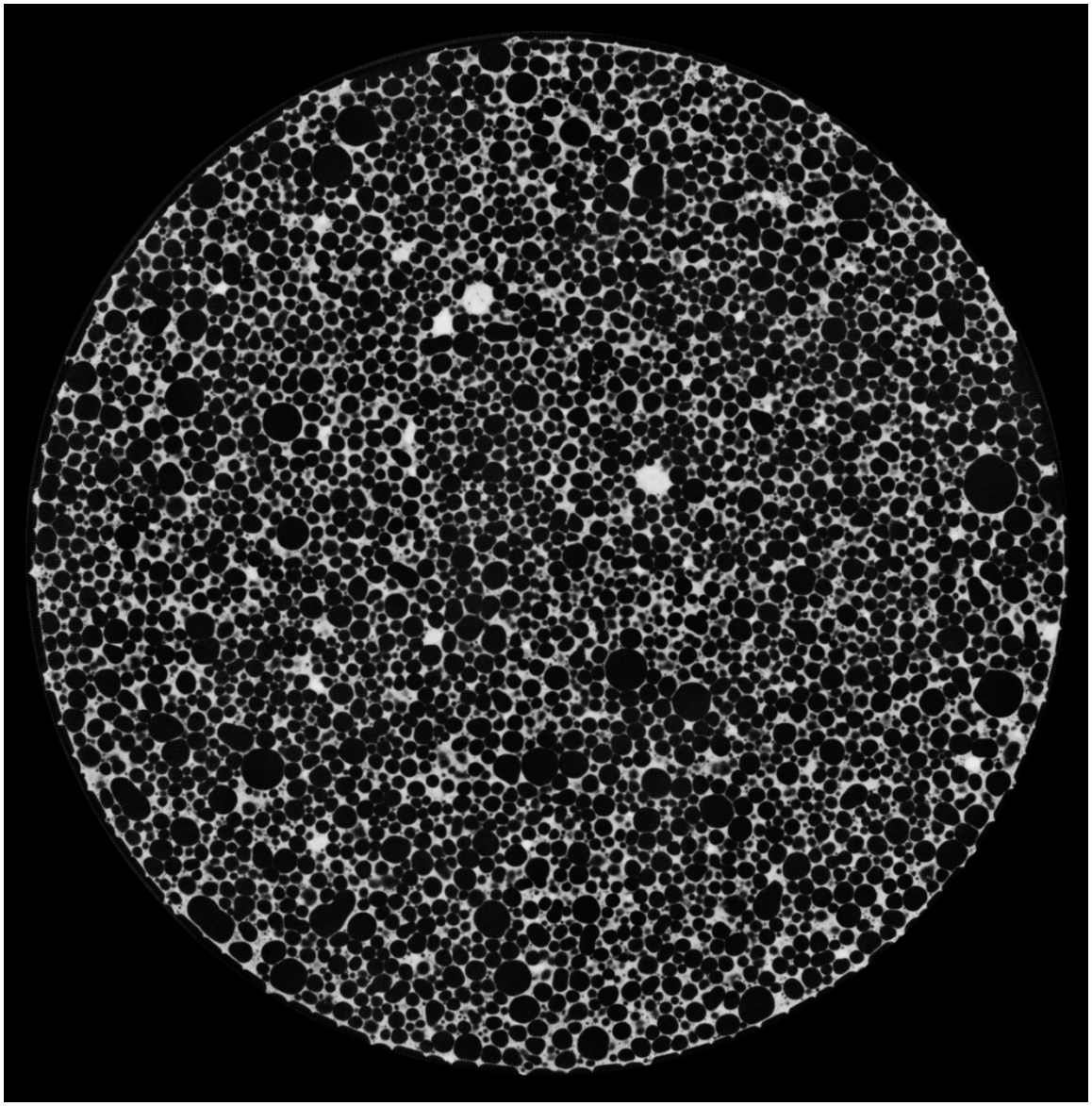

Figure 71. CT scan image of specimen B1-24 after the D1 treatment, No. 0729.

The image cross-section is located 0.778” below the center of the specimen. The dark spherical objects are the foamed air voids, and the light matrix being the concrete skeleton structure. The degree of saturation is 16.35%. No free pore water is visible in the image.

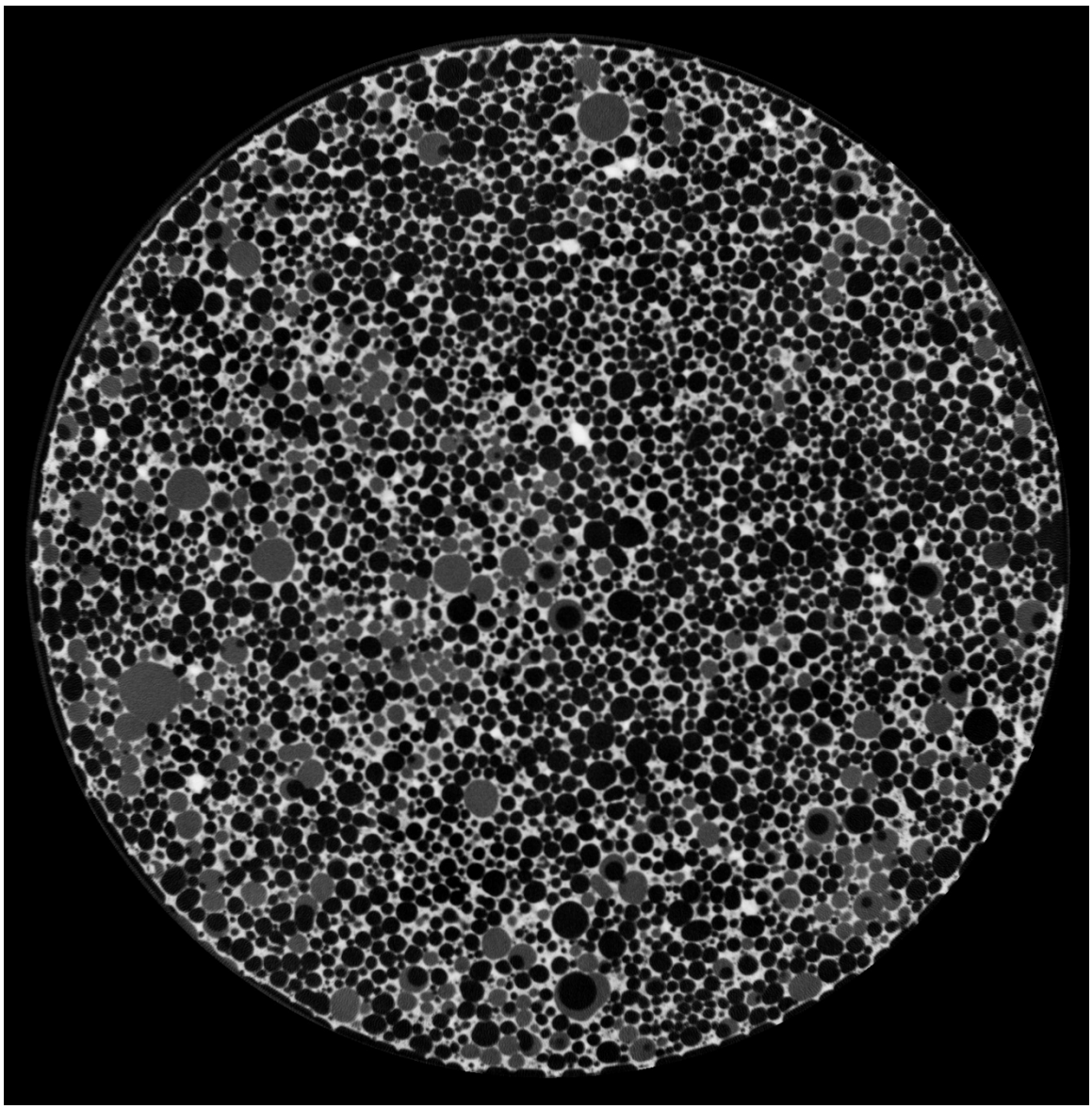

Figure 72. CT scan image of specimen B1-24 after the V8 treatment, No. 0243.

The image cross-section is located 0.778” above the center of the specimen. The dark spherical objects are the foamed air voids, and the light matrix being the concrete skeleton structure. The degree of saturation is 24.67%. Free pore water is visible in the image as grey spheres.

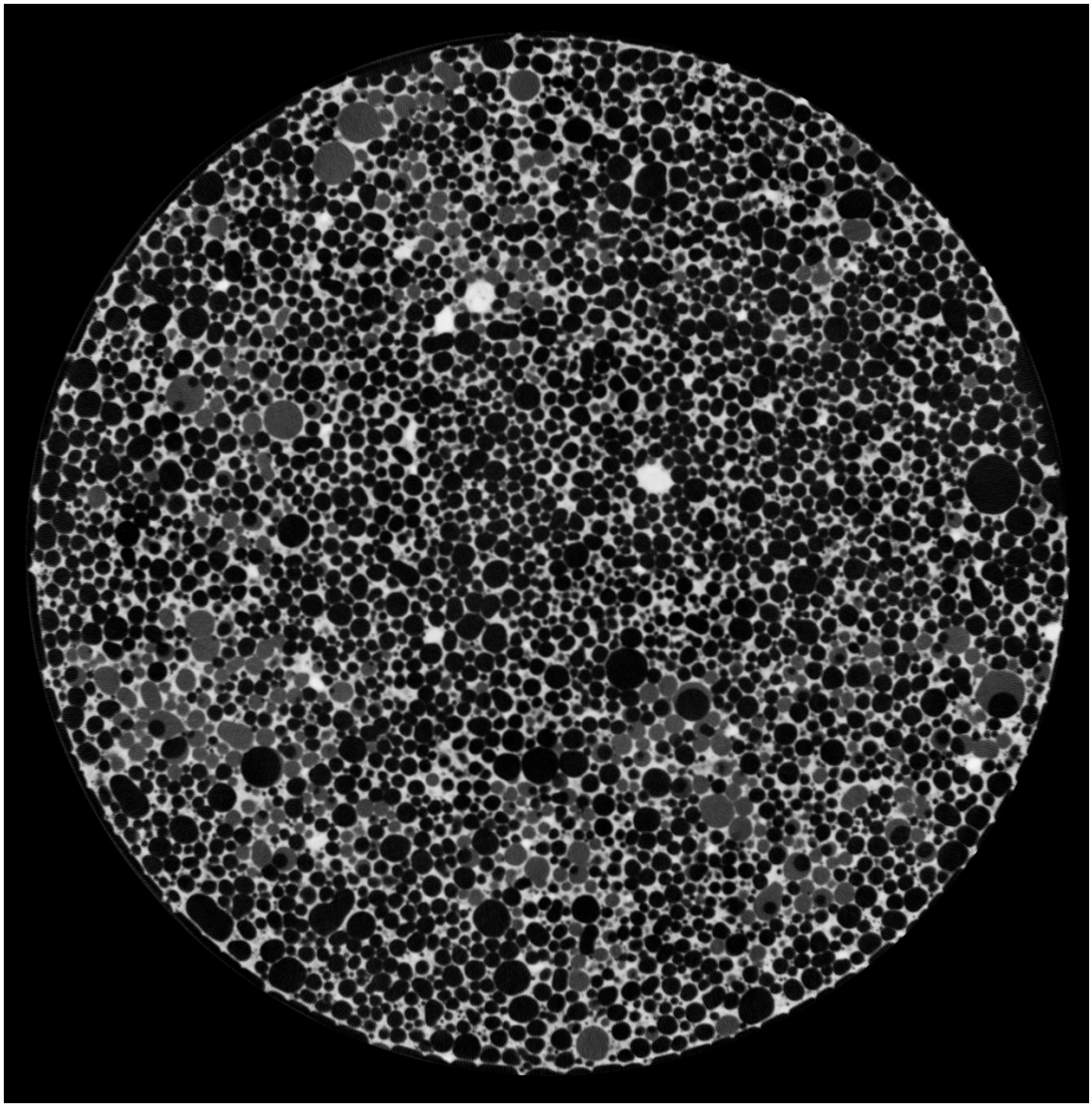

Figure 73. CT scan image of specimen B1-24 after the V8 treatment, No. 0729.

The image cross-section is located 0.778” below the center of the specimen. The dark spherical objects are the foamed air voids, and the light matrix being the concrete skeleton structure. The degree of saturation is 24.67%. Free pore water is visible in the image as grey spheres.

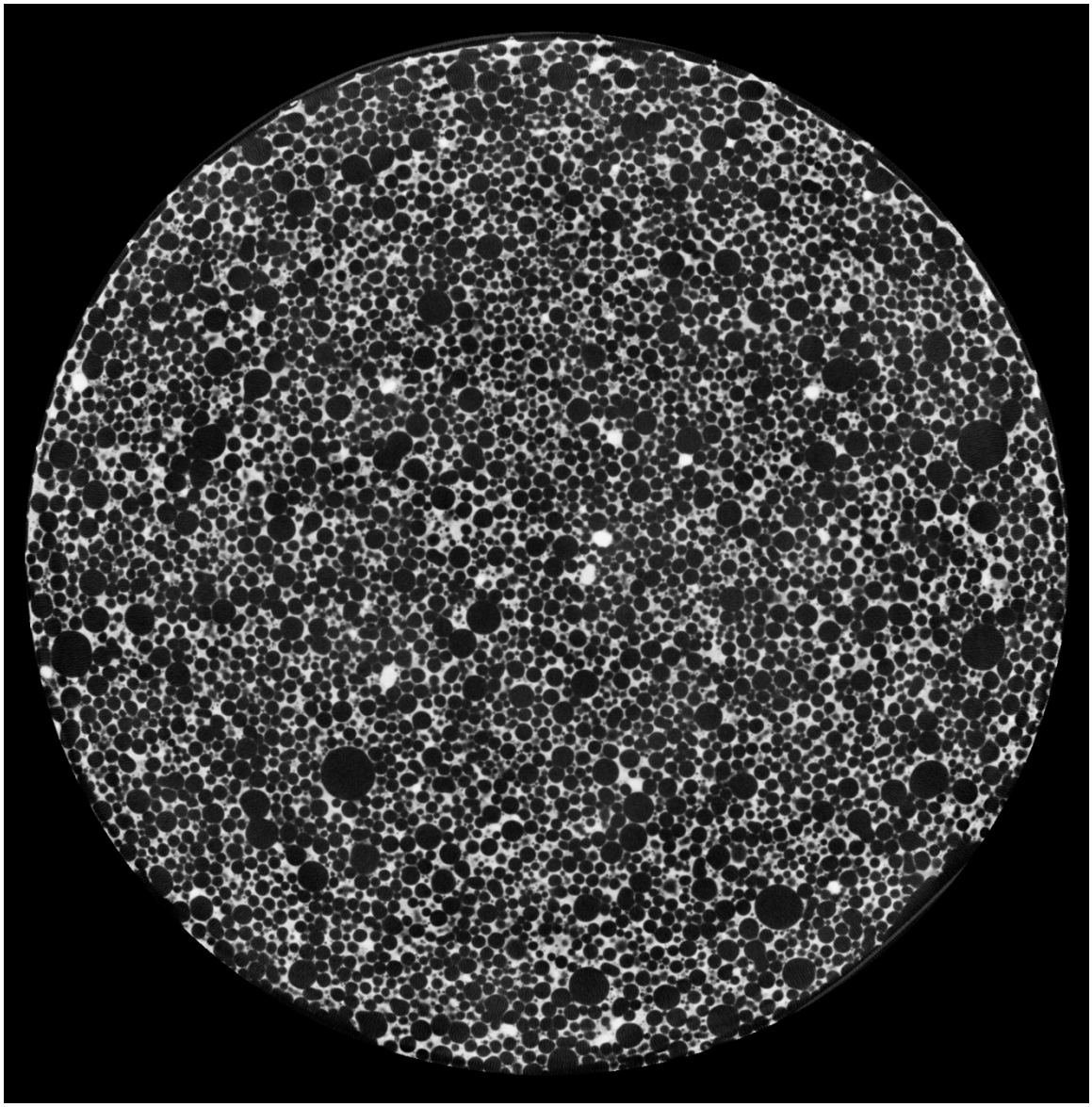

Figure 74. CT scan image of specimen B3-24 after the AD treatment, No. 0243.

The image cross-section is located 0.778” above the center of the specimen. The dark spherical objects are the foamed air voids, and the light matrix being the concrete skeleton structure. The degree of saturation is 1.67%. No free pore water is visible in the image.

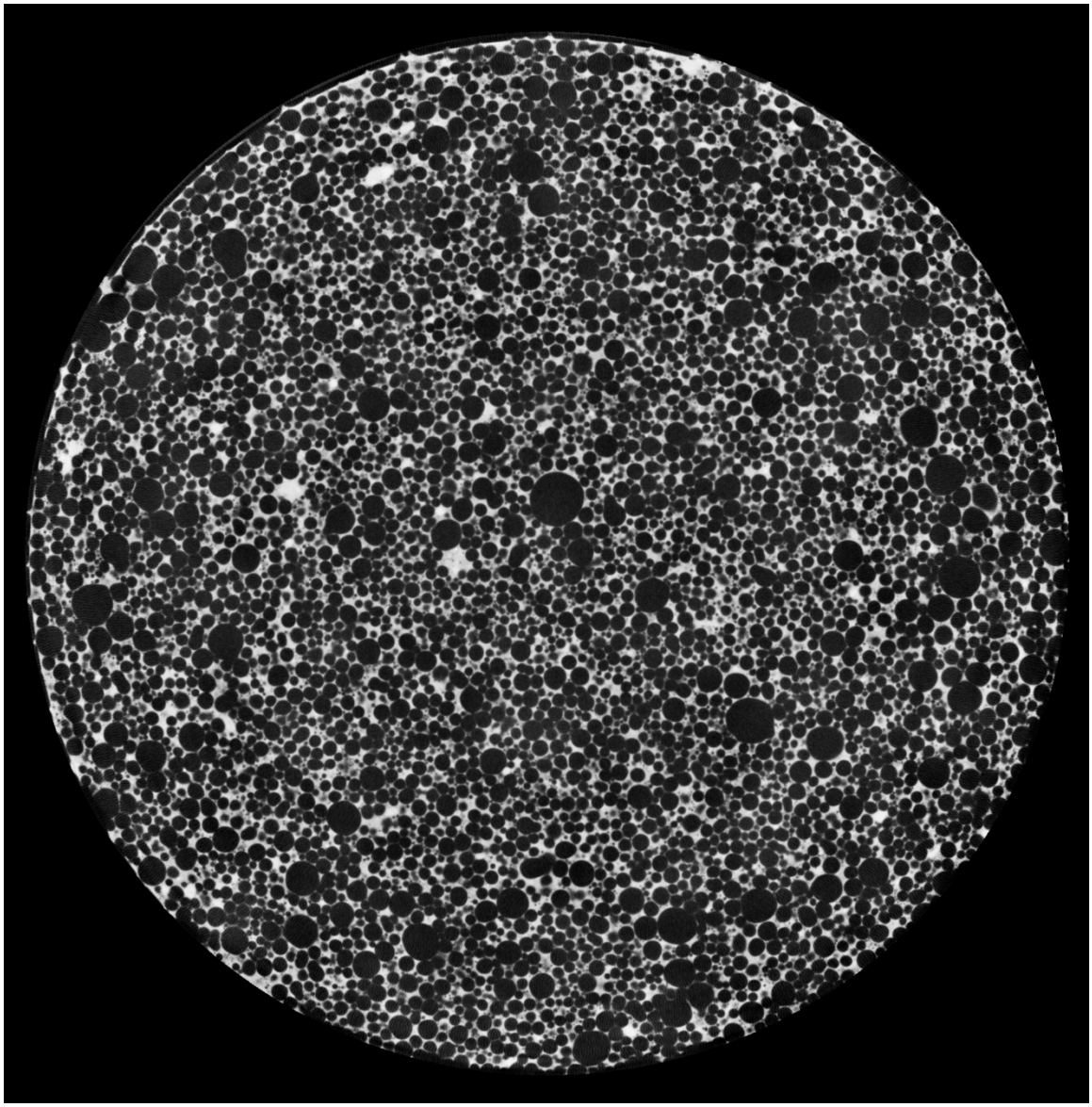

Figure 75. CT scan image of specimen B3-24 after the AD treatment, No. 0729.

The image cross-section is located 0.778” below the center of the specimen. The dark spherical objects are the foamed air voids, and the light matrix being the concrete skeleton structure. The degree of saturation is 1.67%. No free pore water is visible in the image.

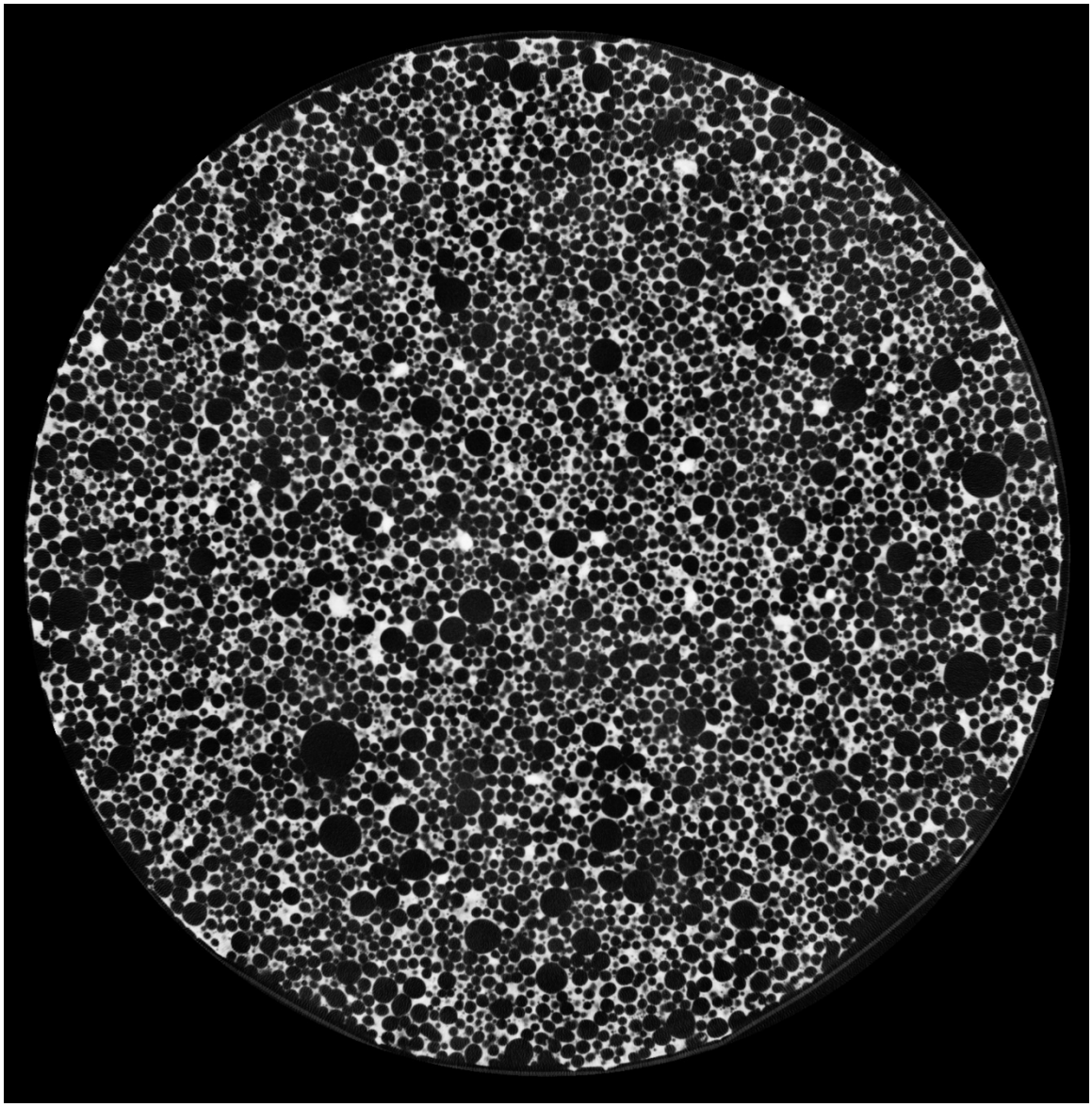

Figure 76. CT scan image of specimen B3-24 after the M5 treatment, No. 0243.

The image cross-section is located 0.778” above the center of the specimen. The dark spherical objects are the foamed air voids, and the light matrix being the concrete skeleton structure. The degree of saturation is 10.80%. No free pore water is visible in the image.

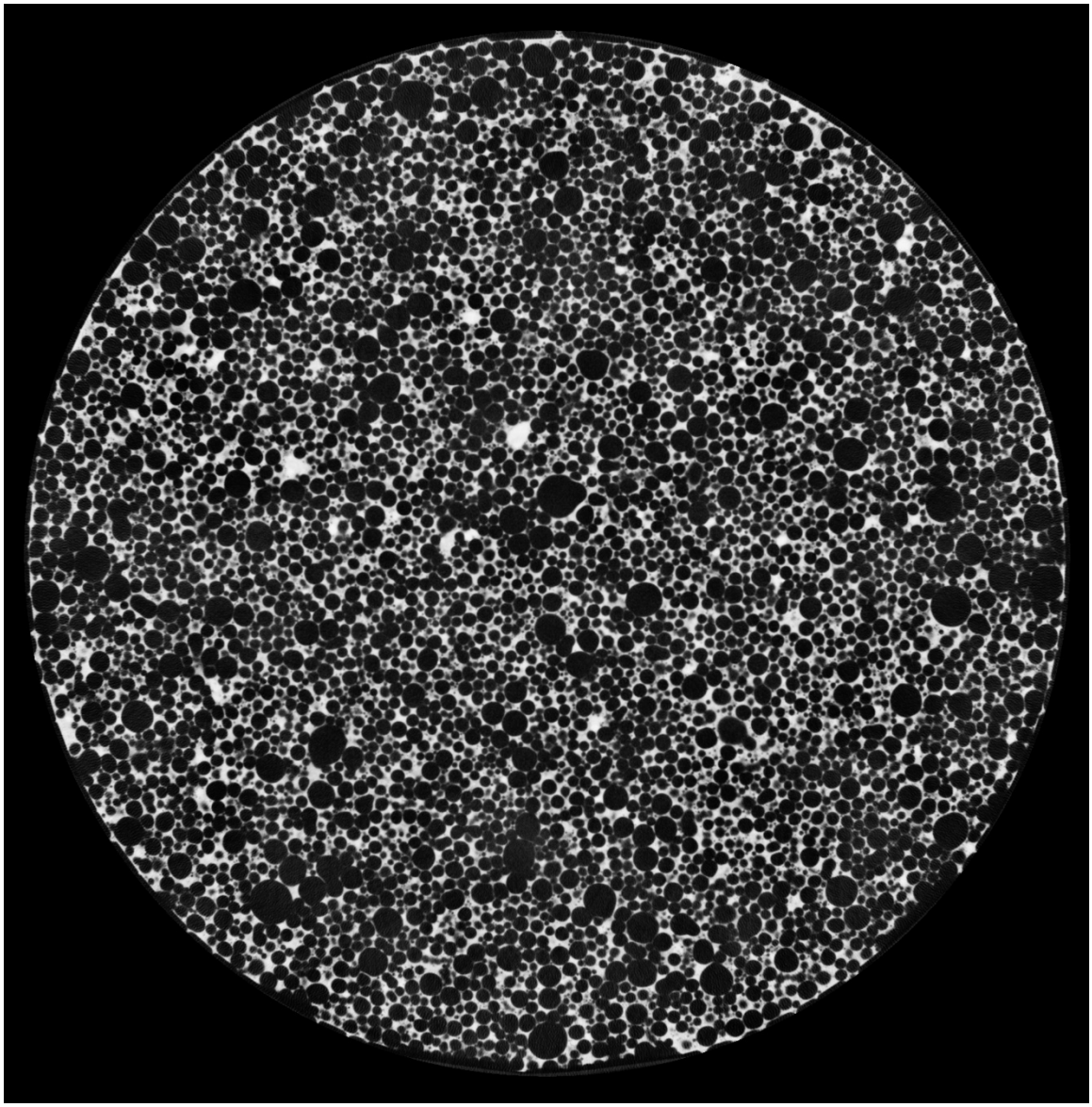

Figure 77. CT scan image of specimen B3-24 after the M5 treatment, No. 0729.

The image cross-section is located 0.778” below the center of the specimen. The dark spherical objects are the foamed air voids, and the light matrix being the concrete skeleton structure. The degree of saturation is 10.80%. No free pore water is visible in the image.

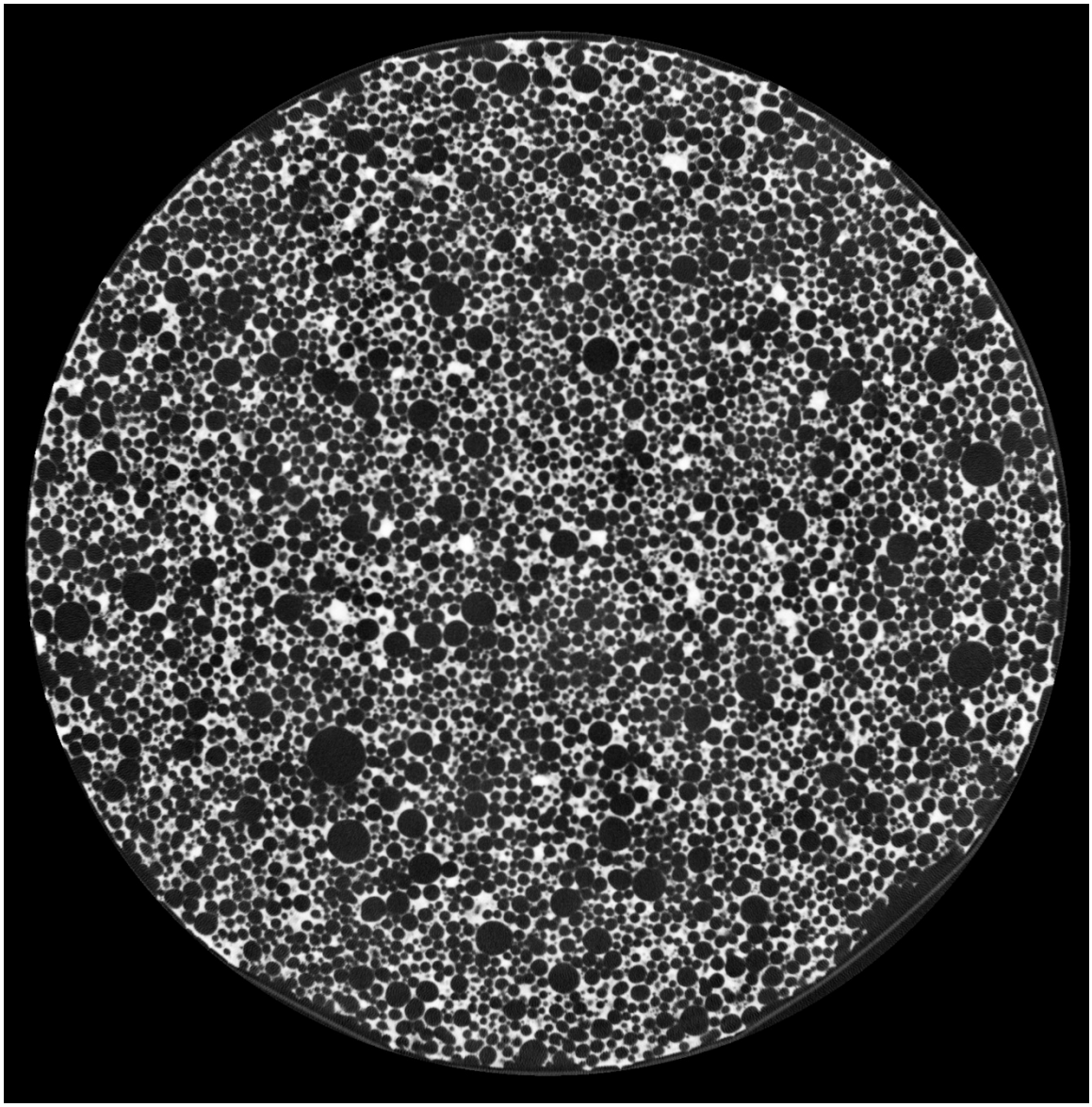

Figure 78. CT scan image of specimen B3-24 after the D1 treatment, No. 0243.

The image cross-section is located 0.778” above the center of the specimen. The dark spherical objects are the foamed air voids, and the light matrix being the concrete skeleton structure. The degree of saturation is 16.43%. Free pore water is visible in the image as grey spheres.

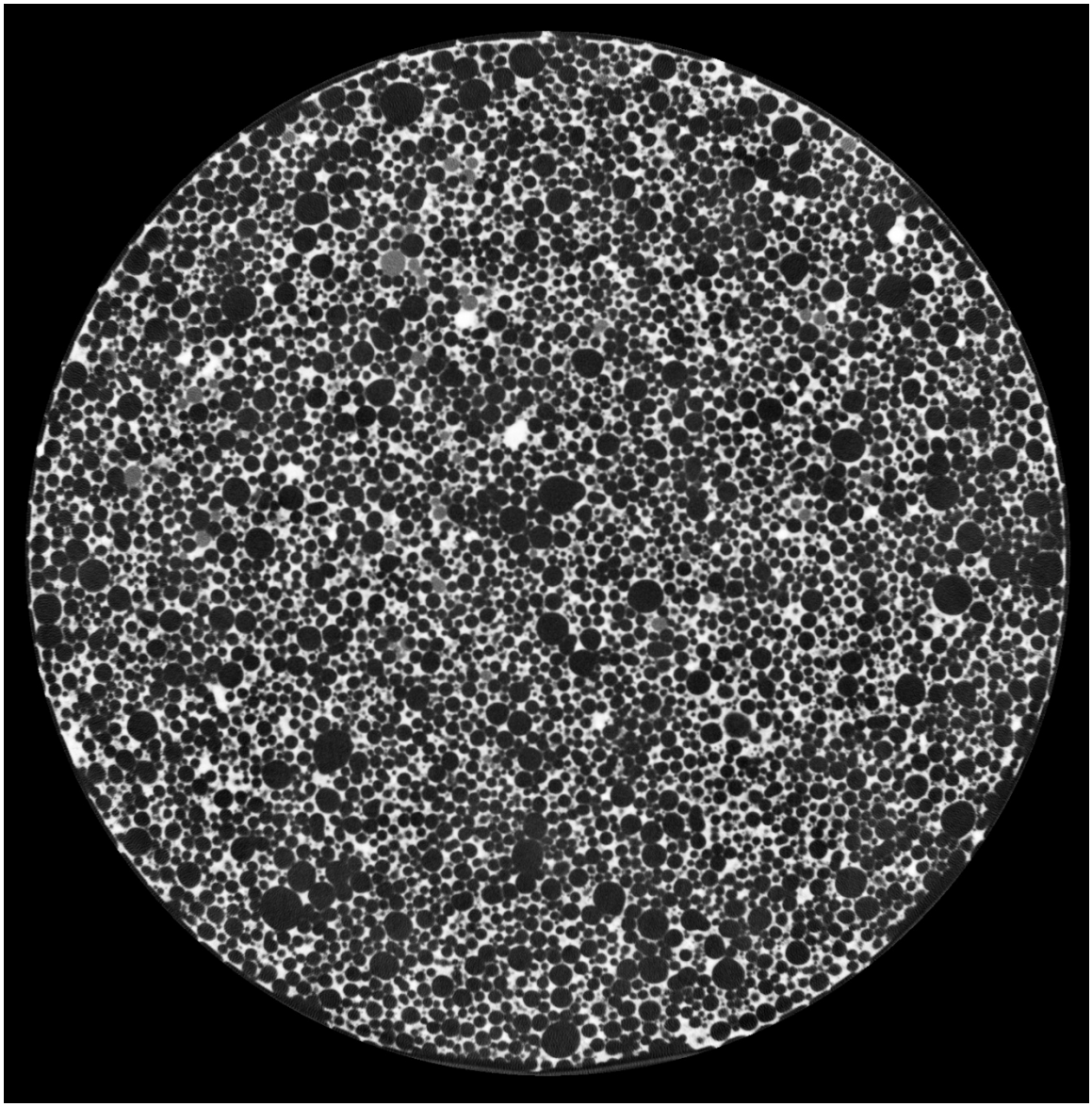

Figure 79. CT scan image of specimen B3-24 after the D1 treatment, No. 0729.

The image cross-section is located 0.778” below the center of the specimen. The dark spherical objects are the foamed air voids, and the light matrix being the concrete skeleton structure. The degree of saturation is 16.43%. Free pore water is visible in the image as grey spheres.

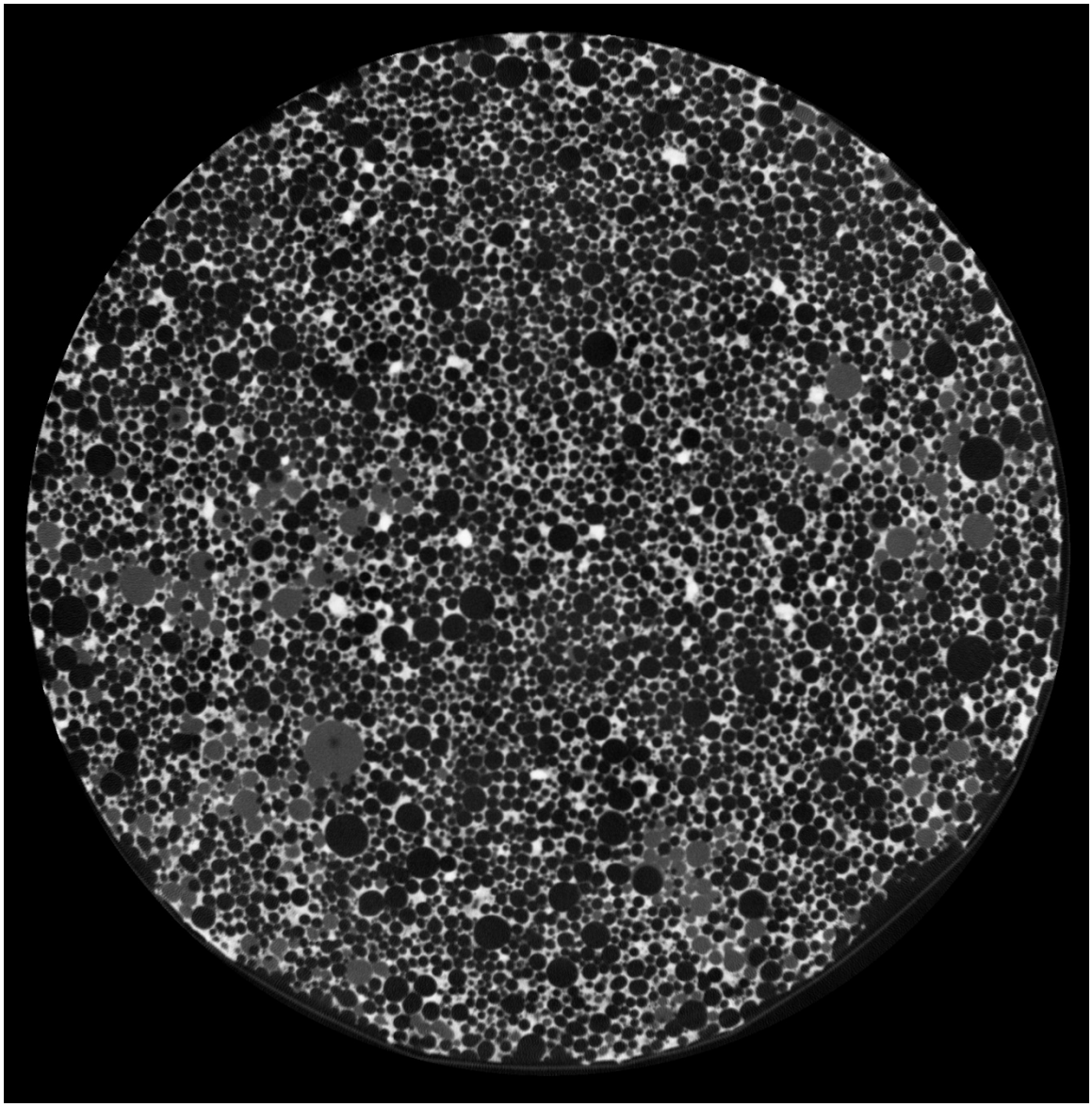

Figure 80. CT scan image of specimen B3-24 after the V8 treatment, No. 0243.

The image cross-section is located 0.778” above the center of the specimen. The dark spherical objects are the foamed air voids, and the light matrix being the concrete skeleton structure. The degree of saturation is 30.61%. Free pore water is visible in the image as grey spheres.

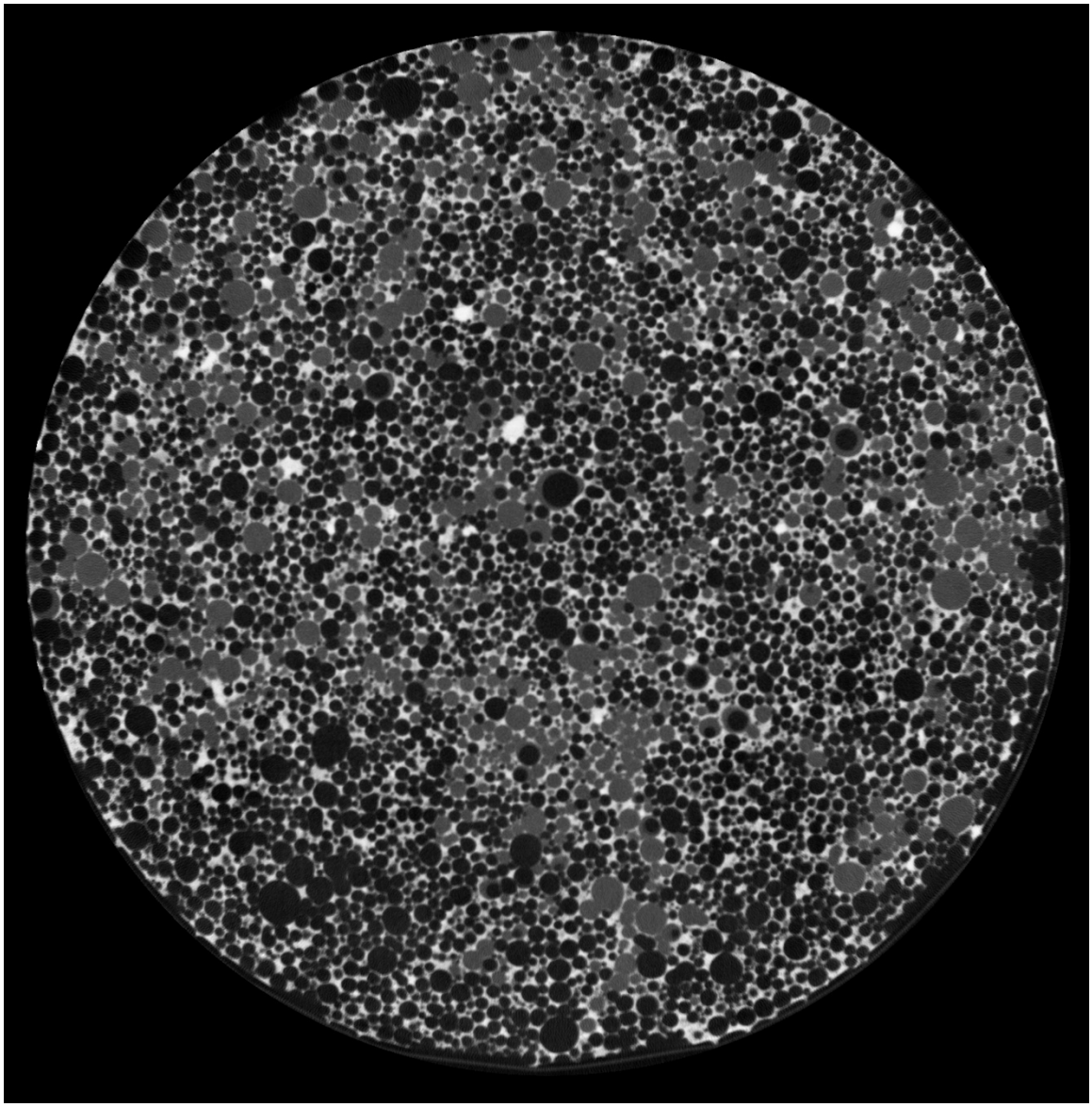

Figure 81. CT scan image of specimen B3-24 after the V8 treatment, No. 0729.

The image cross-section is located 0.778” below the center of the specimen. The dark spherical objects are the foamed air voids, and the light matrix being the concrete skeleton structure. The degree of saturation is 30.61%. Free pore water is visible in the image as grey spheres.

APPENDIX C

RESILIENT MODULUS TEST RESULTS

Dan Seely
9/11/2023

$SampleNo := \text{“B2}-\text{24”}$

$Treatment = \text{“AD”}$

$S = 3.067$ Degree of Saturation (%)

Test Sequence : Base/Subbase

Test summary data (psi) :

$$\sigma_3 = \begin{bmatrix} 2.615 \\ 2.566 \\ 2.561 \\ 4.616 \\ 4.584 \\ 4.587 \\ 9.615 \\ 9.640 \\ 9.604 \\ 14.640 \\ 14.660 \\ 14.640 \\ 19.710 \\ 19.680 \\ 19.670 \end{bmatrix} \quad \sigma_d = \begin{bmatrix} 3.124 \\ 6.071 \\ 9.052 \\ 5.188 \\ 10.050 \\ 14.640 \\ 10.020 \\ 19.680 \\ 29.770 \\ 10.030 \\ 14.640 \\ 30.170 \\ 14.660 \\ 20.000 \\ 40.160 \end{bmatrix} \quad \sigma_B = \begin{bmatrix} 10.970 \\ 13.770 \\ 16.730 \\ 19.040 \\ 23.800 \\ 28.410 \\ 38.860 \\ 48.600 \\ 58.580 \\ 53.940 \\ 58.620 \\ 74.100 \\ 73.800 \\ 79.040 \\ 99.170 \end{bmatrix} \quad M_R = \begin{bmatrix} 19420.4 \\ 21627.8 \\ 24330.6 \\ 28095.0 \\ 28541.0 \\ 33735.6 \\ 41972.8 \\ 44077.2 \\ 44842.0 \\ 47415.4 \\ 39935.4 \\ 45952.4 \\ 36155.2 \\ 40127.2 \\ 53498.8 \end{bmatrix}$$

σ_3 = mean confining stress
σ_d = mean deviator stress
σ_B = mean bulk stress
M_R = resilient modulus
p_a = atmospheric pressure = 14.6959 psi

Dan Seely
9/11/2023

$$M_{R.1}\left(\sigma_B, K_1, K_2\right) := K_1 \cdot {\sigma_B}^{K_2}$$

Equation 1
AASHTO Publication No. FHWA-RD-97-083

$K_1 = 9277.355$

$K_2 = 0.3698$

Equation 1 fitting parameters

${R_1}^2 = 0.8064$

Coefficient of determination

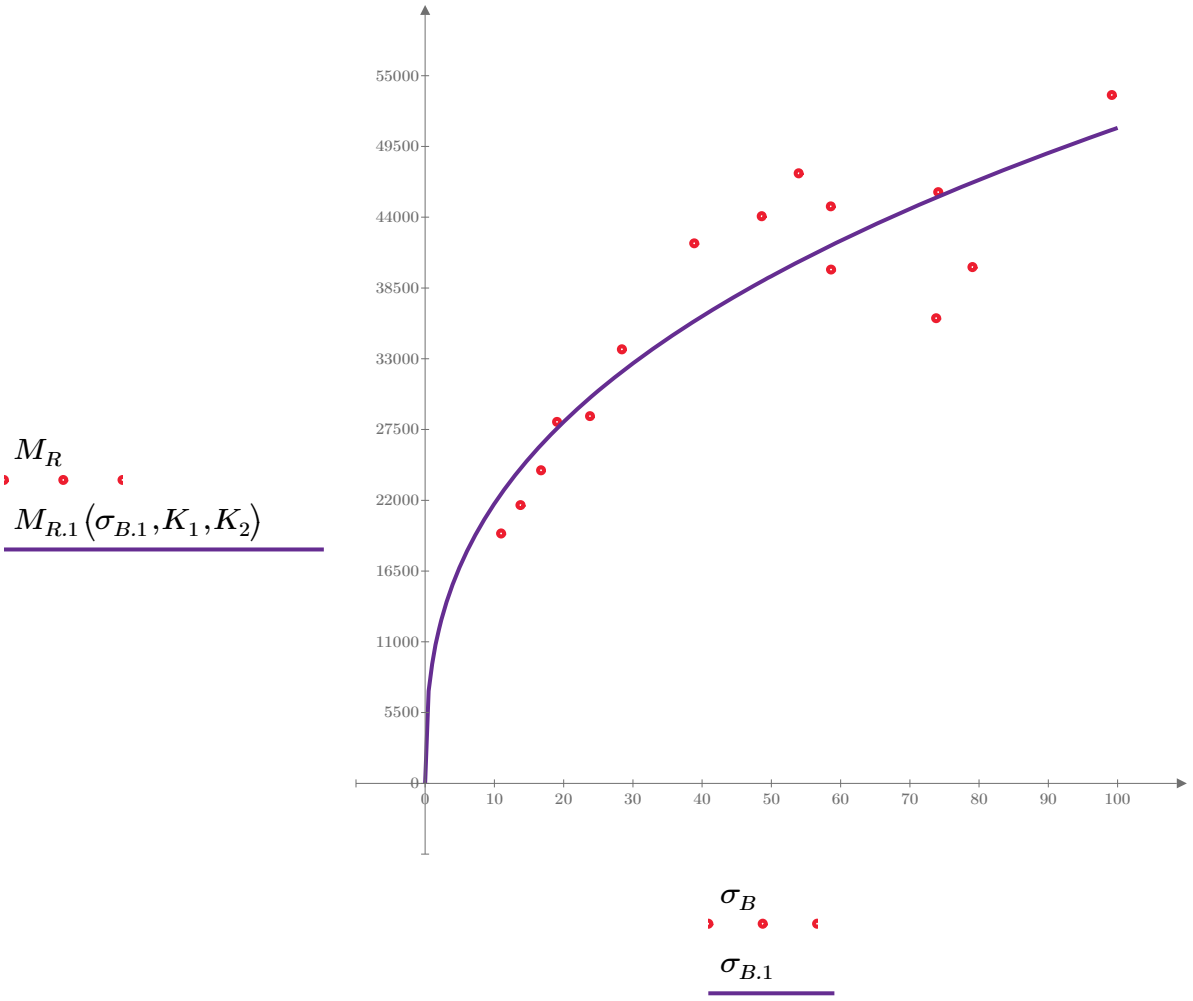

Figure 1. Plot of the test data (red points) vs. the fitted Equation 1 model (purple line).

Dan Seely
9/11/2023

$$M_{R.2}(\sigma_d, K_3, K_4) := K_3 \cdot \sigma_d^{K_4}$$

Equation 2
AASHTO Publication No. FHWA-RD-97-083

$K_3 = 15201.358$

$K_4 = 0.3357$

Equation 2 fitting parameters

$R_2^2 = 0.6908$

Coefficient of determination

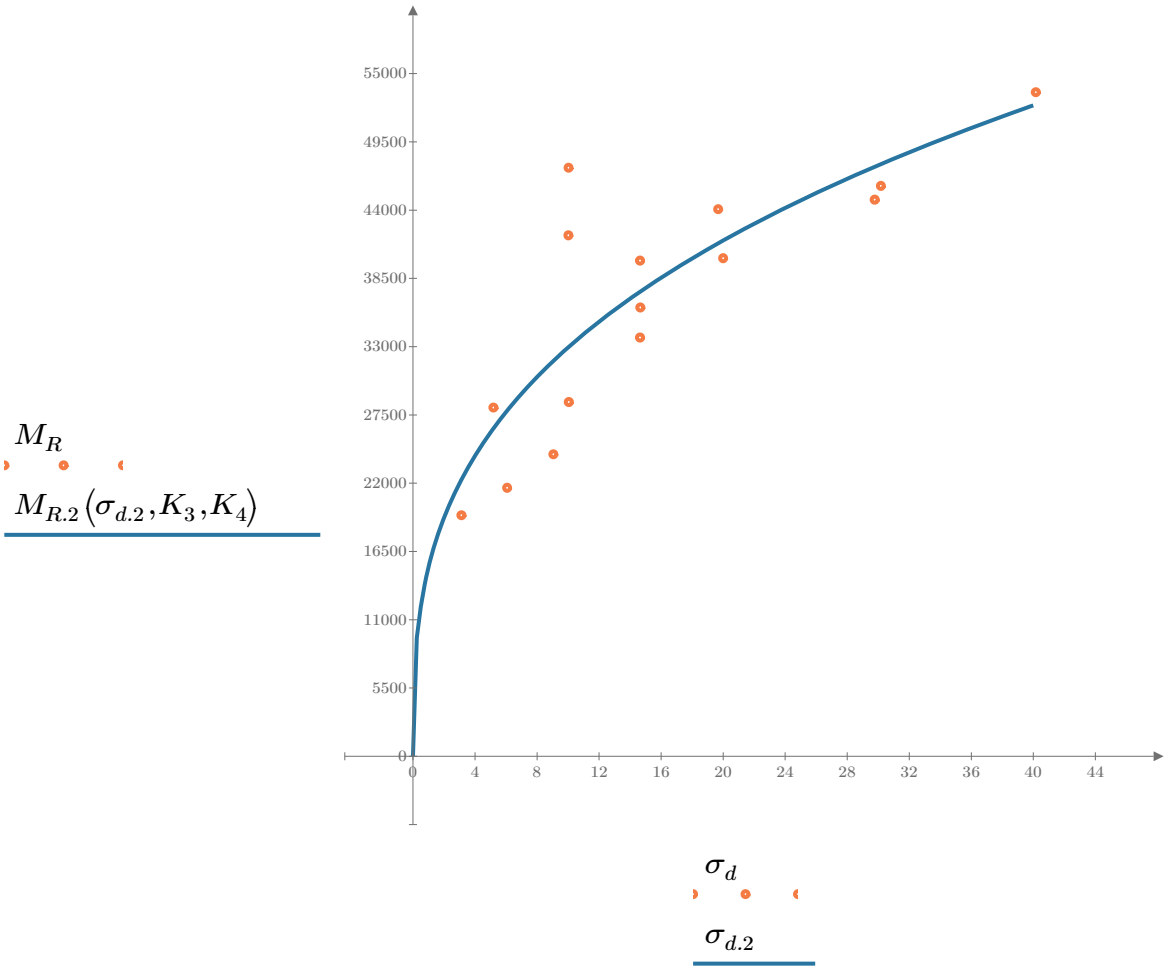

Figure 2. Plot of the test data (orange points) vs. the fitted Equation 2 model (blue line).

Dan Seely
9/11/2023

$$M_{R.3}\left(\sigma_d,\sigma_3,K_5,K_6,K_7\right) := K_5 \cdot {\sigma_d}^{K_6} \cdot \left(1+\sigma_3\right)^{K_7}$$

Equation 3 AASHTO Publication No. FHWA-RD-97-083

$K_5 = 13574.578$

$K_6 = 0.1941$ Equation 3 fitting parameters

$K_7 = 0.2109$

${R_3}^2 = 0.8093$ Coefficient of determination

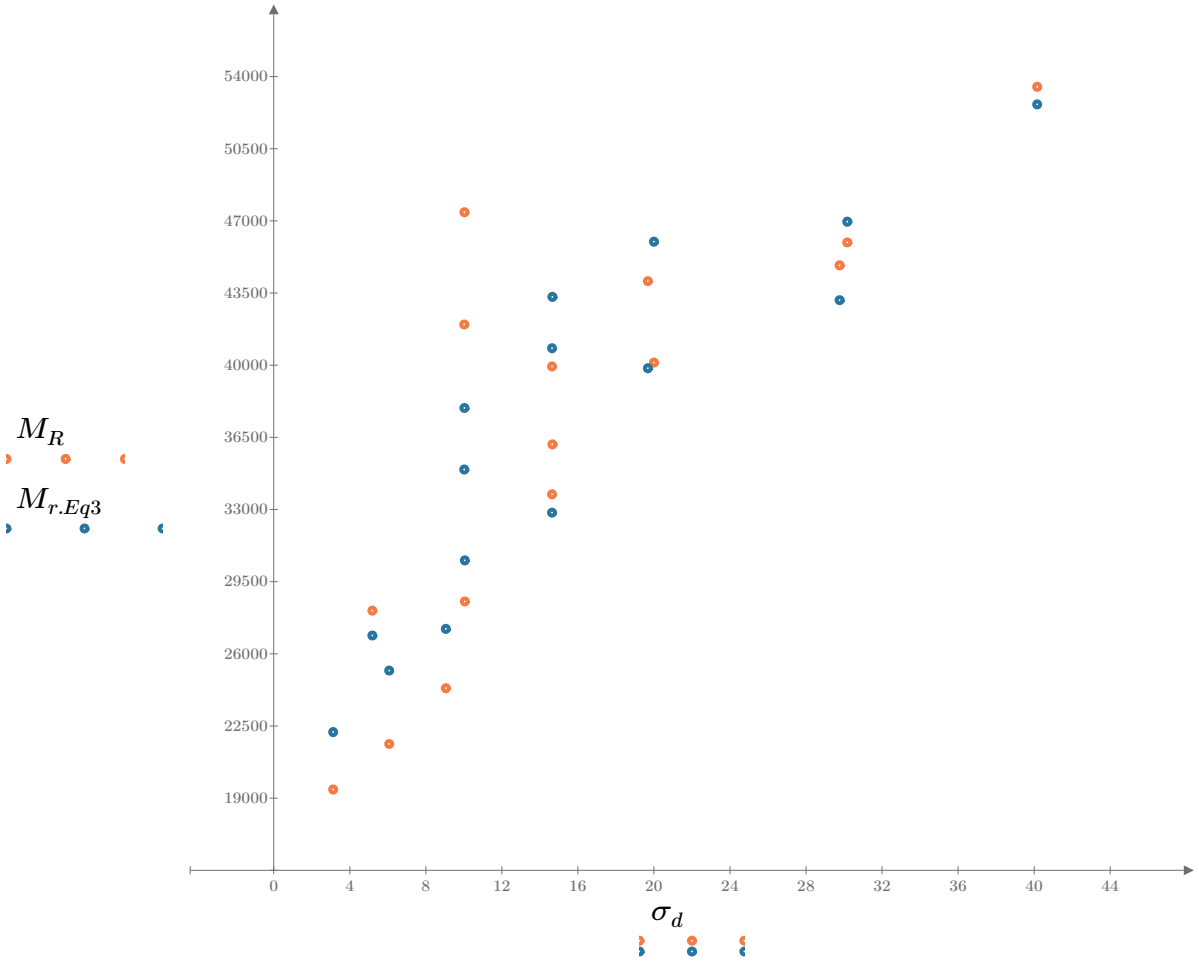

Figure 3. Plot of the test data (orange points) vs. the fitted Equation 3 model (blue points).

Dan Seely
9/11/2023

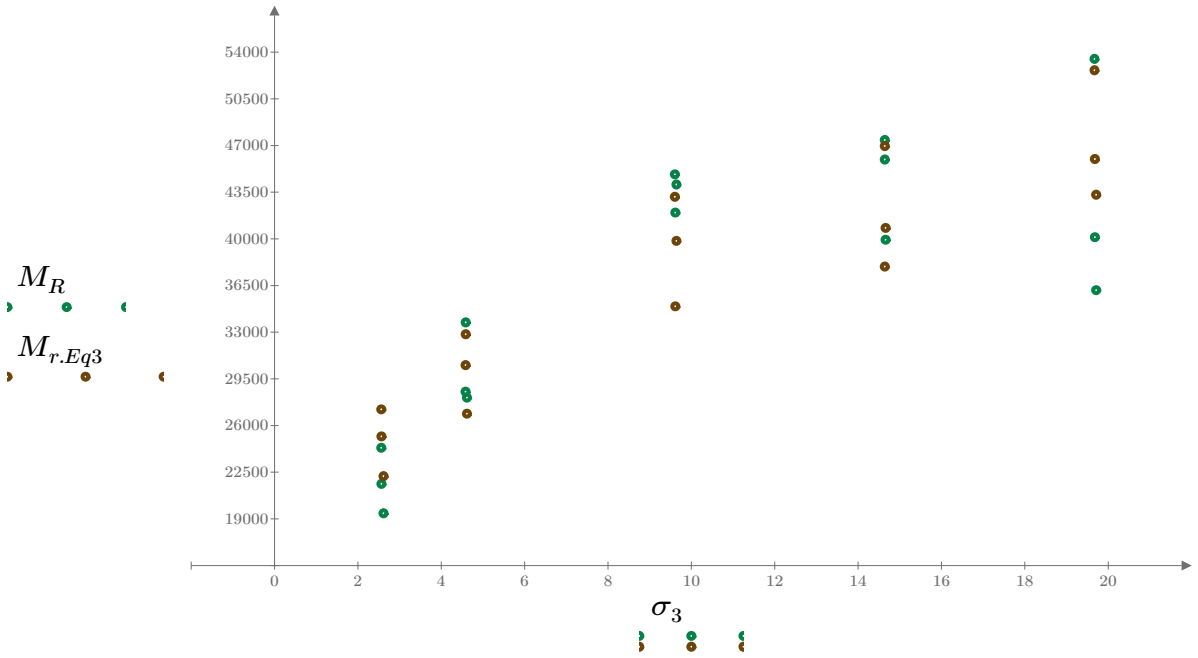

Figure 4. Plot of the test data (green points) vs. the fitted Equation 3 model (brown points).

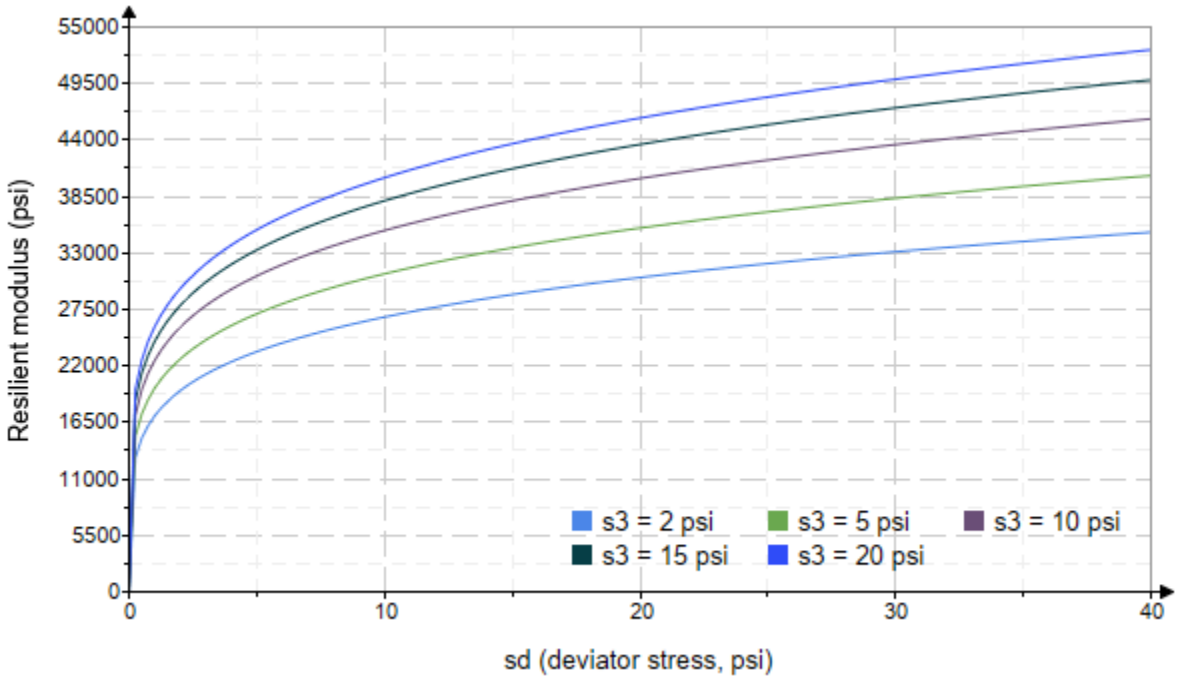

Figure 5. Plot of the fitted Equation 3 model for various confining stresses.

Dan Seely
9/11/2023

$$M_{R.4}\left(\sigma_B,\sigma_d,K_8,K_9,K_{10}\right) := K_8 \cdot p_a \left(\frac{\sigma_B}{p_a}\right)^{K_9} \cdot \left(\frac{\sigma_d}{p_a}\right)^{K_{10}}$$

Equation 4 AASHTO Publication No. FHWA-RD-97-083

$K_8 = 1854.439$

$K_9 = 0.2939$ Equation 4 fitting parameters

$K_{10} = 0.0883$

$R_4^{\ 2} = 0.8187$ Coefficient of determination

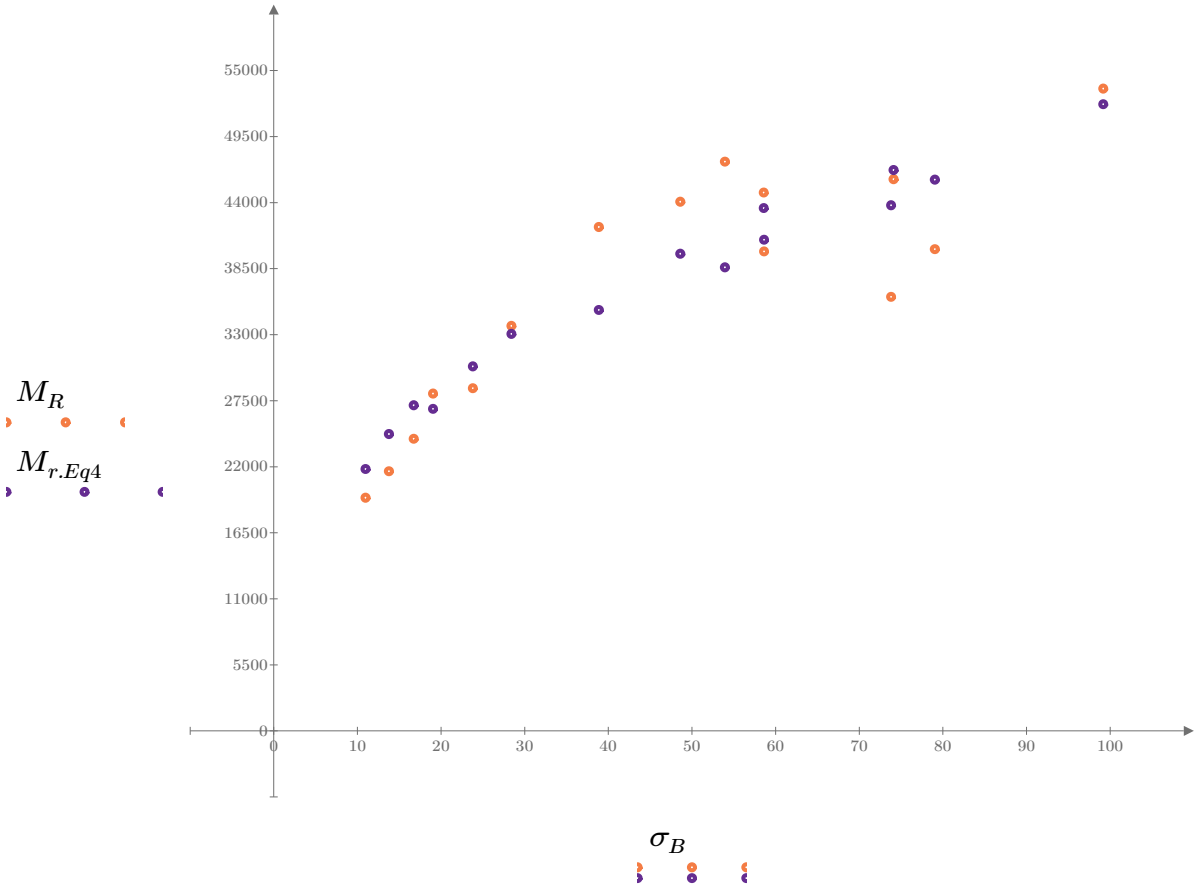

Figure 6. Plot of the test data (orange points) vs. the fitted Equation 4 model (purple points).

Dan Seely
9/11/2023

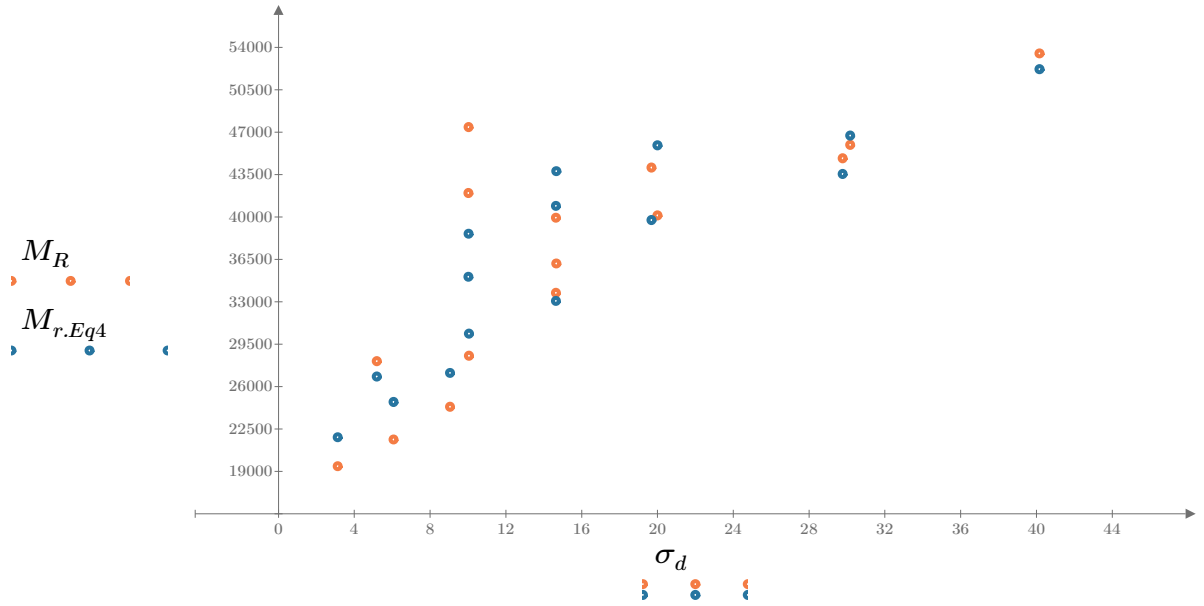

Figure 7. Plot of the test data (orange points) vs. the fitted Equation 4 model (blue points).

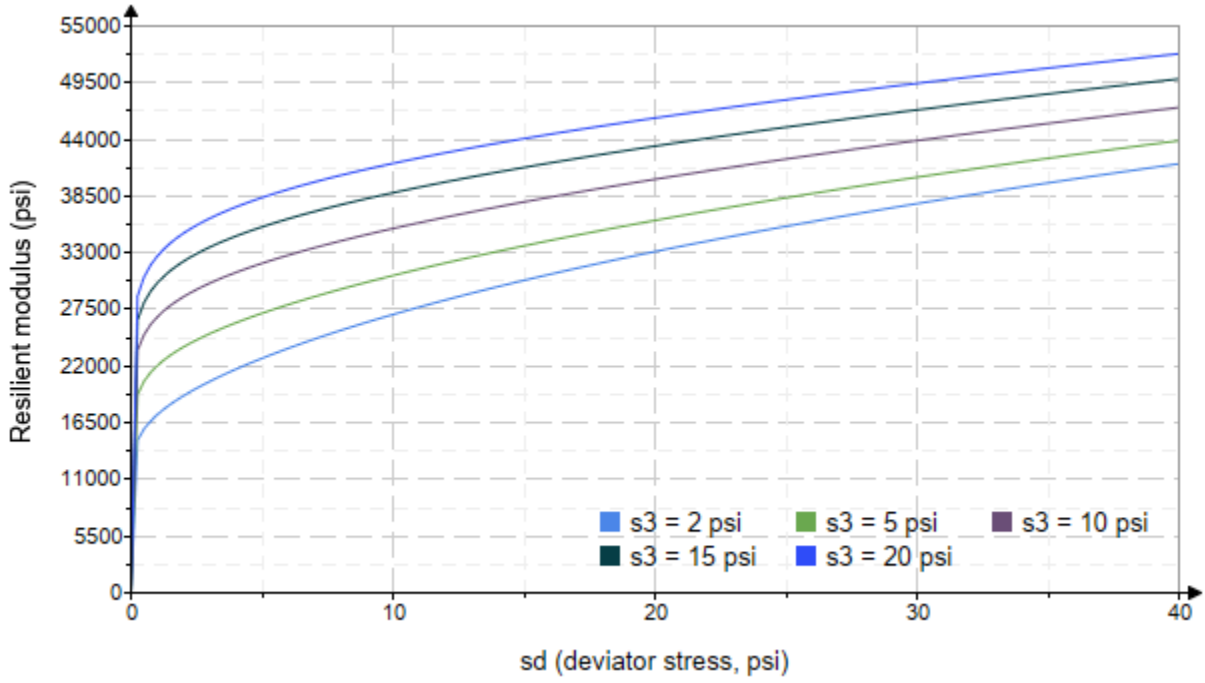

Figure 8. Plot of the fitted Equation 4 model for various confining stresses.

Dan Seely
9/11/2023

$SampleNo := \text{“B2}-\text{25”}$

$Treatment = \text{“AD”}$

$S = 3.122$ Degree of Saturation (%)

Test Sequence : Base/Subbase

Test summary data (psi) :

$$\sigma_3 = \begin{bmatrix} 2.137 \\ 2.010 \\ 1.843 \\ 3.726 \\ 3.851 \\ 4.080 \\ 9.257 \\ 8.953 \\ 9.449 \\ 14.440 \\ 14.260 \\ 14.300 \\ 19.360 \\ 19.150 \\ 19.430 \end{bmatrix} \quad \sigma_d = \begin{bmatrix} 3.296 \\ 6.251 \\ 9.159 \\ 5.311 \\ 10.030 \\ 14.640 \\ 9.919 \\ 19.740 \\ 30.260 \\ 10.020 \\ 14.770 \\ 30.060 \\ 14.780 \\ 20.150 \\ 40.620 \end{bmatrix} \quad \sigma_B = \begin{bmatrix} 9.706 \\ 12.280 \\ 14.690 \\ 16.490 \\ 21.580 \\ 26.880 \\ 37.690 \\ 46.600 \\ 58.610 \\ 53.340 \\ 57.550 \\ 72.950 \\ 72.870 \\ 77.600 \\ 98.910 \end{bmatrix} \quad M_R = \begin{bmatrix} 57748.3 \\ 46032.8 \\ 37091.0 \\ 42374.2 \\ 33169.0 \\ 36626.8 \\ 42037.6 \\ 52130.2 \\ 54378.6 \\ 56467.0 \\ 58700.6 \\ 58495.4 \\ 60163.2 \\ 57753.2 \\ 64028.8 \end{bmatrix}$$

σ_3 = mean confining stress
σ_d = mean deviator stress
σ_B = mean bulk stress
M_R = resilient modulus
p_a = atmospheric pressure = 14.6959 psi

Dan Seely
9/11/2023

$$M_{R.1}(\sigma_B, K_1, K_2) := K_1 \cdot {\sigma_B}^{K_2}$$

Equation 1
AASHTO Publication No. FHWA-RD-97-083

$K_1 = 25527.182$

$K_2 = 0.1876$

Equation 1 fitting parameters

${R_1}^2 = 0.4382$

Coefficient of determination

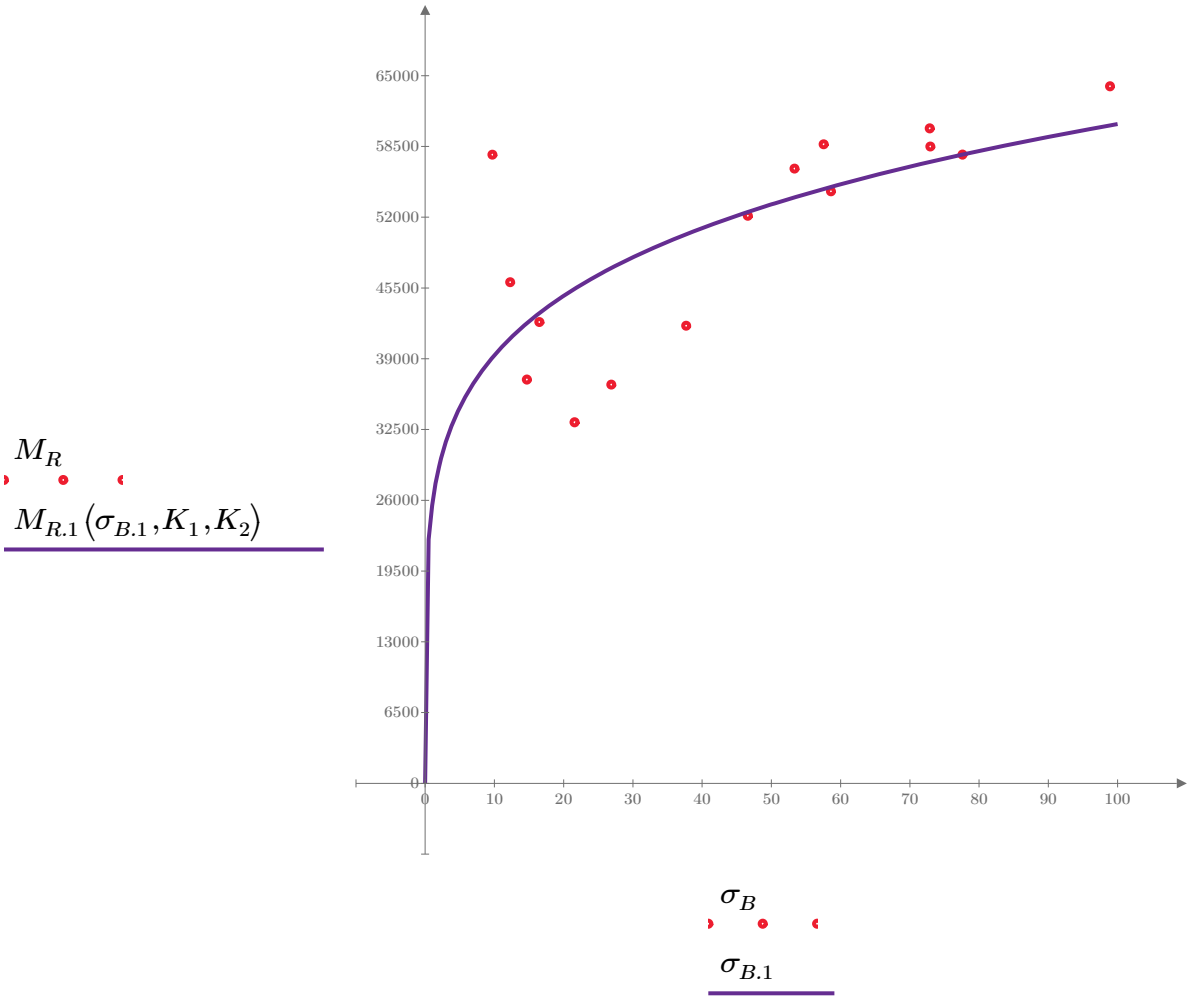

Figure 1. Plot of the test data (red points) vs. the fitted Equation 1 model (purple line).

Dan Seely
9/11/2023

$$M_{R.2}(\sigma_d, K_3, K_4) := K_3 \cdot \sigma_d^{K_4}$$

Equation 2
AASHTO Publication No. FHWA-RD-97-083

$K_3 = 35677.427$

$K_4 = 0.1339$

Equation 2 fitting parameters

$R_2^2 = 0.1951$

Coefficient of determination

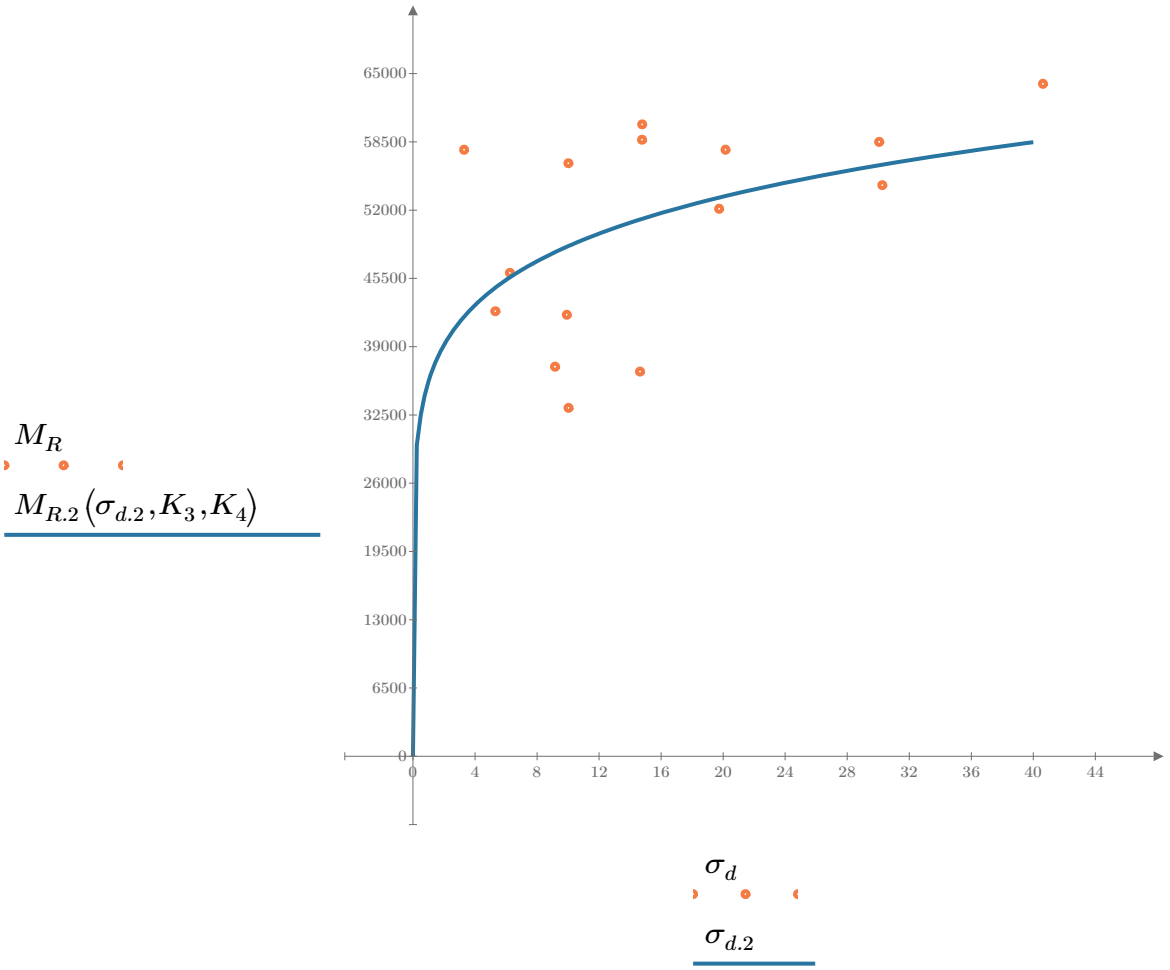

Figure 2. Plot of the test data (orange points) vs. the fitted Equation 2 model (blue line).

Dan Seely
9/11/2023

$$M_{R.3}(\sigma_d, \sigma_3, K_5, K_6, K_7) := K_5 \cdot \sigma_d^{K_6} \cdot (1 + \sigma_3)^{K_7}$$

Equation 3 AASHTO Publication No. FHWA-RD-97-083

$K_5 = 33731.323$

$K_6 = -0.0354$ Equation 3 fitting parameters

$K_7 = 0.2249$

$R_3^2 = 0.5298$ Coefficient of determination

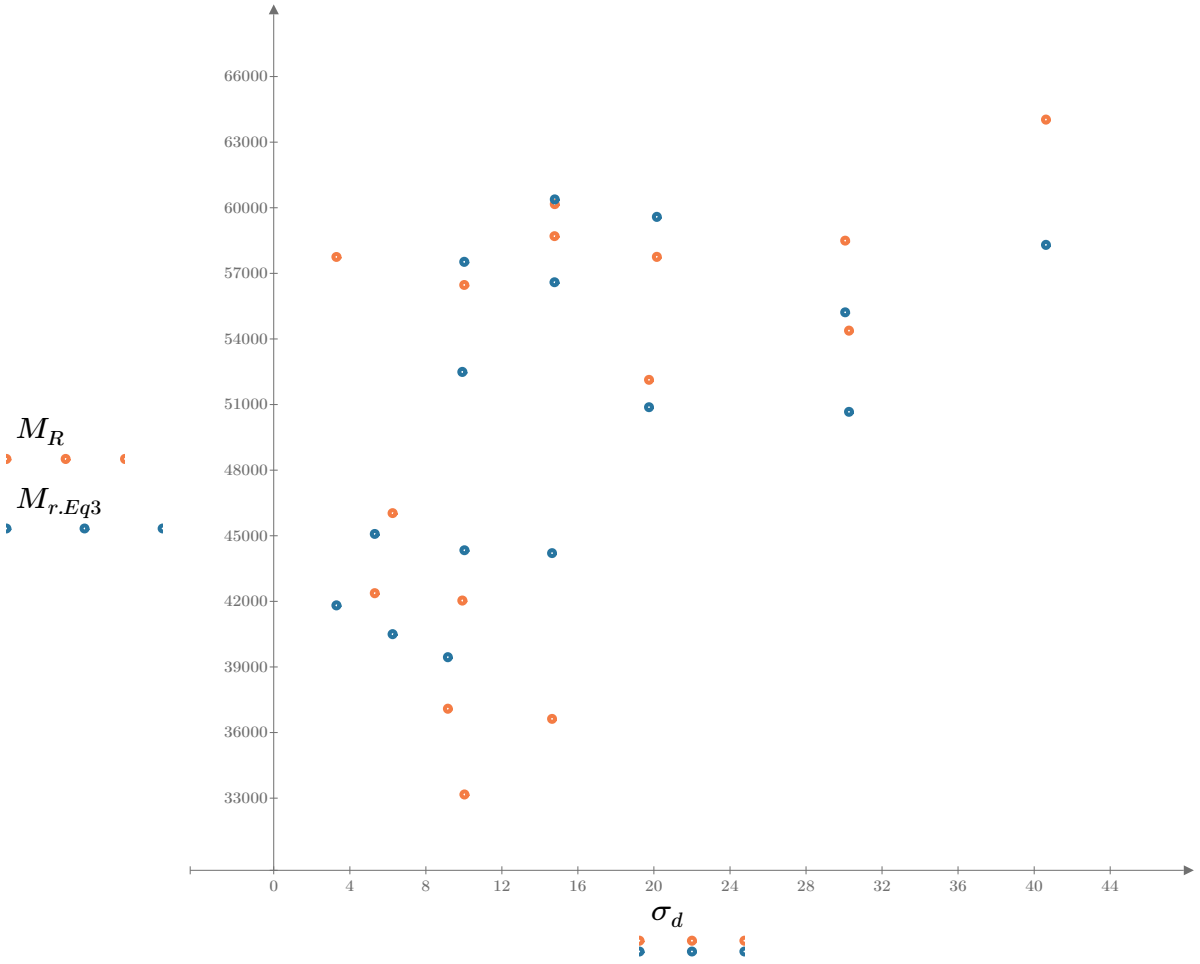

Figure 3. Plot of the test data (orange points) vs. the fitted Equation 3 model (blue points).

Dan Seely
9/11/2023

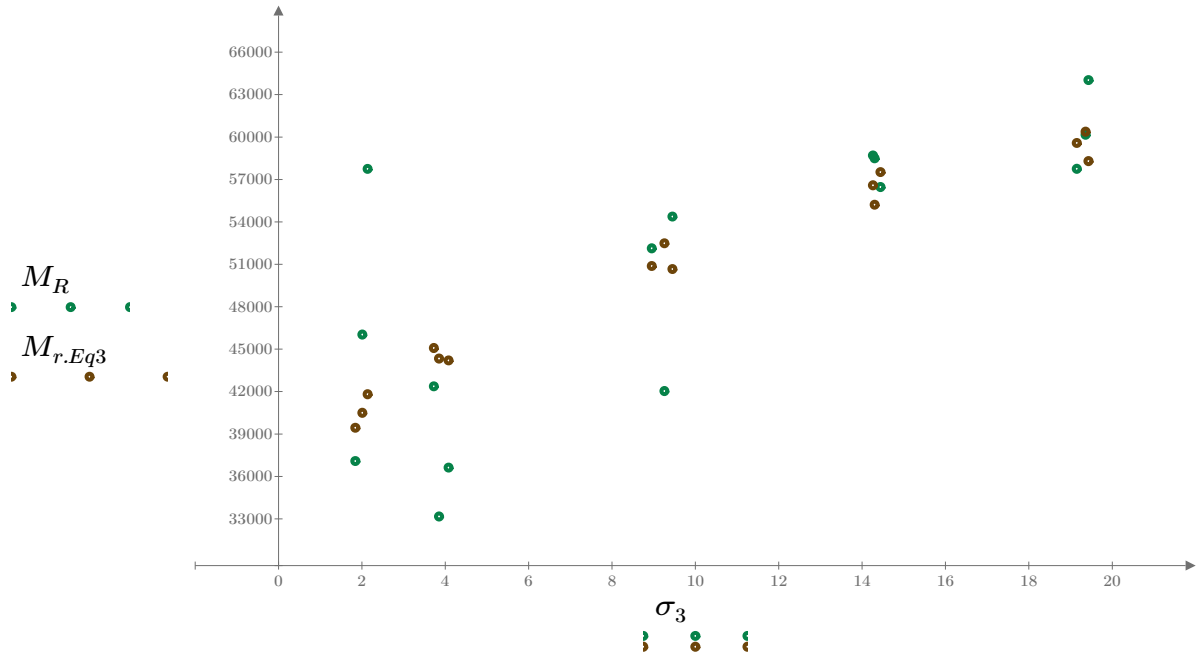

Figure 4. Plot of the test data (green points) vs. the fitted Equation 3 model (brown points).

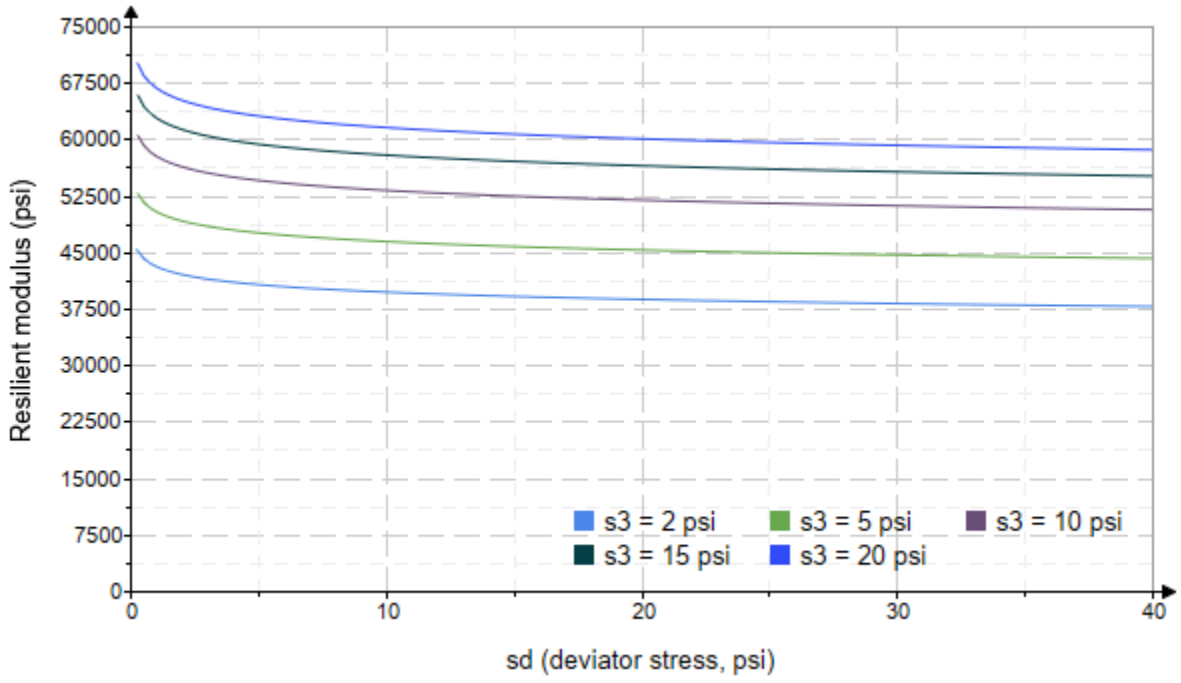

Figure 5. Plot of the fitted Equation 3 model for various confining stresses.

Dan Seely
9/11/2023

$$M_{R.4}\left(\sigma_B,\sigma_d,K_8,K_9,K_{10}\right) := K_8 \cdot p_a \left(\frac{\sigma_B}{p_a}\right)^{K_9} \cdot \left(\frac{\sigma_d}{p_a}\right)^{K_{10}}$$

Equation 4 AASHTO Publication No. FHWA-RD-97-083

$K_8 = 2597.540$

$K_9 = 0.2833$ Equation 4 fitting parameters

$K_{10} = -0.1251$

$R_4^{\,2} = 0.4866$ Coefficient of determination

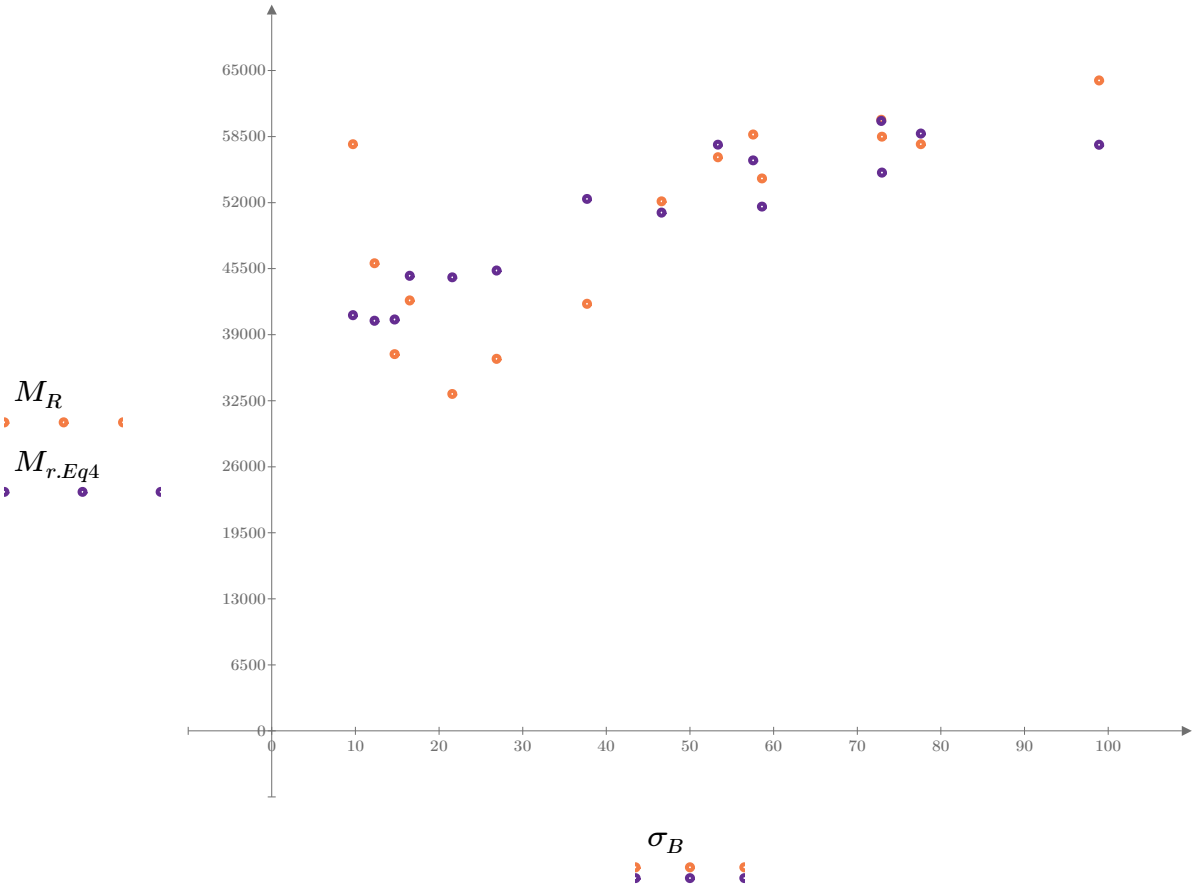

Figure 6. Plot of the test data (orange points) vs. the fitted Equation 4 model (purple points).

Dan Seely
9/11/2023

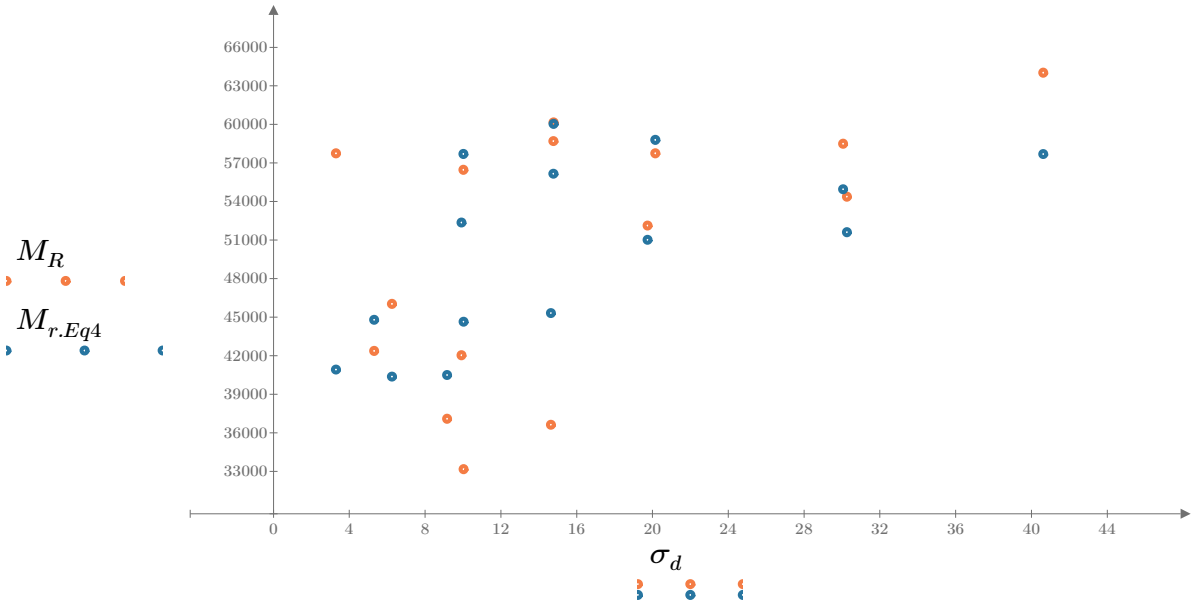

Figure 7. Plot of the test data (orange points) vs. the fitted Equation 4 model (blue points).

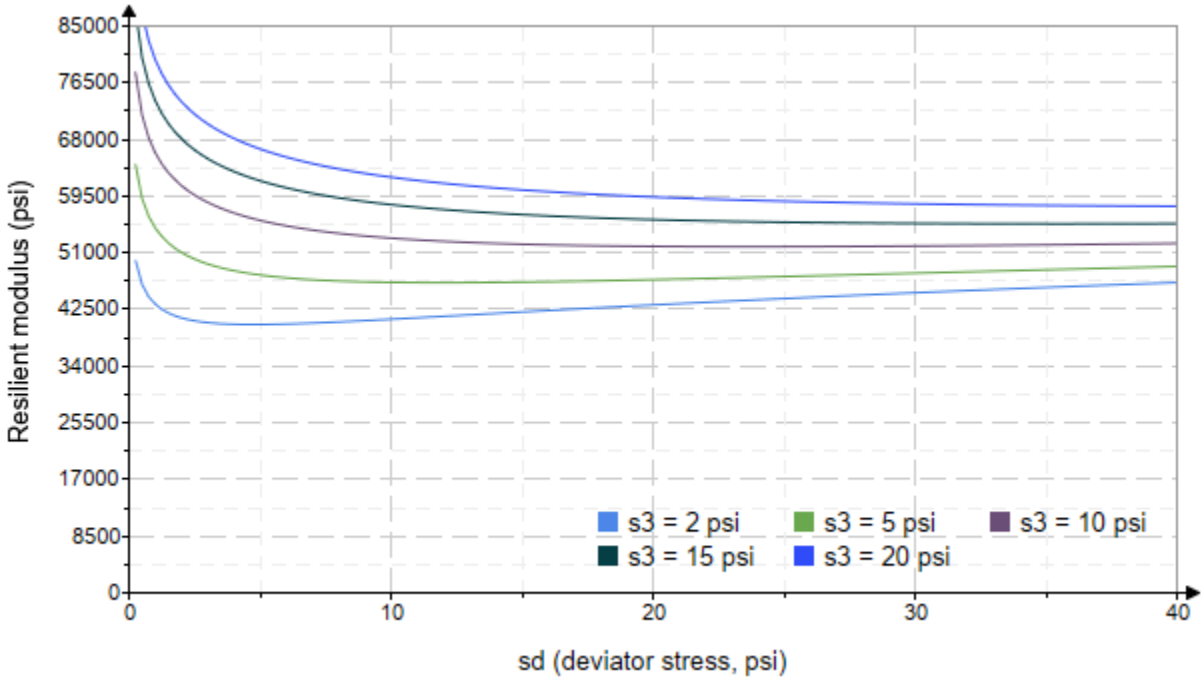

Figure 8. Plot of the fitted Equation 4 model for various confining stresses.

Dan Seely
9/11/2023

$SampleNo := \text{“B2}-\text{26”}$

$Treatment = \text{“AD”}$

$S = 3.620$ Degree of Saturation (%)

Test Sequence : Base/Subbase

Test summary data (psi) :

$$\sigma_3 = \begin{bmatrix} 2.790 \\ 2.778 \\ 2.759 \\ 4.557 \\ 4.585 \\ 4.573 \\ 9.615 \\ 9.597 \\ 9.595 \\ 14.650 \\ 14.630 \\ 14.630 \\ 19.650 \\ 19.640 \\ 19.640 \end{bmatrix} \quad \sigma_d = \begin{bmatrix} 3.148 \\ 6.008 \\ 8.844 \\ 5.089 \\ 9.692 \\ 14.270 \\ 9.697 \\ 19.380 \\ 29.570 \\ 9.735 \\ 14.440 \\ 29.600 \\ 14.290 \\ 19.610 \\ 40.020 \end{bmatrix} \quad \sigma_B = \begin{bmatrix} 11.520 \\ 14.340 \\ 17.120 \\ 18.760 \\ 23.450 \\ 27.990 \\ 38.540 \\ 48.170 \\ 58.350 \\ 53.680 \\ 58.320 \\ 73.490 \\ 73.250 \\ 78.540 \\ 98.950 \end{bmatrix} \quad M_R = \begin{bmatrix} 39839.8 \\ 46321.2 \\ 45306.8 \\ 45914.2 \\ 51544.0 \\ 53961.8 \\ 53829.6 \\ 69377.2 \\ 68868.6 \\ 46547.0 \\ 64757.8 \\ 73187.6 \\ 85386.2 \\ 88371.0 \\ 81176.8 \end{bmatrix}$$

σ_3 = mean confining stress
σ_d = mean deviator stress
σ_B = mean bulk stress
M_R = resilient modulus
p_a = atmospheric pressure = 14.6959 psi

Dan Seely
9/11/2023

$$M_{R.1}\left(\sigma_B, K_1, K_2\right) := K_1 \cdot {\sigma_B}^{K_2}$$

Equation 1
AASHTO Publication No. FHWA-RD-97-083

$K_1 = 16046.691$

$K_2 = 0.3591$

Equation 1 fitting parameters

${R_1}^2 = 0.7846$

Coefficient of determination

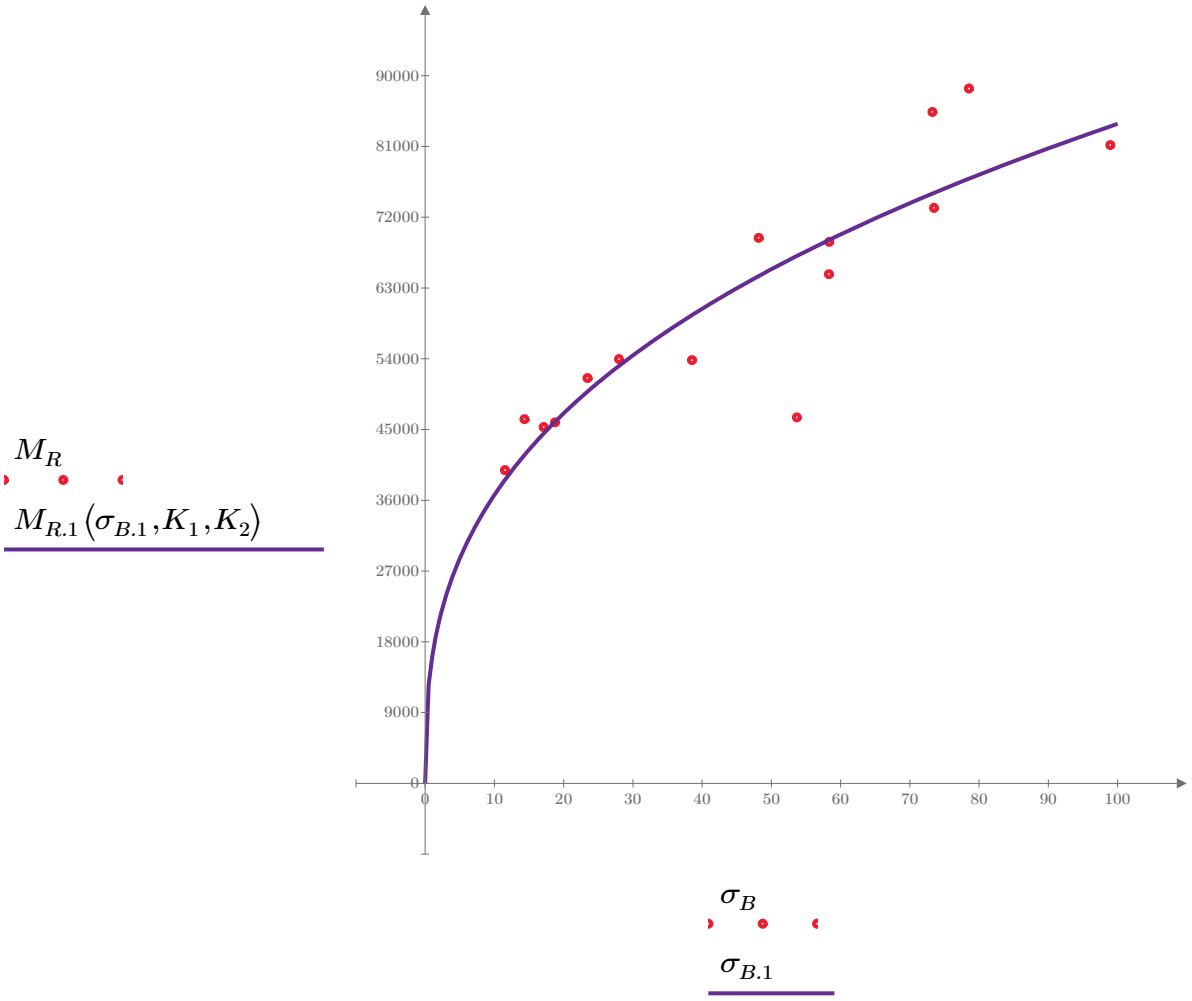

Figure 1. Plot of the test data (red points) vs. the fitted Equation 1 model (purple line).

Dan Seely
9/11/2023

$$M_{R.2}(\sigma_d, K_3, K_4) := K_3 \cdot \sigma_d^{K_4}$$

Equation 2
AASHTO Publication No. FHWA-RD-97-083

$K_3 = 27966.567$

$K_4 = 0.3002$

Equation 2 fitting parameters

$R_2^2 = 0.6413$

Coefficient of determination

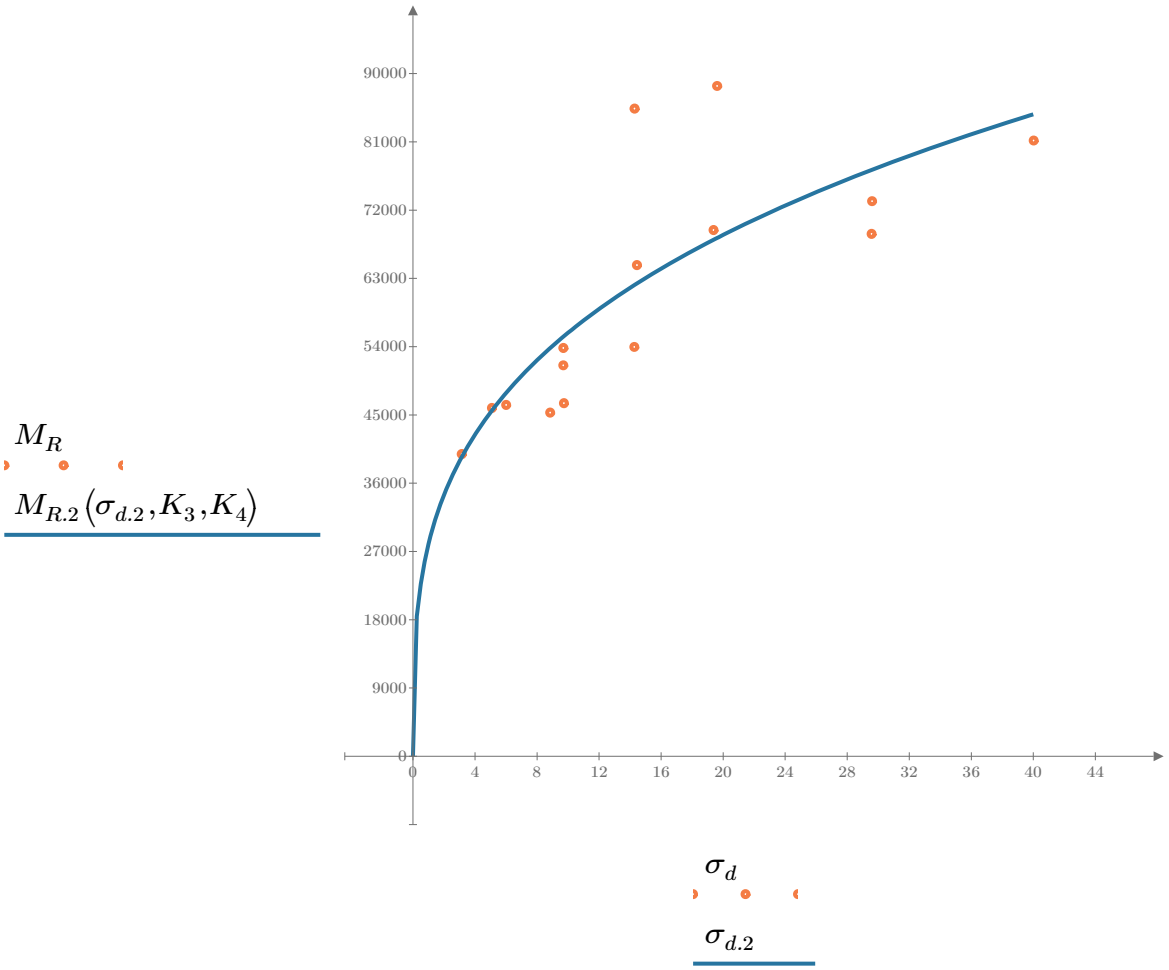

Figure 2. Plot of the test data (orange points) vs. the fitted Equation 2 model (blue line).

Dan Seely
9/11/2023

$$M_{R.3}\left(\sigma_d,\sigma_3,K_5,K_6,K_7\right):=K_5\cdot{\sigma_d}^{K_6}\cdot\left(1+\sigma_3\right)^{K_7}$$

Equation 3 AASHTO Publication No. FHWA-RD-97-083

$K_5=23425.962$

$K_6=0.1571$ Equation 3 fitting parameters

$K_7=0.2373$

${R_3}^2=0.8015$ Coefficient of determination

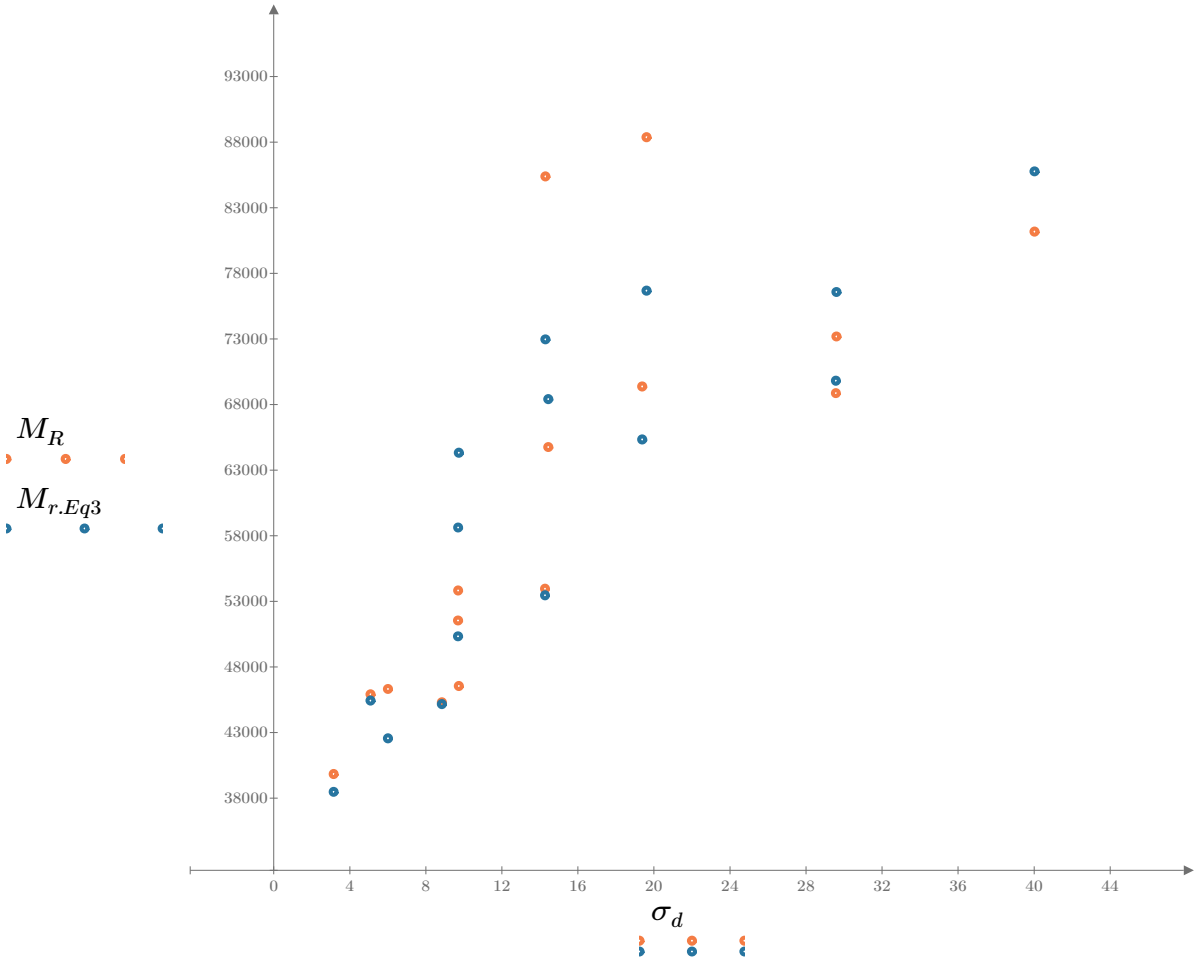

Figure 3. Plot of the test data (orange points) vs. the fitted Equation 3 model (blue points).

Dan Seely
9/11/2023

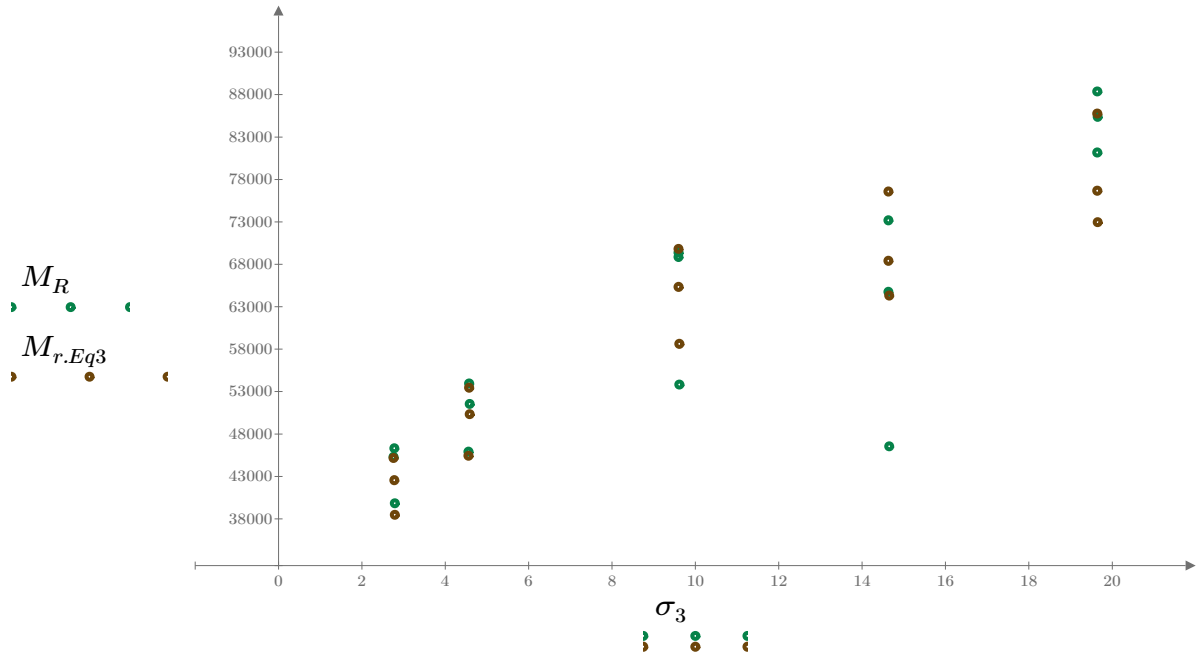

Figure 4. Plot of the test data (green points) vs. the fitted Equation 3 model (brown points).

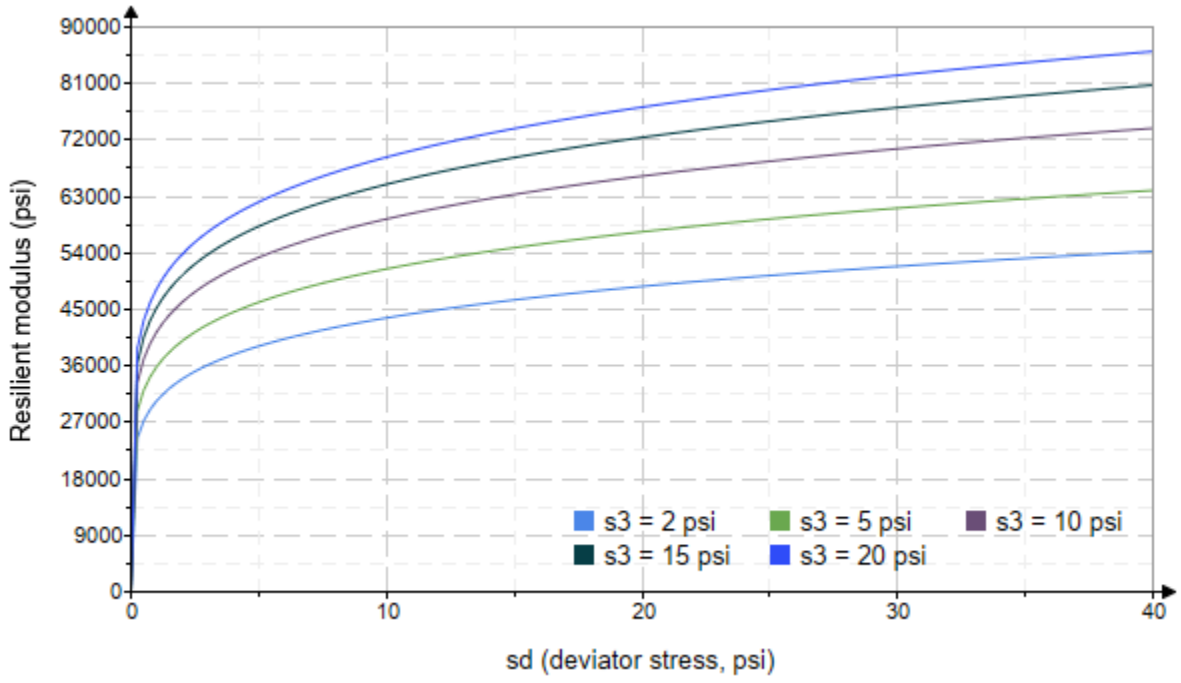

Figure 5. Plot of the fitted Equation 3 model for various confining stresses.

Dan Seely
9/11/2023

$$M_{R.4}\left(\sigma_B,\sigma_d,K_8,K_9,K_{10}\right) := K_8 \cdot p_a \left(\frac{\sigma_B}{p_a}\right)^{K_9} \cdot \left(\frac{\sigma_d}{p_a}\right)^{K_{10}}$$

Equation 4 AASHTO Publication No. FHWA-RD-97-083

$K_8 = 3048.626$

$K_9 = 0.3044$ Equation 4 fitting parameters

$K_{10} = 0.0603$

$R_4^{\,2} = 0.7917$ Coefficient of determination

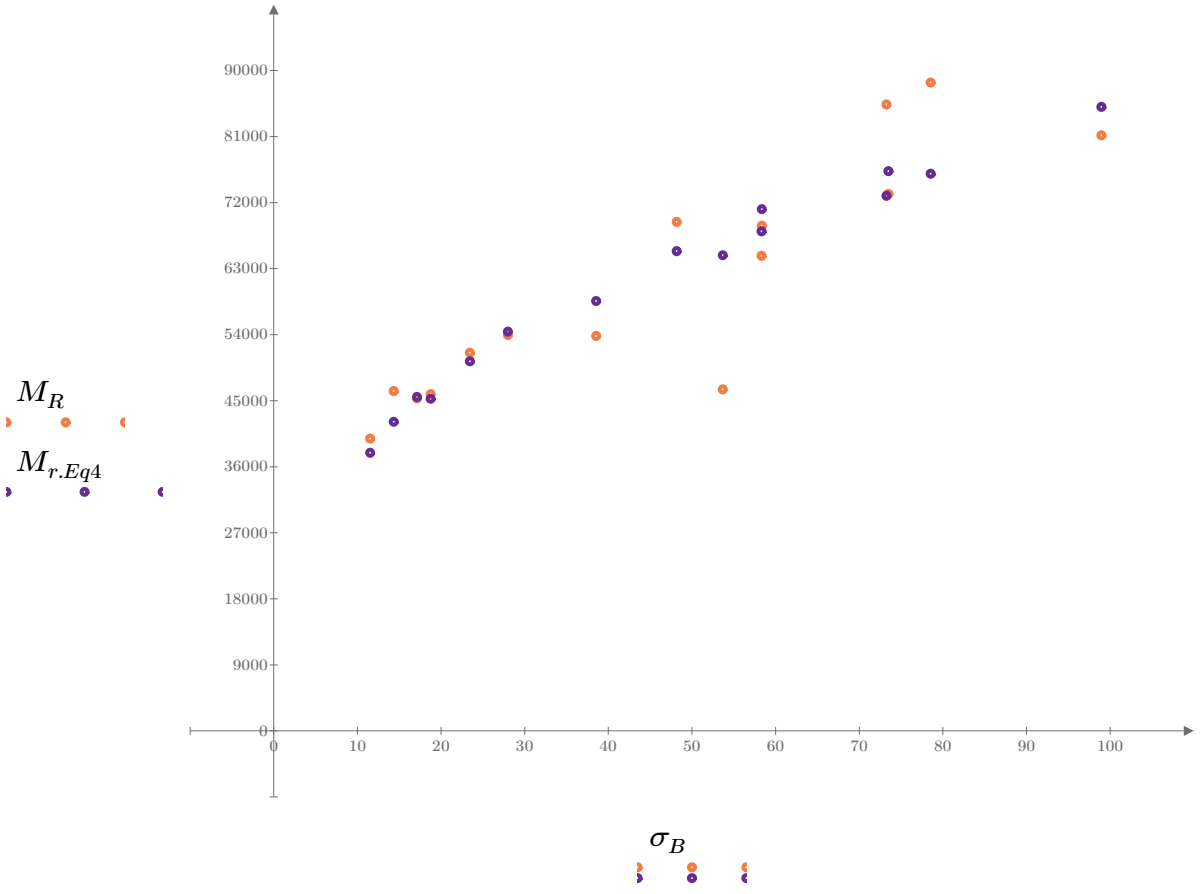

Figure 6. Plot of the test data (orange points) vs. the fitted Equation 4 model (purple points).

Dan Seely
9/11/2023

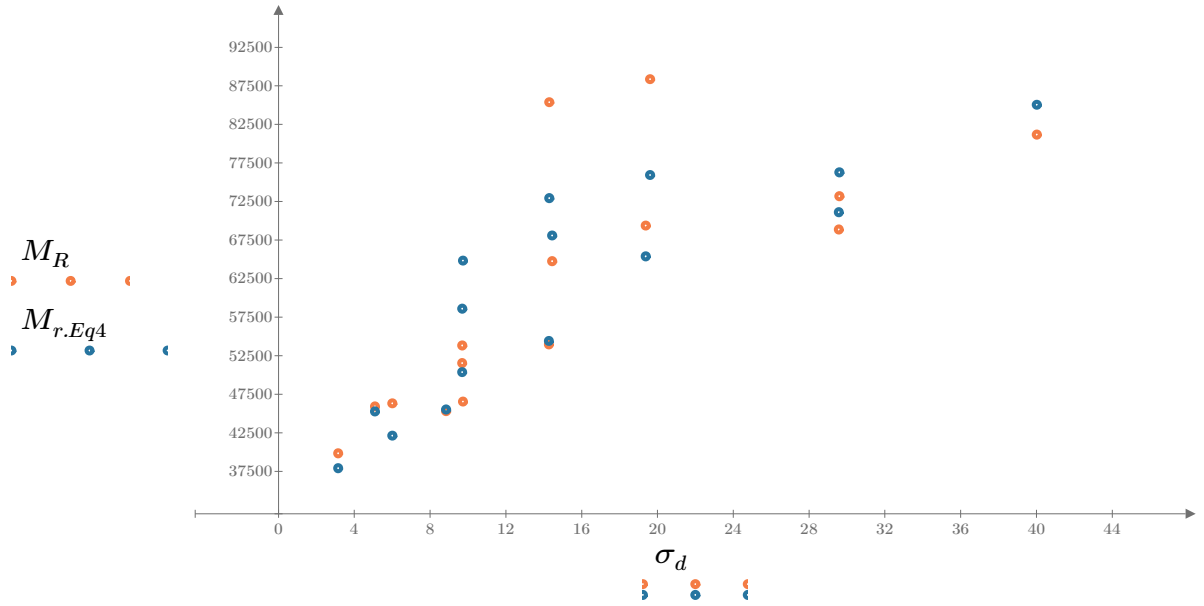

Figure 7. Plot of the test data (orange points) vs. the fitted Equation 4 model (blue points).

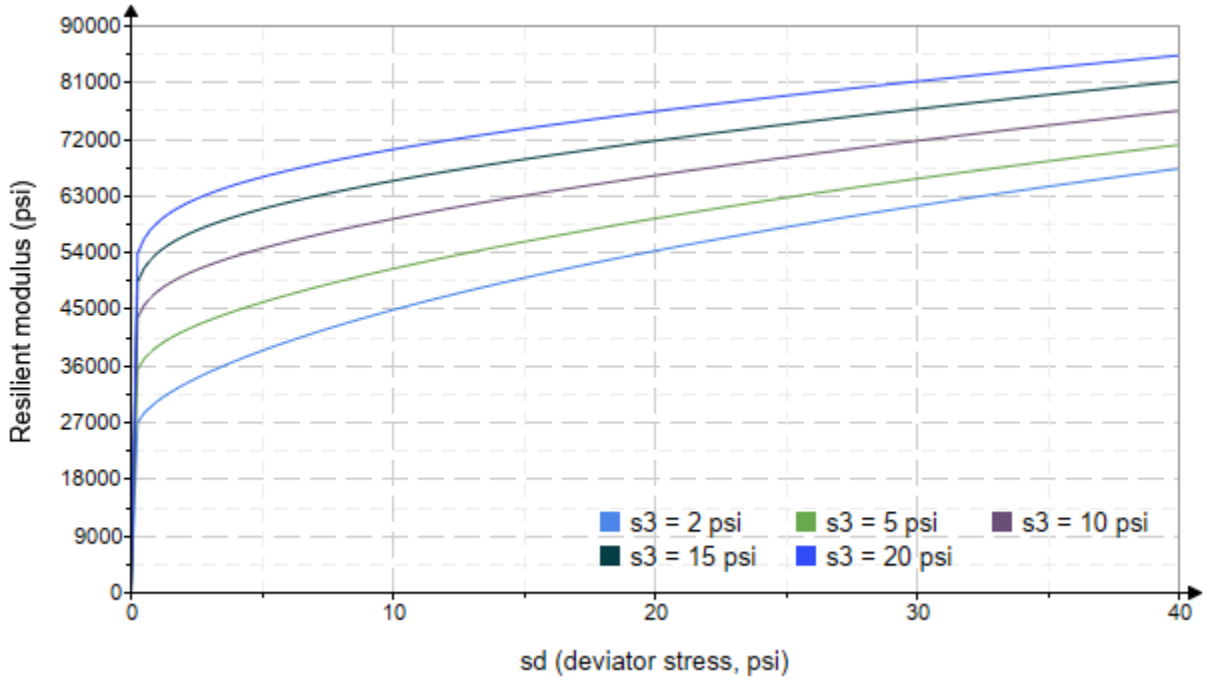

Figure 8. Plot of the fitted Equation 4 model for various confining stresses.

Dan Seely
9/11/2023

$SampleNo := \text{“B2}-\text{27”}$

$Treatment = \text{“H100”}$

$S = 4.449$ Degree of Saturation (%)

Test Sequence : Base/Subbase

Test summary data (psi) :

$$\sigma_3 = \begin{bmatrix} 2.714 \\ 2.762 \\ 2.796 \\ 4.604 \\ 4.641 \\ 4.636 \\ 9.701 \\ 9.632 \\ 9.627 \\ 14.650 \\ 14.620 \\ 14.560 \\ 19.640 \\ 19.590 \\ 19.640 \end{bmatrix} \quad \sigma_d = \begin{bmatrix} 3.195 \\ 6.113 \\ 8.936 \\ 5.064 \\ 9.879 \\ 14.580 \\ 9.852 \\ 19.670 \\ 29.910 \\ 9.923 \\ 14.670 \\ 30.050 \\ 14.610 \\ 19.940 \\ 40.190 \end{bmatrix} \quad \sigma_B = \begin{bmatrix} 11.340 \\ 14.400 \\ 17.320 \\ 18.880 \\ 23.800 \\ 28.490 \\ 38.950 \\ 48.570 \\ 58.790 \\ 53.870 \\ 58.520 \\ 73.720 \\ 73.510 \\ 78.710 \\ 99.100 \end{bmatrix} \quad M_R = \begin{bmatrix} 47618.8 \\ 50045.2 \\ 52726.6 \\ 57001.4 \\ 67192.2 \\ 71901.4 \\ 87922.6 \\ 61075.4 \\ 64057.0 \\ 65550.2 \\ 54213.2 \\ 67509.0 \\ 58583.2 \\ 66273.0 \\ 77090.0 \end{bmatrix}$$

σ_3 = mean confining stress
σ_d = mean deviator stress
σ_B = mean bulk stress
M_R = resilient modulus
p_a = atmospheric pressure = 14.6959 psi

Dan Seely
9/11/2023

$$M_{R.1}\left(\sigma_B, K_1, K_2\right) := K_1 \cdot {\sigma_B}^{K_2}$$

Equation 1
AASHTO Publication No. FHWA-RD-97-083

$K_1 = 40598.849$

$K_2 = 0.1209$

Equation 1 fitting parameters

${R_1}^2 = 0.2473$

Coefficient of determination

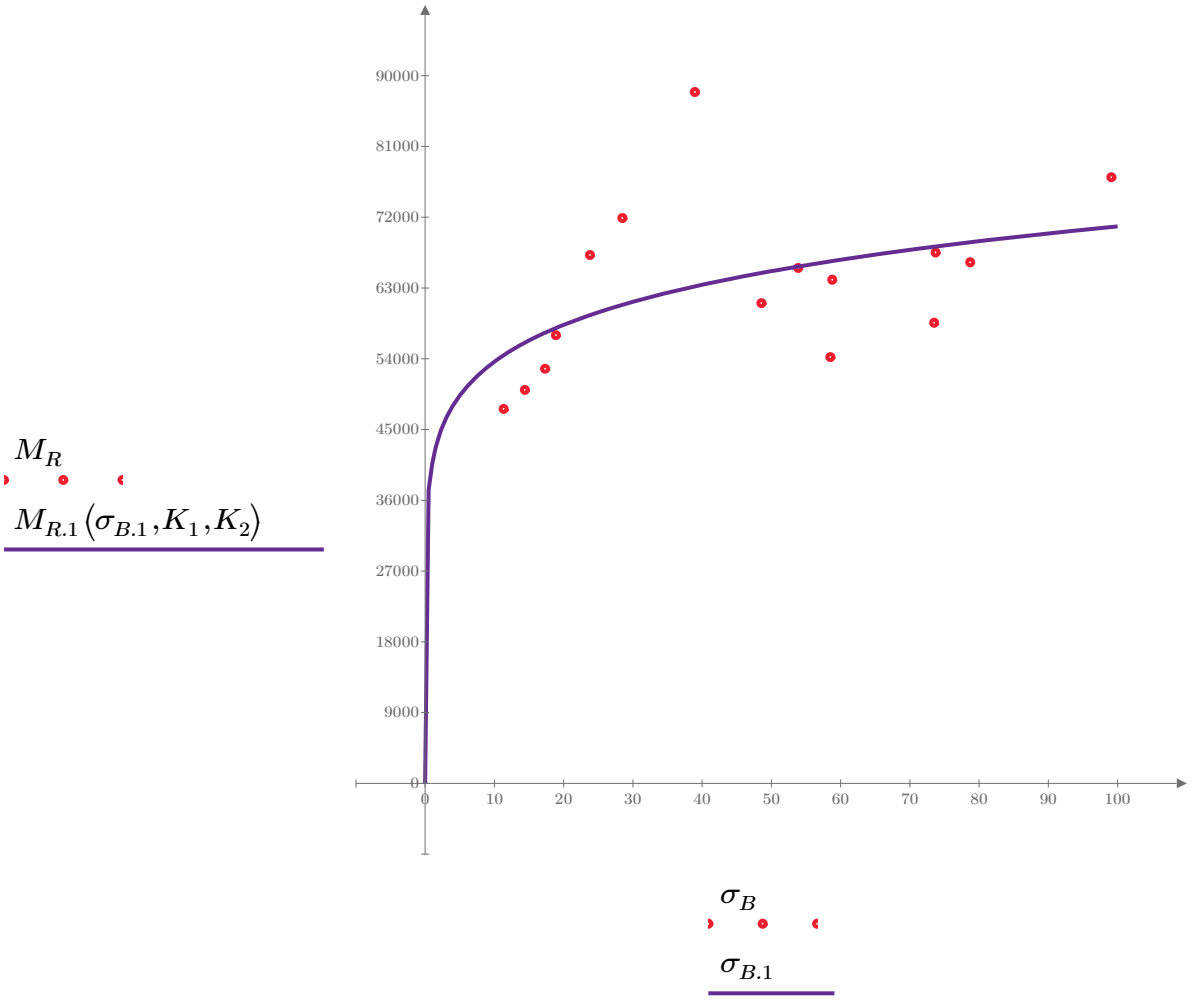

Figure 1. Plot of the test data (red points) vs. the fitted Equation 1 model (purple line).

Dan Seely
9/11/2023

$$M_{R.2}(\sigma_d, K_3, K_4) := K_3 \cdot \sigma_d^{K_4}$$

Equation 2
AASHTO Publication No. FHWA-RD-97-083

$K_3 = 46548.067$

$K_4 = 0.1193$

Equation 2 fitting parameters

$R_2^2 = 0.2471$

Coefficient of determination

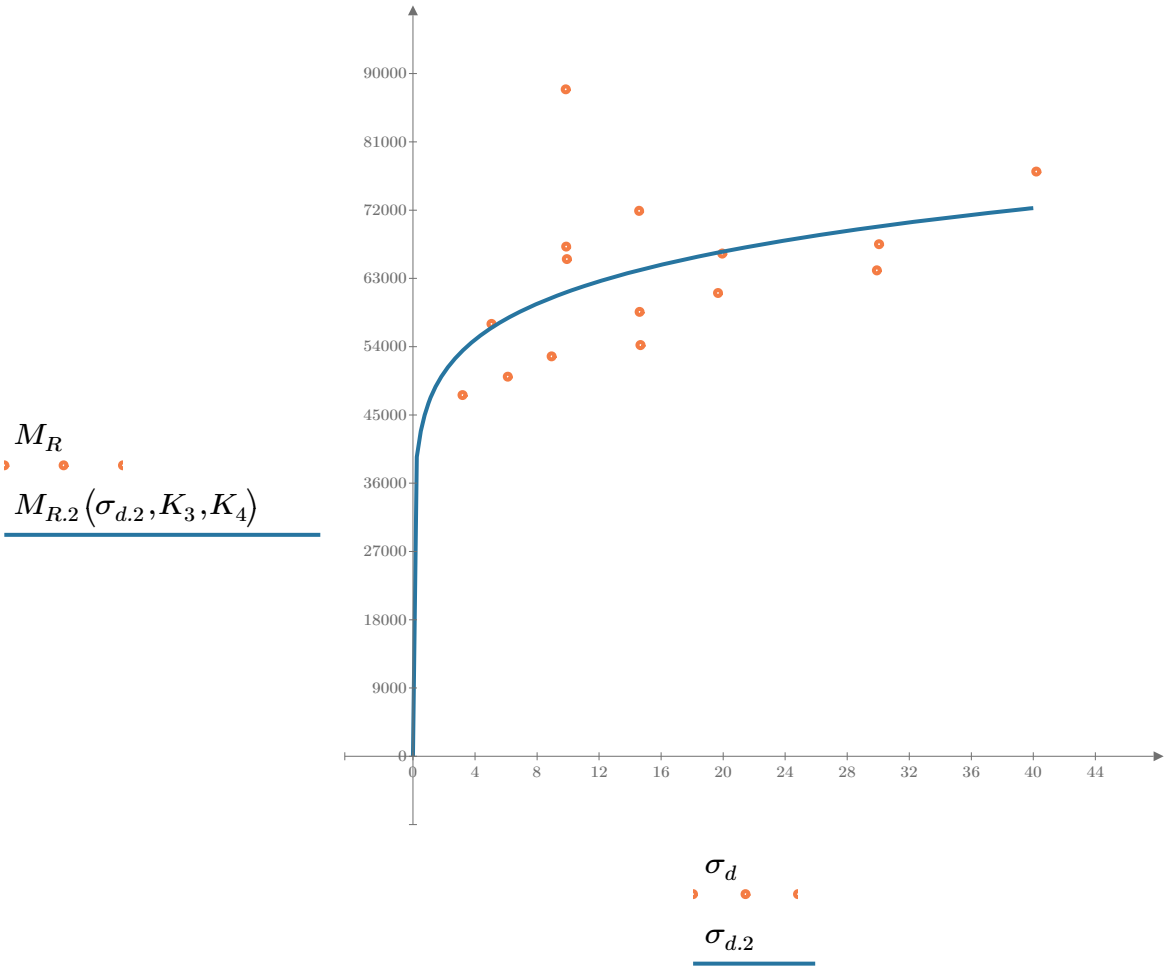

Figure 2. Plot of the test data (orange points) vs. the fitted Equation 2 model (blue line).

Dan Seely
9/11/2023

$$M_{R.3}(\sigma_d, \sigma_3, K_5, K_6, K_7) := K_5 \cdot {\sigma_d}^{K_6} \cdot (1 + \sigma_3)^{K_7}$$

Equation 3 AASHTO Publication No. FHWA-RD-97-083

$K_5 = 45508.854$

$K_6 = 0.0897$ Equation 3 fitting parameters

$K_7 = 0.0436$

${R_3}^2 = 0.2605$ Coefficient of determination

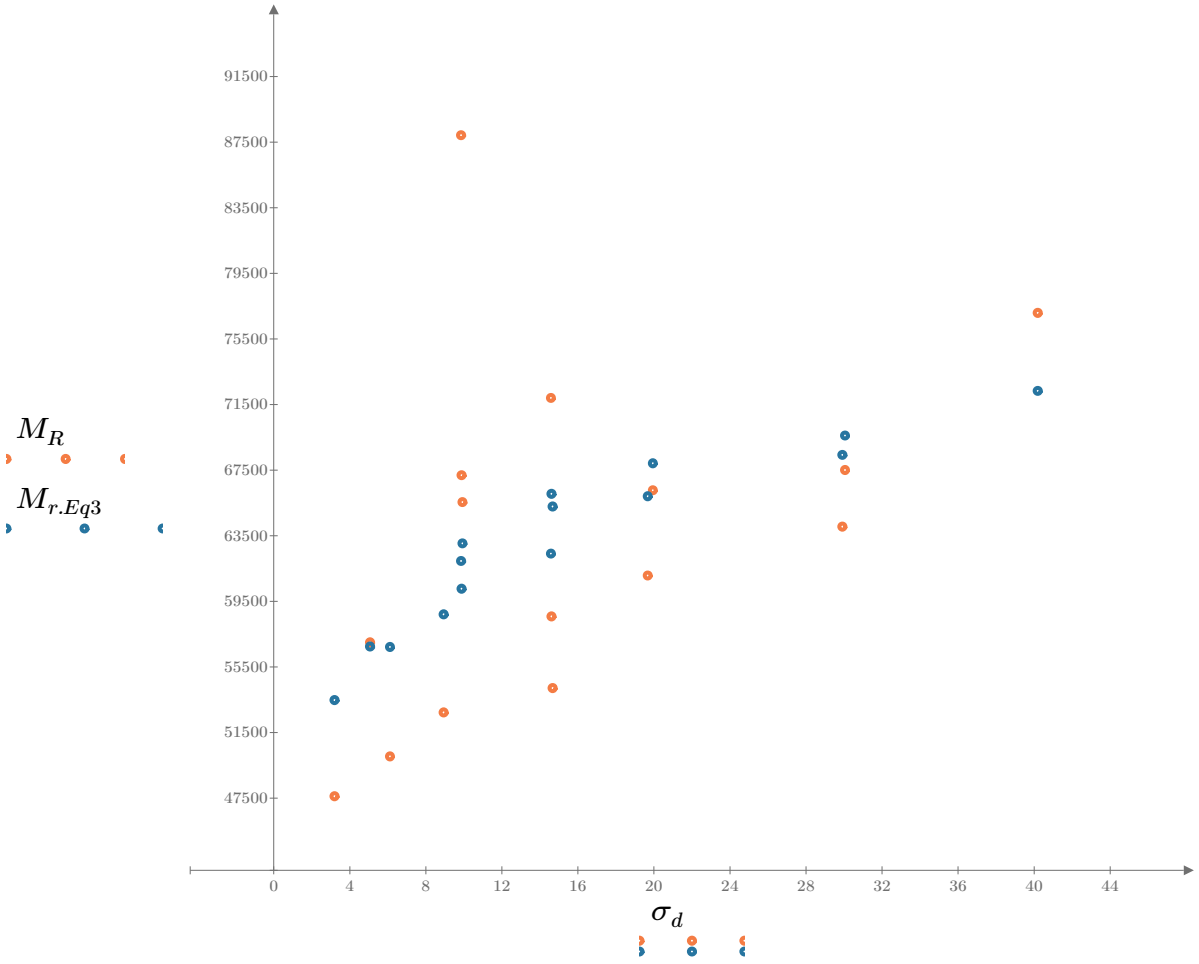

Figure 3. Plot of the test data (orange points) vs. the fitted Equation 3 model (blue points).

Dan Seely
9/11/2023

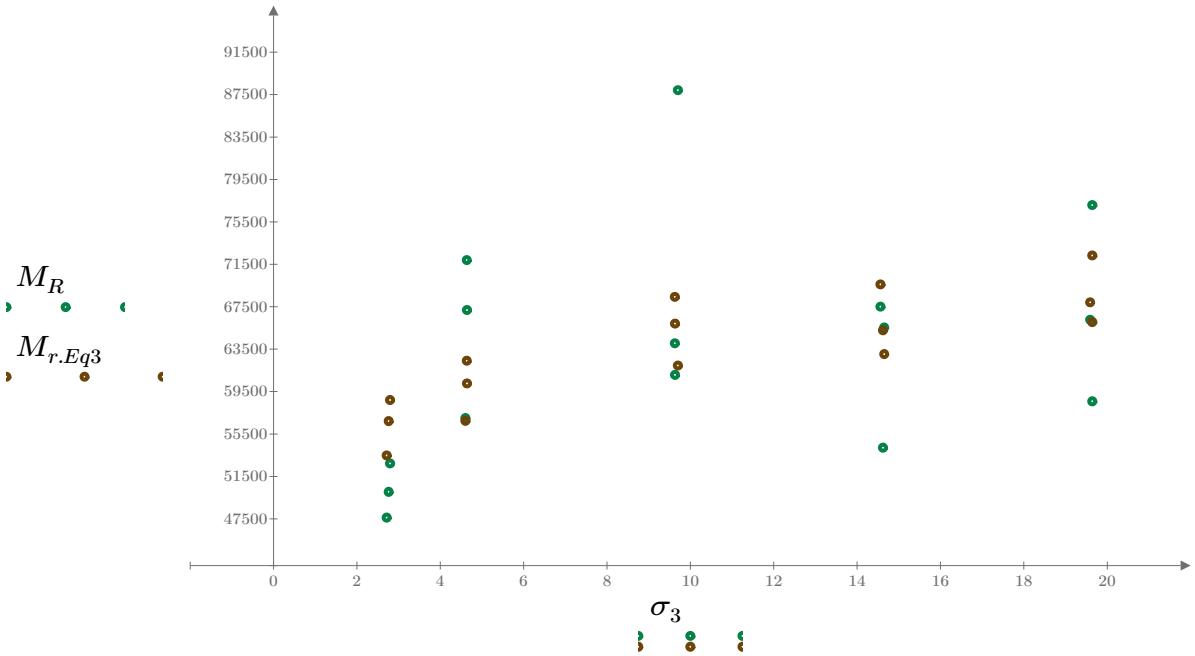

Figure 4. Plot of the test data (green points) vs. the fitted Equation 3 model (brown points).

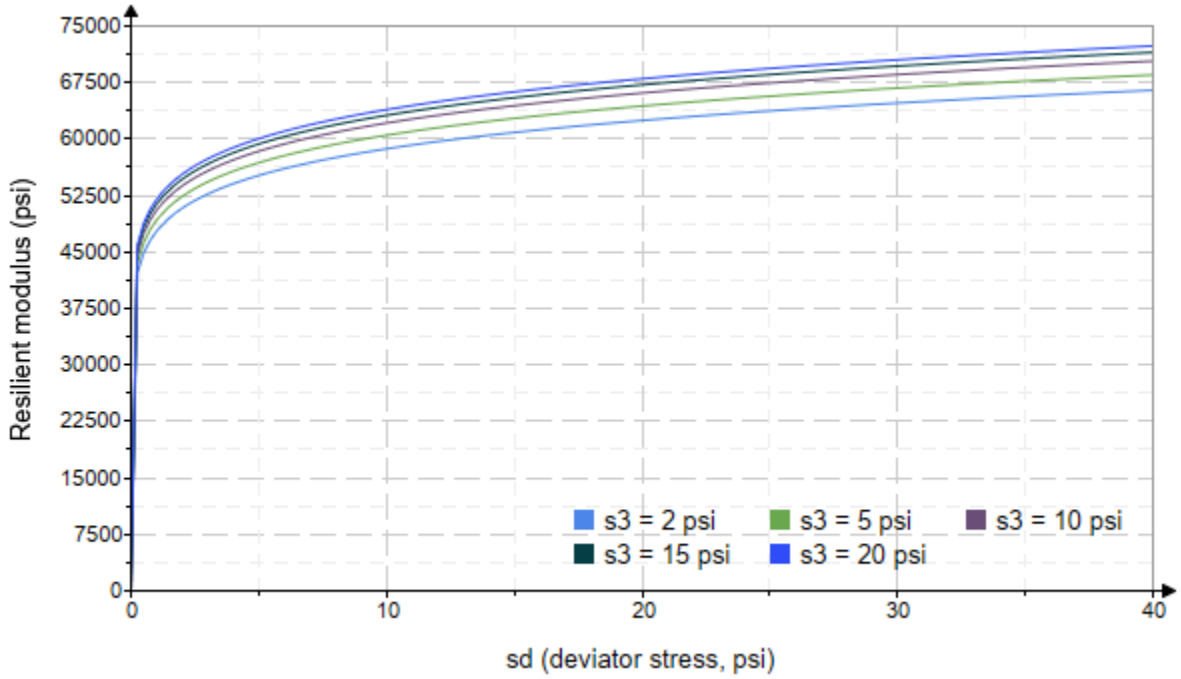

Figure 5. Plot of the fitted Equation 3 model for various confining stresses.

Dan Seely
9/11/2023

$$M_{R.4}\left(\sigma_B,\sigma_d,K_8,K_9,K_{10}\right) := K_8 \cdot p_a \left(\frac{\sigma_B}{p_a}\right)^{K_9} \cdot \left(\frac{\sigma_d}{p_a}\right)^{K_{10}}$$

Equation 4 AASHTO Publication No. FHWA-RD-97-083

$K_8 = 4067.799$

$K_9 = 0.0651$ Equation 4 fitting parameters

$K_{10} = 0.0635$

${R_4}^2 = 0.2640$ Coefficient of determination

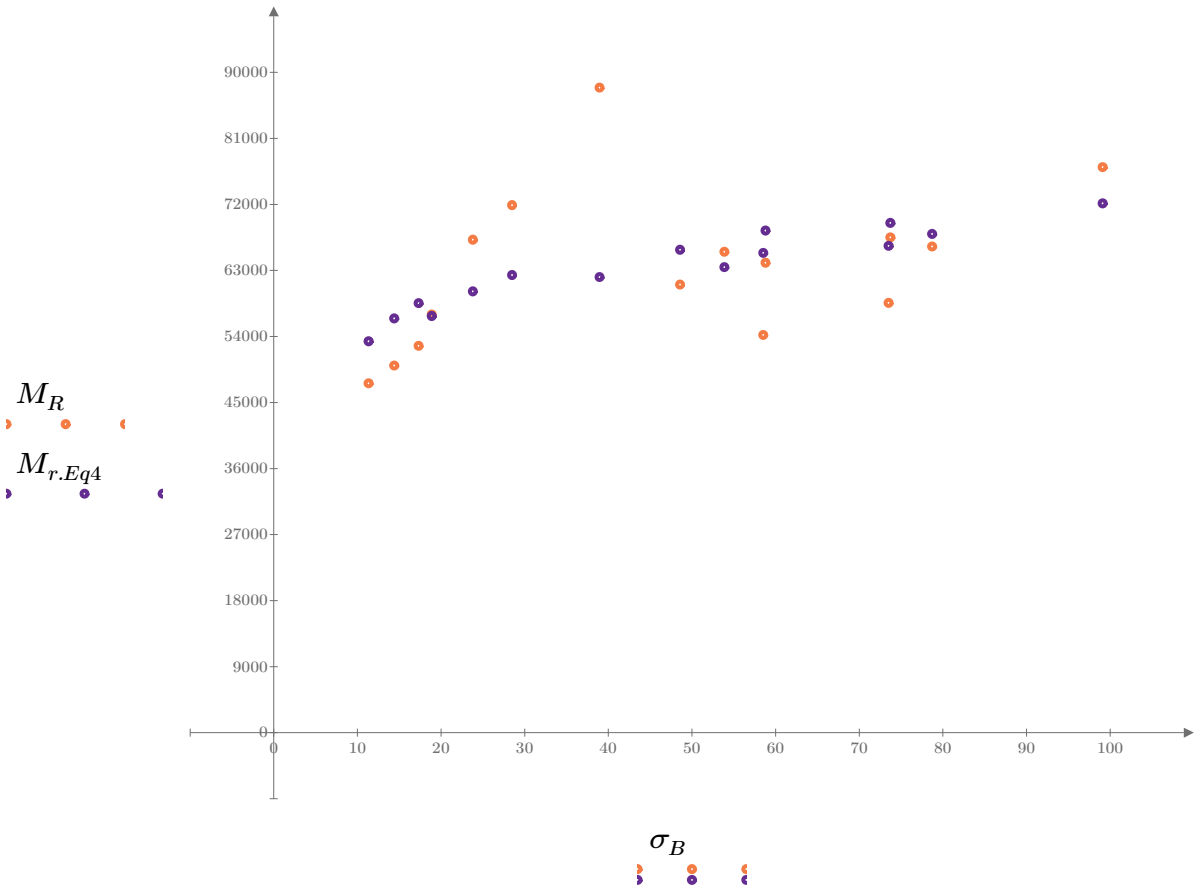

Figure 6. Plot of the test data (orange points) vs. the fitted Equation 4 model (purple points).

Dan Seely
9/11/2023

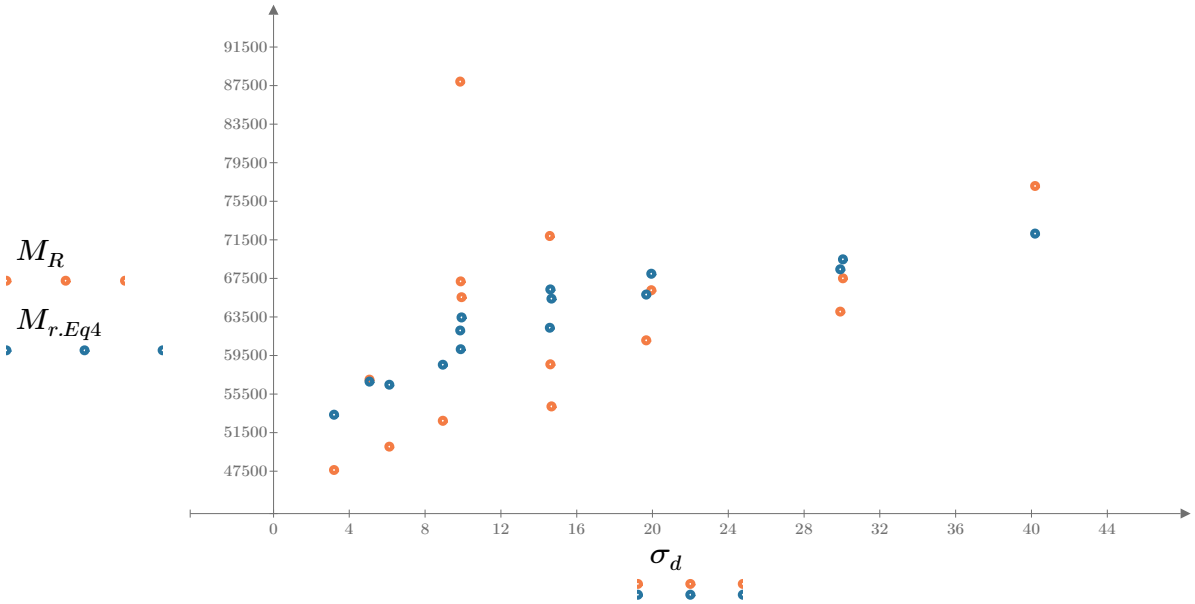

Figure 7. Plot of the test data (orange points) vs. the fitted Equation 4 model (blue points).

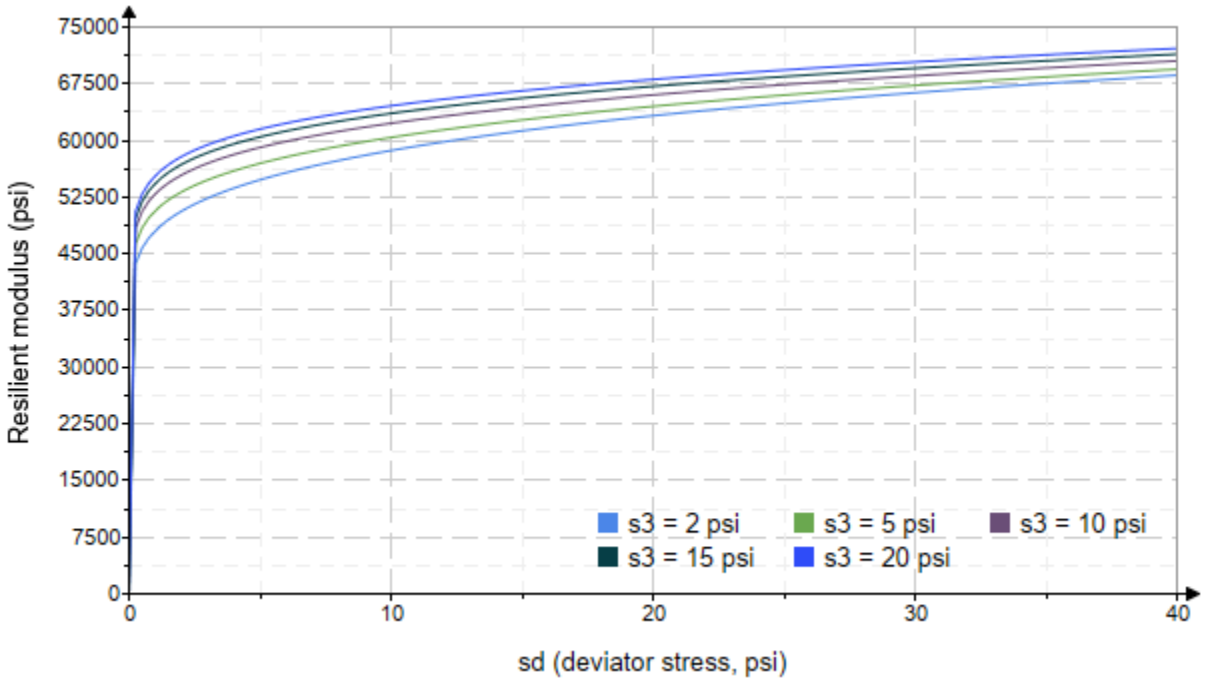

Figure 8. Plot of the fitted Equation 4 model for various confining stresses.

Dan Seely
9/11/2023

$SampleNo := \text{“B2}-\text{28”}$

$Treatment = \text{“H100”}$

$S = 4.441$ Degree of Saturation (%)

Test Sequence : Base/Subbase

Test summary data (psi) :

$$\sigma_3 = \begin{bmatrix} 2.165 \\ 2.264 \\ 2.444 \\ 4.081 \\ 4.161 \\ 4.438 \\ 9.308 \\ 9.202 \\ 9.031 \\ 14.830 \\ 14.710 \\ 14.180 \\ 19.420 \\ 19.490 \\ 19.540 \end{bmatrix} \quad \sigma_d = \begin{bmatrix} 3.234 \\ 6.239 \\ 9.087 \\ 5.187 \\ 9.972 \\ 14.590 \\ 10.110 \\ 19.800 \\ 30.200 \\ 10.140 \\ 14.790 \\ 30.280 \\ 14.780 \\ 20.060 \\ 40.350 \end{bmatrix} \quad \sigma_B = \begin{bmatrix} 9.730 \\ 13.030 \\ 16.420 \\ 17.430 \\ 22.460 \\ 27.910 \\ 38.030 \\ 47.410 \\ 57.290 \\ 54.620 \\ 58.910 \\ 72.810 \\ 73.050 \\ 78.520 \\ 98.980 \end{bmatrix} \quad M_R = \begin{bmatrix} 115067.5 \\ 93785.5 \\ 69081.4 \\ 73085.4 \\ 77089.4 \\ 56722.4 \\ 94632.6 \\ 82732.4 \\ 83761.8 \\ 184680.0 \\ 127474.0 \\ 89247.4 \\ 160236.0 \\ 118162.0 \\ 97209.6 \end{bmatrix}$$

σ_3 = mean confining stress
σ_d = mean deviator stress
σ_B = mean bulk stress
M_R = resilient modulus
p_a = atmospheric pressure = 14.6959 psi

Dan Seely
9/11/2023

$$M_{R.1}\left(\sigma_B, K_1, K_2\right) := K_1 \cdot {\sigma_B}^{K_2}$$

Equation 1
AASHTO Publication No. FHWA-RD-97-083

$K_1 = 50174.193$

$K_2 = 0.1928$

Equation 1 fitting parameters

${R_1}^2 = 0.1513$

Coefficient of determination

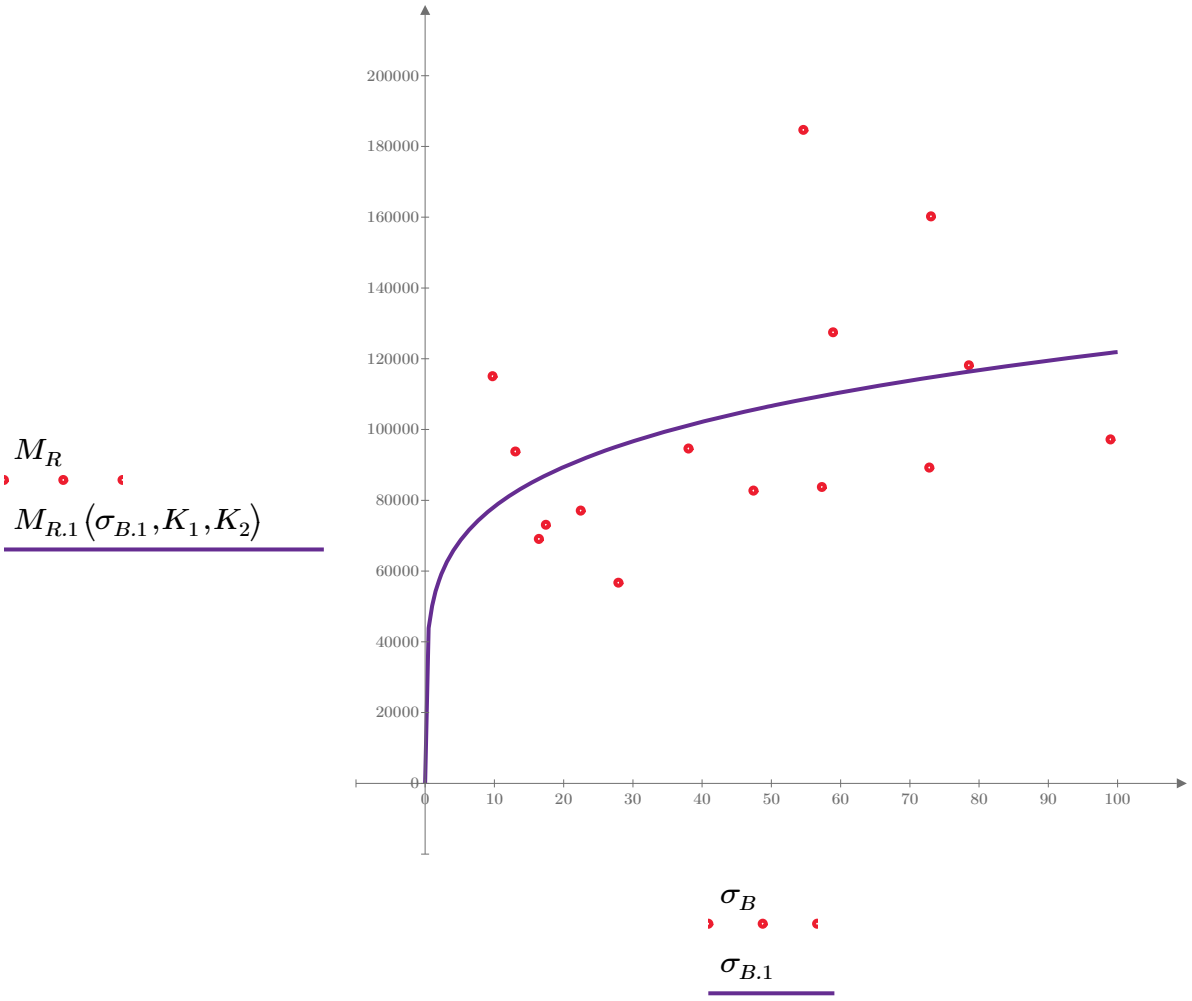

Figure 1. Plot of the test data (red points) vs. the fitted Equation 1 model (purple line).

Dan Seely
9/11/2023

$$M_{R.2}(\sigma_d, K_3, K_4) := K_3 \cdot \sigma_d^{K_4}$$

Equation 2
AASHTO Publication No. FHWA-RD-97-083

$K_3 = 106358.710$

$K_4 = -0.0182$

Equation 2 fitting parameters

$R_2^2 = 0.0014$

Coefficient of determination

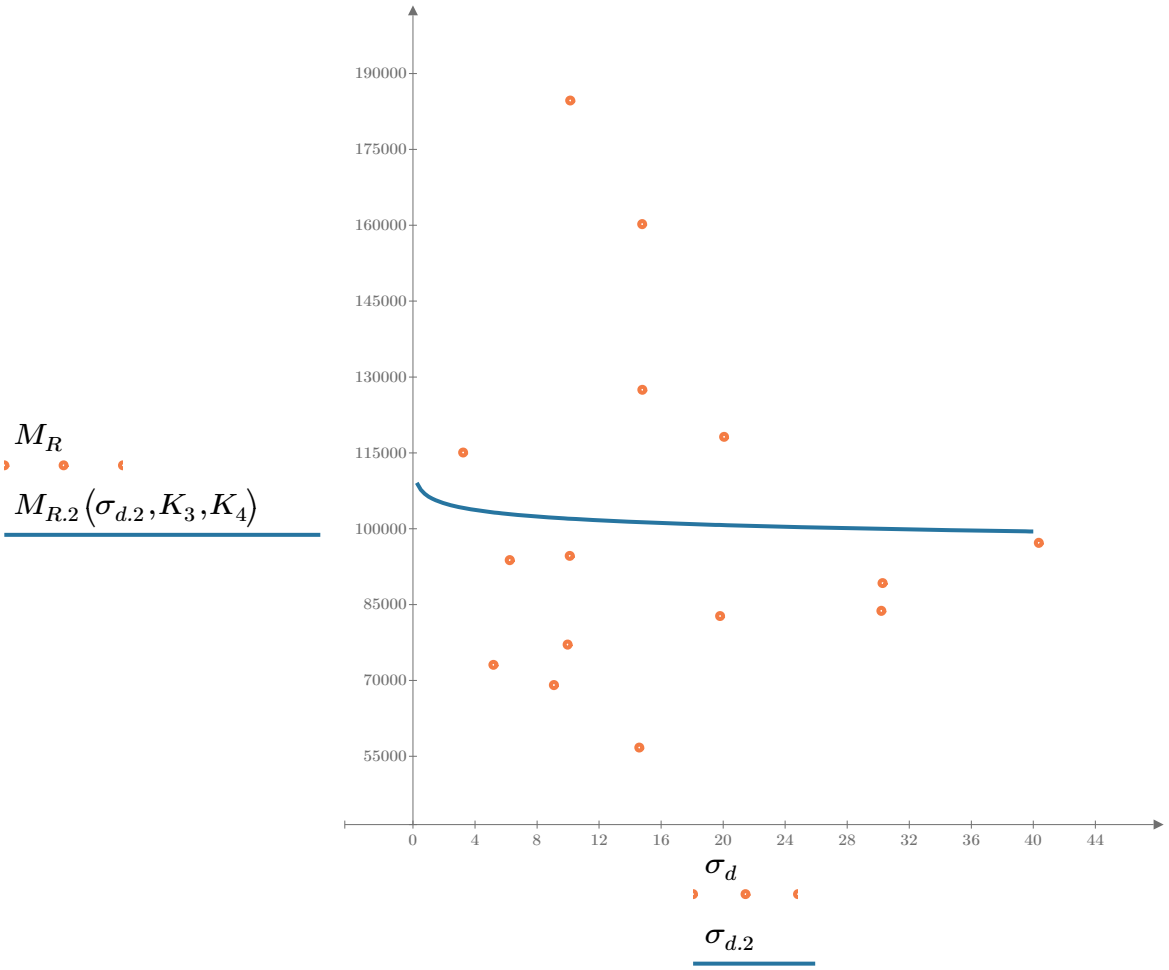

Figure 2. Plot of the test data (orange points) vs. the fitted Equation 2 model (blue line).

Dan Seely
9/11/2023

$$M_{R.3}\left(\sigma_d,\sigma_3,K_5,K_6,K_7\right):=K_5\cdot{\sigma_d}^{K_6}\cdot\left(1+\sigma_3\right)^{K_7}$$

Equation 3 AASHTO Publication No. FHWA-RD-97-083

$K_5=85434.053$

$K_6=-0.5042$ Equation 3 fitting parameters

$K_7=0.647$

${R_3}^2=0.7768$ Coefficient of determination

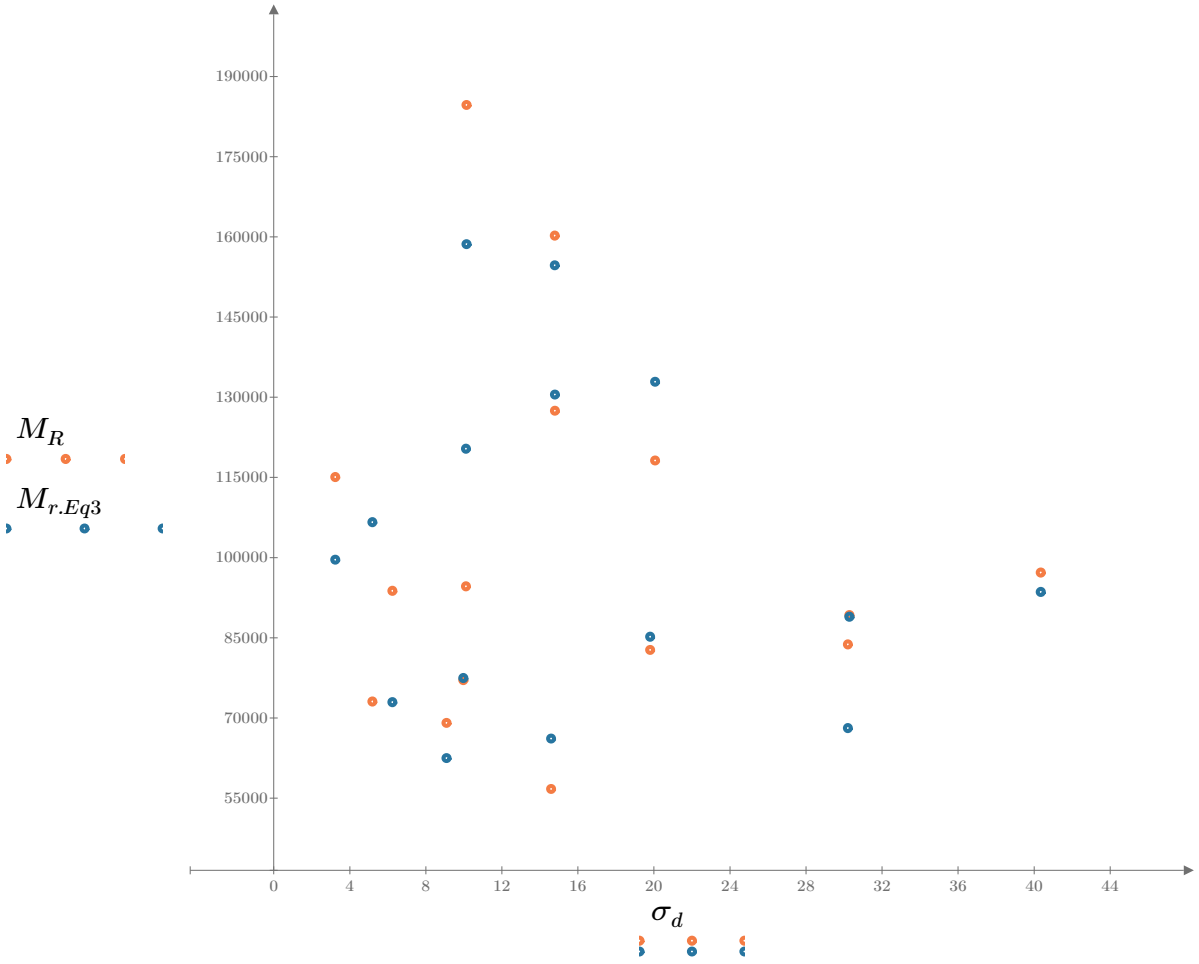

Figure 3. Plot of the test data (orange points) vs. the fitted Equation 3 model (blue points).

Dan Seely
9/11/2023

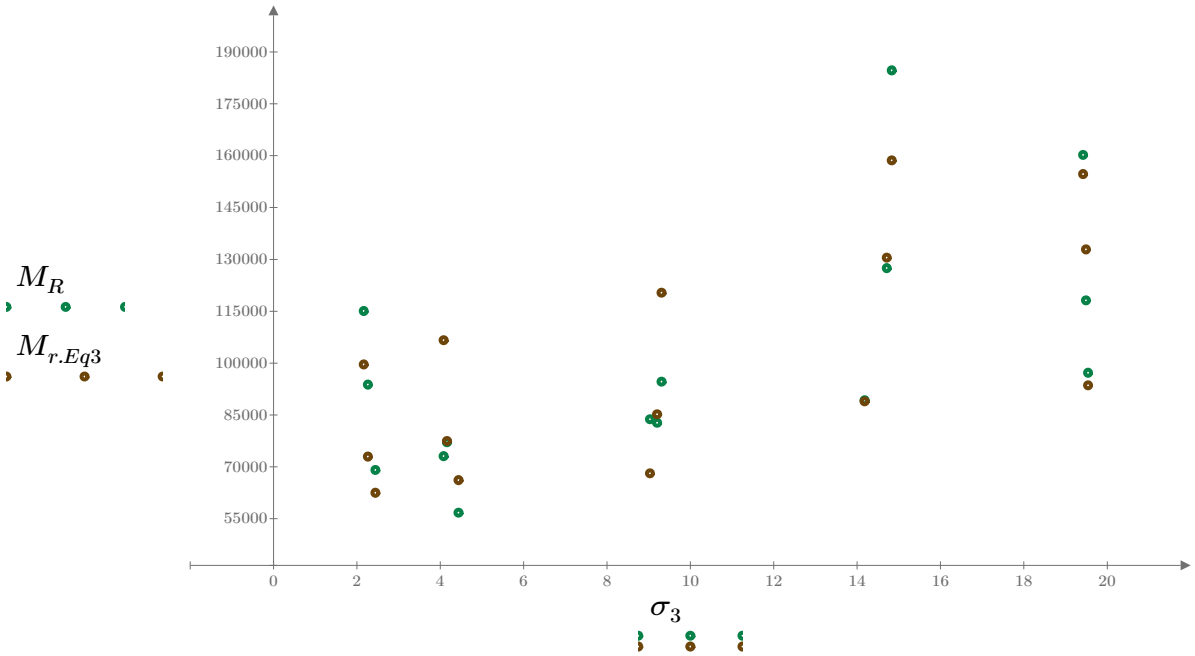

Figure 4. Plot of the test data (green points) vs. the fitted Equation 3 model (brown points).

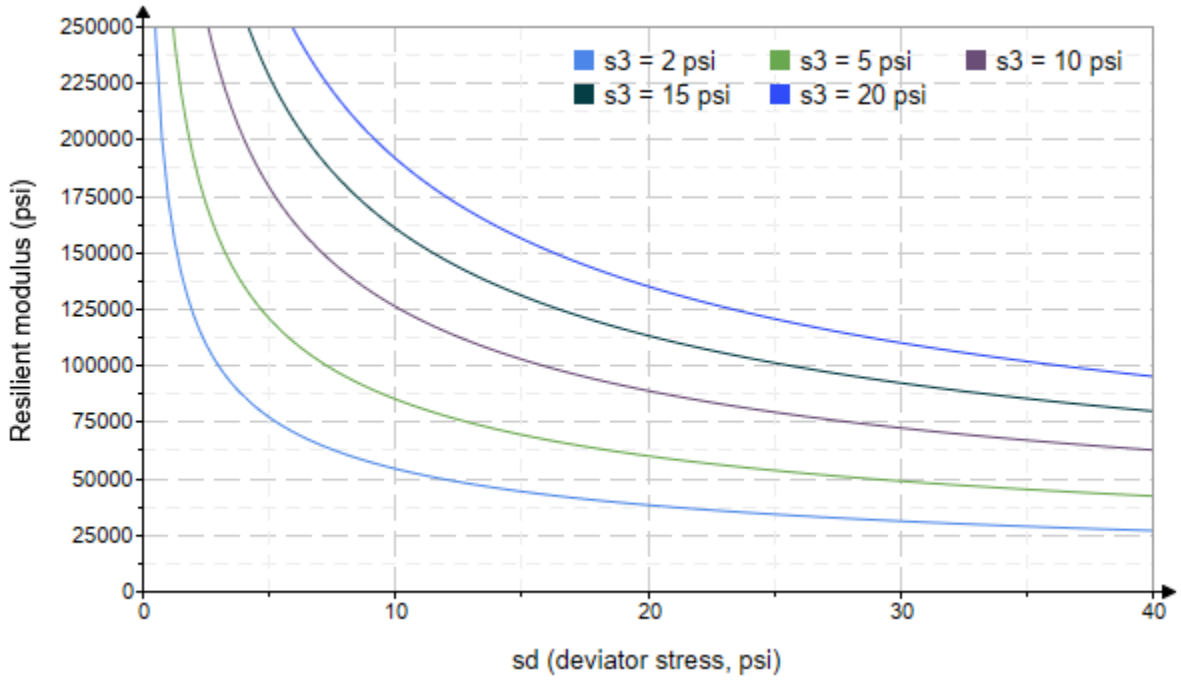

Figure 5. Plot of the fitted Equation 3 model for various confining stresses.

Dan Seely
9/11/2023

$$M_{R.4}\left(\sigma_B,\sigma_d,K_8,K_9,K_{10}\right) := K_8 \cdot p_a \left(\frac{\sigma_B}{p_a}\right)^{K_9} \cdot \left(\frac{\sigma_d}{p_a}\right)^{K_{10}}$$

Equation 4 AASHTO Publication No. FHWA-RD-97-083

$K_8 = 2731.515$

$K_9 = 0.8468$ Equation 4 fitting parameters

$K_{10} = -0.7953$

$R_4^{\,2} = 0.7832$ Coefficient of determination

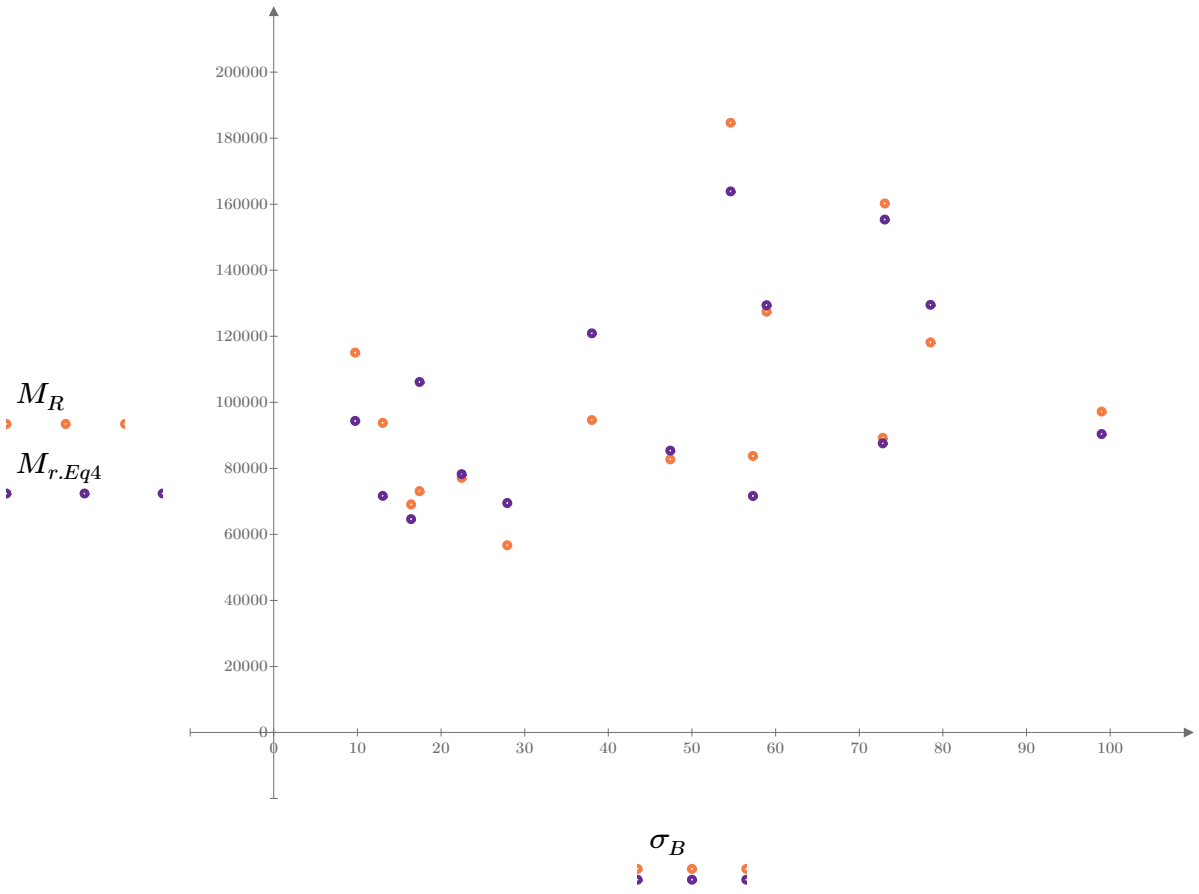

Figure 6. Plot of the test data (orange points) vs. the fitted Equation 4 model (purple points).

Dan Seely
9/11/2023

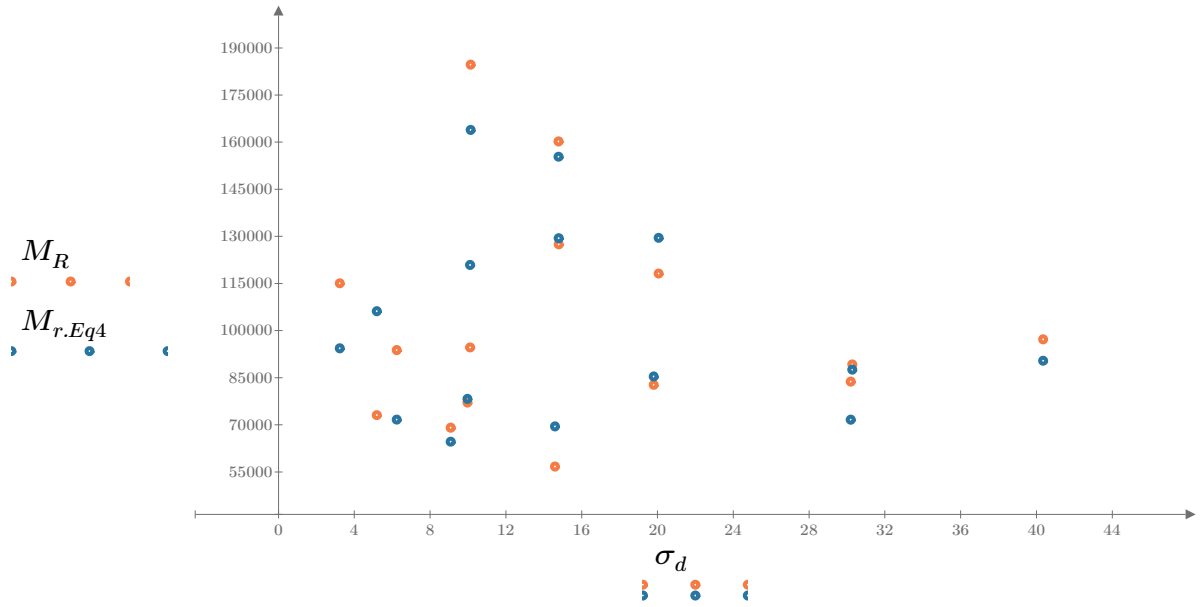

Figure 7. Plot of the test data (orange points) vs. the fitted Equation 4 model (blue points).

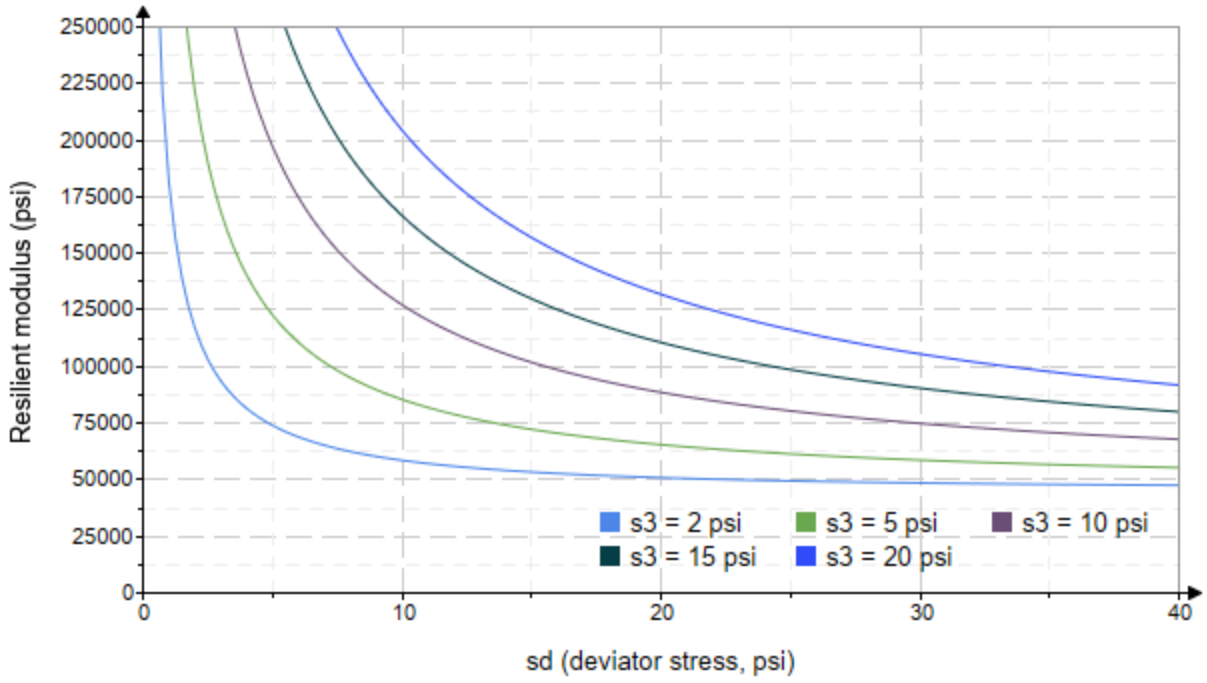

Figure 8. Plot of the fitted Equation 4 model for various confining stresses.

Dan Seely
9/11/2023

$SampleNo := \text{“B2}-\text{29”}$

$Treatment = \text{“H100”}$

$S = 4.275$ Degree of Saturation (%)

Test Sequence : Base/Subbase

Test summary data (psi) :

$$\sigma_3 = \begin{bmatrix} 2.625 \\ 2.624 \\ 2.601 \\ 4.628 \\ 4.616 \\ 4.618 \\ 9.662 \\ 9.646 \\ 9.616 \\ 14.680 \\ 14.690 \\ 14.640 \\ 19.690 \\ 19.690 \\ 19.700 \end{bmatrix} \quad \sigma_d = \begin{bmatrix} 3.306 \\ 6.168 \\ 8.998 \\ 5.178 \\ 9.940 \\ 14.700 \\ 9.978 \\ 19.850 \\ 30.390 \\ 10.050 \\ 14.790 \\ 30.480 \\ 14.870 \\ 19.950 \\ 40.560 \end{bmatrix} \quad \sigma_B = \begin{bmatrix} 11.180 \\ 14.040 \\ 16.800 \\ 19.060 \\ 23.790 \\ 28.560 \\ 38.970 \\ 48.780 \\ 59.240 \\ 54.090 \\ 58.860 \\ 74.410 \\ 73.950 \\ 79.030 \\ 99.660 \end{bmatrix} \quad M_R = \begin{bmatrix} 30640.2 \\ 37771.6 \\ 39532.8 \\ 43540.2 \\ 48502.0 \\ 51839.0 \\ 68995.0 \\ 74354.2 \\ 71655.4 \\ 74371.8 \\ 77149.8 \\ 65796.0 \\ 70989.8 \\ 67185.2 \\ 71093.8 \end{bmatrix}$$

σ_3 = mean confining stress
σ_d = mean deviator stress
σ_B = mean bulk stress
M_R = resilient modulus
p_a = atmospheric pressure = 14.6959 psi

Dan Seely
9/11/2023

$$M_{R.1}\left(\sigma_B, K_1, K_2\right) := K_1 \cdot {\sigma_B}^{K_2}$$

Equation 1
AASHTO Publication No. FHWA-RD-97-083

$K_1 = 16845.622$

$K_2 = 0.3403$

Equation 1 fitting parameters

${R_1}^2 = 0.7947$

Coefficient of determination

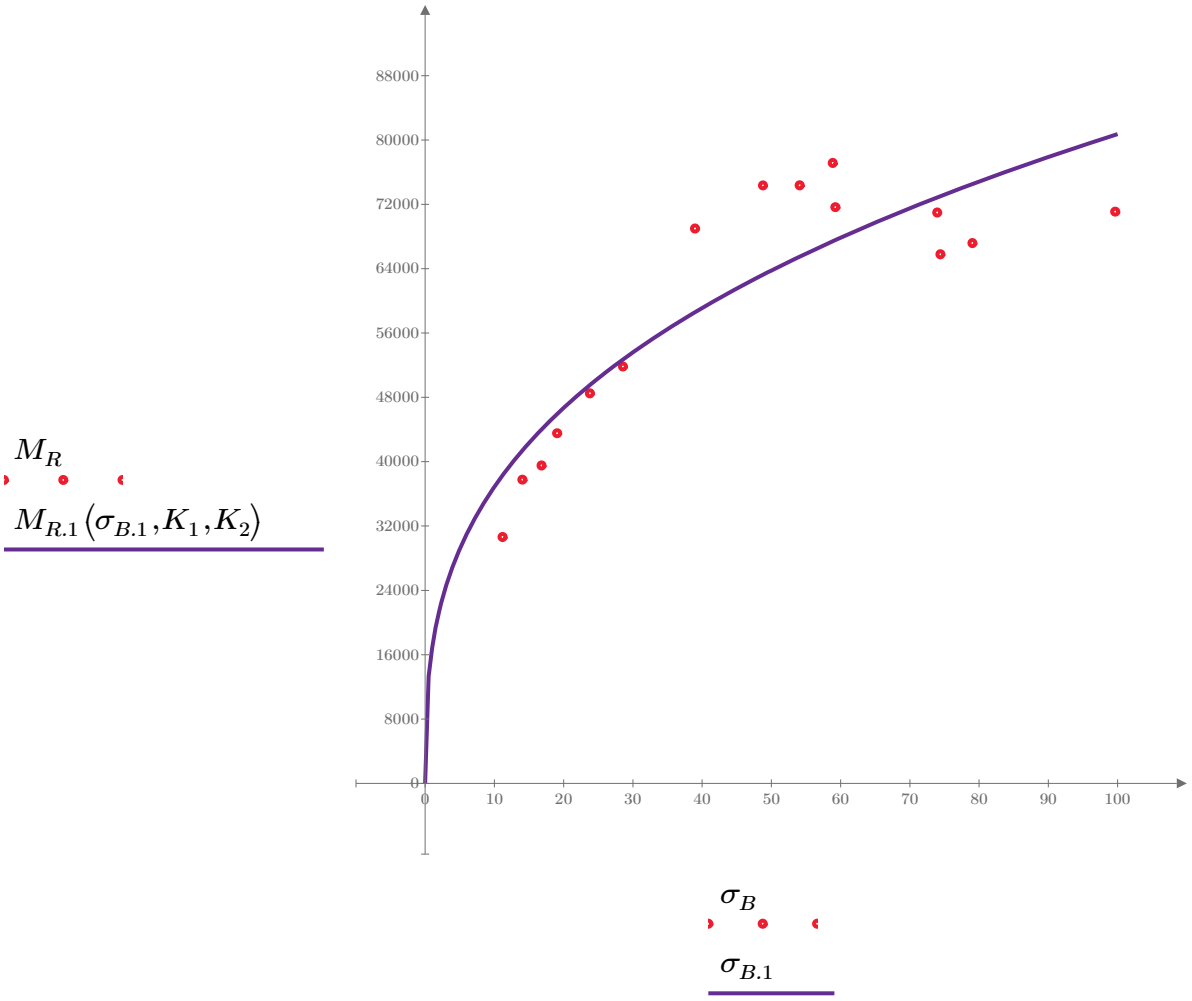

Figure 1. Plot of the test data (red points) vs. the fitted Equation 1 model (purple line).

Dan Seely
9/11/2023

$M_{R.2}(\sigma_d, K_3, K_4) := K_3 \cdot \sigma_d^{K_4}$ Equation 2
AASHTO Publication No. FHWA-RD-97-083

$K_3 = 29911.980$

$K_4 = 0.2639$ Equation 2 fitting parameters

$R_2^2 = 0.5180$ Coefficient of determination

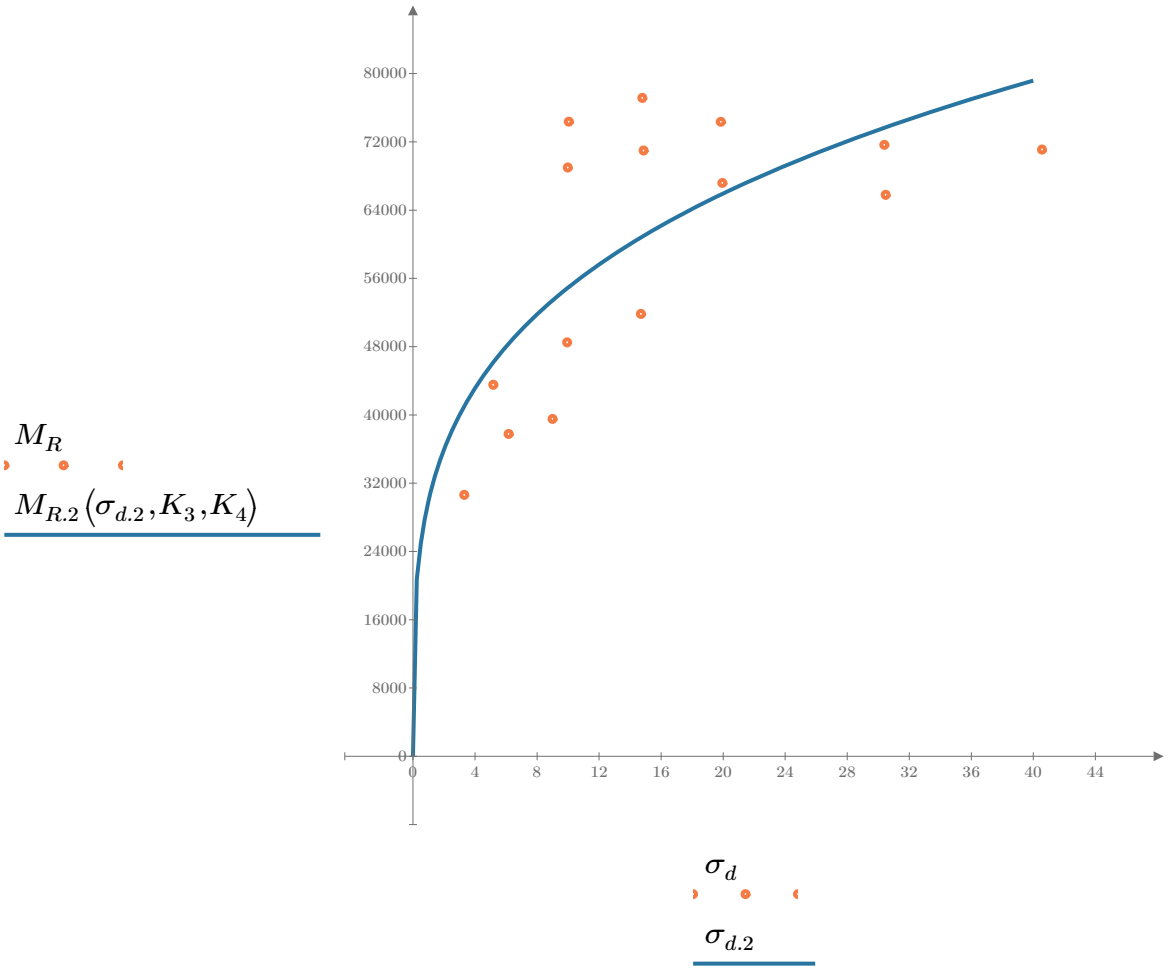

Figure 2. Plot of the test data (orange points) vs. the fitted Equation 2 model (blue line).

Dan Seely
9/11/2023

$$M_{R.3}\left(\sigma_d,\sigma_3,K_5,K_6,K_7\right):=K_5\cdot{\sigma_d}^{K_6}\cdot\left(1+\sigma_3\right)^{K_7}$$

Equation 3 AASHTO Publication No. FHWA-RD-97-083

$K_5=25382.207$

$K_6=0.0596$ Equation 3 fitting parameters

$K_7=0.3036$

${R_3}^2=0.7855$ Coefficient of determination

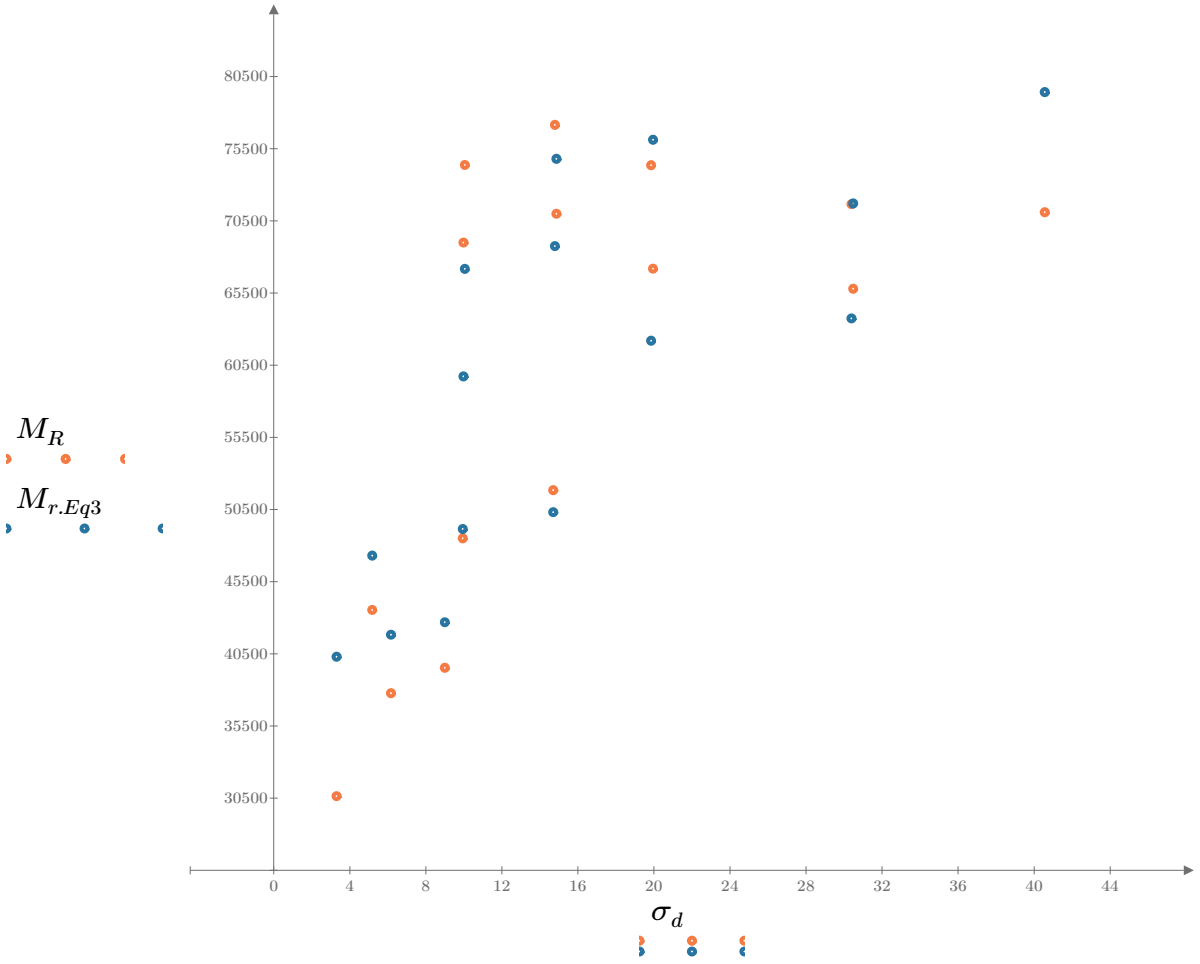

Figure 3. Plot of the test data (orange points) vs. the fitted Equation 3 model (blue points).

Dan Seely
9/11/2023

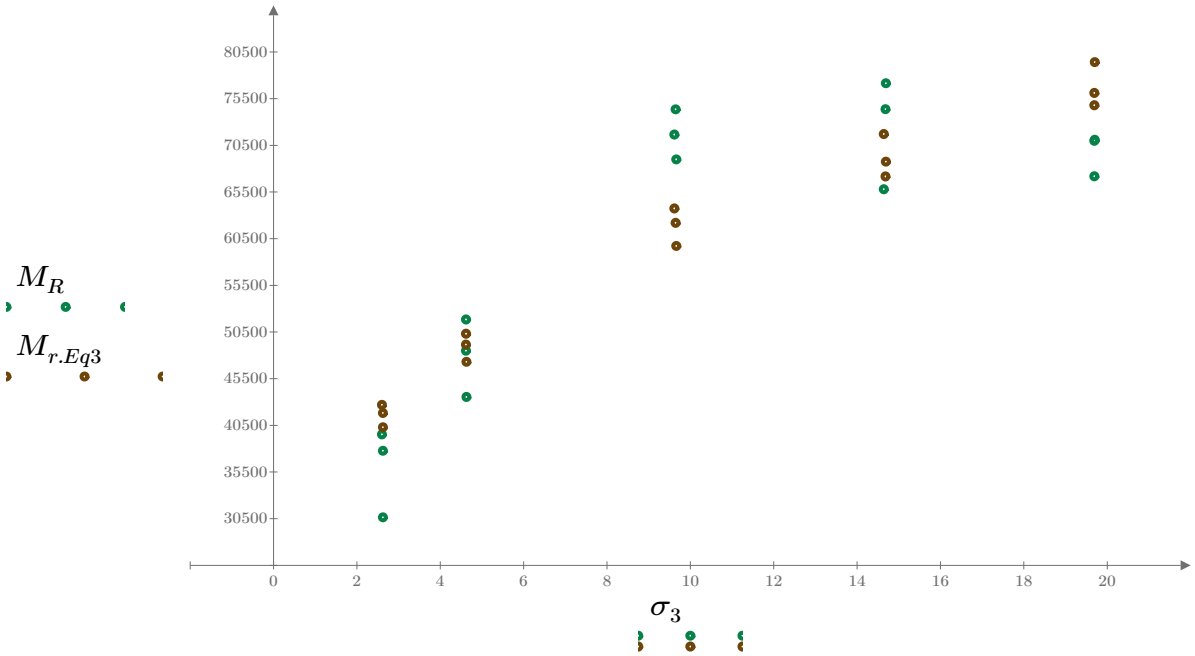

Figure 4. Plot of the test data (green points) vs. the fitted Equation 3 model (brown points).

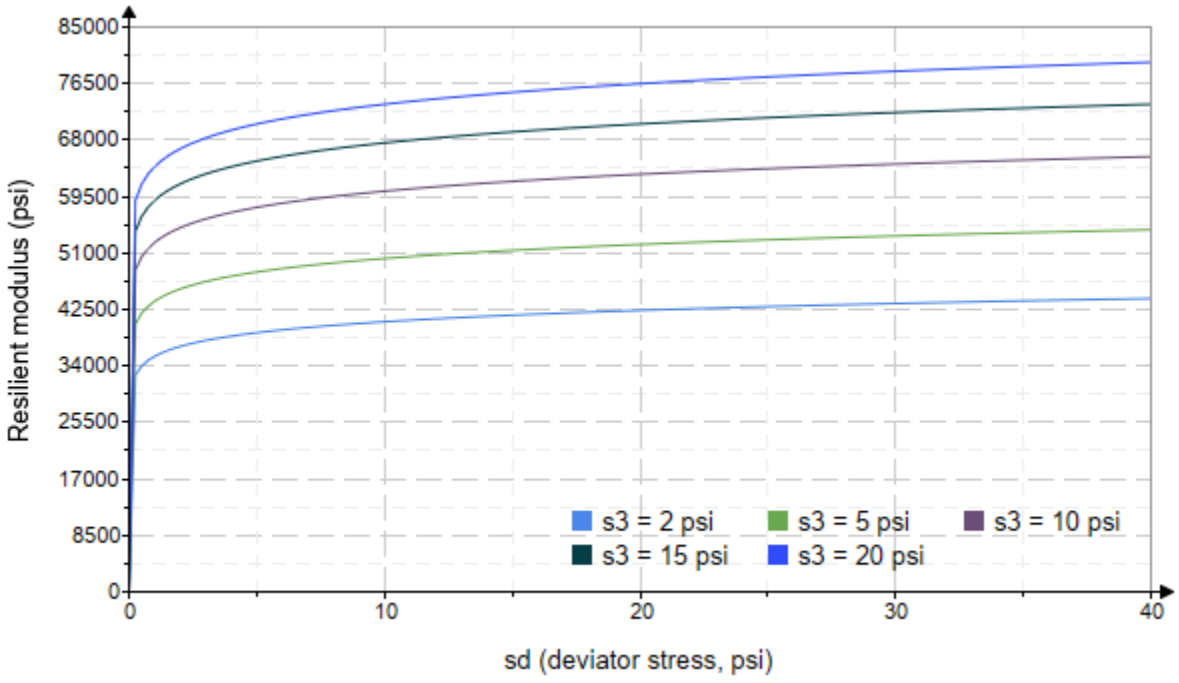

Figure 5. Plot of the fitted Equation 3 model for various confining stresses.

Dan Seely
9/11/2023

$$M_{R.4}\left(\sigma_B,\sigma_d,K_8,K_9,K_{10}\right) := K_8 \cdot p_a \left(\frac{\sigma_B}{p_a}\right)^{K_9} \cdot \left(\frac{\sigma_d}{p_a}\right)^{K_{10}}$$

Equation 4 AASHTO Publication No. FHWA-RD-97-083

$K_8 = 2613.978$

$K_9 = 0.4214$ Equation 4 fitting parameters

$K_{10} = -0.0917$

$R_4^{\,2} = 0.8096$ Coefficient of determination

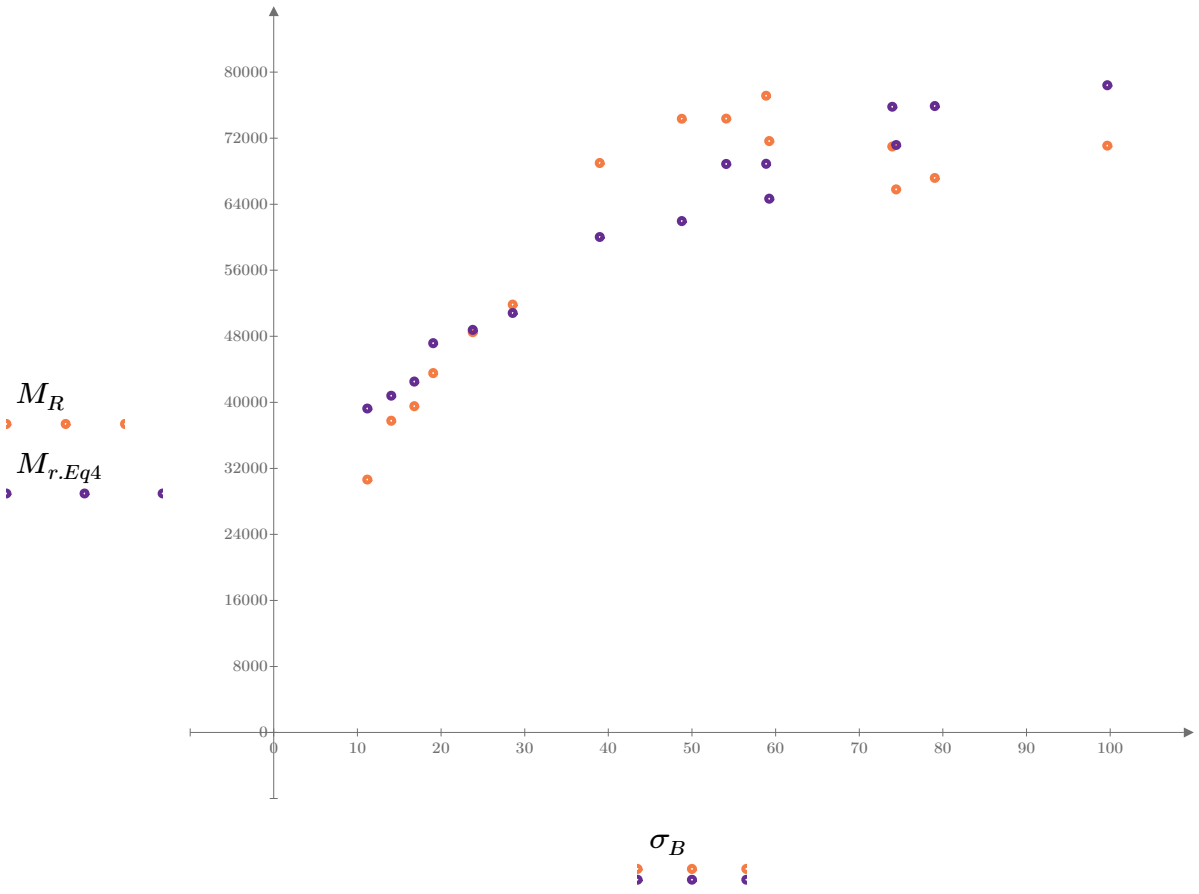

Figure 6. Plot of the test data (orange points) vs. the fitted Equation 4 model (purple points).

Dan Seely
9/11/2023

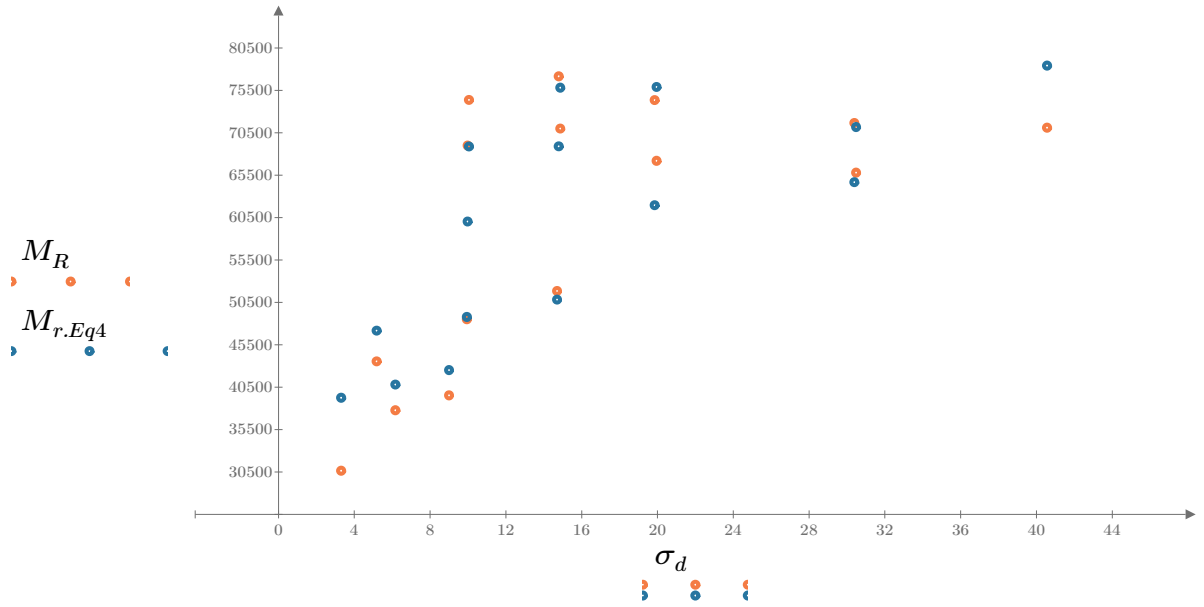

Figure 7. Plot of the test data (orange points) vs. the fitted Equation 4 model (blue points).

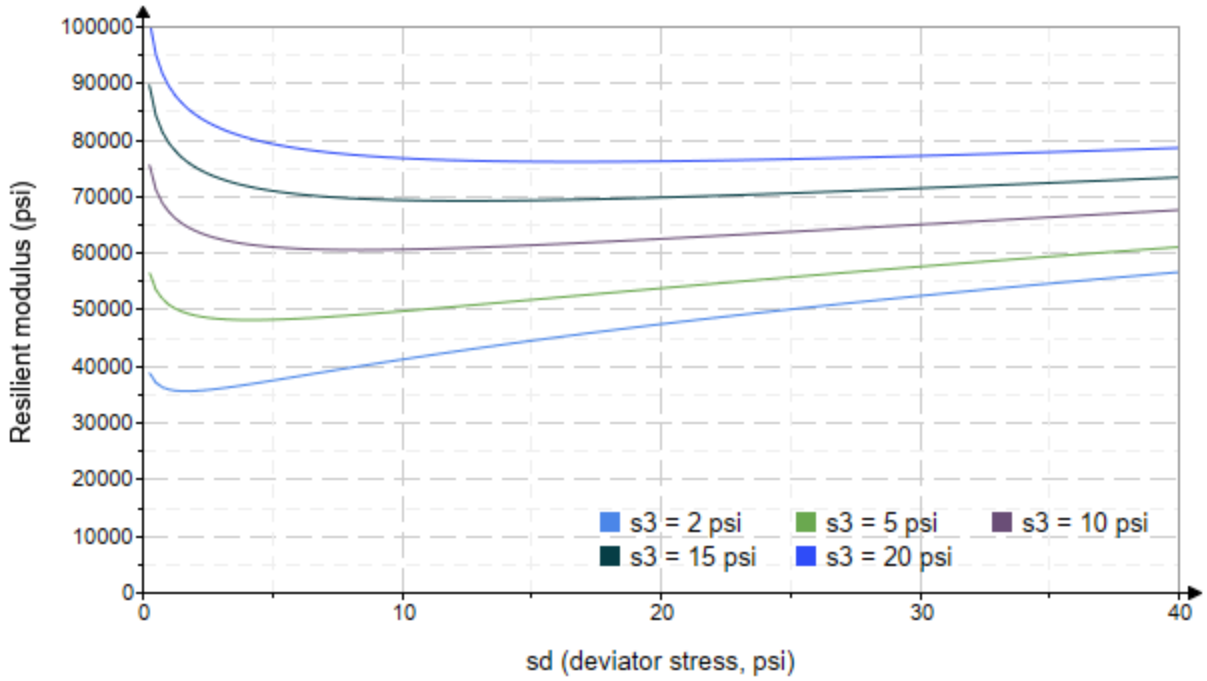

Figure 8. Plot of the fitted Equation 4 model for various confining stresses.

Dan Seely
9/11/2023

$SampleNo := \text{“B2}-\text{30”}$

$Treatment = \text{“H100”}$

$S = 4.227$ Degree of Saturation (%)

Test Sequence : Base/Subbase

Test summary data (psi) :

$$\sigma_3 = \begin{bmatrix} 1.926 \\ 1.829 \\ 1.939 \\ 4.106 \\ 4.132 \\ 4.241 \\ 9.239 \\ 8.975 \\ 9.045 \\ 14.720 \\ 14.640 \\ 14.430 \\ 19.710 \\ 19.460 \\ 19.310 \end{bmatrix} \quad \sigma_d = \begin{bmatrix} 3.143 \\ 6.159 \\ 8.900 \\ 5.191 \\ 9.926 \\ 14.560 \\ 9.961 \\ 19.730 \\ 30.050 \\ 9.941 \\ 14.780 \\ 30.110 \\ 14.810 \\ 19.940 \\ 40.210 \end{bmatrix} \quad \sigma_B = \begin{bmatrix} 8.920 \\ 11.650 \\ 14.720 \\ 17.510 \\ 22.320 \\ 27.280 \\ 37.680 \\ 46.660 \\ 57.190 \\ 54.100 \\ 58.690 \\ 73.390 \\ 73.940 \\ 78.330 \\ 98.130 \end{bmatrix} \quad M_R = \begin{bmatrix} 79587.0 \\ 55471.6 \\ 52498.6 \\ 50342.6 \\ 48186.6 \\ 42758.8 \\ 51725.0 \\ 53107.6 \\ 59975.6 \\ 79515.2 \\ 77226.6 \\ 72441.2 \\ 110518.0 \\ 90905.6 \\ 62919.2 \end{bmatrix}$$

σ_3 = mean confining stress
σ_d = mean deviator stress
σ_B = mean bulk stress
M_R = resilient modulus
p_a = atmospheric pressure = 14.6959 psi

Dan Seely
9/11/2023

$$M_{R.1}\left(\sigma_B, K_1, K_2\right) := K_1 \cdot {\sigma_B}^{K_2}$$

Equation 1
AASHTO Publication No. FHWA-RD-97-083

$K_1 = 32797.589$

$K_2 = 0.1914$

Equation 1 fitting parameters

${R_1}^2 = 0.2180$

Coefficient of determination

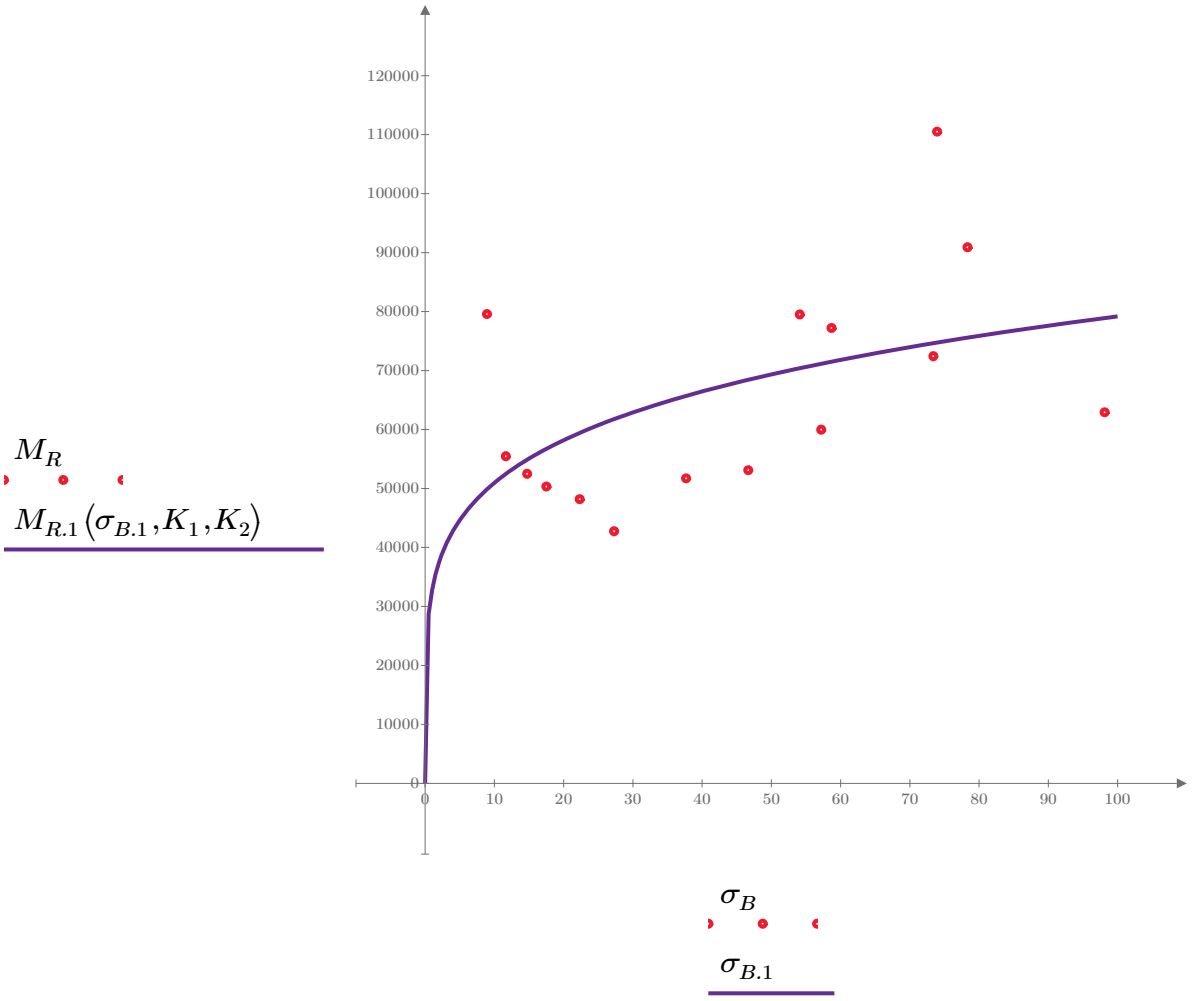

Figure 1. Plot of the test data (red points) vs. the fitted Equation 1 model (purple line).

Dan Seely
9/11/2023

$$M_{R.2}(\sigma_d, K_3, K_4) := K_3 \cdot \sigma_d^{K_4}$$

Equation 2
AASHTO Publication No. FHWA-RD-97-083

$K_3 = 58689.308$

$K_4 = 0.0448$

Equation 2 fitting parameters

$R_2^2 = 0.0117$

Coefficient of determination

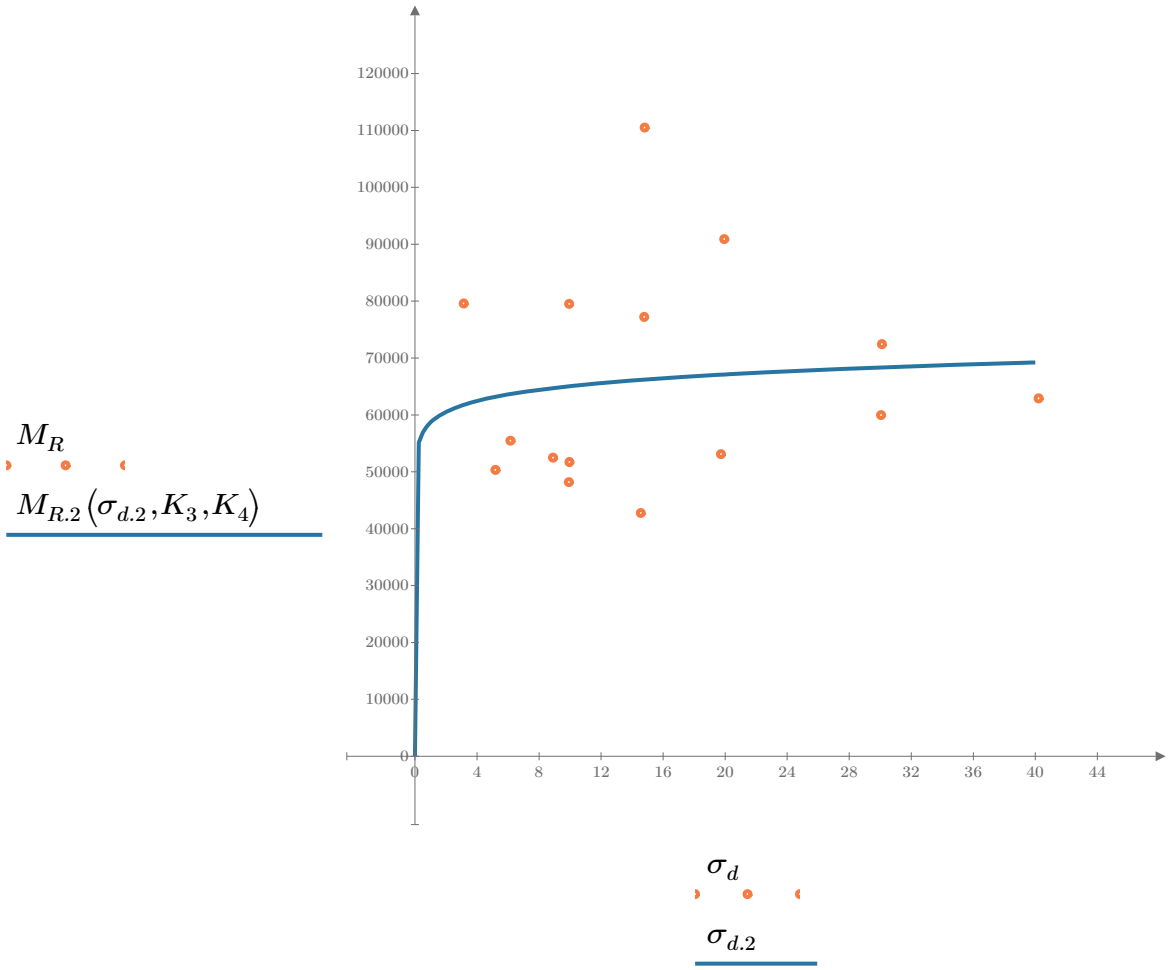

Figure 2. Plot of the test data (orange points) vs. the fitted Equation 2 model (blue line).

Dan Seely
9/11/2023

$$M_{R.3}(\sigma_d, \sigma_3, K_5, K_6, K_7) := K_5 \cdot {\sigma_d}^{K_6} \cdot (1 + \sigma_3)^{K_7}$$

Equation 3 AASHTO Publication No. FHWA-RD-97-083

$K_5 = 50193.104$

$K_6 = -0.2688$ Equation 3 fitting parameters

$K_7 = 0.4319$

${R_3}^2 = 0.5735$ Coefficient of determination

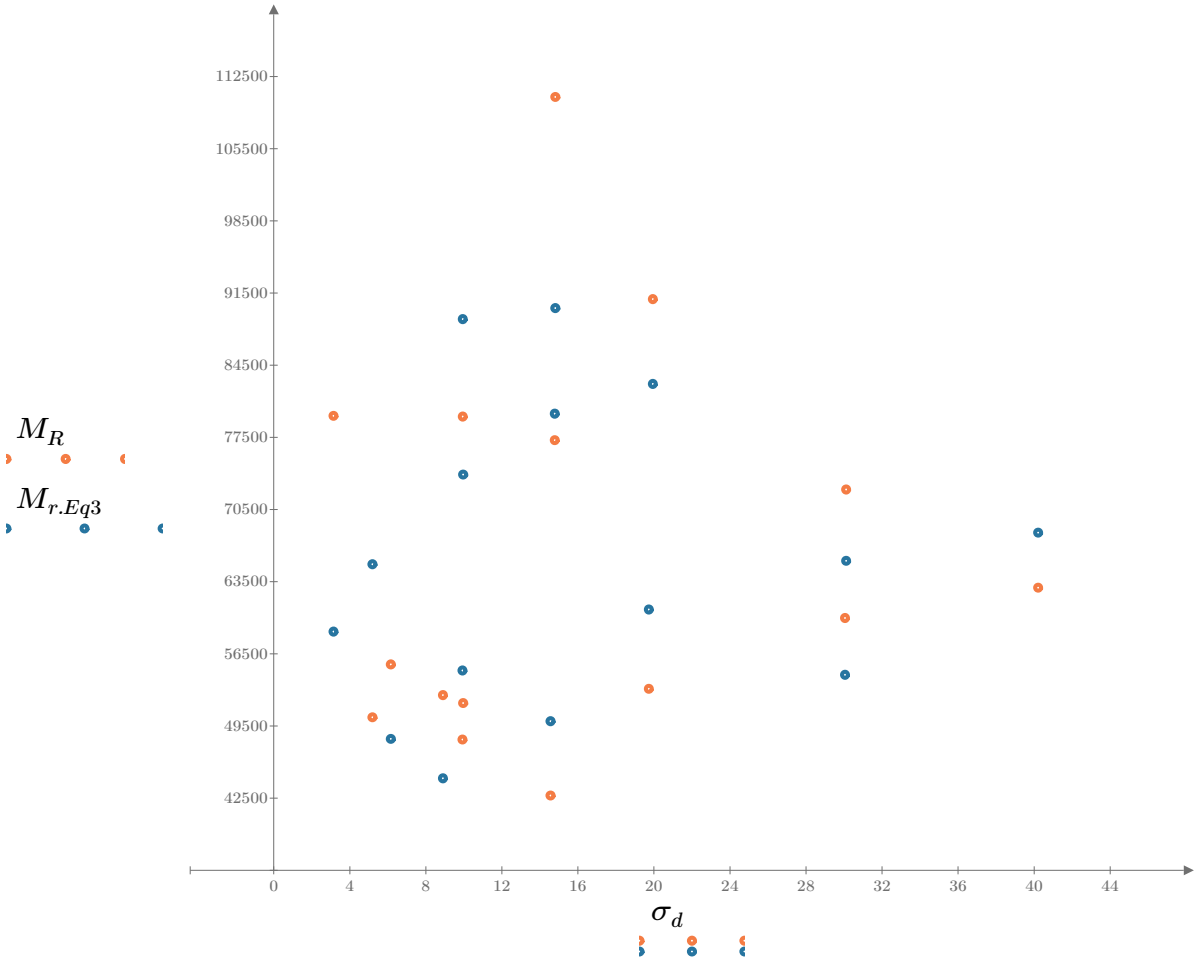

Figure 3. Plot of the test data (orange points) vs. the fitted Equation 3 model (blue points).

Dan Seely
9/11/2023

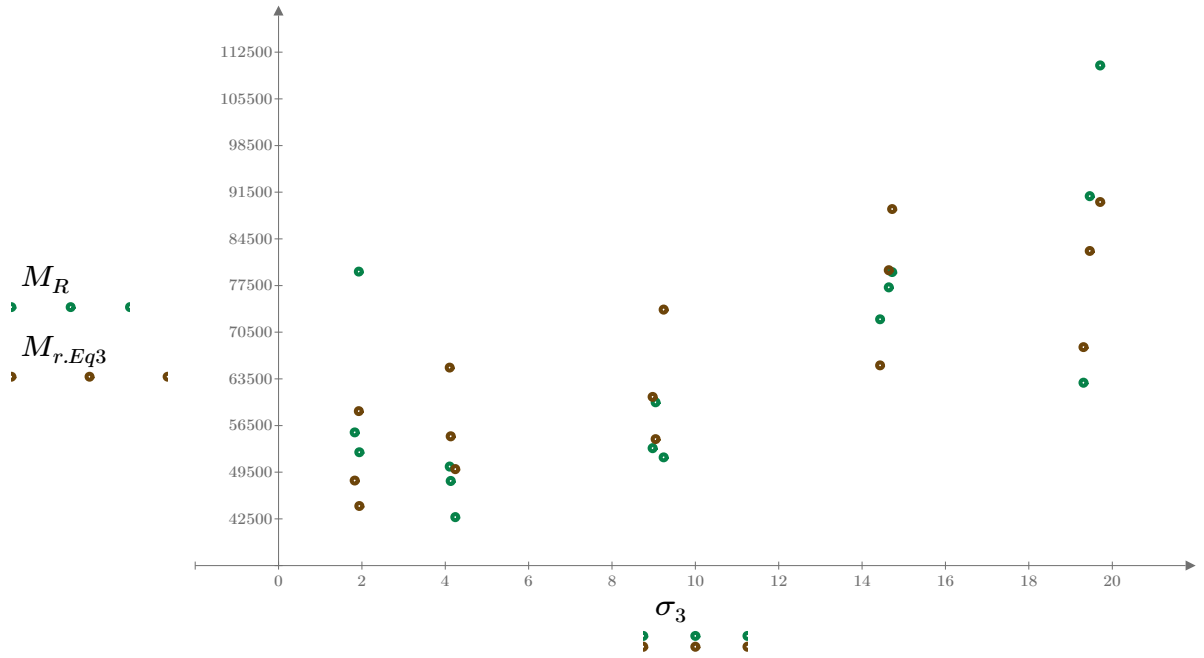

Figure 4. Plot of the test data (green points) vs. the fitted Equation 3 model (brown points).

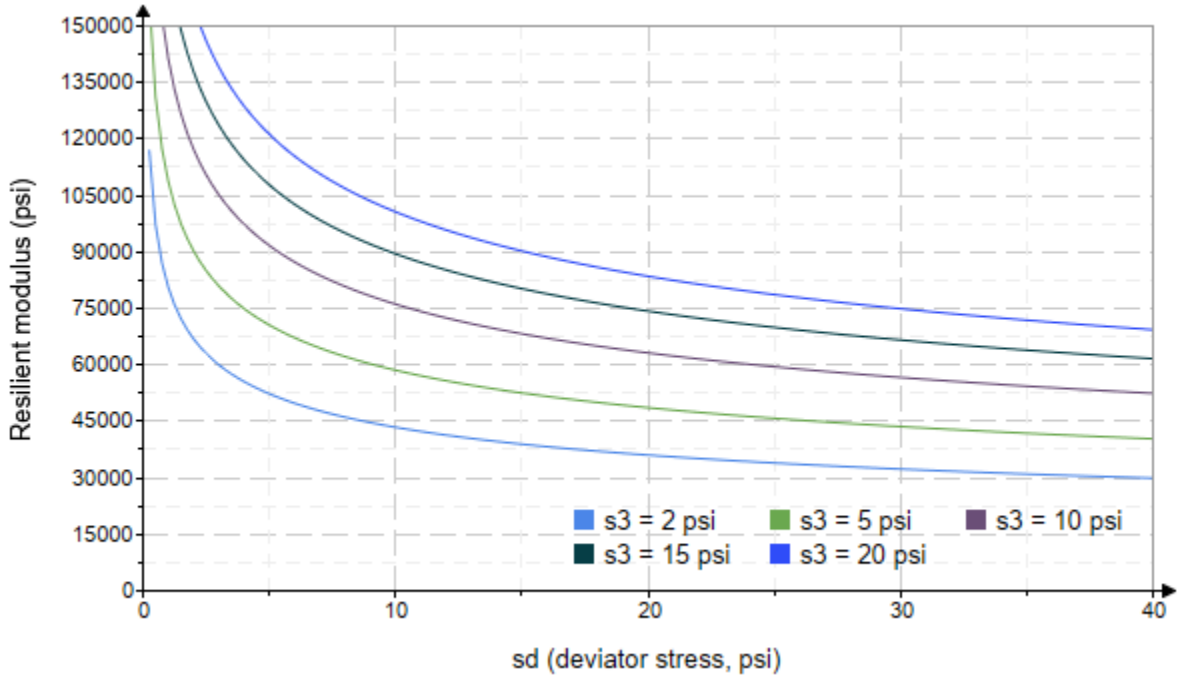

Figure 5. Plot of the fitted Equation 3 model for various confining stresses.

Dan Seely
9/11/2023

$$M_{R.4}\left(\sigma_B,\sigma_d,K_8,K_9,K_{10}\right) := K_8 \cdot p_a \left(\frac{\sigma_B}{p_a}\right)^{K_9} \cdot \left(\frac{\sigma_d}{p_a}\right)^{K_{10}}$$

Equation 4 AASHTO Publication No. FHWA-RD-97-083

$K_8 = 2516.448$

$K_9 = 0.5495$ Equation 4 fitting parameters

$K_{10} = -0.4477$

$R_4^{\,2} = 0.5371$ Coefficient of determination

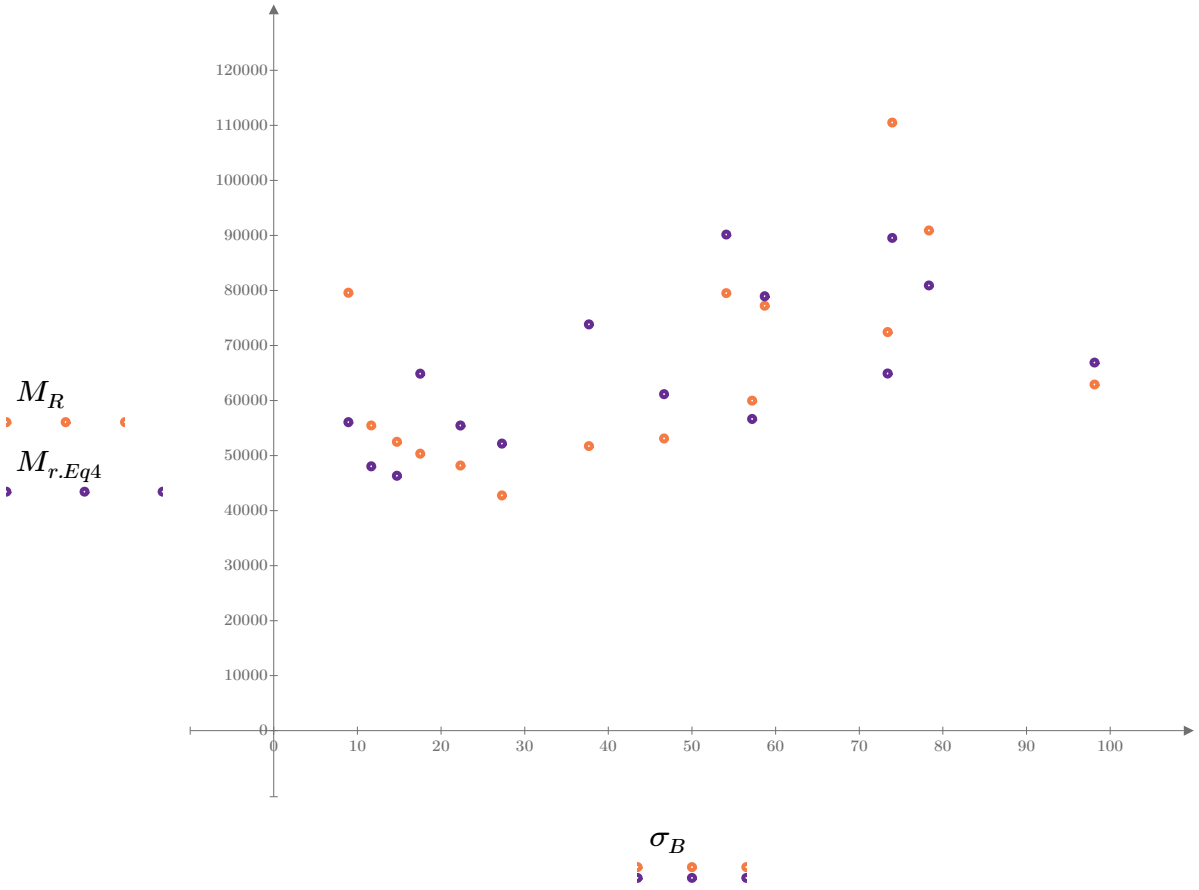

Figure 6. Plot of the test data (orange points) vs. the fitted Equation 4 model (purple points).

Dan Seely
9/11/2023

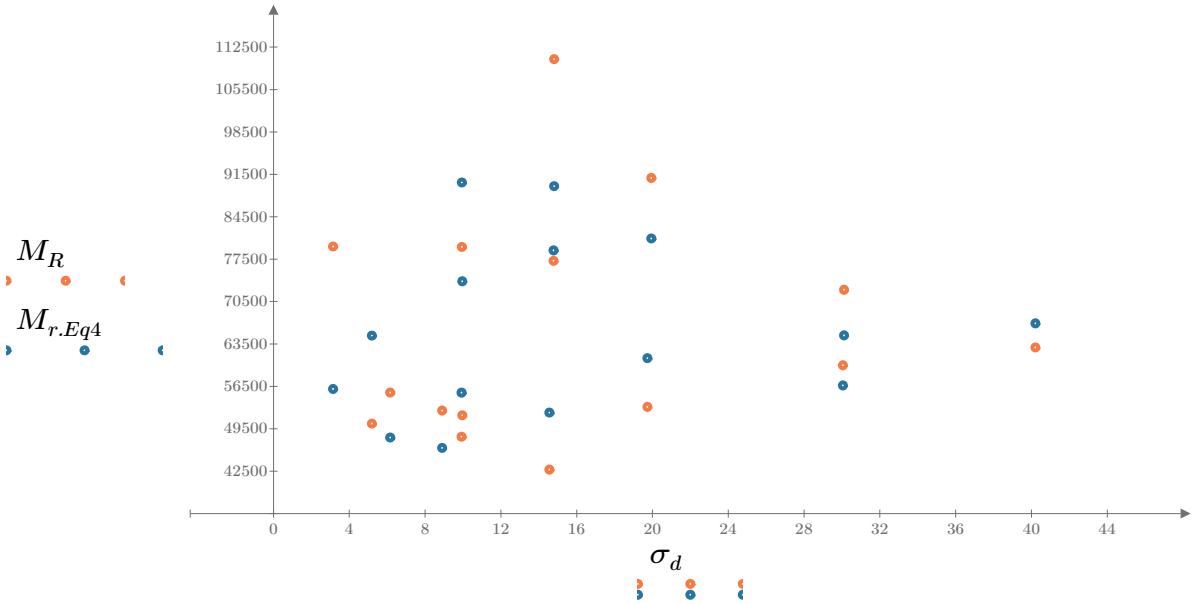

Figure 7. Plot of the test data (orange points) vs. the fitted Equation 4 model (blue points).

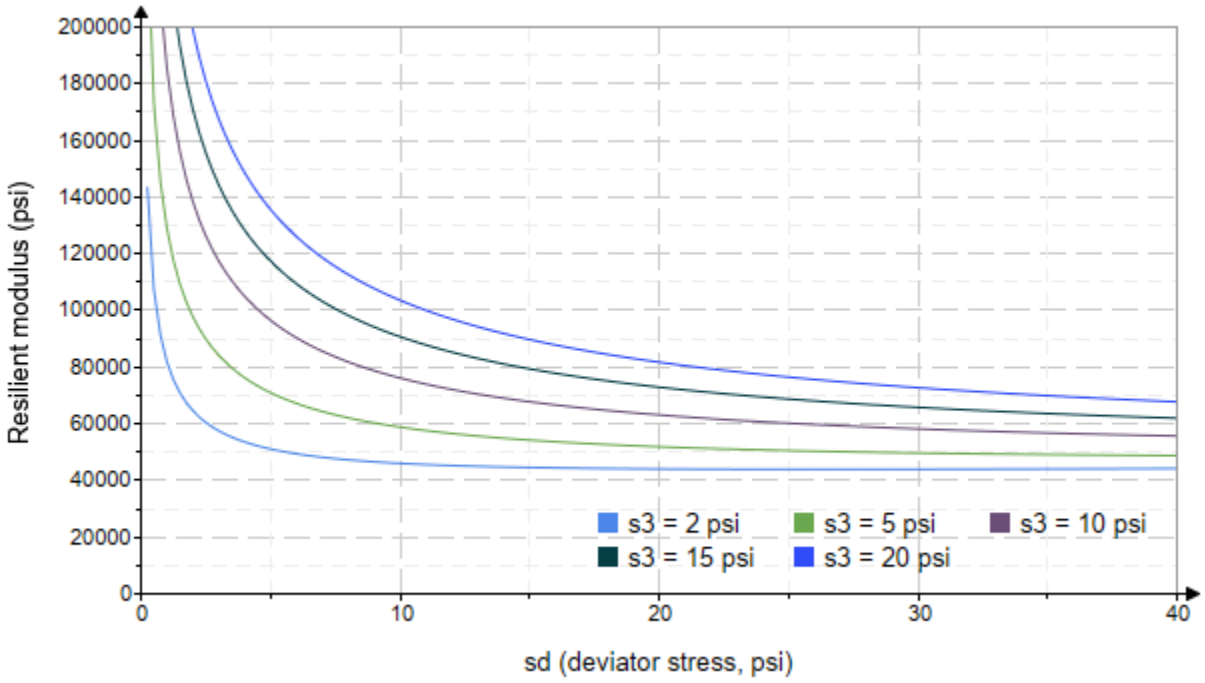

Figure 8. Plot of the fitted Equation 4 model for various confining stresses.

Dan Seely
9/12/2023

$SampleNo := \text{“B2–31”}$

$Treatment = \text{“H100”}$

$S = 4.981$ Degree of Saturation (%)

Test Sequence : Base/Subbase

Test summary data (psi) :

$$\sigma_3 = \begin{bmatrix} 2.743 \\ 2.680 \\ 2.623 \\ 4.565 \\ 4.576 \\ 4.555 \\ 9.600 \\ 9.593 \\ 9.576 \\ 14.620 \\ 14.620 \\ 14.620 \\ 19.660 \\ 19.640 \\ 19.630 \end{bmatrix} \quad \sigma_d = \begin{bmatrix} 3.147 \\ 6.079 \\ 9.065 \\ 5.162 \\ 10.020 \\ 14.620 \\ 9.929 \\ 19.510 \\ 30.420 \\ 9.823 \\ 14.690 \\ 30.240 \\ 14.700 \\ 20.110 \\ 40.460 \end{bmatrix} \quad \sigma_B = \begin{bmatrix} 11.380 \\ 14.120 \\ 16.930 \\ 18.860 \\ 23.750 \\ 28.280 \\ 38.730 \\ 48.280 \\ 59.150 \\ 53.690 \\ 58.560 \\ 74.110 \\ 73.660 \\ 79.030 \\ 99.340 \end{bmatrix} \quad M_R = \begin{bmatrix} 21880.8 \\ 22747.2 \\ 22682.0 \\ 24107.2 \\ 26853.8 \\ 29129.6 \\ 34106.4 \\ 35364.8 \\ 39419.0 \\ 30885.2 \\ 31699.8 \\ 45017.2 \\ 44033.0 \\ 50227.4 \\ 53361.8 \end{bmatrix}$$

σ_3 = mean confining stress
σ_d = mean deviator stress
σ_B = mean bulk stress
M_R = resilient modulus
p_a = atmospheric pressure = 14.6959 psi

Dan Seely
9/12/2023

$$M_{R.1}\left(\sigma_B, K_1, K_2\right) := K_1 \cdot {\sigma_B}^{K_2}$$

Equation 1
AASHTO Publication No. FHWA-RD-97-083

$K_1 = 6368.515$

$K_2 = 0.4485$

Equation 1 fitting parameters

${R_1}^2 = 0.8896$

Coefficient of determination

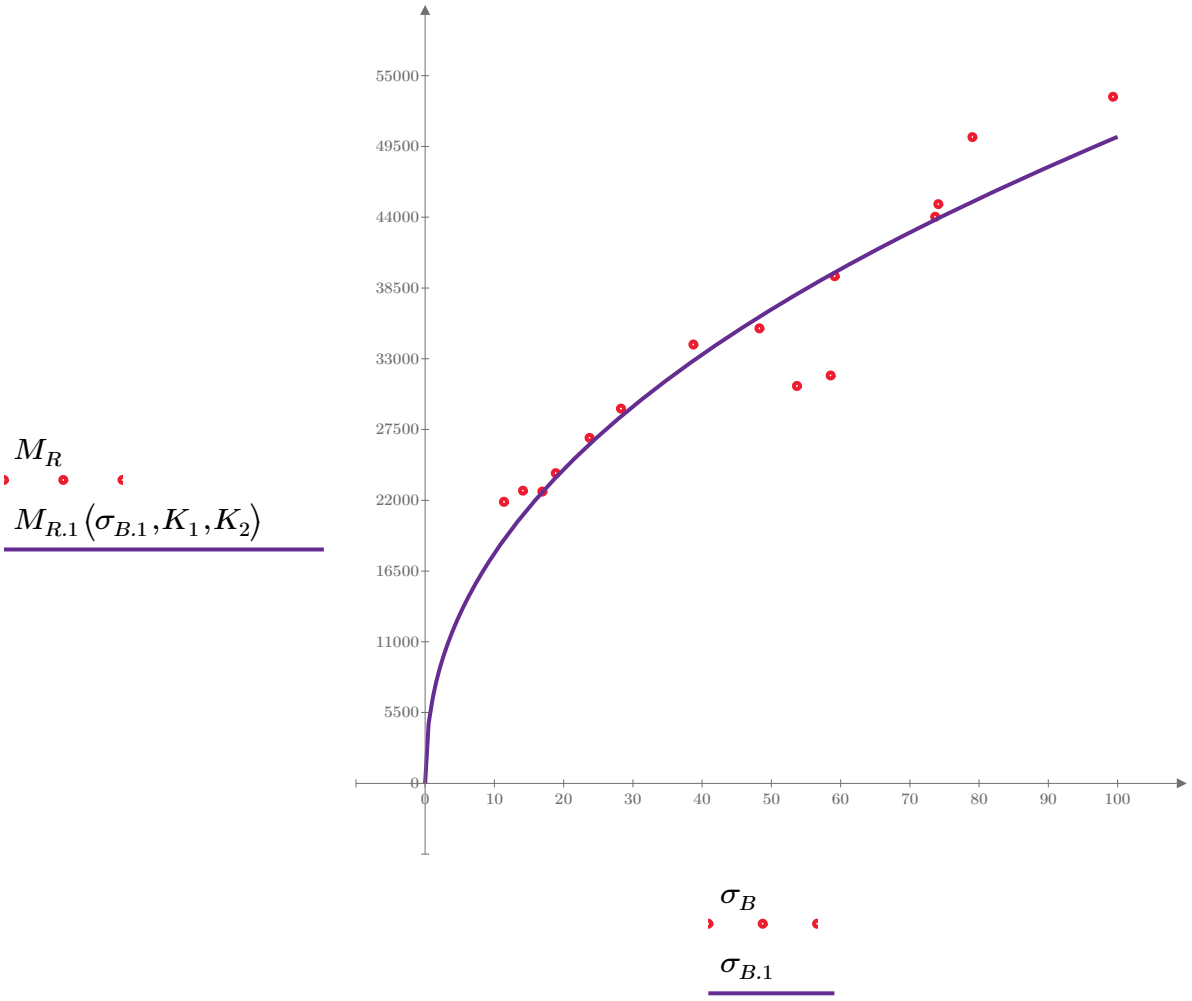

Figure 1. Plot of the test data (red points) vs. the fitted Equation 1 model (purple line).

Dan Seely
9/12/2023

$$M_{R.2}(\sigma_d, K_3, K_4) := K_3 \cdot \sigma_d^{K_4}$$

Equation 2
AASHTO Publication No. FHWA-RD-97-083

$K_3 = 12553.450$

$K_4 = 0.3792$

Equation 2 fitting parameters

$R_2^2 = 0.7395$

Coefficient of determination

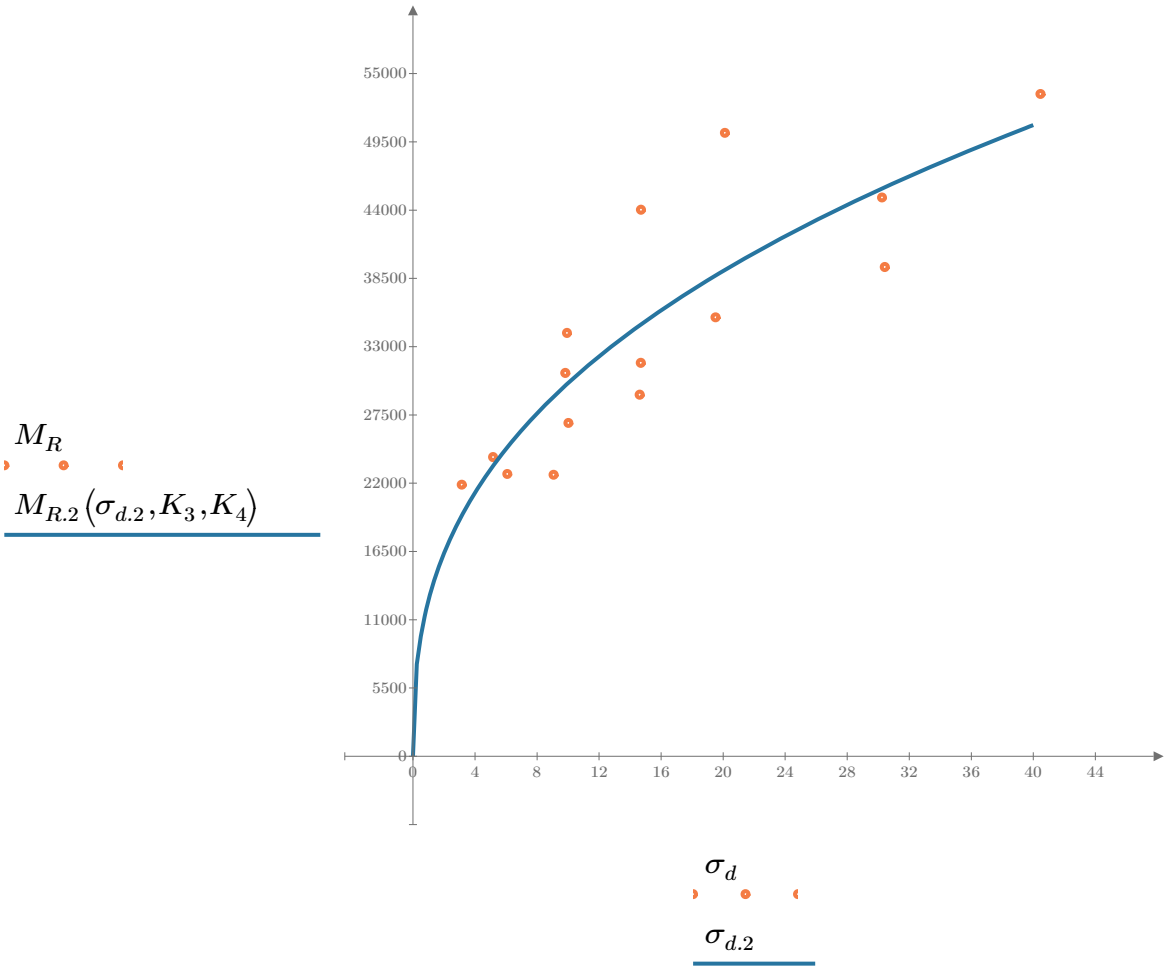

Figure 2. Plot of the test data (orange points) vs. the fitted Equation 2 model (blue line).

Dan Seely
9/12/2023

$$M_{R.3}\left(\sigma_d,\sigma_3,K_5,K_6,K_7\right):=K_5\cdot{\sigma_d}^{K_6}\cdot\left(1+\sigma_3\right)^{K_7}$$

Equation 3 AASHTO Publication No. FHWA-RD-97-083

$K_5=10159.115$

$K_6=0.2129$ Equation 3 fitting parameters

$K_7=0.2793$

${R_3}^2=0.9135$ Coefficient of determination

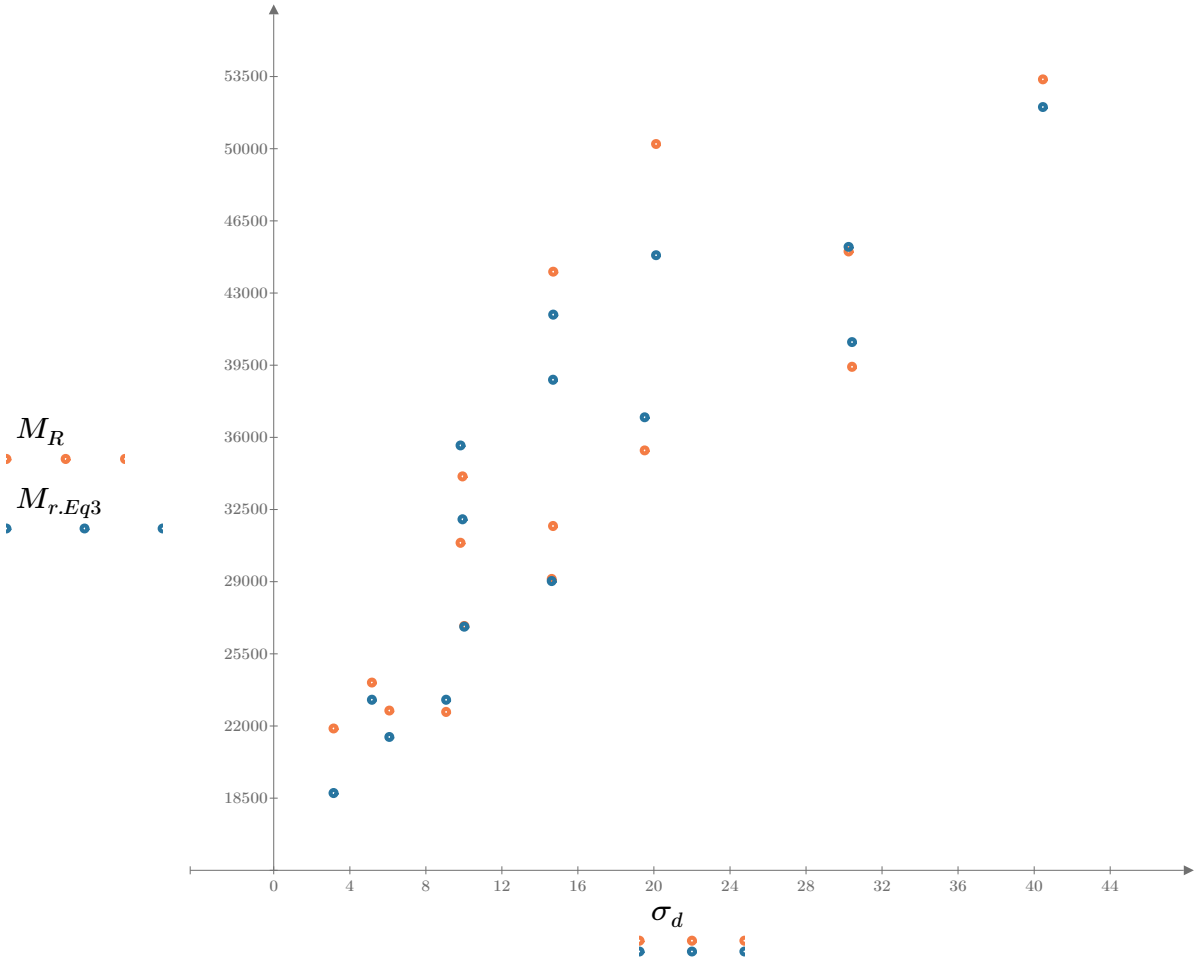

Figure 3. Plot of the test data (orange points) vs. the fitted Equation 3 model (blue points).

Dan Seely
9/12/2023

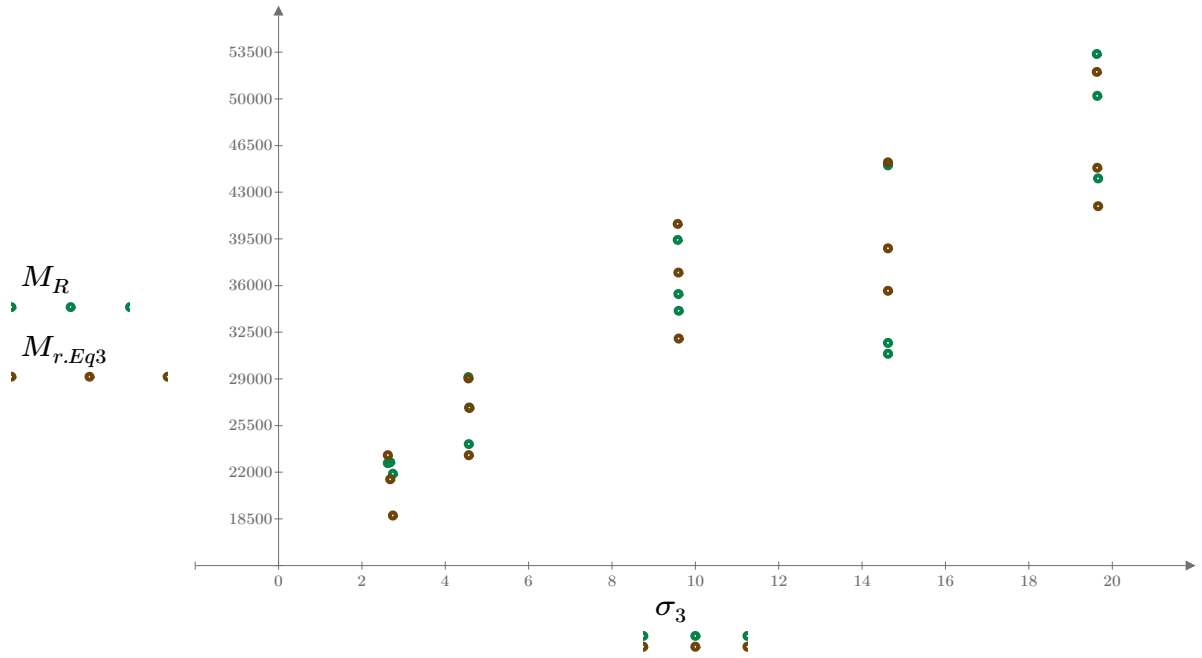

Figure 4. Plot of the test data (green points) vs. the fitted Equation 3 model (brown points).

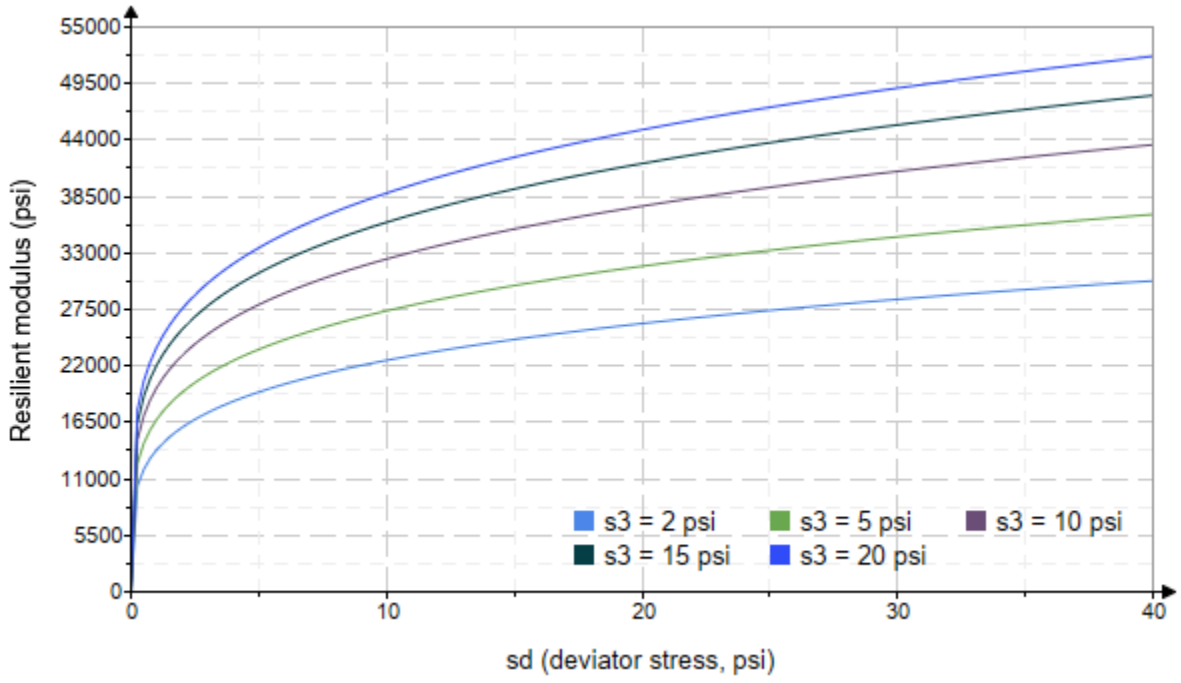

Figure 5. Plot of the fitted Equation 3 model for various confining stresses.

Dan Seely
9/12/2023

$$M_{R.4}\left(\sigma_B,\sigma_d,K_8,K_9,K_{10}\right) := K_8 \cdot p_a \left(\frac{\sigma_B}{p_a}\right)^{K_9} \cdot \left(\frac{\sigma_d}{p_a}\right)^{K_{10}}$$

Equation 4 AASHTO Publication No. FHWA-RD-97-083

$K_8 = 1588.980$

$K_9 = 0.3636$ Equation 4 fitting parameters

$K_{10} = 0.0954$

$R_4^{\,2} = 0.9033$ Coefficient of determination

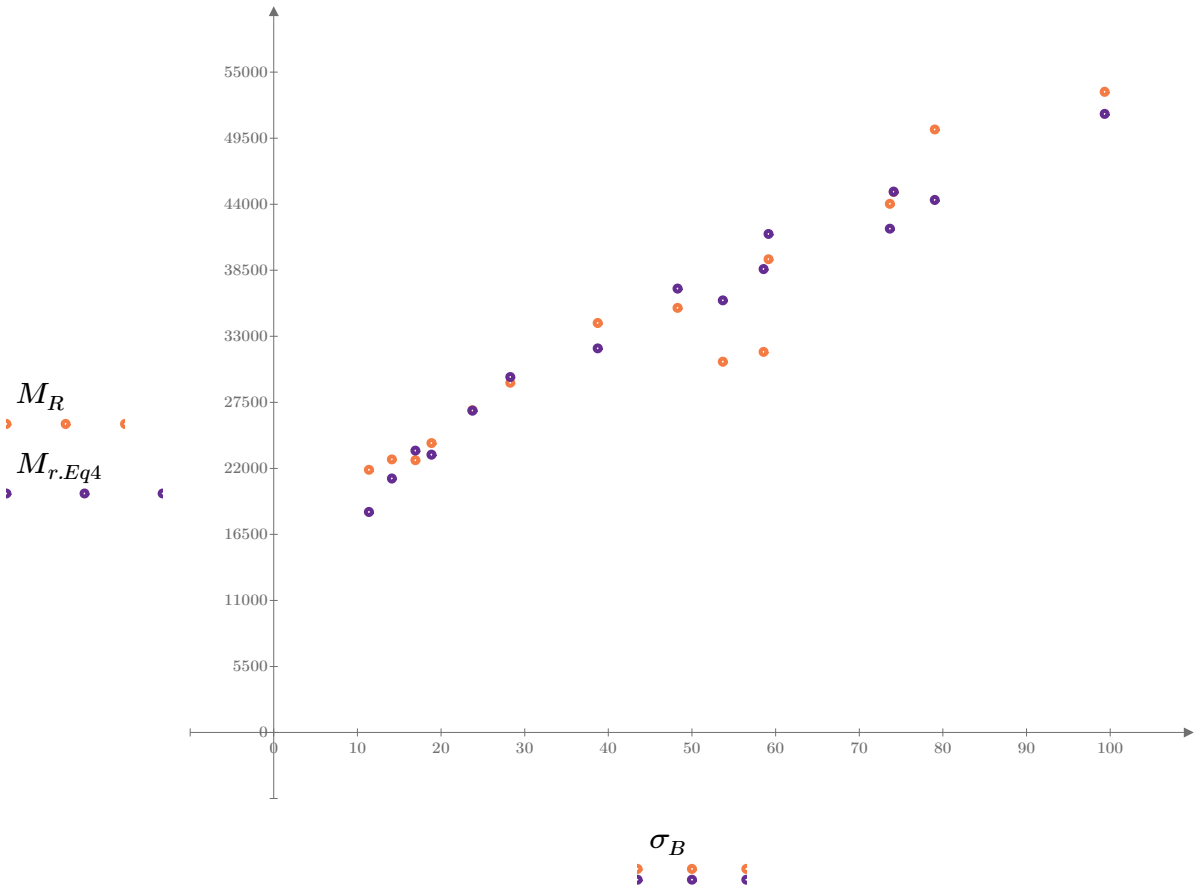

Figure 6. Plot of the test data (orange points) vs. the fitted Equation 4 model (purple points).

Dan Seely
9/12/2023

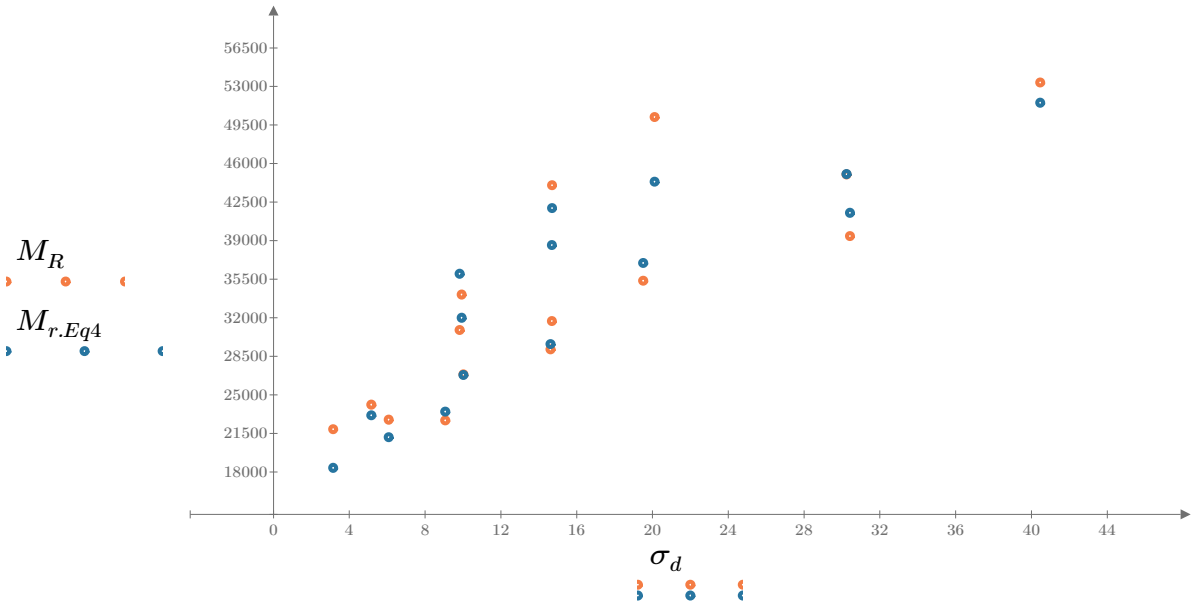

Figure 7. Plot of the test data (orange points) vs. the fitted Equation 4 model (blue points).

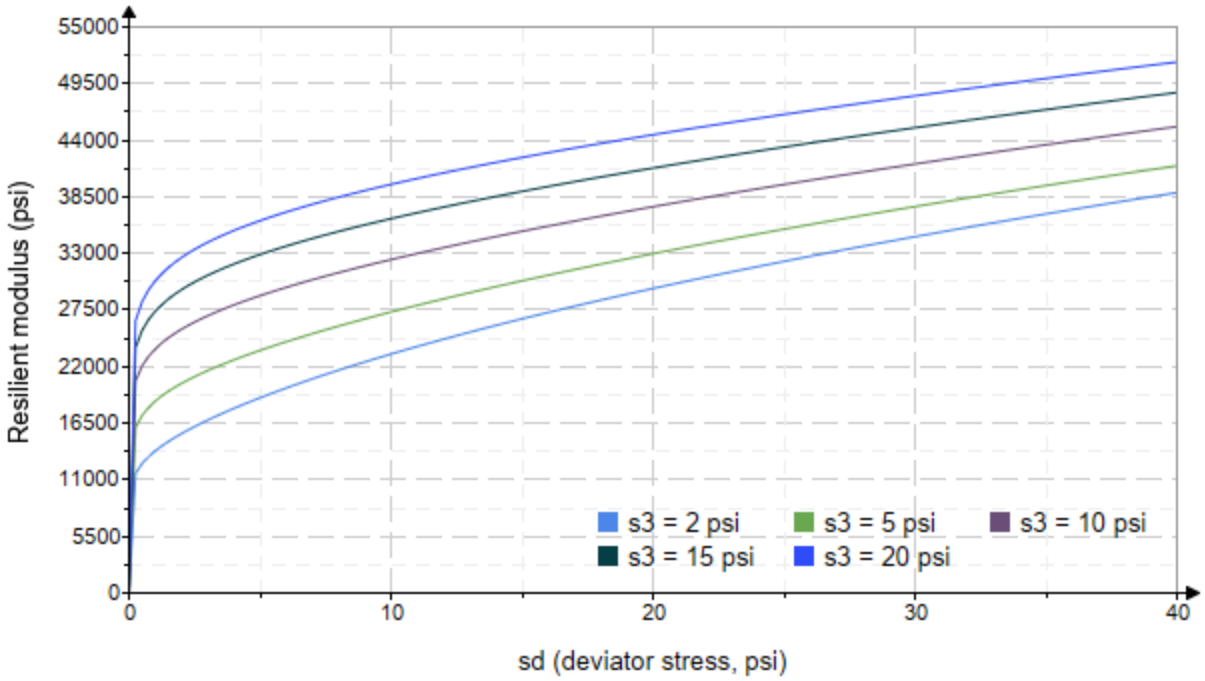

Figure 8. Plot of the fitted Equation 4 model for various confining stresses.

Dan Seely
9/12/2023

$SampleNo := \text{“B2–32”}$

$Treatment = \text{“D1”}$

$S = 15.986$ Degree of Saturation (%)

Test Sequence : Base/Subbase

Test summary data (psi) :

$$\sigma_3 = \begin{bmatrix} 2.627 \\ 2.275 \\ 2.239 \\ 4.183 \\ 4.155 \\ 4.263 \\ 9.255 \\ 8.928 \\ 8.798 \\ 14.310 \\ 14.430 \\ 13.880 \\ 19.640 \\ 19.550 \\ 19.510 \end{bmatrix} \quad \sigma_d = \begin{bmatrix} 3.167 \\ 6.166 \\ 9.112 \\ 5.239 \\ 9.997 \\ 14.340 \\ 10.050 \\ 19.430 \\ 29.660 \\ 10.150 \\ 14.520 \\ 29.890 \\ 14.600 \\ 19.740 \\ 39.990 \end{bmatrix} \quad \sigma_B = \begin{bmatrix} 11.050 \\ 12.990 \\ 15.830 \\ 17.790 \\ 22.460 \\ 27.130 \\ 37.820 \\ 46.220 \\ 56.060 \\ 53.080 \\ 57.810 \\ 71.530 \\ 73.520 \\ 78.390 \\ 98.520 \end{bmatrix} \quad M_R = \begin{bmatrix} 48621.0 \\ 39778.0 \\ 34574.0 \\ 60817.2 \\ 31980.8 \\ 30846.4 \\ 47726.0 \\ 58447.8 \\ 62450.6 \\ 145708.0 \\ 109638.0 \\ 61797.0 \\ 88392.2 \\ 78146.0 \\ 57394.6 \end{bmatrix}$$

σ_3 = mean confining stress
σ_d = mean deviator stress
σ_B = mean bulk stress
M_R = resilient modulus
p_a = atmospheric pressure = 14.6959 psi

Dan Seely
9/12/2023

$$M_{R.1}\left(\sigma_B, K_1, K_2\right) := K_1 \cdot {\sigma_B}^{K_2}$$

Equation 1
AASHTO Publication No. FHWA-RD-97-083

$K_1 = 16909.755$

$K_2 = 0.3605$

Equation 1 fitting parameters

${R_1}^2 = 0.2658$

Coefficient of determination

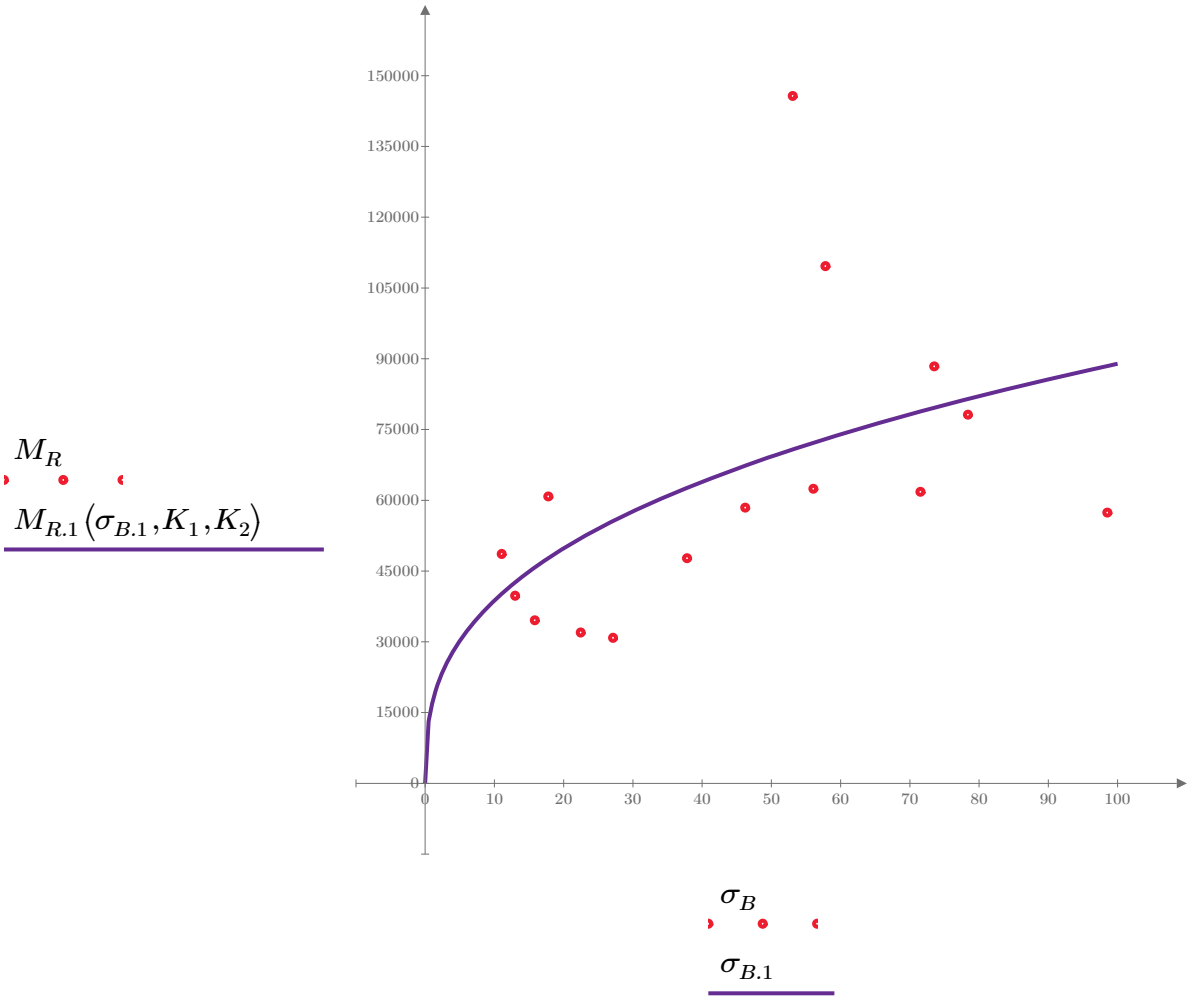

Figure 1. Plot of the test data (red points) vs. the fitted Equation 1 model (purple line).

Dan Seely
9/12/2023

$$M_{R.2}(\sigma_d, K_3, K_4) := K_3 \cdot \sigma_d^{K_4}$$

Equation 2
AASHTO Publication No. FHWA-RD-97-083

$K_3 = 50461.281$

$K_4 = 0.0912$

Equation 2 fitting parameters

$R_2^2 = 0.0183$

Coefficient of determination

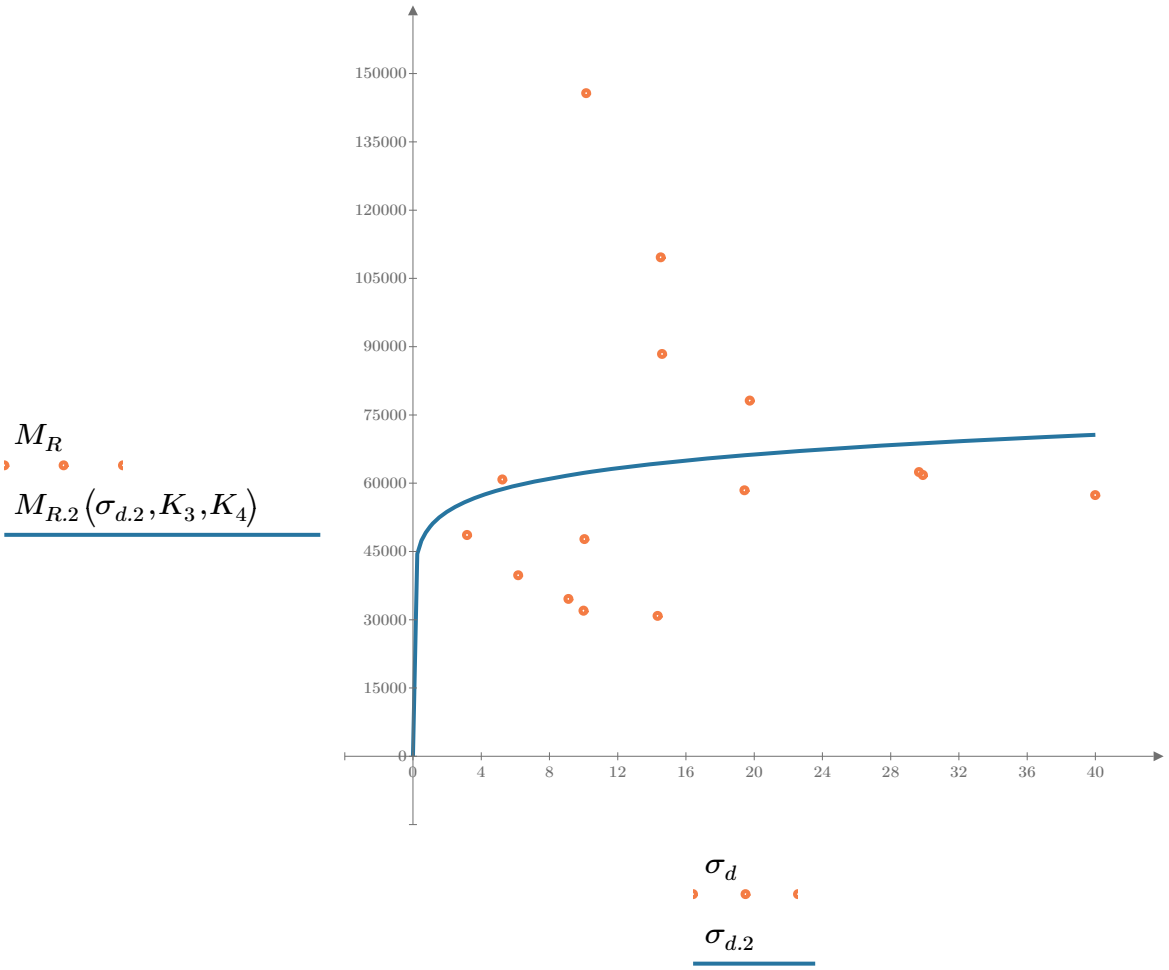

Figure 2. Plot of the test data (orange points) vs. the fitted Equation 2 model (blue line).

Dan Seely
9/12/2023

$$M_{R.3}\left(\sigma_d,\sigma_3,K_5,K_6,K_7\right):=K_5\cdot{\sigma_d}^{K_6}\cdot\left(1+\sigma_3\right)^{K_7}$$

Equation 3 AASHTO Publication No. FHWA-RD-97-083

$K_5=36314.323$

$K_6=-0.5337$ Equation 3 fitting parameters

$K_7=0.8436$

${R_3}^2=0.6696$ Coefficient of determination

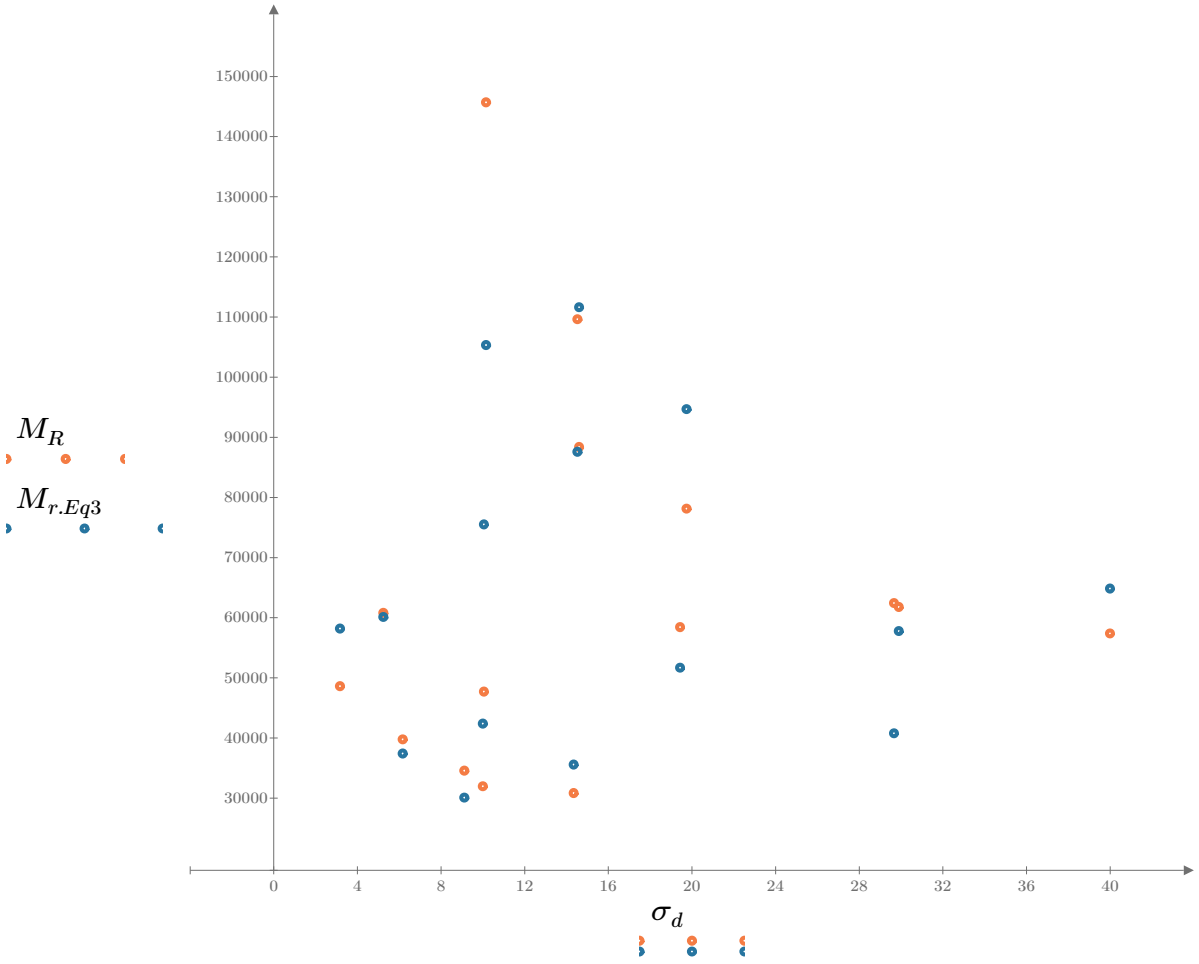

Figure 3. Plot of the test data (orange points) vs. the fitted Equation 3 model (blue points).

Dan Seely
9/12/2023

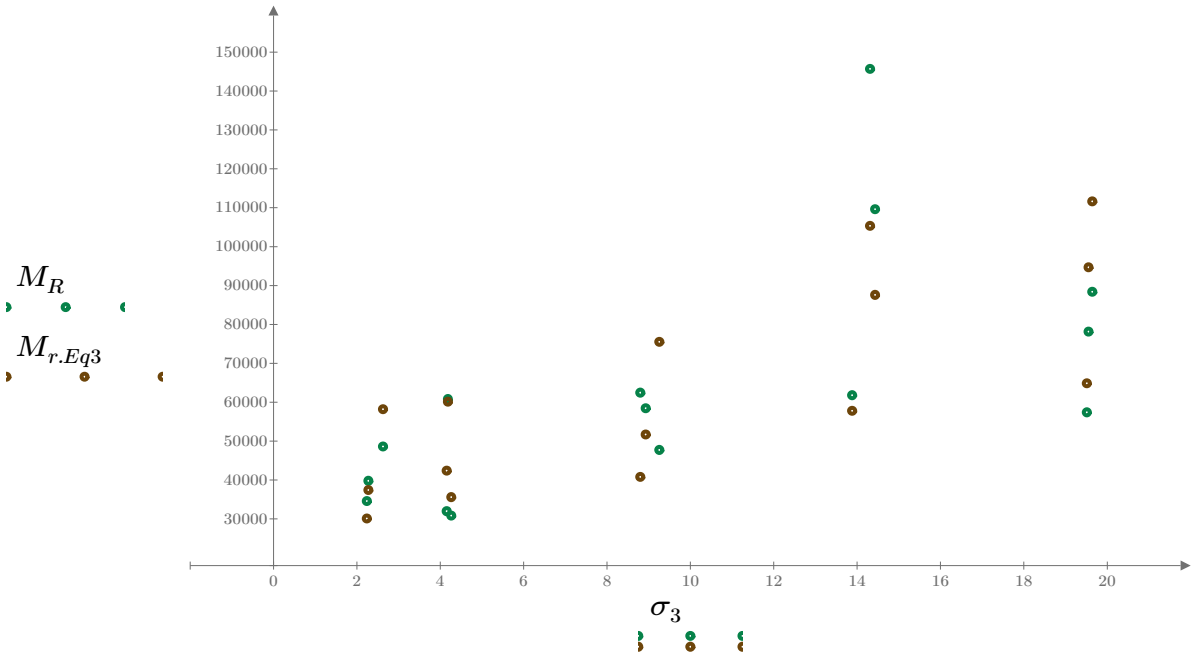

Figure 4. Plot of the test data (green points) vs. the fitted Equation 3 model (brown points).

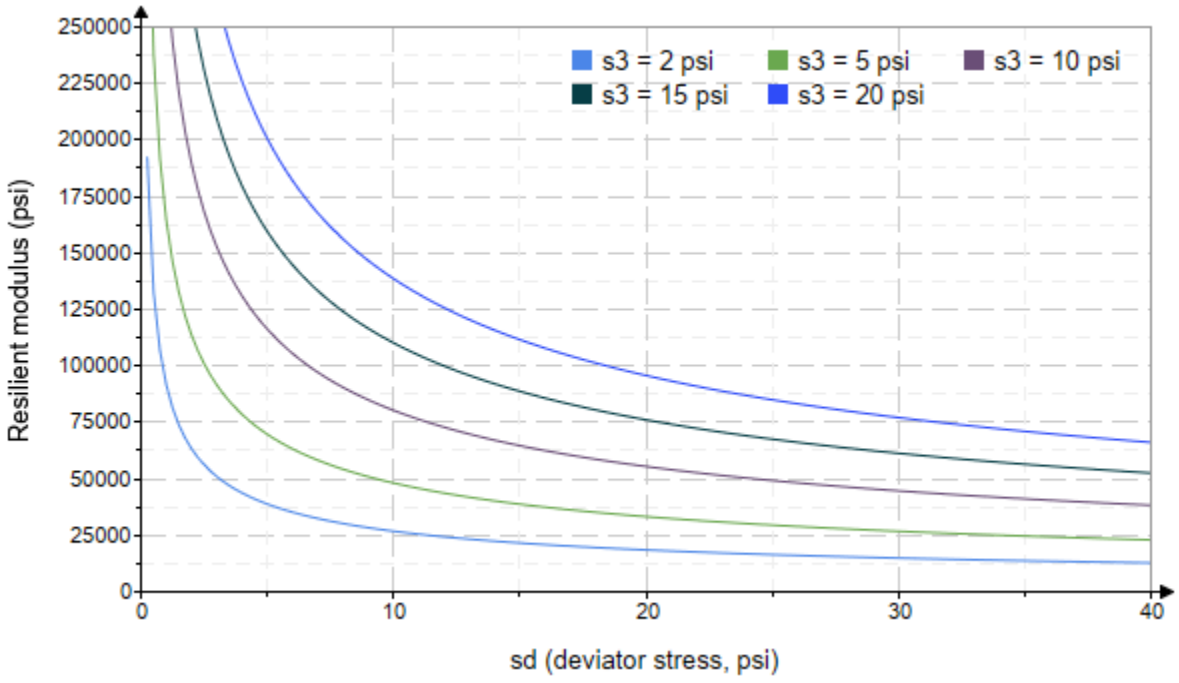

Figure 5. Plot of the fitted Equation 3 model for various confining stresses.

Dan Seely
9/12/2023

$$M_{R.4}\left(\sigma_B,\sigma_d,K_8,K_9,K_{10}\right) := K_8 \cdot p_a \left(\frac{\sigma_B}{p_a}\right)^{K_9} \cdot \left(\frac{\sigma_d}{p_a}\right)^{K_{10}}$$

Equation 4 AASHTO Publication No. FHWA-RD-97-083

$K_8 = 1248.189$

$K_9 = 1.1295$ Equation 4 fitting parameters

$K_{10} = -0.9268$

$R_4^{\,2} = 0.7024$ Coefficient of determination

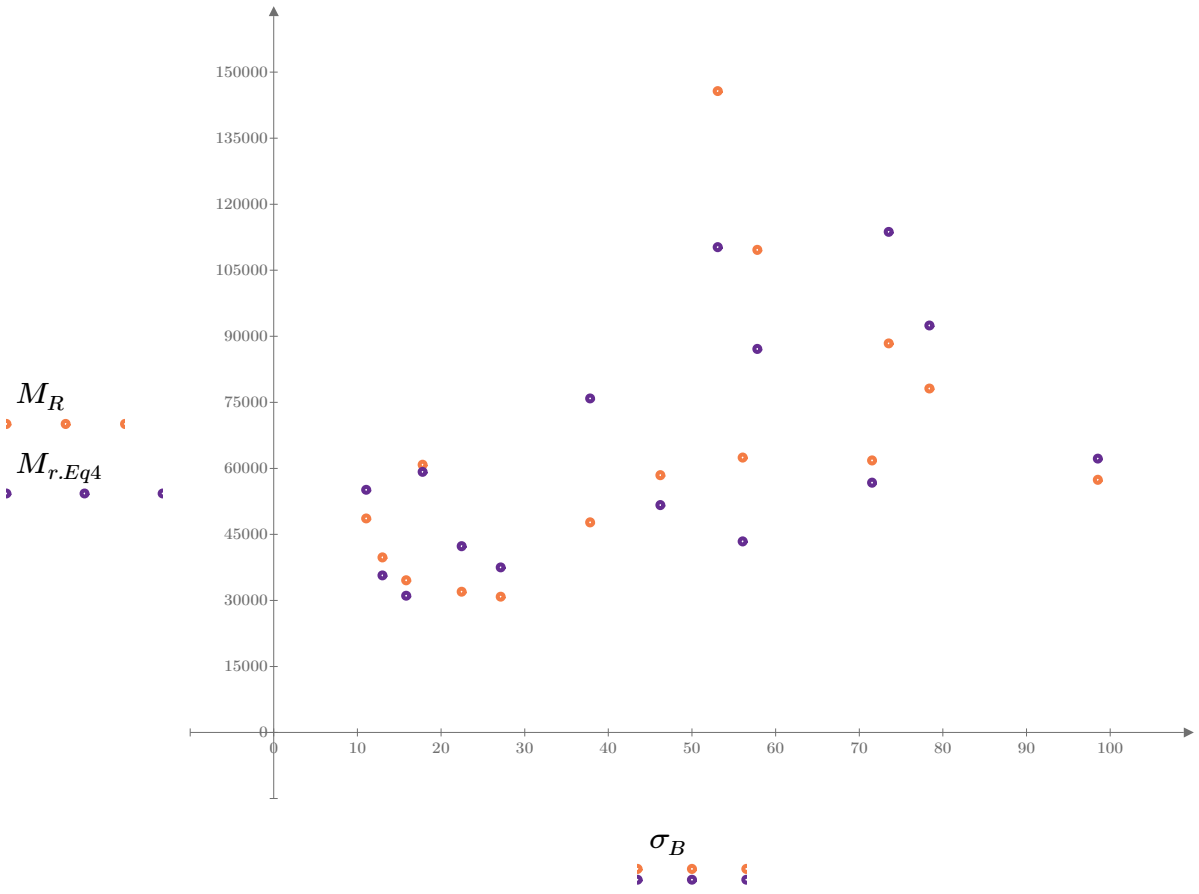

Figure 6. Plot of the test data (orange points) vs. the fitted Equation 4 model (purple points).

Dan Seely
9/12/2023

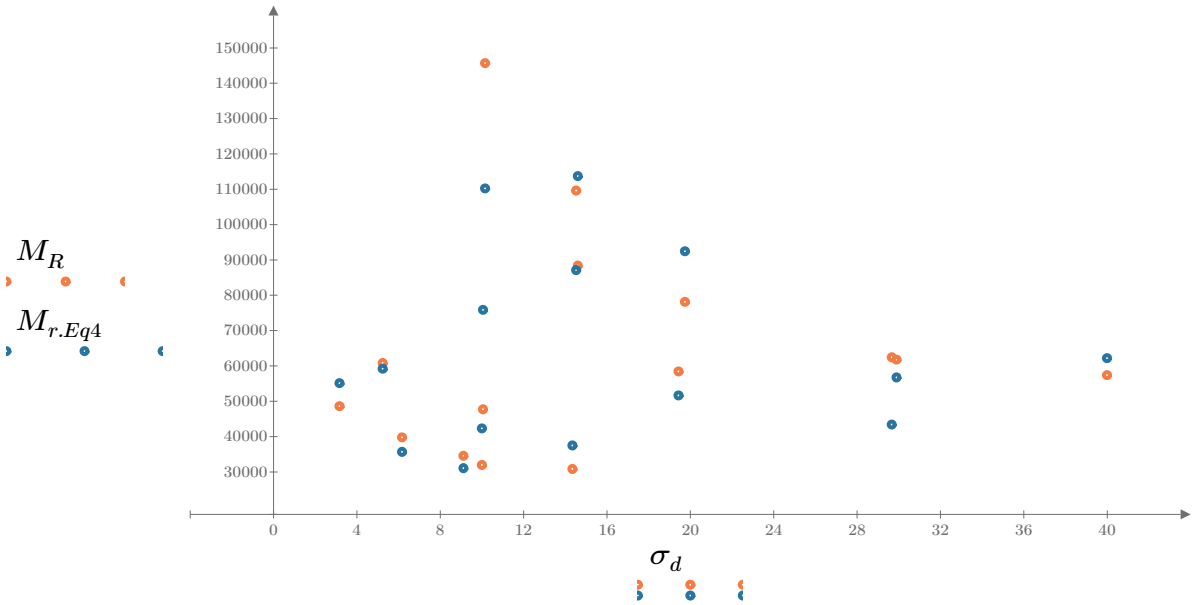

Figure 7. Plot of the test data (orange points) vs. the fitted Equation 4 model (blue points).

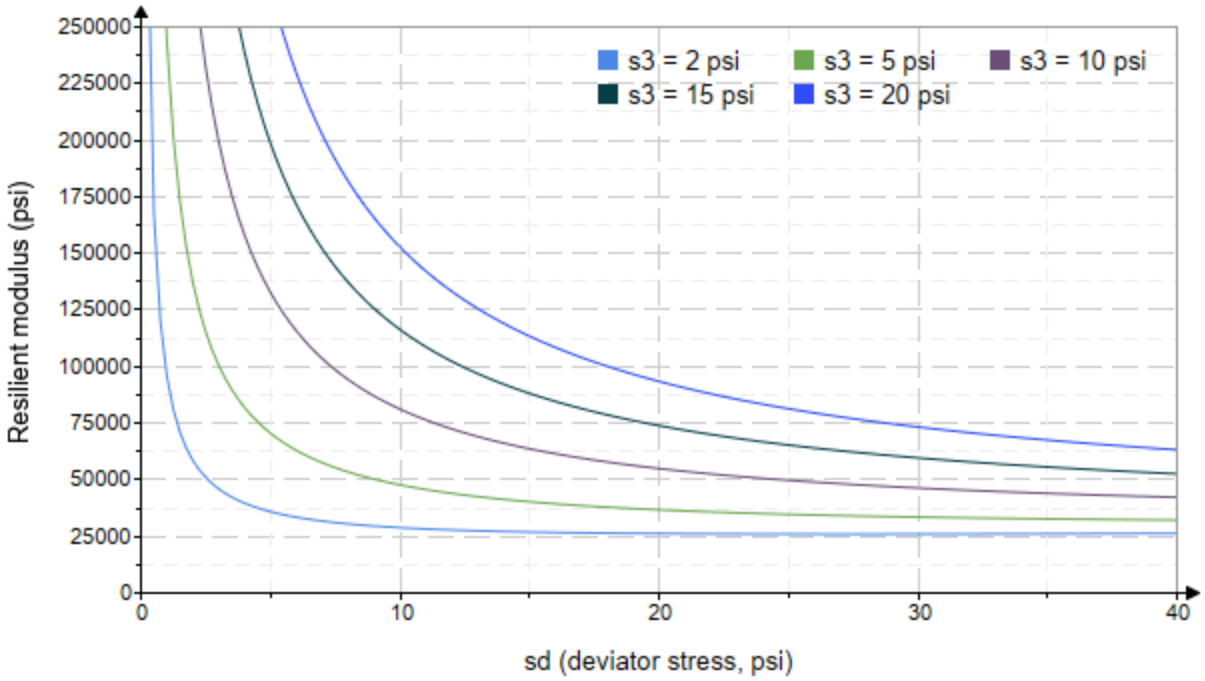

Figure 8. Plot of the fitted Equation 4 model for various confining stresses.

Dan Seely
9/12/2023

$SampleNo :=$ "B2−33"

$Treatment =$ "D1"

$S = 15.504$ Degree of Saturation (%)

Test Sequence : Base/Subbase

Test summary data (psi) :

$$\sigma_3 = \begin{bmatrix} 2.910 \\ 2.909 \\ 2.797 \\ 4.665 \\ 4.625 \\ 4.593 \\ 9.630 \\ 9.649 \\ 9.612 \\ 14.630 \\ 14.660 \\ 14.630 \\ 19.680 \\ 19.690 \\ 19.680 \end{bmatrix} \quad \sigma_d = \begin{bmatrix} 3.110 \\ 6.152 \\ 9.129 \\ 5.175 \\ 10.020 \\ 14.550 \\ 10.110 \\ 19.250 \\ 29.520 \\ 10.160 \\ 14.480 \\ 29.650 \\ 14.520 \\ 19.560 \\ 40.190 \end{bmatrix} \quad \sigma_B = \begin{bmatrix} 11.840 \\ 14.880 \\ 17.520 \\ 19.170 \\ 23.890 \\ 28.330 \\ 39.000 \\ 48.200 \\ 58.350 \\ 54.040 \\ 58.450 \\ 73.550 \\ 73.570 \\ 78.620 \\ 99.230 \end{bmatrix} \quad M_R = \begin{bmatrix} 22008.0 \\ 22779.8 \\ 24797.6 \\ 30282.2 \\ 31116.6 \\ 29135.2 \\ 30501.8 \\ 33120.4 \\ 39905.4 \\ 51824.6 \\ 51727.6 \\ 47174.6 \\ 62331.4 \\ 58987.8 \\ 60574.2 \end{bmatrix}$$

σ_3 = mean confining stress
σ_d = mean deviator stress
σ_B = mean bulk stress
M_R = resilient modulus
p_a = atmospheric pressure = 14.6959 psi

Dan Seely
9/12/2023

$$M_{R.1}\left(\sigma_B, K_1, K_2\right) := K_1 \cdot {\sigma_B}^{K_2}$$

Equation 1
AASHTO Publication No. FHWA-RD-97-083

$K_1 = 5261.696$

$K_2 = 0.5376$

Equation 1 fitting parameters

${R_1}^2 = 0.8511$

Coefficient of determination

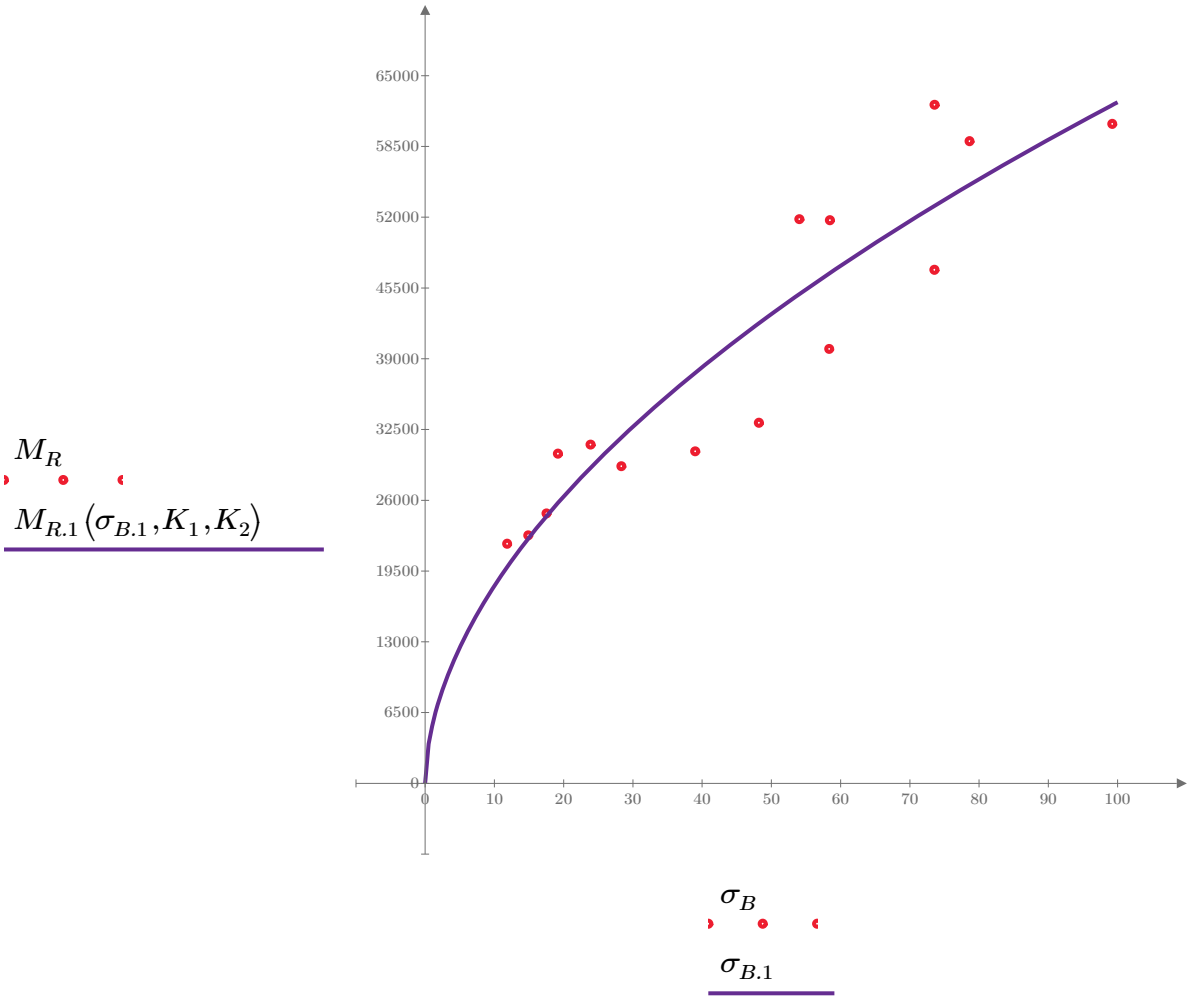

Figure 1. Plot of the test data (red points) vs. the fitted Equation 1 model (purple line).

Dan Seely
9/12/2023

$$M_{R.2}(\sigma_d, K_3, K_4) := K_3 \cdot \sigma_d^{K_4}$$

Equation 2
AASHTO Publication No. FHWA-RD-97-083

$K_3 = 16594.673$

$K_4 = 0.3341$

Equation 2 fitting parameters

$R_2^2 = 0.4143$

Coefficient of determination

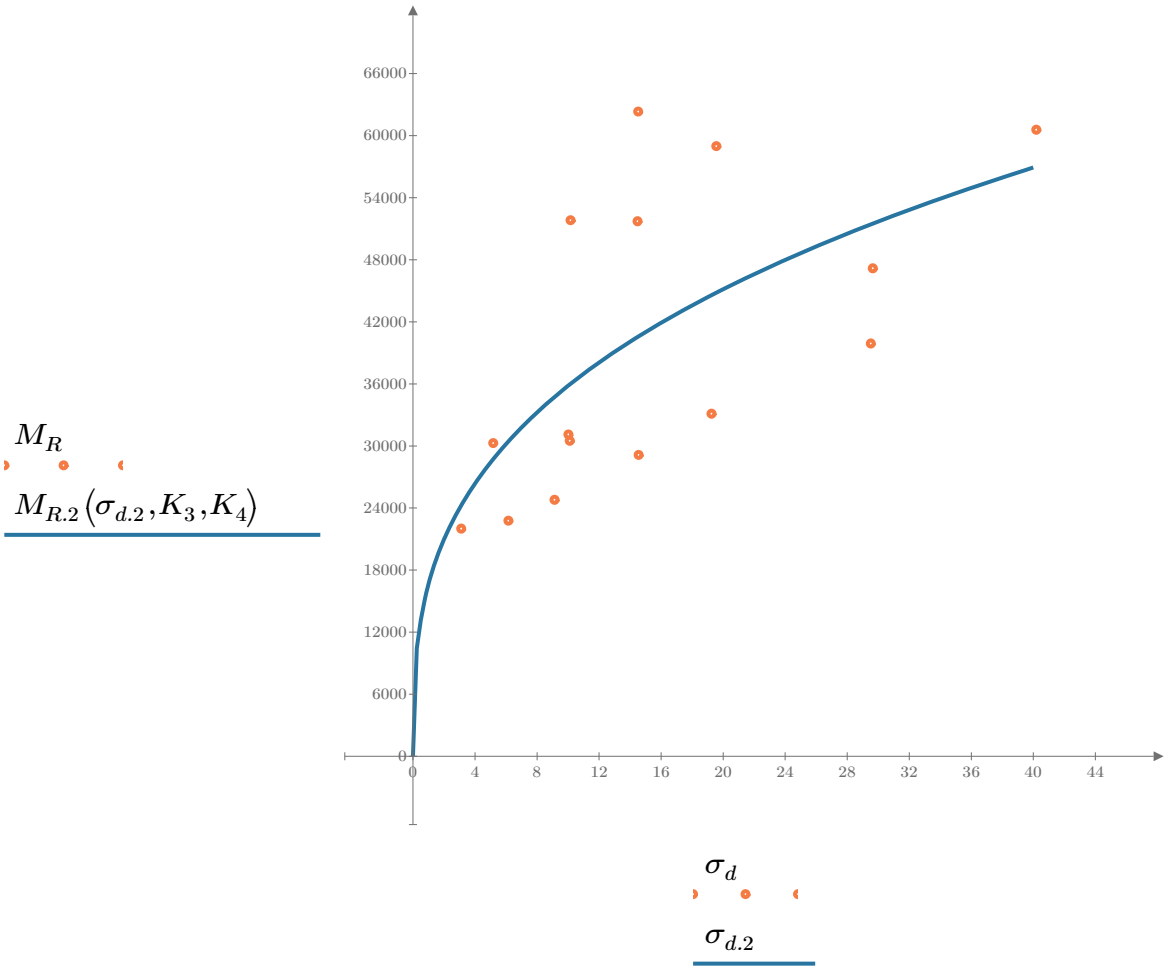

Figure 2. Plot of the test data (orange points) vs. the fitted Equation 2 model (blue line).

Dan Seely
9/12/2023

$$M_{R.3}\left(\sigma_d,\sigma_3,K_5,K_6,K_7\right) := K_5 \cdot {\sigma_d}^{K_6} \cdot \left(1+\sigma_3\right)^{K_7}$$

Equation 3 AASHTO Publication No. FHWA-RD-97-083

$K_5 = 10193.405$

$K_6 = -0.0220$ Equation 3 fitting parameters

$K_7 = 0.6016$

${R_3}^2 = 0.9335$ Coefficient of determination

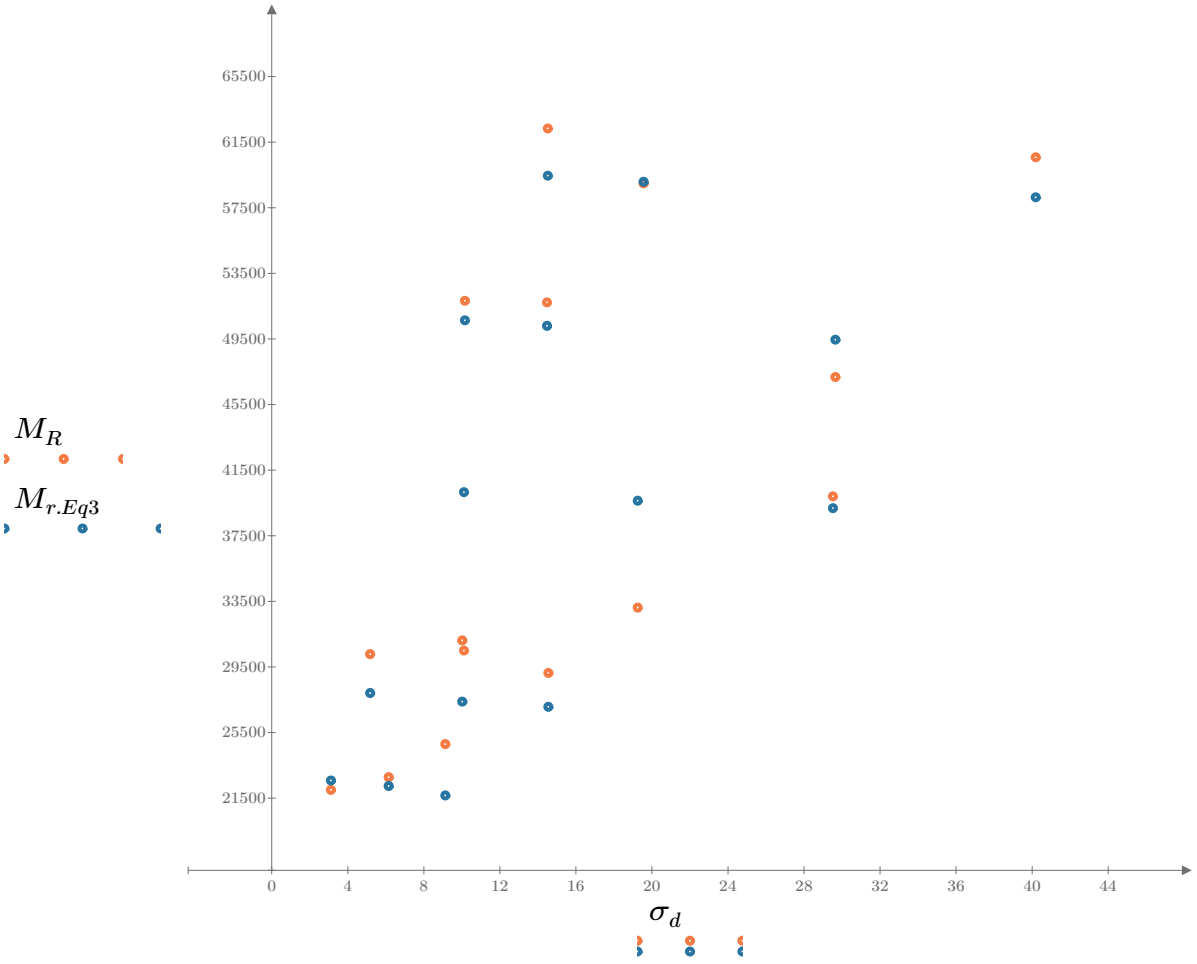

Figure 3. Plot of the test data (orange points) vs. the fitted Equation 3 model (blue points).

Dan Seely
9/12/2023

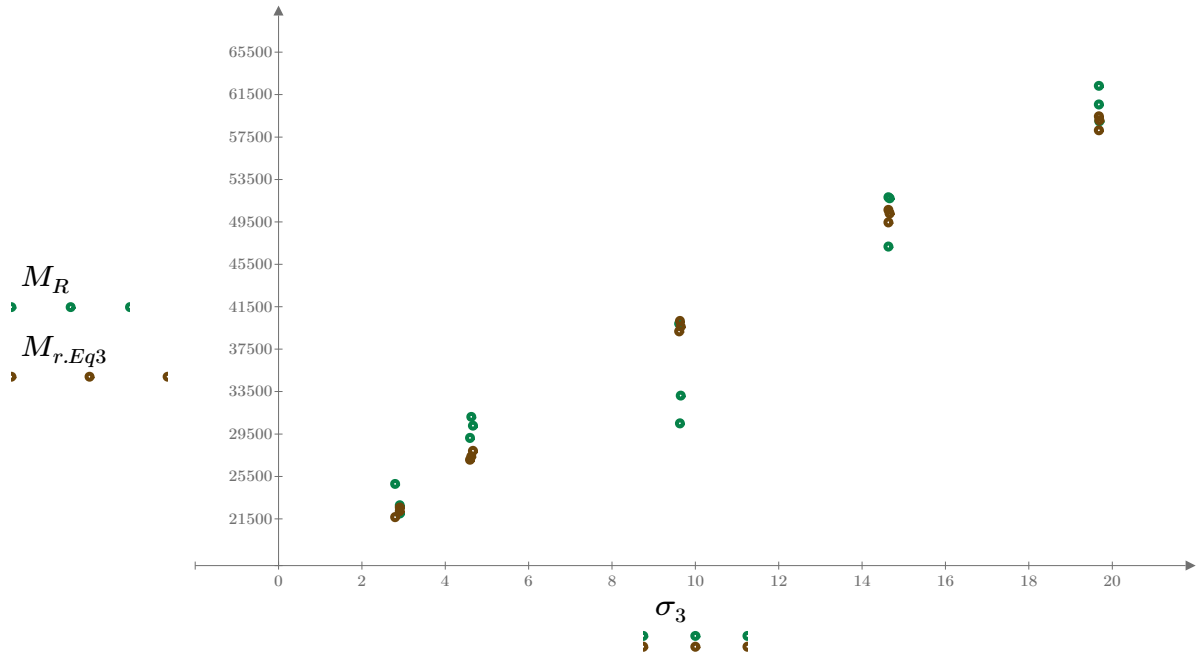

Figure 4. Plot of the test data (green points) vs. the fitted Equation 3 model (brown points).

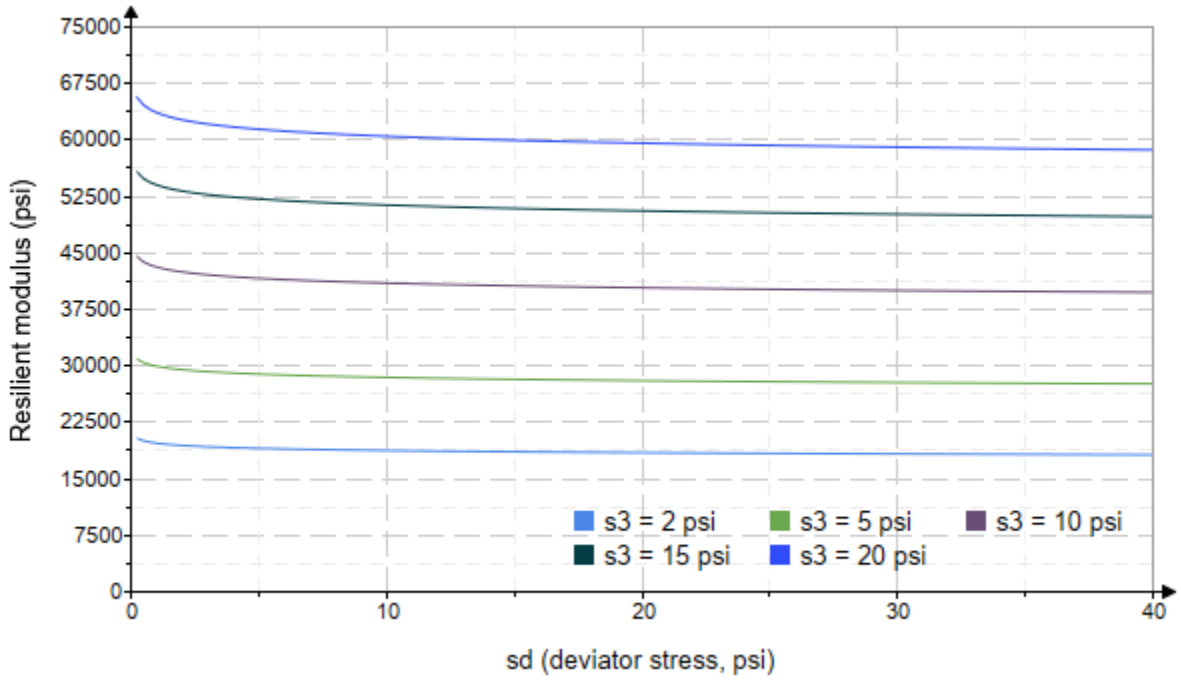

Figure 5. Plot of the fitted Equation 3 model for various confining stresses.

Dan Seely
9/12/2023

$$M_{R.4}\left(\sigma_B,\sigma_d,K_8,K_9,K_{10}\right) := K_8 \cdot p_a \left(\frac{\sigma_B}{p_a}\right)^{K_9} \cdot \left(\frac{\sigma_d}{p_a}\right)^{K_{10}}$$

Equation 4 AASHTO Publication No. FHWA-RD-97-083

$K_8 = 1129.208$

$K_9 = 0.7961$ Equation 4 fitting parameters

$K_{10} = -0.2817$

$R_4^{\,2} = 0.9335$ Coefficient of determination

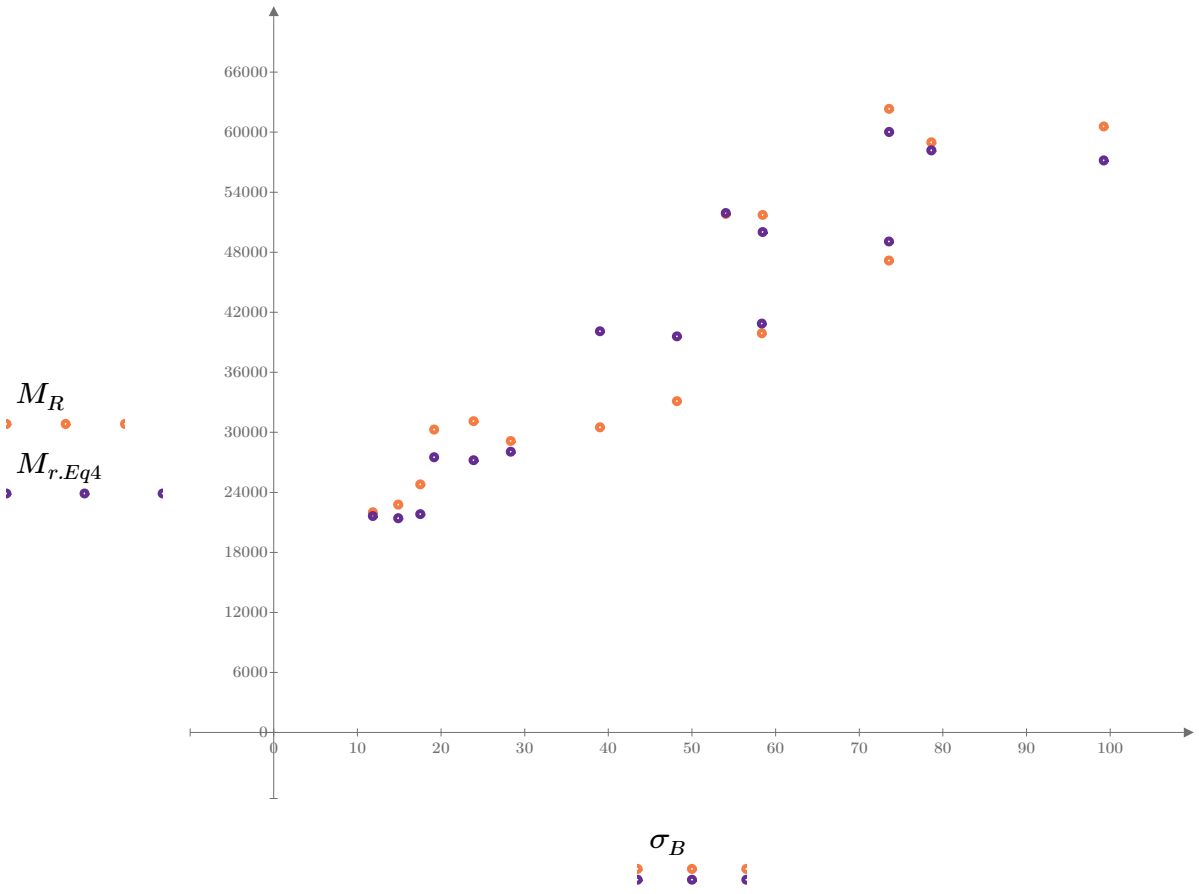

Figure 6. Plot of the test data (orange points) vs. the fitted Equation 4 model (purple points).

Dan Seely
9/12/2023

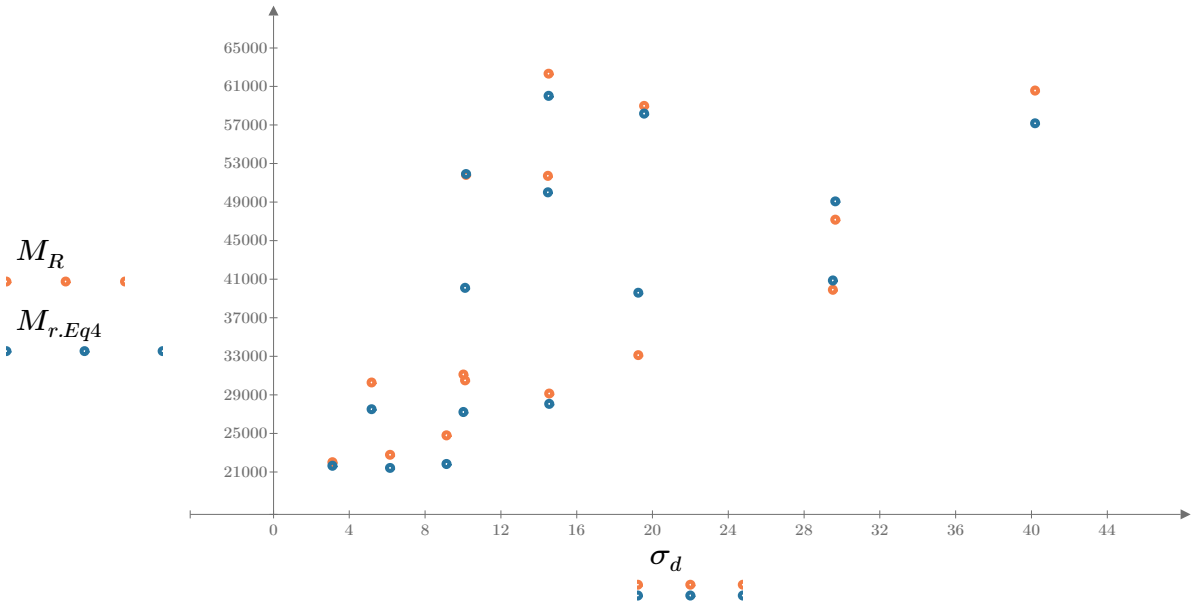

Figure 7. Plot of the test data (orange points) vs. the fitted Equation 4 model (blue points).

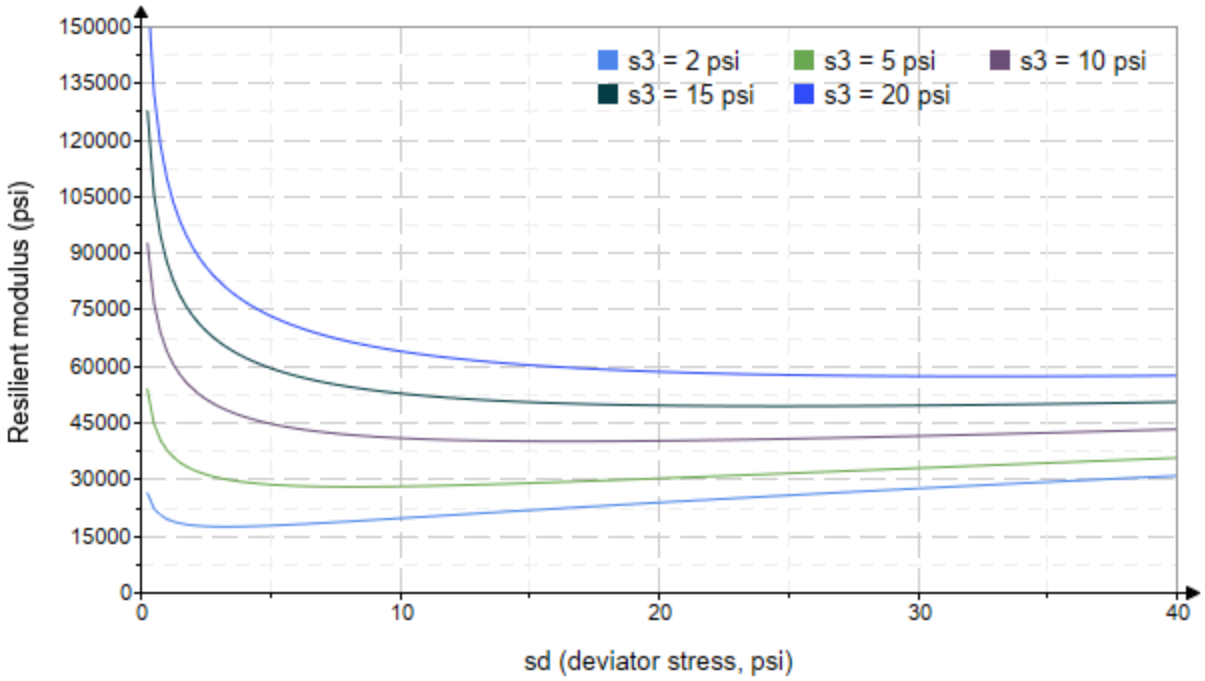

Figure 8. Plot of the fitted Equation 4 model for various confining stresses.

Dan Seely
9/12/2023

$SampleNo := \text{“B2–34”}$

$Treatment = \text{“D1”}$

$S = 15.480$ Degree of Saturation (%)

Test Sequence : Base/Subbase

Test summary data (psi) :

$$\sigma_3 = \begin{bmatrix} 2.788 \\ 2.394 \\ 2.345 \\ 4.317 \\ 4.335 \\ 4.135 \\ 9.051 \\ 9.312 \\ 9.041 \\ 14.320 \\ 14.510 \\ 14.030 \\ 19.520 \\ 19.530 \\ 19.560 \end{bmatrix} \quad \sigma_d = \begin{bmatrix} 3.090 \\ 6.146 \\ 9.105 \\ 5.213 \\ 10.020 \\ 14.460 \\ 10.040 \\ 19.480 \\ 29.620 \\ 9.897 \\ 14.570 \\ 29.900 \\ 14.650 \\ 19.850 \\ 39.870 \end{bmatrix} \quad \sigma_B = \begin{bmatrix} 11.450 \\ 13.330 \\ 16.140 \\ 18.160 \\ 23.030 \\ 26.860 \\ 37.200 \\ 47.420 \\ 56.740 \\ 52.860 \\ 58.090 \\ 72.000 \\ 73.200 \\ 78.440 \\ 98.550 \end{bmatrix} \quad M_R = \begin{bmatrix} 53131.2 \\ 30341.6 \\ 29247.2 \\ 114486.2 \\ 51200.4 \\ 46256.8 \\ 132424.0 \\ 55838.8 \\ 50287.2 \\ 176180.0 \\ 75114.2 \\ 61787.8 \\ 143570.0 \\ 101239.6 \\ 61202.0 \end{bmatrix}$$

σ_3 = mean confining stress
σ_d = mean deviator stress
σ_B = mean bulk stress
M_R = resilient modulus
p_a = atmospheric pressure = 14.6959 psi

Dan Seely
9/12/2023

$$M_{R.1}\left(\sigma_B, K_1, K_2\right) := K_1 \cdot {\sigma_B}^{K_2}$$

Equation 1
AASHTO Publication No. FHWA-RD-97-083

$K_1 = 27883.965$

$K_2 = 0.2831$

Equation 1 fitting parameters

${R_1}^2 = 0.1316$

Coefficient of determination

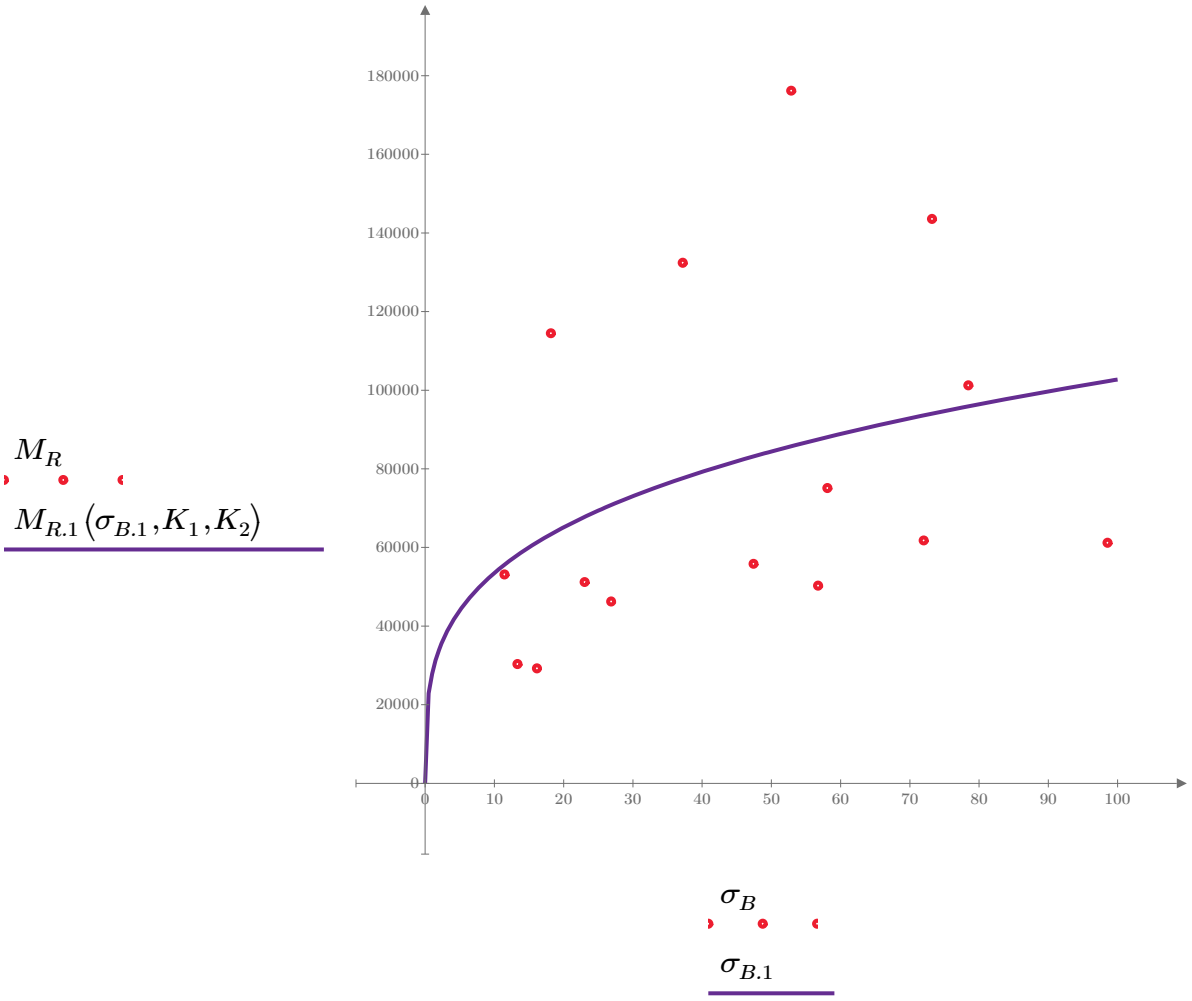

Figure 1. Plot of the test data (red points) vs. the fitted Equation 1 model (purple line).

Dan Seely
9/12/2023

$$M_{R.2}(\sigma_d, K_3, K_4) := K_3 \cdot {\sigma_d}^{K_4}$$

Equation 2
AASHTO Publication No. FHWA-RD-97-083

$K_3 = 88106.659$

$K_4 = -0.0439$

Equation 2 fitting parameters

${R_2}^2 = 0.0036$

Coefficient of determination

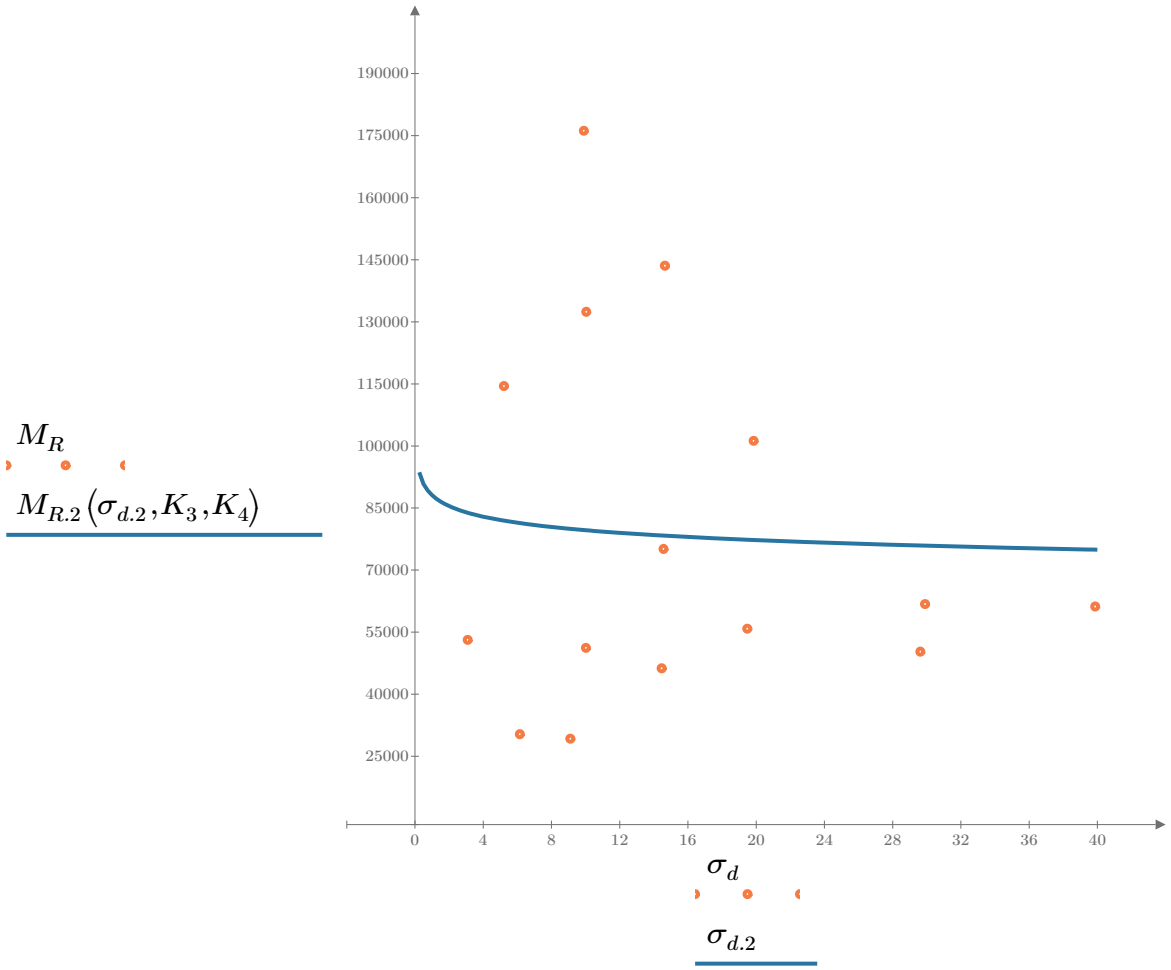

Figure 2. Plot of the test data (orange points) vs. the fitted Equation 2 model (blue line).

Dan Seely
9/12/2023

$$M_{R.3}\left(\sigma_d,\sigma_3,K_5,K_6,K_7\right):=K_5\cdot{\sigma_d}^{K_6}\cdot\left(1+\sigma_3\right)^{K_7}$$

Equation 3 AASHTO Publication No. FHWA-RD-97-083

$K_5=55847.465$

$K_6=-0.8332$ Equation 3 fitting parameters

$K_7=1.0656$

${R_3}^2=0.7693$ Coefficient of determination

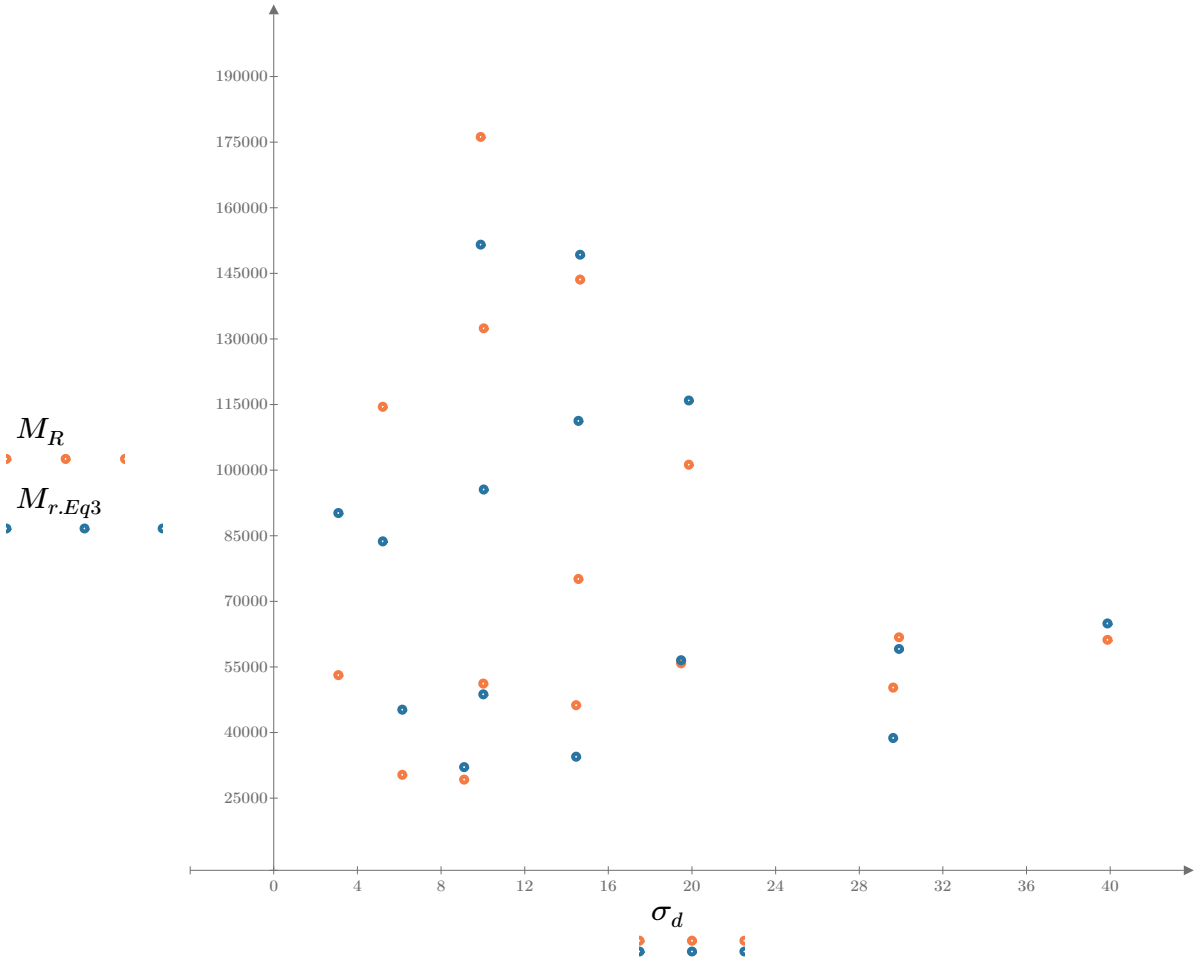

Figure 3. Plot of the test data (orange points) vs. the fitted Equation 3 model (blue points).

Dan Seely
9/12/2023

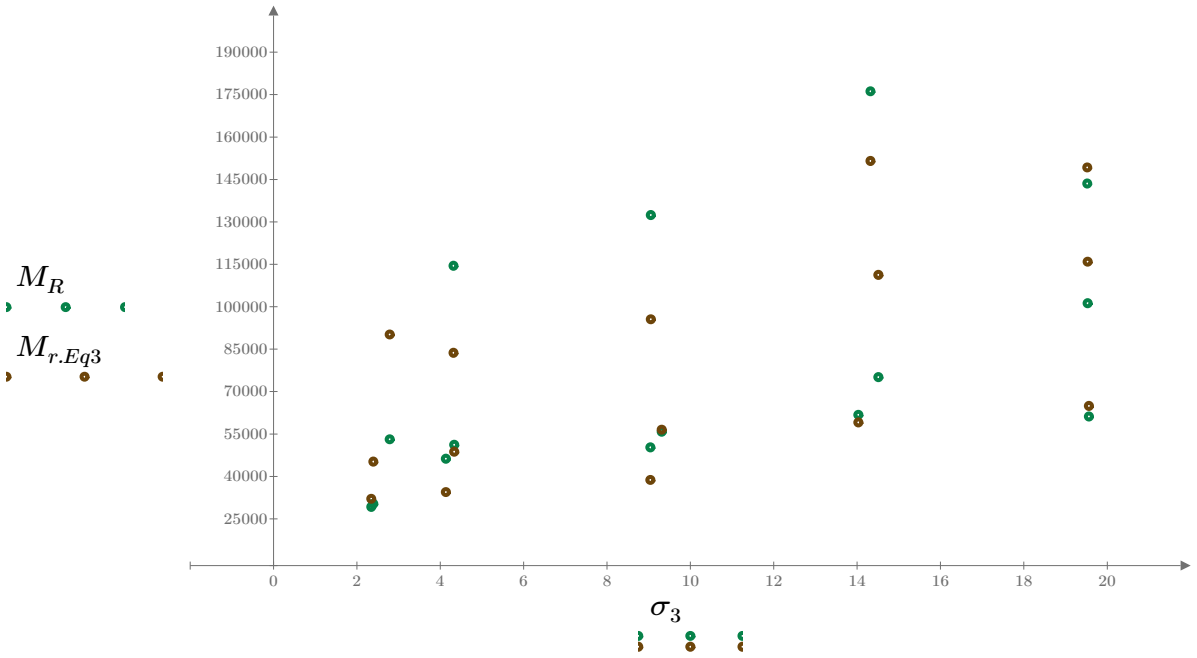

Figure 4. Plot of the test data (green points) vs. the fitted Equation 3 model (brown points).

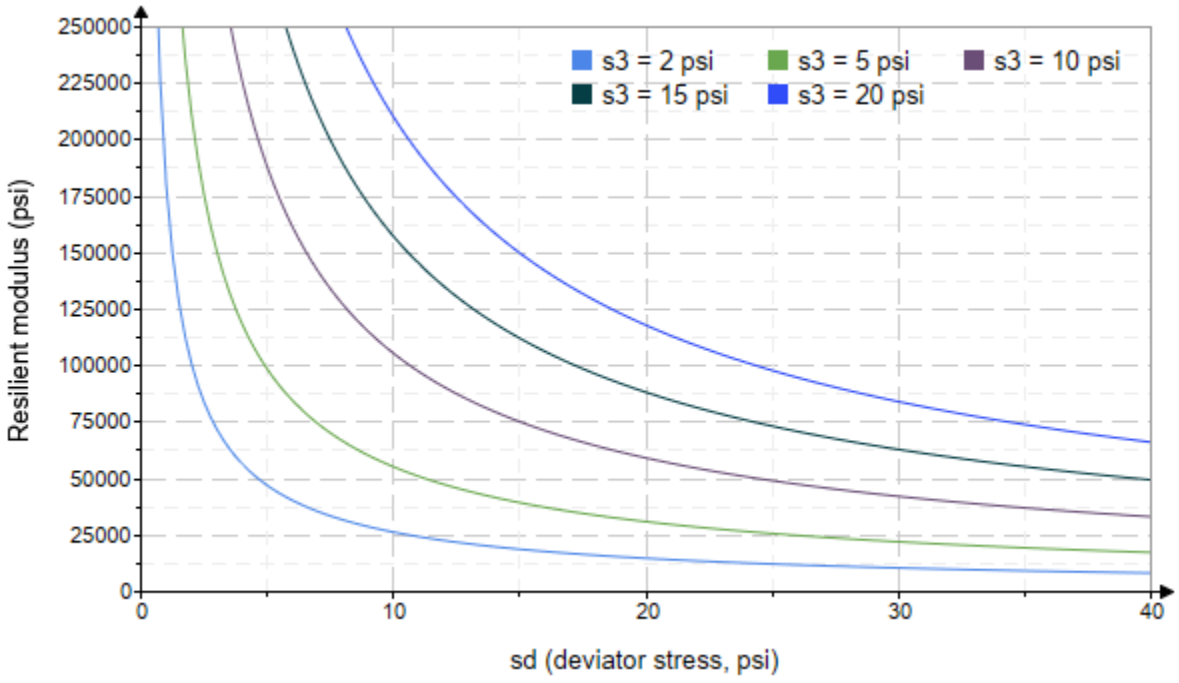

Figure 5. Plot of the fitted Equation 3 model for various confining stresses.

Dan Seely
9/12/2023

$$M_{R.4}\left(\sigma_B,\sigma_d,K_8,K_9,K_{10}\right) := K_8 \cdot p_a \left(\frac{\sigma_B}{p_a}\right)^{K_9} \cdot \left(\frac{\sigma_d}{p_a}\right)^{K_{10}}$$

Equation 4 AASHTO Publication No. FHWA-RD-97-083

$K_8 = 1086.436$

$K_9 = 1.3953$ Equation 4 fitting parameters

$K_{10} = -1.3065$

$R_4^{\,2} = 0.8036$ Coefficient of determination

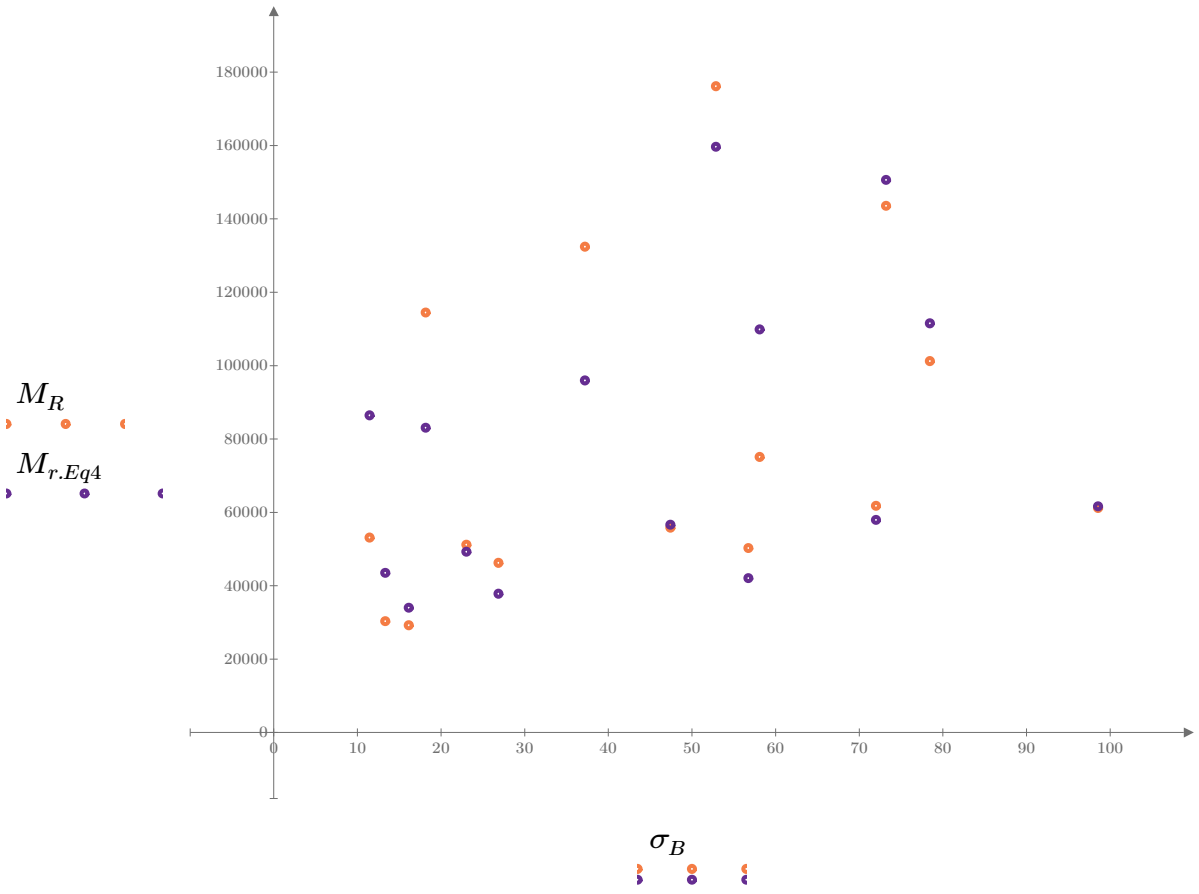

Figure 6. Plot of the test data (orange points) vs. the fitted Equation 4 model (purple points).

Dan Seely
9/12/2023

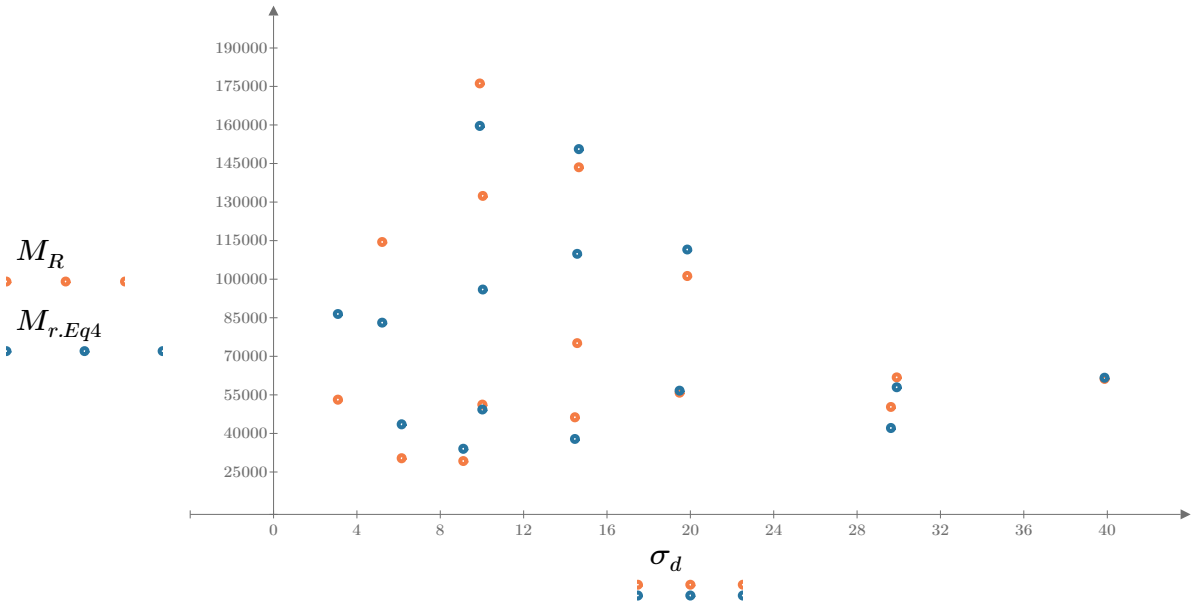

Figure 7. Plot of the test data (orange points) vs. the fitted Equation 4 model (blue points).

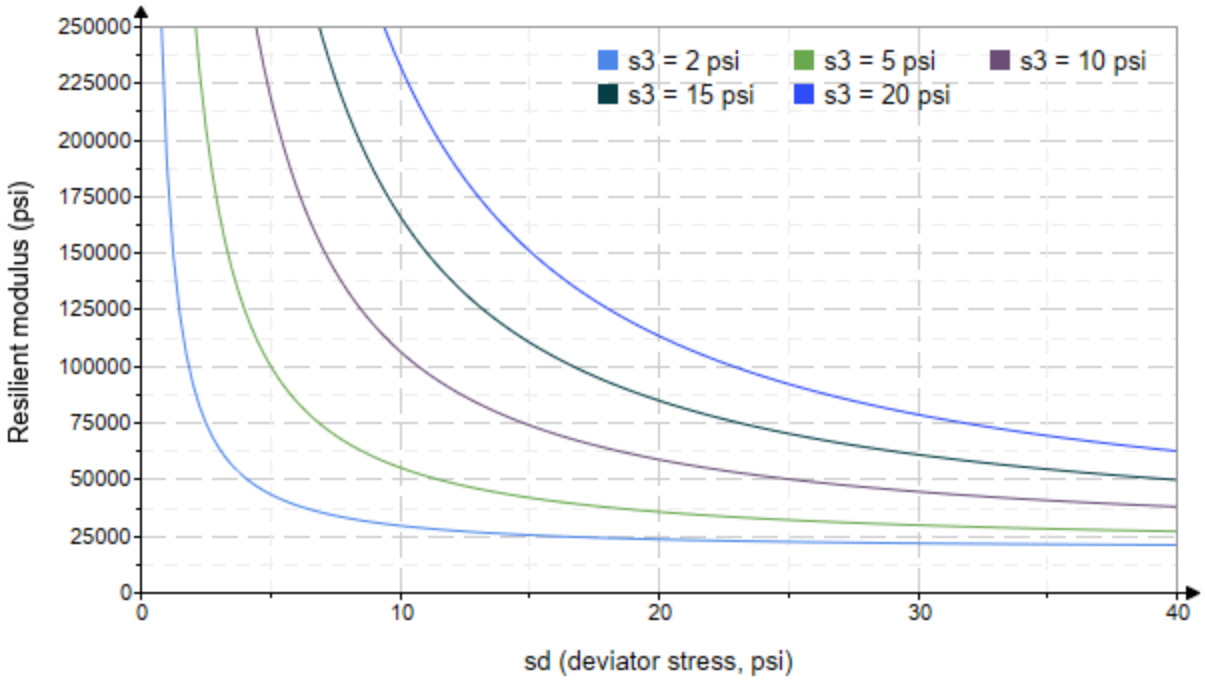

Figure 8. Plot of the fitted Equation 4 model for various confining stresses.

Dan Seely
9/12/2023

$SampleNo := \text{“B2–35”}$

$Treatment = \text{“D1”}$

$S = 15.802$ Degree of Saturation (%)

Test Sequence : Base/Subbase

Test summary data (psi) :

$$\sigma_3 = \begin{bmatrix} 2.886 \\ 2.902 \\ 2.897 \\ 4.607 \\ 4.611 \\ 4.580 \\ 9.628 \\ 9.601 \\ 9.622 \\ 14.630 \\ 14.620 \\ 14.630 \\ 19.640 \\ 19.650 \\ 19.640 \end{bmatrix} \quad \sigma_d = \begin{bmatrix} 3.148 \\ 6.117 \\ 9.080 \\ 5.092 \\ 10.010 \\ 14.550 \\ 9.949 \\ 19.320 \\ 29.370 \\ 10.050 \\ 14.490 \\ 29.550 \\ 14.450 \\ 19.390 \\ 40.130 \end{bmatrix} \quad \sigma_B = \begin{bmatrix} 11.810 \\ 14.820 \\ 17.770 \\ 18.910 \\ 23.840 \\ 28.290 \\ 38.830 \\ 48.120 \\ 58.230 \\ 53.930 \\ 58.360 \\ 73.460 \\ 73.360 \\ 78.350 \\ 99.060 \end{bmatrix} \quad M_R = \begin{bmatrix} 23941.6 \\ 23858.6 \\ 24658.8 \\ 26292.8 \\ 27955.2 \\ 29742.8 \\ 38912.4 \\ 47150.6 \\ 52840.4 \\ 49233.0 \\ 51699.8 \\ 51197.6 \\ 61295.6 \\ 59452.0 \\ 47448.6 \end{bmatrix}$$

σ_3 = mean confining stress
σ_d = mean deviator stress
σ_B = mean bulk stress
M_R = resilient modulus
p_a = atmospheric pressure = 14.6959 psi

Dan Seely
9/12/2023

$$M_{R.1}(\sigma_B, K_1, K_2) := K_1 \cdot {\sigma_B}^{K_2}$$

Equation 1
AASHTO Publication No. FHWA-RD-97-083

$K_1 = 7051.343$

$K_2 = 0.4711$

Equation 1 fitting parameters

${R_1}^2 = 0.8523$

Coefficient of determination

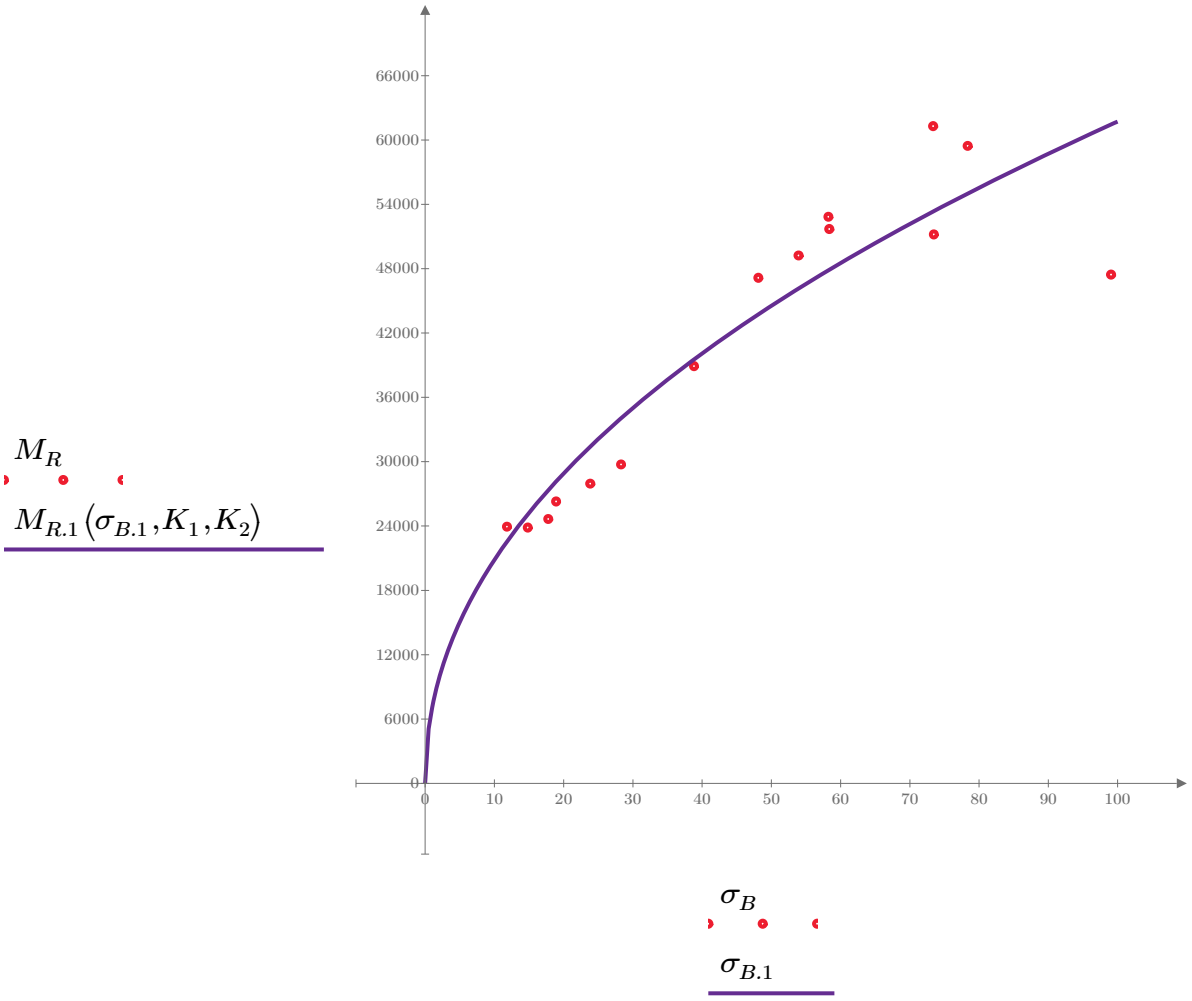

Figure 1. Plot of the test data (red points) vs. the fitted Equation 1 model (purple line).

Dan Seely
9/12/2023

$$M_{R.2}(\sigma_d, K_3, K_4) := K_3 \cdot \sigma_d^{K_4}$$

Equation 2
AASHTO Publication No. FHWA-RD-97-083

$K_3 = 17630.262$

$K_4 = 0.3244$

Equation 2 fitting parameters

$R_2^2 = 0.4829$

Coefficient of determination

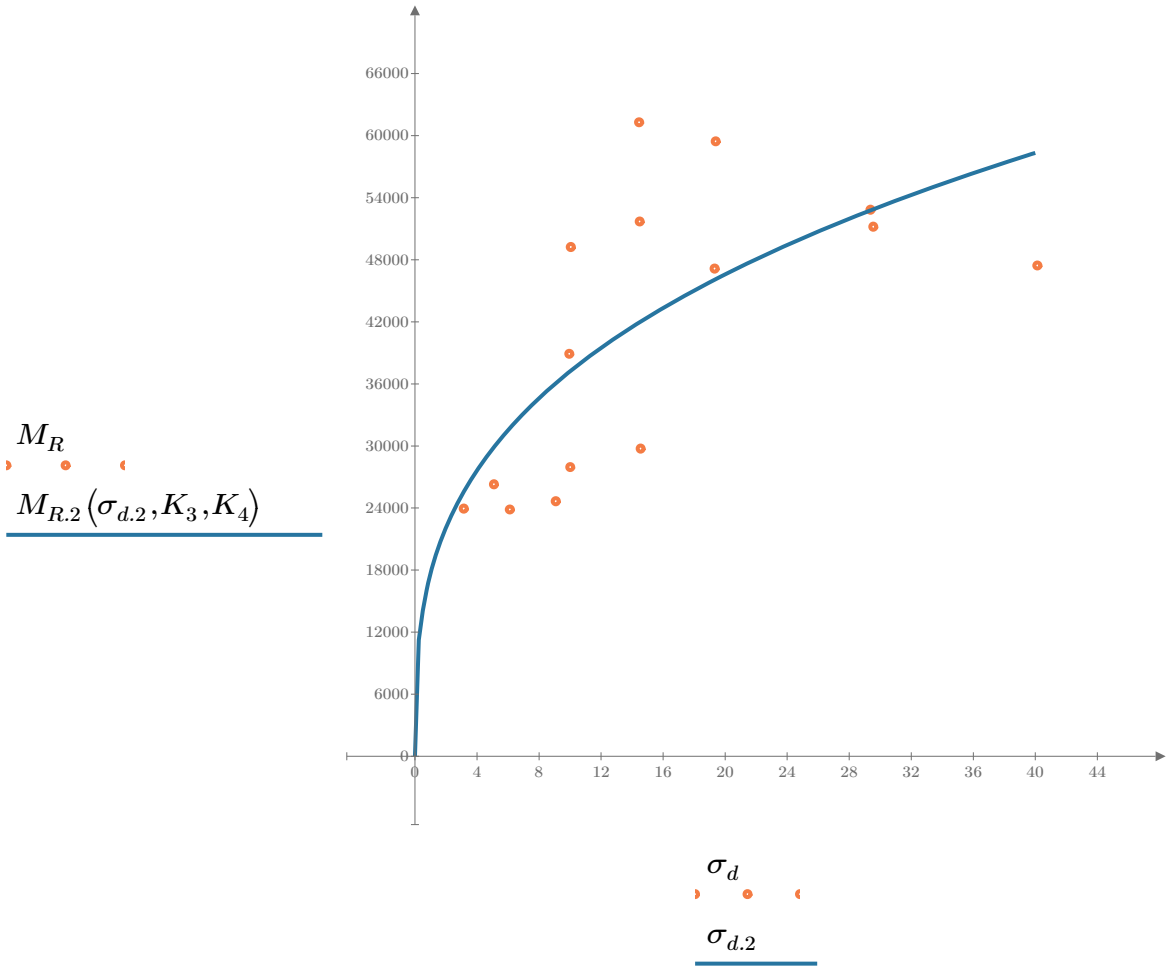

Figure 2. Plot of the test data (orange points) vs. the fitted Equation 2 model (blue line).

Dan Seely
9/12/2023

$$M_{R.3}\left(\sigma_d,\sigma_3,K_5,K_6,K_7\right):=K_5\cdot{\sigma_d}^{K_6}\cdot\left(1+\sigma_3\right)^{K_7}$$

Equation 3 AASHTO Publication No. FHWA-RD-97-083

$K_5=12560.402$

$K_6=0.0215$ Equation 3 fitting parameters

$K_7=0.4831$

${R_3}^2=0.8807$ Coefficient of determination

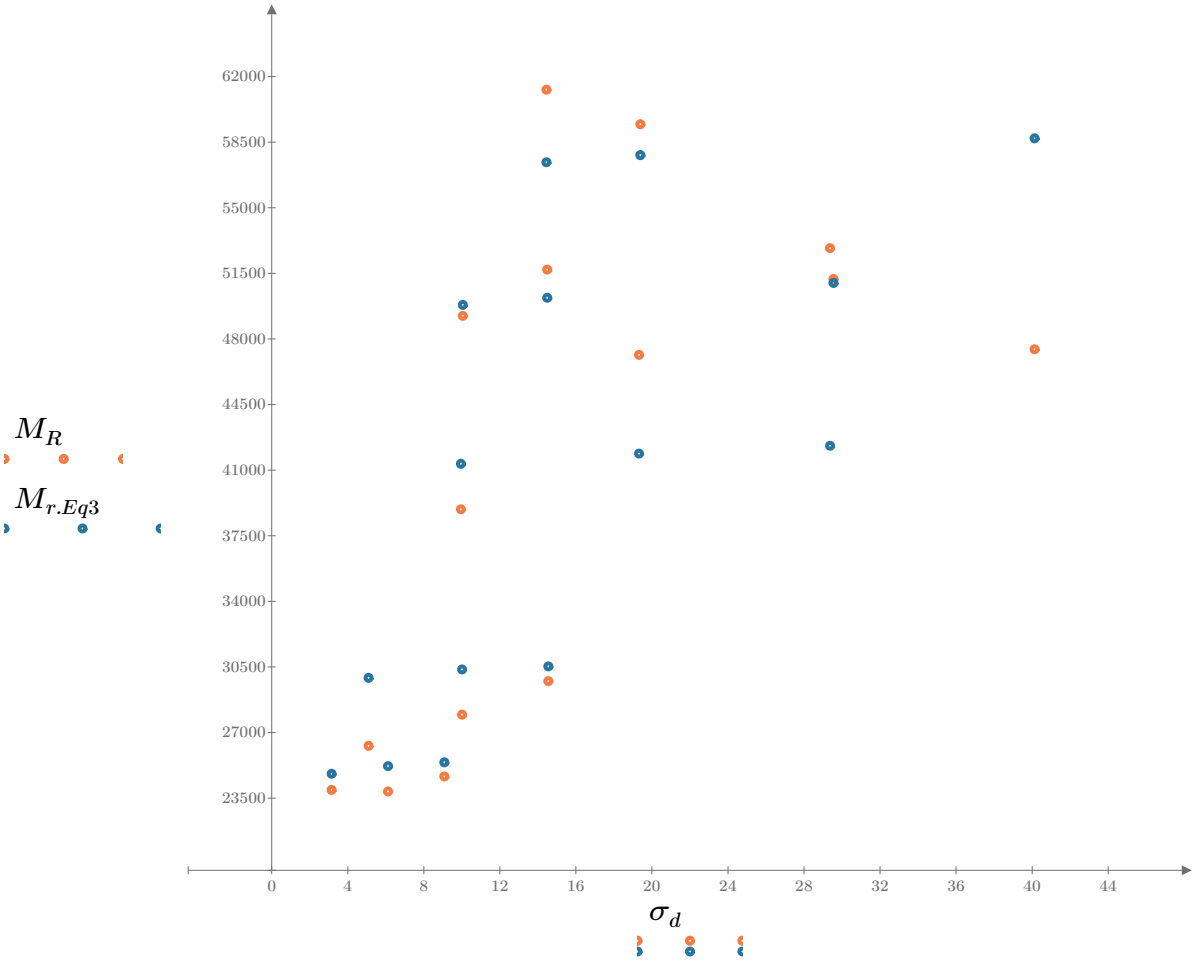

Figure 3. Plot of the test data (orange points) vs. the fitted Equation 3 model (blue points).

Dan Seely
9/12/2023

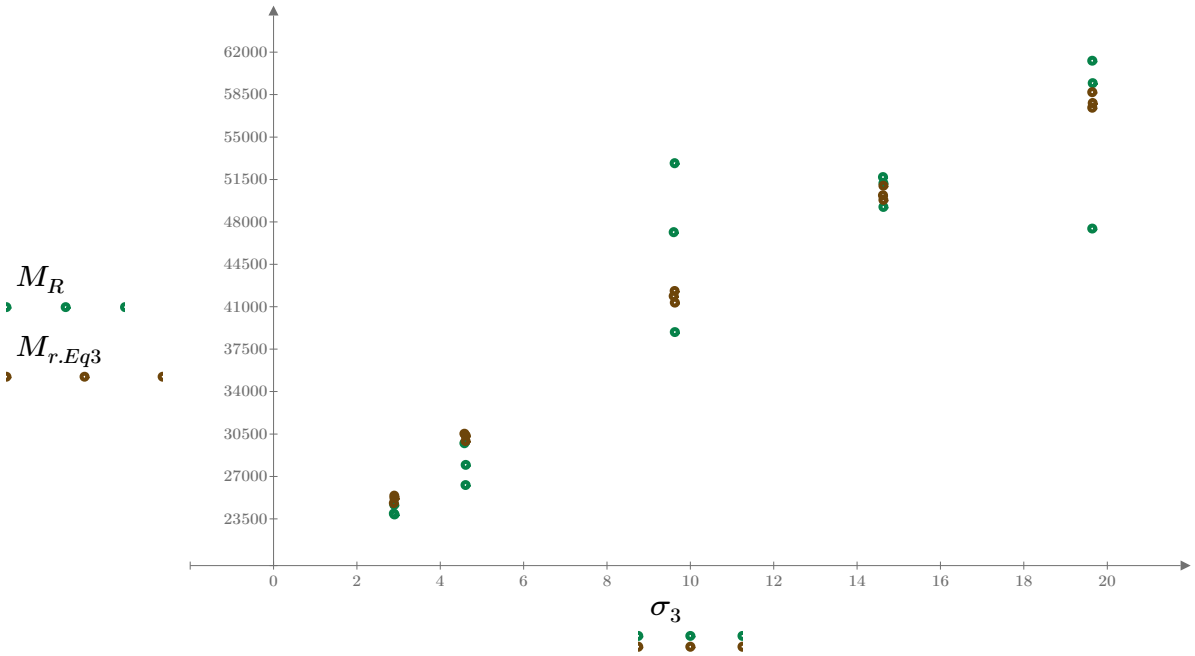

Figure 4. Plot of the test data (green points) vs. the fitted Equation 3 model (brown points).

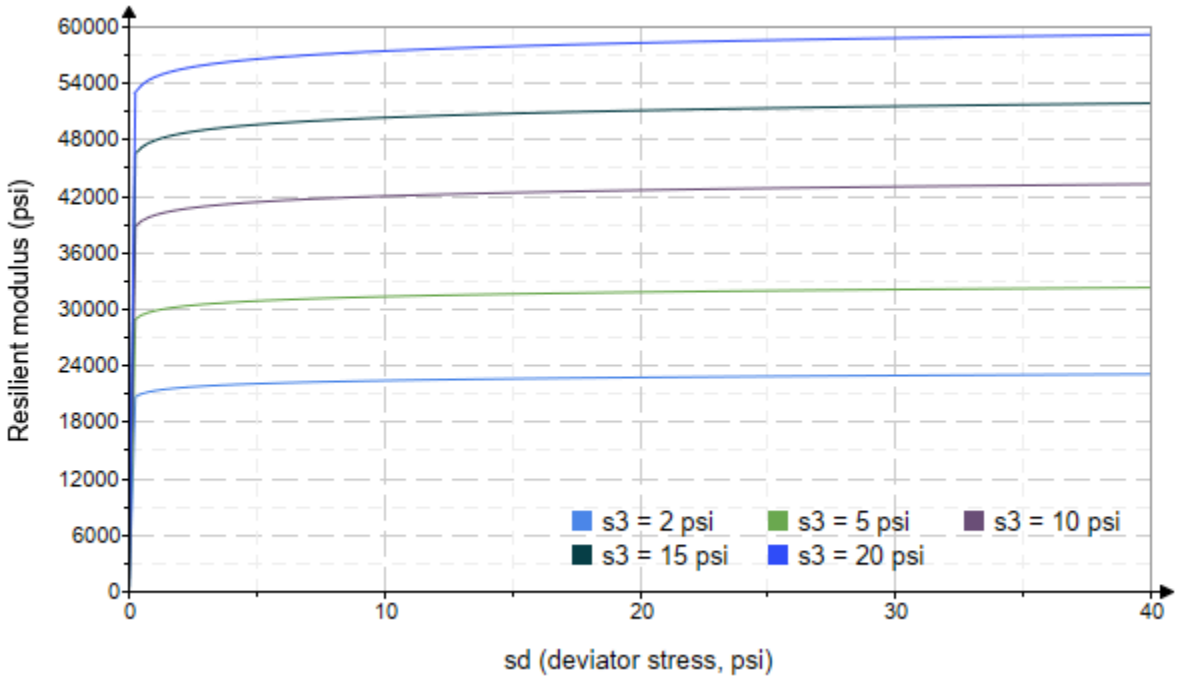

Figure 5. Plot of the fitted Equation 3 model for various confining stresses.

Dan Seely
9/12/2023

$$M_{R.4}\left(\sigma_B,\sigma_d,K_8,K_9,K_{10}\right) := K_8 \cdot p_a \left(\frac{\sigma_B}{p_a}\right)^{K_9} \cdot \left(\frac{\sigma_d}{p_a}\right)^{K_{10}}$$

Equation 4 AASHTO Publication No. FHWA-RD-97-083

$K_8 = 1385.842$

$K_9 = 0.6509$ Equation 4 fitting parameters

$K_{10} = -0.1958$

$R_4^{\,2} = 0.8977$ Coefficient of determination

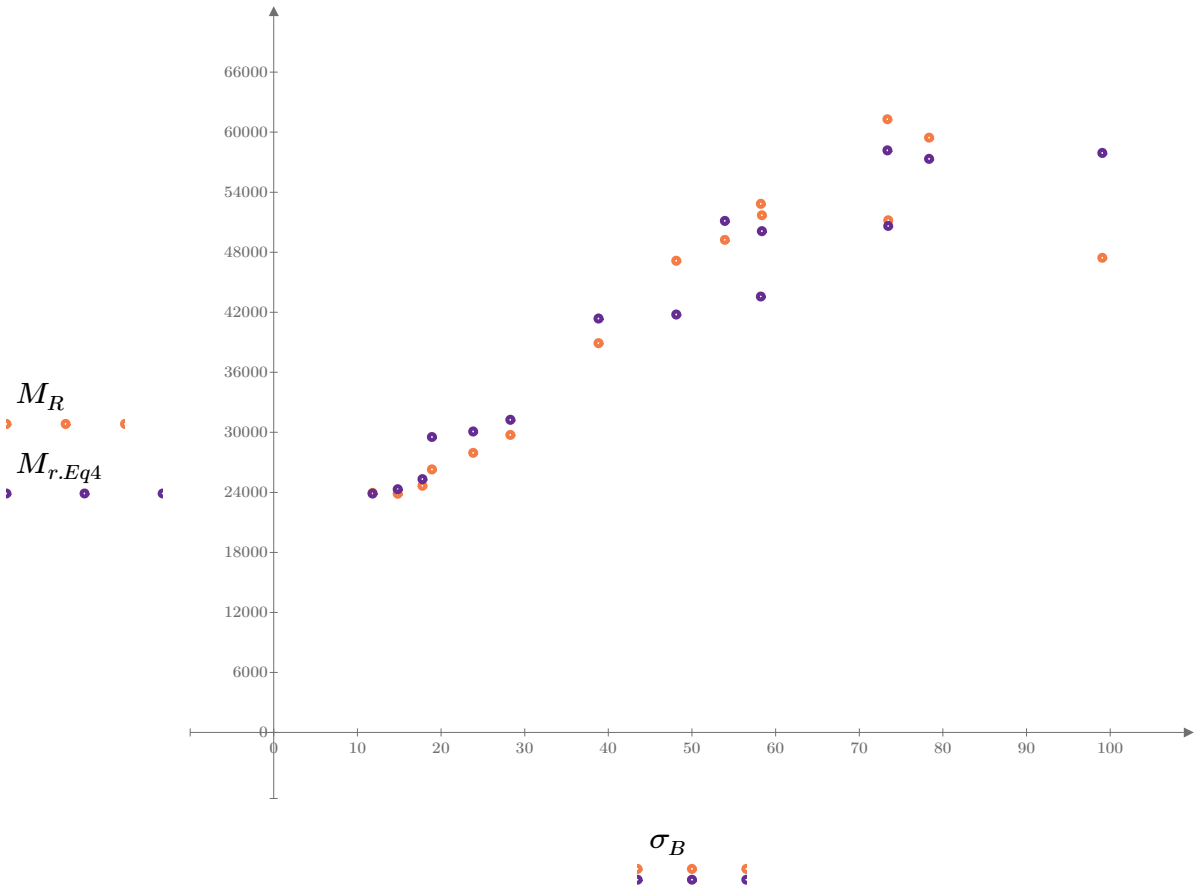

Figure 6. Plot of the test data (orange points) vs. the fitted Equation 4 model (purple points).

Dan Seely
9/12/2023

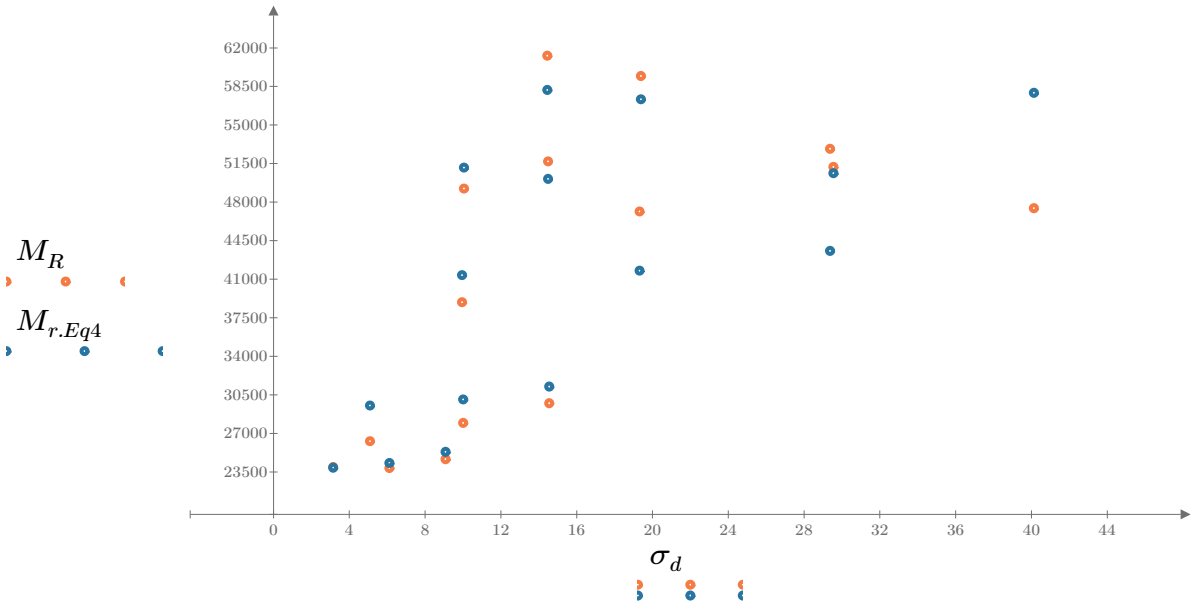

Figure 7. Plot of the test data (orange points) vs. the fitted Equation 4 model (blue points).

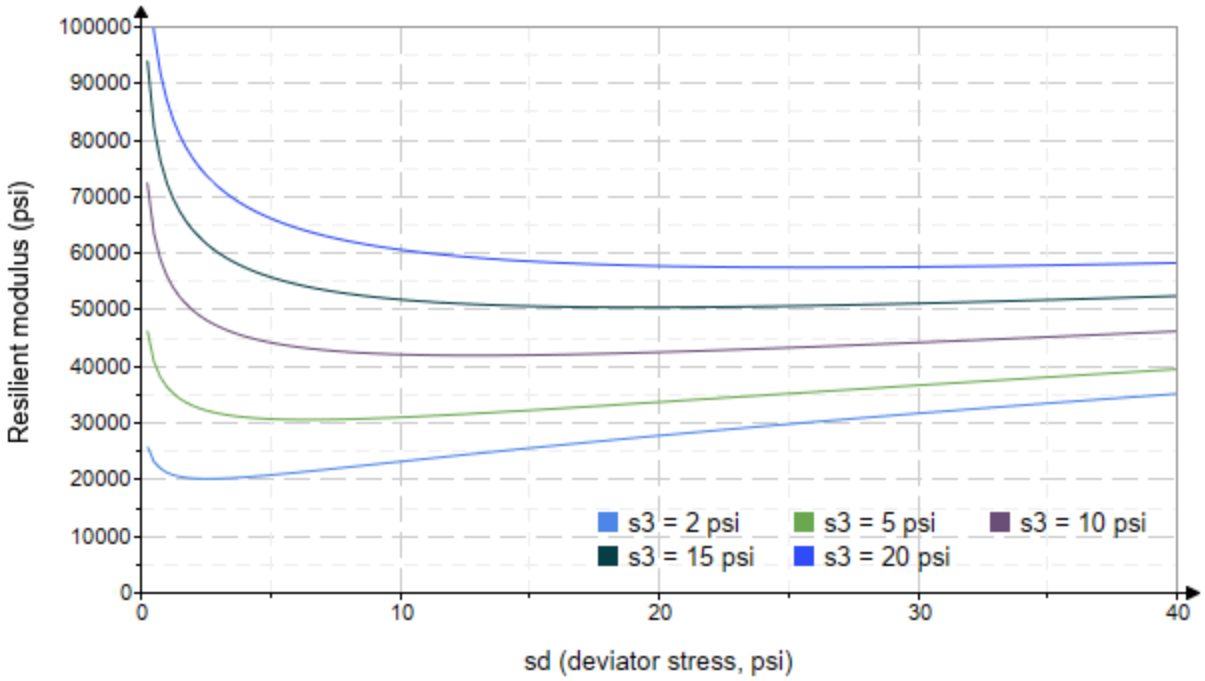

Figure 8. Plot of the fitted Equation 4 model for various confining stresses.

Dan Seely
9/12/2023

$SampleNo := \text{“B2–36”}$

$Treatment = \text{“D1”}$

$S = 17.123$ Degree of Saturation (%)

Test Sequence : Base/Subbase

Test summary data (psi) :

$$\sigma_3 = \begin{bmatrix} 2.840 \\ 2.829 \\ 2.828 \\ 4.574 \\ 4.581 \\ 4.609 \\ 9.589 \\ 9.644 \\ 9.616 \\ 14.670 \\ 14.680 \\ 14.640 \\ 19.700 \\ 19.670 \\ 19.650 \end{bmatrix} \quad \sigma_d = \begin{bmatrix} 3.178 \\ 6.179 \\ 8.988 \\ 5.163 \\ 9.838 \\ 14.270 \\ 9.813 \\ 19.280 \\ 29.650 \\ 9.849 \\ 14.340 \\ 29.830 \\ 14.400 \\ 19.560 \\ 40.120 \end{bmatrix} \quad \sigma_B = \begin{bmatrix} 11.700 \\ 14.670 \\ 17.470 \\ 18.880 \\ 23.580 \\ 28.100 \\ 38.580 \\ 48.210 \\ 58.500 \\ 53.870 \\ 58.390 \\ 73.740 \\ 73.500 \\ 78.570 \\ 99.060 \end{bmatrix} \quad M_R = \begin{bmatrix} 24082.6 \\ 22891.6 \\ 25137.2 \\ 23149.0 \\ 28131.8 \\ 30553.0 \\ 38791.0 \\ 51580.2 \\ 56467.0 \\ 59020.0 \\ 54669.4 \\ 56509.0 \\ 57530.6 \\ 64036.4 \\ 56569.6 \end{bmatrix}$$

σ_3 = mean confining stress
σ_d = mean deviator stress
σ_B = mean bulk stress
M_R = resilient modulus
p_a = atmospheric pressure = 14.6959 psi

Dan Seely
9/12/2023

$$M_{R.1}(\sigma_B, K_1, K_2) := K_1 \cdot {\sigma_B}^{K_2}$$

Equation 1
AASHTO Publication No. FHWA-RD-97-083

$K_1 = 5904.861$

$K_2 = 0.5313$

Equation 1 fitting parameters

${R_1}^2 = 0.8923$

Coefficient of determination

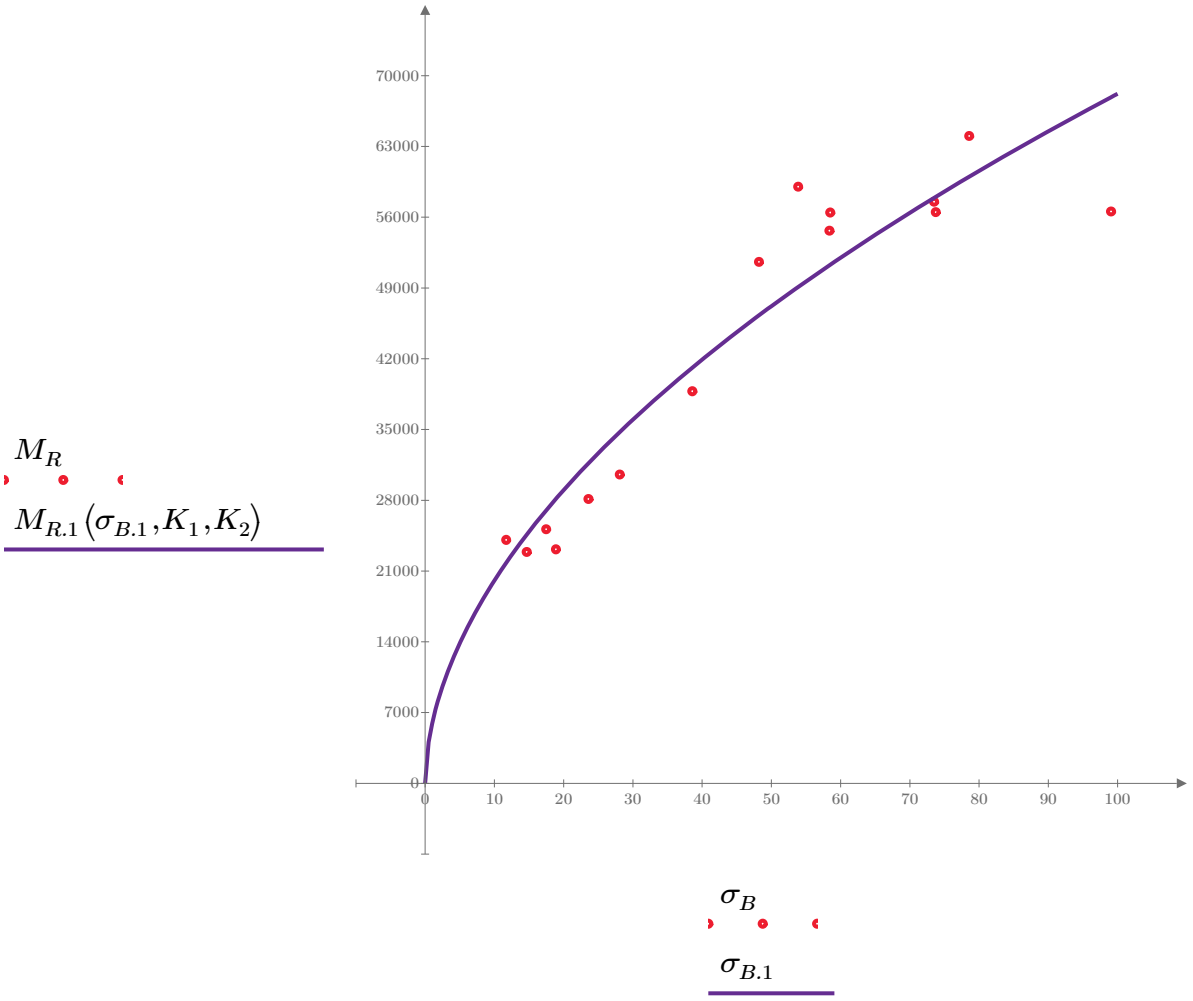

Figure 1. Plot of the test data (red points) vs. the fitted Equation 1 model (purple line).

Dan Seely
9/12/2023

$$M_{R.2}(\sigma_d, K_3, K_4) := K_3 \cdot \sigma_d^{K_4}$$

Equation 2
AASHTO Publication No. FHWA-RD-97-083

$K_3 = 15823.649$

$K_4 = 0.3847$

Equation 2 fitting parameters

$R_2^2 = 0.5579$

Coefficient of determination

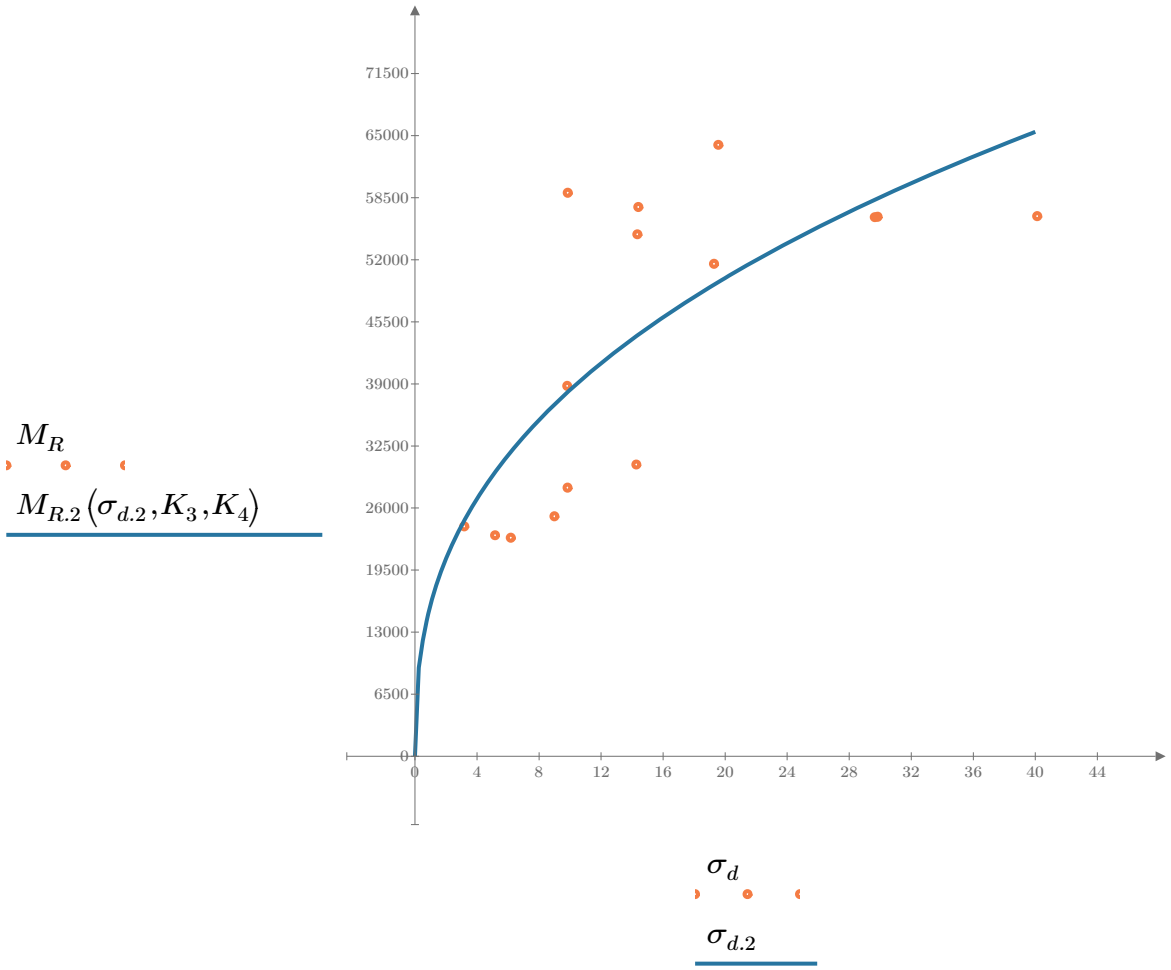

Figure 2. Plot of the test data (orange points) vs. the fitted Equation 2 model (blue line).

Dan Seely
9/12/2023

$$M_{R.3}\left(\sigma_d,\sigma_3,K_5,K_6,K_7\right):=K_5\cdot{\sigma_d}^{K_6}\cdot\left(1+\sigma_3\right)^{K_7}$$

Equation 3 AASHTO Publication No. FHWA-RD-97-083

$K_5=11191.382$

$K_6=0.0829$ Equation 3 fitting parameters

$K_7=0.485$

${R_3}^2=0.8949$ Coefficient of determination

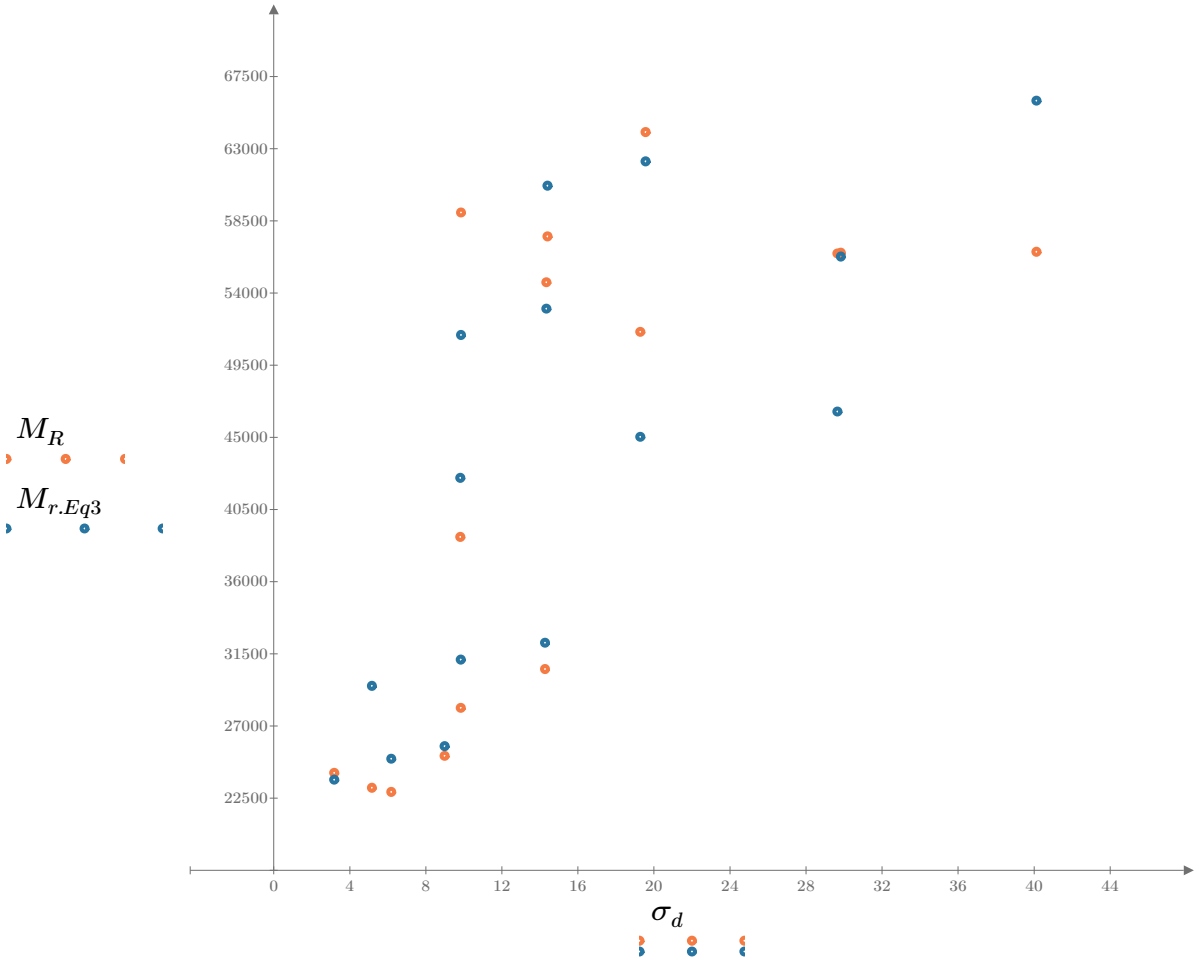

Figure 3. Plot of the test data (orange points) vs. the fitted Equation 3 model (blue points).

Dan Seely
9/12/2023

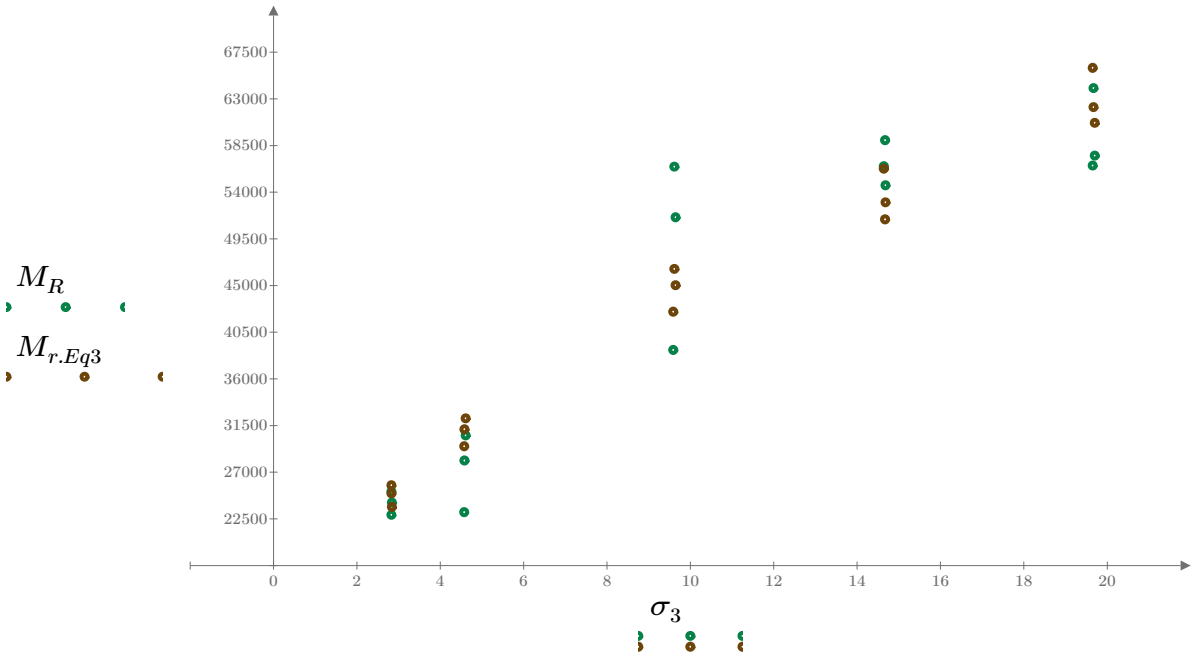

Figure 4. Plot of the test data (green points) vs. the fitted Equation 3 model (brown points).

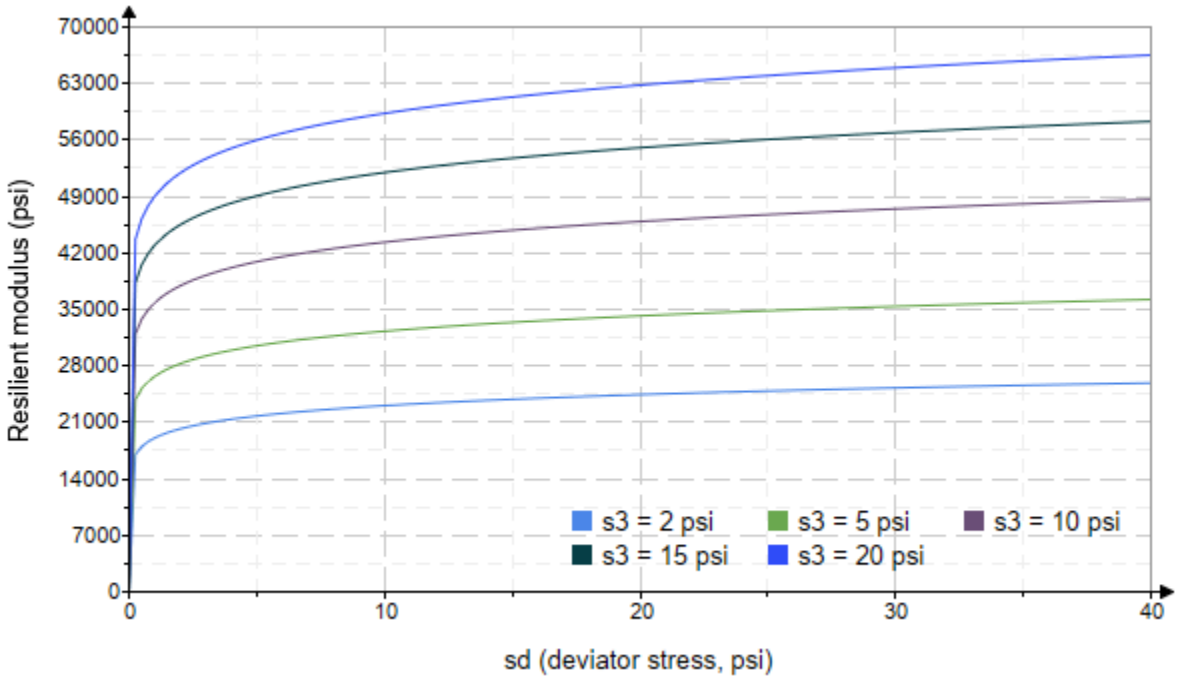

Figure 5. Plot of the fitted Equation 3 model for various confining stresses.

Dan Seely
9/12/2023

$$M_{R.4}\left(\sigma_B,\sigma_d,K_8,K_9,K_{10}\right) := K_8 \cdot p_a \left(\frac{\sigma_B}{p_a}\right)^{K_9} \cdot \left(\frac{\sigma_d}{p_a}\right)^{K_{10}}$$

Equation 4 AASHTO Publication No. FHWA-RD-97-083

$K_8 = 1453.508$

$K_9 = 0.6560$ Equation 4 fitting parameters

$K_{10} = -0.1362$

$R_4^{\,2} = 0.9110$ Coefficient of determination

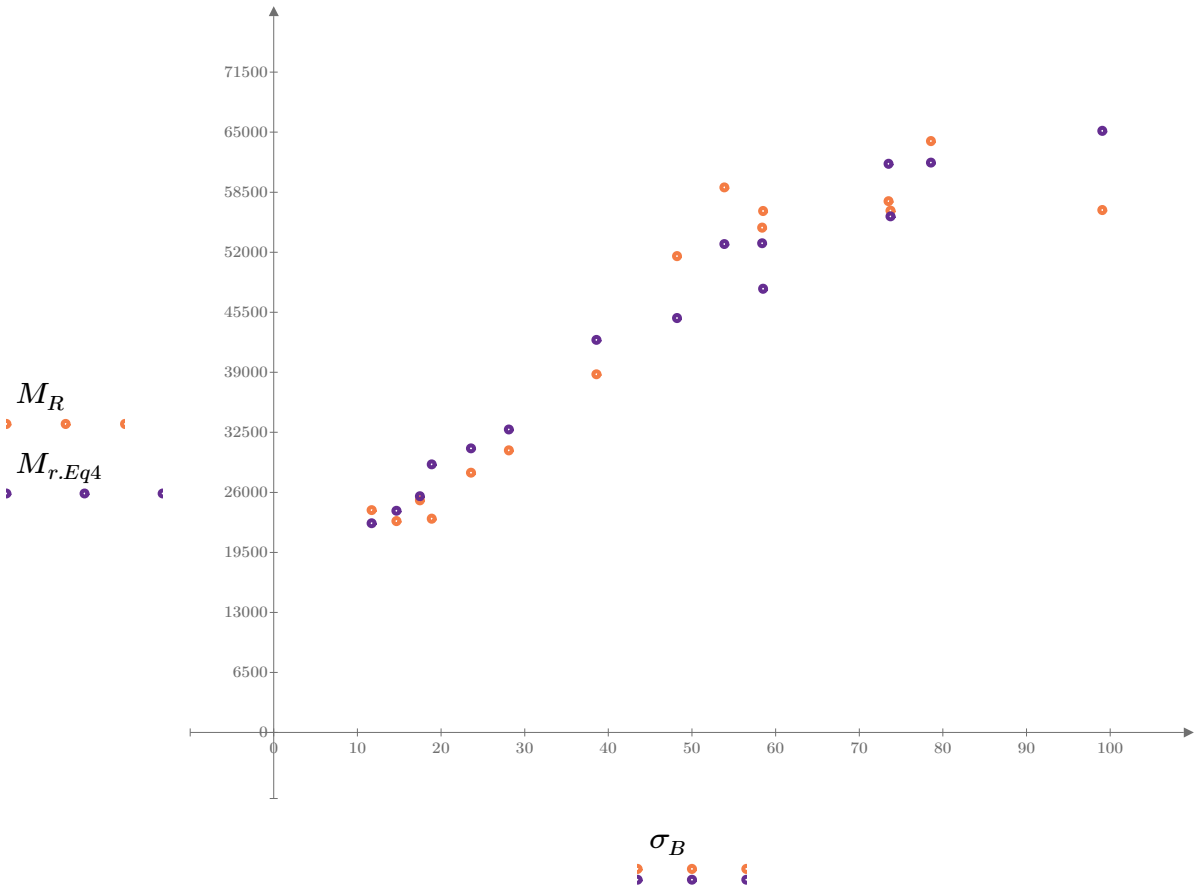

Figure 6. Plot of the test data (orange points) vs. the fitted Equation 4 model (purple points).

Dan Seely
9/12/2023

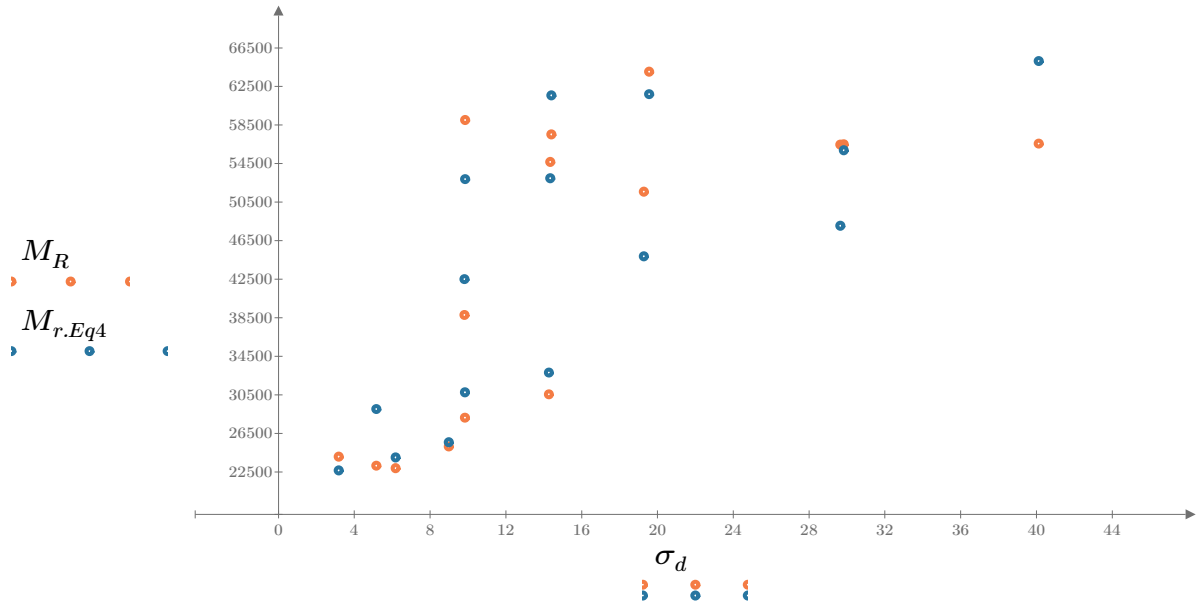

Figure 7. Plot of the test data (orange points) vs. the fitted Equation 4 model (blue points).

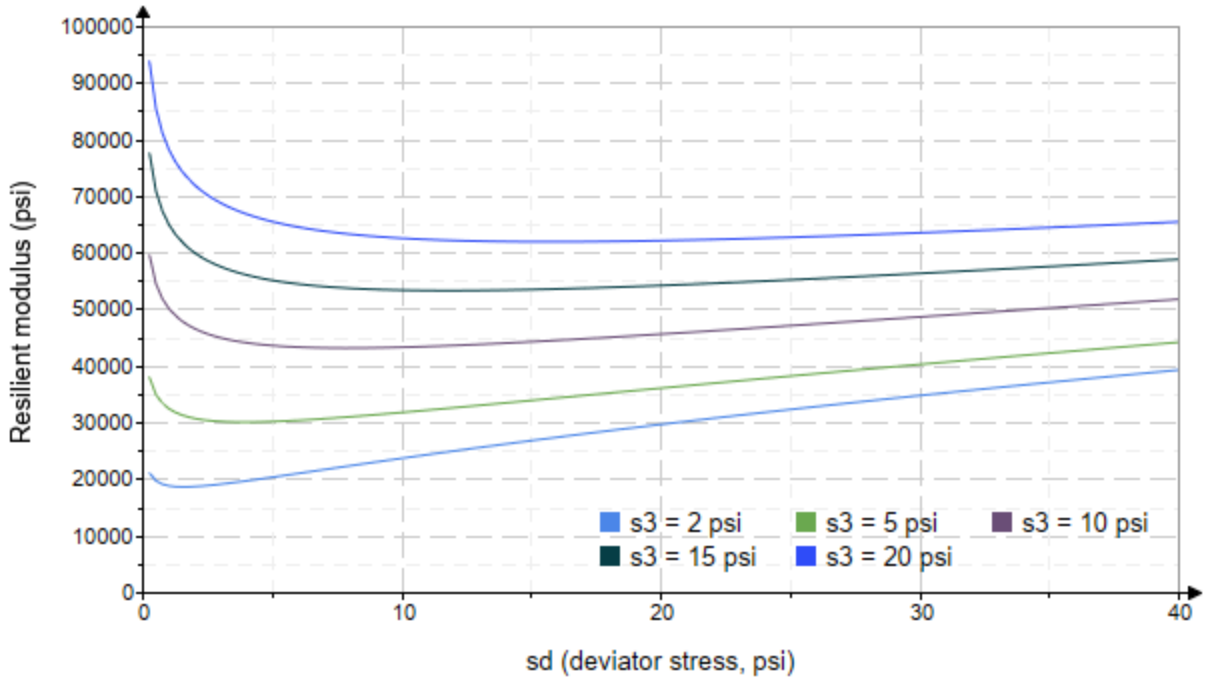

Figure 8. Plot of the fitted Equation 4 model for various confining stresses.

Dan Seely
9/12/2023

$SampleNo := \text{“B2–37”}$

$Treatment = \text{“W1”}$

$S = 17.531$ Degree of Saturation (%)

Test Sequence : Base/Subbase

Test summary data (psi) :

$$\sigma_3 = \begin{bmatrix} 2.819 \\ 2.804 \\ 2.740 \\ 4.739 \\ 4.683 \\ 4.642 \\ 9.646 \\ 9.699 \\ 9.704 \\ 14.660 \\ 14.680 \\ 14.720 \\ 19.720 \\ 19.740 \\ 19.670 \end{bmatrix} \quad \sigma_d = \begin{bmatrix} 3.230 \\ 6.150 \\ 9.163 \\ 5.108 \\ 10.130 \\ 14.630 \\ 10.250 \\ 19.370 \\ 29.450 \\ 10.310 \\ 14.460 \\ 29.660 \\ 14.580 \\ 19.400 \\ 40.280 \end{bmatrix} \quad \sigma_B = \begin{bmatrix} 11.690 \\ 14.560 \\ 17.380 \\ 19.330 \\ 24.180 \\ 28.550 \\ 39.190 \\ 48.470 \\ 58.560 \\ 54.290 \\ 58.490 \\ 73.810 \\ 73.730 \\ 78.620 \\ 99.300 \end{bmatrix} \quad M_R = \begin{bmatrix} 22305.4 \\ 23671.0 \\ 25384.6 \\ 29025.6 \\ 31966.0 \\ 36158.0 \\ 49020.0 \\ 55733.4 \\ 57378.6 \\ 54382.6 \\ 62882.2 \\ 63626.0 \\ 61899.6 \\ 65816.4 \\ 70515.0 \end{bmatrix}$$

σ_3 = mean confining stress
σ_d = mean deviator stress
σ_B = mean bulk stress
M_R = resilient modulus
p_a = atmospheric pressure = 14.6959 psi

Dan Seely
9/12/2023

$$M_{R.1}\left(\sigma_B, K_1, K_2\right) := K_1 \cdot {\sigma_B}^{K_2}$$

Equation 1
AASHTO Publication No. FHWA-RD-97-083

$K_1 = 5812.098$

$K_2 = 0.5577$

Equation 1 fitting parameters

${R_1}^2 = 0.9662$

Coefficient of determination

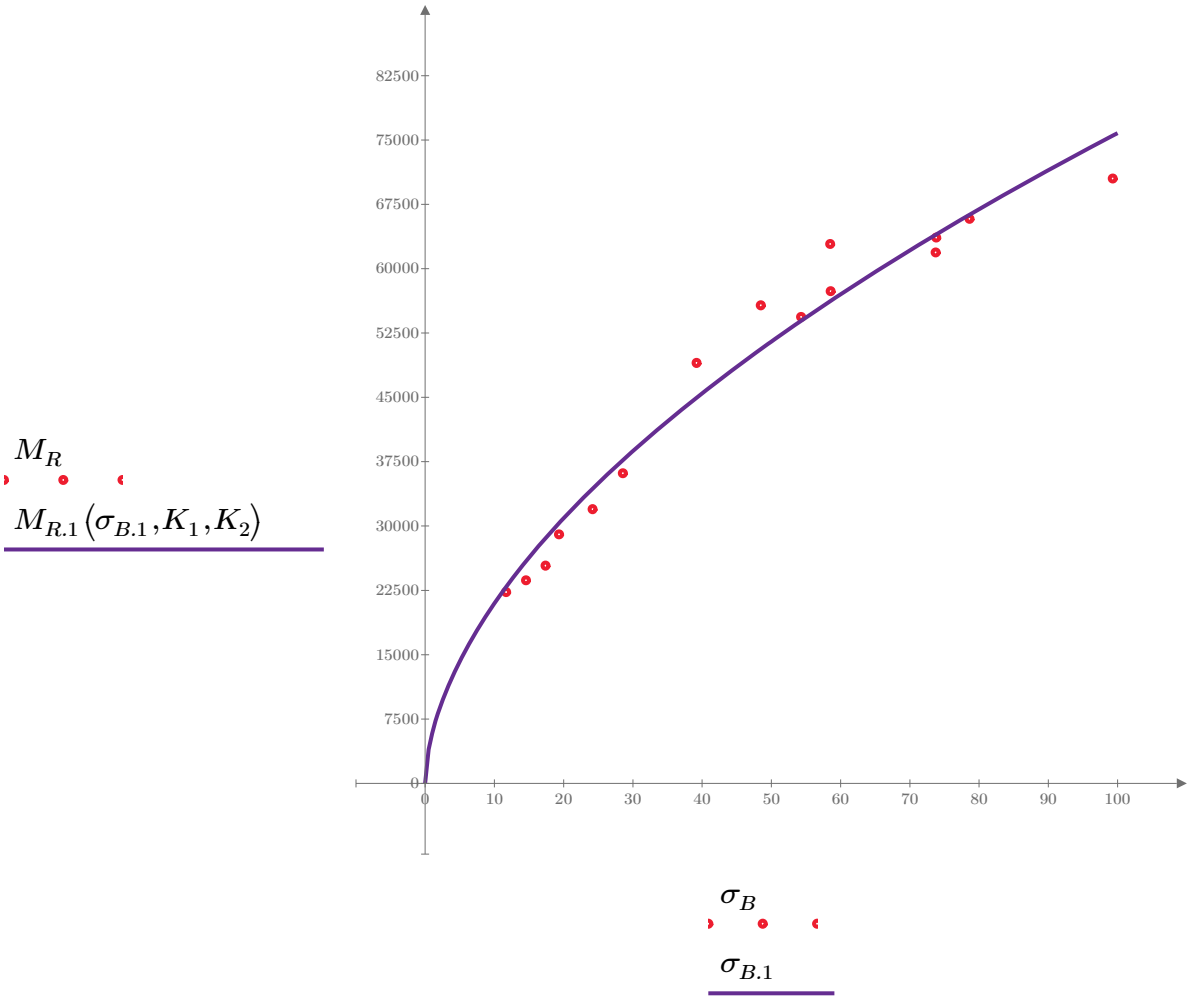

Figure 1. Plot of the test data (red points) vs. the fitted Equation 1 model (purple line).

Dan Seely
9/12/2023

$$M_{R.2}(\sigma_d, K_3, K_4) := K_3 \cdot \sigma_d^{K_4}$$

Equation 2
AASHTO Publication No. FHWA-RD-97-083

$K_3 = 15313.772$

$K_4 = 0.4281$

Equation 2 fitting parameters

$R_2^2 = 0.6723$

Coefficient of determination

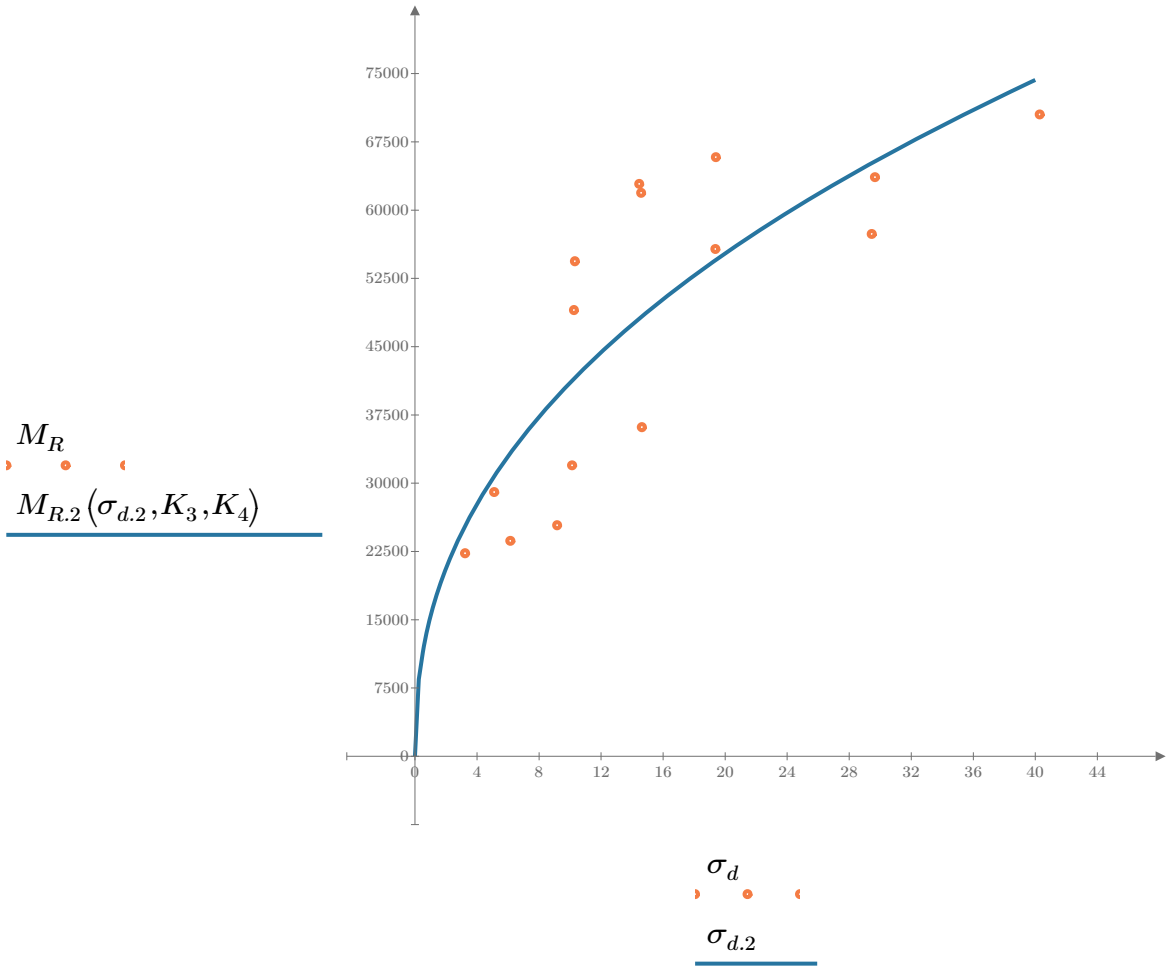

Figure 2. Plot of the test data (orange points) vs. the fitted Equation 2 model (blue line).

Dan Seely
9/12/2023

$$M_{R.3}\left(\sigma_d,\sigma_3,K_5,K_6,K_7\right):=K_5\cdot{\sigma_d}^{K_6}\cdot\left(1+\sigma_3\right)^{K_7}$$

Equation 3 AASHTO Publication No. FHWA-RD-97-083

$K_5=11083.875$

$K_6=0.1549$ Equation 3 fitting parameters

$K_7=0.4442$

${R_3}^2=0.9637$ Coefficient of determination

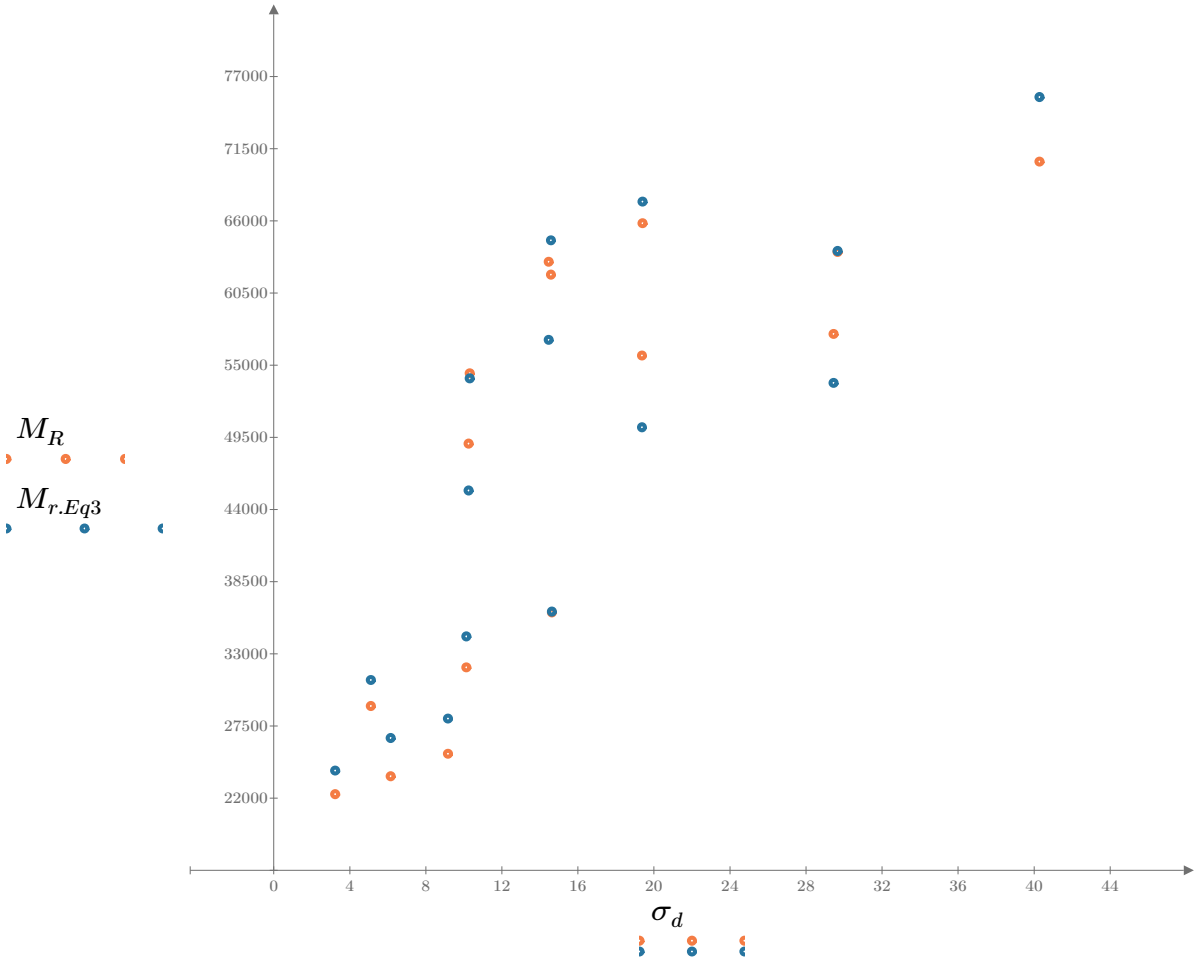

Figure 3. Plot of the test data (orange points) vs. the fitted Equation 3 model (blue points).

Dan Seely
9/12/2023

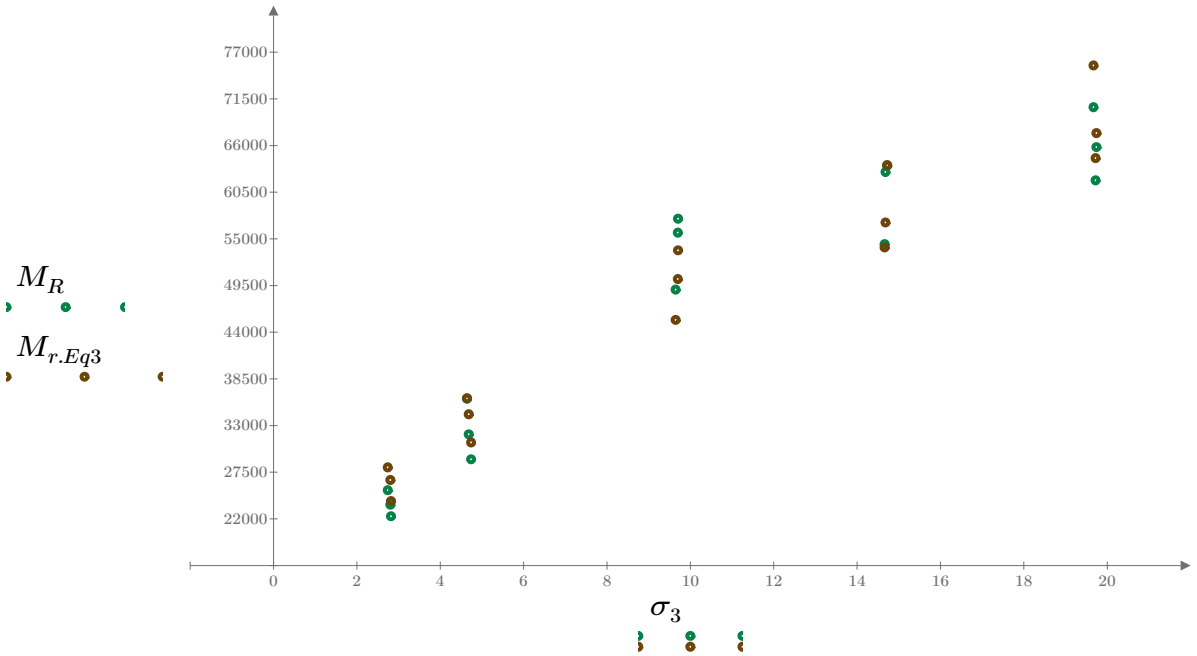

Figure 4. Plot of the test data (green points) vs. the fitted Equation 3 model (brown points).

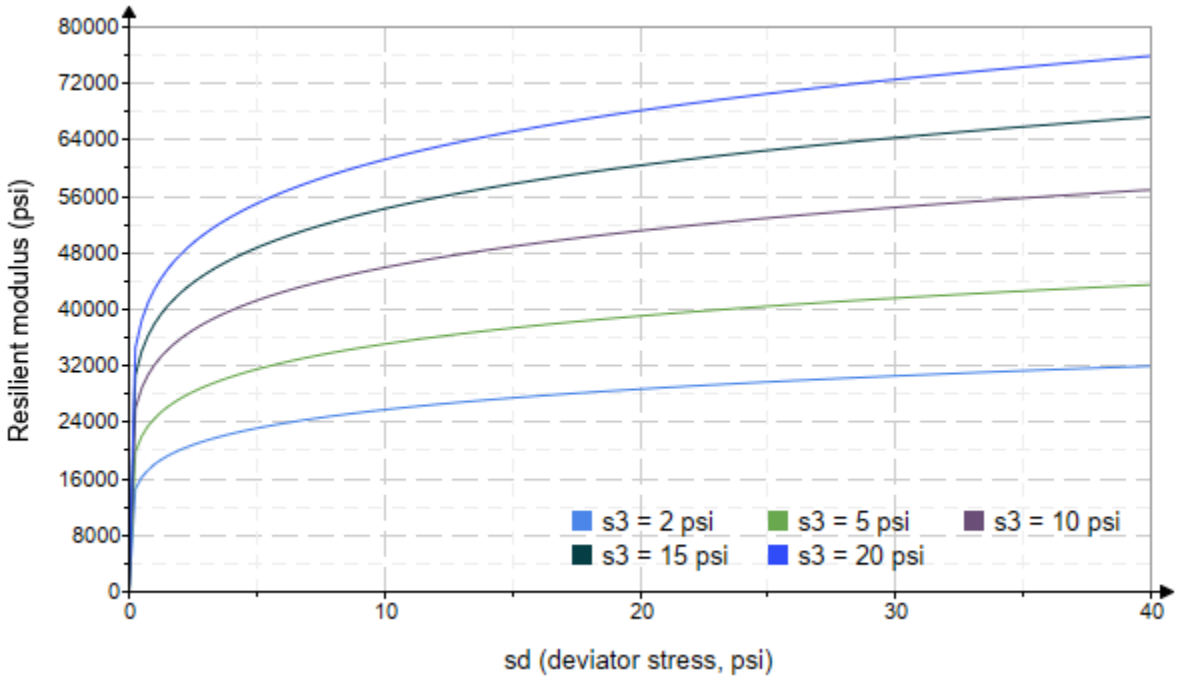

Figure 5. Plot of the fitted Equation 3 model for various confining stresses.

Dan Seely
9/12/2023

$$M_{R.4}\left(\sigma_B,\sigma_d,K_8,K_9,K_{10}\right) := K_8 \cdot p_a \left(\frac{\sigma_B}{p_a}\right)^{K_9} \cdot \left(\frac{\sigma_d}{p_a}\right)^{K_{10}}$$

Equation 4 AASHTO Publication No. FHWA-RD-97-083

$K_8 = 1694.787$

$K_9 = 0.5965$ Equation 4 fitting parameters

$K_{10} = -0.0429$

$R_4^{\,2} = 0.9681$ Coefficient of determination

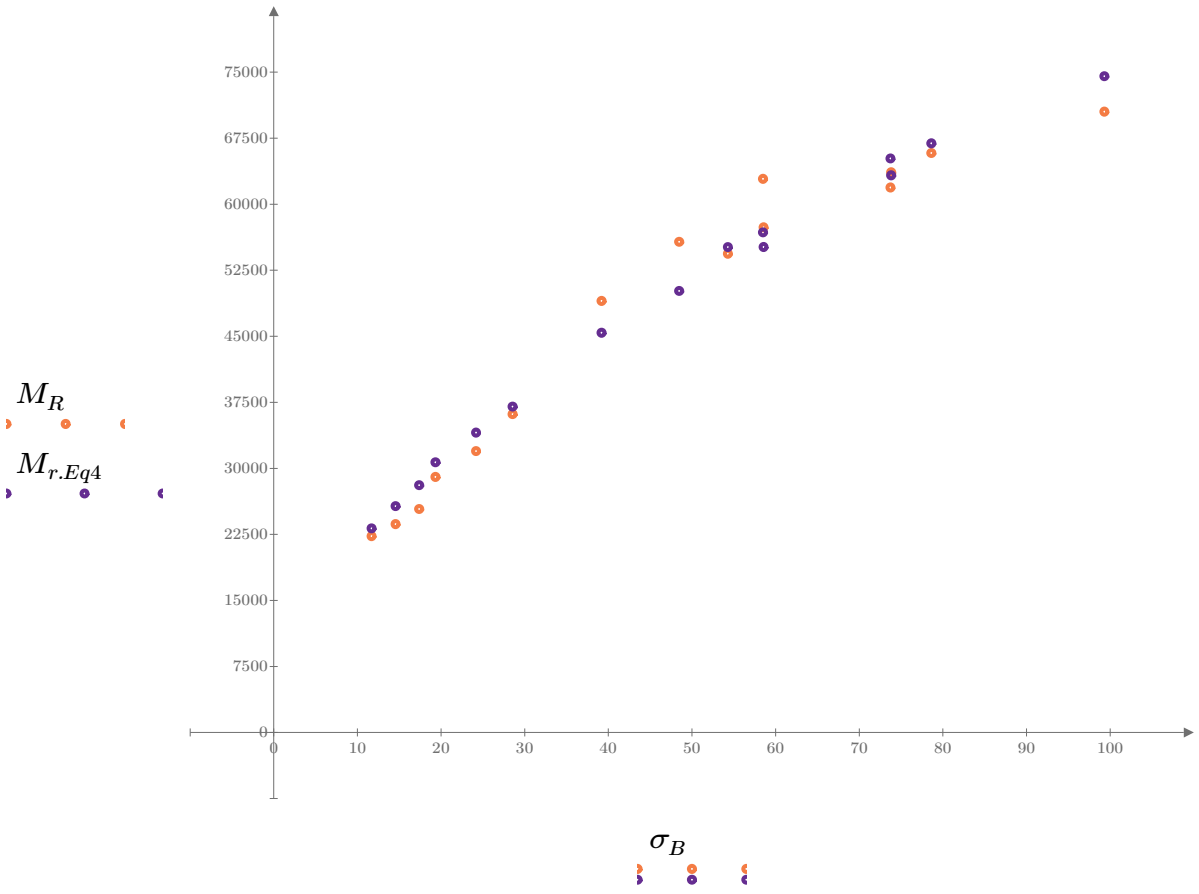

Figure 6. Plot of the test data (orange points) vs. the fitted Equation 4 model (purple points).

Dan Seely
9/12/2023

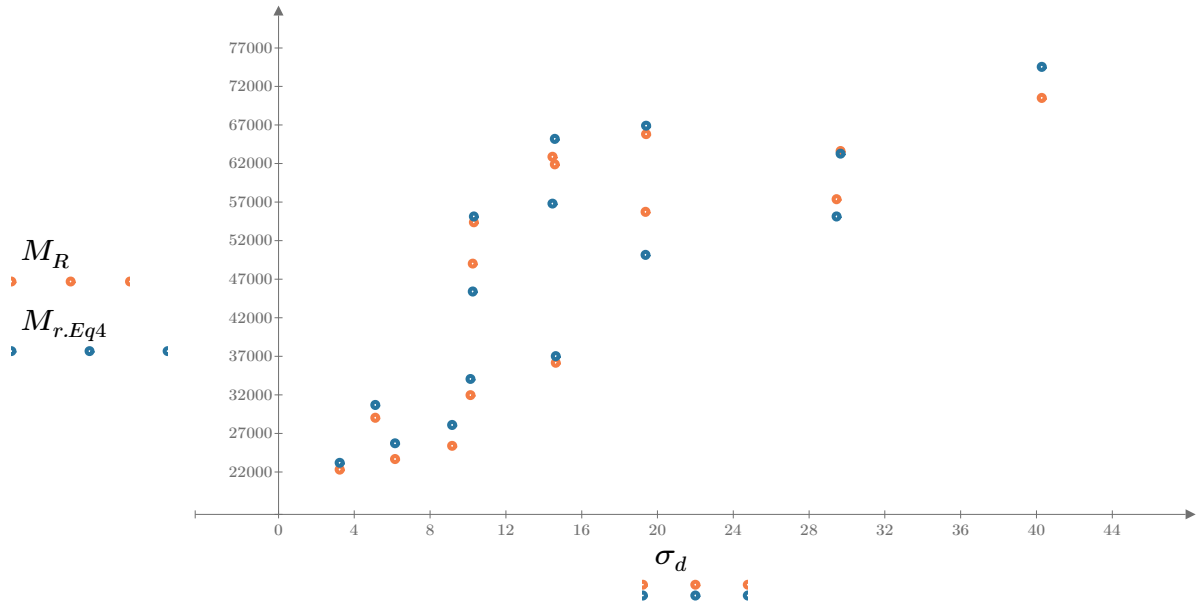

Figure 7. Plot of the test data (orange points) vs. the fitted Equation 4 model (blue points).

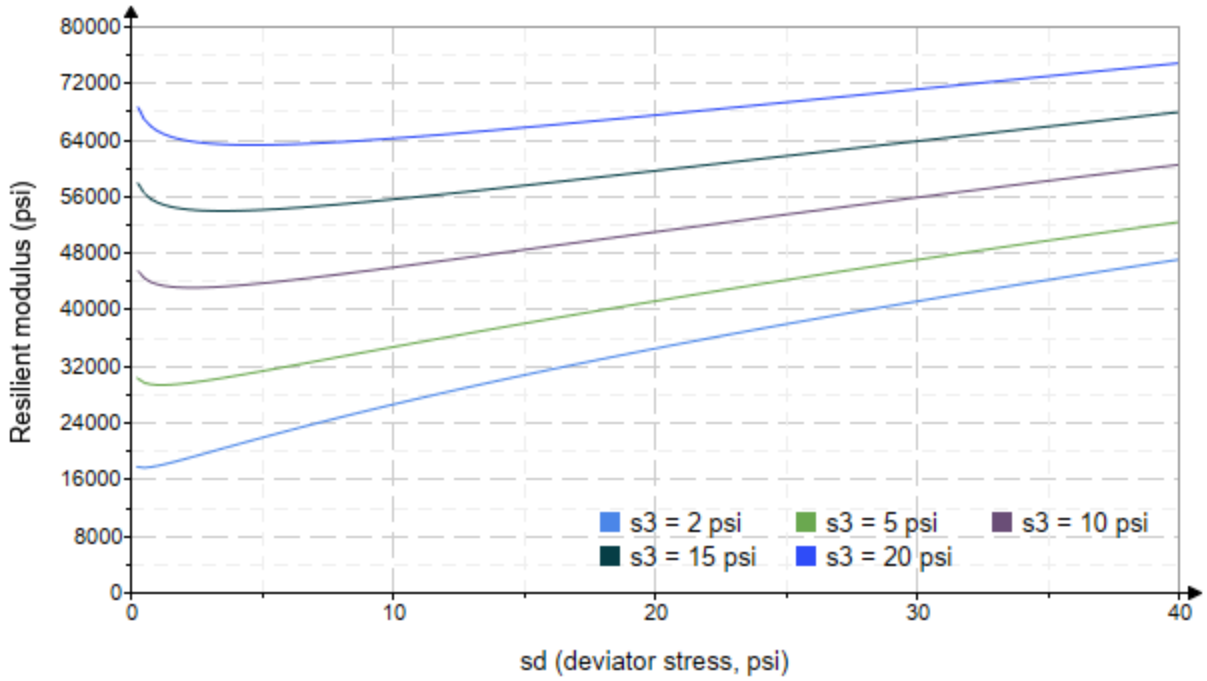

Figure 8. Plot of the fitted Equation 4 model for various confining stresses.

Dan Seely
9/12/2023

$SampleNo := \text{“B2–38”}$

$Treatment = \text{“W1”}$

$S = 18.374$ Degree of Saturation (%)

Test Sequence : Base/Subbase

Test summary data (psi) :

$$\sigma_3 = \begin{bmatrix} 1.757 \\ 2.213 \\ 2.196 \\ 3.518 \\ 3.460 \\ 4.310 \\ 9.280 \\ 9.032 \\ 8.727 \\ 14.560 \\ 14.140 \\ 13.600 \\ 19.030 \\ 18.520 \\ 18.570 \end{bmatrix} \quad \sigma_d = \begin{bmatrix} 3.498 \\ 6.077 \\ 8.966 \\ 5.330 \\ 9.951 \\ 14.440 \\ 10.010 \\ 19.400 \\ 29.460 \\ 10.370 \\ 14.340 \\ 29.670 \\ 14.430 \\ 19.660 \\ 39.980 \end{bmatrix} \quad \sigma_B = \begin{bmatrix} 8.768 \\ 12.720 \\ 15.550 \\ 15.880 \\ 20.330 \\ 27.370 \\ 37.850 \\ 46.500 \\ 55.640 \\ 54.050 \\ 56.750 \\ 70.460 \\ 71.530 \\ 75.230 \\ 95.680 \end{bmatrix} \quad M_R = \begin{bmatrix} 298838.0 \\ 73173.0 \\ 57382.6 \\ 266094.0 \\ 83559.2 \\ 48422.0 \\ 168572.0 \\ 64701.2 \\ 61450.6 \\ 228946.0 \\ 152390.0 \\ 87443.2 \\ 244658.0 \\ 157838.0 \\ 88756.0 \end{bmatrix}$$

σ_3 = mean confining stress
σ_d = mean deviator stress
σ_B = mean bulk stress
M_R = resilient modulus
p_a = atmospheric pressure = 14.6959 psi

Dan Seely
9/12/2023

$$M_{R.1}(\sigma_B, K_1, K_2) := K_1 \cdot {\sigma_B}^{K_2}$$

Equation 1
AASHTO Publication No. FHWA-RD-97-083

$K_1 = 237914.005$

$K_2 = -0.1532$

Equation 1 fitting parameters

${R_1}^2 = 0.0308$

Coefficient of determination

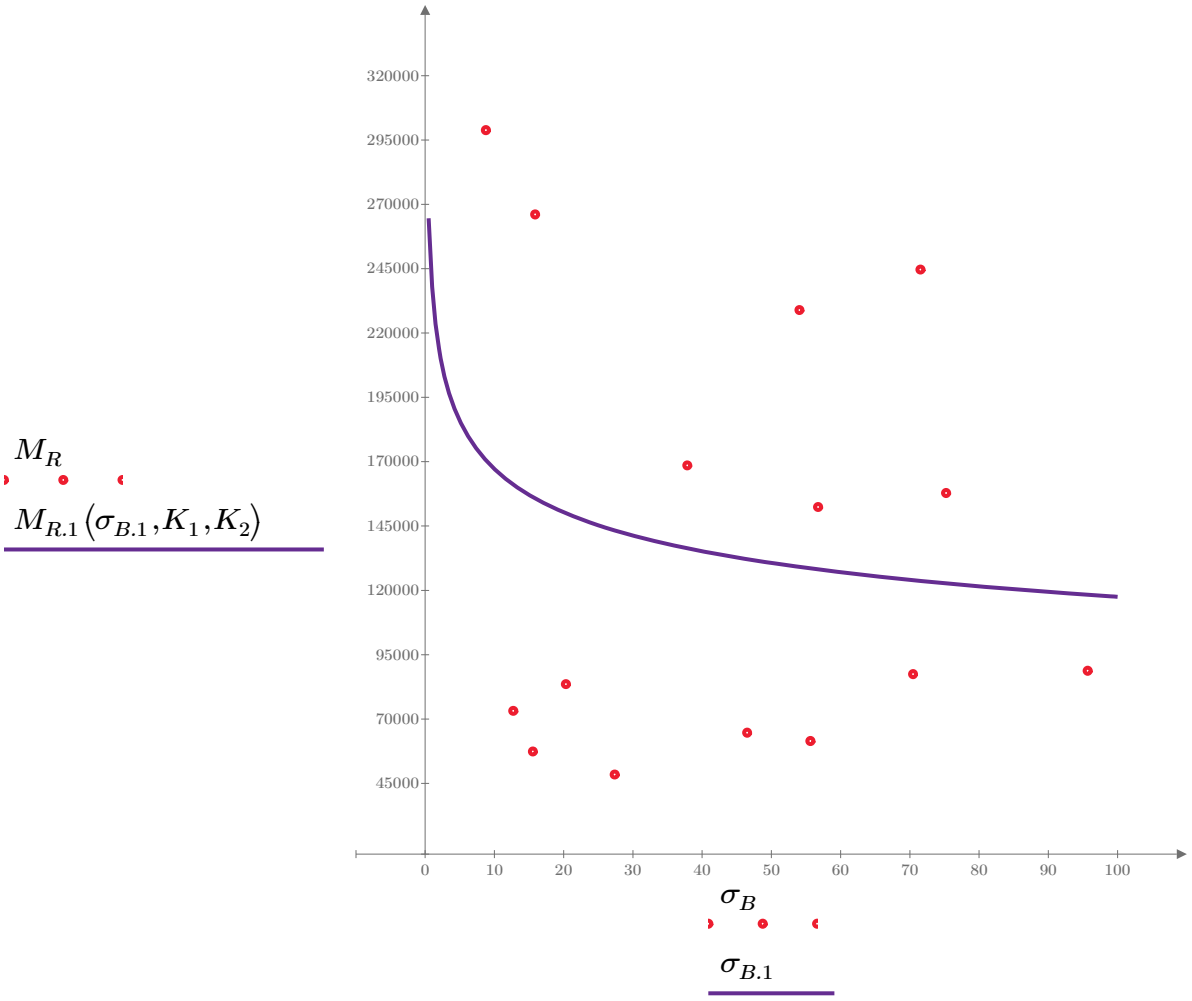

Figure 1. Plot of the test data (red points) vs. the fitted Equation 1 model (purple line).

Dan Seely
9/12/2023

$$M_{R.2}(\sigma_d, K_3, K_4) := K_3 \cdot \sigma_d^{K_4}$$

Equation 2
AASHTO Publication No. FHWA-RD-97-083

$K_3 = 504209.829$

$K_4 = -0.5315$

Equation 2 fitting parameters

$R_2^2 = 0.3326$

Coefficient of determination

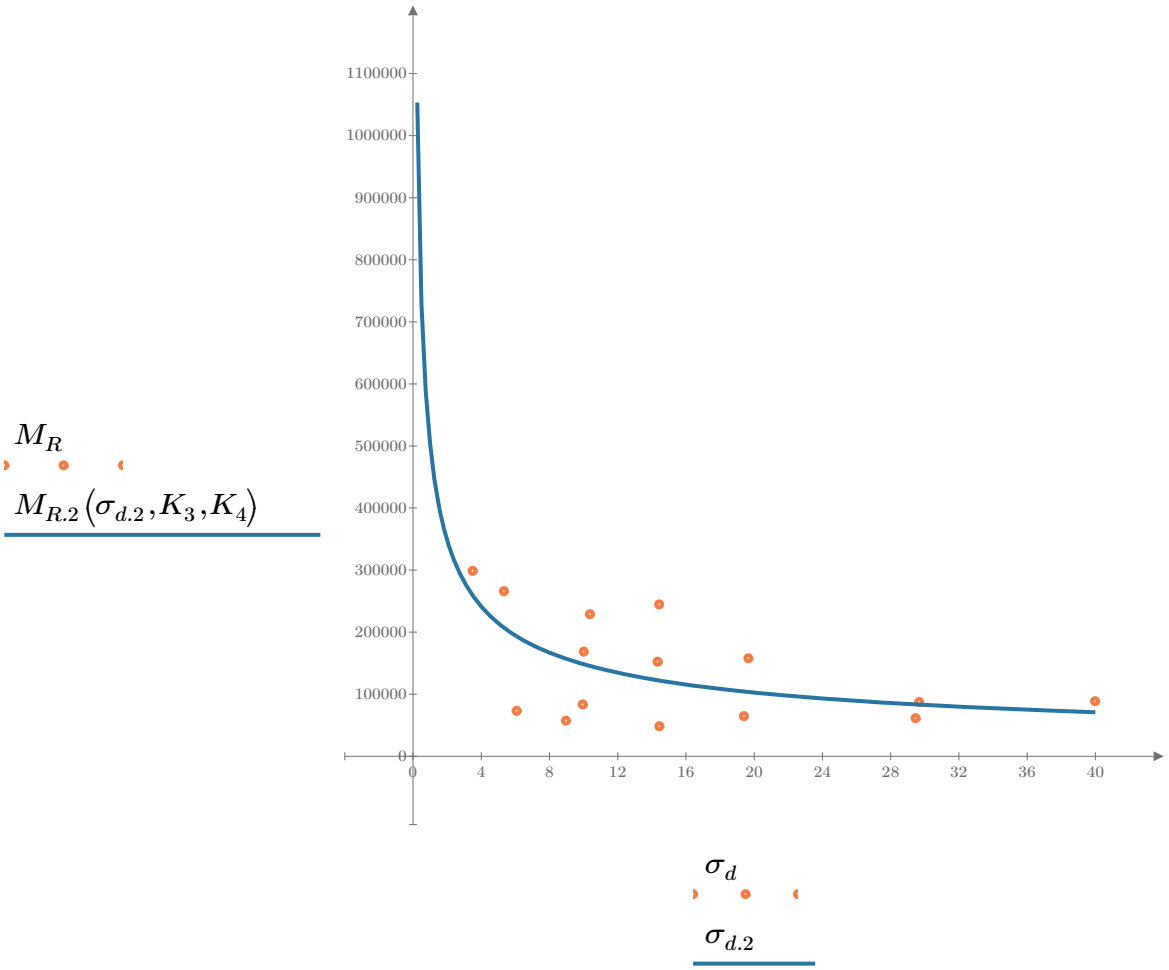

Figure 2. Plot of the test data (orange points) vs. the fitted Equation 2 model (blue line).

Dan Seely
9/12/2023

$$M_{R.3}\left(\sigma_d,\sigma_3,K_5,K_6,K_7\right):=K_5\cdot{\sigma_d}^{K_6}\cdot\left(1+\sigma_3\right)^{K_7}$$

Equation 3 AASHTO Publication No. FHWA-RD-97-083

$K_5=659695.937$

$K_6=-1.4553$ Equation 3 fitting parameters

$K_7=0.9155$

${R_3}^2=0.8536$ Coefficient of determination

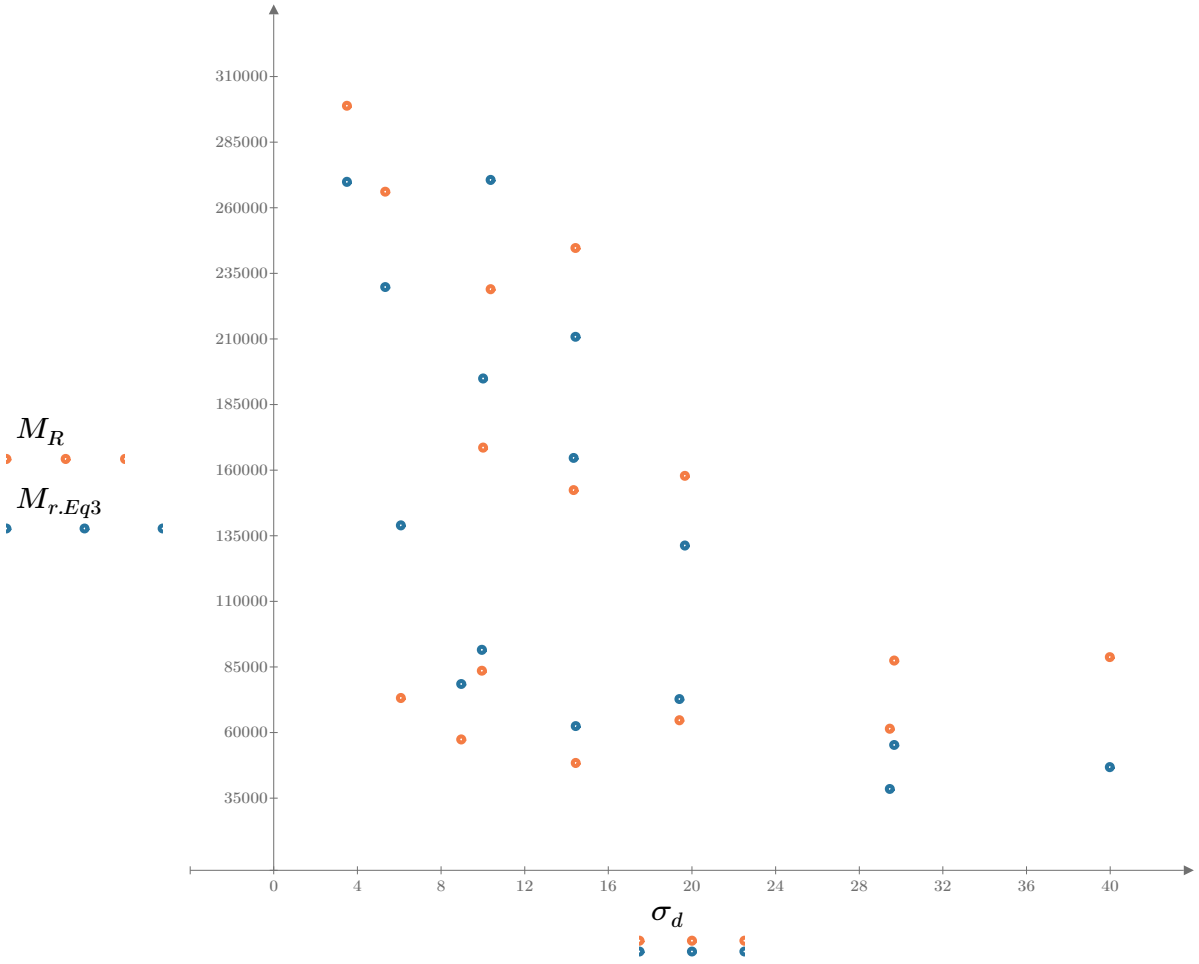

Figure 3. Plot of the test data (orange points) vs. the fitted Equation 3 model (blue points).

Dan Seely
9/12/2023

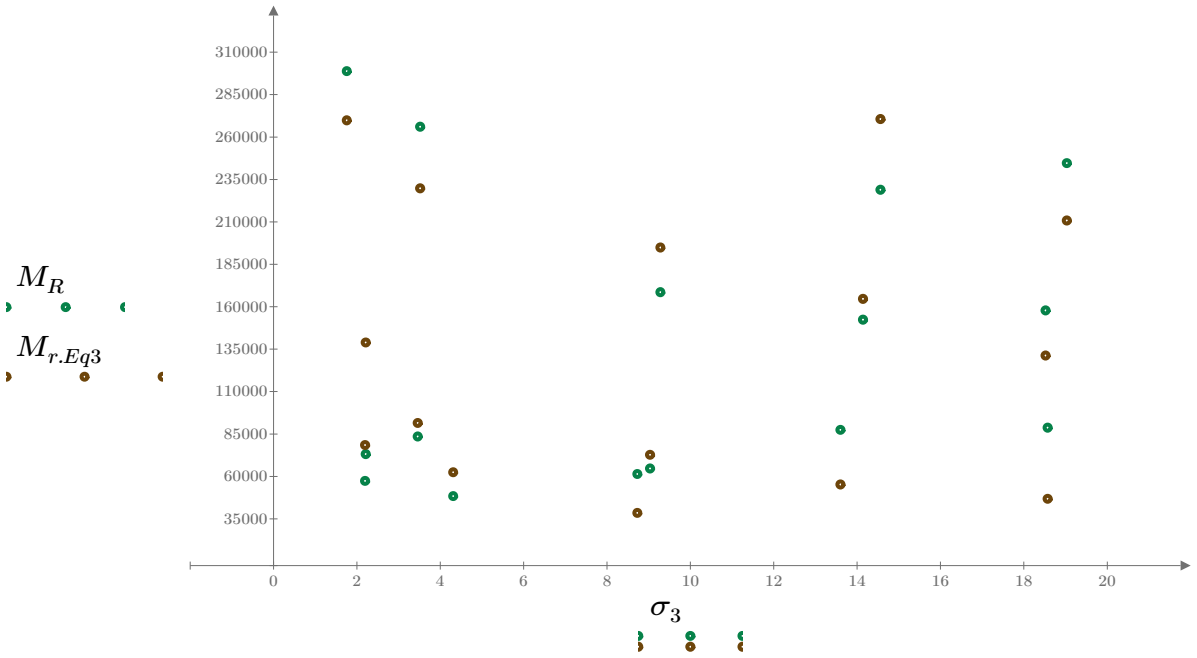

Figure 4. Plot of the test data (green points) vs. the fitted Equation 3 model (brown points).

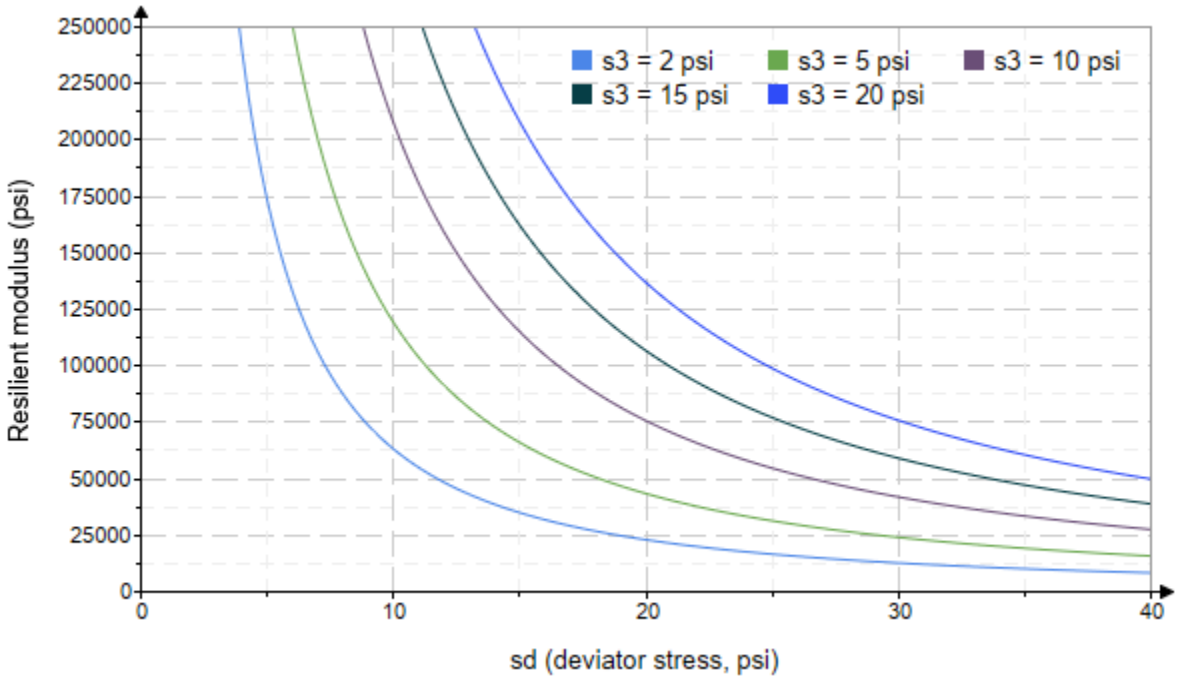

Figure 5. Plot of the fitted Equation 3 model for various confining stresses.

Dan Seely
9/12/2023

$$M_{R.4}\left(\sigma_B,\sigma_d,K_8,K_9,K_{10}\right):=K_8\cdot p_a\left(\frac{\sigma_B}{p_a}\right)^{K_9}\cdot\left(\frac{\sigma_d}{p_a}\right)^{K_{10}}$$

Equation 4 AASHTO Publication No. FHWA-RD-97-083

$K_8=2227.866$

$K_9=1.1360$ Equation 4 fitting parameters

$K_{10}=-1.854$

$R_4{}^2=0.8212$ Coefficient of determination

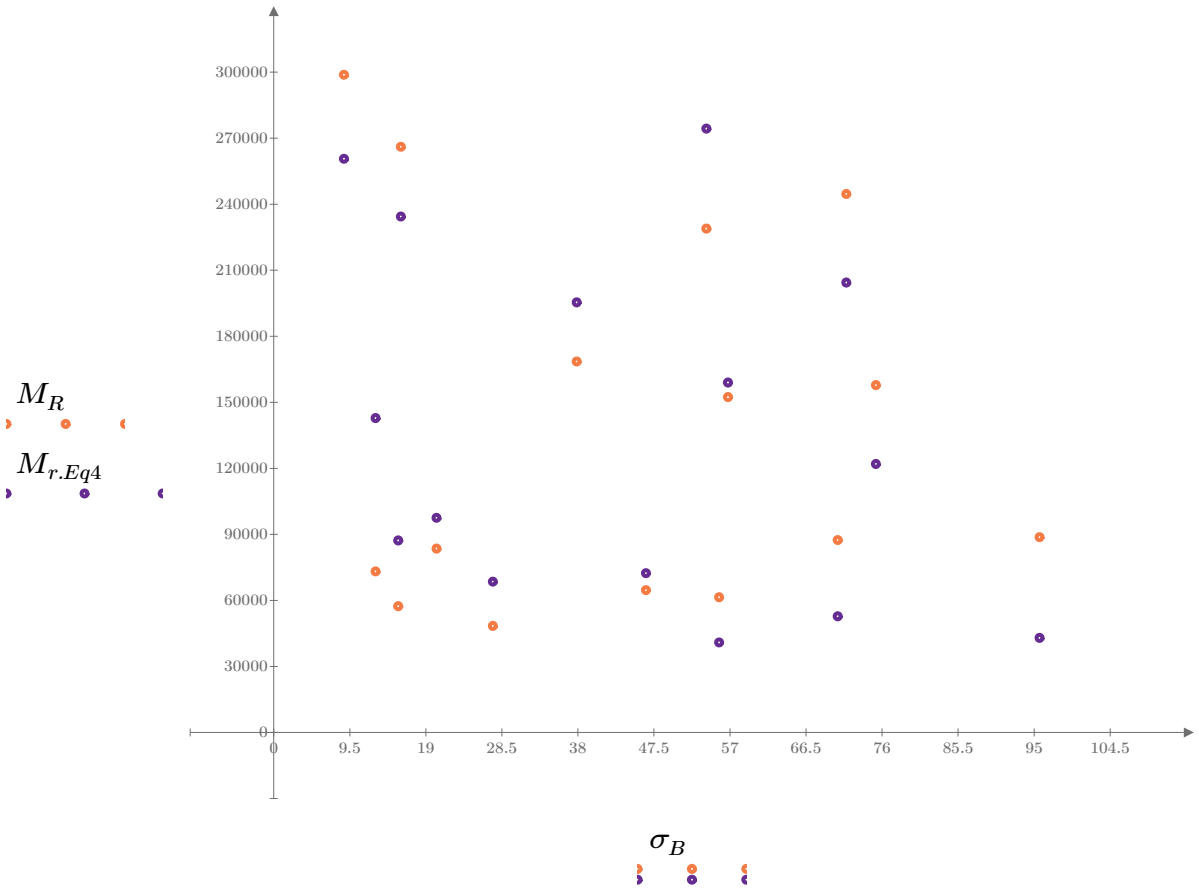

Figure 6. Plot of the test data (orange points) vs. the fitted Equation 4 model (purple points).

Dan Seely
9/12/2023

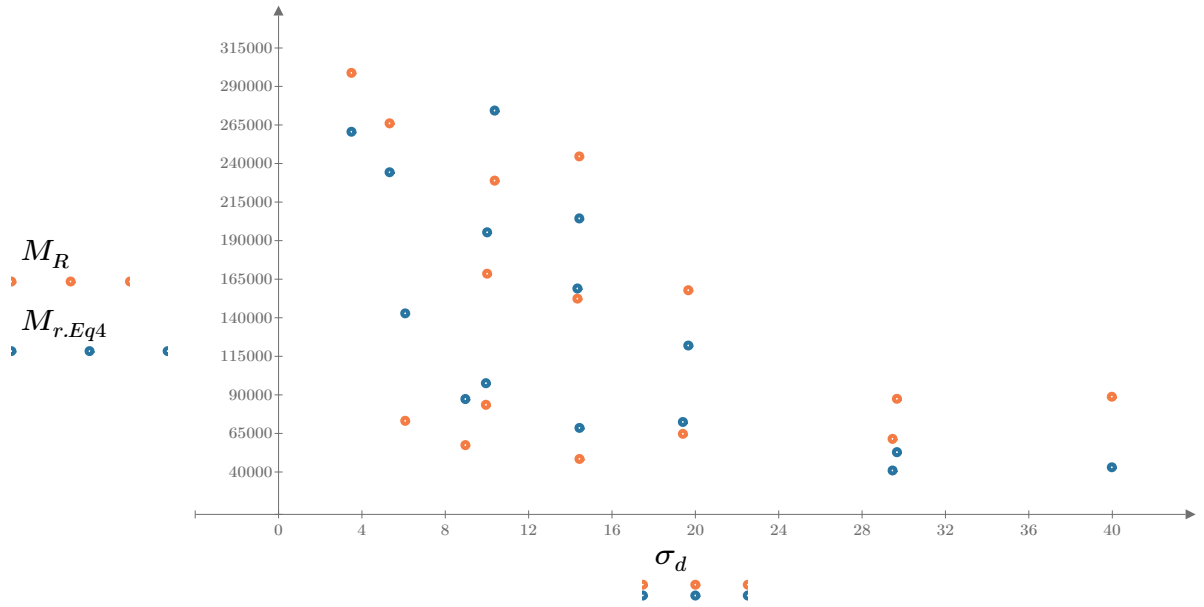

Figure 7. Plot of the test data (orange points) vs. the fitted Equation 4 model (blue points).

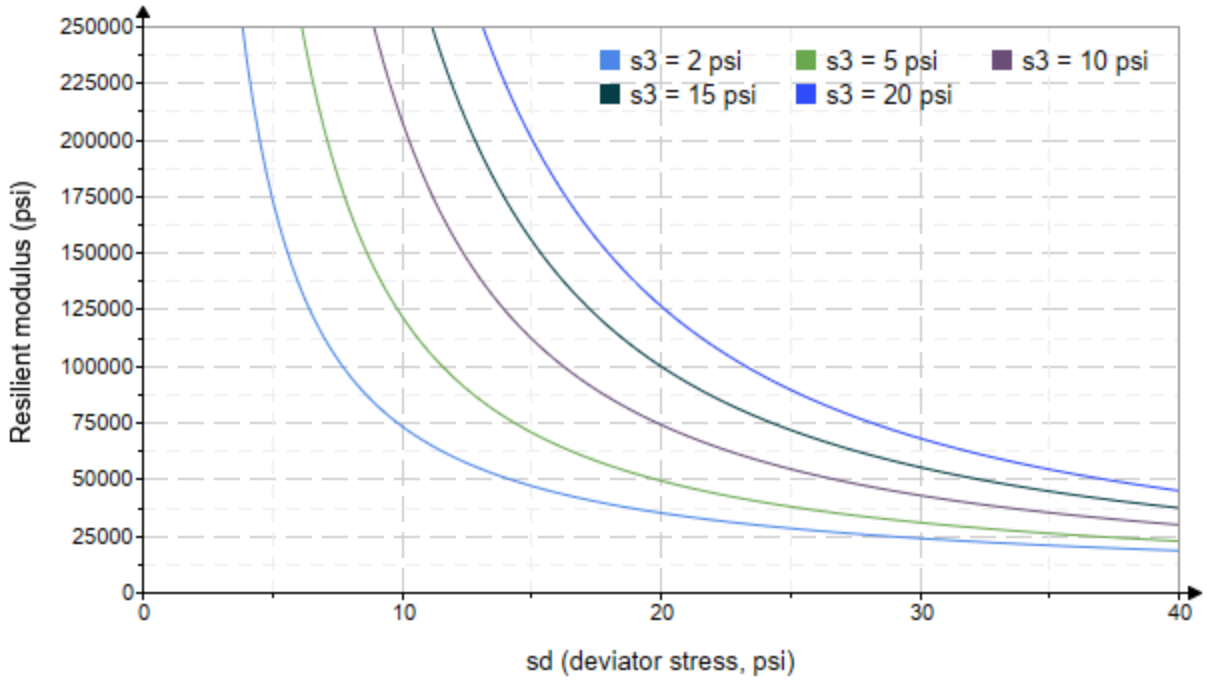

Figure 8. Plot of the fitted Equation 4 model for various confining stresses.

Dan Seely
9/12/2023

$SampleNo := \text{“B2}-39\text{”}$

$Treatment = \text{“W1”}$

$S = 20.368$ Degree of Saturation (%)

Test Sequence : Base/Subbase

Test summary data (psi) :

$$\sigma_3 = \begin{bmatrix} 2.770 \\ 2.814 \\ 2.787 \\ 4.733 \\ 4.702 \\ 4.655 \\ 9.725 \\ 9.645 \\ 9.688 \\ 14.700 \\ 14.670 \\ 14.700 \\ 19.680 \\ 19.720 \\ 19.680 \end{bmatrix} \quad \sigma_d = \begin{bmatrix} 3.142 \\ 6.140 \\ 9.031 \\ 5.089 \\ 10.020 \\ 14.540 \\ 10.110 \\ 19.380 \\ 29.630 \\ 9.930 \\ 14.480 \\ 29.860 \\ 14.650 \\ 19.460 \\ 40.330 \end{bmatrix} \quad \sigma_B = \begin{bmatrix} 11.450 \\ 14.580 \\ 17.390 \\ 19.290 \\ 24.120 \\ 28.510 \\ 39.280 \\ 48.310 \\ 58.690 \\ 54.040 \\ 58.490 \\ 73.970 \\ 73.700 \\ 78.610 \\ 99.360 \end{bmatrix} \quad M_R = \begin{bmatrix} 36435.6 \\ 32917.4 \\ 35084.8 \\ 37438.8 \\ 36983.6 \\ 40088.4 \\ 42016.0 \\ 45775.8 \\ 50982.2 \\ 60913.8 \\ 51542.8 \\ 54494.4 \\ 53639.4 \\ 58849.4 \\ 57514.6 \end{bmatrix}$$

σ_3 = mean confining stress
σ_d = mean deviator stress
σ_B = mean bulk stress
M_R = resilient modulus
p_a = atmospheric pressure = 14.6959 psi

Dan Seely
9/12/2023

$$M_{R.1}\left(\sigma_B, K_1, K_2\right) := K_1 \cdot {\sigma_B}^{K_2}$$

Equation 1
AASHTO Publication No. FHWA-RD-97-083

$K_1 = 15664.269$

$K_2 = 0.2921$

Equation 1 fitting parameters

${R_1}^2 = 0.8563$

Coefficient of determination

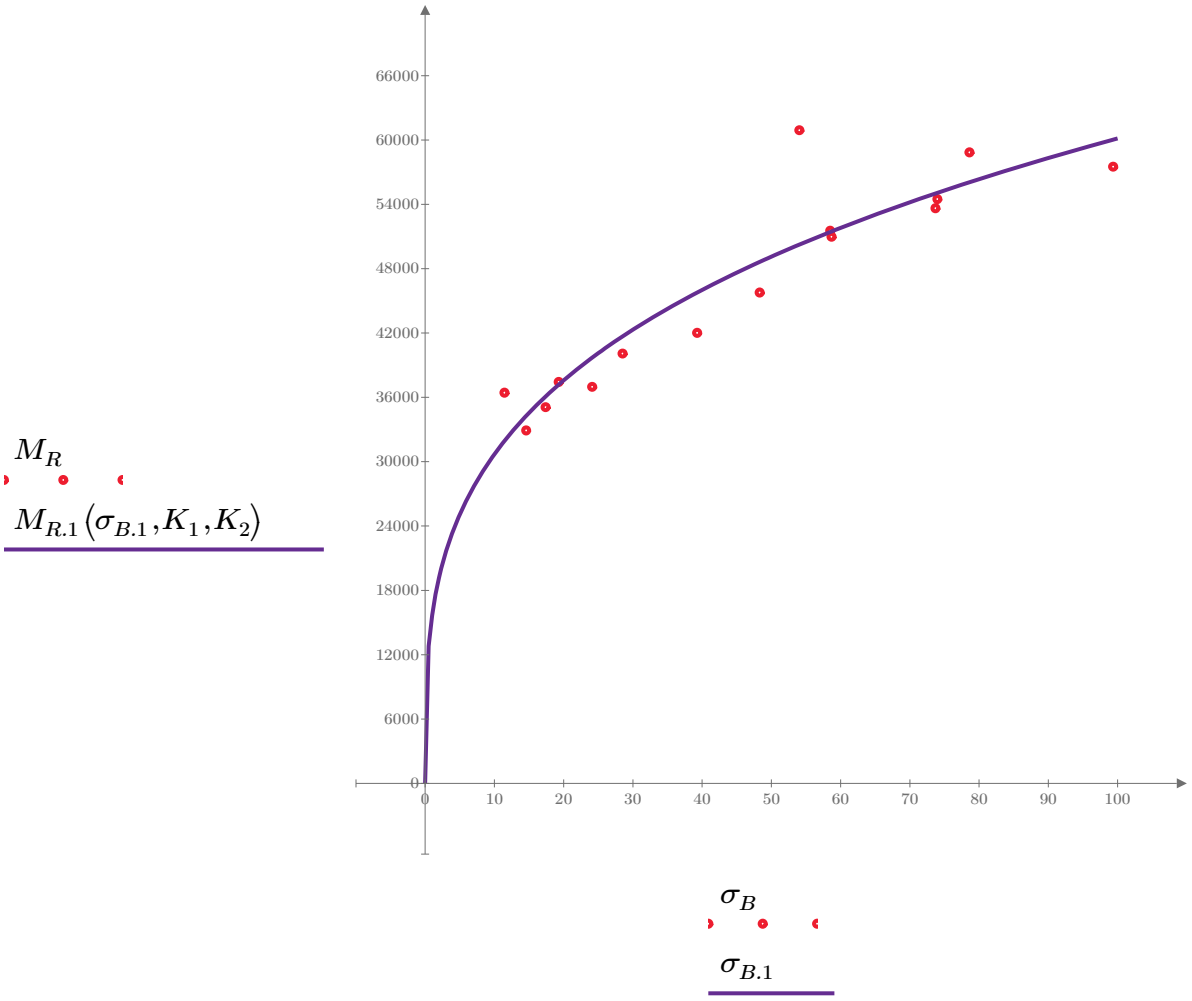

Figure 1. Plot of the test data (red points) vs. the fitted Equation 1 model (purple line).

Dan Seely
9/12/2023

$$M_{R.2}(\sigma_d, K_3, K_4) := K_3 \cdot \sigma_d^{K_4}$$

Equation 2
AASHTO Publication No. FHWA-RD-97-083

$K_3 = 27055.895$

$K_4 = 0.2076$

Equation 2 fitting parameters

$R_2^2 = 0.4788$

Coefficient of determination

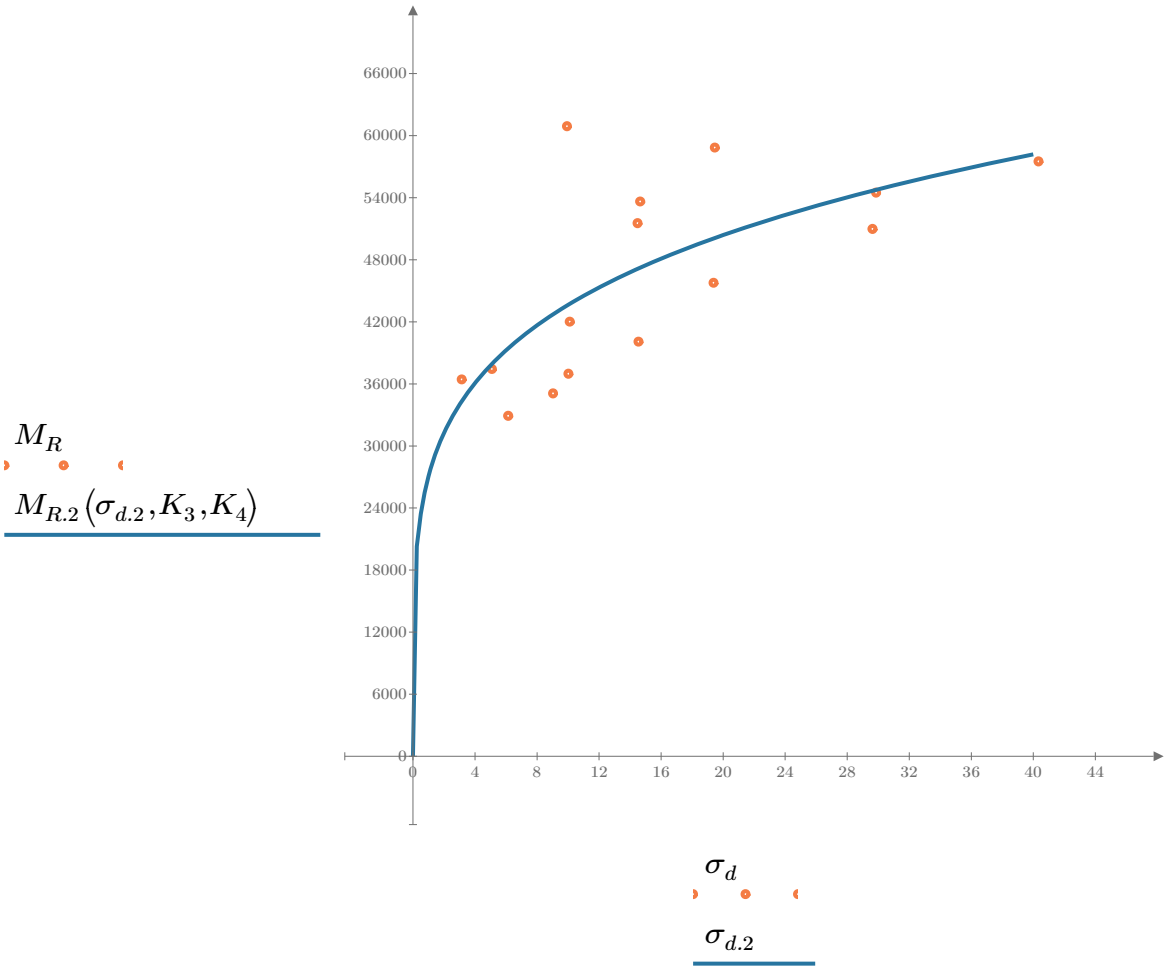

Figure 2. Plot of the test data (orange points) vs. the fitted Equation 2 model (blue line).

Dan Seely
9/12/2023

$$M_{R.3}\left(\sigma_d,\sigma_3,K_5,K_6,K_7\right):=K_5\cdot{\sigma_d}^{K_6}\cdot\left(1+\sigma_3\right)^{K_7}$$

Equation 3 AASHTO Publication No. FHWA-RD-97-083

$K_5=22469.869$

$K_6=0.0121$ Equation 3 fitting parameters

$K_7=0.3002$

${R_3}^2=0.8907$ Coefficient of determination

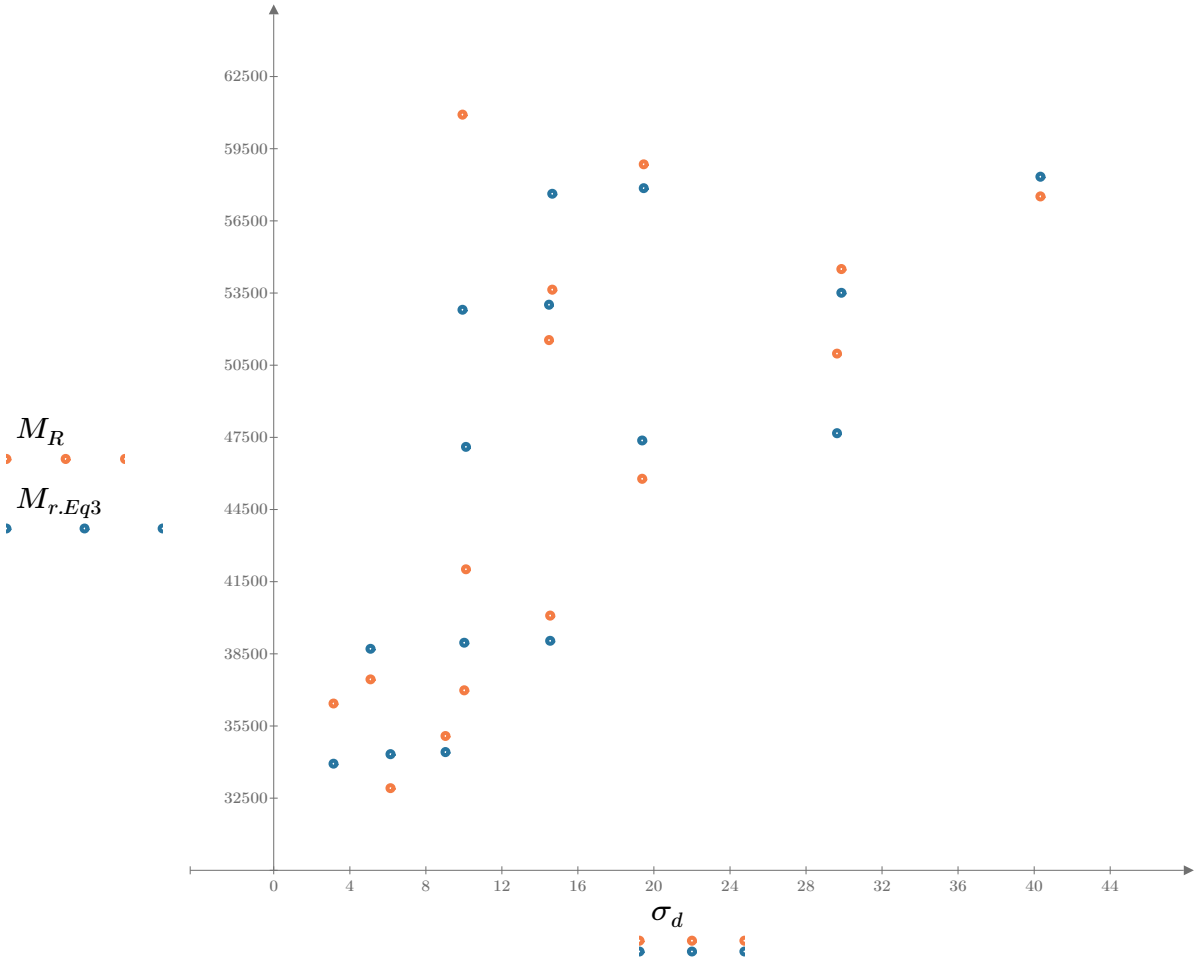

Figure 3. Plot of the test data (orange points) vs. the fitted Equation 3 model (blue points).

Dan Seely
9/12/2023

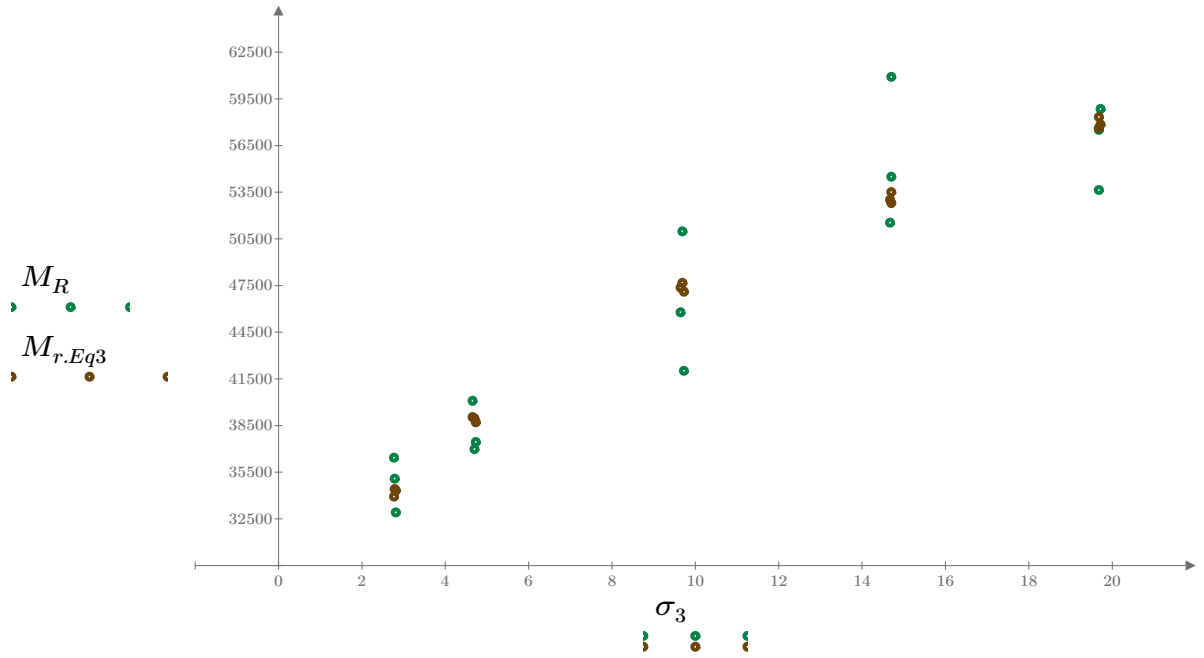

Figure 4. Plot of the test data (green points) vs. the fitted Equation 3 model (brown points).

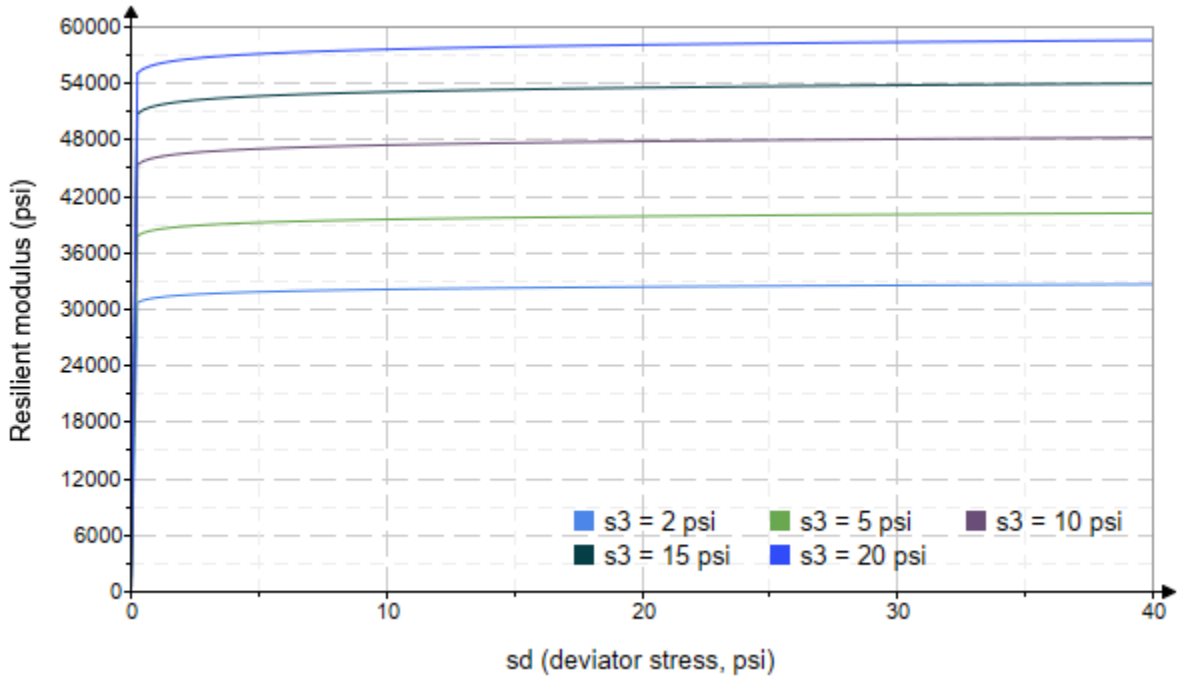

Figure 5. Plot of the fitted Equation 3 model for various confining stresses.

Dan Seely
9/12/2023

$$M_{R.4}\left(\sigma_B,\sigma_d,K_8,K_9,K_{10}\right) := K_8 \cdot p_a \left(\frac{\sigma_B}{p_a}\right)^{K_9} \cdot \left(\frac{\sigma_d}{p_a}\right)^{K_{10}}$$

Equation 4 AASHTO Publication No. FHWA-RD-97-083

$K_8 = 2062.977$

$K_9 = 0.4025$ Equation 4 fitting parameters

$K_{10} = -0.1254$

$R_4^{\,2} = 0.9015$ Coefficient of determination

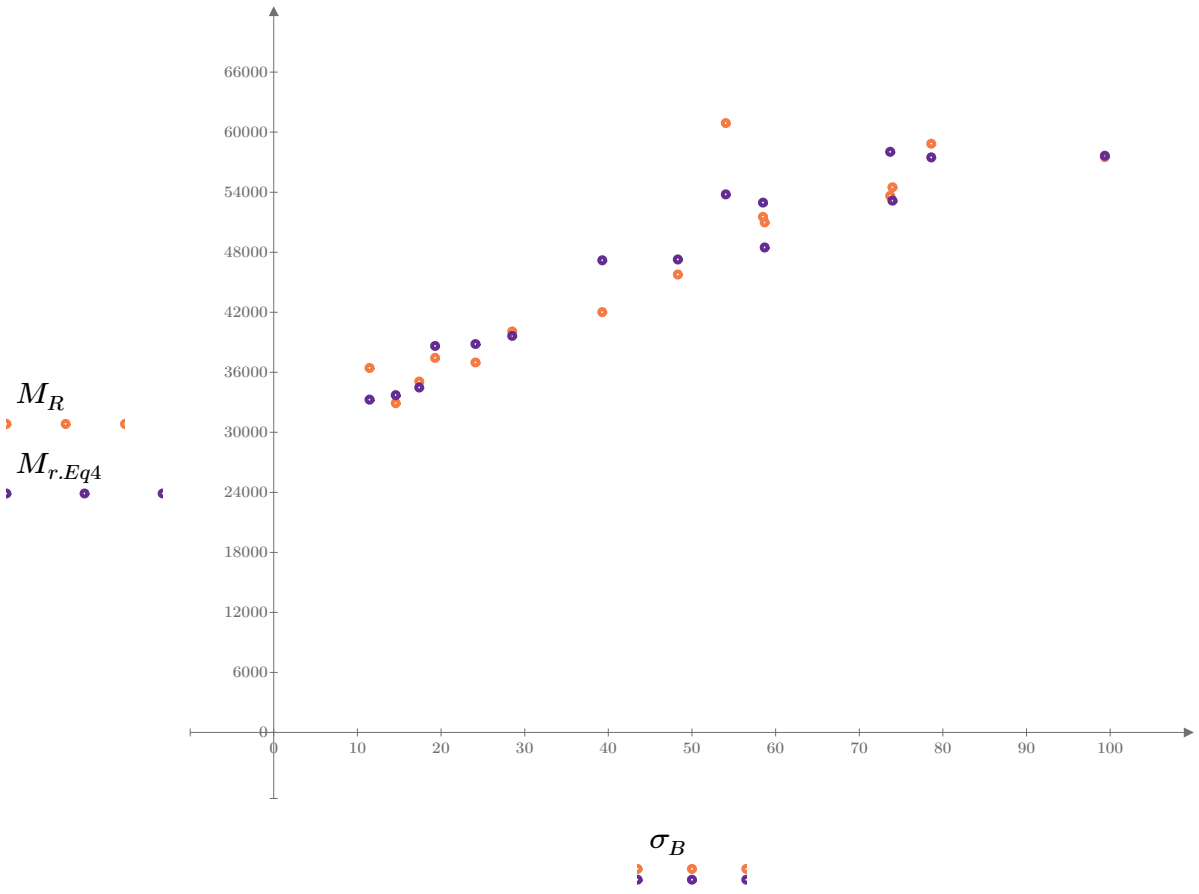

Figure 6. Plot of the test data (orange points) vs. the fitted Equation 4 model (purple points).

Dan Seely
9/12/2023

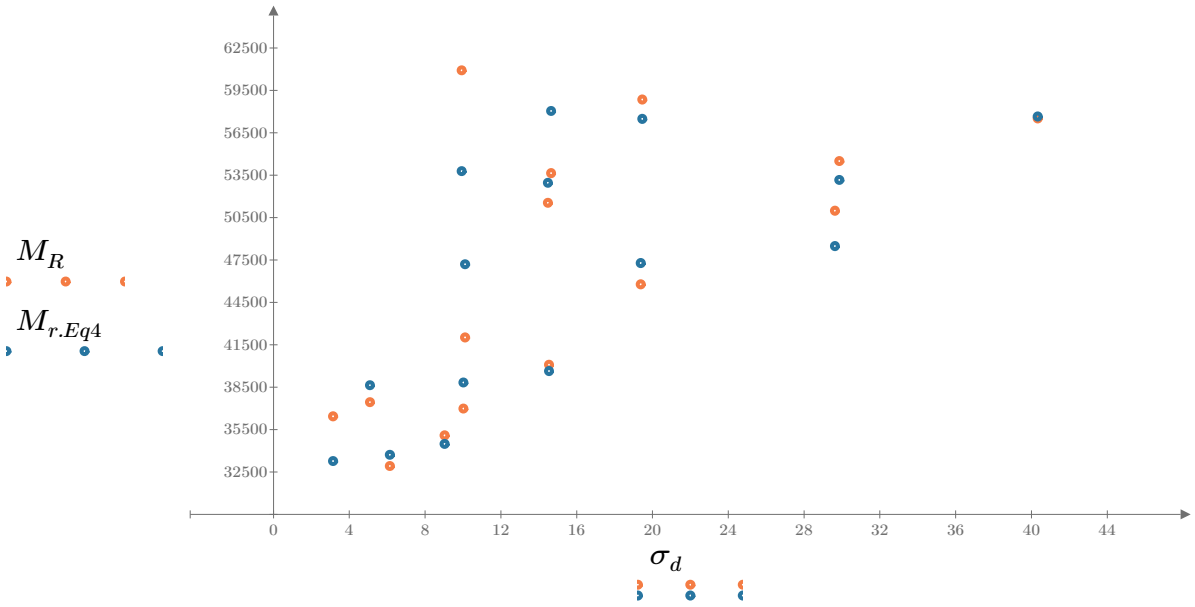

Figure 7. Plot of the test data (orange points) vs. the fitted Equation 4 model (blue points).

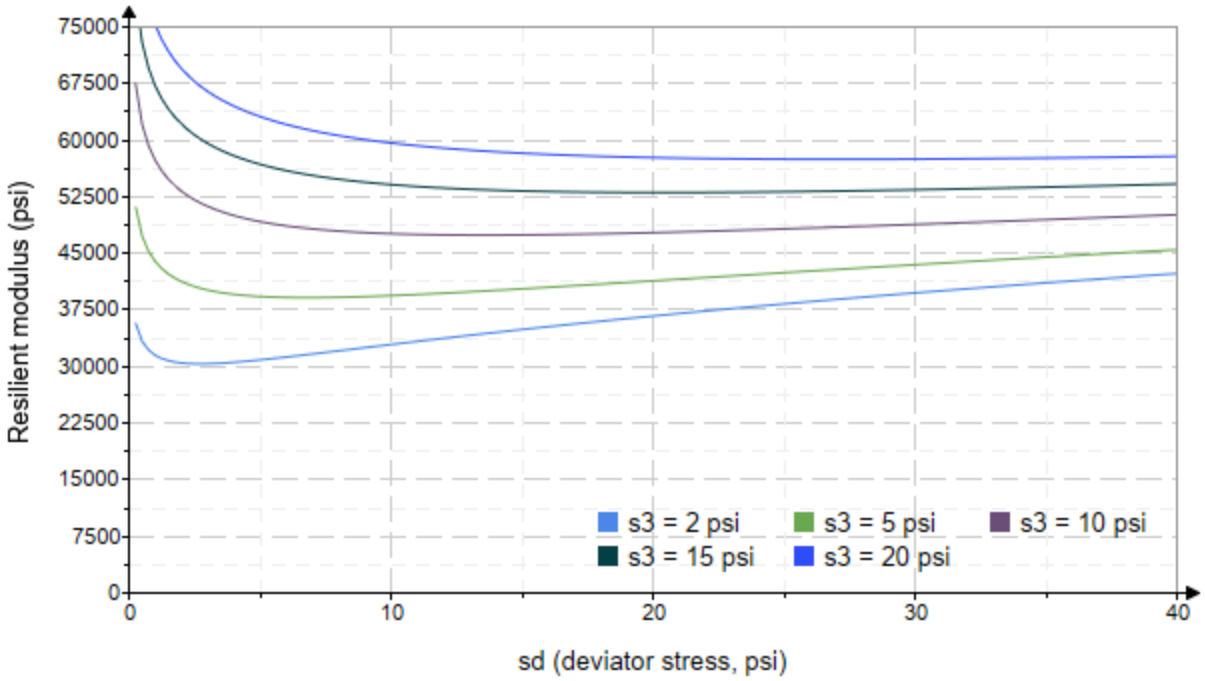

Figure 8. Plot of the fitted Equation 4 model for various confining stresses.

Dan Seely
9/12/2023

$SampleNo := \text{“B2}-\text{40”}$

$Treatment = \text{“W1”}$

$S = 19.438$ Degree of Saturation (%)

Test Sequence : Base/Subbase

Test summary data (psi) :

$$\sigma_3 = \begin{bmatrix} 2.193 \\ 2.391 \\ 2.402 \\ 3.935 \\ 4.131 \\ 4.413 \\ 9.117 \\ 9.327 \\ 8.729 \\ 14.430 \\ 14.770 \\ 13.990 \\ 19.370 \\ 19.120 \\ 19.280 \end{bmatrix} \quad \sigma_d = \begin{bmatrix} 3.160 \\ 6.235 \\ 9.079 \\ 5.186 \\ 9.994 \\ 14.480 \\ 10.100 \\ 19.260 \\ 29.490 \\ 10.210 \\ 14.440 \\ 29.770 \\ 14.610 \\ 19.600 \\ 39.850 \end{bmatrix} \quad \sigma_B = \begin{bmatrix} 9.740 \\ 13.410 \\ 16.290 \\ 16.990 \\ 22.390 \\ 27.720 \\ 37.450 \\ 47.240 \\ 55.680 \\ 53.490 \\ 58.750 \\ 71.730 \\ 72.710 \\ 76.950 \\ 97.700 \end{bmatrix} \quad M_R = \begin{bmatrix} 46049.8 \\ 34415.6 \\ 36513.2 \\ 51752.0 \\ 44696.2 \\ 43596.0 \\ 50220.0 \\ 49867.6 \\ 49710.6 \\ 60581.8 \\ 58453.4 \\ 54938.2 \\ 58227.0 \\ 58918.6 \\ 57557.0 \end{bmatrix}$$

σ_3 = mean confining stress
σ_d = mean deviator stress
σ_B = mean bulk stress
M_R = resilient modulus
p_a = atmospheric pressure = 14.6959 psi

Dan Seely
9/12/2023

$$M_{R.1}\left(\sigma_B, K_1, K_2\right) := K_1 \cdot {\sigma_B}^{K_2}$$

Equation 1
AASHTO Publication No. FHWA-RD-97-083

$K_1 = 25729.834$

$K_2 = 0.1844$

Equation 1 fitting parameters

${R_1}^2 = 0.6438$

Coefficient of determination

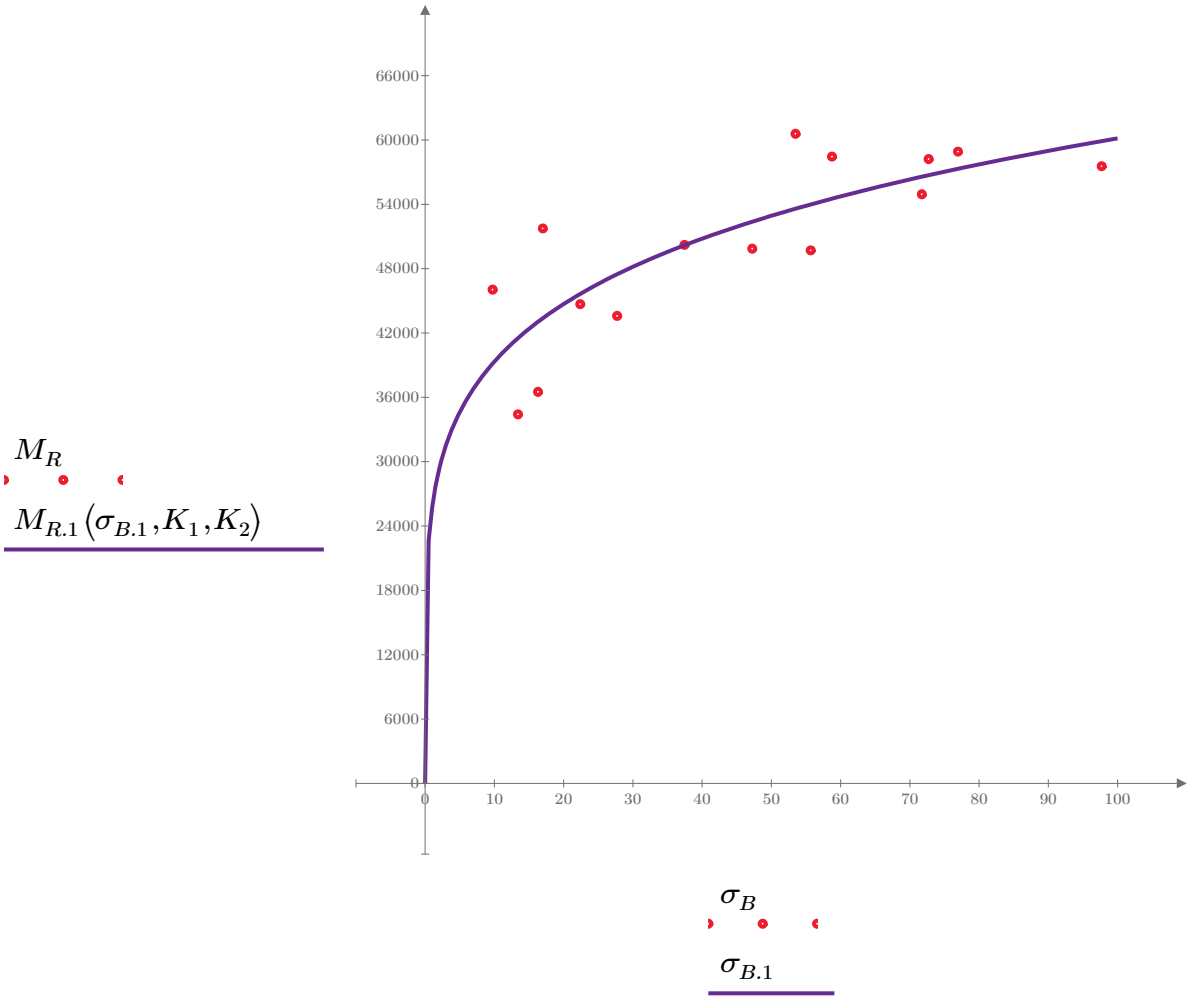

Figure 1. Plot of the test data (red points) vs. the fitted Equation 1 model (purple line).

Dan Seely
9/12/2023

$$M_{R.2}(\sigma_d, K_3, K_4) := K_3 \cdot \sigma_d^{K_4}$$

Equation 2
AASHTO Publication No. FHWA-RD-97-083

$K_3 = 38045.445$

$K_4 = 0.1091$

Equation 2 fitting parameters

$R_2^2 = 0.2145$

Coefficient of determination

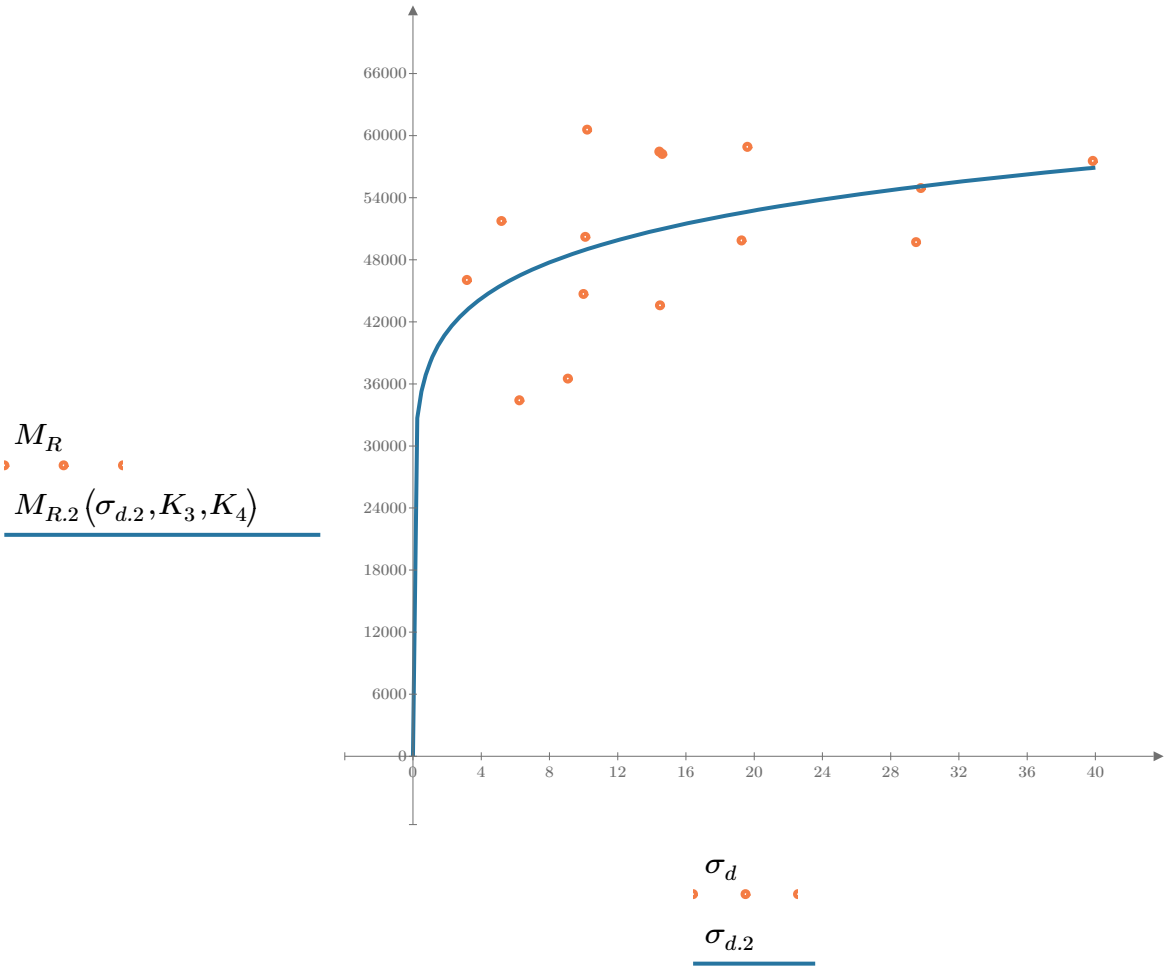

Figure 2. Plot of the test data (orange points) vs. the fitted Equation 2 model (blue line).

Dan Seely
9/12/2023

$$M_{R.3}\left(\sigma_d,\sigma_3,K_5,K_6,K_7\right):=K_5\cdot{\sigma_d}^{K_6}\cdot\left(1+\sigma_3\right)^{K_7}$$

Equation 3 AASHTO Publication No. FHWA-RD-97-083

$K_5=34712.965$

$K_6=-0.0886$ Equation 3 fitting parameters

$K_7=0.2698$

${R_3}^2=0.8619$ Coefficient of determination

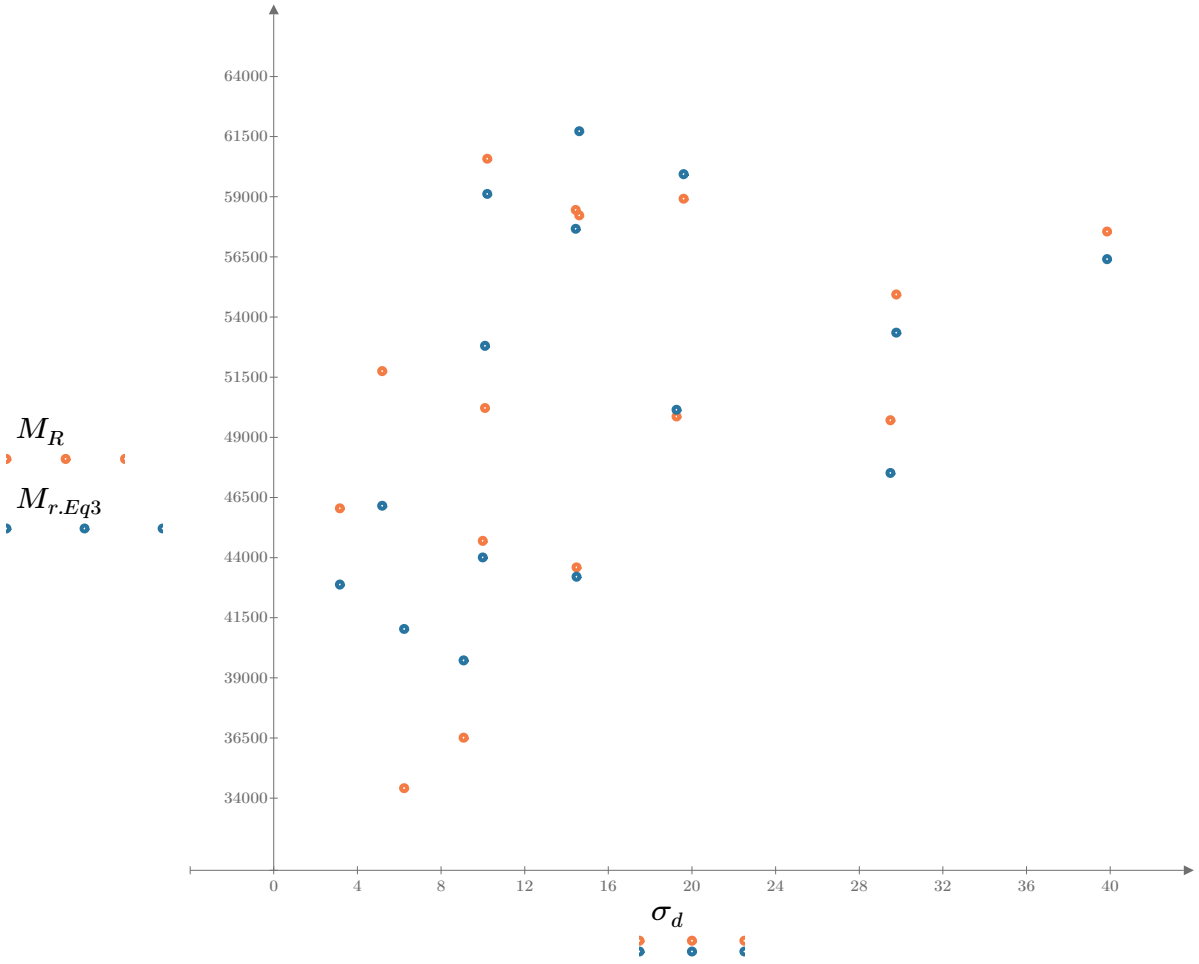

Figure 3. Plot of the test data (orange points) vs. the fitted Equation 3 model (blue points).

Dan Seely
9/12/2023

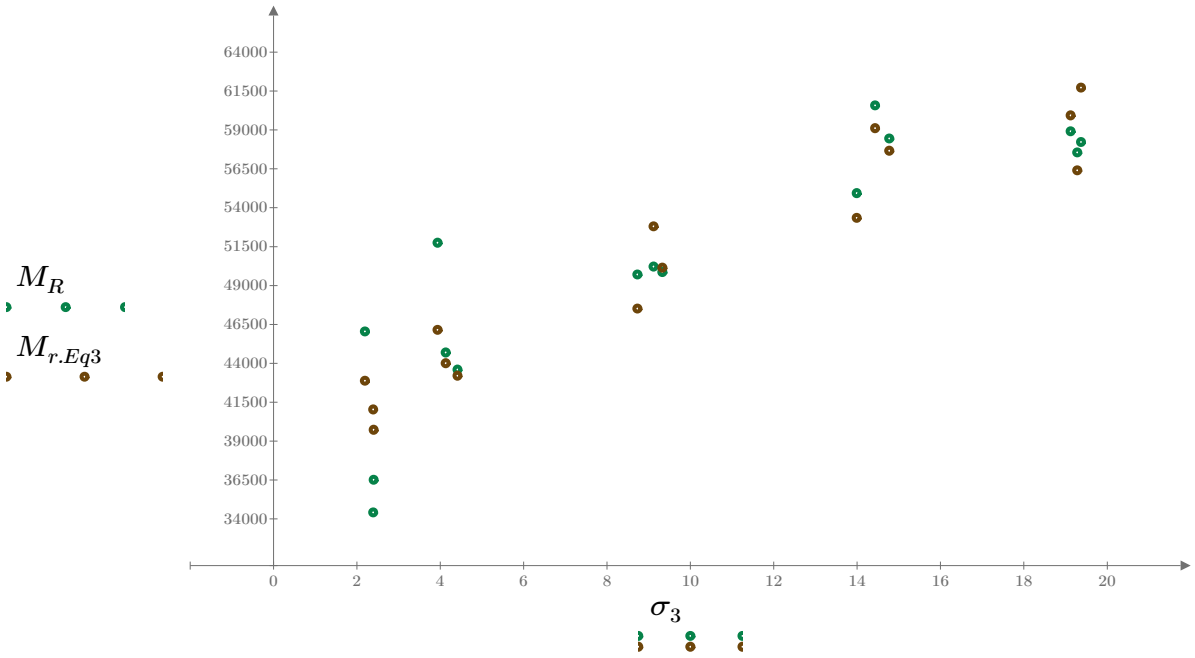

Figure 4. Plot of the test data (green points) vs. the fitted Equation 3 model (brown points).

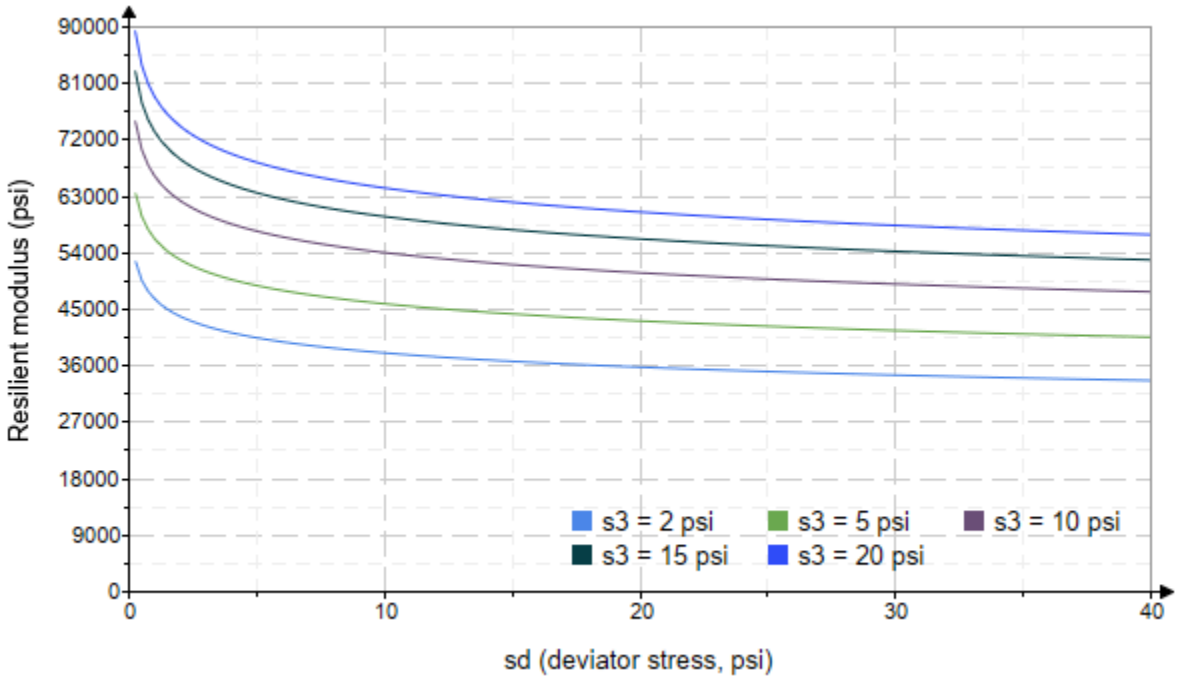

Figure 5. Plot of the fitted Equation 3 model for various confining stresses.

Dan Seely
9/12/2023

$$M_{R.4}\left(\sigma_B,\sigma_d,K_8,K_9,K_{10}\right) := K_8 \cdot p_a \left(\frac{\sigma_B}{p_a}\right)^{K_9} \cdot \left(\frac{\sigma_d}{p_a}\right)^{K_{10}}$$

Equation 4 AASHTO Publication No. FHWA-RD-97-083

$K_8 = 2379.033$

$K_9 = 0.3570$ Equation 4 fitting parameters

$K_{10} = -0.2141$

$R_4^{\,2} = 0.8539$ Coefficient of determination

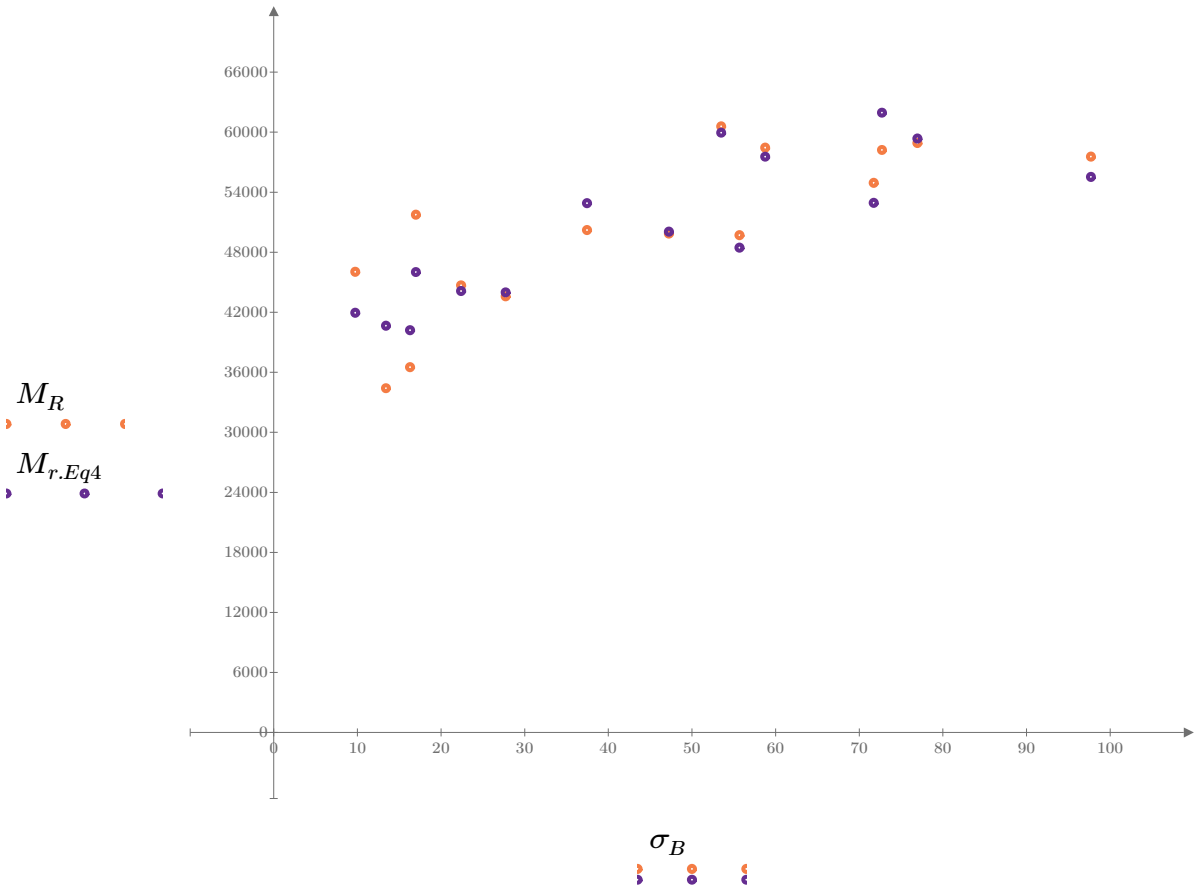

Figure 6. Plot of the test data (orange points) vs. the fitted Equation 4 model (purple points).

Dan Seely
9/12/2023

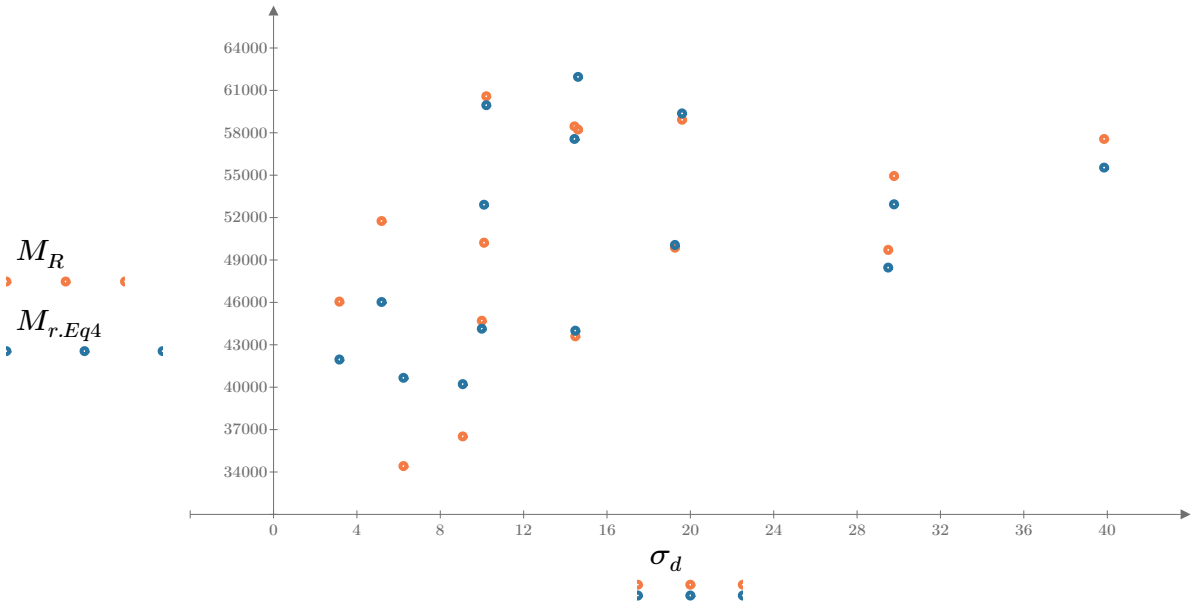

Figure 7. Plot of the test data (orange points) vs. the fitted Equation 4 model (blue points).

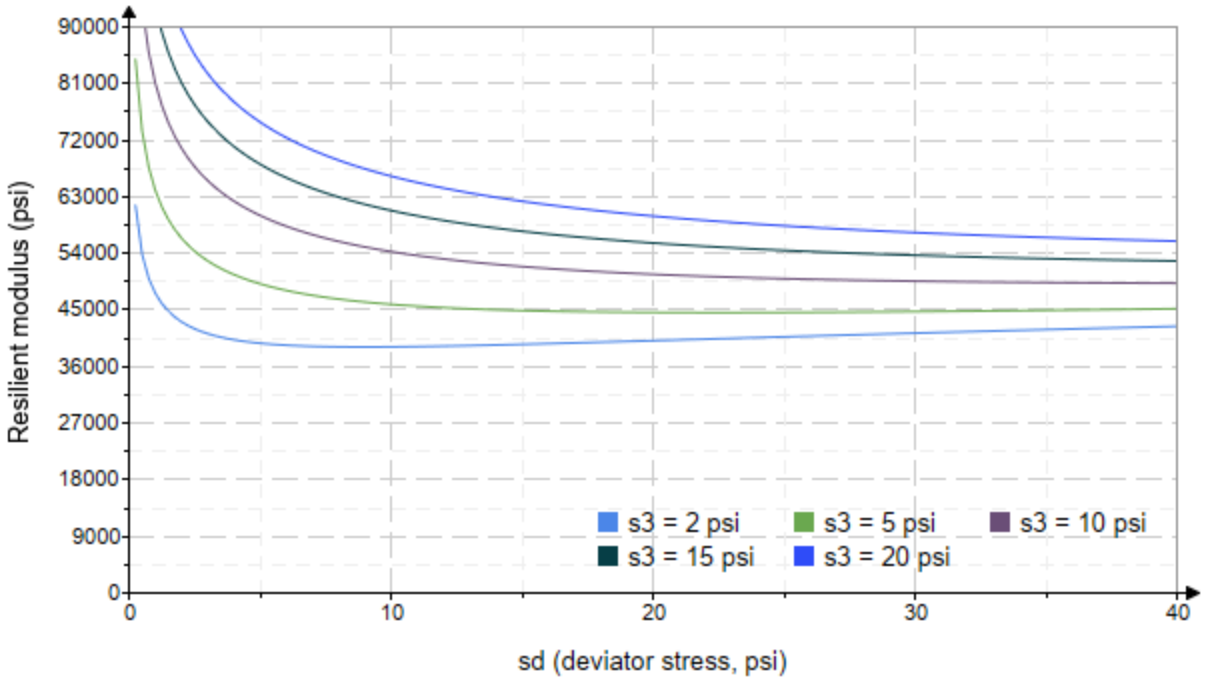

Figure 8. Plot of the fitted Equation 4 model for various confining stresses.

Dan Seely
9/12/2023

$SampleNo := \text{“B2−41”}$

$Treatment = \text{“W1”}$

$S = 18.652$ Degree of Saturation (%)

Test Sequence : Base/Subbase

Test summary data (psi) :

$$\sigma_3 = \begin{bmatrix} 2.927 \\ 2.456 \\ 2.157 \\ 4.423 \\ 3.775 \\ 3.637 \\ 8.826 \\ 8.360 \\ 8.519 \\ 13.870 \\ 13.450 \\ 13.800 \\ 18.480 \\ 18.980 \\ 19.080 \end{bmatrix} \quad \sigma_d = \begin{bmatrix} 3.132 \\ 6.086 \\ 9.059 \\ 5.147 \\ 9.966 \\ 14.350 \\ 9.906 \\ 19.200 \\ 29.490 \\ 9.756 \\ 14.410 \\ 29.720 \\ 14.420 \\ 19.590 \\ 40.000 \end{bmatrix} \quad \sigma_B = \begin{bmatrix} 11.910 \\ 13.450 \\ 15.530 \\ 18.420 \\ 21.290 \\ 25.260 \\ 36.380 \\ 44.280 \\ 55.050 \\ 51.370 \\ 54.750 \\ 71.110 \\ 69.860 \\ 76.530 \\ 97.240 \end{bmatrix} \quad M_R = \begin{bmatrix} 64764.6 \\ 45436.4 \\ 44088.8 \\ 49284.2 \\ 54479.6 \\ 44670.6 \\ 98009.2 \\ 76863.6 \\ 54638.8 \\ 76952.9 \\ 99267.0 \\ 64500.6 \\ 83885.2 \\ 70602.8 \\ 65817.8 \end{bmatrix}$$

σ_3 = mean confining stress
σ_d = mean deviator stress
σ_B = mean bulk stress
M_R = resilient modulus
p_a = atmospheric pressure = 14.6959 psi

Dan Seely
9/12/2023

$$M_{R.1}\left(\sigma_B, K_1, K_2\right) := K_1 \cdot {\sigma_B}^{K_2}$$

Equation 1
AASHTO Publication No. FHWA-RD-97-083

$K_1 = 31479.017$

$K_2 = 0.2050$

Equation 1 fitting parameters

${R_1}^2 = 0.2738$

Coefficient of determination

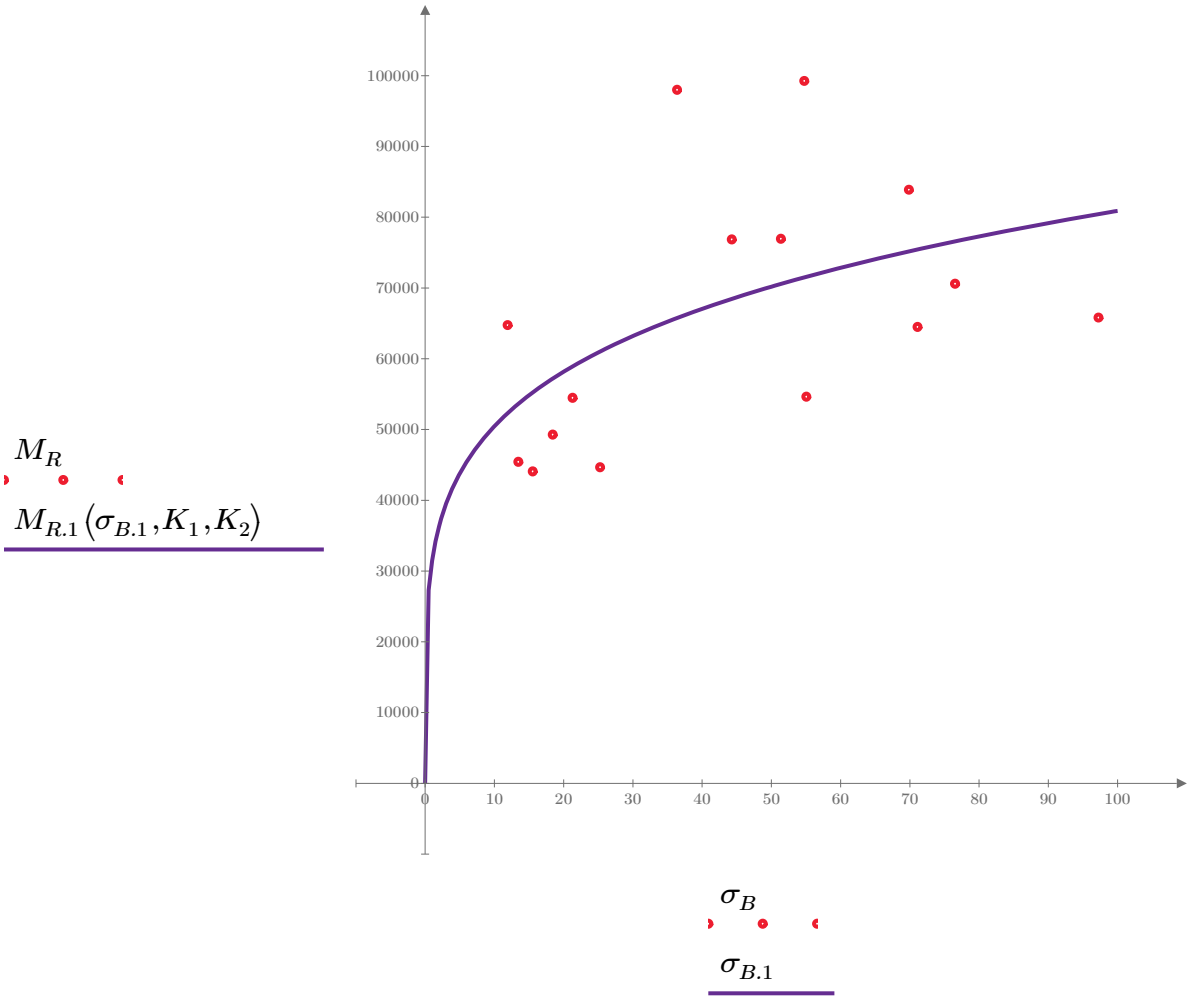

Figure 1. Plot of the test data (red points) vs. the fitted Equation 1 model (purple line).

Dan Seely
9/12/2023

$$M_{R.2}\left(\sigma_d, K_3, K_4\right) := K_3 \cdot \sigma_d^{K_4}$$

Equation 2
AASHTO Publication No. FHWA-RD-97-083

$K_3 = 56244.149$

$K_4 = 0.0640$

Equation 2 fitting parameters

$R_2^2 = 0.0281$

Coefficient of determination

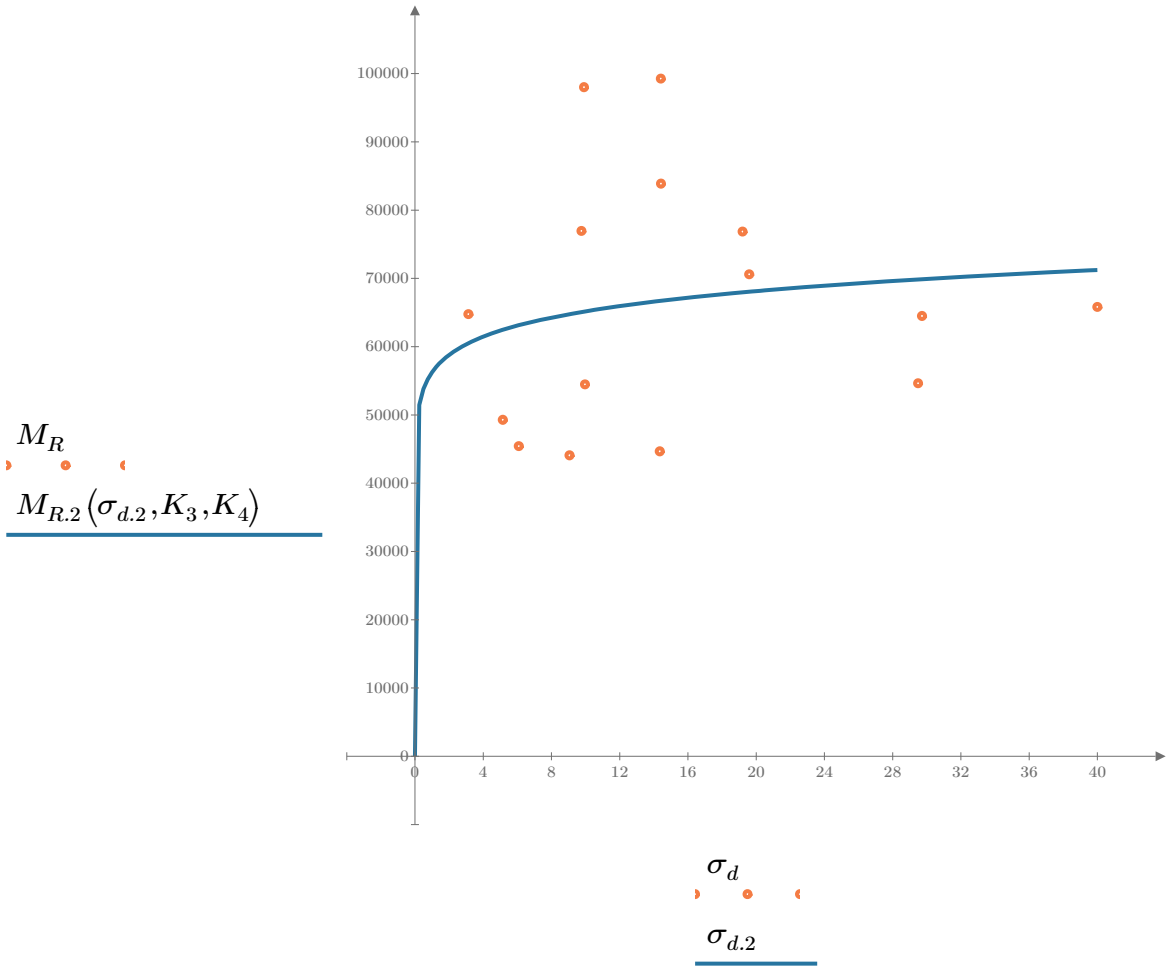

Figure 2. Plot of the test data (orange points) vs. the fitted Equation 2 model (blue line).

Dan Seely
9/12/2023

$$M_{R.3}\left(\sigma_d,\sigma_3,K_5,K_6,K_7\right):=K_5\cdot{\sigma_d}^{K_6}\cdot\left(1+\sigma_3\right)^{K_7}$$

Equation 3 AASHTO Publication No. FHWA-RD-97-083

$K_5=45786.731$

$K_6=-0.2055$ Equation 3 fitting parameters

$K_7=0.4044$

${R_3}^2=0.5697$ Coefficient of determination

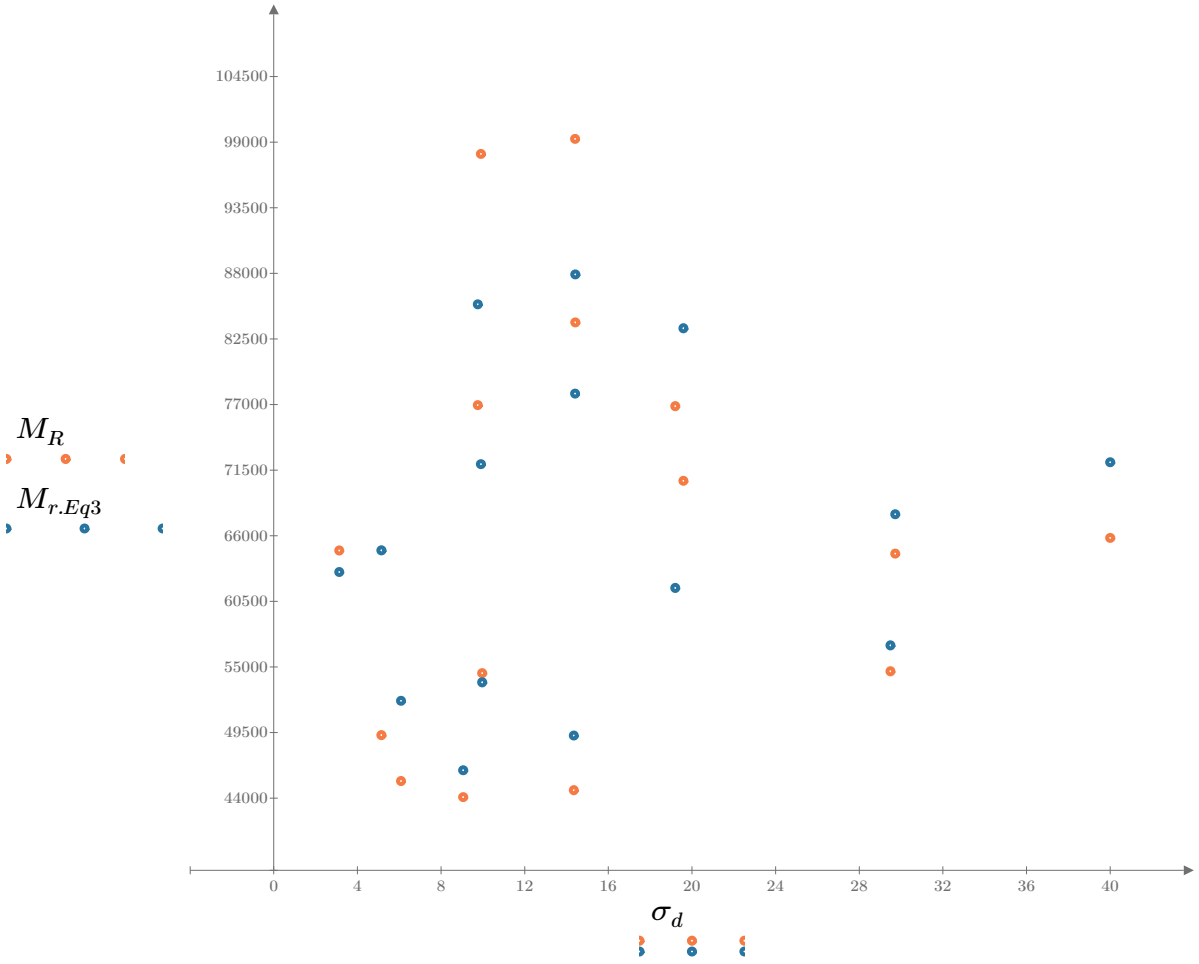

Figure 3. Plot of the test data (orange points) vs. the fitted Equation 3 model (blue points).

Dan Seely
9/12/2023

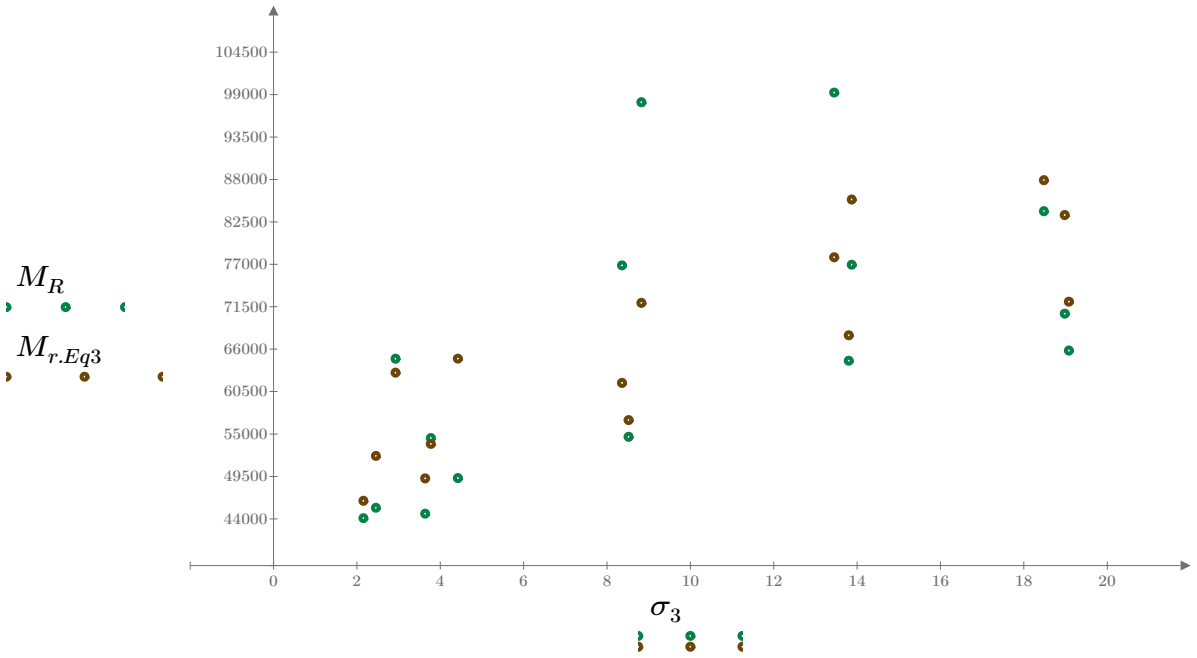

Figure 4. Plot of the test data (green points) vs. the fitted Equation 3 model (brown points).

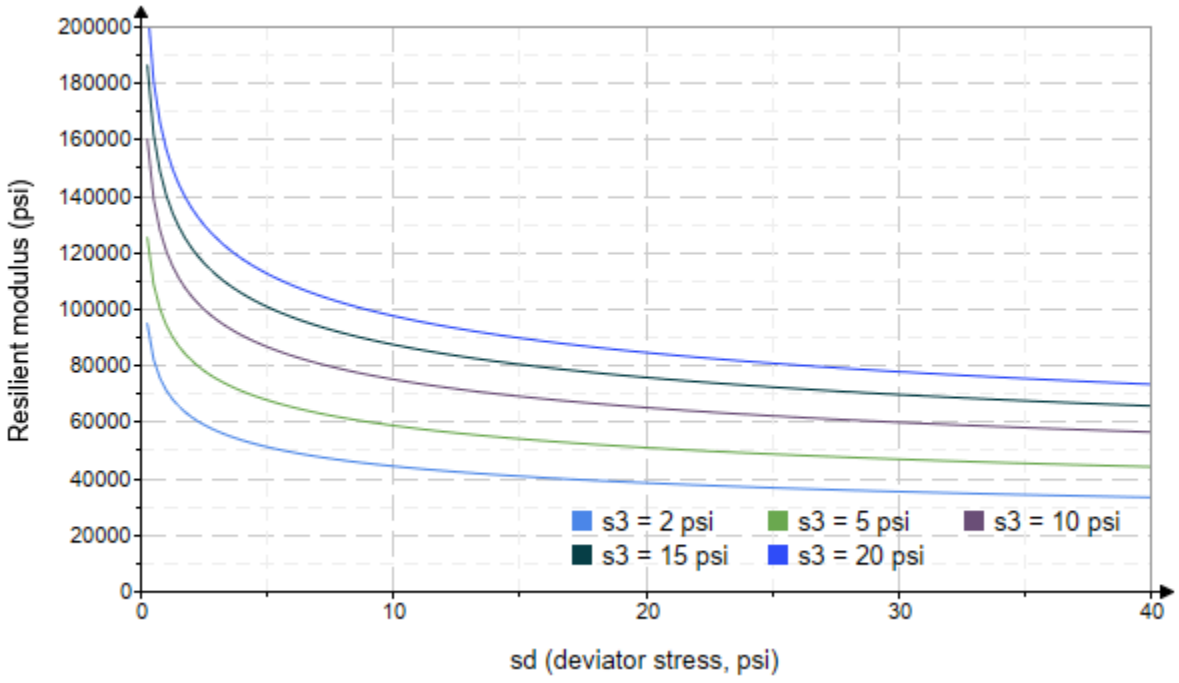

Figure 5. Plot of the fitted Equation 3 model for various confining stresses.

Dan Seely
9/12/2023

$$M_{R.4}\left(\sigma_B,\sigma_d,K_8,K_9,K_{10}\right) := K_8 \cdot p_a \left(\frac{\sigma_B}{p_a}\right)^{K_9} \cdot \left(\frac{\sigma_d}{p_a}\right)^{K_{10}}$$

Equation 4 AASHTO Publication No. FHWA-RD-97-083

$K_8 = 2567.767$

$K_9 = 0.5408$ Equation 4 fitting parameters

$K_{10} = -0.3936$

$R_4^{\,2} = 0.5645$ Coefficient of determination

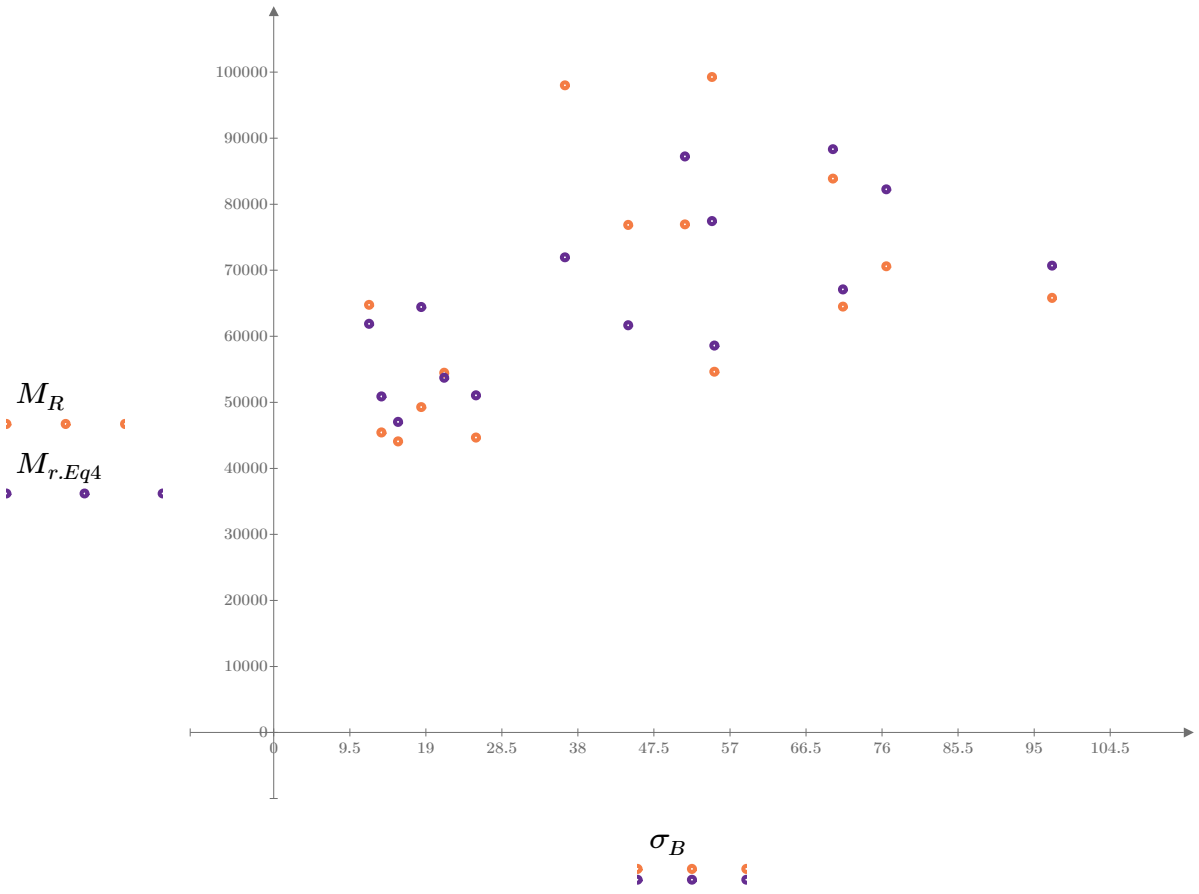

Figure 6. Plot of the test data (orange points) vs. the fitted Equation 4 model (purple points).

Dan Seely
9/12/2023

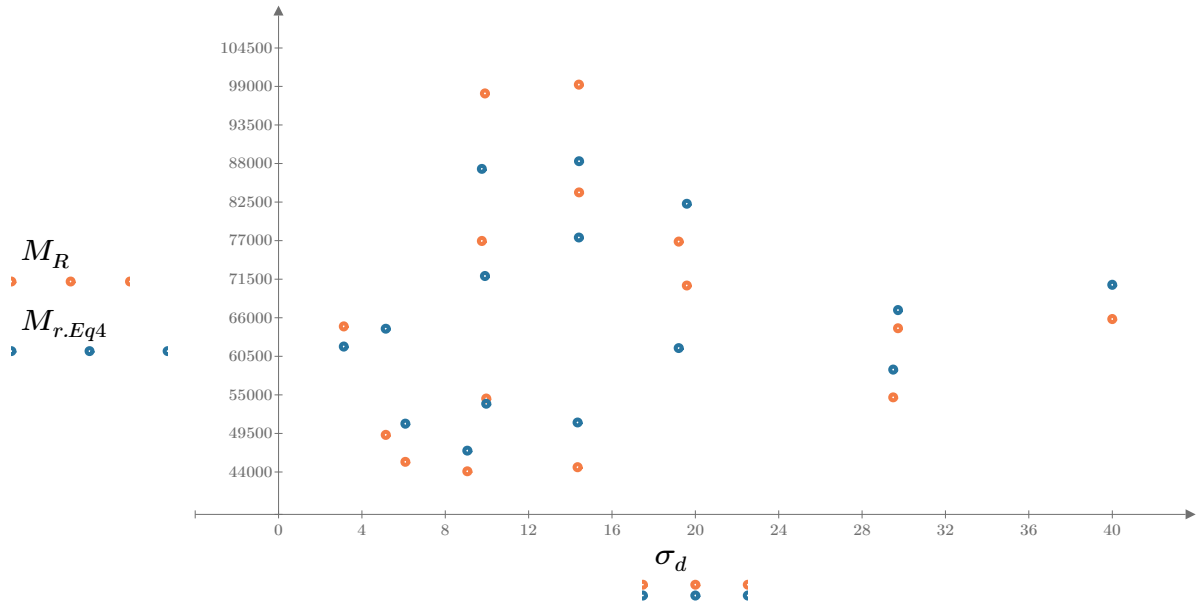

Figure 7. Plot of the test data (orange points) vs. the fitted Equation 4 model (blue points).

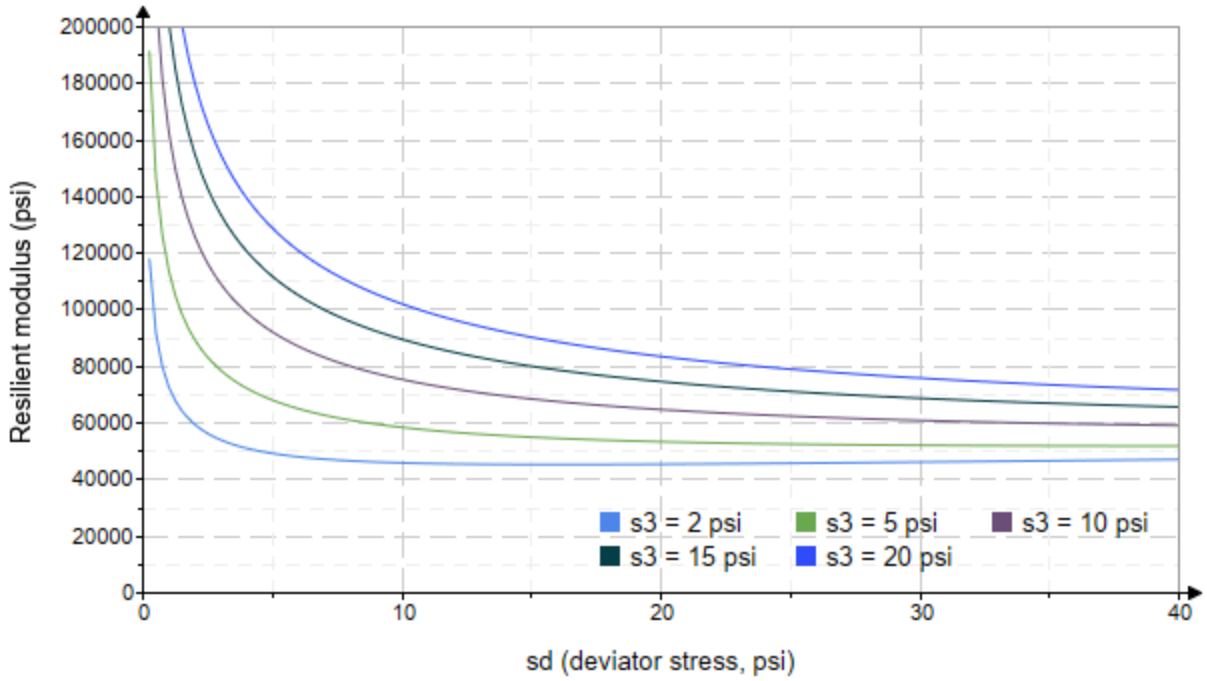

Figure 8. Plot of the fitted Equation 4 model for various confining stresses.

Dan Seely
9/12/2023

$SampleNo := \text{“B2–42”}$

$Treatment = \text{“AD”}$

$S = 3.716$ Degree of Saturation (%)

Test Sequence : Base/Subbase

Test summary data (psi) :

$$\sigma_3 = \begin{bmatrix} 2.318 \\ 2.385 \\ 2.430 \\ 4.137 \\ 4.700 \\ 4.457 \\ 9.689 \\ 9.298 \\ 9.363 \\ 14.800 \\ 14.370 \\ 14.420 \\ 19.490 \\ 19.670 \\ 19.580 \end{bmatrix} \quad \sigma_d = \begin{bmatrix} 3.140 \\ 6.163 \\ 9.009 \\ 5.167 \\ 10.020 \\ 14.600 \\ 10.030 \\ 19.670 \\ 30.000 \\ 10.020 \\ 14.630 \\ 29.990 \\ 14.760 \\ 19.760 \\ 40.360 \end{bmatrix} \quad \sigma_B = \begin{bmatrix} 10.090 \\ 13.320 \\ 16.300 \\ 17.580 \\ 24.120 \\ 27.970 \\ 39.090 \\ 47.570 \\ 58.090 \\ 54.430 \\ 57.730 \\ 73.250 \\ 73.220 \\ 78.770 \\ 99.110 \end{bmatrix} \quad M_R = \begin{bmatrix} 40259.4 \\ 38319.0 \\ 38086.8 \\ 46267.4 \\ 50298.6 \\ 59793.2 \\ 79378.6 \\ 78820.4 \\ 52826.2 \\ 106848.0 \\ 85619.6 \\ 48790.2 \\ 60201.2 \\ 46223.4 \\ 51072.4 \end{bmatrix}$$

σ_3 = mean confining stress
σ_d = mean deviator stress
σ_B = mean bulk stress
M_R = resilient modulus
p_a = atmospheric pressure = 14.6959 psi

Dan Seely
9/12/2023

$$M_{R.1}\left(\sigma_B, K_1, K_2\right) := K_1 \cdot {\sigma_B}^{K_2}$$

Equation 1
AASHTO Publication No. FHWA-RD-97-083

$K_1 = 30706.189$

$K_2 = 0.1781$

Equation 1 fitting parameters

${R_1}^2 = 0.1566$

Coefficient of determination

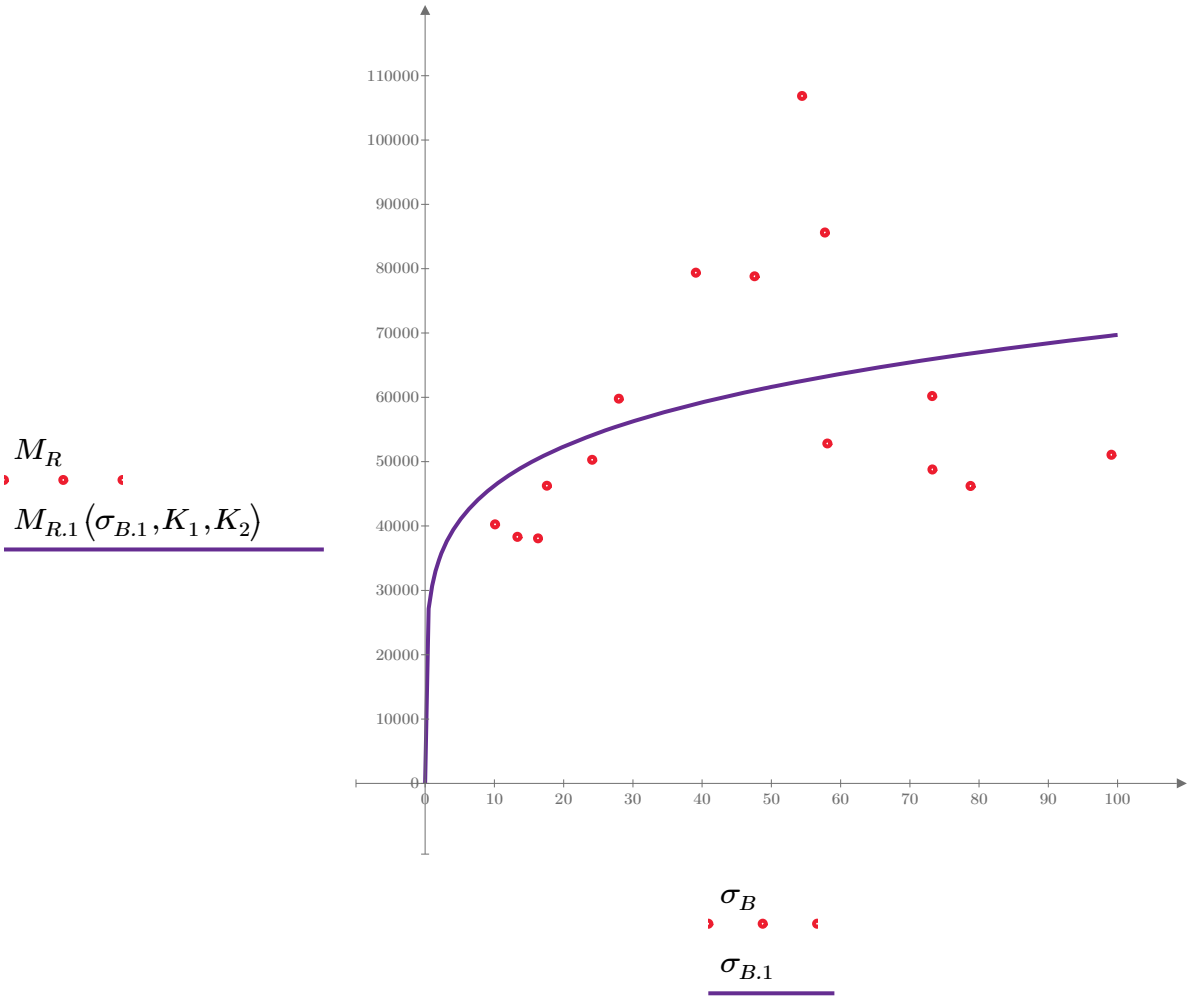

Figure 1. Plot of the test data (red points) vs. the fitted Equation 1 model (purple line).

Dan Seely
9/12/2023

$M_{R.2}(\sigma_d, K_3, K_4) := K_3 \cdot \sigma_d^{K_4}$ Equation 2
AASHTO Publication No. FHWA-RD-97-083

$K_3 = 50162.760$

$K_4 = 0.0624$ Equation 2 fitting parameters

$R_2^2 = 0.0193$ Coefficient of determination

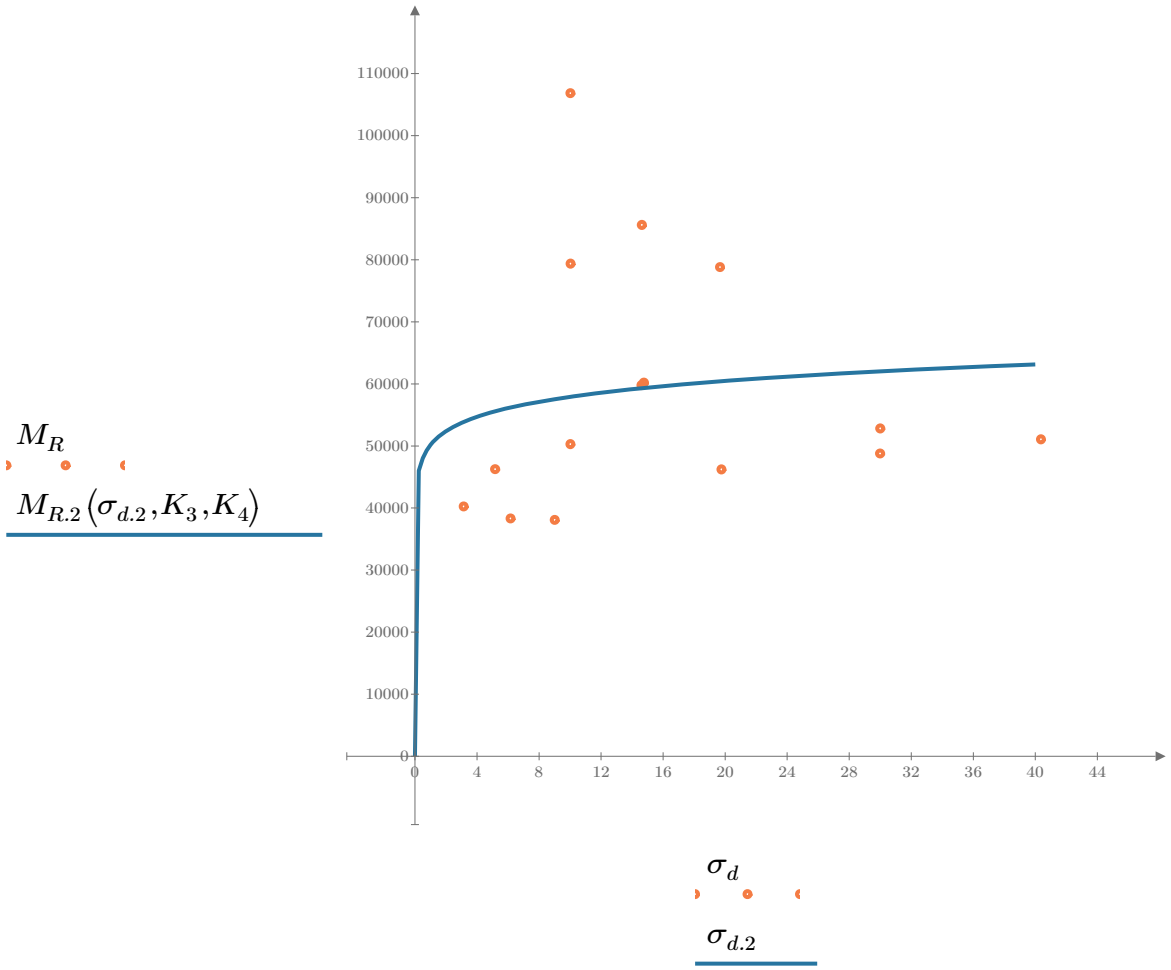

Figure 2. Plot of the test data (orange points) vs. the fitted Equation 2 model (blue line).

Dan Seely
9/12/2023

$$M_{R.3}\left(\sigma_d,\sigma_3,K_5,K_6,K_7\right):=K_5\cdot{\sigma_d}^{K_6}\cdot\left(1+\sigma_3\right)^{K_7}$$

Equation 3 AASHTO Publication No. FHWA-RD-97-083

$K_5=44133.644$

$K_6=-0.2551$ Equation 3 fitting parameters

$K_7=0.4172$

${R_3}^2=0.3372$ Coefficient of determination

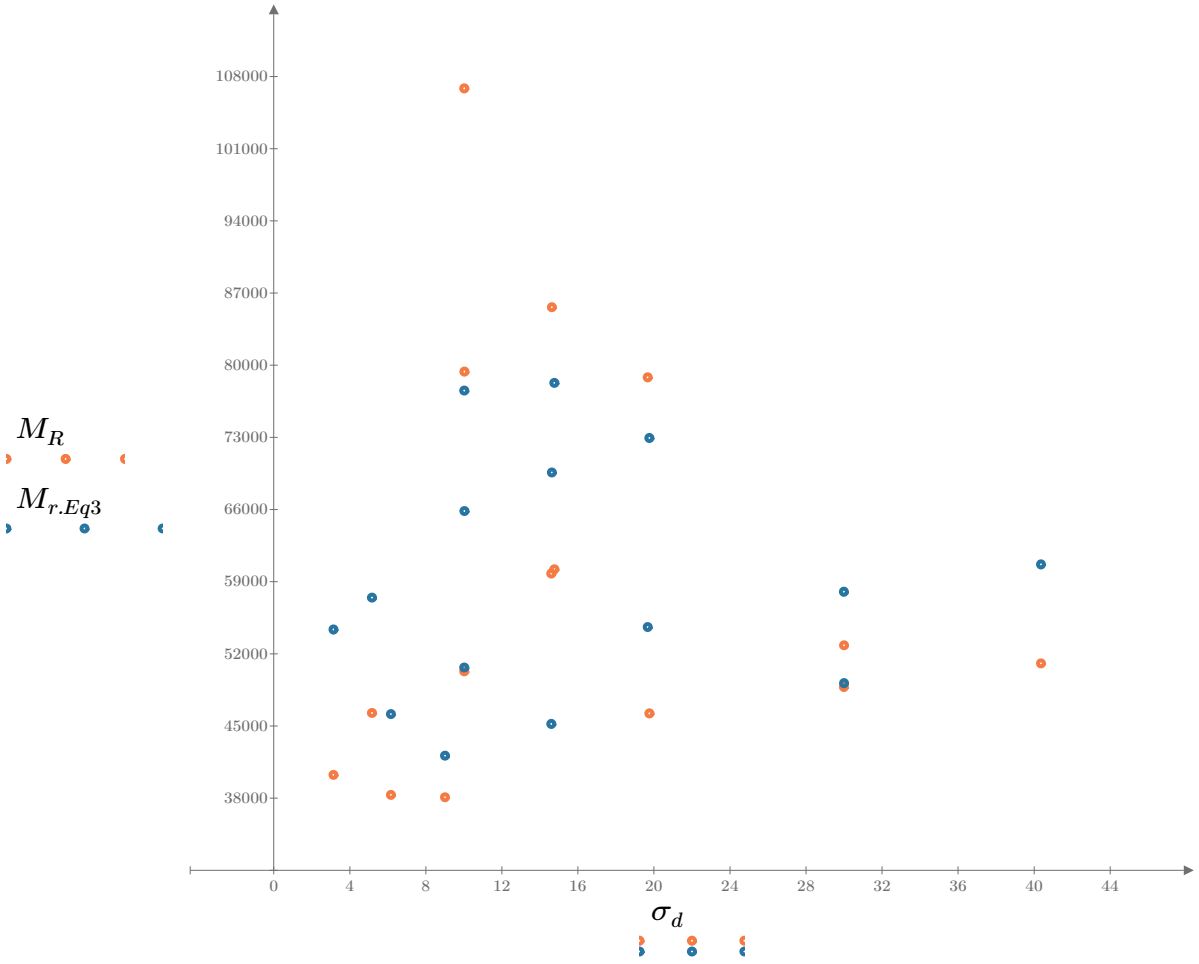

Figure 3. Plot of the test data (orange points) vs. the fitted Equation 3 model (blue points).

Dan Seely
9/12/2023

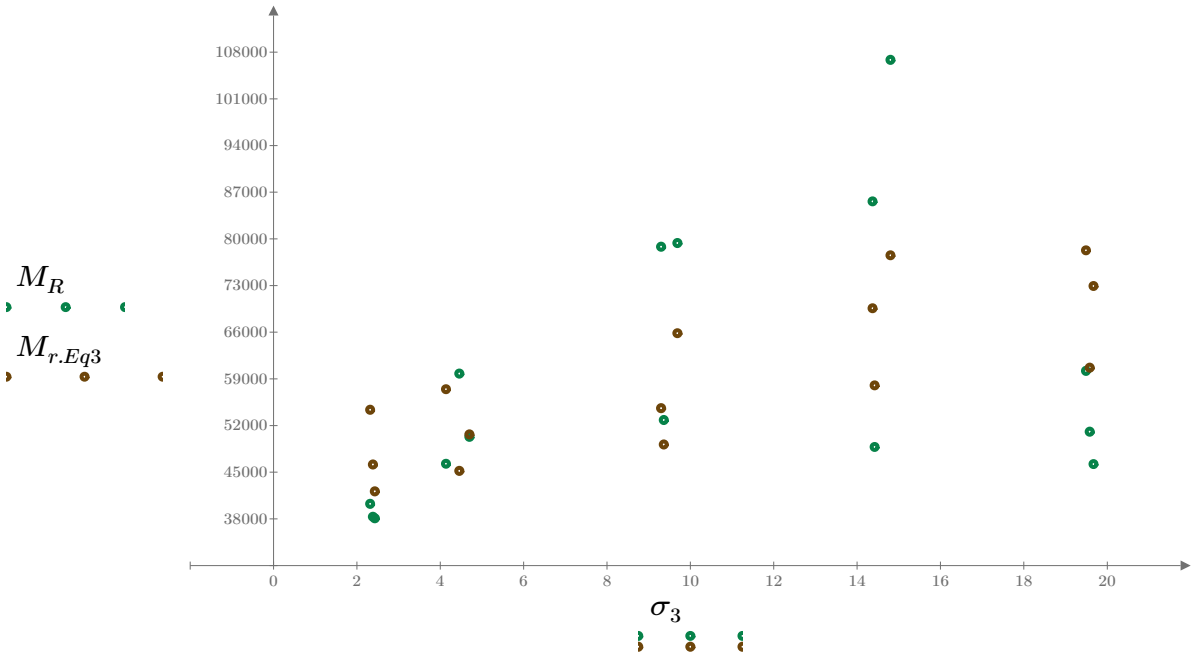

Figure 4. Plot of the test data (green points) vs. the fitted Equation 3 model (brown points).

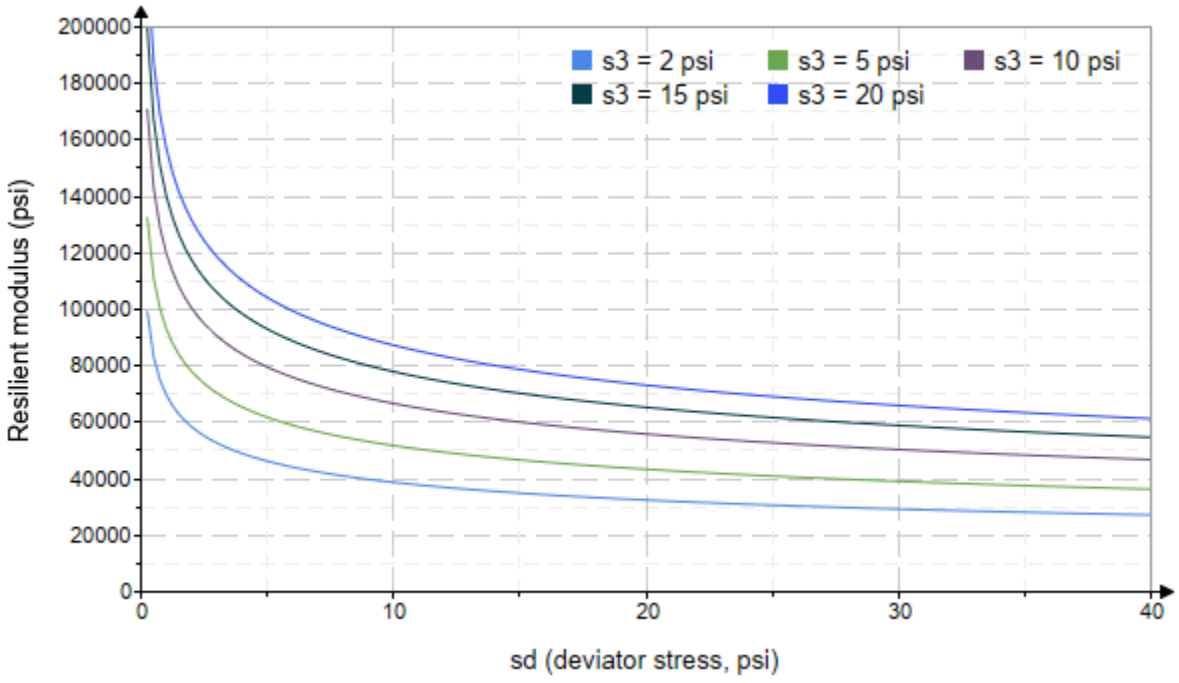

Figure 5. Plot of the fitted Equation 3 model for various confining stresses.

Dan Seely
9/12/2023

$$M_{R.4}\left(\sigma_B,\sigma_d,K_8,K_9,K_{10}\right) := K_8 \cdot p_a \left(\frac{\sigma_B}{p_a}\right)^{K_9} \cdot \left(\frac{\sigma_d}{p_a}\right)^{K_{10}}$$

Equation 4 AASHTO Publication No. FHWA-RD-97-083

$K_8 = 2118.807$

$K_9 = 0.5899$ Equation 4 fitting parameters

$K_{10} = -0.4837$

$R_4^{\,2} = 0.3882$ Coefficient of determination

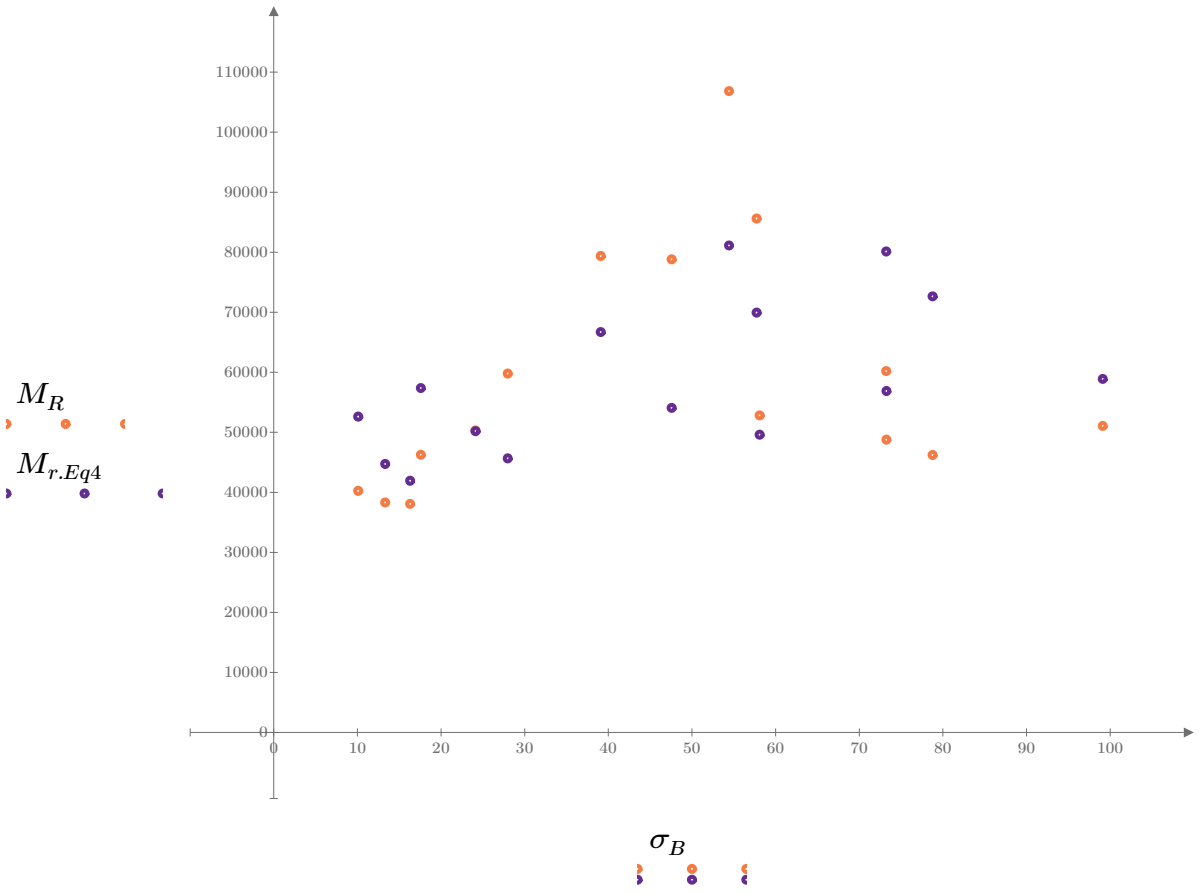

Figure 6. Plot of the test data (orange points) vs. the fitted Equation 4 model (purple points).

Dan Seely
9/12/2023

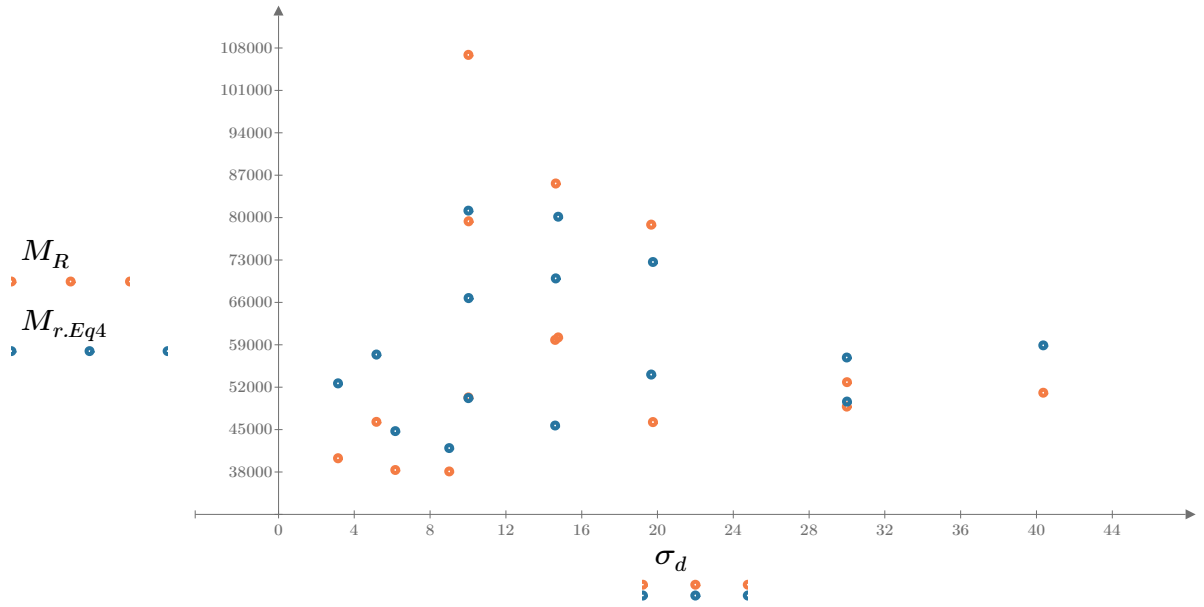

Figure 7. Plot of the test data (orange points) vs. the fitted Equation 4 model (blue points).

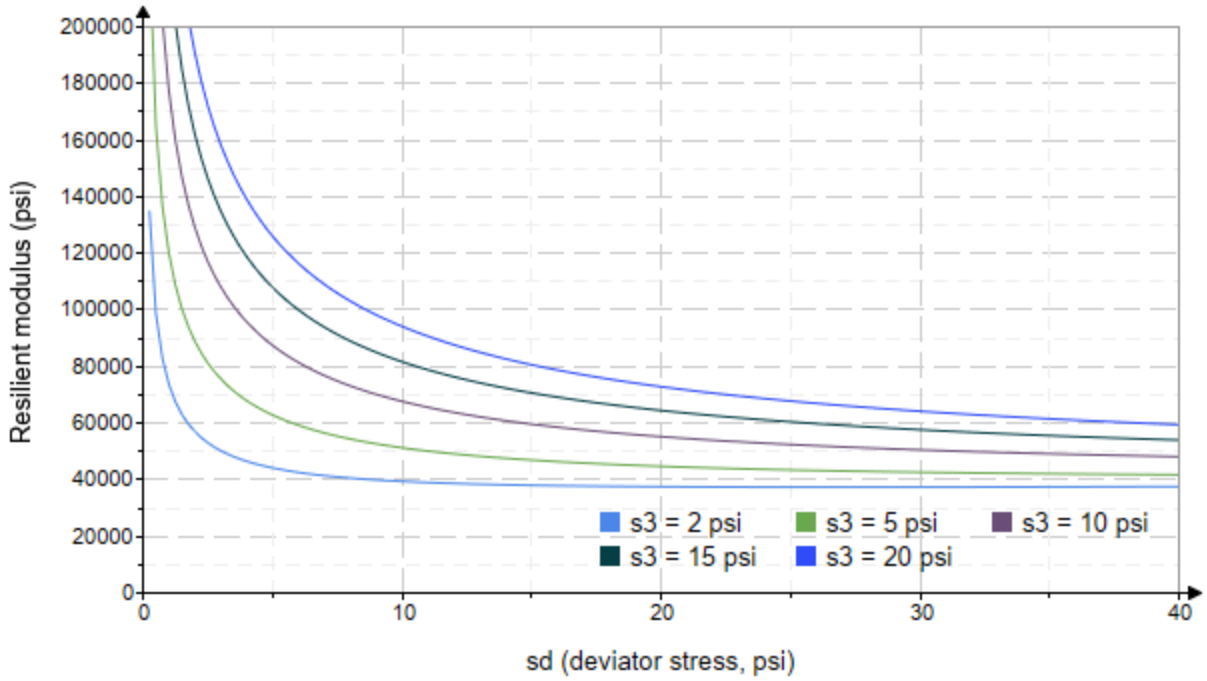

Figure 8. Plot of the fitted Equation 4 model for various confining stresses.

Dan Seely
9/12/2023

$SampleNo := \text{“B2–43”}$

$Treatment = \text{“AD”}$

$S = 3.541$ Degree of Saturation (%)

Test Sequence : Base/Subbase

Test summary data (psi) :

$$\sigma_3 = \begin{bmatrix} 2.875 \\ 2.884 \\ 2.874 \\ 4.595 \\ 4.591 \\ 4.616 \\ 9.631 \\ 9.616 \\ 9.626 \\ 14.660 \\ 14.660 \\ 14.640 \\ 19.670 \\ 19.660 \\ 19.670 \end{bmatrix} \quad \sigma_d = \begin{bmatrix} 3.185 \\ 6.079 \\ 8.966 \\ 5.084 \\ 9.828 \\ 14.450 \\ 9.985 \\ 19.830 \\ 30.350 \\ 9.911 \\ 14.850 \\ 30.190 \\ 14.830 \\ 20.010 \\ 40.080 \end{bmatrix} \quad \sigma_B = \begin{bmatrix} 11.810 \\ 14.730 \\ 17.590 \\ 18.870 \\ 23.600 \\ 28.300 \\ 38.880 \\ 48.680 \\ 59.220 \\ 53.900 \\ 58.820 \\ 74.110 \\ 73.830 \\ 78.980 \\ 99.100 \end{bmatrix} \quad M_R = \begin{bmatrix} 29894.4 \\ 31584.4 \\ 35110.0 \\ 30912.8 \\ 39503.2 \\ 44259.6 \\ 55853.2 \\ 62883.2 \\ 55355.4 \\ 52950.0 \\ 54826.0 \\ 55479.6 \\ 49500.0 \\ 52954.2 \\ 68352.2 \end{bmatrix}$$

σ_3 = mean confining stress
σ_d = mean deviator stress
σ_B = mean bulk stress
M_R = resilient modulus
p_a = atmospheric pressure = 14.6959 psi

Dan Seely
9/12/2023

$$M_{R.1}\left(\sigma_B, K_1, K_2\right) := K_1 \cdot {\sigma_B}^{K_2}$$

Equation 1
AASHTO Publication No. FHWA-RD-97-083

$K_1 = 13747.084$

$K_2 = 0.3361$

Equation 1 fitting parameters

${R_1}^2 = 0.7930$

Coefficient of determination

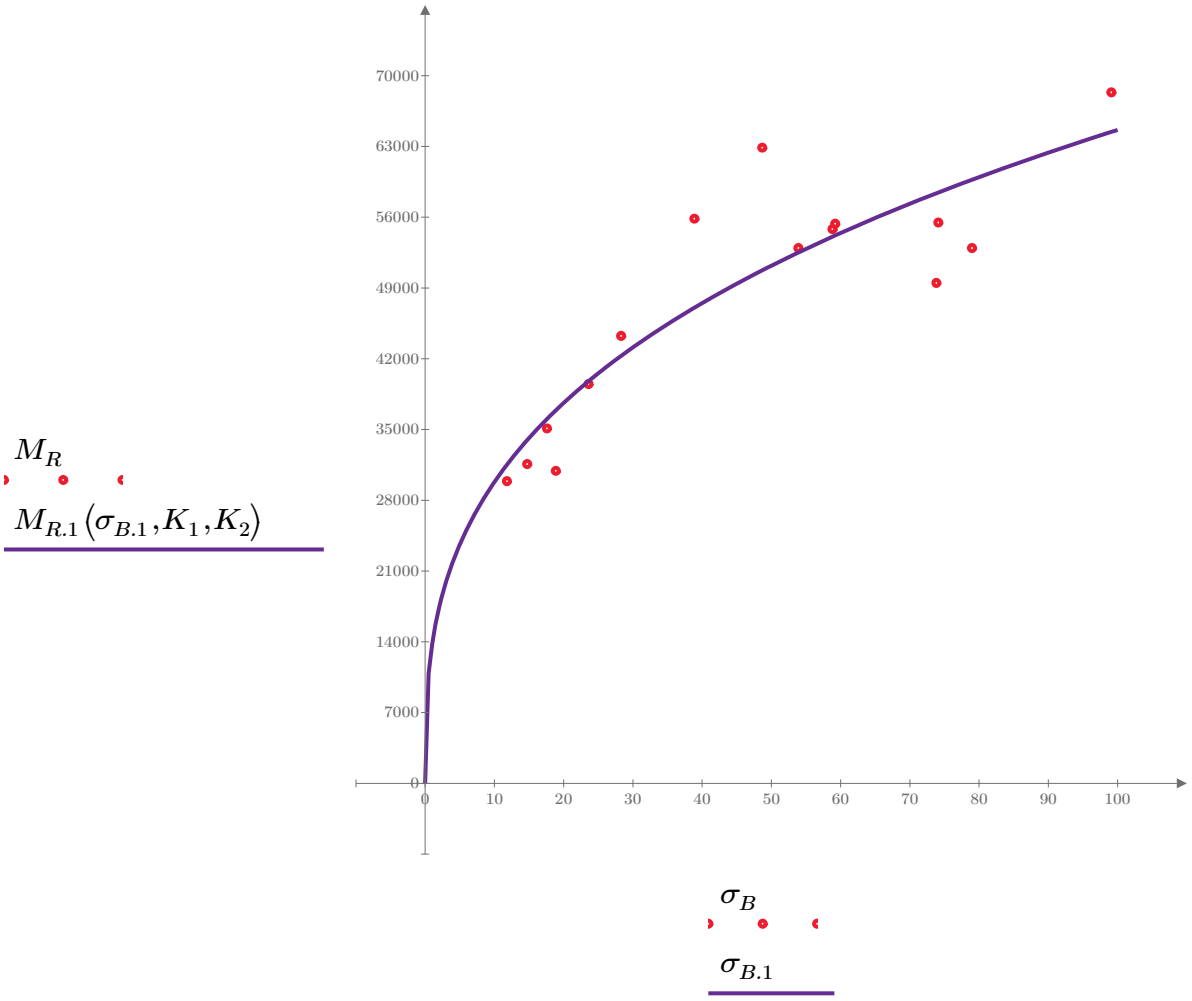

Figure 1. Plot of the test data (red points) vs. the fitted Equation 1 model (purple line).

Dan Seely
9/12/2023

$$M_{R.2}(\sigma_d, K_3, K_4) := K_3 \cdot \sigma_d^{K_4}$$

Equation 2
AASHTO Publication No. FHWA-RD-97-083

$K_3 = 21590.123$

$K_4 = 0.3053$

Equation 2 fitting parameters

$R_2^2 = 0.7236$

Coefficient of determination

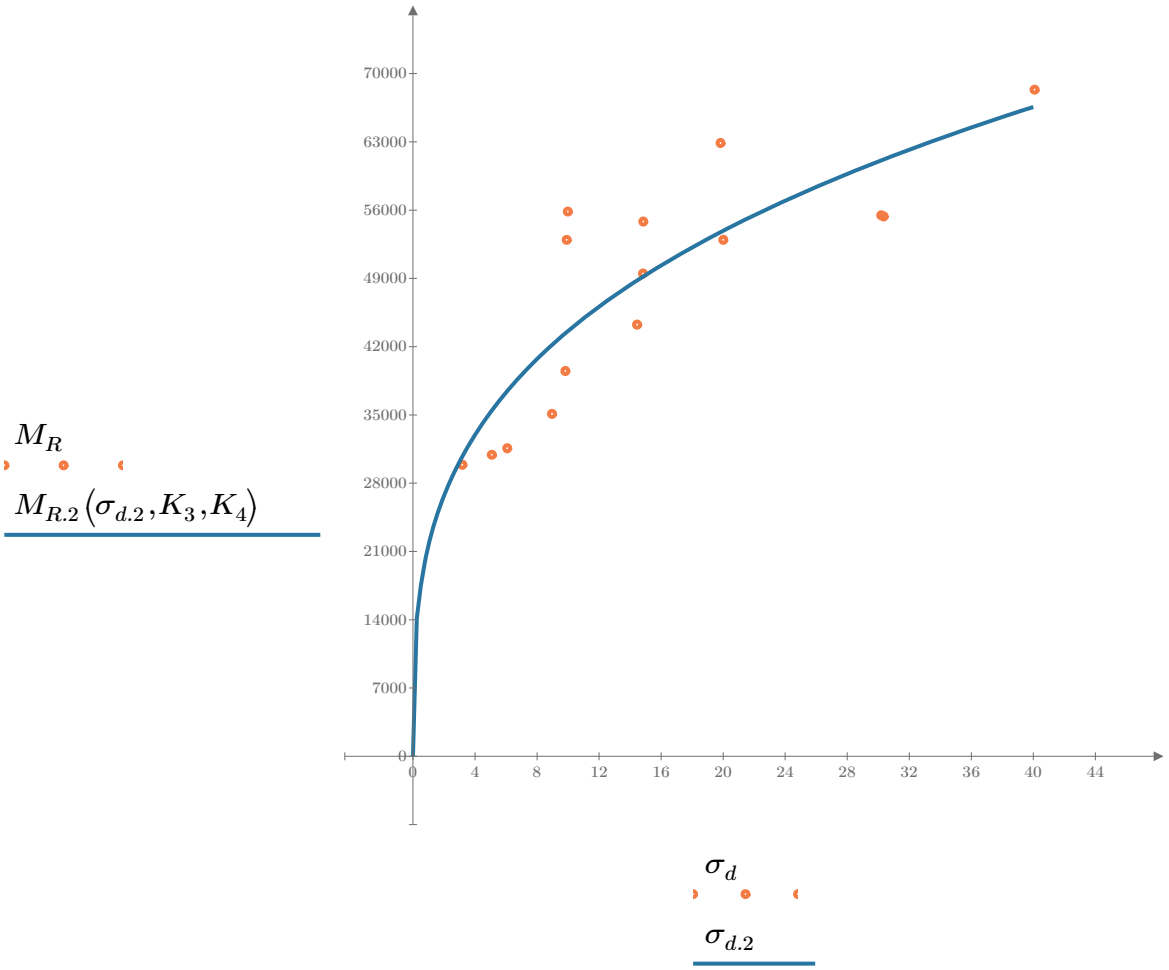

Figure 2. Plot of the test data (orange points) vs. the fitted Equation 2 model (blue line).

Dan Seely
9/12/2023

$$M_{R.3}\left(\sigma_d,\sigma_3,K_5,K_6,K_7\right):=K_5\cdot{\sigma_d}^{K_6}\cdot\left(1+\sigma_3\right)^{K_7}$$

Equation 3 AASHTO Publication No. FHWA-RD-97-083

$K_5=19350.683$

$K_6=0.1959$ Equation 3 fitting parameters

$K_7=0.1716$

${R_3}^2=0.8154$ Coefficient of determination

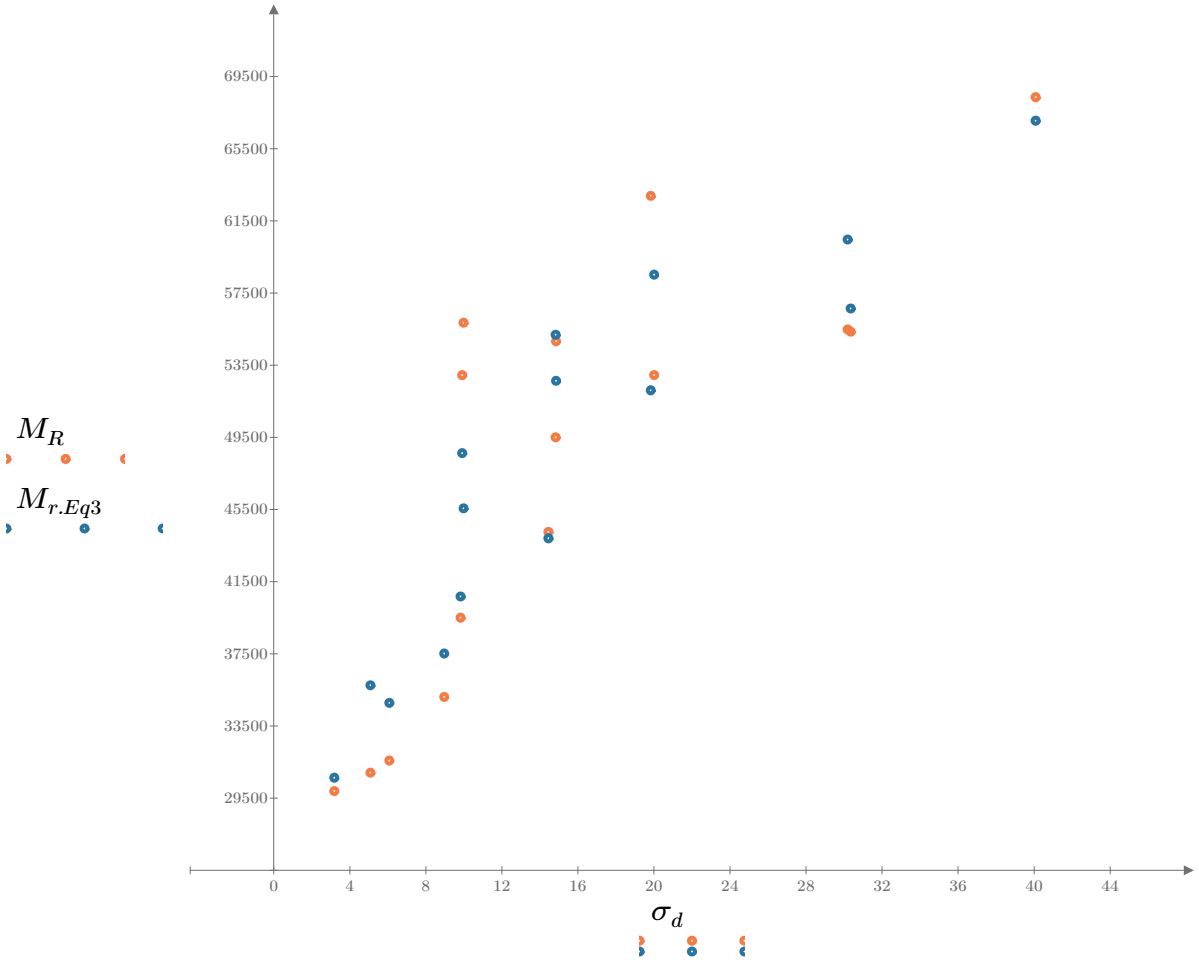

Figure 3. Plot of the test data (orange points) vs. the fitted Equation 3 model (blue points).

Dan Seely
9/12/2023

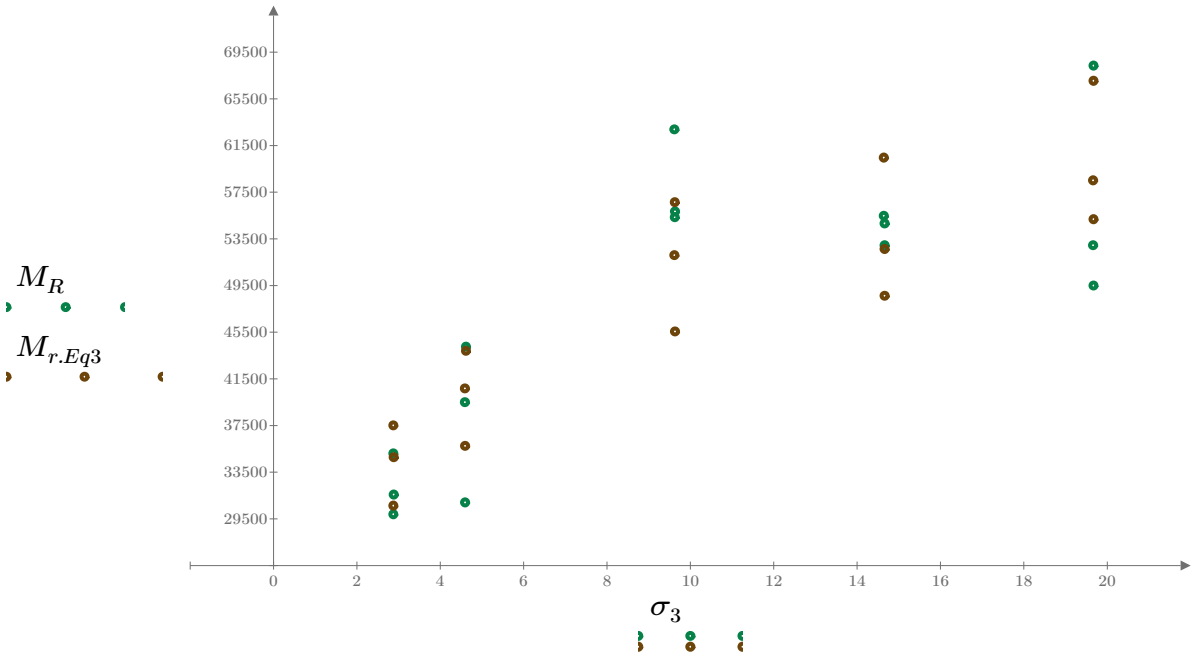

Figure 4. Plot of the test data (green points) vs. the fitted Equation 3 model (brown points).

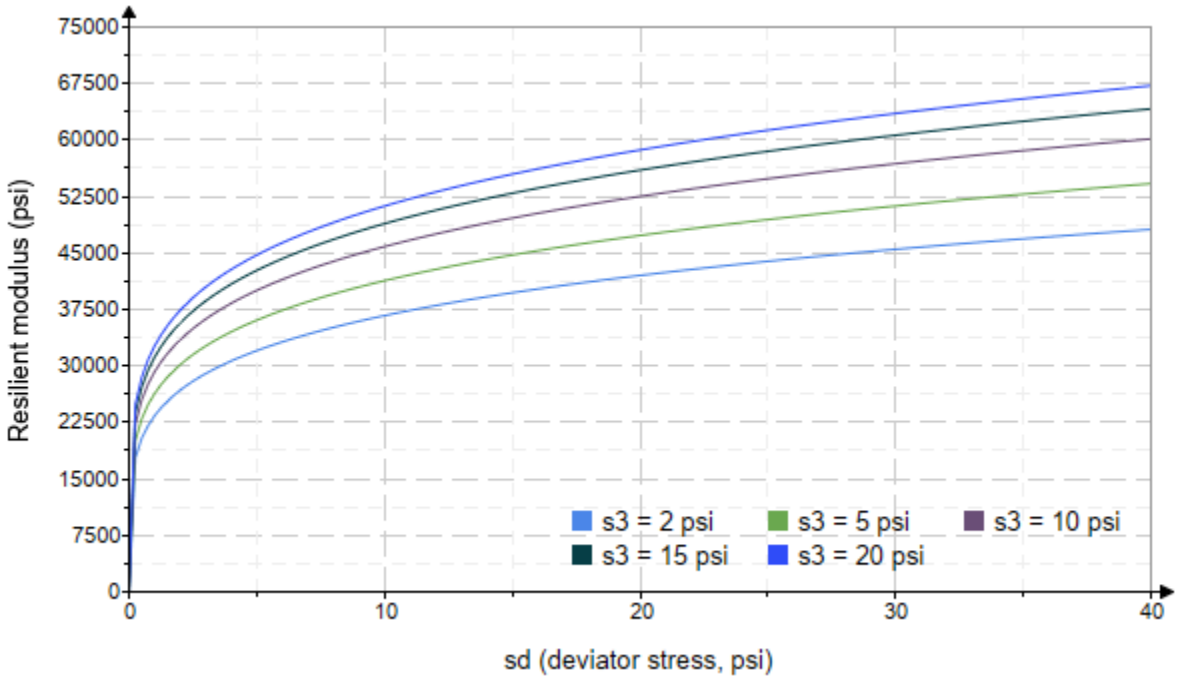

Figure 5. Plot of the fitted Equation 3 model for various confining stresses.

Dan Seely
9/12/2023

$$M_{R.4}\left(\sigma_B,\sigma_d,K_8,K_9,K_{10}\right) := K_8 \cdot p_a \left(\frac{\sigma_B}{p_a}\right)^{K_9} \cdot \left(\frac{\sigma_d}{p_a}\right)^{K_{10}}$$

Equation 4 AASHTO Publication No. FHWA-RD-97-083

$K_8 = 2584.284$

$K_9 = 0.2344$ Equation 4 fitting parameters

$K_{10} = 0.1137$

$R_4^{\,2} = 0.8187$ Coefficient of determination

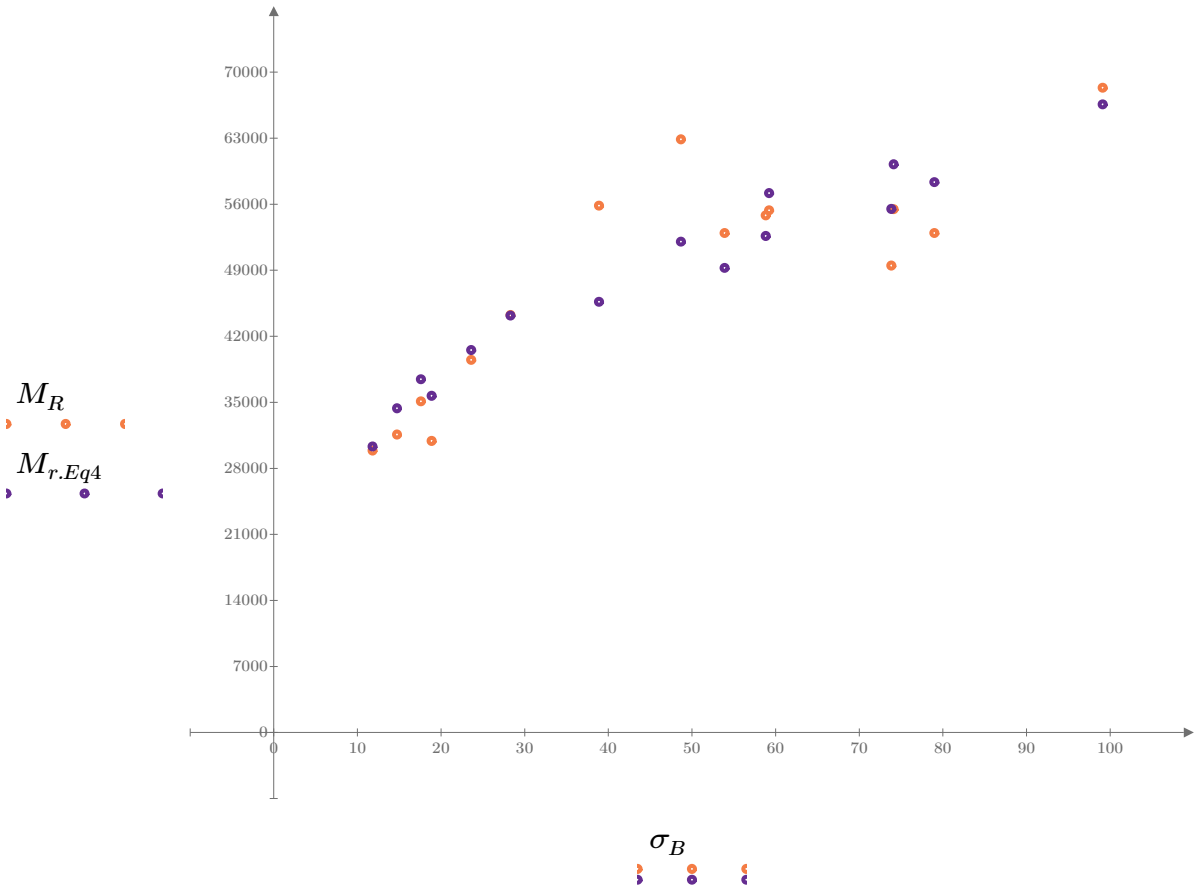

Figure 6. Plot of the test data (orange points) vs. the fitted Equation 4 model (purple points).

Dan Seely
9/12/2023

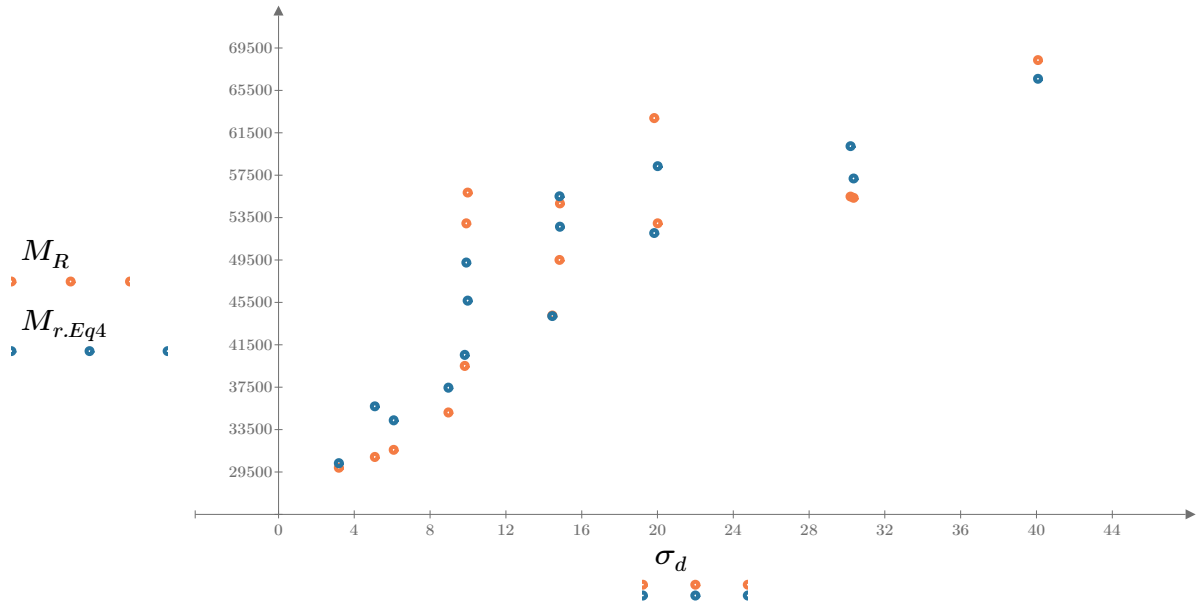

Figure 7. Plot of the test data (orange points) vs. the fitted Equation 4 model (blue points).

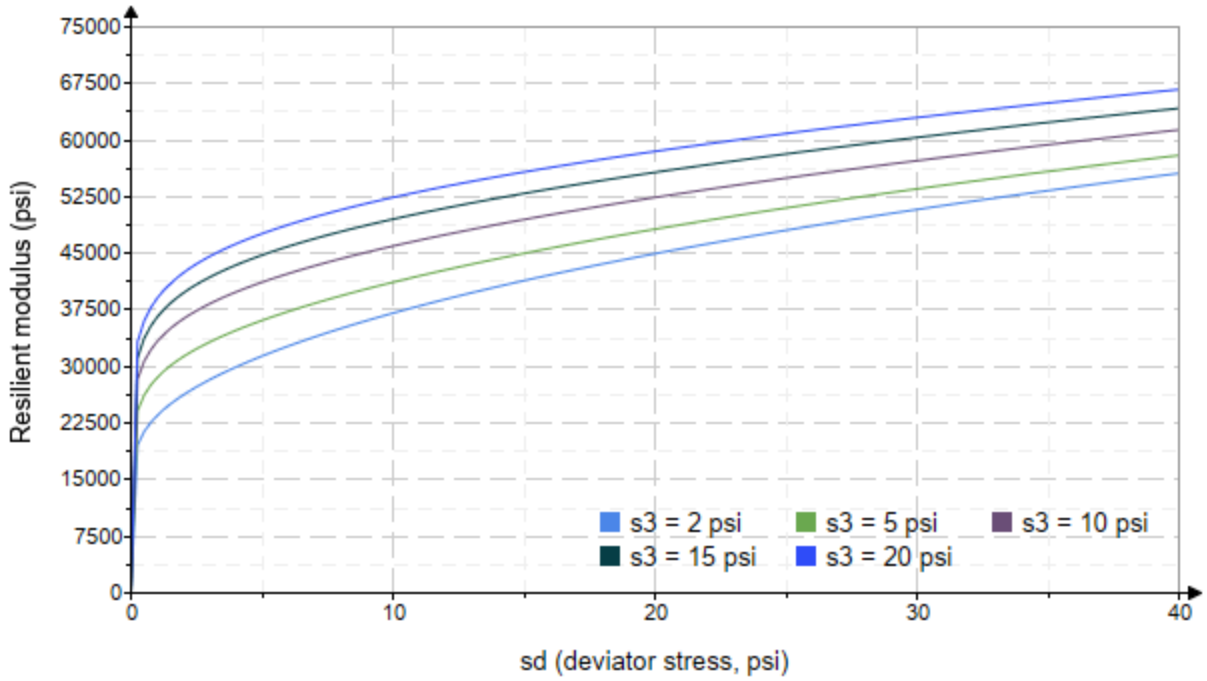

Figure 8. Plot of the fitted Equation 4 model for various confining stresses.

Dan Seely
9/12/2023

$SampleNo :=$ "B2−44"

$Treatment =$ "AD"

$S = 3.455$ Degree of Saturation (%)

Test Sequence : Base/Subbase

Test summary data (psi) :

$$\sigma_3 = \begin{bmatrix} 2.738 \\ 2.733 \\ 2.690 \\ 4.603 \\ 4.580 \\ 4.596 \\ 9.580 \\ 9.612 \\ 9.576 \\ 14.620 \\ 14.640 \\ 14.600 \\ 19.680 \\ 19.670 \\ 19.670 \end{bmatrix} \quad \sigma_d = \begin{bmatrix} 3.238 \\ 6.115 \\ 8.935 \\ 5.124 \\ 9.785 \\ 14.660 \\ 9.903 \\ 19.520 \\ 30.020 \\ 9.956 \\ 14.520 \\ 30.200 \\ 14.490 \\ 19.690 \\ 40.260 \end{bmatrix} \quad \sigma_B = \begin{bmatrix} 11.450 \\ 14.320 \\ 17.010 \\ 18.930 \\ 23.520 \\ 28.440 \\ 38.640 \\ 48.350 \\ 58.750 \\ 53.800 \\ 58.450 \\ 74.000 \\ 73.530 \\ 78.690 \\ 99.270 \end{bmatrix} \quad M_R = \begin{bmatrix} 52603.0 \\ 49173.2 \\ 50368.4 \\ 58768.8 \\ 58381.0 \\ 57373.4 \\ 67365.6 \\ 53109.0 \\ 59636.8 \\ 56293.8 \\ 55443.8 \\ 70300.4 \\ 55107.2 \\ 66377.8 \\ 65113.2 \end{bmatrix}$$

σ_3 = mean confining stress
σ_d = mean deviator stress
σ_B = mean bulk stress
M_R = resilient modulus
p_a = atmospheric pressure = 14.6959 psi

Dan Seely
9/12/2023

$$M_{R.1}\left(\sigma_B, K_1, K_2\right) := K_1 \cdot {\sigma_B}^{K_2}$$

Equation 1
AASHTO Publication No. FHWA-RD-97-083

$K_1 = 40790.097$

$K_2 = 0.0978$

Equation 1 fitting parameters

${R_1}^2 = 0.3757$

Coefficient of determination

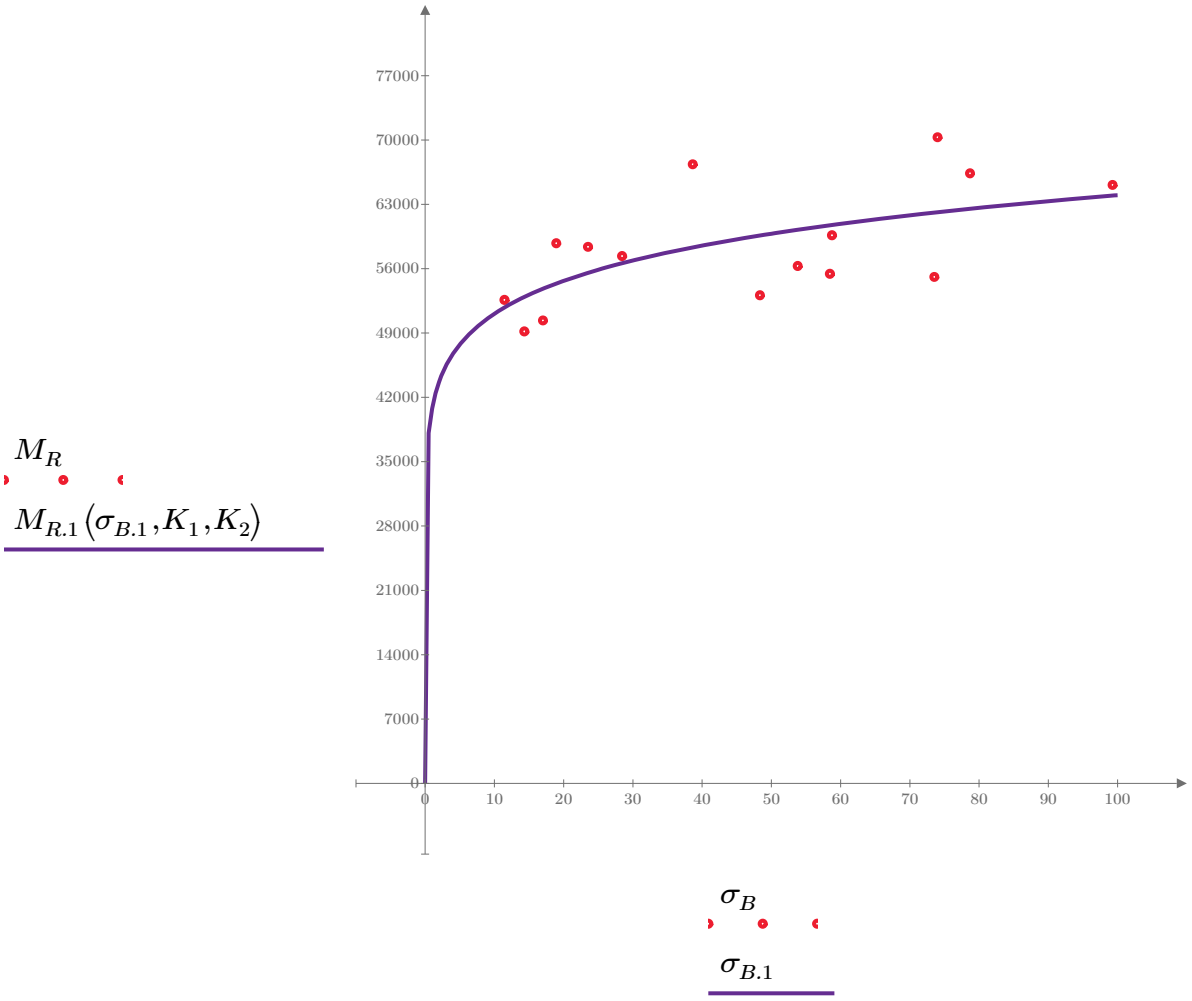

Figure 1. Plot of the test data (red points) vs. the fitted Equation 1 model (purple line).

Dan Seely
9/12/2023

$$M_{R.2}\left(\sigma_d, K_3, K_4\right) := K_3 \cdot {\sigma_d}^{K_4}$$

Equation 2
AASHTO Publication No. FHWA-RD-97-083

$K_3 = 46345.947$

$K_4 = 0.0899$

Equation 2 fitting parameters

${R_2}^2 = 0.3195$

Coefficient of determination

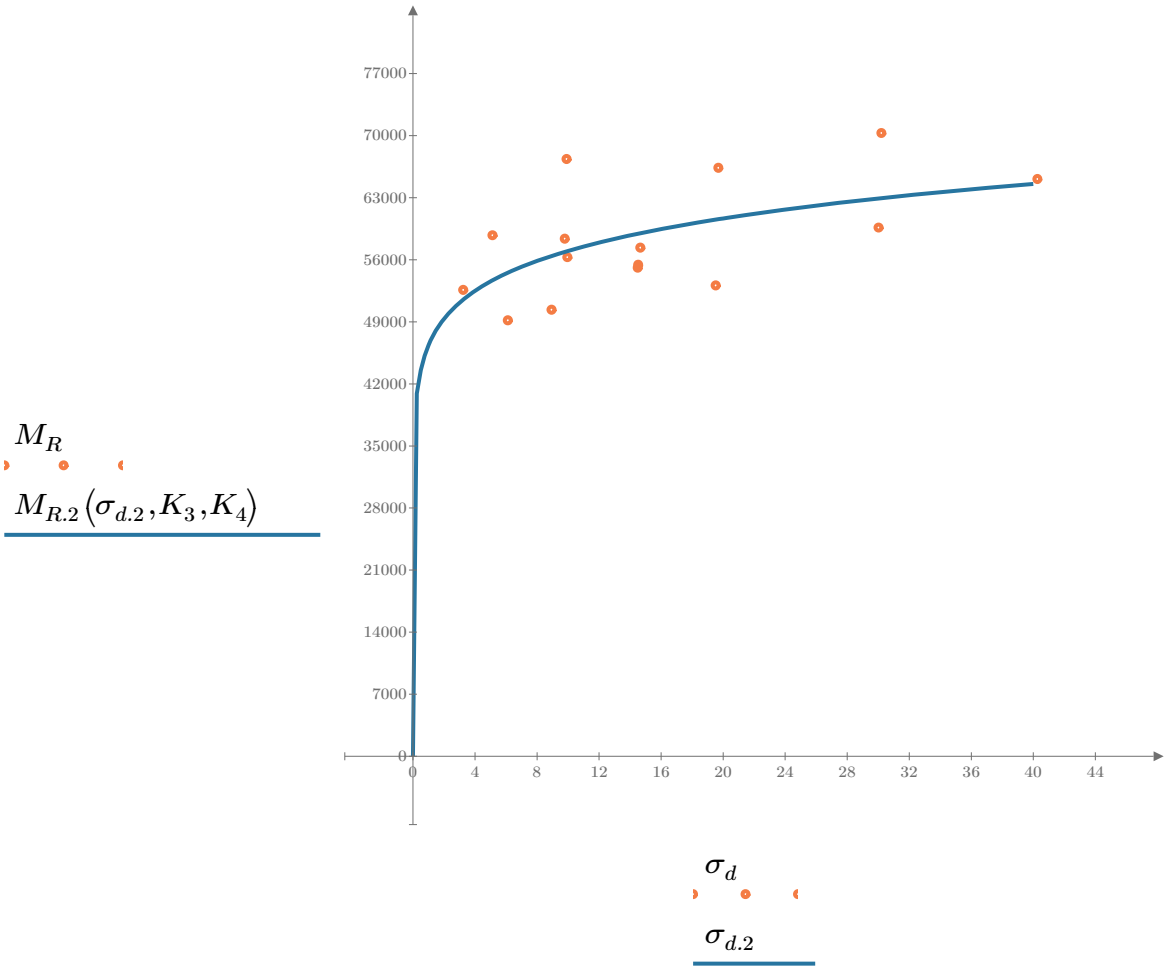

Figure 2. Plot of the test data (orange points) vs. the fitted Equation 2 model (blue line).

Dan Seely
9/12/2023

$$M_{R.3}\left(\sigma_d,\sigma_3,K_5,K_6,K_7\right):=K_5\cdot{\sigma_d}^{K_6}\cdot\left(1+\sigma_3\right)^{K_7}$$

Equation 3 AASHTO Publication No. FHWA-RD-97-083

$K_5=44880.187$

$K_6=0.0478$ Equation 3 fitting parameters

$K_7=0.0621$

${R_3}^2=0.3882$ Coefficient of determination

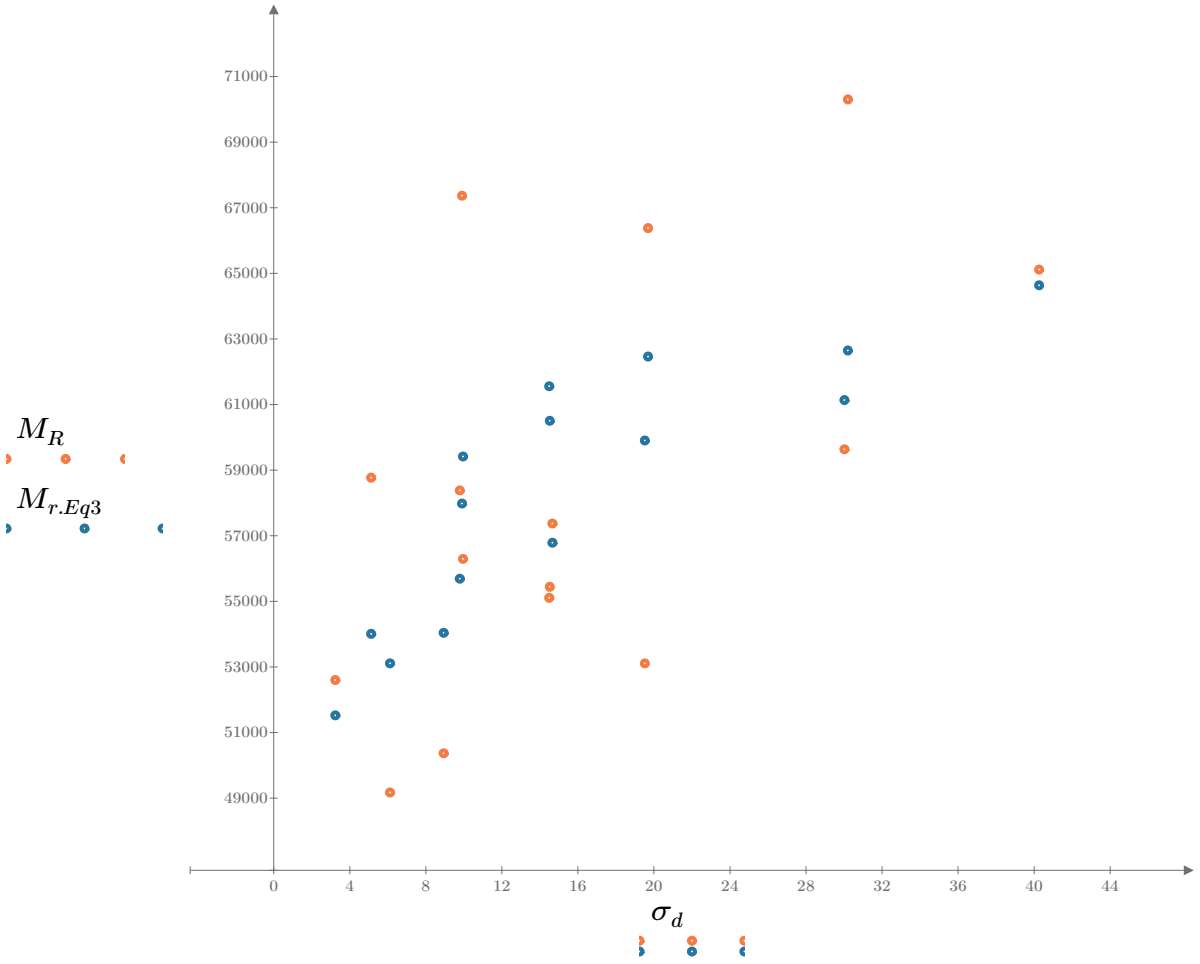

Figure 3. Plot of the test data (orange points) vs. the fitted Equation 3 model (blue points).

Dan Seely
9/12/2023

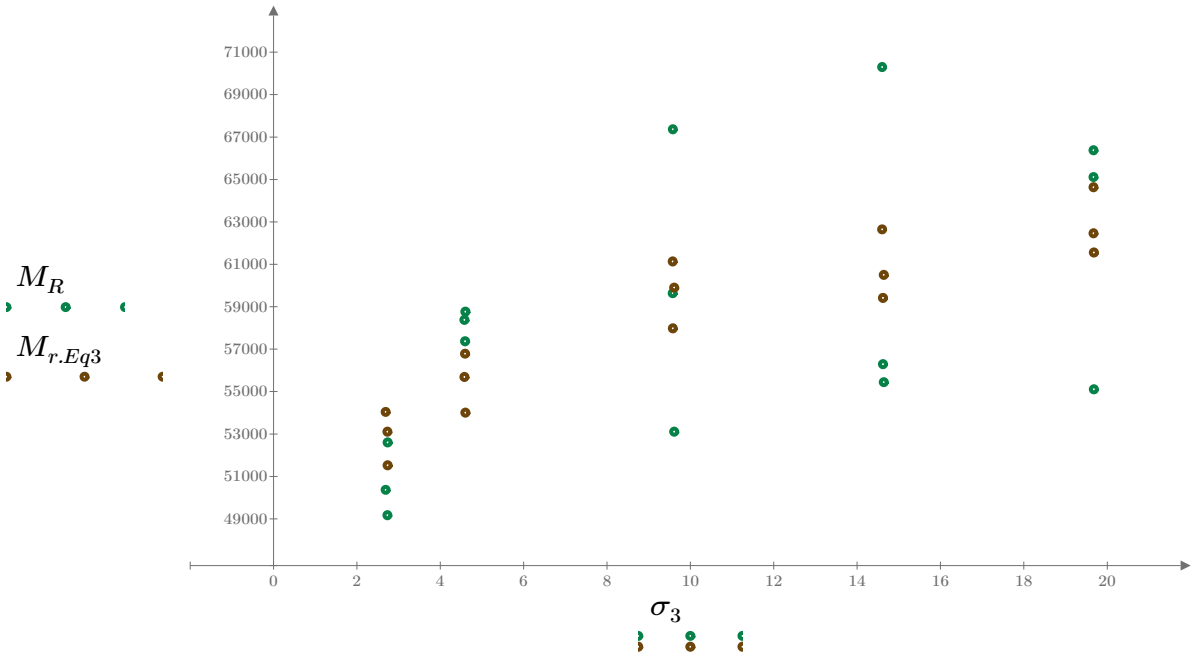

Figure 4. Plot of the test data (green points) vs. the fitted Equation 3 model (brown points).

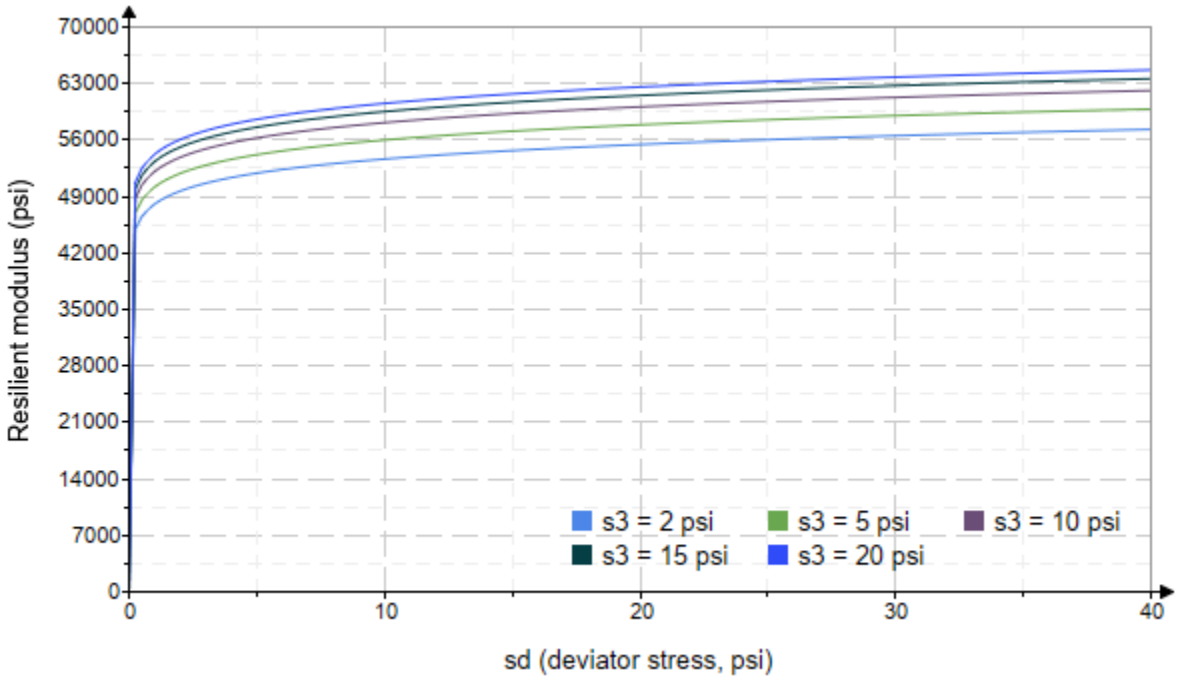

Figure 5. Plot of the fitted Equation 3 model for various confining stresses.

Dan Seely
9/12/2023

$$M_{R.4}\left(\sigma_B,\sigma_d,K_8,K_9,K_{10}\right):=K_8\cdot p_a\left(\frac{\sigma_B}{p_a}\right)^{K_9}\cdot\left(\frac{\sigma_d}{p_a}\right)^{K_{10}}$$

Equation 4 AASHTO Publication No. FHWA-RD-97-083

$K_8=3689.912$

$K_9=0.0782$ Equation 4 fitting parameters

$K_{10}=0.0228$

$R_4{}^2=0.3810$ Coefficient of determination

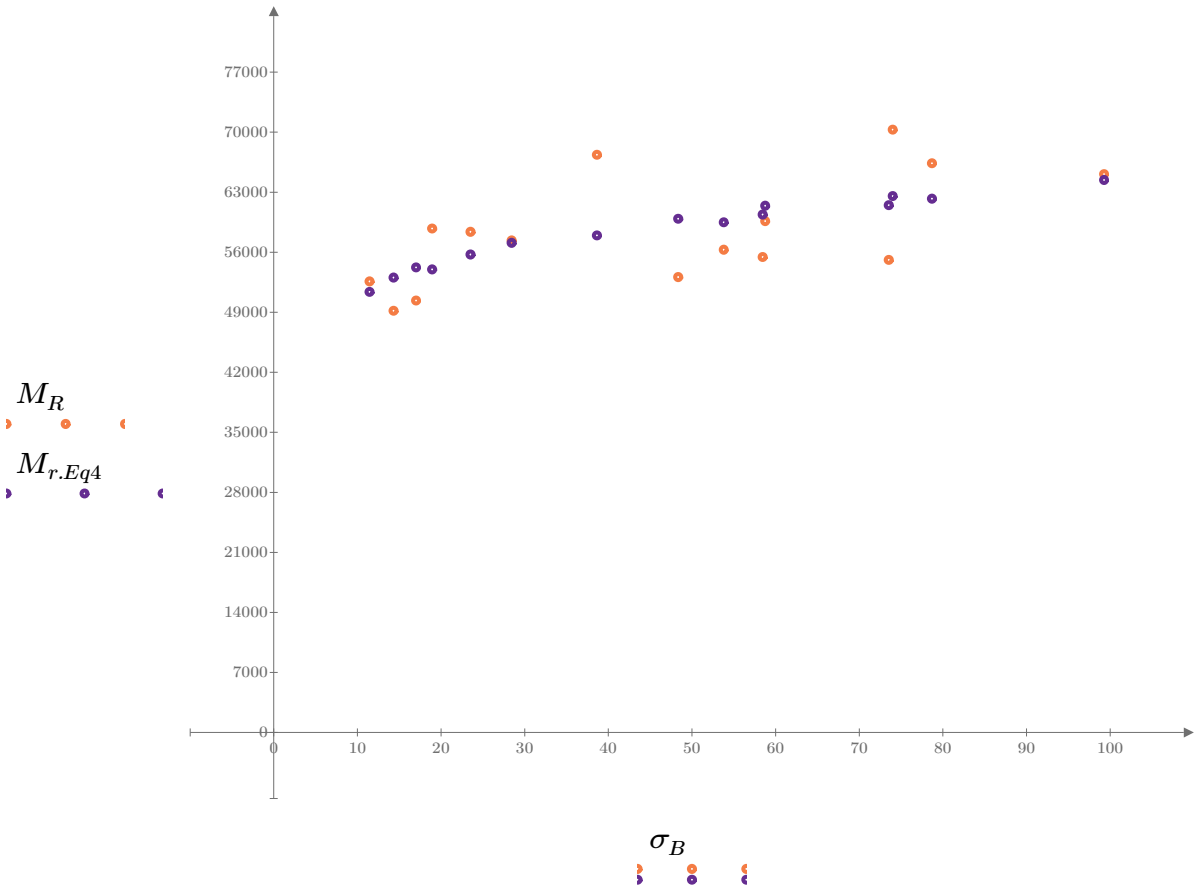

Figure 6. Plot of the test data (orange points) vs. the fitted Equation 4 model (purple points).

Dan Seely
9/12/2023

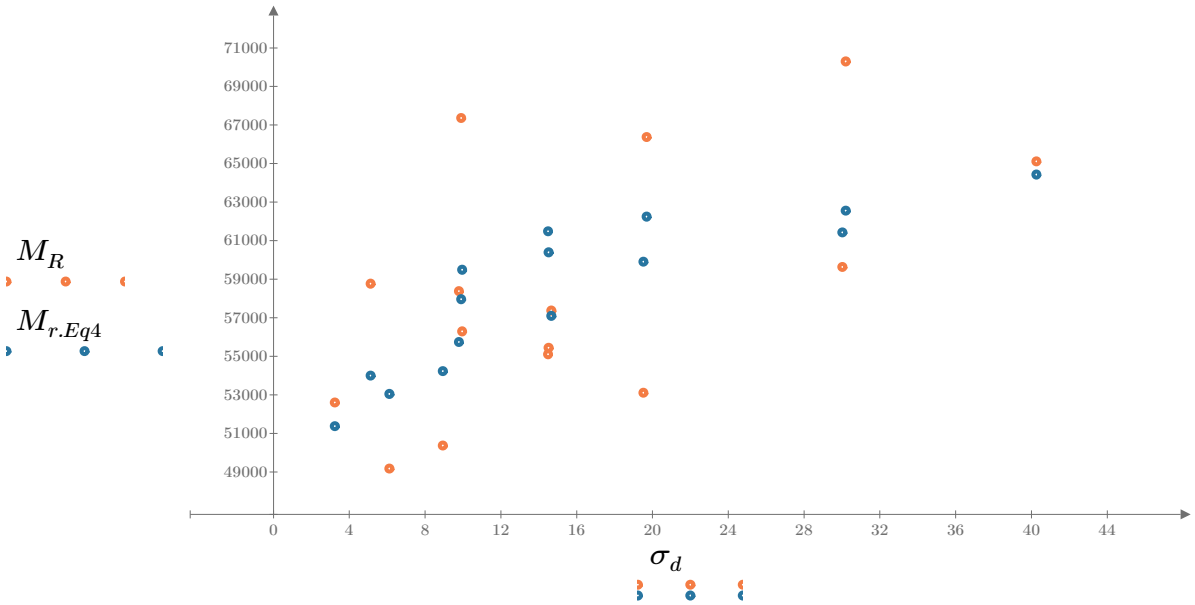

Figure 7. Plot of the test data (orange points) vs. the fitted Equation 4 model (blue points).

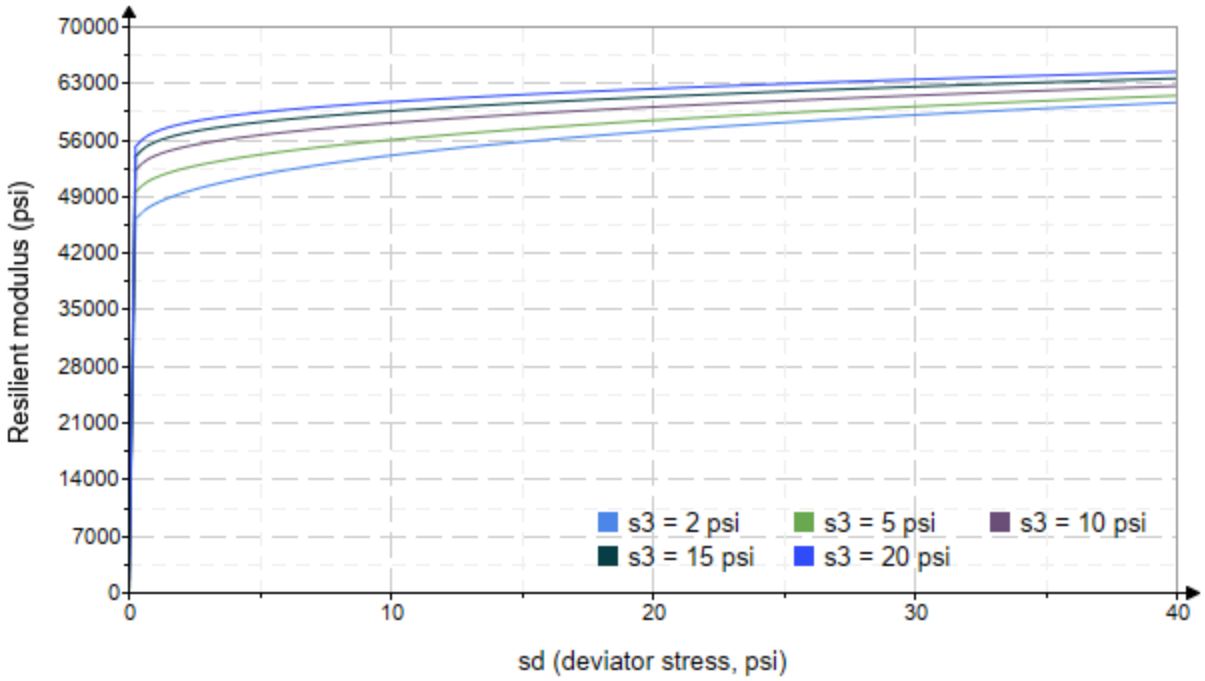

Figure 8. Plot of the fitted Equation 4 model for various confining stresses.

Dan Seely
9/12/2023

$SampleNo := \text{“B2–45”}$

$Treatment = \text{“AD”}$

$S = 3.449$ Degree of Saturation (%)

Test Sequence : Base/Subbase

Test summary data (psi) :

$$\sigma_3 = \begin{bmatrix} 2.526 \\ 2.154 \\ 2.071 \\ 4.406 \\ 3.647 \\ 3.802 \\ 9.120 \\ 9.525 \\ 9.365 \\ 14.290 \\ 14.450 \\ 14.330 \\ 19.280 \\ 19.460 \\ 19.460 \end{bmatrix} \quad \sigma_d = \begin{bmatrix} 3.169 \\ 6.075 \\ 9.164 \\ 5.153 \\ 10.060 \\ 14.750 \\ 9.989 \\ 19.740 \\ 30.160 \\ 9.950 \\ 14.700 \\ 30.250 \\ 14.790 \\ 19.880 \\ 40.530 \end{bmatrix} \quad \sigma_B = \begin{bmatrix} 10.750 \\ 12.540 \\ 15.380 \\ 18.370 \\ 21.000 \\ 26.160 \\ 37.350 \\ 48.320 \\ 58.250 \\ 52.820 \\ 58.060 \\ 73.250 \\ 72.630 \\ 78.250 \\ 98.910 \end{bmatrix} \quad M_R = \begin{bmatrix} 26364.6 \\ 25646.2 \\ 29064.0 \\ 30109.0 \\ 33518.0 \\ 40432.6 \\ 48354.0 \\ 58668.0 \\ 54044.8 \\ 62202.2 \\ 65191.8 \\ 56925.6 \\ 51372.8 \\ 53292.4 \\ 52606.6 \end{bmatrix}$$

σ_3 = mean confining stress
σ_d = mean deviator stress
σ_B = mean bulk stress
M_R = resilient modulus
p_a = atmospheric pressure = 14.6959 psi

Dan Seely
9/12/2023

$$M_{R.1}\left(\sigma_B, K_1, K_2\right) := K_1 \cdot {\sigma_B}^{K_2}$$

Equation 1
AASHTO Publication No. FHWA-RD-97-083

$K_1 = 12212.603$

$K_2 = 0.3597$

Equation 1 fitting parameters

${R_1}^2 = 0.7565$

Coefficient of determination

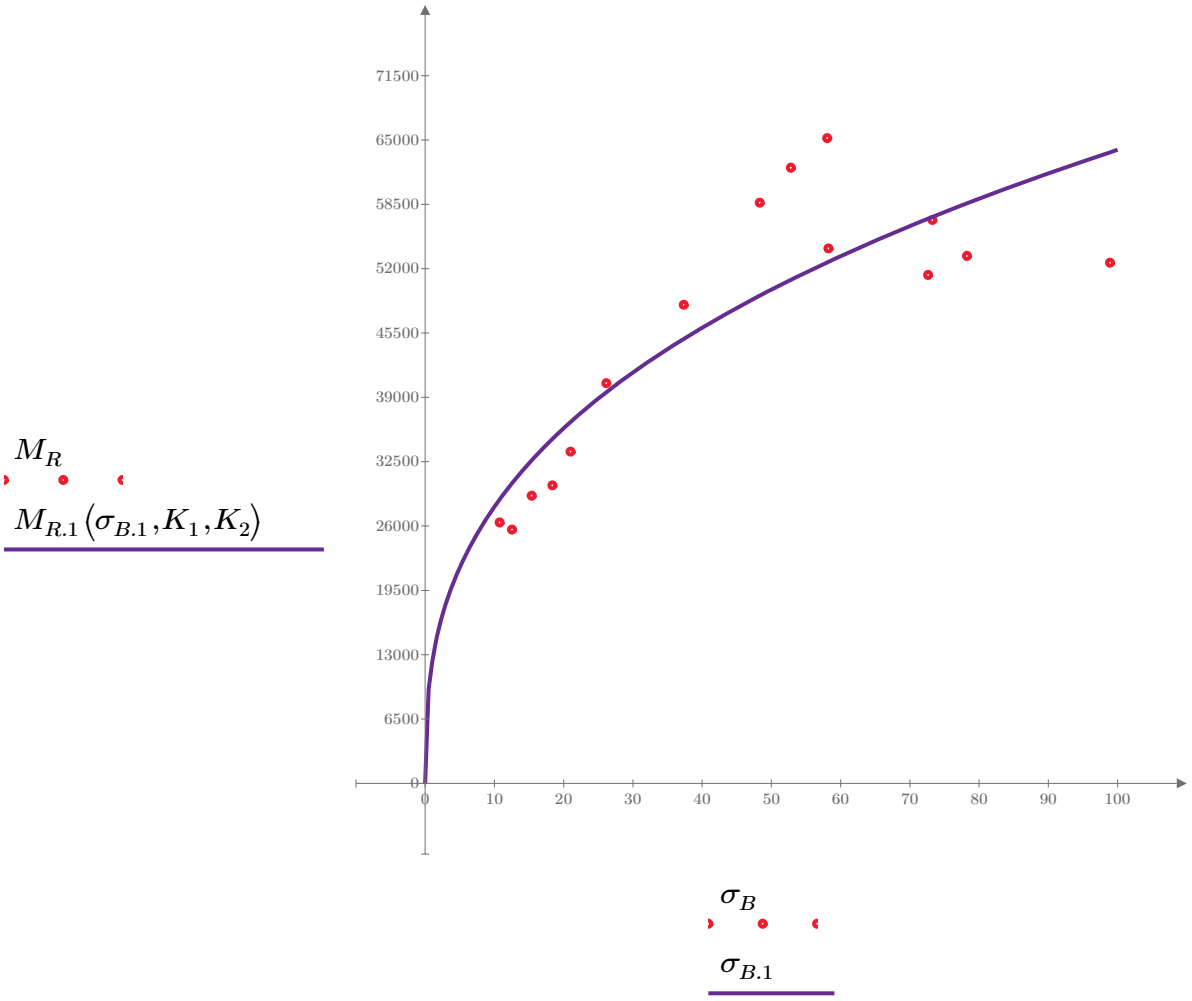

Figure 1. Plot of the test data (red points) vs. the fitted Equation 1 model (purple line).

Dan Seely
9/12/2023

$$M_{R.2}(\sigma_d, K_3, K_4) := K_3 \cdot \sigma_d^{K_4}$$

Equation 2
AASHTO Publication No. FHWA-RD-97-083

$K_3 = 21889.199$

$K_4 = 0.2834$

Equation 2 fitting parameters

$R_2^2 = 0.4722$

Coefficient of determination

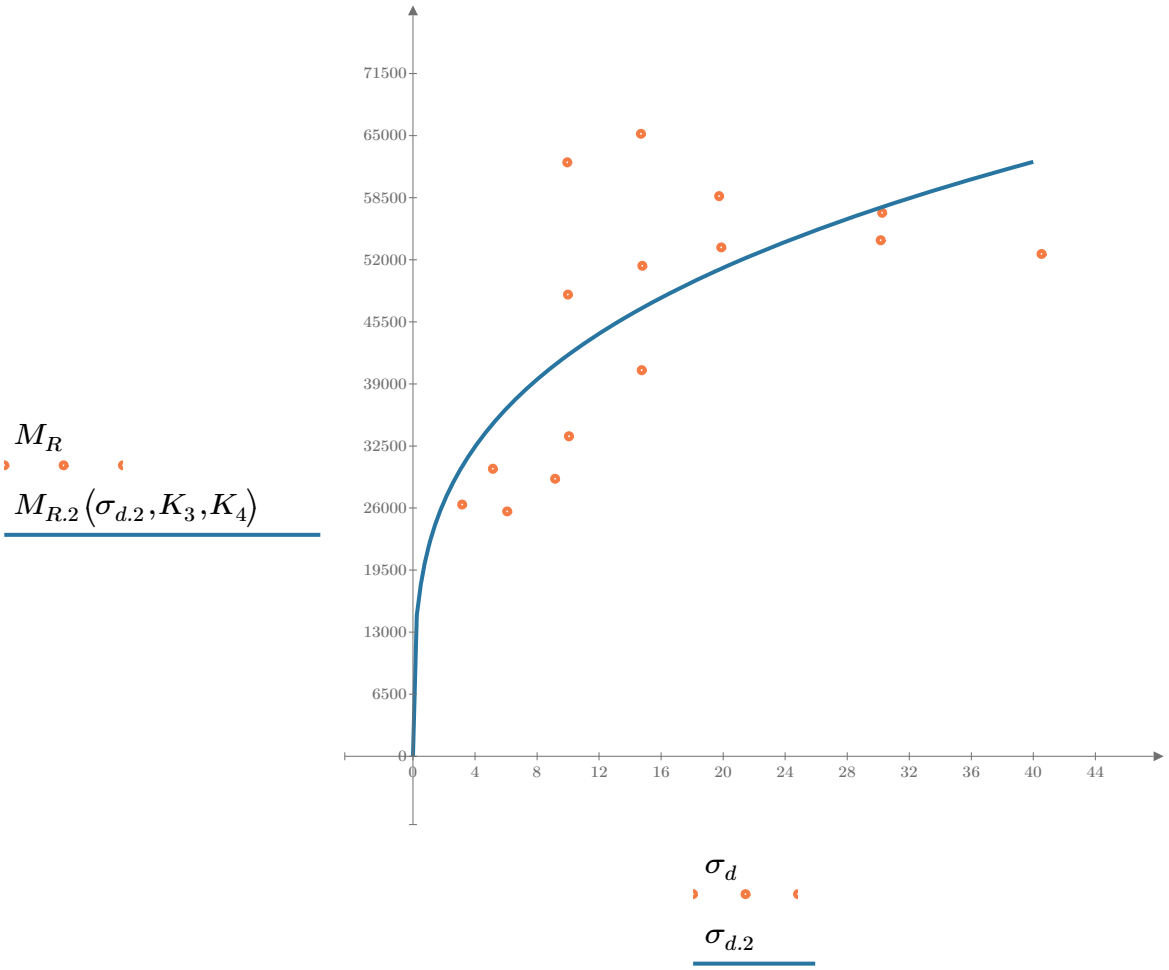

Figure 2. Plot of the test data (orange points) vs. the fitted Equation 2 model (blue line).

Dan Seely
9/12/2023

$$M_{R.3}\left(\sigma_d,\sigma_3,K_5,K_6,K_7\right):=K_5\cdot{\sigma_d}^{K_6}\cdot\left(1+\sigma_3\right)^{K_7}$$

Equation 3 AASHTO Publication No. FHWA-RD-97-083

$K_5=19188.623$

$K_6=0.0563$ Equation 3 fitting parameters

$K_7=0.3221$

${R_3}^2=0.7520$ Coefficient of determination

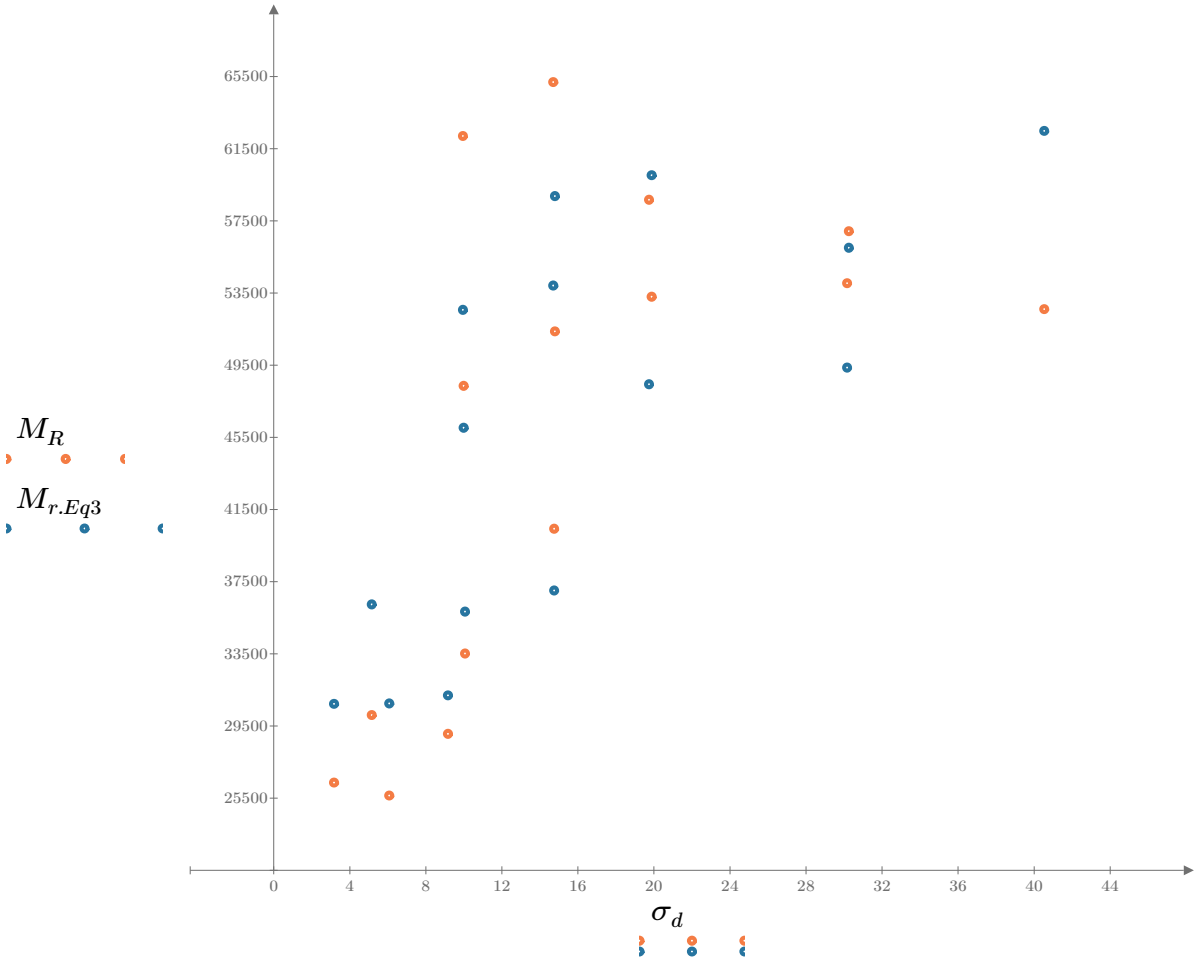

Figure 3. Plot of the test data (orange points) vs. the fitted Equation 3 model (blue points).

Dan Seely
9/12/2023

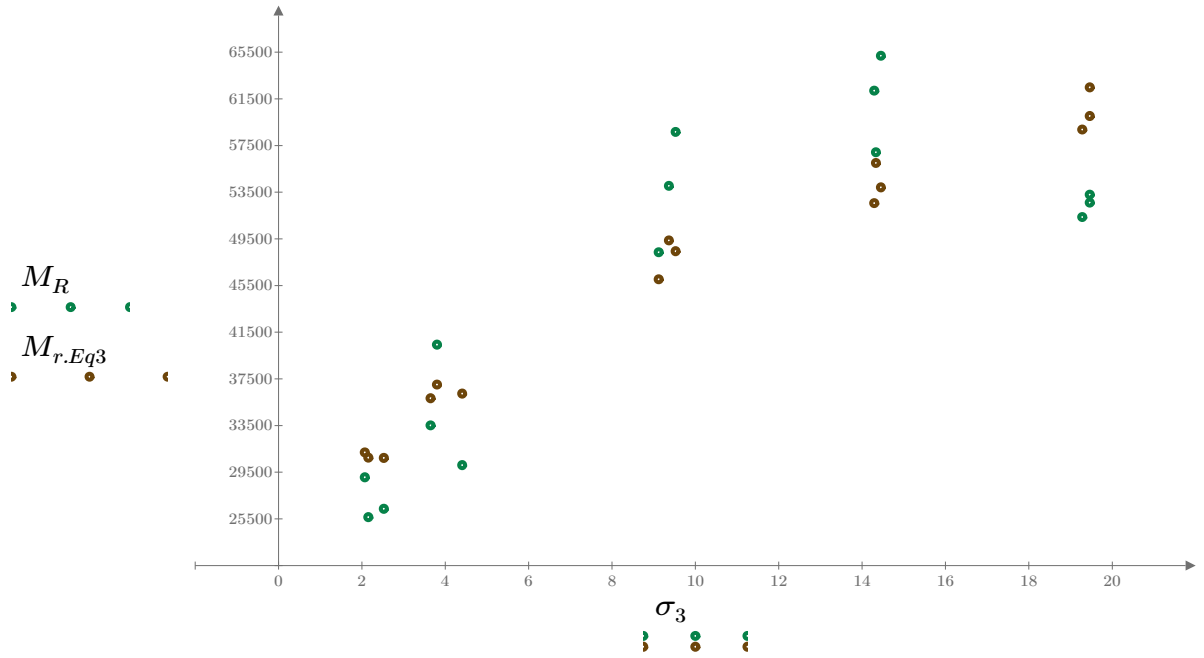

Figure 4. Plot of the test data (green points) vs. the fitted Equation 3 model (brown points).

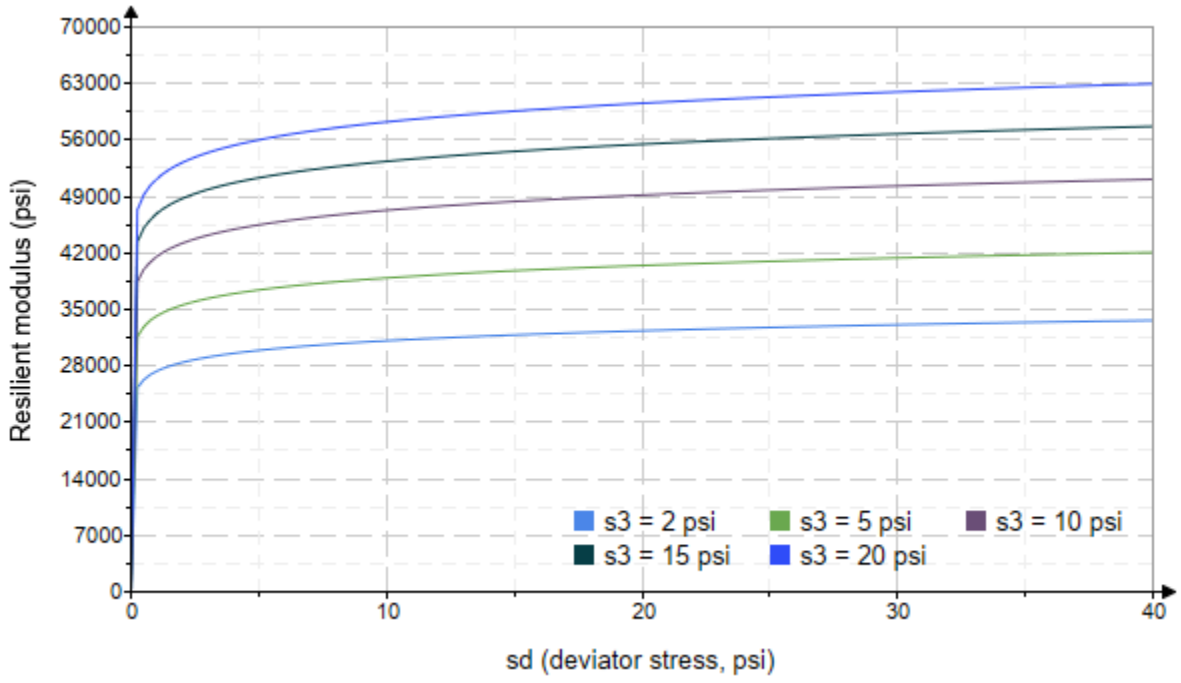

Figure 5. Plot of the fitted Equation 3 model for various confining stresses.

Dan Seely
9/12/2023

$$M_{R.4}\left(\sigma_B,\sigma_d,K_8,K_9,K_{10}\right) := K_8 \cdot p_a \left(\frac{\sigma_B}{p_a}\right)^{K_9} \cdot \left(\frac{\sigma_d}{p_a}\right)^{K_{10}}$$

Equation 4 AASHTO Publication No. FHWA-RD-97-083

$K_8 = 1976.816$

$K_9 = 0.4520$ Equation 4 fitting parameters

$K_{10} = -0.1086$

$R_4^{\,2} = 0.7740$ Coefficient of determination

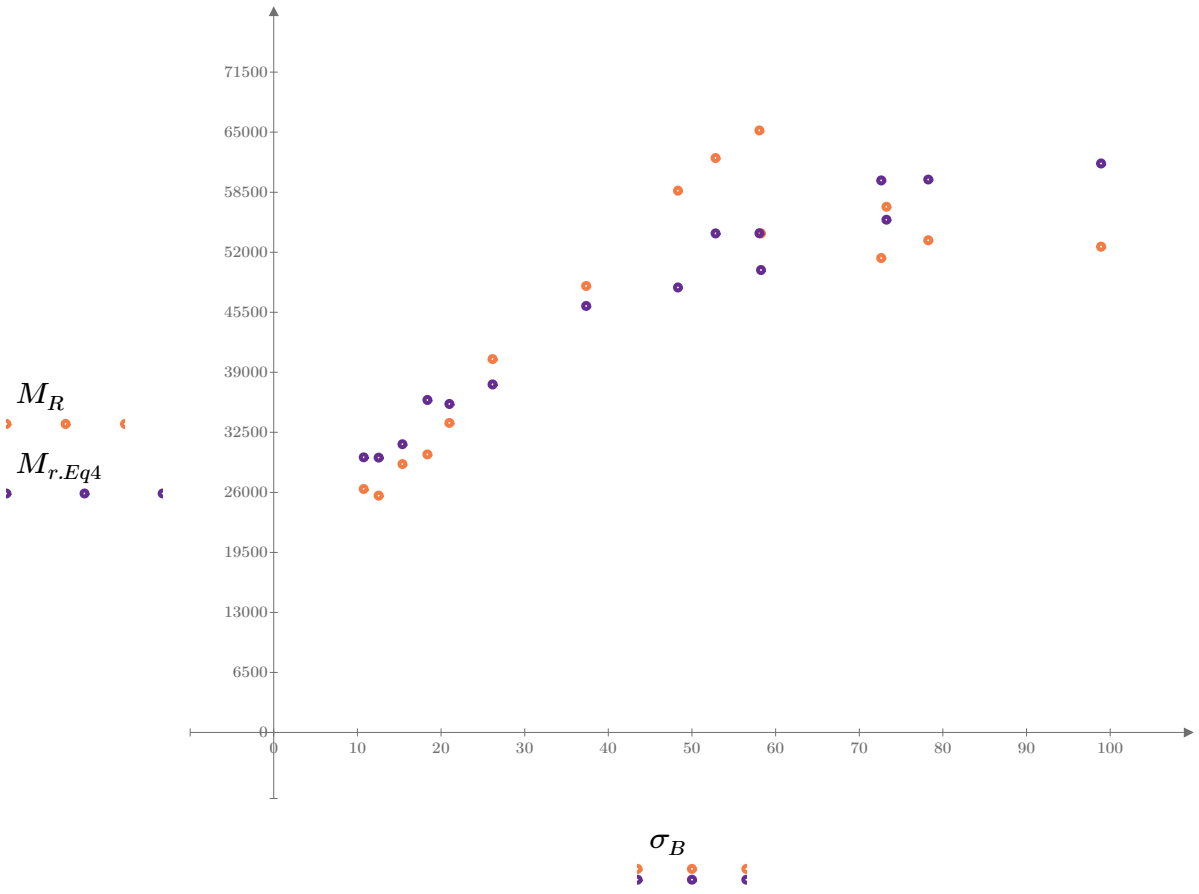

Figure 6. Plot of the test data (orange points) vs. the fitted Equation 4 model (purple points).

Dan Seely
9/12/2023

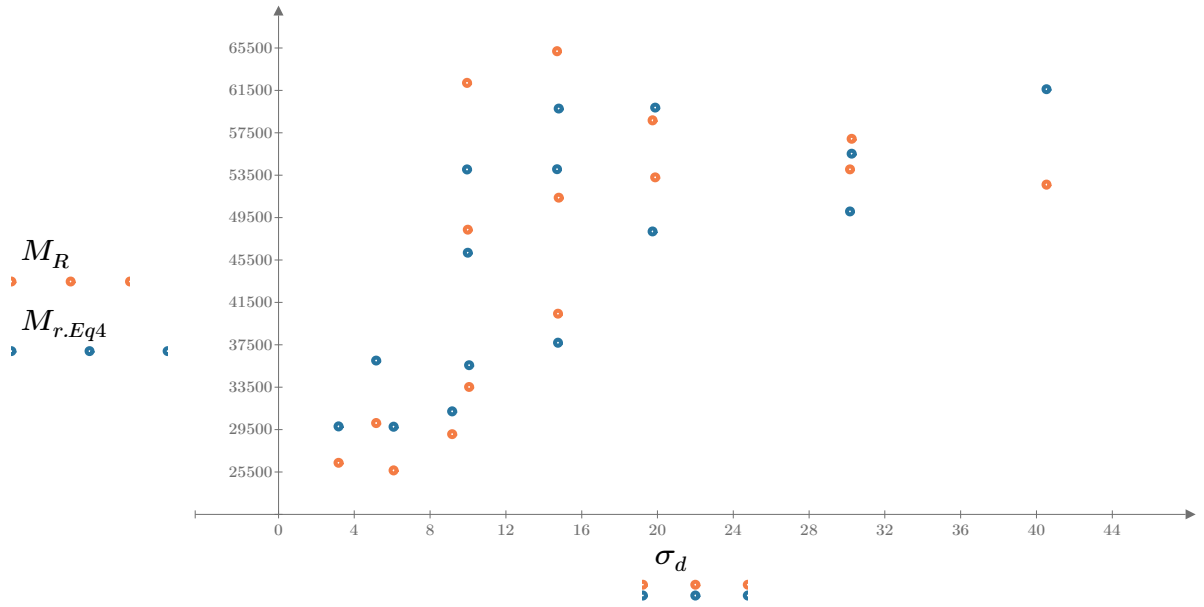

Figure 7. Plot of the test data (orange points) vs. the fitted Equation 4 model (blue points).

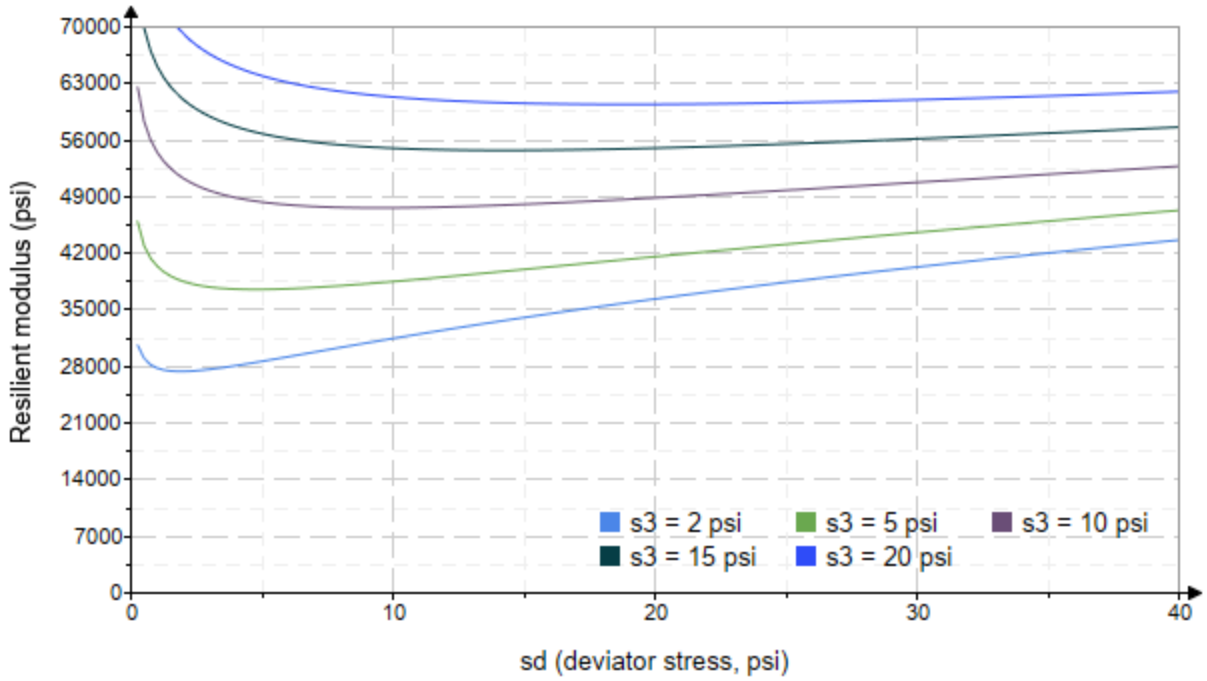

Figure 8. Plot of the fitted Equation 4 model for various confining stresses.

Dan Seely
9/12/2023

$SampleNo := \text{“B2}-\text{46”}$

$Treatment = \text{“AD”}$

$S = 3.329$ Degree of Saturation (%)

Test Sequence : Base/Subbase

Test summary data (psi) :

$$\sigma_3 = \begin{bmatrix} 2.682 \\ 2.635 \\ 2.657 \\ 4.606 \\ 4.668 \\ 4.688 \\ 9.710 \\ 9.644 \\ 9.671 \\ 14.770 \\ 14.700 \\ 14.690 \\ 19.670 \\ 19.680 \\ 19.680 \end{bmatrix} \quad \sigma_d = \begin{bmatrix} 3.115 \\ 6.093 \\ 8.926 \\ 5.125 \\ 9.798 \\ 14.600 \\ 9.822 \\ 19.490 \\ 29.880 \\ 9.758 \\ 14.570 \\ 30.080 \\ 14.620 \\ 19.660 \\ 40.240 \end{bmatrix} \quad \sigma_B = \begin{bmatrix} 11.160 \\ 14.000 \\ 16.900 \\ 18.940 \\ 23.800 \\ 28.670 \\ 38.950 \\ 48.420 \\ 58.890 \\ 54.060 \\ 58.650 \\ 74.150 \\ 73.630 \\ 78.690 \\ 99.270 \end{bmatrix} \quad M_R = \begin{bmatrix} 45390.4 \\ 36808.6 \\ 35861.0 \\ 32097.0 \\ 31492.2 \\ 33950.2 \\ 32110.8 \\ 45629.4 \\ 58545.2 \\ 51655.6 \\ 62738.0 \\ 73967.8 \\ 78218.0 \\ 81508.8 \\ 58175.0 \end{bmatrix}$$

σ_3 = mean confining stress
σ_d = mean deviator stress
σ_B = mean bulk stress
M_R = resilient modulus
p_a = atmospheric pressure = 14.6959 psi

Dan Seely
9/12/2023

$$M_{R.1}\left(\sigma_B, K_1, K_2\right) := K_1 \cdot {\sigma_B}^{K_2}$$

Equation 1
AASHTO Publication No. FHWA-RD-97-083

$K_1 = 9722.310$

$K_2 = 0.4405$

Equation 1 fitting parameters

${R_1}^2 = 0.6302$

Coefficient of determination

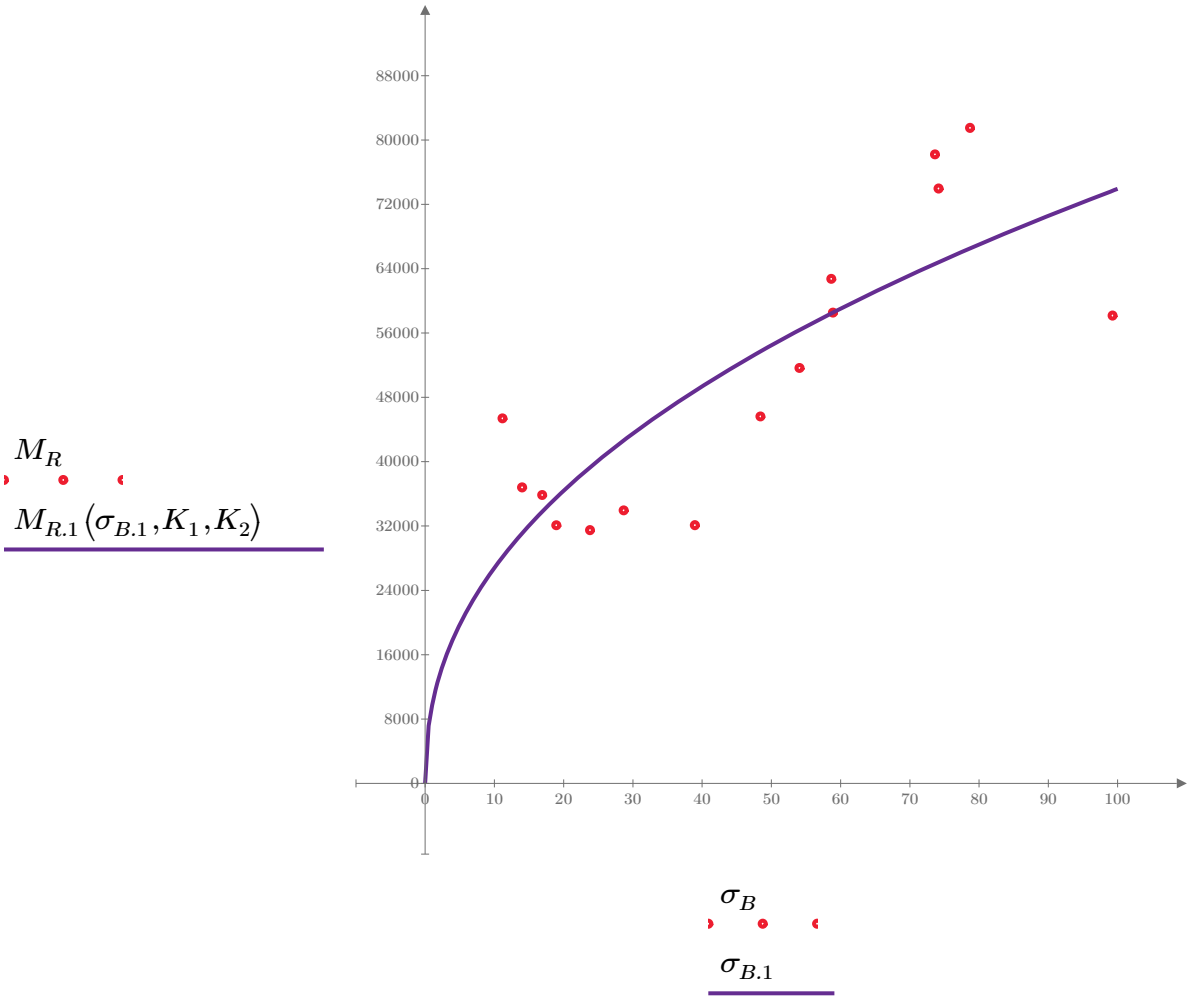

Figure 1. Plot of the test data (red points) vs. the fitted Equation 1 model (purple line).

Dan Seely
9/12/2023

$M_{R.2}(\sigma_d, K_3, K_4) := K_3 \cdot \sigma_d^{K_4}$ Equation 2
AASHTO Publication No. FHWA-RD-97-083

$K_3 = 23559.147$

$K_4 = 0.2929$ Equation 2 fitting parameters

$R_2^2 = 0.3378$ Coefficient of determination

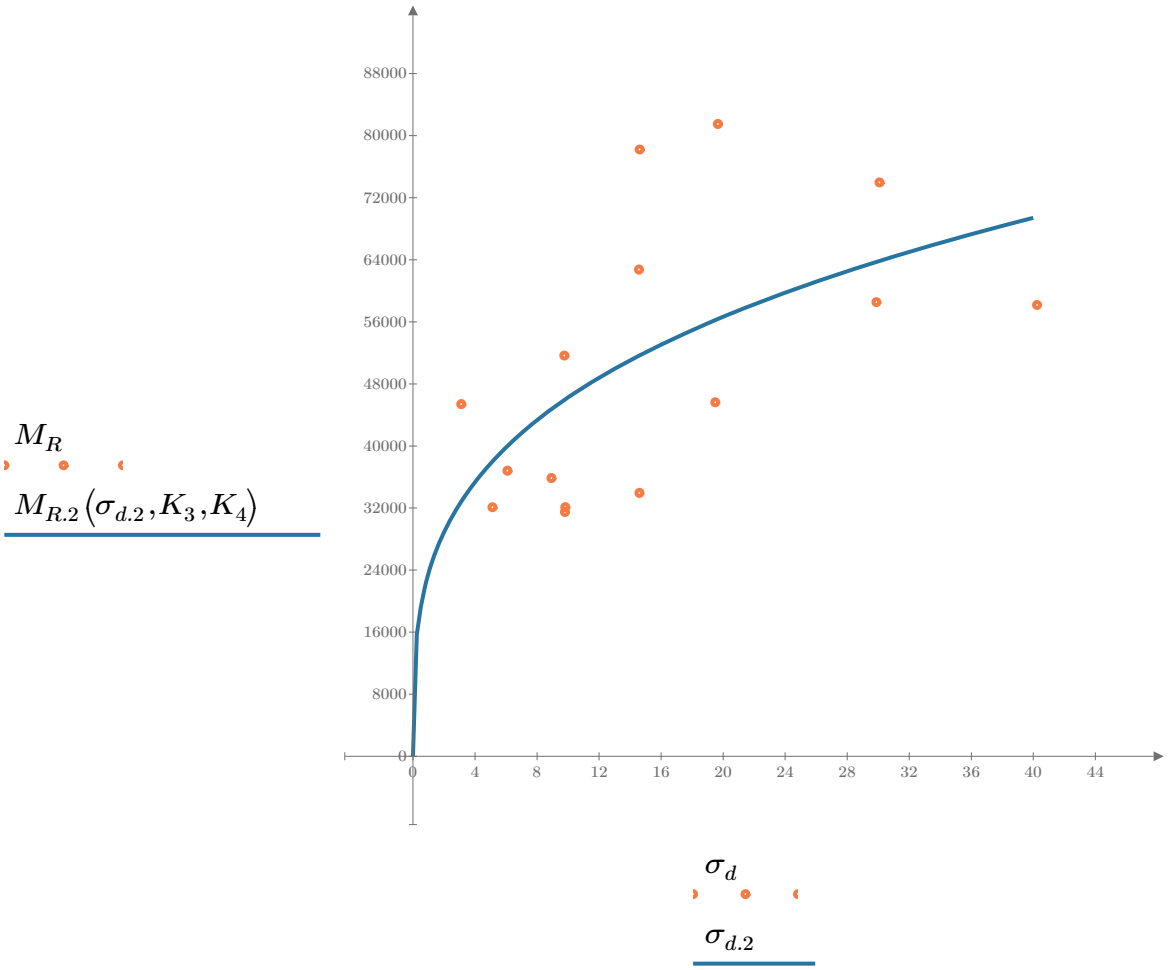

Figure 2. Plot of the test data (orange points) vs. the fitted Equation 2 model (blue line).

Dan Seely
9/12/2023

$$M_{R.3}\left(\sigma_d,\sigma_3,K_5,K_6,K_7\right):=K_5\cdot{\sigma_d}^{K_6}\cdot\left(1+\sigma_3\right)^{K_7}$$

Equation 3 AASHTO Publication No. FHWA-RD-97-083

$K_5=16480.444$

$K_6=0.0198$ Equation 3 fitting parameters

$K_7=0.4575$

${R_3}^2=0.6755$ Coefficient of determination

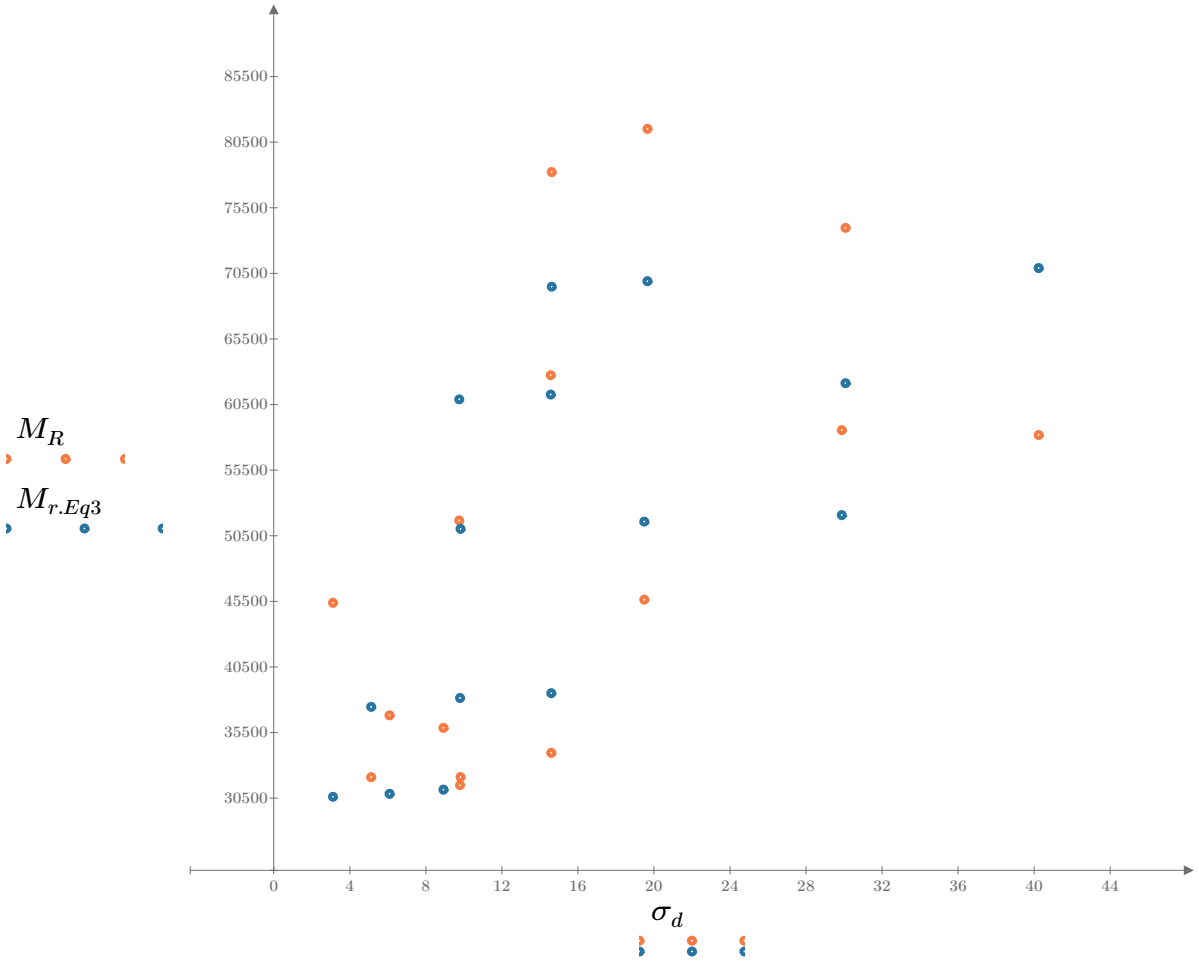

Figure 3. Plot of the test data (orange points) vs. the fitted Equation 3 model (blue points).

Dan Seely
9/12/2023

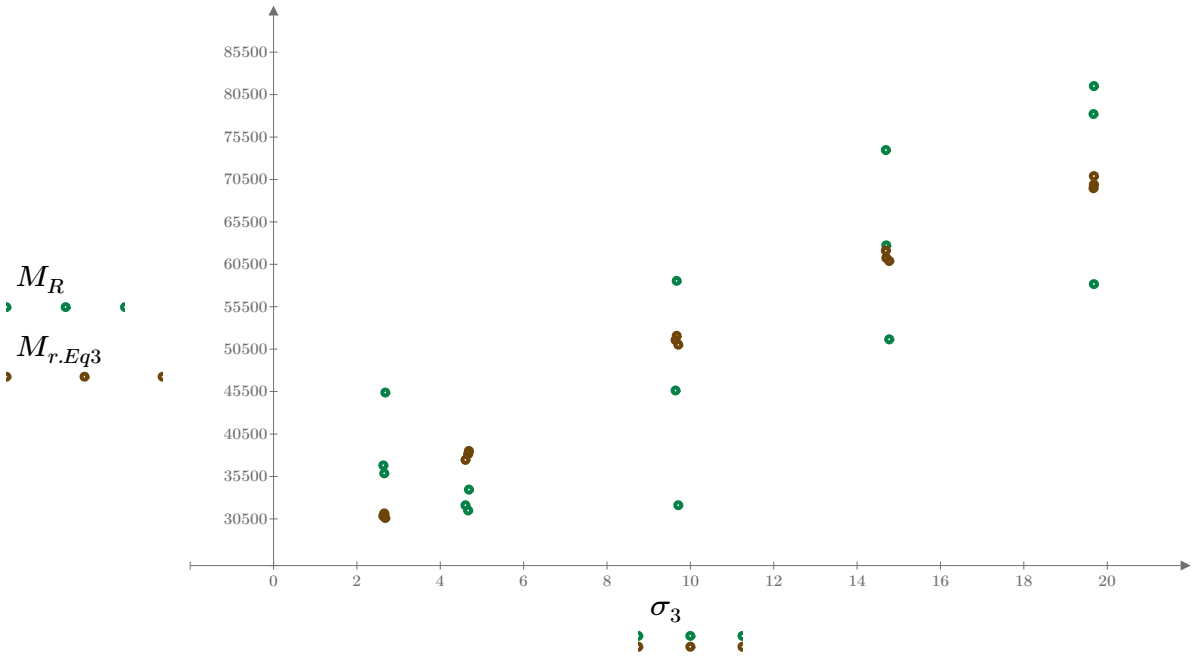

Figure 4. Plot of the test data (green points) vs. the fitted Equation 3 model (brown points).

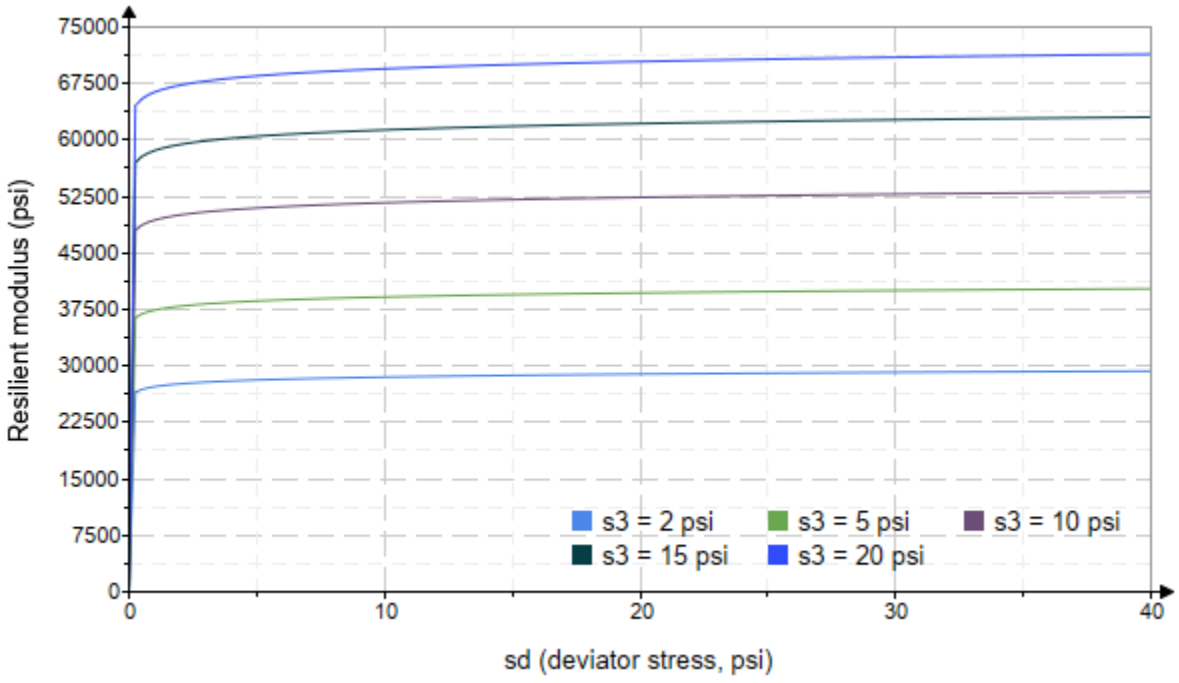

Figure 5. Plot of the fitted Equation 3 model for various confining stresses.

Dan Seely
9/12/2023

$$M_{R.4}\left(\sigma_B,\sigma_d,K_8,K_9,K_{10}\right) := K_8 \cdot p_a \left(\frac{\sigma_B}{p_a}\right)^{K_9} \cdot \left(\frac{\sigma_d}{p_a}\right)^{K_{10}}$$

Equation 4 AASHTO Publication No. FHWA-RD-97-083

$K_8 = 1821.027$

$K_9 = 0.5914$ Equation 4 fitting parameters

$K_{10} = -0.1662$

$R_4^{\,2} = 0.6622$ Coefficient of determination

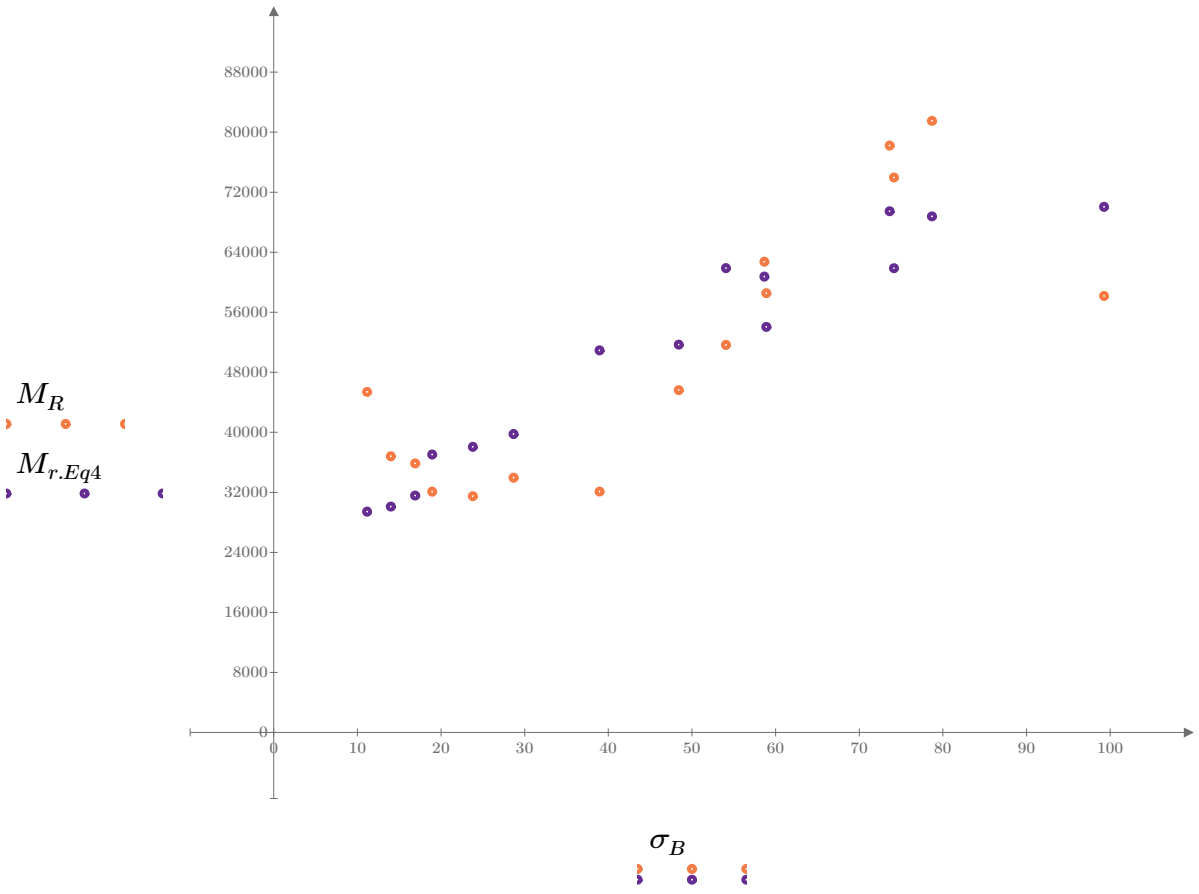

Figure 6. Plot of the test data (orange points) vs. the fitted Equation 4 model (purple points).

Dan Seely
9/12/2023

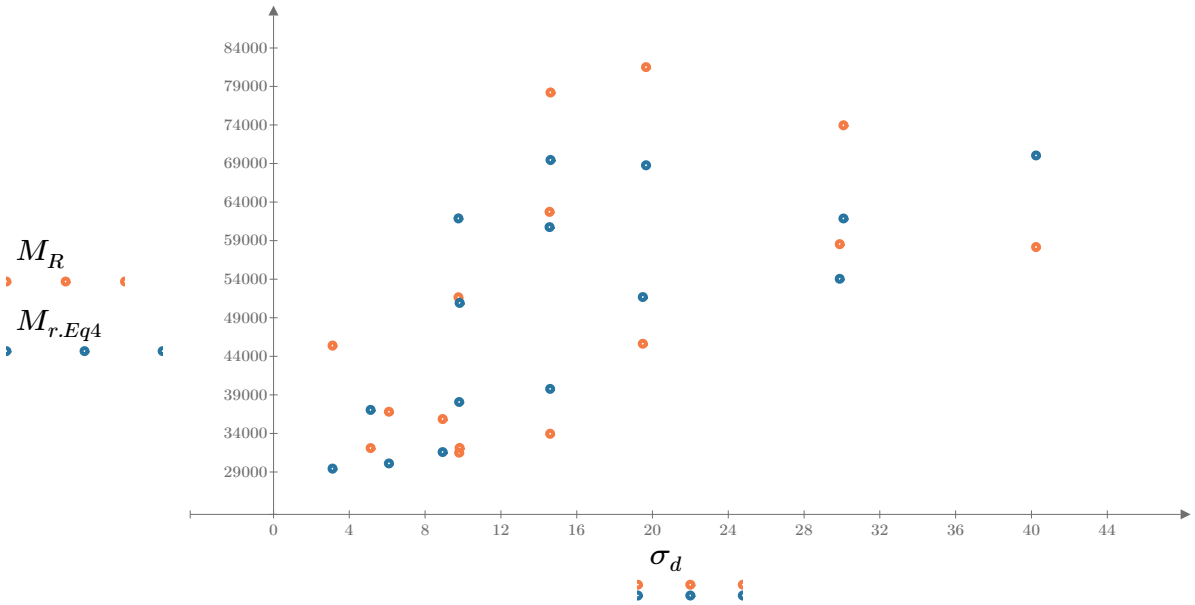

Figure 7. Plot of the test data (orange points) vs. the fitted Equation 4 model (blue points).

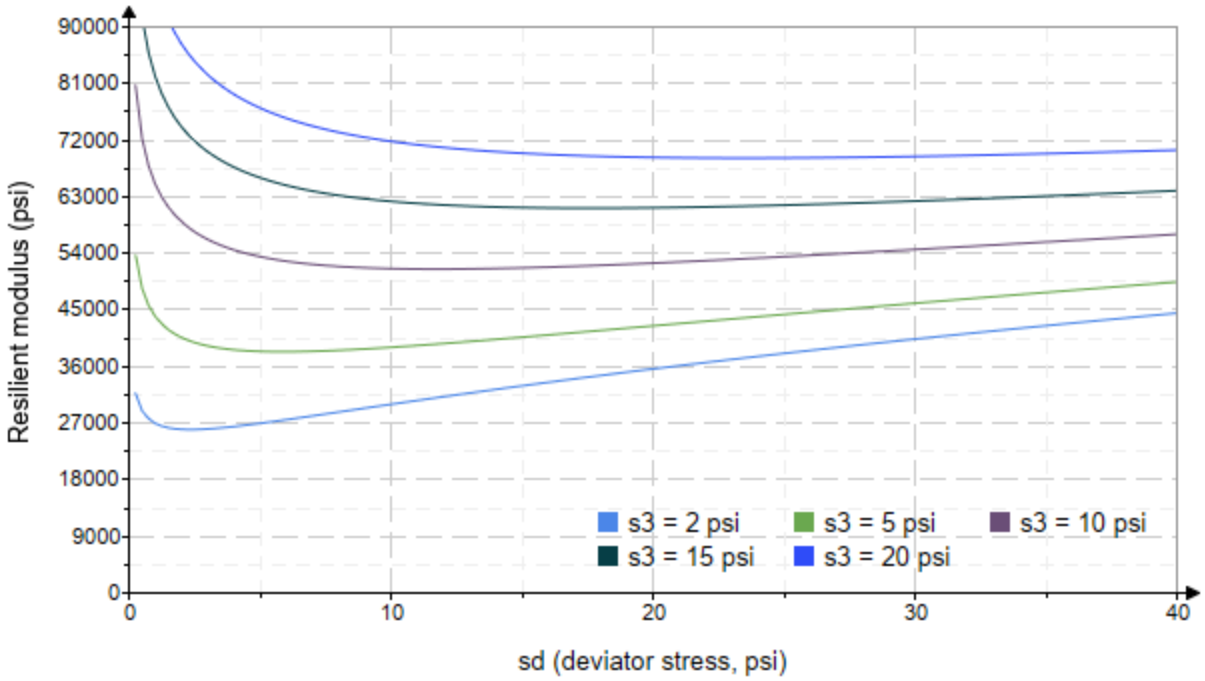

Figure 8. Plot of the fitted Equation 4 model for various confining stresses.

Dan Seely
9/12/2023

$SampleNo := \text{“B2}-\text{47”}$

$Treatment = \text{“H100”}$

$S = 4.647$ Degree of Saturation (%)

Test Sequence : Base/Subbase

Test summary data (psi) :

$$\sigma_3 = \begin{bmatrix} 2.250 \\ 2.409 \\ 2.395 \\ 4.237 \\ 4.361 \\ 4.459 \\ 9.331 \\ 9.137 \\ 9.070 \\ 14.680 \\ 14.310 \\ 14.550 \\ 19.600 \\ 19.410 \\ 19.360 \end{bmatrix} \quad \sigma_d = \begin{bmatrix} 3.189 \\ 6.132 \\ 8.948 \\ 5.146 \\ 9.943 \\ 14.700 \\ 10.070 \\ 19.760 \\ 30.030 \\ 10.070 \\ 14.850 \\ 29.970 \\ 14.940 \\ 20.020 \\ 40.380 \end{bmatrix} \quad \sigma_B = \begin{bmatrix} 9.937 \\ 13.360 \\ 16.130 \\ 17.860 \\ 23.030 \\ 28.080 \\ 38.070 \\ 47.170 \\ 57.240 \\ 54.120 \\ 57.780 \\ 73.610 \\ 73.750 \\ 78.250 \\ 98.450 \end{bmatrix} \quad M_R = \begin{bmatrix} 61174.2 \\ 49191.4 \\ 44366.2 \\ 52657.0 \\ 60947.8 \\ 54183.4 \\ 60126.9 \\ 66070.4 \\ 54771.0 \\ 94586.2 \\ 80672.4 \\ 56544.2 \\ 89131.6 \\ 74373.4 \\ 58135.6 \end{bmatrix}$$

σ_3 = mean confining stress
σ_d = mean deviator stress
σ_B = mean bulk stress
M_R = resilient modulus
p_a = atmospheric pressure = 14.6959 psi

Dan Seely
9/12/2023

$$M_{R.1}\left(\sigma_B, K_1, K_2\right) := K_1 \cdot {\sigma_B}^{K_2}$$

Equation 1
AASHTO Publication No. FHWA-RD-97-083

$K_1 = 34708.101$

$K_2 = 0.1668$

Equation 1 fitting parameters

${R_1}^2 = 0.2680$

Coefficient of determination

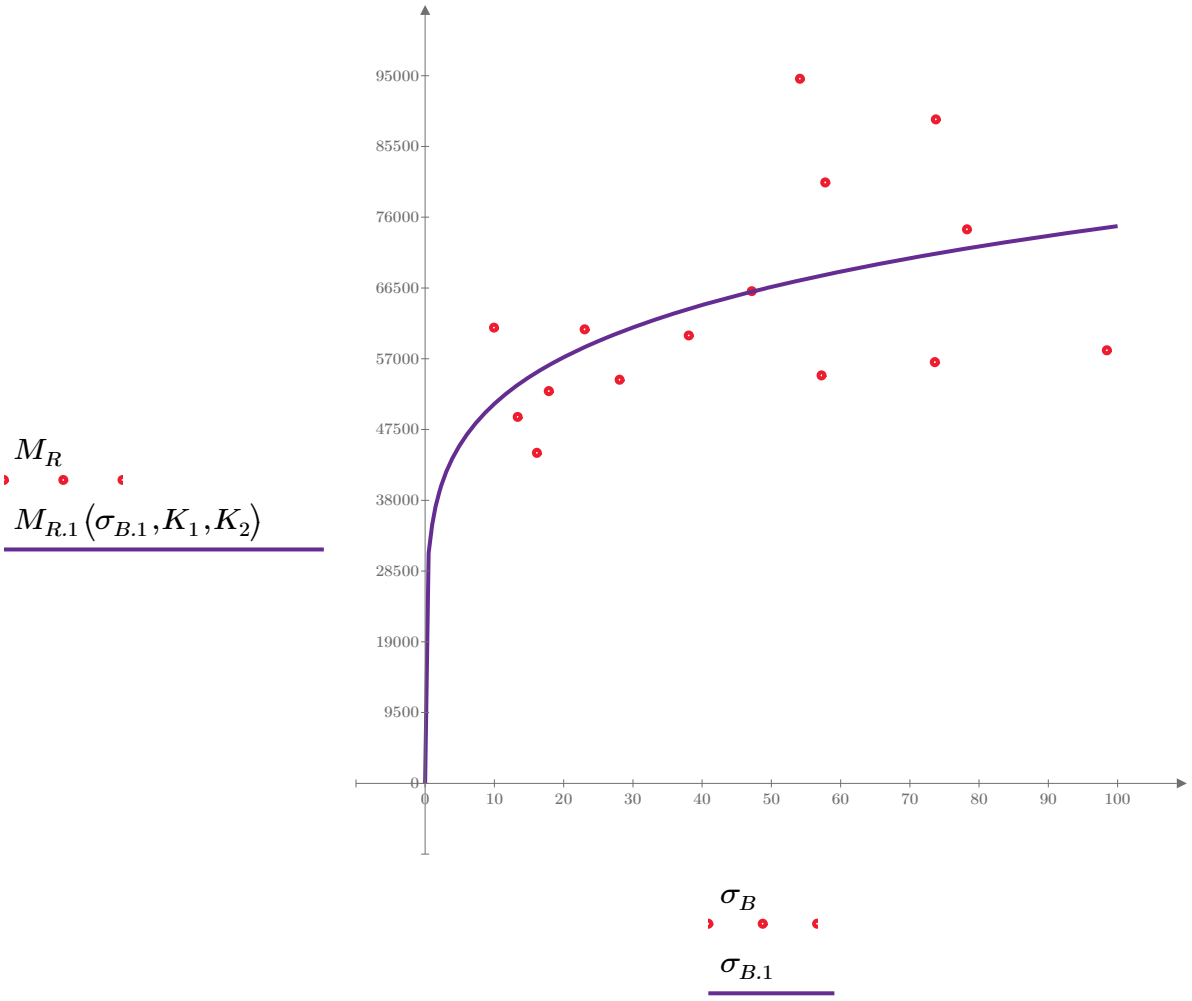

Figure 1. Plot of the test data (red points) vs. the fitted Equation 1 model (purple line).

Dan Seely
9/12/2023

$$M_{R.2}\left(\sigma_d, K_3, K_4\right) := K_3 \cdot {\sigma_d}^{K_4}$$

Equation 2
AASHTO Publication No. FHWA-RD-97-083

$K_3 = 58447.455$

$K_4 = 0.0342$

Equation 2 fitting parameters

${R_2}^2 = 0.0118$

Coefficient of determination

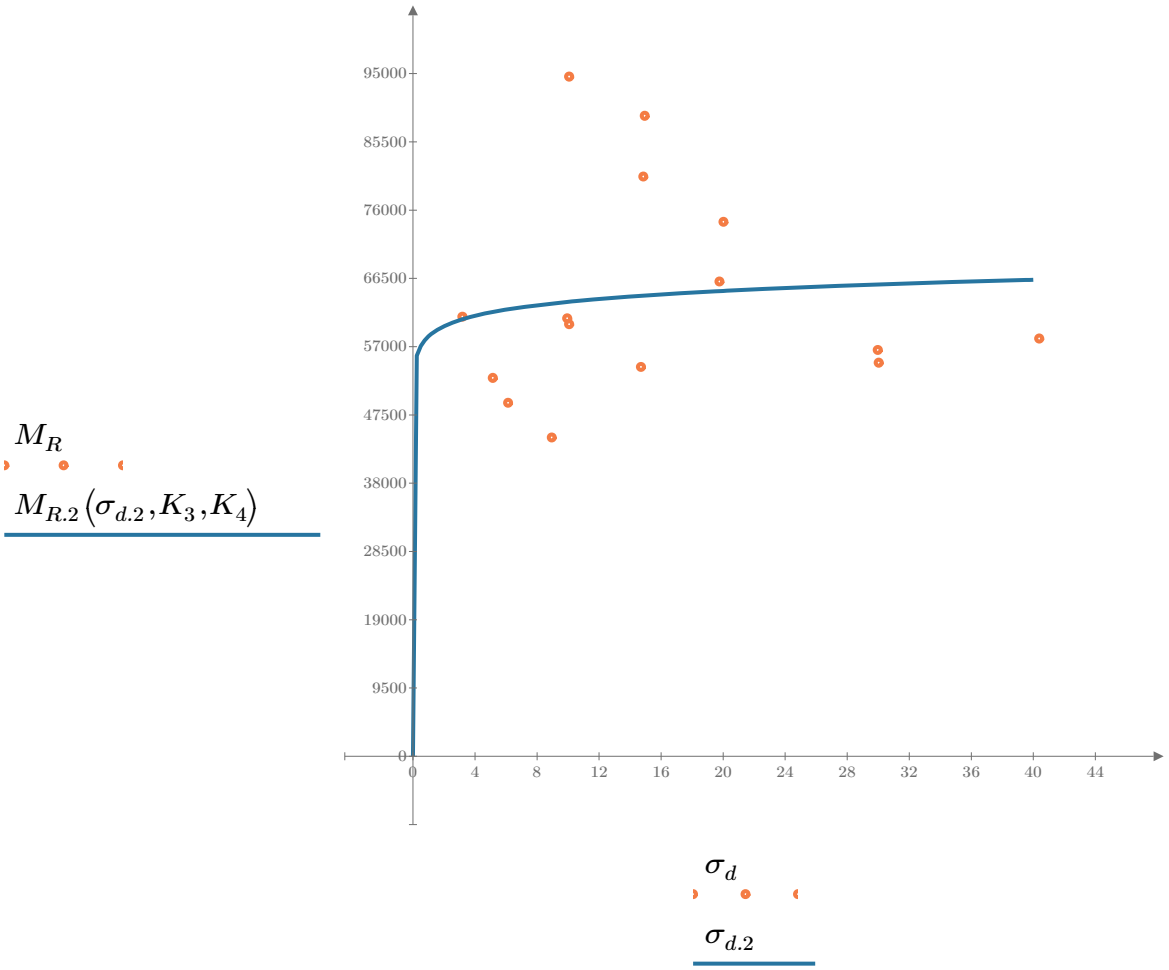

Figure 2. Plot of the test data (orange points) vs. the fitted Equation 2 model (blue line).

Dan Seely
9/12/2023

$$M_{R.3}\left(\sigma_d,\sigma_3,K_5,K_6,K_7\right):=K_5\cdot{\sigma_d}^{K_6}\cdot\left(1+\sigma_3\right)^{K_7}$$

Equation 3 AASHTO Publication No. FHWA-RD-97-083

$K_5=49368.938$

$K_6=-0.2848$ Equation 3 fitting parameters

$K_7=0.4388$

${R_3}^2=0.7906$ Coefficient of determination

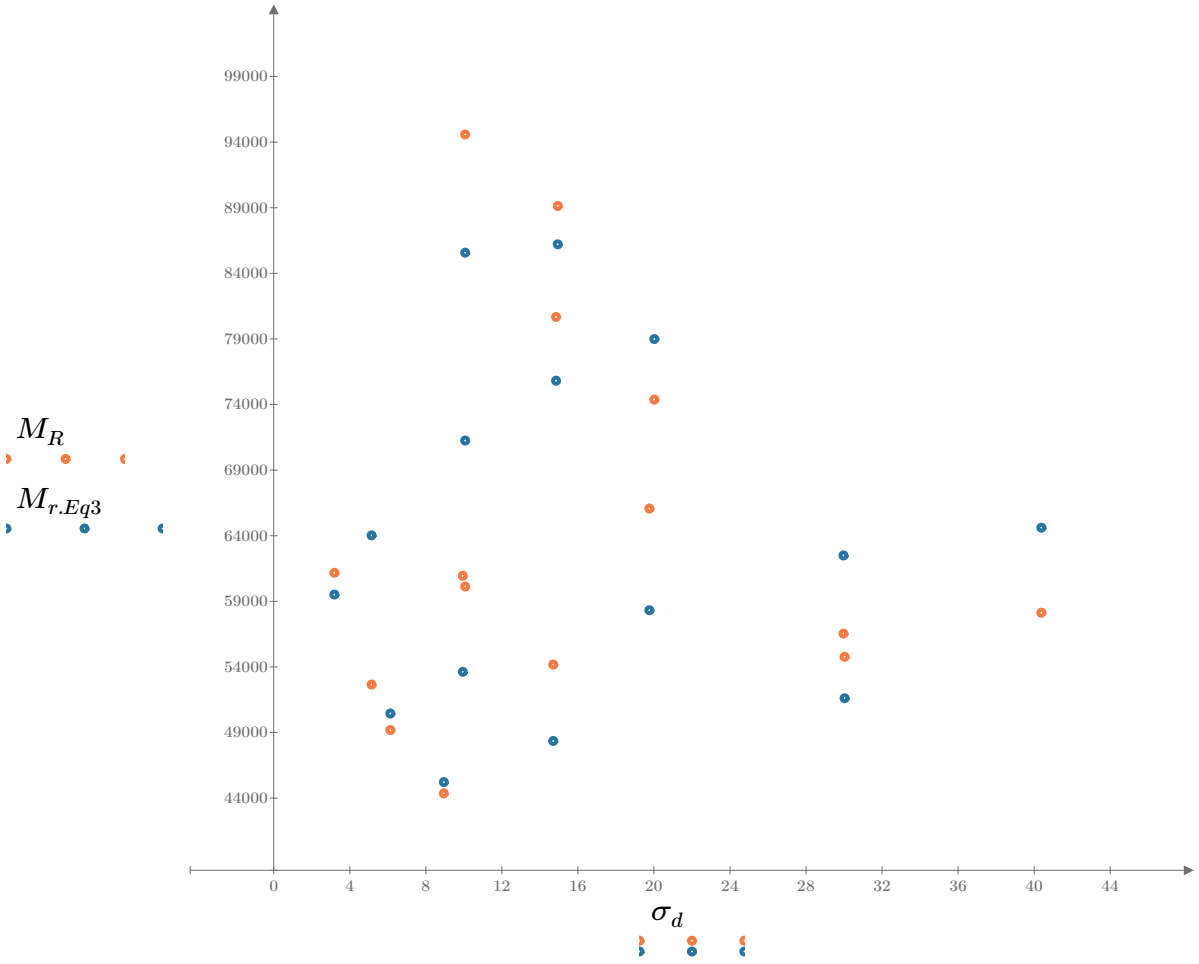

Figure 3. Plot of the test data (orange points) vs. the fitted Equation 3 model (blue points).

Dan Seely
9/12/2023

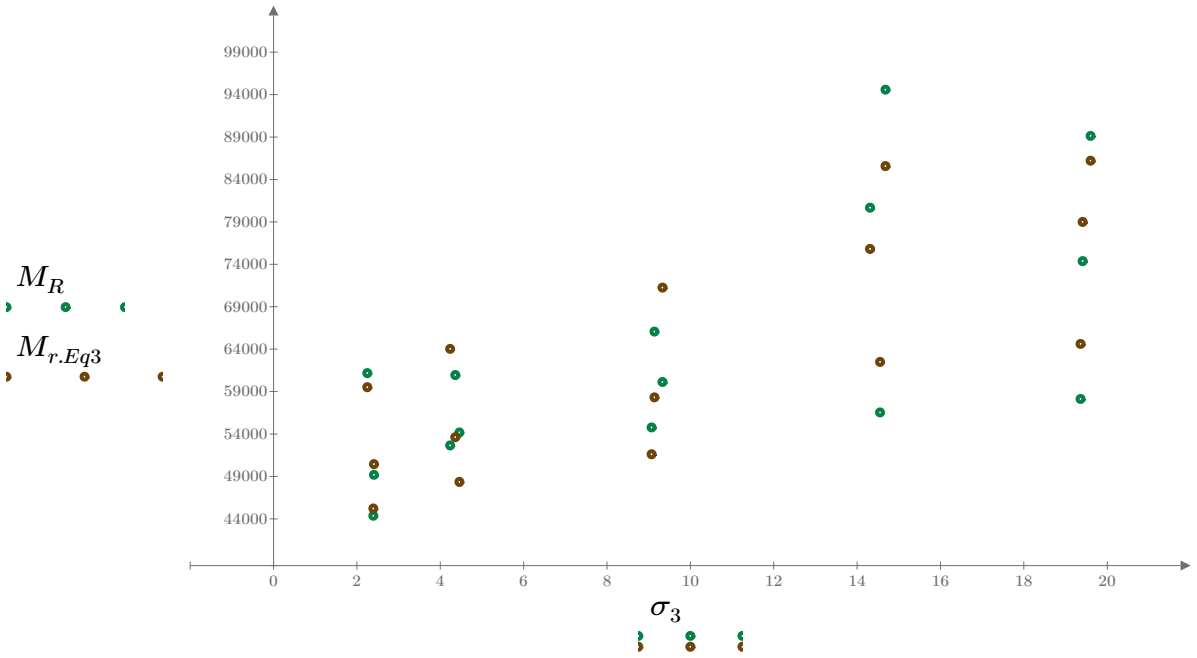

Figure 4. Plot of the test data (green points) vs. the fitted Equation 3 model (brown points).

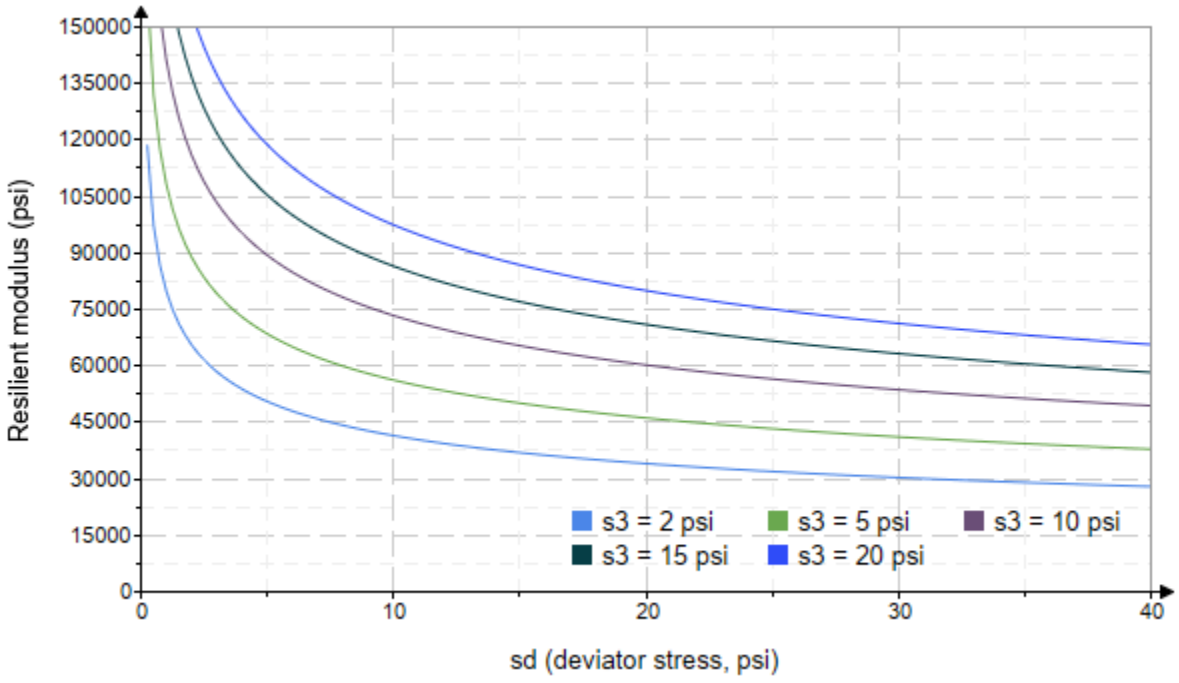

Figure 5. Plot of the fitted Equation 3 model for various confining stresses.

Dan Seely
9/12/2023

$$M_{R.4}\left(\sigma_B,\sigma_d,K_8,K_9,K_{10}\right) := K_8 \cdot p_a \left(\frac{\sigma_B}{p_a}\right)^{K_9} \cdot \left(\frac{\sigma_d}{p_a}\right)^{K_{10}}$$

Equation 4 AASHTO Publication No. FHWA-RD-97-083

$K_8 = 2316.892$

$K_9 = 0.5857$ Equation 4 fitting parameters

$K_{10} = -0.4921$

$R_4^{\,2} = 0.8166$ Coefficient of determination

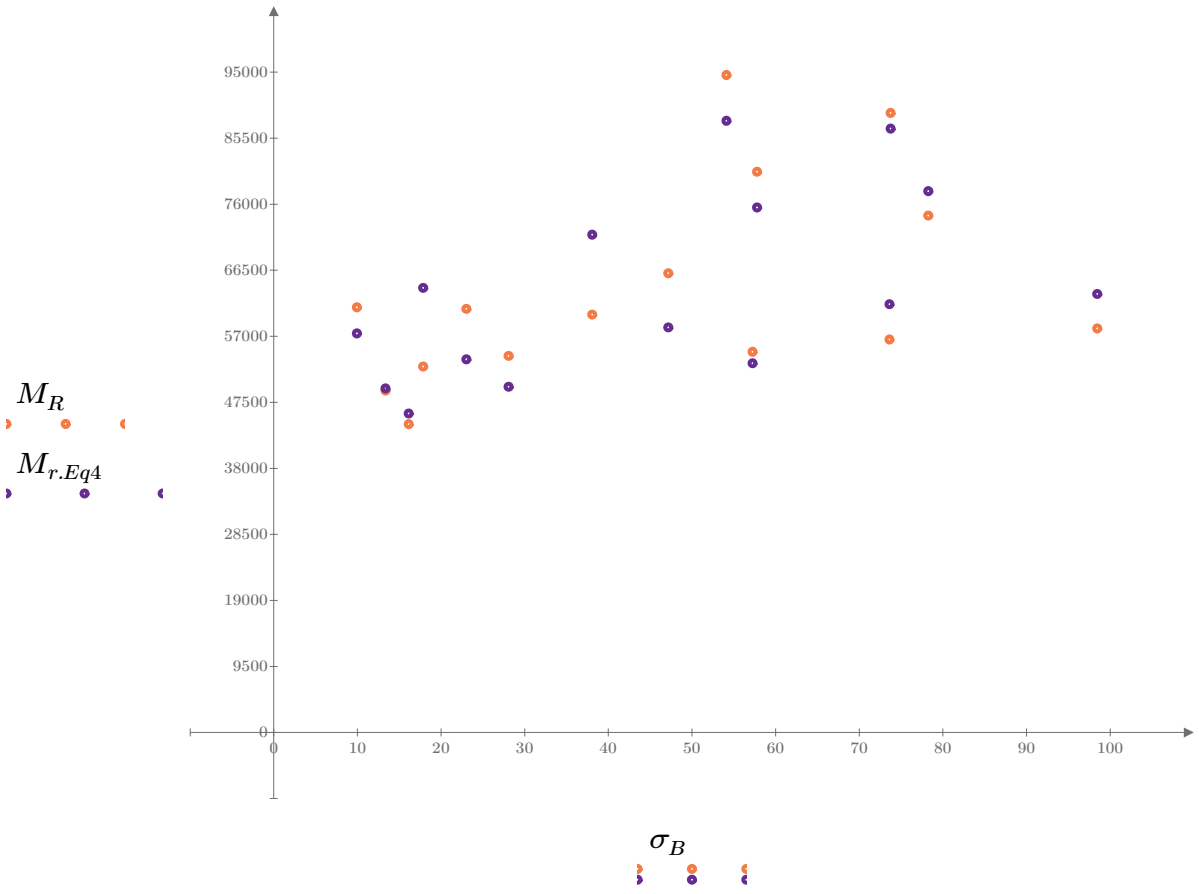

Figure 6. Plot of the test data (orange points) vs. the fitted Equation 4 model (purple points).

Dan Seely
9/12/2023

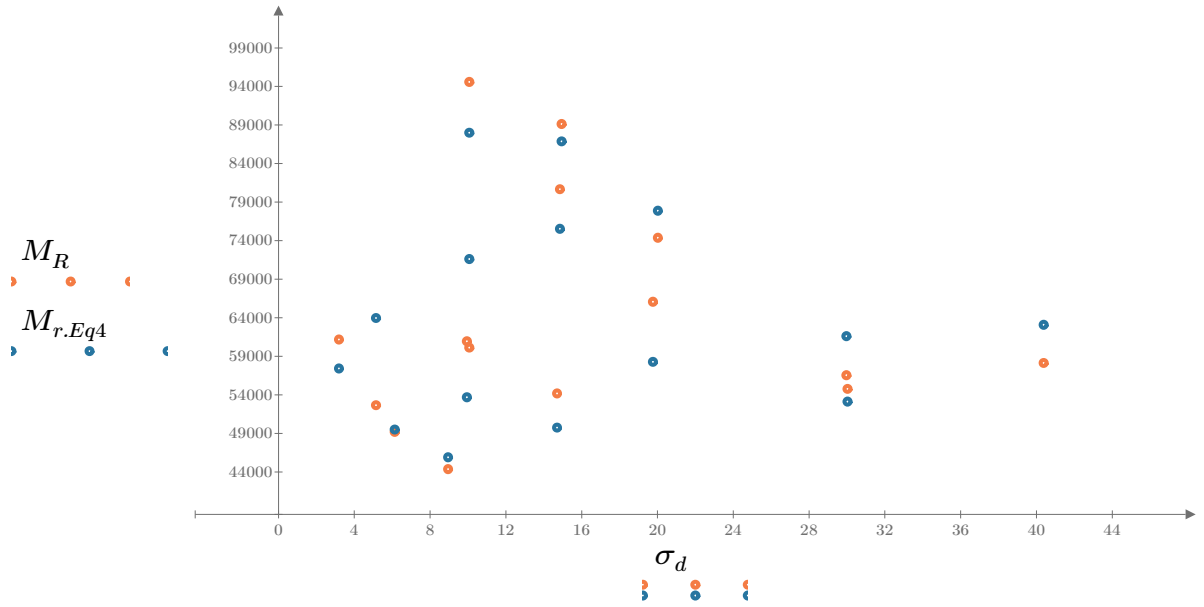

Figure 7. Plot of the test data (orange points) vs. the fitted Equation 4 model (blue points).

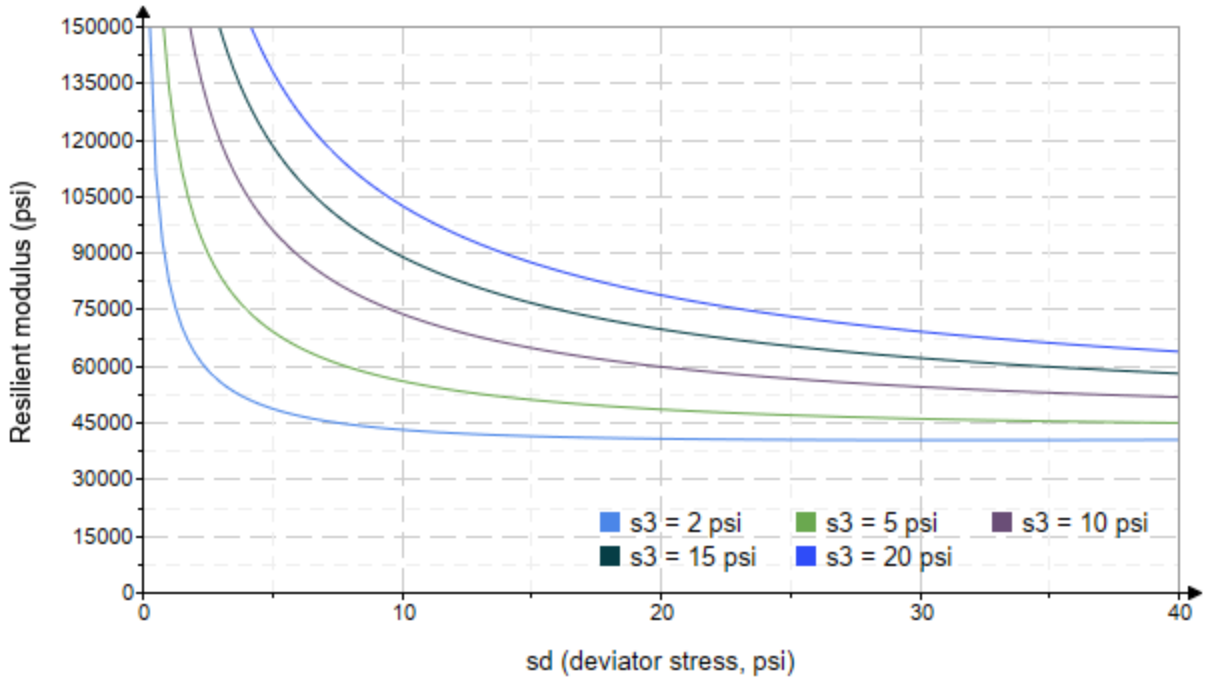

Figure 8. Plot of the fitted Equation 4 model for various confining stresses.

Dan Seely
9/12/2023

$SampleNo := \text{“B2–48”}$

$Treatment = \text{“H100”}$

$S = 4.967$ Degree of Saturation (%)

Test Sequence : Base/Subbase

Test summary data (psi) :

$$\sigma_3 = \begin{bmatrix} 2.833 \\ 2.823 \\ 2.822 \\ 4.560 \\ 4.564 \\ 4.632 \\ 9.623 \\ 9.620 \\ 9.612 \\ 14.680 \\ 14.660 \\ 14.600 \\ 19.630 \\ 19.640 \\ 19.610 \end{bmatrix} \quad \sigma_d = \begin{bmatrix} 3.114 \\ 6.176 \\ 8.910 \\ 5.083 \\ 9.820 \\ 14.550 \\ 9.773 \\ 19.730 \\ 30.060 \\ 9.705 \\ 14.730 \\ 30.140 \\ 14.770 \\ 20.010 \\ 40.370 \end{bmatrix} \quad \sigma_B = \begin{bmatrix} 11.610 \\ 14.640 \\ 17.380 \\ 18.760 \\ 23.510 \\ 28.450 \\ 38.640 \\ 48.590 \\ 58.890 \\ 53.750 \\ 58.700 \\ 73.930 \\ 73.670 \\ 78.920 \\ 99.190 \end{bmatrix} \quad M_R = \begin{bmatrix} 45676.8 \\ 47303.6 \\ 48767.8 \\ 45534.4 \\ 53554.2 \\ 47073.0 \\ 42118.0 \\ 43215.0 \\ 48613.2 \\ 49007.4 \\ 48701.8 \\ 54963.6 \\ 54483.4 \\ 59124.8 \\ 58257.8 \end{bmatrix}$$

σ_3 = mean confining stress
σ_d = mean deviator stress
σ_B = mean bulk stress
M_R = resilient modulus
p_a = atmospheric pressure = 14.6959 psi

Dan Seely
9/12/2023

$$M_{R.1}(\sigma_B, K_1, K_2) := K_1 \cdot {\sigma_B}^{K_2}$$

Equation 1
AASHTO Publication No. FHWA-RD-97-083

$K_1 = 35665.194$

$K_2 = 0.0909$

Equation 1 fitting parameters

${R_1}^2 = 0.3386$

Coefficient of determination

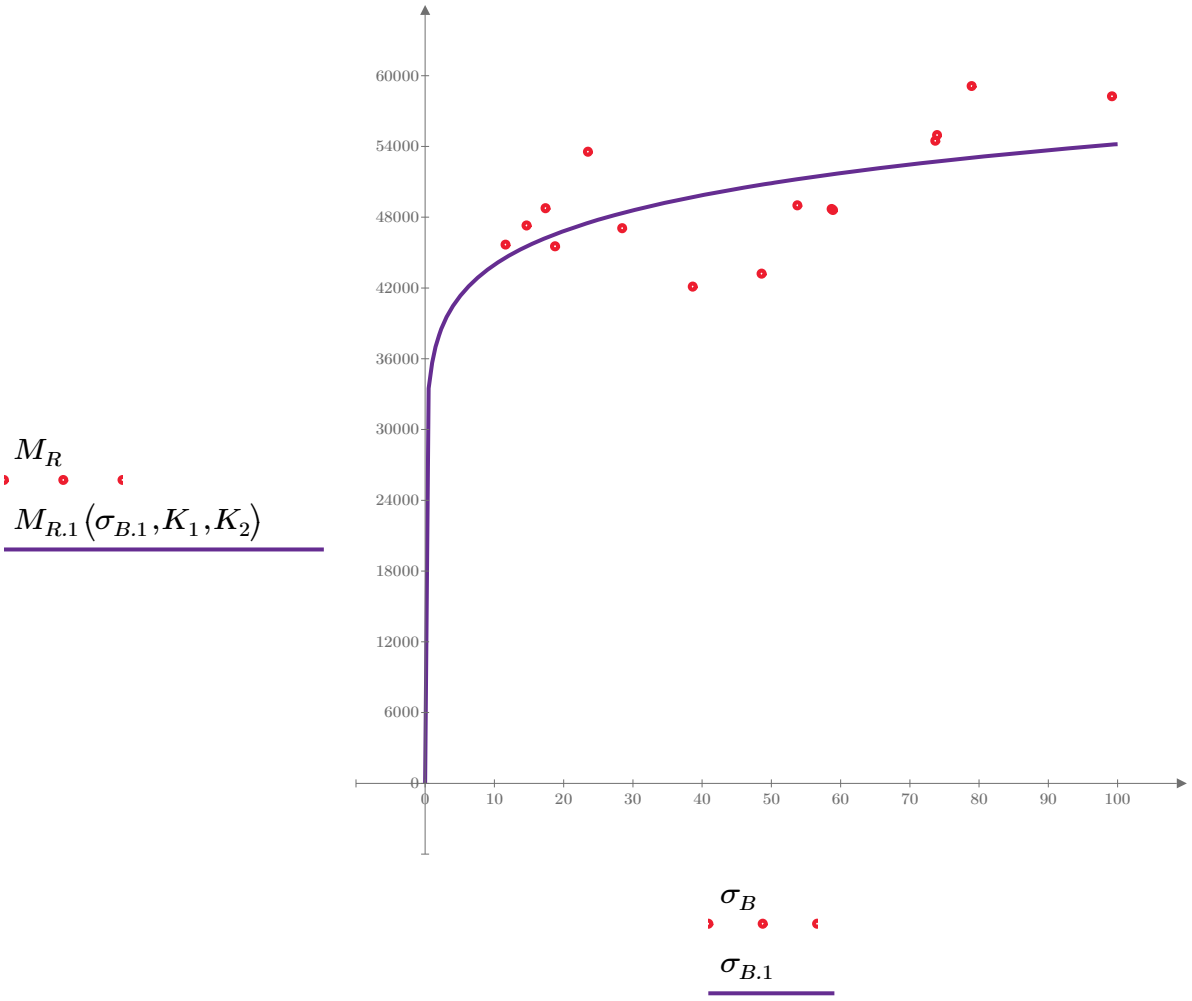

Figure 1. Plot of the test data (red points) vs. the fitted Equation 1 model (purple line).

Dan Seely
9/12/2023

$$M_{R.2}(\sigma_d, K_3, K_4) := K_3 \cdot \sigma_d^{K_4}$$

Equation 2
AASHTO Publication No. FHWA-RD-97-083

$K_3 = 40305.071$

$K_4 = 0.0822$

Equation 2 fitting parameters

$R_2^2 = 0.3010$

Coefficient of determination

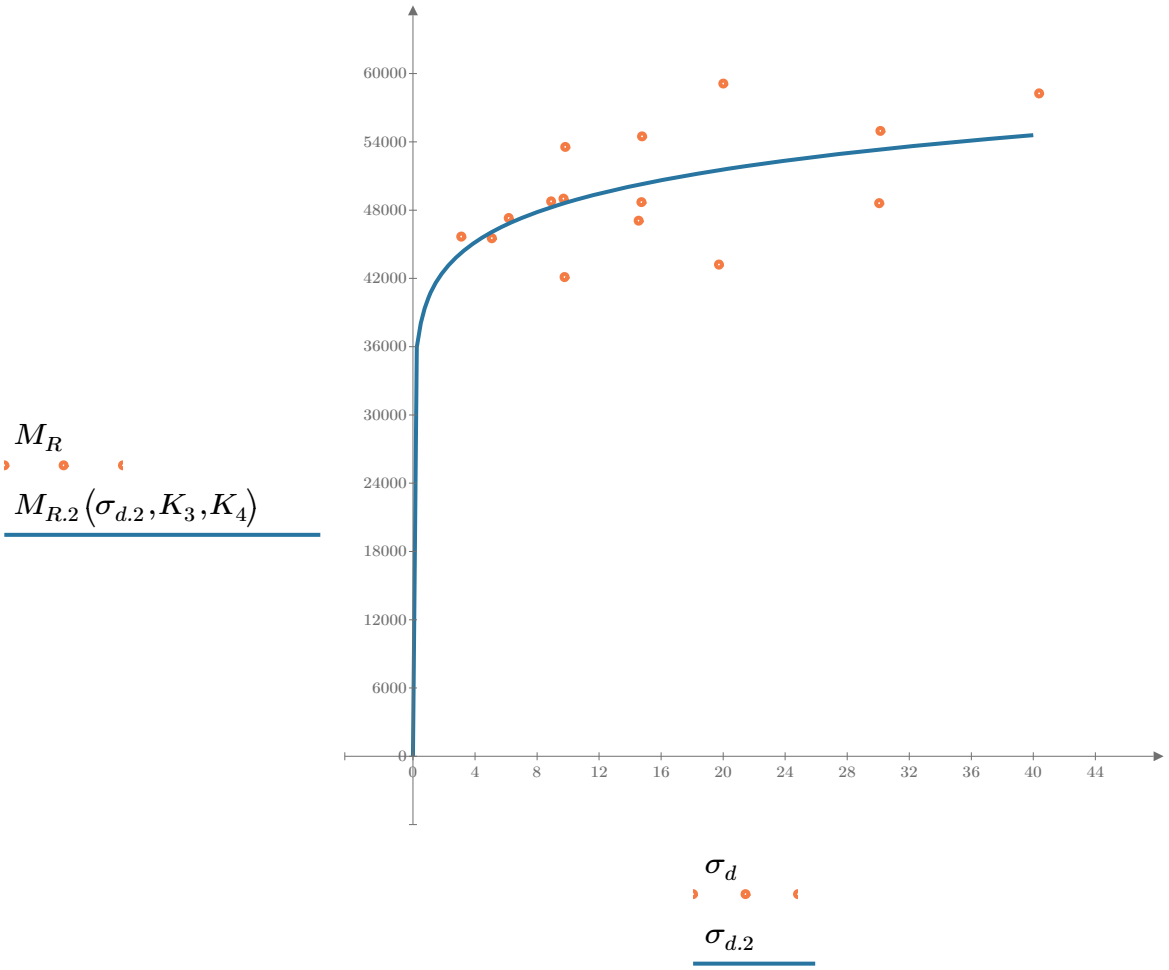

Figure 2. Plot of the test data (orange points) vs. the fitted Equation 2 model (blue line).

Dan Seely
9/12/2023

$$M_{R.3}\left(\sigma_d,\sigma_3,K_5,K_6,K_7\right):=K_5\cdot{\sigma_d}^{K_6}\cdot\left(1+\sigma_3\right)^{K_7}$$

Equation 3 AASHTO Publication No. FHWA-RD-97-083

$K_5=38913.864$

$K_6=0.0456$ Equation 3 fitting parameters

$K_7=0.057$

${R_3}^2=0.3602$ Coefficient of determination

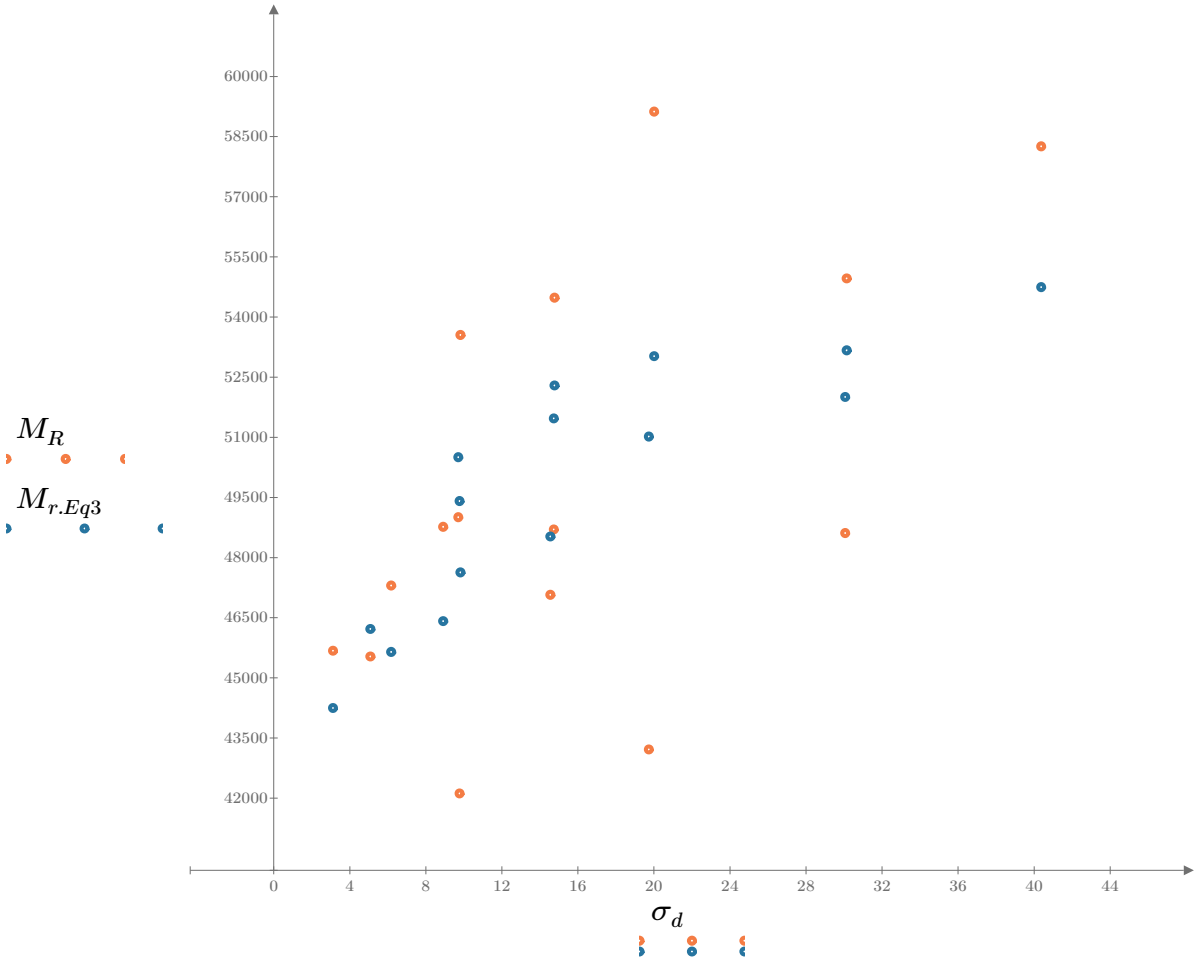

Figure 3. Plot of the test data (orange points) vs. the fitted Equation 3 model (blue points).

Dan Seely
9/12/2023

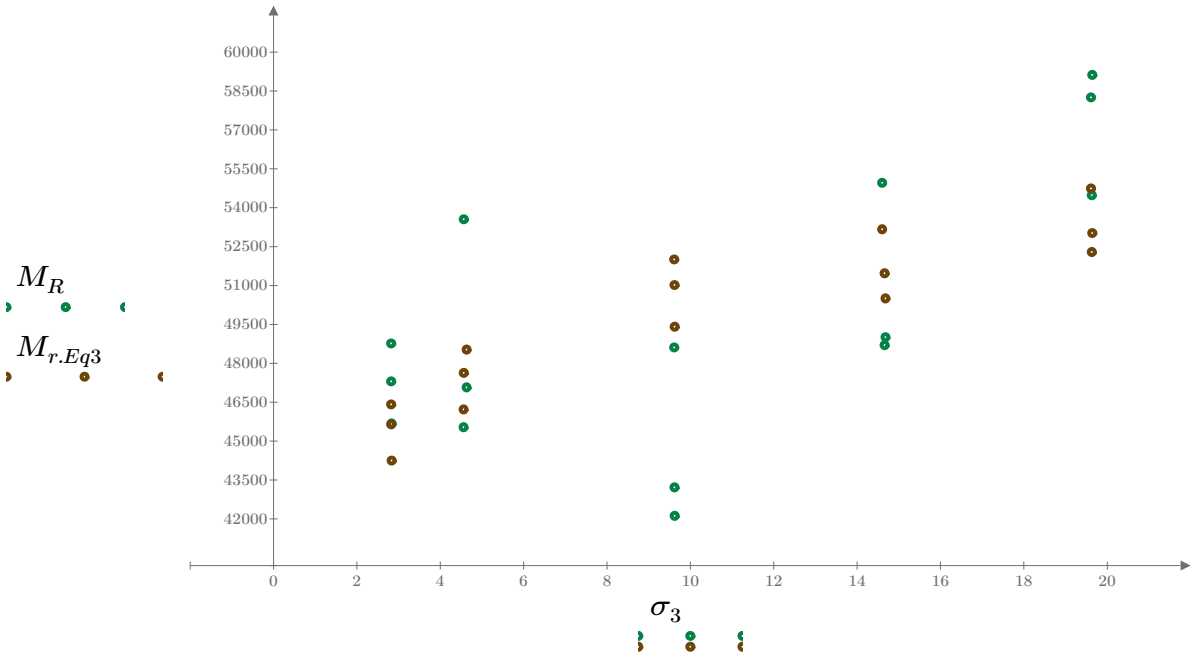

Figure 4. Plot of the test data (green points) vs. the fitted Equation 3 model (brown points).

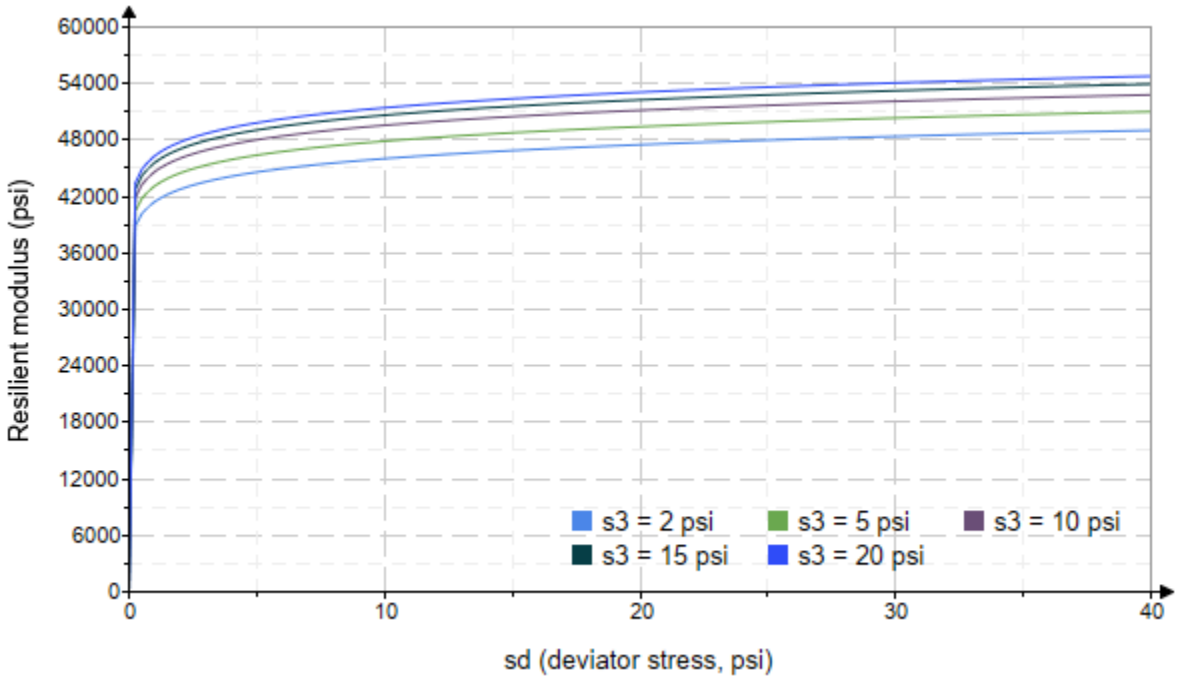

Figure 5. Plot of the fitted Equation 3 model for various confining stresses.

Dan Seely
9/12/2023

$$M_{R.4}\left(\sigma_B,\sigma_d,K_8,K_9,K_{10}\right) := K_8 \cdot p_a \left(\frac{\sigma_B}{p_a}\right)^{K_9} \cdot \left(\frac{\sigma_d}{p_a}\right)^{K_{10}}$$

Equation 4 AASHTO Publication No. FHWA-RD-97-083

$K_8 = 3182.797$

$K_9 = 0.0667$ Equation 4 fitting parameters

$K_{10} = 0.0269$

$R_4^{\,2} = 0.3467$ Coefficient of determination

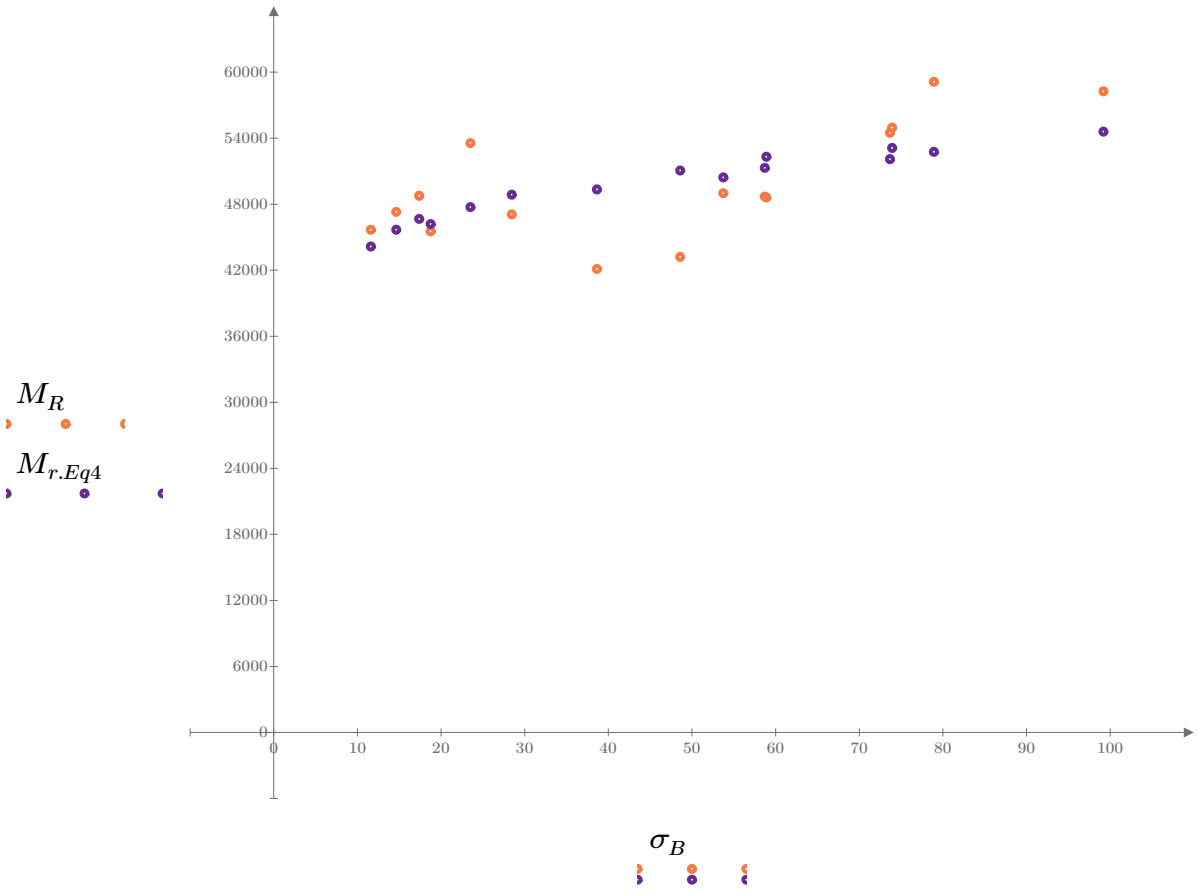

Figure 6. Plot of the test data (orange points) vs. the fitted Equation 4 model (purple points).

Dan Seely
9/12/2023

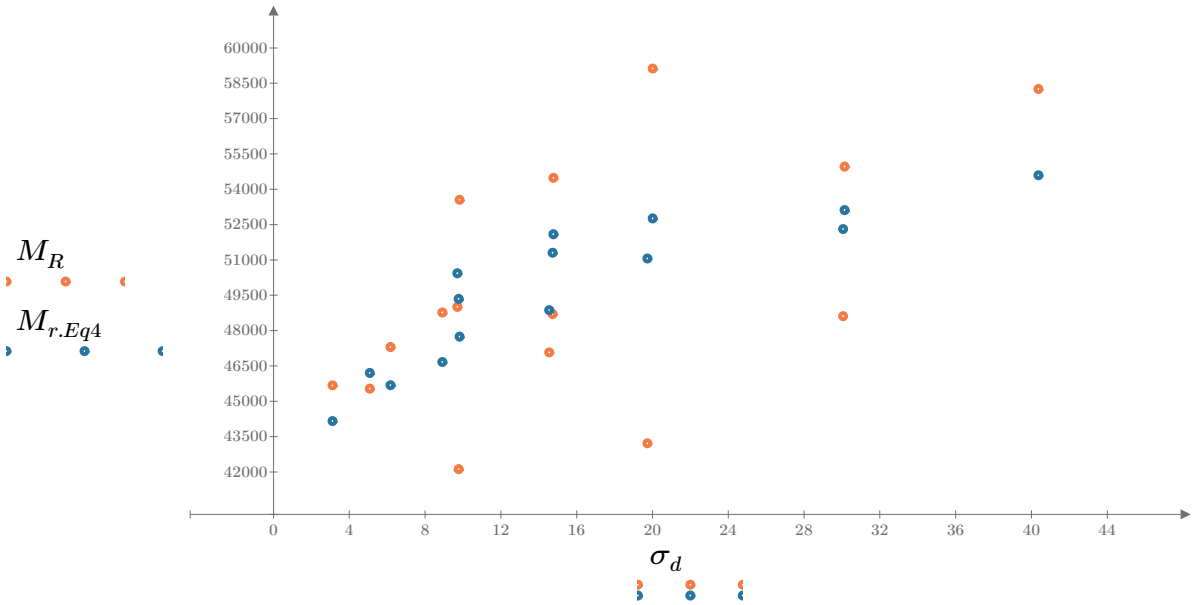

Figure 7. Plot of the test data (orange points) vs. the fitted Equation 4 model (blue points).

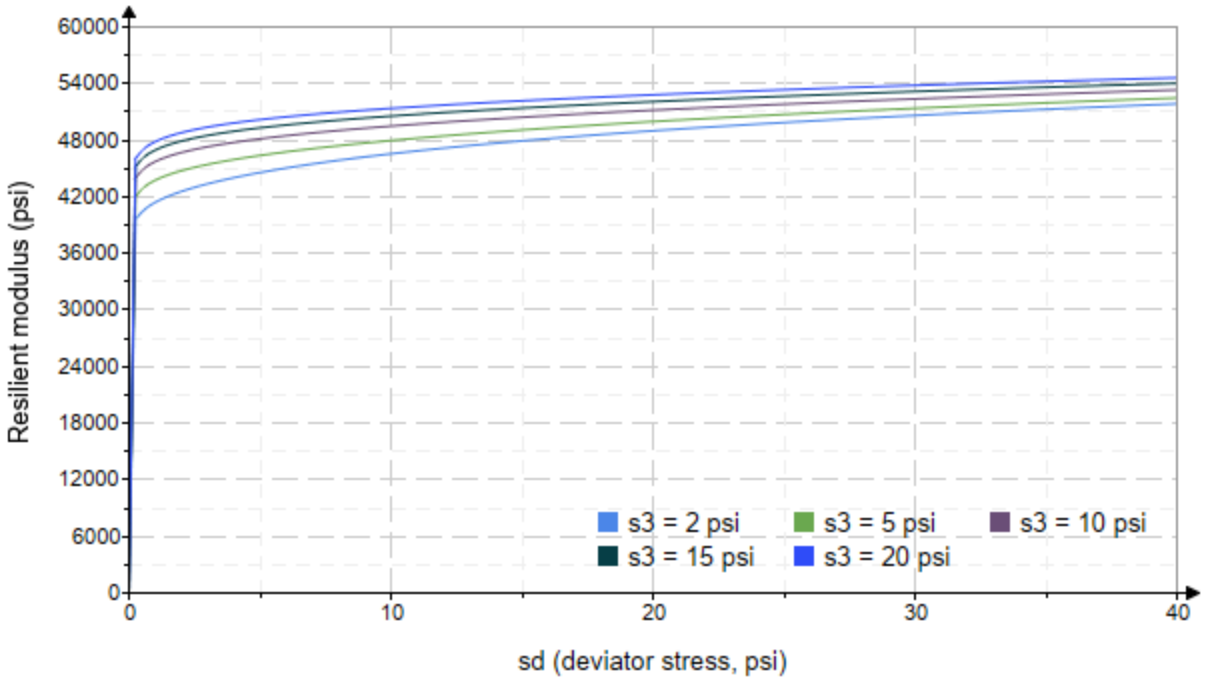

Figure 8. Plot of the fitted Equation 4 model for various confining stresses.

Dan Seely
9/12/2023

$SampleNo := \text{“B2}-\text{49”}$

$Treatment = \text{“H100”}$

$S = 4.996$ Degree of Saturation (%)

Test Sequence : Base/Subbase

Test summary data (psi) :

$$\sigma_3 = \begin{bmatrix} 2.569 \\ 2.503 \\ 2.576 \\ 4.597 \\ 4.582 \\ 4.579 \\ 9.619 \\ 9.650 \\ 9.621 \\ 14.610 \\ 14.660 \\ 14.630 \\ 19.700 \\ 19.680 \\ 19.680 \end{bmatrix} \quad \sigma_d = \begin{bmatrix} 3.200 \\ 6.239 \\ 9.025 \\ 5.176 \\ 10.020 \\ 14.510 \\ 9.998 \\ 19.600 \\ 30.200 \\ 9.938 \\ 14.730 \\ 30.300 \\ 14.660 \\ 19.880 \\ 40.440 \end{bmatrix} \quad \sigma_B = \begin{bmatrix} 10.910 \\ 13.750 \\ 16.750 \\ 18.970 \\ 23.760 \\ 28.250 \\ 38.850 \\ 48.550 \\ 59.060 \\ 53.780 \\ 58.700 \\ 74.170 \\ 73.760 \\ 78.910 \\ 99.480 \end{bmatrix} \quad M_R = \begin{bmatrix} 43041.6 \\ 45952.0 \\ 46697.6 \\ 52948.6 \\ 39978.6 \\ 43245.2 \\ 42608.6 \\ 53184.8 \\ 53289.6 \\ 53085.4 \\ 53778.6 \\ 53935.4 \\ 51775.4 \\ 53430.2 \\ 55776.0 \end{bmatrix}$$

σ_3 = mean confining stress
σ_d = mean deviator stress
σ_B = mean bulk stress
M_R = resilient modulus
p_a = atmospheric pressure = 14.6959 psi

Dan Seely
9/12/2023

$$M_{R.1}\left(\sigma_B, K_1, K_2\right) := K_1 \cdot {\sigma_B}^{K_2}$$

Equation 1
AASHTO Publication No. FHWA-RD-97-083

$K_1 = 33057.260$

$K_2 = 0.1103$

Equation 1 fitting parameters

${R_1}^2 = 0.5078$

Coefficient of determination

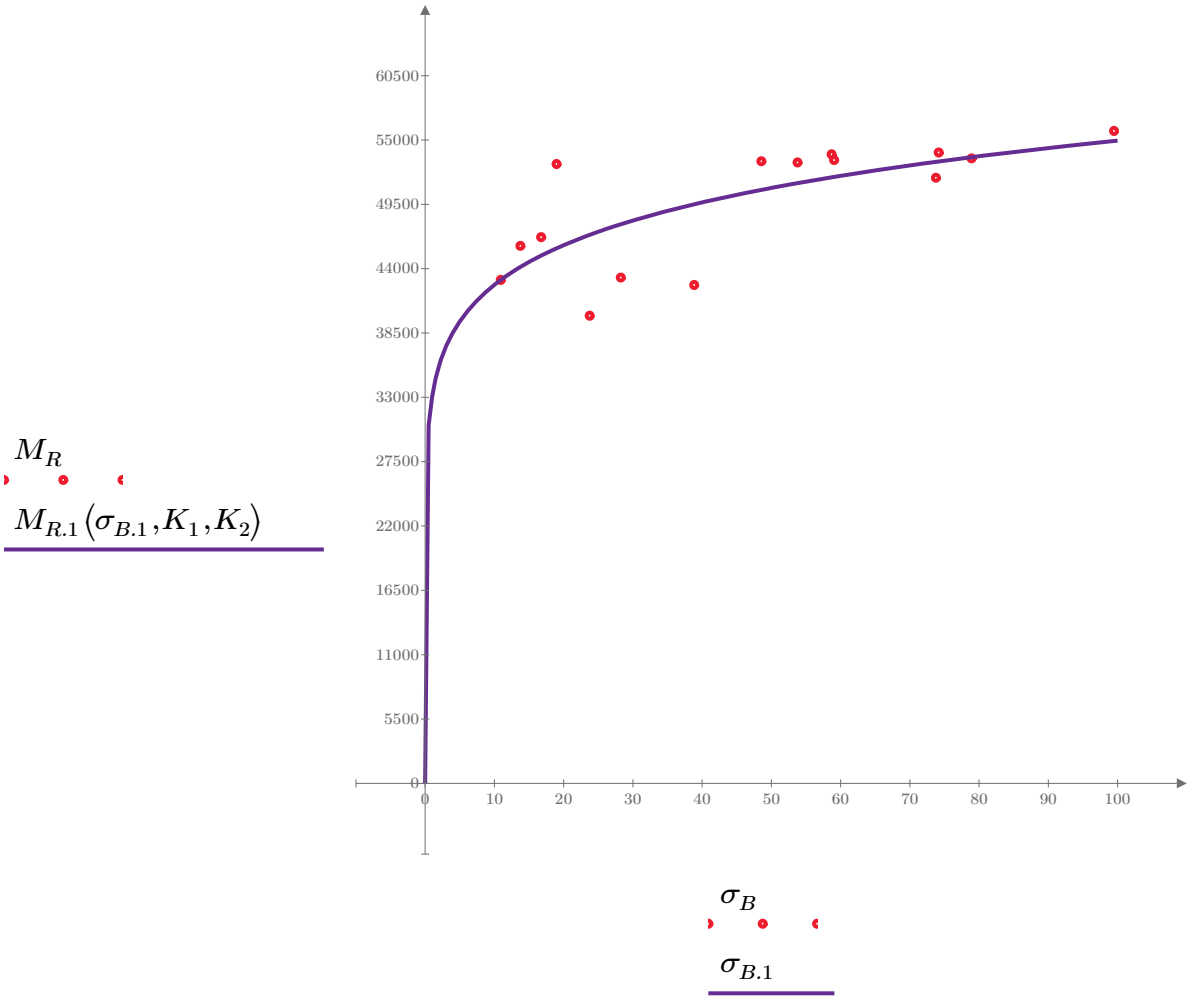

Figure 1. Plot of the test data (red points) vs. the fitted Equation 1 model (purple line).

Dan Seely
9/12/2023

$$M_{R.2}(\sigma_d, K_3, K_4) := K_3 \cdot \sigma_d^{K_4}$$

Equation 2
AASHTO Publication No. FHWA-RD-97-083

$K_3 = 39066.194$

$K_4 = 0.0921$

Equation 2 fitting parameters

$R_2^2 = 0.3513$

Coefficient of determination

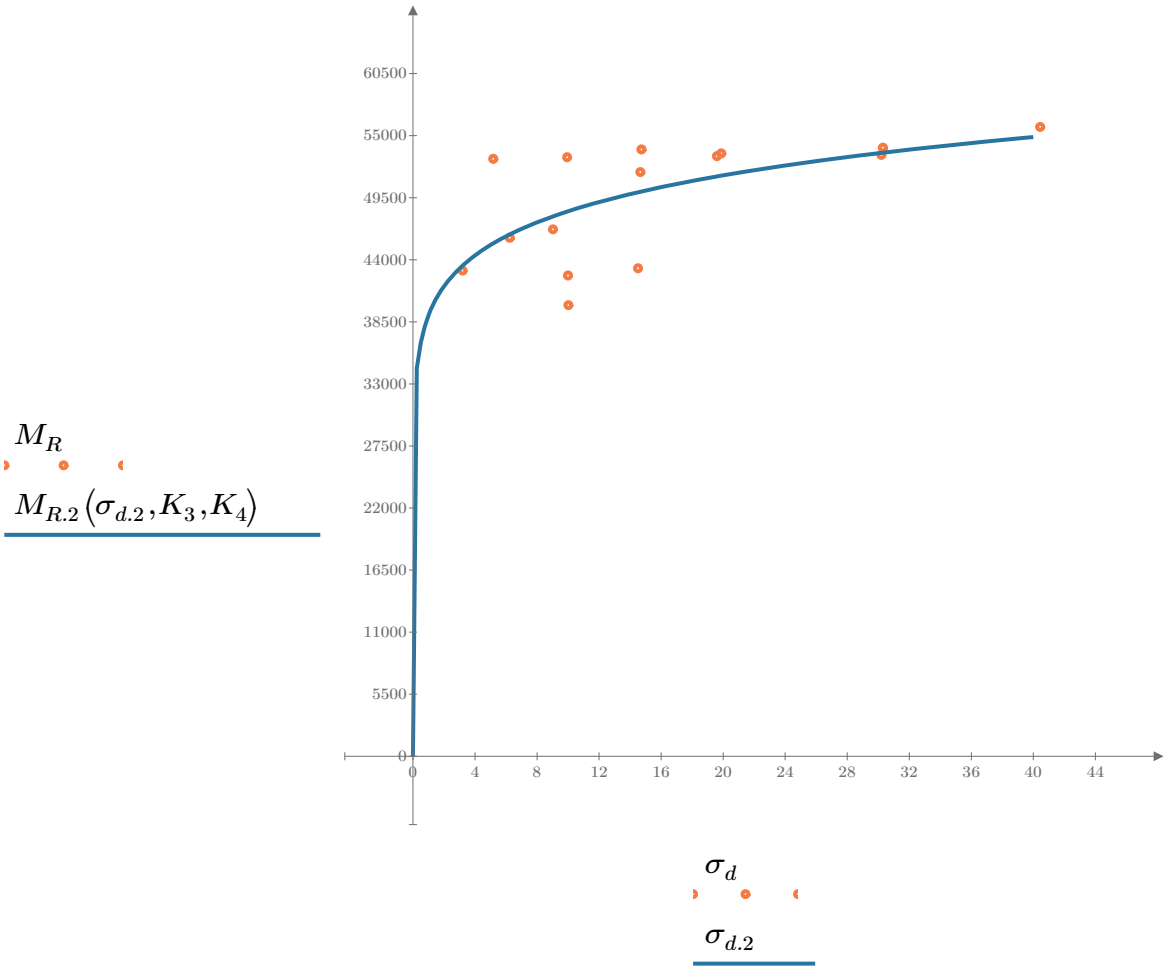

Figure 2. Plot of the test data (orange points) vs. the fitted Equation 2 model (blue line).

Dan Seely
9/12/2023

$$M_{R.3}\left(\sigma_d,\sigma_3,K_5,K_6,K_7\right):=K_5\cdot{\sigma_d}^{K_6}\cdot\left(1+\sigma_3\right)^{K_7}$$

Equation 3 AASHTO Publication No. FHWA-RD-97-083

$K_5=37393.558$

$K_6=0.0272$ Equation 3 fitting parameters

$K_7=0.0937$

${R_3}^2=0.5153$ Coefficient of determination

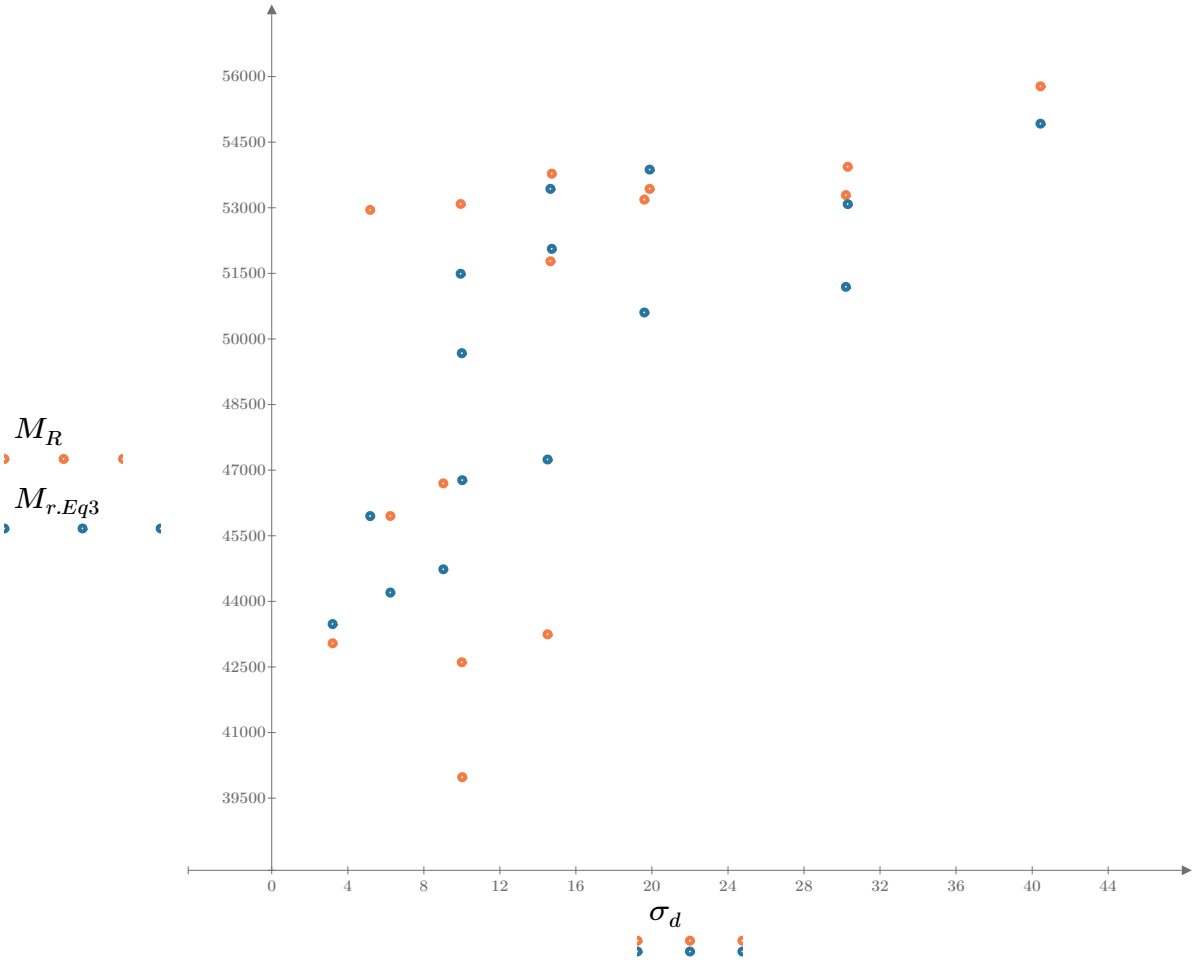

Figure 3. Plot of the test data (orange points) vs. the fitted Equation 3 model (blue points).

Dan Seely
9/12/2023

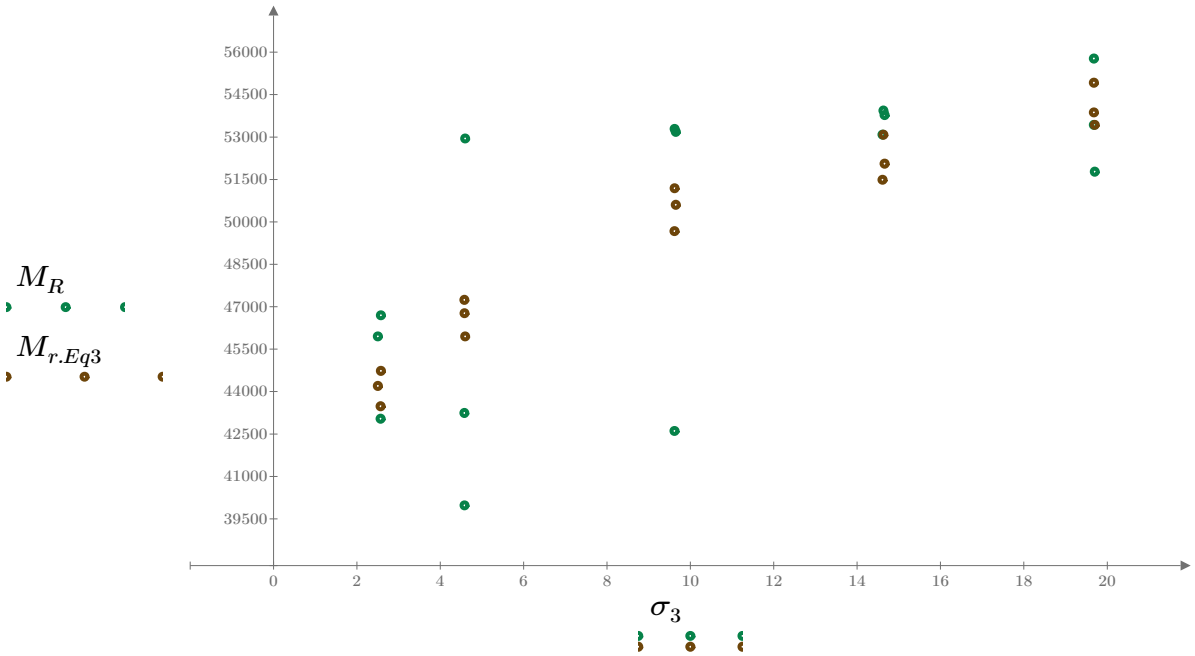

Figure 4. Plot of the test data (green points) vs. the fitted Equation 3 model (brown points).

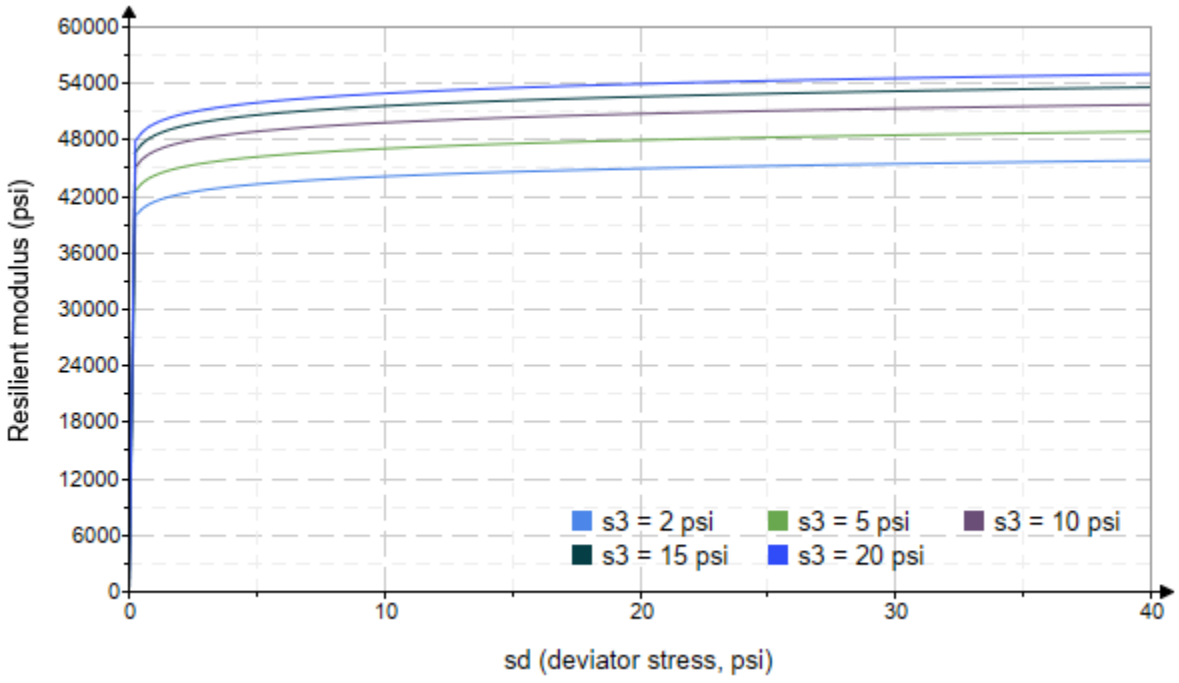

Figure 5. Plot of the fitted Equation 3 model for various confining stresses.

Dan Seely
9/12/2023

$$M_{R.4}\left(\sigma_B,\sigma_d,K_8,K_9,K_{10}\right) := K_8 \cdot p_a \left(\frac{\sigma_B}{p_a}\right)^{K_9} \cdot \left(\frac{\sigma_d}{p_a}\right)^{K_{10}}$$

Equation 4 AASHTO Publication No. FHWA-RD-97-083

$K_8 = 2984.771$

$K_9 = 0.1227$ Equation 4 fitting parameters

$K_{10} = -0.0145$

$R_4^{\,2} = 0.5100$ Coefficient of determination

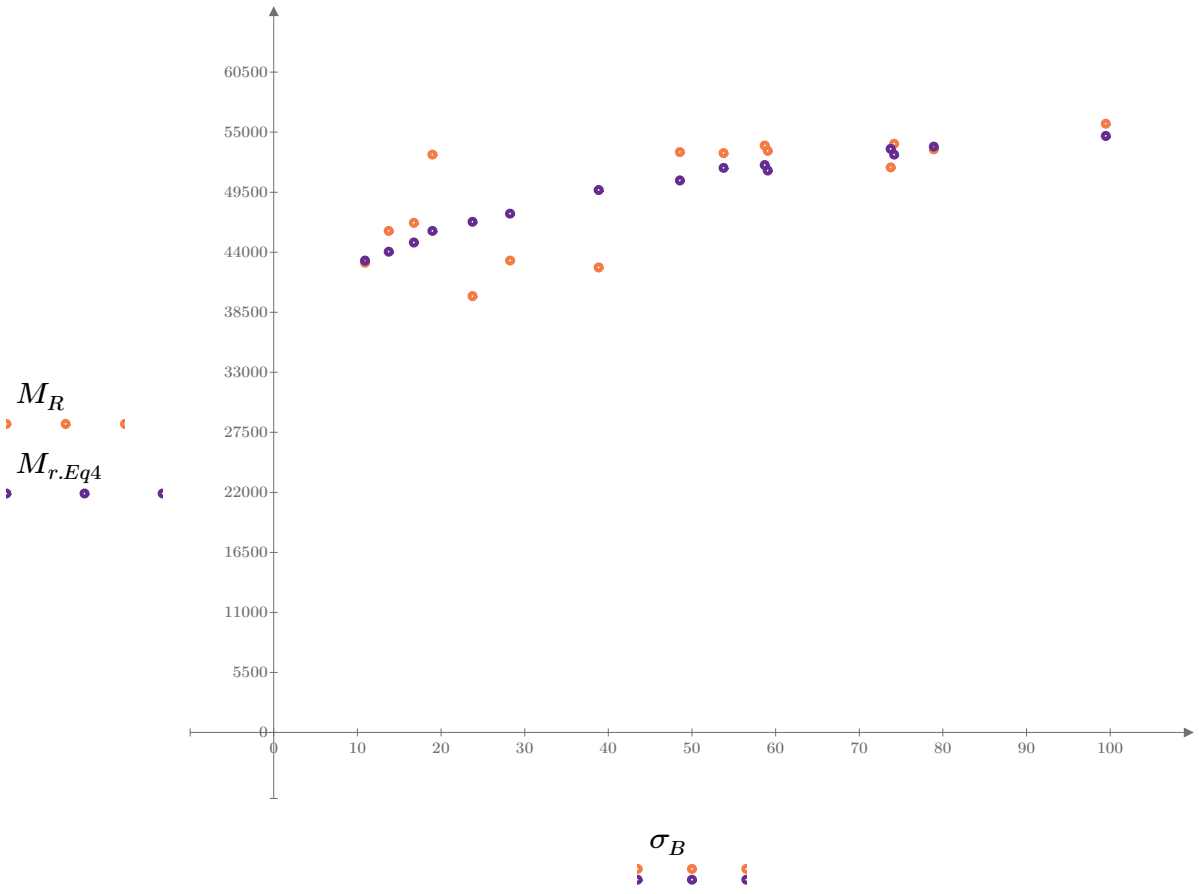

Figure 6. Plot of the test data (orange points) vs. the fitted Equation 4 model (purple points).

Dan Seely
9/12/2023

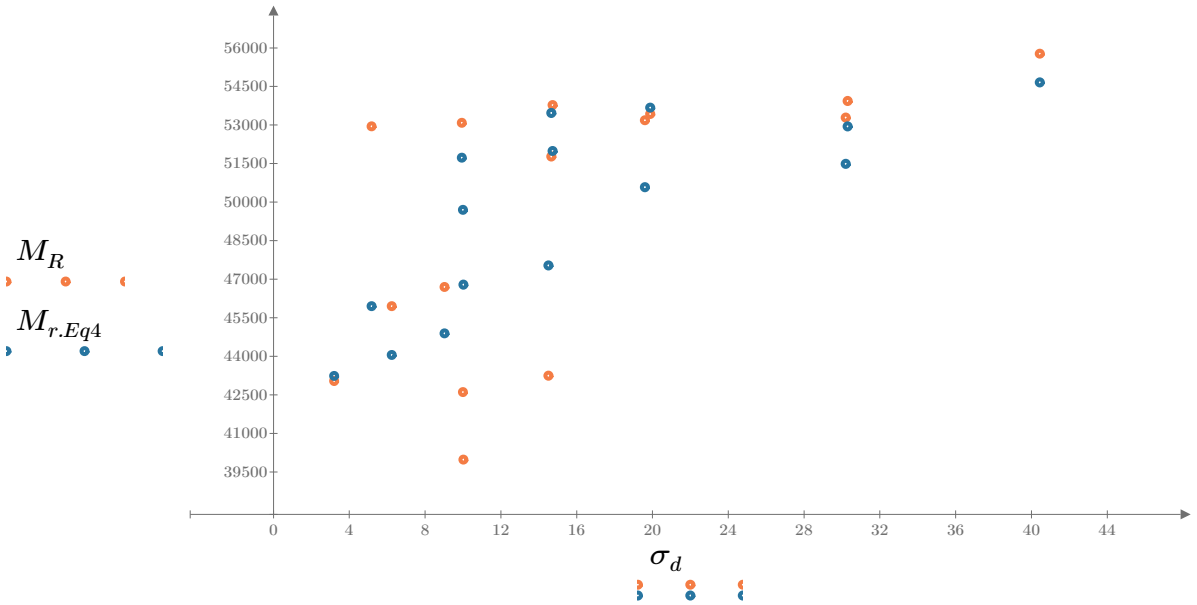

Figure 7. Plot of the test data (orange points) vs. the fitted Equation 4 model (blue points).

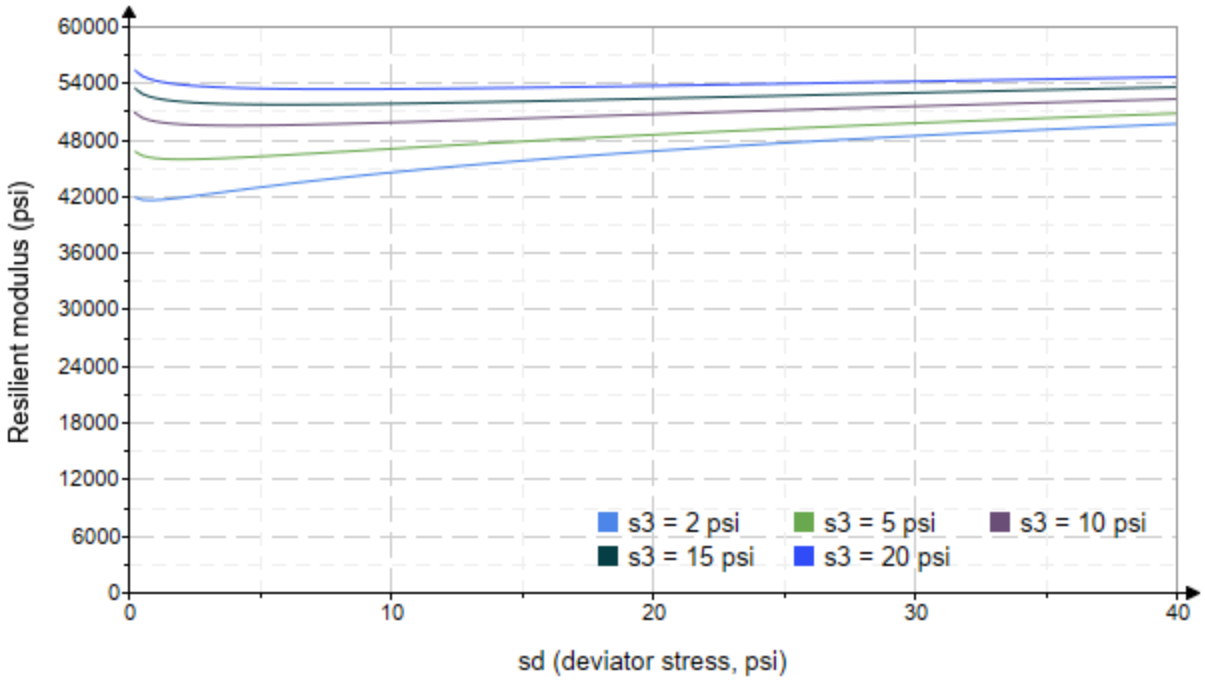

Figure 8. Plot of the fitted Equation 4 model for various confining stresses.

Dan Seely
9/12/2023

$SampleNo := \text{“B2}-\text{50”}$

$Treatment = \text{“H100”}$

$S = 5.033$ Degree of Saturation (%)

Test Sequence : Base/Subbase

Test summary data (psi) :

$$\sigma_3 = \begin{bmatrix} 2.219 \\ 2.233 \\ 2.202 \\ 3.977 \\ 4.372 \\ 4.211 \\ 9.103 \\ 8.917 \\ 8.909 \\ 14.490 \\ 14.320 \\ 13.930 \\ 19.500 \\ 19.350 \\ 19.460 \end{bmatrix} \quad \sigma_d = \begin{bmatrix} 3.184 \\ 6.175 \\ 9.156 \\ 5.192 \\ 10.070 \\ 14.600 \\ 9.955 \\ 19.610 \\ 29.600 \\ 9.953 \\ 14.720 \\ 29.800 \\ 14.850 \\ 19.730 \\ 40.150 \end{bmatrix} \quad \sigma_B = \begin{bmatrix} 9.842 \\ 12.870 \\ 15.760 \\ 17.120 \\ 23.180 \\ 27.230 \\ 37.260 \\ 46.360 \\ 56.320 \\ 53.410 \\ 57.660 \\ 71.590 \\ 73.340 \\ 77.780 \\ 98.530 \end{bmatrix} \quad M_R = \begin{bmatrix} 56156.7 \\ 52556.4 \\ 53400.0 \\ 61327.2 \\ 55913.4 \\ 54867.4 \\ 60946.2 \\ 59466.6 \\ 55986.2 \\ 58146.4 \\ 60638.2 \\ 54454.8 \\ 62868.4 \\ 58271.0 \\ 61999.4 \end{bmatrix}$$

σ_3 = mean confining stress
σ_d = mean deviator stress
σ_B = mean bulk stress
M_R = resilient modulus
p_a = atmospheric pressure = 14.6959 psi

Dan Seely
9/12/2023

$$M_{R.1}\left(\sigma_B, K_1, K_2\right) := K_1 \cdot {\sigma_B}^{K_2}$$

Equation 1
AASHTO Publication No. FHWA-RD-97-083

$K_1 = 49988.698$

$K_2 = 0.0403$

Equation 1 fitting parameters

${R_1}^2 = 0.2613$

Coefficient of determination

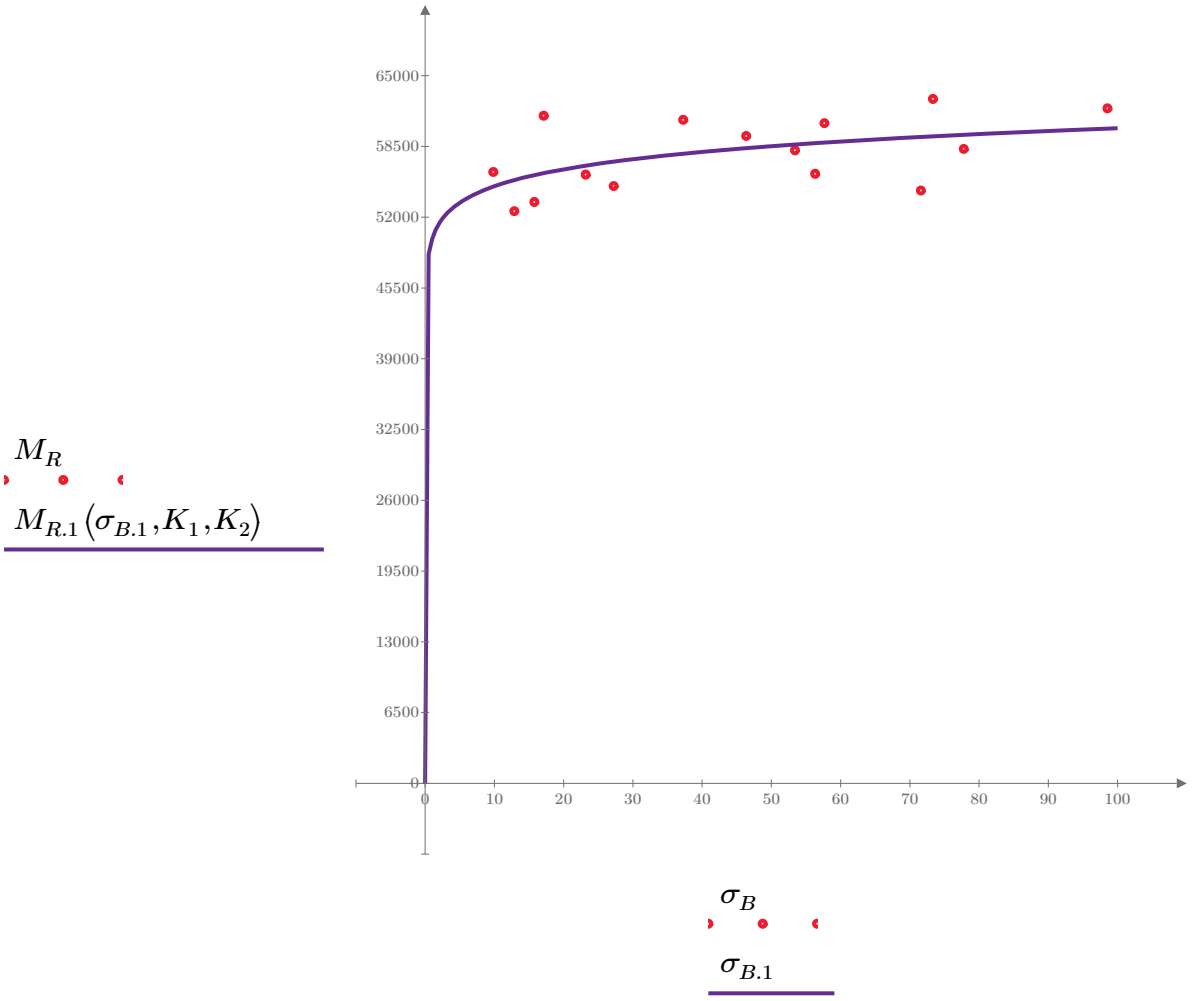

Figure 1. Plot of the test data (red points) vs. the fitted Equation 1 model (purple line).

Dan Seely
9/12/2023

$$M_{R.2}\left(\sigma_d, K_3, K_4\right) := K_3 \cdot \sigma_d^{K_4}$$

Equation 2
AASHTO Publication No. FHWA-RD-97-083

$K_3 = 55527.325$

$K_4 = 0.0157$

Equation 2 fitting parameters

$R_2^{\,2} = 0.0362$

Coefficient of determination

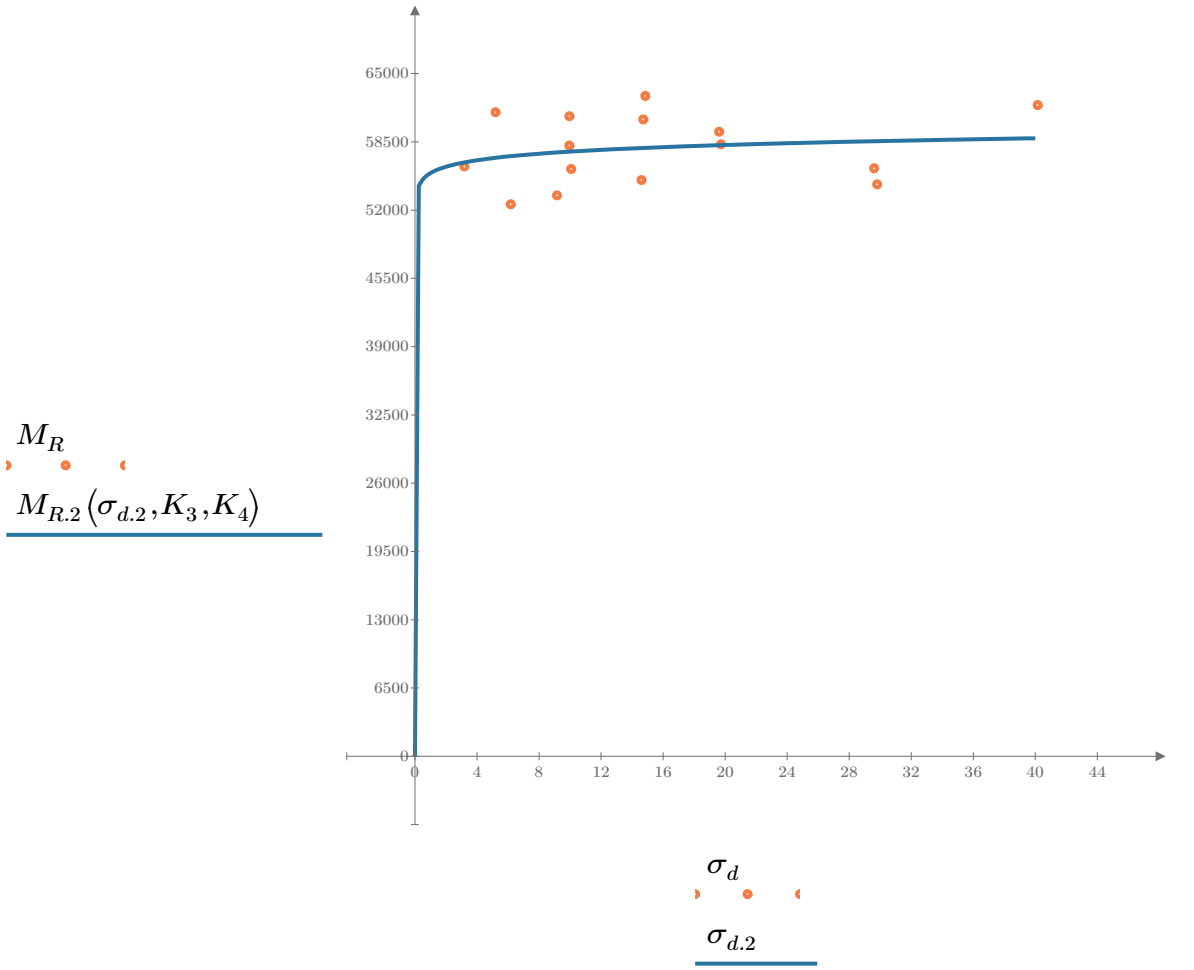

Figure 2. Plot of the test data (orange points) vs. the fitted Equation 2 model (blue line).

Dan Seely
9/12/2023

$$M_{R.3}\left(\sigma_d,\sigma_3,K_5,K_6,K_7\right) := K_5 \cdot {\sigma_d}^{K_6} \cdot \left(1+\sigma_3\right)^{K_7}$$

Equation 3 AASHTO Publication No. FHWA-RD-97-083

$K_5 = 54195.134$

$K_6 = -0.0457$ Equation 3 fitting parameters

$K_7 = 0.083$

${R_3}^2 = 0.5362$ Coefficient of determination

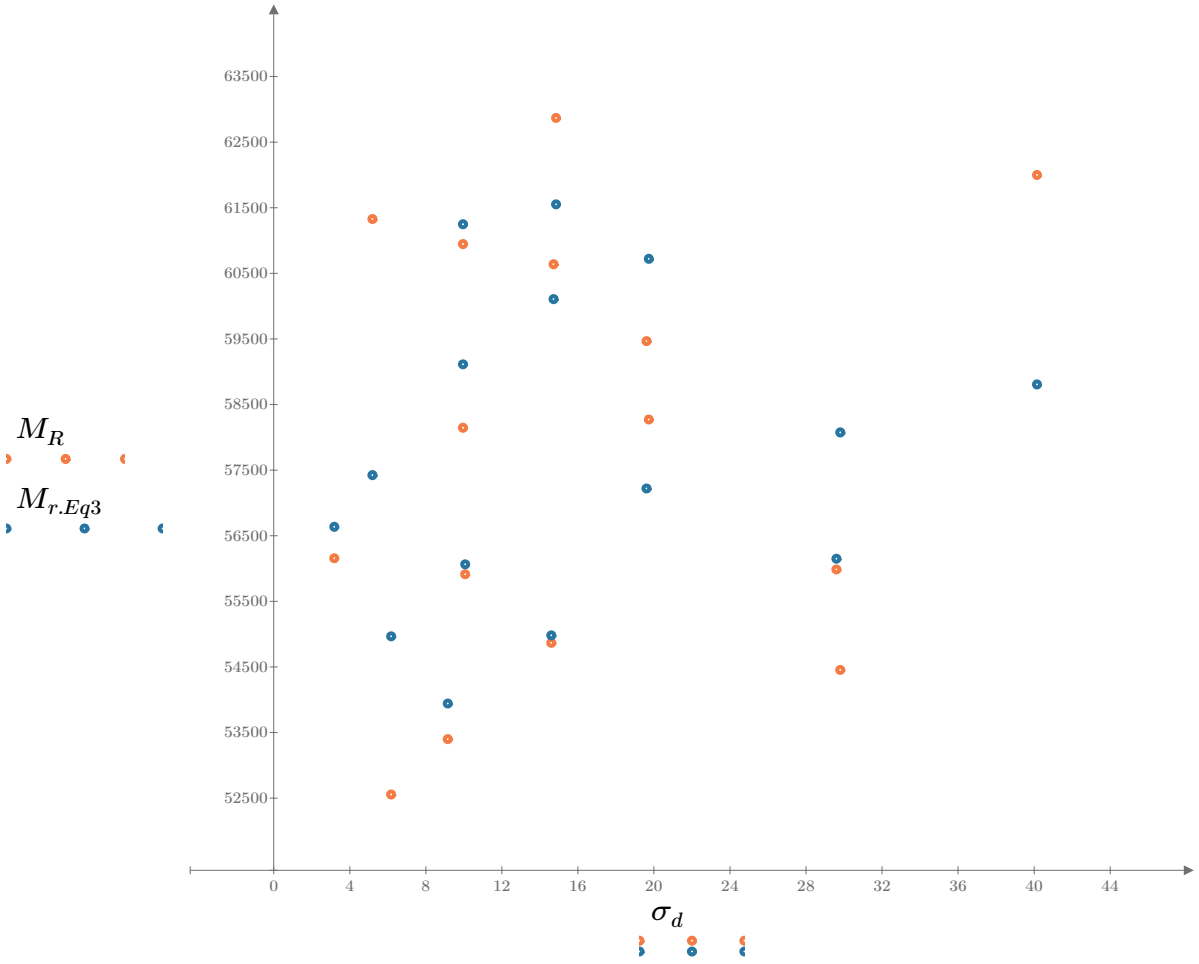

Figure 3. Plot of the test data (orange points) vs. the fitted Equation 3 model (blue points).

Dan Seely
9/12/2023

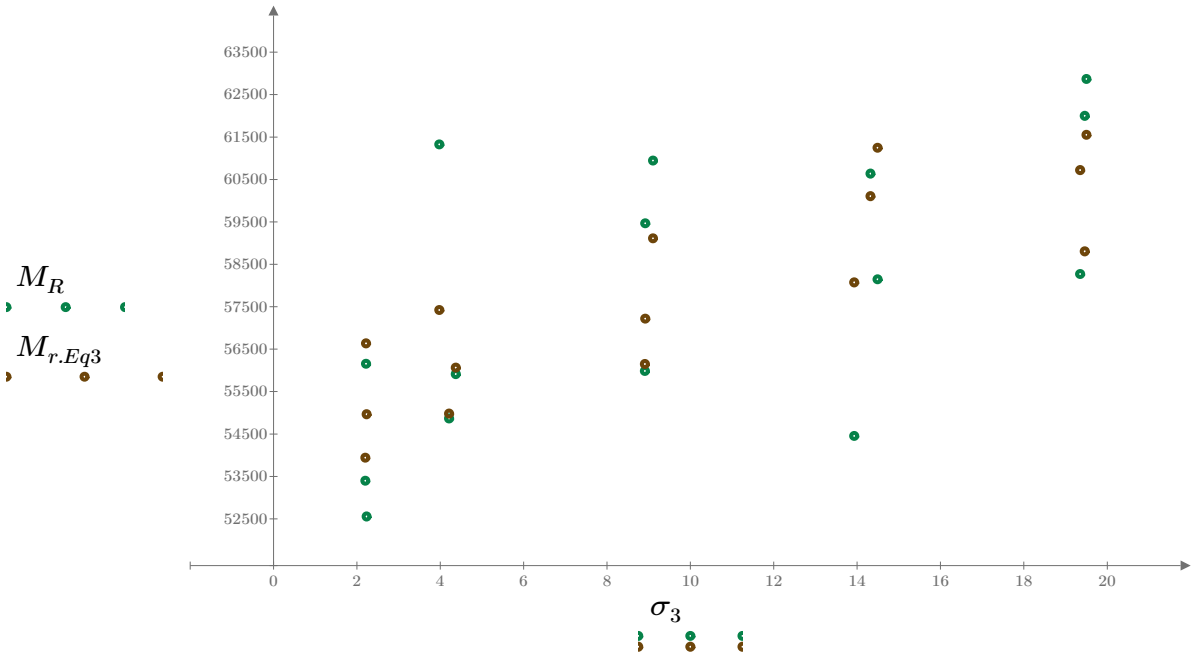

Figure 4. Plot of the test data (green points) vs. the fitted Equation 3 model (brown points).

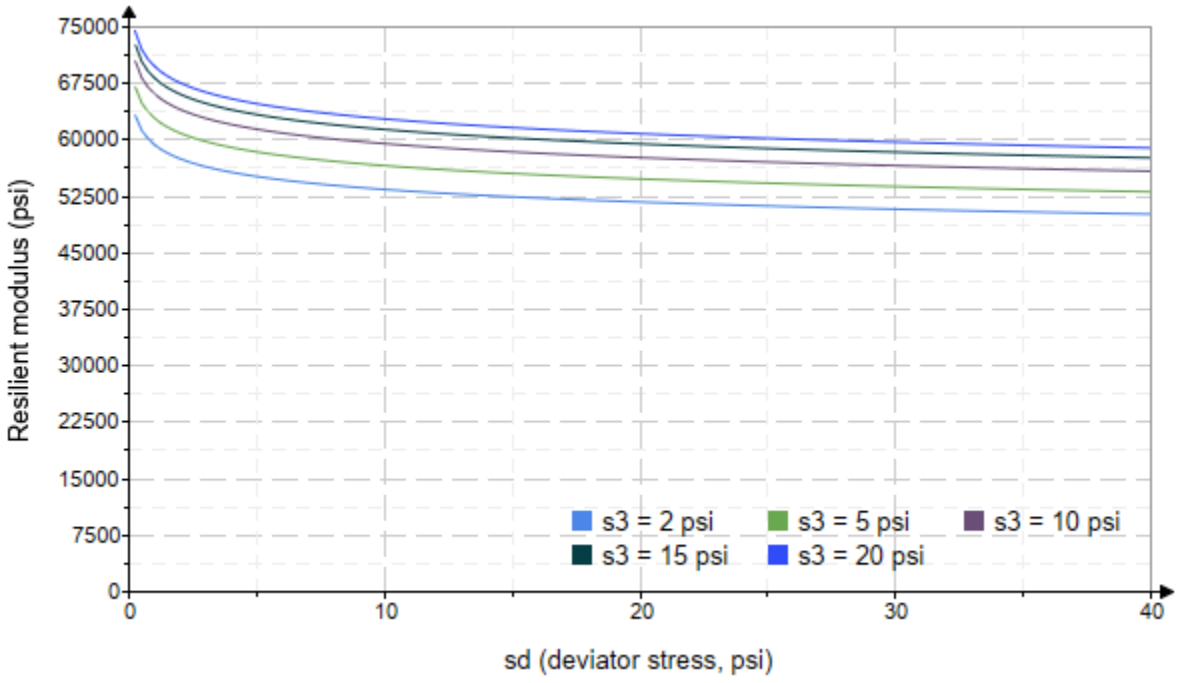

Figure 5. Plot of the fitted Equation 3 model for various confining stresses.

Dan Seely
9/12/2023

$$M_{R.4}\left(\sigma_B,\sigma_d,K_8,K_9,K_{10}\right) := K_8 \cdot p_a \left(\frac{\sigma_B}{p_a}\right)^{K_9} \cdot \left(\frac{\sigma_d}{p_a}\right)^{K_{10}}$$

Equation 4 AASHTO Publication No. FHWA-RD-97-083

$K_8 = 3514.899$

$K_9 = 0.1101$ Equation 4 fitting parameters

$K_{10} = -0.0853$

${R_4}^2 = 0.5239$ Coefficient of determination

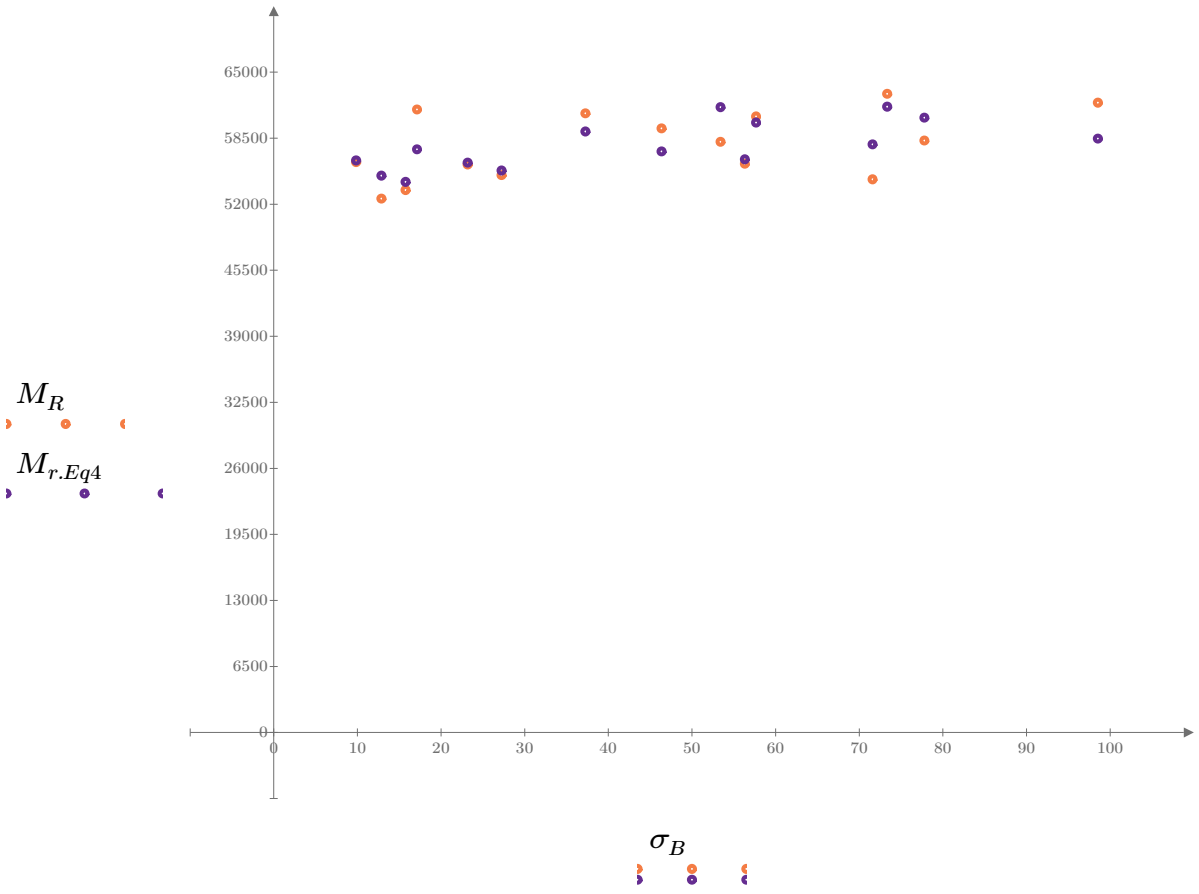

Figure 6. Plot of the test data (orange points) vs. the fitted Equation 4 model (purple points).

Dan Seely
9/12/2023

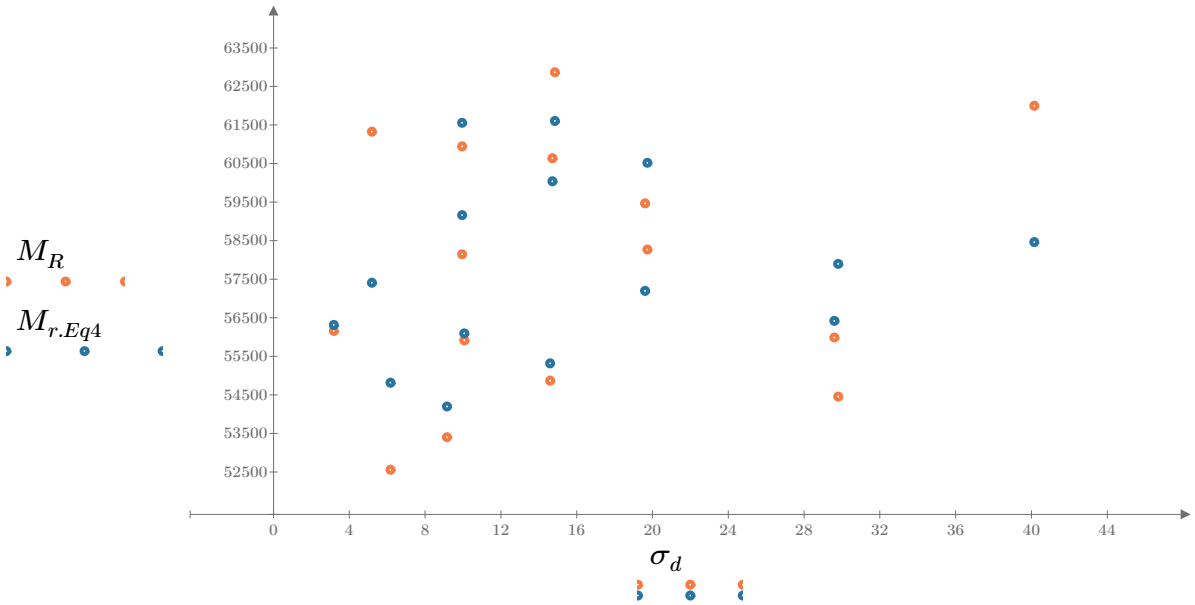

Figure 7. Plot of the test data (orange points) vs. the fitted Equation 4 model (blue points).

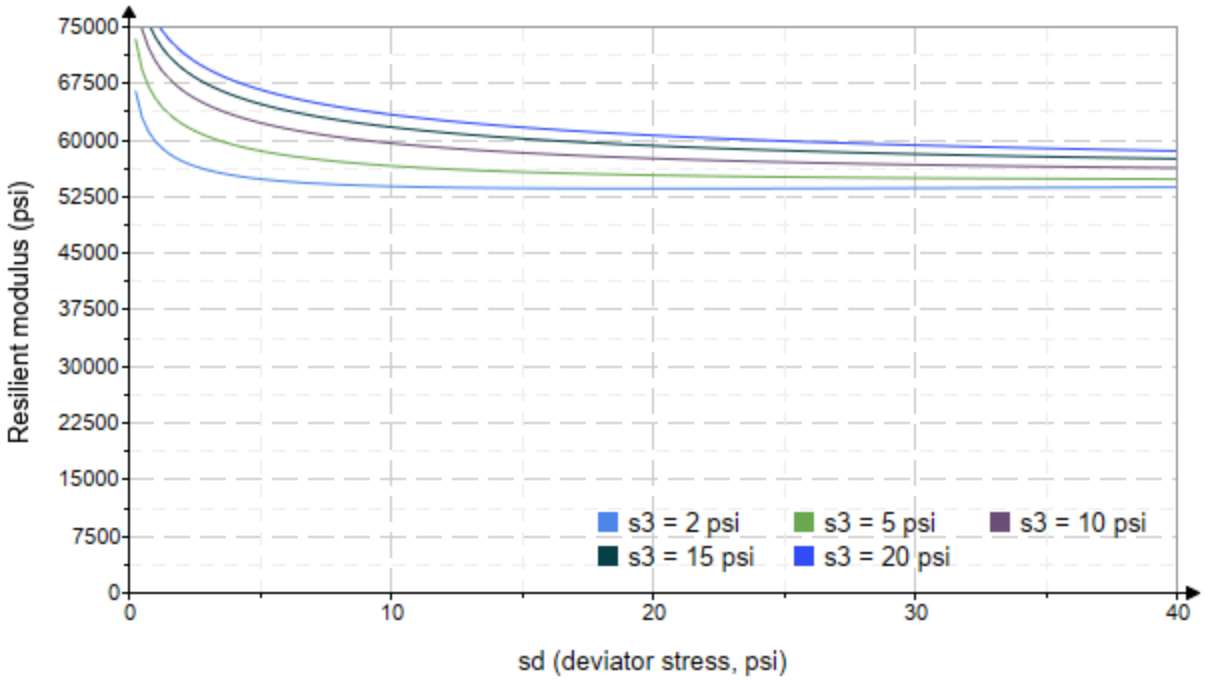

Figure 8. Plot of the fitted Equation 4 model for various confining stresses.

Dan Seely
9/12/2023

$SampleNo := \text{“B2}-\text{51”}$

$Treatment = \text{“H100”}$

$S = 5.100$ Degree of Saturation (%)

Test Sequence : Base/Subbase

Test summary data (psi) :

$$\sigma_3 = \begin{bmatrix} 2.792 \\ 2.729 \\ 2.665 \\ 4.749 \\ 4.666 \\ 4.621 \\ 9.668 \\ 9.706 \\ 9.668 \\ 14.630 \\ 14.740 \\ 14.670 \\ 19.780 \\ 19.760 \\ 19.700 \end{bmatrix} \quad \sigma_d = \begin{bmatrix} 3.191 \\ 6.090 \\ 9.323 \\ 5.102 \\ 10.170 \\ 14.650 \\ 10.120 \\ 19.570 \\ 29.590 \\ 9.936 \\ 14.900 \\ 29.940 \\ 14.790 \\ 19.700 \\ 40.340 \end{bmatrix} \quad \sigma_B = \begin{bmatrix} 11.570 \\ 14.280 \\ 17.320 \\ 19.350 \\ 24.160 \\ 28.510 \\ 39.120 \\ 48.690 \\ 58.590 \\ 53.820 \\ 59.120 \\ 73.950 \\ 74.110 \\ 78.990 \\ 99.440 \end{bmatrix} \quad M_R = \begin{bmatrix} 39105.2 \\ 40213.4 \\ 40693.0 \\ 43692.2 \\ 42966.6 \\ 42926.4 \\ 44921.2 \\ 52928.8 \\ 64112.8 \\ 64282.6 \\ 63175.0 \\ 69411.0 \\ 70800.6 \\ 71595.0 \\ 69900.8 \end{bmatrix}$$

σ_3 = mean confining stress
σ_d = mean deviator stress
σ_B = mean bulk stress
M_R = resilient modulus
p_a = atmospheric pressure = 14.6959 psi

Dan Seely
9/12/2023

$$M_{R.1}\left(\sigma_B, K_1, K_2\right) := K_1 \cdot {\sigma_B}^{K_2}$$

Equation 1
AASHTO Publication No. FHWA-RD-97-083

$K_1 = 14840.260$

$K_2 = 0.3503$

Equation 1 fitting parameters

${R_1}^2 = 0.9030$

Coefficient of determination

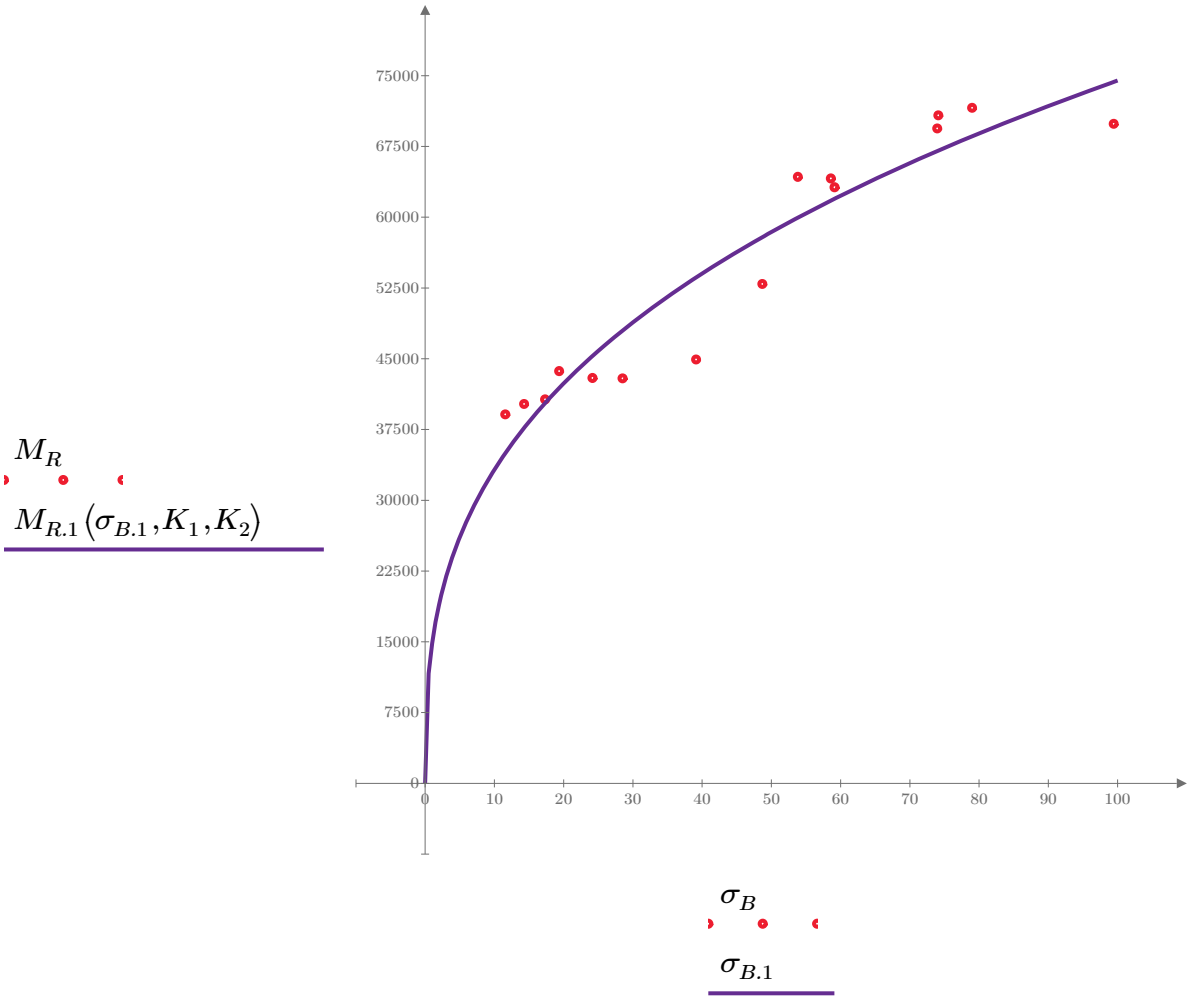

Figure 1. Plot of the test data (red points) vs. the fitted Equation 1 model (purple line).

Dan Seely
9/12/2023

$$M_{R.2}(\sigma_d, K_3, K_4) := K_3 \cdot \sigma_d^{K_4}$$

Equation 2
AASHTO Publication No. FHWA-RD-97-083

$K_3 = 27531.676$

$K_4 = 0.2632$

Equation 2 fitting parameters

$R_2^2 = 0.5711$

Coefficient of determination

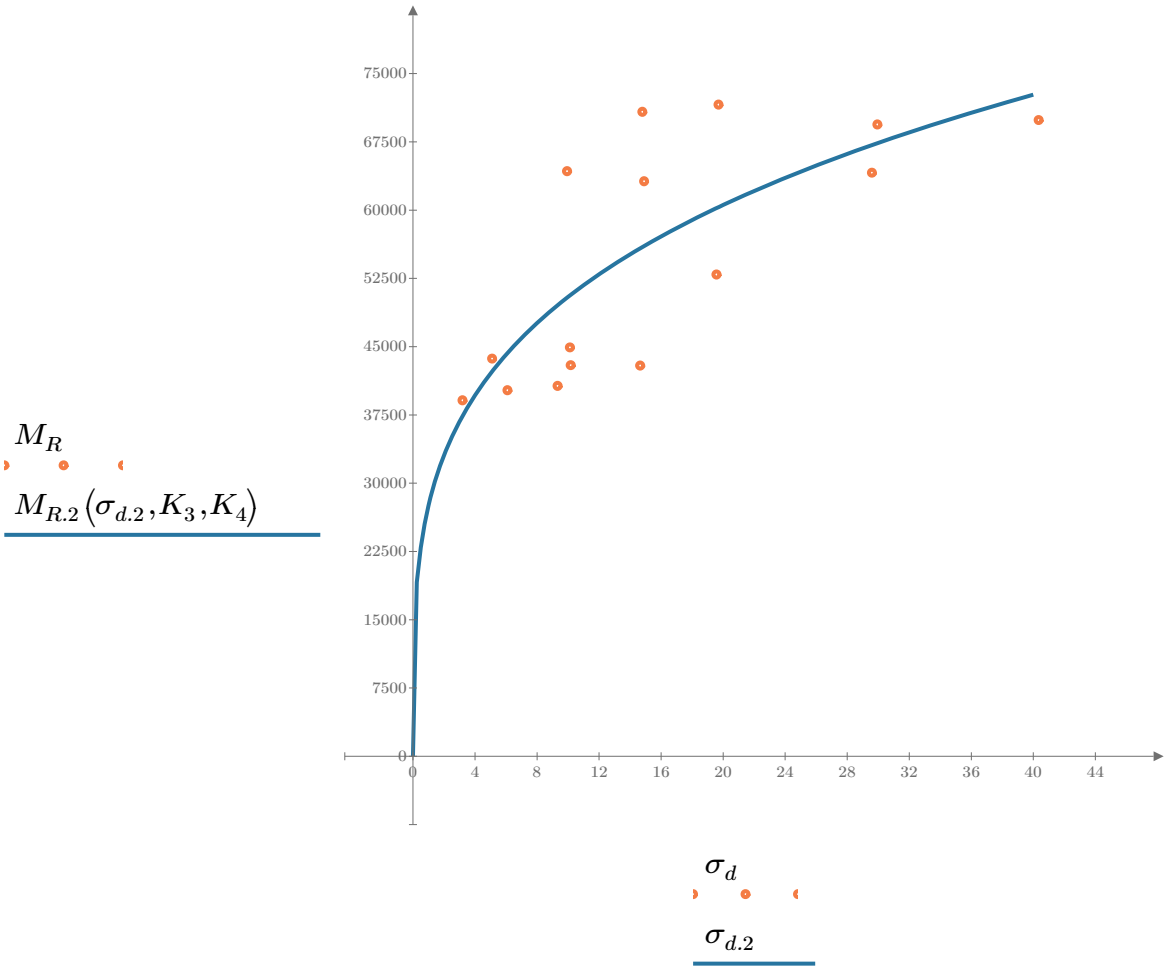

Figure 2. Plot of the test data (orange points) vs. the fitted Equation 2 model (blue line).

Dan Seely
9/12/2023

$$M_{R.3}\left(\sigma_d,\sigma_3,K_5,K_6,K_7\right):=K_5\cdot{\sigma_d}^{K_6}\cdot\left(1+\sigma_3\right)^{K_7}$$

Equation 3 AASHTO Publication No. FHWA-RD-97-083

$K_5=22478.189$

$K_6=0.0627$ Equation 3 fitting parameters

$K_7=0.3138$

${R_3}^2=0.9143$ Coefficient of determination

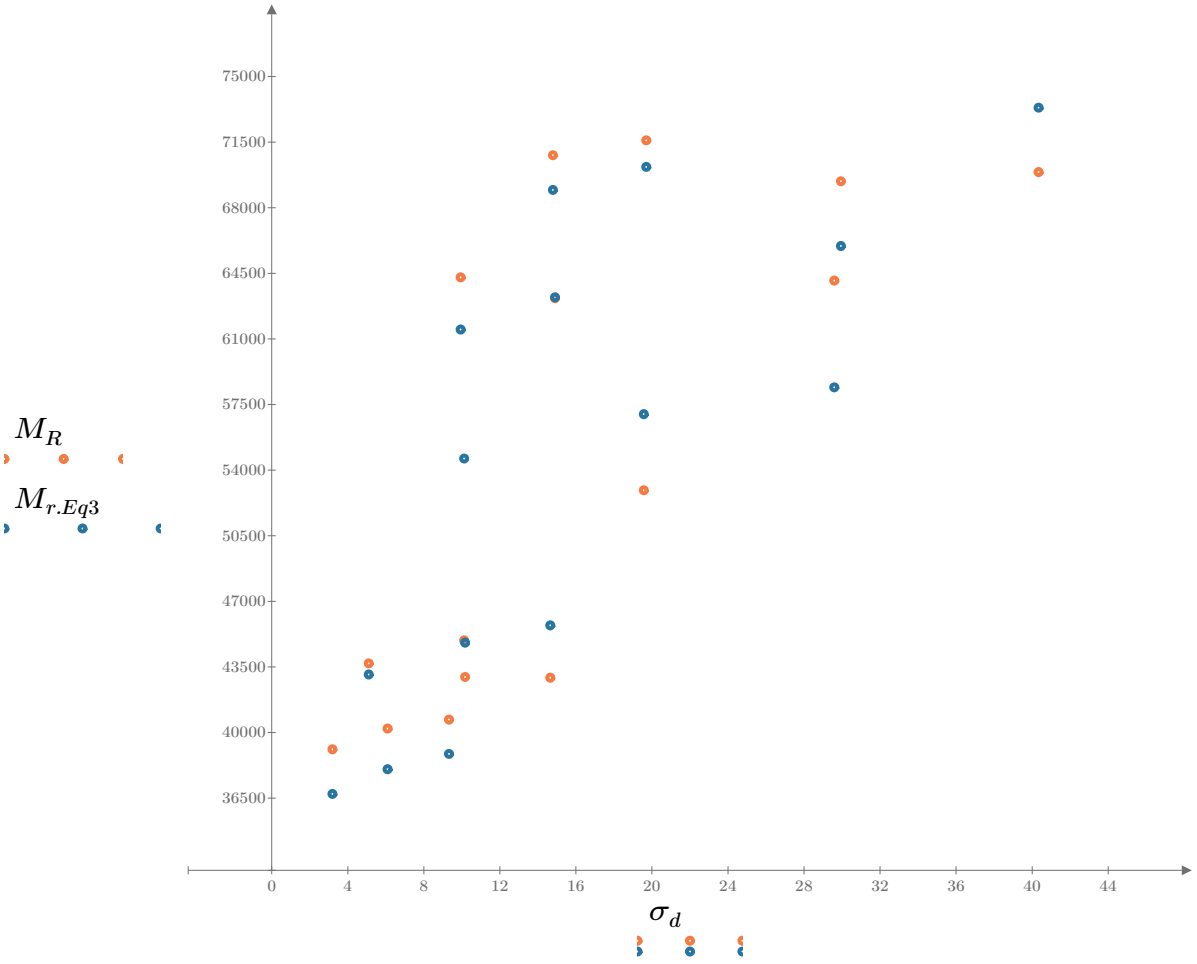

Figure 3. Plot of the test data (orange points) vs. the fitted Equation 3 model (blue points).

Dan Seely
9/12/2023

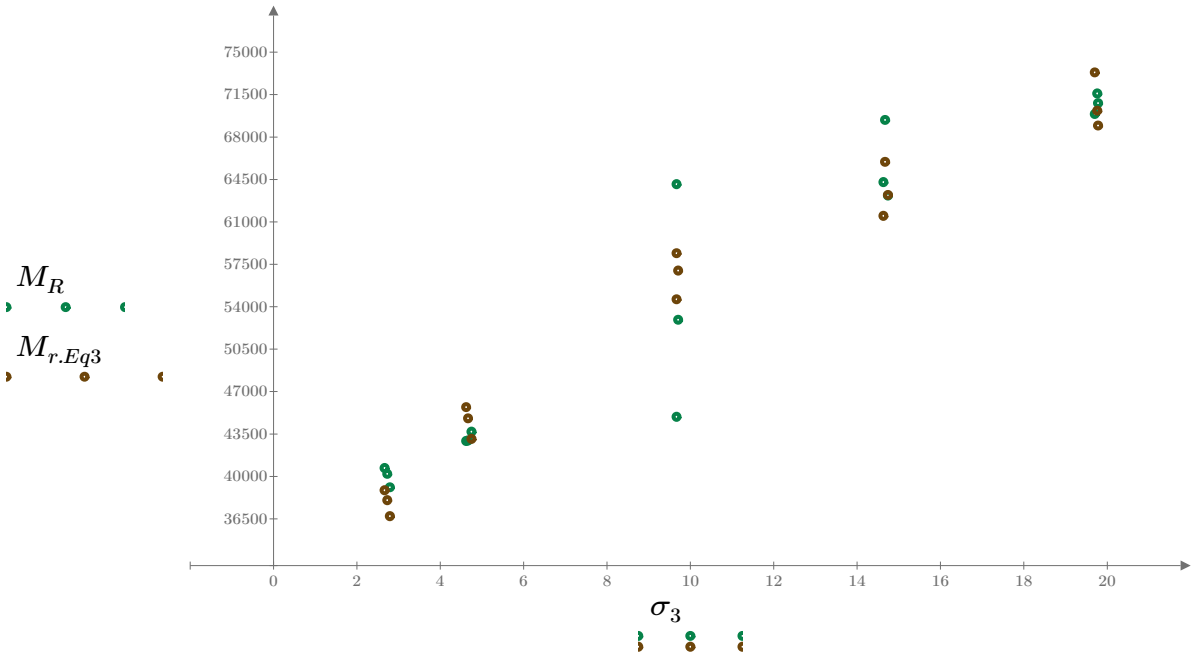

Figure 4. Plot of the test data (green points) vs. the fitted Equation 3 model (brown points).

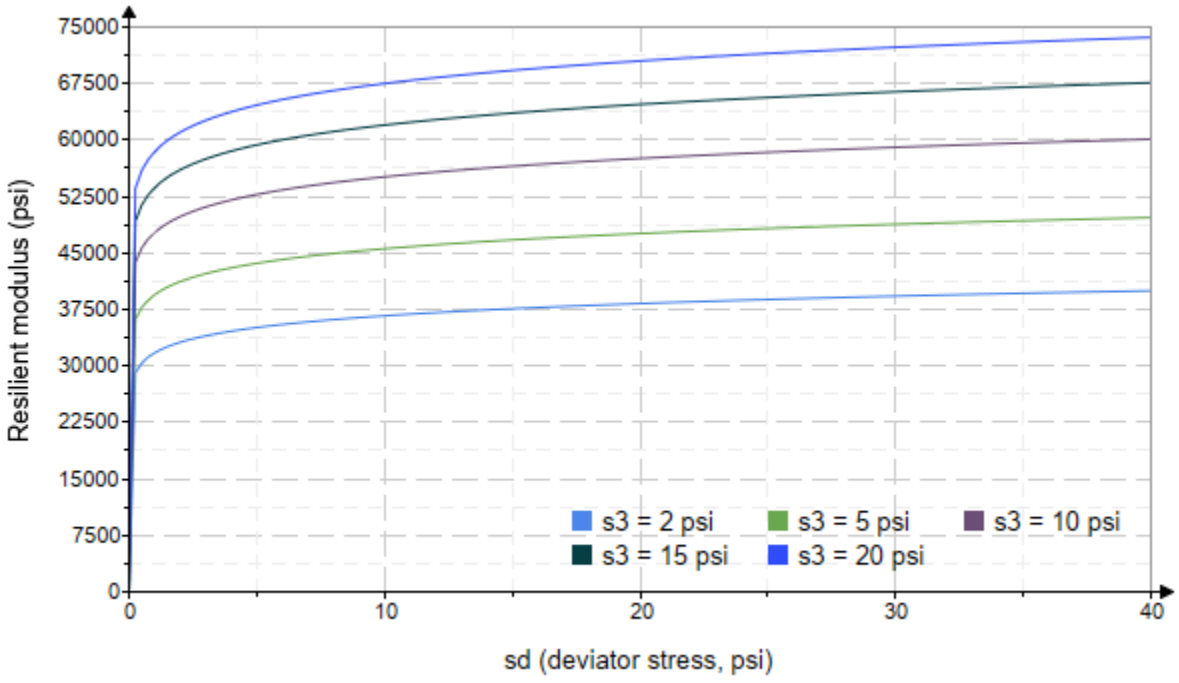

Figure 5. Plot of the fitted Equation 3 model for various confining stresses.

Dan Seely
9/12/2023

$$M_{R.4}\left(\sigma_B,\sigma_d,K_8,K_9,K_{10}\right) := K_8 \cdot p_a \left(\frac{\sigma_B}{p_a}\right)^{K_9} \cdot \left(\frac{\sigma_d}{p_a}\right)^{K_{10}}$$

Equation 4 AASHTO Publication No. FHWA-RD-97-083

$K_8 = 2395.959$

$K_9 = 0.4194$ Equation 4 fitting parameters

$K_{10} = -0.0783$

$R_4^{\,2} = 0.9166$ Coefficient of determination

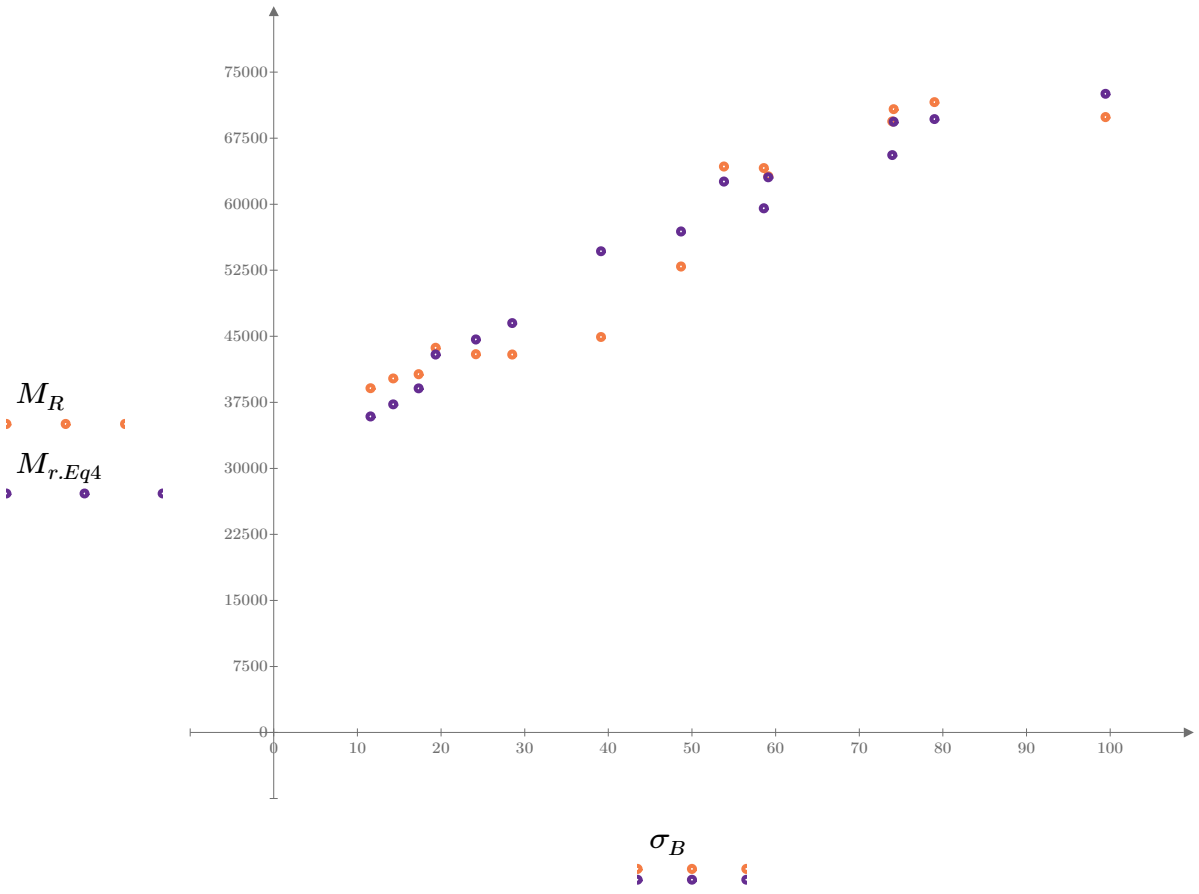

Figure 6. Plot of the test data (orange points) vs. the fitted Equation 4 model (purple points).

Dan Seely
9/12/2023

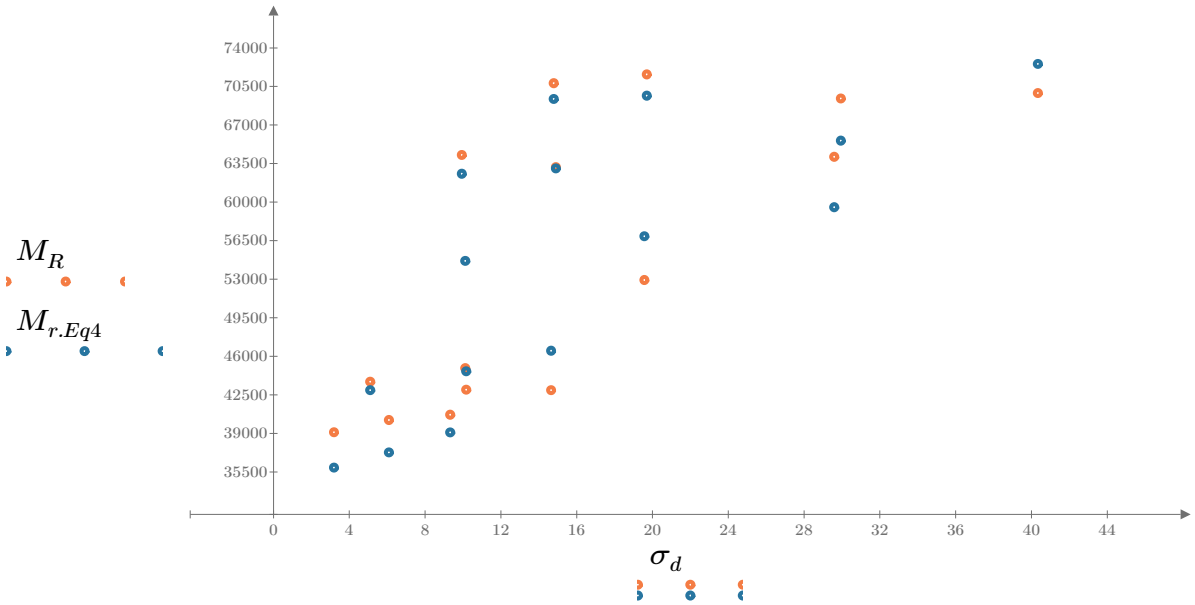

Figure 7. Plot of the test data (orange points) vs. the fitted Equation 4 model (blue points).

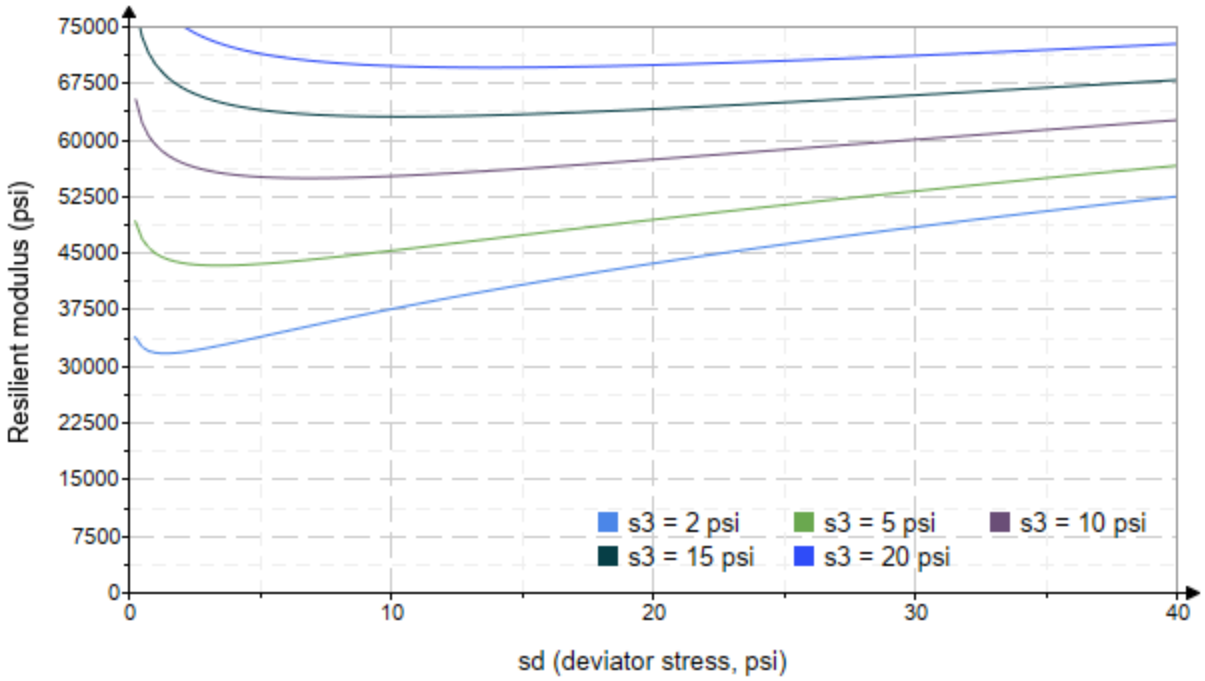

Figure 8. Plot of the fitted Equation 4 model for various confining stresses.

Dan Seely
9/12/2023

$SampleNo := \text{“B2}-\text{52”}$

$Treatment = \text{“D1”}$

$S = 17.533$ Degree of Saturation (%)

Test Sequence : Base/Subbase

Test summary data (psi) :

$$\sigma_3 = \begin{bmatrix} 2.556 \\ 2.605 \\ 2.325 \\ 4.399 \\ 4.021 \\ 3.774 \\ 9.203 \\ 8.969 \\ 8.613 \\ 13.830 \\ 13.570 \\ 14.160 \\ 18.940 \\ 19.240 \\ 19.220 \end{bmatrix} \quad \sigma_d = \begin{bmatrix} 2.992 \\ 6.084 \\ 9.031 \\ 5.179 \\ 10.070 \\ 14.530 \\ 9.923 \\ 19.230 \\ 29.400 \\ 9.887 \\ 14.420 \\ 29.730 \\ 14.470 \\ 19.510 \\ 39.910 \end{bmatrix} \quad \sigma_B = \begin{bmatrix} 10.660 \\ 13.900 \\ 16.010 \\ 18.380 \\ 22.130 \\ 25.850 \\ 37.530 \\ 46.130 \\ 55.240 \\ 51.380 \\ 55.110 \\ 72.210 \\ 71.300 \\ 77.240 \\ 97.570 \end{bmatrix} \quad M_R = \begin{bmatrix} 30204.2 \\ 19426.6 \\ 19123.0 \\ 35576.2 \\ 27825.4 \\ 27801.4 \\ 62629.4 \\ 45084.8 \\ 47477.0 \\ 67659.9 \\ 87842.8 \\ 57992.8 \\ 96284.0 \\ 86778.8 \\ 63263.0 \end{bmatrix}$$

σ_3 = mean confining stress
σ_d = mean deviator stress
σ_B = mean bulk stress
M_R = resilient modulus
p_a = atmospheric pressure = 14.6959 psi

Dan Seely
9/12/2023

$$M_{R.1}\left(\sigma_B, K_1, K_2\right) := K_1 \cdot {\sigma_B}^{K_2}$$

Equation 1
AASHTO Publication No. FHWA-RD-97-083

$K_1 = 5662.368$

$K_2 = 0.5950$

Equation 1 fitting parameters

${R_1}^2 = 0.6536$

Coefficient of determination

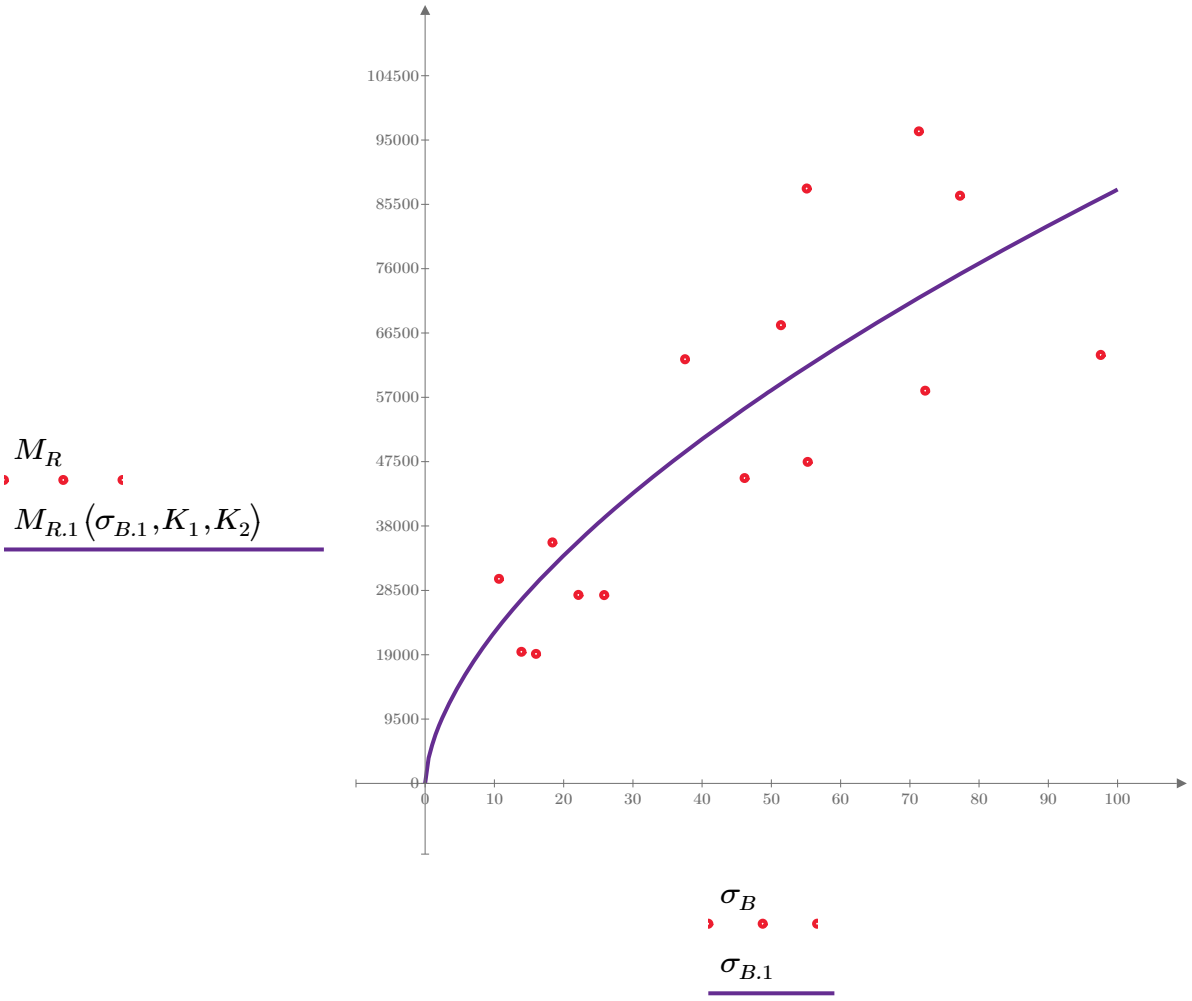

Figure 1. Plot of the test data (red points) vs. the fitted Equation 1 model (purple line).

Dan Seely
9/12/2023

$$M_{R.2}(\sigma_d, K_3, K_4) := K_3 \cdot \sigma_d^{K_4}$$

Equation 2
AASHTO Publication No. FHWA-RD-97-083

$K_3 = 24431.041$

$K_4 = 0.2889$

Equation 2 fitting parameters

$R_2^2 = 0.1857$

Coefficient of determination

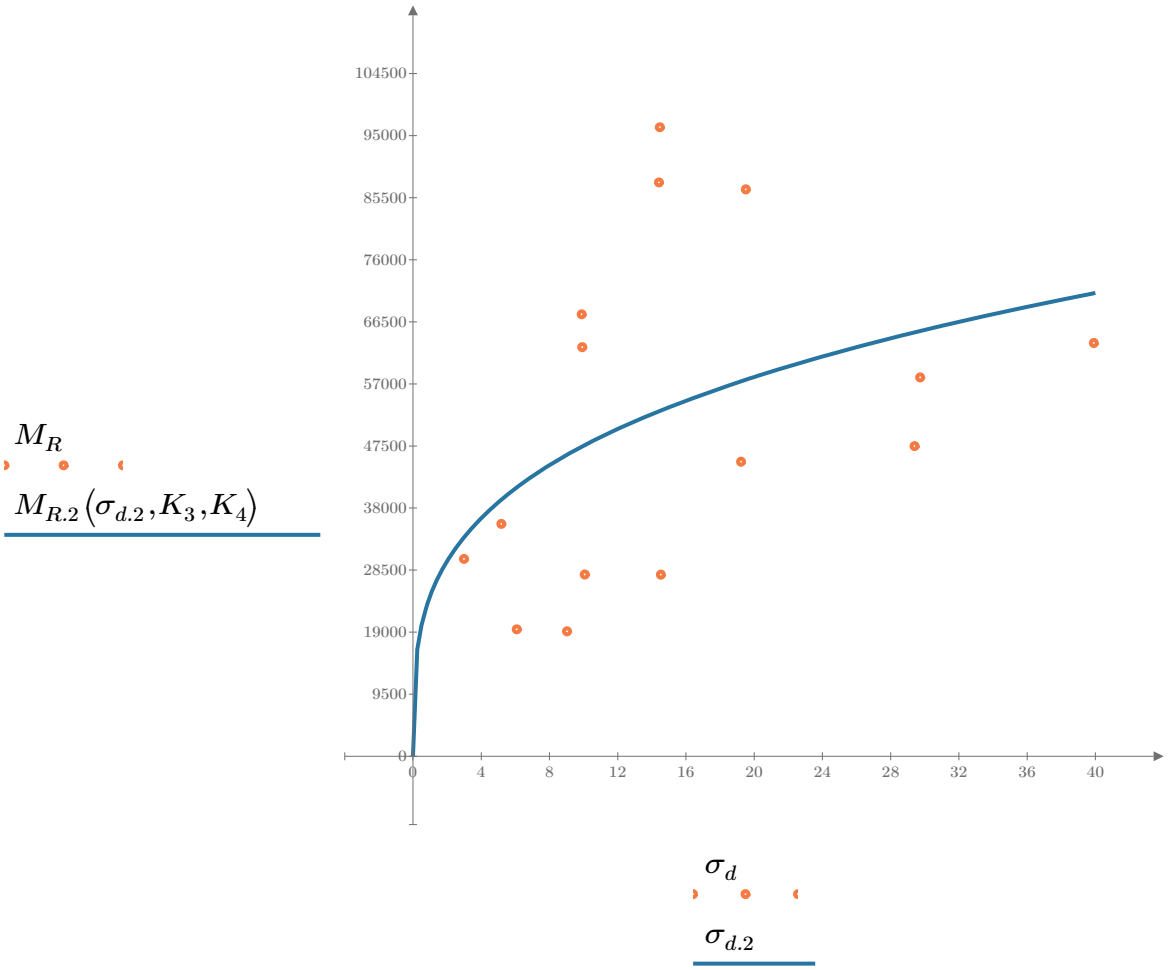

Figure 2. Plot of the test data (orange points) vs. the fitted Equation 2 model (blue line).

Dan Seely
9/12/2023

$$M_{R.3}\left(\sigma_d,\sigma_3,K_5,K_6,K_7\right):=K_5\cdot{\sigma_d}^{K_6}\cdot\left(1+\sigma_3\right)^{K_7}$$

Equation 3 AASHTO Publication No. FHWA-RD-97-083

$K_5=13099.160$

$K_6=-0.2755$ Equation 3 fitting parameters

$K_7=0.9033$

${R_3}^2=0.9264$ Coefficient of determination

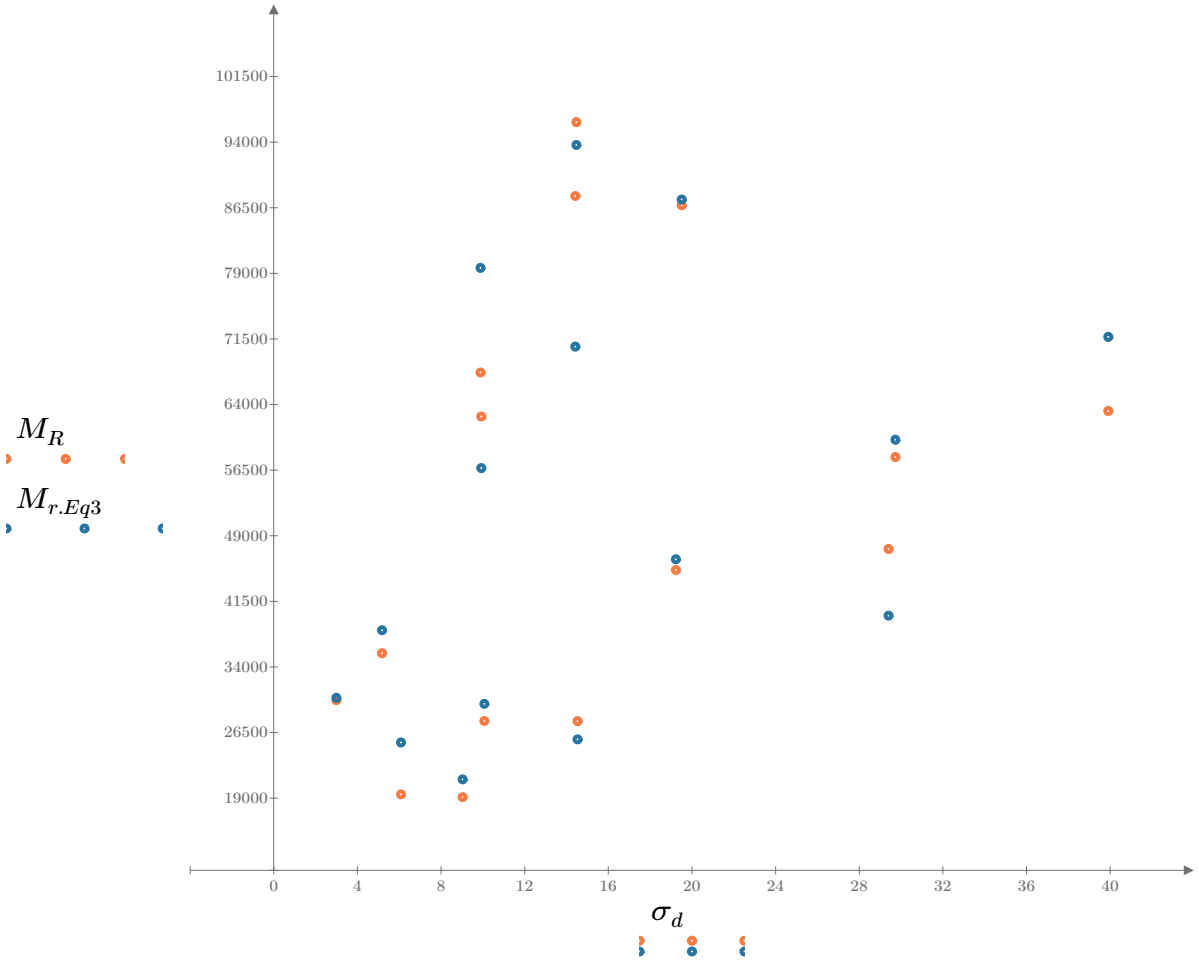

Figure 3. Plot of the test data (orange points) vs. the fitted Equation 3 model (blue points).

Dan Seely
9/12/2023

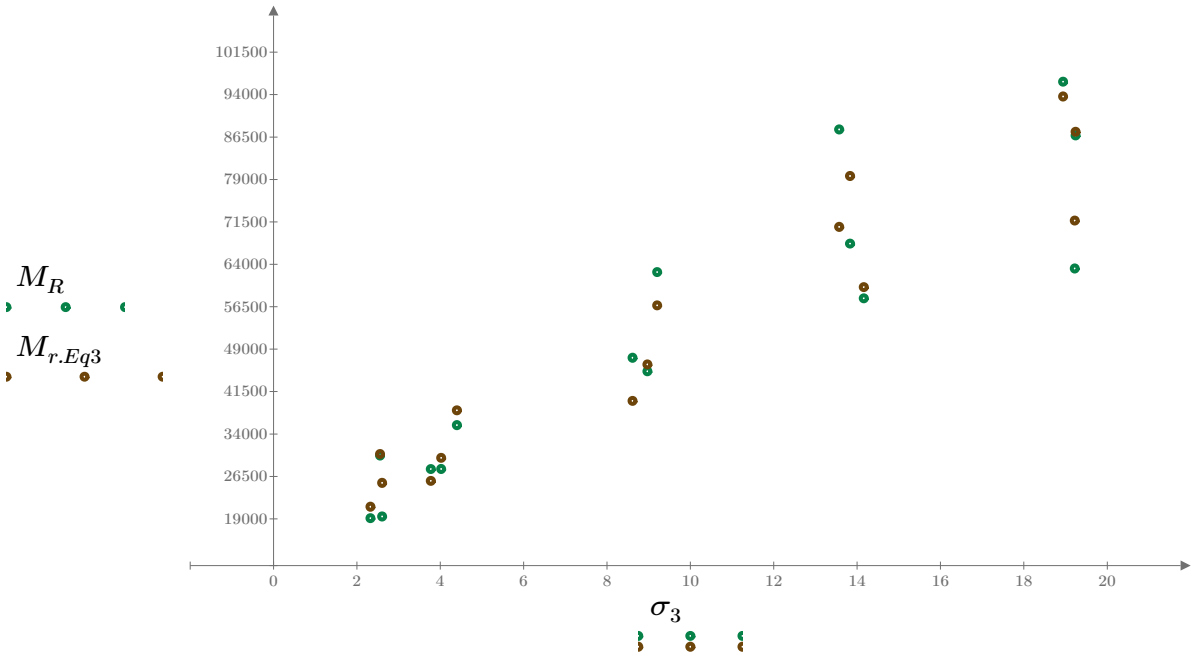

Figure 4. Plot of the test data (green points) vs. the fitted Equation 3 model (brown points).

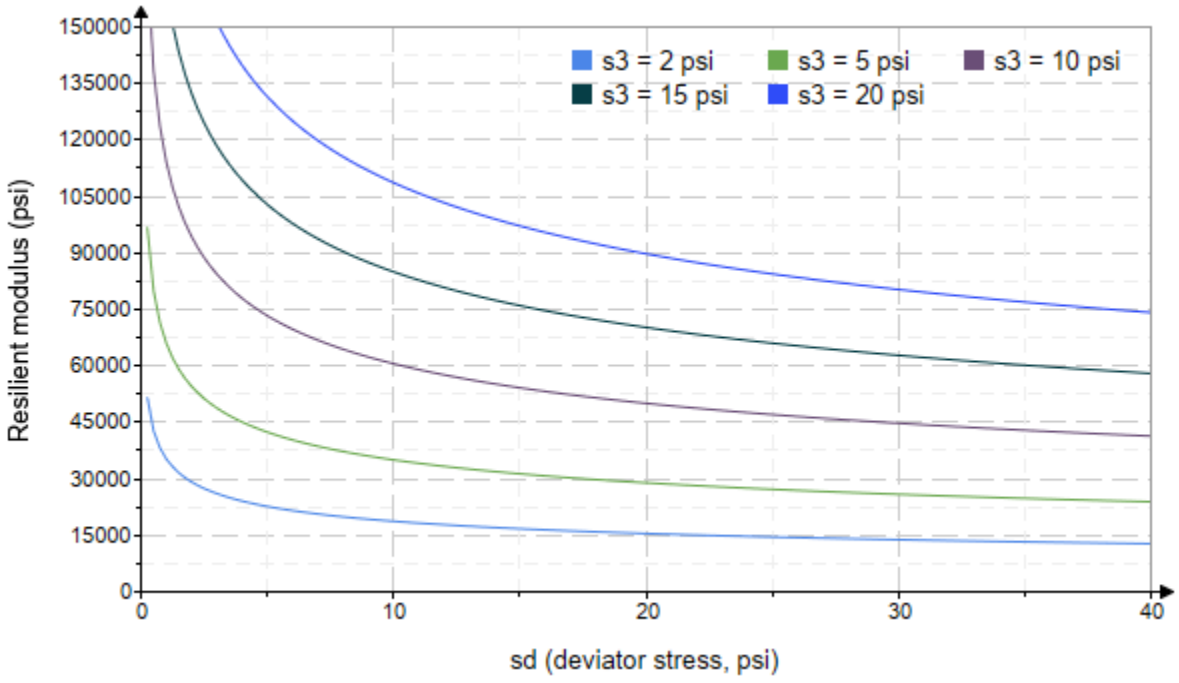

Figure 5. Plot of the fitted Equation 3 model for various confining stresses.

Dan Seely
9/12/2023

$$M_{R.4}\left(\sigma_B,\sigma_d,K_8,K_9,K_{10}\right) := K_8 \cdot p_a \left(\frac{\sigma_B}{p_a}\right)^{K_9} \cdot \left(\frac{\sigma_d}{p_a}\right)^{K_{10}}$$

Equation 4 AASHTO Publication No. FHWA-RD-97-083

$K_8 = 974.453$

$K_9 = 1.1875$ Equation 4 fitting parameters

$K_{10} = -0.6593$

$R_4^{\,2} = 0.9240$ Coefficient of determination

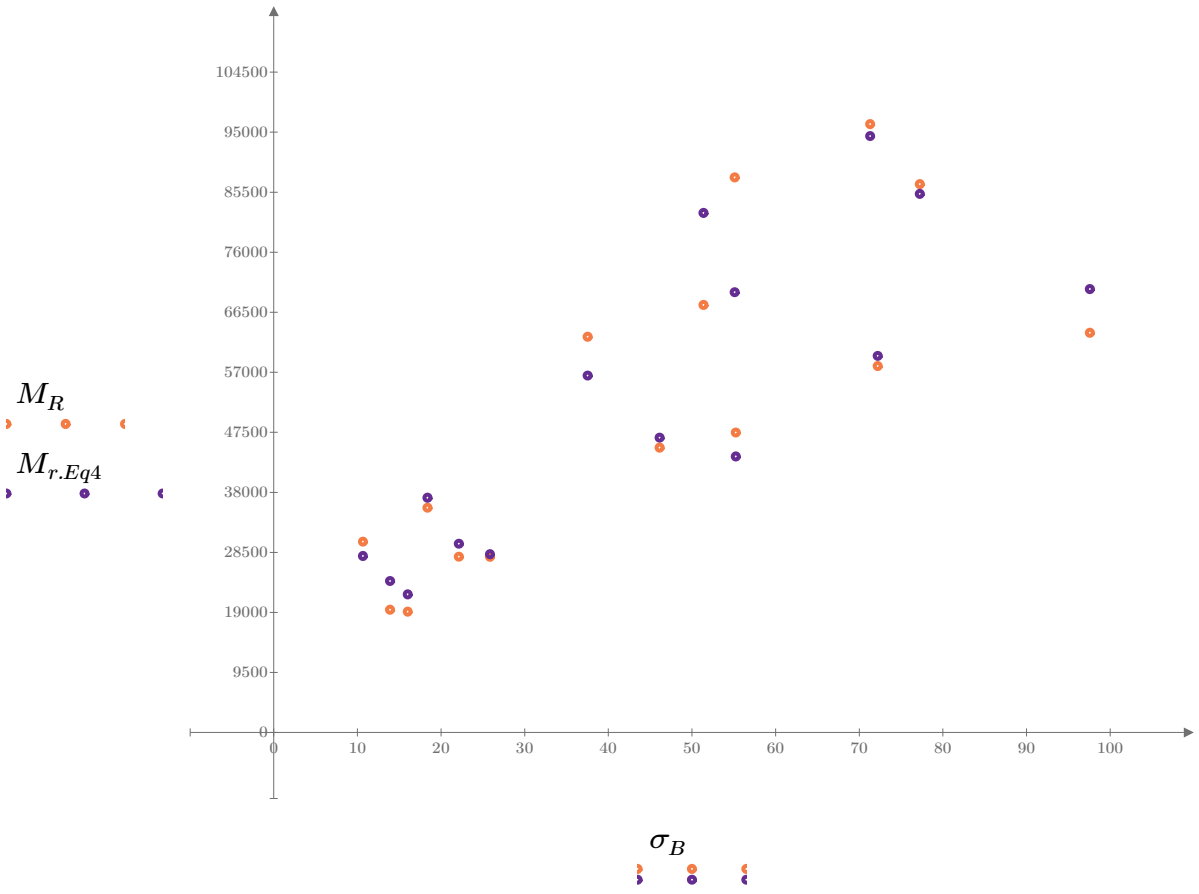

Figure 6. Plot of the test data (orange points) vs. the fitted Equation 4 model (purple points).

Dan Seely
9/12/2023

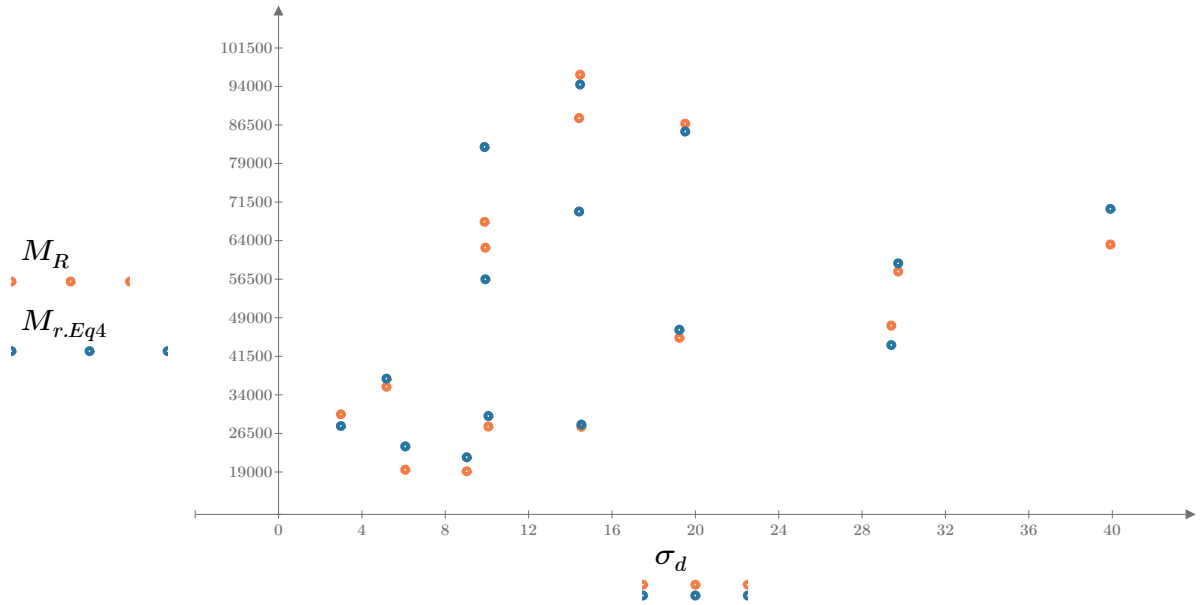

Figure 7. Plot of the test data (orange points) vs. the fitted Equation 4 model (blue points).

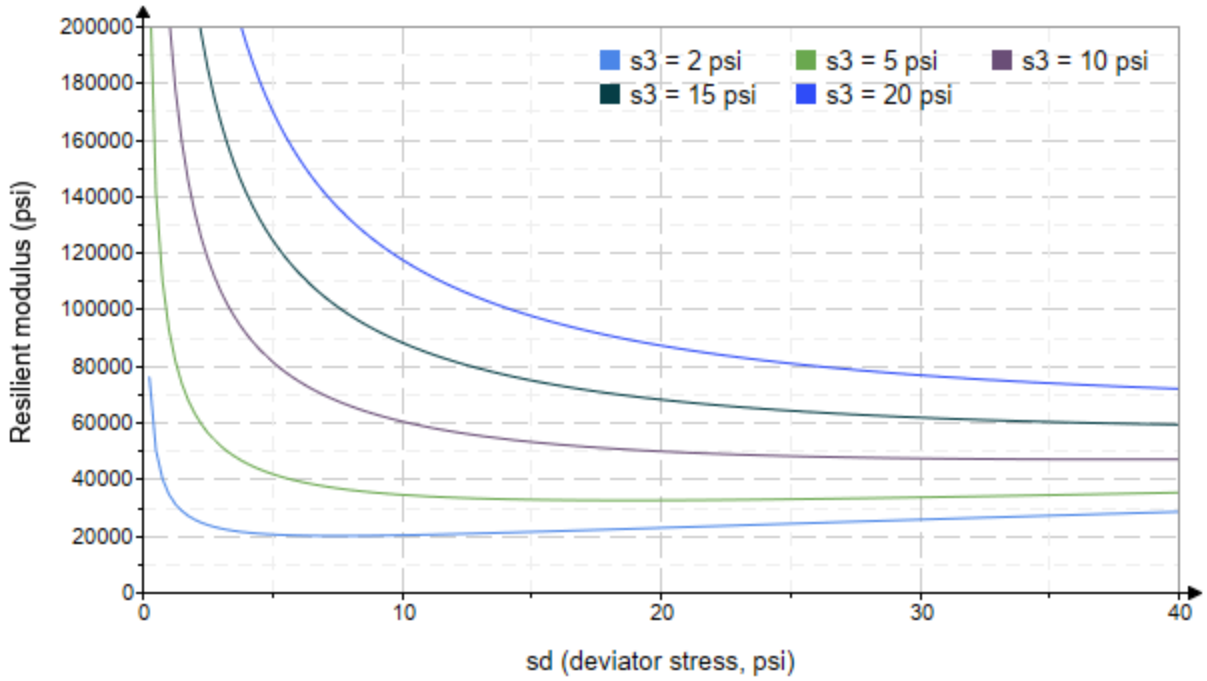

Figure 8. Plot of the fitted Equation 4 model for various confining stresses.

Dan Seely
9/12/2023

$SampleNo := \text{“B2}-\text{53”}$

$Treatment = \text{“D1”}$

$S = 15.493$ Degree of Saturation (%)

Test Sequence : Base/Subbase

Test summary data (psi) :

$$\sigma_3 = \begin{bmatrix} 2.606 \\ 2.602 \\ 2.578 \\ 4.581 \\ 4.584 \\ 4.554 \\ 9.611 \\ 9.595 \\ 9.588 \\ 14.610 \\ 14.620 \\ 14.610 \\ 19.640 \\ 19.650 \\ 19.630 \end{bmatrix} \quad \sigma_d = \begin{bmatrix} 3.217 \\ 6.107 \\ 9.108 \\ 5.187 \\ 10.160 \\ 14.580 \\ 10.190 \\ 19.180 \\ 29.460 \\ 10.230 \\ 14.500 \\ 29.720 \\ 14.490 \\ 19.660 \\ 40.180 \end{bmatrix} \quad \sigma_B = \begin{bmatrix} 11.040 \\ 13.910 \\ 16.840 \\ 18.930 \\ 23.920 \\ 28.240 \\ 39.020 \\ 47.960 \\ 58.220 \\ 54.050 \\ 58.350 \\ 73.560 \\ 73.420 \\ 78.610 \\ 99.080 \end{bmatrix} \quad M_R = \begin{bmatrix} 41930.4 \\ 46501.4 \\ 50622.2 \\ 58938.8 \\ 50397.6 \\ 47599.2 \\ 58666.4 \\ 54151.4 \\ 54481.8 \\ 47876.0 \\ 57989.0 \\ 56170.8 \\ 71311.4 \\ 58969.2 \\ 56056.0 \end{bmatrix}$$

σ_3 = mean confining stress
σ_d = mean deviator stress
σ_B = mean bulk stress
M_R = resilient modulus
p_a = atmospheric pressure = 14.6959 psi

Dan Seely
9/12/2023

$$M_{R.1}(\sigma_B, K_1, K_2) := K_1 \cdot {\sigma_B}^{K_2}$$

Equation 1
AASHTO Publication No. FHWA-RD-97-083

$K_1 = 35051.775$

$K_2 = 0.1186$

Equation 1 fitting parameters

${R_1}^2 = 0.3939$

Coefficient of determination

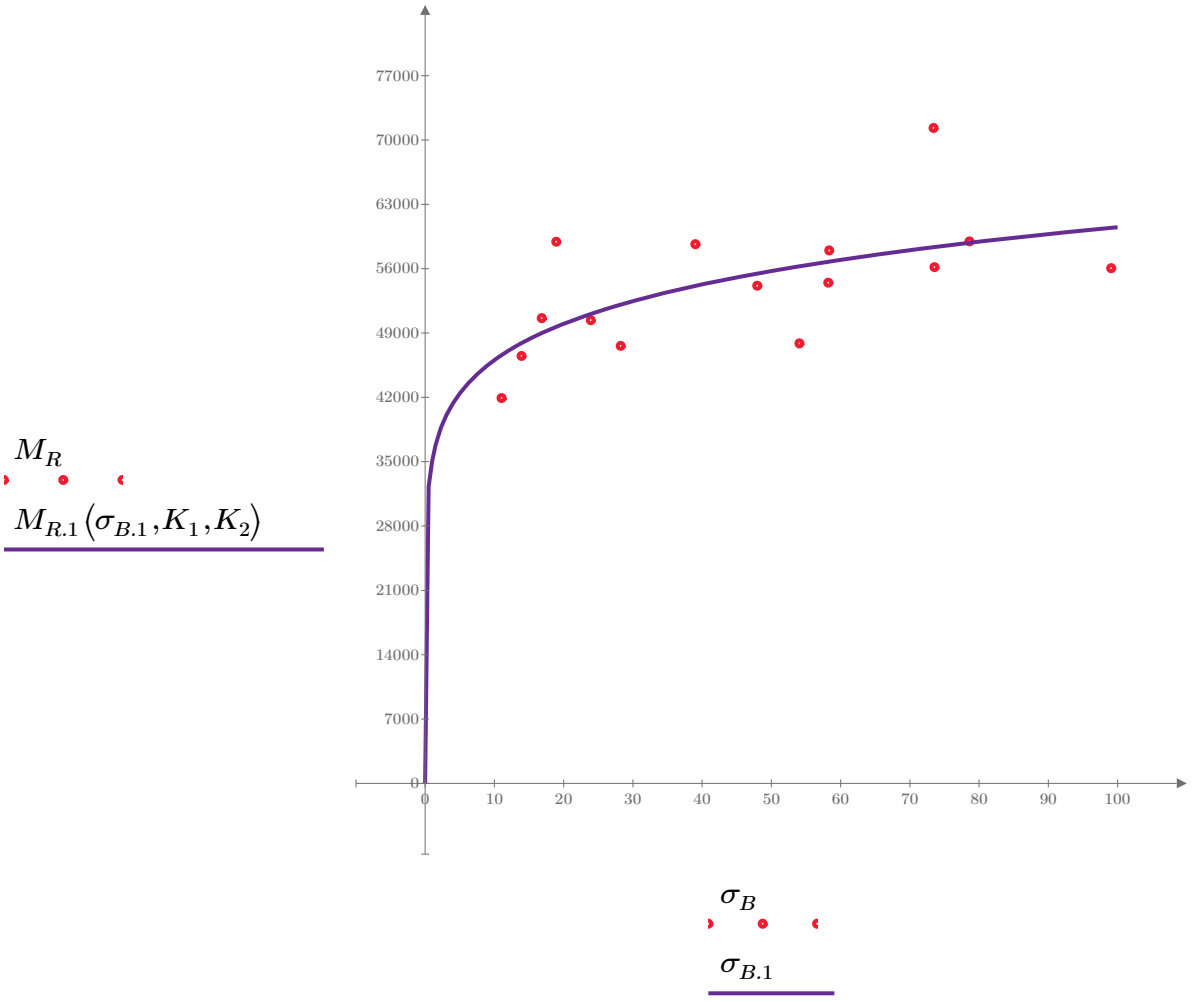

Figure 1. Plot of the test data (red points) vs. the fitted Equation 1 model (purple line).

Dan Seely
9/12/2023

$$M_{R.2}(\sigma_d, K_3, K_4) := K_3 \cdot \sigma_d^{K_4}$$

Equation 2
AASHTO Publication No. FHWA-RD-97-083

$K_3 = 44434.620$

$K_4 = 0.0768$

Equation 2 fitting parameters

$R_2^2 = 0.1692$

Coefficient of determination

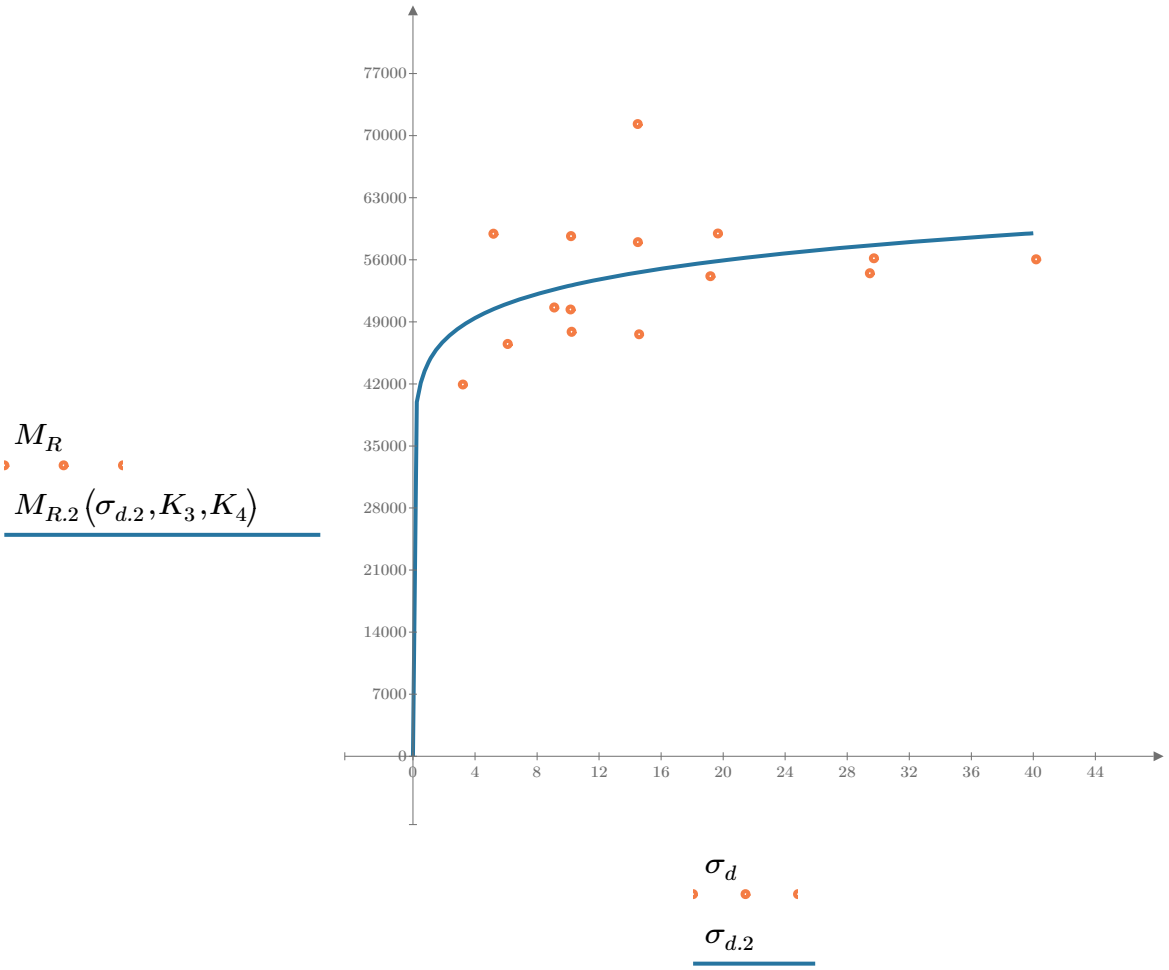

Figure 2. Plot of the test data (orange points) vs. the fitted Equation 2 model (blue line).

Dan Seely
9/12/2023

$$M_{R.3}\left(\sigma_d,\sigma_3,K_5,K_6,K_7\right):=K_5\cdot{\sigma_d}^{K_6}\cdot\left(1+\sigma_3\right)^{K_7}$$

Equation 3 AASHTO Publication No. FHWA-RD-97-083

$K_5=41210.435$

$K_6=-0.0312$ Equation 3 fitting parameters

$K_7=0.1563$

${R_3}^2=0.4650$ Coefficient of determination

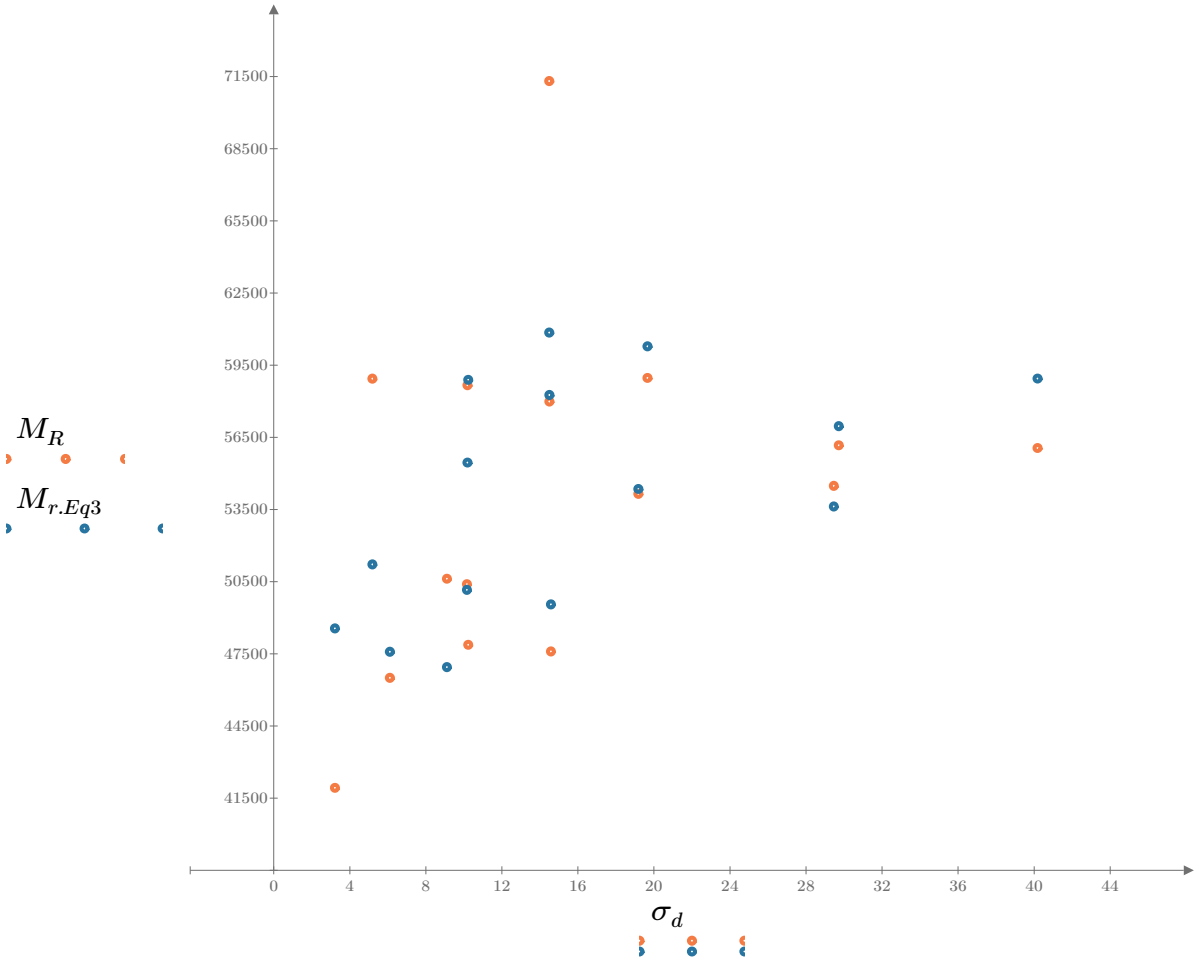

Figure 3. Plot of the test data (orange points) vs. the fitted Equation 3 model (blue points).

Dan Seely
9/12/2023

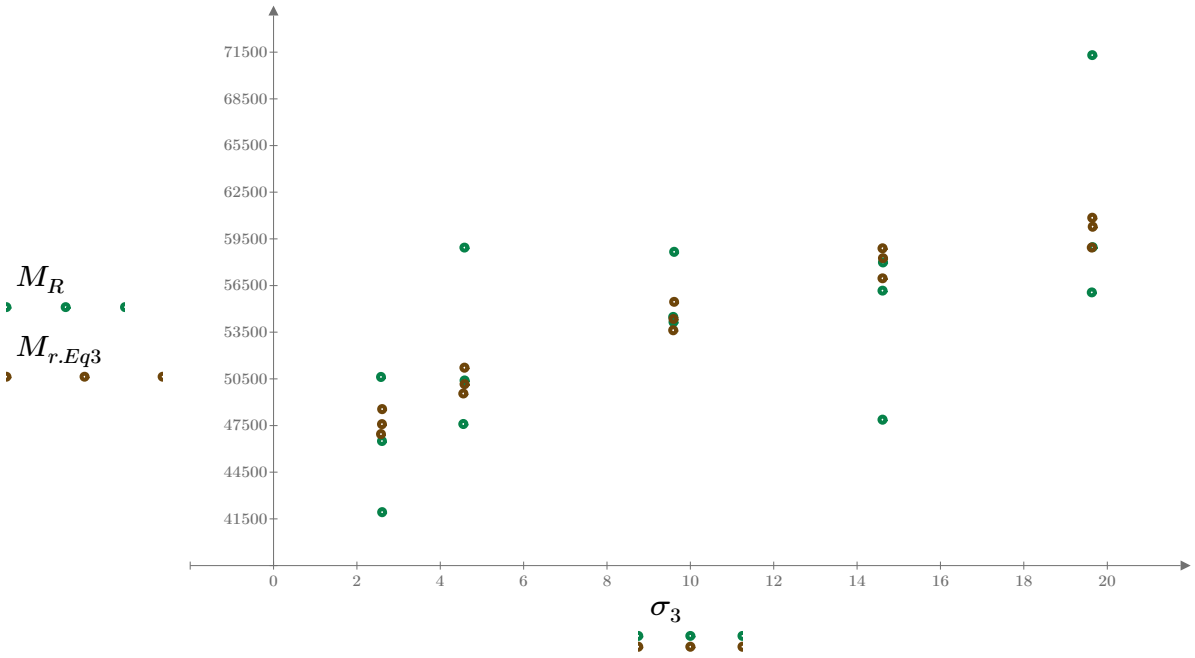

Figure 4. Plot of the test data (green points) vs. the fitted Equation 3 model (brown points).

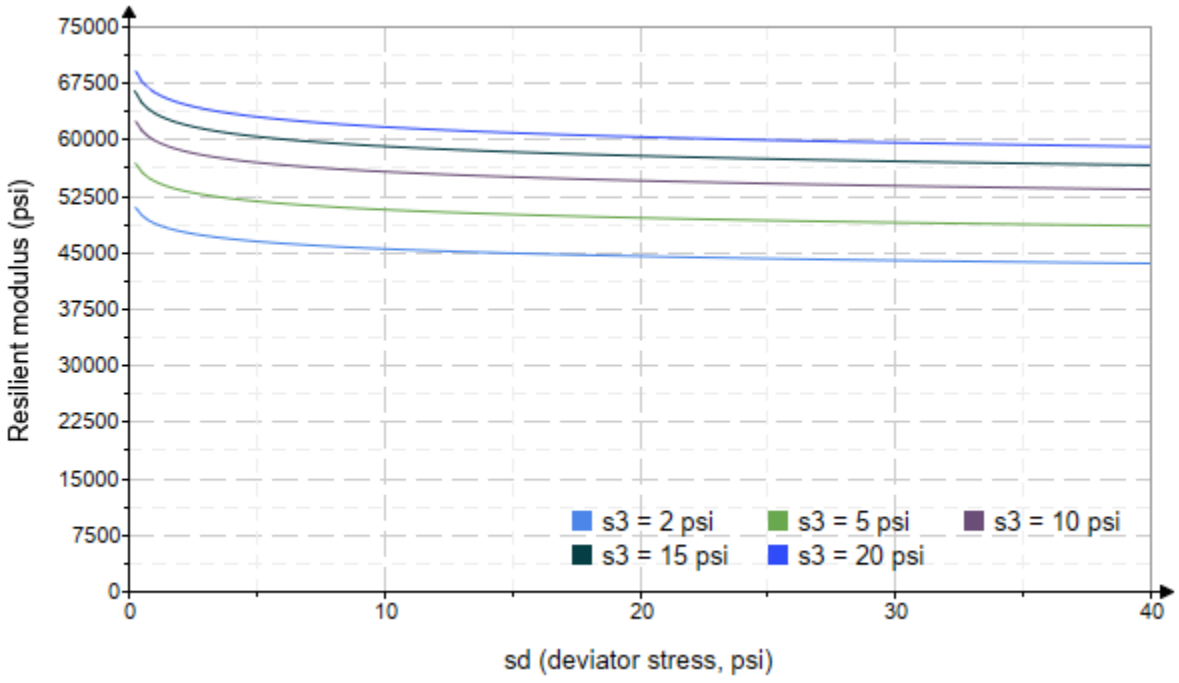

Figure 5. Plot of the fitted Equation 3 model for various confining stresses.

Dan Seely
9/12/2023

$$M_{R.4}\left(\sigma_B,\sigma_d,K_8,K_9,K_{10}\right) := K_8 \cdot p_a \left(\frac{\sigma_B}{p_a}\right)^{K_9} \cdot \left(\frac{\sigma_d}{p_a}\right)^{K_{10}}$$

Equation 4 AASHTO Publication No. FHWA-RD-97-083

$K_8 = 2965.467$

$K_9 = 0.2091$ Equation 4 fitting parameters

$K_{10} = -0.1046$

$R_4^{\,2} = 0.4699$ Coefficient of determination

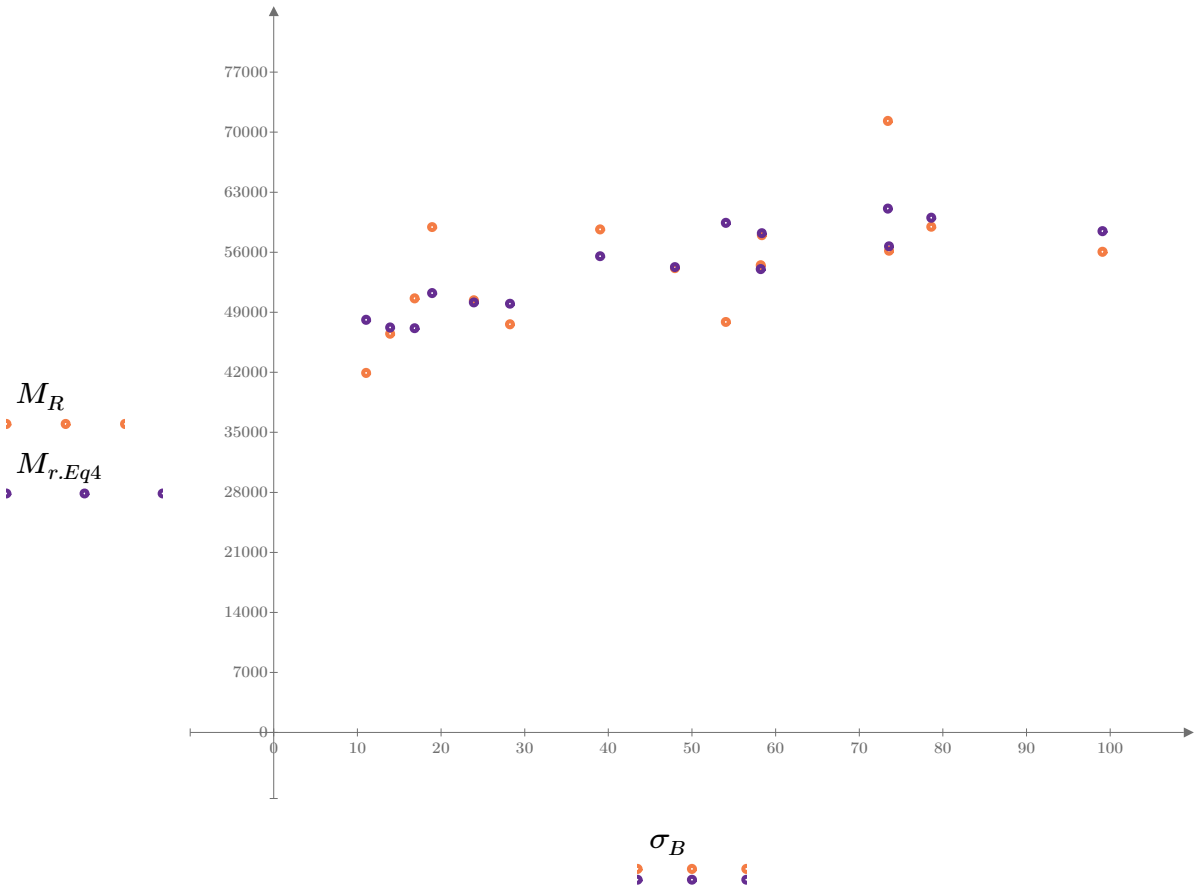

Figure 6. Plot of the test data (orange points) vs. the fitted Equation 4 model (purple points).

Dan Seely
9/12/2023

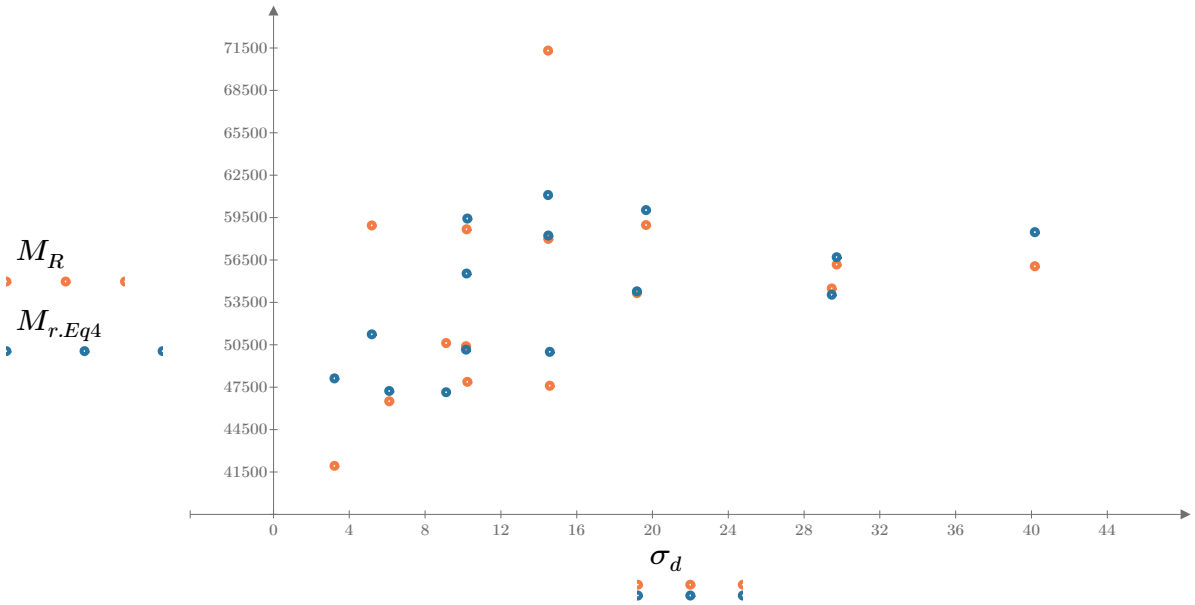

Figure 7. Plot of the test data (orange points) vs. the fitted Equation 4 model (blue points).

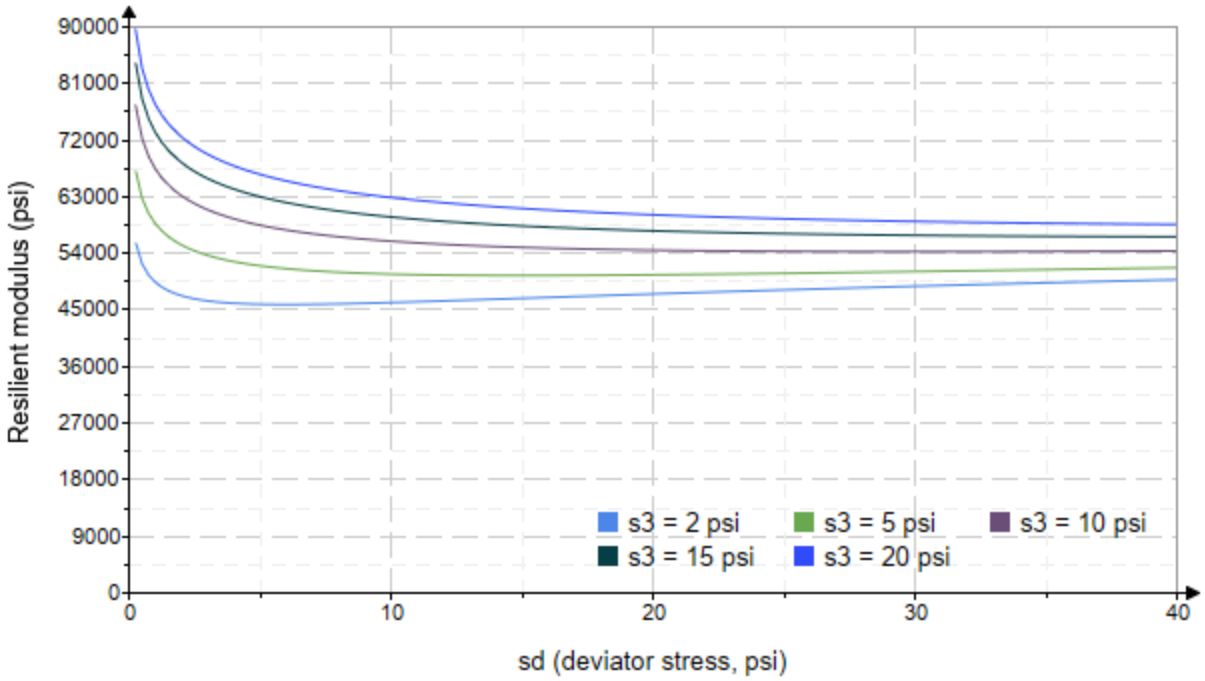

Figure 8. Plot of the fitted Equation 4 model for various confining stresses.

Dan Seely
9/12/2023

$SampleNo := \text{“B2}-\text{54”}$

$Treatment = \text{“D1”}$

$S = 15.764$ Degree of Saturation (%)

Test Sequence : Base/Subbase

Test summary data (psi) :

$$\sigma_3 = \begin{bmatrix} 2.482 \\ 2.020 \\ 1.703 \\ 4.029 \\ 3.784 \\ 3.617 \\ 8.526 \\ 9.549 \\ 9.806 \\ 15.000 \\ 15.310 \\ 14.750 \\ 19.170 \\ 19.540 \\ 18.920 \end{bmatrix} \quad \sigma_d = \begin{bmatrix} 3.415 \\ 6.123 \\ 9.108 \\ 5.238 \\ 10.020 \\ 14.460 \\ 10.100 \\ 19.330 \\ 29.720 \\ 9.945 \\ 14.490 \\ 30.010 \\ 14.730 \\ 19.590 \\ 40.060 \end{bmatrix} \quad \sigma_B = \begin{bmatrix} 10.860 \\ 12.180 \\ 14.220 \\ 17.320 \\ 21.370 \\ 25.310 \\ 35.680 \\ 47.970 \\ 59.140 \\ 54.940 \\ 60.420 \\ 74.270 \\ 72.230 \\ 78.200 \\ 96.810 \end{bmatrix} \quad M_R = \begin{bmatrix} 72935.3 \\ 48073.0 \\ 42196.8 \\ 61479.1 \\ 80761.4 \\ 57912.4 \\ 62631.7 \\ 67351.0 \\ 69008.8 \\ 141608.4 \\ 214208.0 \\ 78917.0 \\ 109588.5 \\ 140260.0 \\ 60775.0 \end{bmatrix}$$

σ_3 = mean confining stress
σ_d = mean deviator stress
σ_B = mean bulk stress
M_R = resilient modulus
p_a = atmospheric pressure = 14.6959 psi

Dan Seely
9/12/2023

$$M_{R.1}\left(\sigma_B, K_1, K_2\right) := K_1 \cdot {\sigma_B}^{K_2}$$

Equation 1
AASHTO Publication No. FHWA-RD-97-083

$K_1 = 24821.552$

$K_2 = 0.3424$

Equation 1 fitting parameters

${R_1}^2 = 0.2237$

Coefficient of determination

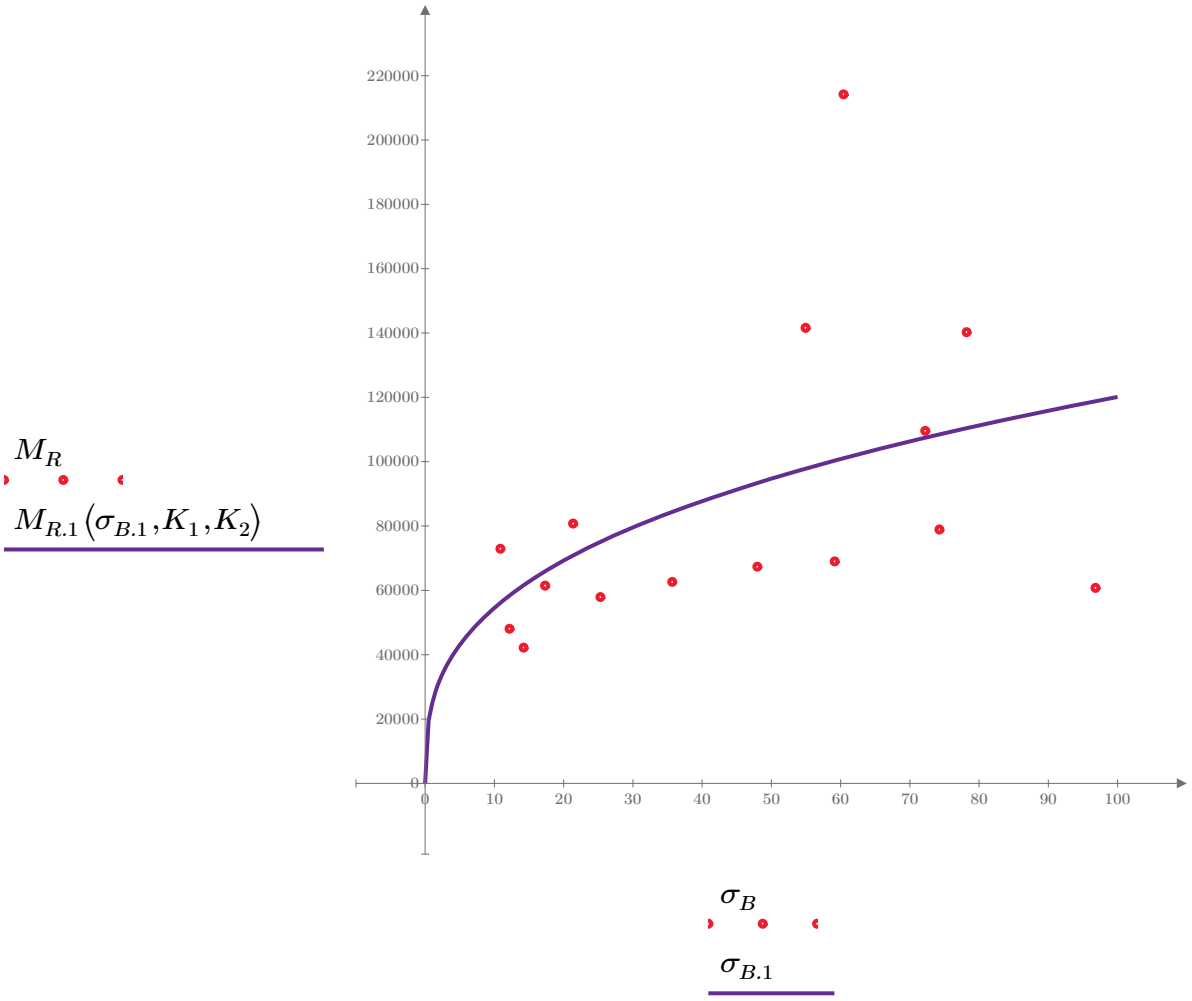

Figure 1. Plot of the test data (red points) vs. the fitted Equation 1 model (purple line).

Dan Seely
9/12/2023

$$M_{R.2}(\sigma_d, K_3, K_4) := K_3 \cdot \sigma_d^{K_4}$$

Equation 2
AASHTO Publication No. FHWA-RD-97-083

$K_3 = 70331.286$

$K_4 = 0.0837$

Equation 2 fitting parameters

$R_2^2 = 0.0140$

Coefficient of determination

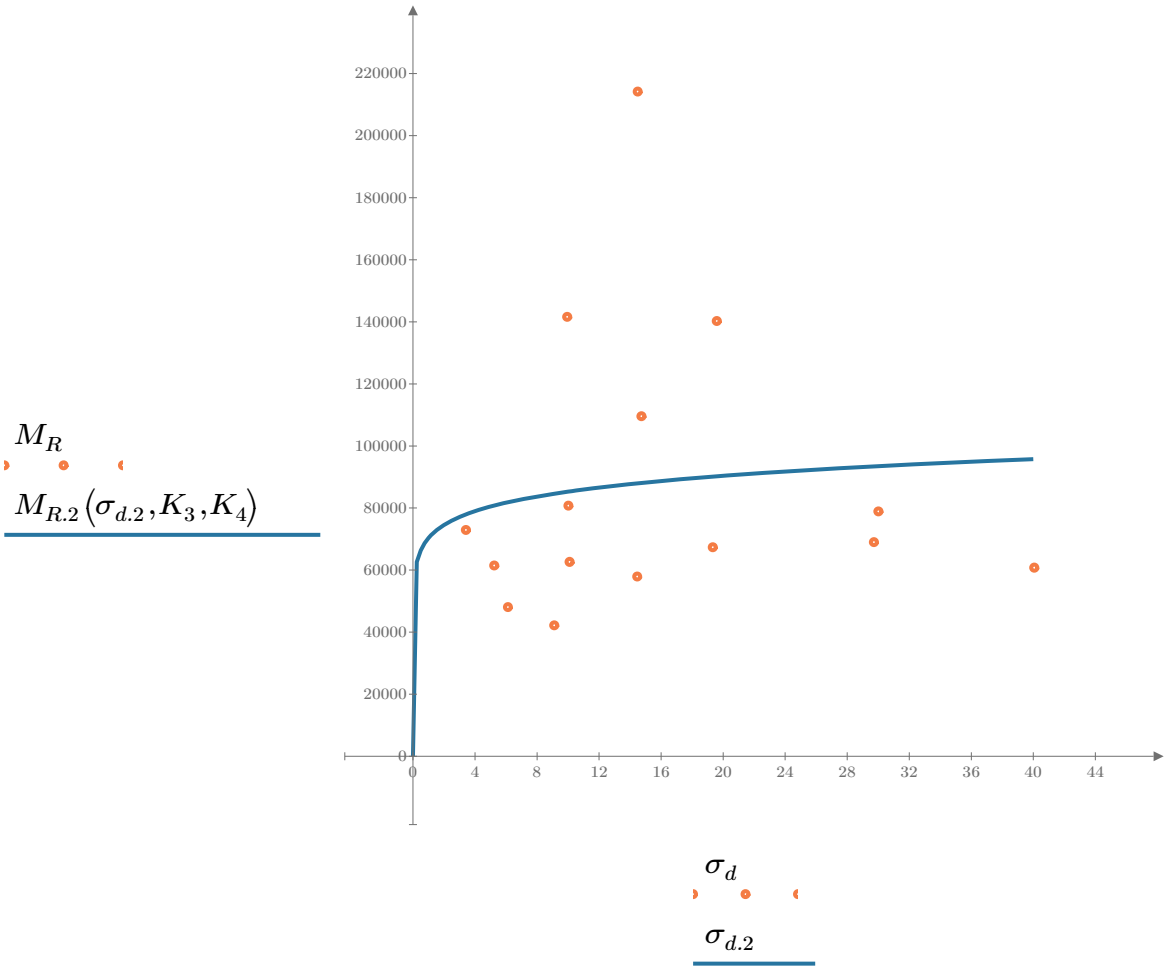

Figure 2. Plot of the test data (orange points) vs. the fitted Equation 2 model (blue line).

Dan Seely
9/12/2023

$$M_{R.3}\left(\sigma_d,\sigma_3,K_5,K_6,K_7\right) := K_5 \cdot {\sigma_d}^{K_6} \cdot \left(1+\sigma_3\right)^{K_7}$$

Equation 3 AASHTO Publication No. FHWA-RD-97-083

$K_5 = 49737.547$

$K_6 = -0.4827$ Equation 3 fitting parameters

$K_7 = 0.7913$

${R_3}^2 = 0.5715$ Coefficient of determination

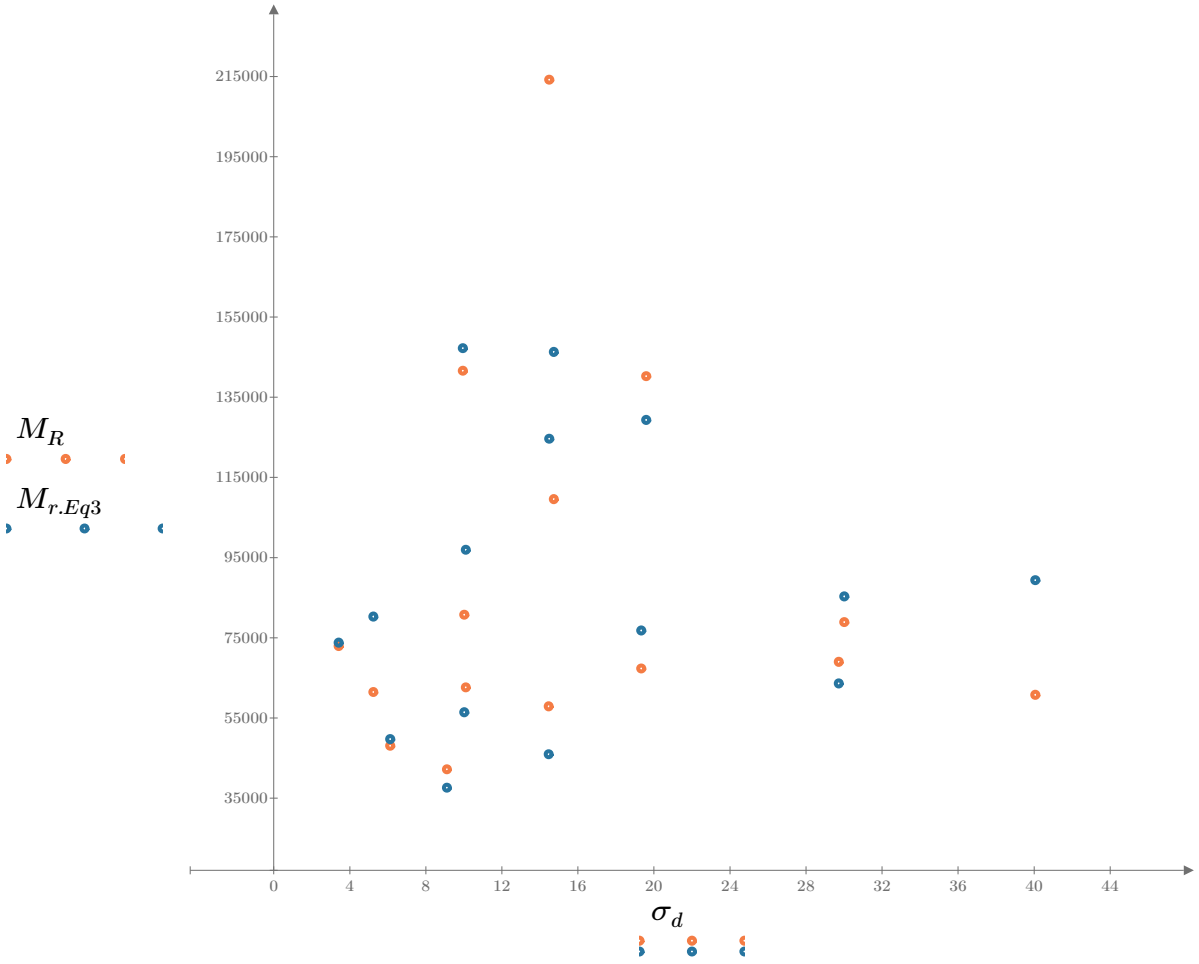

Figure 3. Plot of the test data (orange points) vs. the fitted Equation 3 model (blue points).

Dan Seely
9/12/2023

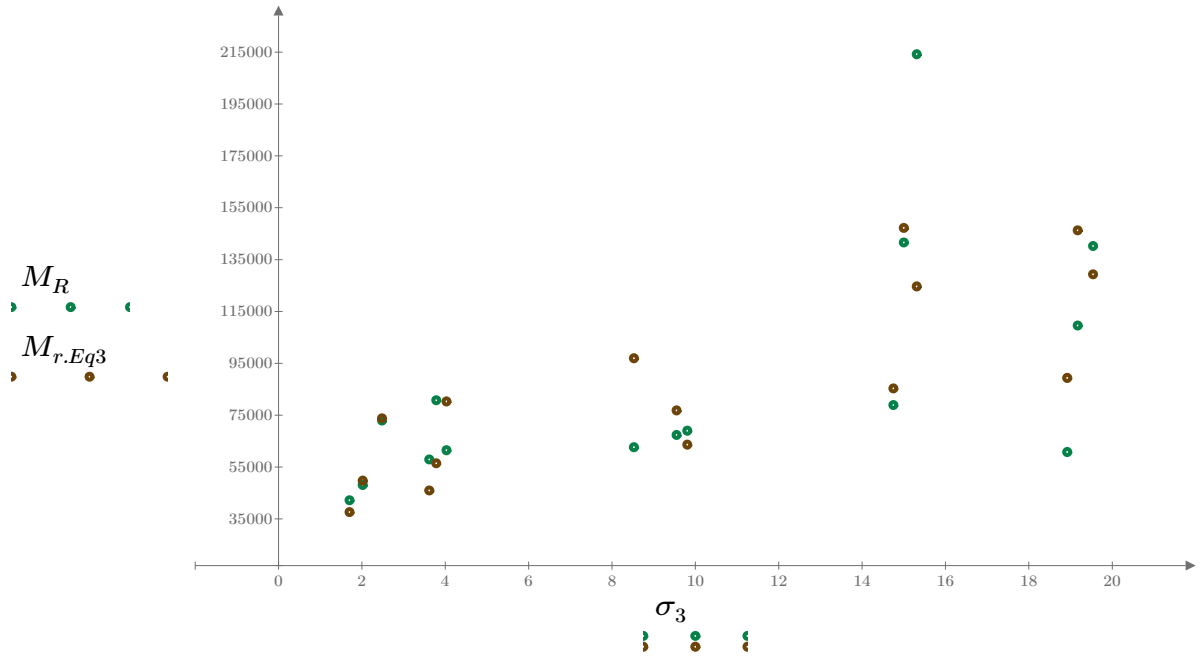

Figure 4. Plot of the test data (green points) vs. the fitted Equation 3 model (brown points).

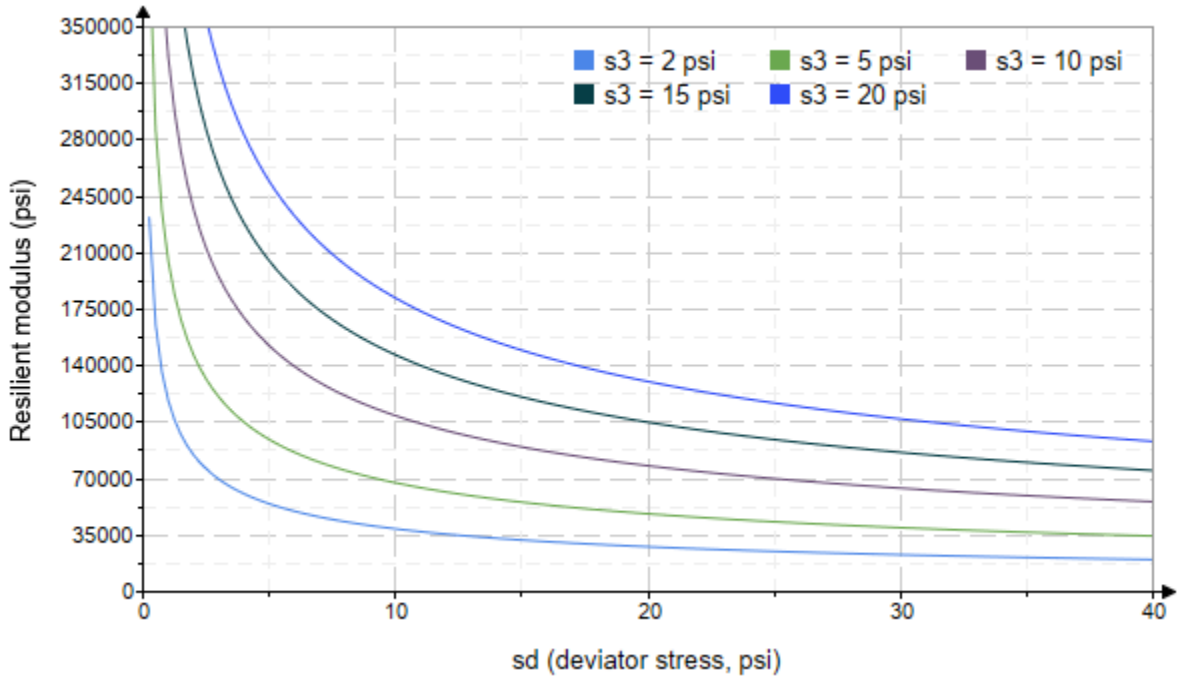

Figure 5. Plot of the fitted Equation 3 model for various confining stresses.

Dan Seely
9/12/2023

$$M_{R.4}\left(\sigma_B,\sigma_d,K_8,K_9,K_{10}\right) := K_8 \cdot p_a \left(\frac{\sigma_B}{p_a}\right)^{K_9} \cdot \left(\frac{\sigma_d}{p_a}\right)^{K_{10}}$$

Equation 4 AASHTO Publication No. FHWA-RD-97-083

$K_8 = 1965.747$

$K_9 = 1.0188$ Equation 4 fitting parameters

$K_{10} = -0.8123$

$R_4^{\,2} = 0.5711$ Coefficient of determination

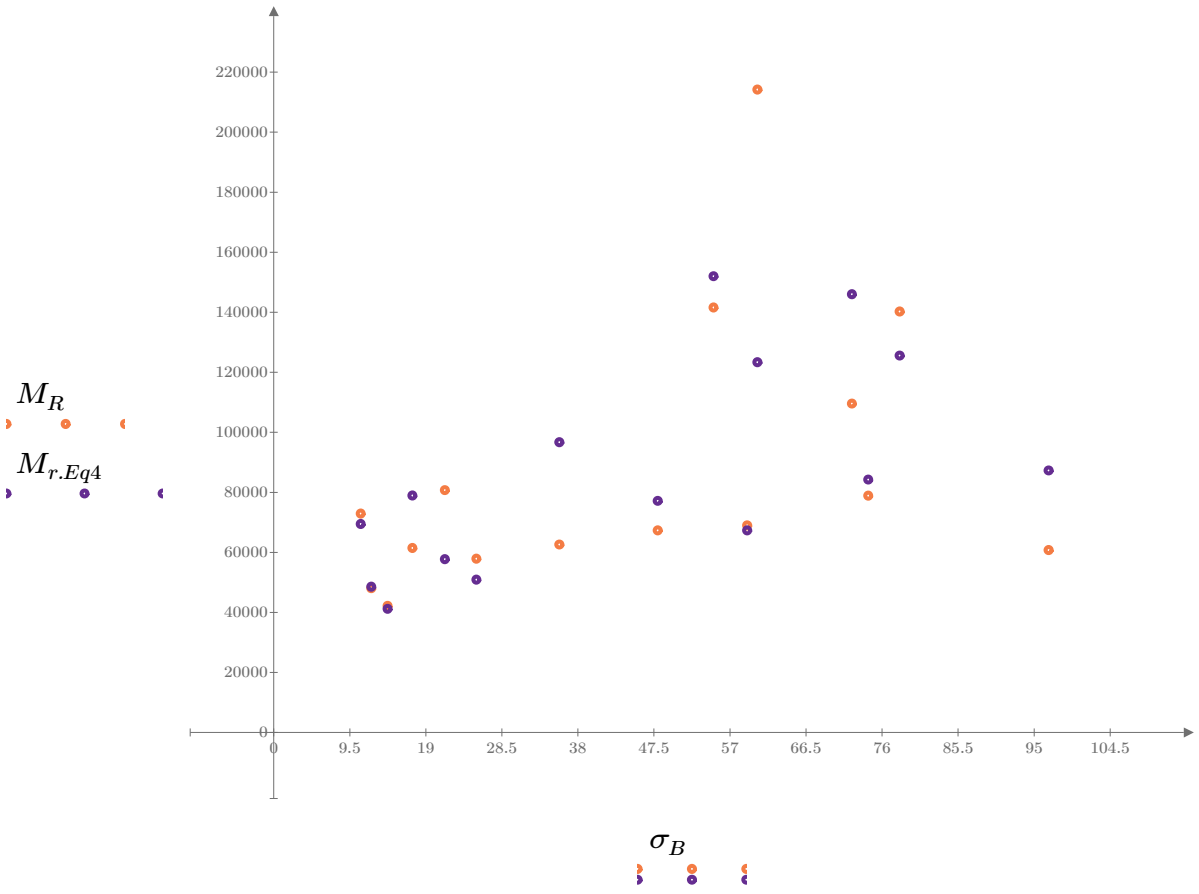

Figure 6. Plot of the test data (orange points) vs. the fitted Equation 4 model (purple points).

Dan Seely
9/12/2023

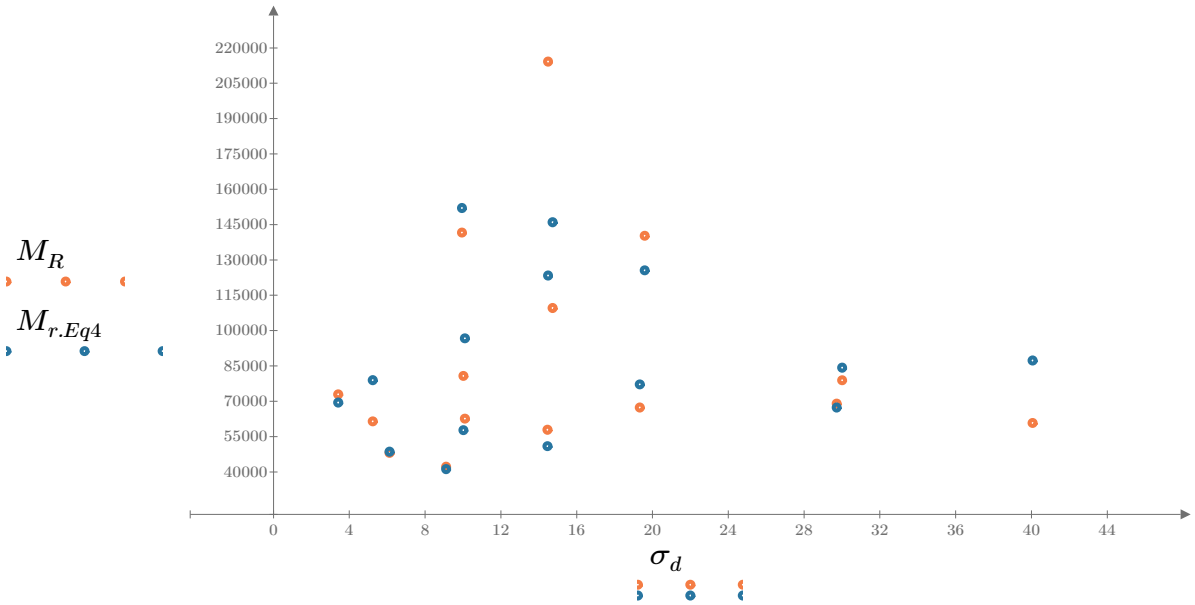

Figure 7. Plot of the test data (orange points) vs. the fitted Equation 4 model (blue points).

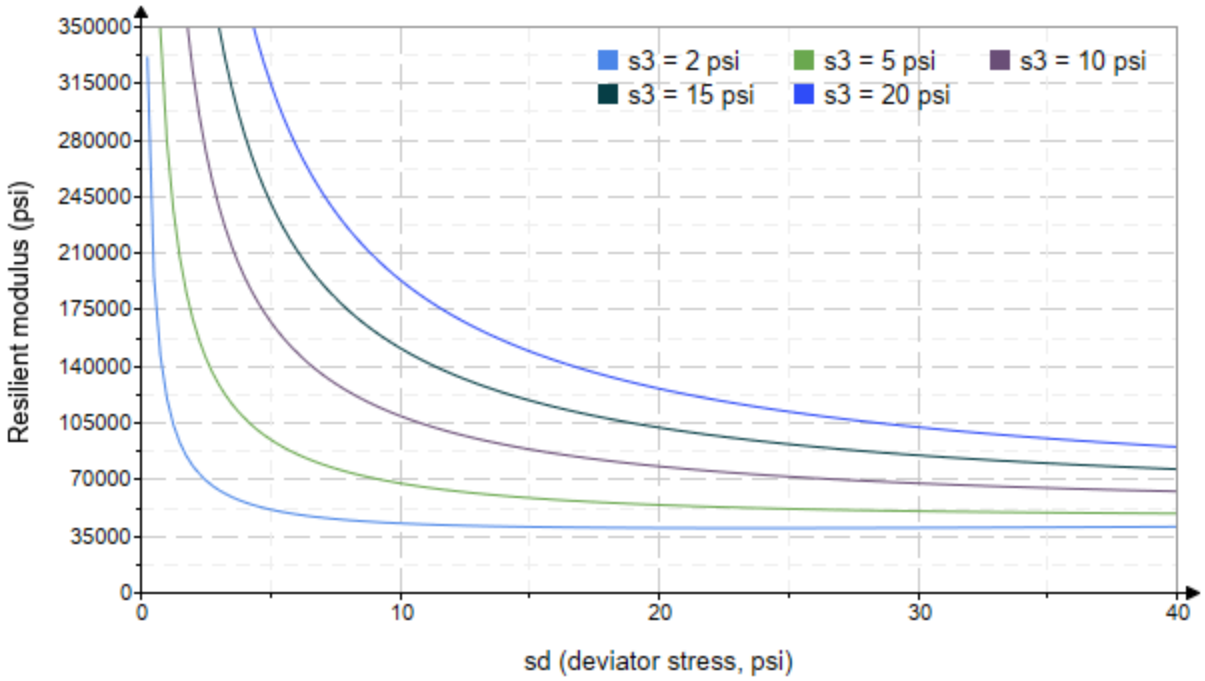

Figure 8. Plot of the fitted Equation 4 model for various confining stresses.

Dan Seely
9/12/2023

$SampleNo := \text{“B2}-\text{55”}$

$Treatment = \text{“D1”}$

$S = 17.973$ Degree of Saturation (%)

Test Sequence : Base/Subbase

Test summary data (psi) :

$$\sigma_3 = \begin{bmatrix} 2.743 \\ 2.752 \\ 2.733 \\ 4.731 \\ 4.699 \\ 4.663 \\ 9.542 \\ 9.495 \\ 9.473 \\ 14.670 \\ 14.650 \\ 14.660 \\ 19.650 \\ 19.650 \\ 19.640 \end{bmatrix} \quad \sigma_d = \begin{bmatrix} 3.193 \\ 6.075 \\ 9.021 \\ 5.069 \\ 10.040 \\ 14.440 \\ 10.150 \\ 19.330 \\ 29.490 \\ 10.270 \\ 14.460 \\ 29.720 \\ 14.520 \\ 19.470 \\ 40.190 \end{bmatrix} \quad \sigma_B = \begin{bmatrix} 11.420 \\ 14.330 \\ 17.220 \\ 19.260 \\ 24.140 \\ 28.430 \\ 38.770 \\ 47.820 \\ 57.910 \\ 54.290 \\ 58.420 \\ 73.690 \\ 73.480 \\ 78.420 \\ 99.120 \end{bmatrix} \quad M_R = \begin{bmatrix} 39076.4 \\ 36102.4 \\ 33660.0 \\ 34628.2 \\ 36103.0 \\ 39976.2 \\ 59097.4 \\ 61756.6 \\ 51722.6 \\ 58754.8 \\ 62456.8 \\ 51916.4 \\ 52135.2 \\ 54622.2 \\ 54468.0 \end{bmatrix}$$

σ_3 = mean confining stress
σ_d = mean deviator stress
σ_B = mean bulk stress
M_R = resilient modulus
p_a = atmospheric pressure = 14.6959 psi

Dan Seely
9/12/2023

$$M_{R.1}\left(\sigma_B, K_1, K_2\right) := K_1 \cdot {\sigma_B}^{K_2}$$

Equation 1
AASHTO Publication No. FHWA-RD-97-083

$K_1 = 18968.696$

$K_2 = 0.2537$

Equation 1 fitting parameters

${R_1}^2 = 0.6188$

Coefficient of determination

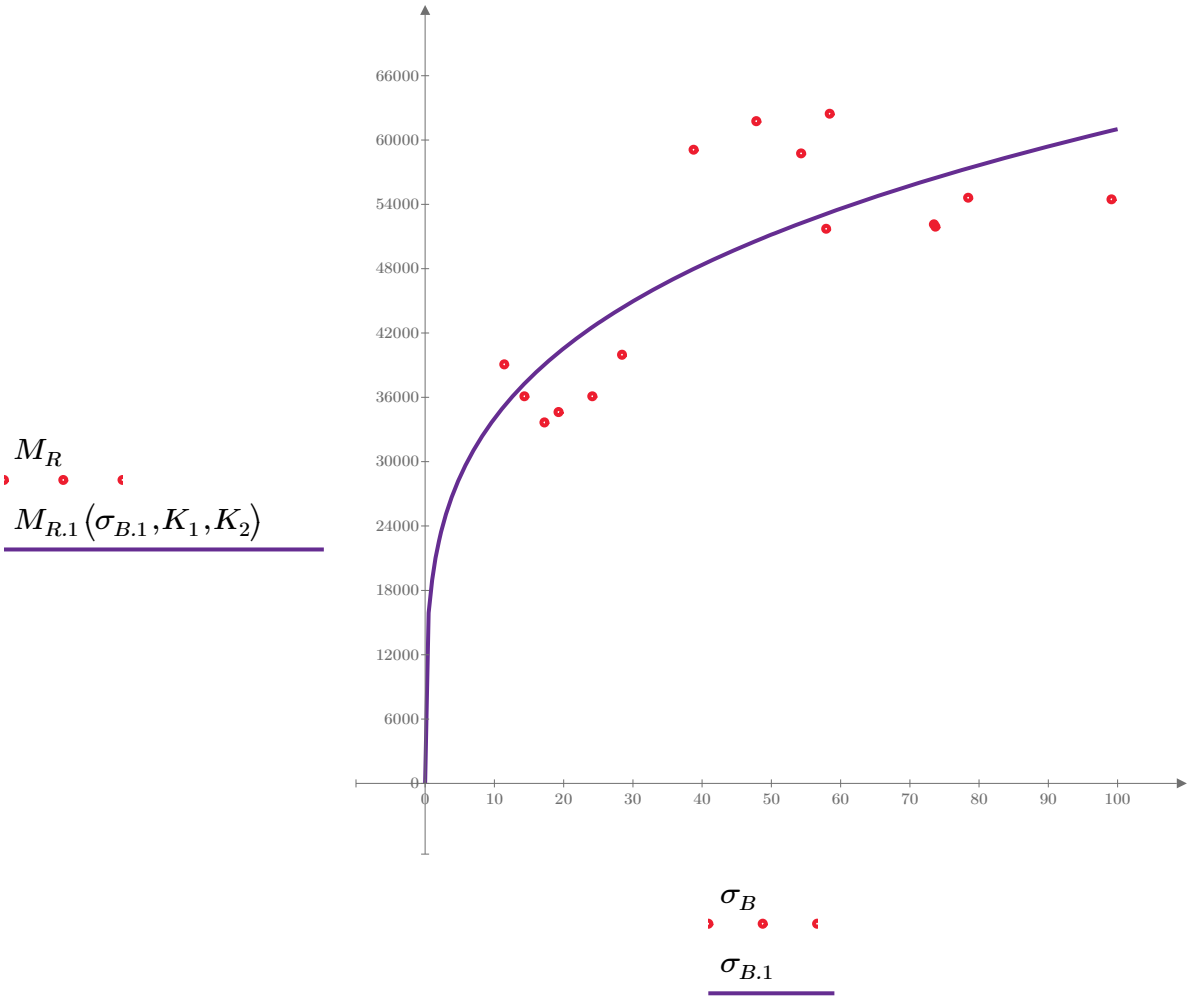

Figure 1. Plot of the test data (red points) vs. the fitted Equation 1 model (purple line).

Dan Seely
9/12/2023

$$M_{R.2}\left(\sigma_d, K_3, K_4\right) := K_3 \cdot \sigma_d^{K_4}$$

Equation 2
AASHTO Publication No. FHWA-RD-97-083

$K_3 = 30579.087$

$K_4 = 0.1781$

Equation 2 fitting parameters

$R_2^2 = 0.3268$

Coefficient of determination

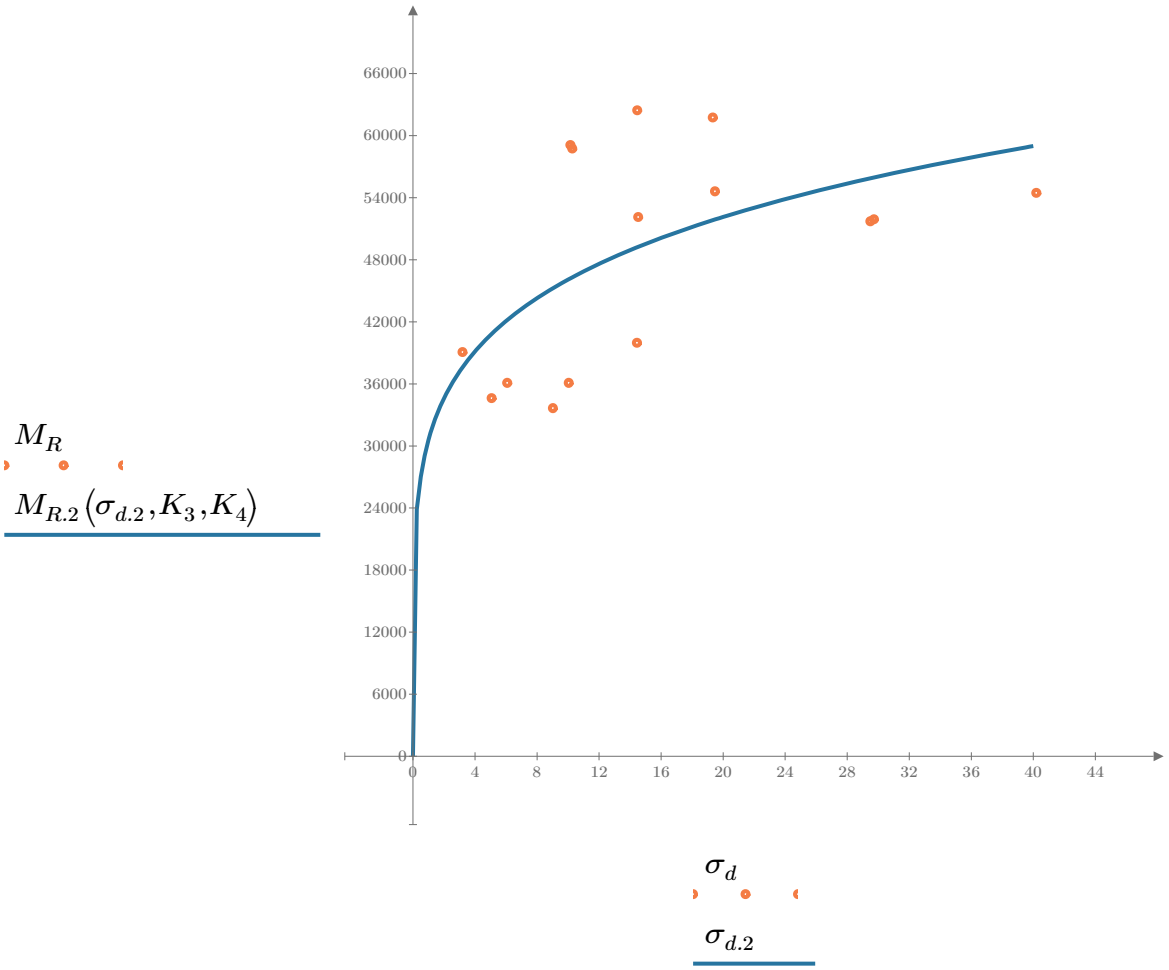

Figure 2. Plot of the test data (orange points) vs. the fitted Equation 2 model (blue line).

Dan Seely
9/12/2023

$$M_{R.3}\left(\sigma_d,\sigma_3,K_5,K_6,K_7\right):=K_5\cdot{\sigma_d}^{K_6}\cdot\left(1+\sigma_3\right)^{K_7}$$

Equation 3 AASHTO Publication No. FHWA-RD-97-083

$K_5=26203.522$

$K_6=-0.0097$ Equation 3 fitting parameters

$K_7=0.2793$

${R_3}^2=0.6618$ Coefficient of determination

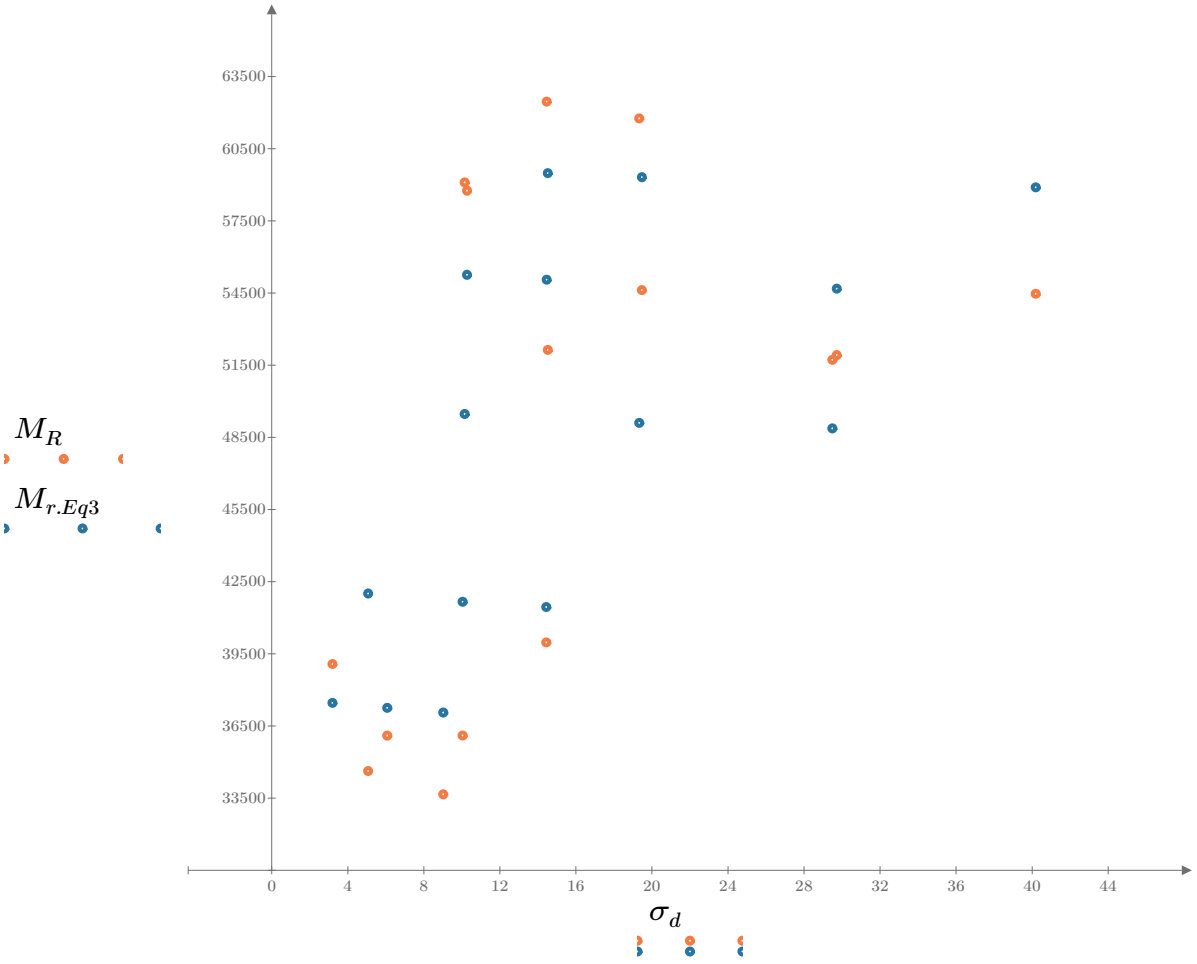

Figure 3. Plot of the test data (orange points) vs. the fitted Equation 3 model (blue points).

Dan Seely
9/12/2023

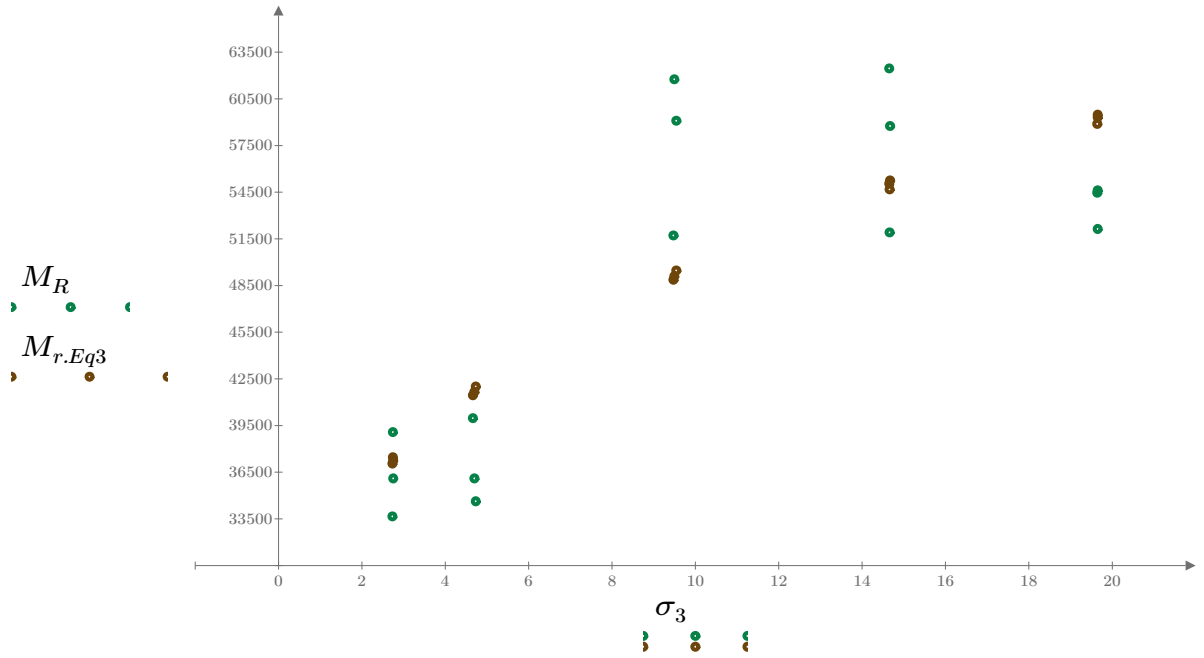

Figure 4. Plot of the test data (green points) vs. the fitted Equation 3 model (brown points).

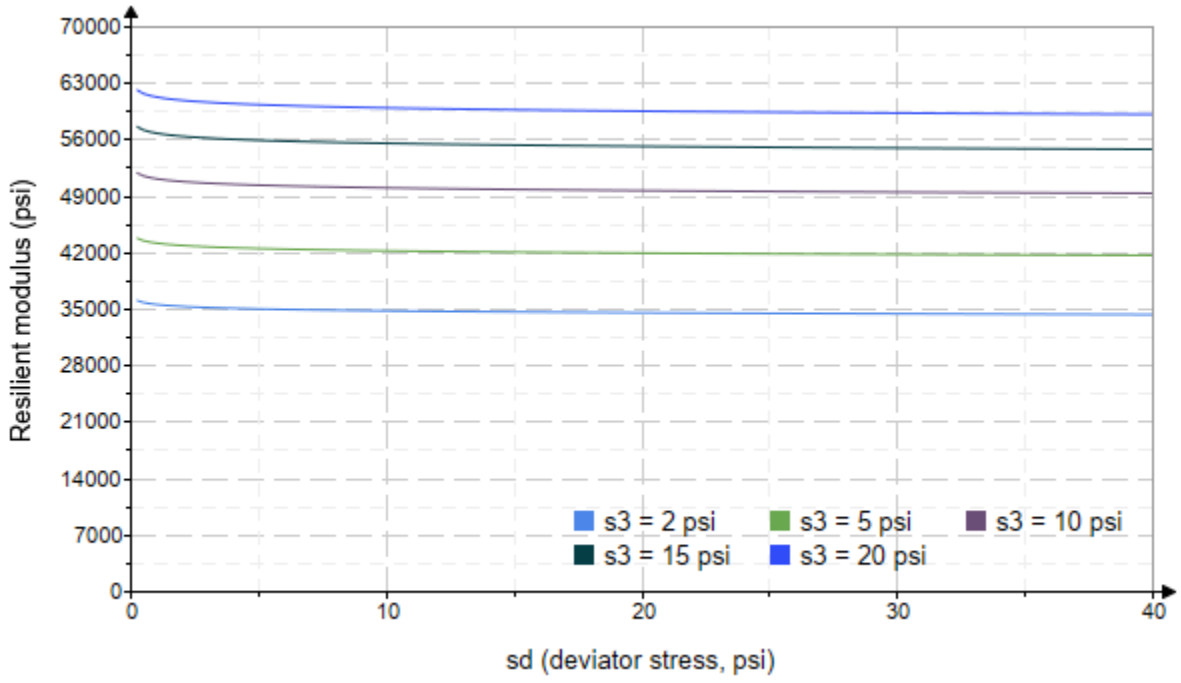

Figure 5. Plot of the fitted Equation 3 model for various confining stresses.

Dan Seely
9/12/2023

$$M_{R.4}\left(\sigma_B,\sigma_d,K_8,K_9,K_{10}\right):=K_8\cdot p_a\left(\frac{\sigma_B}{p_a}\right)^{K_9}\cdot\left(\frac{\sigma_d}{p_a}\right)^{K_{10}}$$

Equation 4 AASHTO Publication No. FHWA-RD-97-083

$K_8=2229.454$

$K_9=0.3738$ Equation 4 fitting parameters

$K_{10}=-0.1379$

$R_4{}^2=0.6680$ Coefficient of determination

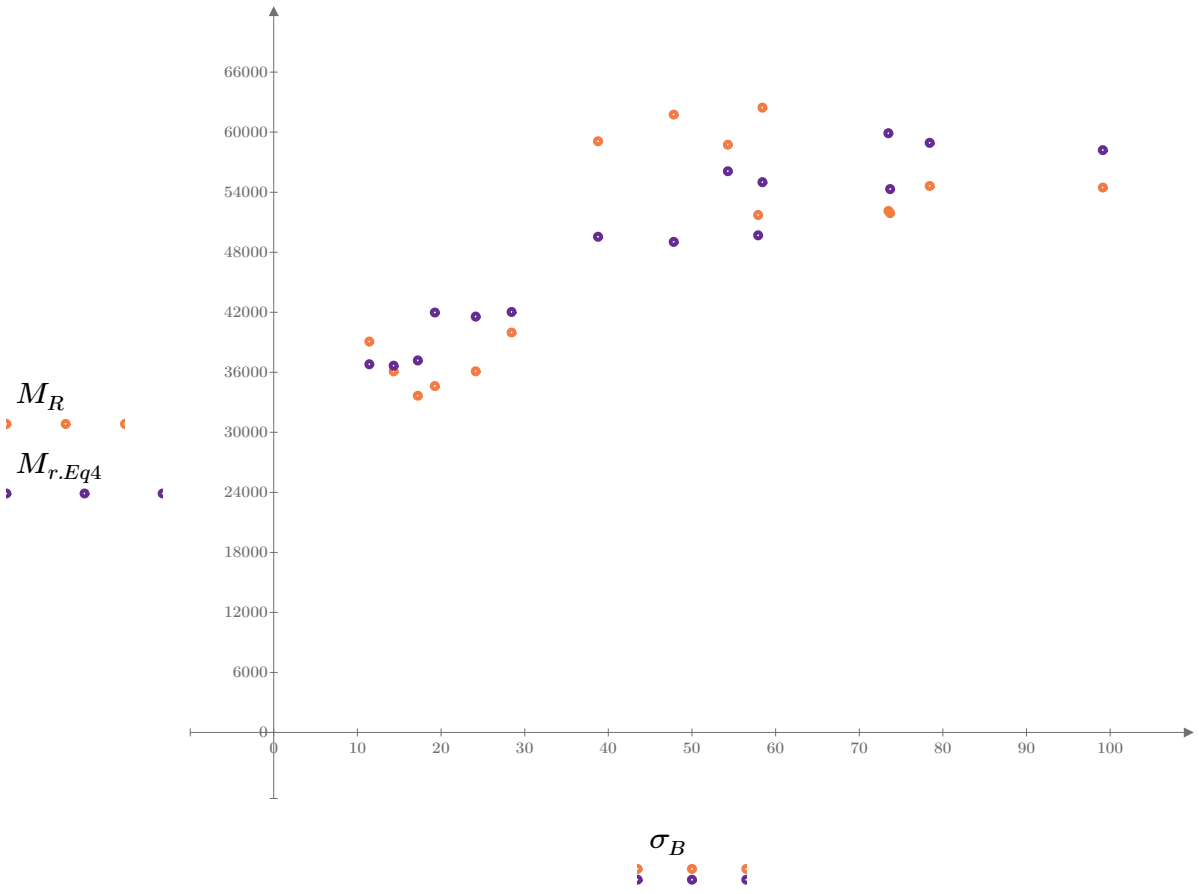

Figure 6. Plot of the test data (orange points) vs. the fitted Equation 4 model (purple points).

Dan Seely
9/12/2023

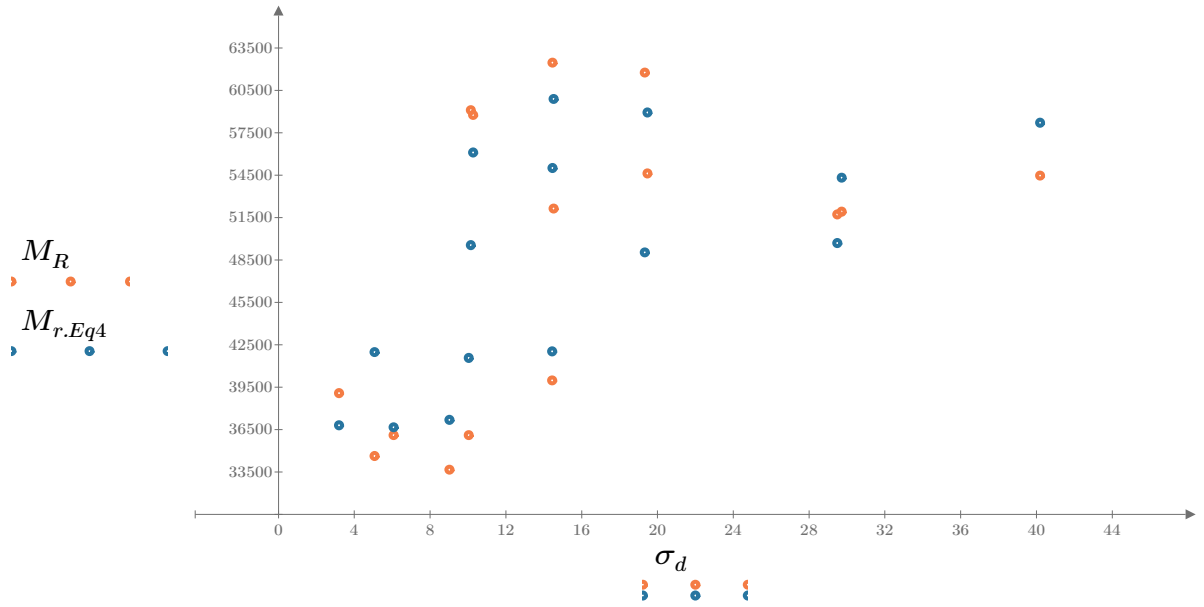

Figure 7. Plot of the test data (orange points) vs. the fitted Equation 4 model (blue points).

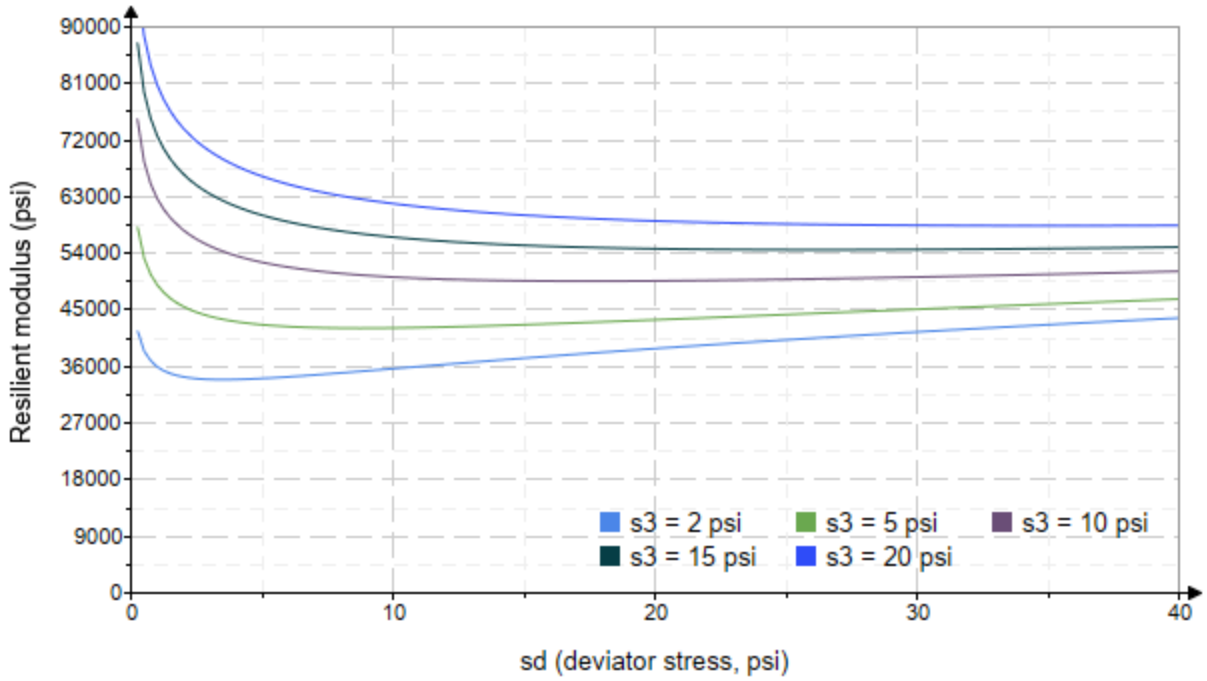

Figure 8. Plot of the fitted Equation 4 model for various confining stresses.

Dan Seely
9/12/2023

$SampleNo := \text{“B2}-\text{56”}$

$Treatment = \text{“D1”}$

$S = 15.708$ Degree of Saturation (%)

Test Sequence : Base/Subbase

Test summary data (psi) :

$$\sigma_3 = \begin{bmatrix} 2.514 \\ 1.995 \\ 2.113 \\ 4.240 \\ 4.044 \\ 3.553 \\ 8.864 \\ 8.886 \\ 8.991 \\ 13.970 \\ 13.630 \\ 14.080 \\ 19.490 \\ 18.870 \\ 19.470 \end{bmatrix} \quad \sigma_d = \begin{bmatrix} 3.179 \\ 6.166 \\ 9.203 \\ 5.136 \\ 10.120 \\ 14.550 \\ 10.190 \\ 19.250 \\ 29.460 \\ 10.220 \\ 14.660 \\ 29.750 \\ 14.490 \\ 19.640 \\ 39.760 \end{bmatrix} \quad \sigma_B = \begin{bmatrix} 10.720 \\ 12.150 \\ 15.540 \\ 17.860 \\ 22.250 \\ 25.210 \\ 36.780 \\ 45.900 \\ 56.440 \\ 52.140 \\ 55.530 \\ 71.990 \\ 72.970 \\ 76.240 \\ 98.170 \end{bmatrix} \quad M_R = \begin{bmatrix} 51916.4 \\ 26379.8 \\ 26883.8 \\ 36659.2 \\ 46434.6 \\ 42431.6 \\ 65119.8 \\ 46431.6 \\ 51532.2 \\ 90952.8 \\ 72947.6 \\ 55711.2 \\ 71247.2 \\ 73335.4 \\ 60003.4 \end{bmatrix}$$

σ_3 = mean confining stress
σ_d = mean deviator stress
σ_B = mean bulk stress
M_R = resilient modulus
p_a = atmospheric pressure = 14.6959 psi

Dan Seely
9/12/2023

$$M_{R.1}\left(\sigma_B, K_1, K_2\right) := K_1 \cdot {\sigma_B}^{K_2}$$

Equation 1
AASHTO Publication No. FHWA-RD-97-083

$K_1 = 16693.319$

$K_2 = 0.3237$

Equation 1 fitting parameters

${R_1}^2 = 0.4735$

Coefficient of determination

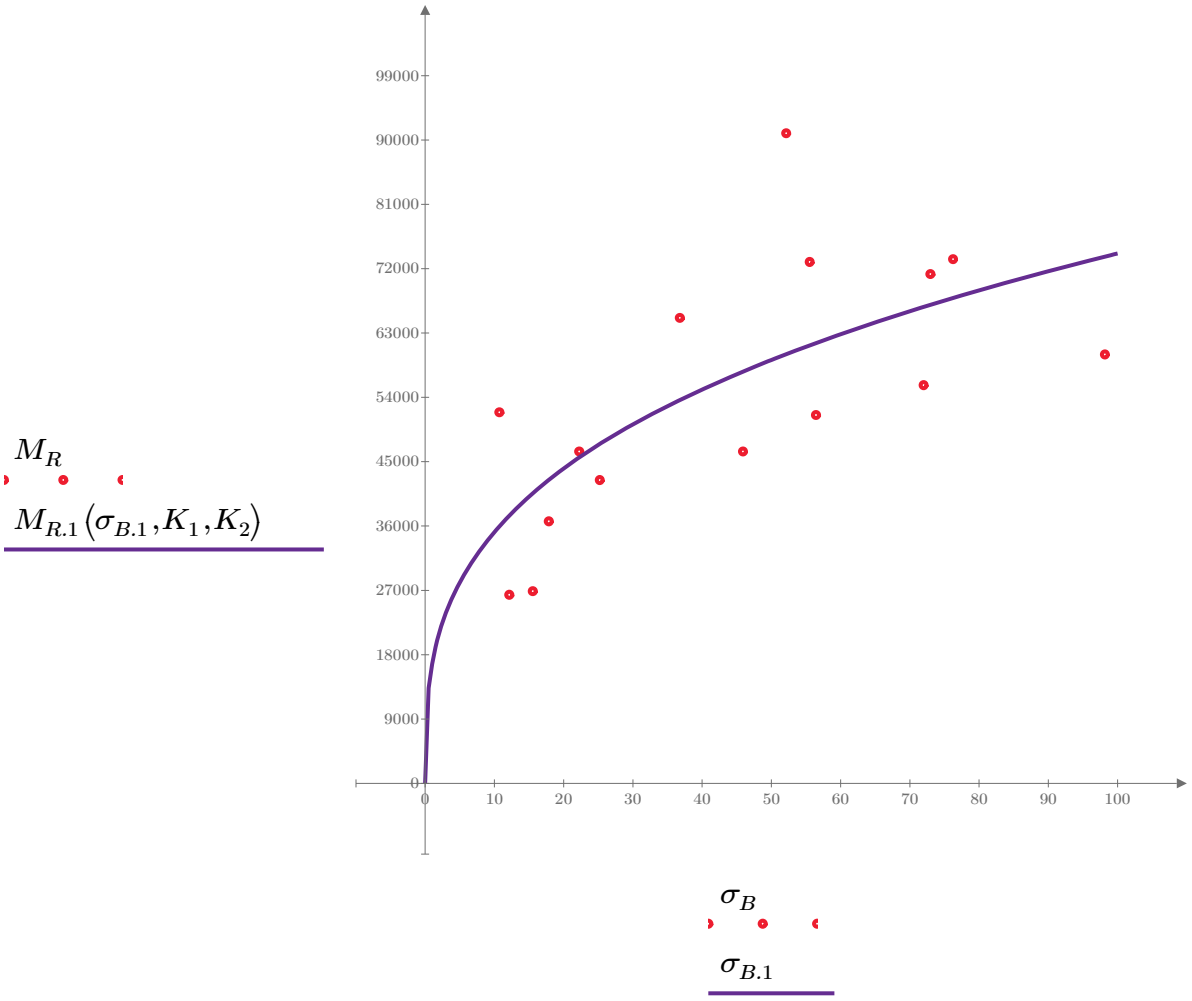

Figure 1. Plot of the test data (red points) vs. the fitted Equation 1 model (purple line).

Dan Seely
9/12/2023

$$M_{R.2}(\sigma_d, K_3, K_4) := K_3 \cdot \sigma_d^{K_4}$$

Equation 2
AASHTO Publication No. FHWA-RD-97-083

$K_3 = 38029.805$

$K_4 = 0.1399$

Equation 2 fitting parameters

$R_2^2 = 0.0877$

Coefficient of determination

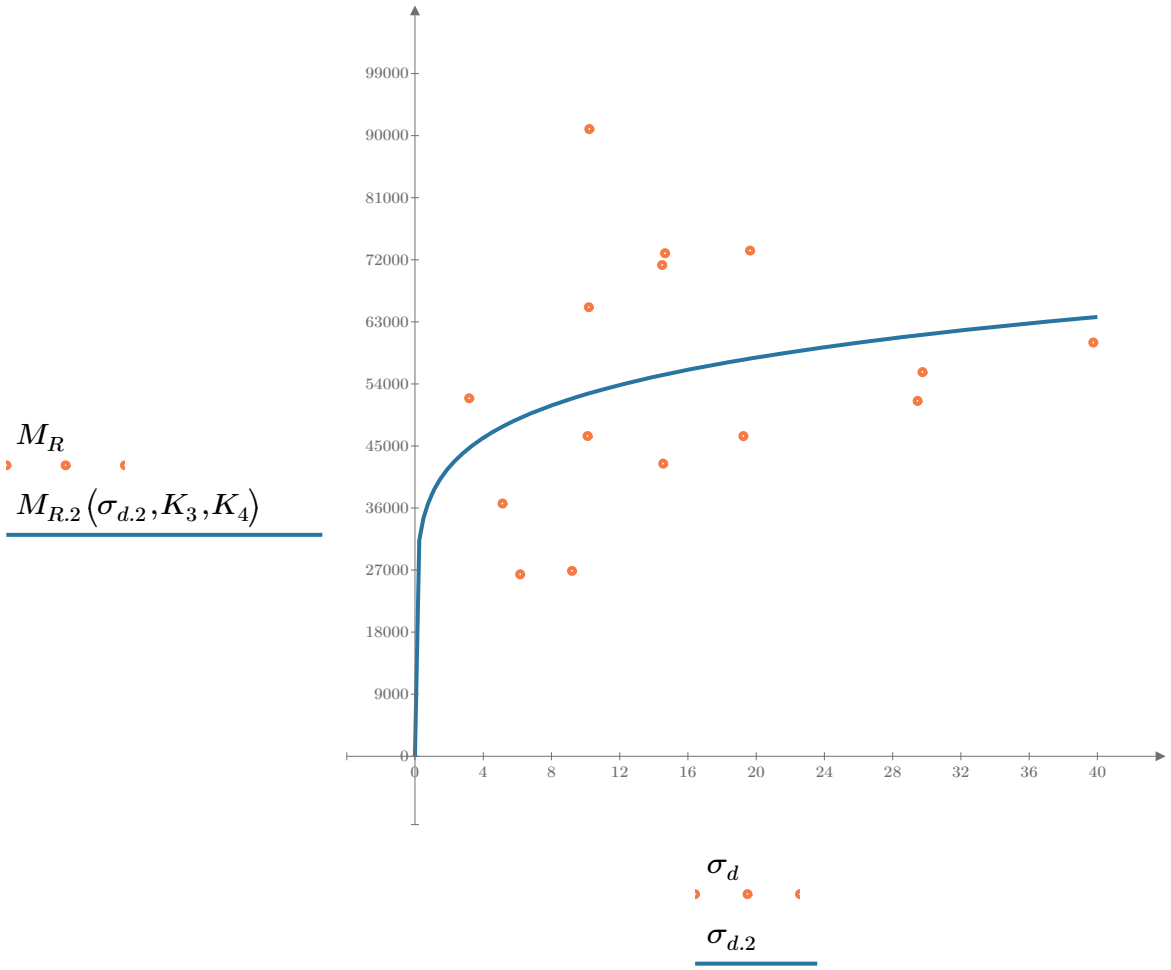

Figure 2. Plot of the test data (orange points) vs. the fitted Equation 2 model (blue line).

Dan Seely
9/12/2023

$$M_{R.3}\left(\sigma_d,\sigma_3,K_5,K_6,K_7\right):=K_5\cdot{\sigma_d}^{K_6}\cdot\left(1+\sigma_3\right)^{K_7}$$

Equation 3 AASHTO Publication No. FHWA-RD-97-083

$K_5=31000.587$

$K_6=-0.2802$ Equation 3 fitting parameters

$K_7=0.5748$

${R_3}^2=0.8093$ Coefficient of determination

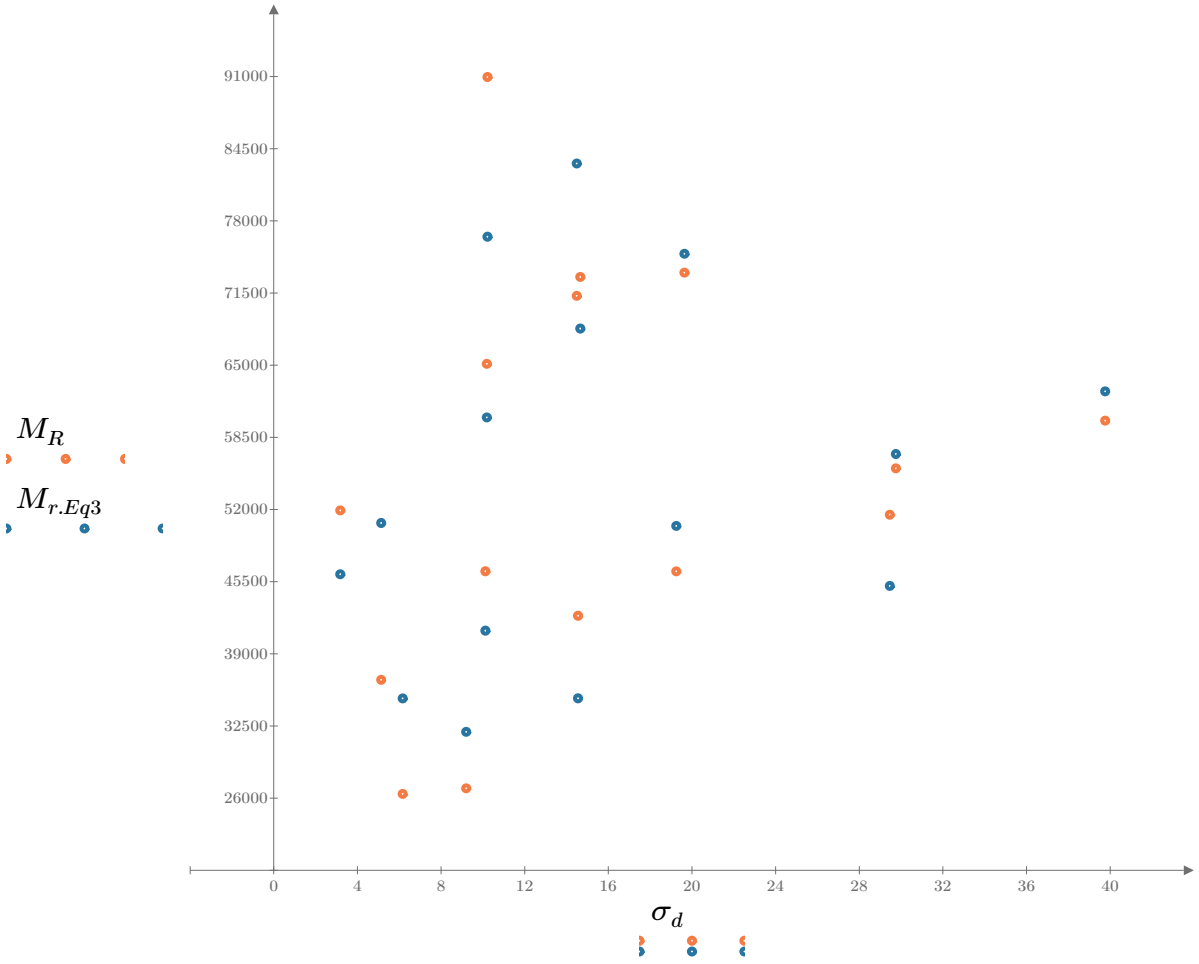

Figure 3. Plot of the test data (orange points) vs. the fitted Equation 3 model (blue points).

Dan Seely
9/12/2023

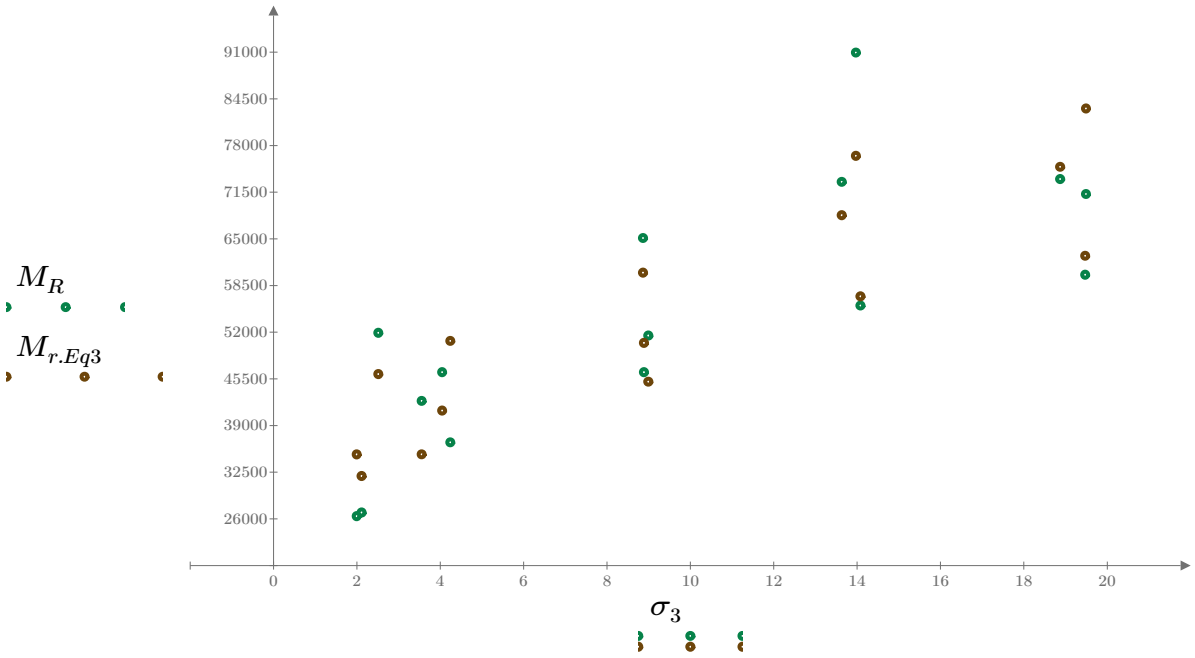

Figure 4. Plot of the test data (green points) vs. the fitted Equation 3 model (brown points).

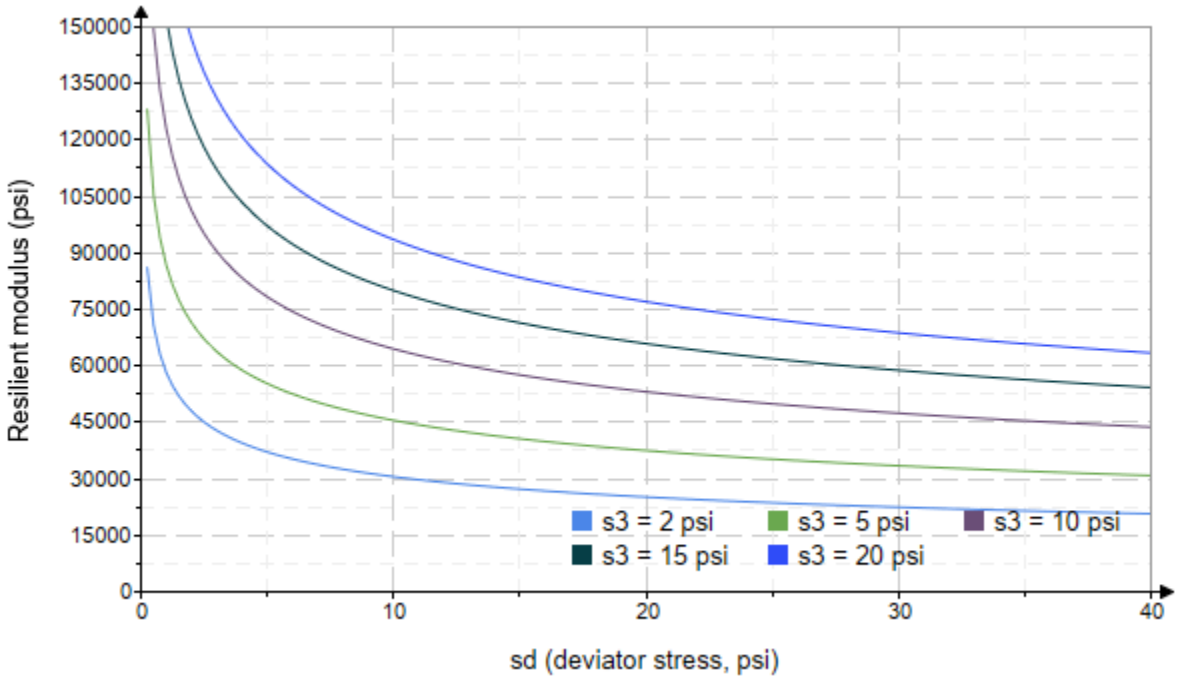

Figure 5. Plot of the fitted Equation 3 model for various confining stresses.

Dan Seely
9/12/2023

$$M_{R.4}\left(\sigma_B,\sigma_d,K_8,K_9,K_{10}\right) := K_8 \cdot p_a \left(\frac{\sigma_B}{p_a}\right)^{K_9} \cdot \left(\frac{\sigma_d}{p_a}\right)^{K_{10}}$$

Equation 4 AASHTO Publication No. FHWA-RD-97-083

$K_8 = 1653.261$

$K_9 = 0.7720$ Equation 4 fitting parameters

$K_{10} = -0.5497$

$R_4^{\,2} = 0.8264$ Coefficient of determination

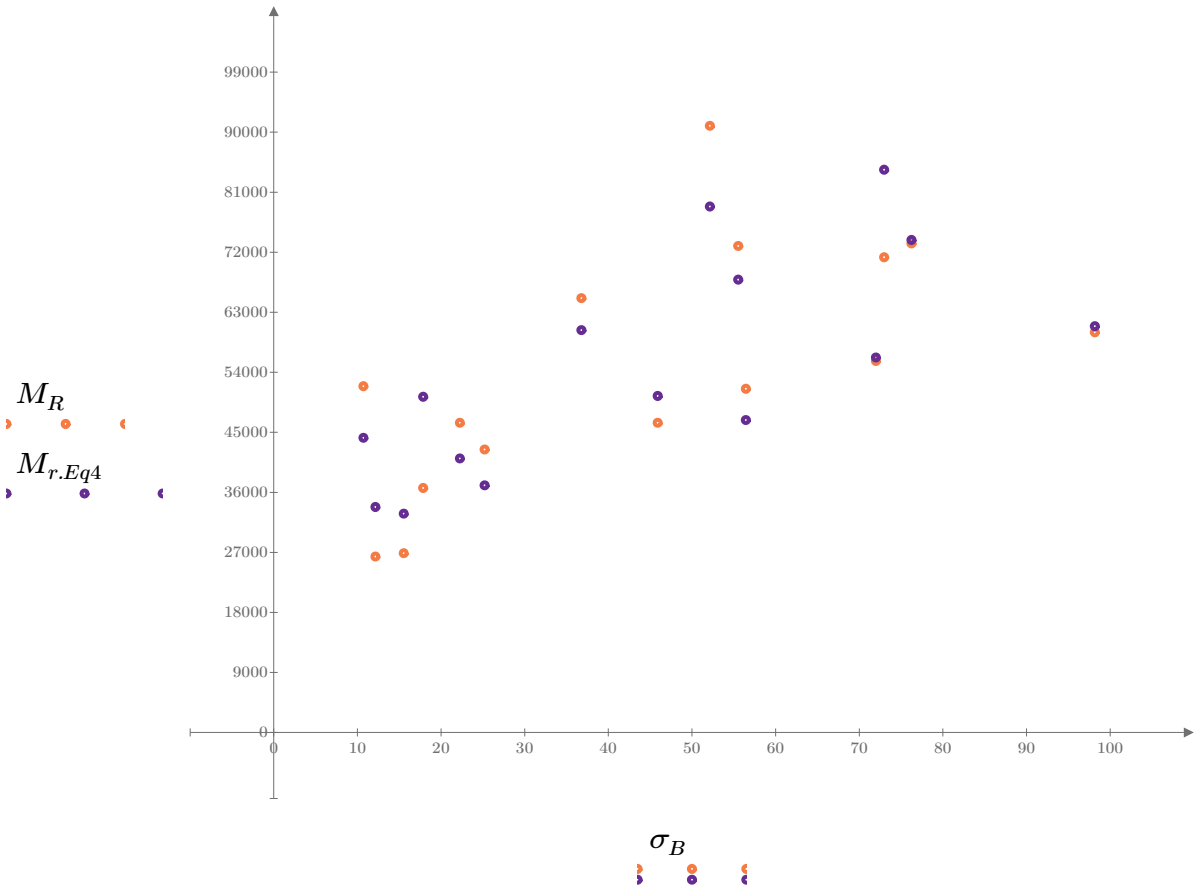

Figure 6. Plot of the test data (orange points) vs. the fitted Equation 4 model (purple points).

Dan Seely
9/12/2023

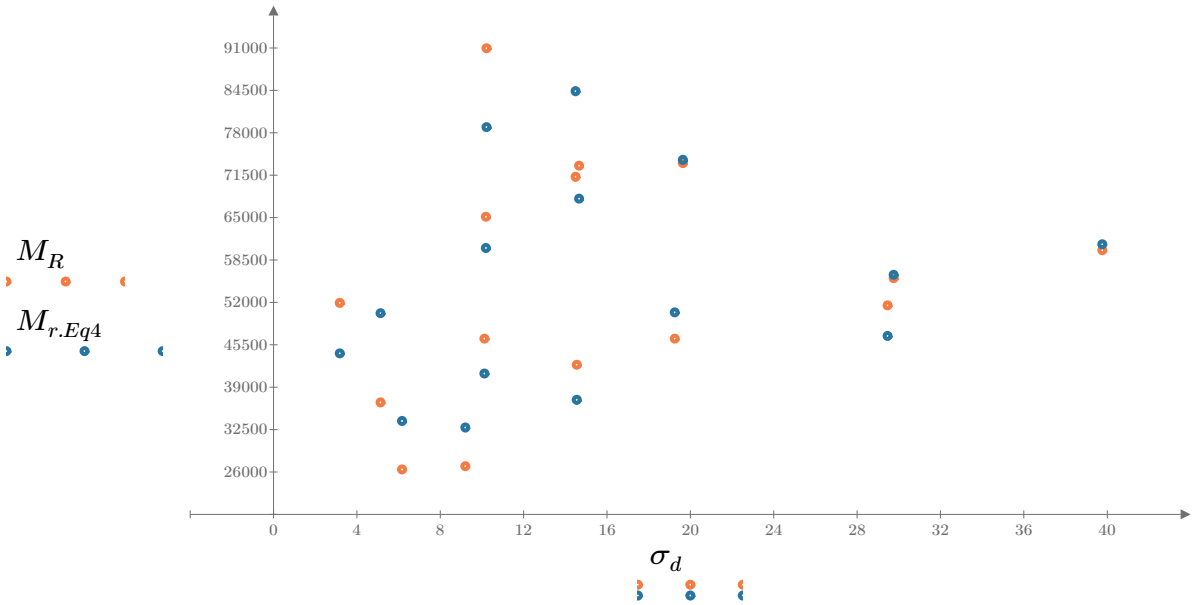

Figure 7. Plot of the test data (orange points) vs. the fitted Equation 4 model (blue points).

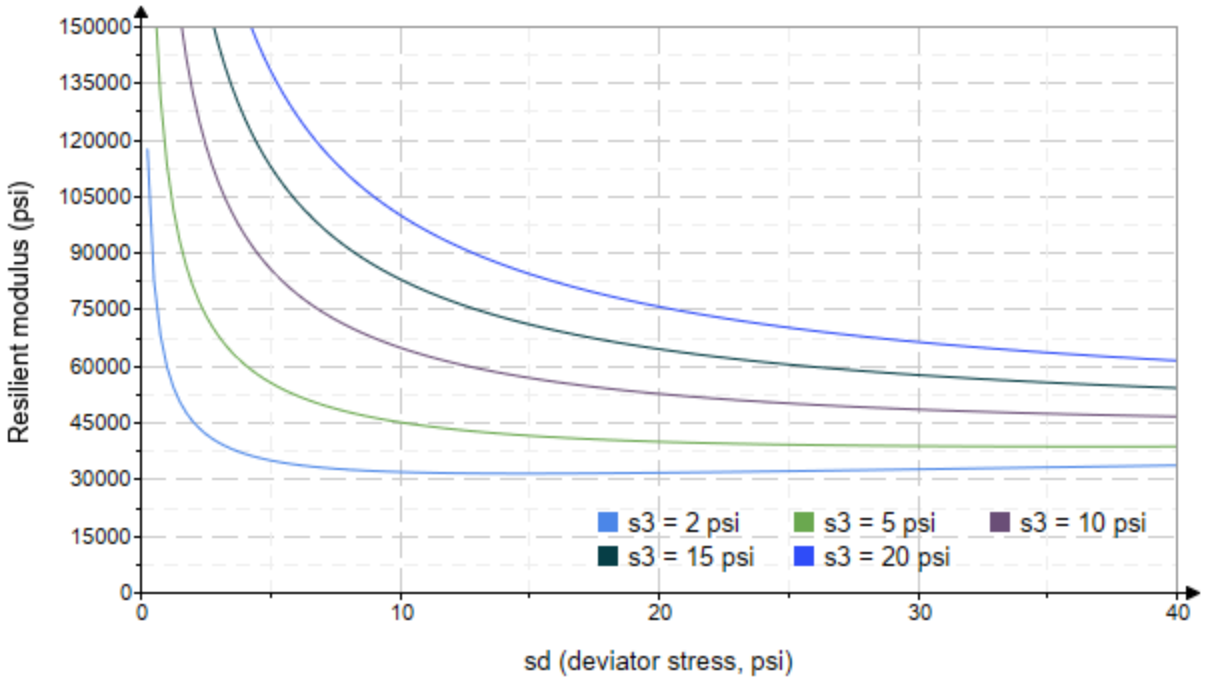

Figure 8. Plot of the fitted Equation 4 model for various confining stresses.

Dan Seely
9/12/2023

$SampleNo := \text{“B2–57”}$

$Treatment = \text{“W1”}$

$S = 16.078$ Degree of Saturation (%)

Test Sequence : Base/Subbase

Test summary data (psi) :

$$\sigma_3 = \begin{bmatrix} 2.783 \\ 2.699 \\ 2.644 \\ 4.546 \\ 4.580 \\ 4.571 \\ 9.602 \\ 9.604 \\ 9.589 \\ 14.640 \\ 14.630 \\ 14.610 \\ 19.650 \\ 19.640 \\ 19.640 \end{bmatrix} \quad \sigma_d = \begin{bmatrix} 3.172 \\ 6.271 \\ 9.035 \\ 5.270 \\ 9.995 \\ 14.560 \\ 10.060 \\ 19.280 \\ 29.340 \\ 10.220 \\ 14.600 \\ 29.580 \\ 14.510 \\ 19.330 \\ 39.890 \end{bmatrix} \quad \sigma_B = \begin{bmatrix} 11.520 \\ 14.370 \\ 16.970 \\ 18.910 \\ 23.740 \\ 28.270 \\ 38.870 \\ 48.090 \\ 58.100 \\ 54.150 \\ 58.470 \\ 73.410 \\ 73.450 \\ 78.260 \\ 98.820 \end{bmatrix} \quad M_R = \begin{bmatrix} 67941.0 \\ 57785.8 \\ 58109.2 \\ 61818.0 \\ 64566.8 \\ 52199.8 \\ 53854.0 \\ 43024.4 \\ 45460.6 \\ 42993.4 \\ 41448.6 \\ 54200.2 \\ 55561.2 \\ 59868.0 \\ 72492.8 \end{bmatrix}$$

σ_3 = mean confining stress
σ_d = mean deviator stress
σ_B = mean bulk stress
M_R = resilient modulus
p_a = atmospheric pressure = 14.6959 psi

Dan Seely
9/12/2023

$$M_{R.1}(\sigma_B, K_1, K_2) := K_1 \cdot {\sigma_B}^{K_2}$$

Equation 1
AASHTO Publication No. FHWA-RD-97-083

$K_1 = 72969.918$

$K_2 = -0.0760$

Equation 1 fitting parameters

${R_1}^2 = 0.0907$

Coefficient of determination

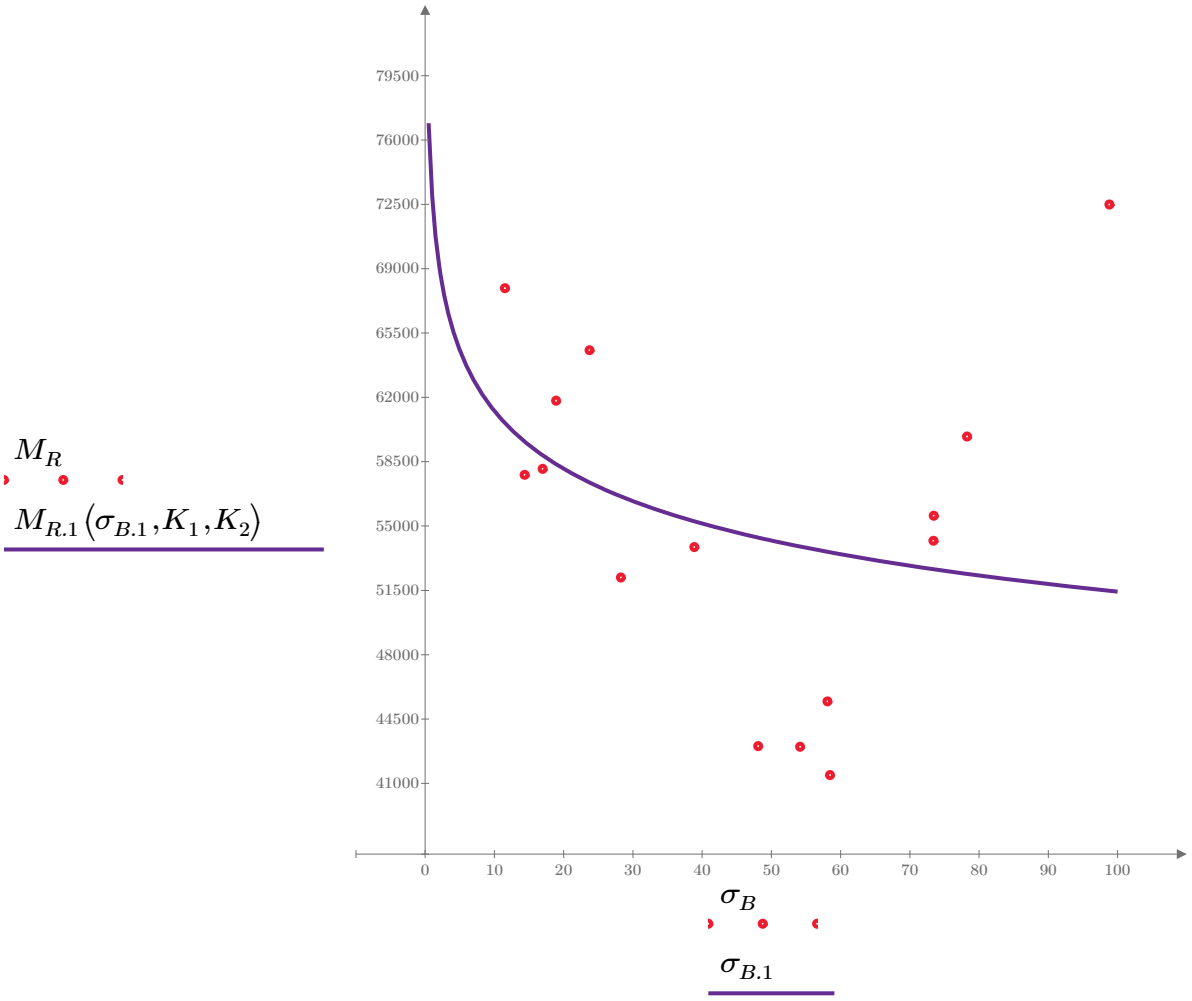

Figure 1. Plot of the test data (red points) vs. the fitted Equation 1 model (purple line).

Dan Seely
9/12/2023

$$M_{R.2}(\sigma_d, K_3, K_4) := K_3 \cdot \sigma_d^{K_4}$$

Equation 2
AASHTO Publication No. FHWA-RD-97-083

$K_3 = 64769.600$

$K_4 = -0.0616$

Equation 2 fitting parameters

$R_2^2 = 0.0570$

Coefficient of determination

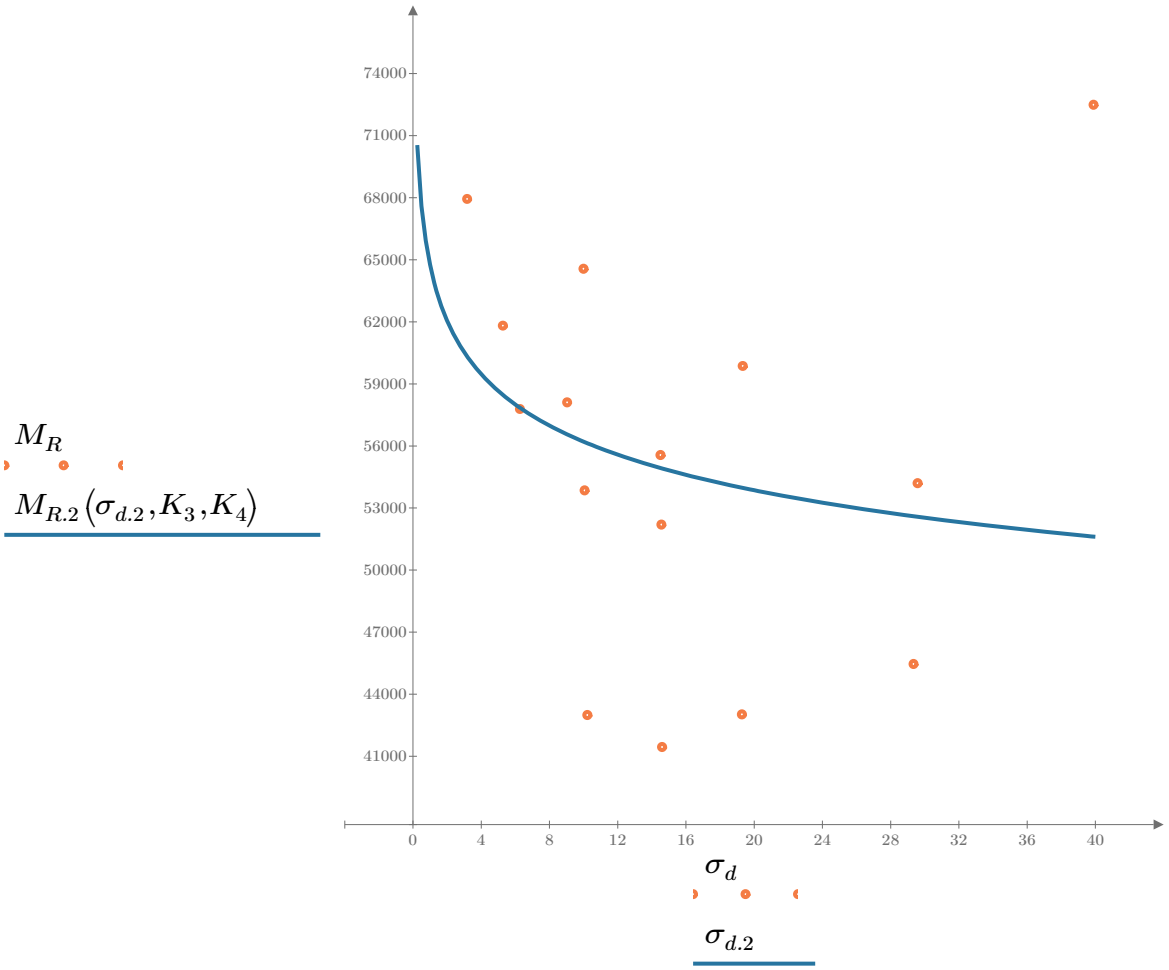

Figure 2. Plot of the test data (orange points) vs. the fitted Equation 2 model (blue line).

Dan Seely
9/12/2023

$$M_{R.3}\left(\sigma_d,\sigma_3,K_5,K_6,K_7\right):=K_5\cdot{\sigma_d}^{K_6}\cdot\left(1+\sigma_3\right)^{K_7}$$

Equation 3 AASHTO Publication No. FHWA-RD-97-083

$K_5=66403.783$

$K_6=-0.0257$ Equation 3 fitting parameters

$K_7=-0.0522$

${R_3}^2=0.0776$ Coefficient of determination

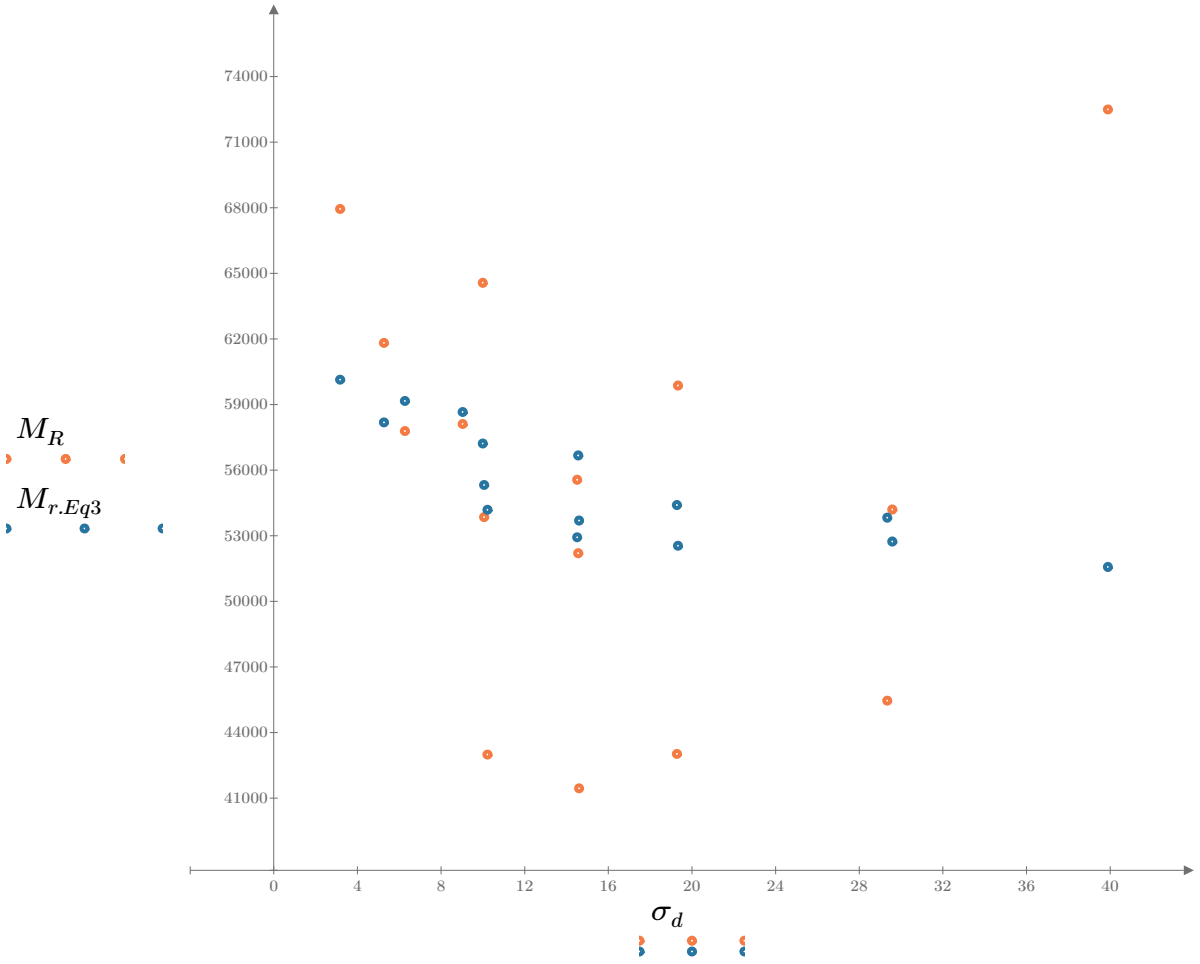

Figure 3. Plot of the test data (orange points) vs. the fitted Equation 3 model (blue points).

Dan Seely
9/12/2023

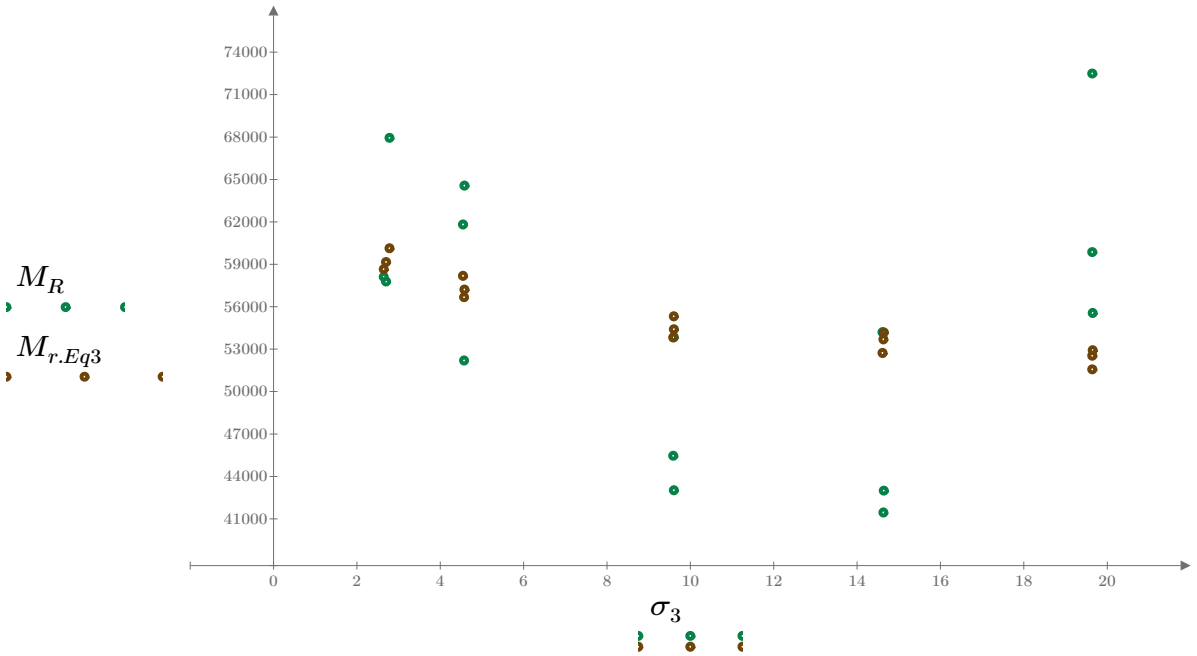

Figure 4. Plot of the test data (green points) vs. the fitted Equation 3 model (brown points).

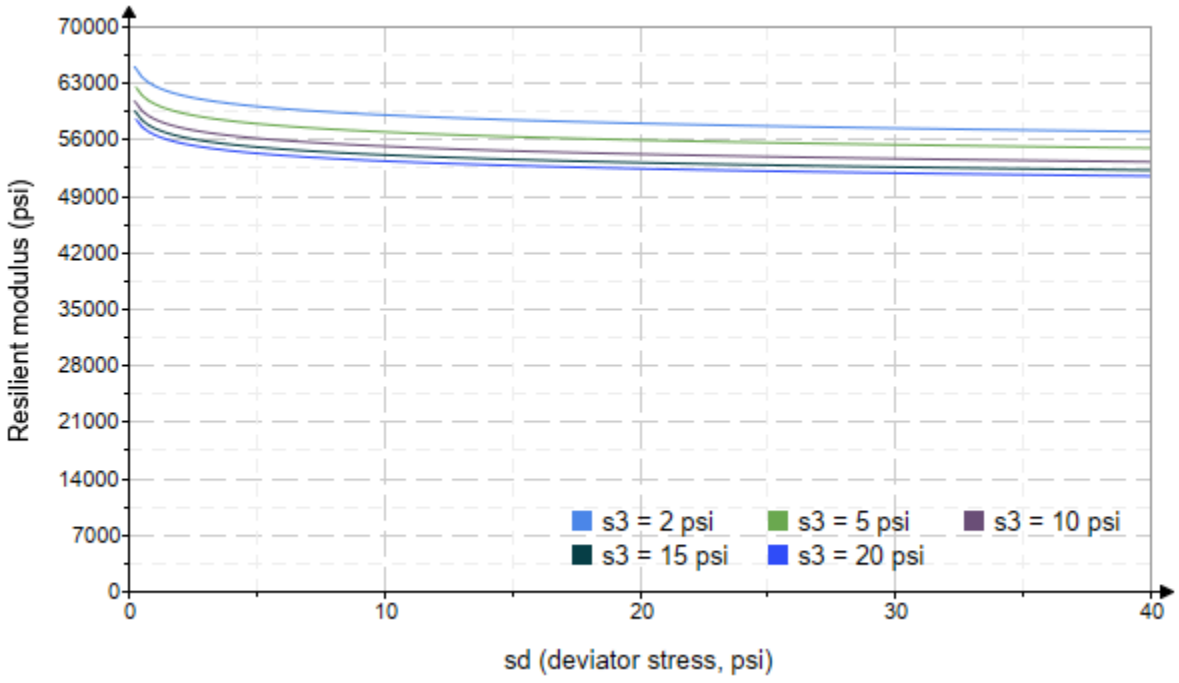

Figure 5. Plot of the fitted Equation 3 model for various confining stresses.

Dan Seely
9/12/2023

$$M_{R.4}\left(\sigma_B,\sigma_d,K_8,K_9,K_{10}\right) := K_8 \cdot p_a \left(\frac{\sigma_B}{p_a}\right)^{K_9} \cdot \left(\frac{\sigma_d}{p_a}\right)^{K_{10}}$$

Equation 4 AASHTO Publication No. FHWA-RD-97-083

$K_8 = 4116.909$

$K_9 = -0.0910$ Equation 4 fitting parameters

$K_{10} = 0.0178$

$R_4^{\,2} = 0.0919$ Coefficient of determination

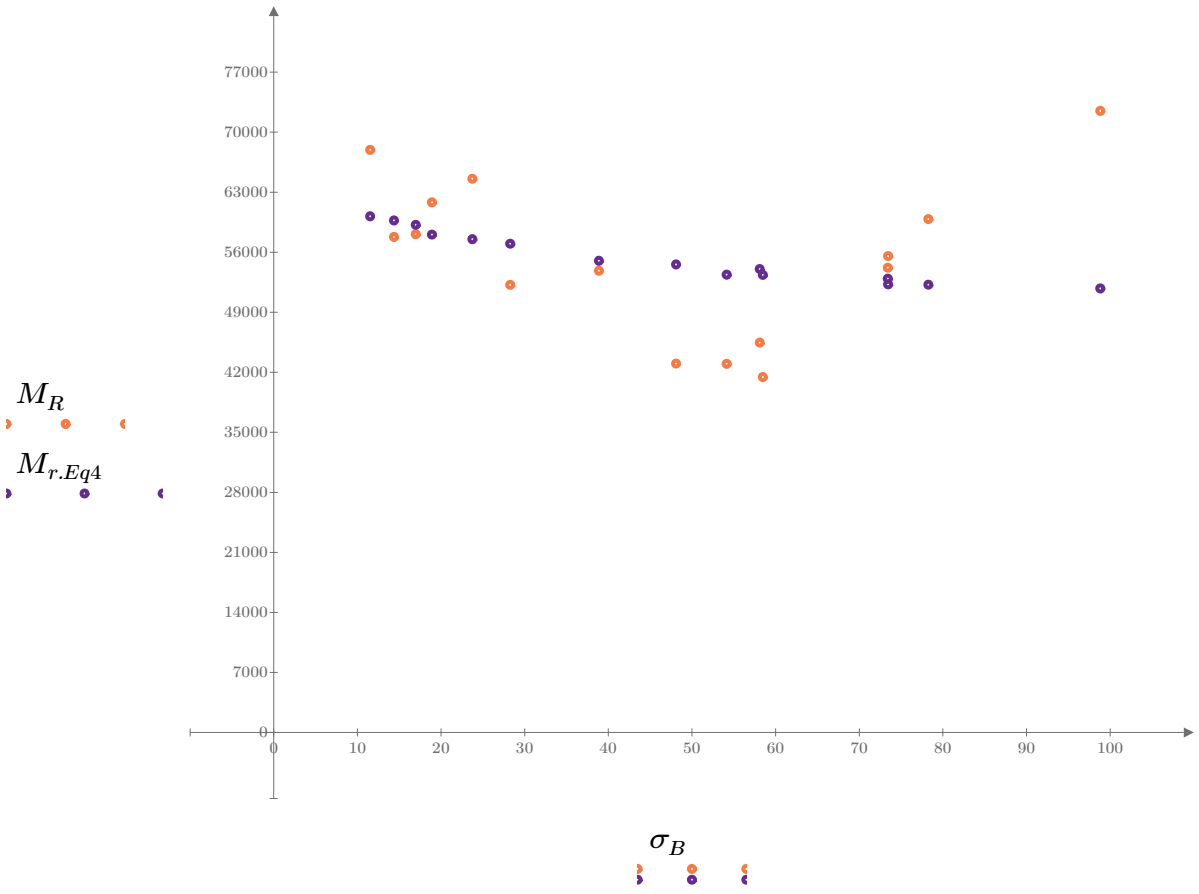

Figure 6. Plot of the test data (orange points) vs. the fitted Equation 4 model (purple points).

Dan Seely
9/12/2023

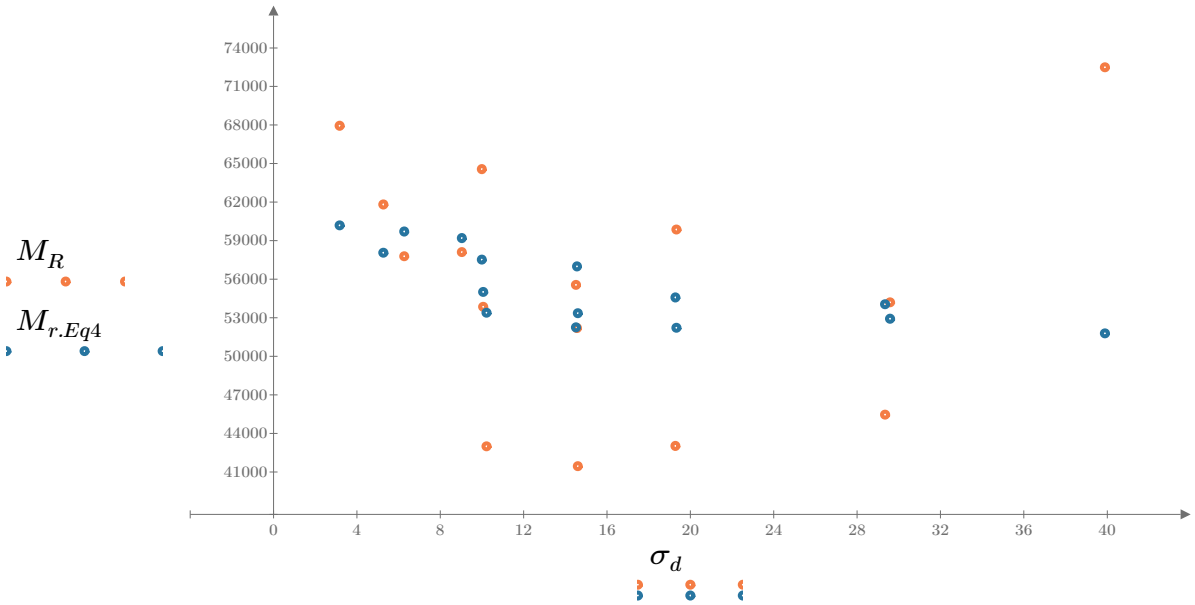

Figure 7. Plot of the test data (orange points) vs. the fitted Equation 4 model (blue points).

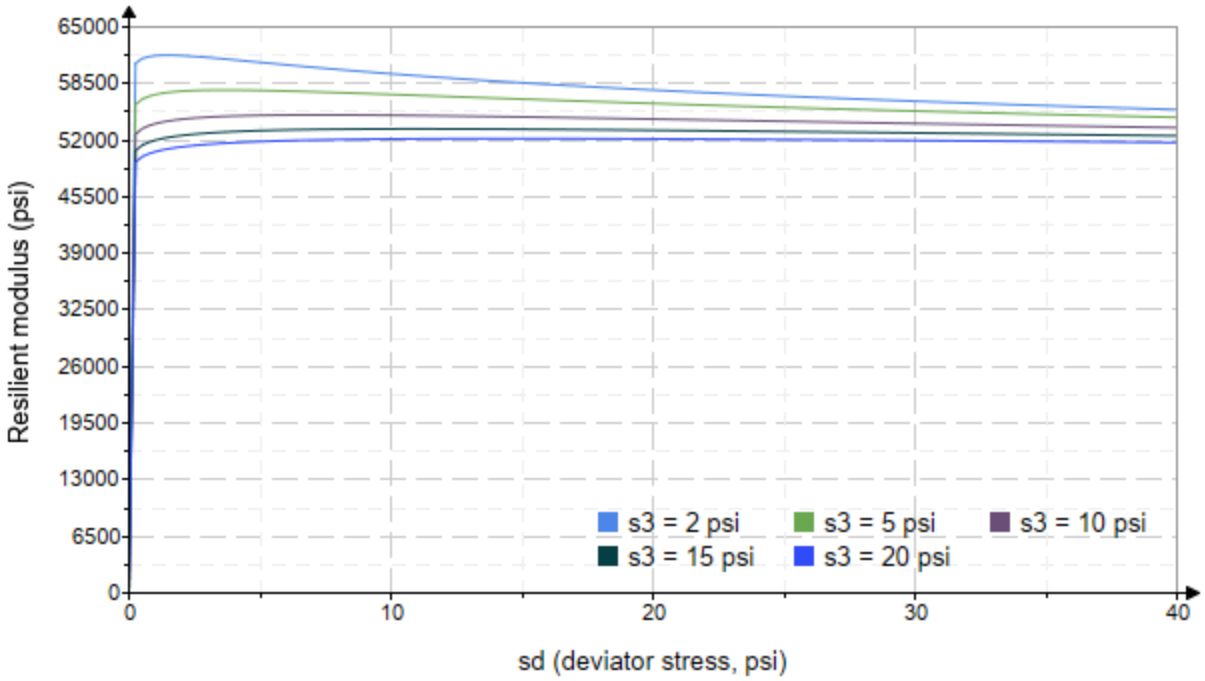

Figure 8. Plot of the fitted Equation 4 model for various confining stresses.

Dan Seely
9/12/2023

$SampleNo := \text{“B2}-\text{58”}$

$Treatment = \text{“W1”}$

$S = 15.842$ Degree of Saturation (%)

Test Sequence : Base/Subbase

Test summary data (psi) :

$$\sigma_3 = \begin{bmatrix} 2.400 \\ 2.738 \\ 2.306 \\ 4.371 \\ 3.819 \\ 3.964 \\ 8.642 \\ 8.669 \\ 8.753 \\ 13.580 \\ 13.840 \\ 13.860 \\ 18.680 \\ 18.990 \\ 19.250 \end{bmatrix} \quad \sigma_d = \begin{bmatrix} 3.311 \\ 6.089 \\ 9.145 \\ 5.164 \\ 10.160 \\ 14.430 \\ 10.220 \\ 19.210 \\ 29.370 \\ 10.150 \\ 14.480 \\ 29.580 \\ 14.570 \\ 19.610 \\ 39.930 \end{bmatrix} \quad \sigma_B = \begin{bmatrix} 10.510 \\ 14.300 \\ 16.060 \\ 18.280 \\ 21.620 \\ 26.320 \\ 36.150 \\ 45.210 \\ 55.630 \\ 50.890 \\ 56.010 \\ 71.170 \\ 70.620 \\ 76.600 \\ 97.670 \end{bmatrix} \quad M_R = \begin{bmatrix} 56168.2 \\ 44676.6 \\ 42806.8 \\ 59237.9 \\ 75669.0 \\ 65240.8 \\ 104606.2 \\ 60457.0 \\ 62738.4 \\ 126880.0 \\ 86395.8 \\ 77331.4 \\ 119860.0 \\ 92410.2 \\ 66634.0 \end{bmatrix}$$

σ_3 = mean confining stress
σ_d = mean deviator stress
σ_B = mean bulk stress
M_R = resilient modulus
p_a = atmospheric pressure = 14.6959 psi

Dan Seely
9/12/2023

$$M_{R.1}(\sigma_B, K_1, K_2) := K_1 \cdot {\sigma_B}^{K_2}$$

Equation 1
AASHTO Publication No. FHWA-RD-97-083

$K_1 = 29698.305$

$K_2 = 0.2582$

Equation 1 fitting parameters

${R_1}^2 = 0.2987$

Coefficient of determination

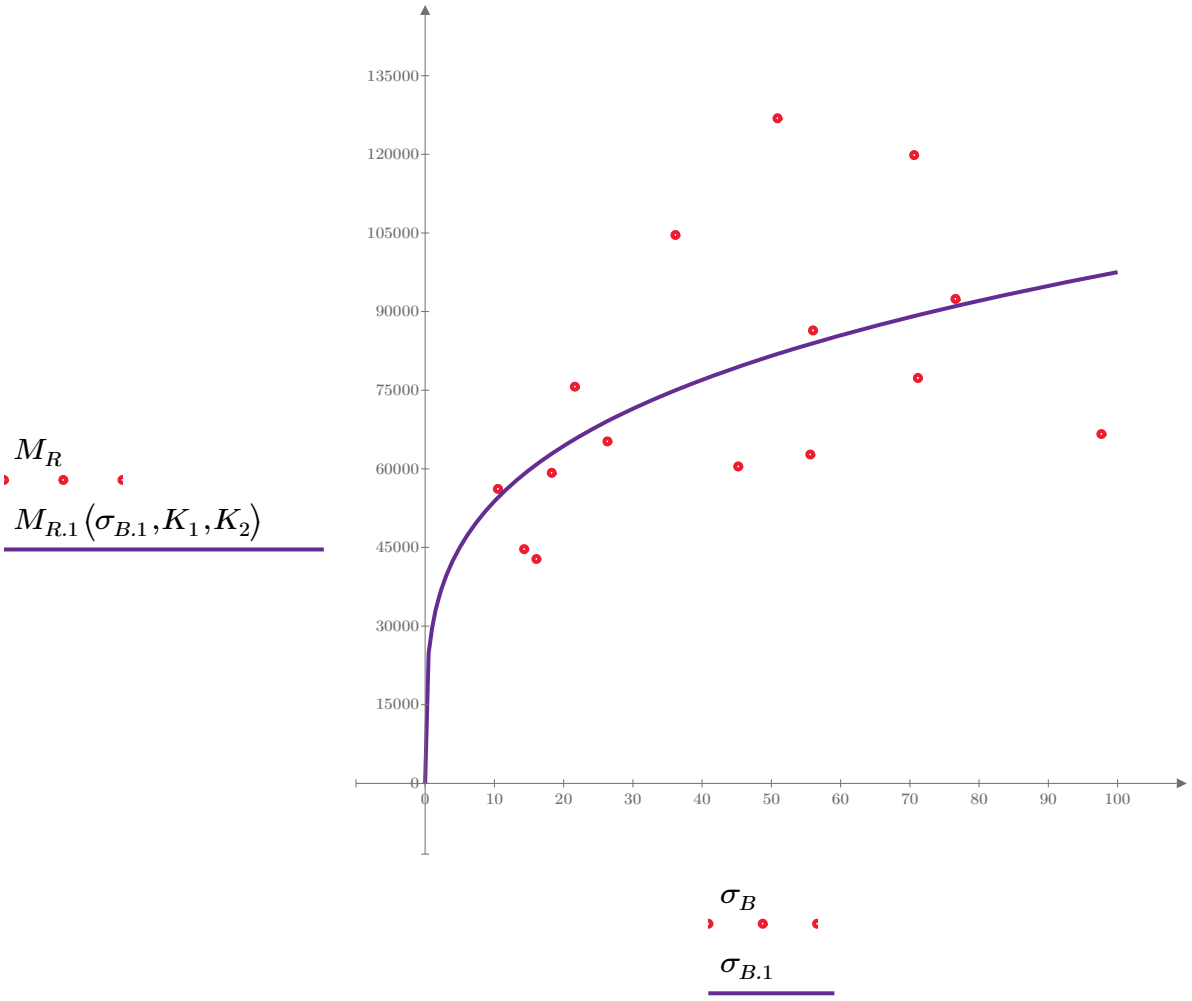

Figure 1. Plot of the test data (red points) vs. the fitted Equation 1 model (purple line).

Dan Seely
9/12/2023

$$M_{R.2}(\sigma_d, K_3, K_4) := K_3 \cdot \sigma_d^{K_4}$$

Equation 2
AASHTO Publication No. FHWA-RD-97-083

$K_3 = 62559.811$

$K_4 = 0.0763$

Equation 2 fitting parameters

$R_2^2 = 0.0282$

Coefficient of determination

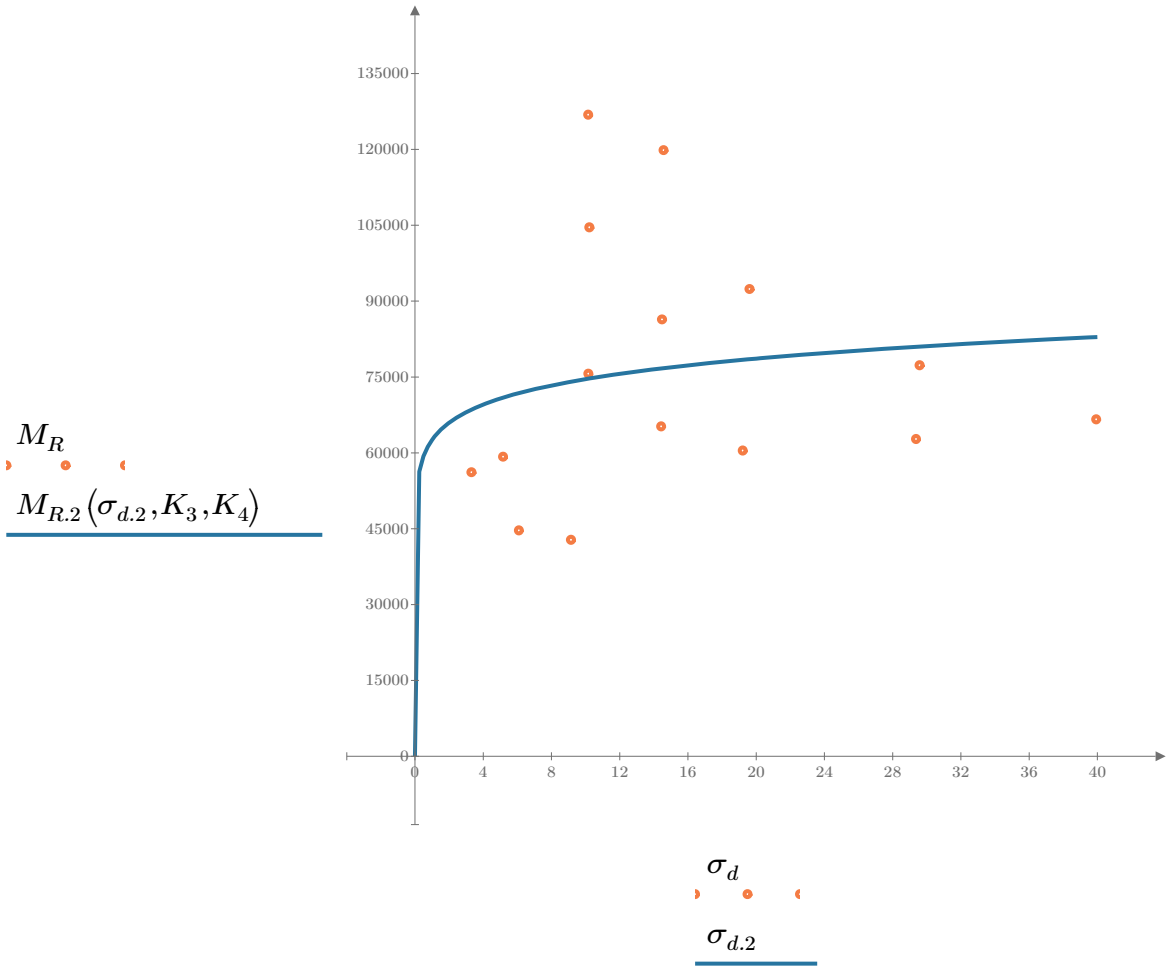

Figure 2. Plot of the test data (orange points) vs. the fitted Equation 2 model (blue line).

Dan Seely
9/12/2023

$$M_{R.3}\left(\sigma_d,\sigma_3,K_5,K_6,K_7\right):=K_5\cdot{\sigma_d}^{K_6}\cdot\left(1+\sigma_3\right)^{K_7}$$

Equation 3 AASHTO Publication No. FHWA-RD-97-083

$K_5=48784.393$

$K_6=-0.3693$ Equation 3 fitting parameters

$K_7=0.6205$

${R_3}^2=0.7268$ Coefficient of determination

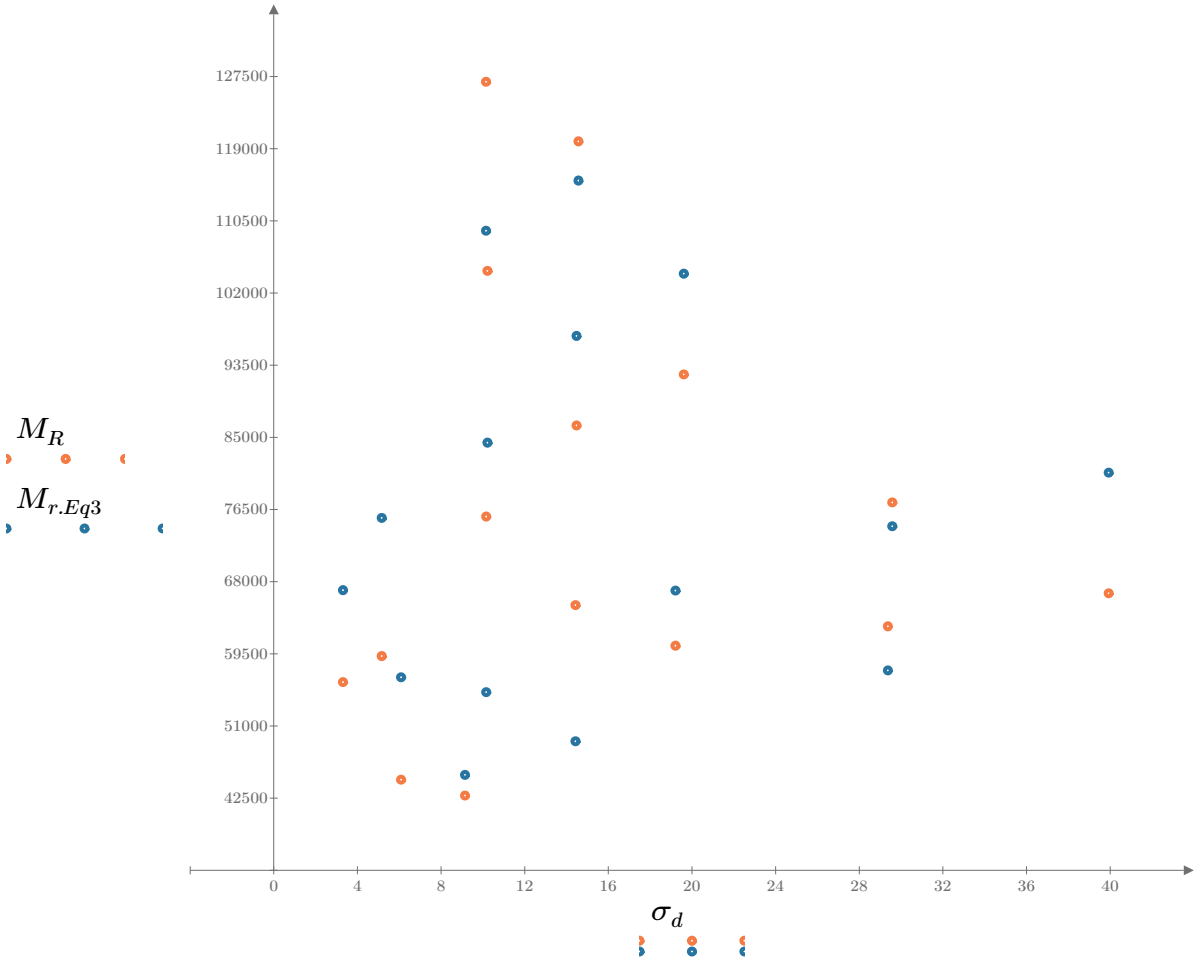

Figure 3. Plot of the test data (orange points) vs. the fitted Equation 3 model (blue points).

Dan Seely
9/12/2023

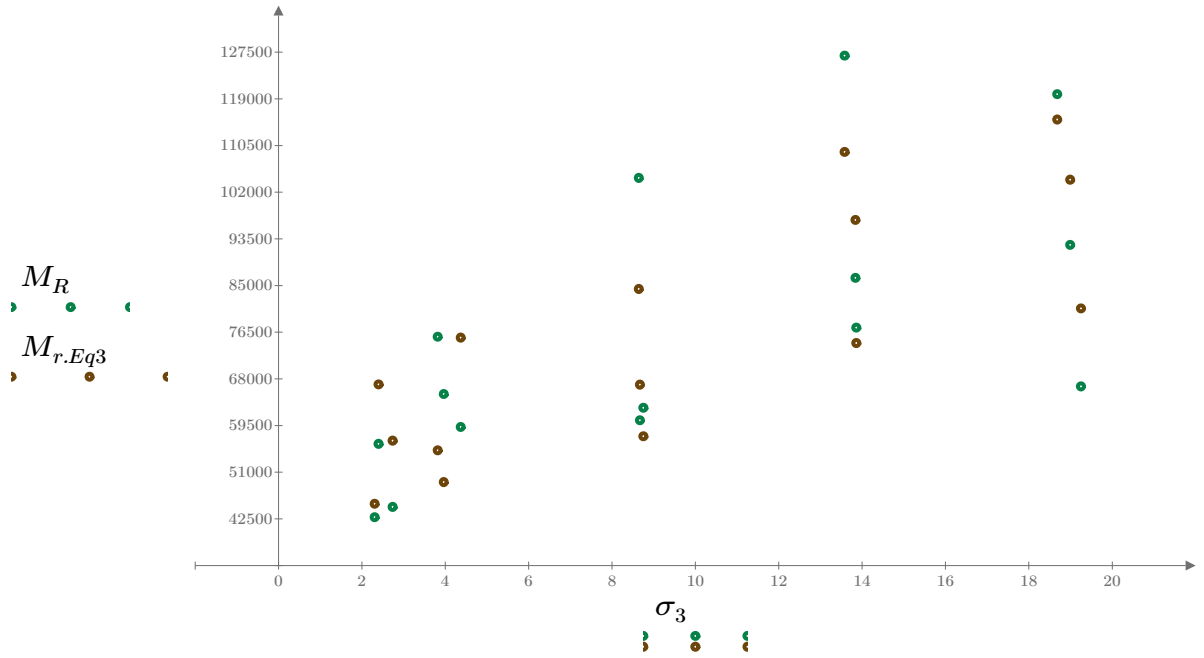

Figure 4. Plot of the test data (green points) vs. the fitted Equation 3 model (brown points).

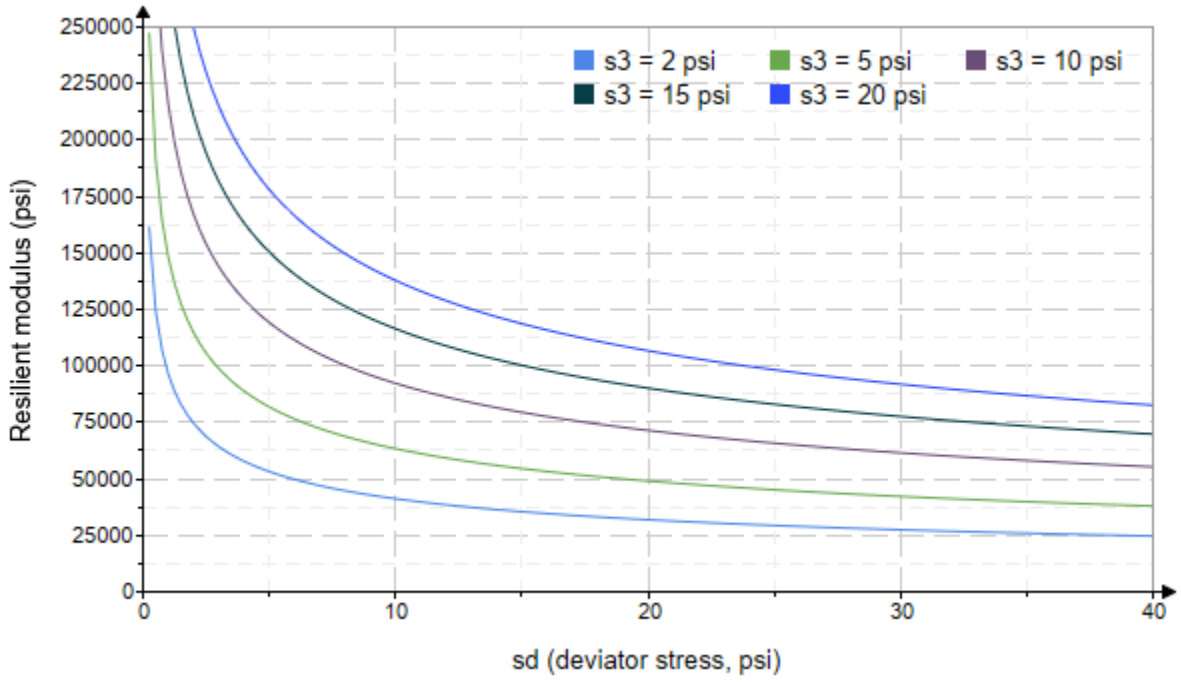

Figure 5. Plot of the fitted Equation 3 model for various confining stresses.

Dan Seely
9/12/2023

$$M_{R.4}\left(\sigma_B,\sigma_d,K_8,K_9,K_{10}\right) := K_8 \cdot p_a \left(\frac{\sigma_B}{p_a}\right)^{K_9} \cdot \left(\frac{\sigma_d}{p_a}\right)^{K_{10}}$$

Equation 4 AASHTO Publication No. FHWA-RD-97-083

$K_8 = 2098.551$

$K_9 = 0.8483$ Equation 4 fitting parameters

$K_{10} = -0.6785$

$R_4^{\,2} = 0.7745$ Coefficient of determination

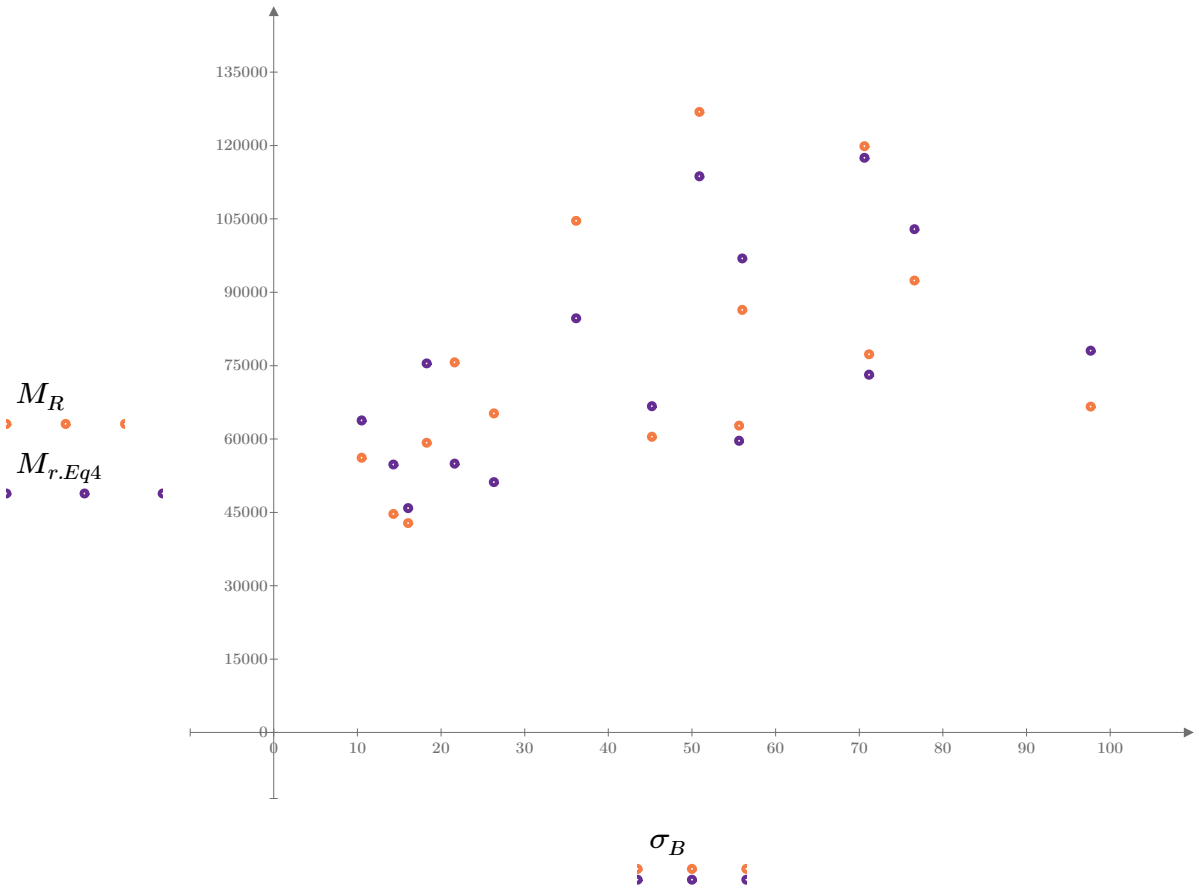

Figure 6. Plot of the test data (orange points) vs. the fitted Equation 4 model (purple points).

Dan Seely
9/12/2023

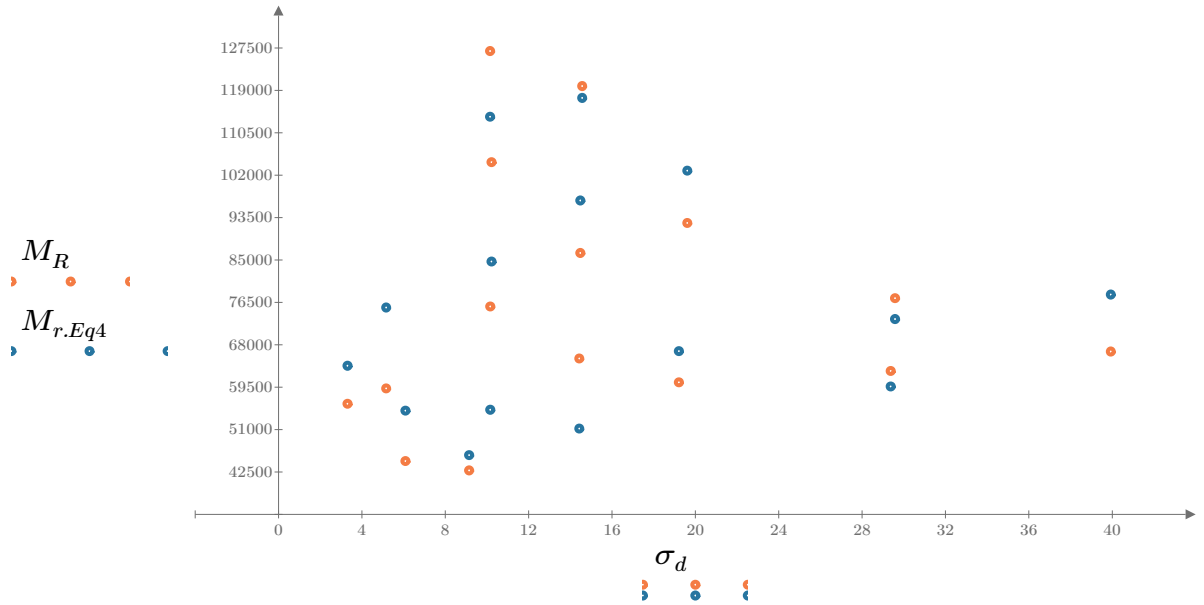

Figure 7. Plot of the test data (orange points) vs. the fitted Equation 4 model (blue points).

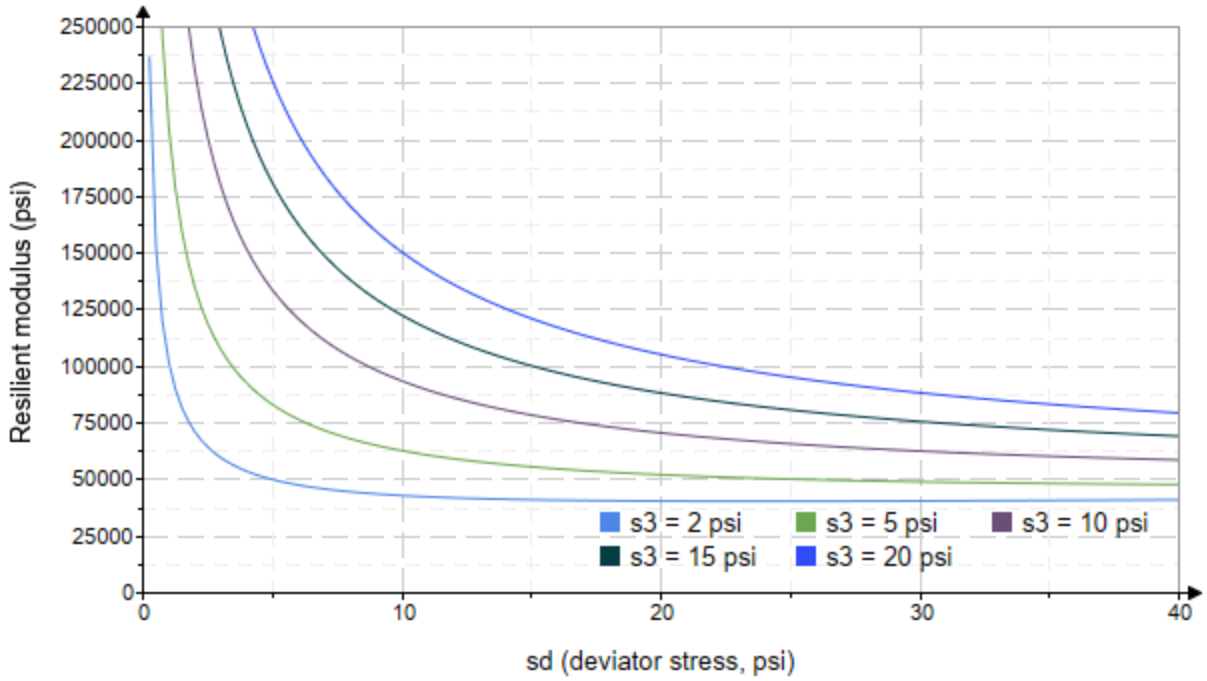

Figure 8. Plot of the fitted Equation 4 model for various confining stresses.

Dan Seely
9/12/2023

$SampleNo := \text{“B2}-\text{59”}$

$Treatment = \text{“W1”}$

$S = 17.084$ Degree of Saturation (%)

Test Sequence : Base/Subbase

Test summary data (psi) :

$$\sigma_3 = \begin{bmatrix} 2.595 \\ 2.568 \\ 2.545 \\ 4.592 \\ 4.536 \\ 4.572 \\ 9.562 \\ 9.575 \\ 9.579 \\ 14.610 \\ 14.610 \\ 14.590 \\ 19.630 \\ 19.660 \\ 19.630 \end{bmatrix} \quad \sigma_d = \begin{bmatrix} 3.208 \\ 6.286 \\ 9.169 \\ 5.291 \\ 10.040 \\ 14.480 \\ 10.050 \\ 19.090 \\ 29.440 \\ 10.220 \\ 14.420 \\ 29.500 \\ 14.470 \\ 19.420 \\ 40.000 \end{bmatrix} \quad \sigma_B = \begin{bmatrix} 10.990 \\ 13.990 \\ 16.800 \\ 19.070 \\ 23.650 \\ 28.190 \\ 38.740 \\ 47.810 \\ 58.170 \\ 54.050 \\ 58.250 \\ 73.270 \\ 73.360 \\ 78.390 \\ 98.880 \end{bmatrix} \quad M_R = \begin{bmatrix} 41488.2 \\ 39403.6 \\ 38748.6 \\ 46304.0 \\ 46990.0 \\ 43753.4 \\ 52691.0 \\ 50438.0 \\ 52561.2 \\ 55008.0 \\ 49793.6 \\ 59996.2 \\ 59670.4 \\ 64354.6 \\ 75807.6 \end{bmatrix}$$

σ_3 = mean confining stress
σ_d = mean deviator stress
σ_B = mean bulk stress
M_R = resilient modulus
p_a = atmospheric pressure = 14.6959 psi

Dan Seely
9/12/2023

$$M_{R.1}\left(\sigma_B, K_1, K_2\right) := K_1 \cdot {\sigma_B}^{K_2}$$

Equation 1
AASHTO Publication No. FHWA-RD-97-083

$K_1 = 19153.741$

$K_2 = 0.2692$

Equation 1 fitting parameters

${R_1}^2 = 0.8190$

Coefficient of determination

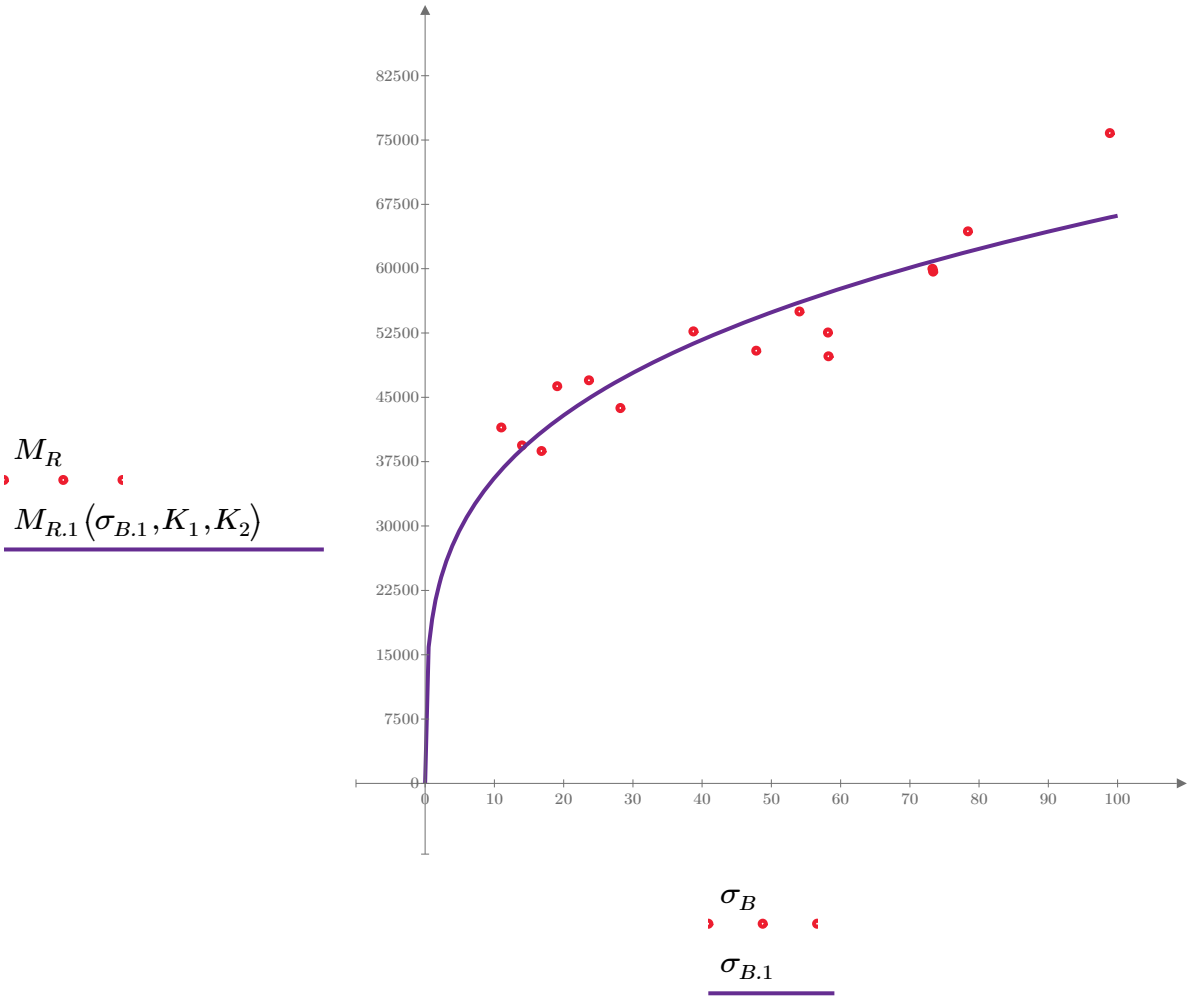

Figure 1. Plot of the test data (red points) vs. the fitted Equation 1 model (purple line).

Dan Seely
9/12/2023

$$M_{R.2}(\sigma_d, K_3, K_4) := K_3 \cdot \sigma_d^{K_4}$$

Equation 2
AASHTO Publication No. FHWA-RD-97-083

$K_3 = 28907.244$

$K_4 = 0.2246$

Equation 2 fitting parameters

$R_2^2 = 0.5782$

Coefficient of determination

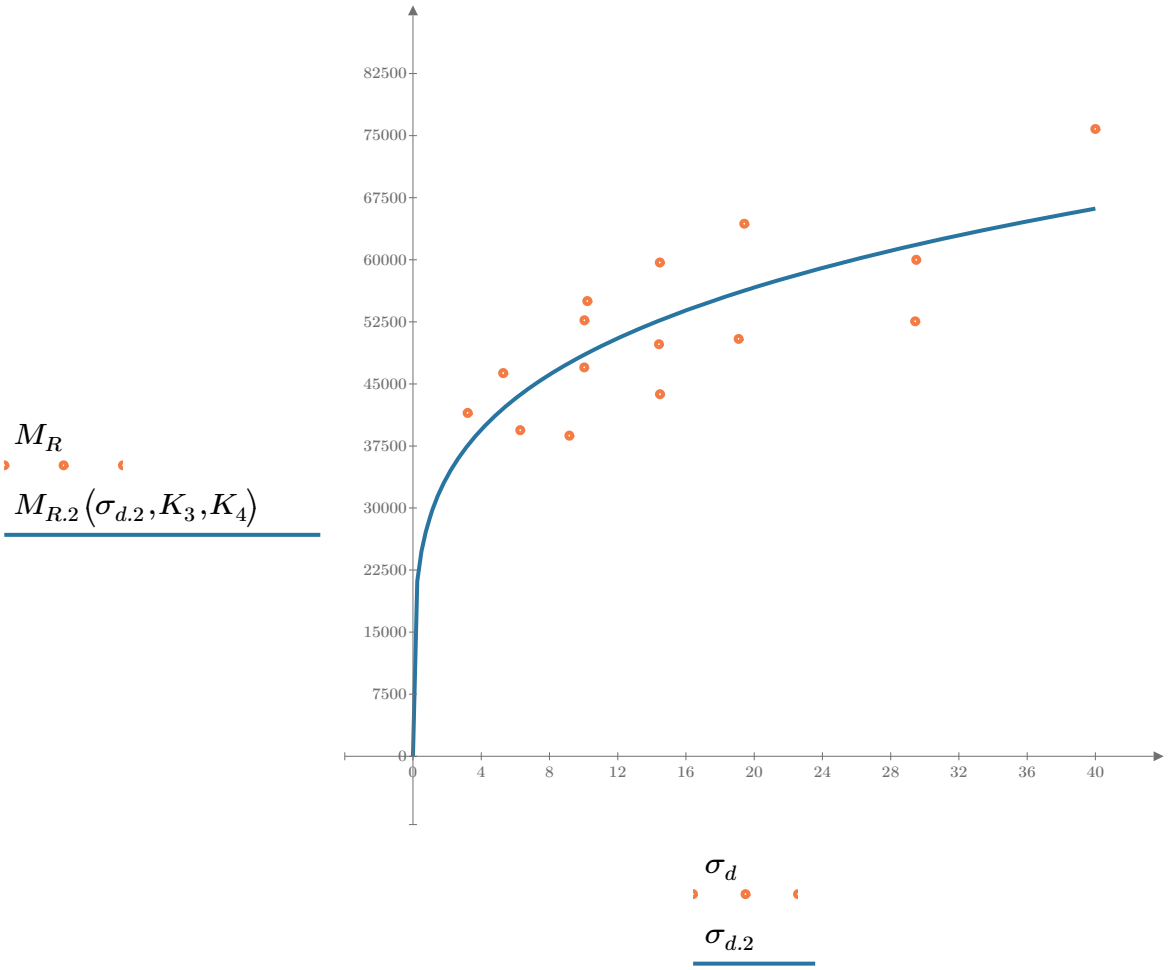

Figure 2. Plot of the test data (orange points) vs. the fitted Equation 2 model (blue line).

Dan Seely
9/12/2023

$$M_{R.3}\left(\sigma_d,\sigma_3,K_5,K_6,K_7\right):=K_5\cdot{\sigma_d}^{K_6}\cdot\left(1+\sigma_3\right)^{K_7}$$

Equation 3 AASHTO Publication No. FHWA-RD-97-083

$K_5=25655.740$

$K_6=0.0817$ Equation 3 fitting parameters

$K_7=0.2148$

${R_3}^2=0.8393$ Coefficient of determination

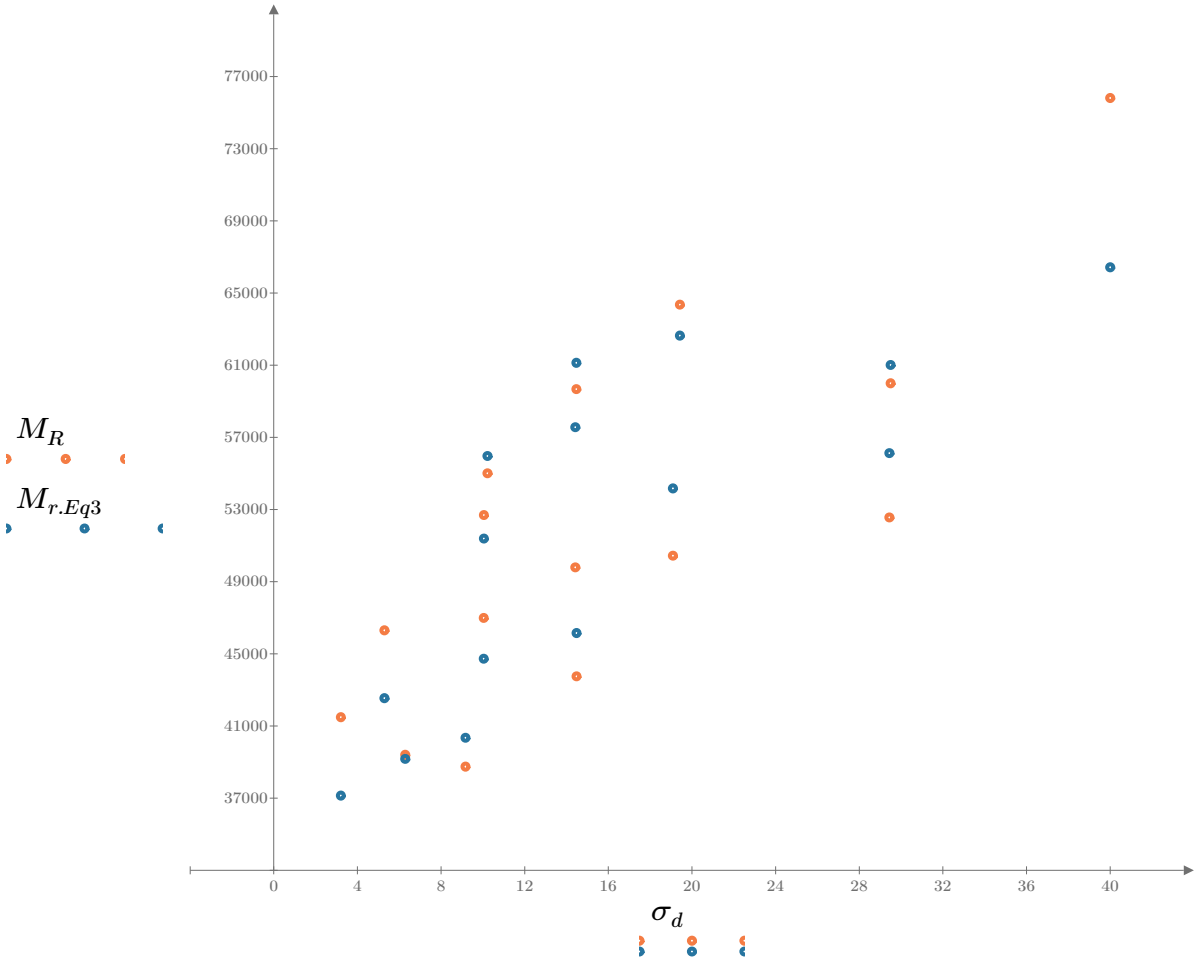

Figure 3. Plot of the test data (orange points) vs. the fitted Equation 3 model (blue points).

Dan Seely
9/12/2023

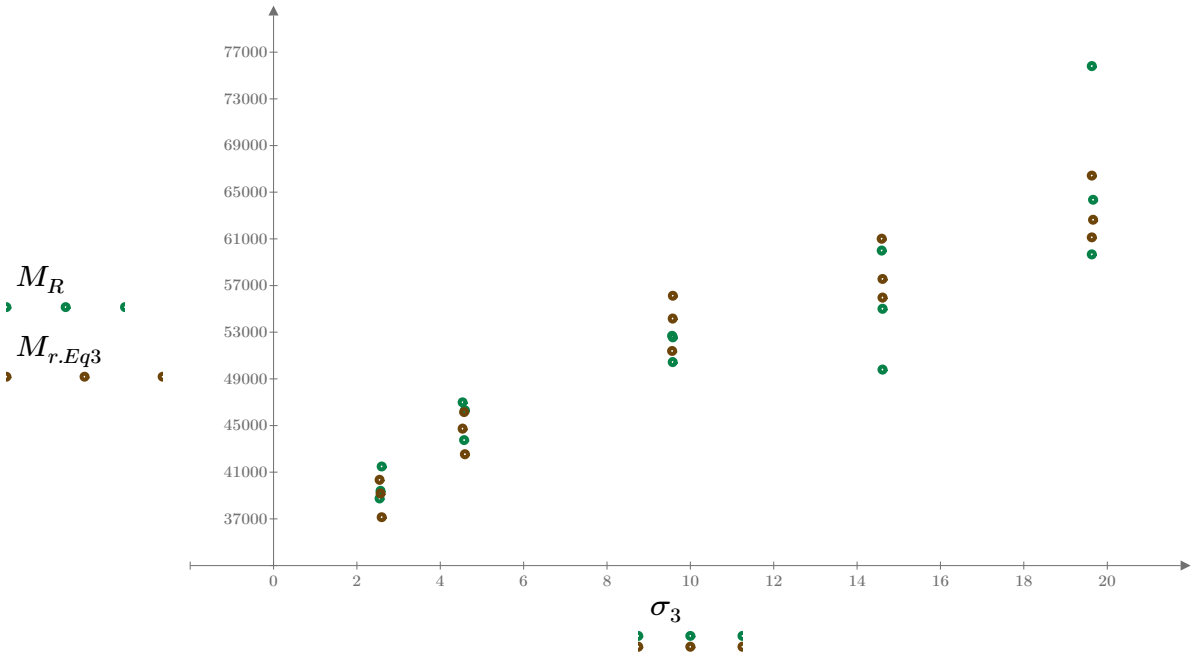

Figure 4. Plot of the test data (green points) vs. the fitted Equation 3 model (brown points).

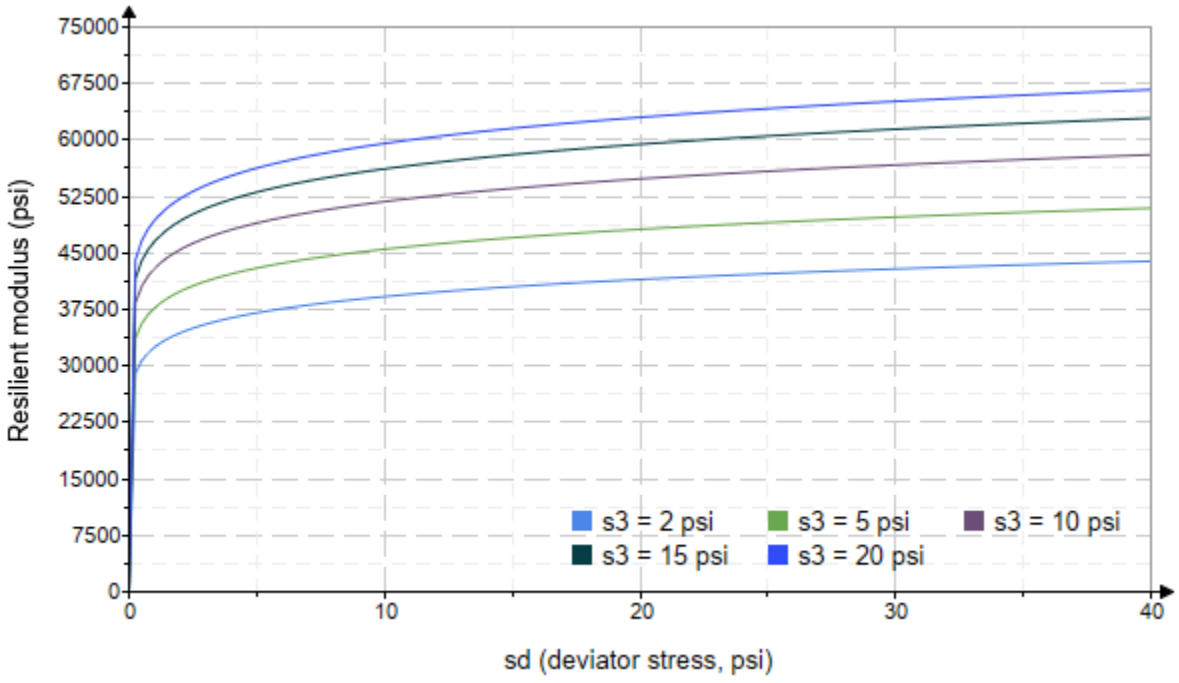

Figure 5. Plot of the fitted Equation 3 model for various confining stresses.

Dan Seely
9/12/2023

$$M_{R.4}\left(\sigma_B,\sigma_d,K_8,K_9,K_{10}\right) := K_8 \cdot p_a \left(\frac{\sigma_B}{p_a}\right)^{K_9} \cdot \left(\frac{\sigma_d}{p_a}\right)^{K_{10}}$$

Equation 4 AASHTO Publication No. FHWA-RD-97-083

$K_8 = 2669.204$

$K_9 = 0.2753$ Equation 4 fitting parameters

$K_{10} = -0.0073$

$R_4^{\,2} = 0.8191$ Coefficient of determination

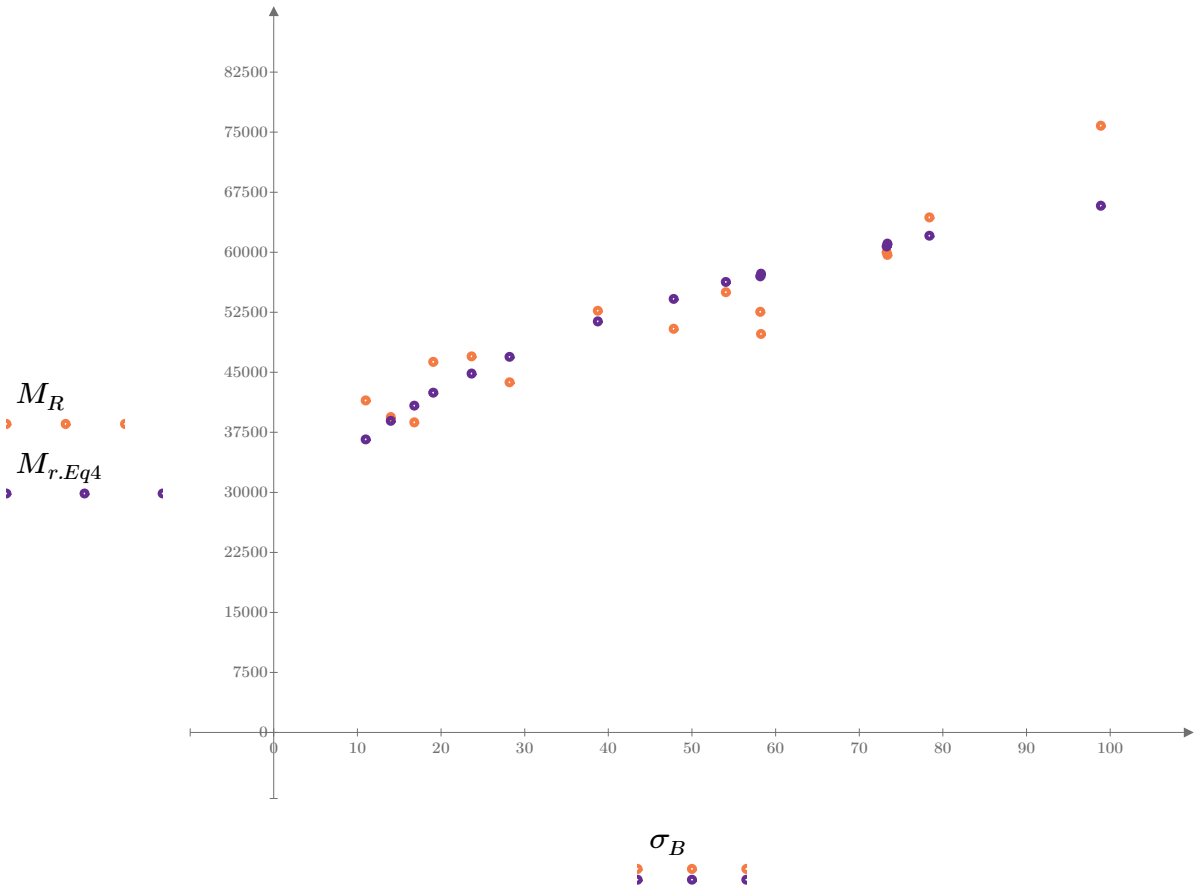

Figure 6. Plot of the test data (orange points) vs. the fitted Equation 4 model (purple points).

Dan Seely
9/12/2023

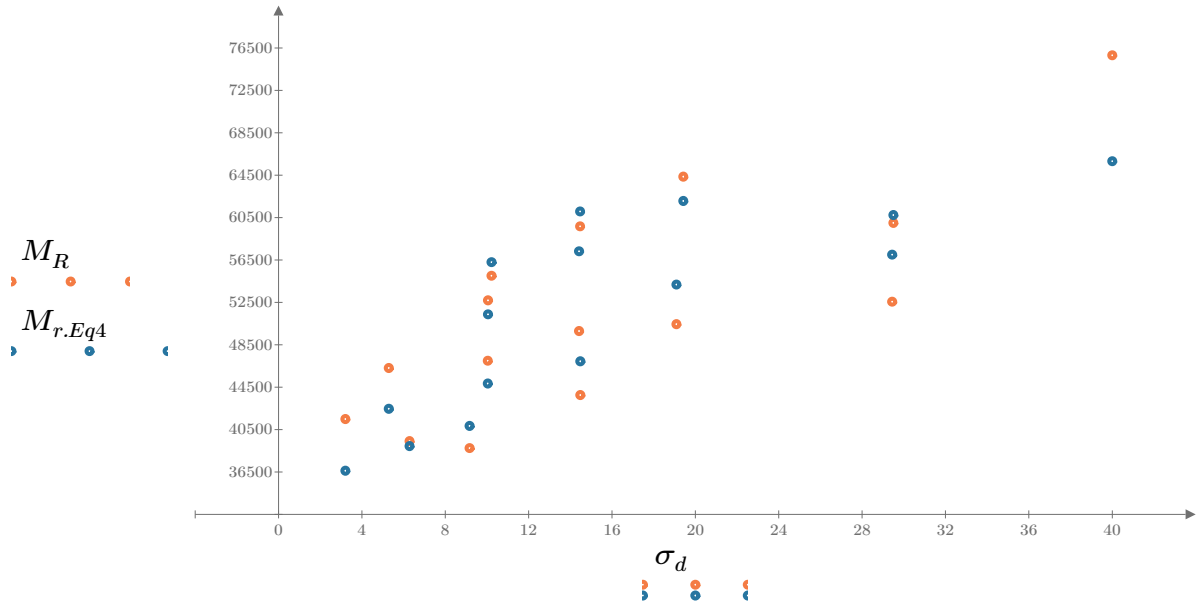

Figure 7. Plot of the test data (orange points) vs. the fitted Equation 4 model (blue points).

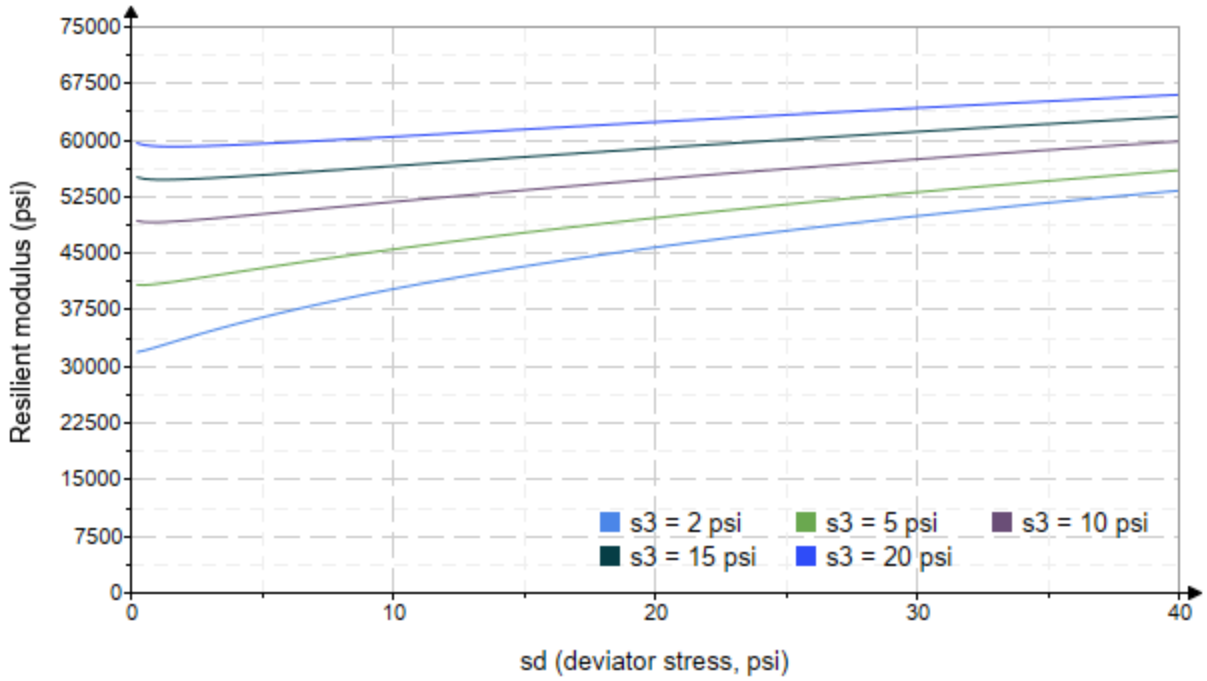

Figure 8. Plot of the fitted Equation 4 model for various confining stresses.

Dan Seely
9/12/2023

$SampleNo := \text{“B2}-\text{60”}$

$Treatment = \text{“W1”}$

$S = 18.536$ Degree of Saturation (%)

Test Sequence : Base/Subbase

Test summary data (psi) :

$$\sigma_3 = \begin{bmatrix} 2.256 \\ 1.969 \\ 2.529 \\ 3.625 \\ 4.021 \\ 4.125 \\ 9.553 \\ 9.081 \\ 9.031 \\ 14.570 \\ 14.380 \\ 14.250 \\ 18.850 \\ 18.900 \\ 19.120 \end{bmatrix} \quad \sigma_d = \begin{bmatrix} 3.221 \\ 6.082 \\ 9.041 \\ 5.238 \\ 10.080 \\ 14.530 \\ 10.140 \\ 19.390 \\ 29.390 \\ 10.200 \\ 14.580 \\ 29.500 \\ 14.580 \\ 19.570 \\ 39.920 \end{bmatrix} \quad \sigma_B = \begin{bmatrix} 9.990 \\ 11.990 \\ 16.630 \\ 16.110 \\ 22.150 \\ 26.910 \\ 38.800 \\ 46.630 \\ 56.490 \\ 53.910 \\ 57.720 \\ 72.260 \\ 71.120 \\ 76.280 \\ 97.270 \end{bmatrix} \quad M_R = \begin{bmatrix} 57314.2 \\ 46507.2 \\ 43344.2 \\ 46575.4 \\ 49806.6 \\ 47632.8 \\ 83543.4 \\ 59629.6 \\ 56031.6 \\ 150252.0 \\ 74902.8 \\ 62833.4 \\ 79367.2 \\ 83041.6 \\ 67132.4 \end{bmatrix}$$

σ_3 = mean confining stress
σ_d = mean deviator stress
σ_B = mean bulk stress
M_R = resilient modulus
p_a = atmospheric pressure = 14.6959 psi

Dan Seely
9/12/2023

$$M_{R.1}\left(\sigma_B, K_1, K_2\right) := K_1 \cdot {\sigma_B}^{K_2}$$

Equation 1
AASHTO Publication No. FHWA-RD-97-083

$K_1 = 25815.118$

$K_2 = 0.2622$

Equation 1 fitting parameters

${R_1}^2 = 0.2255$

Coefficient of determination

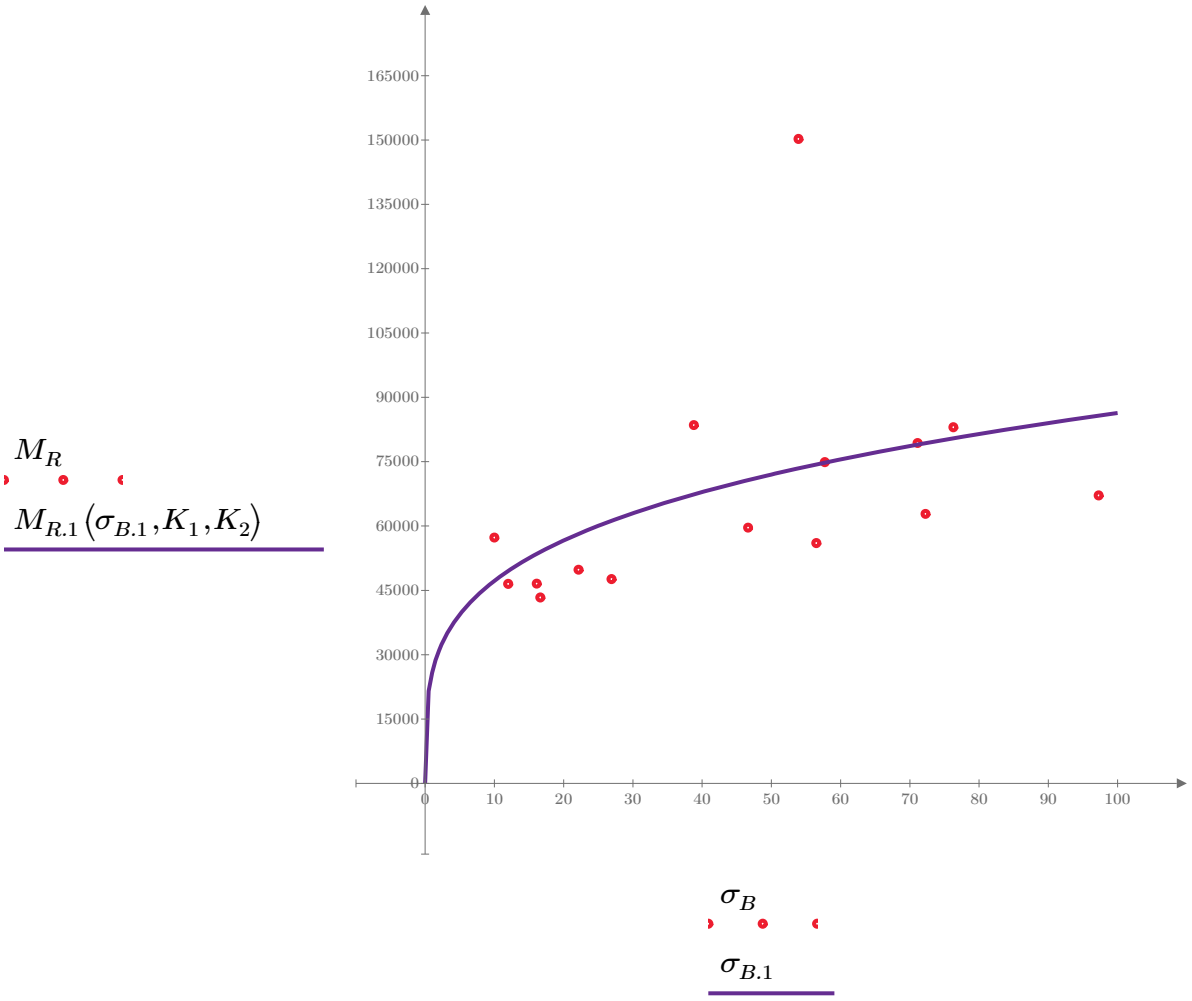

Figure 1. Plot of the test data (red points) vs. the fitted Equation 1 model (purple line).

Dan Seely
9/12/2023

$$M_{R.2}(\sigma_d, K_3, K_4) := K_3 \cdot \sigma_d^{K_4}$$

Equation 2
AASHTO Publication No. FHWA-RD-97-083

$K_3 = 58146.062$

$K_4 = 0.0565$

Equation 2 fitting parameters

$R_2^2 = 0.0106$

Coefficient of determination

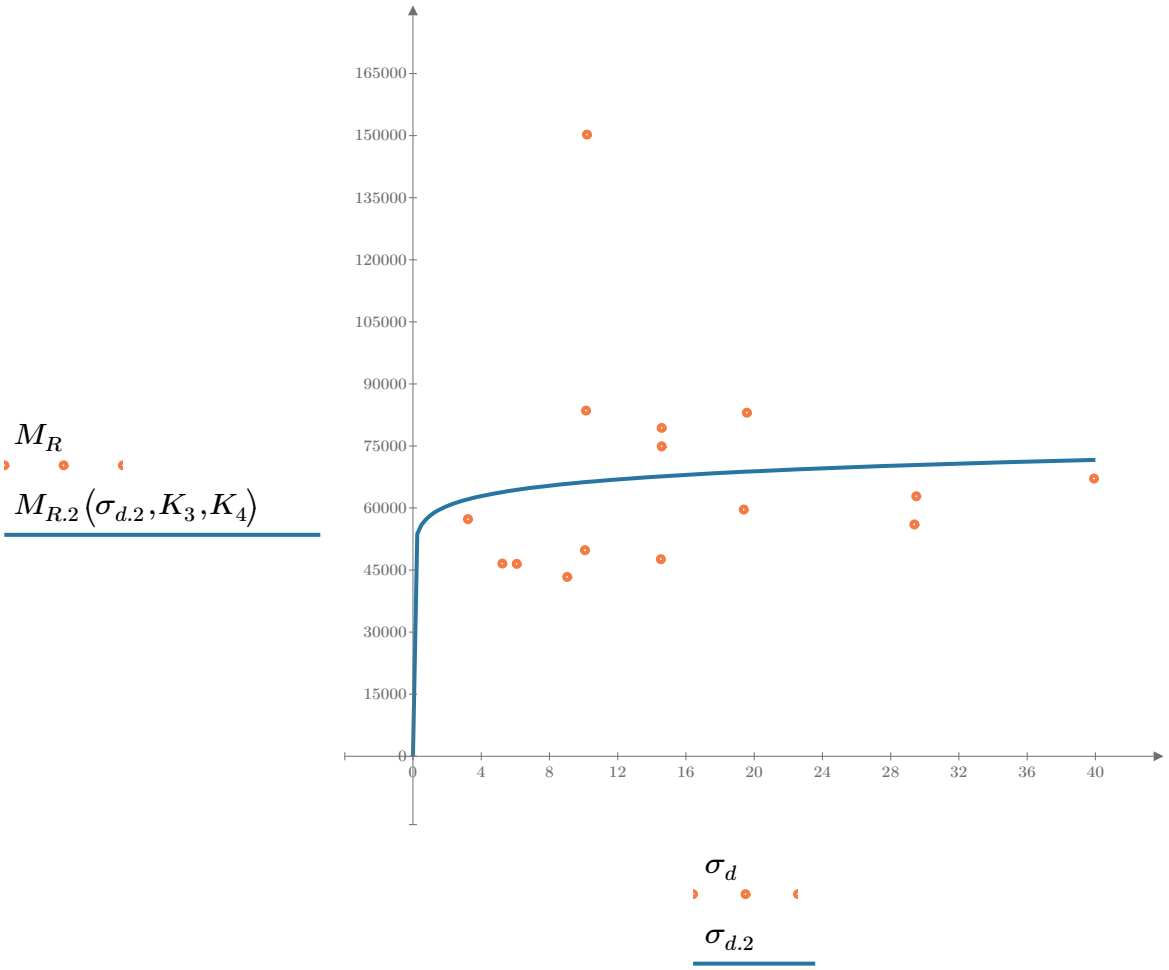

Figure 2. Plot of the test data (orange points) vs. the fitted Equation 2 model (blue line).

Dan Seely
9/12/2023

$$M_{R.3}\left(\sigma_d,\sigma_3,K_5,K_6,K_7\right):=K_5\cdot{\sigma_d}^{K_6}\cdot\left(1+\sigma_3\right)^{K_7}$$

Equation 3 AASHTO Publication No. FHWA-RD-97-083

$K_5=49416.772$

$K_6=-0.4893$ Equation 3 fitting parameters

$K_7=0.6926$

${R_3}^2=0.6658$ Coefficient of determination

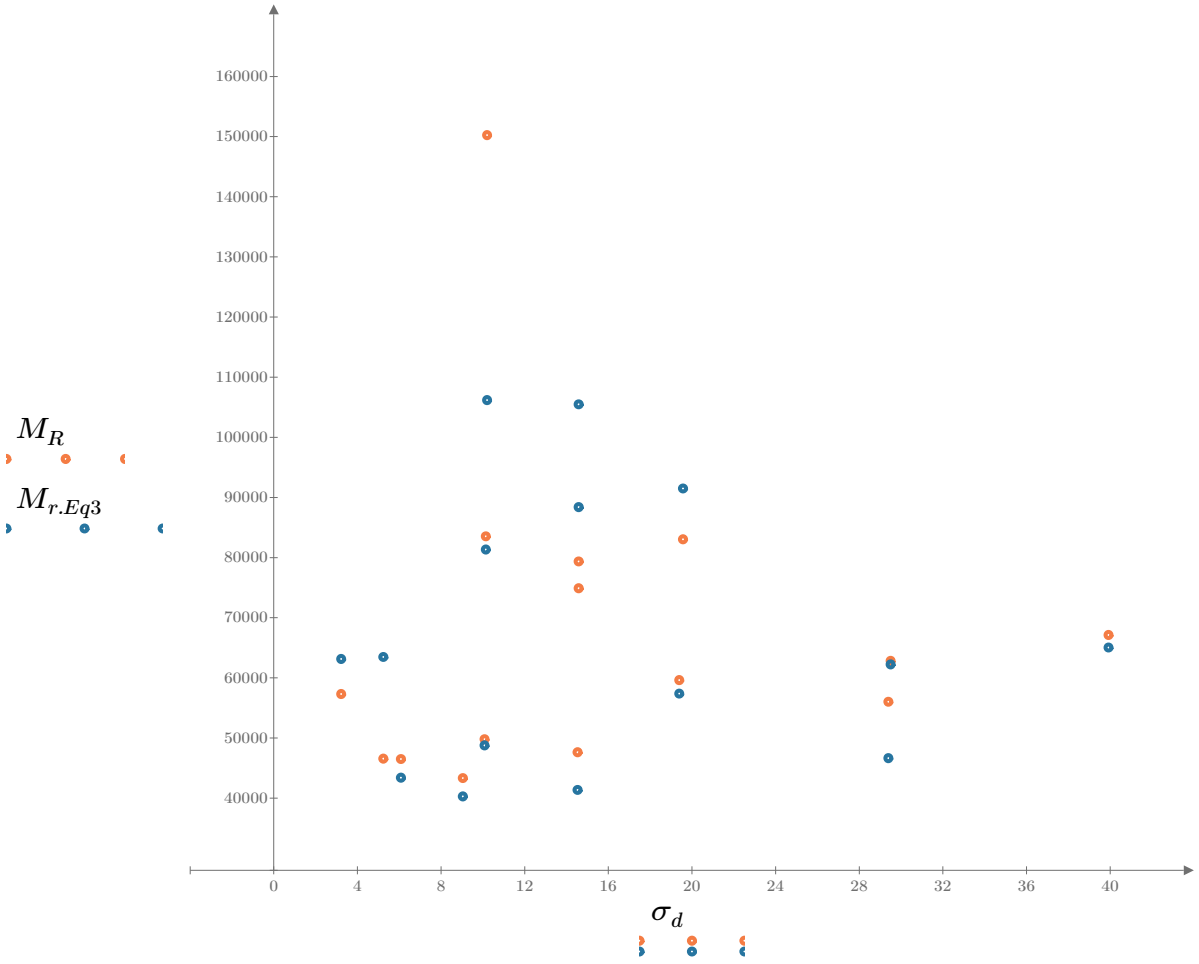

Figure 3. Plot of the test data (orange points) vs. the fitted Equation 3 model (blue points).

Dan Seely
9/12/2023

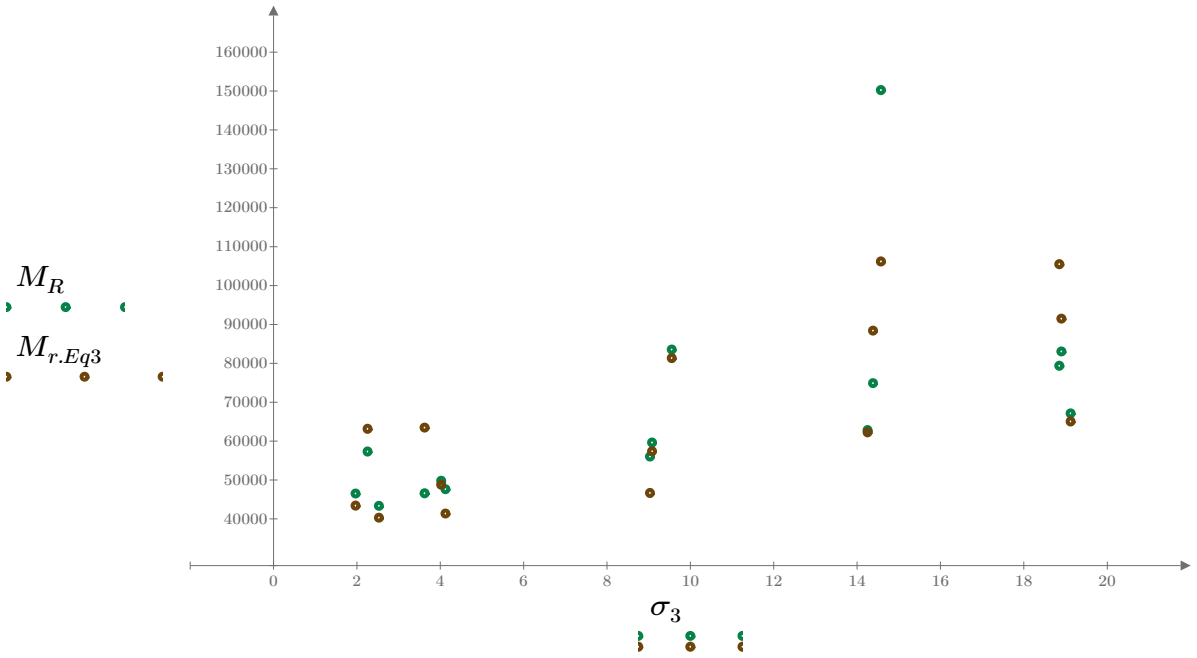

Figure 4. Plot of the test data (green points) vs. the fitted Equation 3 model (brown points).

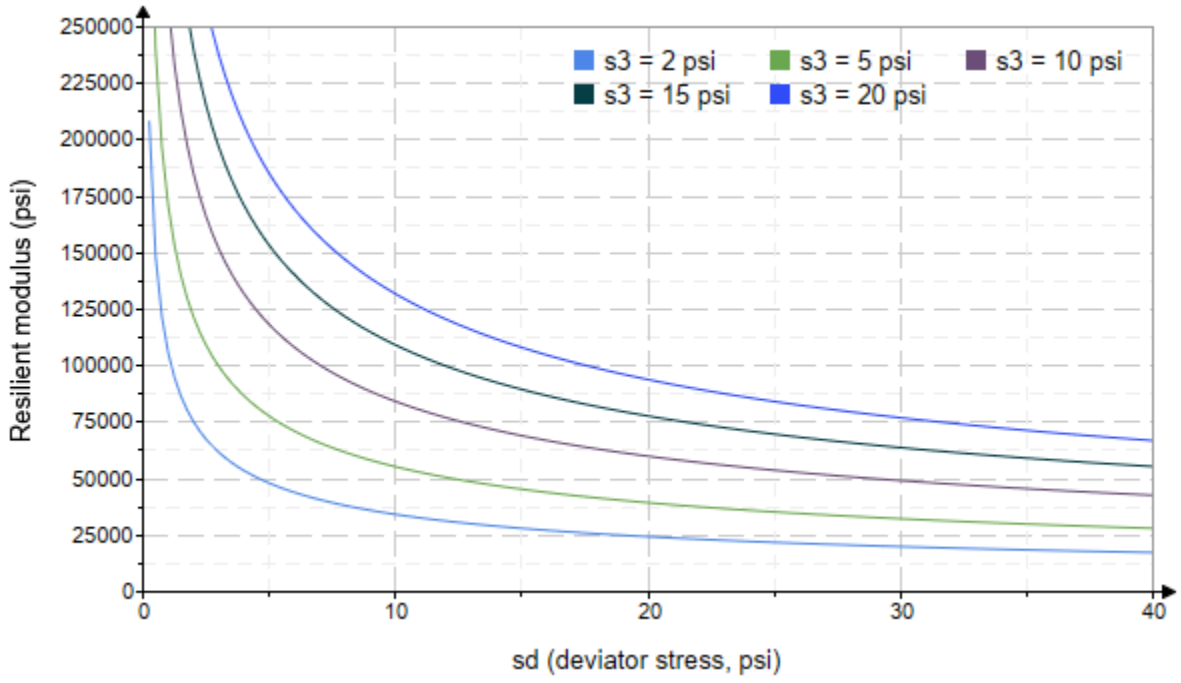

Figure 5. Plot of the fitted Equation 3 model for various confining stresses.

Dan Seely
9/12/2023

$$M_{R.4}\left(\sigma_B,\sigma_d,K_8,K_9,K_{10}\right) := K_8 \cdot p_a \left(\frac{\sigma_B}{p_a}\right)^{K_9} \cdot \left(\frac{\sigma_d}{p_a}\right)^{K_{10}}$$

Equation 4 AASHTO Publication No. FHWA-RD-97-083

$K_8 = 1660.553$

$K_9 = 0.9344$ Equation 4 fitting parameters

$K_{10} = -0.8307$

$R_4^{\,2} = 0.7098$ Coefficient of determination

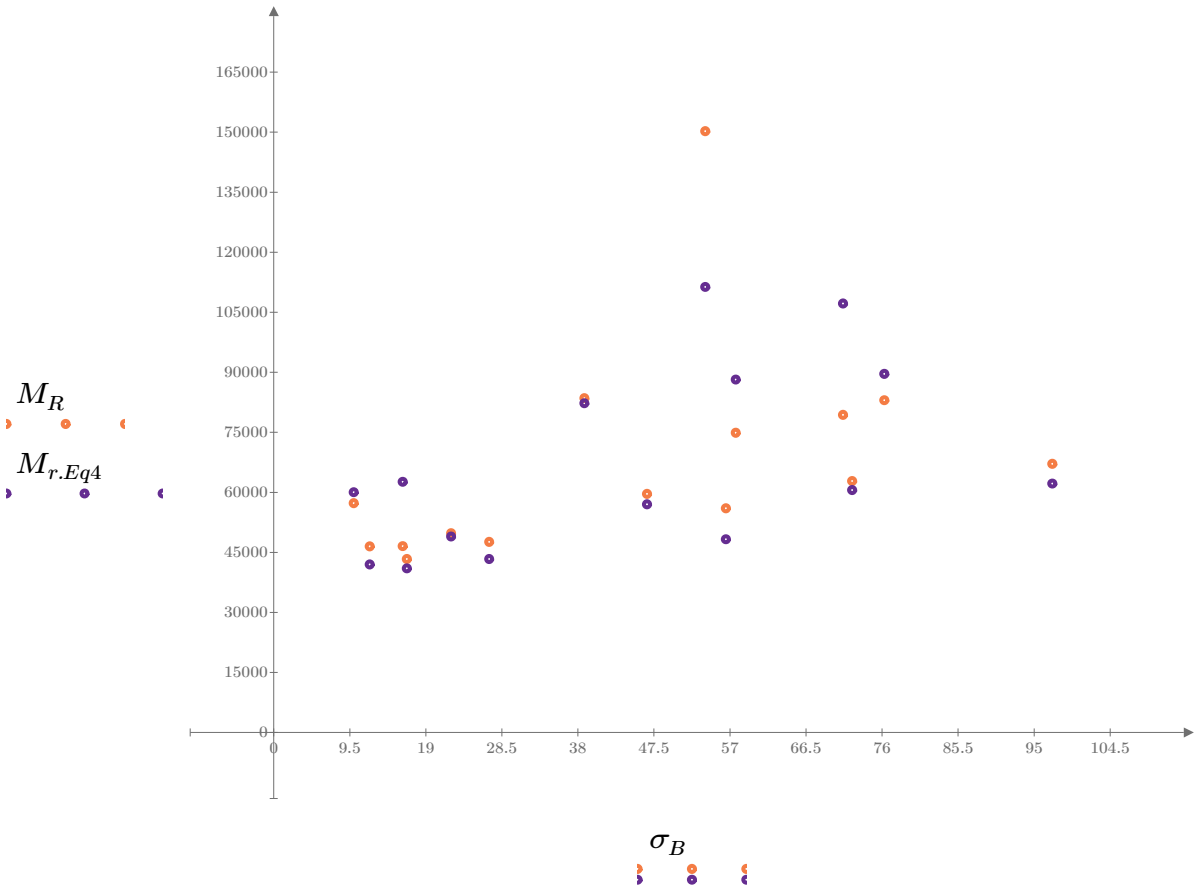

Figure 6. Plot of the test data (orange points) vs. the fitted Equation 4 model (purple points).

Dan Seely
9/12/2023

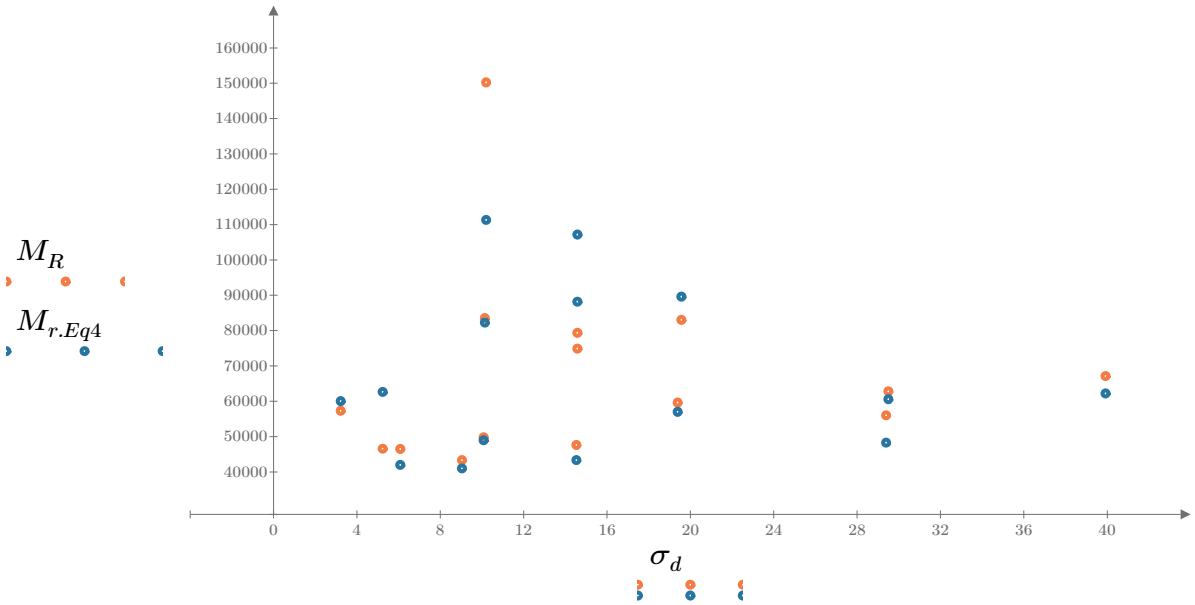

Figure 7. Plot of the test data (orange points) vs. the fitted Equation 4 model (blue points).

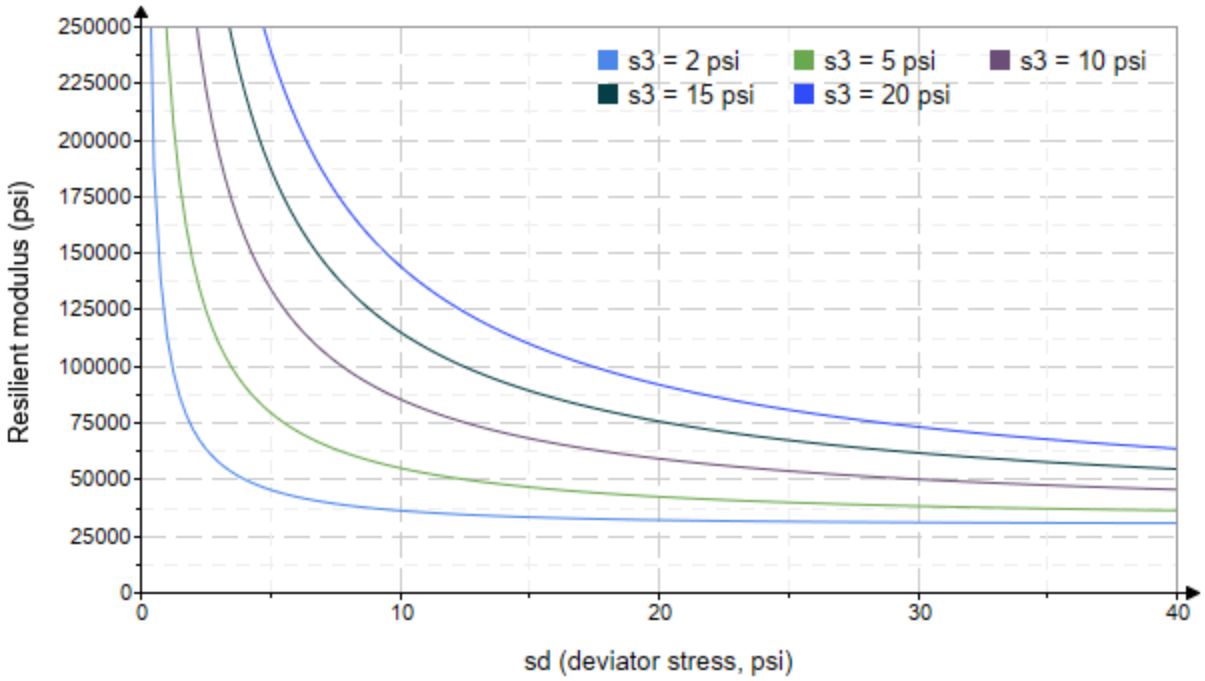

Figure 8. Plot of the fitted Equation 4 model for various confining stresses.

Dan Seely
9/12/2023

$SampleNo := \text{“B2}-\text{61”}$

$Treatment = \text{“W1”}$

$S = 18.283$ Degree of Saturation (%)

Test Sequence : Base/Subbase

Test summary data (psi) :

$$\sigma_3 = \begin{bmatrix} 2.059 \\ 2.066 \\ 2.280 \\ 3.893 \\ 4.192 \\ 4.494 \\ 9.600 \\ 9.190 \\ 9.044 \\ 15.000 \\ 14.260 \\ 14.020 \\ 19.480 \\ 19.080 \\ 19.160 \end{bmatrix} \quad \sigma_d = \begin{bmatrix} 3.362 \\ 6.151 \\ 8.848 \\ 5.359 \\ 9.909 \\ 14.470 \\ 9.988 \\ 19.540 \\ 29.730 \\ 9.997 \\ 14.500 \\ 29.800 \\ 14.710 \\ 19.360 \\ 40.090 \end{bmatrix} \quad \sigma_B = \begin{bmatrix} 9.540 \\ 12.350 \\ 15.690 \\ 17.040 \\ 22.480 \\ 27.950 \\ 38.790 \\ 47.110 \\ 56.860 \\ 54.990 \\ 57.290 \\ 71.850 \\ 73.130 \\ 76.610 \\ 97.580 \end{bmatrix} \quad M_R = \begin{bmatrix} 148031.3 \\ 110074.7 \\ 72118.0 \\ 89814.0 \\ 107510.0 \\ 67066.2 \\ 93305.1 \\ 119544.0 \\ 81230.0 \\ 173607.0 \\ 265984.0 \\ 82348.4 \\ 164483.2 \\ 246618.0 \\ 92464.4 \end{bmatrix}$$

σ_3 = mean confining stress
σ_d = mean deviator stress
σ_B = mean bulk stress
M_R = resilient modulus
p_a = atmospheric pressure = 14.6959 psi

Dan Seely
9/12/2023

$$M_{R.1}\left(\sigma_B, K_1, K_2\right) := K_1 \cdot {\sigma_B}^{K_2}$$

Equation 1
AASHTO Publication No. FHWA-RD-97-083

$K_1 = 56604.083$

$K_2 = 0.2227$

Equation 1 fitting parameters

${R_1}^2 = 0.1033$

Coefficient of determination

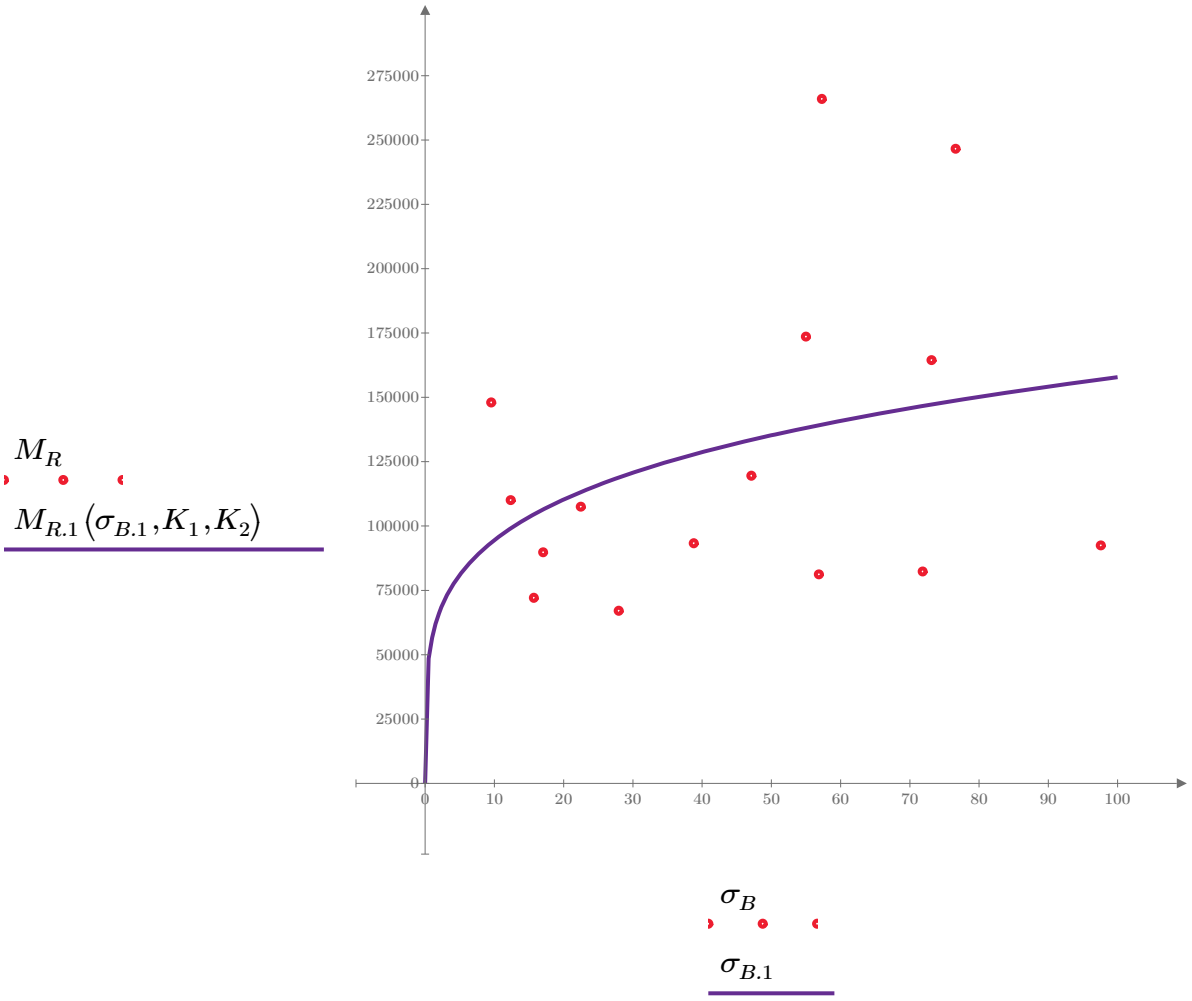

Figure 1. Plot of the test data (red points) vs. the fitted Equation 1 model (purple line).

Dan Seely
9/12/2023

$$M_{R.2}(\sigma_d, K_3, K_4) := K_3 \cdot \sigma_d^{K_4}$$

Equation 2
AASHTO Publication No. FHWA-RD-97-083

$K_3 = 133088.957$

$K_4 = -0.0165$

Equation 2 fitting parameters

$R_2^2 = 0.0006$

Coefficient of determination

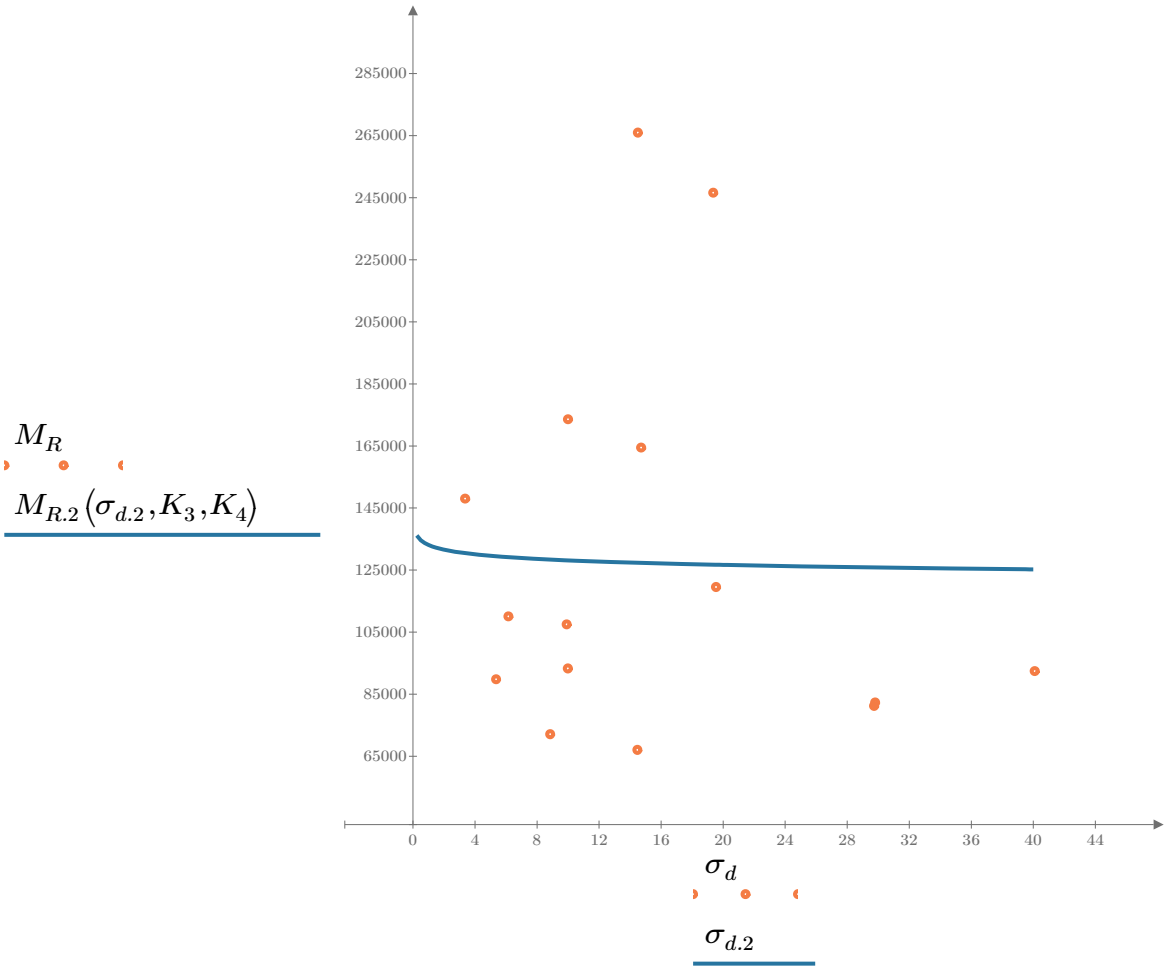

Figure 2. Plot of the test data (orange points) vs. the fitted Equation 2 model (blue line).

Dan Seely
9/12/2023

$$M_{R.3}\left(\sigma_d,\sigma_3,K_5,K_6,K_7\right):=K_5\cdot{\sigma_d}^{K_6}\cdot\left(1+\sigma_3\right)^{K_7}$$

Equation 3 AASHTO Publication No. FHWA-RD-97-083

$K_5=98474.361$

$K_6=-0.4854$ Equation 3 fitting parameters

$K_7=0.6669$

${R_3}^2=0.4866$ Coefficient of determination

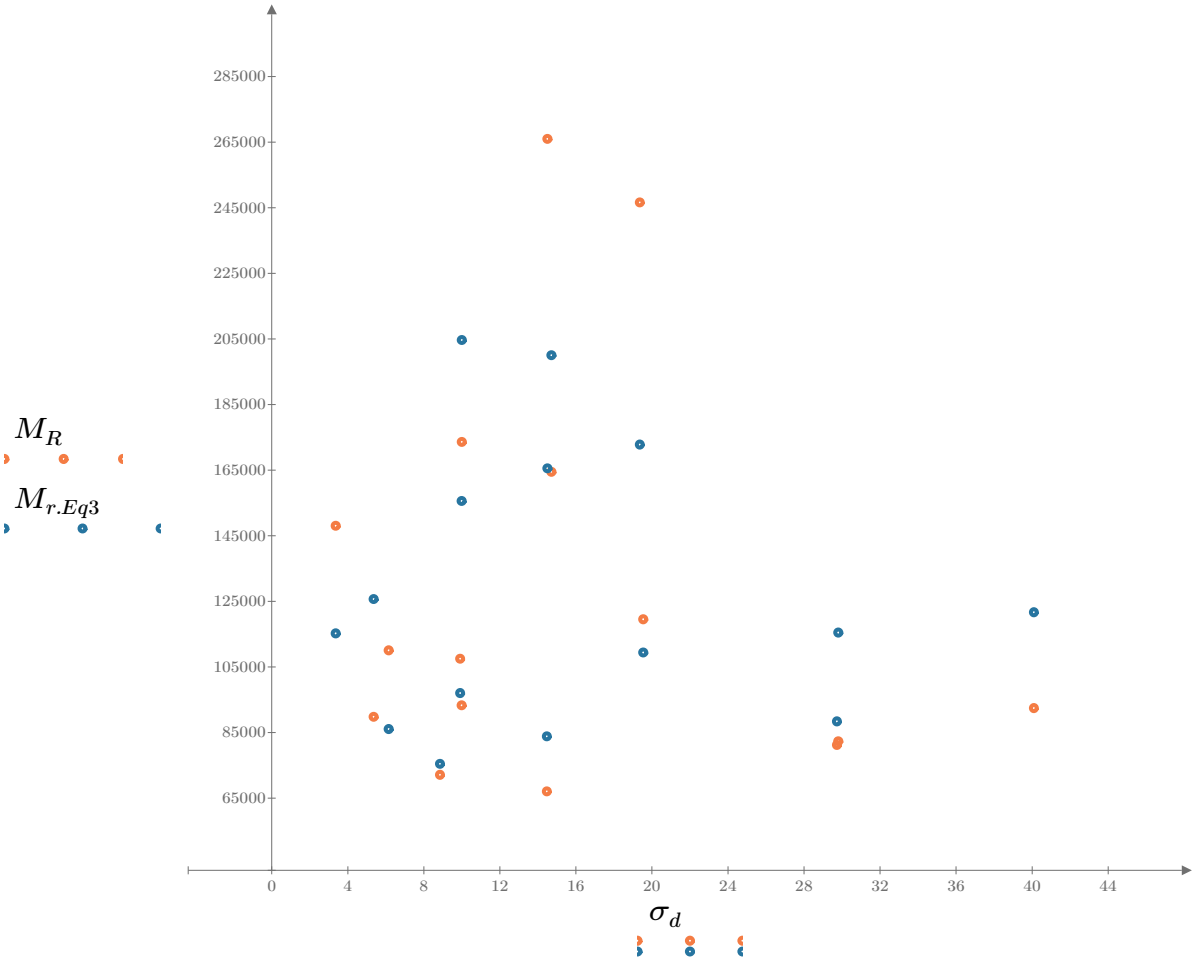

Figure 3. Plot of the test data (orange points) vs. the fitted Equation 3 model (blue points).

Dan Seely
9/12/2023

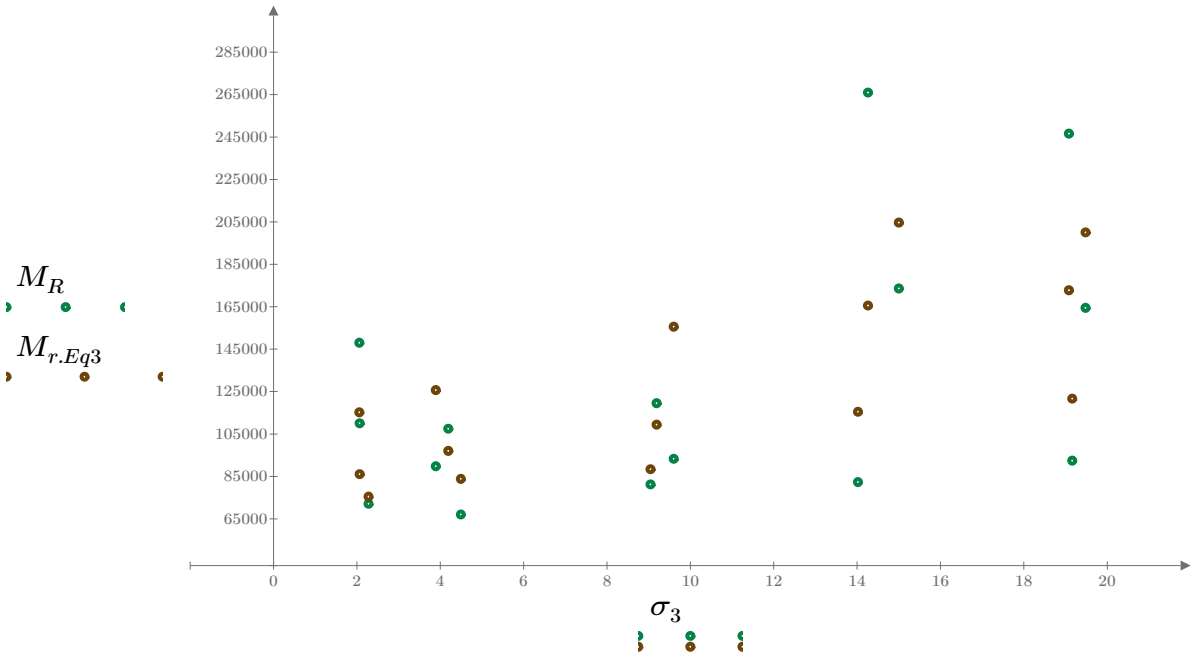

Figure 4. Plot of the test data (green points) vs. the fitted Equation 3 model (brown points).

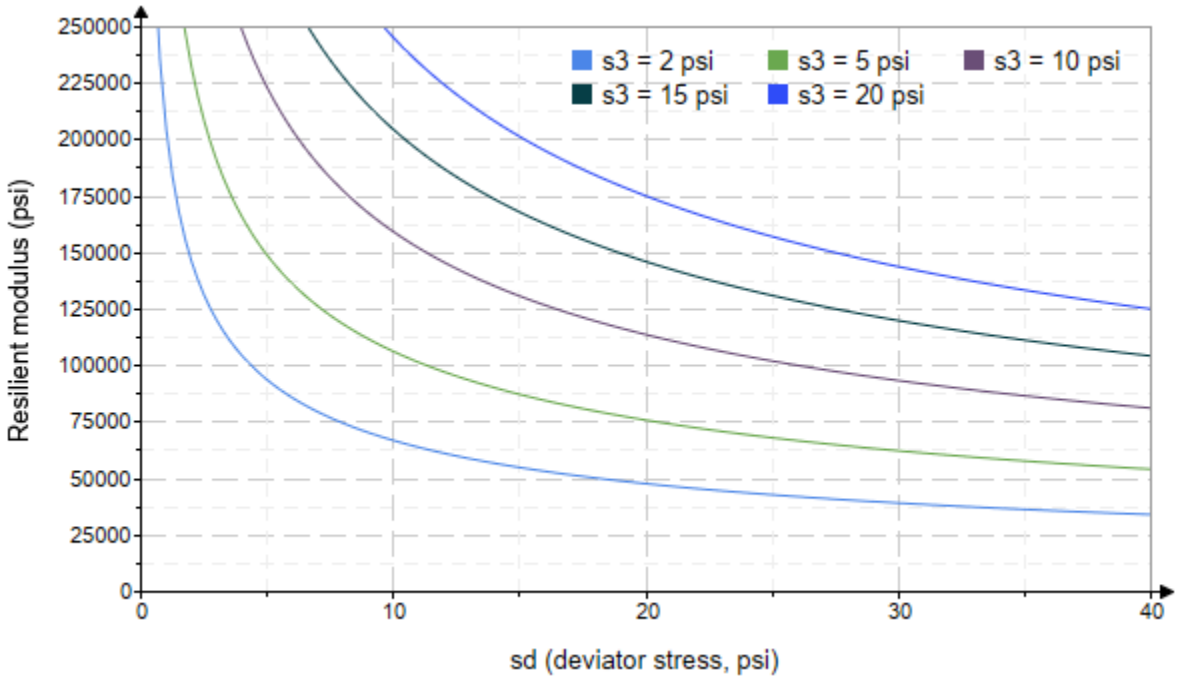

Figure 5. Plot of the fitted Equation 3 model for various confining stresses.

Dan Seely
9/12/2023

$$M_{R.4}\left(\sigma_B,\sigma_d,K_8,K_9,K_{10}\right) := K_8 \cdot p_a \left(\frac{\sigma_B}{p_a}\right)^{K_9} \cdot \left(\frac{\sigma_d}{p_a}\right)^{K_{10}}$$

Equation 4 AASHTO Publication No. FHWA-RD-97-083

$K_8 = 3562.412$

$K_9 = 0.8252$ Equation 4 fitting parameters

$K_{10} = -0.7424$

$R_4^{\,2} = 0.4501$ Coefficient of determination

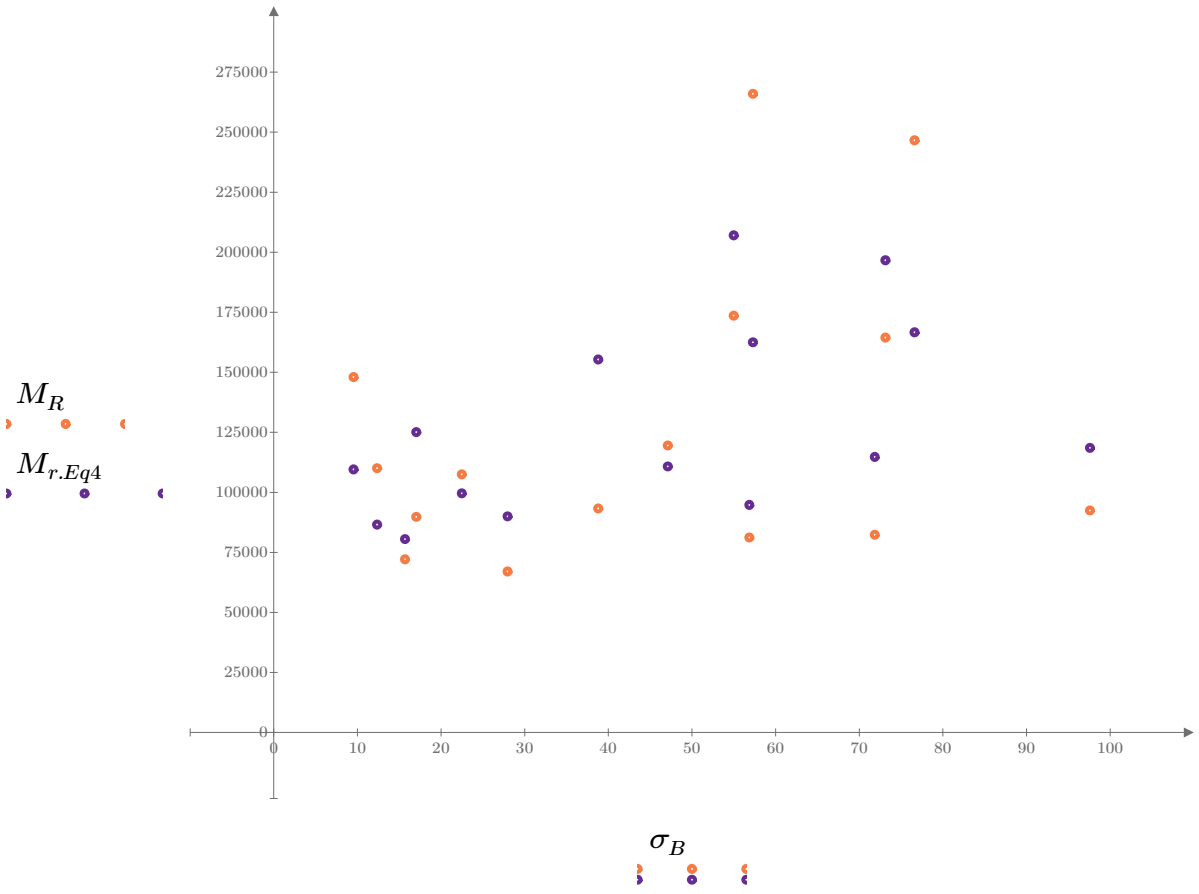

Figure 6. Plot of the test data (orange points) vs. the fitted Equation 4 model (purple points).

Dan Seely
9/12/2023

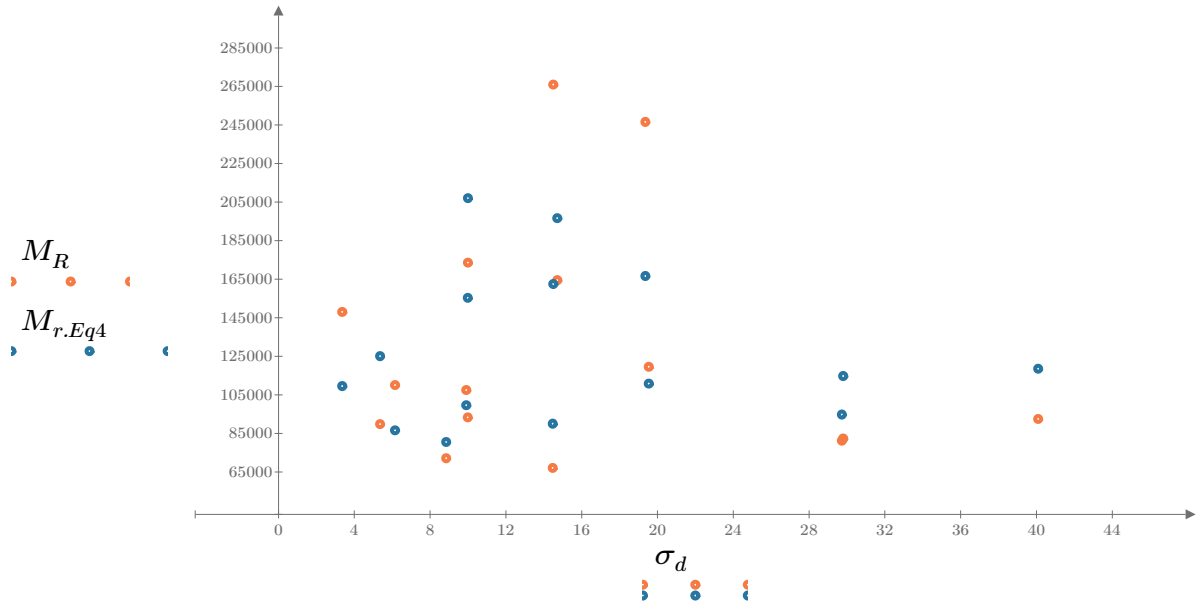

Figure 7. Plot of the test data (orange points) vs. the fitted Equation 4 model (blue points).

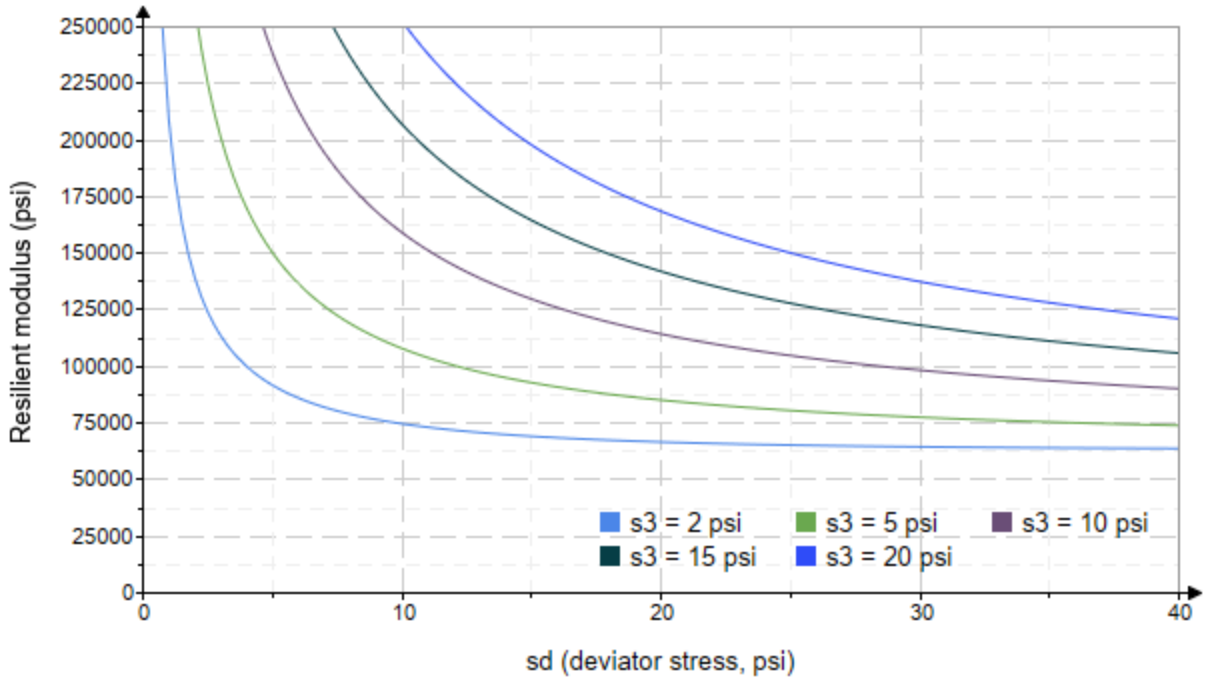

Figure 8. Plot of the fitted Equation 4 model for various confining stresses.

Dan Seely
9/12/2023

$SampleNo := \text{“B2–62”}$

$Treatment = \text{“AD”}$

$S = 4.014$ Degree of Saturation (%)

Test Sequence : Base/Subbase

Test summary data (psi) :

$$\sigma_3 = \begin{bmatrix} 2.861 \\ 2.884 \\ 2.819 \\ 4.861 \\ 4.823 \\ 4.512 \\ 9.445 \\ 9.297 \\ 9.238 \\ 14.140 \\ 14.260 \\ 14.400 \\ 19.370 \\ 19.150 \\ 19.150 \end{bmatrix} \quad \sigma_d = \begin{bmatrix} 3.089 \\ 6.094 \\ 8.991 \\ 5.107 \\ 9.870 \\ 14.760 \\ 9.955 \\ 19.790 \\ 30.200 \\ 10.010 \\ 14.700 \\ 30.220 \\ 14.780 \\ 19.910 \\ 40.650 \end{bmatrix} \quad \sigma_B = \begin{bmatrix} 11.670 \\ 14.750 \\ 17.450 \\ 19.690 \\ 24.340 \\ 28.290 \\ 38.290 \\ 47.680 \\ 57.910 \\ 52.430 \\ 57.470 \\ 73.420 \\ 72.900 \\ 77.370 \\ 98.110 \end{bmatrix} \quad M_R = \begin{bmatrix} 41461.6 \\ 28981.2 \\ 29560.6 \\ 32085.8 \\ 34949.6 \\ 40895.8 \\ 48546.6 \\ 52995.0 \\ 52561.6 \\ 60447.6 \\ 60584.2 \\ 52273.6 \\ 65100.8 \\ 55866.0 \\ 52699.4 \end{bmatrix}$$

σ_3 = mean confining stress
σ_d = mean deviator stress
σ_B = mean bulk stress
M_R = resilient modulus
p_a = atmospheric pressure = 14.6959 psi

Dan Seely
9/12/2023

$$M_{R.1}\left(\sigma_B, K_1, K_2\right) := K_1 \cdot {\sigma_B}^{K_2}$$

Equation 1
AASHTO Publication No. FHWA-RD-97-083

$K_1 = 14381.742$

$K_2 = 0.3211$

Equation 1 fitting parameters

${R_1}^2 = 0.7074$

Coefficient of determination

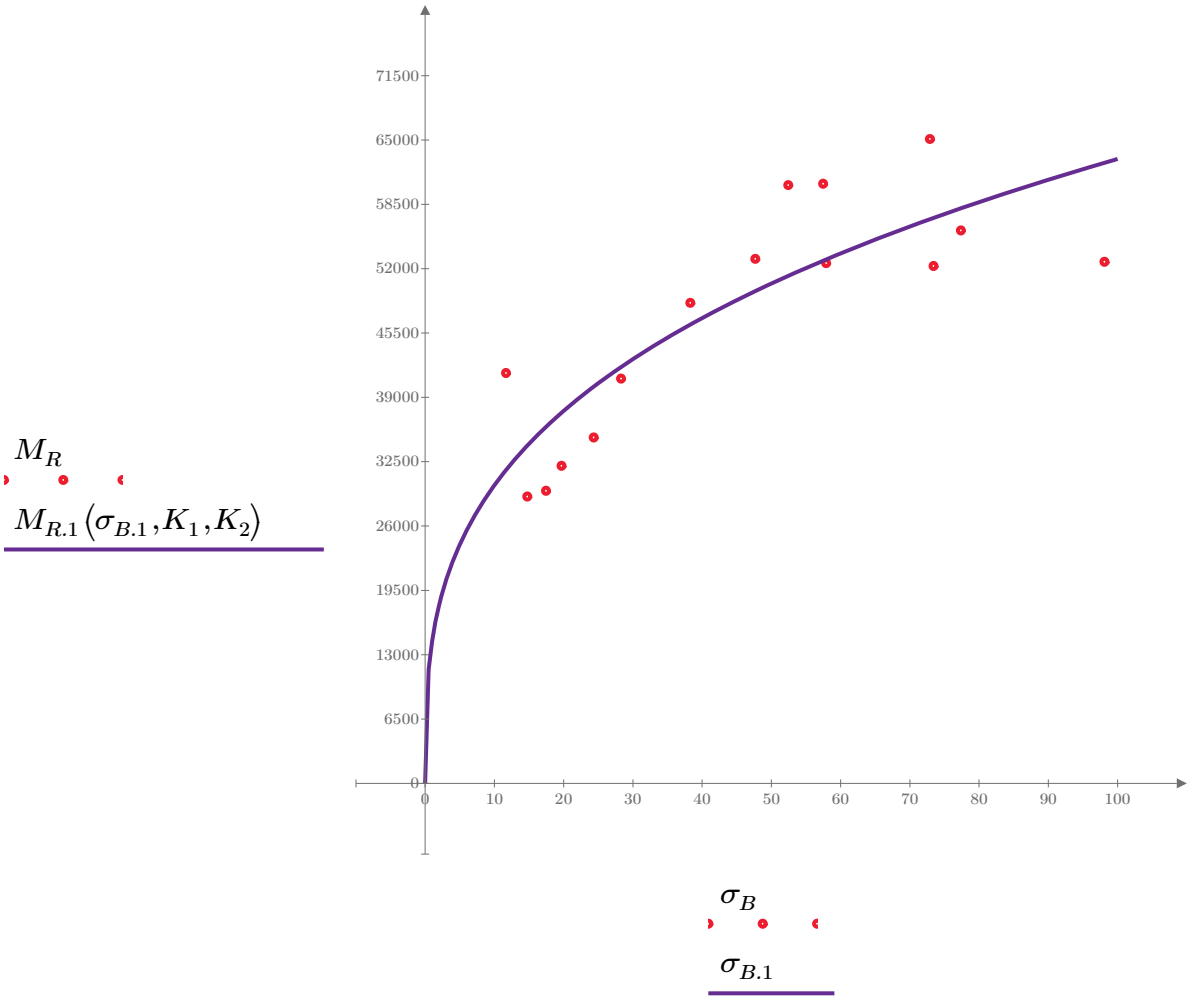

Figure 1. Plot of the test data (red points) vs. the fitted Equation 1 model (purple line).

Dan Seely
9/12/2023

$$M_{R.2}(\sigma_d, K_3, K_4) := K_3 \cdot \sigma_d^{K_4}$$

Equation 2
AASHTO Publication No. FHWA-RD-97-083

$K_3 = 28407.740$

$K_4 = 0.1965$

Equation 2 fitting parameters

$R_2^2 = 0.3122$

Coefficient of determination

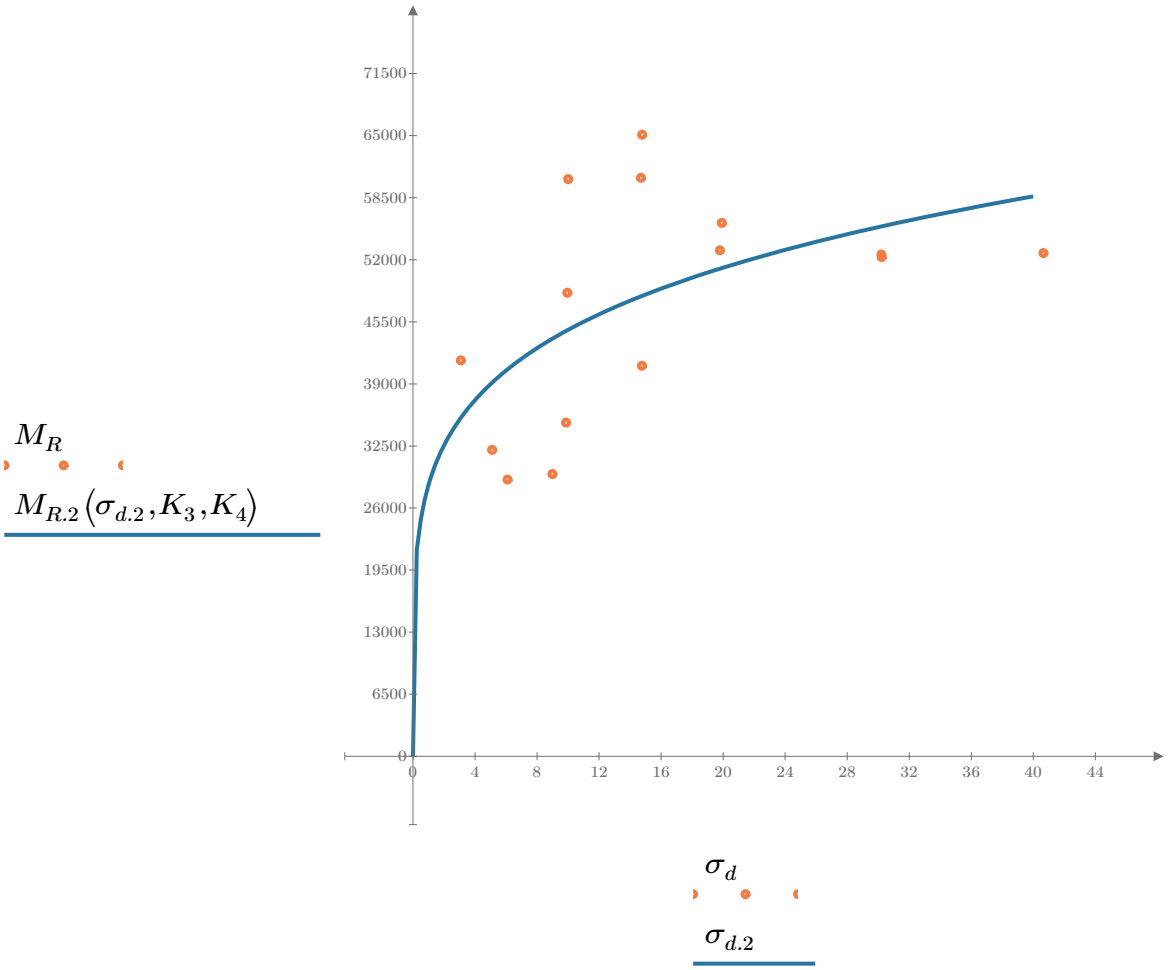

Figure 2. Plot of the test data (orange points) vs. the fitted Equation 2 model (blue line).

Dan Seely
9/12/2023

$$M_{R.3}\left(\sigma_d,\sigma_3,K_5,K_6,K_7\right):=K_5\cdot{\sigma_d}^{K_6}\cdot\left(1+\sigma_3\right)^{K_7}$$

Equation 3 AASHTO Publication No. FHWA-RD-97-083

$K_5=21792.188$

$K_6=-0.0614$ Equation 3 fitting parameters

$K_7=0.4065$

${R_3}^2=0.8114$ Coefficient of determination

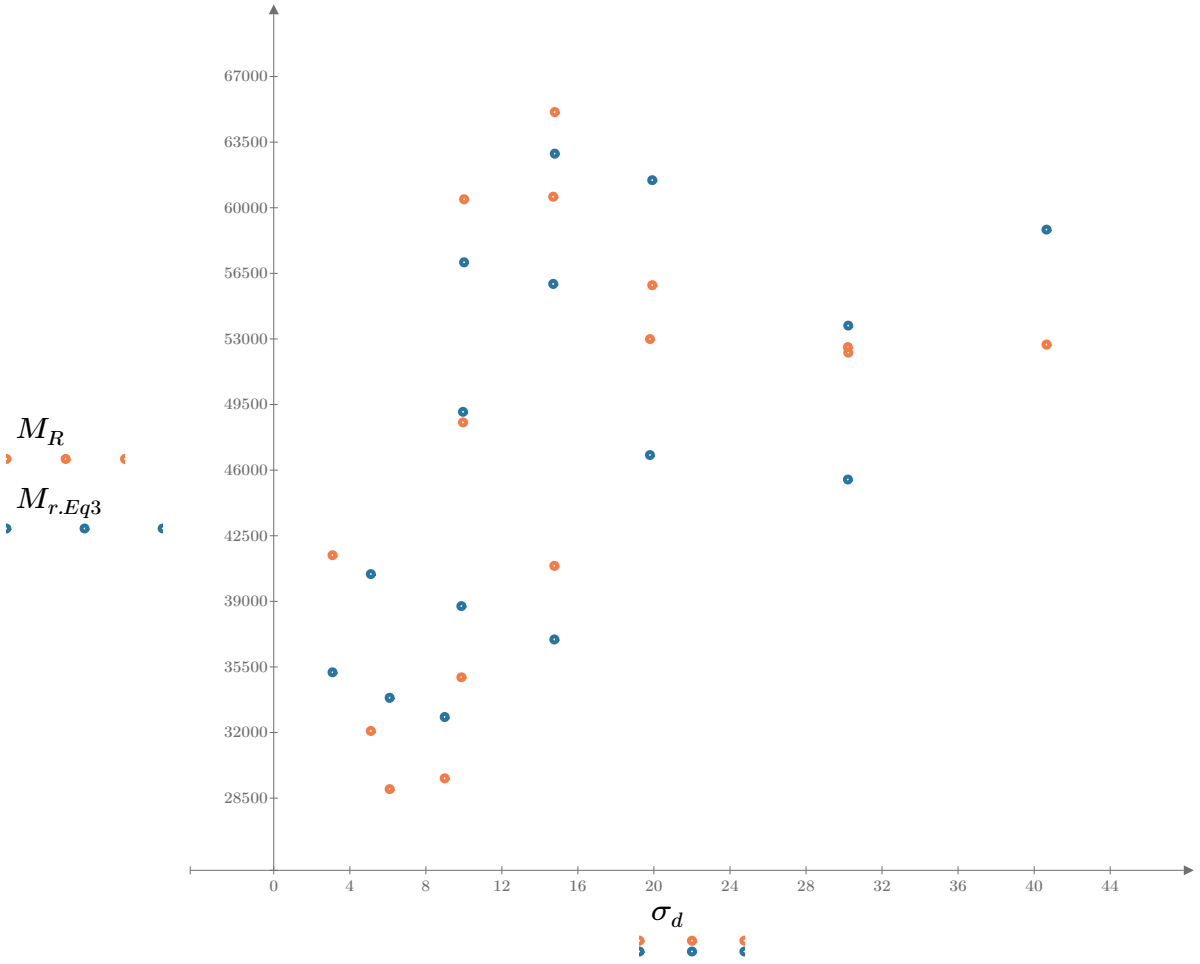

Figure 3. Plot of the test data (orange points) vs. the fitted Equation 3 model (blue points).

Dan Seely
9/12/2023

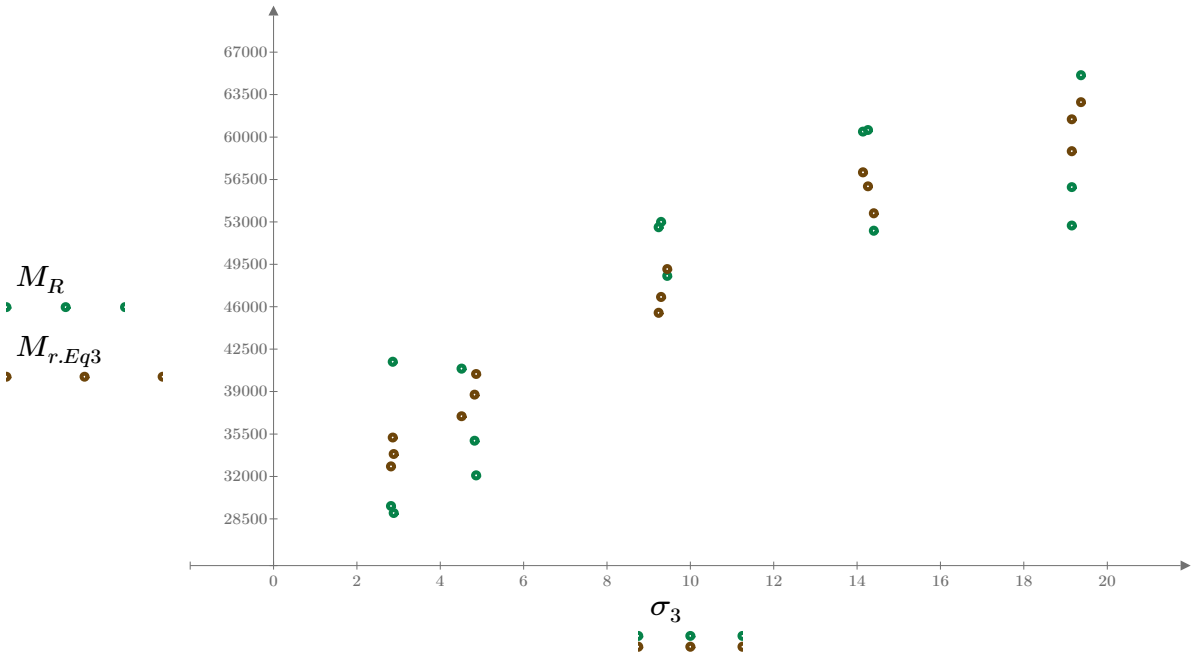

Figure 4. Plot of the test data (green points) vs. the fitted Equation 3 model (brown points).

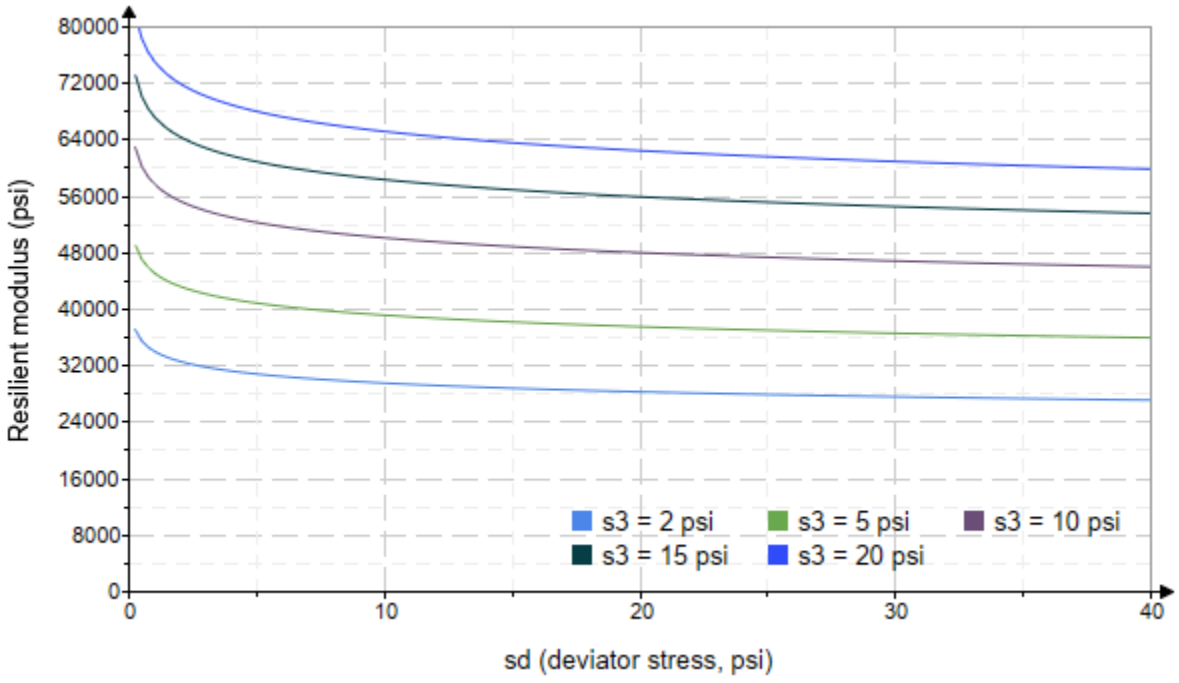

Figure 5. Plot of the fitted Equation 3 model for various confining stresses.

Dan Seely
9/12/2023

$$M_{R.4}\left(\sigma_B,\sigma_d,K_8,K_9,K_{10}\right):=K_8\cdot p_a\left(\frac{\sigma_B}{p_a}\right)^{K_9}\cdot\left(\frac{\sigma_d}{p_a}\right)^{K_{10}}$$

Equation 4 AASHTO Publication No. FHWA-RD-97-083

$K_8=1787.302$

$K_9=0.5532$ Equation 4 fitting parameters

$K_{10}=-0.2537$

$R_4{}^2=0.8349$ Coefficient of determination

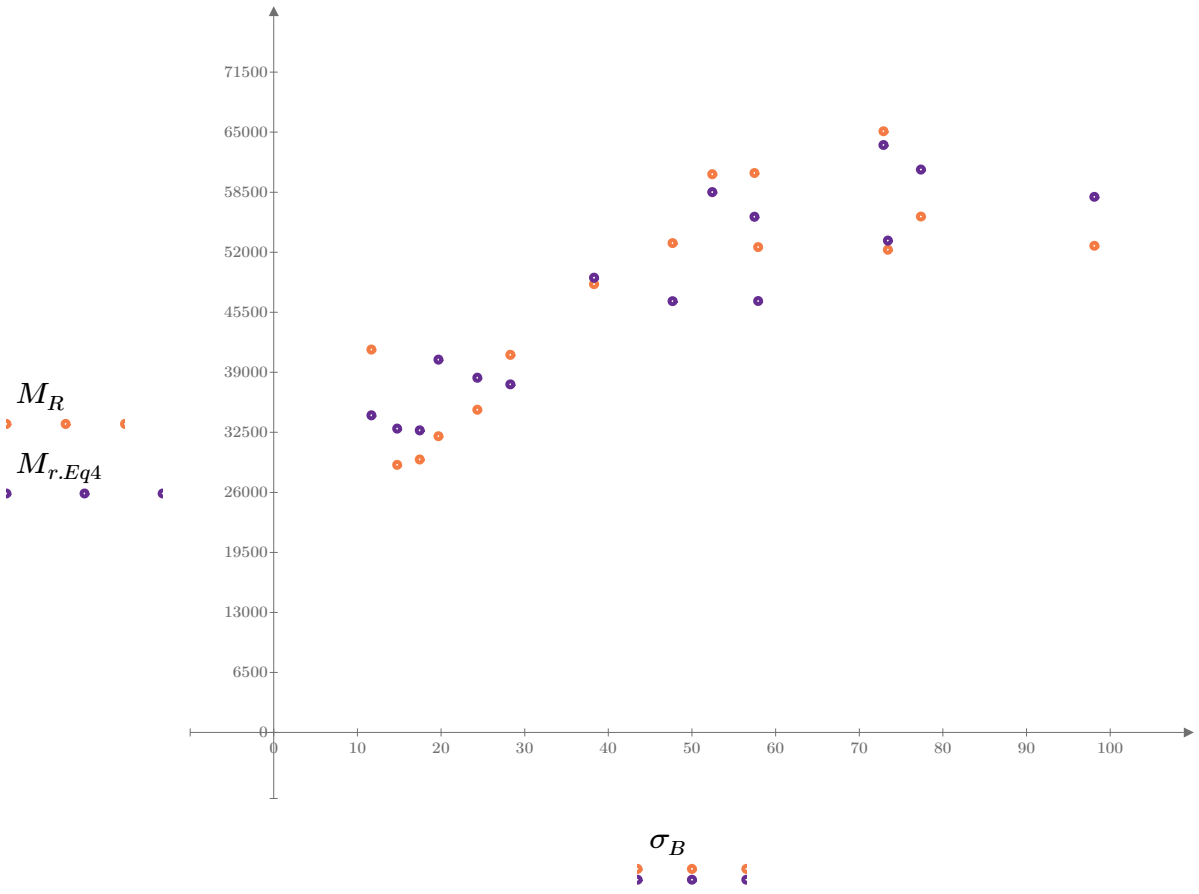

Figure 6. Plot of the test data (orange points) vs. the fitted Equation 4 model (purple points).

Dan Seely
9/12/2023

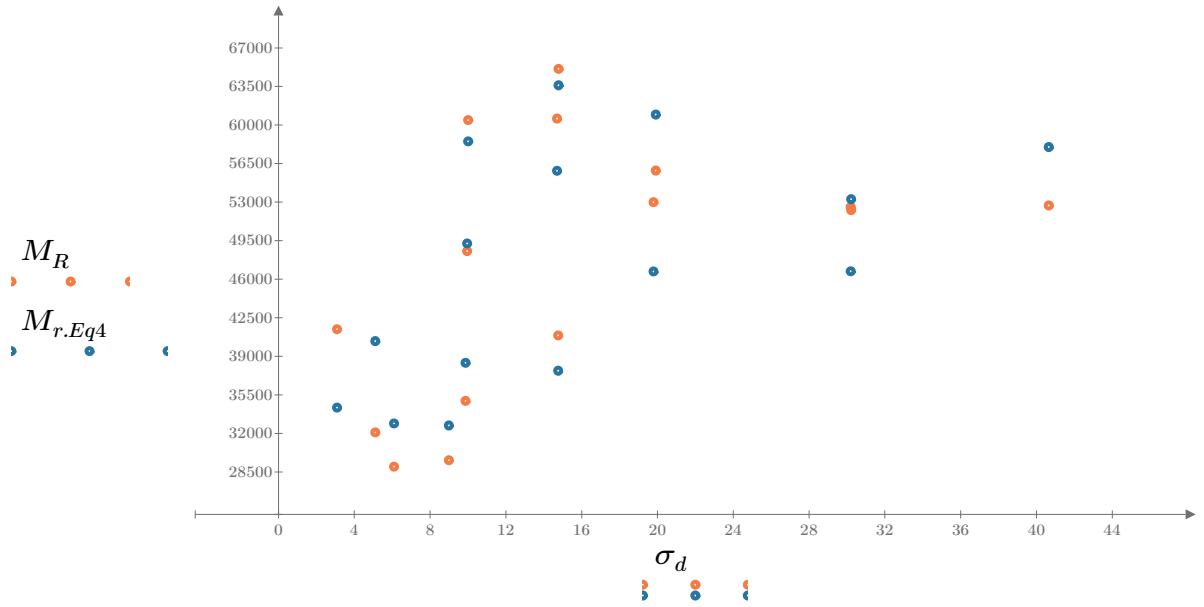

Figure 7. Plot of the test data (orange points) vs. the fitted Equation 4 model (blue points).

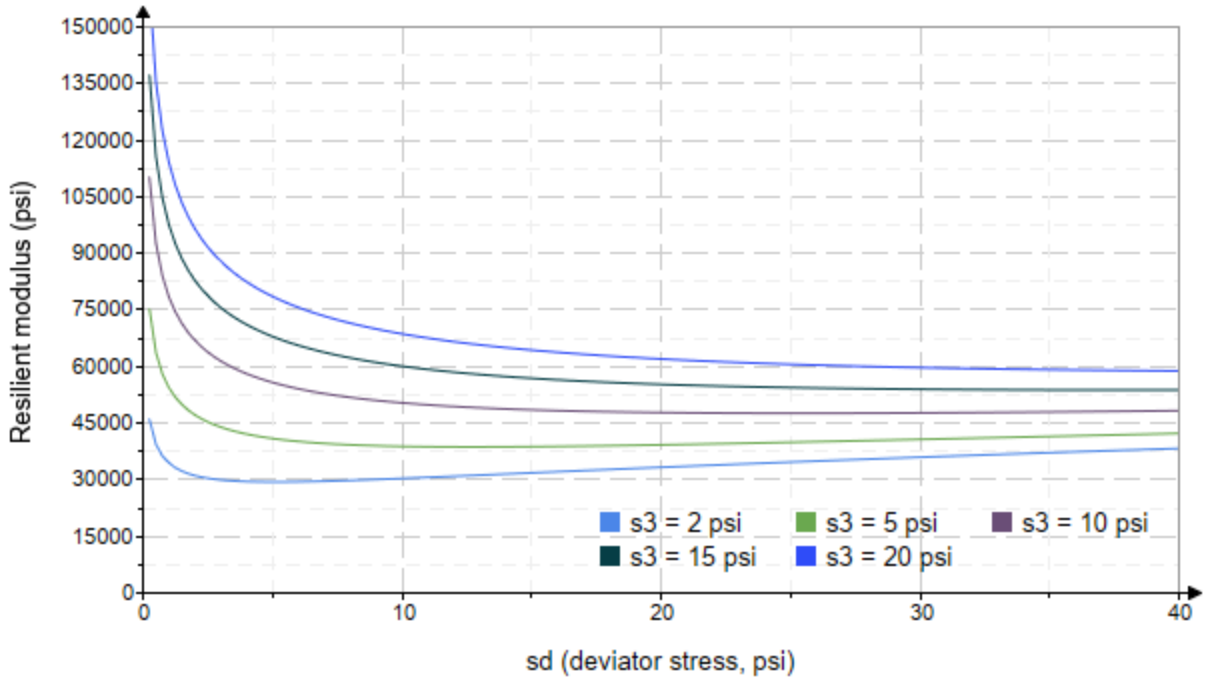

Figure 8. Plot of the fitted Equation 4 model for various confining stresses.

Dan Seely
9/12/2023

$SampleNo := \text{“B2}-\text{63”}$

$Treatment = \text{“AD”}$

$S = 3.825$ Degree of Saturation (%)

Test Sequence : Base/Subbase

Test summary data (psi) :

$$\sigma_3 = \begin{bmatrix} 2.800 \\ 2.780 \\ 2.783 \\ 4.564 \\ 4.593 \\ 4.603 \\ 9.624 \\ 9.587 \\ 9.604 \\ 14.660 \\ 14.660 \\ 14.640 \\ 19.650 \\ 19.640 \\ 19.640 \end{bmatrix} \quad \sigma_d = \begin{bmatrix} 3.284 \\ 6.167 \\ 8.978 \\ 5.232 \\ 9.756 \\ 14.660 \\ 9.804 \\ 19.750 \\ 30.020 \\ 9.850 \\ 14.780 \\ 30.140 \\ 14.740 \\ 19.970 \\ 40.470 \end{bmatrix} \quad \sigma_B = \begin{bmatrix} 11.690 \\ 14.510 \\ 17.330 \\ 18.920 \\ 23.530 \\ 28.470 \\ 38.680 \\ 48.510 \\ 58.830 \\ 53.820 \\ 58.750 \\ 74.050 \\ 73.690 \\ 78.890 \\ 99.380 \end{bmatrix} \quad M_R = \begin{bmatrix} 36685.0 \\ 43321.4 \\ 44283.8 \\ 49831.8 \\ 44433.6 \\ 49111.4 \\ 43993.0 \\ 53513.6 \\ 53057.2 \\ 53923.6 \\ 58890.8 \\ 55963.6 \\ 56312.4 \\ 58080.8 \\ 59697.4 \end{bmatrix}$$

σ_3 = mean confining stress
σ_d = mean deviator stress
σ_B = mean bulk stress
M_R = resilient modulus
p_a = atmospheric pressure = 14.6959 psi

Dan Seely
9/12/2023

$$M_{R.1}\left(\sigma_B, K_1, K_2\right) := K_1 \cdot {\sigma_B}^{K_2}$$

Equation 1
AASHTO Publication No. FHWA-RD-97-083

$K_1 = 25860.219$

$K_2 = 0.1829$

Equation 1 fitting parameters

${R_1}^2 = 0.8226$

Coefficient of determination

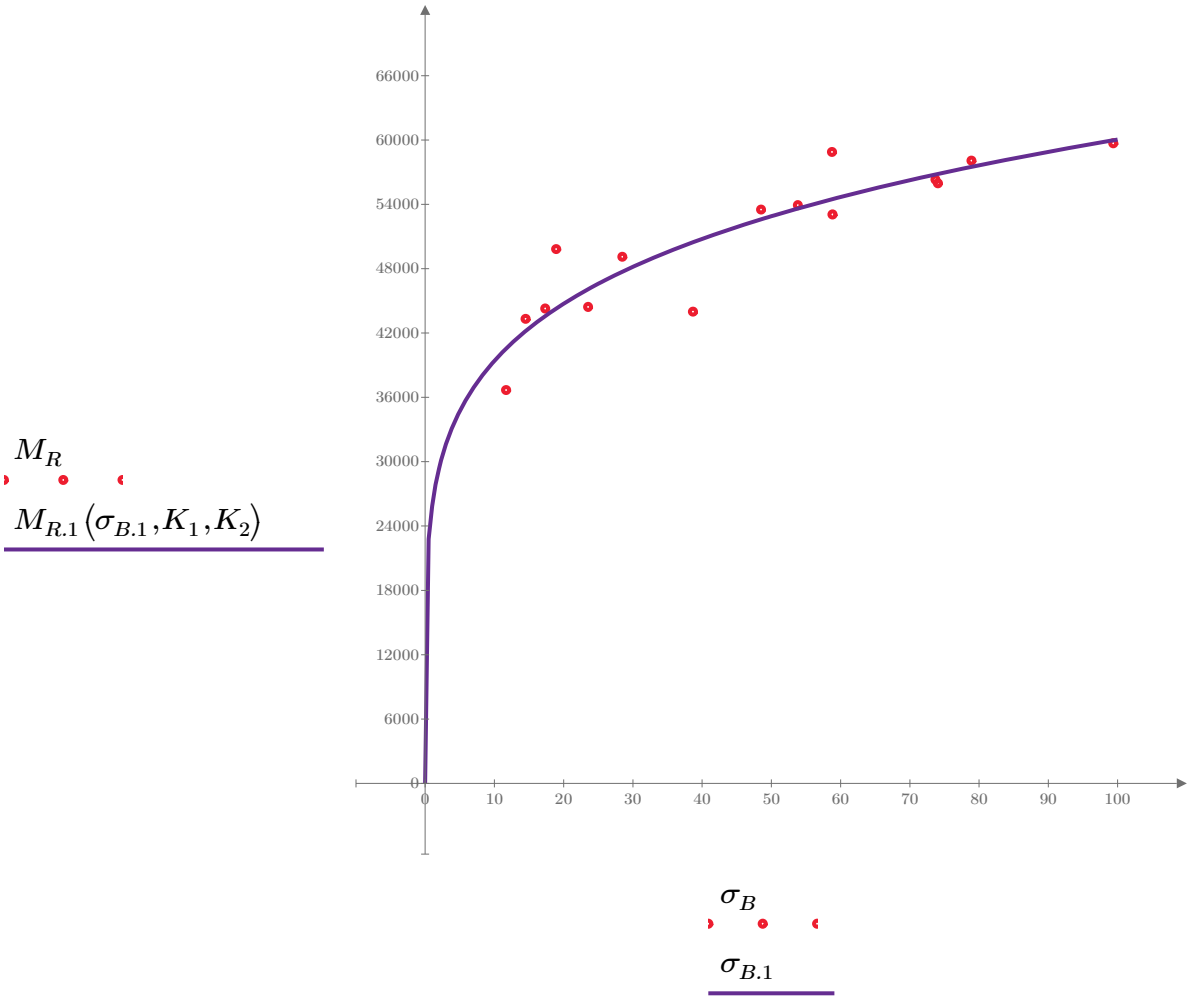

Figure 1. Plot of the test data (red points) vs. the fitted Equation 1 model (purple line).

Dan Seely
9/12/2023

$$M_{R.2}(\sigma_d, K_3, K_4) := K_3 \cdot \sigma_d^{K_4}$$

Equation 2
AASHTO Publication No. FHWA-RD-97-083

$K_3 = 34165.492$

$K_4 = 0.1531$

Equation 2 fitting parameters

$R_2^2 = 0.6182$

Coefficient of determination

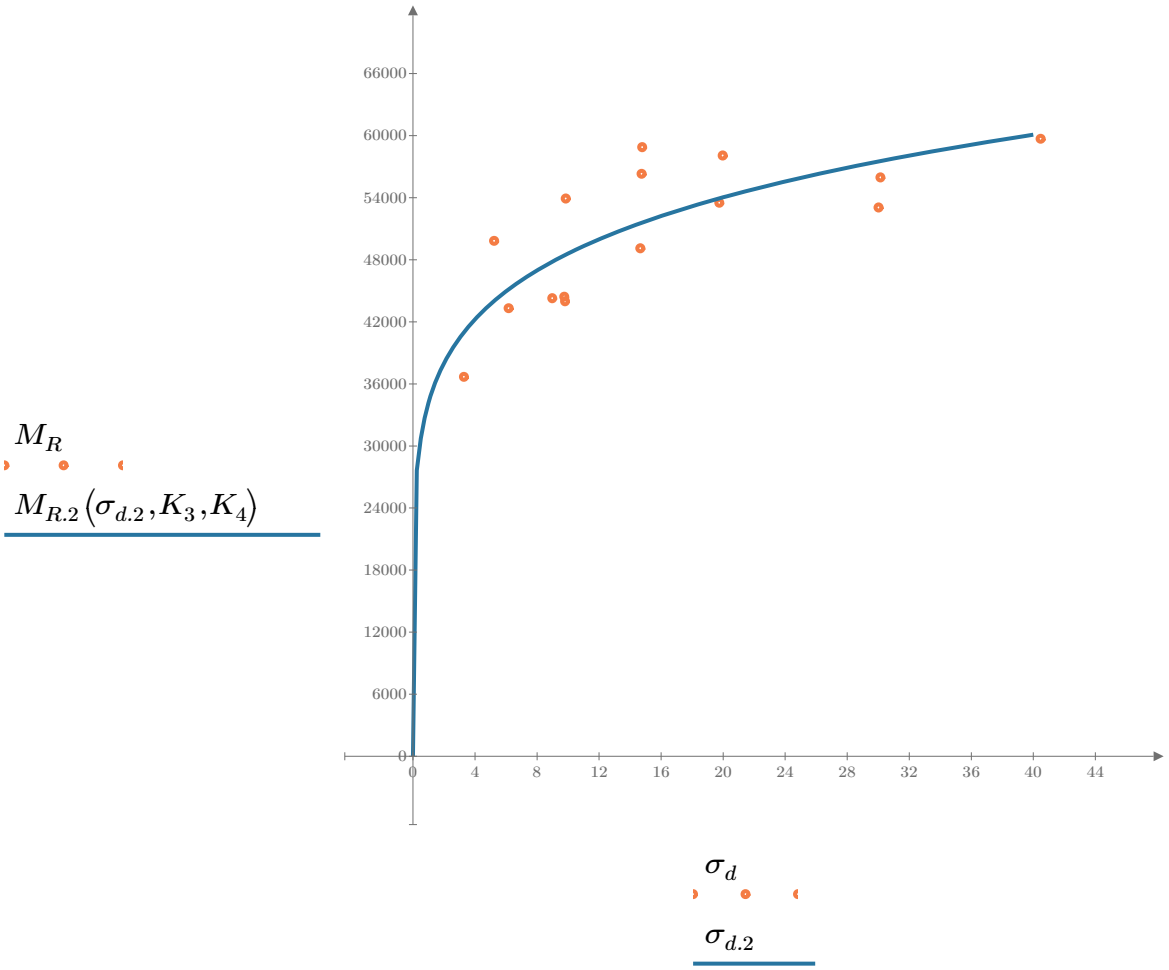

Figure 2. Plot of the test data (orange points) vs. the fitted Equation 2 model (blue line).

Dan Seely
9/12/2023

$$M_{R.3}\left(\sigma_d,\sigma_3,K_5,K_6,K_7\right) := K_5 \cdot {\sigma_d}^{K_6} \cdot \left(1+\sigma_3\right)^{K_7}$$

Equation 3 AASHTO Publication No. FHWA-RD-97-083

$K_5 = 31559.574$

$K_6 = 0.0629$ Equation 3 fitting parameters

$K_7 = 0.1373$

${R_3}^2 = 0.8210$ Coefficient of determination

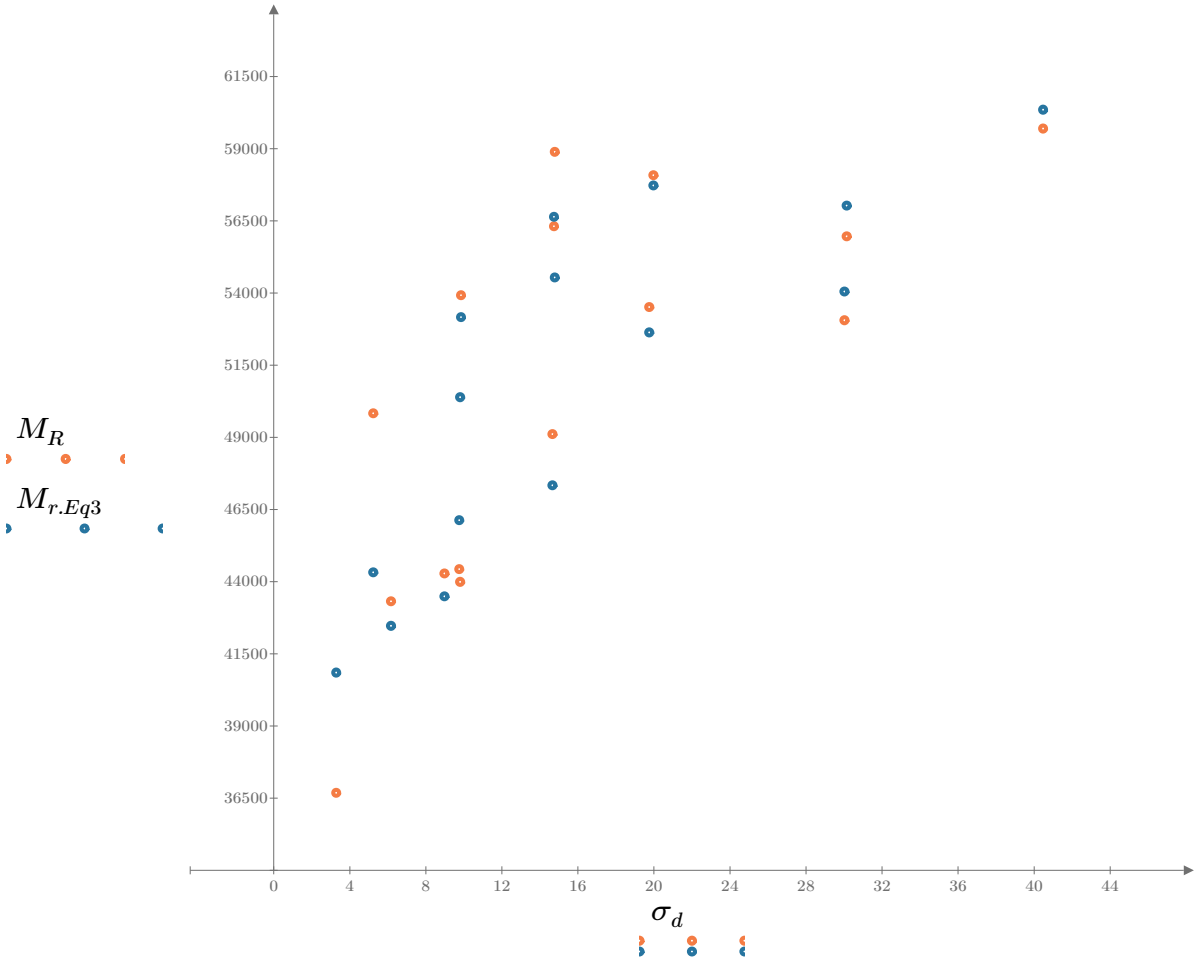

Figure 3. Plot of the test data (orange points) vs. the fitted Equation 3 model (blue points).

Dan Seely
9/12/2023

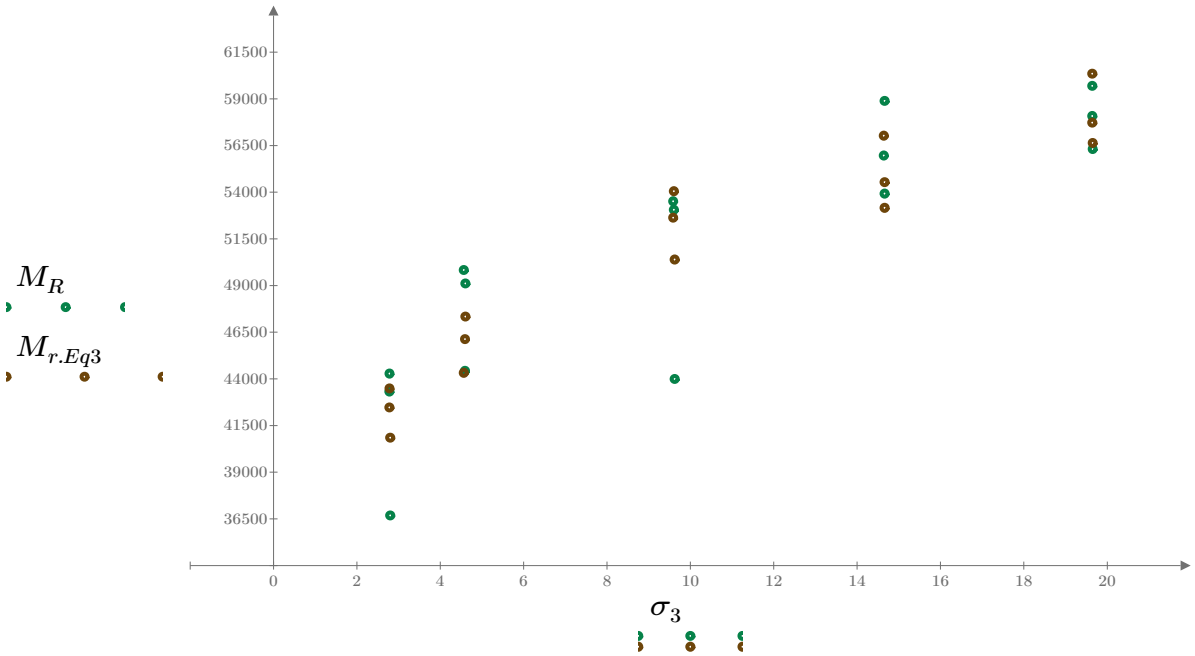

Figure 4. Plot of the test data (green points) vs. the fitted Equation 3 model (brown points).

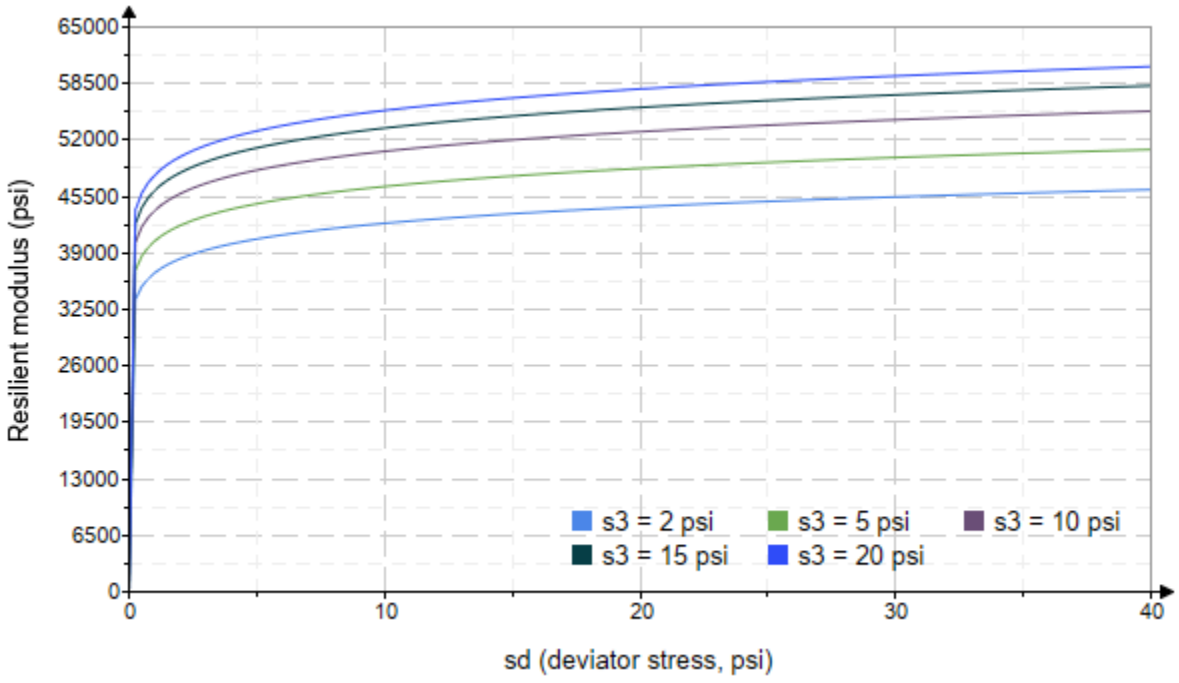

Figure 5. Plot of the fitted Equation 3 model for various confining stresses.

Dan Seely
9/12/2023

$$M_{R.4}\left(\sigma_B,\sigma_d,K_8,K_9,K_{10}\right) := K_8 \cdot p_a \left(\frac{\sigma_B}{p_a}\right)^{K_9} \cdot \left(\frac{\sigma_d}{p_a}\right)^{K_{10}}$$

Equation 4 AASHTO Publication No. FHWA-RD-97-083

$K_8 = 2875.574$

$K_9 = 0.1834$ Equation 4 fitting parameters

$K_{10} = -0.0005$

$R_4^{\,2} = 0.8226$ Coefficient of determination

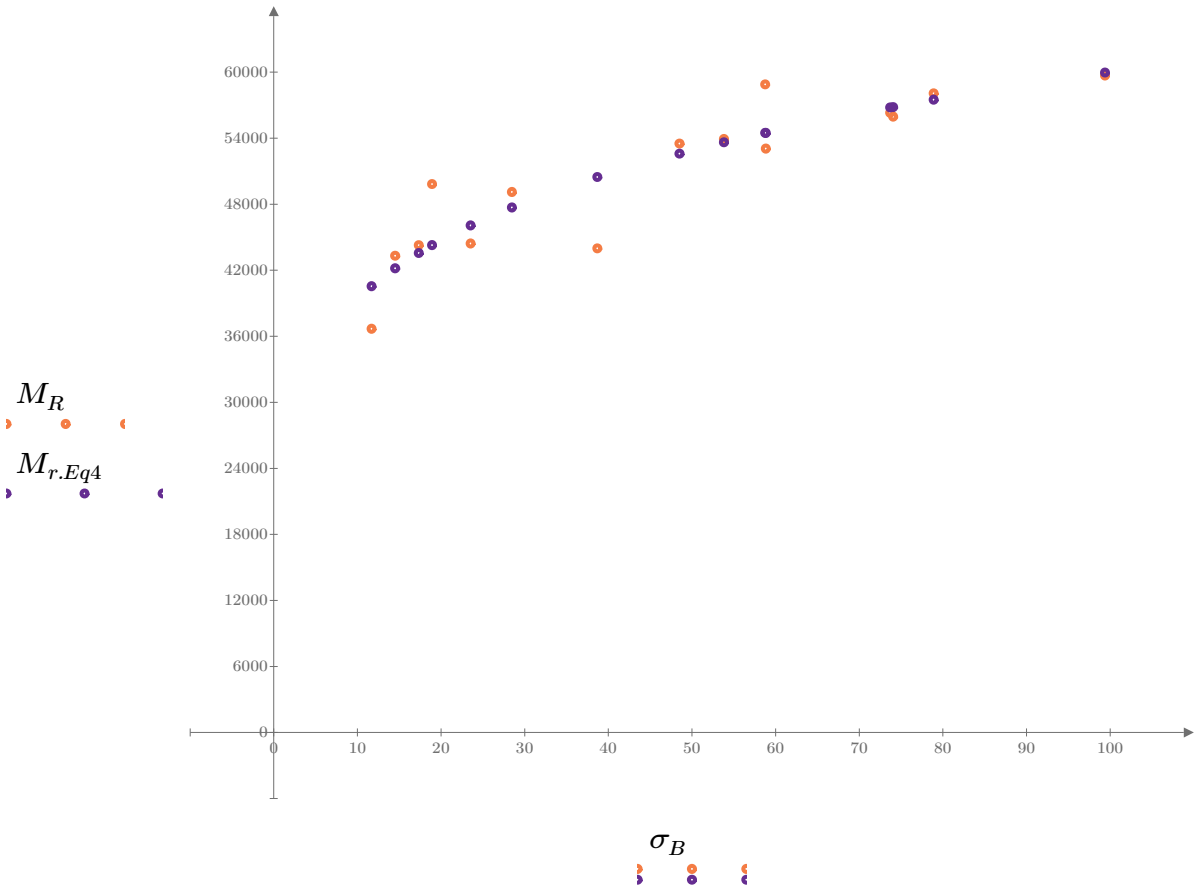

Figure 6. Plot of the test data (orange points) vs. the fitted Equation 4 model (purple points).

Dan Seely
9/12/2023

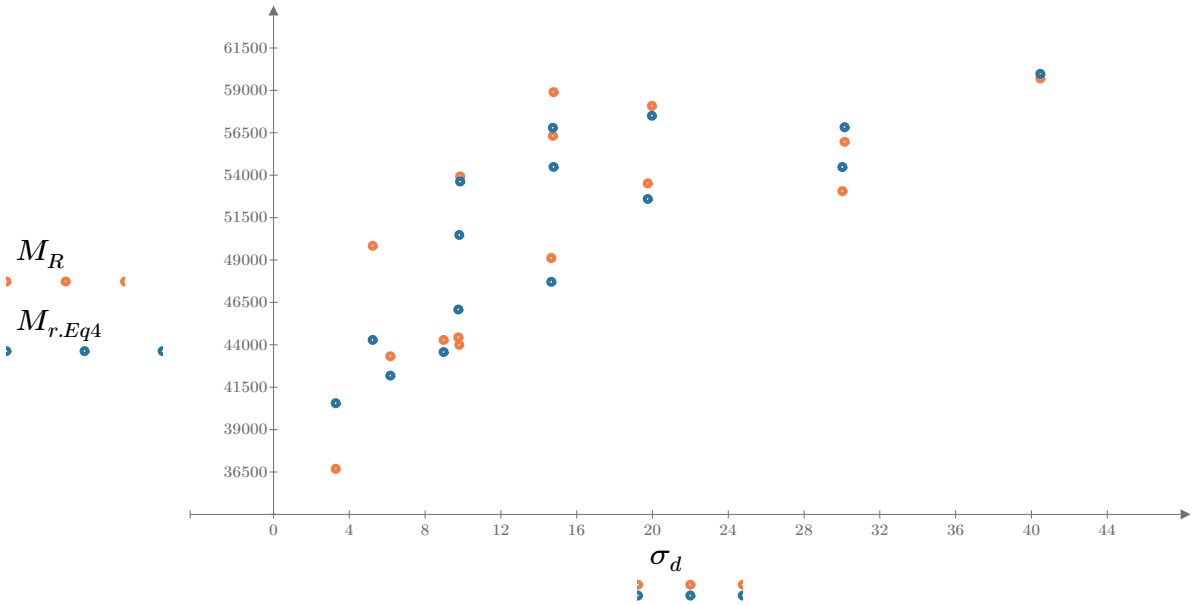

Figure 7. Plot of the test data (orange points) vs. the fitted Equation 4 model (blue points).

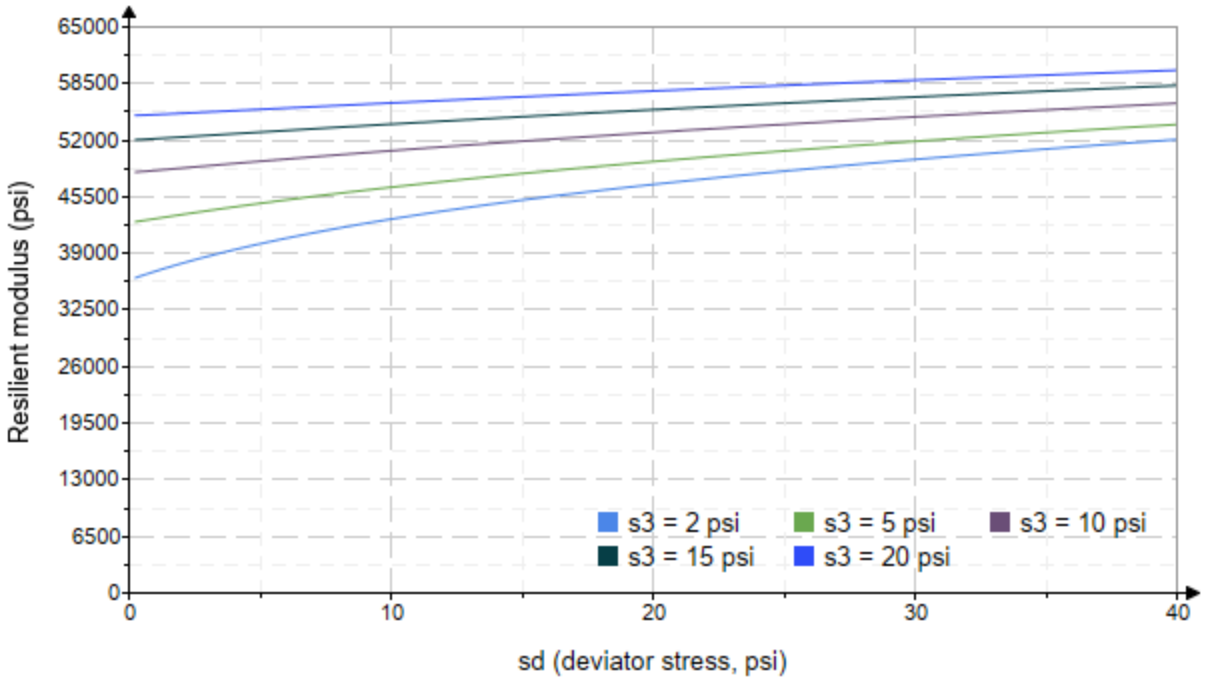

Figure 8. Plot of the fitted Equation 4 model for various confining stresses.

Dan Seely
9/12/2023

$SampleNo := \text{“B2}-\text{64”}$

$Treatment = \text{“H100”}$

$S = 5.288$ Degree of Saturation (%)

Test Sequence : Base/Subbase

Test summary data (psi) :

$$\sigma_3 = \begin{bmatrix} 2.687 \\ 2.698 \\ 2.697 \\ 4.701 \\ 4.686 \\ 4.628 \\ 9.669 \\ 9.641 \\ 9.622 \\ 14.640 \\ 14.610 \\ 14.640 \\ 19.630 \\ 19.650 \\ 19.600 \end{bmatrix} \quad \sigma_d = \begin{bmatrix} 3.164 \\ 6.121 \\ 9.157 \\ 5.193 \\ 10.090 \\ 14.590 \\ 10.030 \\ 19.210 \\ 29.390 \\ 10.250 \\ 14.530 \\ 29.540 \\ 14.520 \\ 19.470 \\ 40.120 \end{bmatrix} \quad \sigma_B = \begin{bmatrix} 11.230 \\ 14.210 \\ 17.250 \\ 19.300 \\ 24.140 \\ 28.470 \\ 39.040 \\ 48.130 \\ 58.260 \\ 54.160 \\ 58.360 \\ 73.470 \\ 73.420 \\ 78.410 \\ 98.920 \end{bmatrix} \quad M_R = \begin{bmatrix} 30723.6 \\ 34321.8 \\ 36037.8 \\ 48906.4 \\ 44059.6 \\ 41884.2 \\ 49052.4 \\ 47535.2 \\ 44317.6 \\ 44314.6 \\ 48405.0 \\ 49533.2 \\ 50082.4 \\ 51122.8 \\ 56803.6 \end{bmatrix}$$

σ_3 = mean confining stress
σ_d = mean deviator stress
σ_B = mean bulk stress
M_R = resilient modulus
p_a = atmospheric pressure = 14.6959 psi

Dan Seely
9/12/2023

$$M_{R.1}(\sigma_B, K_1, K_2) := K_1 \cdot {\sigma_B}^{K_2}$$

Equation 1
AASHTO Publication No. FHWA-RD-97-083

$K_1 = 22210.292$

$K_2 = 0.1926$

Equation 1 fitting parameters

${R_1}^2 = 0.7119$

Coefficient of determination

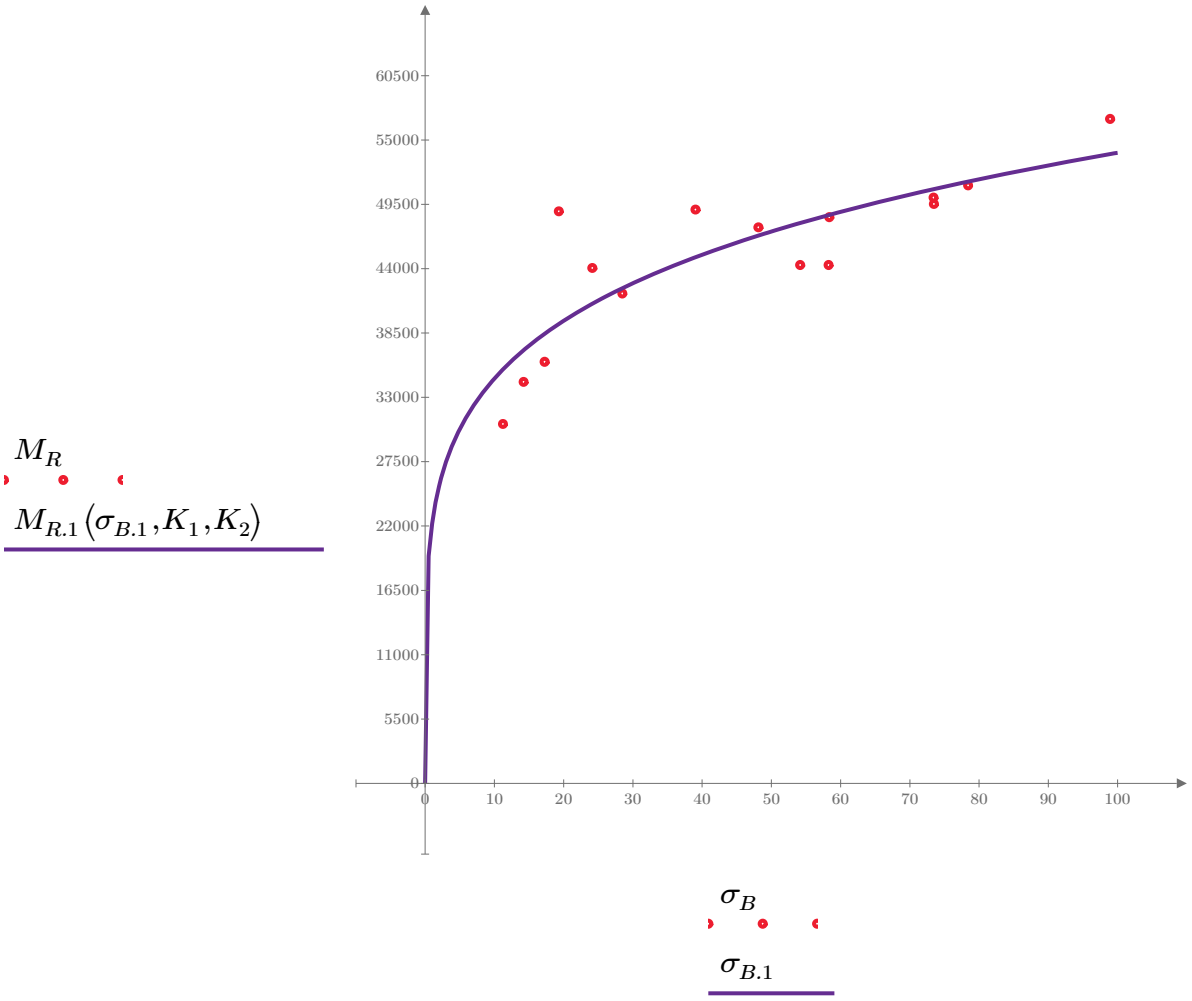

Figure 1. Plot of the test data (red points) vs. the fitted Equation 1 model (purple line).

Dan Seely
9/12/2023

$$M_{R.2}(\sigma_d, K_3, K_4) := K_3 \cdot \sigma_d^{K_4}$$

Equation 2
AASHTO Publication No. FHWA-RD-97-083

$K_3 = 30112.633$

$K_4 = 0.1569$

Equation 2 fitting parameters

$R_2^2 = 0.4902$

Coefficient of determination

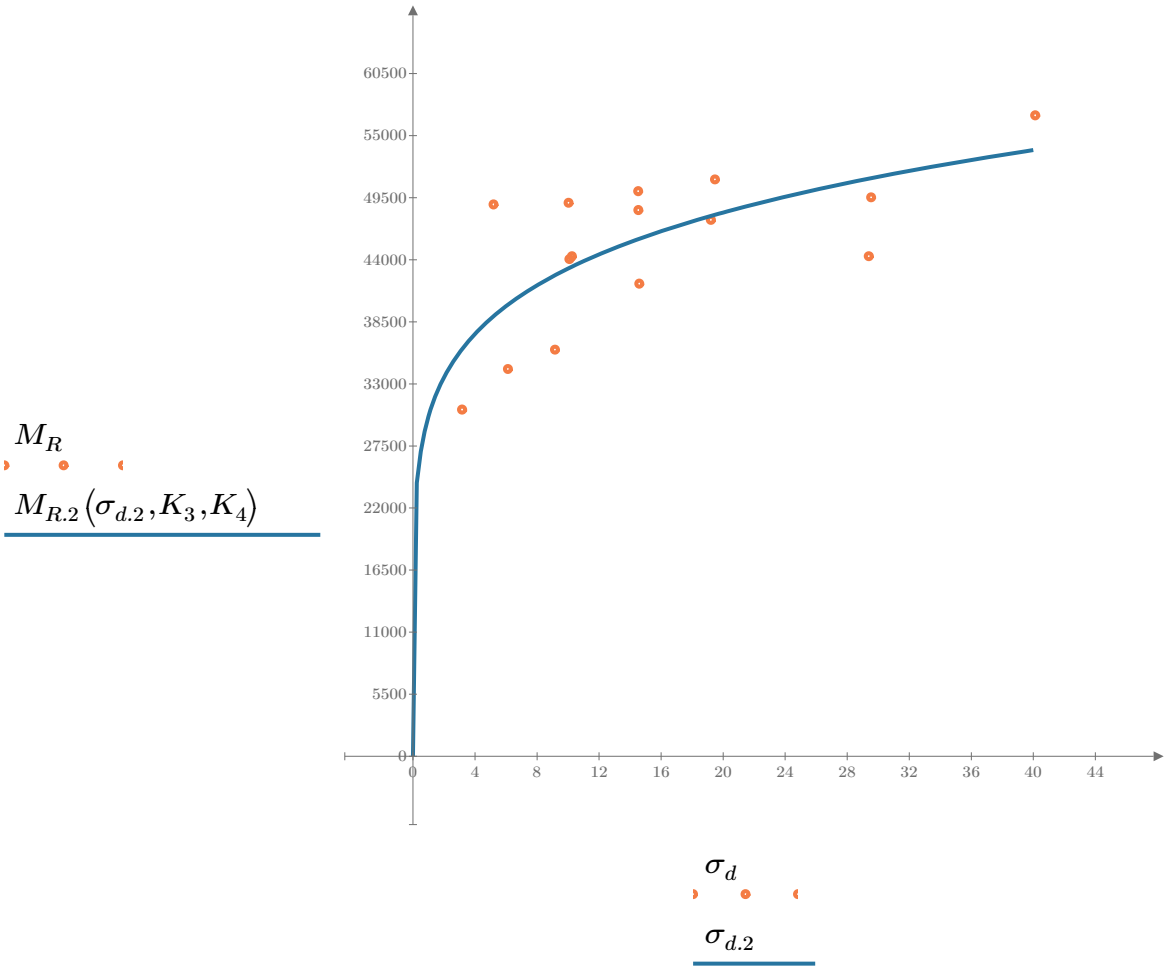

Figure 2. Plot of the test data (orange points) vs. the fitted Equation 2 model (blue line).

Dan Seely
9/12/2023

$$M_{R.3}\left(\sigma_d,\sigma_3,K_5,K_6,K_7\right):=K_5\cdot{\sigma_d}^{K_6}\cdot\left(1+\sigma_3\right)^{K_7}$$

Equation 3 AASHTO Publication No. FHWA-RD-97-083

$K_5=27555.593$

$K_6=0.0479$ Equation 3 fitting parameters

$K_7=0.1625$

${R_3}^2=0.7202$ Coefficient of determination

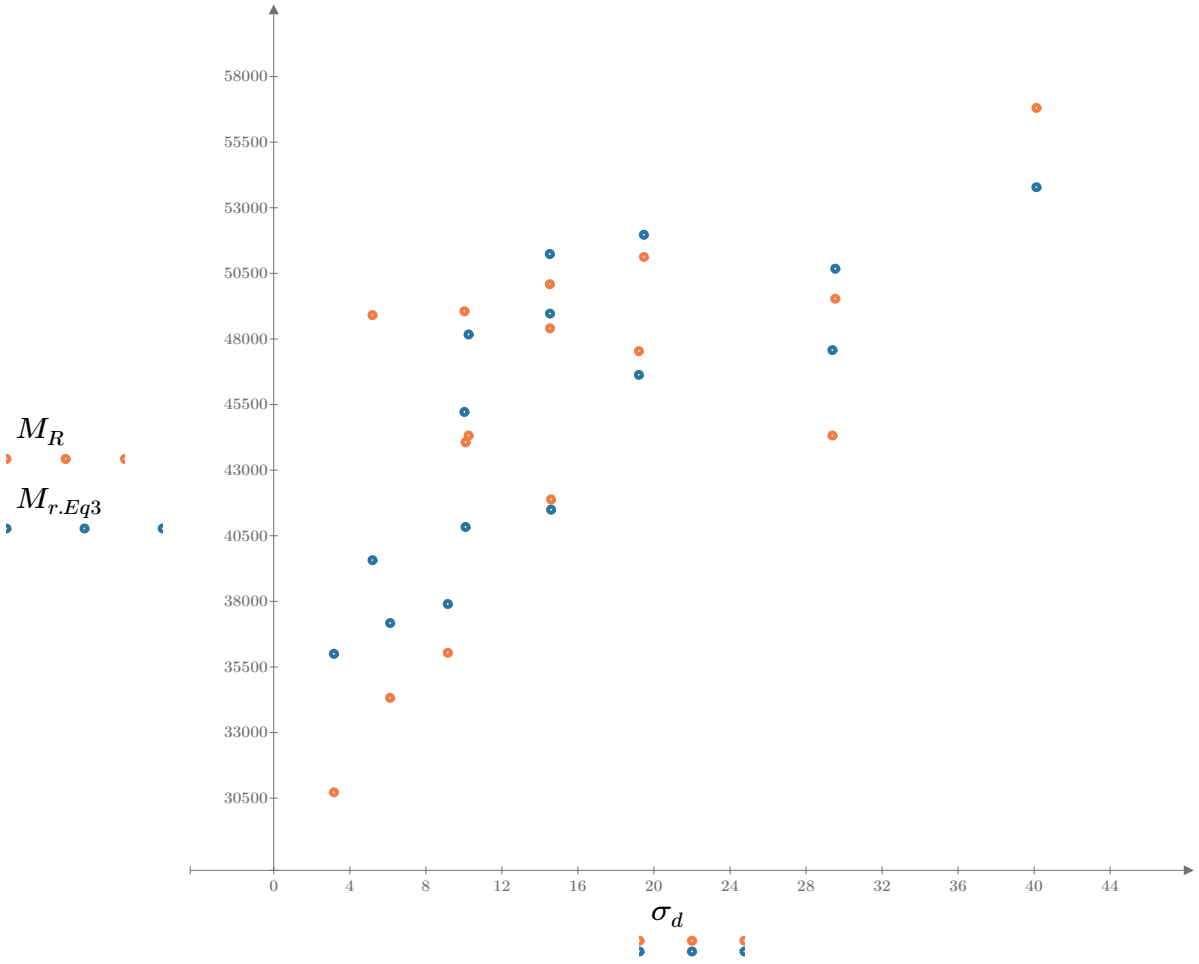

Figure 3. Plot of the test data (orange points) vs. the fitted Equation 3 model (blue points).

Dan Seely
9/12/2023

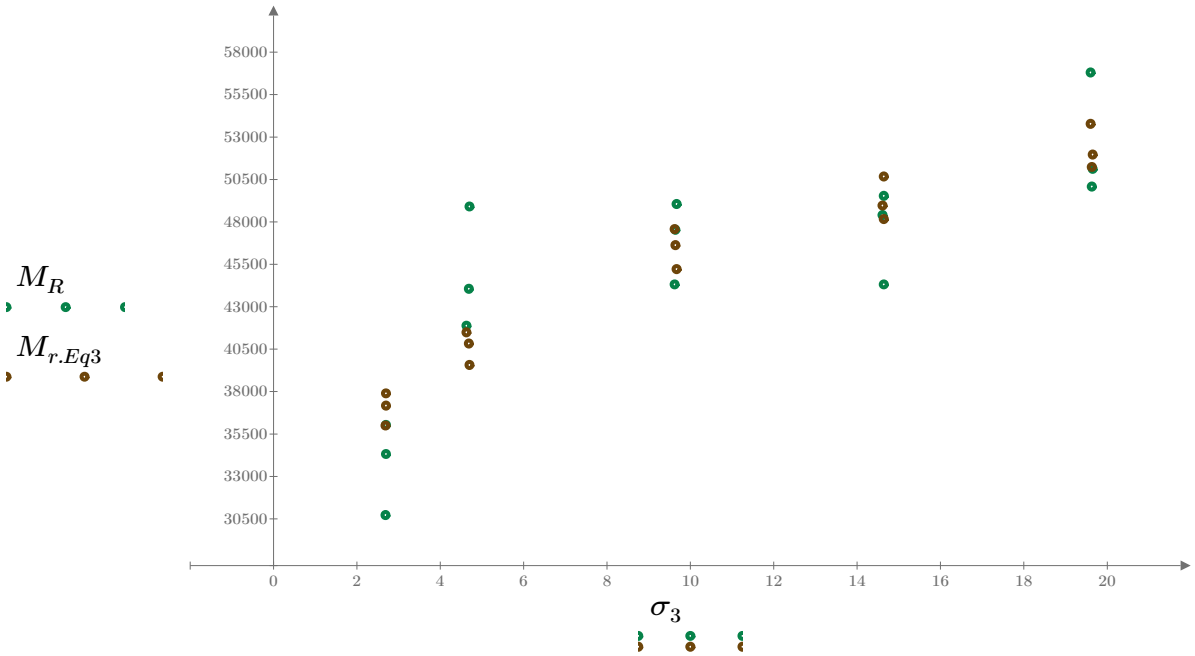

Figure 4. Plot of the test data (green points) vs. the fitted Equation 3 model (brown points).

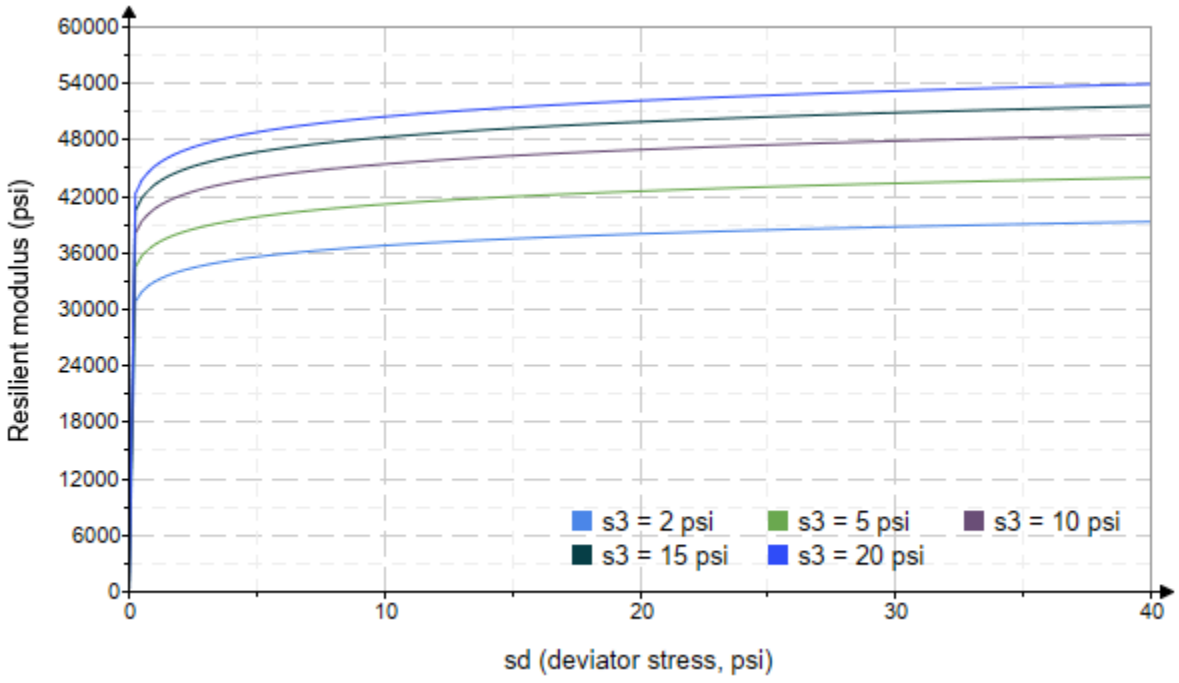

Figure 5. Plot of the fitted Equation 3 model for various confining stresses.

Dan Seely
9/12/2023

$$M_{R.4}\left(\sigma_B,\sigma_d,K_8,K_9,K_{10}\right) := K_8 \cdot p_a \left(\frac{\sigma_B}{p_a}\right)^{K_9} \cdot \left(\frac{\sigma_d}{p_a}\right)^{K_{10}}$$

Equation 4 AASHTO Publication No. FHWA-RD-97-083

$K_8 = 2476.407$

$K_9 = 0.2137$ Equation 4 fitting parameters

$K_{10} = -0.0246$

$R_4^{\,2} = 0.7150$ Coefficient of determination

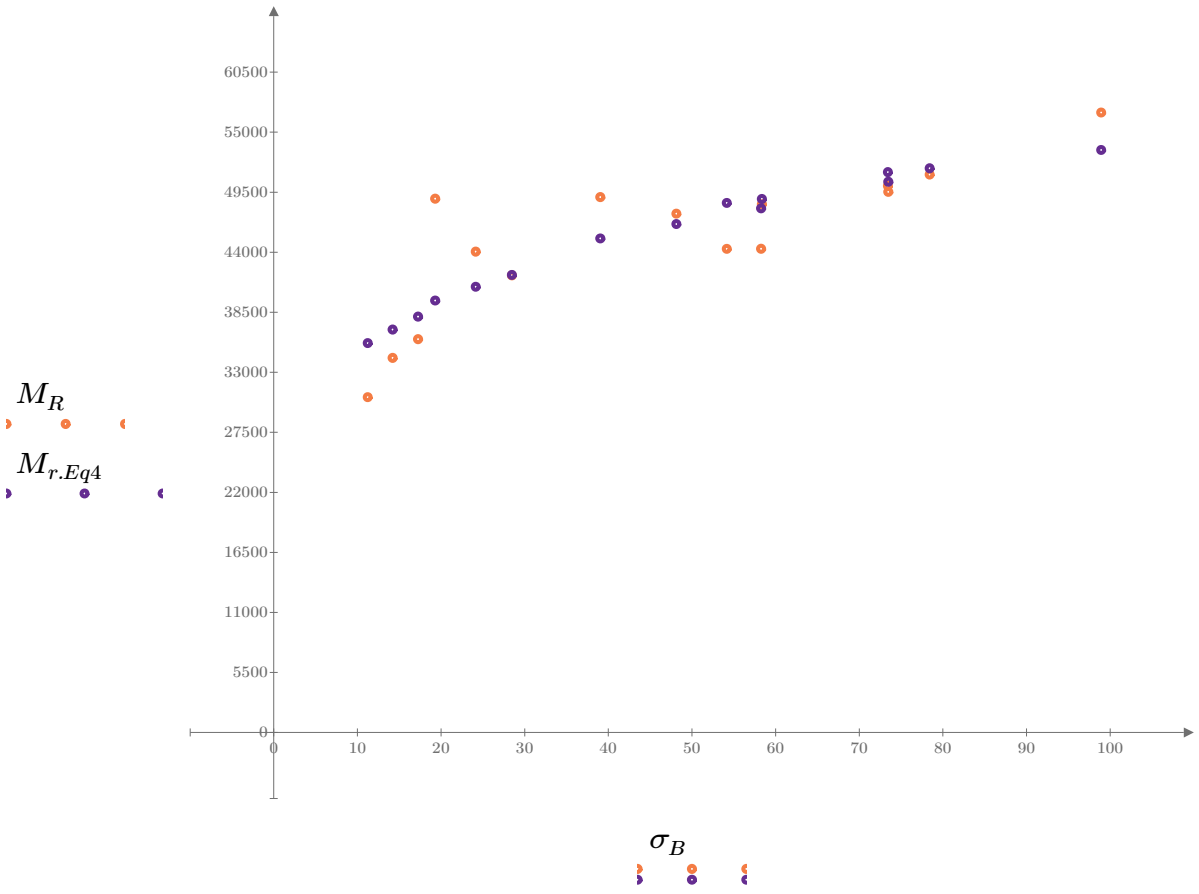

Figure 6. Plot of the test data (orange points) vs. the fitted Equation 4 model (purple points).

Dan Seely
9/12/2023

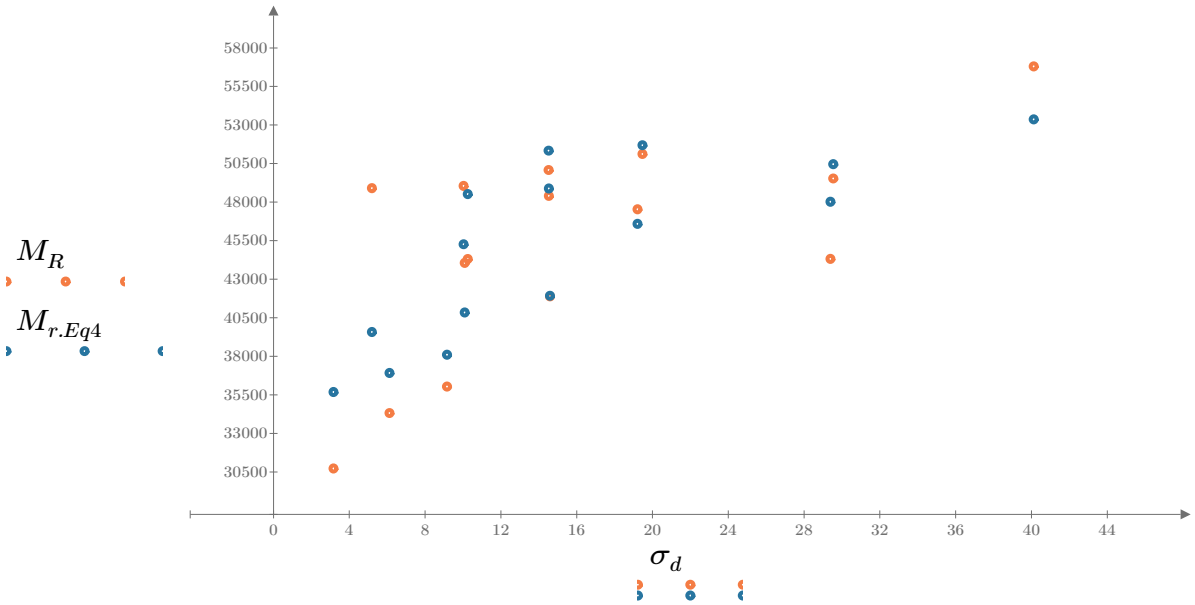

Figure 7. Plot of the test data (orange points) vs. the fitted Equation 4 model (blue points).

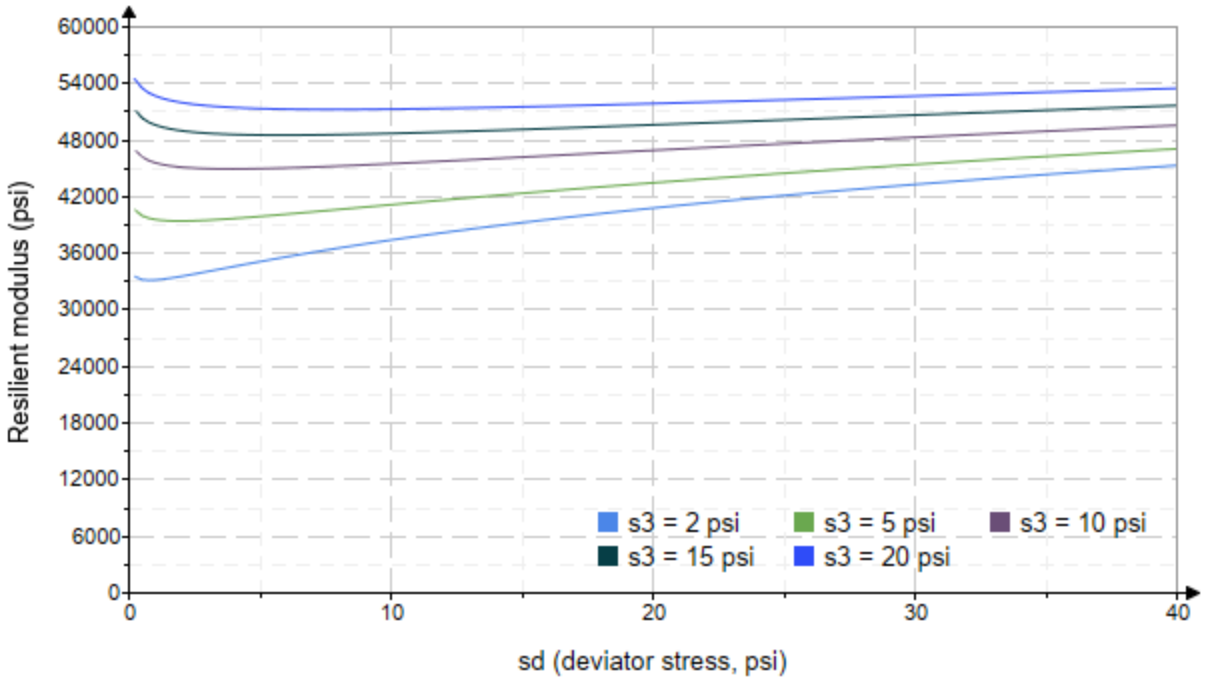

Figure 8. Plot of the fitted Equation 4 model for various confining stresses.

Dan Seely
9/12/2023

$SampleNo :=$ "B2−65"

$Treatment =$ "H100"

$S = 5.112$ Degree of Saturation (%)

Test Sequence : Base/Subbase

Test summary data (psi) :

$$\sigma_3 = \begin{bmatrix} 3.048 \\ 2.833 \\ 2.460 \\ 5.127 \\ 4.806 \\ 3.450 \\ 9.463 \\ 8.925 \\ 9.217 \\ 14.050 \\ 13.610 \\ 13.740 \\ 18.820 \\ 18.690 \\ 19.110 \end{bmatrix} \quad \sigma_d = \begin{bmatrix} 3.186 \\ 6.231 \\ 9.255 \\ 5.115 \\ 10.090 \\ 14.370 \\ 9.978 \\ 19.370 \\ 29.640 \\ 9.763 \\ 14.520 \\ 29.830 \\ 14.550 \\ 19.530 \\ 40.220 \end{bmatrix} \quad \sigma_B = \begin{bmatrix} 12.330 \\ 14.730 \\ 16.630 \\ 20.490 \\ 24.510 \\ 24.720 \\ 38.370 \\ 46.150 \\ 57.300 \\ 51.920 \\ 55.350 \\ 71.050 \\ 71.010 \\ 75.600 \\ 97.560 \end{bmatrix} \quad M_R = \begin{bmatrix} 86621.5 \\ 64431.0 \\ 49404.6 \\ 56537.9 \\ 63671.2 \\ 58066.2 \\ 94452.8 \\ 78487.6 \\ 64877.0 \\ 89337.5 \\ 113798.0 \\ 62734.6 \\ 116916.0 \\ 81946.2 \\ 65981.2 \end{bmatrix}$$

σ_3 = mean confining stress
σ_d = mean deviator stress
σ_B = mean bulk stress
M_R = resilient modulus
p_a = atmospheric pressure = 14.6959 psi

Dan Seely
9/12/2023

$$M_{R.1}\left(\sigma_B, K_1, K_2\right) := K_1 \cdot {\sigma_B}^{K_2}$$

Equation 1
AASHTO Publication No. FHWA-RD-97-083

$K_1 = 43797.400$

$K_2 = 0.1525$

Equation 1 fitting parameters

${R_1}^2 = 0.1426$

Coefficient of determination

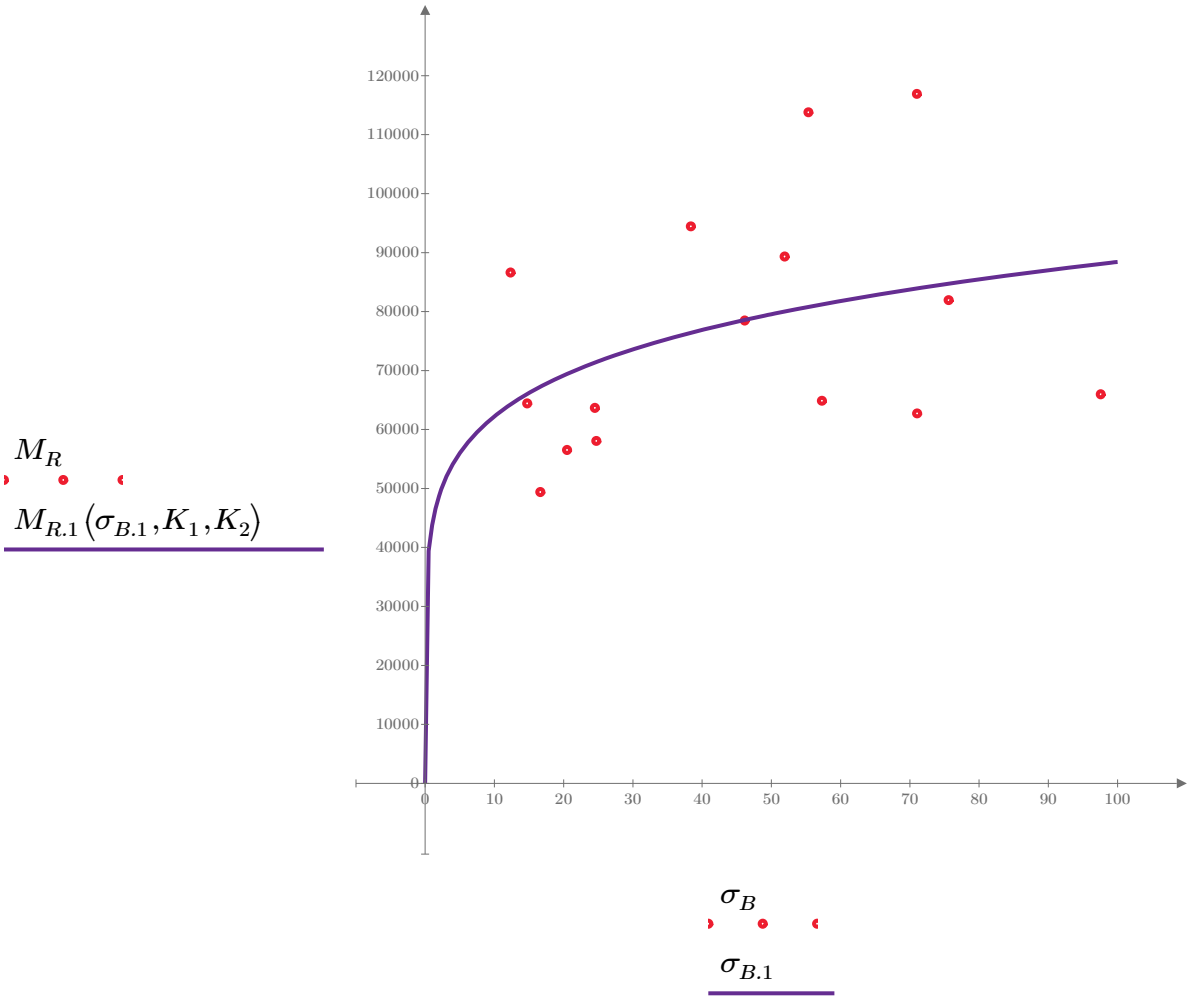

Figure 1. Plot of the test data (red points) vs. the fitted Equation 1 model (purple line).

Dan Seely
9/12/2023

$$M_{R.2}(\sigma_d, K_3, K_4) := K_3 \cdot \sigma_d^{K_4}$$

Equation 2
AASHTO Publication No. FHWA-RD-97-083

$K_3 = 78551.929$

$K_4 = -0.0105$

Equation 2 fitting parameters

$R_2^2 = 0.0008$

Coefficient of determination

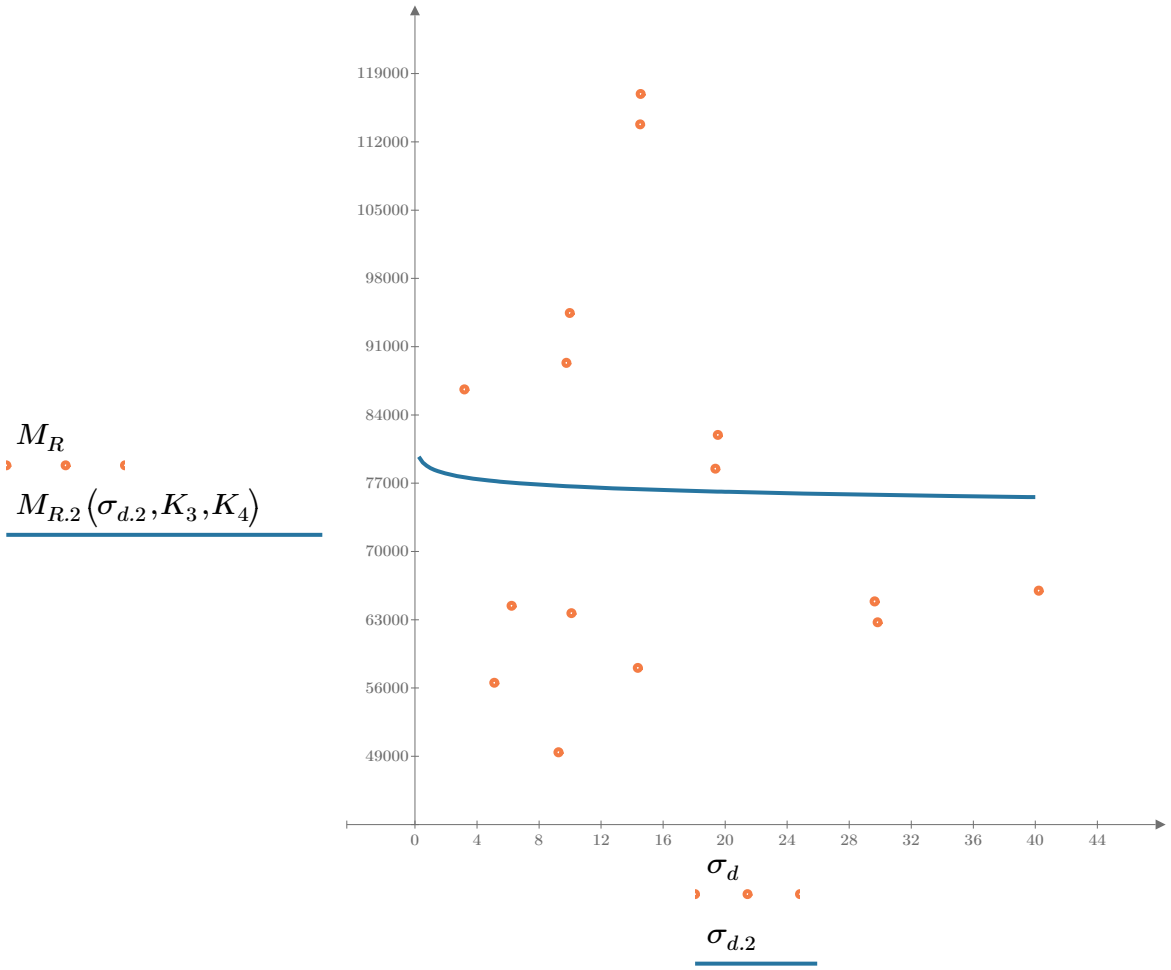

Figure 2. Plot of the test data (orange points) vs. the fitted Equation 2 model (blue line).

Dan Seely
9/12/2023

$$M_{R.3}\left(\sigma_d,\sigma_3,K_5,K_6,K_7\right):=K_5\cdot{\sigma_d}^{K_6}\cdot\left(1+\sigma_3\right)^{K_7}$$

Equation 3 AASHTO Publication No. FHWA-RD-97-083

$K_5=57883.189$

$K_6=-0.2932$ Equation 3 fitting parameters

$K_7=0.4549$

${R_3}^2=0.6153$ Coefficient of determination

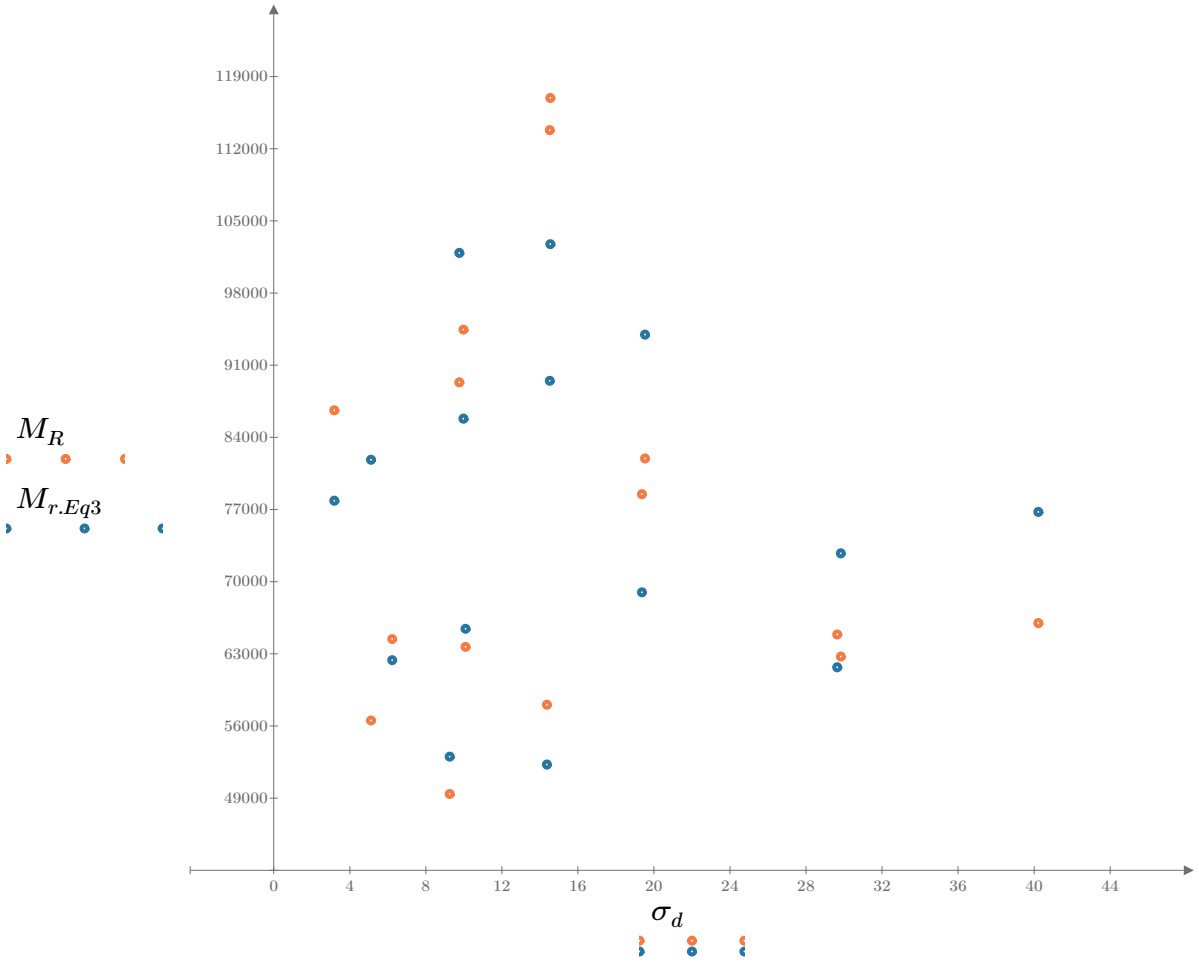

Figure 3. Plot of the test data (orange points) vs. the fitted Equation 3 model (blue points).

Dan Seely
9/12/2023

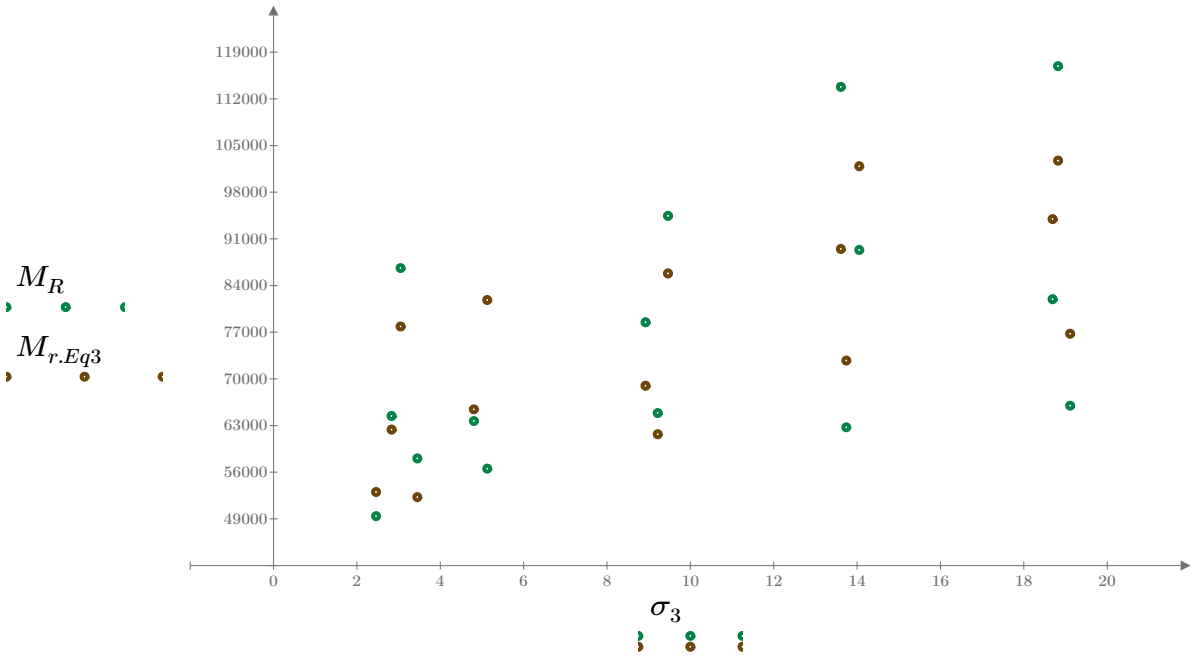

Figure 4. Plot of the test data (green points) vs. the fitted Equation 3 model (brown points).

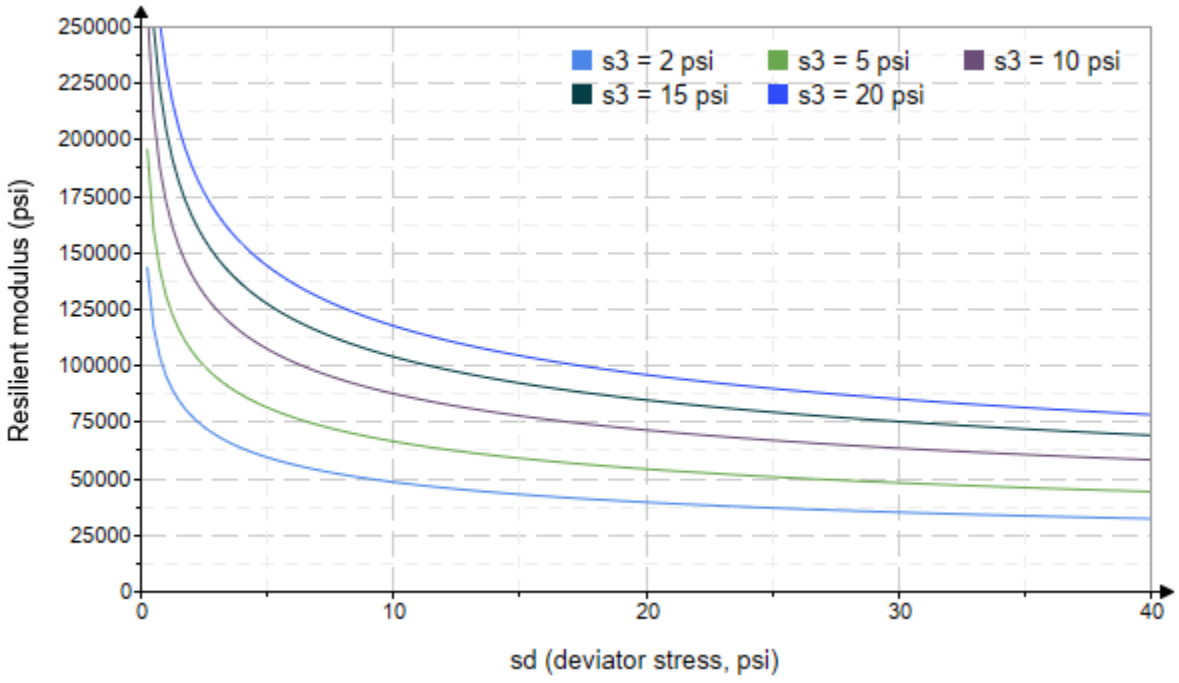

Figure 5. Plot of the fitted Equation 3 model for various confining stresses.

Dan Seely
9/12/2023

$$M_{R.4}\left(\sigma_B,\sigma_d,K_8,K_9,K_{10}\right) := K_8 \cdot p_a \left(\frac{\sigma_B}{p_a}\right)^{K_9} \cdot \left(\frac{\sigma_d}{p_a}\right)^{K_{10}}$$

Equation 4 AASHTO Publication No. FHWA-RD-97-083

$K_8 = 2700.947$

$K_9 = 0.6027$ Equation 4 fitting parameters

$K_{10} = -0.4964$

$R_4^{\,2} = 0.6108$ Coefficient of determination

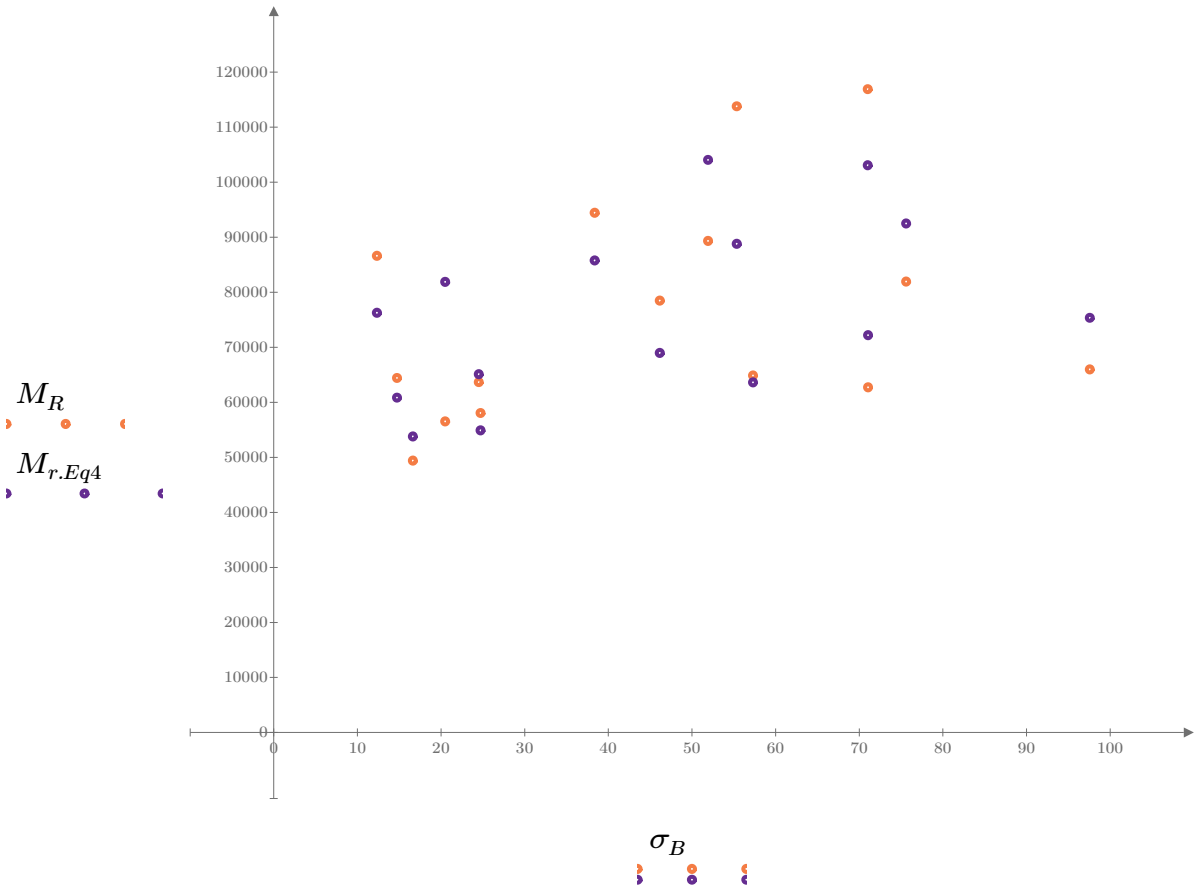

Figure 6. Plot of the test data (orange points) vs. the fitted Equation 4 model (purple points).

Dan Seely
9/12/2023

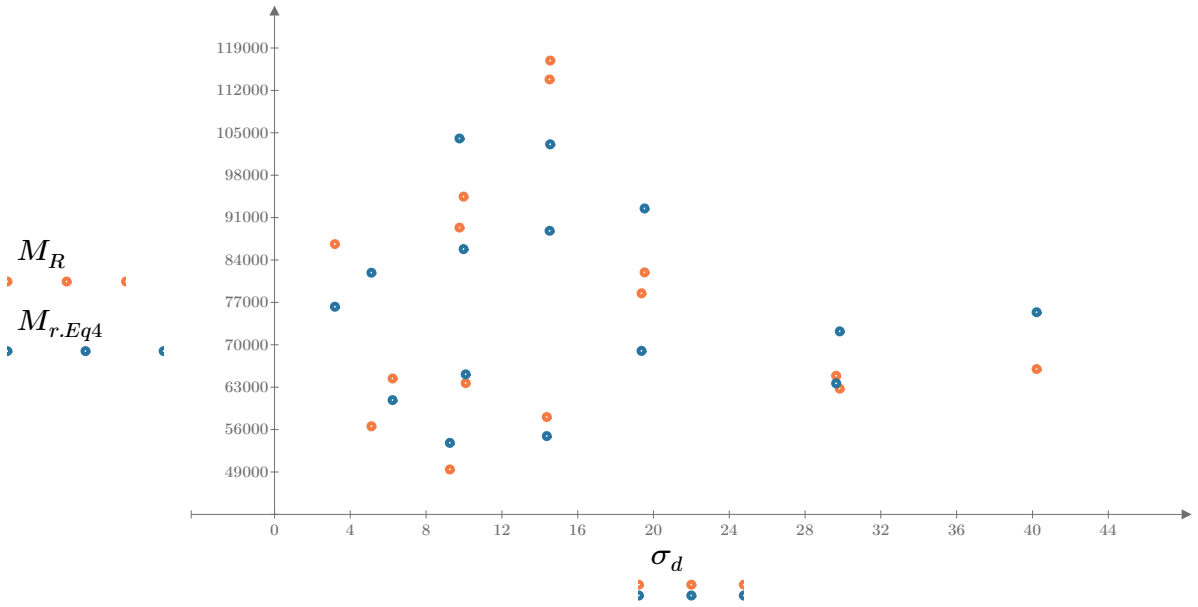

Figure 7. Plot of the test data (orange points) vs. the fitted Equation 4 model (blue points).

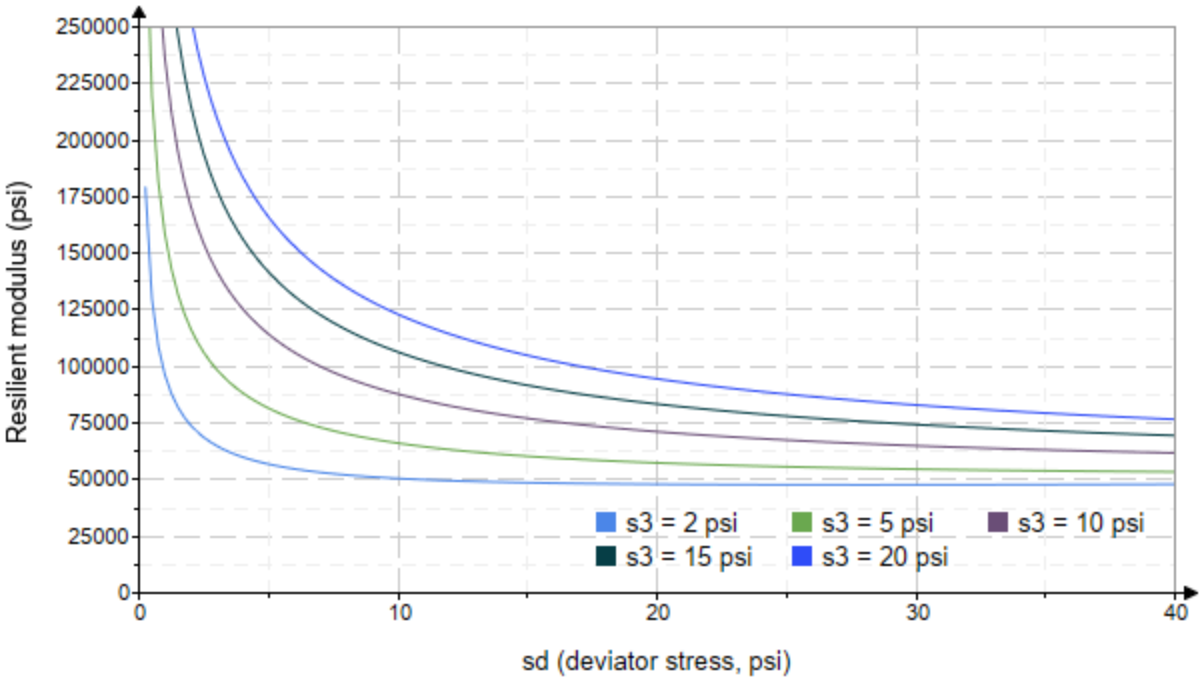

Figure 8. Plot of the fitted Equation 4 model for various confining stresses.

Dan Seely
9/12/2023

$SampleNo := \text{“B2–66”}$

$Treatment = \text{“D1”}$

$S = 15.832$ Degree of Saturation (%)

Test Sequence : Base/Subbase

Test summary data (psi) :

$$\sigma_3 = \begin{bmatrix} 2.590 \\ 2.503 \\ 2.488 \\ 4.497 \\ 4.519 \\ 4.478 \\ 9.537 \\ 9.530 \\ 9.543 \\ 14.630 \\ 14.600 \\ 14.630 \\ 19.660 \\ 19.650 \\ 19.650 \end{bmatrix} \quad \sigma_d = \begin{bmatrix} 3.156 \\ 6.211 \\ 9.132 \\ 5.020 \\ 10.050 \\ 14.510 \\ 10.160 \\ 19.140 \\ 29.250 \\ 10.060 \\ 14.460 \\ 29.490 \\ 14.400 \\ 19.510 \\ 39.970 \end{bmatrix} \quad \sigma_B = \begin{bmatrix} 10.930 \\ 13.720 \\ 16.590 \\ 18.510 \\ 23.600 \\ 27.950 \\ 38.770 \\ 47.730 \\ 57.880 \\ 53.950 \\ 58.250 \\ 73.380 \\ 73.370 \\ 78.460 \\ 98.910 \end{bmatrix} \quad M_R = \begin{bmatrix} 39338.6 \\ 30639.0 \\ 28894.8 \\ 31220.8 \\ 32471.2 \\ 36887.8 \\ 61911.4 \\ 56151.8 \\ 55233.6 \\ 67674.4 \\ 60362.4 \\ 60285.8 \\ 55433.4 \\ 59748.2 \\ 62901.6 \end{bmatrix}$$

σ_3 = mean confining stress
σ_d = mean deviator stress
σ_B = mean bulk stress
M_R = resilient modulus
p_a = atmospheric pressure = 14.6959 psi

Dan Seely
9/12/2023

$$M_{R.1}(\sigma_B, K_1, K_2) := K_1 \cdot {\sigma_B}^{K_2}$$

Equation 1
AASHTO Publication No. FHWA-RD-97-083

$K_1 = 12771.996$

$K_2 = 0.3643$

Equation 1 fitting parameters

${R_1}^2 = 0.7429$

Coefficient of determination

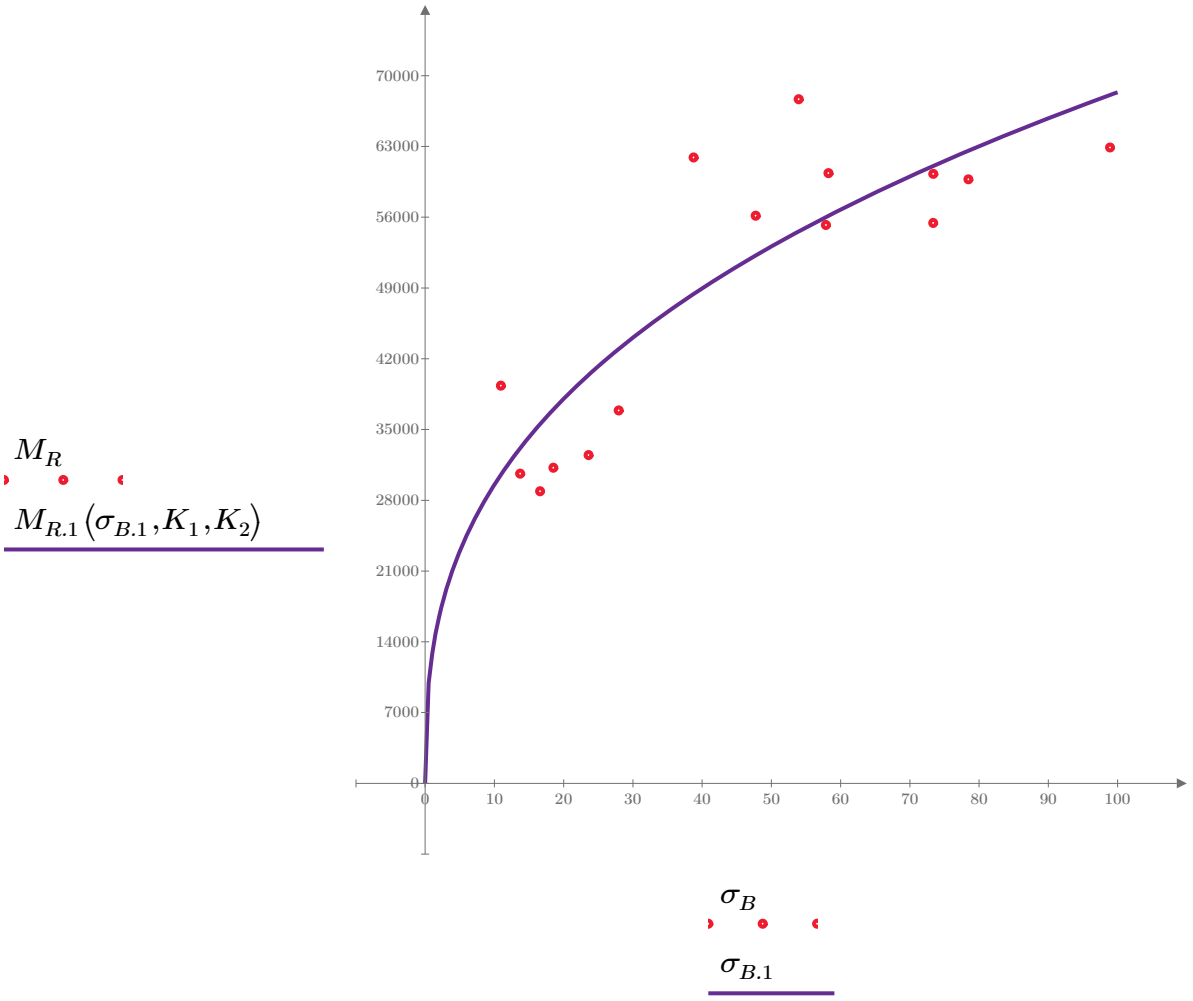

Figure 1. Plot of the test data (red points) vs. the fitted Equation 1 model (purple line).

Dan Seely
9/12/2023

$$M_{R.2}(\sigma_d, K_3, K_4) := K_3 \cdot \sigma_d^{K_4}$$

Equation 2
AASHTO Publication No. FHWA-RD-97-083

$K_3 = 25224.051$

$K_4 = 0.2579$

Equation 2 fitting parameters

$R_2^2 = 0.3852$

Coefficient of determination

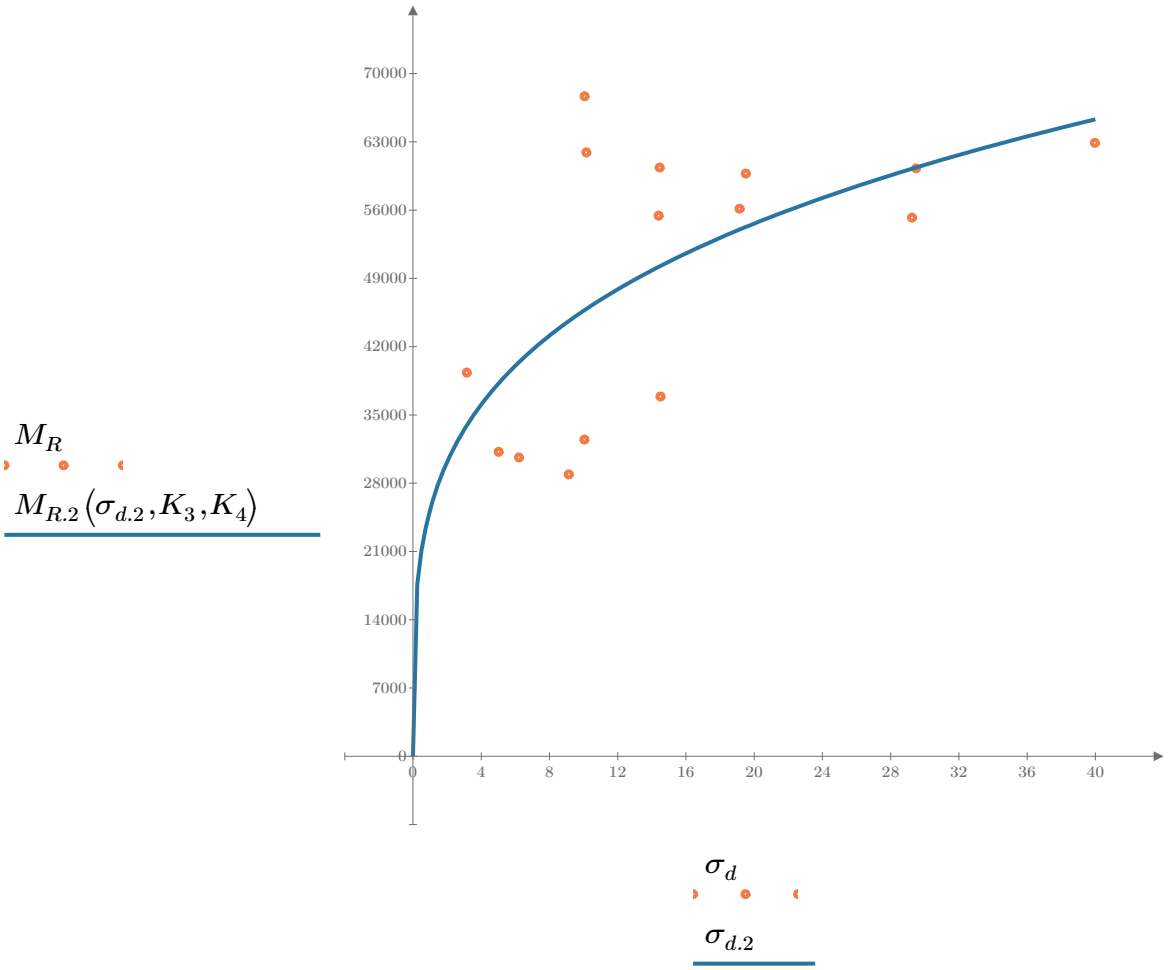

Figure 2. Plot of the test data (orange points) vs. the fitted Equation 2 model (blue line).

Dan Seely
9/12/2023

$$M_{R.3}\left(\sigma_d,\sigma_3,K_5,K_6,K_7\right):=K_5\cdot{\sigma_d}^{K_6}\cdot\left(1+\sigma_3\right)^{K_7}$$

Equation 3 AASHTO Publication No. FHWA-RD-97-083

$K_5=20695.090$

$K_6=-0.0077$ Equation 3 fitting parameters

$K_7=0.3868$

${R_3}^2=0.7907$ Coefficient of determination

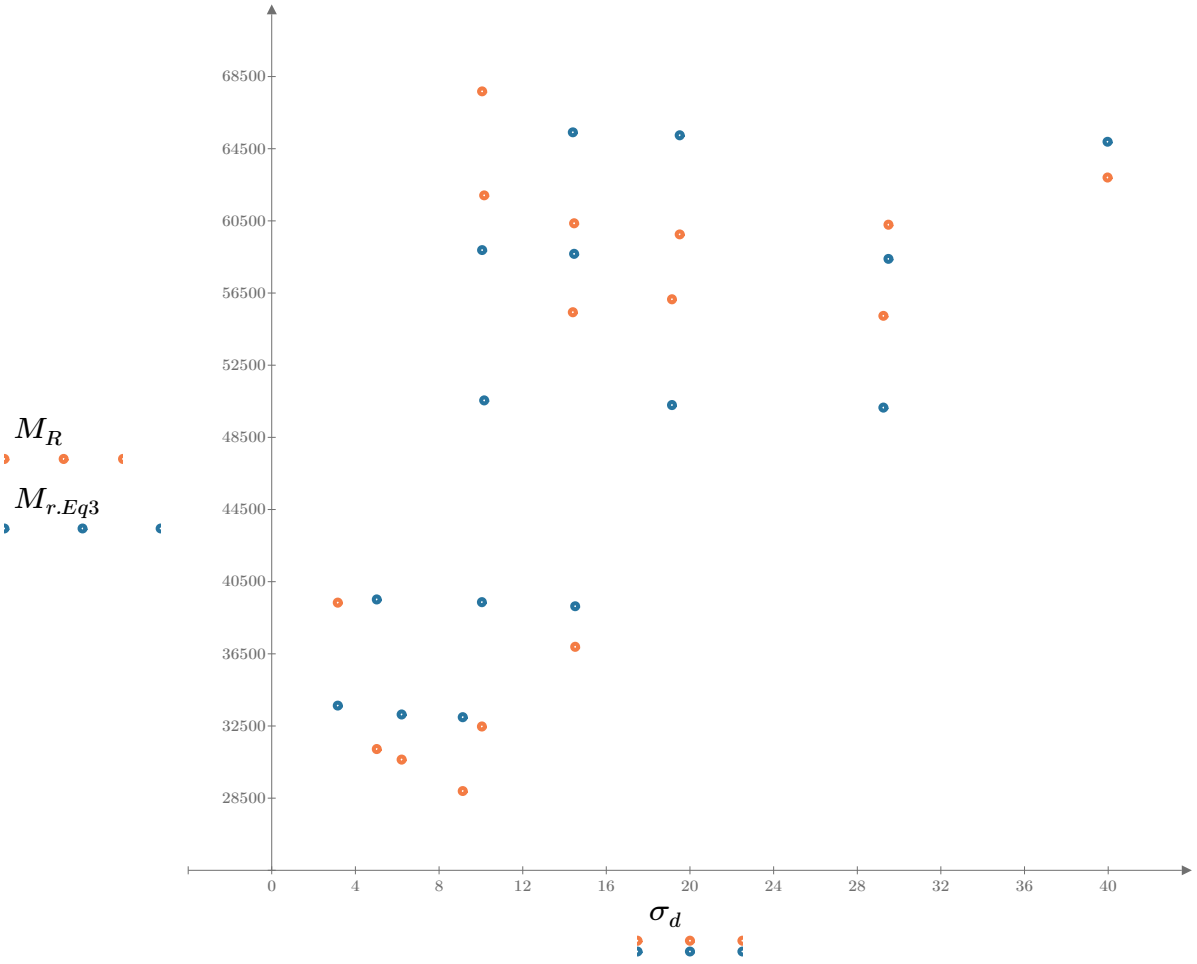

Figure 3. Plot of the test data (orange points) vs. the fitted Equation 3 model (blue points).

Dan Seely
9/12/2023

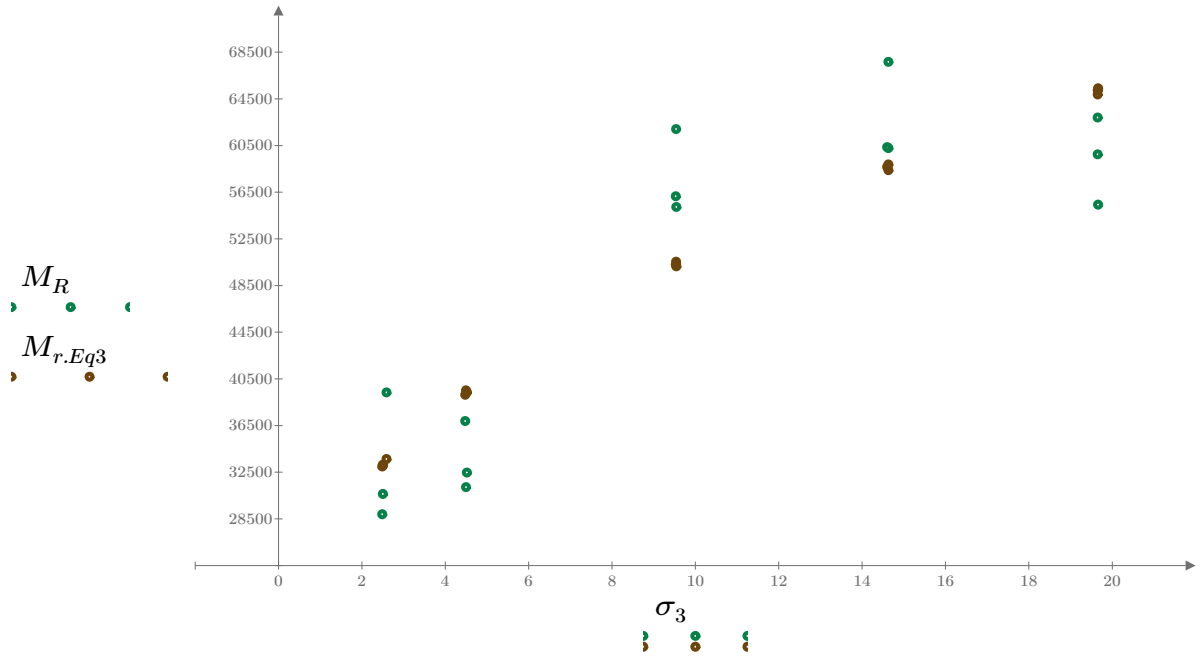

Figure 4. Plot of the test data (green points) vs. the fitted Equation 3 model (brown points).

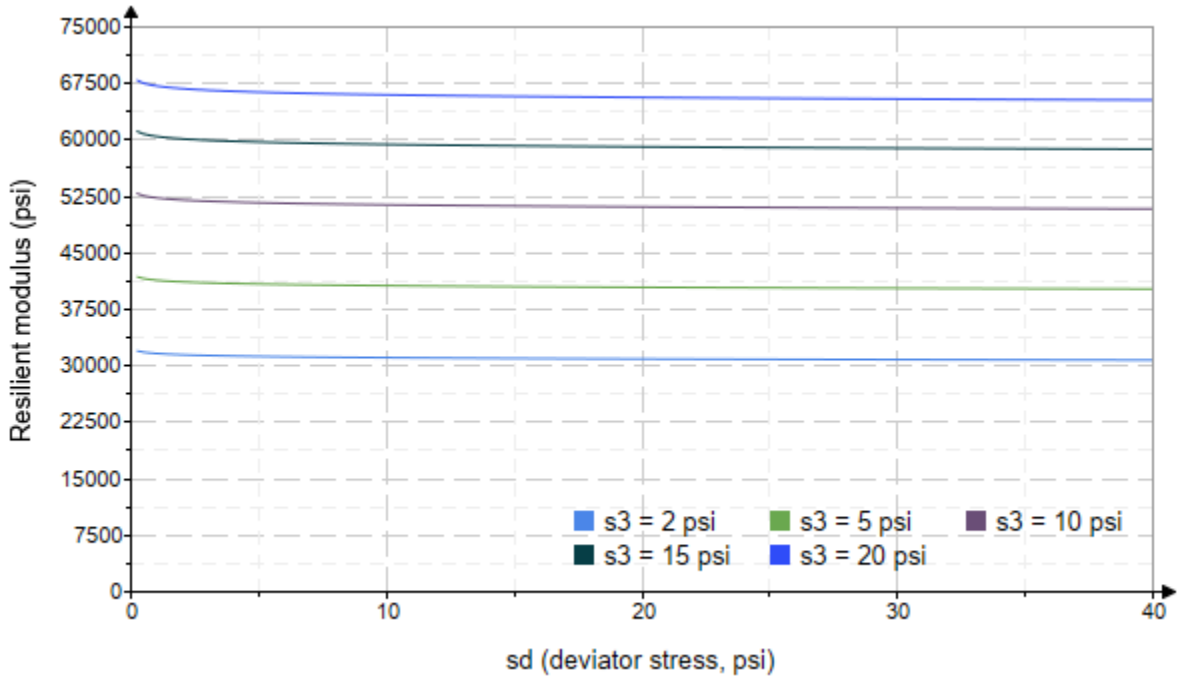

Figure 5. Plot of the fitted Equation 3 model for various confining stresses.

Dan Seely
9/12/2023

$$M_{R.4}\left(\sigma_B,\sigma_d,K_8,K_9,K_{10}\right) := K_8 \cdot p_a \left(\frac{\sigma_B}{p_a}\right)^{K_9} \cdot \left(\frac{\sigma_d}{p_a}\right)^{K_{10}}$$

Equation 4 AASHTO Publication No. FHWA-RD-97-083

$K_8 = 1951.689$

$K_9 = 0.5159$ Equation 4 fitting parameters

$K_{10} = -0.1814$

$R_4^{\,2} = 0.7953$ Coefficient of determination

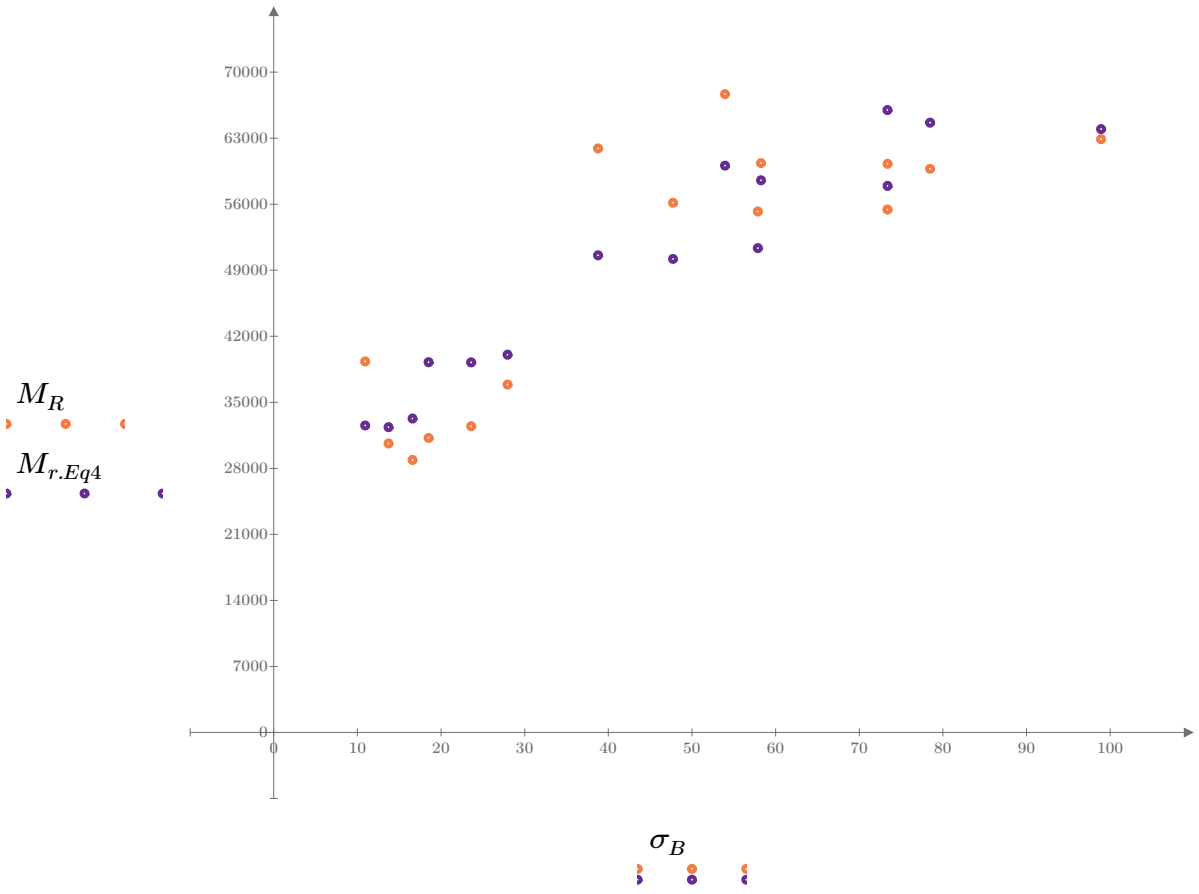

Figure 6. Plot of the test data (orange points) vs. the fitted Equation 4 model (purple points).

Dan Seely
9/12/2023

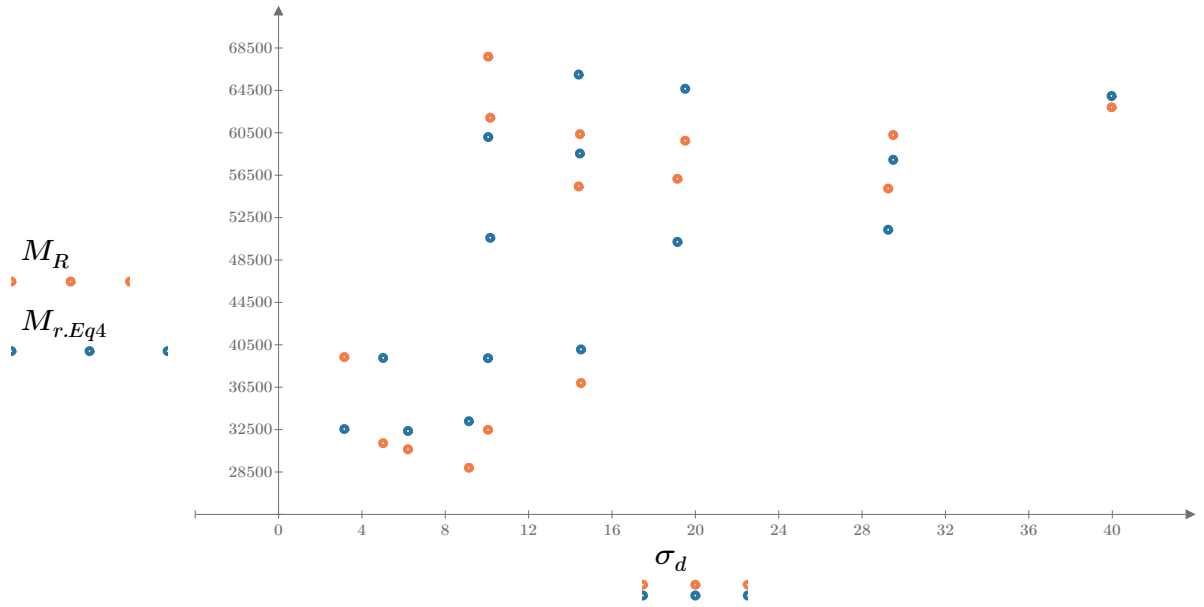

Figure 7. Plot of the test data (orange points) vs. the fitted Equation 4 model (blue points).

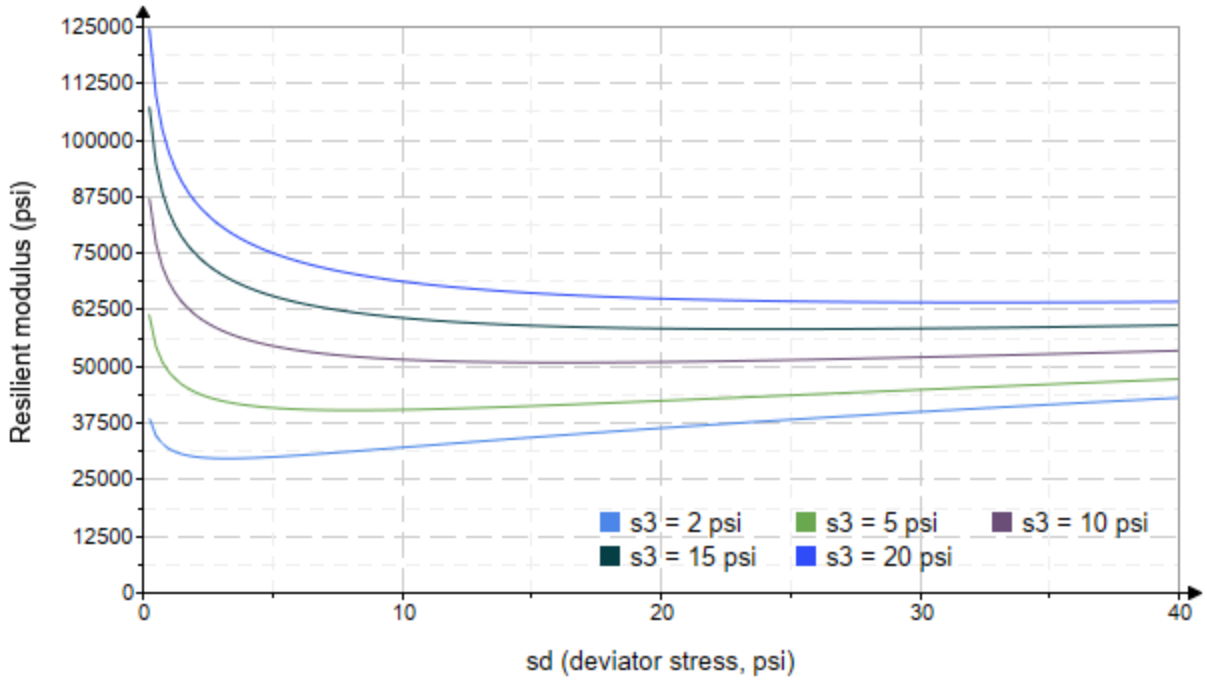

Figure 8. Plot of the fitted Equation 4 model for various confining stresses.

Dan Seely
9/12/2023

$SampleNo := \text{“B2–67”}$

$Treatment = \text{“D1”}$

$S = 17.547$ Degree of Saturation (%)

Test Sequence : Base/Subbase

Test summary data (psi) :

$$\sigma_3 = \begin{bmatrix} 2.587 \\ 2.603 \\ 2.602 \\ 4.641 \\ 4.623 \\ 4.582 \\ 9.664 \\ 9.641 \\ 9.582 \\ 14.590 \\ 14.610 \\ 14.570 \\ 19.600 \\ 19.610 \\ 19.610 \end{bmatrix} \quad \sigma_d = \begin{bmatrix} 3.115 \\ 6.081 \\ 9.084 \\ 5.087 \\ 10.030 \\ 14.650 \\ 10.050 \\ 19.360 \\ 29.560 \\ 9.844 \\ 14.380 \\ 29.840 \\ 14.460 \\ 19.560 \\ 40.190 \end{bmatrix} \quad \sigma_B = \begin{bmatrix} 10.880 \\ 13.890 \\ 16.890 \\ 19.010 \\ 23.900 \\ 28.390 \\ 39.040 \\ 48.280 \\ 58.310 \\ 53.620 \\ 58.210 \\ 73.550 \\ 73.260 \\ 78.390 \\ 99.010 \end{bmatrix} \quad M_R = \begin{bmatrix} 60856.0 \\ 31357.6 \\ 26111.0 \\ 27987.2 \\ 29863.4 \\ 29161.0 \\ 69331.6 \\ 47711.4 \\ 43250.0 \\ 90911.6 \\ 58780.0 \\ 59931.8 \\ 80991.2 \\ 73880.4 \\ 53364.2 \end{bmatrix}$$

σ_3 = mean confining stress
σ_d = mean deviator stress
σ_B = mean bulk stress
M_R = resilient modulus
p_a = atmospheric pressure = 14.6959 psi

Dan Seely
9/12/2023

$$M_{R.1}\left(\sigma_B, K_1, K_2\right) := K_1 \cdot {\sigma_B}^{K_2}$$

Equation 1
AASHTO Publication No. FHWA-RD-97-083

$K_1 = 13875.191$

$K_2 = 0.3569$

Equation 1 fitting parameters

${R_1}^2 = 0.3441$

Coefficient of determination

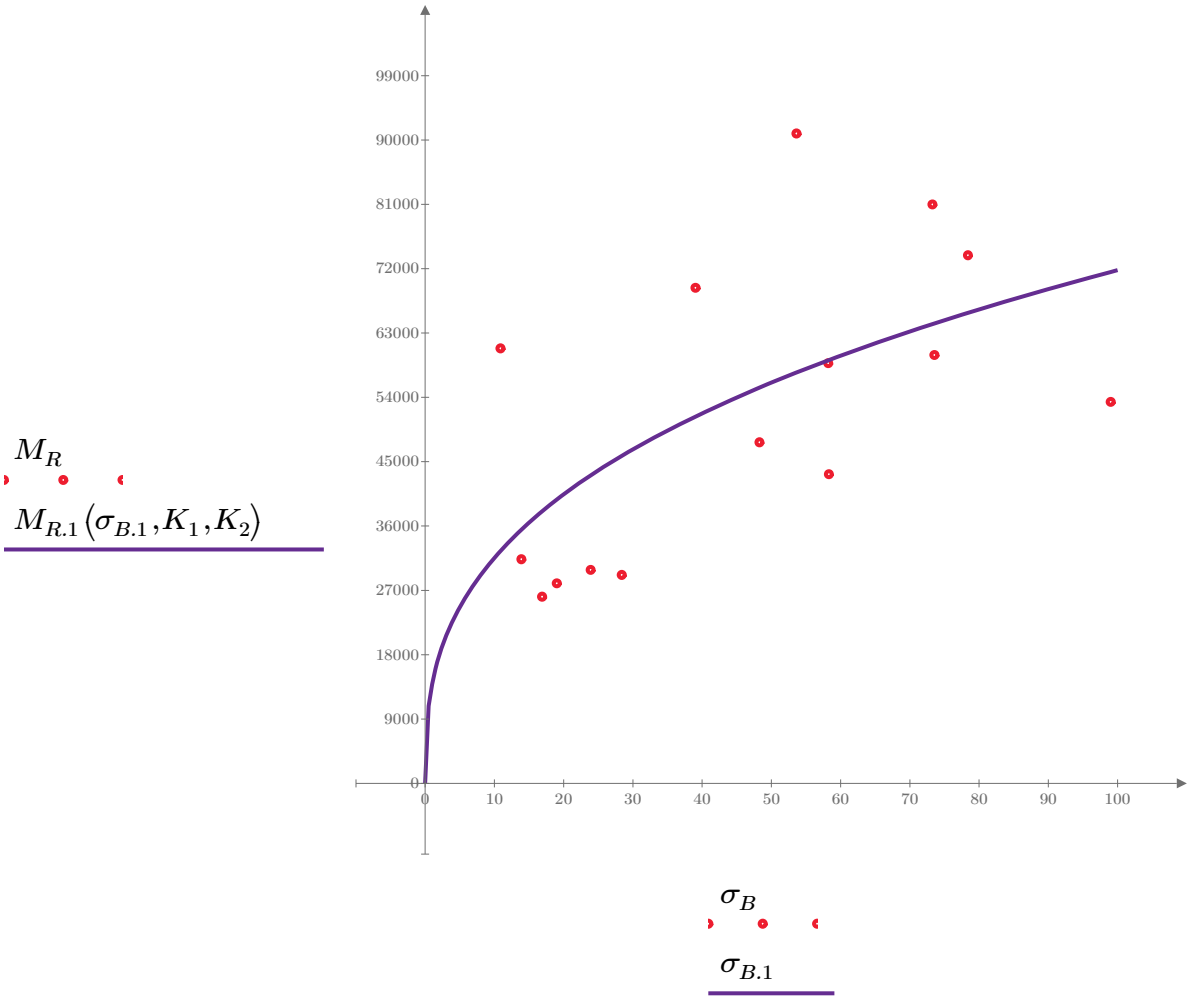

Figure 1. Plot of the test data (red points) vs. the fitted Equation 1 model (purple line).

Dan Seely
9/12/2023

$$M_{R.2}(\sigma_d, K_3, K_4) := K_3 \cdot \sigma_d^{K_4}$$

Equation 2
AASHTO Publication No. FHWA-RD-97-083

$K_3 = 40898.498$

$K_4 = 0.0955$

Equation 2 fitting parameters

$R_2^2 = 0.0281$

Coefficient of determination

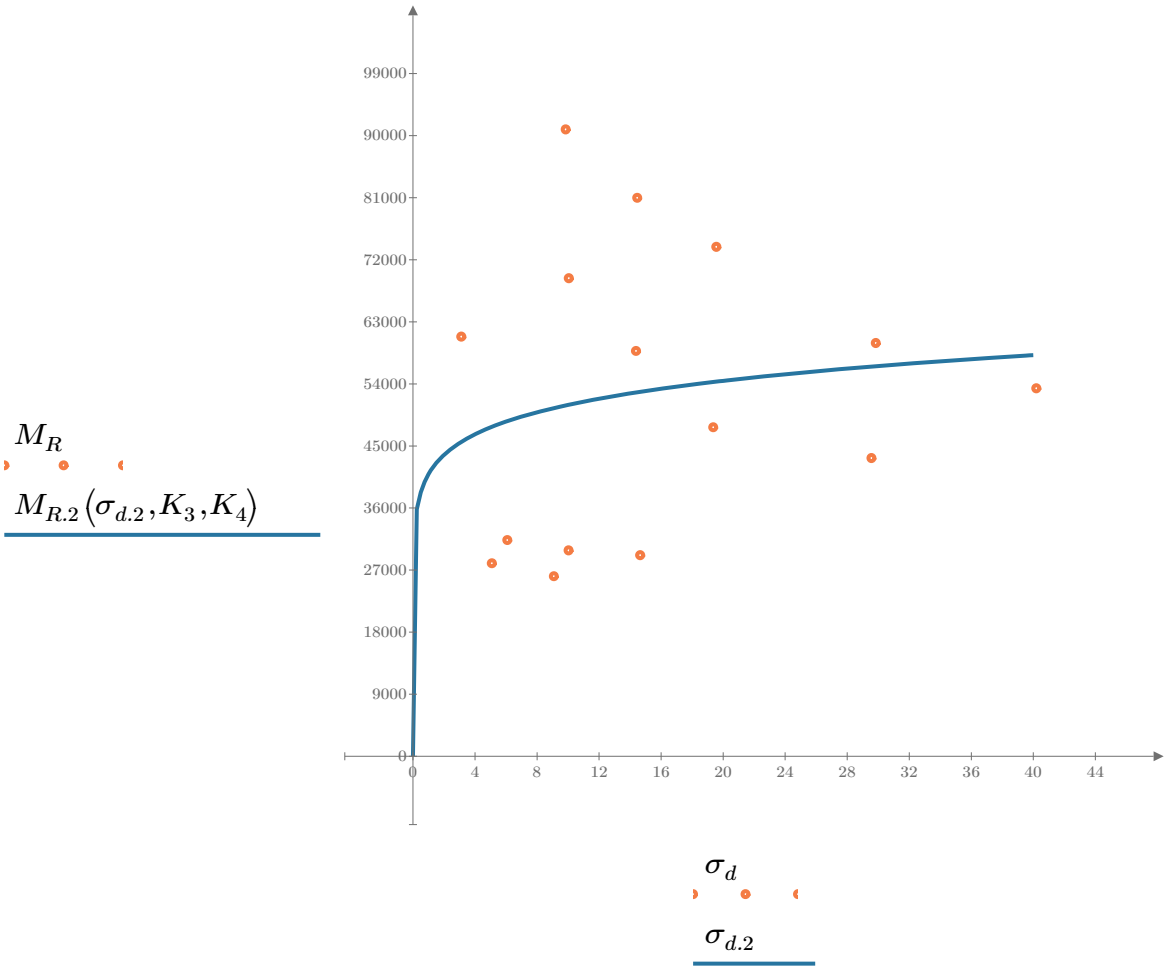

Figure 2. Plot of the test data (orange points) vs. the fitted Equation 2 model (blue line).

Dan Seely
9/12/2023

$$M_{R.3}\left(\sigma_d,\sigma_3,K_5,K_6,K_7\right):=K_5\cdot{\sigma_d}^{K_6}\cdot\left(1+\sigma_3\right)^{K_7}$$

Equation 3 AASHTO Publication No. FHWA-RD-97-083

$K_5=26669.590$

$K_6=-0.4234$ Equation 3 fitting parameters

$K_7=0.7584$

${R_3}^2=0.7930$ Coefficient of determination

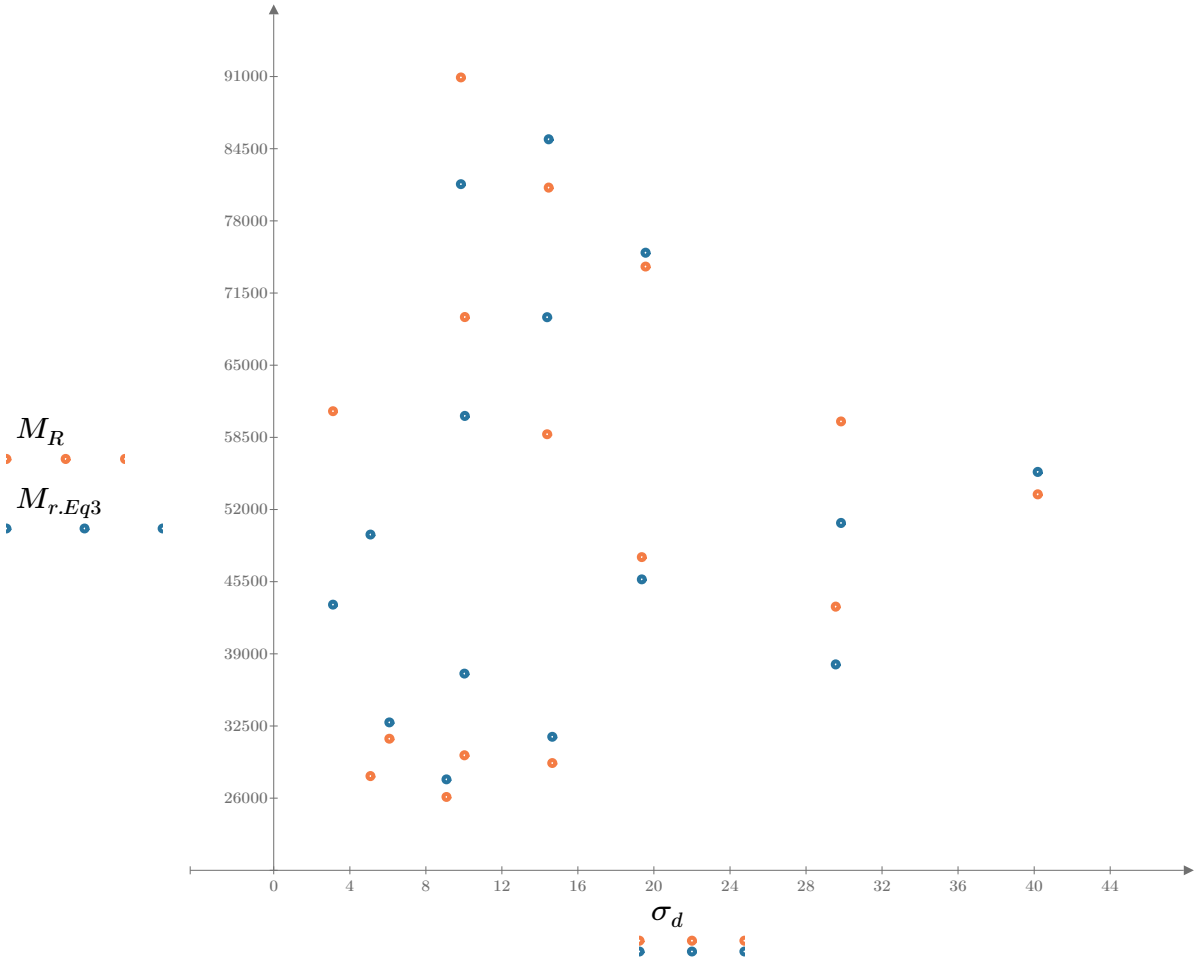

Figure 3. Plot of the test data (orange points) vs. the fitted Equation 3 model (blue points).

Dan Seely
9/12/2023

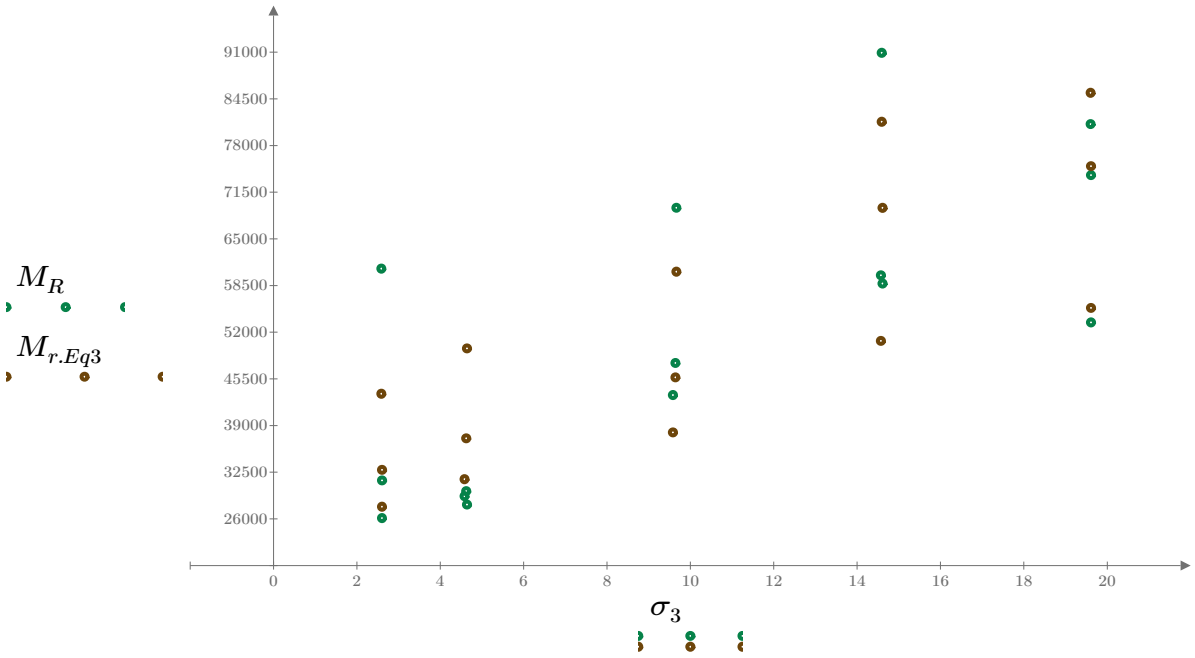

Figure 4. Plot of the test data (green points) vs. the fitted Equation 3 model (brown points).

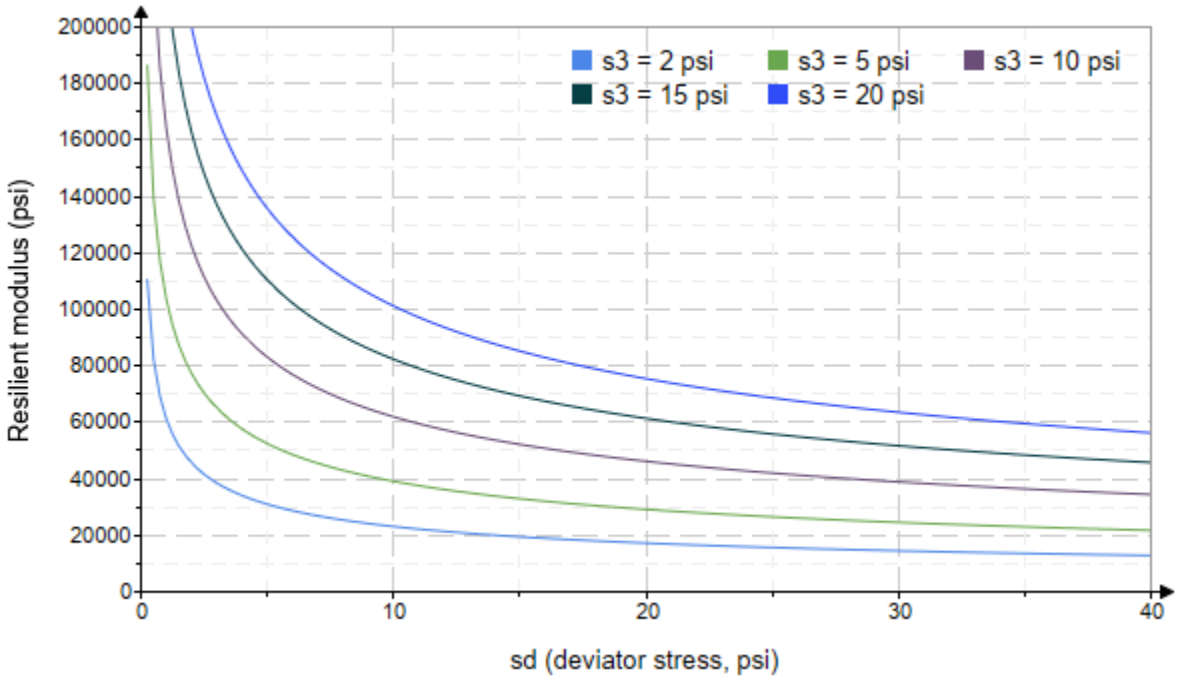

Figure 5. Plot of the fitted Equation 3 model for various confining stresses.

Dan Seely
9/12/2023

$$M_{R.4}\left(\sigma_B,\sigma_d,K_8,K_9,K_{10}\right) := K_8 \cdot p_a \left(\frac{\sigma_B}{p_a}\right)^{K_9} \cdot \left(\frac{\sigma_d}{p_a}\right)^{K_{10}}$$

Equation 4 AASHTO Publication No. FHWA-RD-97-083

$K_8 = 1189.254$

$K_9 = 0.9822$ Equation 4 fitting parameters

$K_{10} = -0.7392$

$R_4^{\,2} = 0.7894$ Coefficient of determination

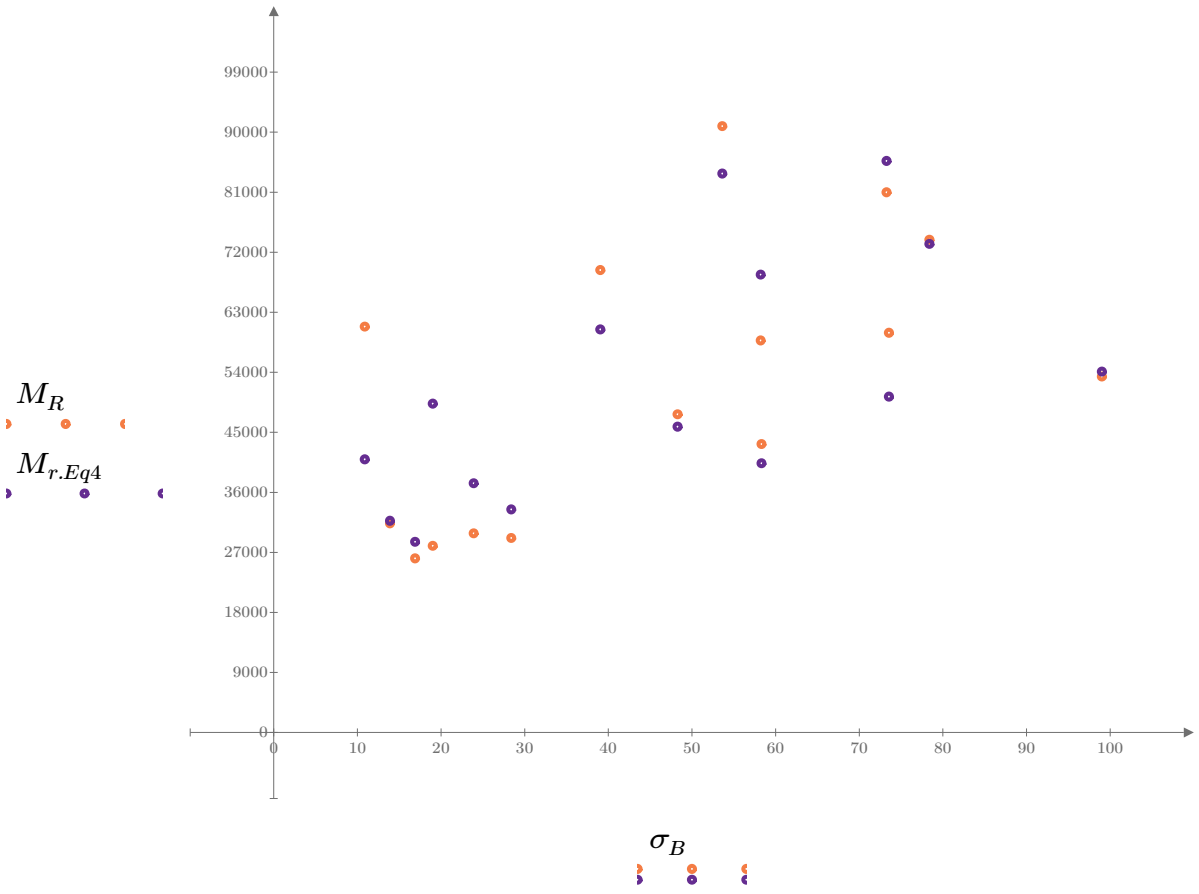

Figure 6. Plot of the test data (orange points) vs. the fitted Equation 4 model (purple points).

Dan Seely
9/12/2023

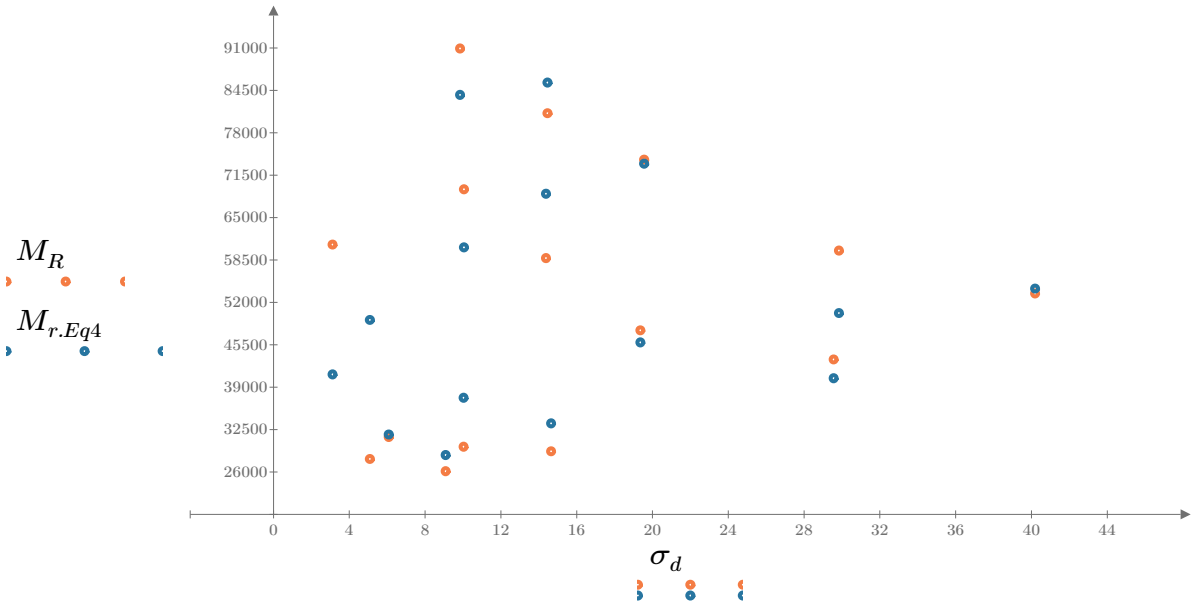

Figure 7. Plot of the test data (orange points) vs. the fitted Equation 4 model (blue points).

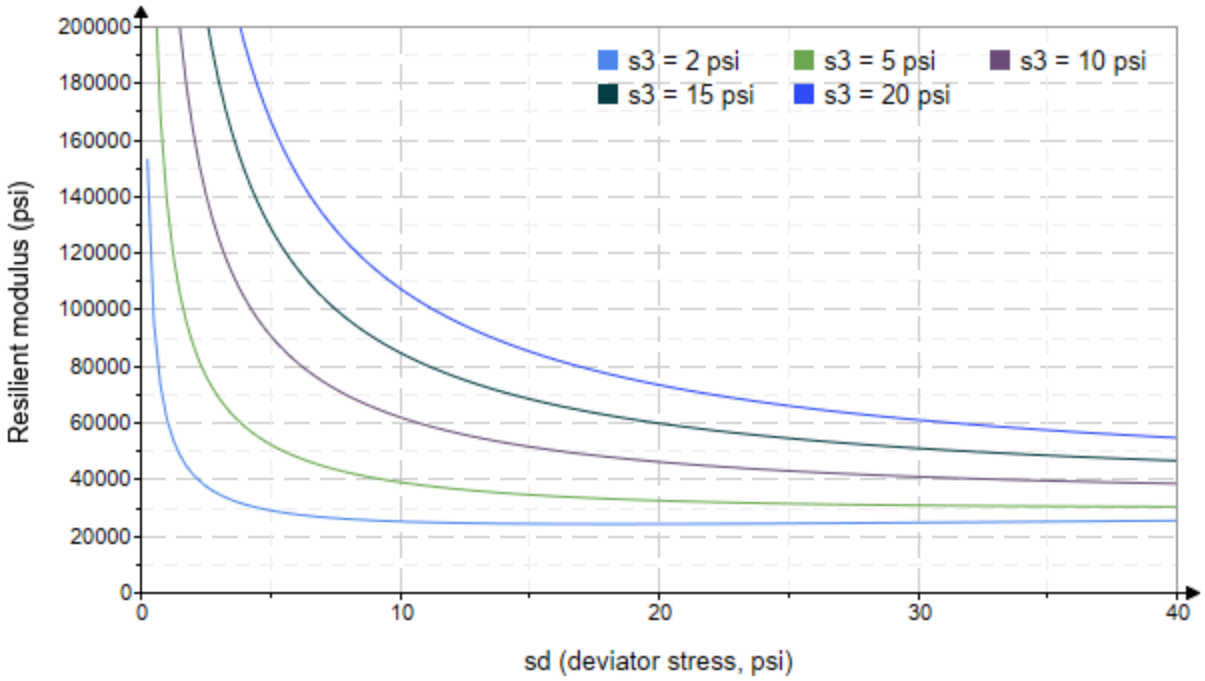

Figure 8. Plot of the fitted Equation 4 model for various confining stresses.

Dan Seely
9/12/2023

$SampleNo := \text{“B2–68”}$

$Treatment = \text{“W1”}$

$S = 17.781$ Degree of Saturation (%)

Test Sequence : Base/Subbase

Test summary data (psi) :

$$\sigma_3 = \begin{bmatrix} 2.857 \\ 2.865 \\ 2.677 \\ 4.615 \\ 4.638 \\ 4.595 \\ 9.653 \\ 9.599 \\ 9.626 \\ 14.630 \\ 14.620 \\ 14.650 \\ 19.630 \\ 19.670 \\ 19.670 \end{bmatrix} \quad \sigma_d = \begin{bmatrix} 3.145 \\ 6.069 \\ 9.075 \\ 5.214 \\ 10.040 \\ 14.620 \\ 10.090 \\ 19.270 \\ 29.110 \\ 10.280 \\ 14.540 \\ 29.300 \\ 14.580 \\ 19.360 \\ 39.720 \end{bmatrix} \quad \sigma_B = \begin{bmatrix} 11.720 \\ 14.660 \\ 17.110 \\ 19.060 \\ 23.950 \\ 28.400 \\ 39.050 \\ 48.070 \\ 57.990 \\ 54.180 \\ 58.410 \\ 73.270 \\ 73.470 \\ 78.360 \\ 98.710 \end{bmatrix} \quad M_R = \begin{bmatrix} 31701.4 \\ 32391.2 \\ 31721.8 \\ 57206.4 \\ 41539.8 \\ 42078.6 \\ 58614.8 \\ 49536.4 \\ 49642.2 \\ 77194.6 \\ 62634.2 \\ 56159.8 \\ 75238.6 \\ 65912.0 \\ 59838.2 \end{bmatrix}$$

σ_3 = mean confining stress
σ_d = mean deviator stress
σ_B = mean bulk stress
M_R = resilient modulus
p_a = atmospheric pressure = 14.6959 psi

Dan Seely
9/12/2023

$$M_{R.1}\left(\sigma_B, K_1, K_2\right) := K_1 \cdot {\sigma_B}^{K_2}$$

Equation 1
AASHTO Publication No. FHWA-RD-97-083

$K_1 = 16055.255$

$K_2 = 0.3208$

Equation 1 fitting parameters

${R_1}^2 = 0.5910$

Coefficient of determination

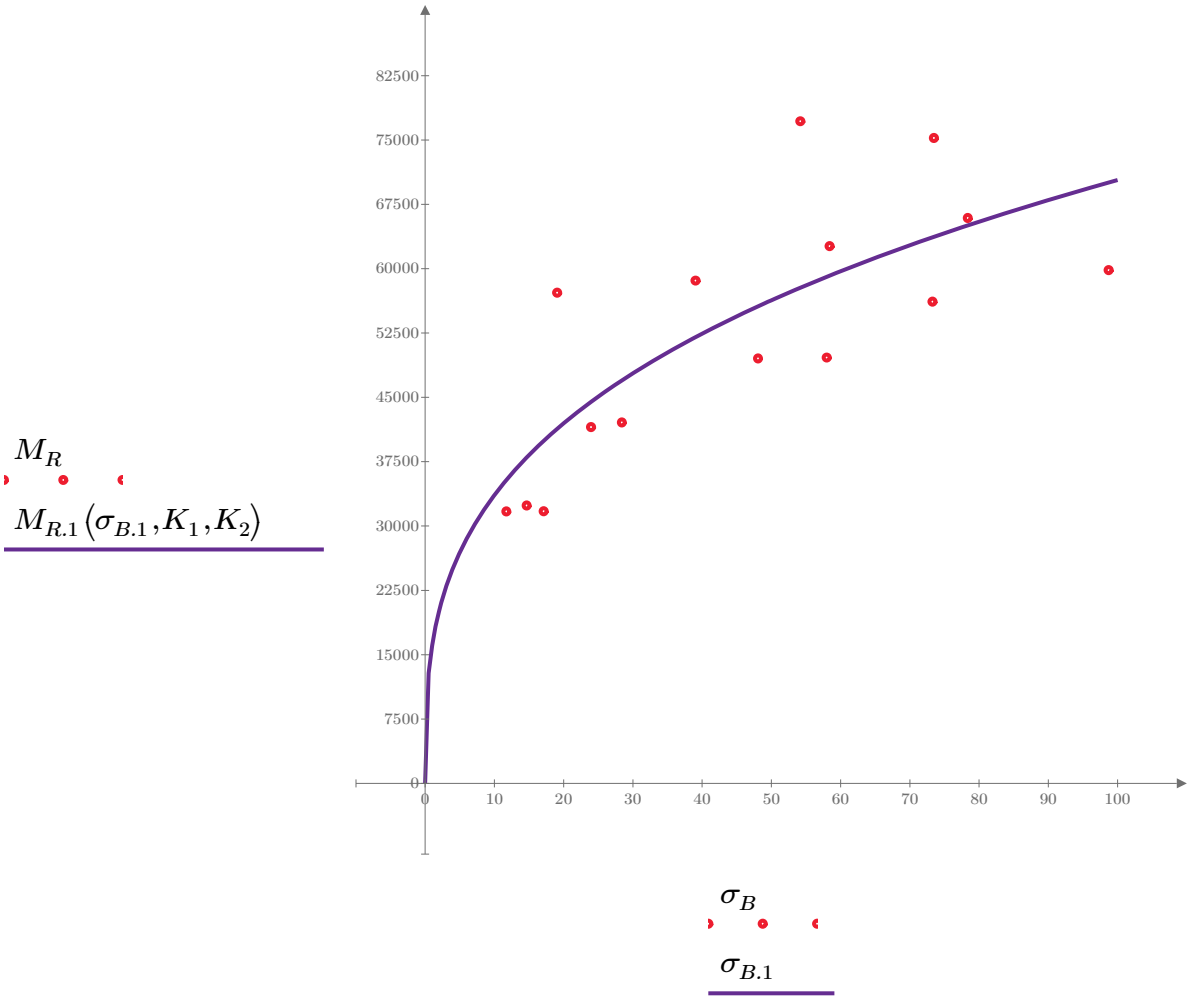

Figure 1. Plot of the test data (red points) vs. the fitted Equation 1 model (purple line).

Dan Seely
9/12/2023

$$M_{R.2}\left(\sigma_d, K_3, K_4\right) := K_3 \cdot {\sigma_d}^{K_4}$$

Equation 2
AASHTO Publication No. FHWA-RD-97-083

$K_3 = 35246.863$

$K_4 = 0.1567$

Equation 2 fitting parameters

${R_2}^2 = 0.1591$

Coefficient of determination

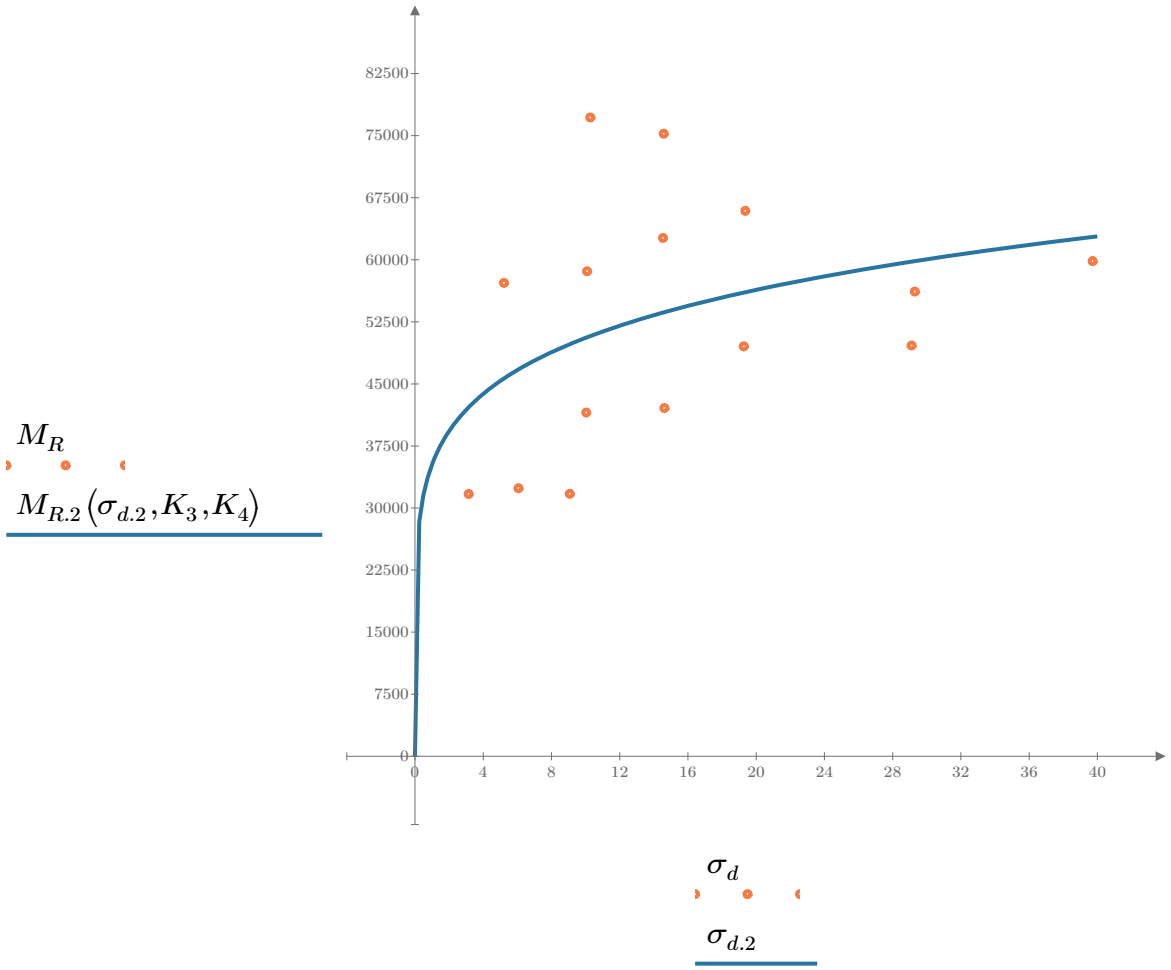

Figure 2. Plot of the test data (orange points) vs. the fitted Equation 2 model (blue line).

Dan Seely
9/12/2023

$$M_{R.3}\left(\sigma_d,\sigma_3,K_5,K_6,K_7\right):=K_5\cdot{\sigma_d}^{K_6}\cdot\left(1+\sigma_3\right)^{K_7}$$

Equation 3 AASHTO Publication No. FHWA-RD-97-083

$K_5=26004.577$

$K_6=-0.2041$ Equation 3 fitting parameters

$K_7=0.5333$

${R_3}^2=0.8771$ Coefficient of determination

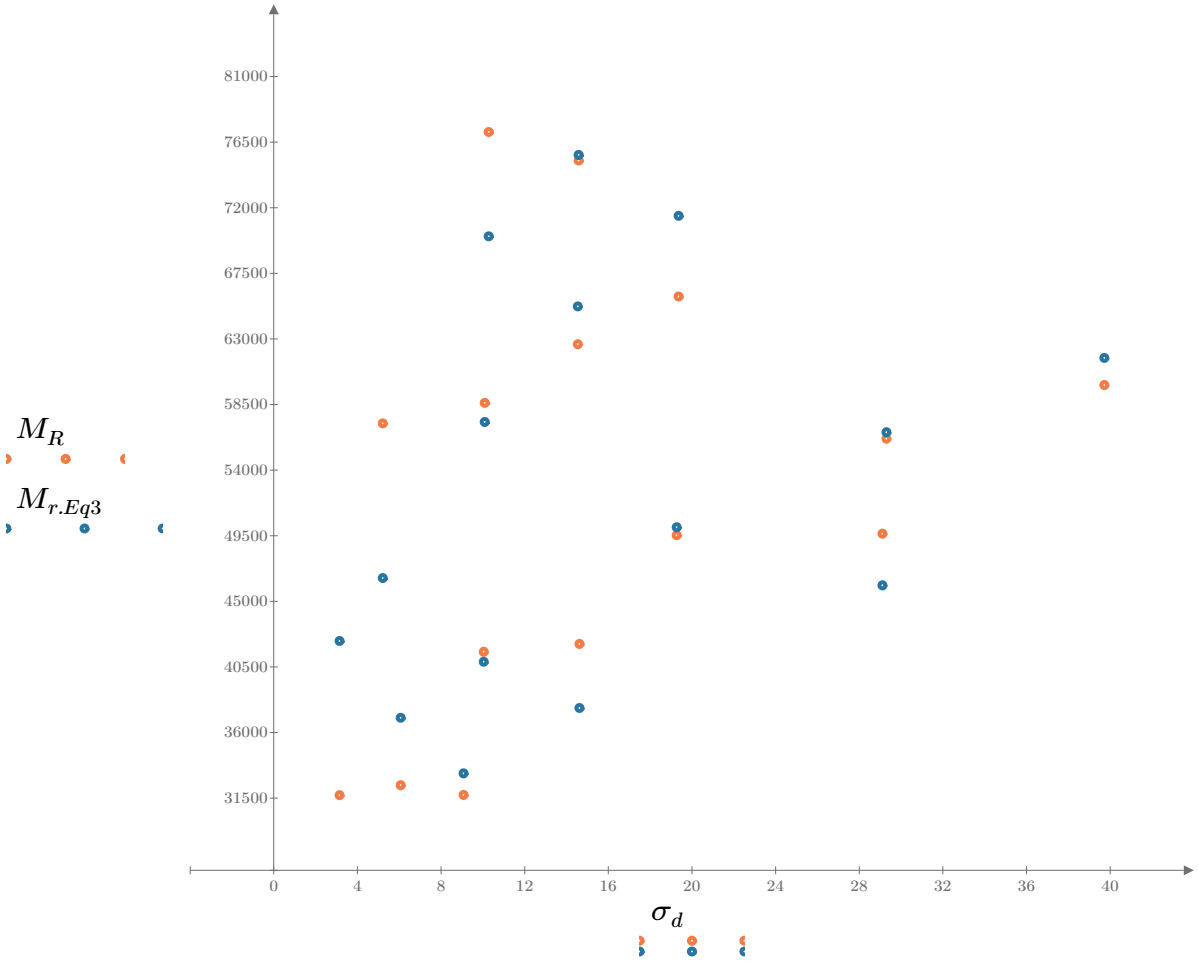

Figure 3. Plot of the test data (orange points) vs. the fitted Equation 3 model (blue points).

Dan Seely
9/12/2023

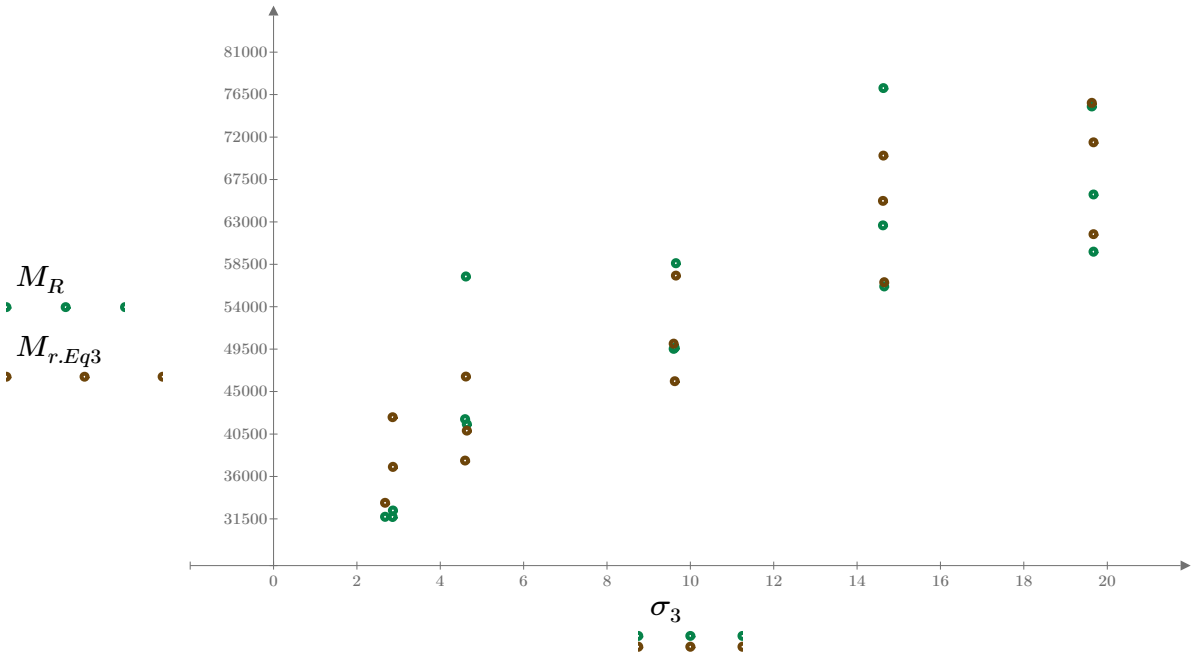

Figure 4. Plot of the test data (green points) vs. the fitted Equation 3 model (brown points).

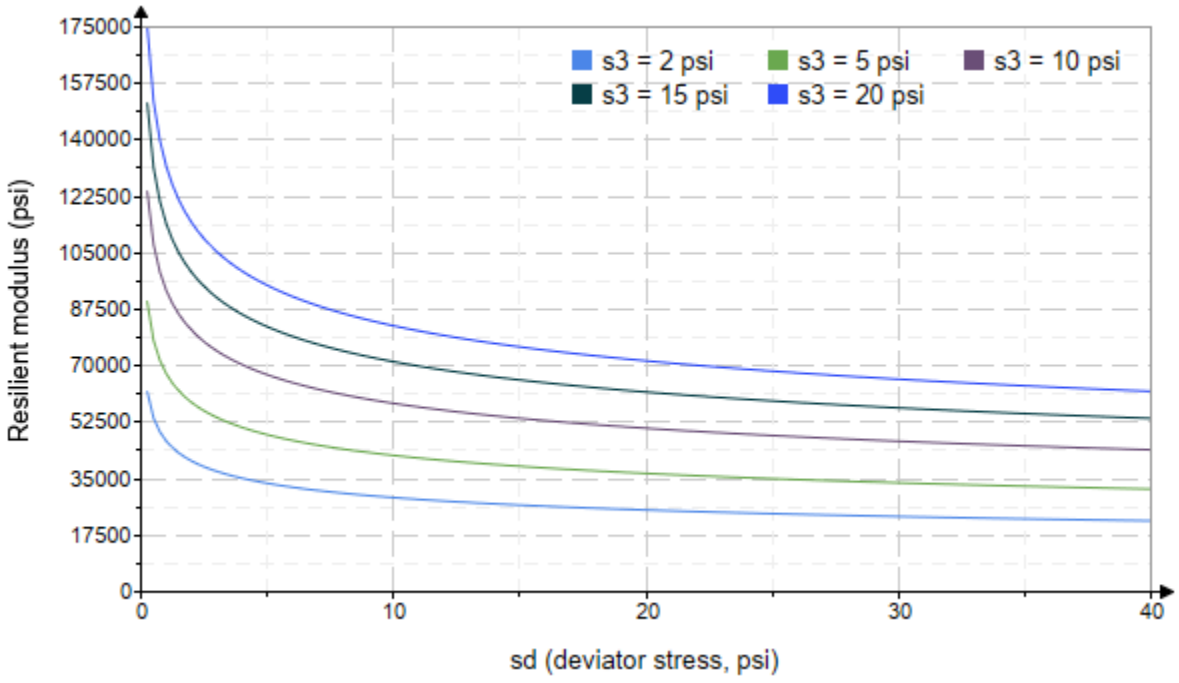

Figure 5. Plot of the fitted Equation 3 model for various confining stresses.

Dan Seely
9/12/2023

$$M_{R.4}\left(\sigma_B,\sigma_d,K_8,K_9,K_{10}\right) := K_8 \cdot p_a \left(\frac{\sigma_B}{p_a}\right)^{K_9} \cdot \left(\frac{\sigma_d}{p_a}\right)^{K_{10}}$$

Equation 4 AASHTO Publication No. FHWA-RD-97-083

$K_8 = 1648.461$

$K_9 = 0.7128$ Equation 4 fitting parameters

$K_{10} = -0.4474$

$R_4^{\,2} = 0.9032$ Coefficient of determination

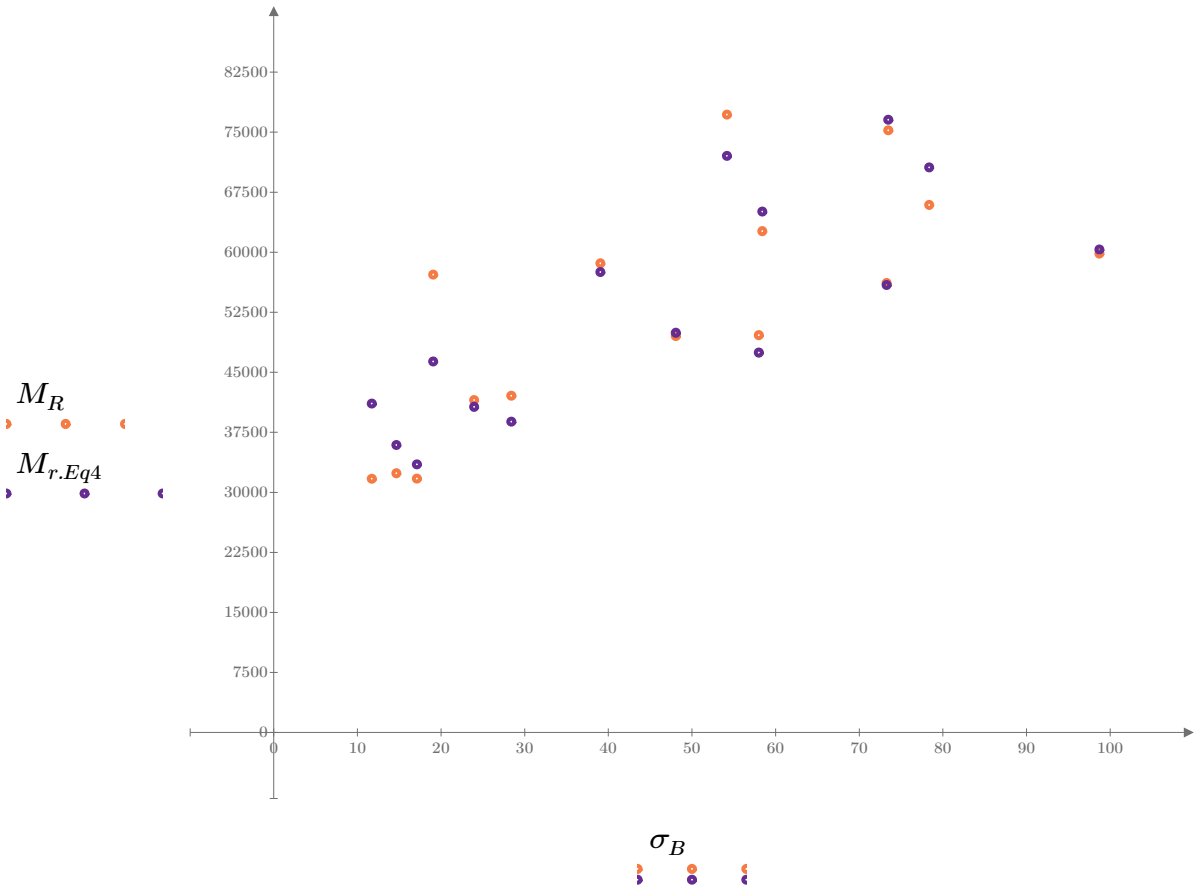

Figure 6. Plot of the test data (orange points) vs. the fitted Equation 4 model (purple points).

Dan Seely
9/12/2023

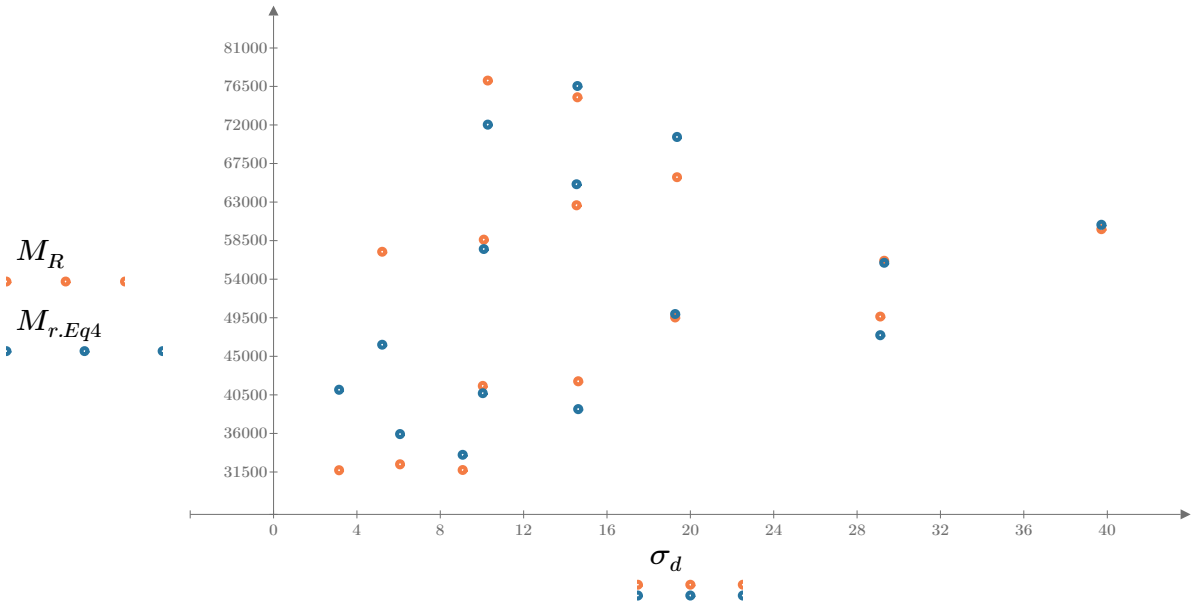

Figure 7. Plot of the test data (orange points) vs. the fitted Equation 4 model (blue points).

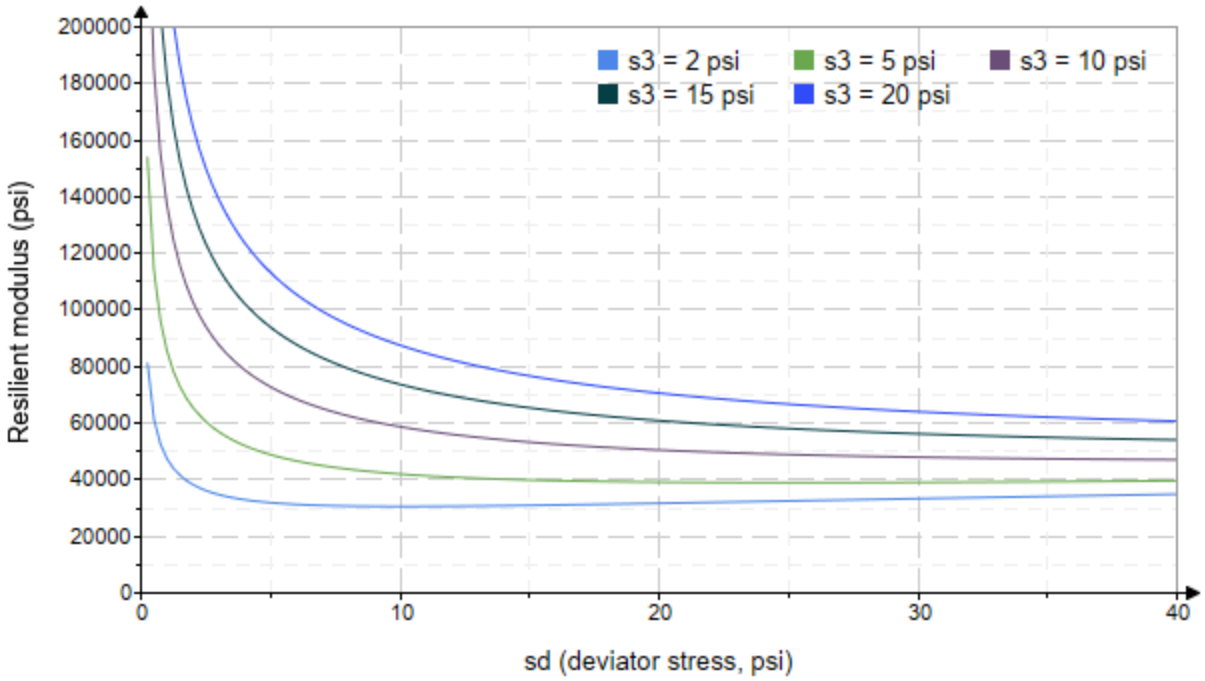

Figure 8. Plot of the fitted Equation 4 model for various confining stresses.

Dan Seely
9/12/2023

$SampleNo := \text{“B2}-\text{69”}$

$Treatment = \text{“W1”}$

$S = 18.503$ Degree of Saturation (%)

Test Sequence : Base/Subbase

Test summary data (psi) :

$$\sigma_3 = \begin{bmatrix} 2.322 \\ 1.935 \\ 2.266 \\ 3.954 \\ 4.222 \\ 4.264 \\ 9.465 \\ 8.992 \\ 8.864 \\ 15.120 \\ 14.240 \\ 14.500 \\ 19.140 \\ 19.040 \\ 19.400 \end{bmatrix} \quad \sigma_d = \begin{bmatrix} 3.390 \\ 6.060 \\ 9.045 \\ 5.382 \\ 9.981 \\ 14.380 \\ 9.908 \\ 19.460 \\ 29.500 \\ 10.070 \\ 14.380 \\ 29.640 \\ 14.580 \\ 19.570 \\ 39.910 \end{bmatrix} \quad \sigma_B = \begin{bmatrix} 10.350 \\ 11.860 \\ 15.840 \\ 17.240 \\ 22.650 \\ 27.170 \\ 38.300 \\ 46.440 \\ 56.090 \\ 55.420 \\ 57.100 \\ 73.150 \\ 72.010 \\ 76.680 \\ 98.100 \end{bmatrix} \quad M_R = \begin{bmatrix} 71820.6 \\ 49482.0 \\ 37849.0 \\ 49614.5 \\ 61380.0 \\ 45652.4 \\ 109965.6 \\ 54615.4 \\ 58759.2 \\ 96059.6 \\ 133360.0 \\ 81189.4 \\ 254558.0 \\ 157348.0 \\ 57492.4 \end{bmatrix}$$

σ_3 = mean confining stress
σ_d = mean deviator stress
σ_B = mean bulk stress
M_R = resilient modulus
p_a = atmospheric pressure = 14.6959 psi

Dan Seely
9/12/2023

$$M_{R.1}(\sigma_B, K_1, K_2) := K_1 \cdot {\sigma_B}^{K_2}$$

Equation 1
AASHTO Publication No. FHWA-RD-97-083

$K_1 = 14792.009$

$K_2 = 0.4811$

Equation 1 fitting parameters

${R_1}^2 = 0.2515$

Coefficient of determination

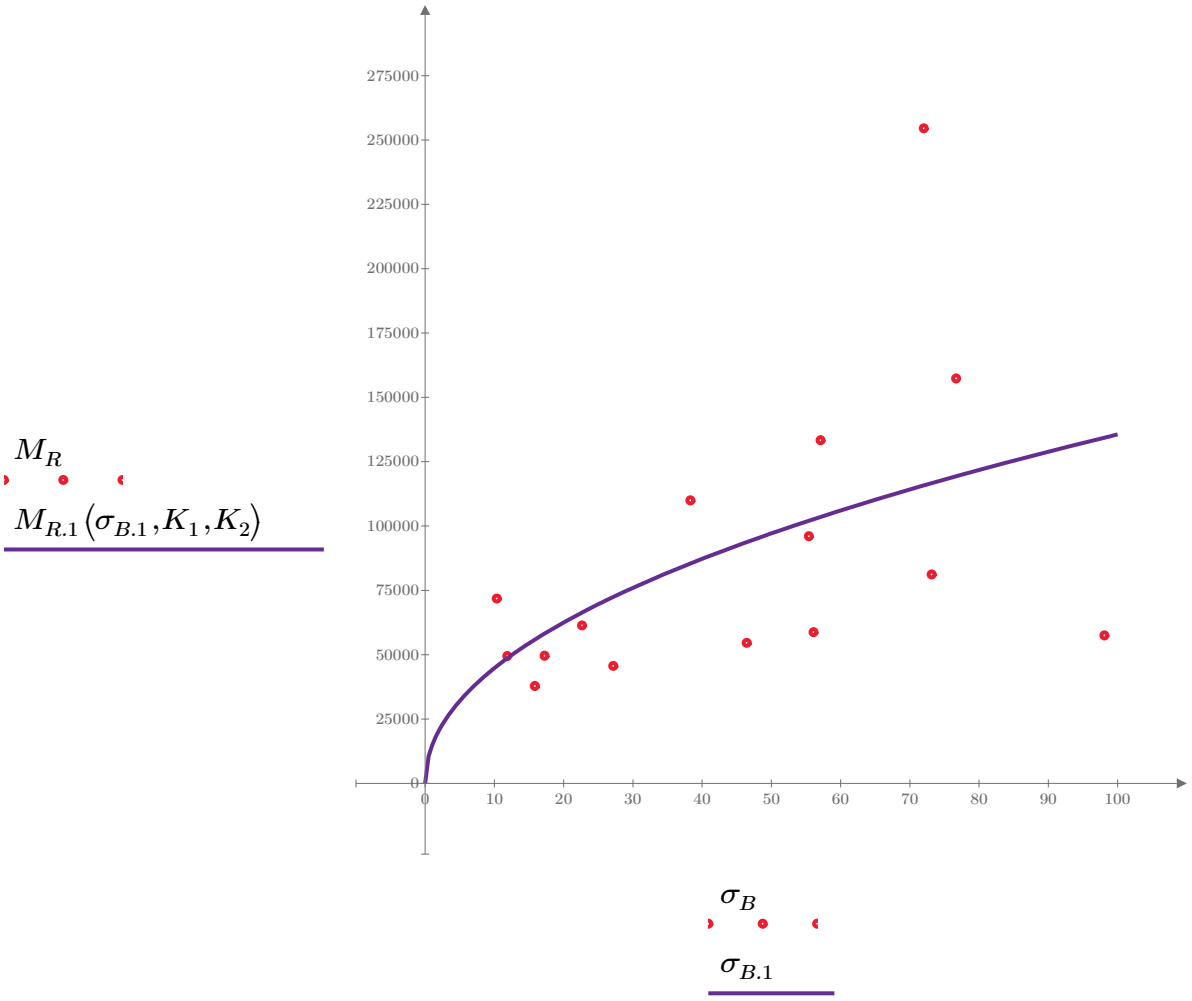

Figure 1. Plot of the test data (red points) vs. the fitted Equation 1 model (purple line).

Dan Seely
9/12/2023

$$M_{R.2}(\sigma_d, K_3, K_4) := K_3 \cdot \sigma_d^{K_4}$$

Equation 2
AASHTO Publication No. FHWA-RD-97-083

$K_3 = 67482.483$

$K_4 = 0.1032$

Equation 2 fitting parameters

$R_2^2 = 0.0144$

Coefficient of determination

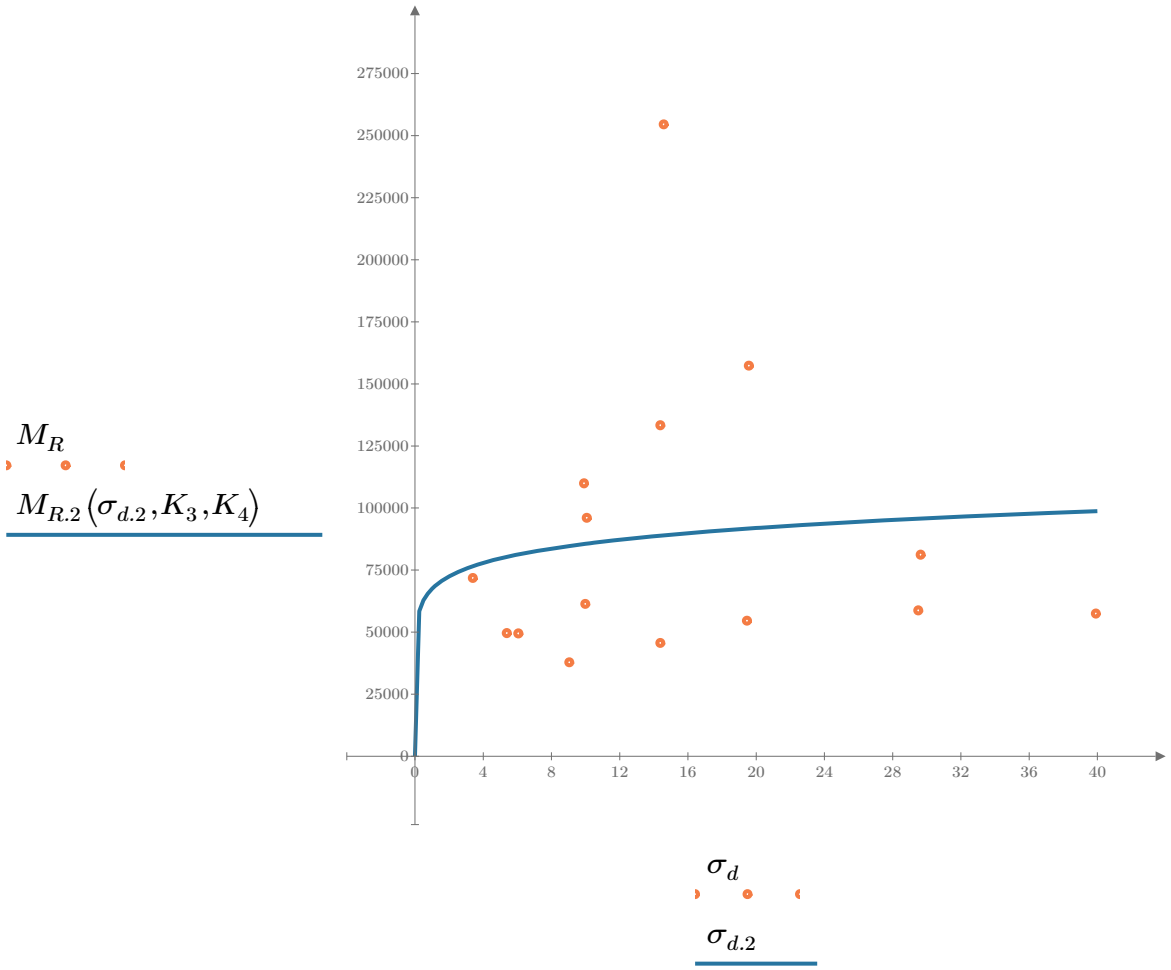

Figure 2. Plot of the test data (orange points) vs. the fitted Equation 2 model (blue line).

Dan Seely
9/12/2023

$$M_{R.3}\left(\sigma_d,\sigma_3,K_5,K_6,K_7\right):=K_5\cdot{\sigma_d}^{K_6}\cdot\left(1+\sigma_3\right)^{K_7}$$

Equation 3 AASHTO Publication No. FHWA-RD-97-083

$K_5=29745.993$

$K_6=-0.6115$ Equation 3 fitting parameters

$K_7=1.1394$

${R_3}^2=0.6820$ Coefficient of determination

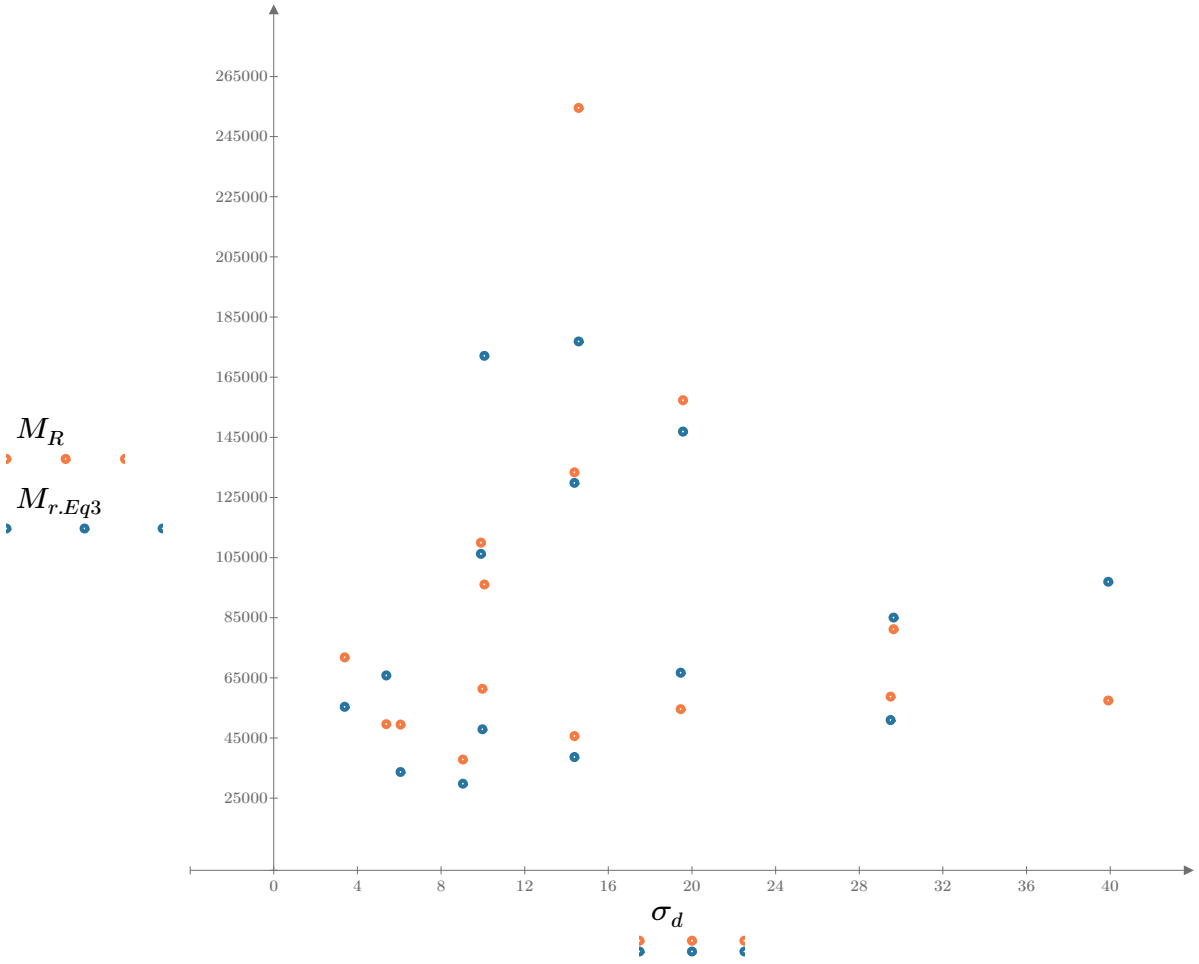

Figure 3. Plot of the test data (orange points) vs. the fitted Equation 3 model (blue points).

Dan Seely
9/12/2023

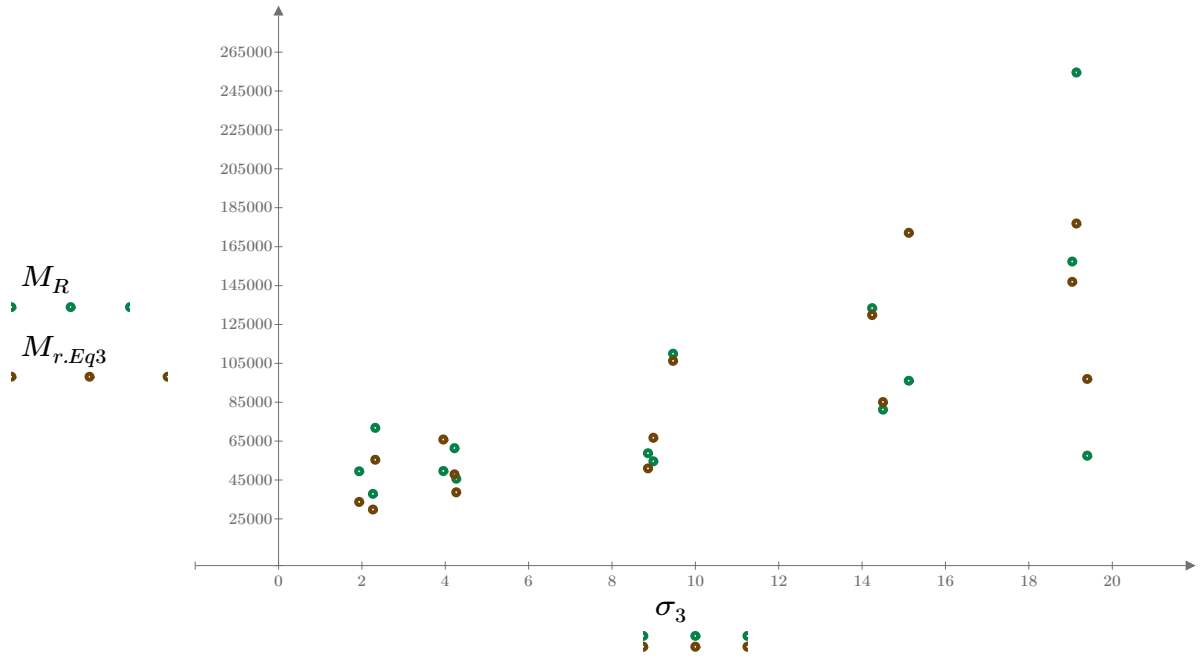

Figure 4. Plot of the test data (green points) vs. the fitted Equation 3 model (brown points).

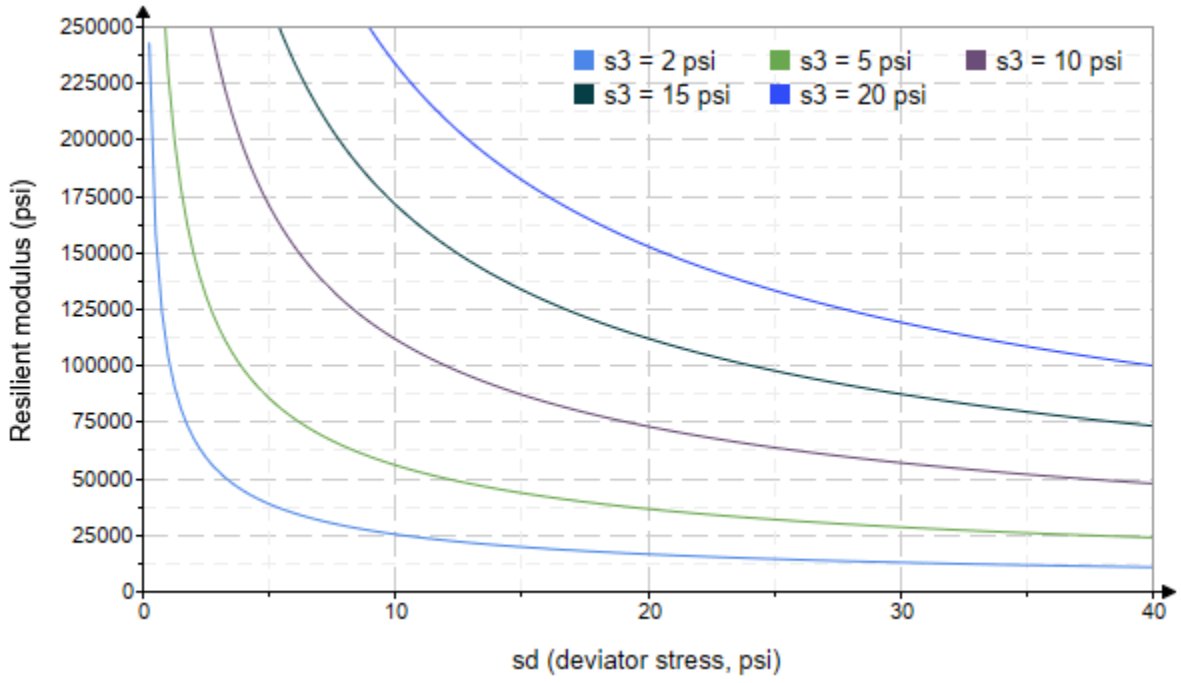

Figure 5. Plot of the fitted Equation 3 model for various confining stresses.

Dan Seely
9/12/2023

$$M_{R.4}\left(\sigma_B,\sigma_d,K_8,K_9,K_{10}\right) := K_8 \cdot p_a \left(\frac{\sigma_B}{p_a}\right)^{K_9} \cdot \left(\frac{\sigma_d}{p_a}\right)^{K_{10}}$$

Equation 4 AASHTO Publication No. FHWA-RD-97-083

$K_8 = 1241.035$

$K_9 = 1.4138$ Equation 4 fitting parameters

$K_{10} = -1.0273$

$R_4^{\,2} = 0.6560$ Coefficient of determination

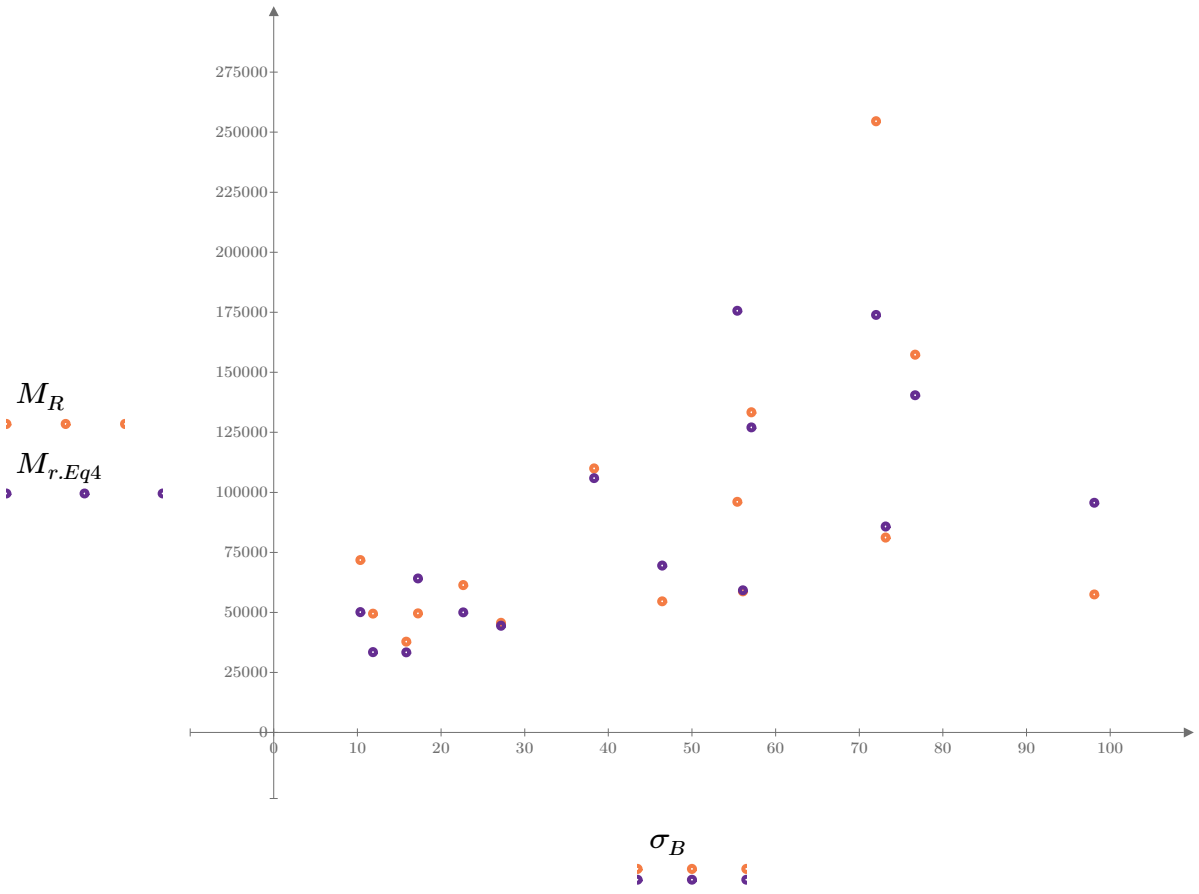

Figure 6. Plot of the test data (orange points) vs. the fitted Equation 4 model (purple points).

Dan Seely
9/12/2023

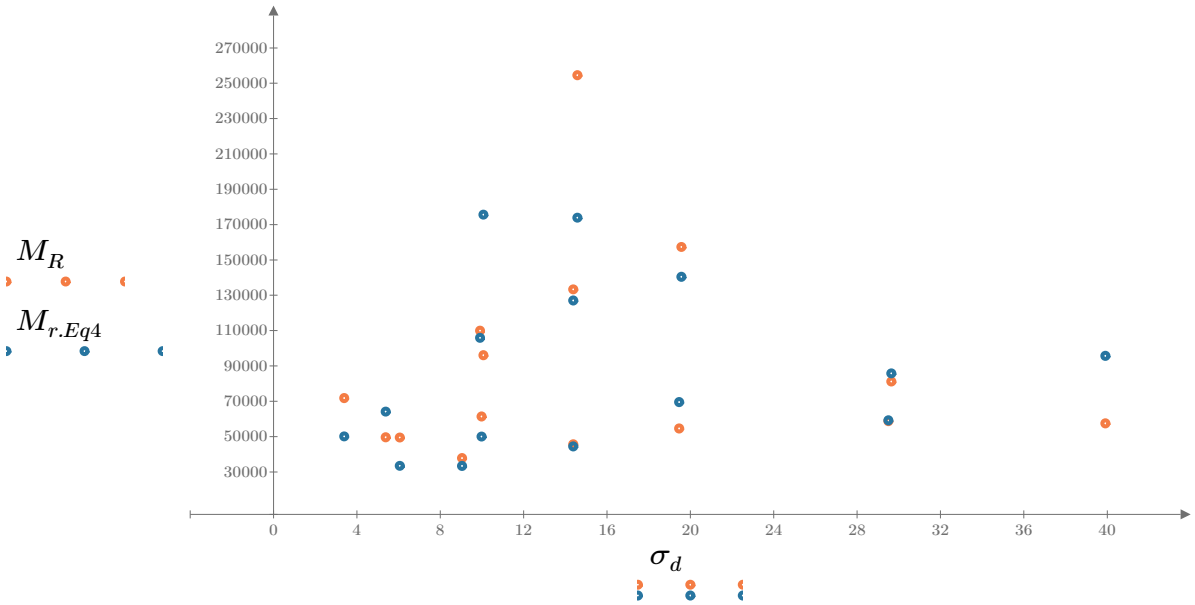

Figure 7. Plot of the test data (orange points) vs. the fitted Equation 4 model (blue points).

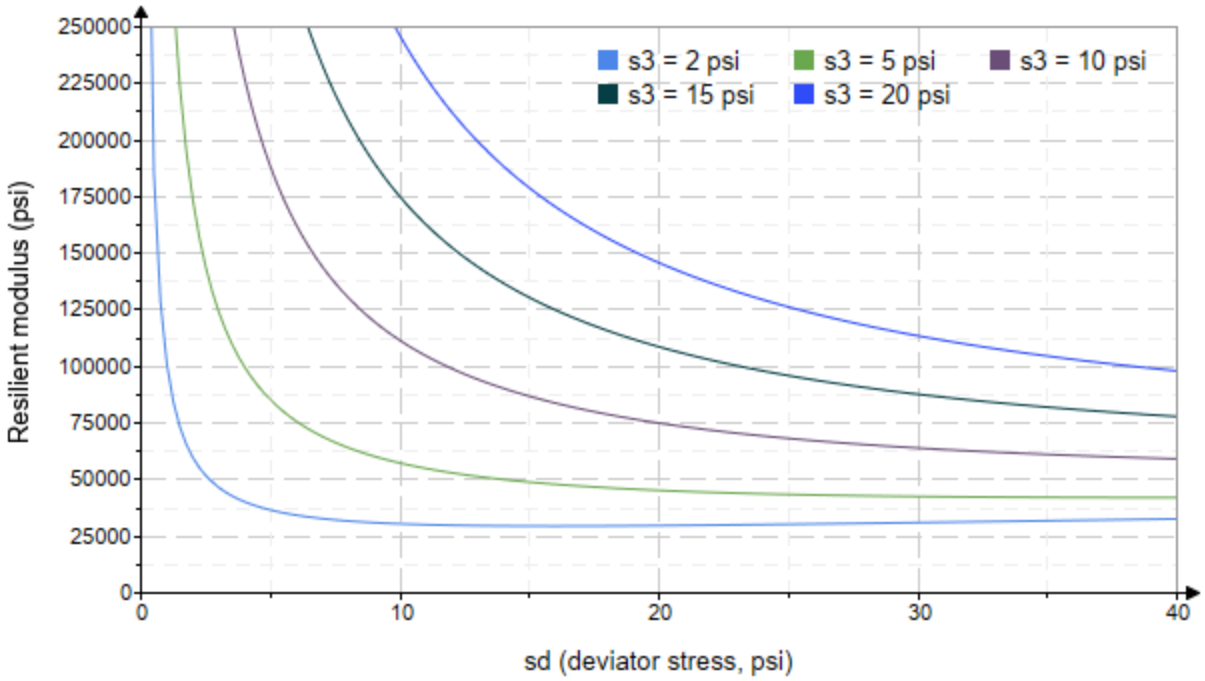

Figure 8. Plot of the fitted Equation 4 model for various confining stresses.

Dan Seely
9/12/2023

$SampleNo := \text{“B2}-\text{70”}$

$Treatment = \text{“M5”}$

$S = 11.907$ Degree of Saturation (%)

Test Sequence : Base/Subbase

Test summary data (psi) :

$$\sigma_3 = \begin{bmatrix} 2.760 \\ 2.757 \\ 2.756 \\ 4.514 \\ 4.505 \\ 4.550 \\ 9.529 \\ 9.579 \\ 9.541 \\ 14.630 \\ 14.620 \\ 14.570 \\ 19.620 \\ 19.630 \\ 19.580 \end{bmatrix} \quad \sigma_d = \begin{bmatrix} 3.224 \\ 6.151 \\ 9.082 \\ 5.166 \\ 10.040 \\ 14.350 \\ 10.140 \\ 19.340 \\ 29.720 \\ 10.140 \\ 14.410 \\ 29.960 \\ 14.560 \\ 19.780 \\ 40.290 \end{bmatrix} \quad \sigma_B = \begin{bmatrix} 11.500 \\ 14.420 \\ 17.350 \\ 18.710 \\ 23.560 \\ 28.000 \\ 38.730 \\ 48.070 \\ 58.340 \\ 54.030 \\ 58.270 \\ 73.660 \\ 73.400 \\ 78.670 \\ 99.020 \end{bmatrix} \quad M_R = \begin{bmatrix} 30680.2 \\ 34382.4 \\ 39249.4 \\ 47183.2 \\ 58251.4 \\ 63162.0 \\ 85506.0 \\ 64157.8 \\ 53011.2 \\ 61395.8 \\ 53622.2 \\ 54193.4 \\ 52853.6 \\ 55647.8 \\ 64553.8 \end{bmatrix}$$

σ_3 = mean confining stress
σ_d = mean deviator stress
σ_B = mean bulk stress
M_R = resilient modulus
p_a = atmospheric pressure = 14.6959 psi

Dan Seely
9/12/2023

$$M_{R.1}\left(\sigma_B, K_1, K_2\right) := K_1 \cdot {\sigma_B}^{K_2}$$

Equation 1
AASHTO Publication No. FHWA-RD-97-083

$K_1 = 27287.101$

$K_2 = 0.1883$

Equation 1 fitting parameters

${R_1}^2 = 0.2919$

Coefficient of determination

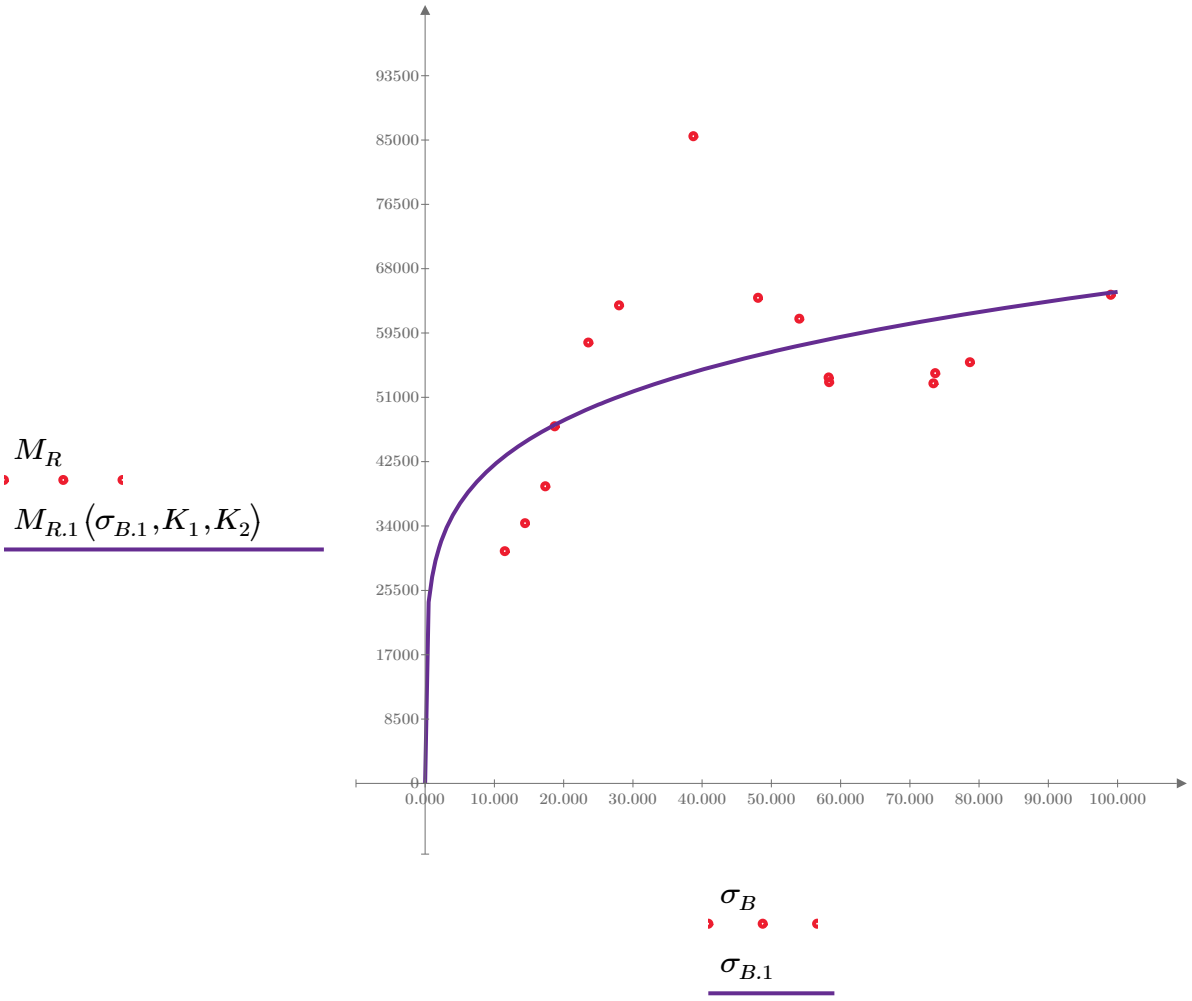

Figure 1. Plot of the test data (red points) vs. the fitted Equation 1 model (purple line).

Dan Seely
9/12/2023

$$M_{R.2}(\sigma_d, K_3, K_4) := K_3 \cdot \sigma_d^{K_4}$$

Equation 2
AASHTO Publication No. FHWA-RD-97-083

$K_3 = 35946.766$

$K_4 = 0.1615$

Equation 2 fitting parameters

$R_2^2 = 0.2222$

Coefficient of determination

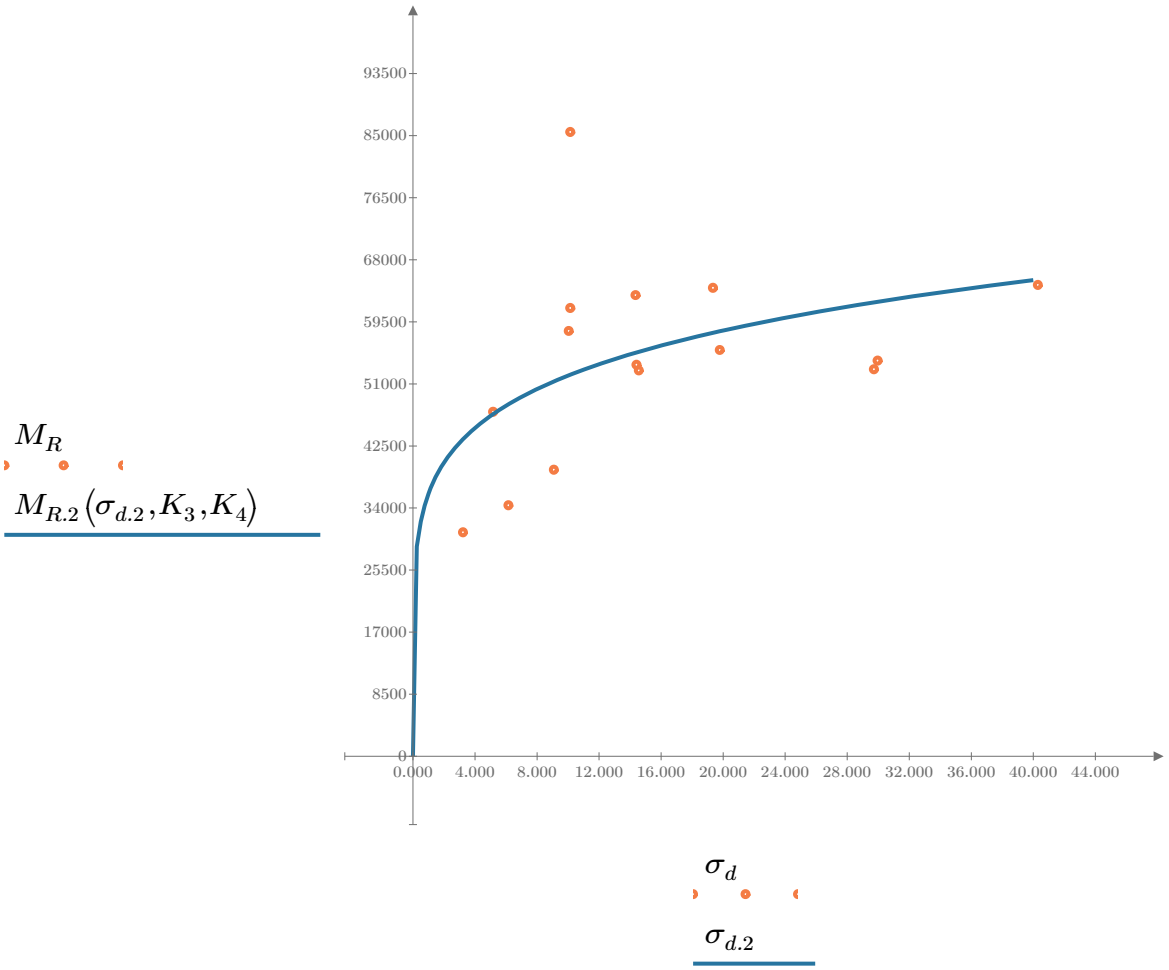

Figure 2. Plot of the test data (orange points) vs. the fitted Equation 2 model (blue line).

Dan Seely
9/12/2023

$$M_{R.3}\left(\sigma_d,\sigma_3,K_5,K_6,K_7\right):=K_5\cdot{\sigma_d}^{K_6}\cdot\left(1+\sigma_3\right)^{K_7}$$

Equation 3 AASHTO Publication No. FHWA-RD-97-083

$K_5=33673.001$

$K_6=0.0706$ Equation 3 fitting parameters

$K_7=0.1323$

${R_3}^2=0.2811$ Coefficient of determination

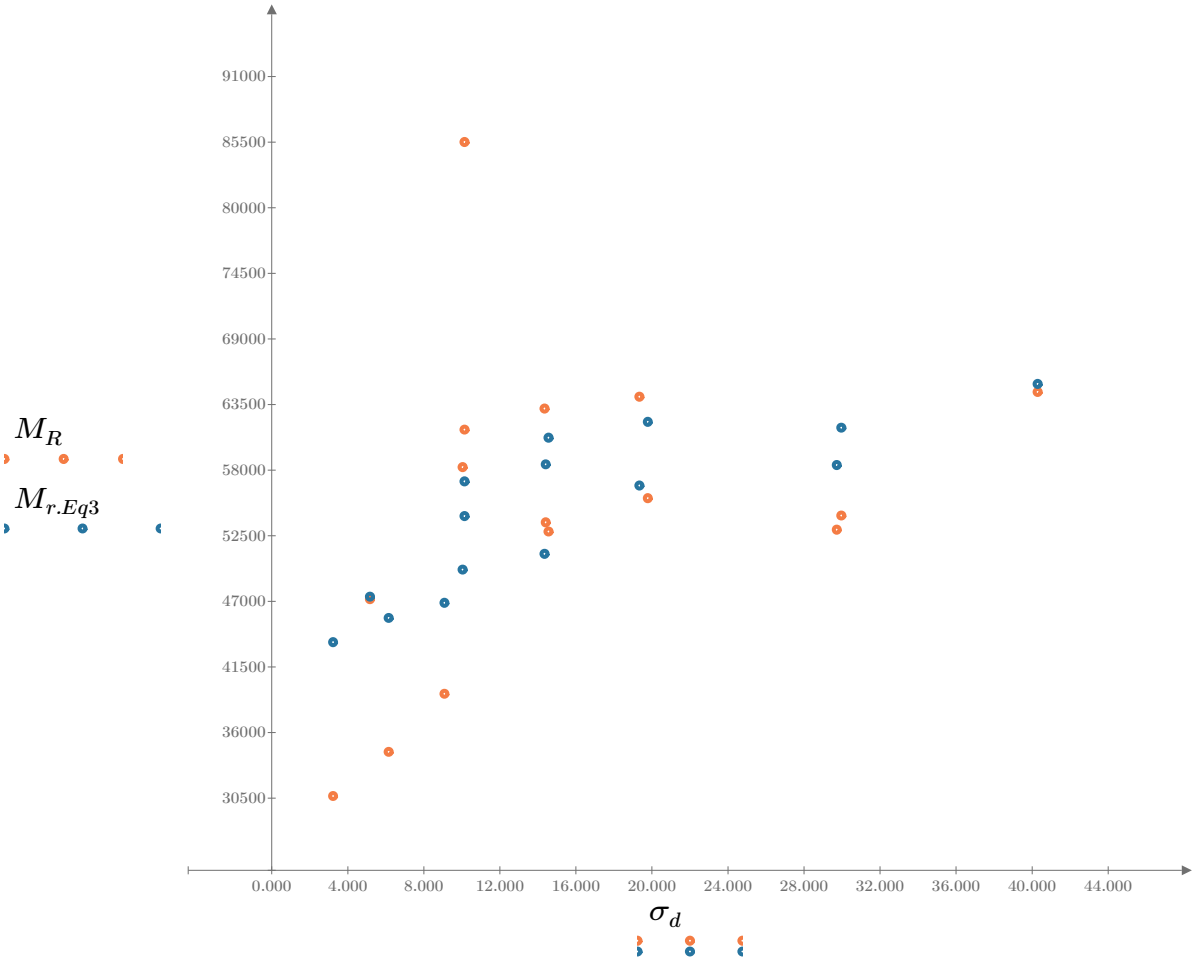

Figure 3. Plot of the test data (orange points) vs. the fitted Equation 3 model (blue points).

Dan Seely
9/12/2023

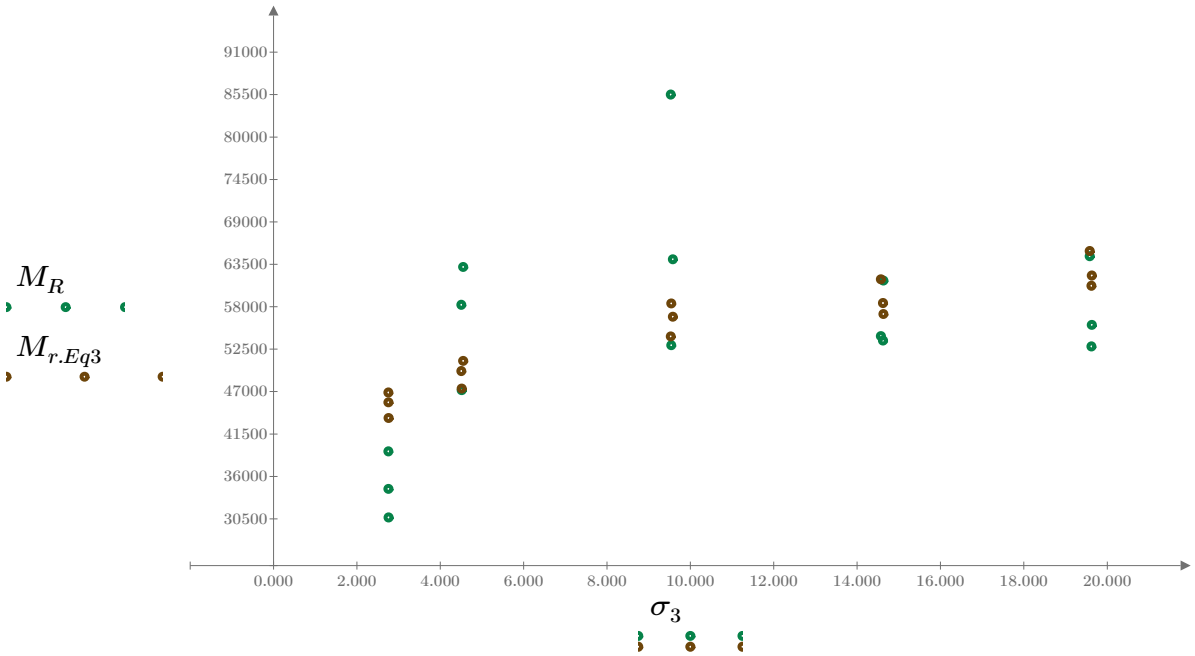

Figure 4. Plot of the test data (green points) vs. the fitted Equation 3 model (brown points).

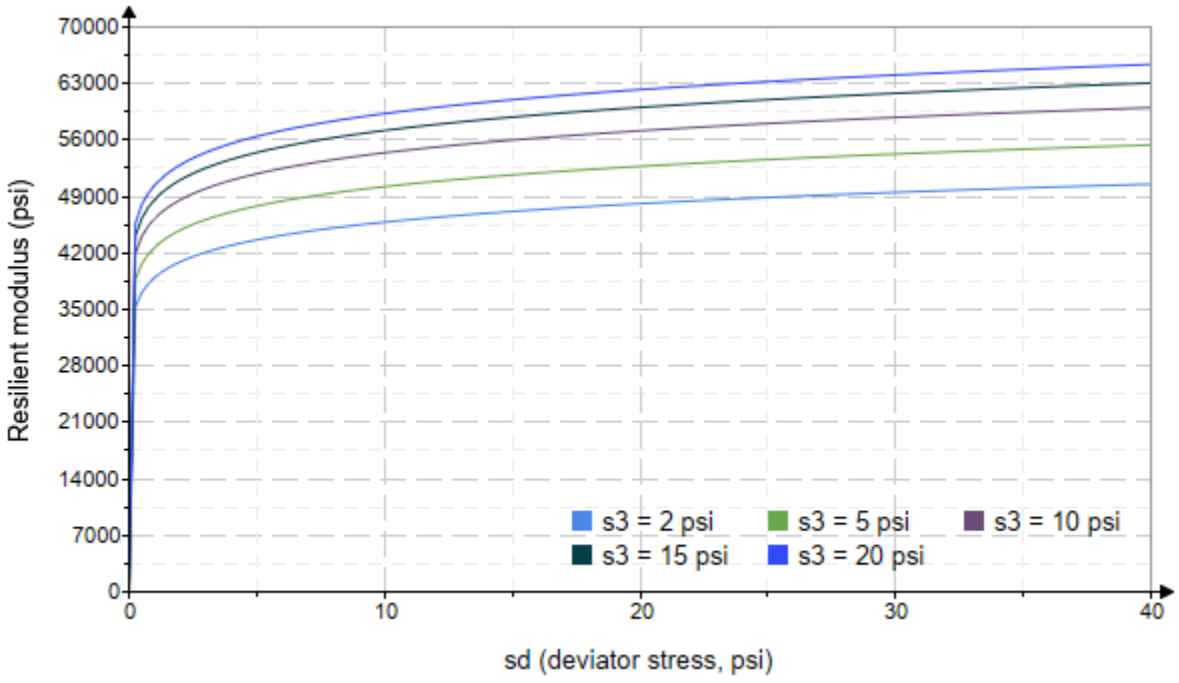

Figure 5. Plot of the fitted Equation 3 model for various confining stresses.

Dan Seely
9/12/2023

$$M_{R.4}\left(\sigma_B,\sigma_d,K_8,K_9,K_{10}\right) := K_8 \cdot p_a \left(\frac{\sigma_B}{p_a}\right)^{K_9} \cdot \left(\frac{\sigma_d}{p_a}\right)^{K_{10}}$$

Equation 4 AASHTO Publication No. FHWA-RD-97-083

$K_8 = 3068.918$

$K_9 = 0.1915$ Equation 4 fitting parameters

$K_{10} = -0.0037$

$R_4^{\,2} = 0.2919$ Coefficient of determination

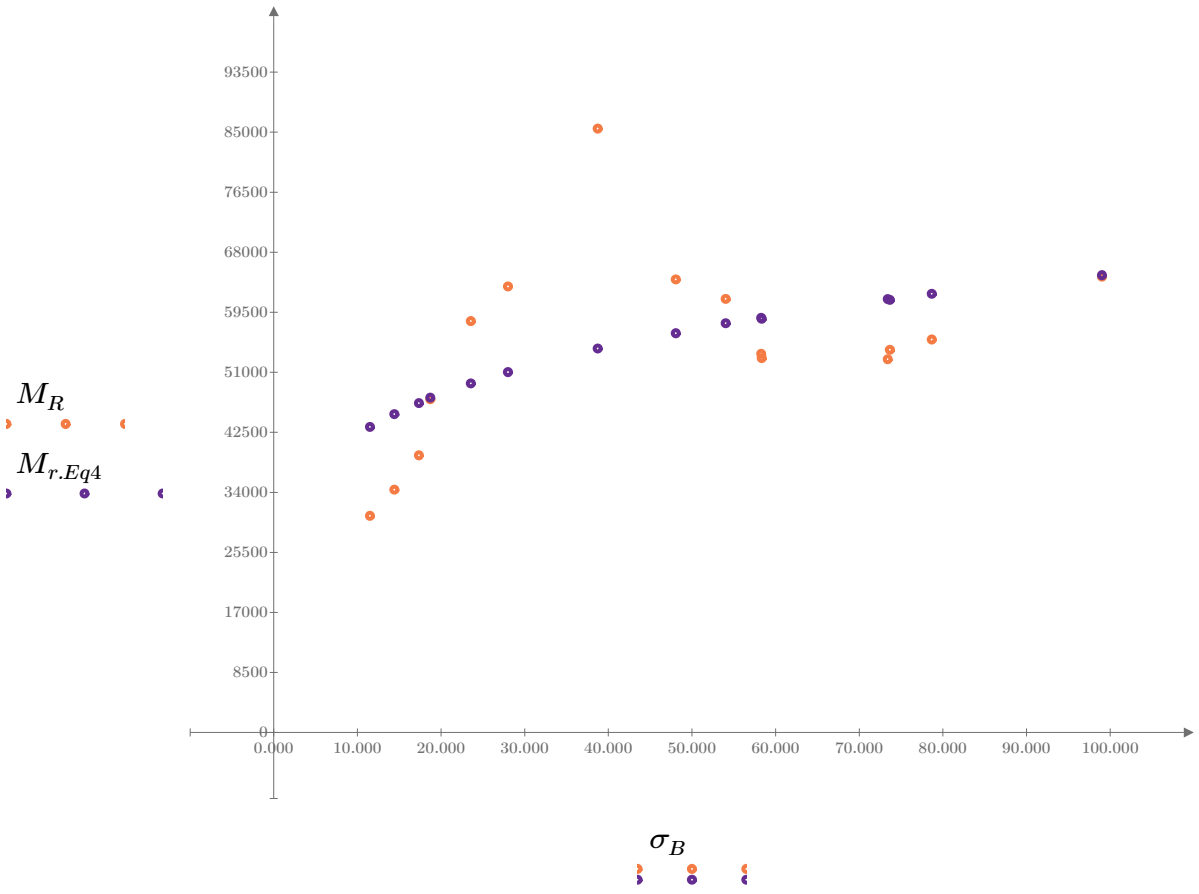

Figure 6. Plot of the test data (orange points) vs. the fitted Equation 4 model (purple points).

Dan Seely
9/12/2023

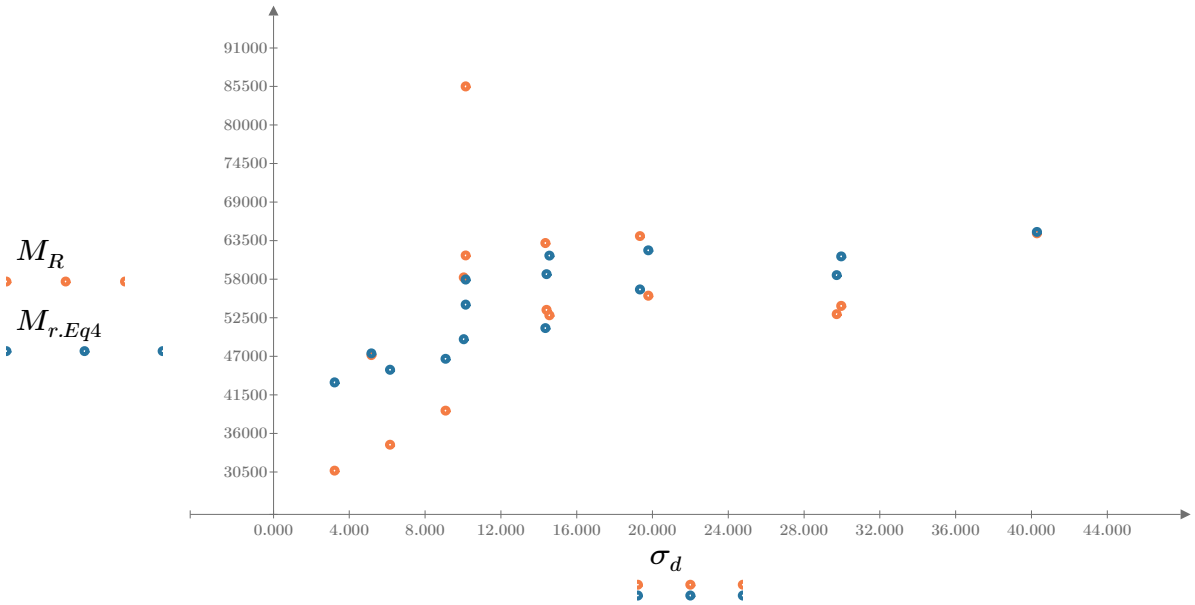

Figure 7. Plot of the test data (orange points) vs. the fitted Equation 4 model (blue points).

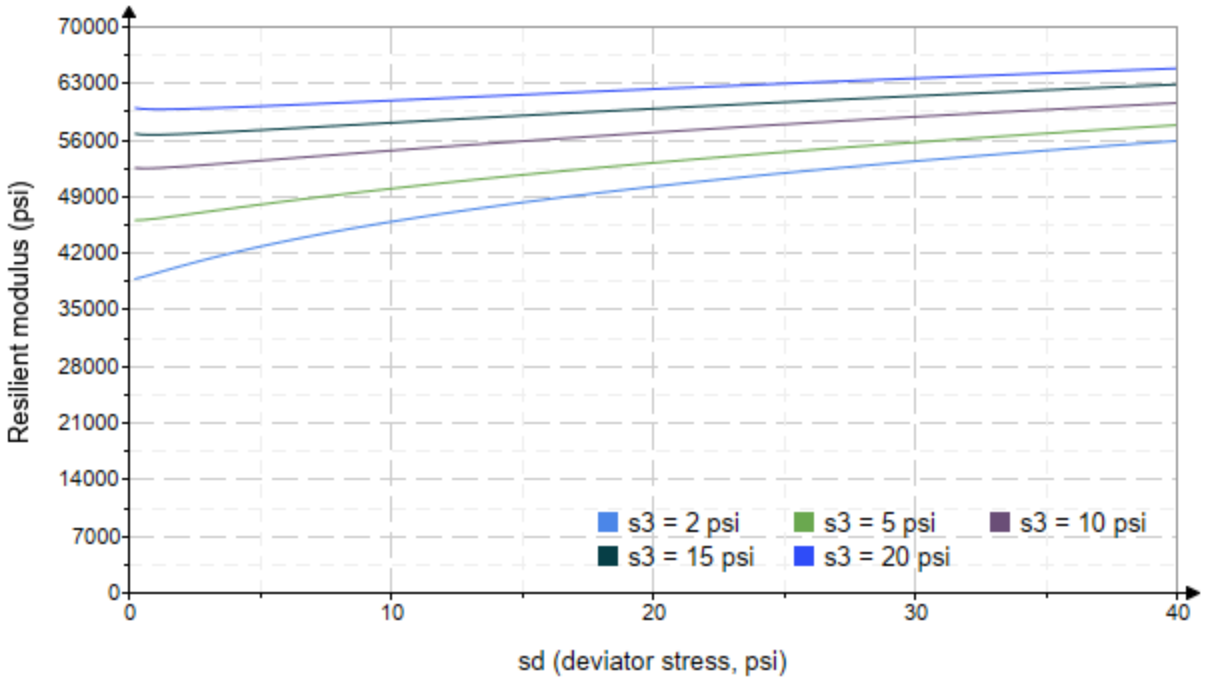

Figure 8. Plot of the fitted Equation 4 model for various confining stresses.

Dan Seely
9/12/2023

$SampleNo := \text{“B2}-\text{71”}$

$Treatment = \text{“M5”}$

$S = 9.783$ Degree of Saturation (%)

Test Sequence : Base/Subbase

Test summary data (psi) :

$$\sigma_3 = \begin{bmatrix} 2.317 \\ 2.329 \\ 2.196 \\ 4.387 \\ 3.988 \\ 4.193 \\ 9.139 \\ 9.125 \\ 9.201 \\ 14.110 \\ 14.210 \\ 13.940 \\ 19.660 \\ 19.030 \\ 19.090 \end{bmatrix} \quad \sigma_d = \begin{bmatrix} 3.463 \\ 6.127 \\ 9.221 \\ 5.308 \\ 10.160 \\ 14.390 \\ 10.100 \\ 19.240 \\ 29.580 \\ 10.290 \\ 14.410 \\ 29.740 \\ 14.520 \\ 19.470 \\ 39.990 \end{bmatrix} \quad \sigma_B = \begin{bmatrix} 10.410 \\ 13.110 \\ 15.810 \\ 18.470 \\ 22.130 \\ 26.970 \\ 37.520 \\ 46.620 \\ 57.180 \\ 52.610 \\ 57.040 \\ 71.550 \\ 73.520 \\ 76.550 \\ 97.270 \end{bmatrix} \quad M_R = \begin{bmatrix} 135160.0 \\ 51827.2 \\ 57894.2 \\ 71036.7 \\ 84179.2 \\ 72927.4 \\ 153568.0 \\ 69557.2 \\ 61901.4 \\ 311692.0 \\ 106637.2 \\ 76812.4 \\ 188984.0 \\ 114570.0 \\ 77089.4 \end{bmatrix}$$

σ_3 = mean confining stress
σ_d = mean deviator stress
σ_B = mean bulk stress
M_R = resilient modulus
p_a = atmospheric pressure = 14.6959 psi

Dan Seely
9/12/2023

$$M_{R.1}\left(\sigma_B, K_1, K_2\right) := K_1 \cdot {\sigma_B}^{K_2}$$

Equation 1
AASHTO Publication No. FHWA-RD-97-083

$K_1 = 50530.452$

$K_2 = 0.2107$

Equation 1 fitting parameters

${R_1}^2 = 0.0579$

Coefficient of determination

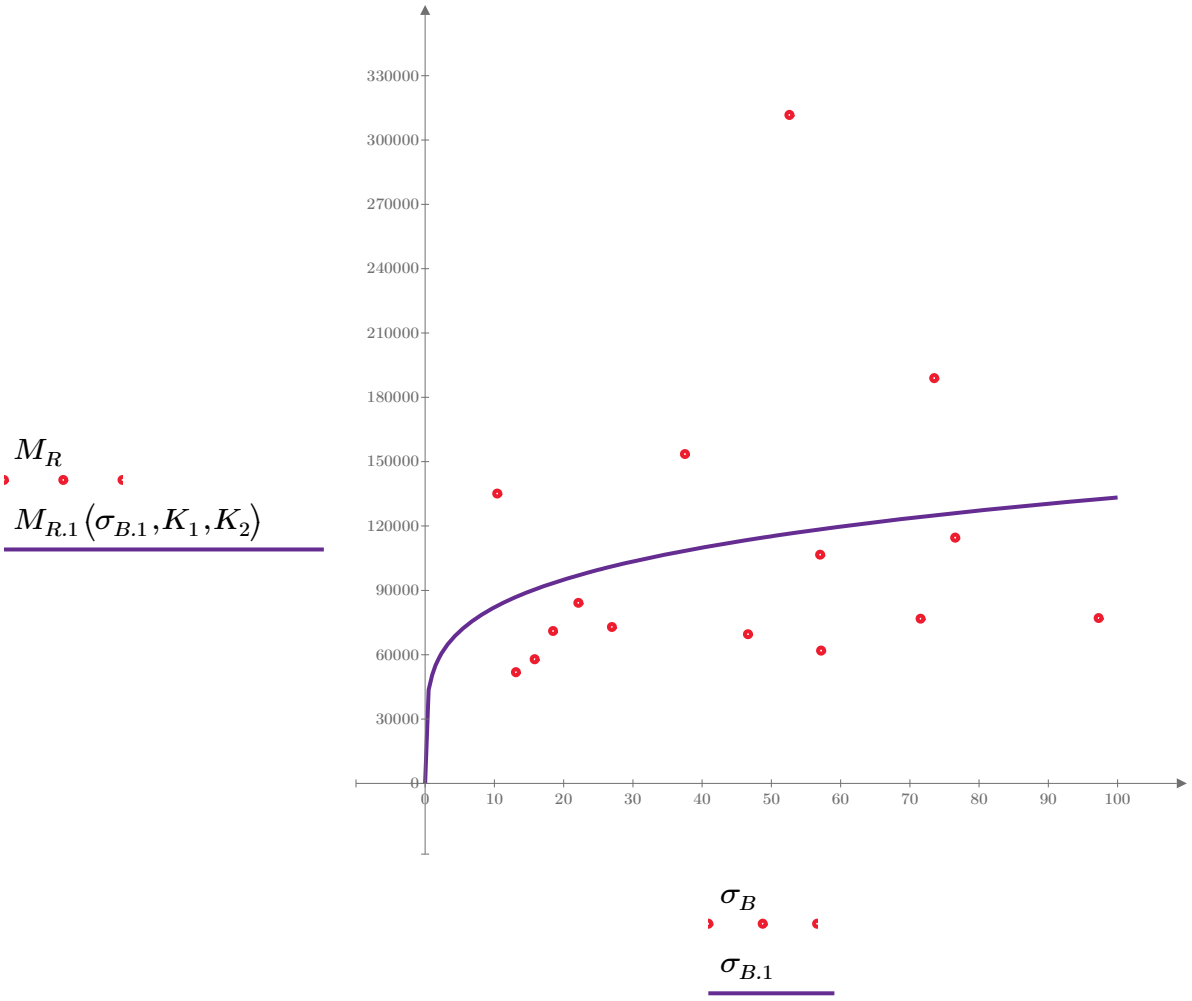

Figure 1. Plot of the test data (red points) vs. the fitted Equation 1 model (purple line).

Dan Seely
9/12/2023

$$M_{R.2}(\sigma_d, K_3, K_4) := K_3 \cdot \sigma_d^{K_4}$$

Equation 2
AASHTO Publication No. FHWA-RD-97-083

$K_3 = 149096.051$

$K_4 = -0.1240$

Equation 2 fitting parameters

$R_2^2 = 0.0214$

Coefficient of determination

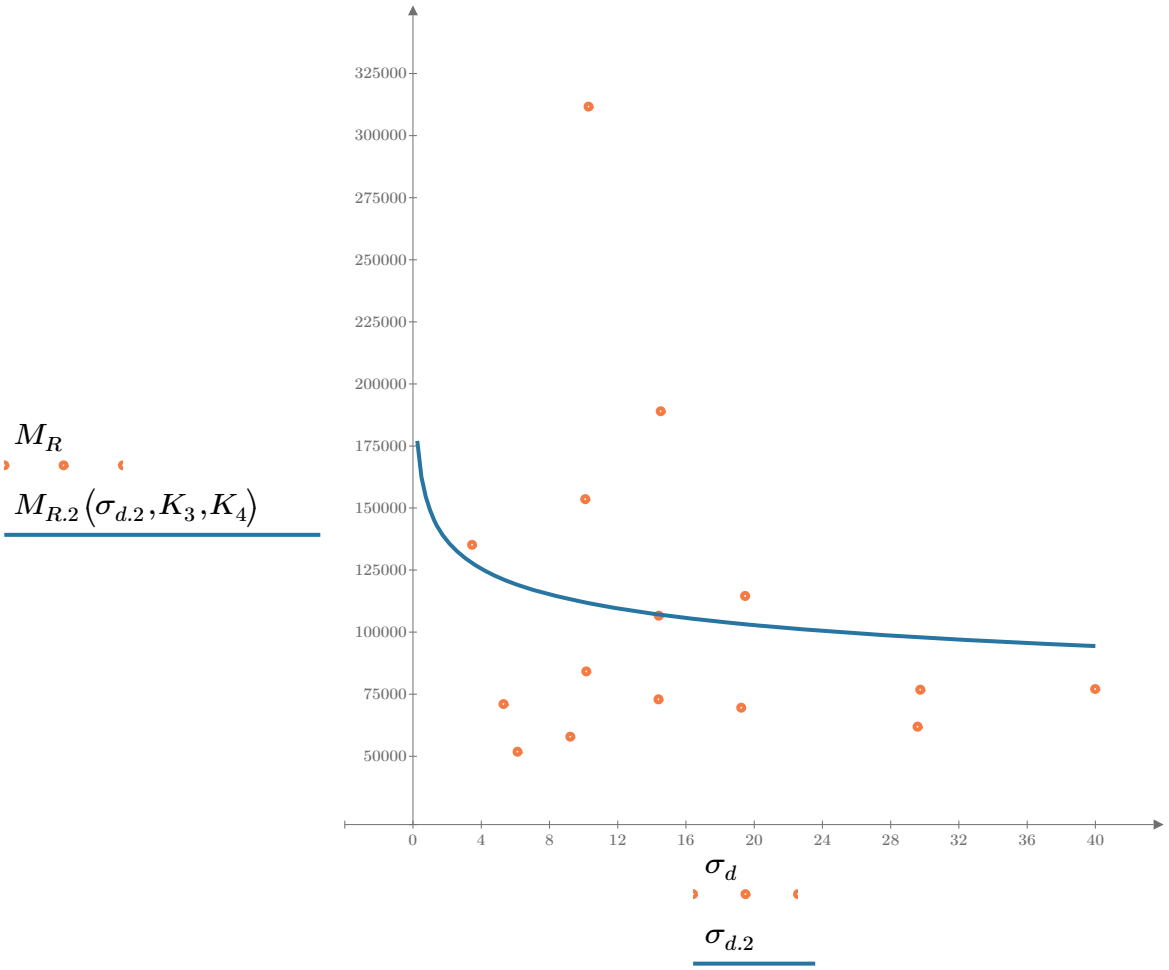

Figure 2. Plot of the test data (orange points) vs. the fitted Equation 2 model (blue line).

Dan Seely
9/12/2023

$$M_{R.3}\left(\sigma_d,\sigma_3,K_5,K_6,K_7\right):=K_5\cdot{\sigma_d}^{K_6}\cdot\left(1+\sigma_3\right)^{K_7}$$

Equation 3 AASHTO Publication No. FHWA-RD-97-083

$K_5=121872.085$

$K_6=-1.1421$ Equation 3 fitting parameters

$K_7=1.2022$

${R_3}^2=0.7053$ Coefficient of determination

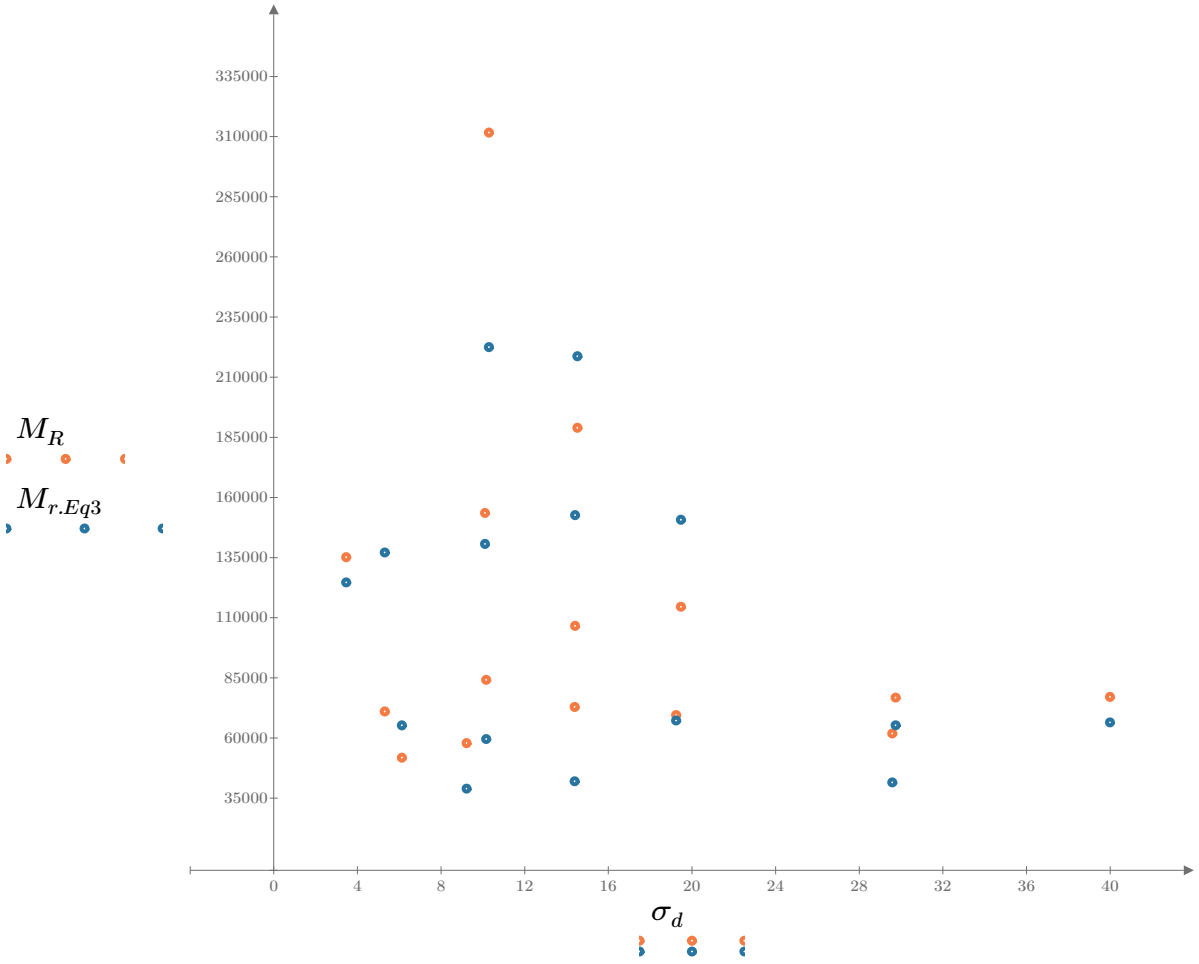

Figure 3. Plot of the test data (orange points) vs. the fitted Equation 3 model (blue points).

Dan Seely
9/12/2023

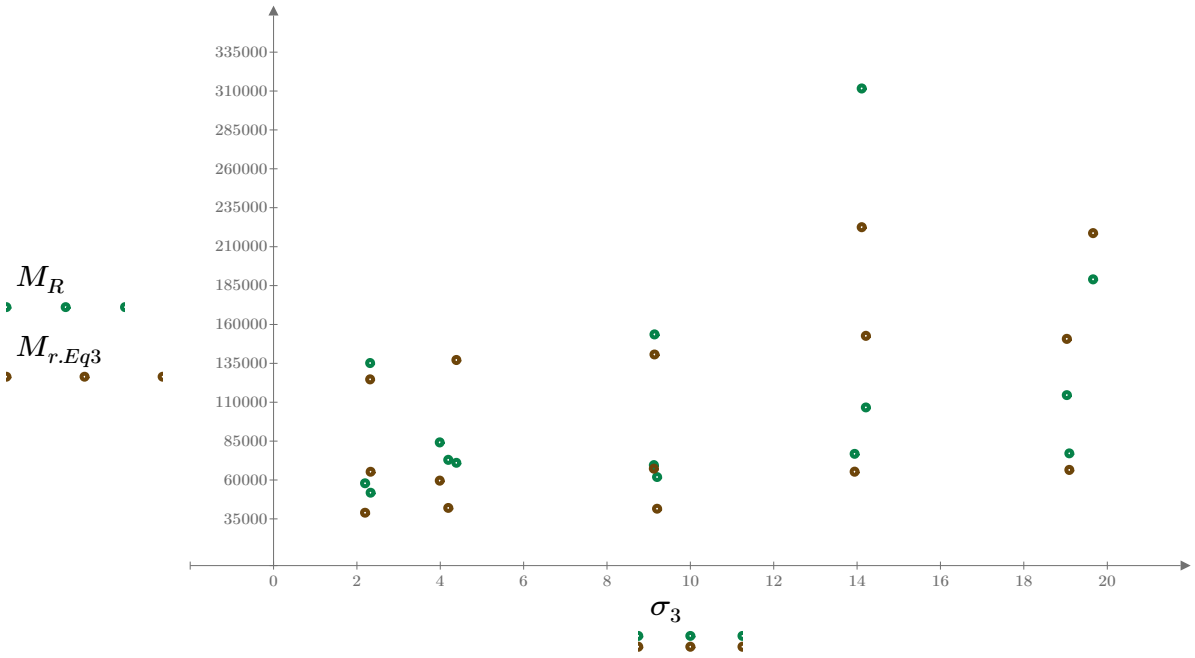

Figure 4. Plot of the test data (green points) vs. the fitted Equation 3 model (brown points).

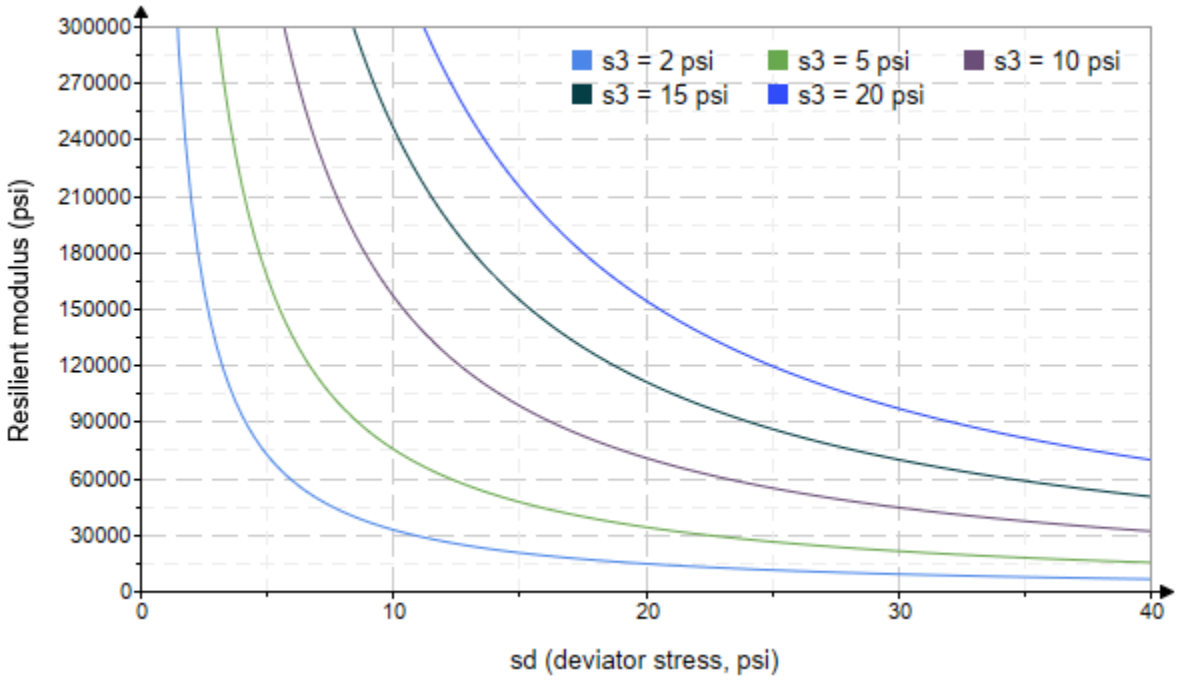

Figure 5. Plot of the fitted Equation 3 model for various confining stresses.

Dan Seely
9/12/2023

$$M_{R.4}\left(\sigma_B,\sigma_d,K_8,K_9,K_{10}\right) := K_8 \cdot p_a \left(\frac{\sigma_B}{p_a}\right)^{K_9} \cdot \left(\frac{\sigma_d}{p_a}\right)^{K_{10}}$$

Equation 4 AASHTO Publication No. FHWA-RD-97-083

$K_8 = 1175.165$

$K_9 = 1.5723$ Equation 4 fitting parameters

$K_{10} = -1.6892$

$R_4^{\,2} = 0.7424$ Coefficient of determination

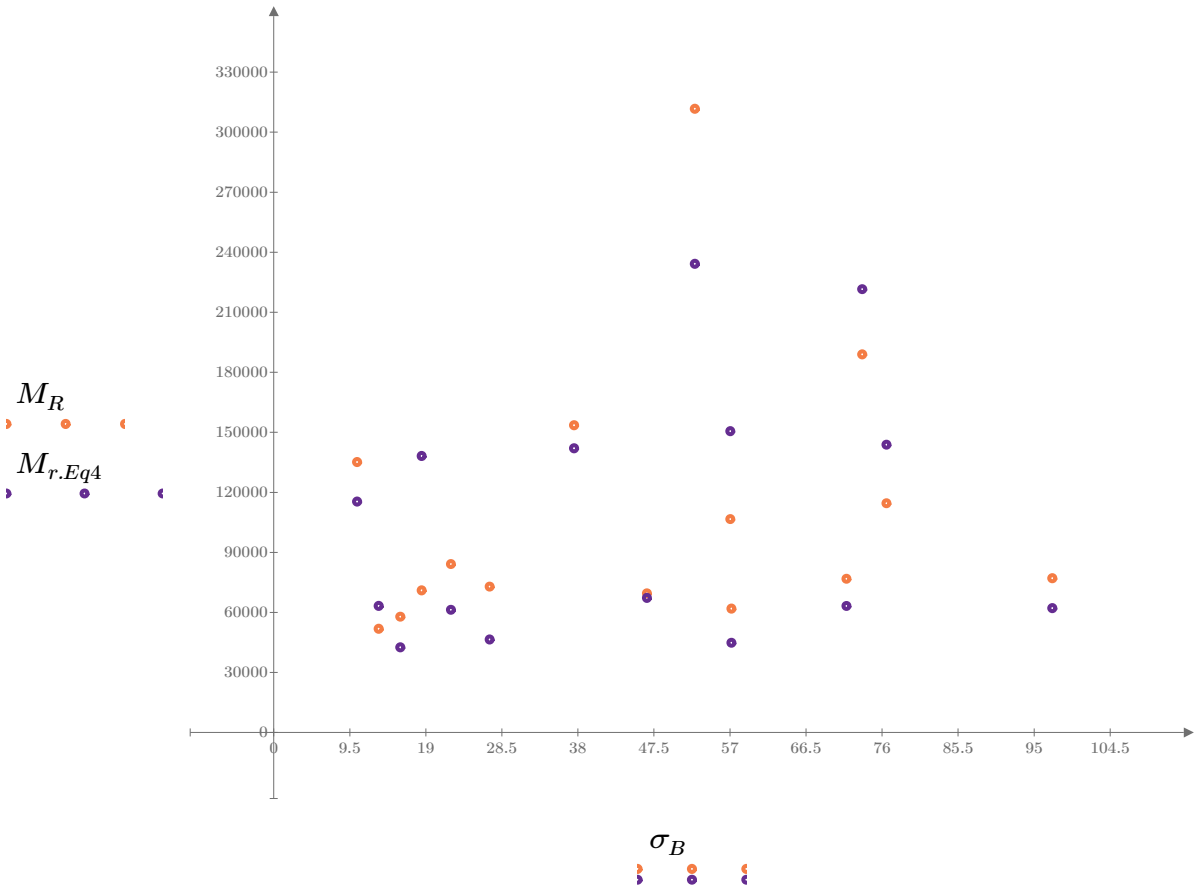

Figure 6. Plot of the test data (orange points) vs. the fitted Equation 4 model (purple points).

Dan Seely
9/12/2023

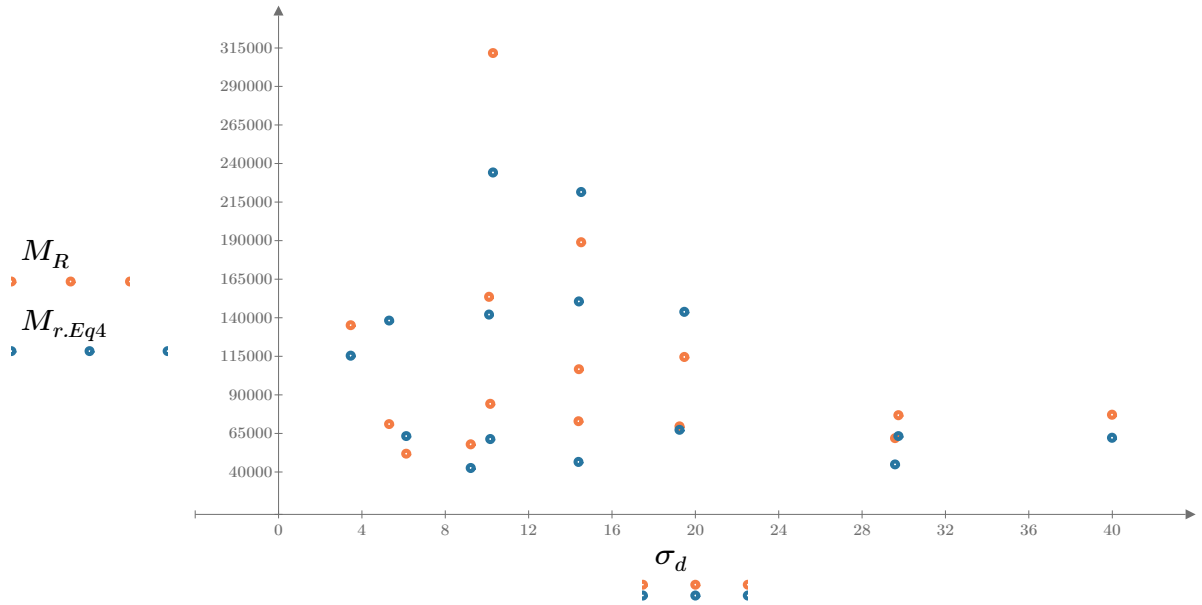

Figure 7. Plot of the test data (orange points) vs. the fitted Equation 4 model (blue points).

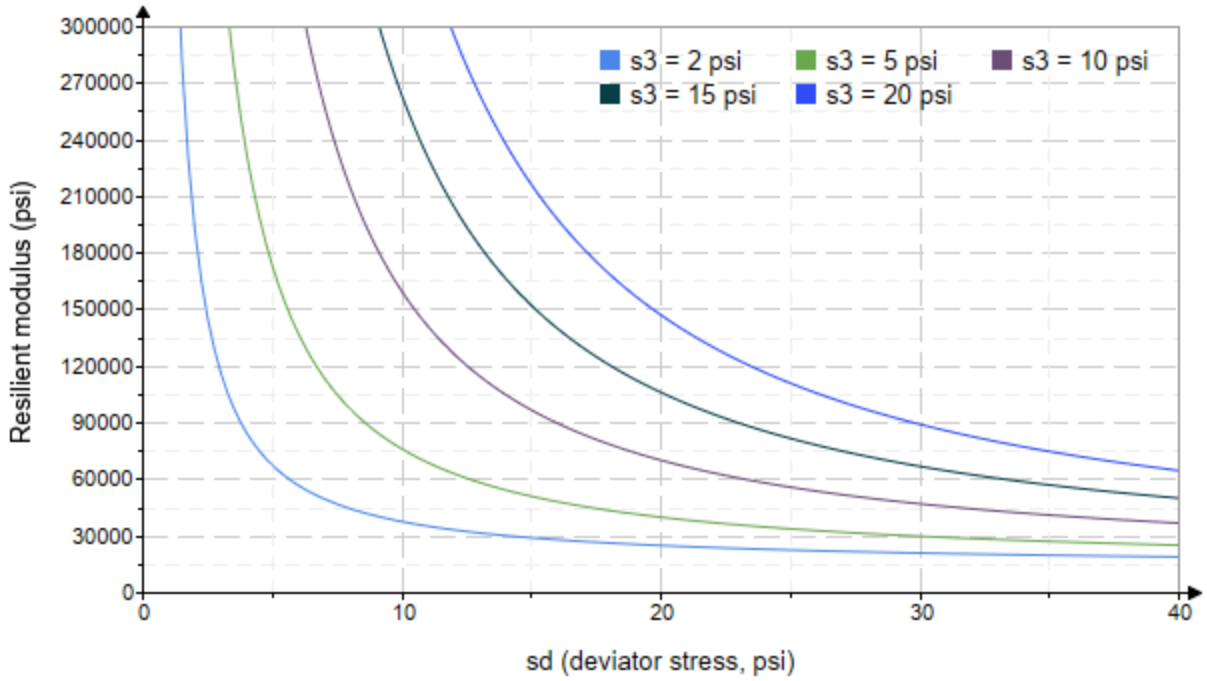

Figure 8. Plot of the fitted Equation 4 model for various confining stresses.

Dan Seely
9/12/2023

$SampleNo := \text{“B2}-\text{72”}$

$Treatment = \text{“M5”}$

$S = 10.281$ Degree of Saturation (%)

Test Sequence : Base/Subbase

Test summary data (psi) :

$$\sigma_3 = \begin{bmatrix} 2.782 \\ 2.797 \\ 2.796 \\ 4.556 \\ 4.591 \\ 4.543 \\ 9.595 \\ 9.560 \\ 9.588 \\ 14.600 \\ 14.600 \\ 14.590 \\ 19.600 \\ 19.610 \\ 19.600 \end{bmatrix} \quad \sigma_d = \begin{bmatrix} 3.137 \\ 6.239 \\ 9.111 \\ 5.234 \\ 10.140 \\ 14.690 \\ 10.290 \\ 19.330 \\ 29.250 \\ 10.270 \\ 14.660 \\ 29.450 \\ 14.560 \\ 19.460 \\ 40.030 \end{bmatrix} \quad \sigma_B = \begin{bmatrix} 11.480 \\ 14.630 \\ 17.500 \\ 18.900 \\ 23.920 \\ 28.320 \\ 39.070 \\ 48.010 \\ 58.010 \\ 54.080 \\ 58.450 \\ 73.230 \\ 73.370 \\ 78.300 \\ 98.820 \end{bmatrix} \quad M_R = \begin{bmatrix} 21739.2 \\ 22209.4 \\ 23791.8 \\ 48178.0 \\ 39685.0 \\ 38174.2 \\ 51258.6 \\ 46935.6 \\ 44844.8 \\ 87588.4 \\ 61580.8 \\ 55367.2 \\ 60879.8 \\ 59128.6 \\ 61328.2 \end{bmatrix}$$

σ_3 = mean confining stress
σ_d = mean deviator stress
σ_B = mean bulk stress
M_R = resilient modulus
p_a = atmospheric pressure = 14.6959 psi

Dan Seely
9/12/2023

$$M_{R.1}\left(\sigma_B, K_1, K_2\right) := K_1 \cdot {\sigma_B}^{K_2}$$

Equation 1
AASHTO Publication No. FHWA-RD-97-083

$K_1 = 10236.833$

$K_2 = 0.4160$

Equation 1 fitting parameters

${R_1}^2 = 0.5822$

Coefficient of determination

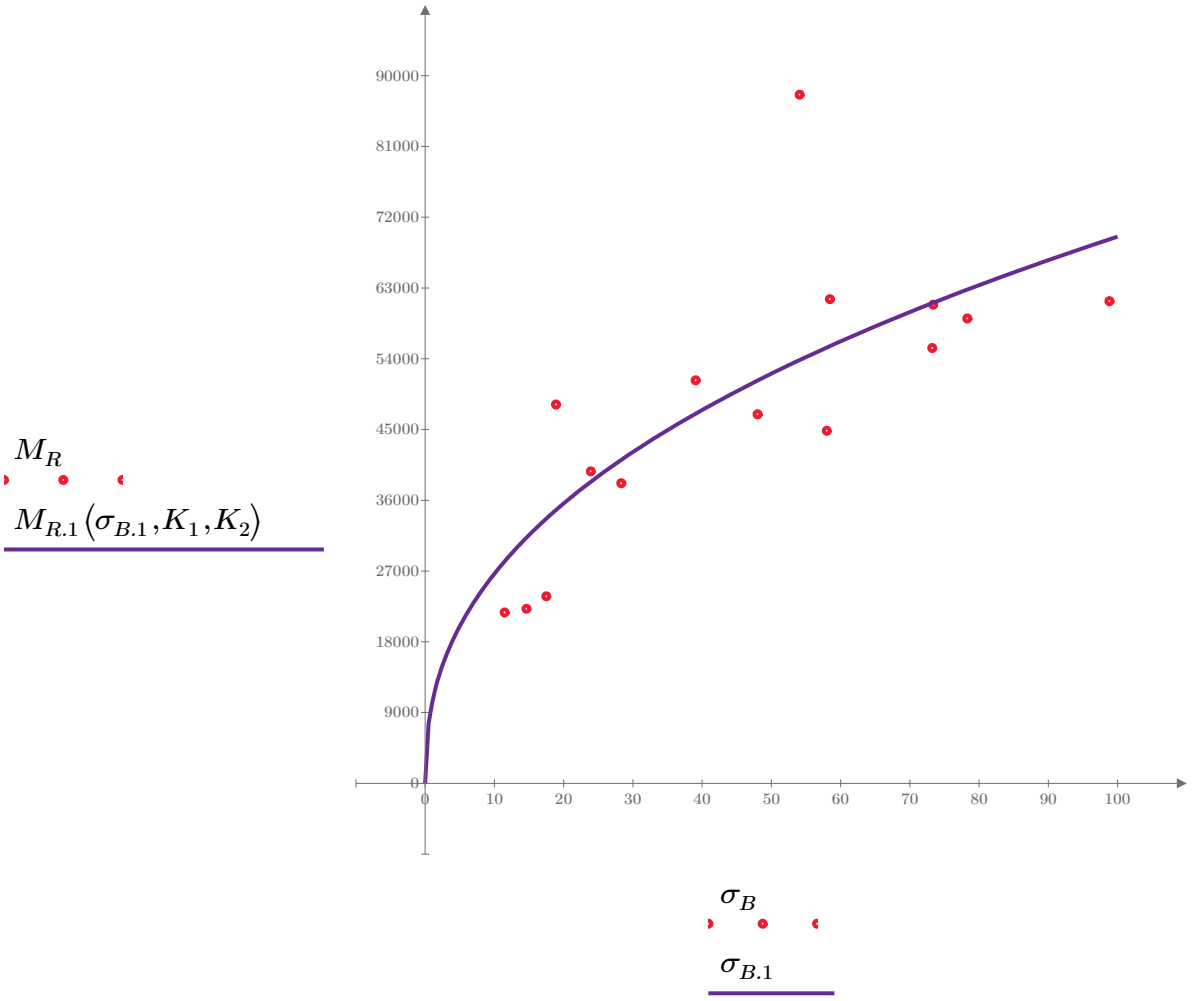

Figure 1. Plot of the test data (red points) vs. the fitted Equation 1 model (purple line).

Dan Seely
9/12/2023

$$M_{R.2}(\sigma_d, K_3, K_4) := K_3 \cdot \sigma_d^{K_4}$$

Equation 2
AASHTO Publication No. FHWA-RD-97-083

$K_3 = 26351.287$

$K_4 = 0.2326$

Equation 2 fitting parameters

$R_2^2 = 0.2045$

Coefficient of determination

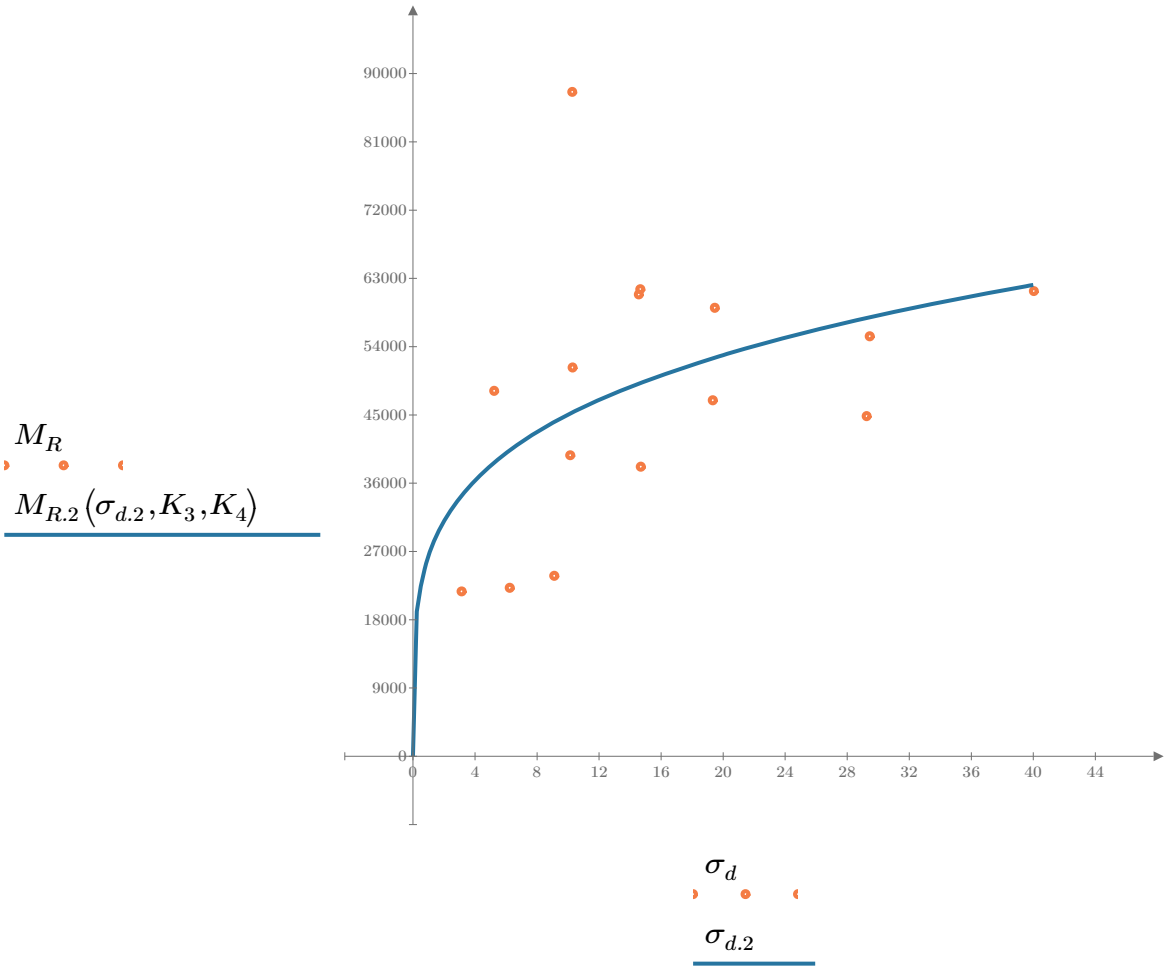

Figure 2. Plot of the test data (orange points) vs. the fitted Equation 2 model (blue line).

Dan Seely
9/12/2023

$$M_{R.3}\left(\sigma_d,\sigma_3,K_5,K_6,K_7\right):=K_5\cdot{\sigma_d}^{K_6}\cdot\left(1+\sigma_3\right)^{K_7}$$

Equation 3 AASHTO Publication No. FHWA-RD-97-083

$K_5=18854.771$

$K_6=-0.1798$ Equation 3 fitting parameters

$K_7=0.6051$

${R_3}^2=0.7490$ Coefficient of determination

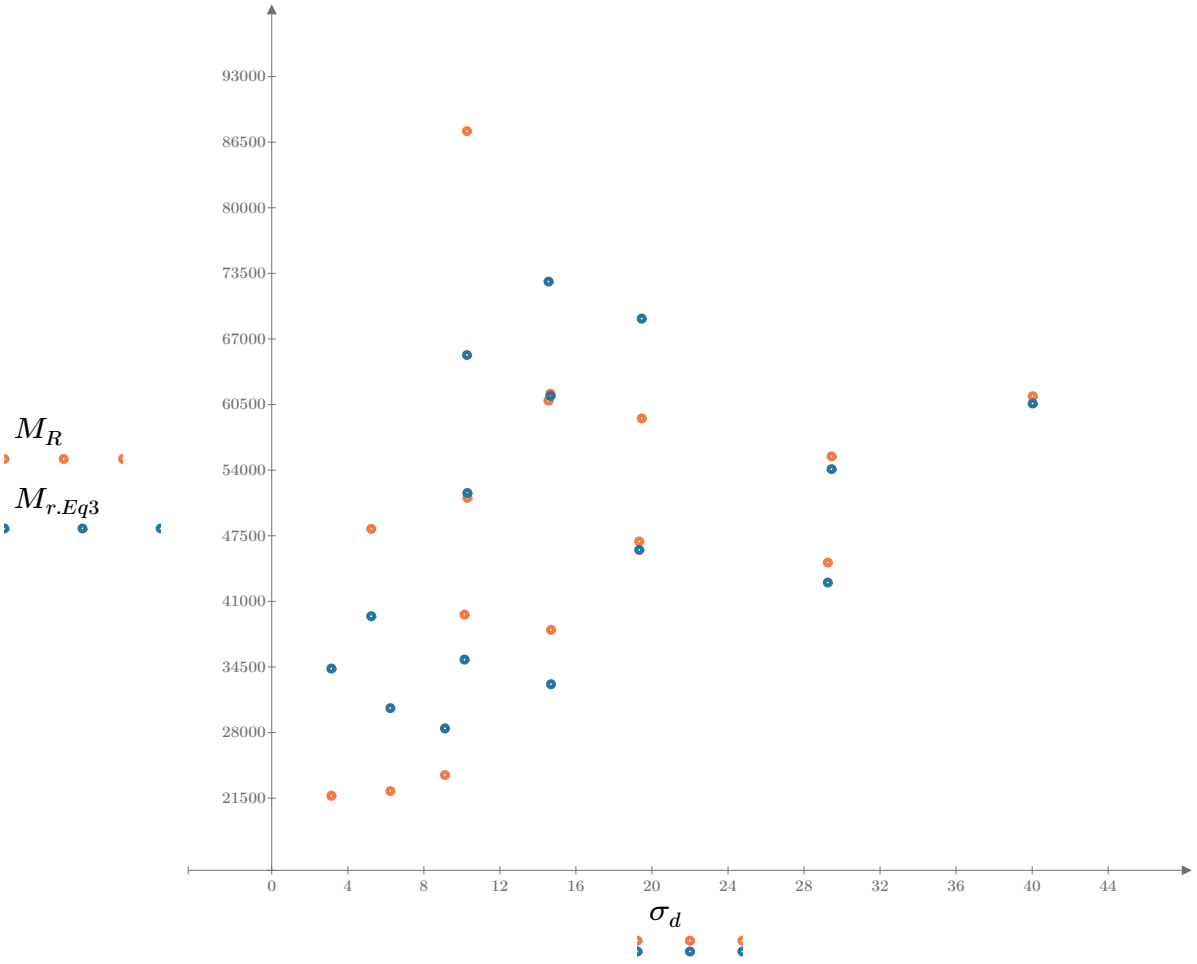

Figure 3. Plot of the test data (orange points) vs. the fitted Equation 3 model (blue points).

Dan Seely
9/12/2023

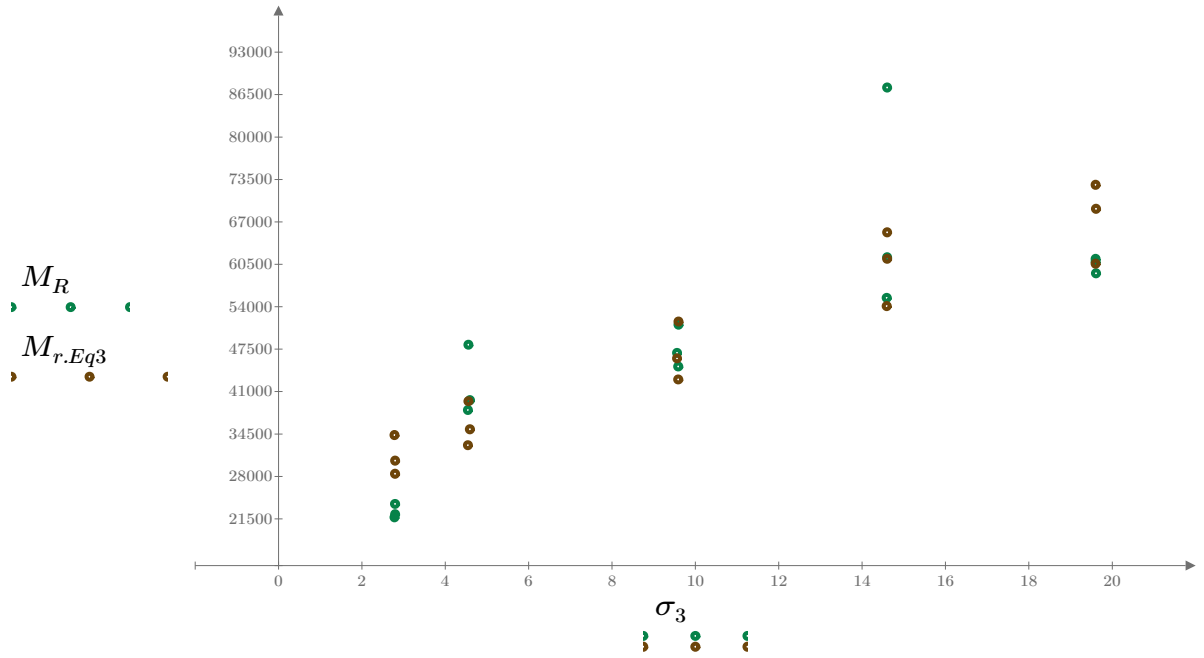

Figure 4. Plot of the test data (green points) vs. the fitted Equation 3 model (brown points).

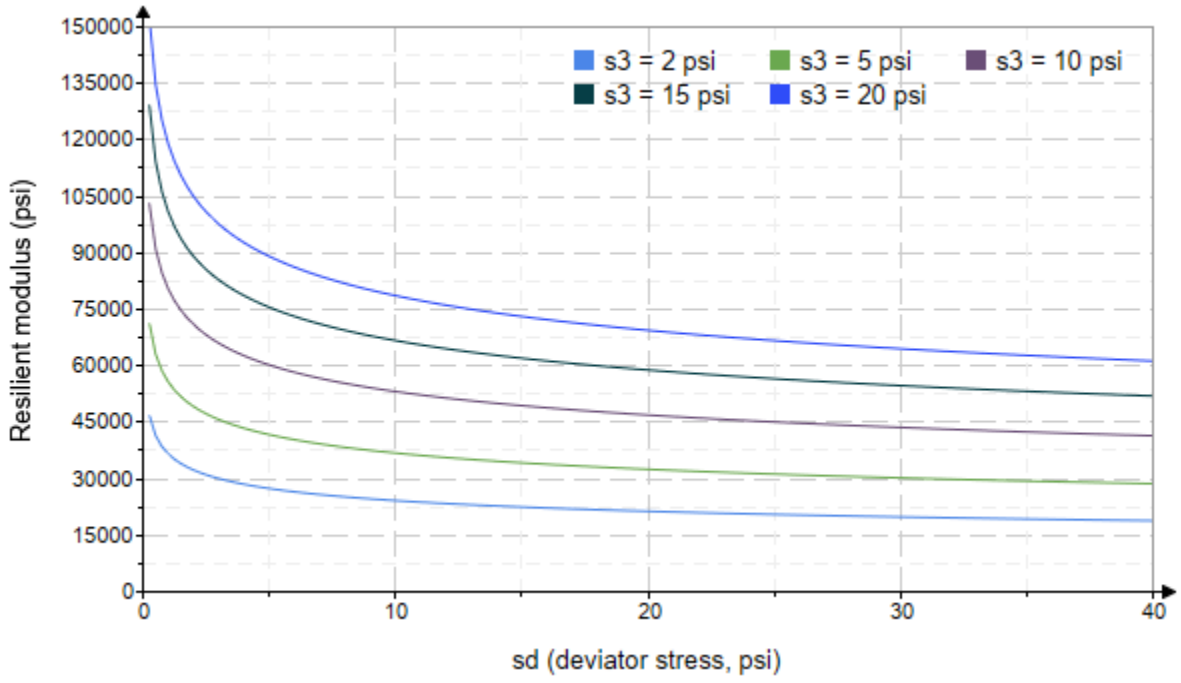

Figure 5. Plot of the fitted Equation 3 model for various confining stresses.

Dan Seely
9/12/2023

$$M_{R.4}\left(\sigma_B,\sigma_d,K_8,K_9,K_{10}\right) := K_8 \cdot p_a \left(\frac{\sigma_B}{p_a}\right)^{K_9} \cdot \left(\frac{\sigma_d}{p_a}\right)^{K_{10}}$$

Equation 4 AASHTO Publication No. FHWA-RD-97-083

$K_8 = 1347.375$

$K_9 = 0.8171$ Equation 4 fitting parameters

$K_{10} = -0.4625$

$R_4^{\,2} = 0.7779$ Coefficient of determination

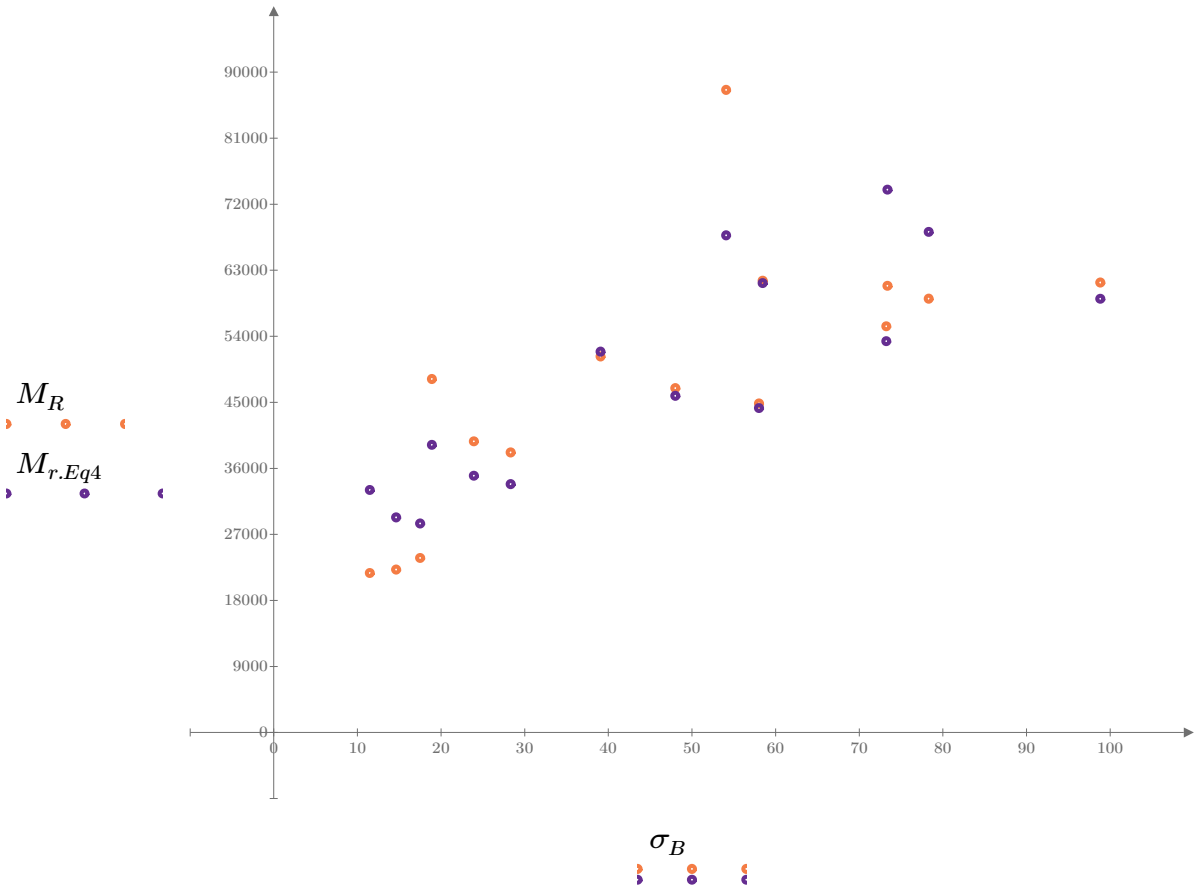

Figure 6. Plot of the test data (orange points) vs. the fitted Equation 4 model (purple points).

Dan Seely
9/12/2023

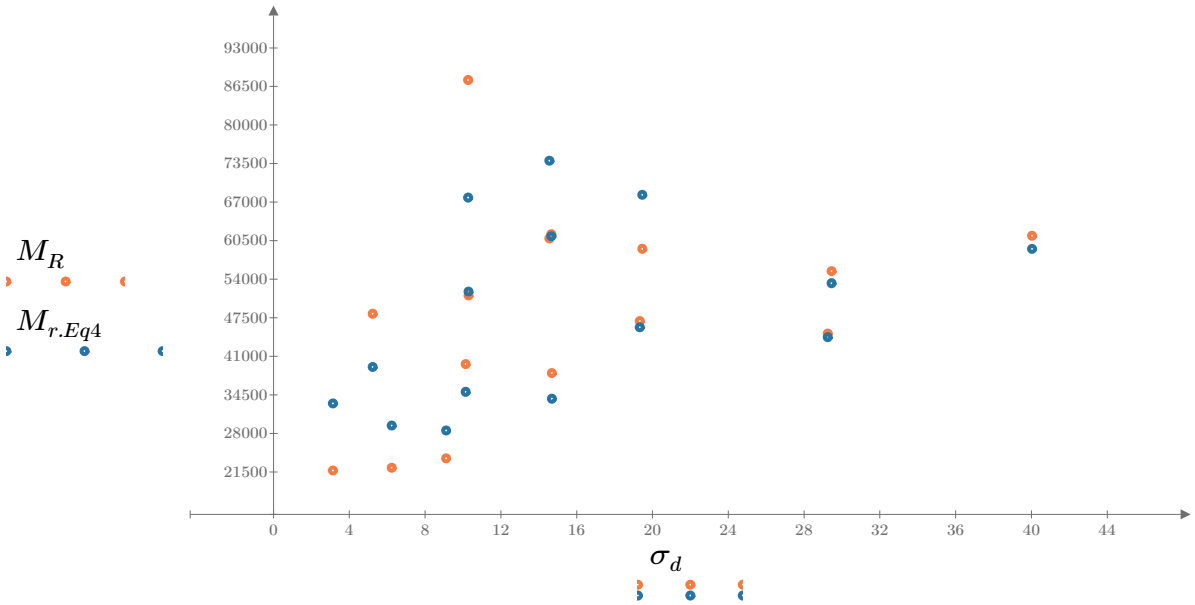

Figure 7. Plot of the test data (orange points) vs. the fitted Equation 4 model (blue points).

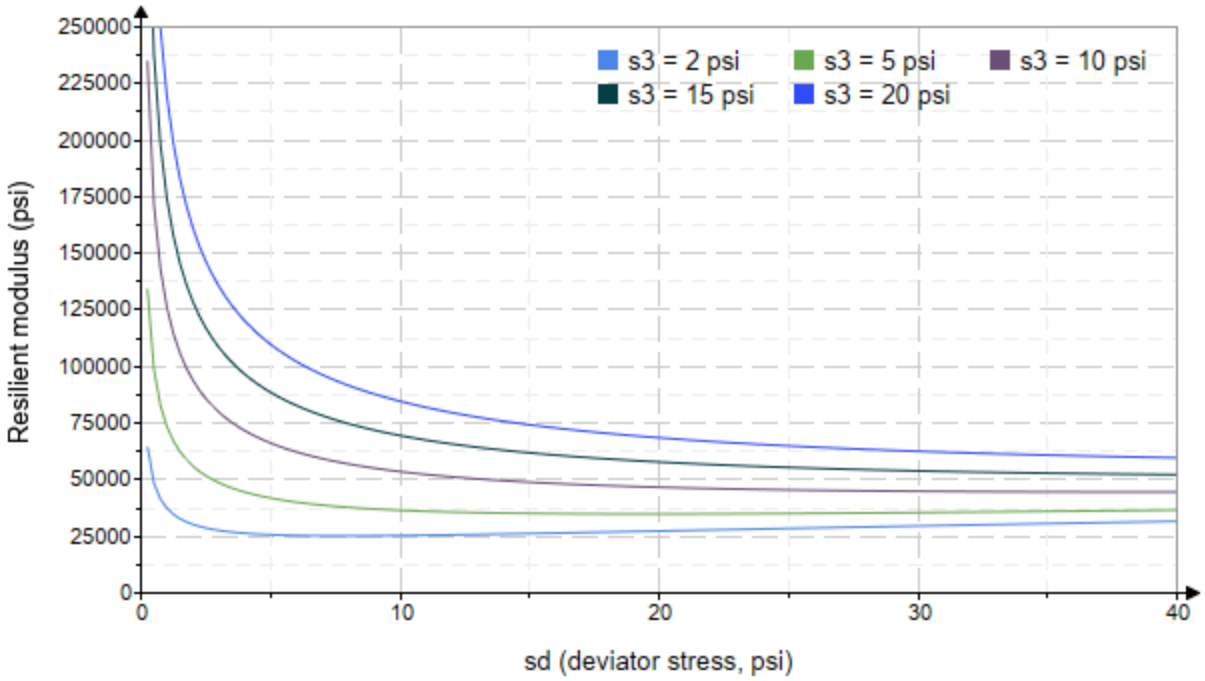

Figure 8. Plot of the fitted Equation 4 model for various confining stresses.

Dan Seely
9/12/2023

$SampleNo := \text{“B2}-\text{73”}$

$Treatment = \text{“M5”}$

$S = 9.679$ Degree of Saturation (%)

Test Sequence : Base/Subbase

Test summary data (psi) :

$$\sigma_3 = \begin{bmatrix} 2.129 \\ 2.227 \\ 2.215 \\ 4.118 \\ 4.228 \\ 4.351 \\ 8.810 \\ 8.872 \\ 8.738 \\ 14.330 \\ 14.350 \\ 13.740 \\ 19.570 \\ 19.340 \\ 19.470 \end{bmatrix} \quad \sigma_d = \begin{bmatrix} 3.213 \\ 6.179 \\ 9.113 \\ 5.164 \\ 10.010 \\ 14.370 \\ 10.180 \\ 19.400 \\ 29.610 \\ 10.140 \\ 14.560 \\ 29.850 \\ 14.630 \\ 19.690 \\ 40.010 \end{bmatrix} \quad \sigma_B = \begin{bmatrix} 9.600 \\ 12.860 \\ 15.760 \\ 17.520 \\ 22.690 \\ 27.420 \\ 36.610 \\ 46.020 \\ 55.830 \\ 53.130 \\ 57.600 \\ 71.070 \\ 73.350 \\ 77.710 \\ 98.420 \end{bmatrix} \quad M_R = \begin{bmatrix} 37052.6 \\ 32723.6 \\ 35880.6 \\ 69836.6 \\ 46518.6 \\ 41950.8 \\ 60368.2 \\ 51768.6 \\ 65877.8 \\ 119070.0 \\ 97136.0 \\ 83375.6 \\ 118506.0 \\ 107358.0 \\ 59981.8 \end{bmatrix}$$

σ_3 = mean confining stress
σ_d = mean deviator stress
σ_B = mean bulk stress
M_R = resilient modulus
p_a = atmospheric pressure = 14.6959 psi

Dan Seely
9/12/2023

$$M_{R.1}\left(\sigma_B, K_1, K_2\right) := K_1 \cdot {\sigma_B}^{K_2}$$

Equation 1
AASHTO Publication No. FHWA-RD-97-083

$K_1 = 13869.989$

$K_2 = 0.4331$

Equation 1 fitting parameters

${R_1}^2 = 0.4843$

Coefficient of determination

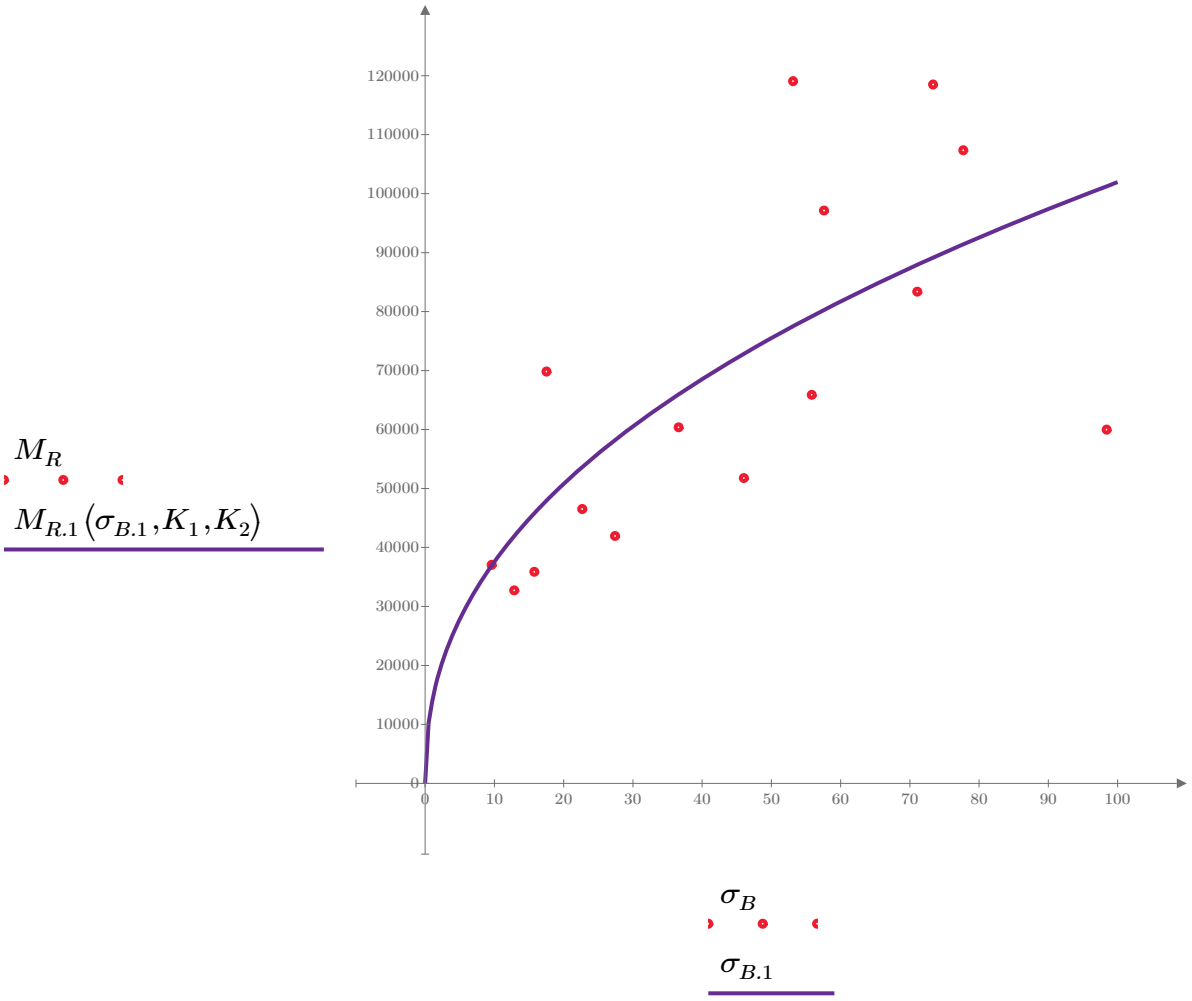

Figure 1. Plot of the test data (red points) vs. the fitted Equation 1 model (purple line).

Dan Seely
9/12/2023

$M_{R.2}(\sigma_d, K_3, K_4) := K_3 \cdot \sigma_d^{K_4}$ Equation 2
AASHTO Publication No. FHWA-RD-97-083

$K_3 = 43294.759$

$K_4 = 0.1777$ Equation 2 fitting parameters

$R_2^2 = 0.0896$ Coefficient of determination

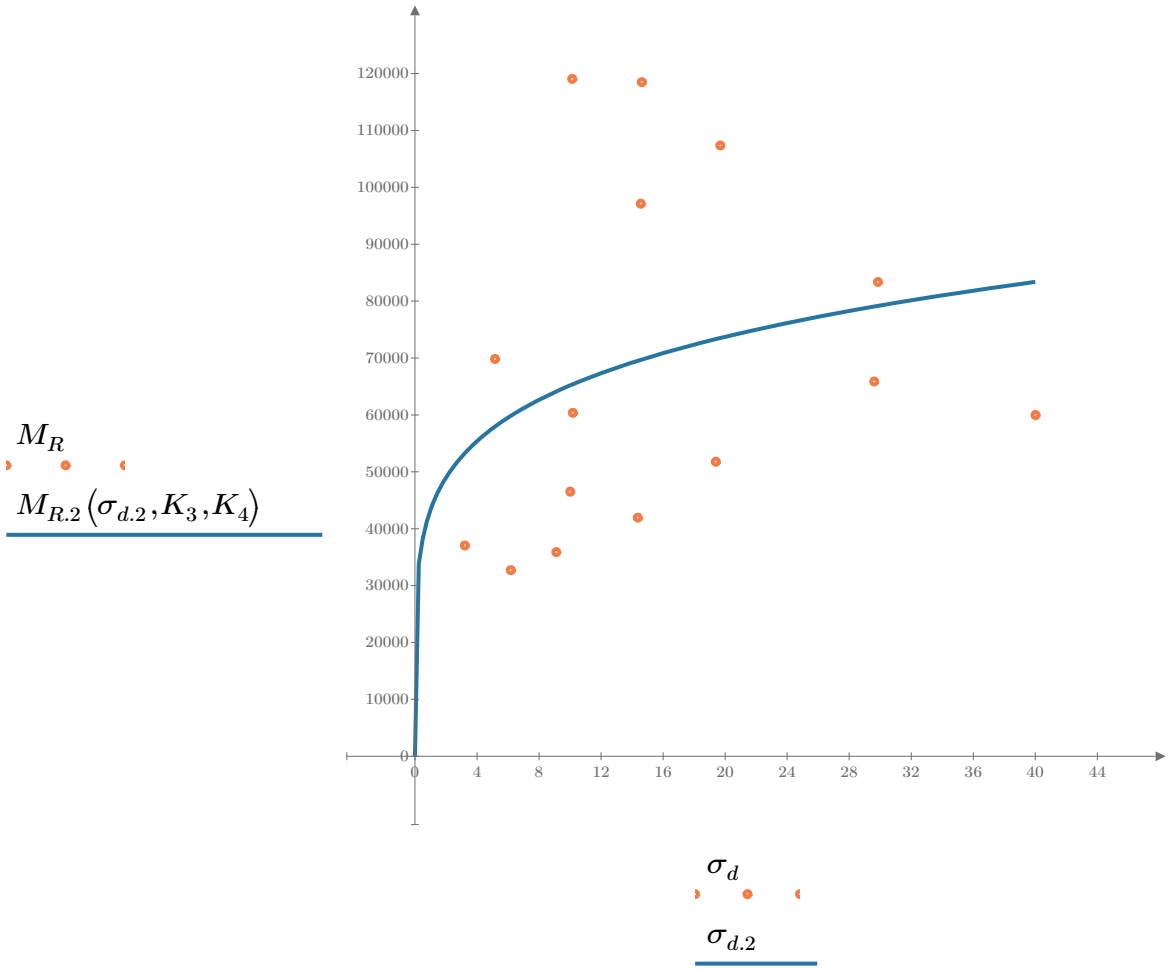

Figure 2. Plot of the test data (orange points) vs. the fitted Equation 2 model (blue line).

Dan Seely
9/12/2023

$$M_{R.3}\left(\sigma_d,\sigma_3,K_5,K_6,K_7\right):=K_5\cdot{\sigma_d}^{K_6}\cdot\left(1+\sigma_3\right)^{K_7}$$

Equation 3 AASHTO Publication No. FHWA-RD-97-083

$K_5=30502.397$

$K_6=-0.4089$ Equation 3 fitting parameters

$K_7=0.8166$

${R_3}^2=0.8758$ Coefficient of determination

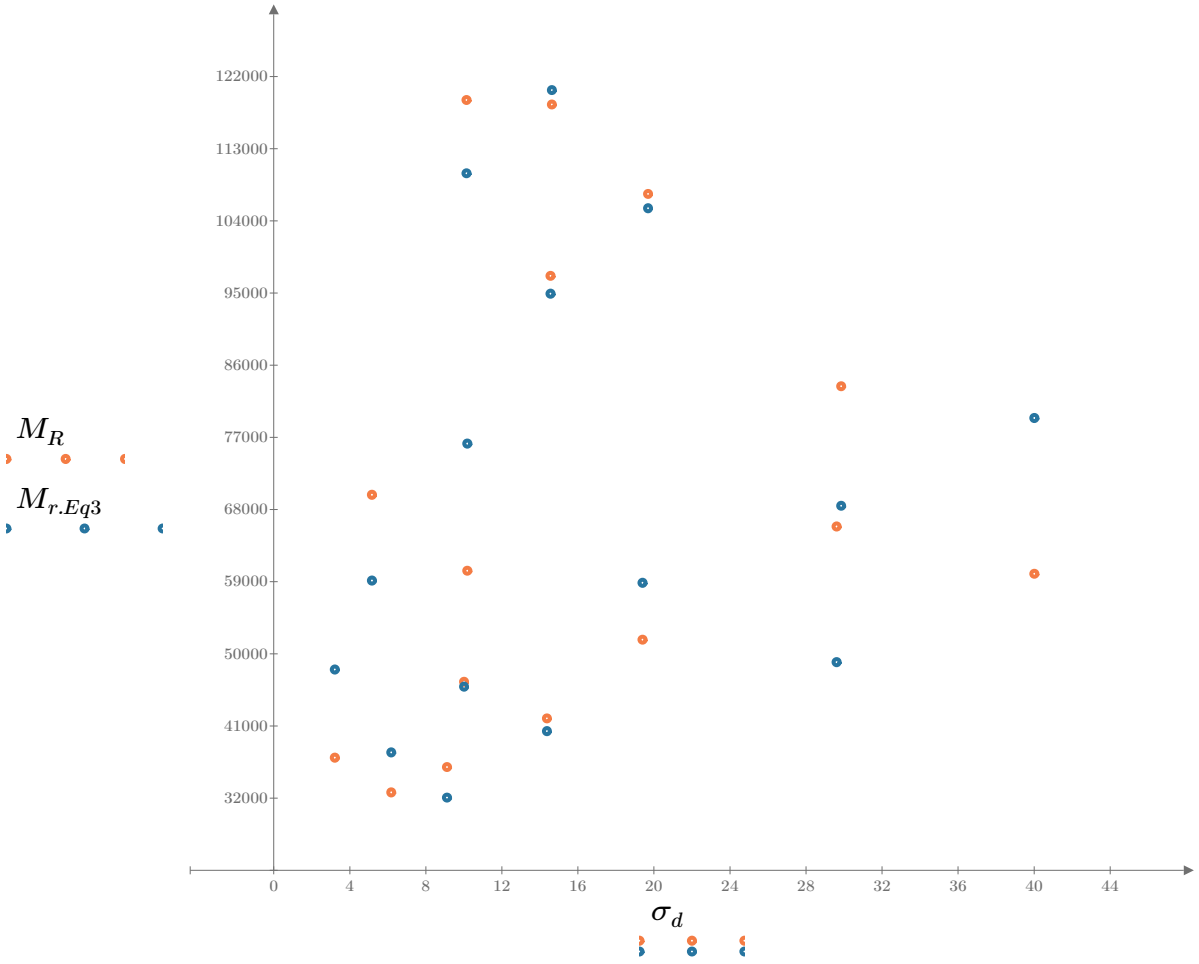

Figure 3. Plot of the test data (orange points) vs. the fitted Equation 3 model (blue points).

Dan Seely
9/12/2023

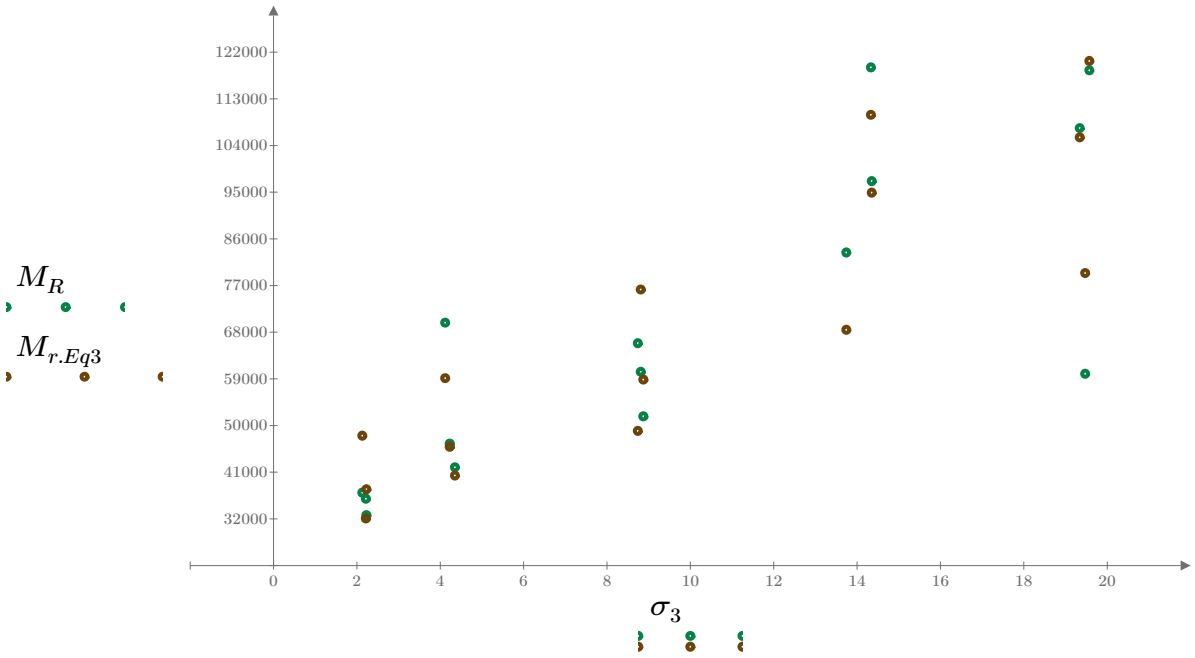

Figure 4. Plot of the test data (green points) vs. the fitted Equation 3 model (brown points).

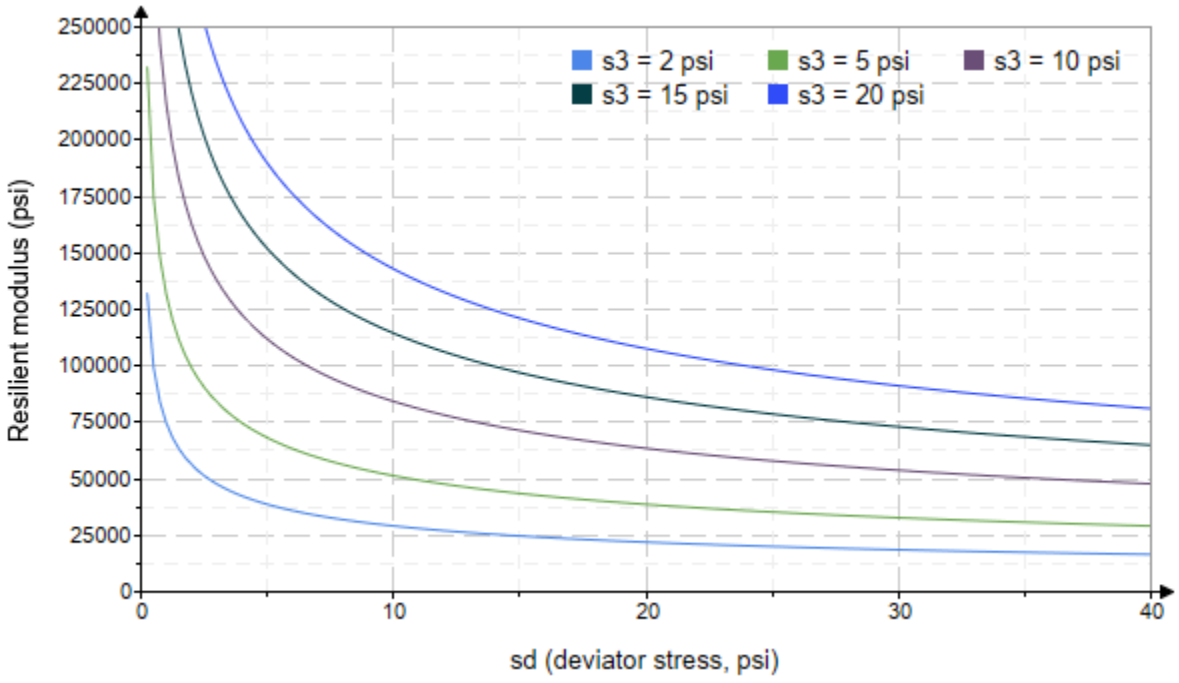

Figure 5. Plot of the fitted Equation 3 model for various confining stresses.

Dan Seely
9/12/2023

$$M_{R.4}\left(\sigma_B,\sigma_d,K_8,K_9,K_{10}\right) := K_8 \cdot p_a \left(\frac{\sigma_B}{p_a}\right)^{K_9} \cdot \left(\frac{\sigma_d}{p_a}\right)^{K_{10}}$$

Equation 4 AASHTO Publication No. FHWA-RD-97-083

$K_8 = 1465.279$

$K_9 = 1.0750$ Equation 4 fitting parameters

$K_{10} = -0.7706$

$R_4^{\,2} = 0.8987$ Coefficient of determination

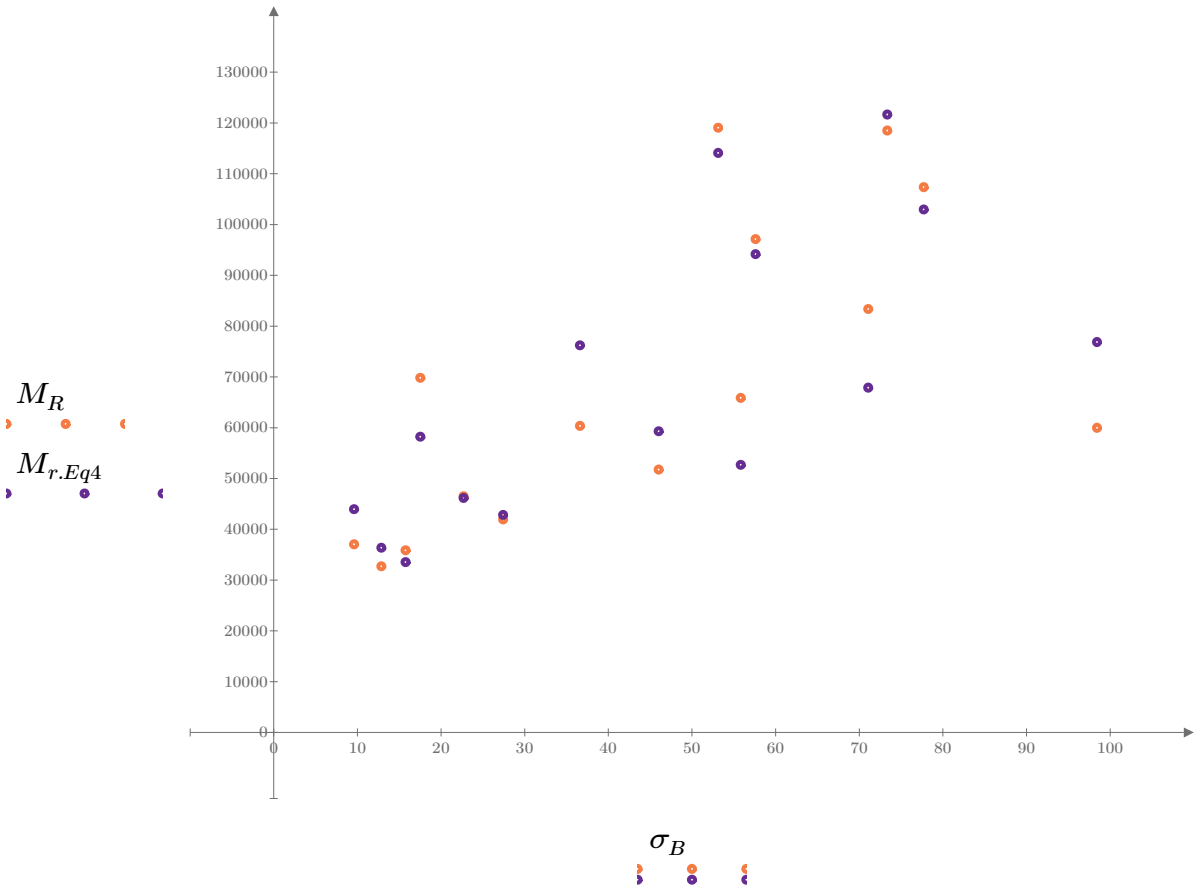

Figure 6. Plot of the test data (orange points) vs. the fitted Equation 4 model (purple points).

Dan Seely
9/12/2023

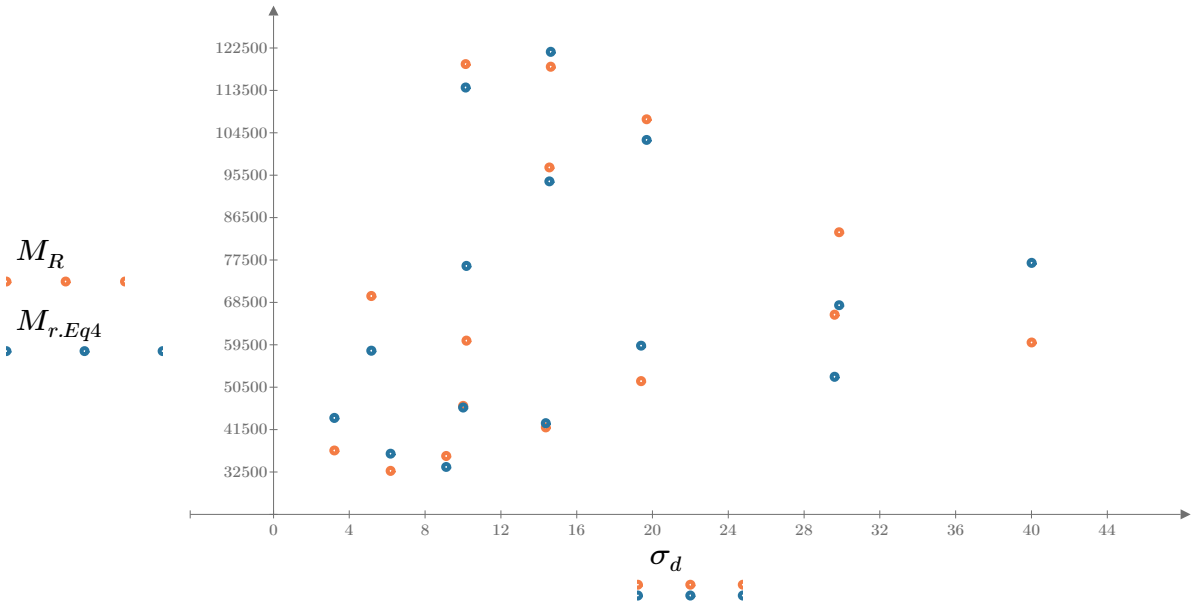

Figure 7. Plot of the test data (orange points) vs. the fitted Equation 4 model (blue points).

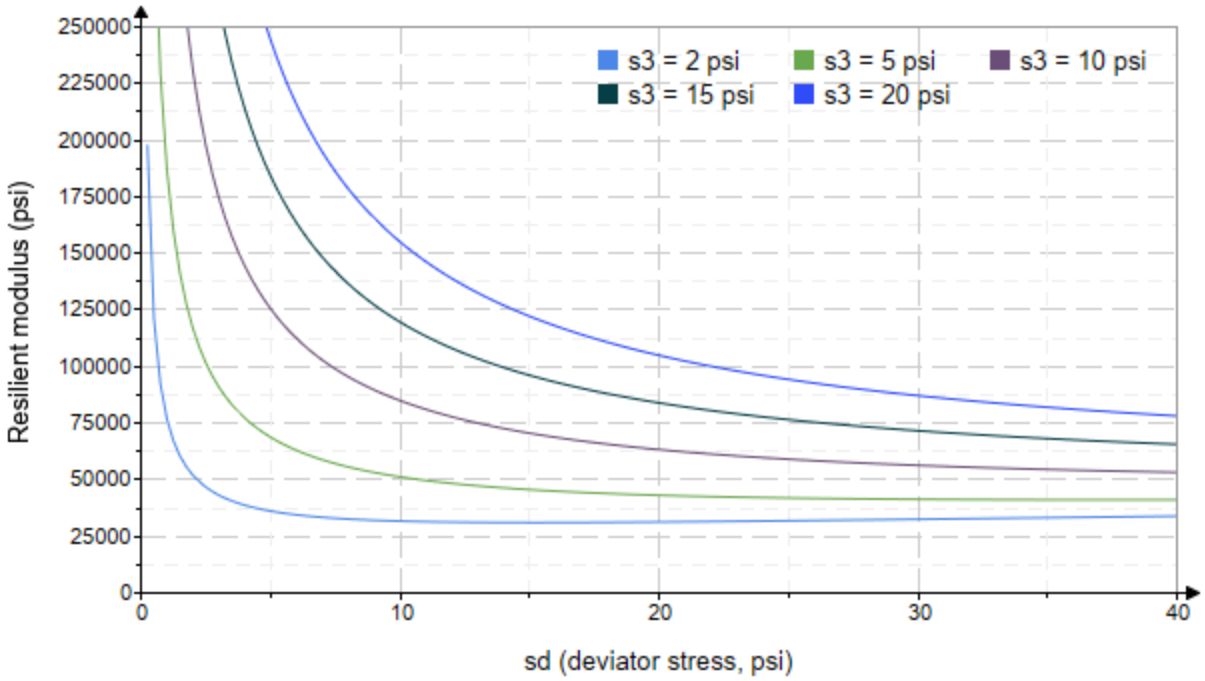

Figure 8. Plot of the fitted Equation 4 model for various confining stresses.

Dan Seely
9/12/2023

$SampleNo := \text{“B2}-\text{74”}$

$Treatment = \text{“M5”}$

$S = 10.444$ Degree of Saturation (%)

Test Sequence : Base/Subbase

Test summary data (psi) :

$$\sigma_3 = \begin{bmatrix} 2.723 \\ 2.692 \\ 2.634 \\ 4.535 \\ 4.549 \\ 4.559 \\ 9.591 \\ 9.559 \\ 9.531 \\ 14.620 \\ 14.600 \\ 14.580 \\ 19.600 \\ 19.620 \\ 19.610 \end{bmatrix} \quad \sigma_d = \begin{bmatrix} 3.318 \\ 6.208 \\ 9.163 \\ 5.281 \\ 10.110 \\ 14.520 \\ 10.090 \\ 19.330 \\ 29.400 \\ 10.180 \\ 14.510 \\ 29.610 \\ 14.460 \\ 19.390 \\ 40.280 \end{bmatrix} \quad \sigma_B = \begin{bmatrix} 11.490 \\ 14.280 \\ 17.060 \\ 18.890 \\ 23.760 \\ 28.200 \\ 38.860 \\ 48.010 \\ 57.990 \\ 54.030 \\ 58.310 \\ 73.340 \\ 73.270 \\ 78.240 \\ 99.110 \end{bmatrix} \quad M_R = \begin{bmatrix} 33955.8 \\ 36100.4 \\ 38472.8 \\ 51254.8 \\ 57660.0 \\ 51675.8 \\ 62387.8 \\ 67846.2 \\ 60964.6 \\ 74647.2 \\ 80018.2 \\ 60581.6 \\ 71811.2 \\ 65142.2 \\ 60352.6 \end{bmatrix}$$

σ_3 = mean confining stress
σ_d = mean deviator stress
σ_B = mean bulk stress
M_R = resilient modulus
p_a = atmospheric pressure = 14.6959 psi

Dan Seely
9/12/2023

$$M_{R.1}\left(\sigma_B, K_1, K_2\right) := K_1 \cdot {\sigma_B}^{K_2}$$

Equation 1
AASHTO Publication No. FHWA-RD-97-083

$K_1 = 21467.813$

$K_2 = 0.2701$

Equation 1 fitting parameters

${R_1}^2 = 0.6287$

Coefficient of determination

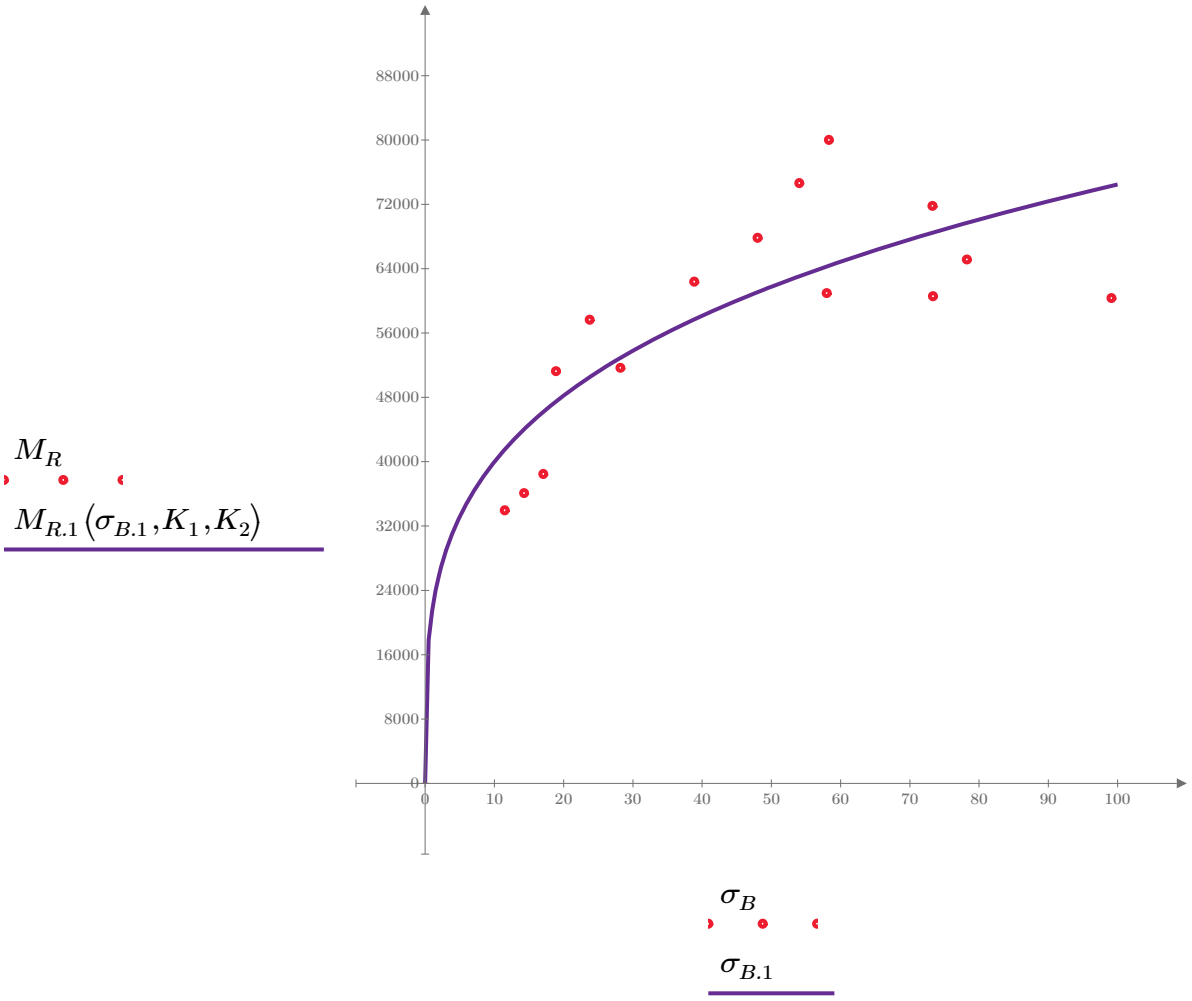

Figure 1. Plot of the test data (red points) vs. the fitted Equation 1 model (purple line).

Dan Seely
9/12/2023

$$M_{R.2}(\sigma_d, K_3, K_4) := K_3 \cdot \sigma_d^{K_4}$$

Equation 2
AASHTO Publication No. FHWA-RD-97-083

$K_3 = 36983.239$

$K_4 = 0.1754$

Equation 2 fitting parameters

$R_2^2 = 0.2828$

Coefficient of determination

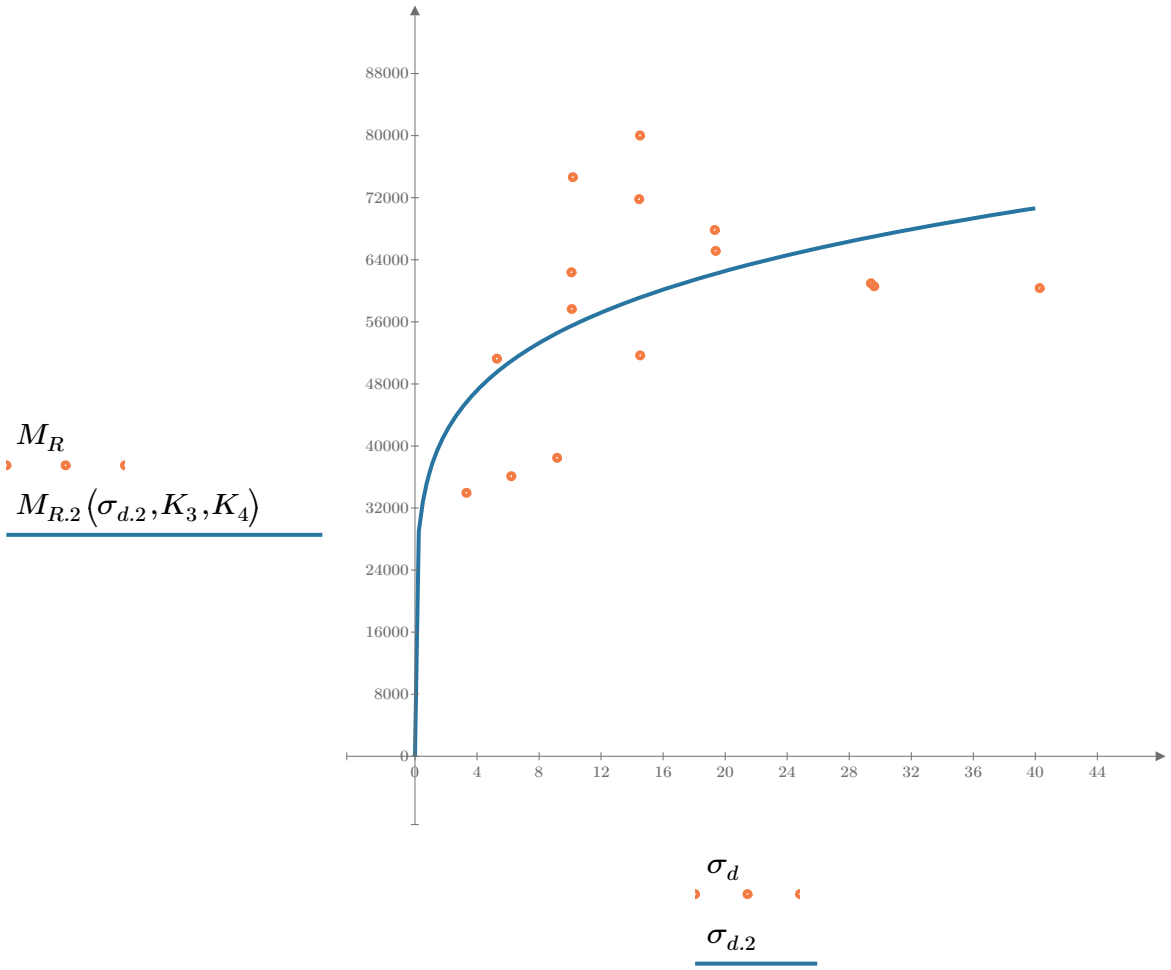

Figure 2. Plot of the test data (orange points) vs. the fitted Equation 2 model (blue line).

Dan Seely
9/12/2023

$$M_{R.3}\left(\sigma_d,\sigma_3,K_5,K_6,K_7\right):=K_5\cdot{\sigma_d}^{K_6}\cdot\left(1+\sigma_3\right)^{K_7}$$

Equation 3 AASHTO Publication No. FHWA-RD-97-083

$K_5=31099.959$

$K_6=-0.0591$ Equation 3 fitting parameters

$K_7=0.3409$

${R_3}^2=0.7088$ Coefficient of determination

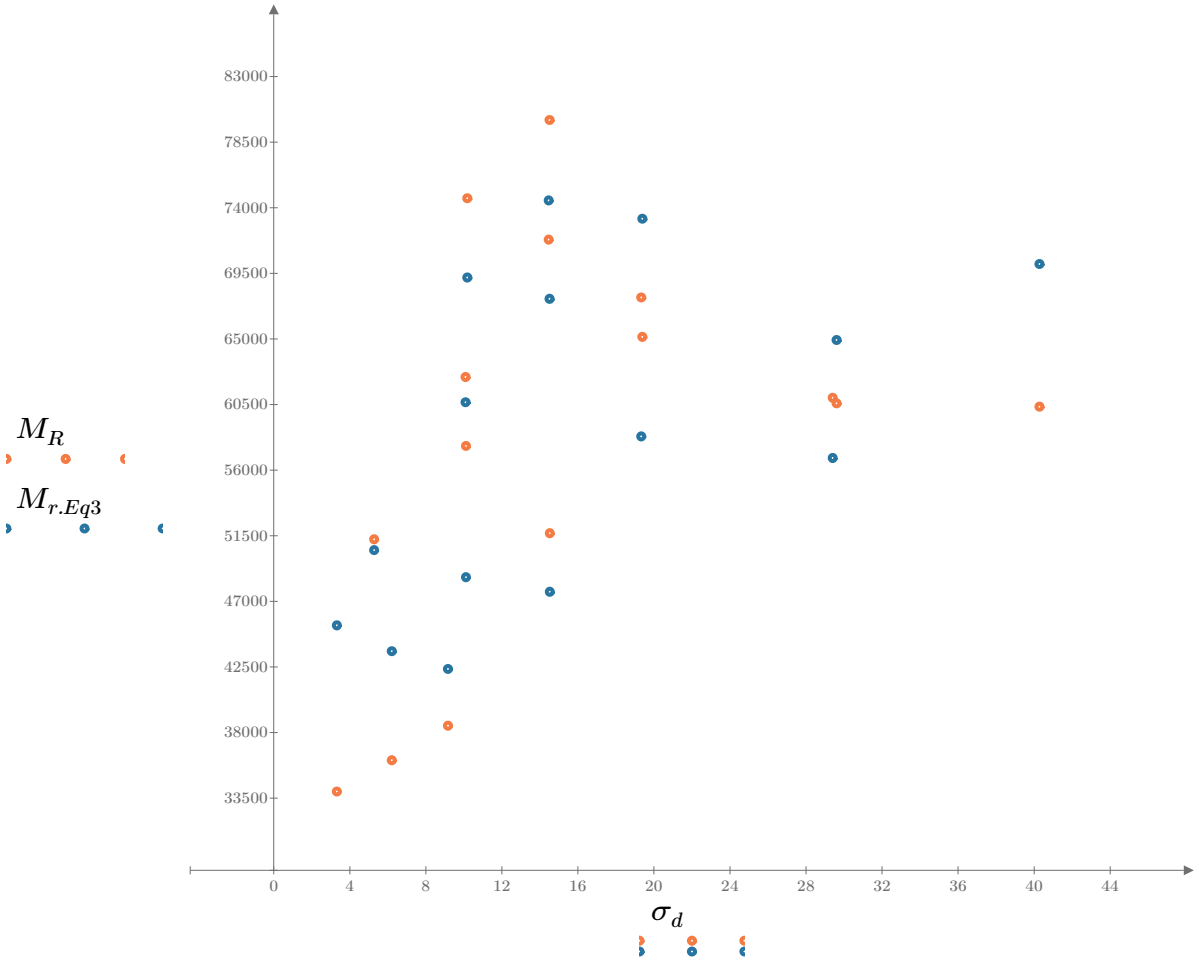

Figure 3. Plot of the test data (orange points) vs. the fitted Equation 3 model (blue points).

Dan Seely
9/12/2023

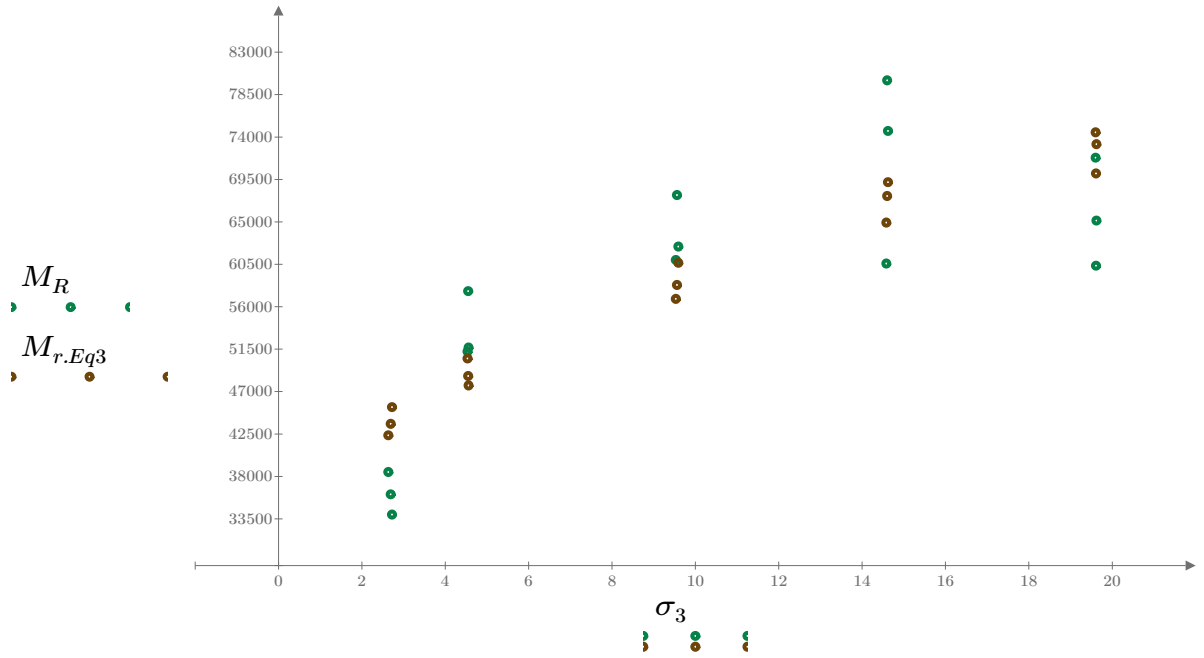

Figure 4. Plot of the test data (green points) vs. the fitted Equation 3 model (brown points).

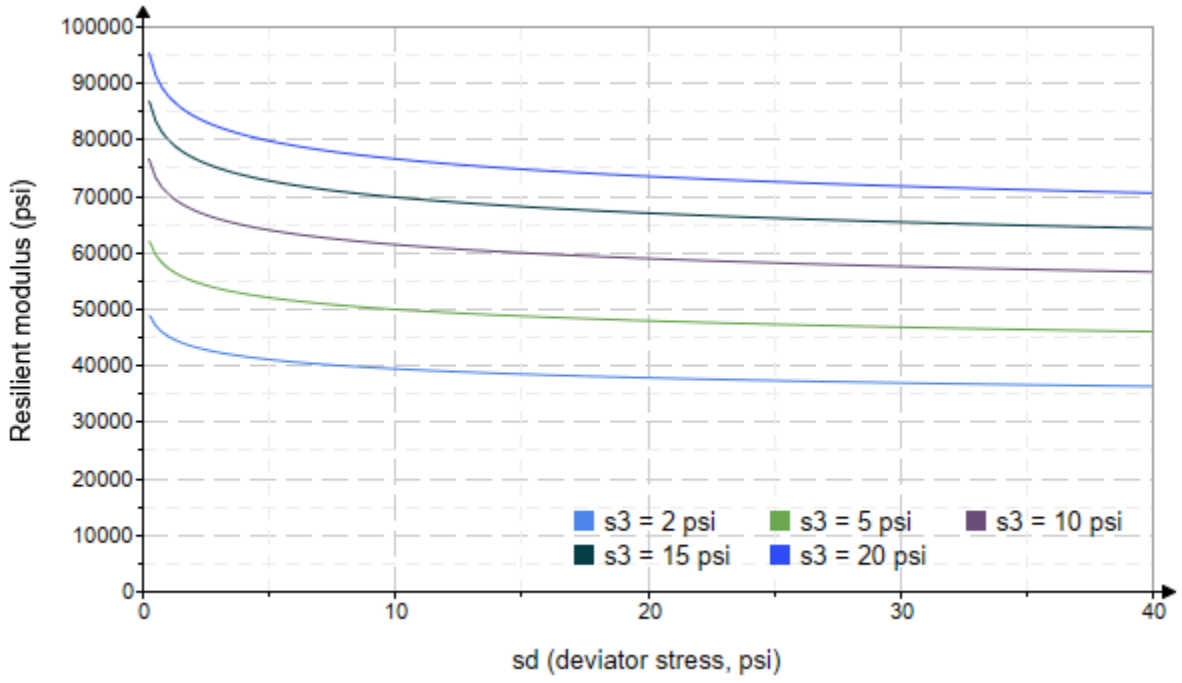

Figure 5. Plot of the fitted Equation 3 model for various confining stresses.

Dan Seely
9/12/2023

$$M_{R.4}\left(\sigma_B,\sigma_d,K_8,K_9,K_{10}\right) := K_8 \cdot p_a \left(\frac{\sigma_B}{p_a}\right)^{K_9} \cdot \left(\frac{\sigma_d}{p_a}\right)^{K_{10}}$$

Equation 4 AASHTO Publication No. FHWA-RD-97-083

$K_8 = 2422.107$

$K_9 = 0.4658$ Equation 4 fitting parameters

$K_{10} = -0.2243$

$R_4^{\,2} = 0.7392$ Coefficient of determination

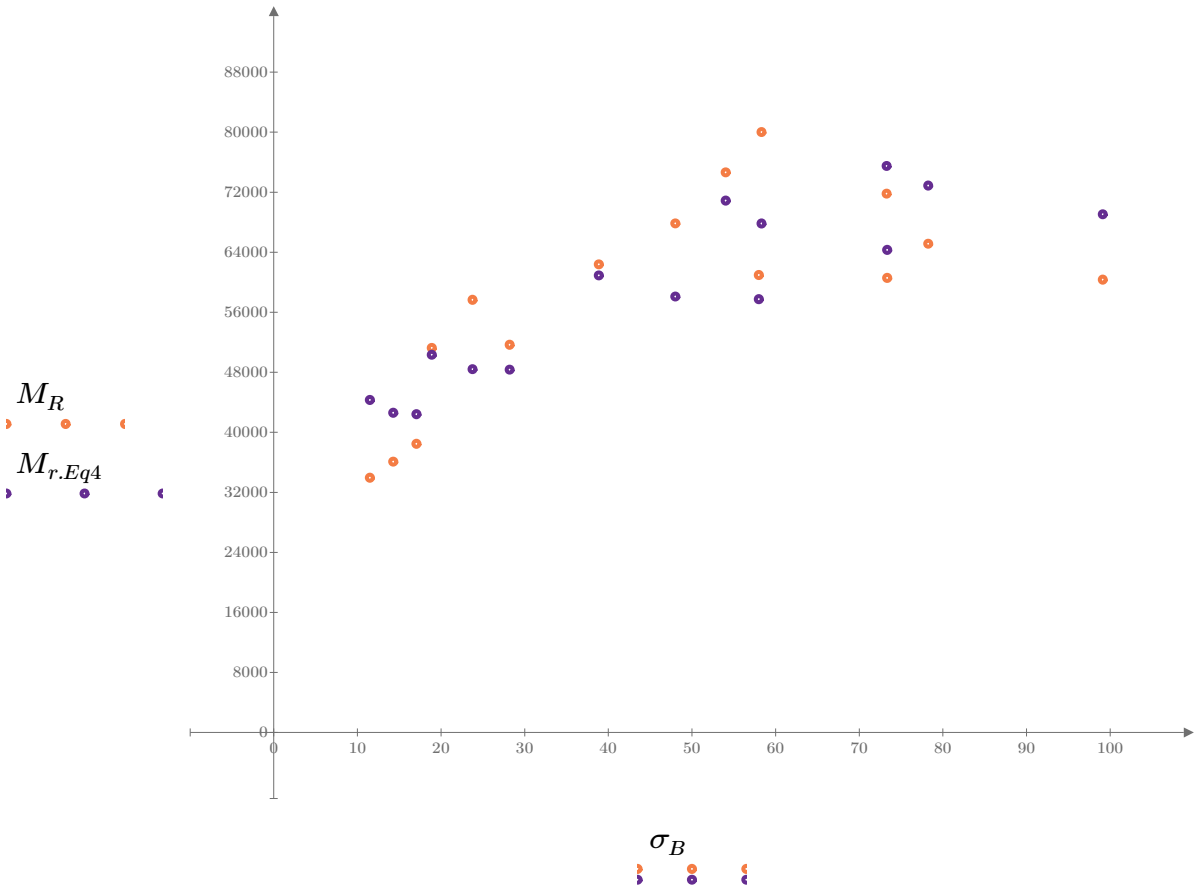

Figure 6. Plot of the test data (orange points) vs. the fitted Equation 4 model (purple points).

Dan Seely
9/12/2023

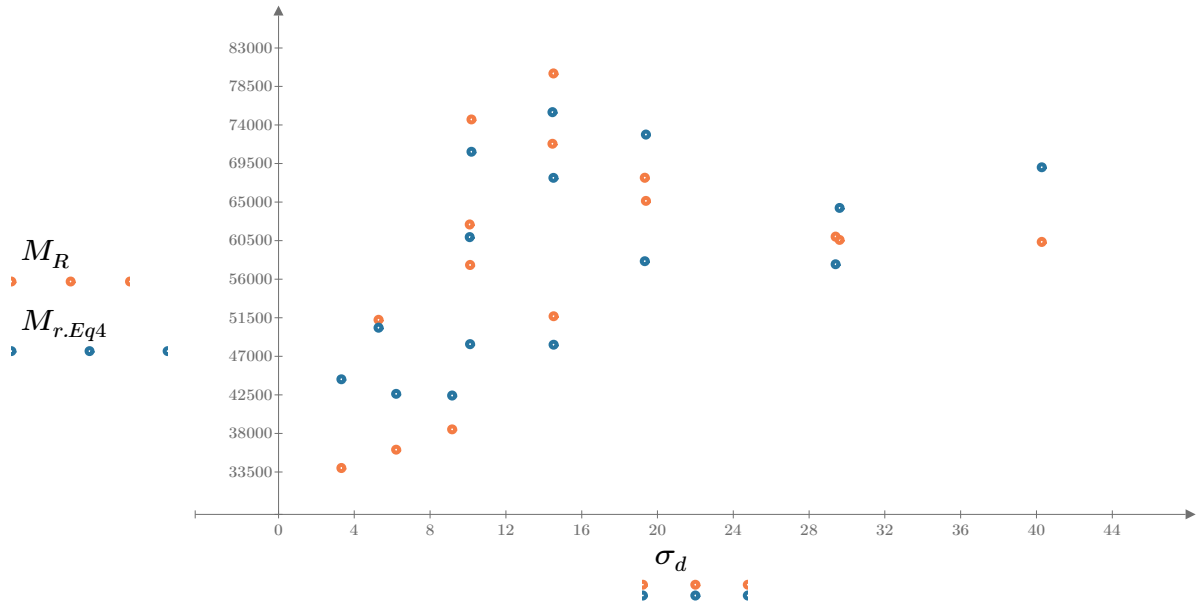

Figure 7. Plot of the test data (orange points) vs. the fitted Equation 4 model (blue points).

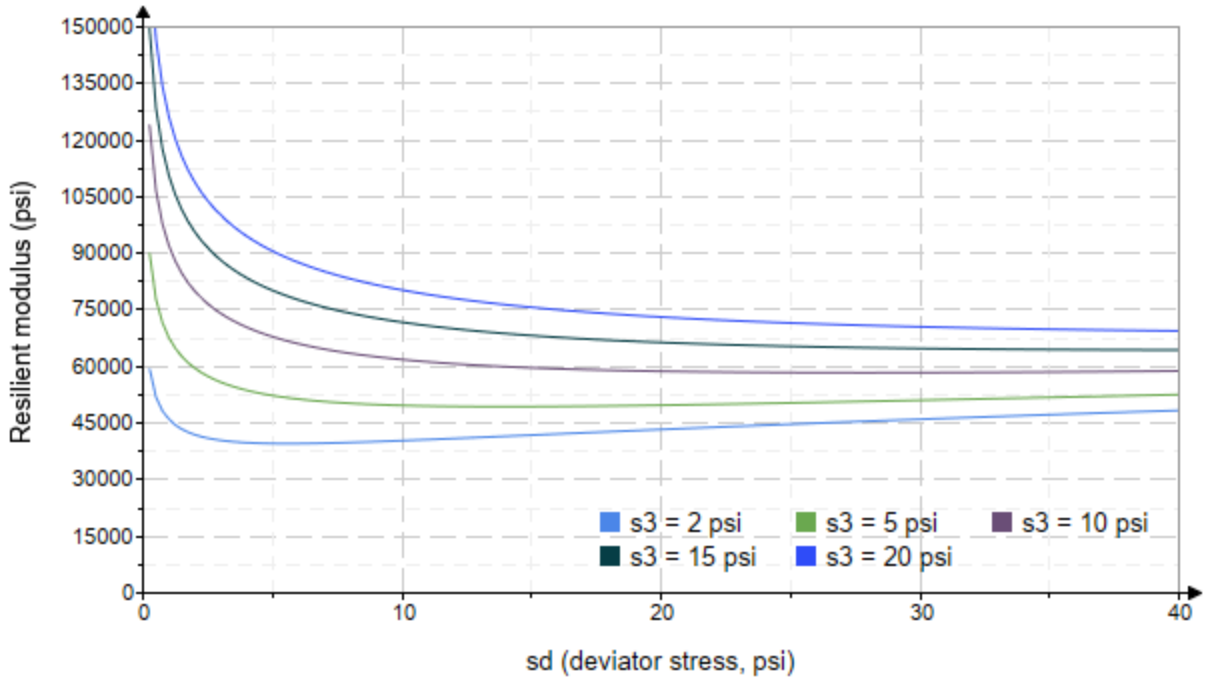

Figure 8. Plot of the fitted Equation 4 model for various confining stresses.

Dan Seely
9/12/2023

$SampleNo := \text{“B2}-75\text{”}$

$Treatment = \text{“M5”}$

$S = 10.055$ Degree of Saturation (%)

Test Sequence : Base/Subbase

Test summary data (psi) :

$$\sigma_3 = \begin{bmatrix} 2.789 \\ 2.204 \\ 1.978 \\ 4.052 \\ 3.682 \\ 3.148 \\ 8.571 \\ 8.712 \\ 8.707 \\ 13.560 \\ 13.160 \\ 13.820 \\ 18.770 \\ 18.390 \\ 19.270 \end{bmatrix} \quad \sigma_d = \begin{bmatrix} 3.108 \\ 6.300 \\ 9.240 \\ 5.212 \\ 10.210 \\ 14.610 \\ 10.240 \\ 19.360 \\ 29.660 \\ 10.170 \\ 14.600 \\ 29.880 \\ 14.580 \\ 19.750 \\ 40.250 \end{bmatrix} \quad \sigma_B = \begin{bmatrix} 11.470 \\ 12.910 \\ 15.170 \\ 17.370 \\ 21.250 \\ 24.050 \\ 35.950 \\ 45.490 \\ 55.780 \\ 50.850 \\ 54.090 \\ 71.360 \\ 70.870 \\ 74.920 \\ 98.060 \end{bmatrix} \quad M_R = \begin{bmatrix} 33593.2 \\ 26456.8 \\ 28727.2 \\ 46165.2 \\ 44385.8 \\ 41021.6 \\ 75104.8 \\ 66216.4 \\ 76302.2 \\ 193686.0 \\ 94895.8 \\ 87337.2 \\ 188624.0 \\ 147176.0 \\ 68962.0 \end{bmatrix}$$

σ_3 = mean confining stress
σ_d = mean deviator stress
σ_B = mean bulk stress
M_R = resilient modulus
p_a = atmospheric pressure = 14.6959 psi

Dan Seely
9/12/2023

$$M_{R.1}\left(\sigma_B, K_1, K_2\right) := K_1 \cdot {\sigma_B}^{K_2}$$

Equation 1
AASHTO Publication No. FHWA-RD-97-083

$K_1 = 8716.605$

$K_2 = 0.6055$

Equation 1 fitting parameters

${R_1}^2 = 0.4238$

Coefficient of determination

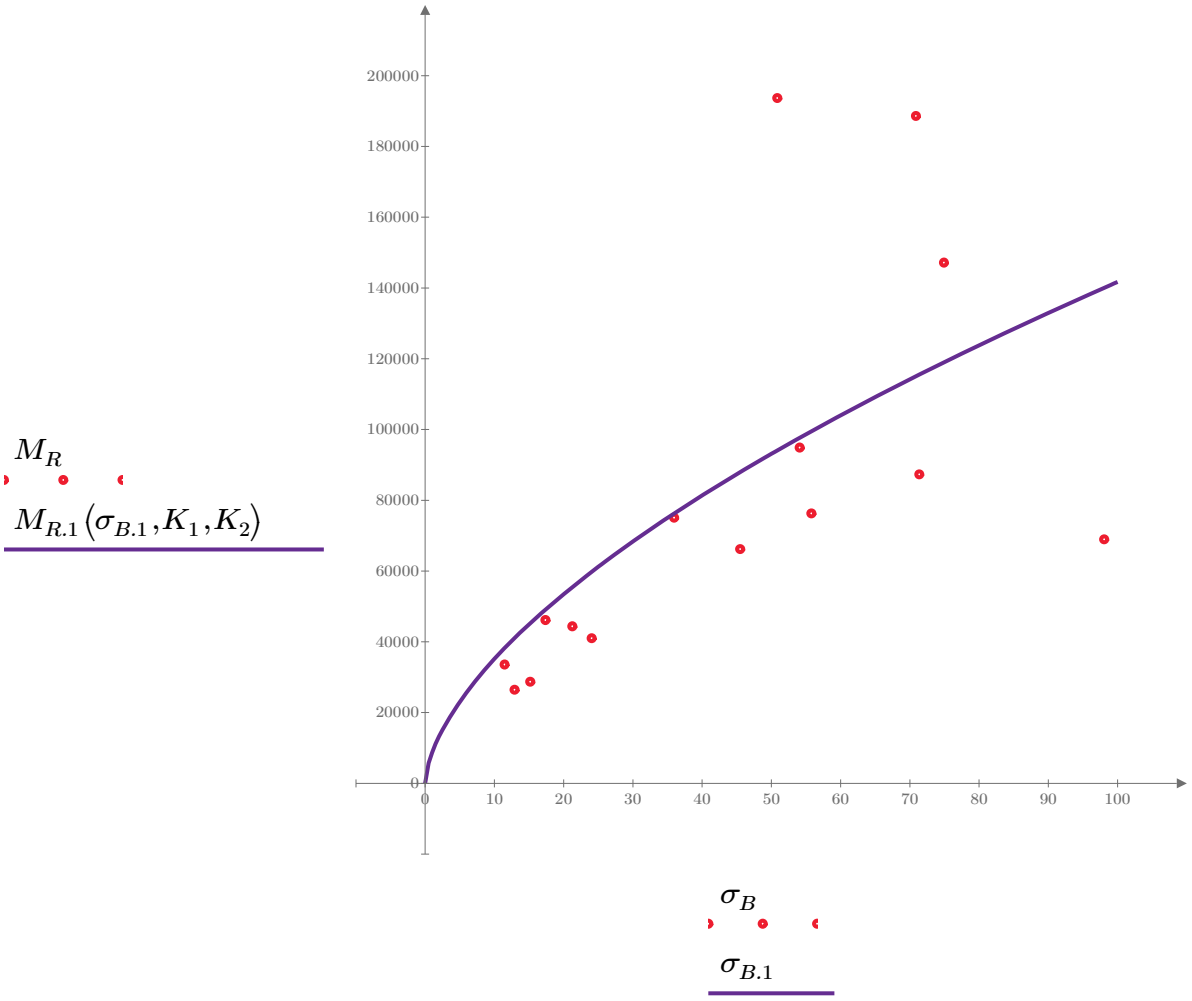

Figure 1. Plot of the test data (red points) vs. the fitted Equation 1 model (purple line).

Dan Seely
9/12/2023

$$M_{R.2}(\sigma_d, K_3, K_4) := K_3 \cdot \sigma_d^{K_4}$$

Equation 2
AASHTO Publication No. FHWA-RD-97-083

$K_3 = 44483.560$

$K_4 = 0.2326$

Equation 2 fitting parameters

$R_2^2 = 0.0728$

Coefficient of determination

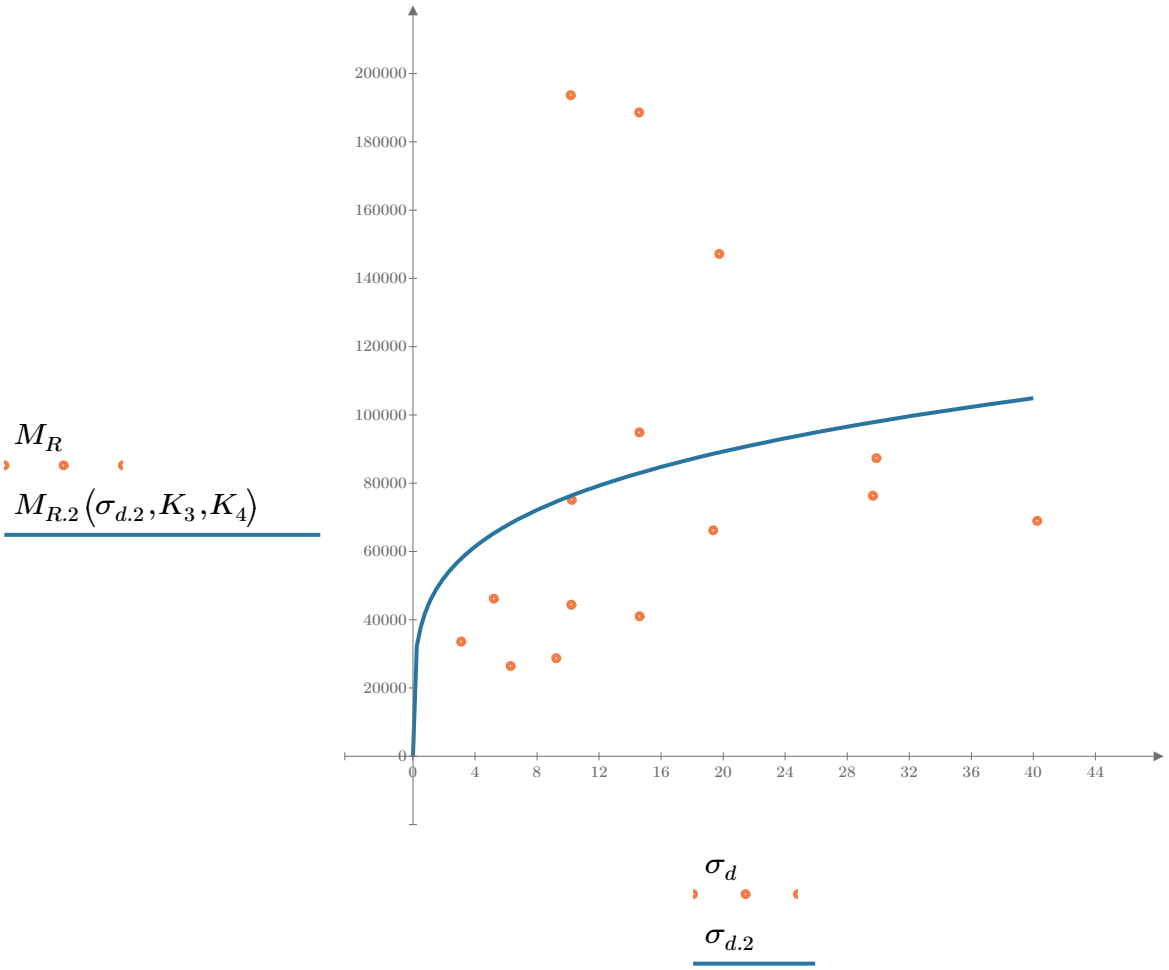

Figure 2. Plot of the test data (orange points) vs. the fitted Equation 2 model (blue line).

Dan Seely
9/12/2023

$$M_{R.3}\left(\sigma_d,\sigma_3,K_5,K_6,K_7\right):=K_5\cdot{\sigma_d}^{K_6}\cdot\left(1+\sigma_3\right)^{K_7}$$

Equation 3 AASHTO Publication No. FHWA-RD-97-083

$K_5=19445.777$

$K_6=-0.7082$ Equation 3 fitting parameters

$K_7=1.3998$

${R_3}^2=0.8765$ Coefficient of determination

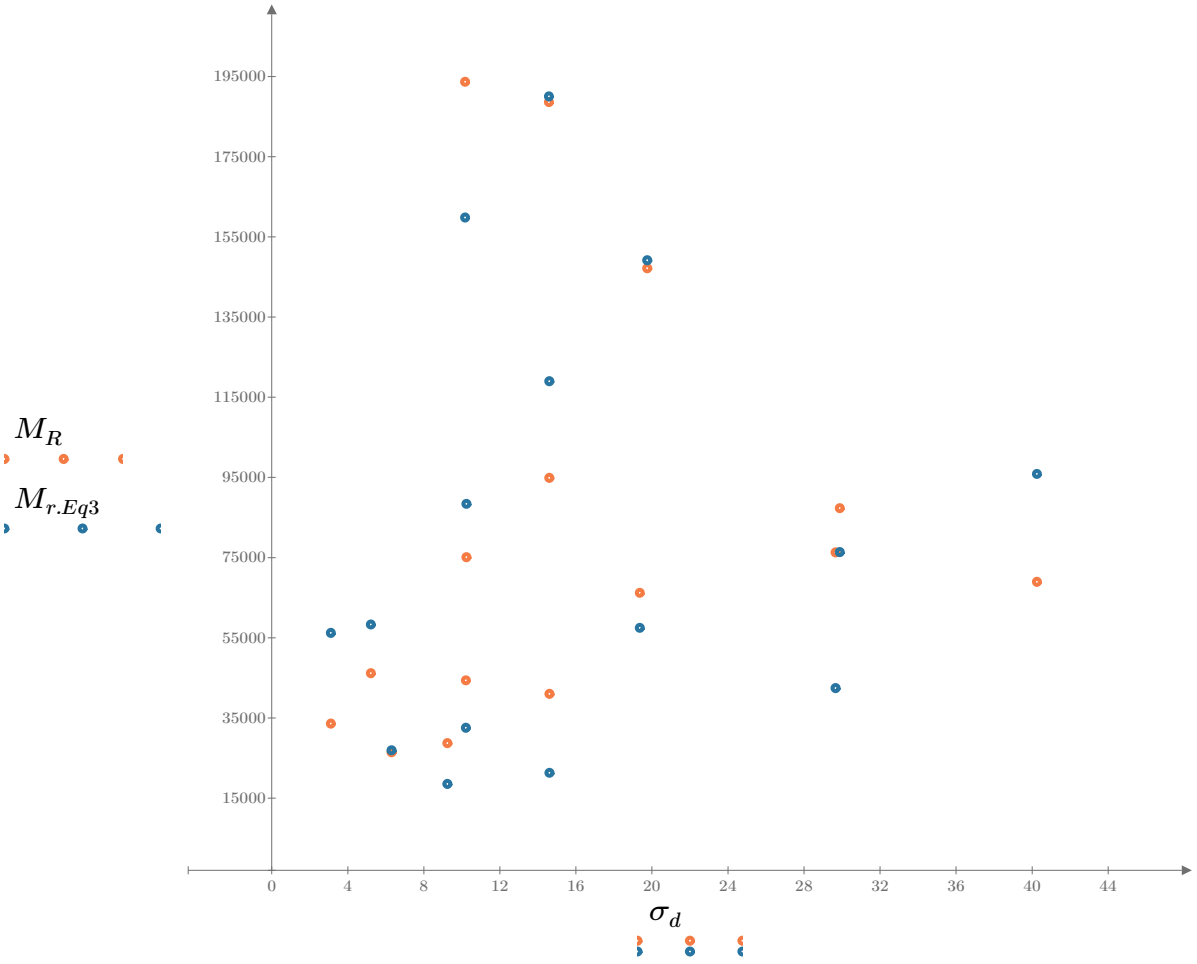

Figure 3. Plot of the test data (orange points) vs. the fitted Equation 3 model (blue points).

Dan Seely
9/12/2023

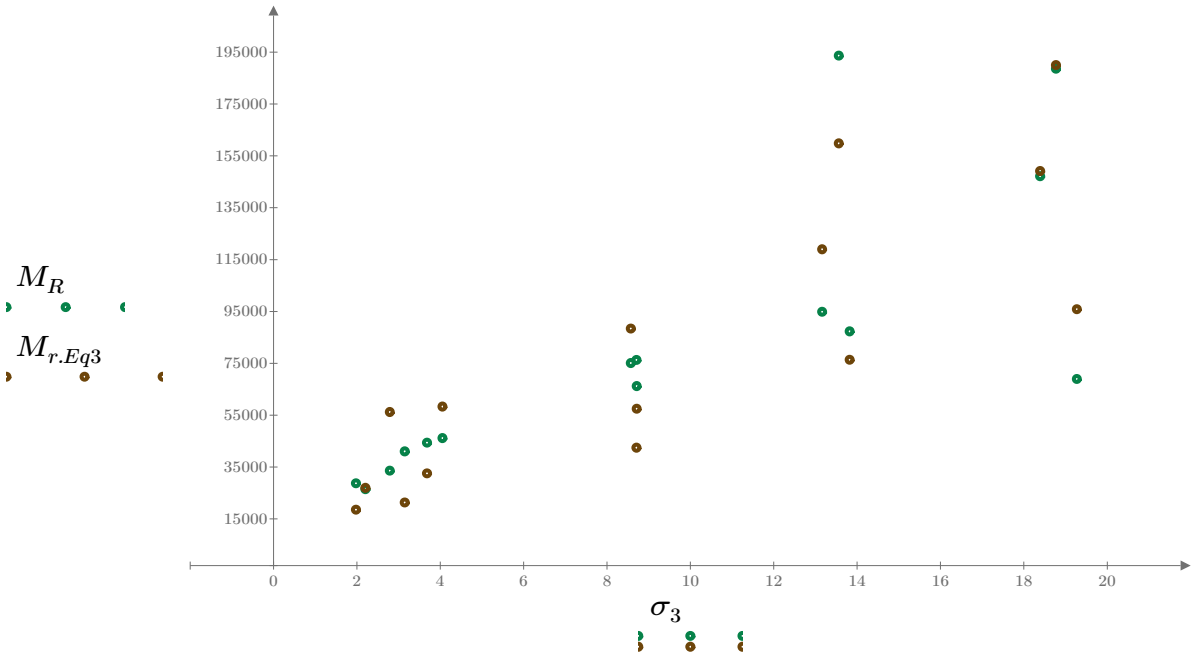

Figure 4. Plot of the test data (green points) vs. the fitted Equation 3 model (brown points).

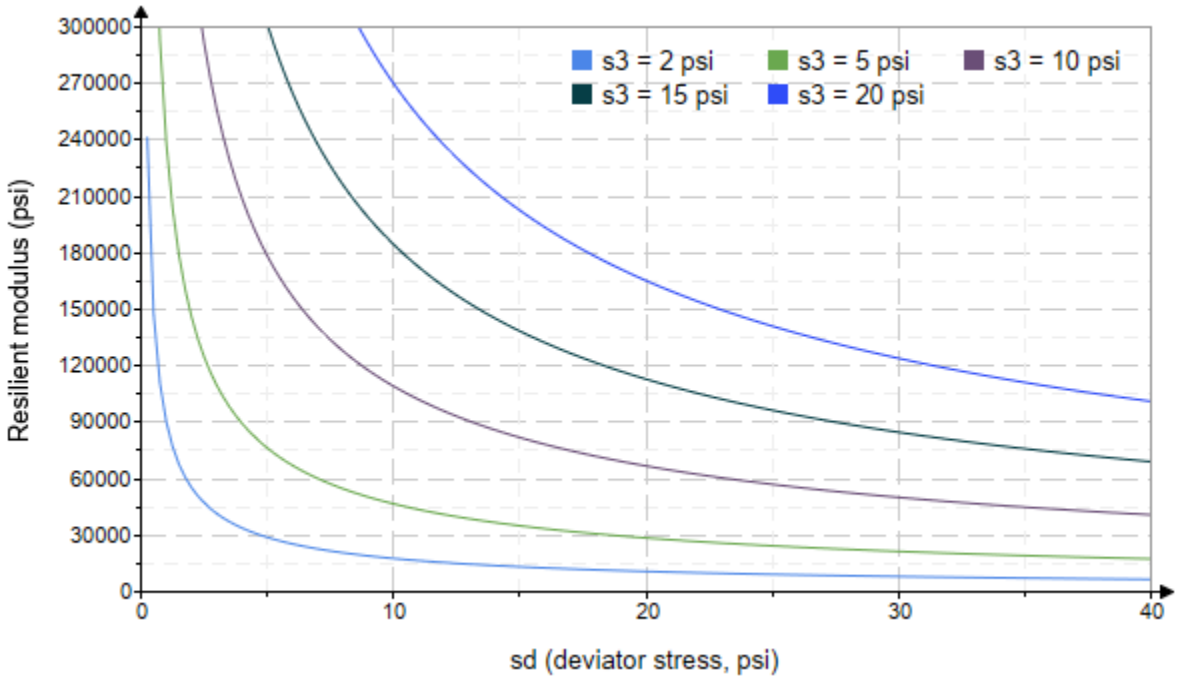

Figure 5. Plot of the fitted Equation 3 model for various confining stresses.

Dan Seely
9/12/2023

$$M_{R.4}\left(\sigma_B,\sigma_d,K_8,K_9,K_{10}\right) := K_8 \cdot p_a \left(\frac{\sigma_B}{p_a}\right)^{K_9} \cdot \left(\frac{\sigma_d}{p_a}\right)^{K_{10}}$$

Equation 4 AASHTO Publication No. FHWA-RD-97-083

$K_8 = 718.899$

$K_9 = 1.8408$ Equation 4 fitting parameters

$K_{10} = -1.306$

$R_4^{\,2} = 0.9137$ Coefficient of determination

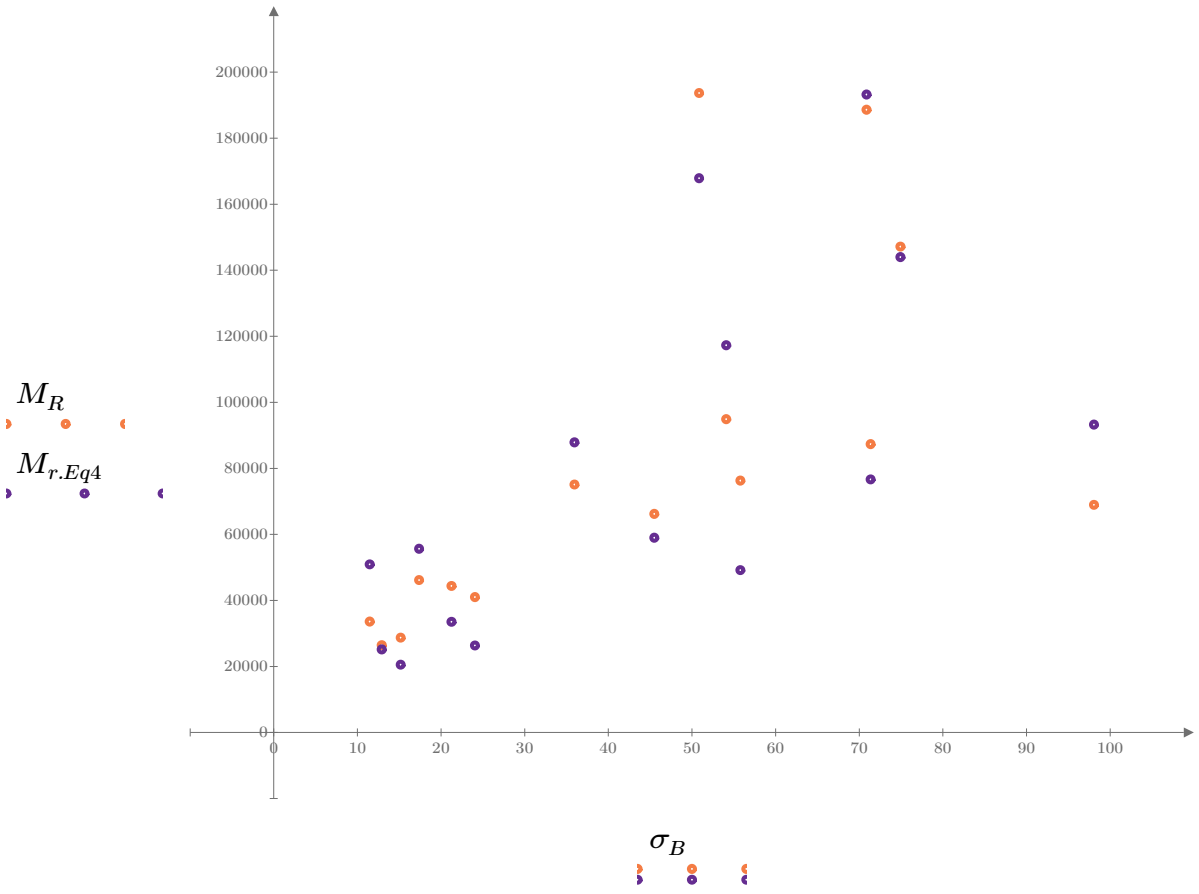

Figure 6. Plot of the test data (orange points) vs. the fitted Equation 4 model (purple points).

Dan Seely
9/12/2023

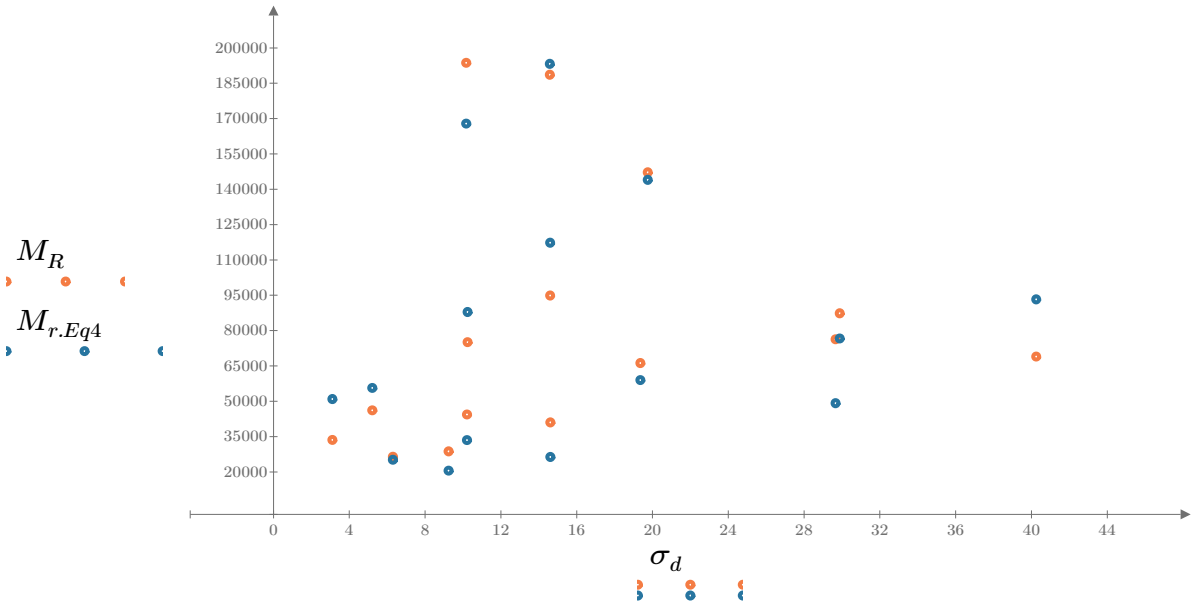

Figure 7. Plot of the test data (orange points) vs. the fitted Equation 4 model (blue points).

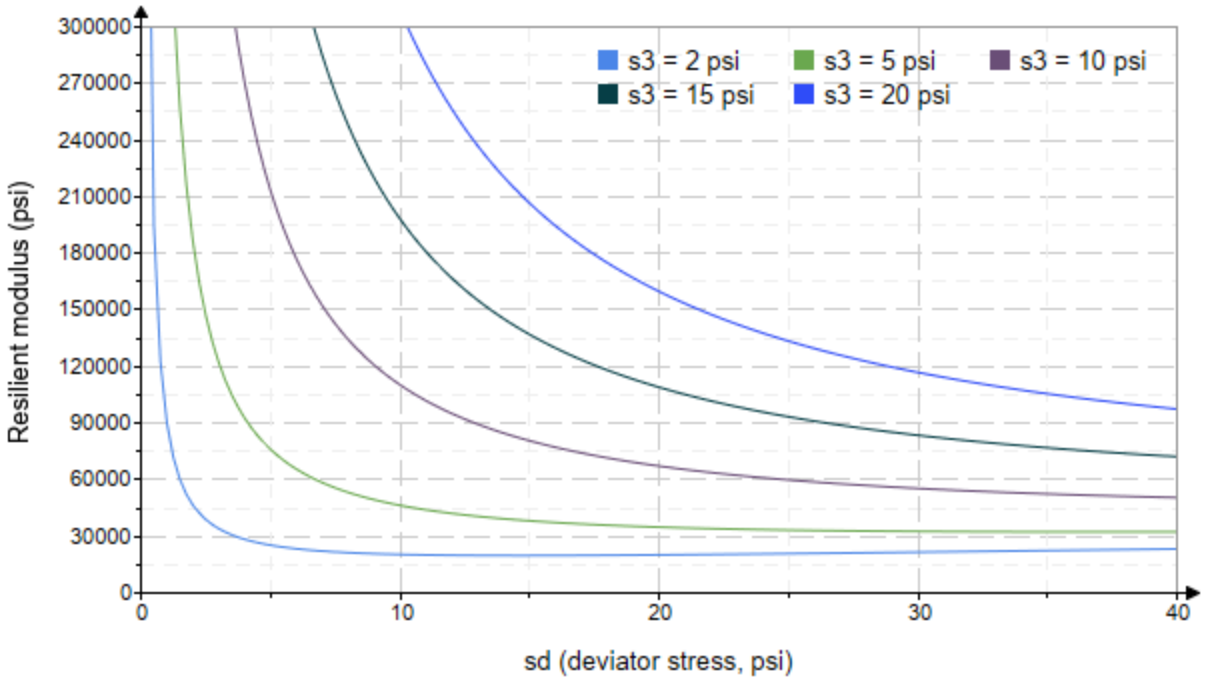

Figure 8. Plot of the fitted Equation 4 model for various confining stresses.

Dan Seely
9/12/2023

$SampleNo := \text{“B2}-\text{76”}$

$Treatment = \text{“M5”}$

$S = 9.884$ Degree of Saturation (%)

Test Sequence : Base/Subbase

Test summary data (psi) :

$$\sigma_3 = \begin{bmatrix} 2.572 \\ 2.570 \\ 2.545 \\ 4.580 \\ 4.531 \\ 4.510 \\ 9.560 \\ 9.554 \\ 9.547 \\ 14.590 \\ 14.580 \\ 14.570 \\ 19.620 \\ 19.610 \\ 19.610 \end{bmatrix} \quad \sigma_d = \begin{bmatrix} 3.156 \\ 6.201 \\ 9.177 \\ 5.246 \\ 10.100 \\ 14.480 \\ 10.040 \\ 19.300 \\ 29.710 \\ 10.200 \\ 14.520 \\ 29.880 \\ 14.540 \\ 19.510 \\ 40.200 \end{bmatrix} \quad \sigma_B = \begin{bmatrix} 10.870 \\ 13.910 \\ 16.810 \\ 18.990 \\ 23.700 \\ 28.010 \\ 38.720 \\ 47.960 \\ 58.350 \\ 53.970 \\ 58.270 \\ 73.600 \\ 73.410 \\ 78.340 \\ 99.020 \end{bmatrix} \quad M_R = \begin{bmatrix} 31077.6 \\ 25273.2 \\ 26699.8 \\ 25163.8 \\ 30091.8 \\ 30948.0 \\ 41707.6 \\ 42680.6 \\ 48636.6 \\ 71910.0 \\ 72675.0 \\ 55817.6 \\ 72918.0 \\ 64033.6 \\ 63560.4 \end{bmatrix}$$

σ_3 = mean confining stress
σ_d = mean deviator stress
σ_B = mean bulk stress
M_R = resilient modulus
p_a = atmospheric pressure = 14.6959 psi

Dan Seely
9/12/2023

$$M_{R.1}\left(\sigma_B, K_1, K_2\right) := K_1 \cdot {\sigma_B}^{K_2}$$

Equation 1
AASHTO Publication No. FHWA-RD-97-083

$K_1 = 6491.671$

$K_2 = 0.5279$

Equation 1 fitting parameters

${R_1}^2 = 0.7559$

Coefficient of determination

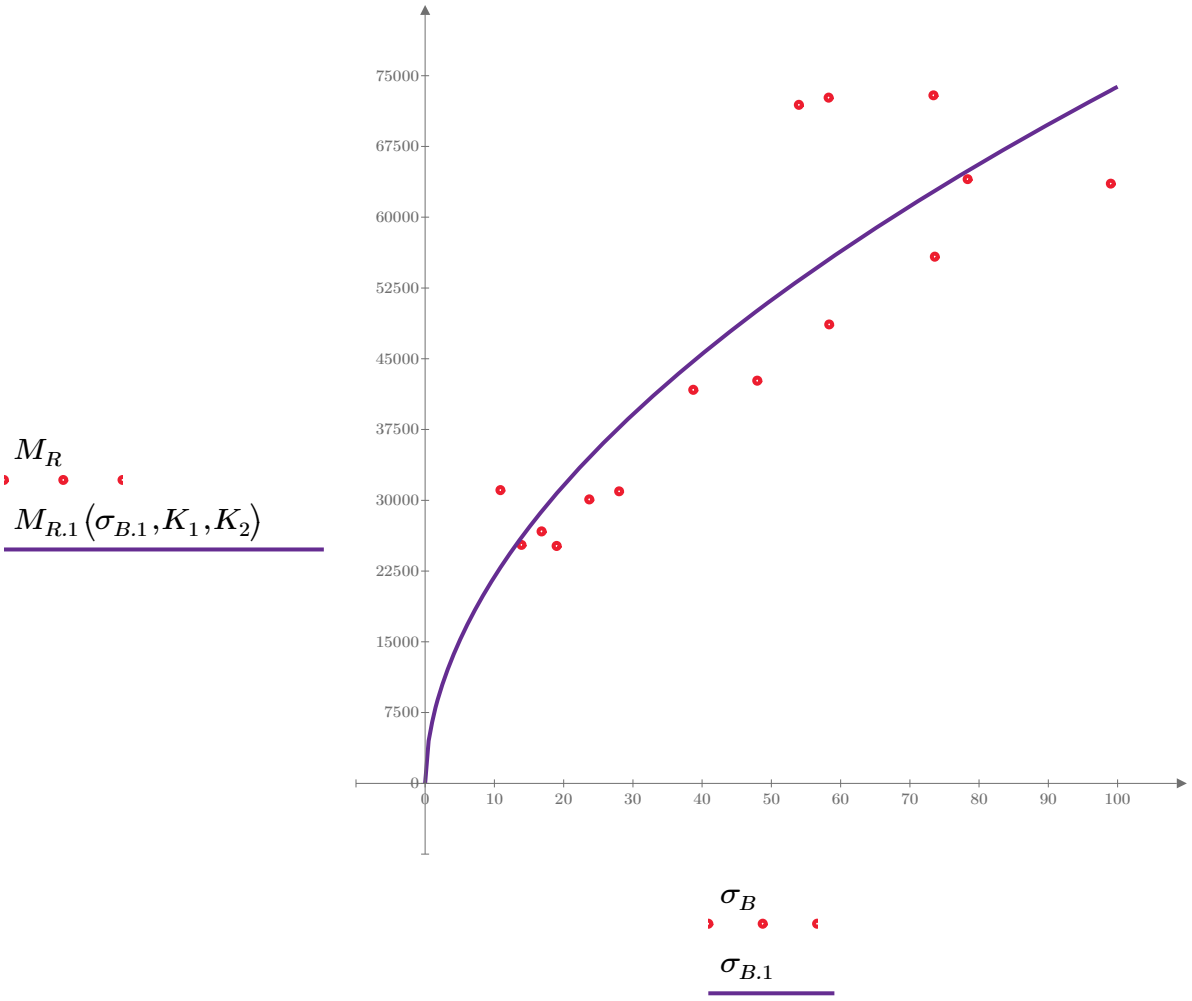

Figure 1. Plot of the test data (red points) vs. the fitted Equation 1 model (purple line).

Dan Seely
9/12/2023

$M_{R.2}(\sigma_d, K_3, K_4) := K_3 \cdot \sigma_d^{K_4}$ Equation 2
AASHTO Publication No. FHWA-RD-97-083

$K_3 = 21019.546$

$K_4 = 0.3073$ Equation 2 fitting parameters

$R_2^2 = 0.3029$ Coefficient of determination

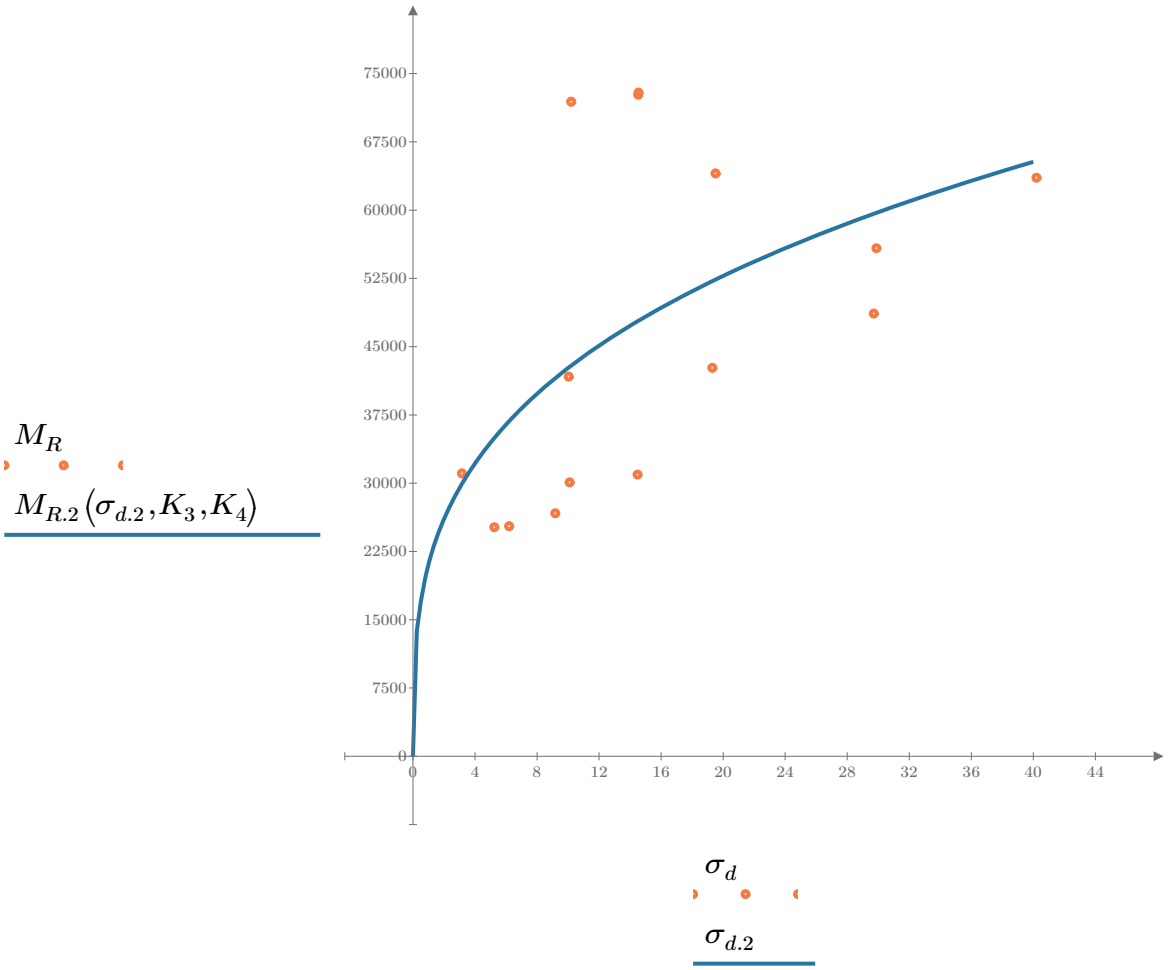

Figure 2. Plot of the test data (orange points) vs. the fitted Equation 2 model (blue line).

Dan Seely
9/12/2023

$$M_{R.3}\left(\sigma_d,\sigma_3,K_5,K_6,K_7\right):=K_5\cdot{\sigma_d}^{K_6}\cdot\left(1+\sigma_3\right)^{K_7}$$

Equation 3 AASHTO Publication No. FHWA-RD-97-083

$K_5=13297.090$

$K_6=-0.1282$ Equation 3 fitting parameters

$K_7=0.6819$

${R_3}^2=0.9036$ Coefficient of determination

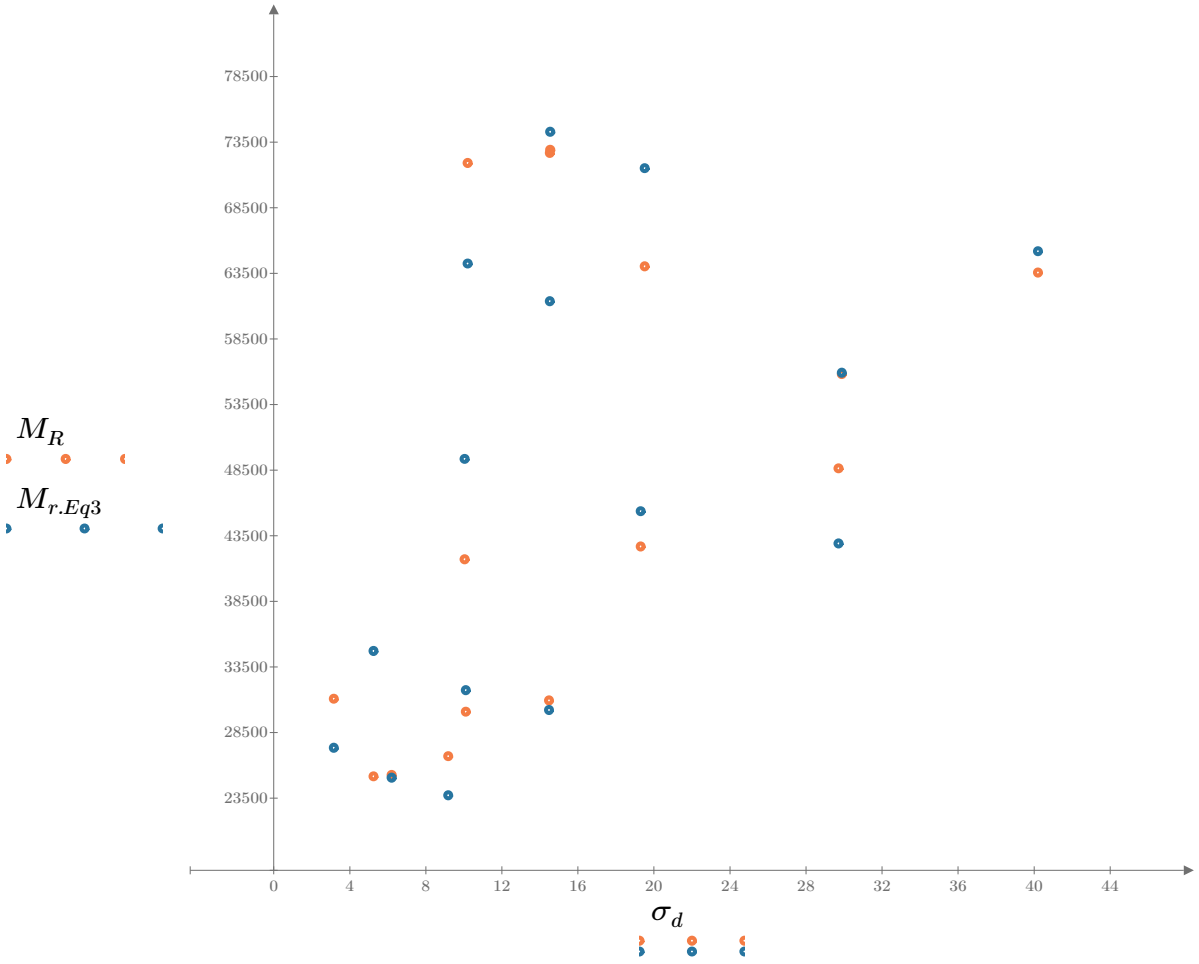

Figure 3. Plot of the test data (orange points) vs. the fitted Equation 3 model (blue points).

Dan Seely
9/12/2023

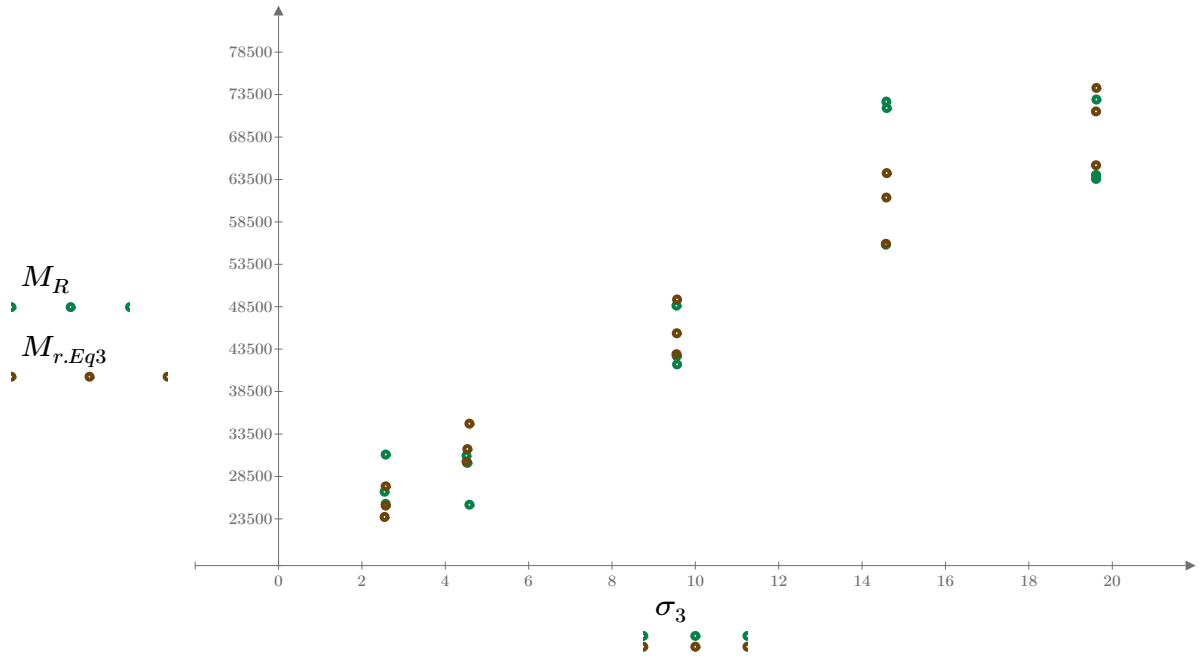

Figure 4. Plot of the test data (green points) vs. the fitted Equation 3 model (brown points).

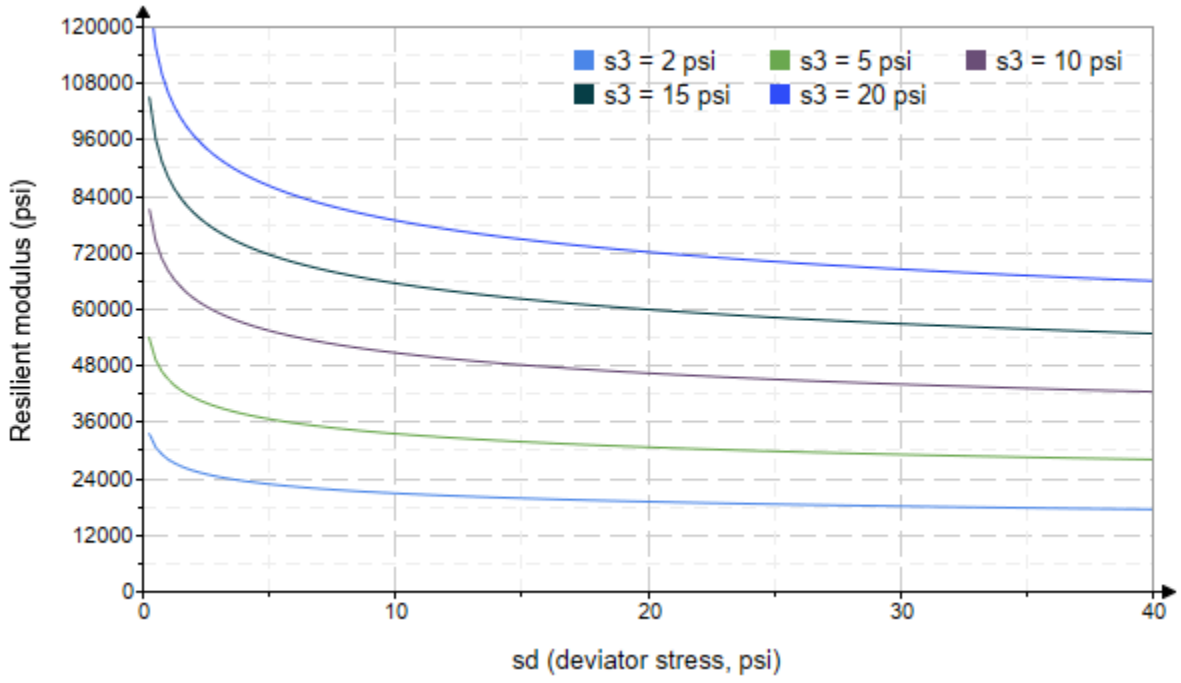

Figure 5. Plot of the fitted Equation 3 model for various confining stresses.

Dan Seely
9/12/2023

$$M_{R.4}\left(\sigma_B,\sigma_d,K_8,K_9,K_{10}\right) := K_8 \cdot p_a \left(\frac{\sigma_B}{p_a}\right)^{K_9} \cdot \left(\frac{\sigma_d}{p_a}\right)^{K_{10}}$$

Equation 4 AASHTO Publication No. FHWA-RD-97-083

$K_8 = 1185.262$

$K_9 = 0.9067$ Equation 4 fitting parameters

$K_{10} = -0.4266$

$R_4^{\,2} = 0.9140$ Coefficient of determination

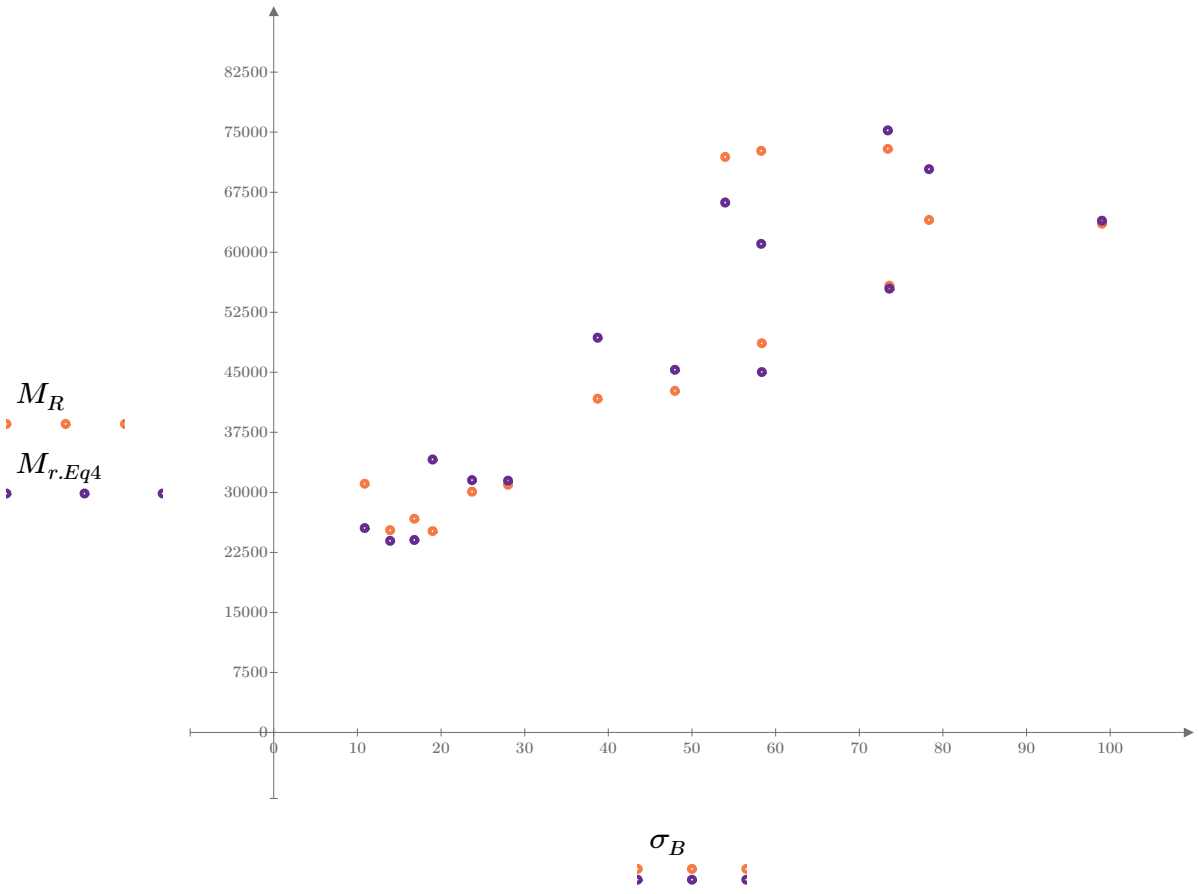

Figure 6. Plot of the test data (orange points) vs. the fitted Equation 4 model (purple points).

Dan Seely
9/12/2023

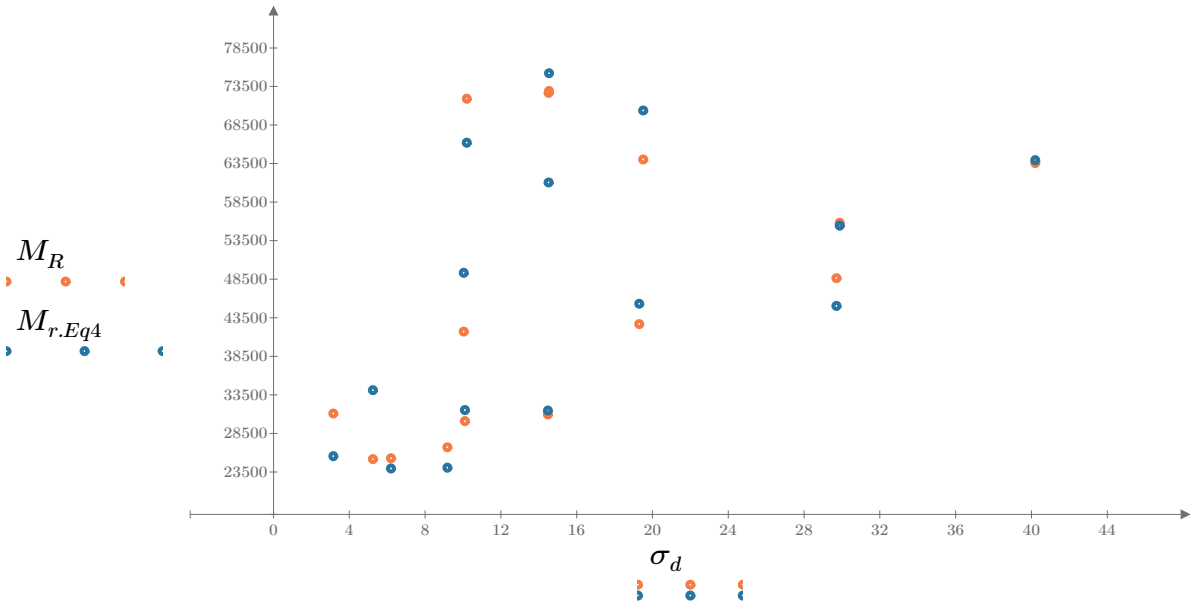

Figure 7. Plot of the test data (orange points) vs. the fitted Equation 4 model (blue points).

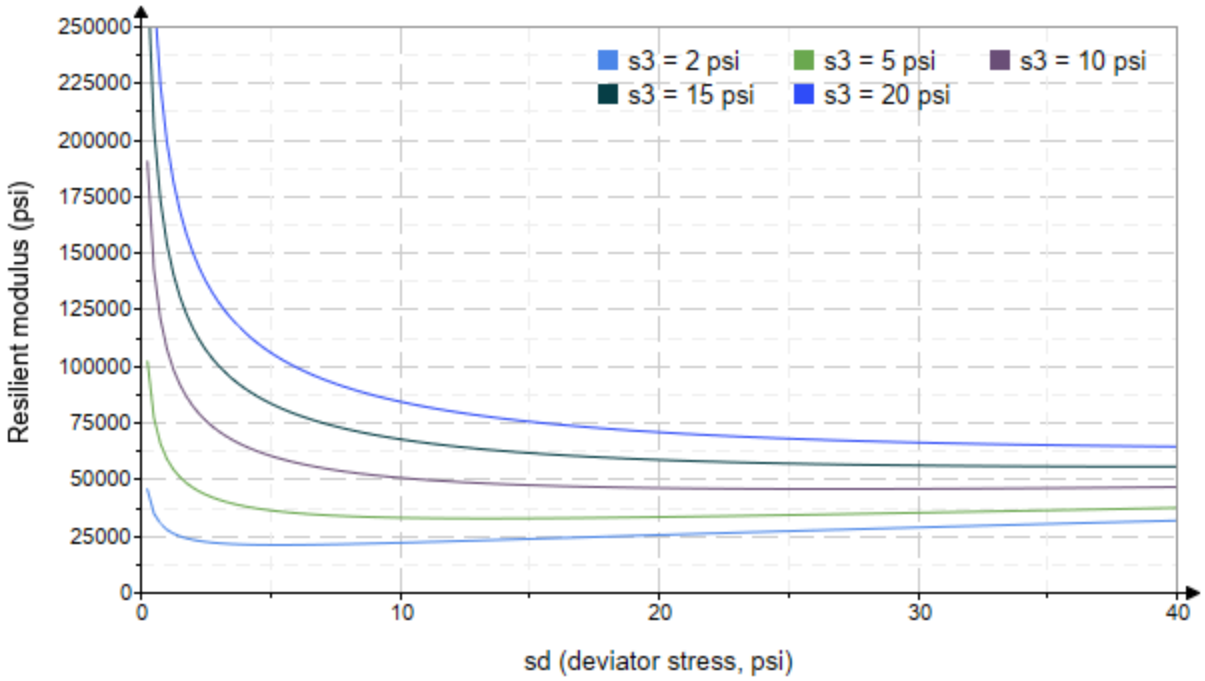

Figure 8. Plot of the fitted Equation 4 model for various confining stresses.

Dan Seely
9/12/2023

$SampleNo := \text{“B2}-\text{77”}$

$Treatment = \text{“M5”}$

$S = 9.860$ Degree of Saturation (%)

Test Sequence : Base/Subbase

Test summary data (psi) :

$$\sigma_3 = \begin{bmatrix} 2.443 \\ 2.387 \\ 2.568 \\ 4.410 \\ 4.564 \\ 5.307 \\ 9.458 \\ 8.614 \\ 8.420 \\ 14.310 \\ 13.940 \\ 13.410 \\ 18.820 \\ 18.430 \\ 18.400 \end{bmatrix} \quad \sigma_d = \begin{bmatrix} 3.178 \\ 6.112 \\ 9.077 \\ 5.100 \\ 10.020 \\ 14.420 \\ 10.180 \\ 19.270 \\ 29.460 \\ 10.200 \\ 14.520 \\ 29.520 \\ 14.650 \\ 19.500 \\ 40.020 \end{bmatrix} \quad \sigma_B = \begin{bmatrix} 10.510 \\ 13.270 \\ 16.780 \\ 18.330 \\ 23.710 \\ 30.340 \\ 38.560 \\ 45.120 \\ 54.720 \\ 53.120 \\ 56.340 \\ 69.740 \\ 71.120 \\ 74.800 \\ 95.220 \end{bmatrix} \quad M_R = \begin{bmatrix} 56428.7 \\ 47779.0 \\ 39456.2 \\ 77299.2 \\ 49891.8 \\ 41676.4 \\ 56985.8 \\ 53295.4 \\ 58701.8 \\ 98750.0 \\ 91249.8 \\ 71704.4 \\ 113352.0 \\ 84663.2 \\ 62806.6 \end{bmatrix}$$

σ_3 = mean confining stress
σ_d = mean deviator stress
σ_B = mean bulk stress
M_R = resilient modulus
p_a = atmospheric pressure = 14.6959 psi

Dan Seely
9/12/2023

$$M_{R.1}\left(\sigma_B, K_1, K_2\right) := K_1 \cdot {\sigma_B}^{K_2}$$

Equation 1
AASHTO Publication No. FHWA-RD-97-083

$K_1 = 24034.862$

$K_2 = 0.2793$

Equation 1 fitting parameters

${R_1}^2 = 0.3126$

Coefficient of determination

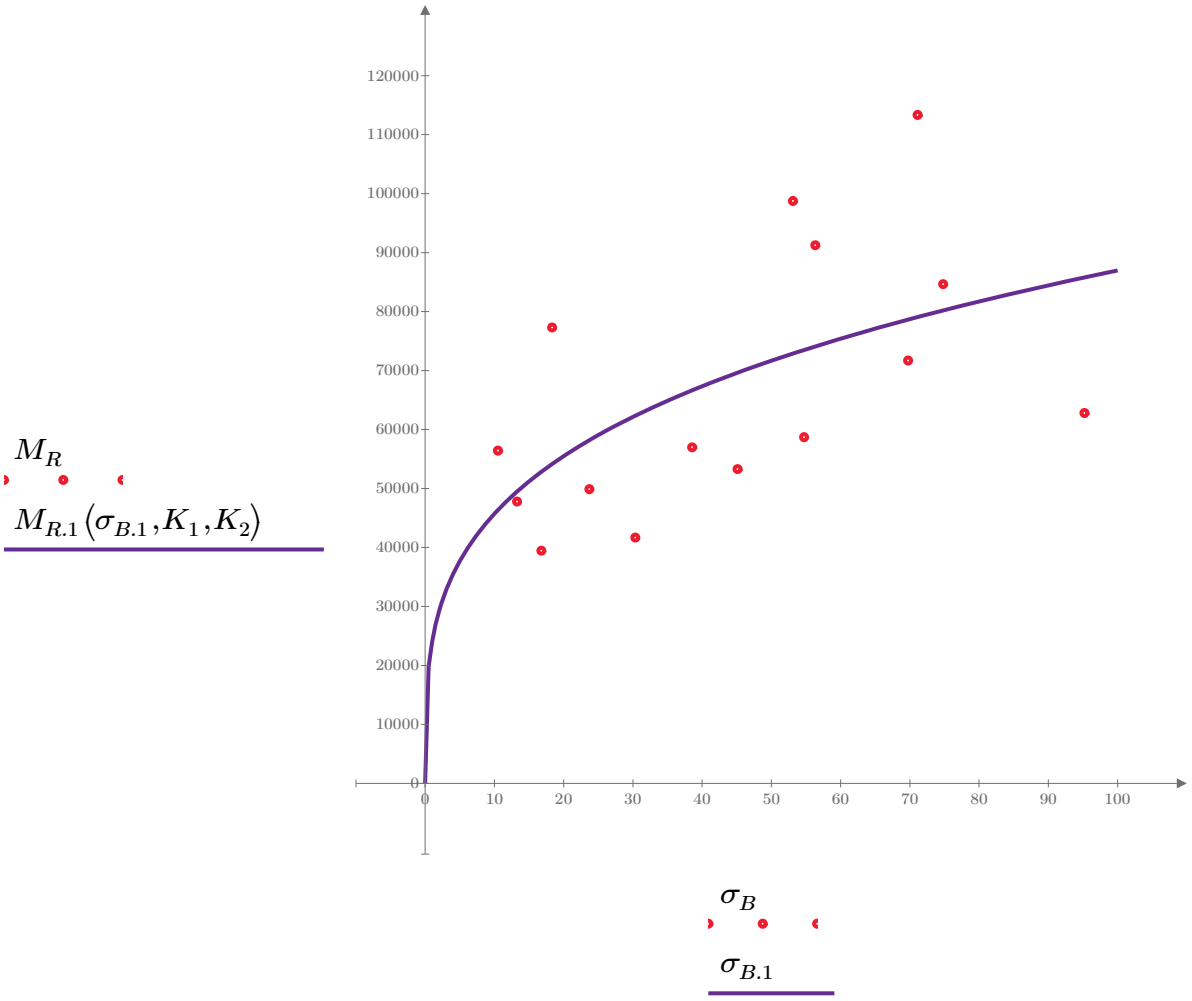

Figure 1. Plot of the test data (red points) vs. the fitted Equation 1 model (purple line).

Dan Seely
9/12/2023

$$M_{R.2}\left(\sigma_d, K_3, K_4\right) := K_3 \cdot {\sigma_d}^{K_4}$$

Equation 2
AASHTO Publication No. FHWA-RD-97-083

$K_3 = 57378.786$

$K_4 = 0.0603$

Equation 2 fitting parameters

${R_2}^2 = 0.0171$

Coefficient of determination

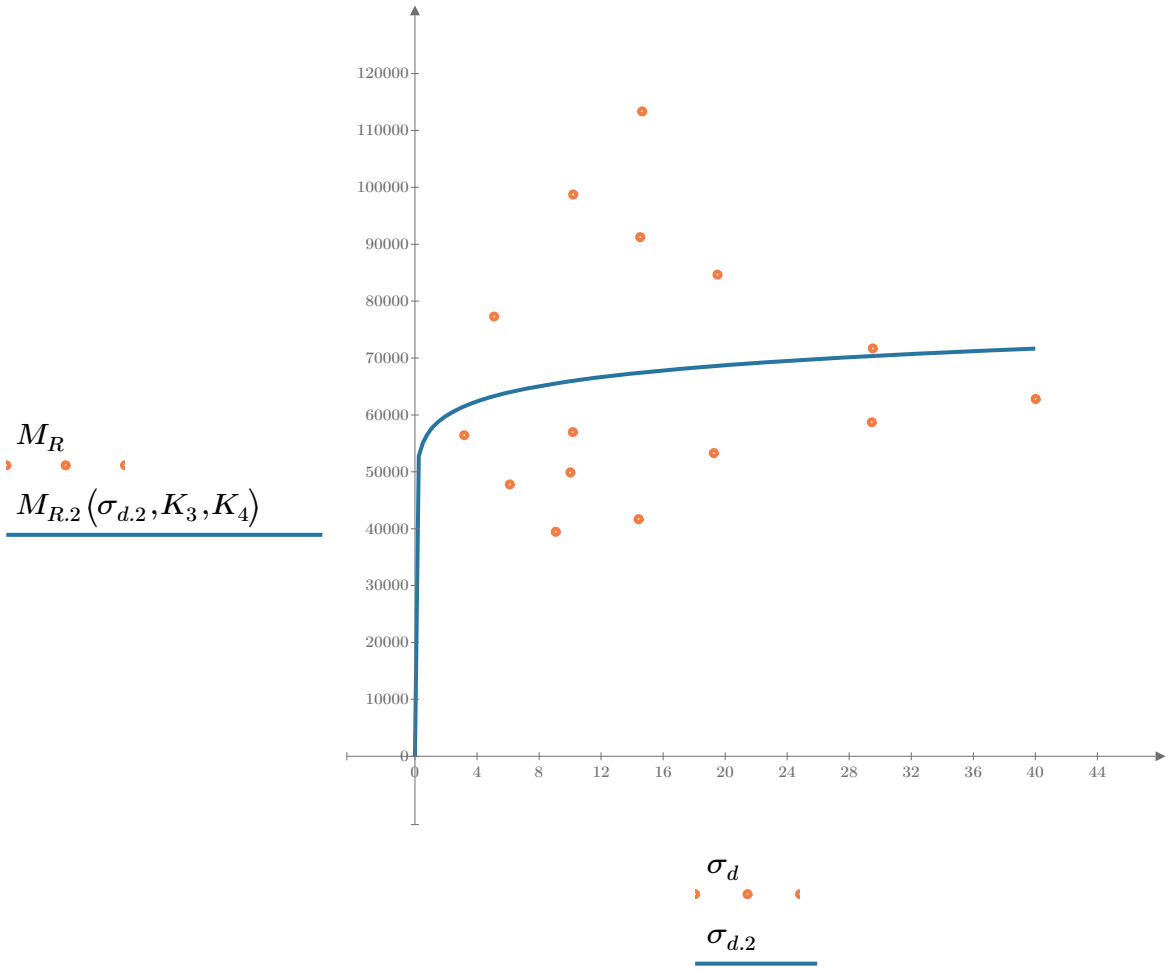

Figure 2. Plot of the test data (orange points) vs. the fitted Equation 2 model (blue line).

Dan Seely
9/12/2023

$$M_{R.3}\left(\sigma_d,\sigma_3,K_5,K_6,K_7\right):=K_5\cdot{\sigma_d}^{K_6}\cdot\left(1+\sigma_3\right)^{K_7}$$

Equation 3 AASHTO Publication No. FHWA-RD-97-083

$K_5=40224.011$

$K_6=-0.3902$ Equation 3 fitting parameters

$K_7=0.666$

${R_3}^2=0.8459$ Coefficient of determination

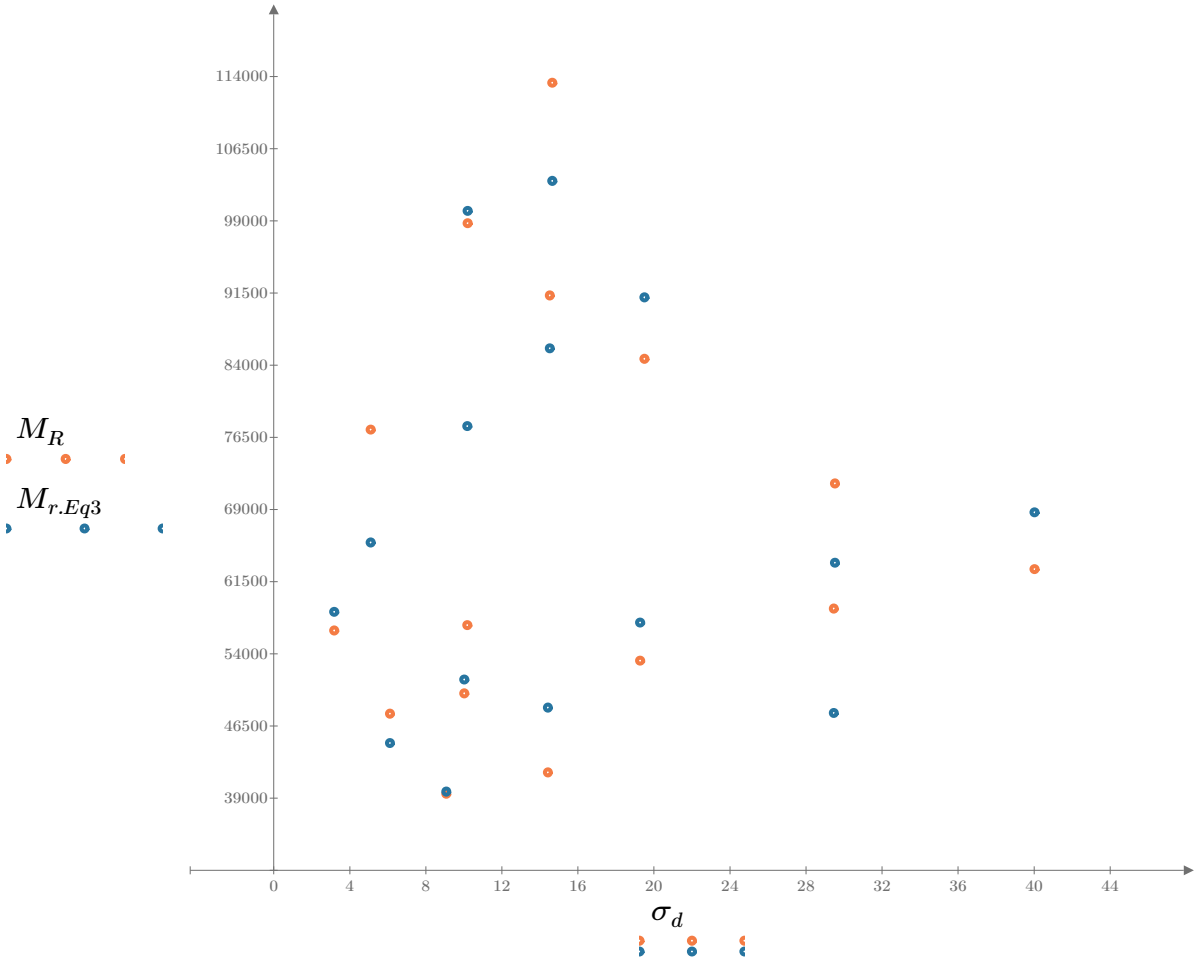

Figure 3. Plot of the test data (orange points) vs. the fitted Equation 3 model (blue points).

Dan Seely
9/12/2023

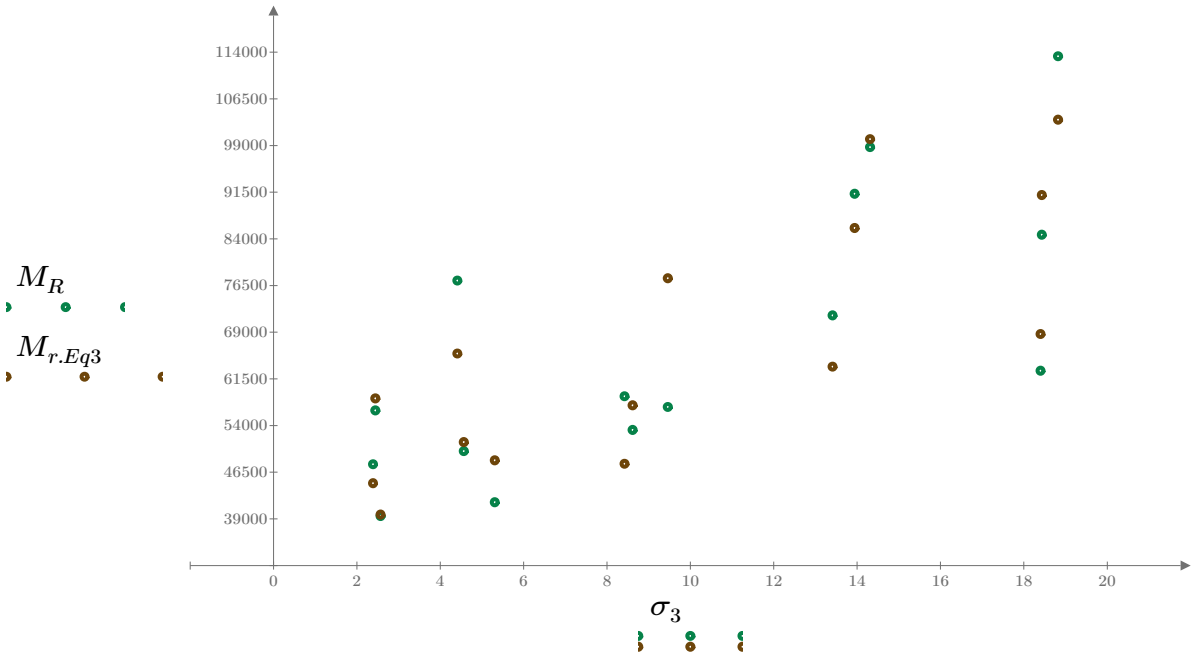

Figure 4. Plot of the test data (green points) vs. the fitted Equation 3 model (brown points).

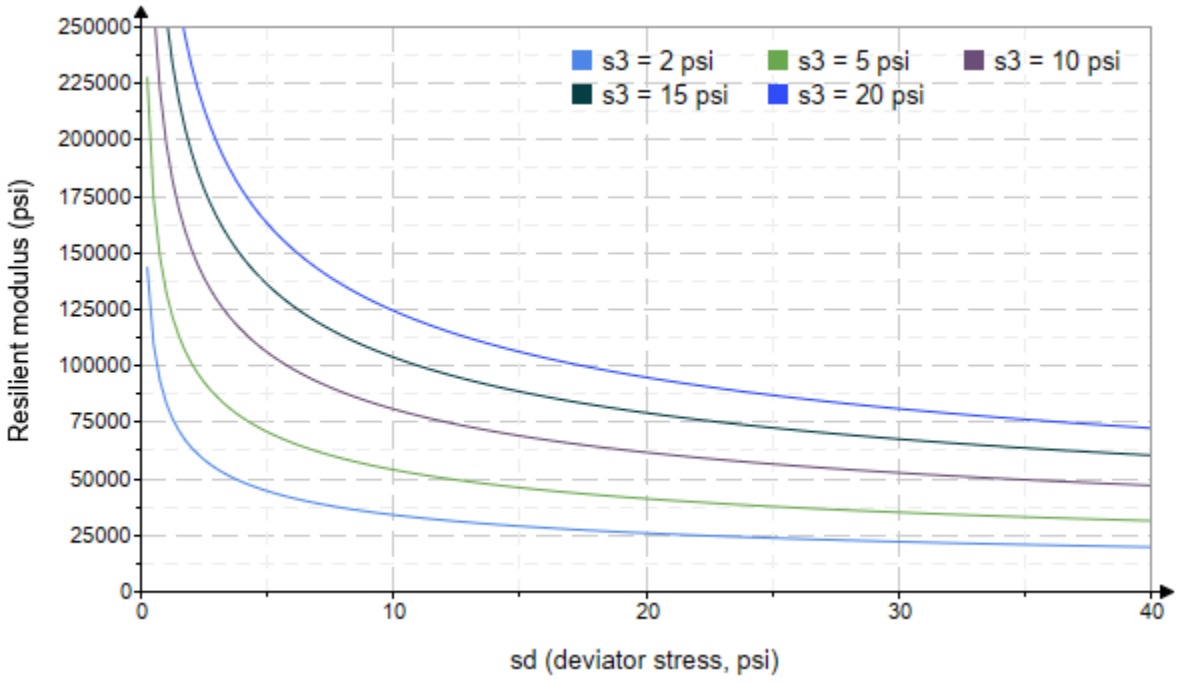

Figure 5. Plot of the fitted Equation 3 model for various confining stresses.

Dan Seely
9/12/2023

$$M_{R.4}\left(\sigma_B,\sigma_d,K_8,K_9,K_{10}\right) := K_8 \cdot p_a \left(\frac{\sigma_B}{p_a}\right)^{K_9} \cdot \left(\frac{\sigma_d}{p_a}\right)^{K_{10}}$$

Equation 4 AASHTO Publication No. FHWA-RD-97-083

$K_8 = 1776.344$

$K_9 = 0.8721$ Equation 4 fitting parameters

$K_{10} = -0.6872$

$R_4^{\,2} = 0.8500$ Coefficient of determination

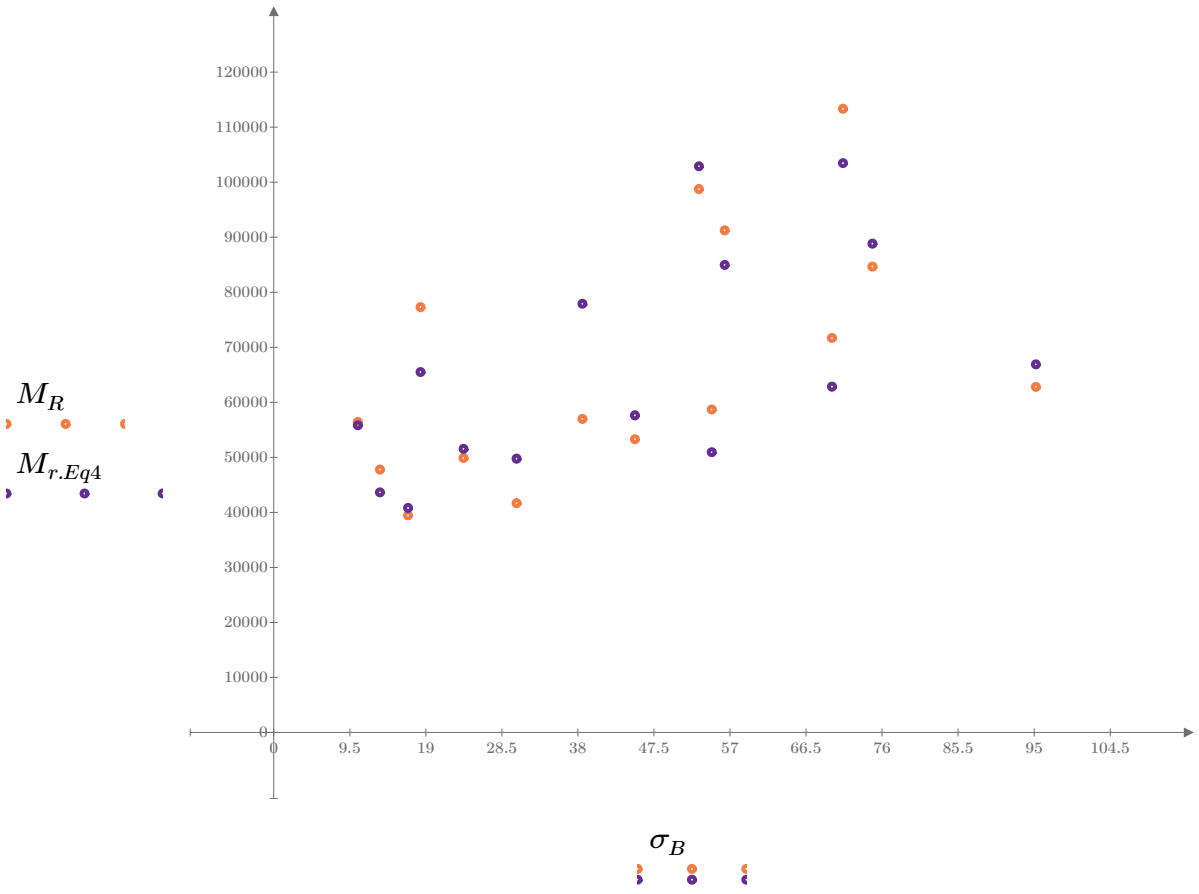

Figure 6. Plot of the test data (orange points) vs. the fitted Equation 4 model (purple points).

Dan Seely
9/12/2023

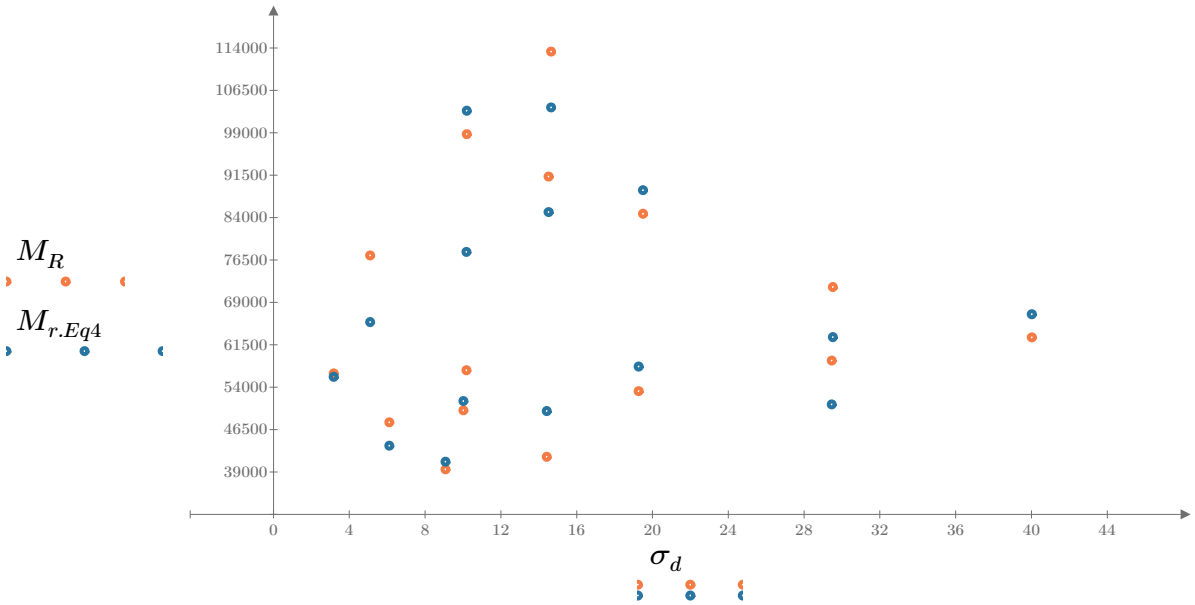

Figure 7. Plot of the test data (orange points) vs. the fitted Equation 4 model (blue points).

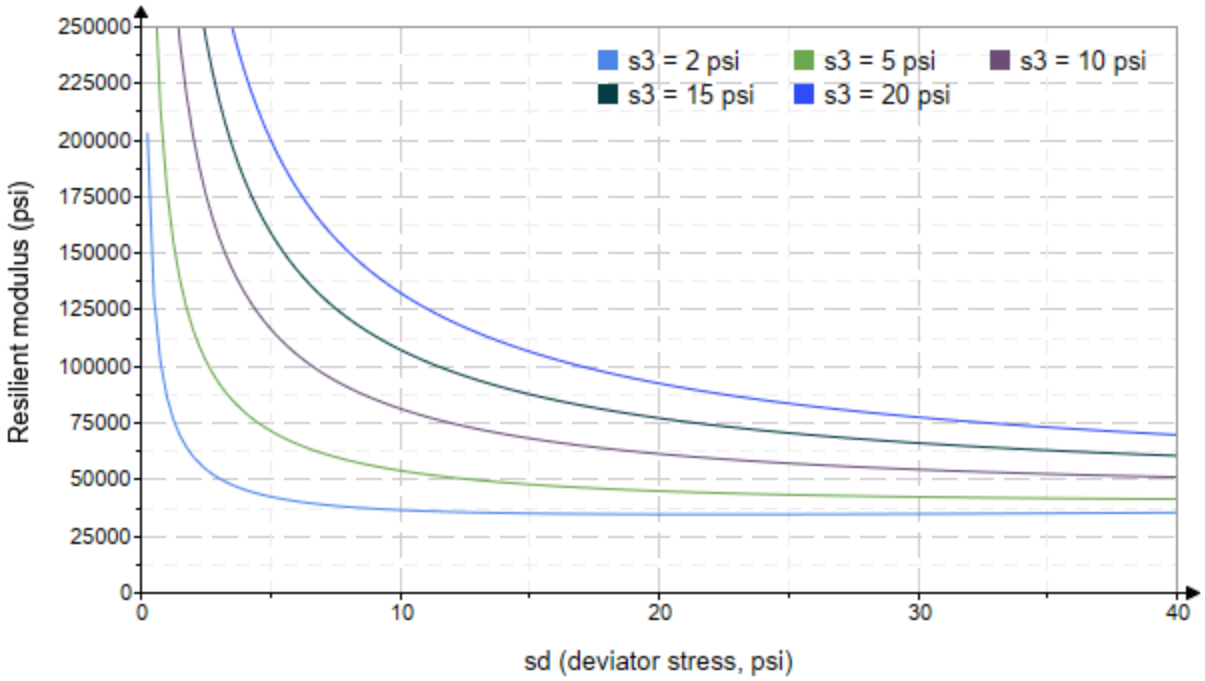

Figure 8. Plot of the fitted Equation 4 model for various confining stresses.

Dan Seely
9/12/2023

$SampleNo := \text{“B3–23”}$

$Treatment = \text{“AD”}$

$S = 2.955$ Degree of Saturation (%)

Test Sequence : Base/Subbase

Test summary data (psi) :

$$\sigma_3 = \begin{bmatrix} 2.231 \\ 2.262 \\ 2.029 \\ 4.128 \\ 4.097 \\ 4.178 \\ 8.943 \\ 9.282 \\ 9.197 \\ 14.000 \\ 15.050 \\ 14.880 \\ 20.130 \\ 19.330 \\ 19.070 \end{bmatrix} \quad \sigma_d = \begin{bmatrix} 3.194 \\ 6.103 \\ 9.080 \\ 5.112 \\ 9.949 \\ 14.520 \\ 9.961 \\ 19.290 \\ 29.710 \\ 10.010 \\ 14.470 \\ 29.930 \\ 14.310 \\ 19.680 \\ 40.010 \end{bmatrix} \quad \sigma_B = \begin{bmatrix} 9.885 \\ 12.890 \\ 15.170 \\ 17.500 \\ 22.240 \\ 27.050 \\ 36.790 \\ 47.130 \\ 57.310 \\ 52.000 \\ 59.630 \\ 74.570 \\ 74.710 \\ 77.680 \\ 97.230 \end{bmatrix} \quad M_R = \begin{bmatrix} 52499.4 \\ 32610.4 \\ 30695.6 \\ 39986.0 \\ 43478.8 \\ 41376.8 \\ 61053.8 \\ 45962.6 \\ 53431.2 \\ 54300.2 \\ 52026.2 \\ 70811.8 \\ 73377.0 \\ 84704.4 \\ 81646.6 \end{bmatrix}$$

σ_3 = mean confining stress
σ_d = mean deviator stress
σ_B = mean bulk stress
M_R = resilient modulus
p_a = atmospheric pressure = 14.6959 psi

Dan Seely
9/12/2023

$$M_{R.1}\left(\sigma_B, K_1, K_2\right) := K_1 \cdot {\sigma_B}^{K_2}$$

Equation 1
AASHTO Publication No. FHWA-RD-97-083

$K_1 = 12978.611$

$K_2 = 0.3882$

Equation 1 fitting parameters

${R_1}^2 = 0.6907$

Coefficient of determination

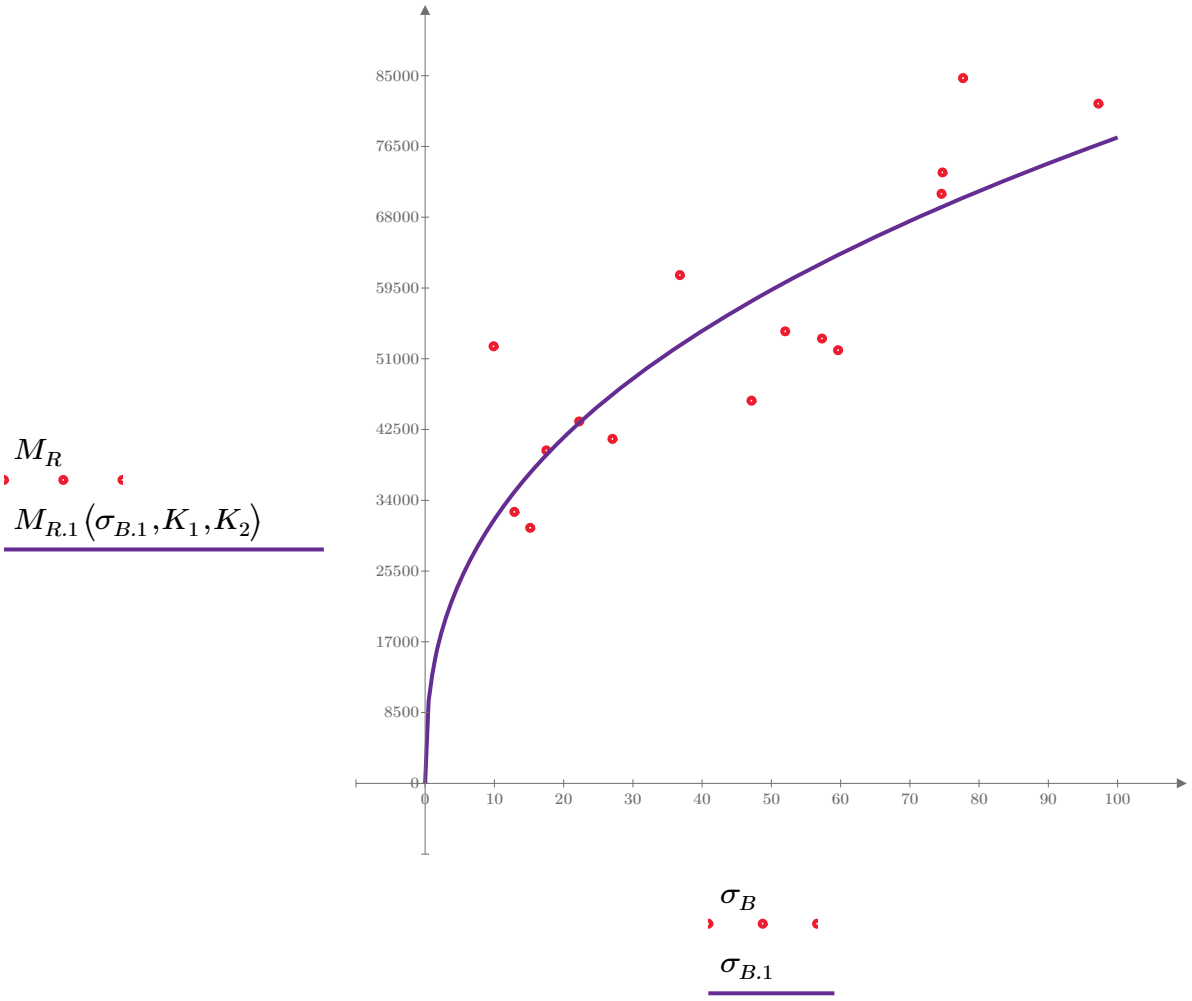

Figure 1. Plot of the test data (red points) vs. the fitted Equation 1 model (purple line).

Dan Seely
9/12/2023

$$M_{R.2}(\sigma_d, K_3, K_4) := K_3 \cdot \sigma_d^{K_4}$$

Equation 2
AASHTO Publication No. FHWA-RD-97-083

$K_3 = 26087.130$

$K_4 = 0.2826$

Equation 2 fitting parameters

$R_2^2 = 0.3685$

Coefficient of determination

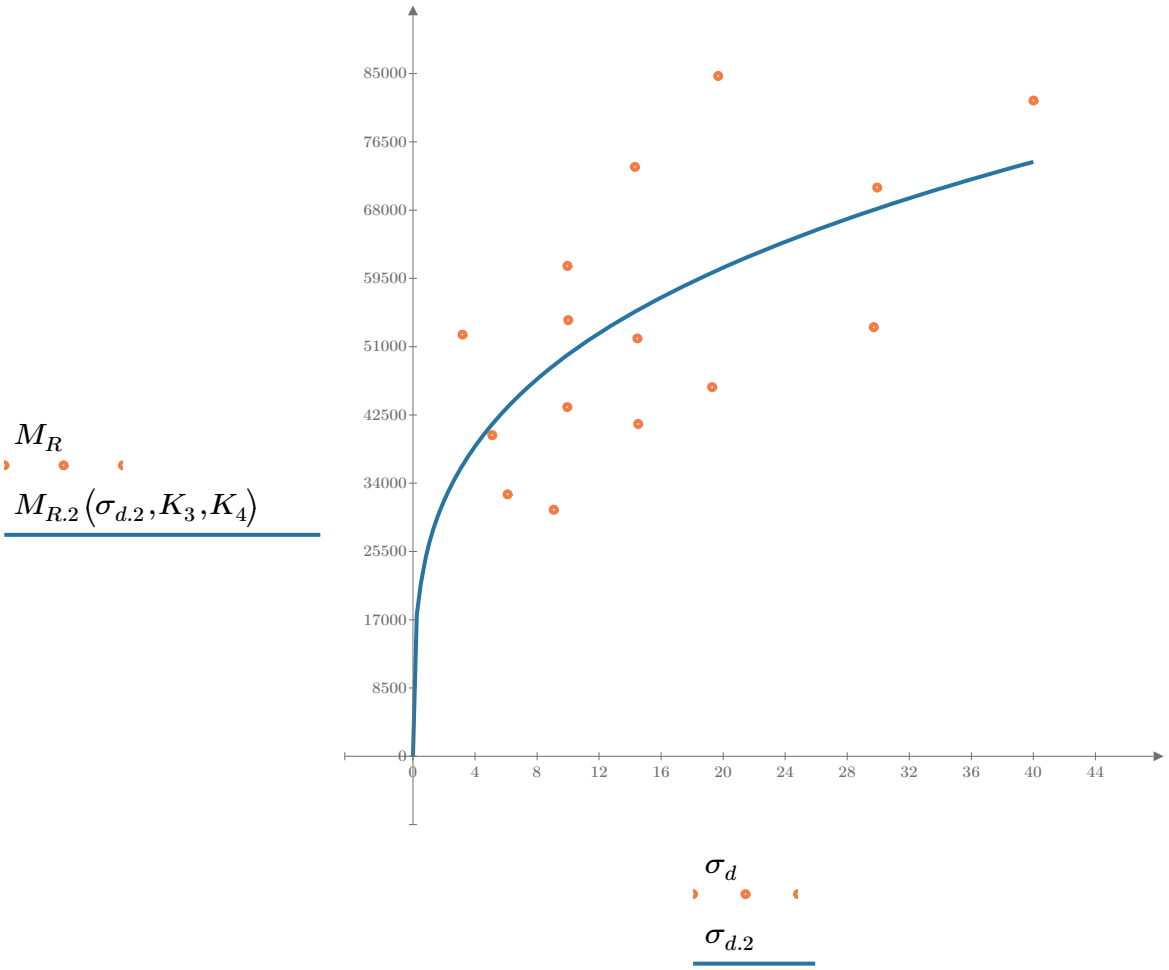

Figure 2. Plot of the test data (orange points) vs. the fitted Equation 2 model (blue line).

Dan Seely
9/12/2023

$$M_{R.3}\left(\sigma_d,\sigma_3,K_5,K_6,K_7\right):=K_5\cdot{\sigma_d}^{K_6}\cdot\left(1+\sigma_3\right)^{K_7}$$

Equation 3 AASHTO Publication No. FHWA-RD-97-083

$K_5=21179.305$

$K_6=0.0319$ Equation 3 fitting parameters

$K_7=0.3793$

${R_3}^2=0.7447$ Coefficient of determination

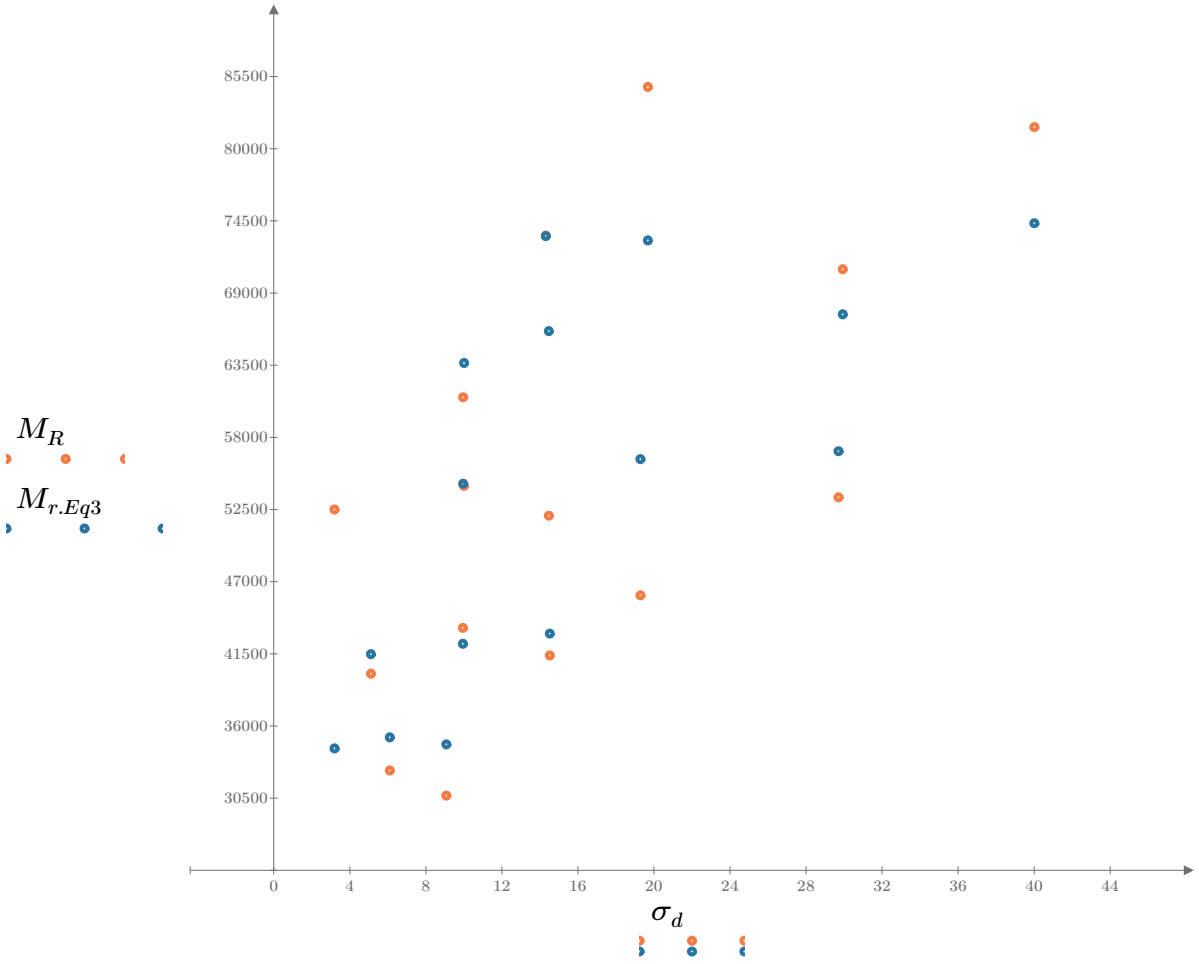

Figure 3. Plot of the test data (orange points) vs. the fitted Equation 3 model (blue points).

Dan Seely
9/12/2023

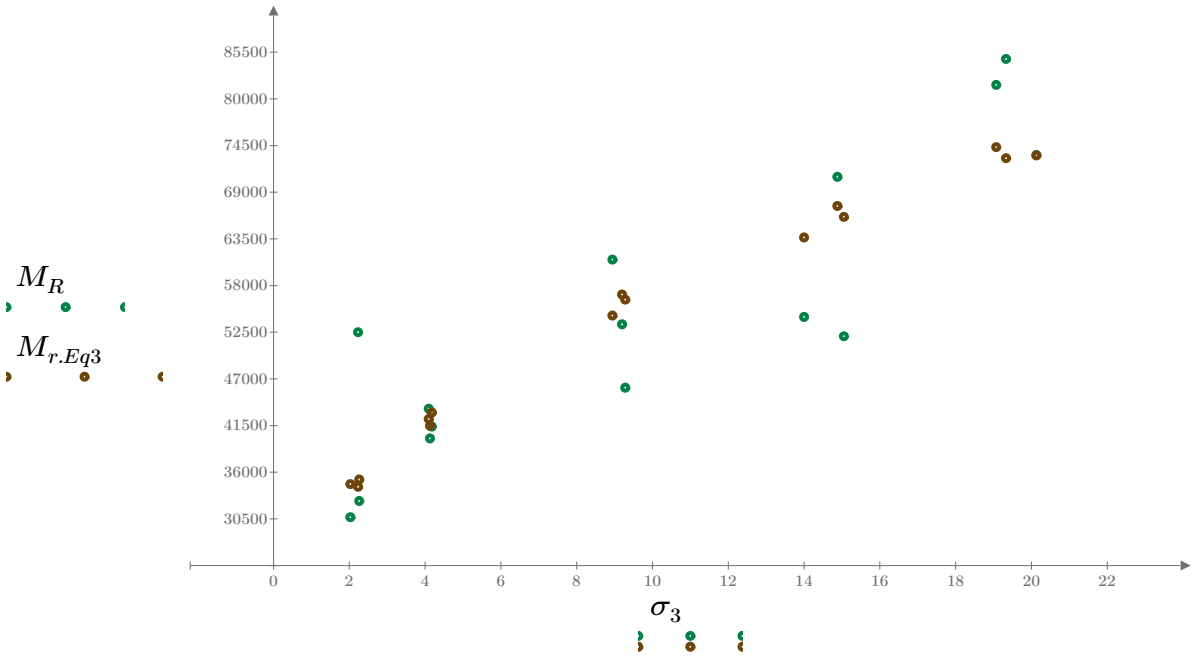

Figure 4. Plot of the test data (green points) vs. the fitted Equation 3 model (brown points).

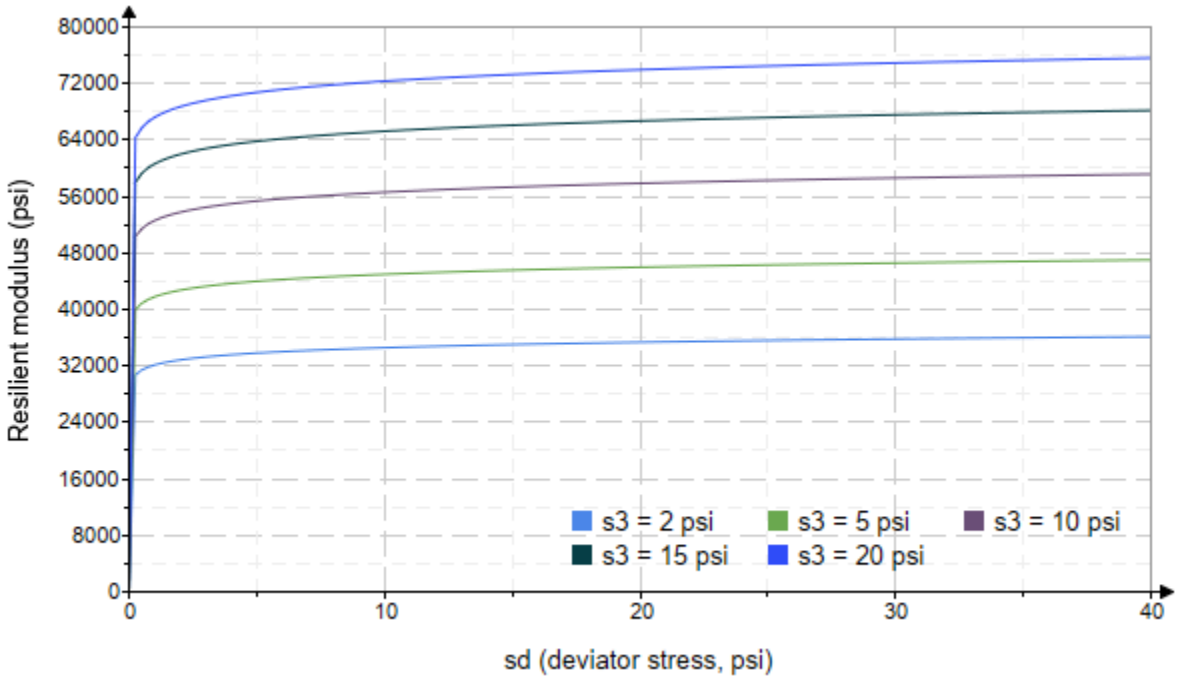

Figure 5. Plot of the fitted Equation 3 model for various confining stresses.

Dan Seely
9/12/2023

$$M_{R.4}\left(\sigma_B,\sigma_d,K_8,K_9,K_{10}\right) := K_8 \cdot p_a \left(\frac{\sigma_B}{p_a}\right)^{K_9} \cdot \left(\frac{\sigma_d}{p_a}\right)^{K_{10}}$$

Equation 4 AASHTO Publication No. FHWA-RD-97-083

$K_8 = 2258.224$

$K_9 = 0.4844$ Equation 4 fitting parameters

$K_{10} = -0.1221$

$R_4^{\,2} = 0.7121$ Coefficient of determination

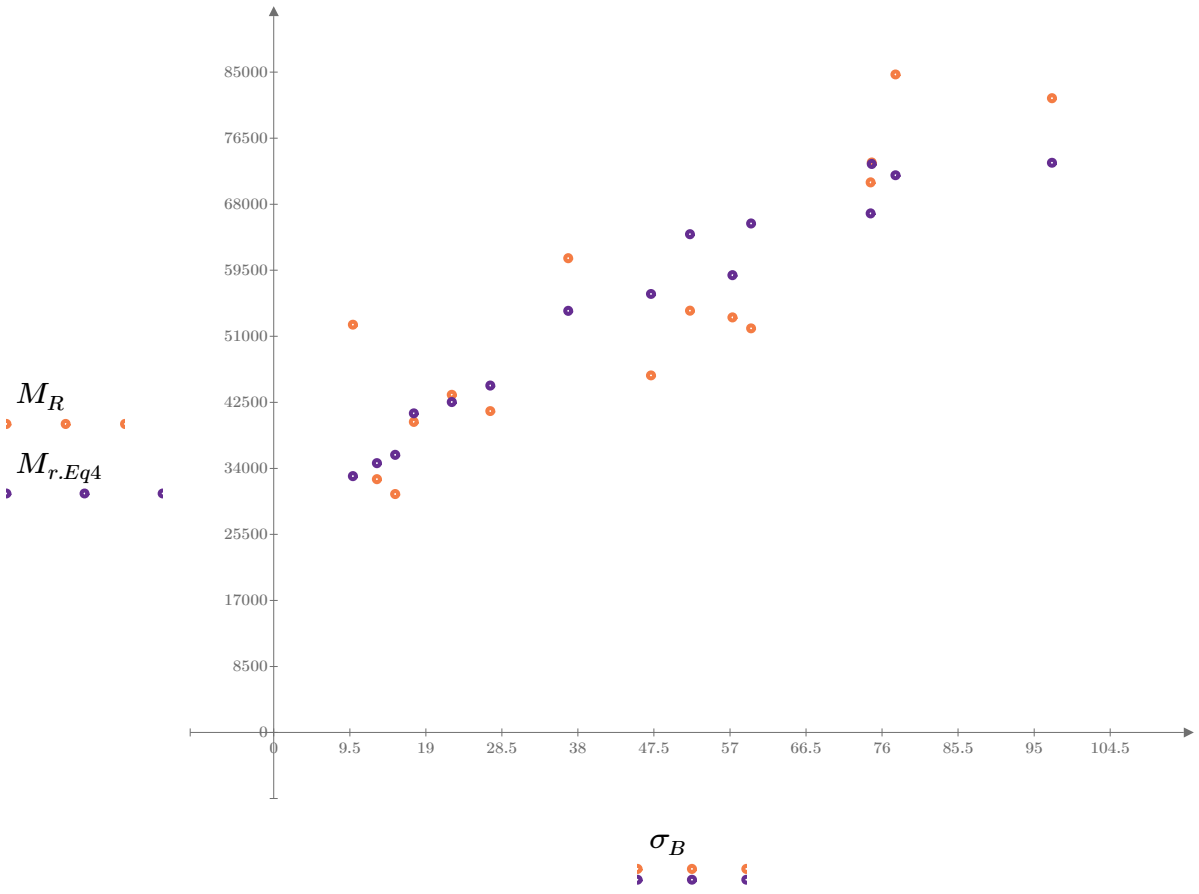

Figure 6. Plot of the test data (orange points) vs. the fitted Equation 4 model (purple points).

Dan Seely
9/12/2023

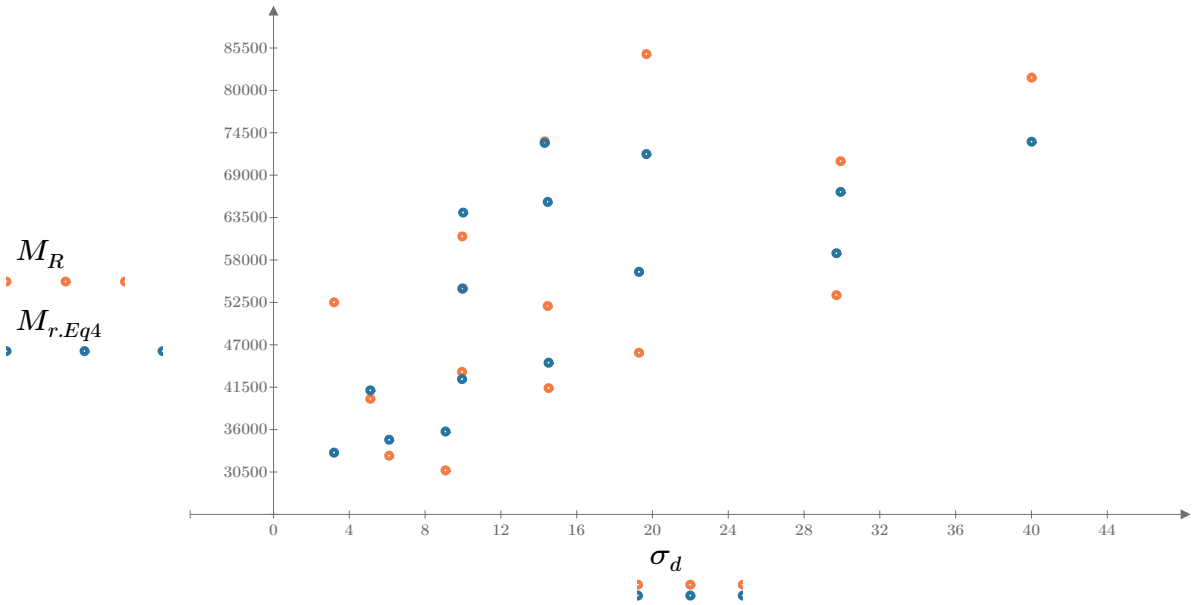

Figure 7. Plot of the test data (orange points) vs. the fitted Equation 4 model (blue points).

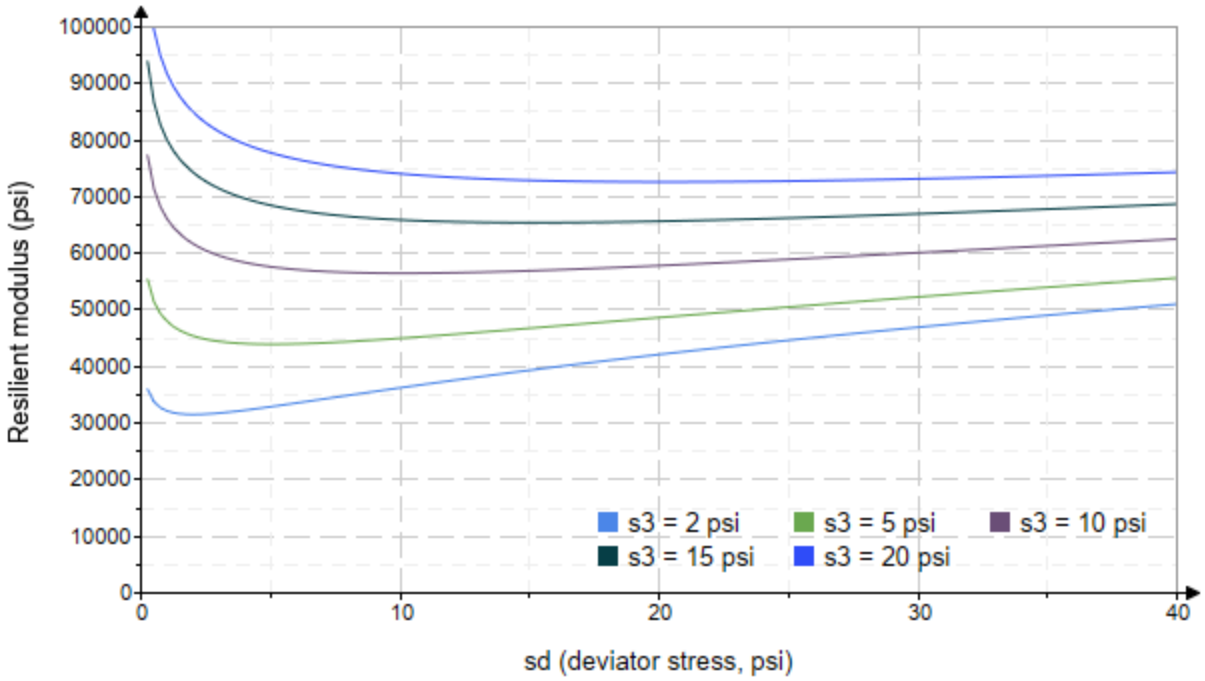

Figure 8. Plot of the fitted Equation 4 model for various confining stresses.

Dan Seely
9/12/2023

$SampleNo := \text{“B3}-25\text{”}$

$Treatment = \text{“AD”}$

$S = 3.091$ Degree of Saturation (%)

Test Sequence : Base/Subbase

Test summary data (psi) :

$$\sigma_3 = \begin{bmatrix} 2.829 \\ 2.838 \\ 2.828 \\ 4.657 \\ 4.663 \\ 4.614 \\ 9.596 \\ 9.570 \\ 9.579 \\ 14.620 \\ 14.600 \\ 14.610 \\ 19.650 \\ 19.650 \\ 19.640 \end{bmatrix} \quad \sigma_d = \begin{bmatrix} 3.185 \\ 6.045 \\ 9.093 \\ 5.026 \\ 9.820 \\ 14.520 \\ 9.806 \\ 19.250 \\ 29.650 \\ 9.933 \\ 14.460 \\ 29.740 \\ 14.330 \\ 19.500 \\ 40.270 \end{bmatrix} \quad \sigma_B = \begin{bmatrix} 11.670 \\ 14.560 \\ 17.580 \\ 19.000 \\ 23.810 \\ 28.360 \\ 38.590 \\ 47.960 \\ 58.390 \\ 53.790 \\ 58.250 \\ 73.570 \\ 73.300 \\ 78.440 \\ 99.200 \end{bmatrix} \quad M_R = \begin{bmatrix} 32720.8 \\ 29654.8 \\ 29510.4 \\ 27083.4 \\ 31064.2 \\ 34353.4 \\ 41055.6 \\ 57242.2 \\ 58350.4 \\ 69492.0 \\ 73961.4 \\ 63657.6 \\ 72484.4 \\ 64841.0 \\ 60472.8 \end{bmatrix}$$

σ_3 = mean confining stress
σ_d = mean deviator stress
σ_B = mean bulk stress
M_R = resilient modulus
p_a = atmospheric pressure = 14.6959 psi

Dan Seely
9/12/2023

$$M_{R.1}\left(\sigma_B, K_1, K_2\right) := K_1 \cdot {\sigma_B}^{K_2}$$

Equation 1
AASHTO Publication No. FHWA-RD-97-083

$K_1 = 8085.279$

$K_2 = 0.4856$

Equation 1 fitting parameters

${R_1}^2 = 0.7848$

Coefficient of determination

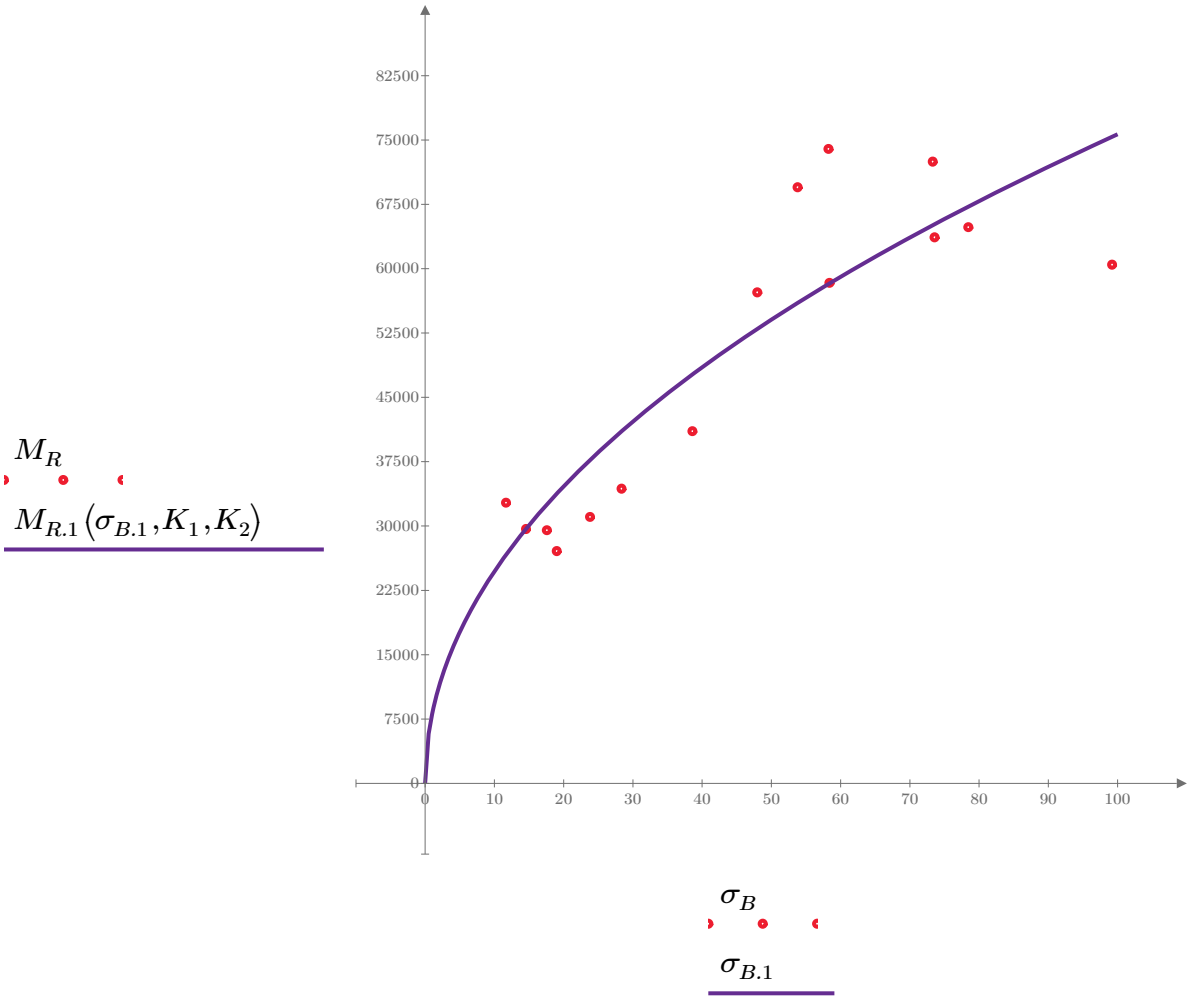

Figure 1. Plot of the test data (red points) vs. the fitted Equation 1 model (purple line).

Dan Seely
9/12/2023

$$M_{R.2}(\sigma_d, K_3, K_4) := K_3 \cdot \sigma_d^{K_4}$$

Equation 2
AASHTO Publication No. FHWA-RD-97-083

$K_3 = 21882.925$

$K_4 = 0.3156$

Equation 2 fitting parameters

$R_2^2 = 0.3994$

Coefficient of determination

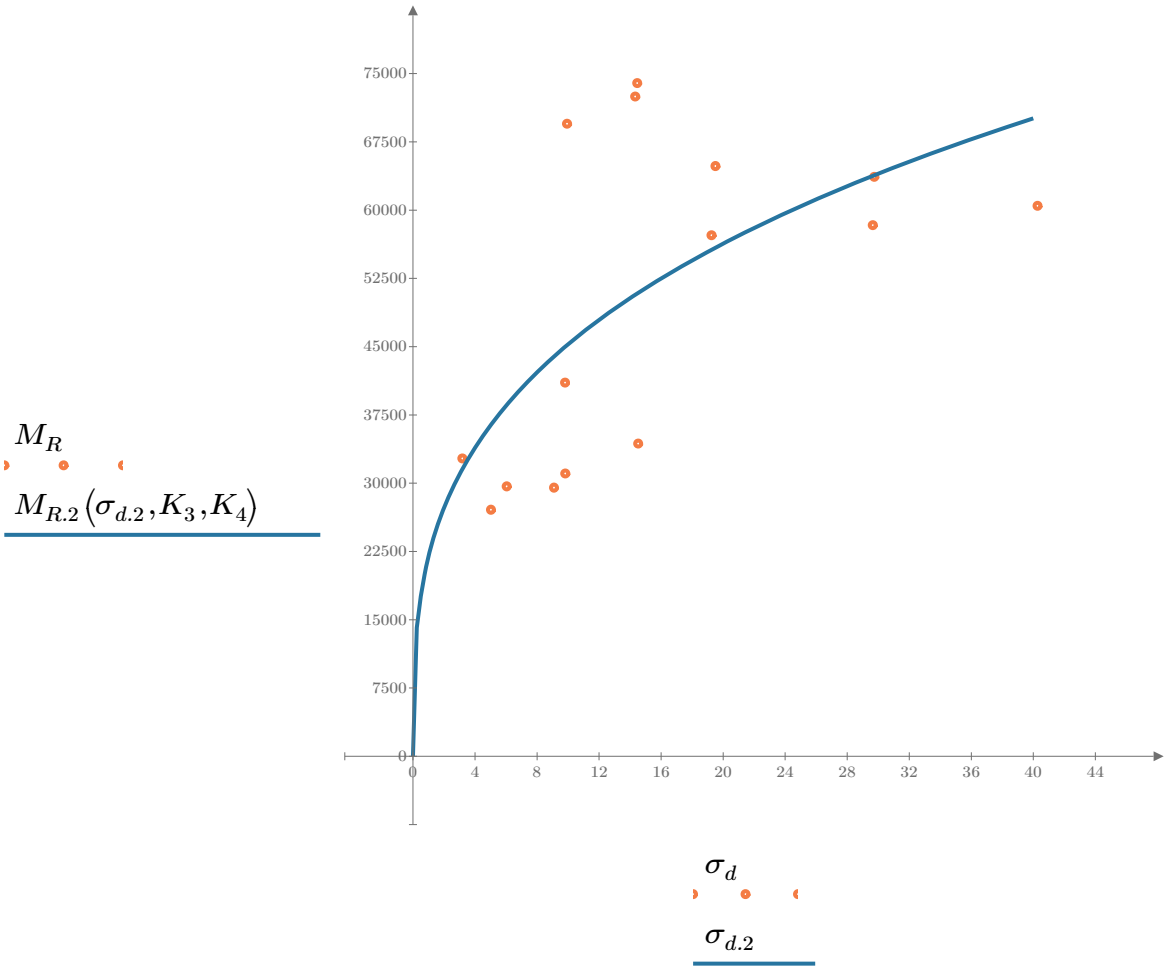

Figure 2. Plot of the test data (orange points) vs. the fitted Equation 2 model (blue line).

Dan Seely
9/12/2023

$$M_{R.3}\left(\sigma_d,\sigma_3,K_5,K_6,K_7\right):=K_5\cdot{\sigma_d}^{K_6}\cdot\left(1+\sigma_3\right)^{K_7}$$

Equation 3 AASHTO Publication No. FHWA-RD-97-083

$K_5=14843.624$

$K_6=-0.0221$ Equation 3 fitting parameters

$K_7=0.5417$

${R_3}^2=0.8427$ Coefficient of determination

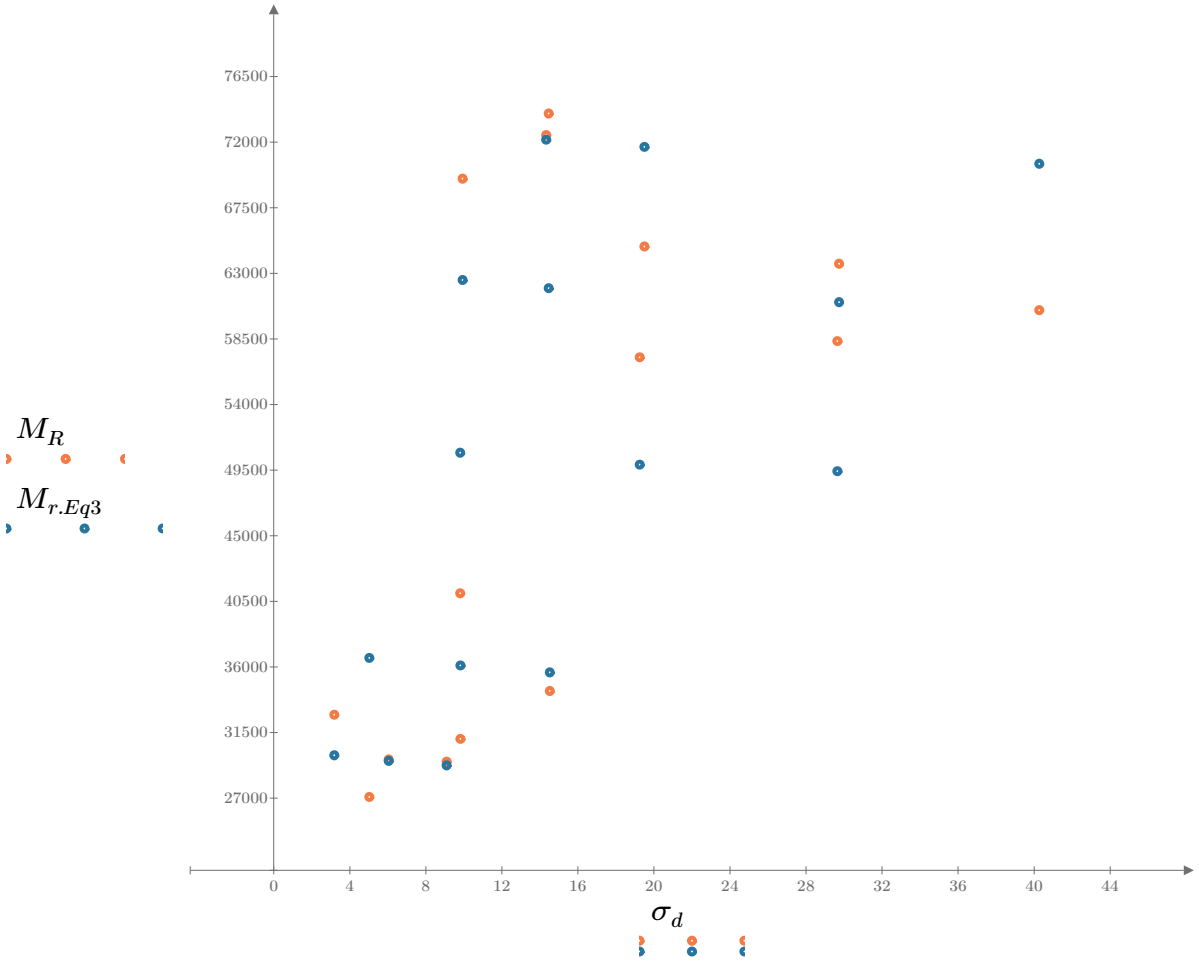

Figure 3. Plot of the test data (orange points) vs. the fitted Equation 3 model (blue points).

Dan Seely
9/12/2023

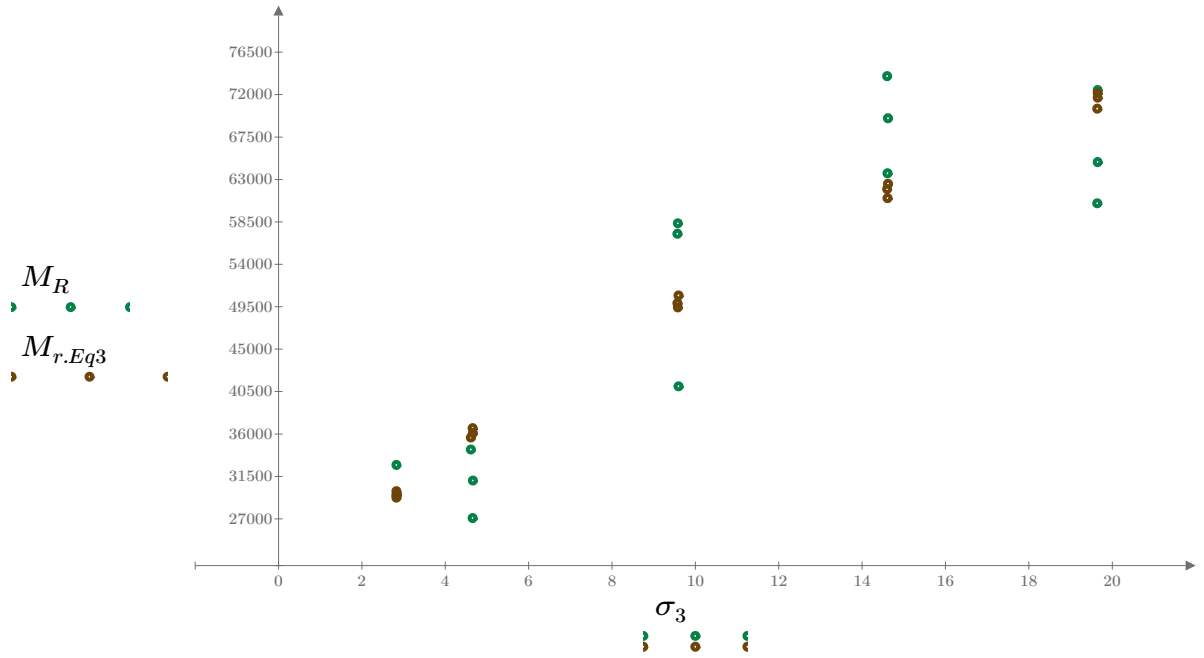

Figure 4. Plot of the test data (green points) vs. the fitted Equation 3 model (brown points).

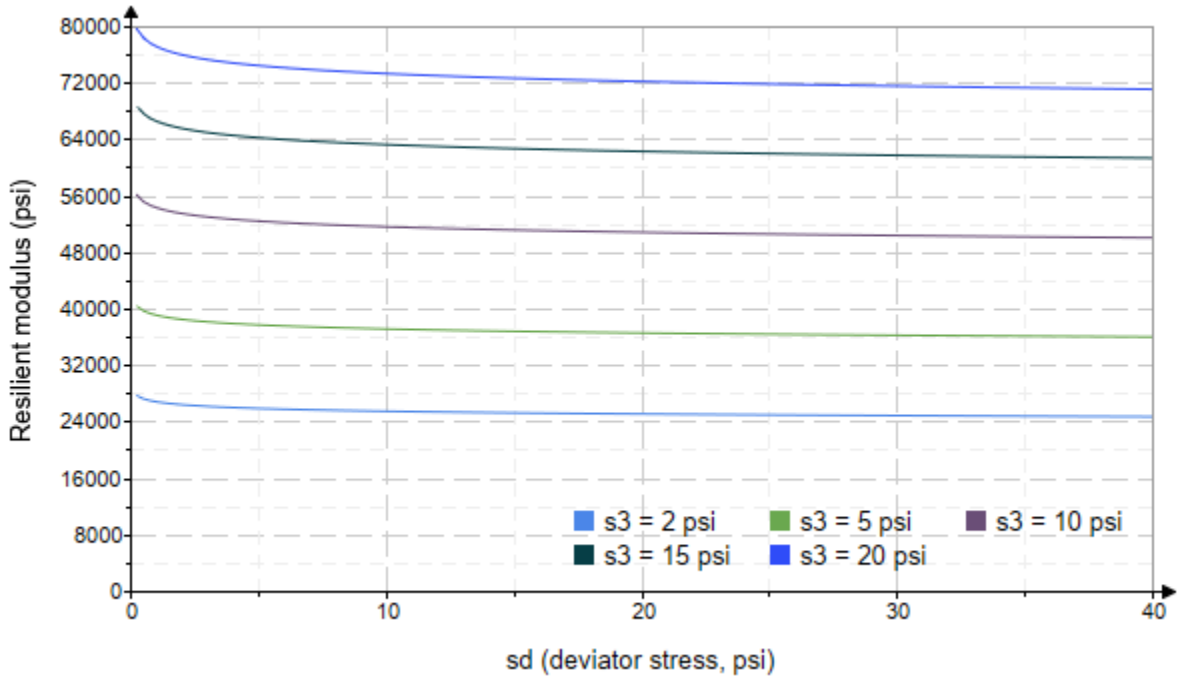

Figure 5. Plot of the fitted Equation 3 model for various confining stresses.

Dan Seely
9/12/2023

$$M_{R.4}\left(\sigma_B,\sigma_d,K_8,K_9,K_{10}\right) := K_8 \cdot p_a \left(\frac{\sigma_B}{p_a}\right)^{K_9} \cdot \left(\frac{\sigma_d}{p_a}\right)^{K_{10}}$$

Equation 4 AASHTO Publication No. FHWA-RD-97-083

$K_8 = 1538.324$

$K_9 = 0.7269$ Equation 4 fitting parameters

$K_{10} = -0.2634$

$R_4^{\,2} = 0.8581$ Coefficient of determination

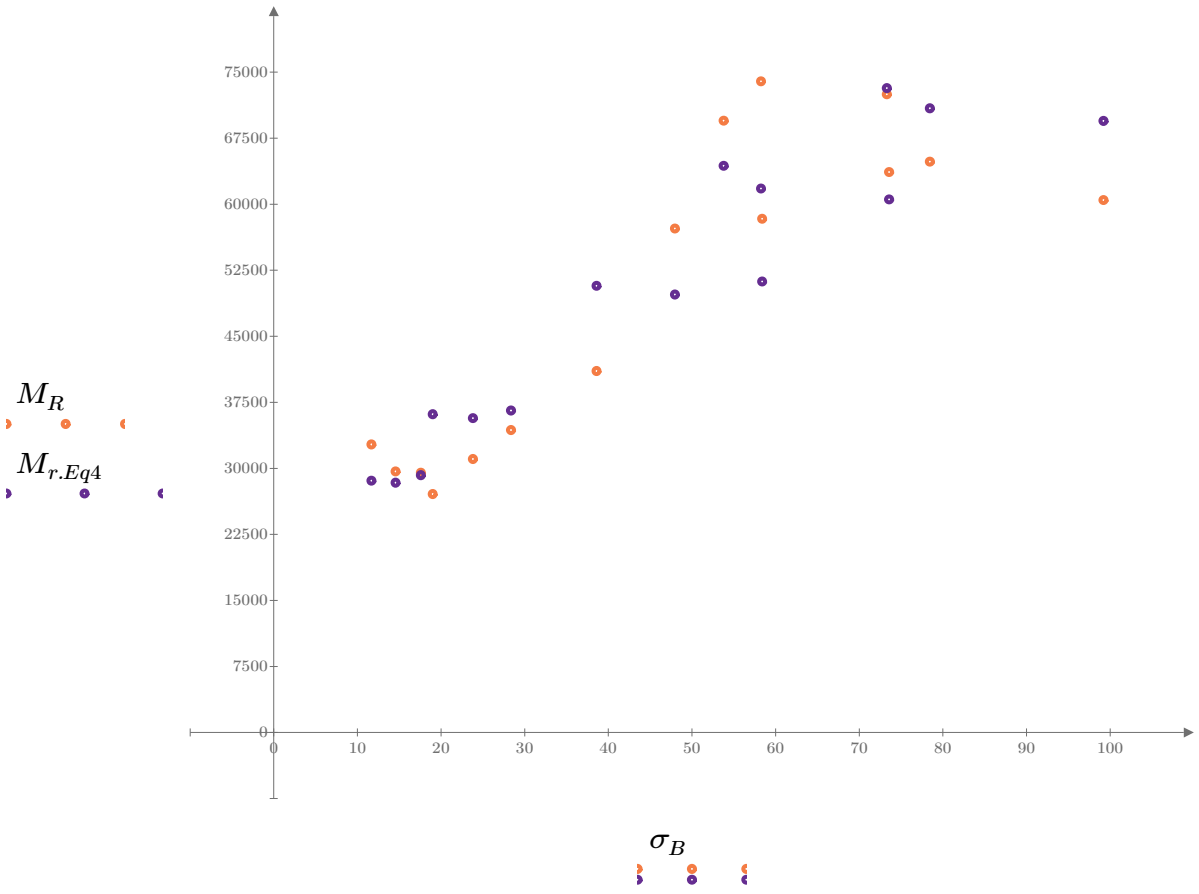

Figure 6. Plot of the test data (orange points) vs. the fitted Equation 4 model (purple points).

Dan Seely
9/12/2023

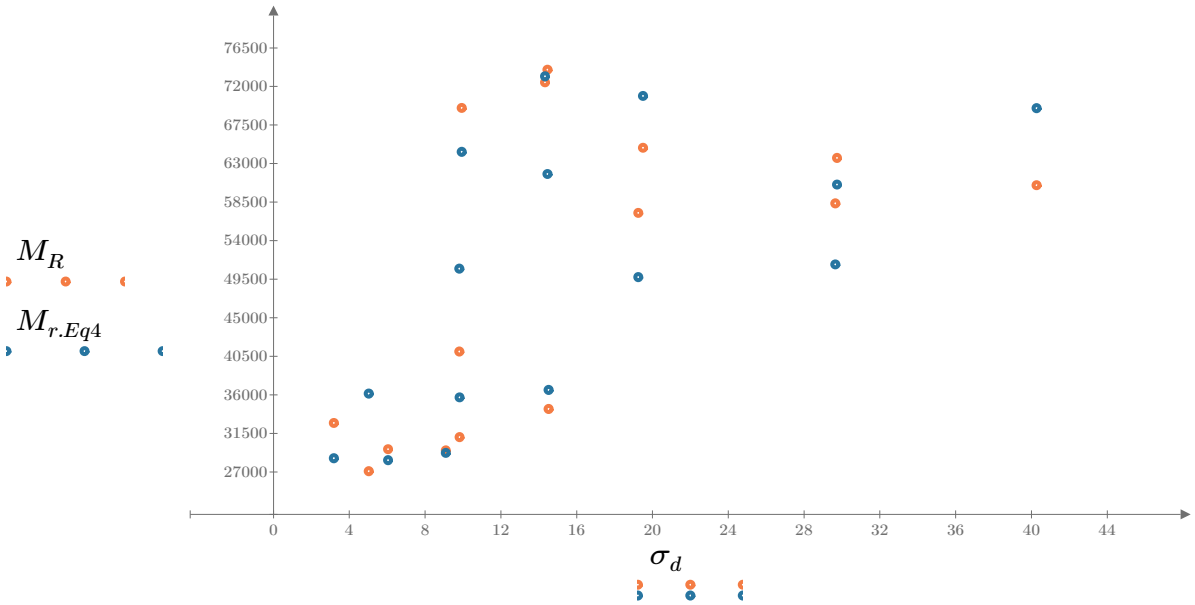

Figure 7. Plot of the test data (orange points) vs. the fitted Equation 4 model (blue points).

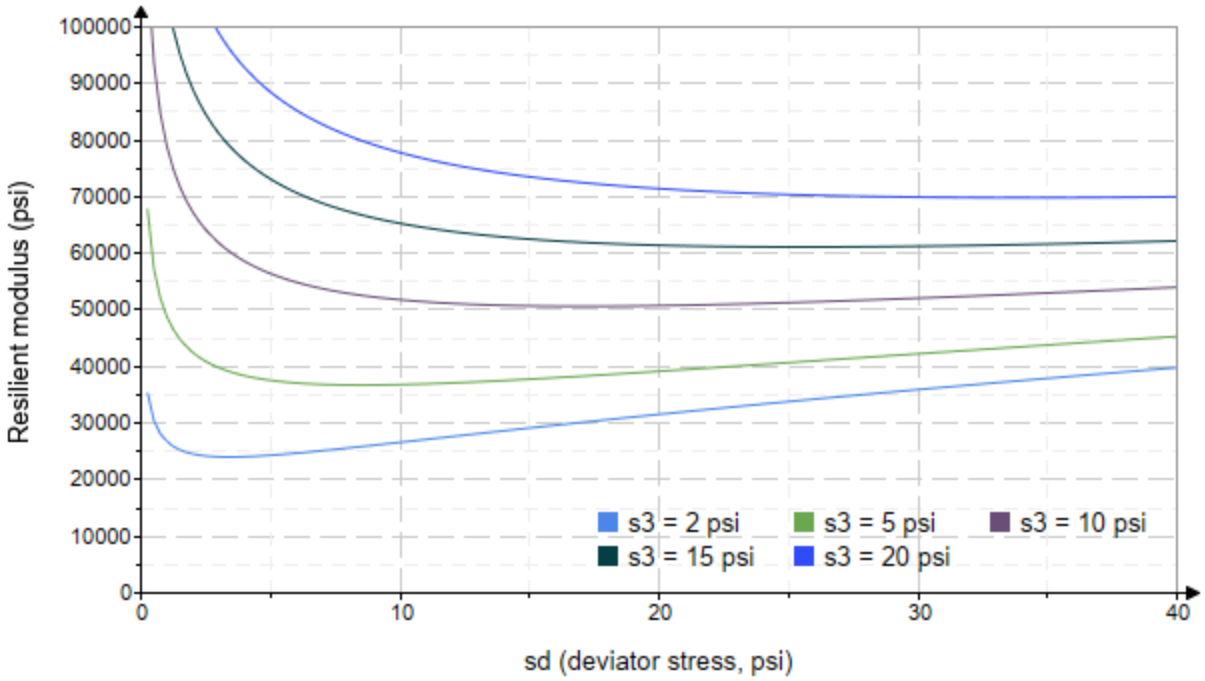

Figure 8. Plot of the fitted Equation 4 model for various confining stresses.

Dan Seely
9/12/2023

$SampleNo := \text{“B3–26”}$

$Treatment = \text{“M5”}$

$S = 9.889$ Degree of Saturation (%)

Test Sequence : Base/Subbase

Test summary data (psi) :

$$\sigma_3 = \begin{bmatrix} 2.804 \\ 2.787 \\ 2.778 \\ 4.545 \\ 4.532 \\ 4.507 \\ 9.544 \\ 9.530 \\ 9.555 \\ 14.550 \\ 14.550 \\ 14.570 \\ 19.580 \\ 19.600 \\ 19.580 \end{bmatrix} \quad \sigma_d = \begin{bmatrix} 3.166 \\ 6.167 \\ 9.121 \\ 5.258 \\ 10.160 \\ 14.590 \\ 10.180 \\ 19.180 \\ 29.200 \\ 10.090 \\ 14.450 \\ 29.370 \\ 14.380 \\ 19.340 \\ 39.920 \end{bmatrix} \quad \sigma_B = \begin{bmatrix} 11.580 \\ 14.530 \\ 17.460 \\ 18.890 \\ 23.750 \\ 28.110 \\ 38.820 \\ 47.770 \\ 57.870 \\ 53.730 \\ 58.090 \\ 73.080 \\ 73.110 \\ 78.140 \\ 98.660 \end{bmatrix} \quad M_R = \begin{bmatrix} 45342.6 \\ 36021.0 \\ 32625.2 \\ 37320.6 \\ 34019.6 \\ 41563.0 \\ 69701.6 \\ 65338.4 \\ 57141.2 \\ 64678.2 \\ 59149.6 \\ 50070.0 \\ 61270.0 \\ 58154.4 \\ 54074.4 \end{bmatrix}$$

σ_3 = mean confining stress
σ_d = mean deviator stress
σ_B = mean bulk stress
M_R = resilient modulus
p_a = atmospheric pressure = 14.6959 psi

Dan Seely
9/12/2023

$$M_{R.1}\left(\sigma_B, K_1, K_2\right) := K_1 \cdot {\sigma_B}^{K_2}$$

Equation 1
AASHTO Publication No. FHWA-RD-97-083

$K_1 = 20393.359$

$K_2 = 0.2489$

Equation 1 fitting parameters

${R_1}^2 = 0.4819$

Coefficient of determination

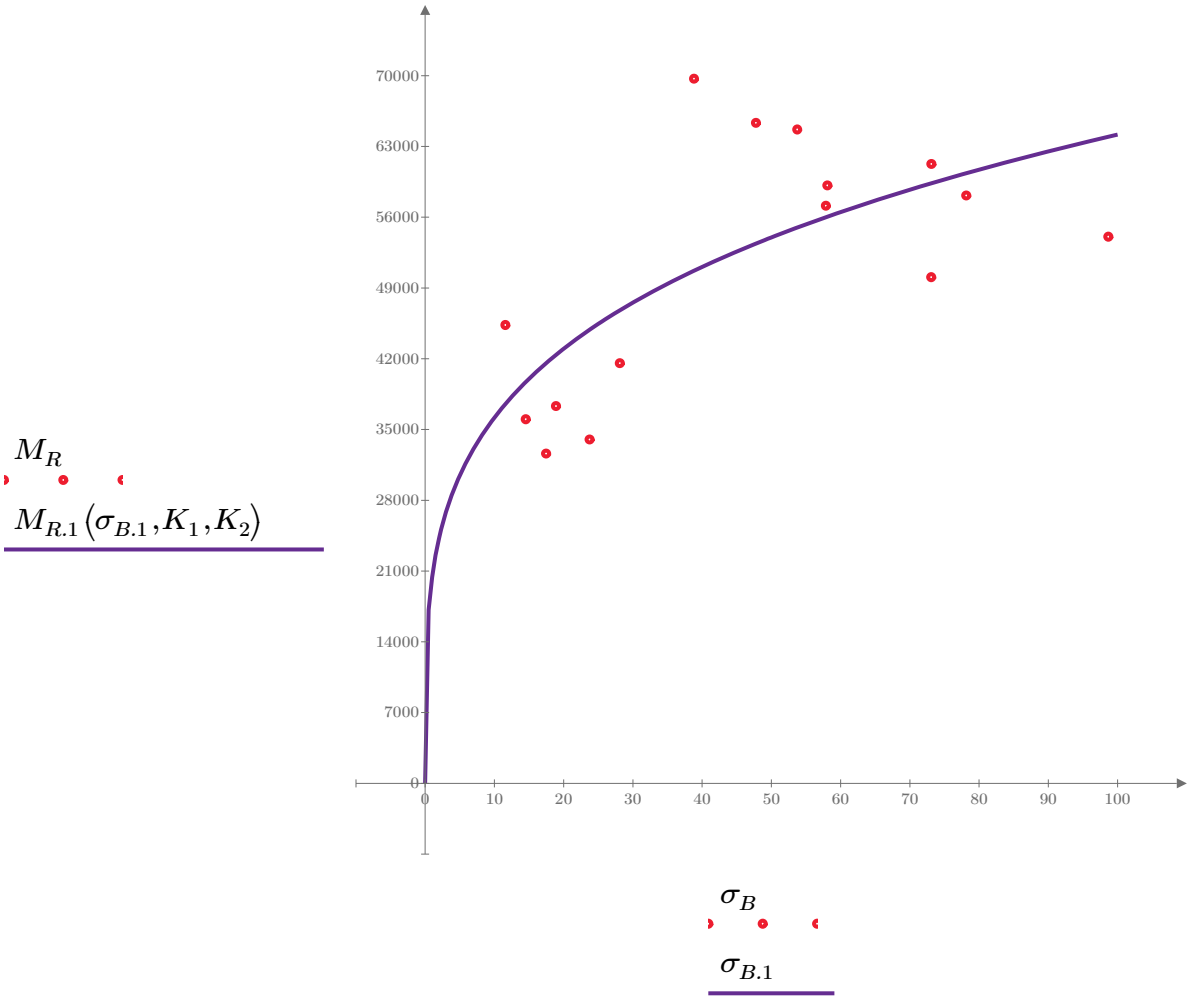

Figure 1. Plot of the test data (red points) vs. the fitted Equation 1 model (purple line).

Dan Seely
9/12/2023

$M_{R.2}(\sigma_d, K_3, K_4) := K_3 \cdot \sigma_d^{K_4}$

Equation 2
AASHTO Publication No. FHWA-RD-97-083

$K_3 = 35032.439$

$K_4 = 0.1466$

Equation 2 fitting parameters

$R_2^2 = 0.1751$

Coefficient of determination

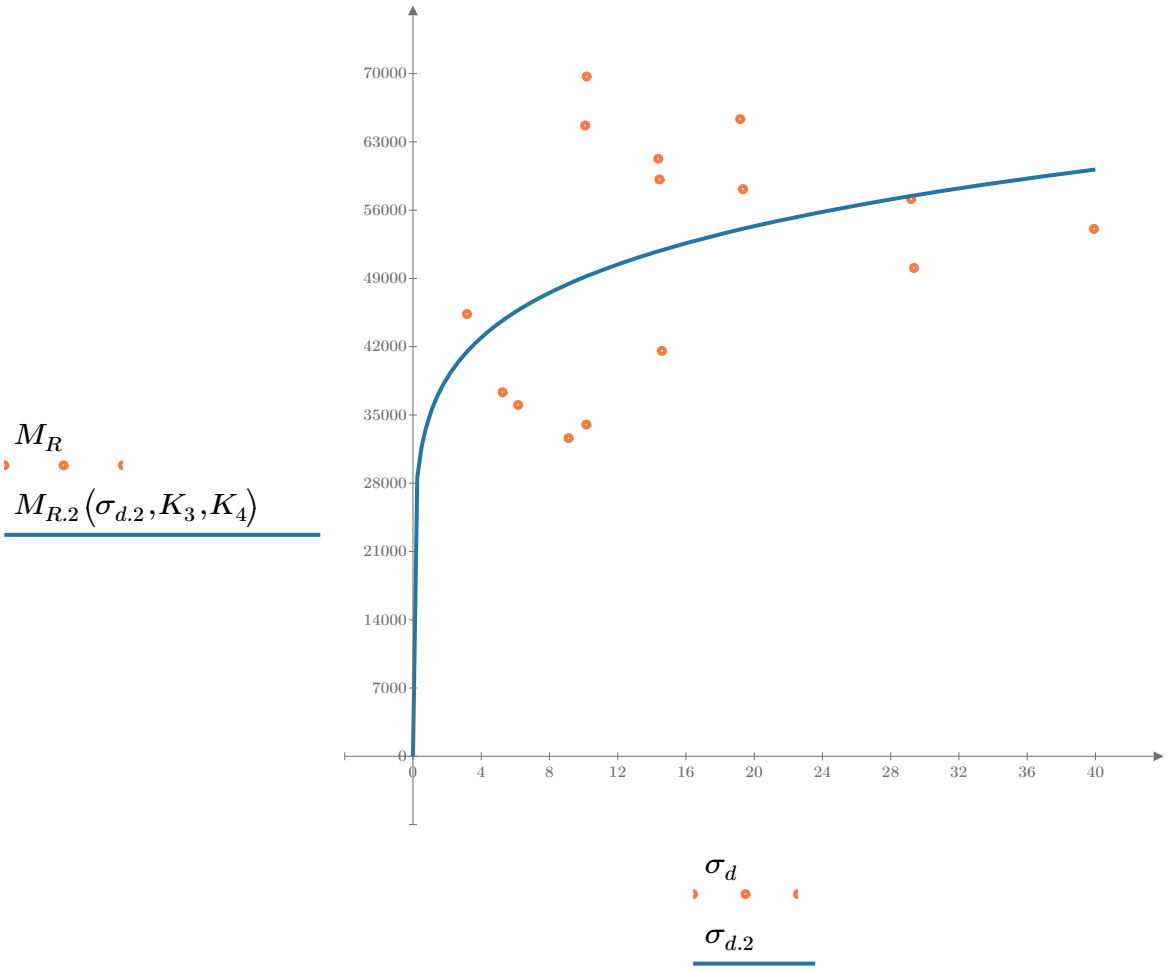

Figure 2. Plot of the test data (orange points) vs. the fitted Equation 2 model (blue line).

Dan Seely
9/12/2023

$$M_{R.3}(\sigma_d, \sigma_3, K_5, K_6, K_7) := K_5 \cdot {\sigma_d}^{K_6} \cdot (1 + \sigma_3)^{K_7}$$

Equation 3 AASHTO Publication No. FHWA-RD-97-083

$K_5 = 29458.543$

$K_6 = -0.0944$ Equation 3 fitting parameters

$K_7 = 0.3475$

${R_3}^2 = 0.6004$ Coefficient of determination

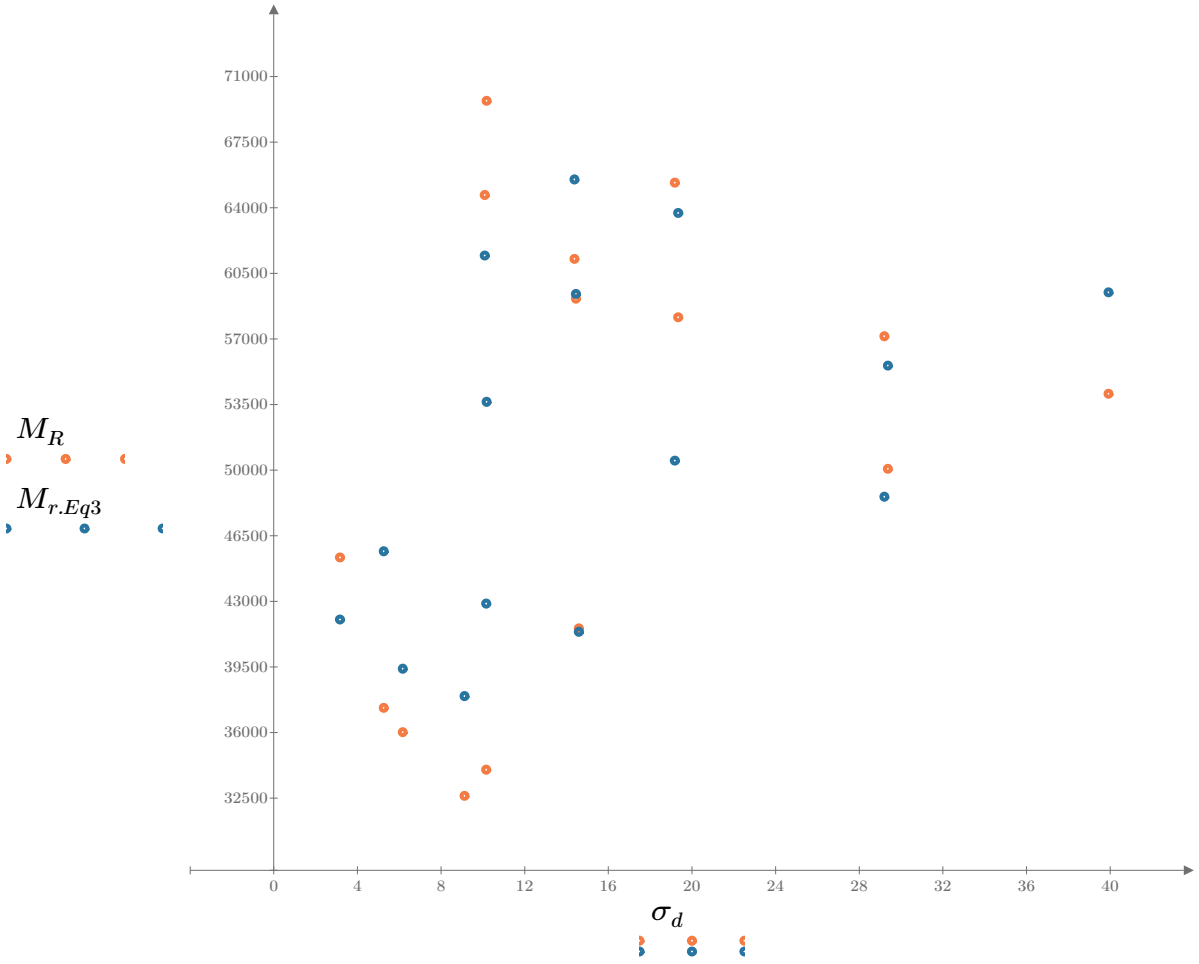

Figure 3. Plot of the test data (orange points) vs. the fitted Equation 3 model (blue points).

Dan Seely
9/12/2023

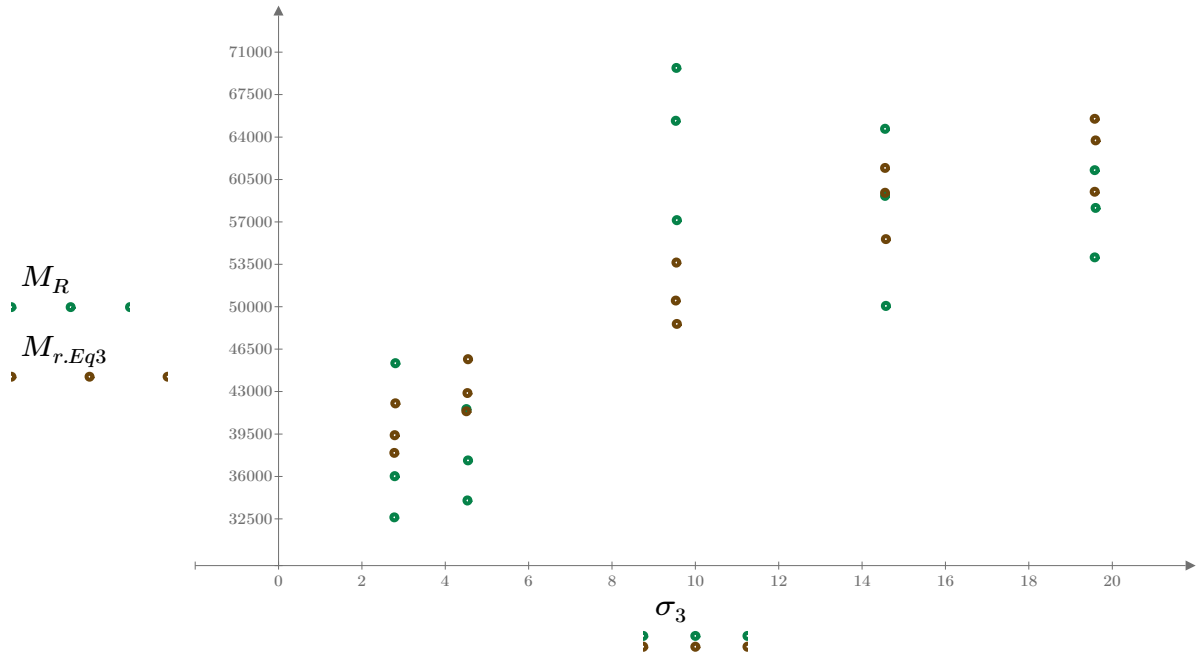

Figure 4. Plot of the test data (green points) vs. the fitted Equation 3 model (brown points).

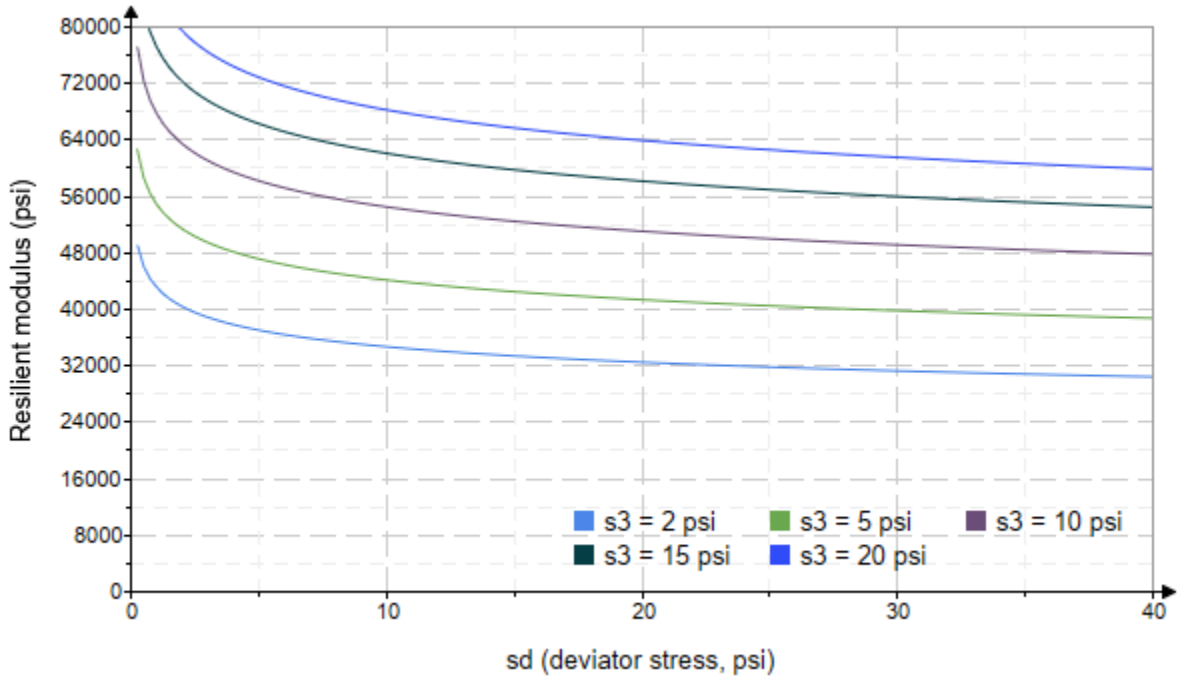

Figure 5. Plot of the fitted Equation 3 model for various confining stresses.

Dan Seely
9/12/2023

$$M_{R.4}\left(\sigma_B,\sigma_d,K_8,K_9,K_{10}\right) := K_8 \cdot p_a \left(\frac{\sigma_B}{p_a}\right)^{K_9} \cdot \left(\frac{\sigma_d}{p_a}\right)^{K_{10}}$$

Equation 4 AASHTO Publication No. FHWA-RD-97-083

$K_8 = 2115.268$

$K_9 = 0.4674$ Equation 4 fitting parameters

$K_{10} = -0.2557$

$R_4^{\,2} = 0.6170$ Coefficient of determination

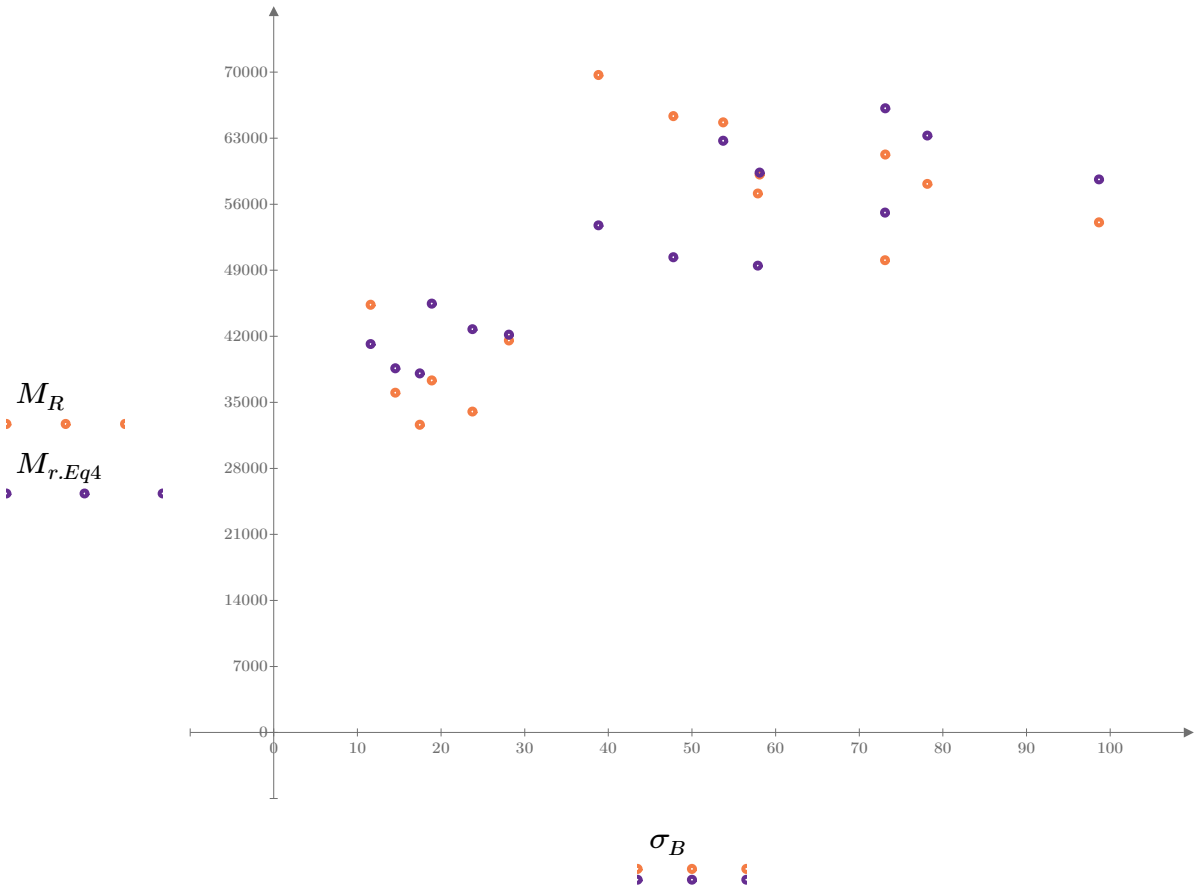

Figure 6. Plot of the test data (orange points) vs. the fitted Equation 4 model (purple points).

Dan Seely
9/12/2023

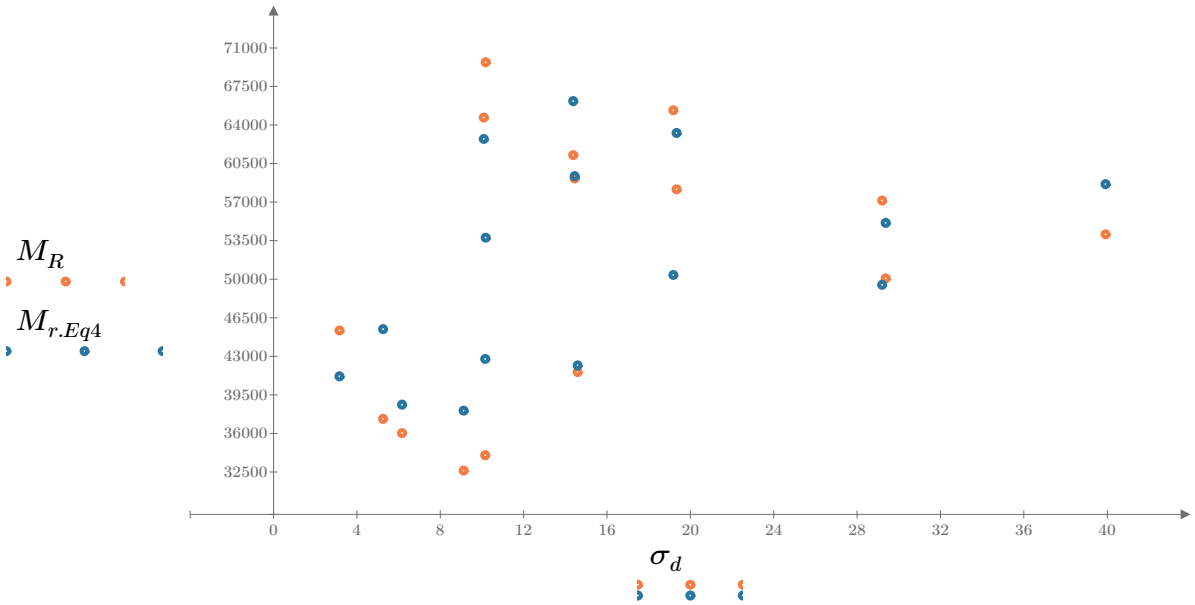

Figure 7. Plot of the test data (orange points) vs. the fitted Equation 4 model (blue points).

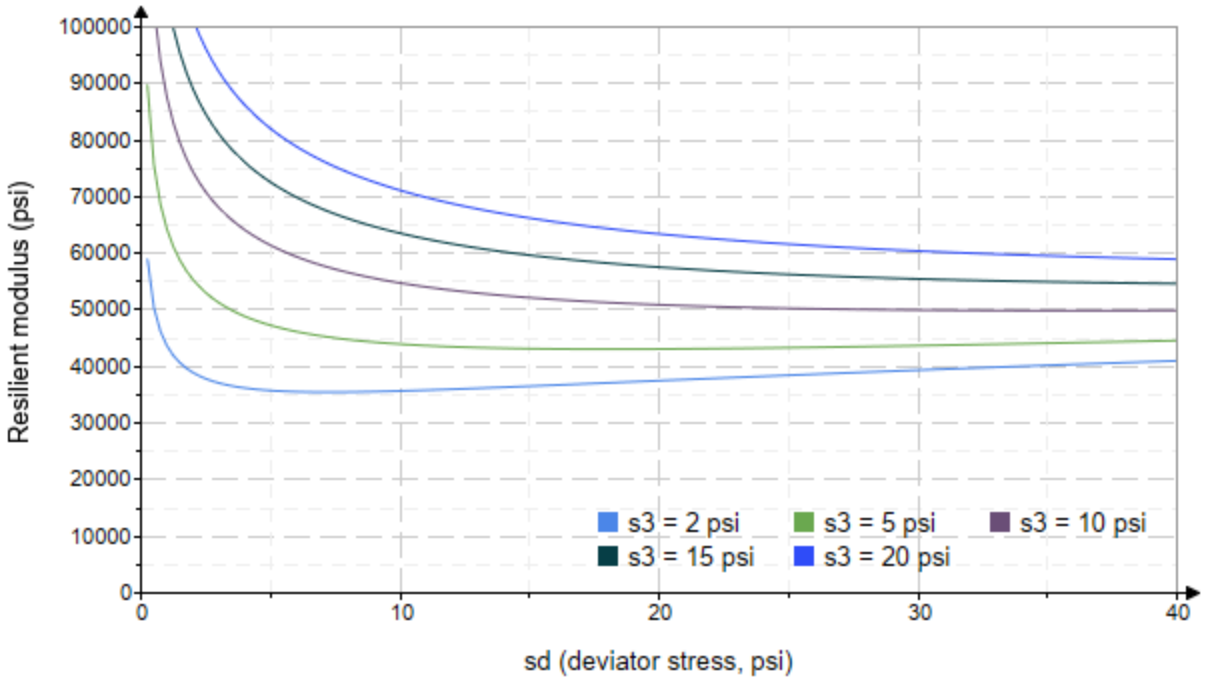

Figure 8. Plot of the fitted Equation 4 model for various confining stresses.

Dan Seely
9/12/2023

$SampleNo := \text{“B3–27”}$

$Treatment = \text{“M5”}$

$S = 9.389$ Degree of Saturation (%)

Test Sequence : Base/Subbase

Test summary data (psi) :

$$\sigma_3 = \begin{bmatrix} 3.311 \\ 2.792 \\ 2.733 \\ 4.490 \\ 4.313 \\ 3.653 \\ 8.479 \\ 8.682 \\ 9.010 \\ 13.810 \\ 14.130 \\ 13.810 \\ 19.210 \\ 19.060 \\ 19.070 \end{bmatrix} \quad \sigma_d = \begin{bmatrix} 3.448 \\ 6.290 \\ 8.977 \\ 5.538 \\ 10.030 \\ 14.820 \\ 10.450 \\ 19.220 \\ 29.130 \\ 10.450 \\ 14.720 \\ 29.270 \\ 14.650 \\ 19.210 \\ 39.930 \end{bmatrix} \quad \sigma_B = \begin{bmatrix} 13.380 \\ 14.670 \\ 17.180 \\ 19.010 \\ 22.970 \\ 25.780 \\ 35.890 \\ 45.260 \\ 56.160 \\ 51.890 \\ 57.110 \\ 70.690 \\ 72.290 \\ 76.380 \\ 97.130 \end{bmatrix} \quad M_R = \begin{bmatrix} 189550.0 \\ 334710.0 \\ 129096.0 \\ 241378.0 \\ 216774.0 \\ 132284.0 \\ 423262.0 \\ 115180.0 \\ 86426.8 \\ 271134.0 \\ 235390.0 \\ 113866.0 \\ 316280.0 \\ 233904.0 \\ 141942.0 \end{bmatrix}$$

σ_3 = mean confining stress
σ_d = mean deviator stress
σ_B = mean bulk stress
M_R = resilient modulus
p_a = atmospheric pressure = 14.6959 psi

Dan Seely
9/12/2023

$$M_{R.1}(\sigma_B, K_1, K_2) := K_1 \cdot {\sigma_B}^{K_2}$$

Equation 1
AASHTO Publication No. FHWA-RD-97-083

$K_1 = 287636.704$

$K_2 = -0.0845$

Equation 1 fitting parameters

${R_1}^2 = 0.0159$

Coefficient of determination

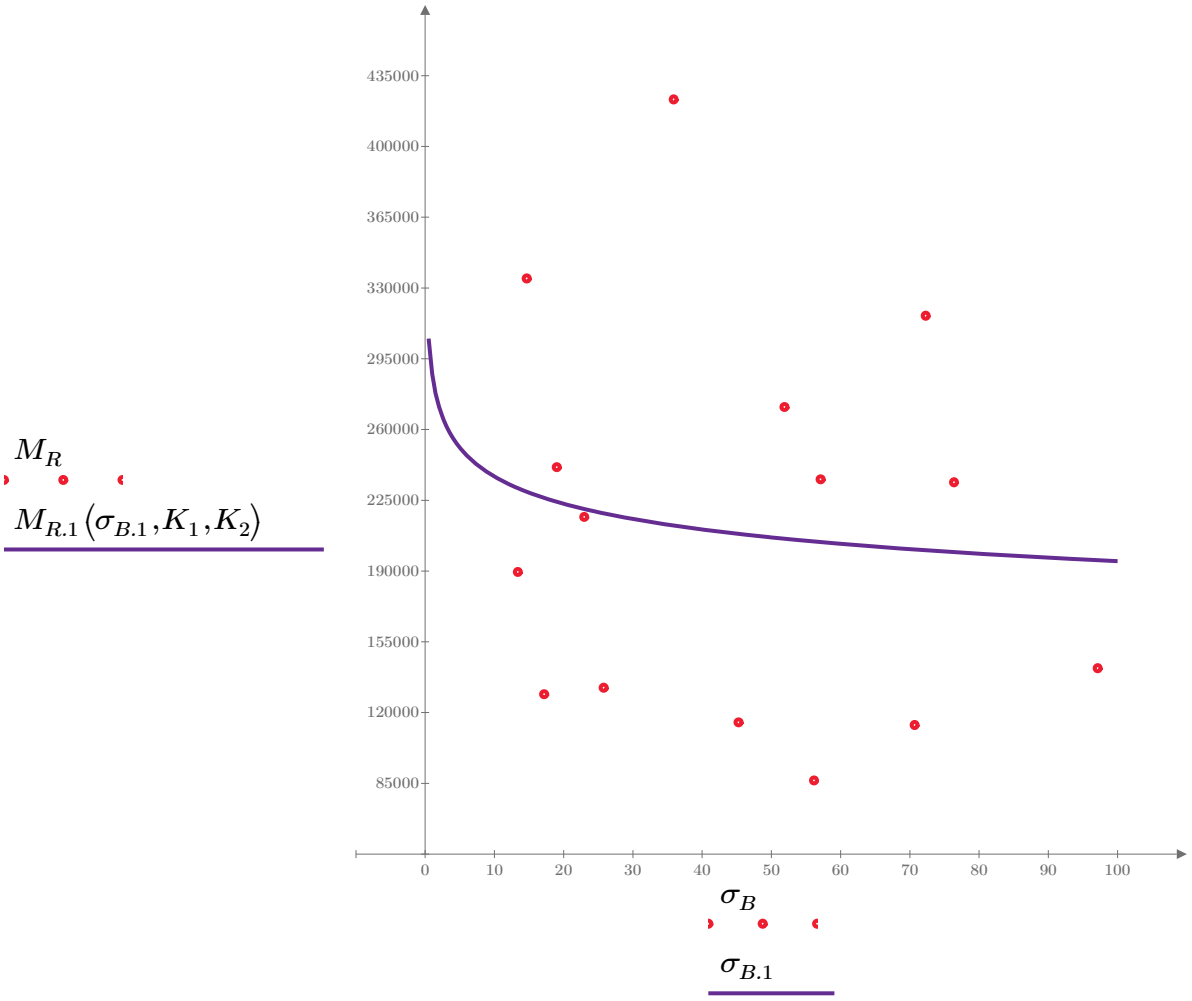

Figure 1. Plot of the test data (red points) vs. the fitted Equation 1 model (purple line).

Dan Seely
9/12/2023

$$M_{R.2}(\sigma_d, K_3, K_4) := K_3 \cdot \sigma_d^{K_4}$$

Equation 2
AASHTO Publication No. FHWA-RD-97-083

$K_3 = 392579.680$

$K_4 = -0.2444$

Equation 2 fitting parameters

$R_2^2 = 0.1648$

Coefficient of determination

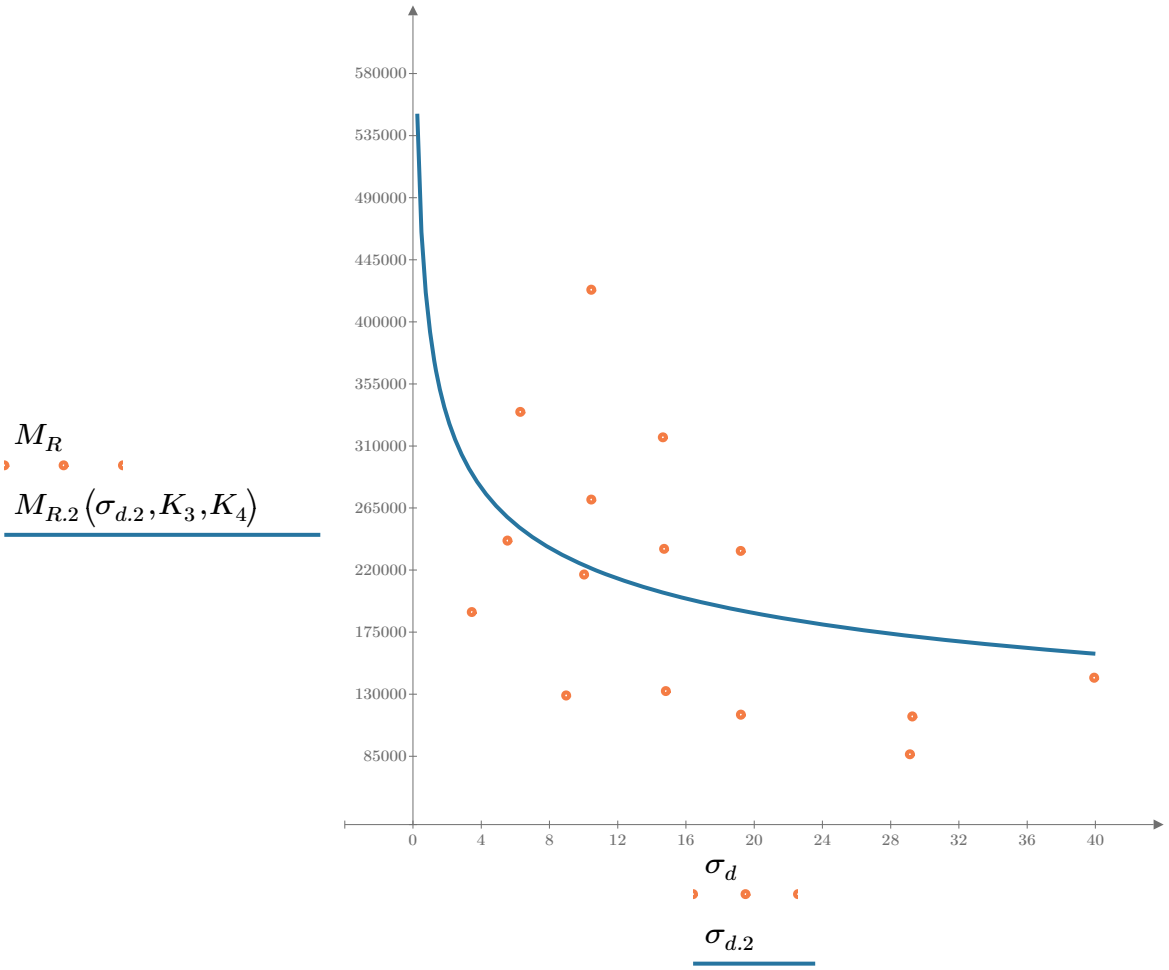

Figure 2. Plot of the test data (orange points) vs. the fitted Equation 2 model (blue line).

Dan Seely
9/12/2023

$$M_{R.3}\left(\sigma_d,\sigma_3,K_5,K_6,K_7\right):=K_5\cdot{\sigma_d}^{K_6}\cdot\left(1+\sigma_3\right)^{K_7}$$

Equation 3 AASHTO Publication No. FHWA-RD-97-083

$K_5=293073.361$

$K_6=-0.5537$ Equation 3 fitting parameters

$K_7=0.4848$

${R_3}^2=0.4004$ Coefficient of determination

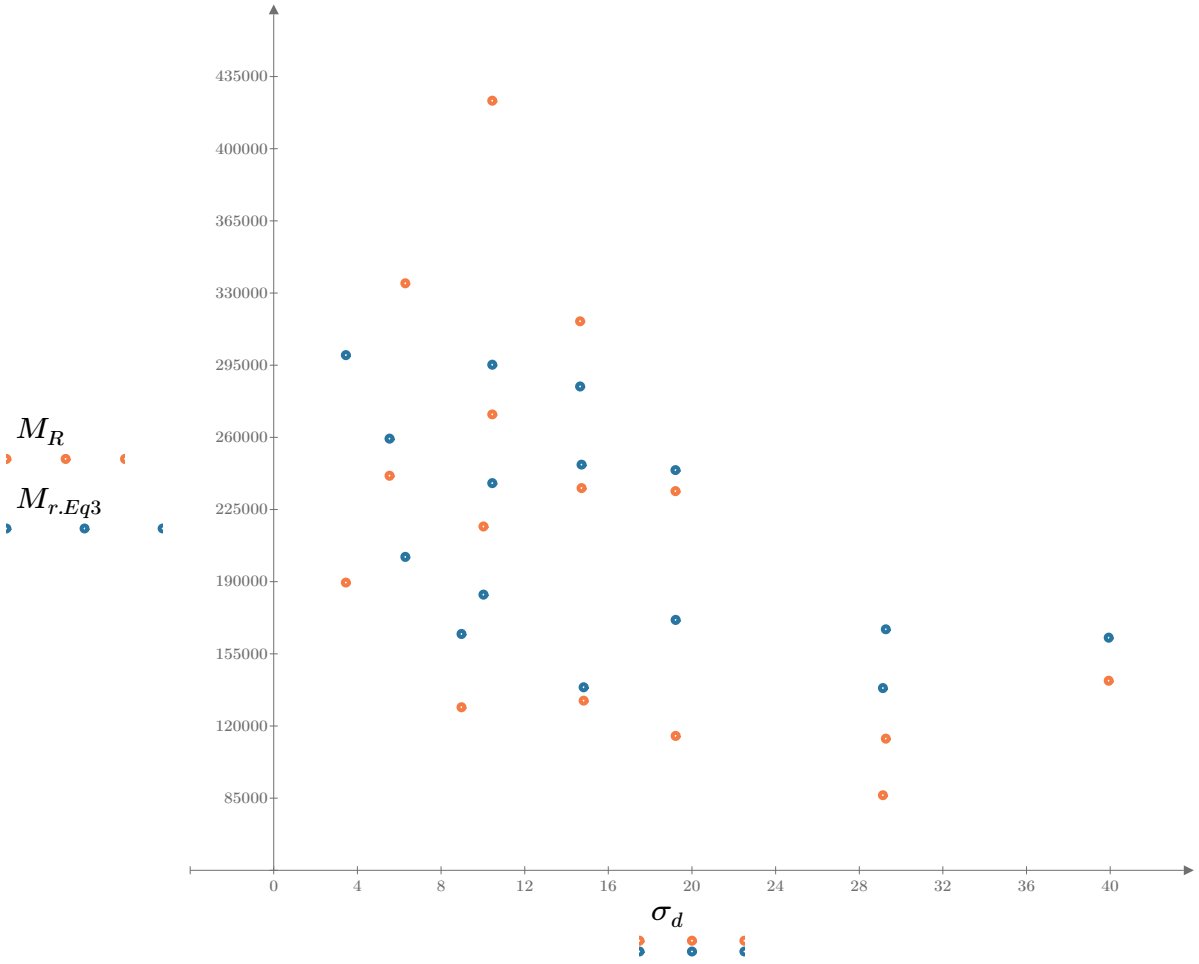

Figure 3. Plot of the test data (orange points) vs. the fitted Equation 3 model (blue points).

Dan Seely
9/12/2023

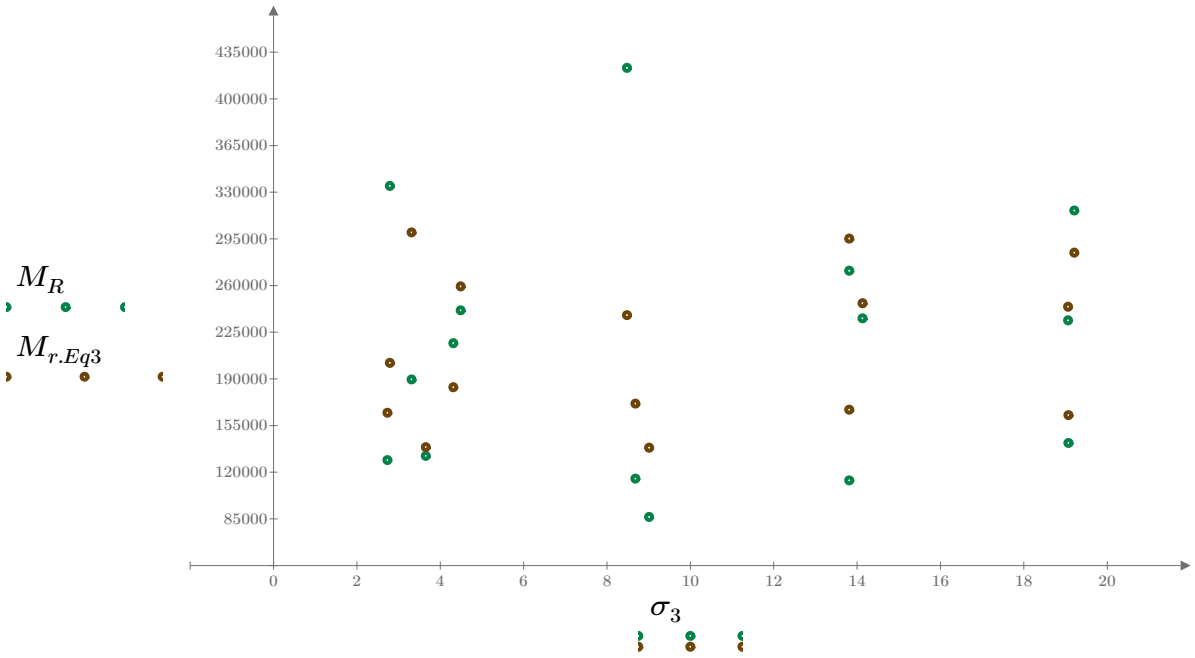

Figure 4. Plot of the test data (green points) vs. the fitted Equation 3 model (brown points).

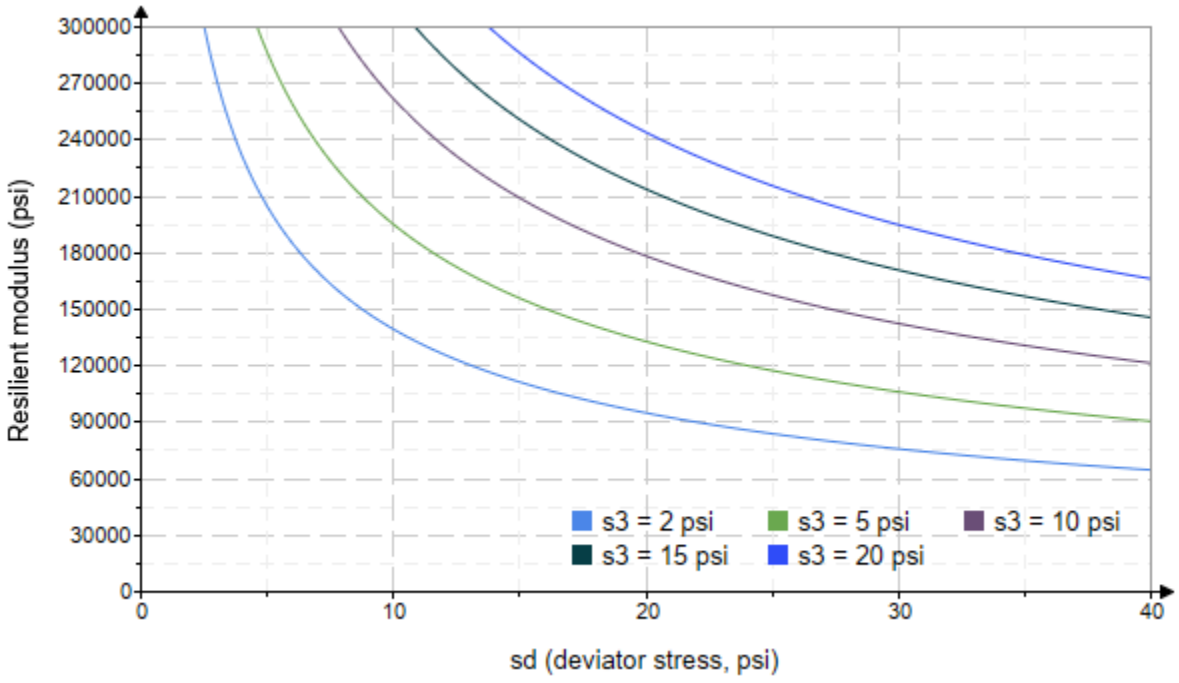

Figure 5. Plot of the fitted Equation 3 model for various confining stresses.

Dan Seely
9/12/2023

$$M_{R.4}\left(\sigma_B,\sigma_d,K_8,K_9,K_{10}\right) := K_8 \cdot p_a \left(\frac{\sigma_B}{p_a}\right)^{K_9} \cdot \left(\frac{\sigma_d}{p_a}\right)^{K_{10}}$$

Equation 4 AASHTO Publication No. FHWA-RD-97-083

$K_8 = 7021.319$

$K_9 = 0.6366$ Equation 4 fitting parameters

$K_{10} = -0.7728$

$R_4^{\ 2} = 0.3909$ Coefficient of determination

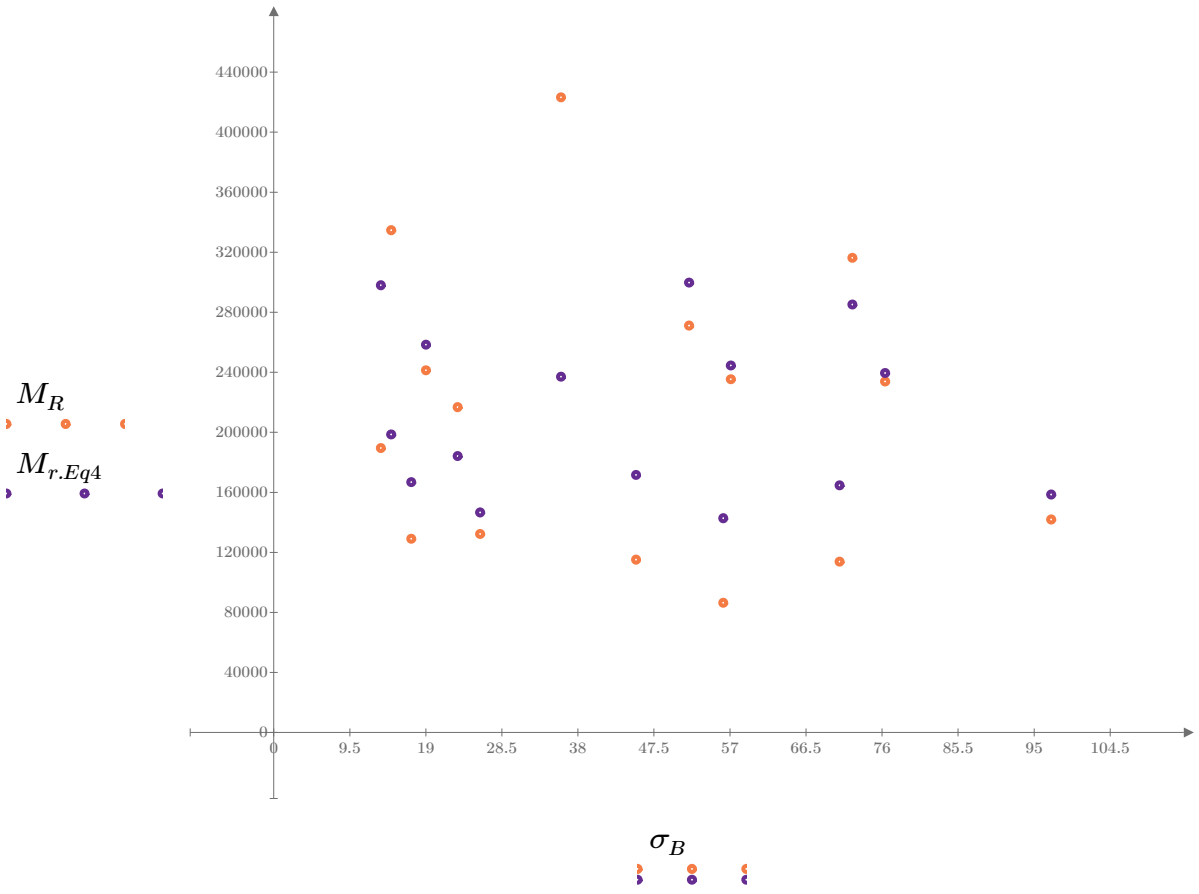

Figure 6. Plot of the test data (orange points) vs. the fitted Equation 4 model (purple points).

Dan Seely
9/12/2023

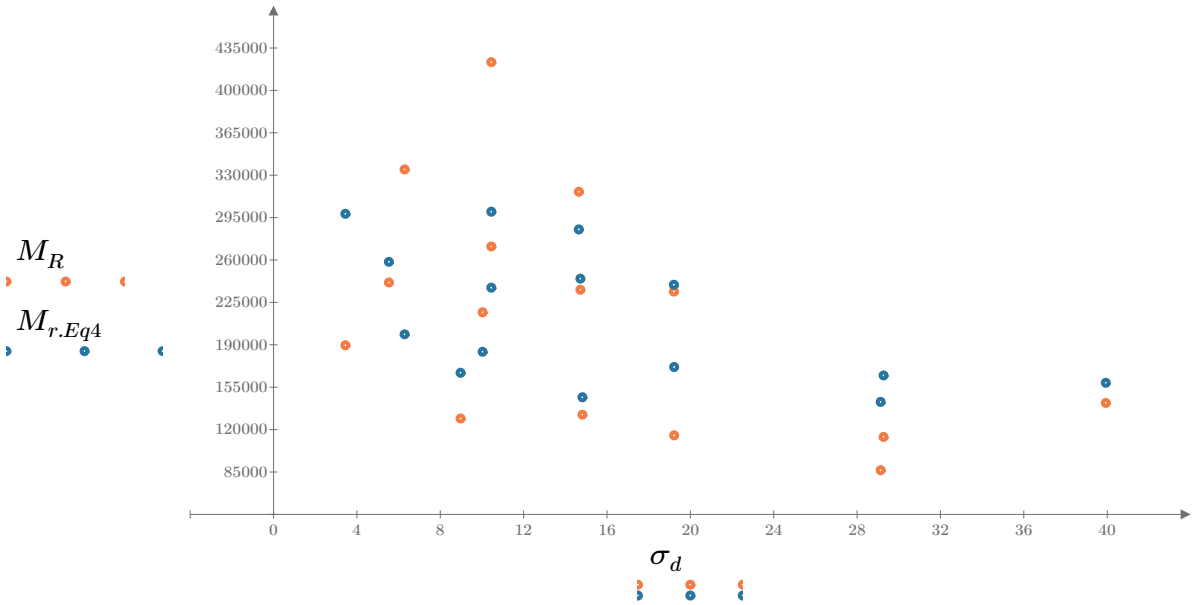

Figure 7. Plot of the test data (orange points) vs. the fitted Equation 4 model (blue points).

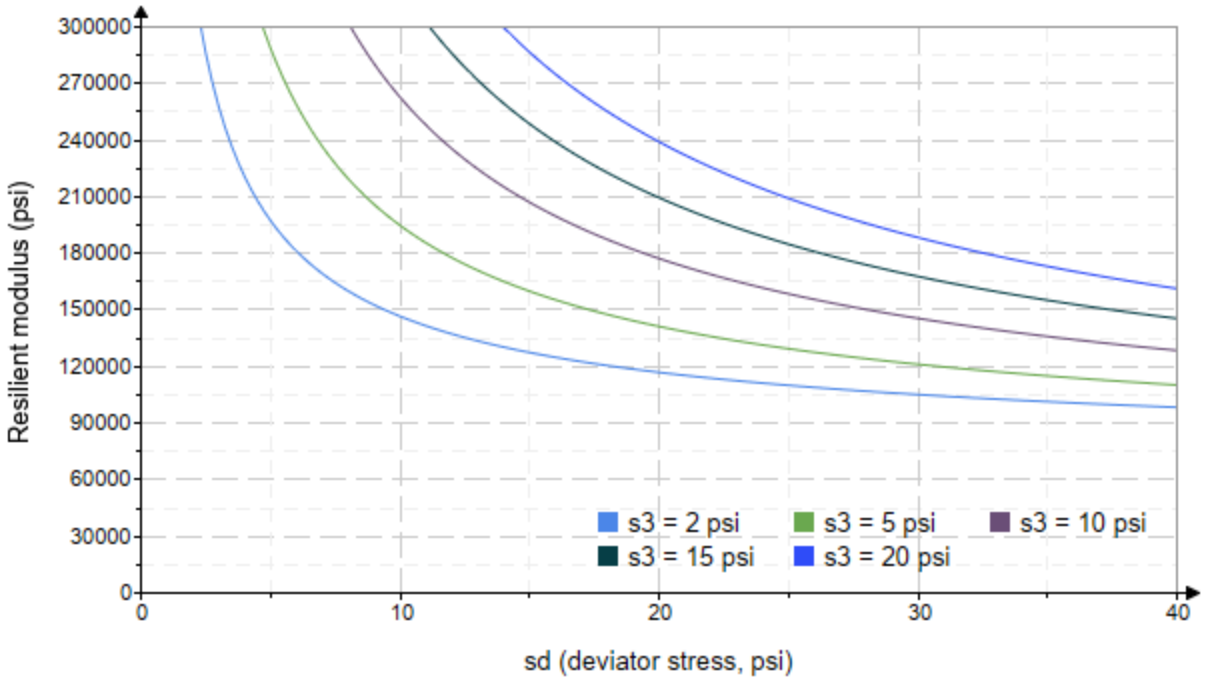

Figure 8. Plot of the fitted Equation 4 model for various confining stresses.

Dan Seely
9/12/2023

$SampleNo := \text{“B3–28”}$

$Treatment = \text{“M5”}$

$S = 9.142$ Degree of Saturation (%)

Test Sequence : Base/Subbase

Test summary data (psi) :

$$\sigma_3 = \begin{bmatrix} 2.709 \\ 2.688 \\ 2.555 \\ 4.565 \\ 4.544 \\ 4.538 \\ 9.577 \\ 9.559 \\ 9.543 \\ 14.620 \\ 14.590 \\ 14.580 \\ 19.600 \\ 19.590 \\ 19.590 \end{bmatrix} \quad \sigma_d = \begin{bmatrix} 3.318 \\ 6.140 \\ 9.065 \\ 5.157 \\ 10.060 \\ 14.430 \\ 10.100 \\ 19.210 \\ 29.340 \\ 10.150 \\ 14.510 \\ 29.440 \\ 14.370 \\ 19.490 \\ 39.970 \end{bmatrix} \quad \sigma_B = \begin{bmatrix} 11.440 \\ 14.200 \\ 16.730 \\ 18.850 \\ 23.700 \\ 28.040 \\ 38.830 \\ 47.880 \\ 57.970 \\ 54.010 \\ 58.280 \\ 73.190 \\ 73.170 \\ 78.260 \\ 98.730 \end{bmatrix} \quad M_R = \begin{bmatrix} 34013.4 \\ 32758.4 \\ 34414.0 \\ 44168.6 \\ 47846.0 \\ 53451.8 \\ 76953.4 \\ 69327.4 \\ 67114.6 \\ 74304.6 \\ 86631.4 \\ 82974.8 \\ 81322.6 \\ 83316.0 \\ 88077.4 \end{bmatrix}$$

σ_3 = mean confining stress
σ_d = mean deviator stress
σ_B = mean bulk stress
M_R = resilient modulus
p_a = atmospheric pressure = 14.6959 psi

Dan Seely
9/12/2023

$$M_{R.1}(\sigma_B, K_1, K_2) := K_1 \cdot {\sigma_B}^{K_2}$$

Equation 1
AASHTO Publication No. FHWA-RD-97-083

$K_1 = 11391.589$

$K_2 = 0.4619$

Equation 1 fitting parameters

${R_1}^2 = 0.9019$

Coefficient of determination

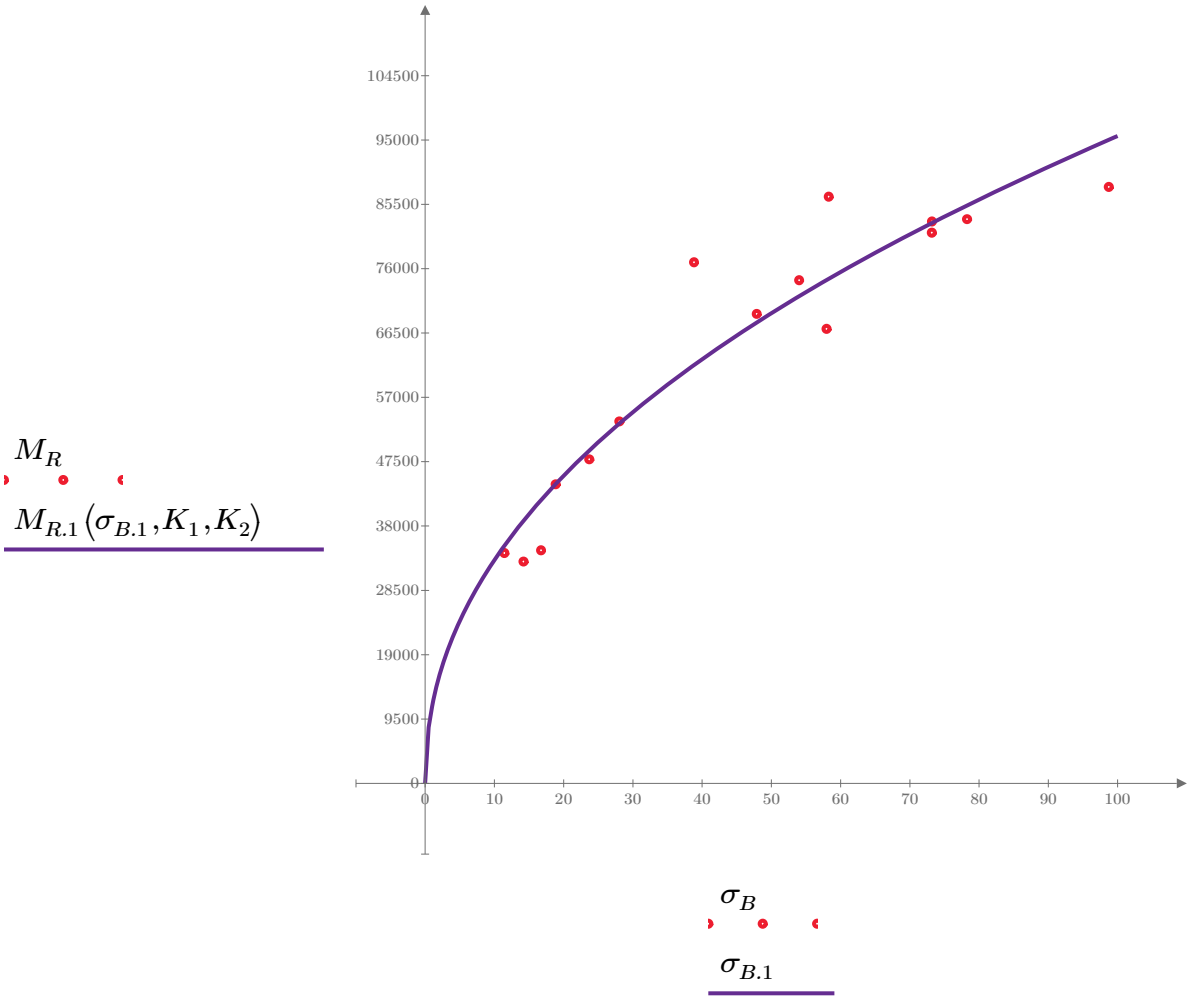

Figure 1. Plot of the test data (red points) vs. the fitted Equation 1 model (purple line).

Dan Seely
9/12/2023

$$M_{R.2}(\sigma_d, K_3, K_4) := K_3 \cdot \sigma_d^{K_4}$$

Equation 2
AASHTO Publication No. FHWA-RD-97-083

$K_3 = 26269.114$

$K_4 = 0.3396$

Equation 2 fitting parameters

$R_2^2 = 0.5421$

Coefficient of determination

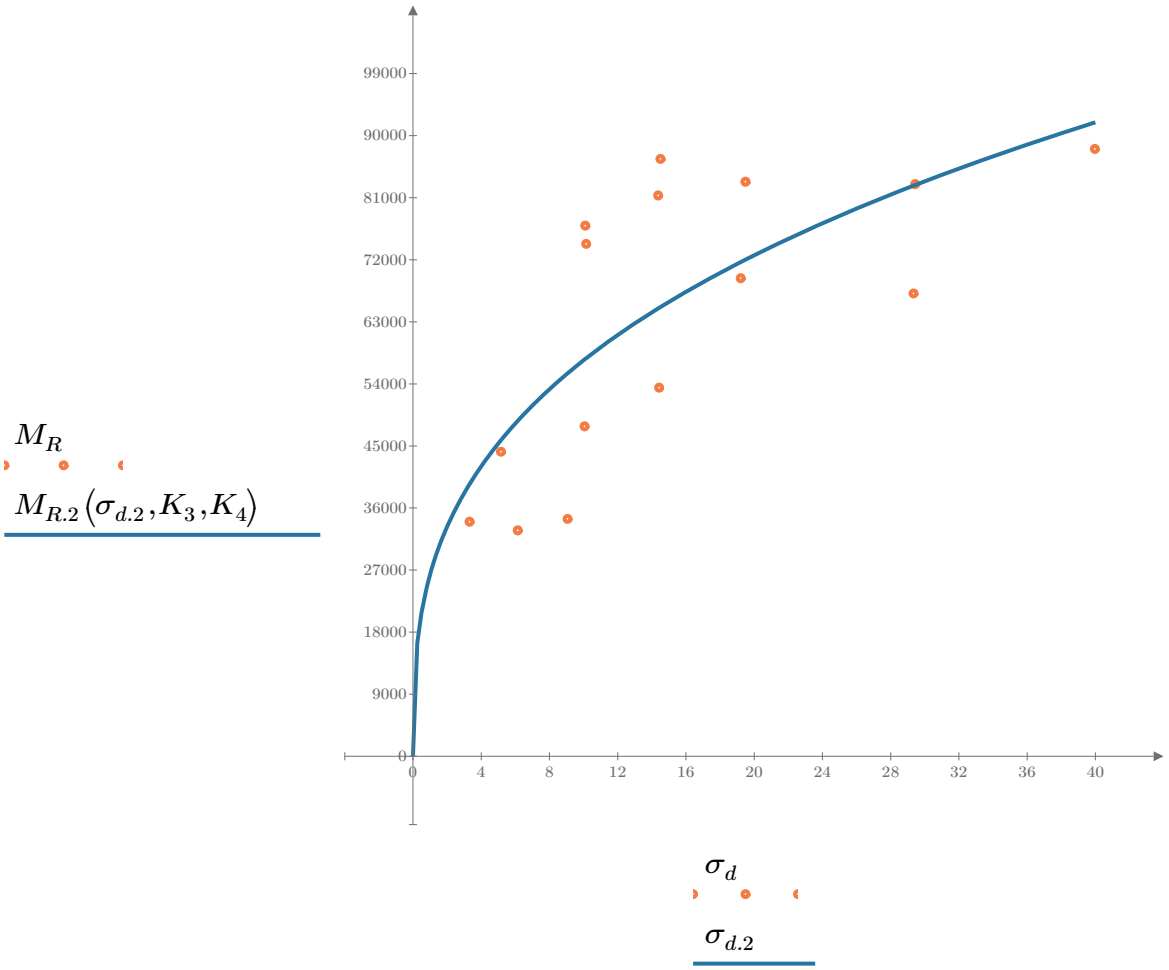

Figure 2. Plot of the test data (orange points) vs. the fitted Equation 2 model (blue line).

Dan Seely
9/12/2023

$$M_{R.3}\left(\sigma_d,\sigma_3,K_5,K_6,K_7\right):=K_5\cdot{\sigma_d}^{K_6}\cdot\left(1+\sigma_3\right)^{K_7}$$

Equation 3 AASHTO Publication No. FHWA-RD-97-083

$K_5=19953.745$

$K_6=0.0592$ Equation 3 fitting parameters

$K_7=0.4345$

${R_3}^2=0.9224$ Coefficient of determination

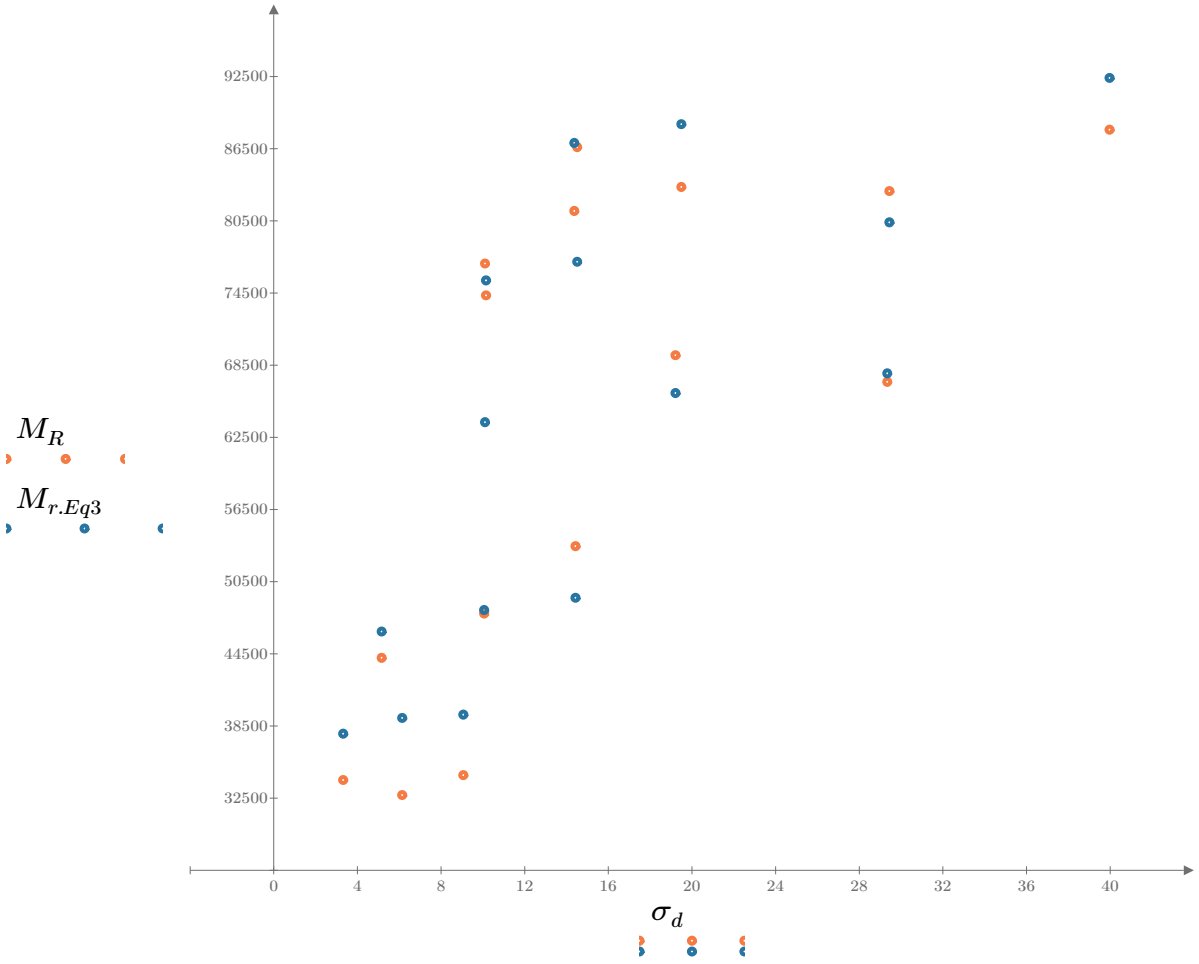

Figure 3. Plot of the test data (orange points) vs. the fitted Equation 3 model (blue points).

Dan Seely
9/12/2023

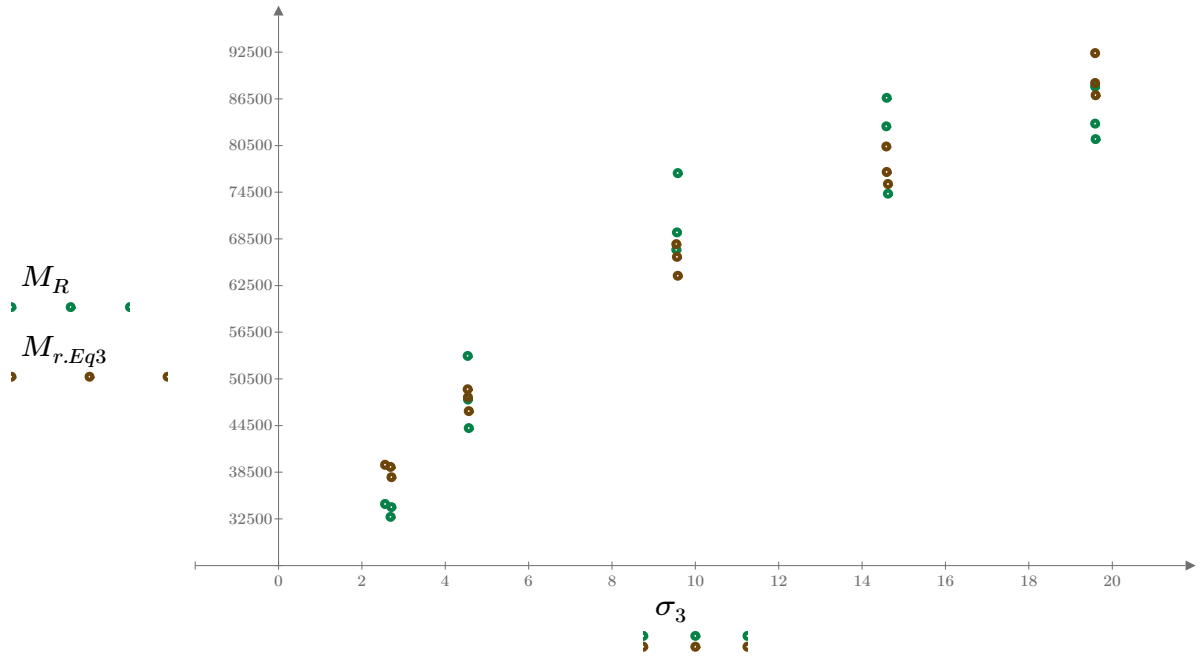

Figure 4. Plot of the test data (green points) vs. the fitted Equation 3 model (brown points).

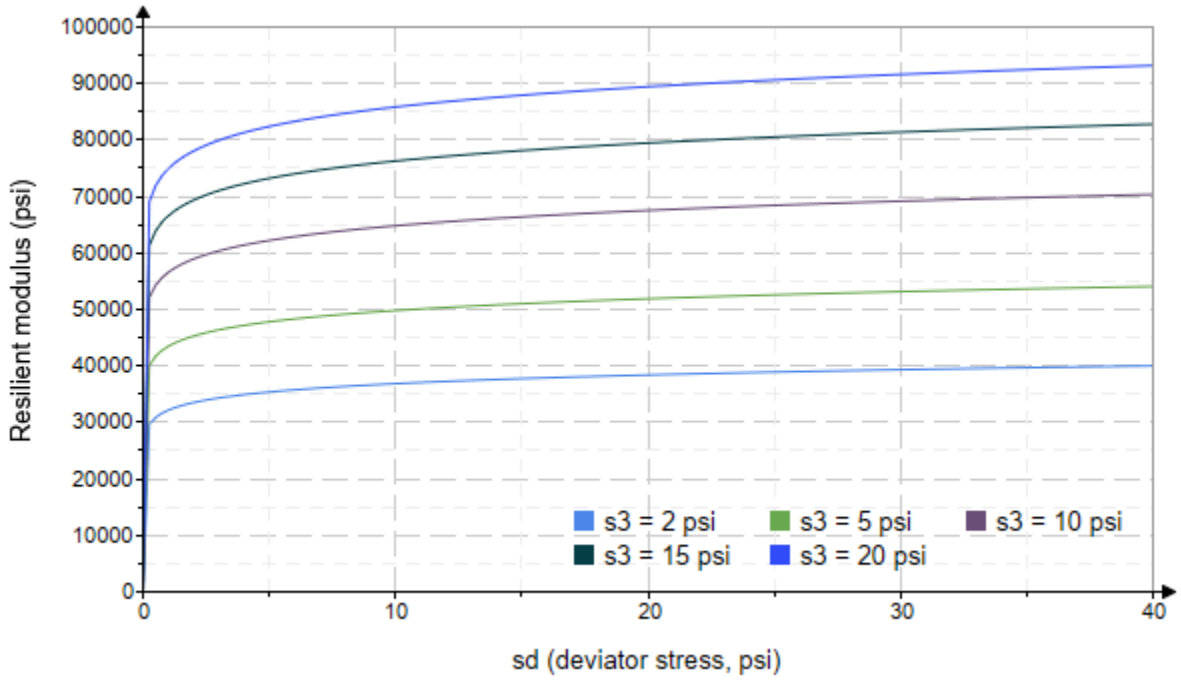

Figure 5. Plot of the fitted Equation 3 model for various confining stresses.

Dan Seely
9/12/2023

$$M_{R.4}\left(\sigma_B,\sigma_d,K_8,K_9,K_{10}\right) := K_8 \cdot p_a \left(\frac{\sigma_B}{p_a}\right)^{K_9} \cdot \left(\frac{\sigma_d}{p_a}\right)^{K_{10}}$$

Equation 4 AASHTO Publication No. FHWA-RD-97-083

$K_8 = 2355.784$

$K_9 = 0.5776$ Equation 4 fitting parameters

$K_{10} = -0.133$

$R_4^{\,2} = 0.9250$ Coefficient of determination

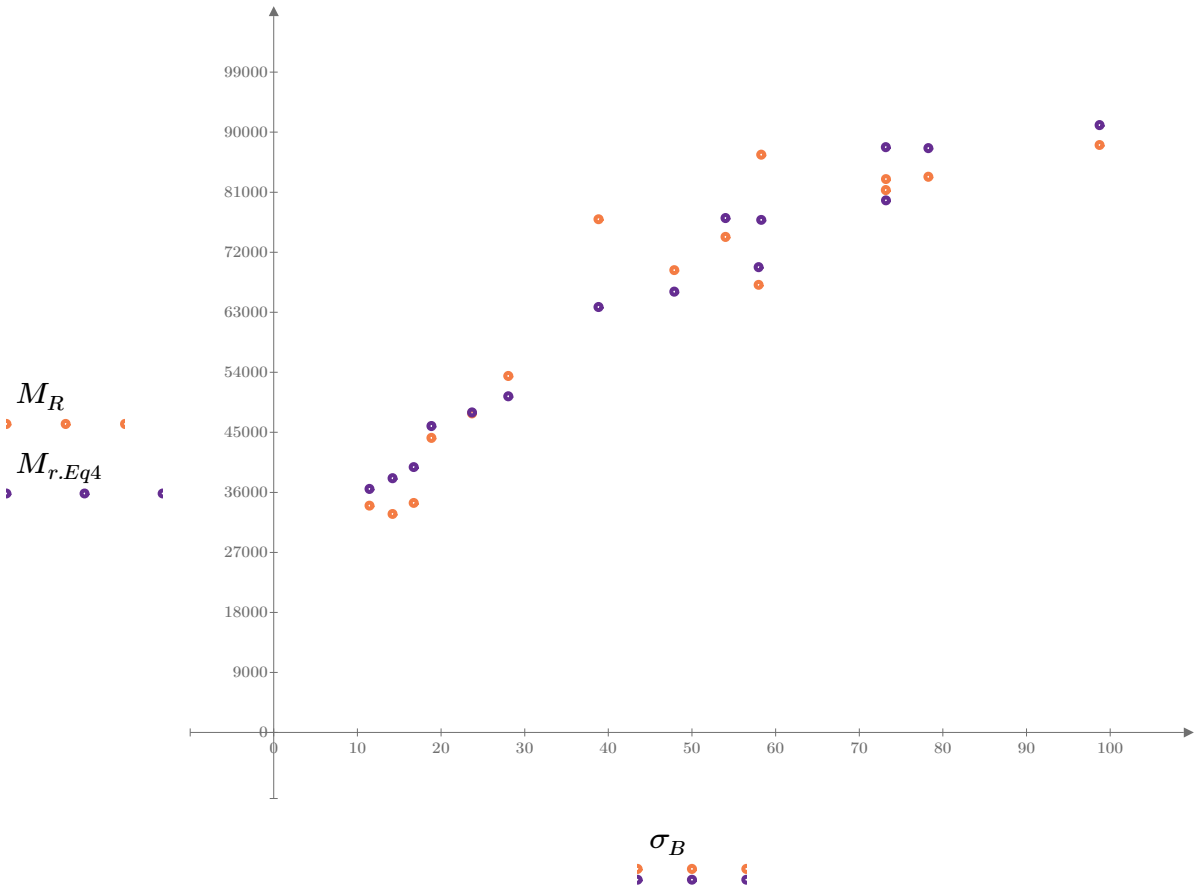

Figure 6. Plot of the test data (orange points) vs. the fitted Equation 4 model (purple points).

Dan Seely
9/12/2023

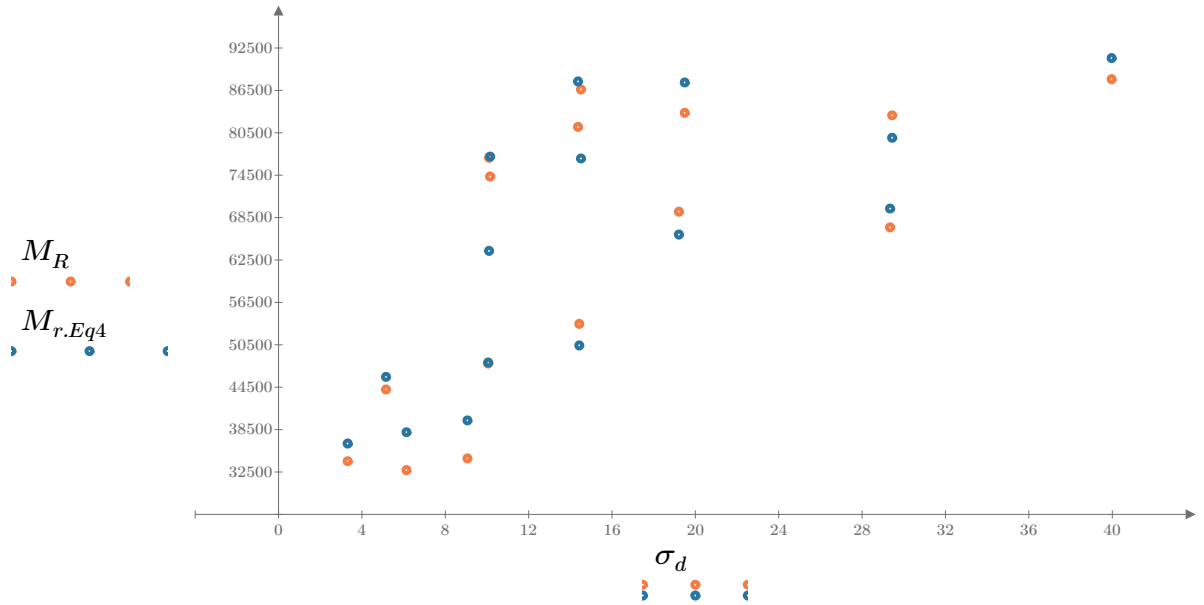

Figure 7. Plot of the test data (orange points) vs. the fitted Equation 4 model (blue points).

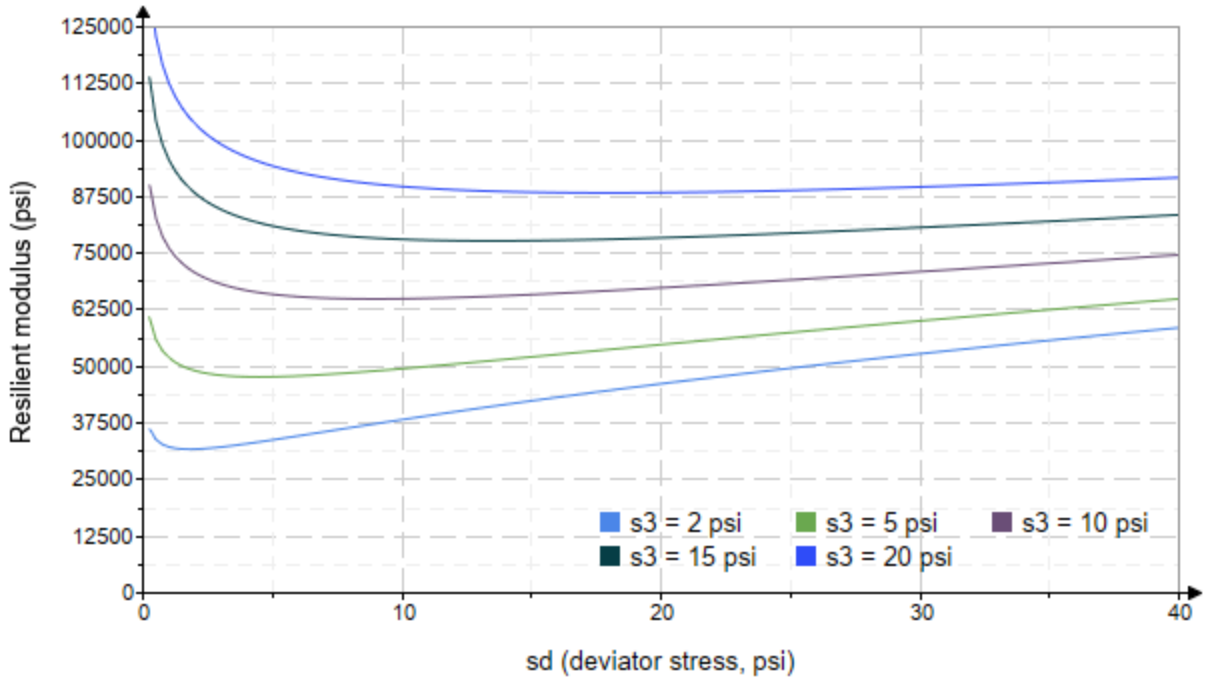

Figure 8. Plot of the fitted Equation 4 model for various confining stresses.

Dan Seely
9/12/2023

$SampleNo := \text{“B3}-29\text{”}$

$Treatment = \text{“M5”}$

$S = 9.293$ Degree of Saturation (%)

Test Sequence : Base/Subbase

Test summary data (psi) :

$$\sigma_3 = \begin{bmatrix} 2.122 \\ 1.948 \\ 1.917 \\ 3.690 \\ 3.845 \\ 3.502 \\ 8.646 \\ 9.098 \\ 9.670 \\ 15.200 \\ 15.220 \\ 15.200 \\ 19.630 \\ 20.060 \\ 19.060 \end{bmatrix} \quad \sigma_d = \begin{bmatrix} 3.623 \\ 6.310 \\ 9.166 \\ 5.213 \\ 9.773 \\ 14.320 \\ 9.871 \\ 19.310 \\ 29.810 \\ 9.800 \\ 14.300 \\ 30.010 \\ 14.610 \\ 19.500 \\ 40.220 \end{bmatrix} \quad \sigma_B = \begin{bmatrix} 9.989 \\ 12.150 \\ 14.920 \\ 16.280 \\ 21.310 \\ 24.830 \\ 35.810 \\ 46.600 \\ 58.820 \\ 55.410 \\ 59.960 \\ 75.610 \\ 73.500 \\ 79.680 \\ 97.410 \end{bmatrix} \quad M_R = \begin{bmatrix} 265800.0 \\ 340194.0 \\ 146196.0 \\ 400430.0 \\ 198440.0 \\ 99298.6 \\ 427118.0 \\ 84406.2 \\ 74829.6 \\ 671128.0 \\ 148850.0 \\ 89644.0 \\ 269240.0 \\ 135368.0 \\ 98370.2 \end{bmatrix}$$

σ_3 = mean confining stress
σ_d = mean deviator stress
σ_B = mean bulk stress
M_R = resilient modulus
p_a = atmospheric pressure = 14.6959 psi

Dan Seely
9/12/2023

$$M_{R.1}(\sigma_B, K_1, K_2) := K_1 \cdot {\sigma_B}^{K_2}$$

Equation 1
AASHTO Publication No. FHWA-RD-97-083

$K_1 = 468800.638$

$K_2 = -0.2017$

Equation 1 fitting parameters

${R_1}^2 = 0.0486$

Coefficient of determination

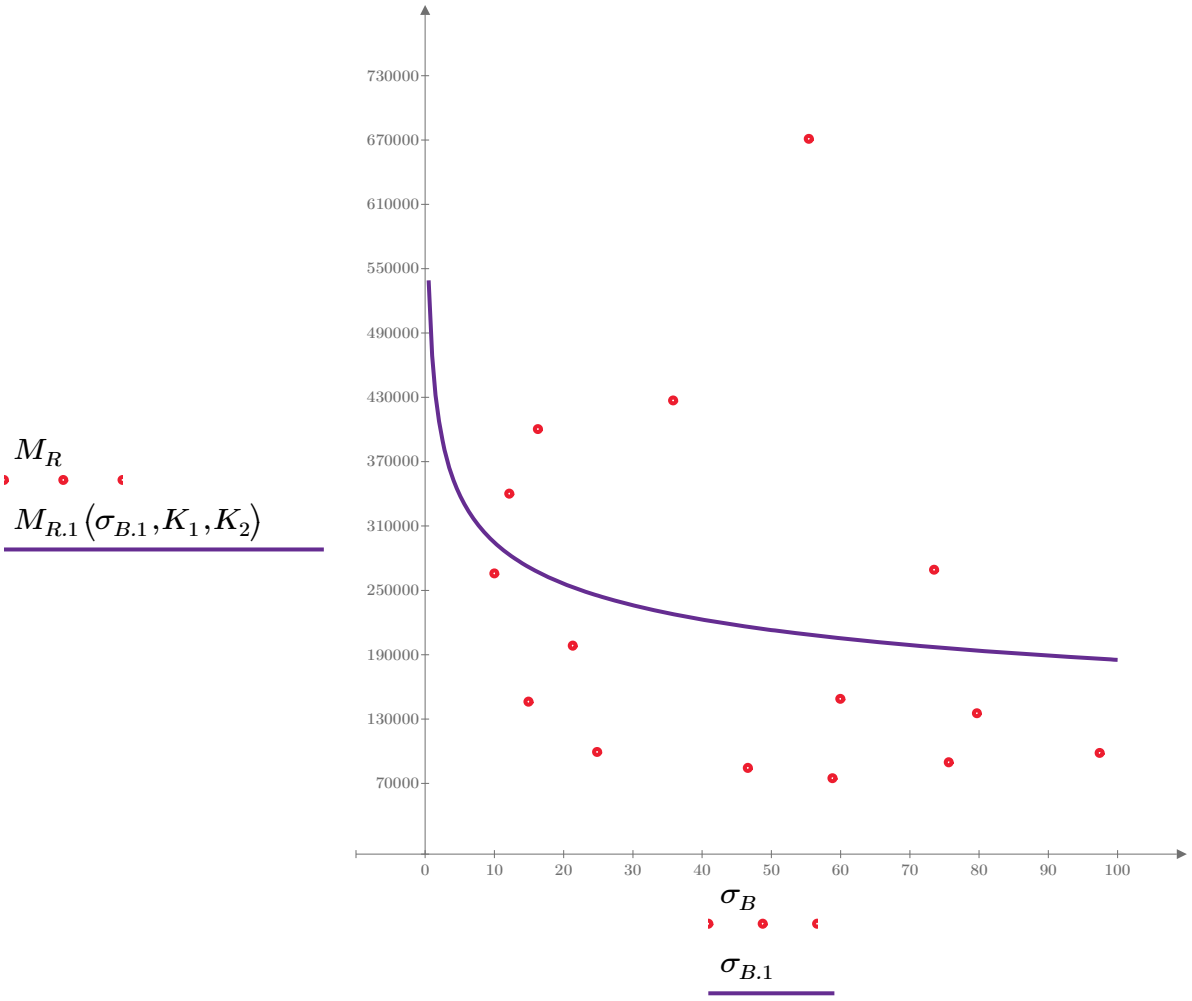

Figure 1. Plot of the test data (red points) vs. the fitted Equation 1 model (purple line).

Dan Seely
9/12/2023

$M_{R.2}(\sigma_d, K_3, K_4) := K_3 \cdot \sigma_d^{K_4}$

Equation 2
AASHTO Publication No. FHWA-RD-97-083

$K_3 = 795881.674$

$K_4 = -0.5022$

Equation 2 fitting parameters

$R_2^2 = 0.2865$

Coefficient of determination

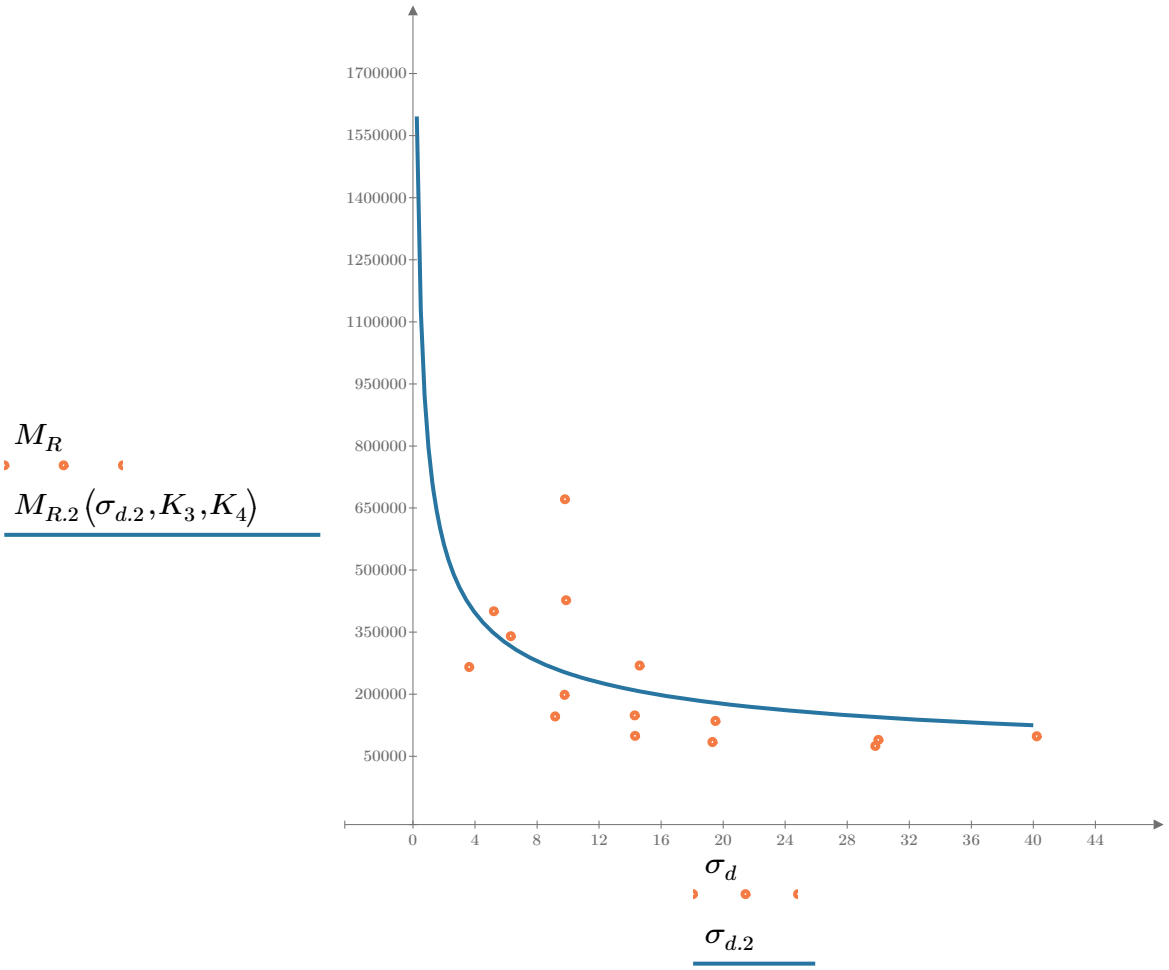

Figure 2. Plot of the test data (orange points) vs. the fitted Equation 2 model (blue line).

Dan Seely
9/12/2023

$$M_{R.3}\left(\sigma_d,\sigma_3,K_5,K_6,K_7\right):=K_5\cdot{\sigma_d}^{K_6}\cdot\left(1+\sigma_3\right)^{K_7}$$

Equation 3 AASHTO Publication No. FHWA-RD-97-083

$K_5=893568.075$

$K_6=-1.4455$ Equation 3 fitting parameters

$K_7=0.9809$

${R_3}^2=0.6502$ Coefficient of determination

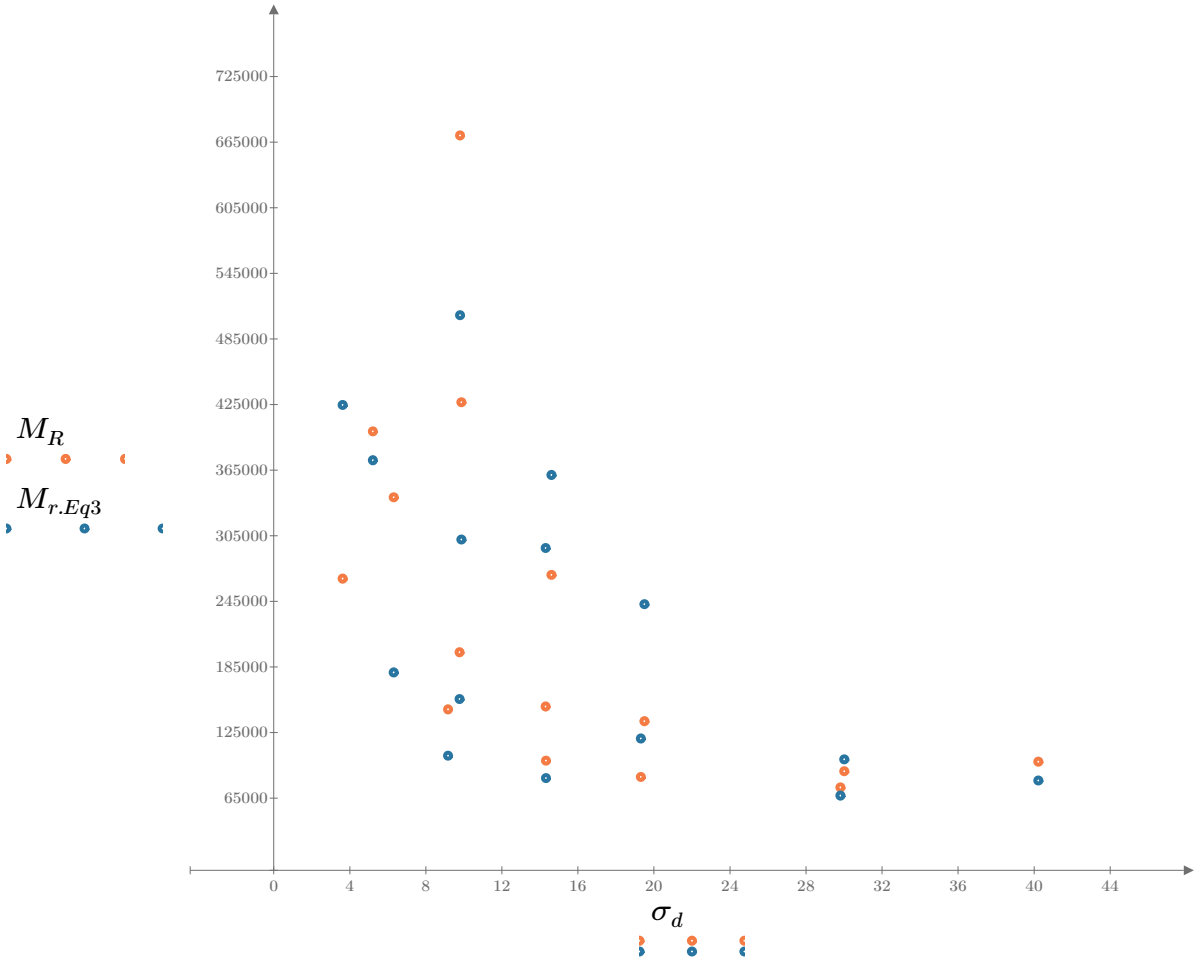

Figure 3. Plot of the test data (orange points) vs. the fitted Equation 3 model (blue points).

Dan Seely
9/12/2023

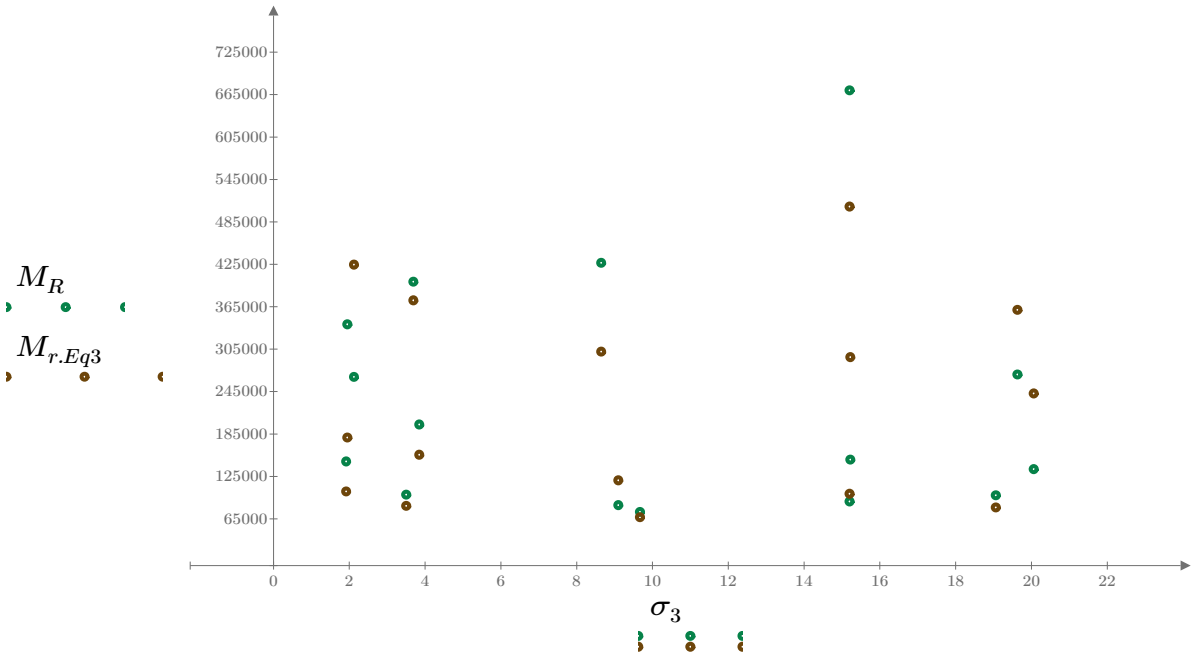

Figure 4. Plot of the test data (green points) vs. the fitted Equation 3 model (brown points).

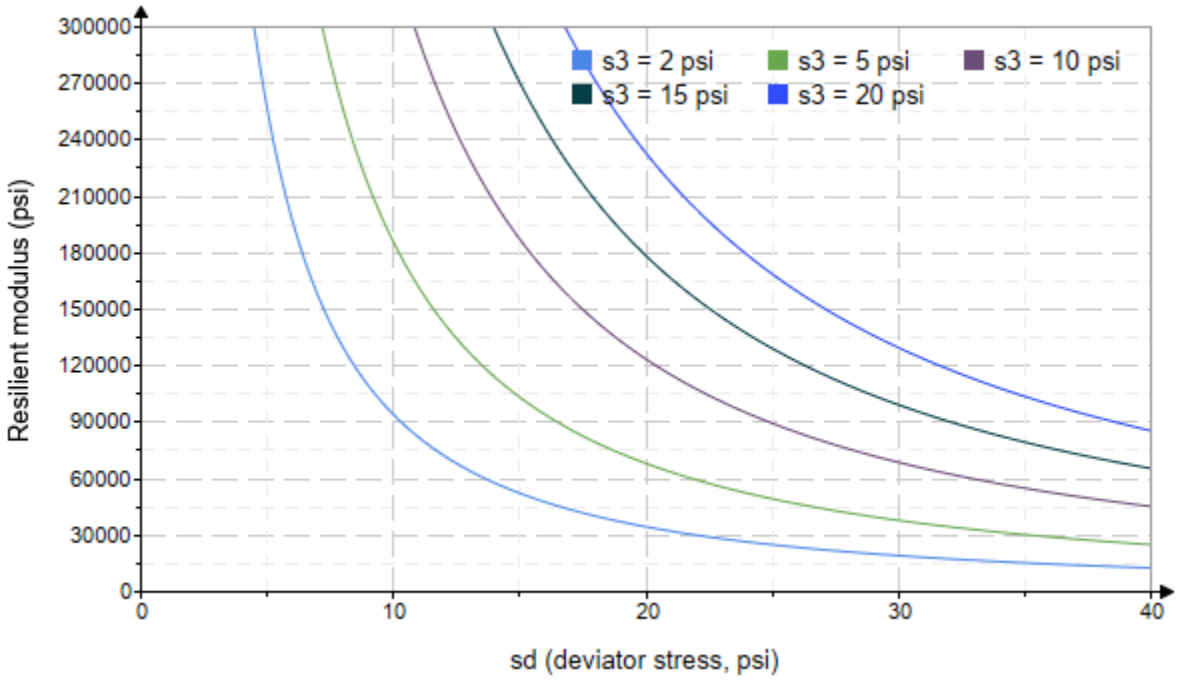

Figure 5. Plot of the fitted Equation 3 model for various confining stresses.

Dan Seely
9/12/2023

$$M_{R.4}\left(\sigma_B,\sigma_d,K_8,K_9,K_{10}\right) := K_8 \cdot p_a \left(\frac{\sigma_B}{p_a}\right)^{K_9} \cdot \left(\frac{\sigma_d}{p_a}\right)^{K_{10}}$$

Equation 4 AASHTO Publication No. FHWA-RD-97-083

$K_8 = 2857.514$

$K_9 = 1.3294$ Equation 4 fitting parameters

$K_{10} = -1.9926$

$R_4^{\,2} = 0.7051$ Coefficient of determination

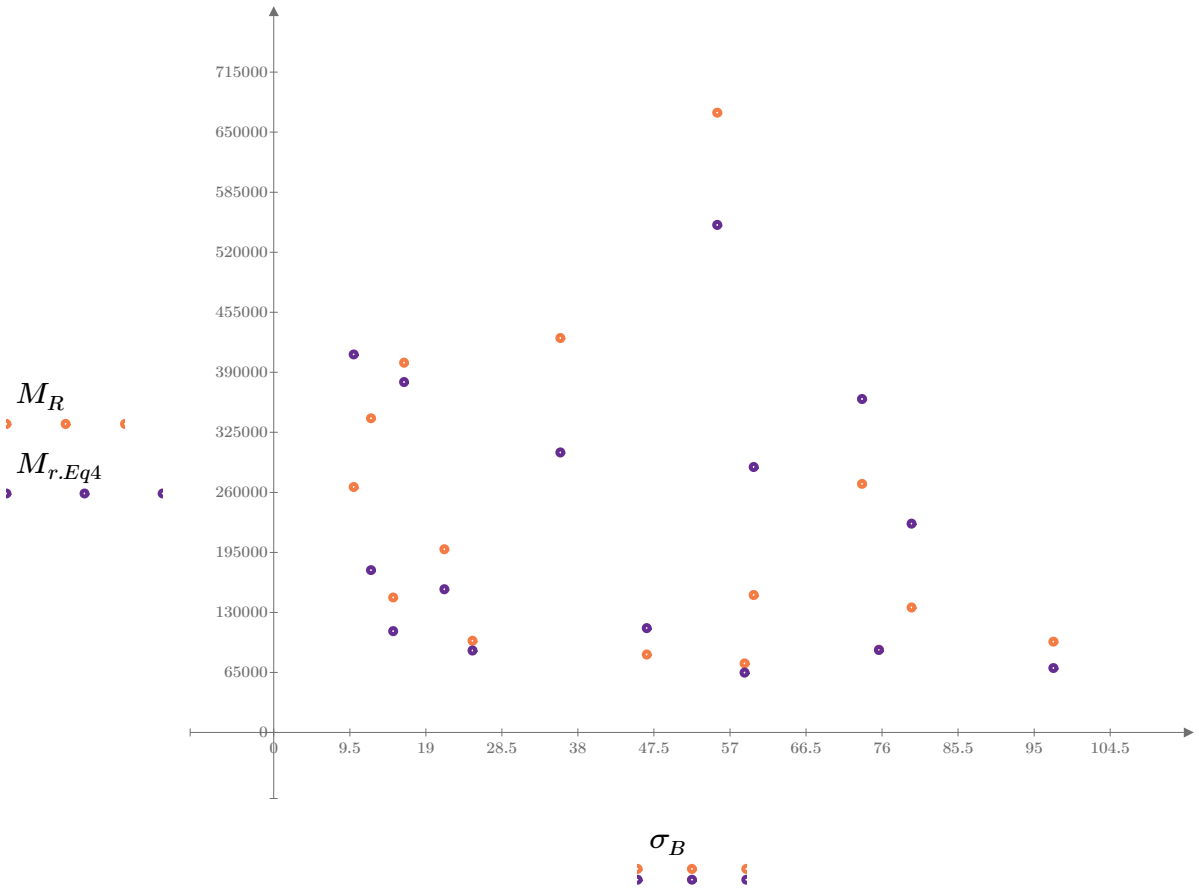

Figure 6. Plot of the test data (orange points) vs. the fitted Equation 4 model (purple points).

Dan Seely
9/12/2023

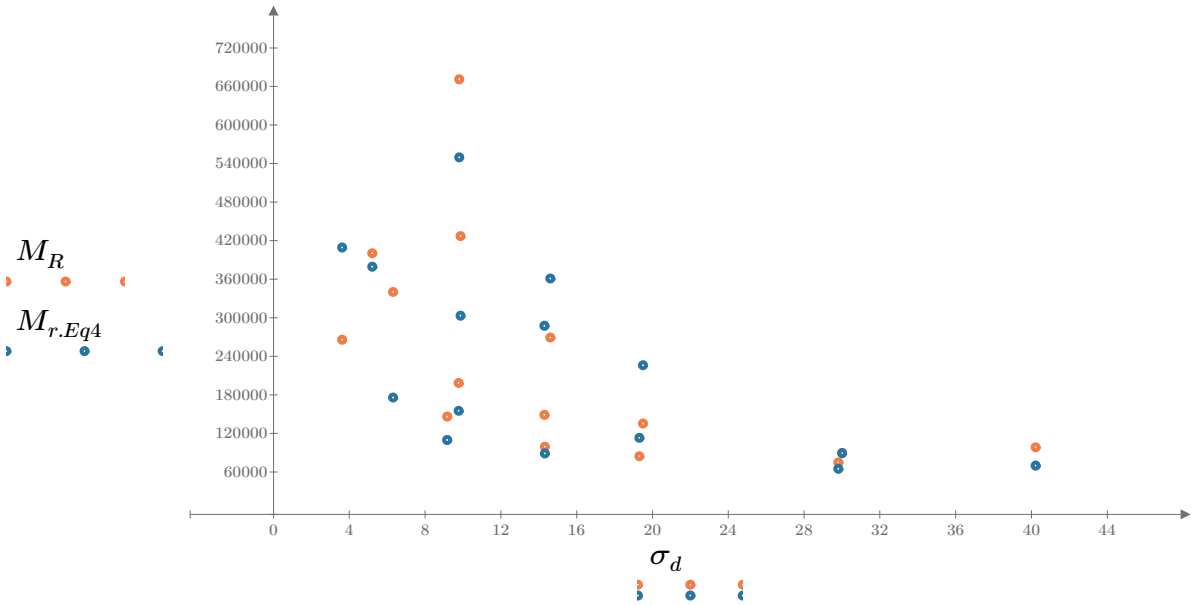

Figure 7. Plot of the test data (orange points) vs. the fitted Equation 4 model (blue points).

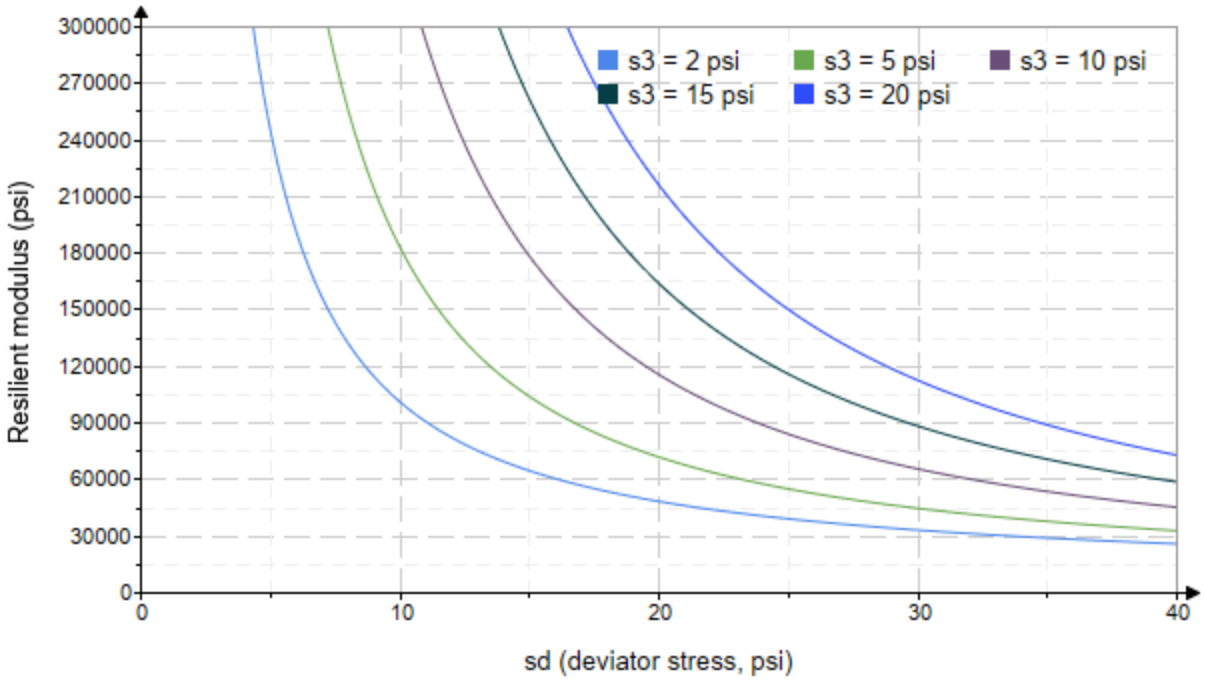

Figure 8. Plot of the fitted Equation 4 model for various confining stresses.

APPENDIX D

UNIAXIAL COMPRESSIVE STRENGTH TEST RESULTS

Uniaxial Compressive Strength of Lightweight Cellular Concrete

Sample ID:	**B1-01**
Height (in):	5.737
Height (mm):	145.7
Diameter (in):	2.984
Diameter (mm)	75.79
Area (in^2):	6.992
Area (mm^2):	4511
Mass (g):	238.89
Weight (lb):	0.5267
Weight (kN):	0.00234271
Volume (in^3):	40.11
Volume (mm^3):	657358
Density (g/mm^3):	0.0003634
Density (kg/m^3):	363.4
Unit Weight (pcf):	**22.69**
Unit Weight (kN/m^3):	3.564
Wet mass + tare (g):	547.58
Dry mass + tare (g):	500.90
Tare (g):	309.44
Water Content (%)	**24.38**
H:D ratio:	1.923
H:D correction:	0.9933

Age (days):	7
Cap:	None, surface ground
Maximum load (lb):	398.5
Maximum load (kN):	1.773
Strain Rate (%/min):	0.5
Time to Failure (min):	3.06
Strain at Failure (%):	1.452
Initial yield (psi):	54.68
Modulus (psi):	24250
ASTM C495	
Comp. Strength (MPa):	0.3930
Comp. Strength (psi):	57.00
Corr. Comp. Strength (psi):	**56.61**
ASTM D2166	
Comp. Strength (kPa):	387.6
Comp. Strength (psi):	56.22
Corr. Comp. Strength (psi):	**55.84**
Treatment:	AD

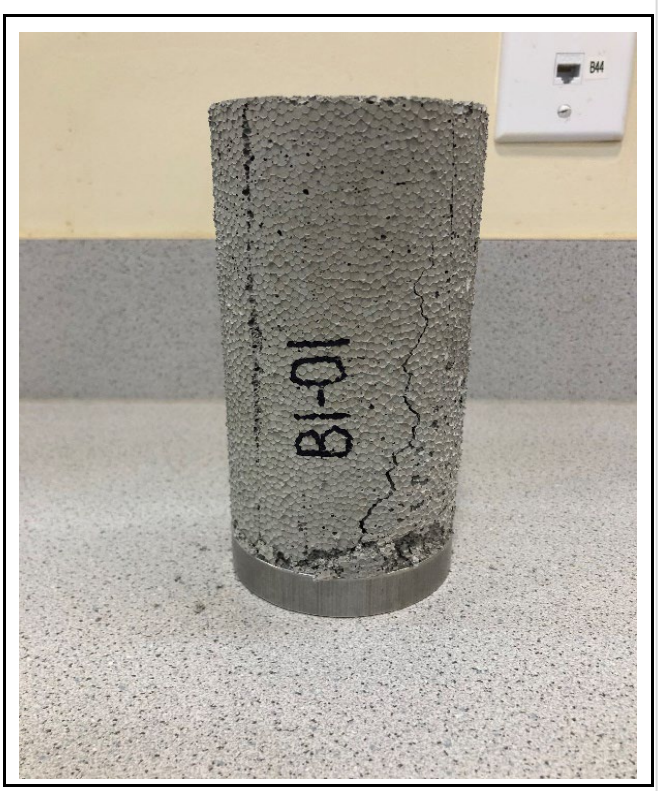

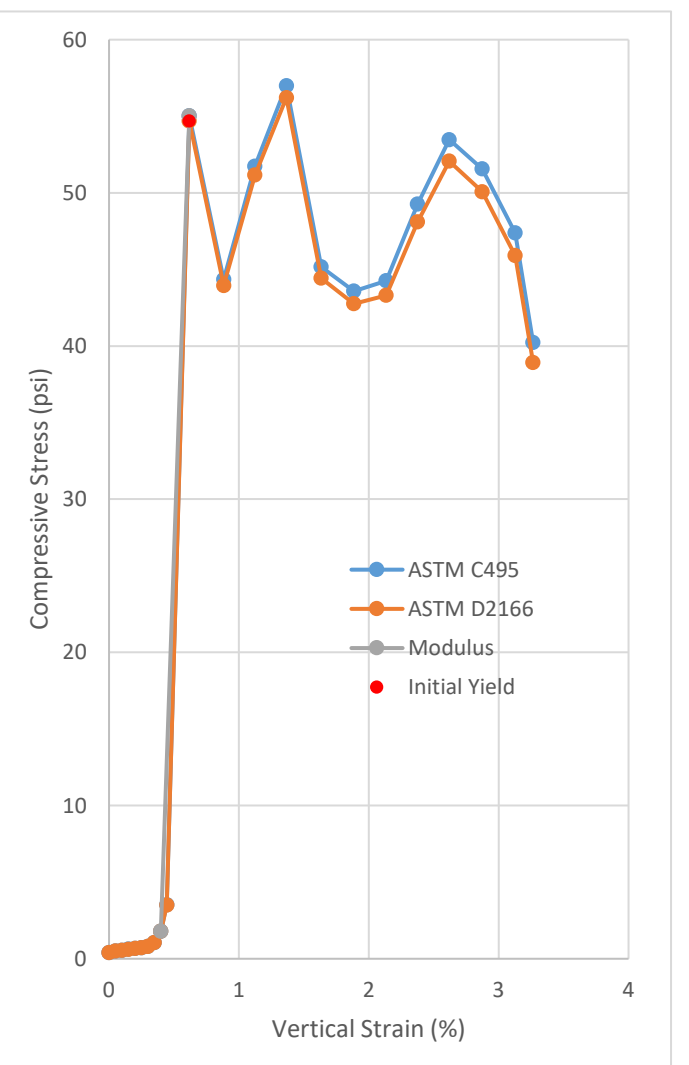

Uniaxial Compressive Strength of Lightweight Cellular Concrete

Sample ID:	**B1-02**
Height (in):	5.840
Height (mm):	148.3
Diameter (in):	2.981
Diameter (mm)	75.72
Area (in^2):	6.979
Area (mm^2):	4503
Mass (g):	241.58
Weight (lb):	0.5326
Weight (kN):	0.00236909
Volume (in^3):	40.76
Volume (mm^3):	667925
Density (g/mm^3):	0.0003617
Density (kg/m^3):	361.7
Unit Weight (pcf):	**22.58**
Unit Weight (kN/m^3):	3.547
Wet mass + tare (g):	551.36
Dry mass + tare (g):	504.02
Tare (g):	310.45
Water Content (%)	**24.46**
H:D ratio:	1.959
H:D correction:	0.9962

Age (days):	7
Cap:	None, surface ground
Maximum load (lb):	377.26
Maximum load (kN):	1.678
Strain Rate (%/min):	0.6
Time to Failure (min):	2.08
Strain at Failure (%):	1.201
Initial yield (psi):	46.29
Modulus (psi):	18010
ASTM C495	
Comp. Strength (MPa):	0.3727
Comp. Strength (psi):	54.05
Corr. Comp. Strength (psi):	**53.85**
ASTM D2166	
Comp. Strength (kPa):	368.5
Comp. Strength (psi):	53.45
Corr. Comp. Strength (psi):	**53.25**
Treatment:	AD

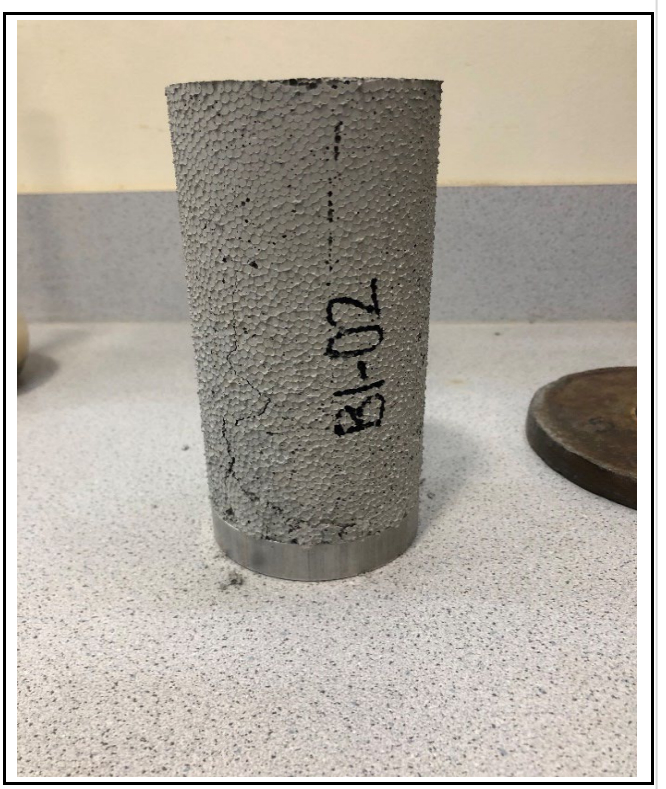

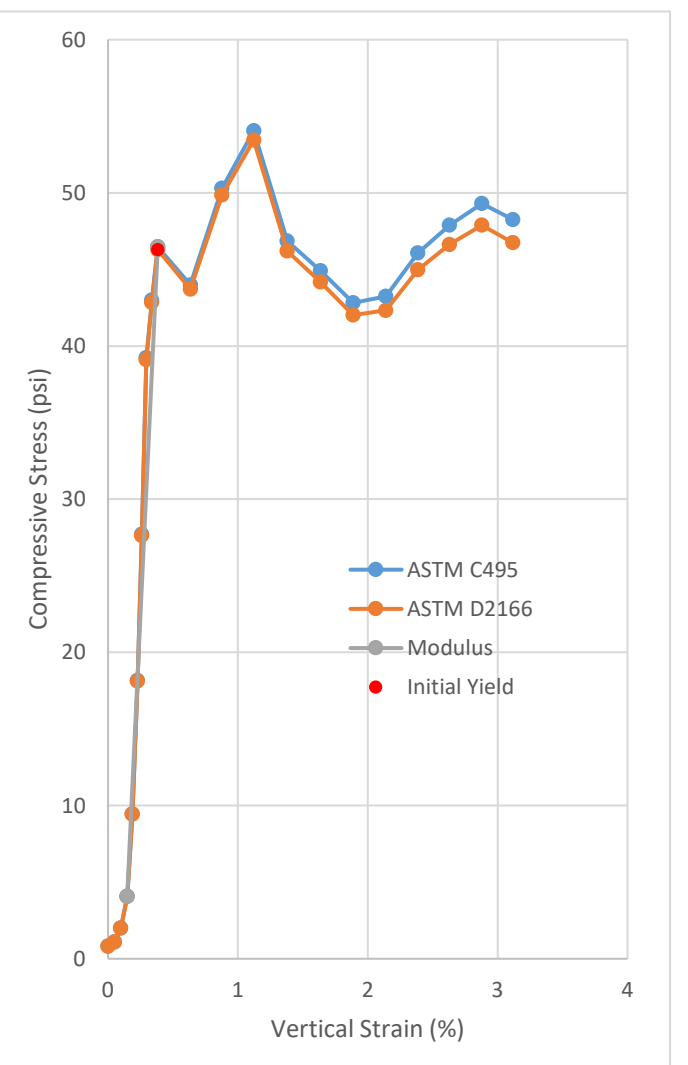

Uniaxial Compressive Strength of Lightweight Cellular Concrete

Sample ID:	**B1-03**
Height (in):	5.825
Height (mm):	148.0
Diameter (in):	2.989
Diameter (mm)	75.93
Area (in^2):	7.018
Area (mm^2):	4528
Mass (g):	240.45
Weight (lb):	0.5301
Weight (kN):	0.00235801
Volume (in^3):	40.88
Volume (mm^3):	669940
Density (g/mm^3):	0.0003589
Density (kg/m^3):	358.9
Unit Weight (pcf):	**22.41**
Unit Weight (kN/m^3):	3.520
Wet mass + tare (g):	647.95
Dry mass + tare (g):	601.18
Tare (g):	408.21
Water Content (%)	**24.24**
H:D ratio:	1.949
H:D correction:	0.9954

Age (days):	7
Cap:	None, surface ground
Maximum load (lb):	384.18
Maximum load (kN):	1.709
Strain Rate (%/min):	0.65
Time to Failure (min):	1.59
Strain at Failure (%):	0.951
Initial yield (psi):	45.18
Modulus (psi):	38764
ASTM C495	
Comp. Strength (MPa):	0.3774
Comp. Strength (psi):	54.74
Corr. Comp. Strength (psi):	**54.49**
ASTM D2166	
Comp. Strength (kPa):	374.1
Comp. Strength (psi):	54.26
Corr. Comp. Strength (psi):	**54.01**
Treatment:	AD

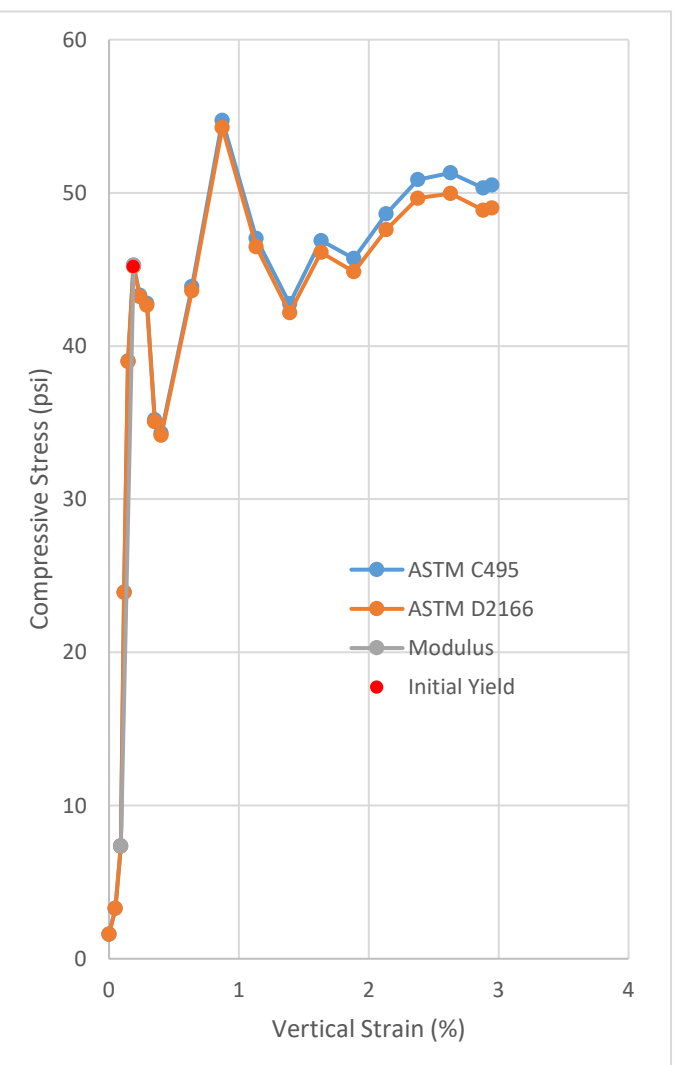

Uniaxial Compressive Strength of Lightweight Cellular Concrete

Sample ID:	**B2-01**
Height (in):	5.862
Height (mm):	148.9
Diameter (in):	2.981
Diameter (mm)	75.73
Area (in^2):	6.981
Area (mm^2):	4504
Mass (g):	246.01
Weight (lb):	0.5424
Weight (kN):	0.00241253
Volume (in^3):	40.92
Volume (mm^3):	670629
Density (g/mm^3):	0.0003668
Density (kg/m^3):	366.8
Unit Weight (pcf):	**22.90**
Unit Weight (kN/m^3):	3.597
Wet mass + tare (g):	709.72
Dry mass + tare (g):	660.96
Tare (g):	464.54
Water Content (%)	**24.82**
H:D ratio:	1.966
H:D correction:	0.9968

Age (days):	7
Cap:	None, surface ground
Maximum load (lb):	586.22
Maximum load (kN):	2.608
Strain Rate (%/min):	0.7
Time to Failure (min):	1.79
Strain at Failure (%):	1.202
Initial yield (psi):	49.43
Modulus (psi):	32132
ASTM C495	
Comp. Strength (MPa):	0.5790
Comp. Strength (psi):	83.97
Corr. Comp. Strength (psi):	**83.71**
ASTM D2166	
Comp. Strength (kPa):	572.7
Comp. Strength (psi):	83.07
Corr. Comp. Strength (psi):	**82.80**
Treatment:	AD

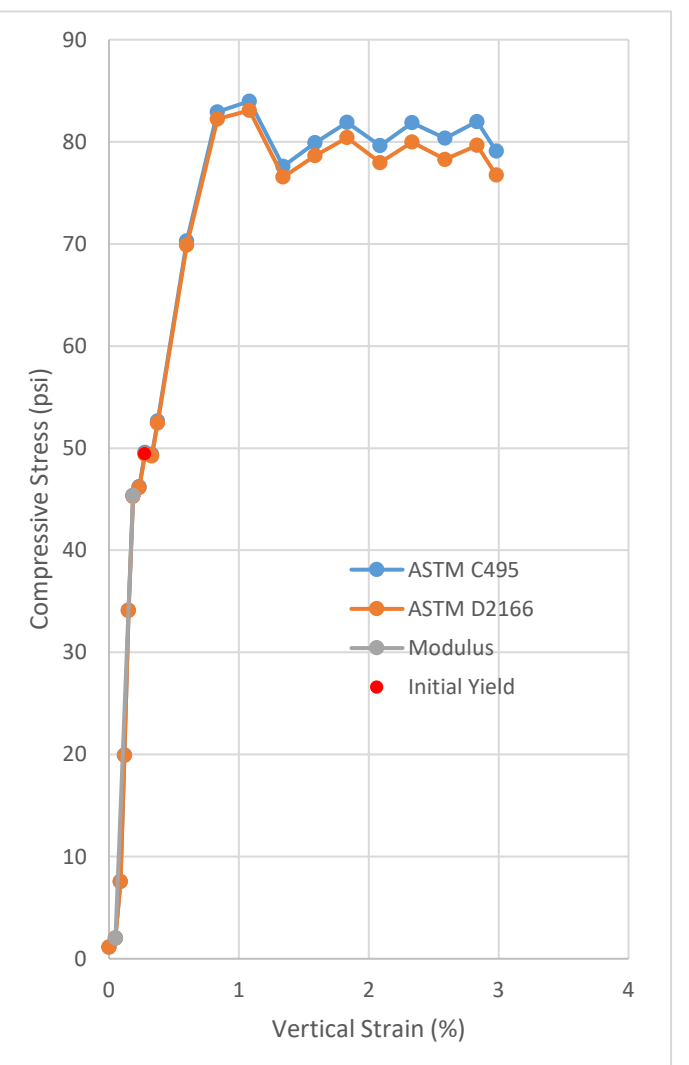

Uniaxial Compressive Strength of Lightweight Cellular Concrete

Sample ID:	**B2-02**
Height (in):	5.885
Height (mm):	149.5
Diameter (in):	2.977
Diameter (mm)	75.62
Area (in^2):	6.961
Area (mm^2):	4491
Mass (g):	248.91
Weight (lb):	0.5488
Weight (kN):	0.00244097
Volume (in^3):	40.97
Volume (mm^3):	671305
Density (g/mm^3):	0.0003708
Density (kg/m^3):	370.8
Unit Weight (pcf):	**23.15**
Unit Weight (kN/m^3):	3.636
Wet mass + tare (g):	713.05
Dry mass + tare (g):	662.20
Tare (g):	465.09
Water Content (%)	**25.80**
H:D ratio:	1.977
H:D correction:	0.9977

Age (days):	7
Cap:	None, surface ground
Maximum load (lb):	634.48
Maximum load (kN):	2.822
Strain Rate (%/min):	0.7
Time to Failure (min):	2.54
Strain at Failure (%):	1.700
Initial yield (psi):	87.80
Modulus (psi):	22953
ASTM C495	
Comp. Strength (MPa):	0.6285
Comp. Strength (psi):	91.15
Corr. Comp. Strength (psi):	**90.94**
ASTM D2166	
Comp. Strength (kPa):	618.6
Comp. Strength (psi):	89.72
Corr. Comp. Strength (psi):	**89.51**
Treatment:	AD

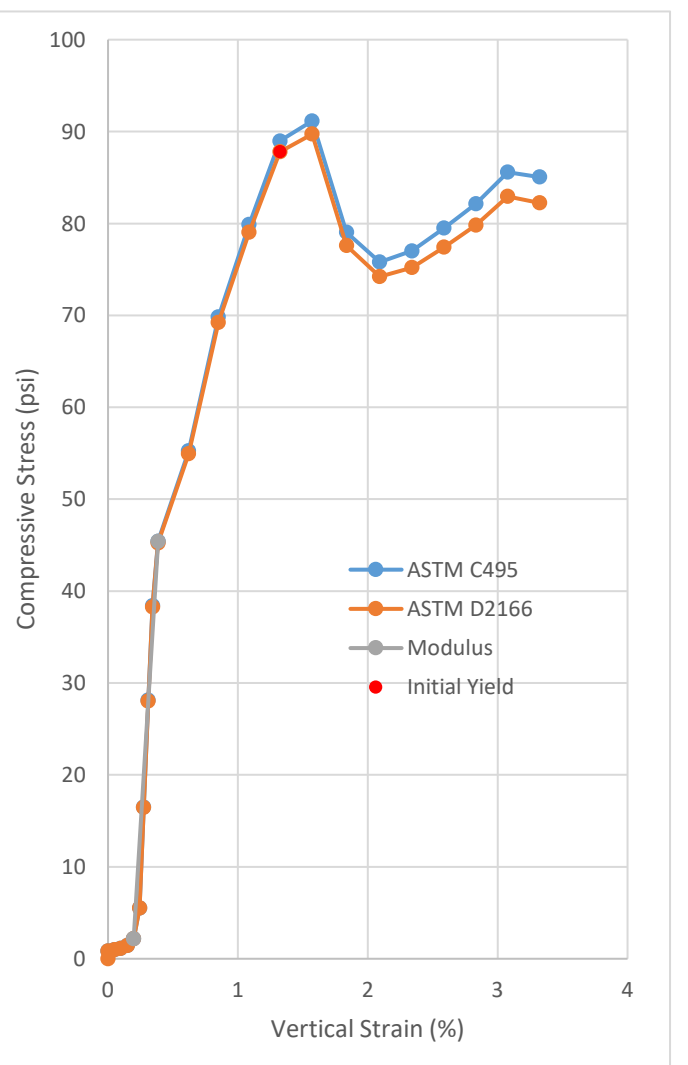

Uniaxial Compressive Strength of Lightweight Cellular Concrete

Sample ID:	**B2-03**
Height (in):	5.868
Height (mm):	149.0
Diameter (in):	2.973
Diameter (mm)	75.51
Area (in^2):	6.940
Area (mm^2):	4478
Mass (g):	249.62
Weight (lb):	0.5503
Weight (kN):	0.00244794
Volume (in^3):	40.73
Volume (mm^3):	667381
Density (g/mm^3):	0.0003740
Density (kg/m^3):	374.0
Unit Weight (pcf):	**23.35**
Unit Weight (kN/m^3):	3.668
Wet mass + tare (g):	658.40
Dry mass + tare (g):	607.63
Tare (g):	409.76
Water Content (%)	**25.66**
H:D ratio:	1.974
H:D correction:	0.9975

Age (days):	7
Cap:	None, surface ground
Maximum load (lb):	593.95
Maximum load (kN):	2.642
Strain Rate (%/min):	0.7
Time to Failure (min):	2.92
Strain at Failure (%):	1.949
Initial yield (psi):	47.95
Modulus (psi):	31377
ASTM C495	
Comp. Strength (MPa):	0.5900
Comp. Strength (psi):	85.58
Corr. Comp. Strength (psi):	**85.36**
ASTM D2166	
Comp. Strength (kPa):	579.3
Comp. Strength (psi):	84.01
Corr. Comp. Strength (psi):	**83.80**
Treatment:	AD

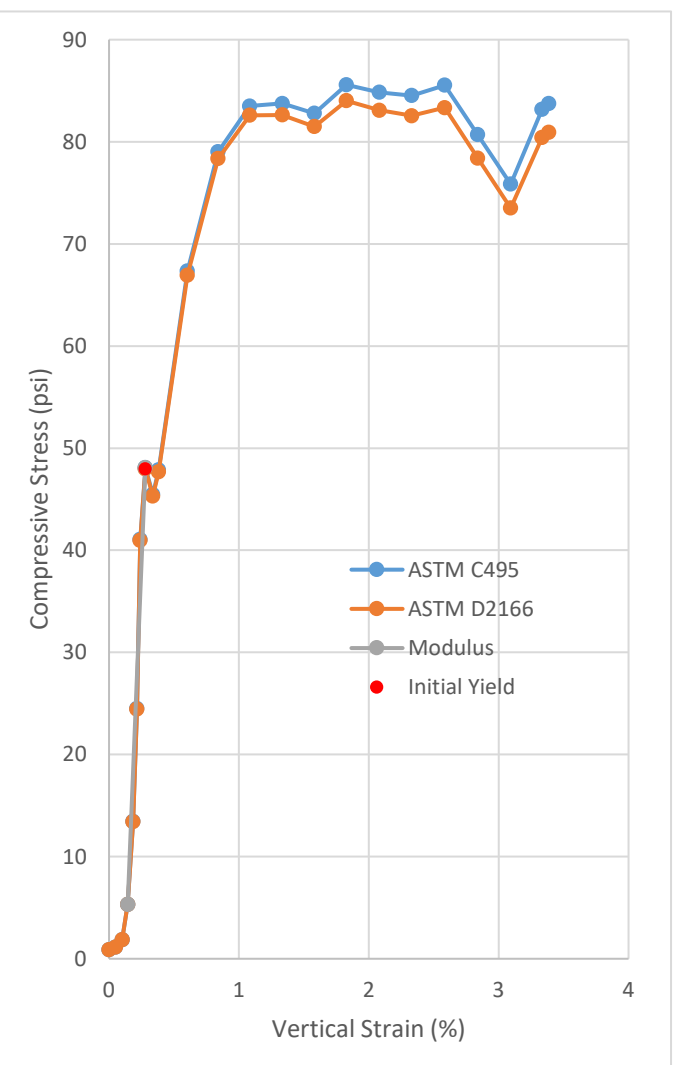

Uniaxial Compressive Strength of Lightweight Cellular Concrete

Sample ID:	**B3-01**
Height (in):	5.876
Height (mm):	149.3
Diameter (in):	2.975
Diameter (mm)	75.57
Area (in^2):	6.953
Area (mm^2):	4486
Mass (g):	255.91
Weight (lb):	0.5642
Weight (kN):	0.00250962
Volume (in^3):	40.86
Volume (mm^3):	669528
Density (g/mm^3):	0.0003822
Density (kg/m^3):	382.2
Unit Weight (pcf):	**23.86**
Unit Weight (kN/m^3):	3.748
Wet mass + tare (g):	565.37
Dry mass + tare (g):	514.72
Tare (g):	310.50
Water Content (%)	**24.80**
H:D ratio:	1.975
H:D correction:	0.9975

Age (days):	7
Cap:	None, surface ground
Maximum load (lb):	700.69
Maximum load (kN):	3.117
Strain Rate (%/min):	0.75
Time to Failure (min):	1.71
Strain at Failure (%):	1.199
Initial yield (psi):	99.71
Modulus (psi):	38912
ASTM C495	
Comp. Strength (MPa):	0.6948
Comp. Strength (psi):	100.78
Corr. Comp. Strength (psi):	**100.53**
ASTM D2166	
Comp. Strength (kPa):	687.5
Comp. Strength (psi):	99.71
Corr. Comp. Strength (psi):	**99.47**
Treatment:	AD

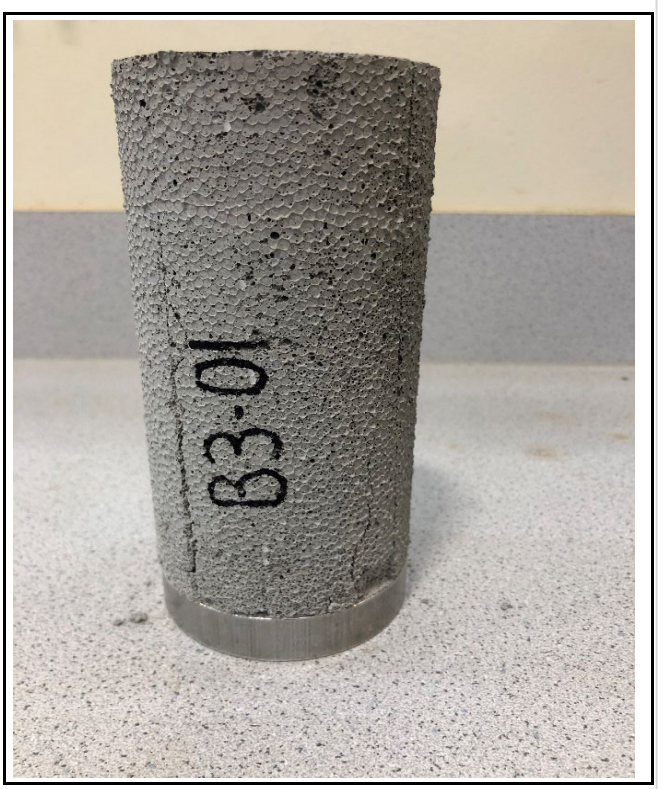

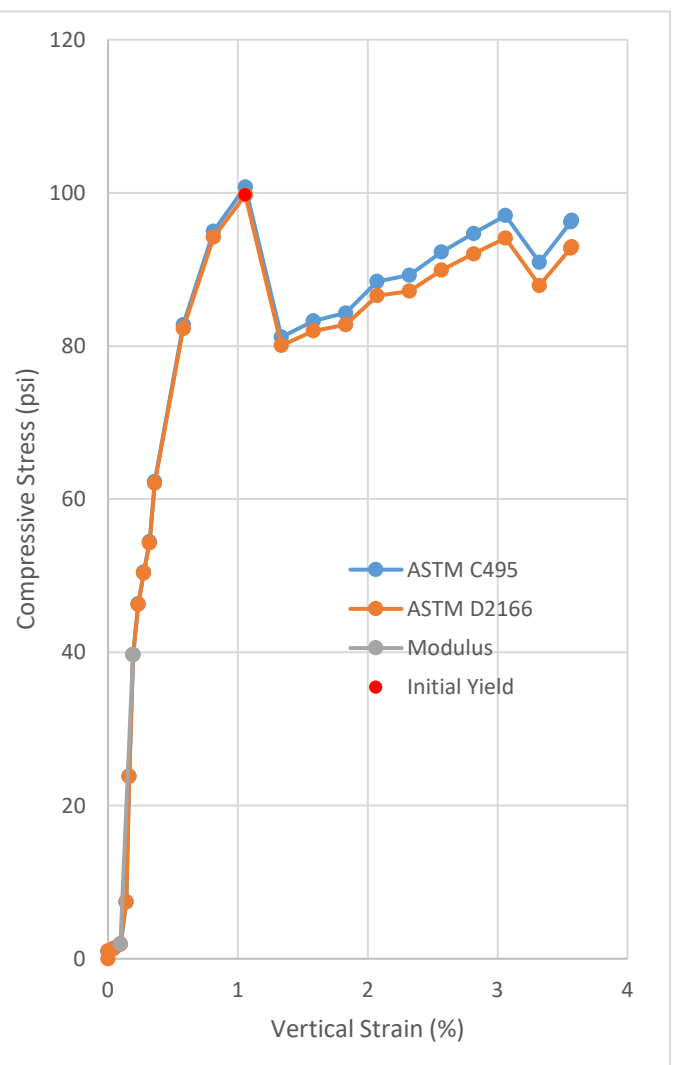

Uniaxial Compressive Strength of Lightweight Cellular Concrete

Sample ID:	**B3-02**
Height (in):	5.888
Height (mm):	149.6
Diameter (in):	2.988
Diameter (mm)	75.90
Area (in^2):	7.012
Area (mm^2):	4524
Mass (g):	256.24
Weight (lb):	0.5649
Weight (kN):	0.00251286
Volume (in^3):	41.29
Volume (mm^3):	676581
Density (g/mm^3):	0.0003787
Density (kg/m^3):	378.7
Unit Weight (pcf):	**23.64**
Unit Weight (kN/m^3):	3.714
Wet mass + tare (g):	565.47
Dry mass + tare (g):	513.23
Tare (g):	310.34
Water Content (%)	**25.75**
H:D ratio:	1.971
H:D correction:	0.9972

Age (days):	7
Cap:	None, surface ground
Maximum load (lb):	649.94
Maximum load (kN):	2.891
Strain Rate (%/min):	0.75
Time to Failure (min):	4.36
Strain at Failure (%):	3.200
Initial yield (psi):	89.22
Modulus (psi):	28495
ASTM C495	
Comp. Strength (MPa):	0.6391
Comp. Strength (psi):	92.69
Corr. Comp. Strength (psi):	**92.43**
ASTM D2166	
Comp. Strength (kPa):	619.4
Comp. Strength (psi):	89.84
Corr. Comp. Strength (psi):	**89.59**
Treatment:	AD

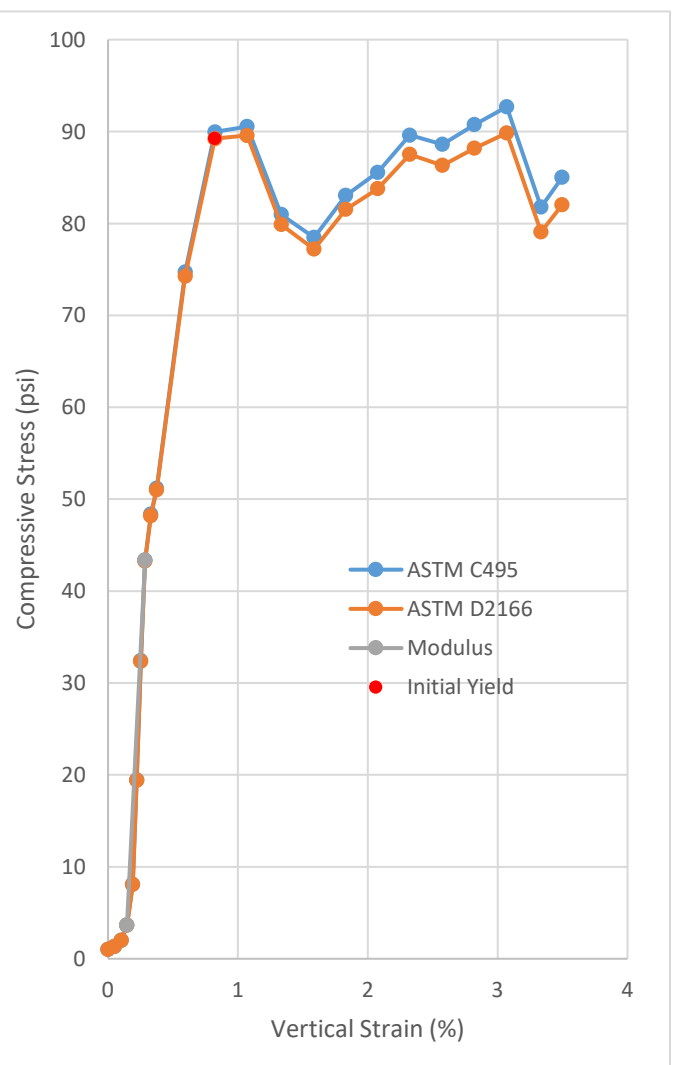

Uniaxial Compressive Strength of Lightweight Cellular Concrete

Sample ID:	**B3-03**
Height (in):	5.868
Height (mm):	149.1
Diameter (in):	2.982
Diameter (mm)	75.75
Area (in^2):	6.986
Area (mm^2):	4507
Mass (g):	258.84
Weight (lb):	0.5706
Weight (kN):	0.00253835
Volume (in^3):	40.99
Volume (mm^3):	671766
Density (g/mm^3):	0.0003853
Density (kg/m^3):	385.3
Unit Weight (pcf):	**24.05**
Unit Weight (kN/m^3):	3.779
Wet mass + tare (g):	570.37
Dry mass + tare (g):	515.84
Tare (g):	312.84
Water Content (%)	**26.86**
H:D ratio:	1.968
H:D correction:	0.9969

Age (days):	7
Cap:	None, surface ground
Maximum load (lb):	783.61
Maximum load (kN):	3.486
Strain Rate (%/min):	0.75
Time to Failure (min):	4.36
Strain at Failure (%):	3.198
Initial yield (psi):	105.98
Modulus (psi):	42653
ASTM C495	
Comp. Strength (MPa):	0.7734
Comp. Strength (psi):	112.18
Corr. Comp. Strength (psi):	**111.83**
ASTM D2166	
Comp. Strength (kPa):	751.2
Comp. Strength (psi):	108.95
Corr. Comp. Strength (psi):	**108.61**
Treatment:	AD

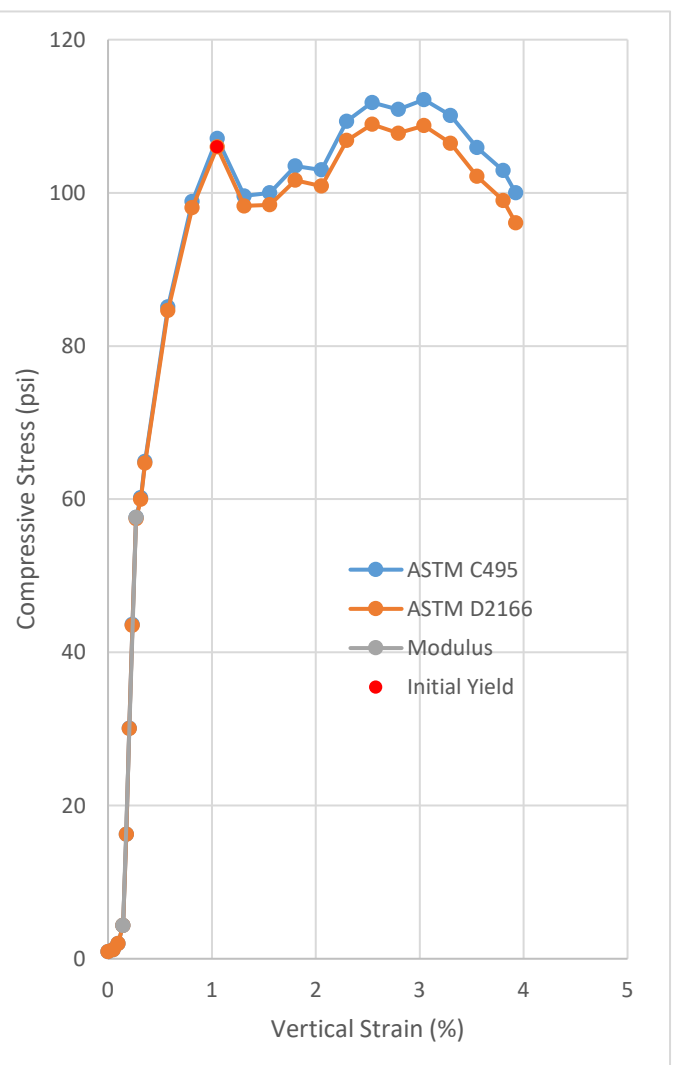

Uniaxial Compressive Strength of Lightweight Cellular Concrete

Sample ID:	**B1-04**
Height (in):	5.653
Height (mm):	143.6
Diameter (in):	2.983
Diameter (mm)	75.76
Area (in^2):	6.987
Area (mm^2):	4508
Mass (g):	237.58
Weight (lb):	0.5238
Weight (kN):	0.00232986
Volume (in^3):	39.50
Volume (mm^3):	647299
Density (g/mm^3):	0.0003670
Density (kg/m^3):	367.0
Unit Weight (pcf):	**22.91**
Unit Weight (kN/m^3):	3.599
Wet mass + tare (g):	547.86
Dry mass + tare (g):	501.89
Tare (g):	310.55
Water Content (%)	**24.03**
H:D ratio:	1.895
H:D correction:	0.9911

Age (days):	14
Cap:	None, surface ground
Maximum load (lb):	440.48
Maximum load (kN):	1.959
Strain Rate (%/min):	1
Time to Failure (min):	1.52
Strain at Failure (%):	1.456
Initial yield (psi):	61.46
Modulus (psi):	13964
ASTM C495	
Comp. Strength (MPa):	0.4347
Comp. Strength (psi):	63.04
Corr. Comp. Strength (psi):	**62.48**
ASTM D2166	
Comp. Strength (kPa):	428.7
Comp. Strength (psi):	62.18
Corr. Comp. Strength (psi):	**61.63**
Treatment:	AD

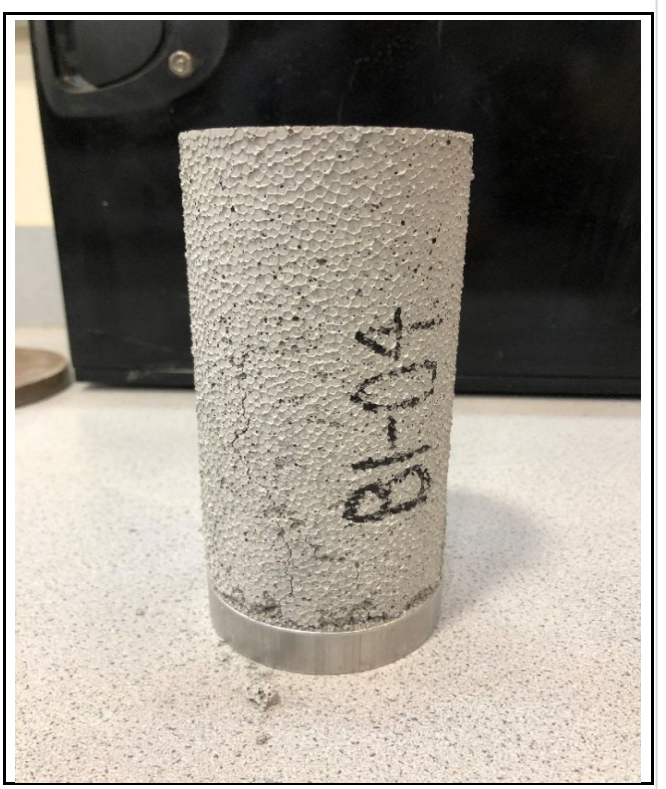

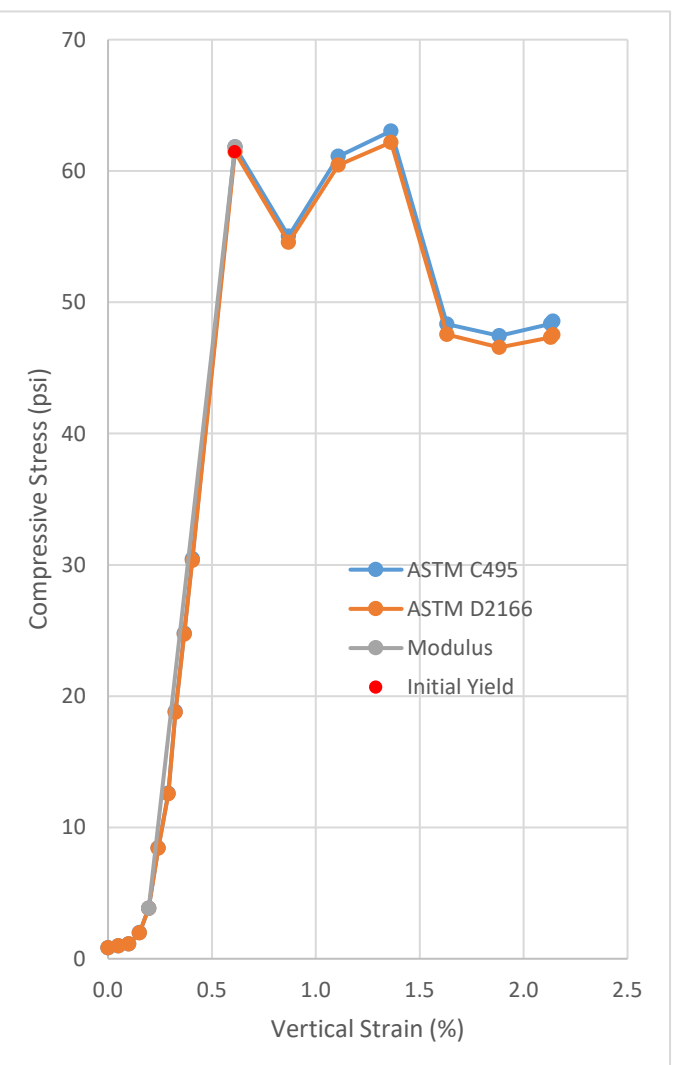

Uniaxial Compressive Strength of Lightweight Cellular Concrete

Sample ID:	**B1-05**
Height (in):	5.754
Height (mm):	146.1
Diameter (in):	2.979
Diameter (mm)	75.68
Area (in^2):	6.972
Area (mm^2):	4498
Mass (g):	248.61
Weight (lb):	0.5481
Weight (kN):	0.00243803
Volume (in^3):	40.11
Volume (mm^3):	657316
Density (g/mm^3):	0.0003782
Density (kg/m^3):	378.2
Unit Weight (pcf):	**23.61**
Unit Weight (kN/m^3):	3.709
Wet mass + tare (g):	641.28
Dry mass + tare (g):	588.55
Tare (g):	393.01
Water Content (%)	**26.97**
H:D ratio:	1.931
H:D correction:	0.9940

Age (days):	14
Cap:	None, surface ground
Maximum load (lb):	633.35
Maximum load (kN):	2.817
Strain Rate (%/min):	1
Time to Failure (min):	0.53
Strain at Failure (%):	0.449
Initial yield (psi):	90.56
Modulus (psi):	47026
ASTM C495	
Comp. Strength (MPa):	0.6264
Comp. Strength (psi):	90.85
Corr. Comp. Strength (psi):	**90.30**
ASTM D2166	
Comp. Strength (kPa):	624.4
Comp. Strength (psi):	90.56
Corr. Comp. Strength (psi):	**90.01**
Treatment:	AD

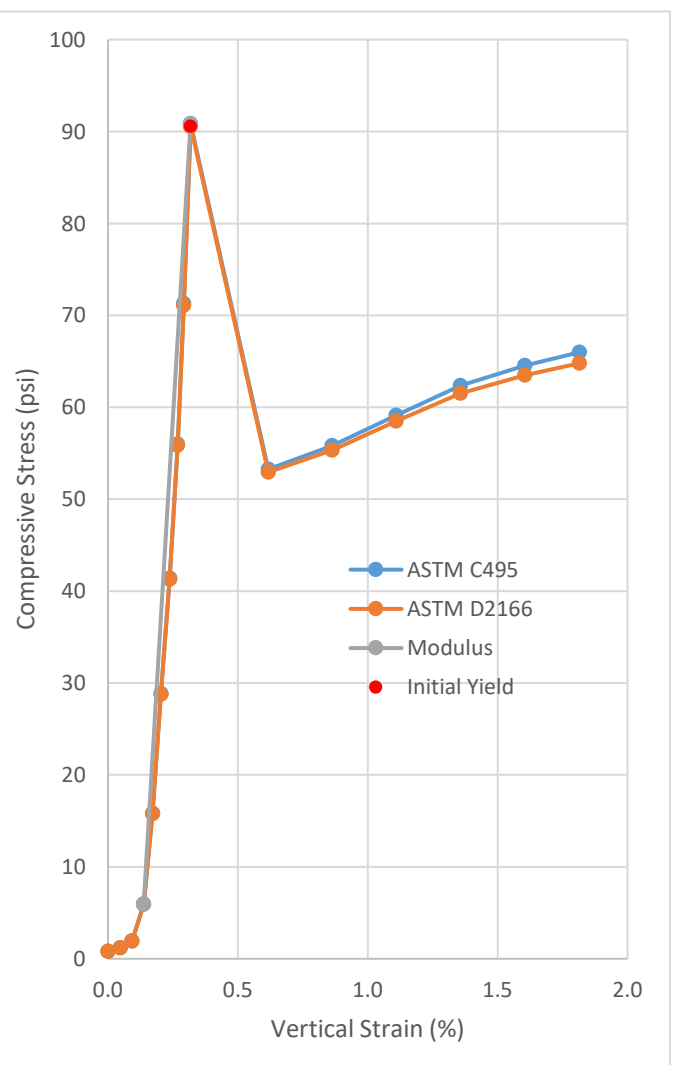

Uniaxial Compressive Strength of Lightweight Cellular Concrete

Sample ID:	**B1-06**
Height (in):	5.650
Height (mm):	143.5
Diameter (in):	2.963
Diameter (mm)	75.27
Area (in^2):	6.897
Area (mm^2):	4450
Mass (g):	238.47
Weight (lb):	0.5257
Weight (kN):	0.00233859
Volume (in^3):	38.97
Volume (mm^3):	638596
Density (g/mm^3):	0.0003734
Density (kg/m^3):	373.4
Unit Weight (pcf):	**23.31**
Unit Weight (kN/m^3):	3.662
Wet mass + tare (g):	629.13
Dry mass + tare (g):	580.69
Tare (g):	391.05
Water Content (%)	**25.54**
H:D ratio:	1.907
H:D correction:	0.9920

Age (days):	14
Cap:	None, surface ground
Maximum load (lb):	696.11
Maximum load (kN):	3.096
Strain Rate (%/min):	1
Time to Failure (min):	0.68
Strain at Failure (%):	0.602
Initial yield (psi):	100.47
Modulus (psi):	40821
ASTM C495	
Comp. Strength (MPa):	0.6959
Comp. Strength (psi):	100.93
Corr. Comp. Strength (psi):	**100.12**
ASTM D2166	
Comp. Strength (kPa):	692.7
Comp. Strength (psi):	100.47
Corr. Comp. Strength (psi):	**99.67**
Treatment:	AD

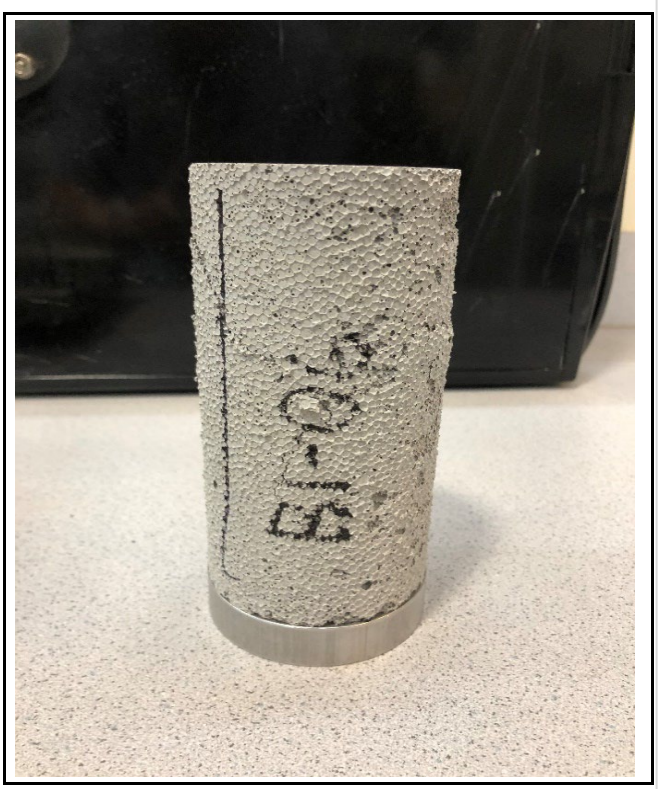

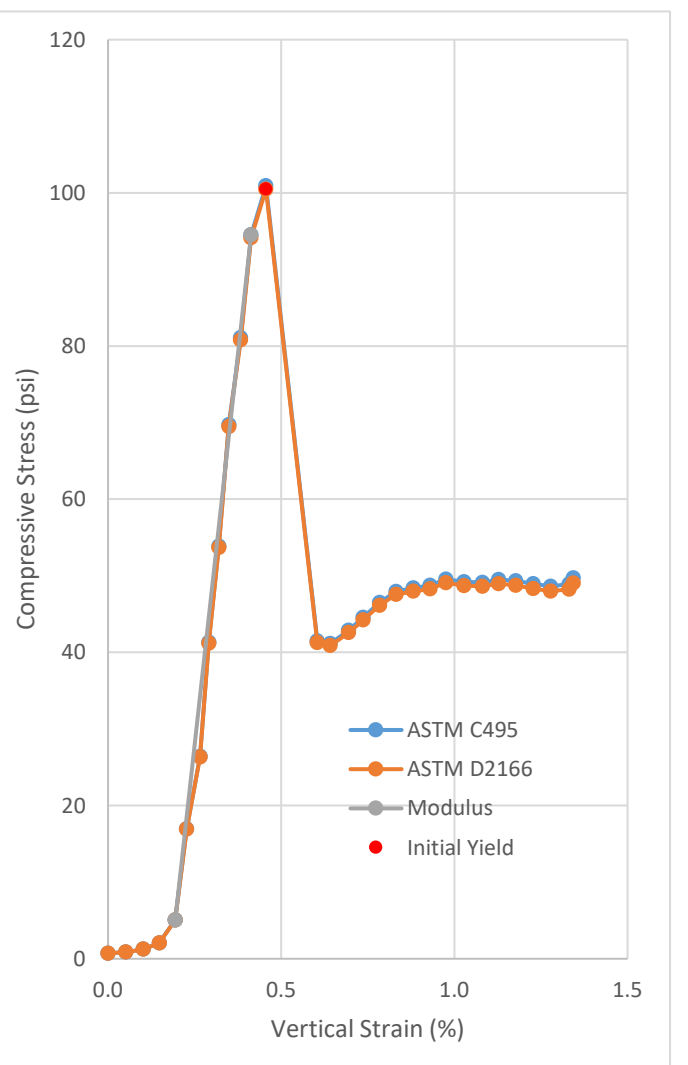

Uniaxial Compressive Strength of Lightweight Cellular Concrete

Sample ID:	**B2-04**
Height (in):	5.739
Height (mm):	145.8
Diameter (in):	2.967
Diameter (mm)	75.36
Area (in^2):	6.914
Area (mm^2):	4461
Mass (g):	253.45
Weight (lb):	0.5588
Weight (kN):	0.0024855
Volume (in^3):	39.68
Volume (mm^3):	650185
Density (g/mm^3):	0.0003898
Density (kg/m^3):	389.8
Unit Weight (pcf):	**24.34**
Unit Weight (kN/m^3):	3.823
Wet mass + tare (g):	563.42
Dry mass + tare (g):	510.08
Tare (g):	310.44
Water Content (%)	**26.72**
H:D ratio:	1.934
H:D correction:	0.9942

Age (days):	14
Cap:	None, surface ground
Maximum load (lb):	682.42
Maximum load (kN):	3.036
Strain Rate (%/min):	1
Time to Failure (min):	0.57
Strain at Failure (%):	0.500
Initial yield (psi):	98.35
Modulus (psi):	48236
ASTM C495	
Comp. Strength (MPa):	0.6805
Comp. Strength (psi):	98.70
Corr. Comp. Strength (psi):	**98.13**
ASTM D2166	
Comp. Strength (kPa):	678.1
Comp. Strength (psi):	98.35
Corr. Comp. Strength (psi):	**97.78**
Treatment:	AD

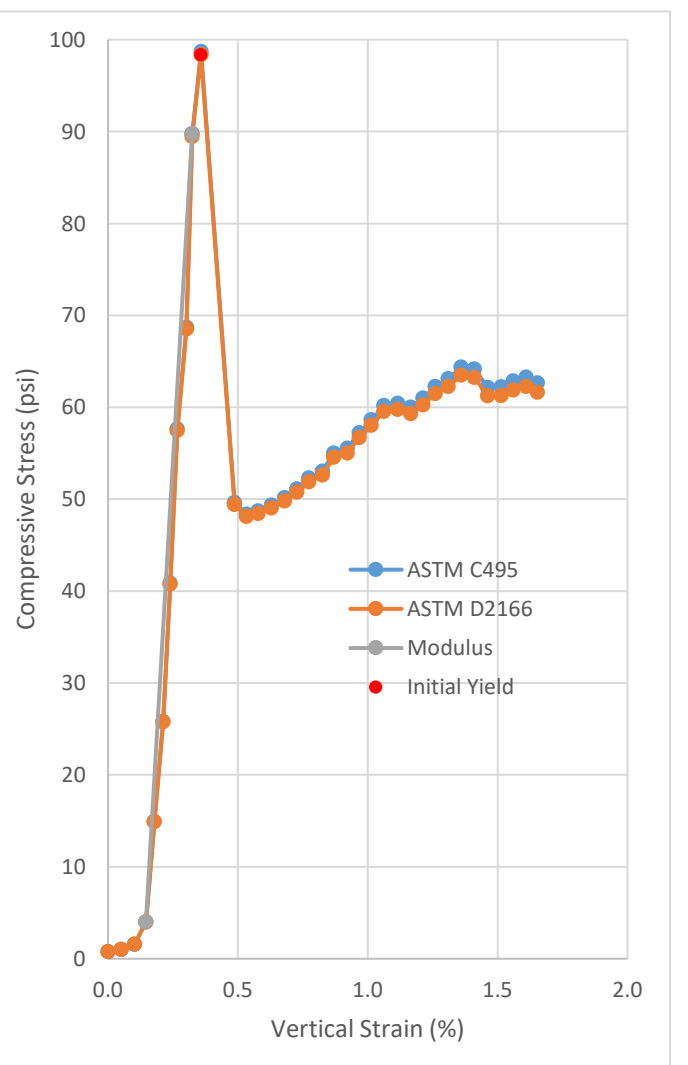

Uniaxial Compressive Strength of Lightweight Cellular Concrete

Sample ID:	**B2-05**
Height (in):	5.736
Height (mm):	145.7
Diameter (in):	2.983
Diameter (mm)	75.76
Area (in^2):	6.987
Area (mm^2):	4508
Mass (g):	247.3
Weight (lb):	0.5452
Weight (kN):	0.00242518
Volume (in^3):	40.08
Volume (mm^3):	656803
Density (g/mm^3):	0.0003765
Density (kg/m^3):	376.5
Unit Weight (pcf):	**23.51**
Unit Weight (kN/m^3):	3.692
Wet mass + tare (g):	571.98
Dry mass + tare (g):	519.85
Tare (g):	324.17
Water Content (%)	**26.64**
H:D ratio:	1.923
H:D correction:	0.9933

Age (days):	14
Cap:	None, surface ground
Maximum load (lb):	915.95
Maximum load (kN):	4.074
Strain Rate (%/min):	1
Time to Failure (min):	0.69
Strain at Failure (%):	0.600
Initial yield (psi):	130.55
Modulus (psi):	54629
ASTM C495	
Comp. Strength (MPa):	0.9038
Comp. Strength (psi):	131.09
Corr. Comp. Strength (psi):	**130.22**
ASTM D2166	
Comp. Strength (kPa):	900.1
Comp. Strength (psi):	130.55
Corr. Comp. Strength (psi):	**129.68**
Treatment:	AD

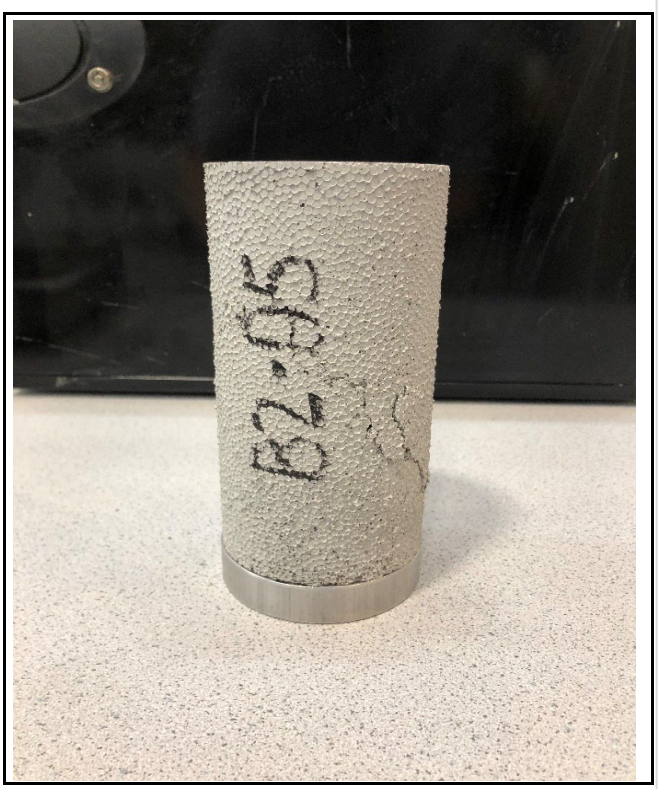

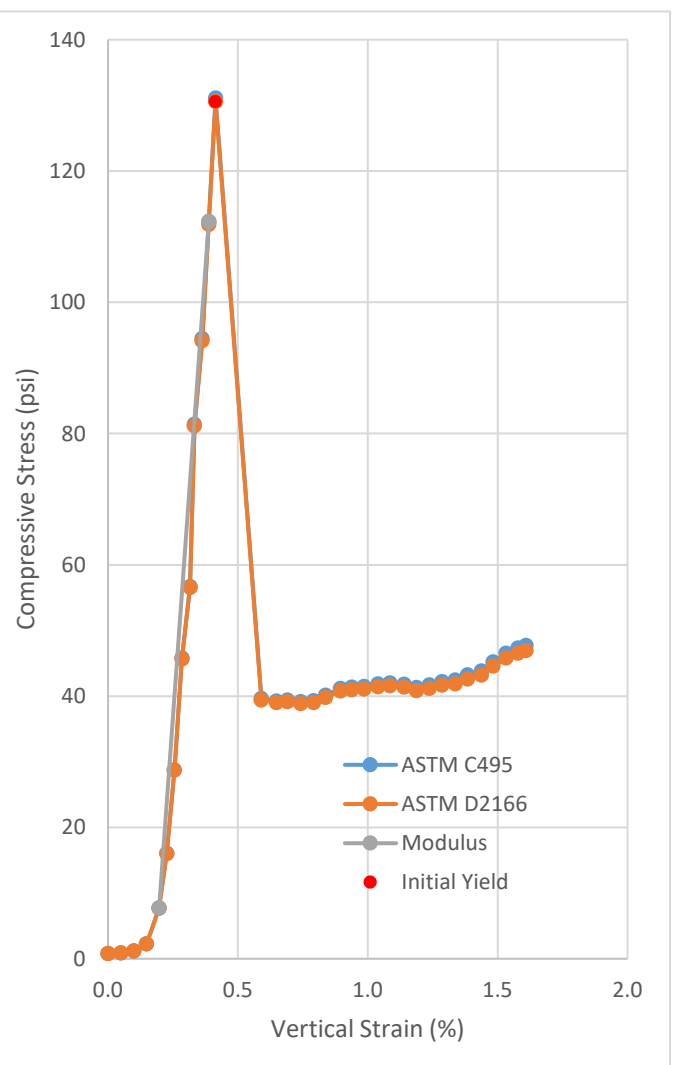

Uniaxial Compressive Strength of Lightweight Cellular Concrete

Sample ID:	**B2-06**
Height (in):	5.721
Height (mm):	145.3
Diameter (in):	2.983
Diameter (mm)	75.77
Area (in^2):	6.989
Area (mm^2):	4509
Mass (g):	246.47
Weight (lb):	0.5434
Weight (kN):	0.00241705
Volume (in^3):	39.98
Volume (mm^3):	655155
Density (g/mm^3):	0.0003762
Density (kg/m^3):	376.2
Unit Weight (pcf):	**23.49**
Unit Weight (kN/m^3):	3.689
Wet mass + tare (g):	556.38
Dry mass + tare (g):	506.58
Tare (g):	310.48
Water Content (%)	**25.40**
H:D ratio:	1.918
H:D correction:	0.9929

Age (days):	14
Cap:	None, surface ground
Maximum load (lb):	727.03
Maximum load (kN):	3.234
Strain Rate (%/min):	1
Time to Failure (min):	0.64
Strain at Failure (%):	0.554
Initial yield (psi):	103.61
Modulus (psi):	50896
ASTM C495	
Comp. Strength (MPa):	0.7173
Comp. Strength (psi):	104.03
Corr. Comp. Strength (psi):	**103.29**
ASTM D2166	
Comp. Strength (kPa):	714.4
Comp. Strength (psi):	103.61
Corr. Comp. Strength (psi):	**102.87**
Treatment:	AD

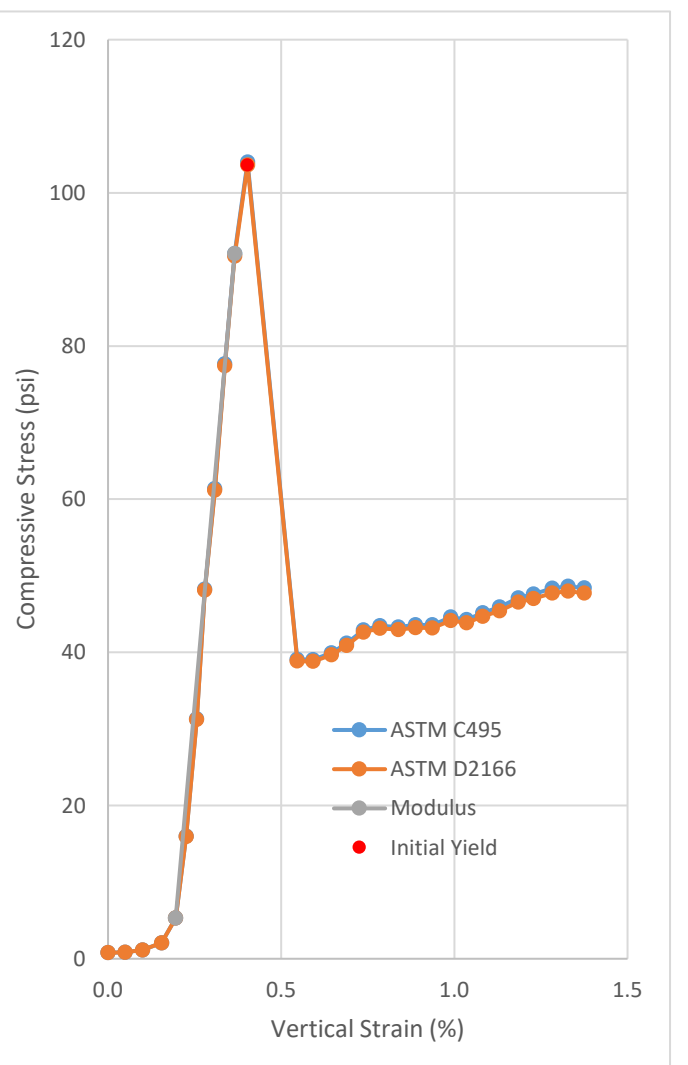

Uniaxial Compressive Strength of Lightweight Cellular Concrete

Sample ID:	**B3-04**
Height (in):	5.733
Height (mm):	145.6
Diameter (in):	2.985
Diameter (mm)	75.82
Area (in^2):	6.998
Area (mm^2):	4515
Mass (g):	255.87
Weight (lb):	0.5641
Weight (kN):	0.00250923
Volume (in^3):	40.12
Volume (mm^3):	657410
Density (g/mm^3):	0.0003892
Density (kg/m^3):	389.2
Unit Weight (pcf):	**24.30**
Unit Weight (kN/m^3):	3.817
Wet mass + tare (g):	583.06
Dry mass + tare (g):	528.46
Tare (g):	327.85
Water Content (%)	**27.22**
H:D ratio:	1.920
H:D correction:	0.9931

Age (days):	14
Cap:	None, surface ground
Maximum load (lb):	992
Maximum load (kN):	4.413
Strain Rate (%/min):	1
Time to Failure (min):	0.66
Strain at Failure (%):	0.550
Initial yield (psi):	141.26
Modulus (psi):	62923
ASTM C495	
Comp. Strength (MPa):	0.9774
Comp. Strength (psi):	141.75
Corr. Comp. Strength (psi):	**140.78**
ASTM D2166	
Comp. Strength (kPa):	973.9
Comp. Strength (psi):	141.26
Corr. Comp. Strength (psi):	**140.28**
Treatment:	AD

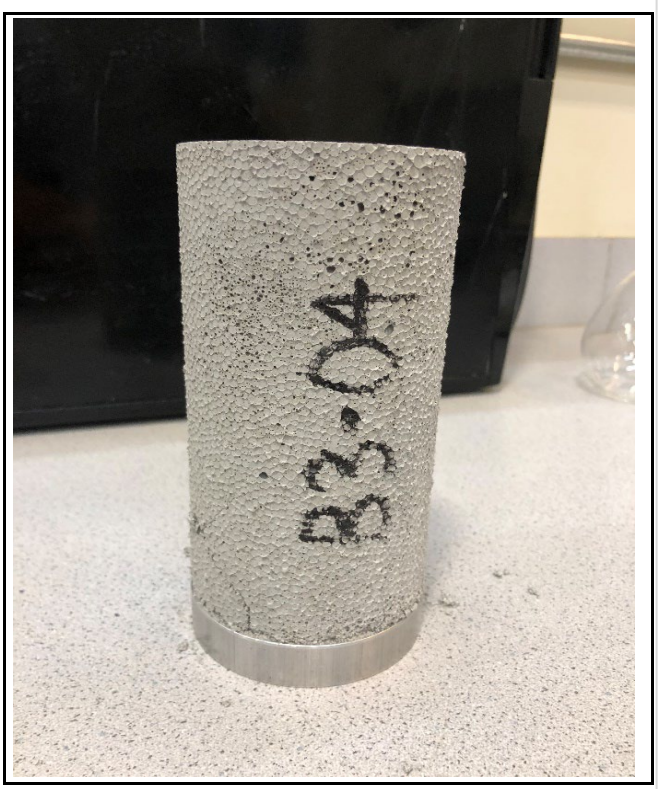

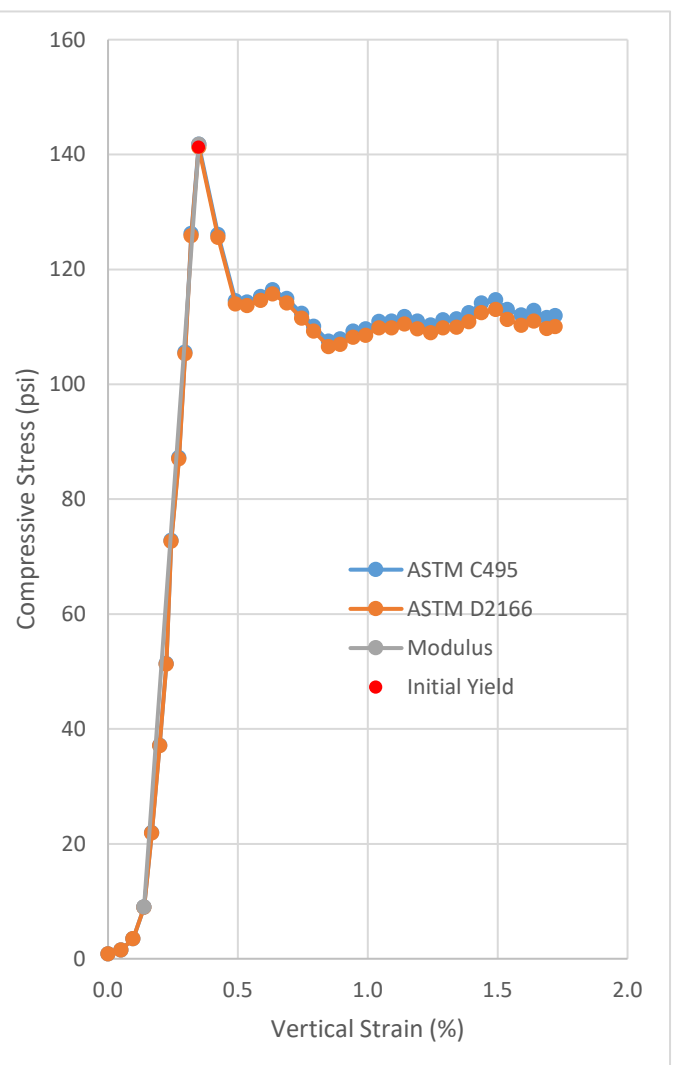

Uniaxial Compressive Strength of Lightweight Cellular Concrete

Sample ID:	**B3-05**
Height (in):	5.754
Height (mm):	146.2
Diameter (in):	2.974
Diameter (mm)	75.55
Area (in^2):	6.948
Area (mm^2):	4483
Mass (g):	254.97
Weight (lb):	0.5621
Weight (kN):	0.0025004
Volume (in^3):	39.98
Volume (mm^3):	655187
Density (g/mm^3):	0.0003892
Density (kg/m^3):	389.2
Unit Weight (pcf):	**24.29**
Unit Weight (kN/m^3):	3.816
Wet mass + tare (g):	720.11
Dry mass + tare (g):	666.01
Tare (g):	465.83
Water Content (%)	**27.03**
H:D ratio:	1.935
H:D correction:	0.9943

Age (days):	14
Cap:	None, surface ground
Maximum load (lb):	1070.4
Maximum load (kN):	4.761
Strain Rate (%/min):	1
Time to Failure (min):	0.66
Strain at Failure (%):	0.550
Initial yield (psi):	153.54
Modulus (psi):	73586
ASTM C495	
Comp. Strength (MPa):	1.0622
Comp. Strength (psi):	154.06
Corr. Comp. Strength (psi):	**153.17**
ASTM D2166	
Comp. Strength (kPa):	1058.6
Comp. Strength (psi):	153.54
Corr. Comp. Strength (psi):	**152.65**
Treatment:	AD

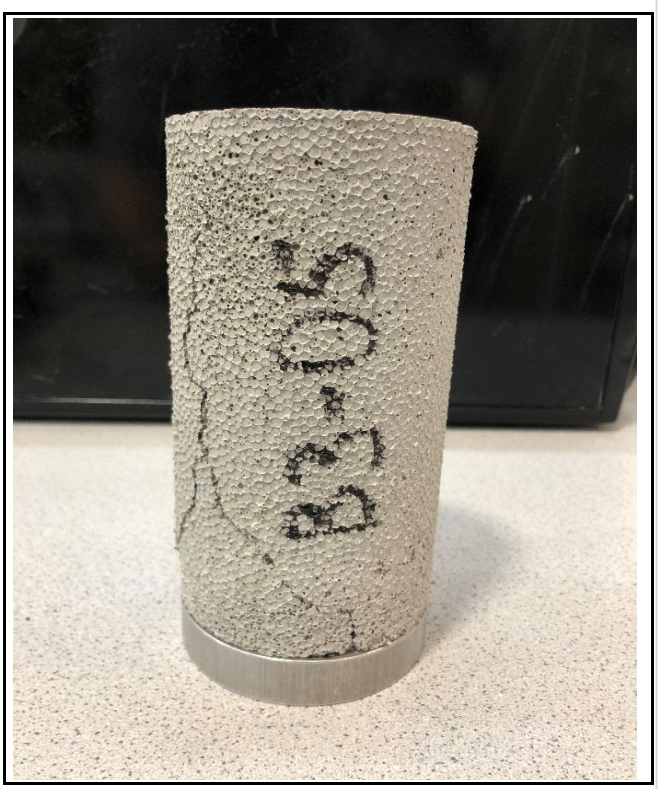

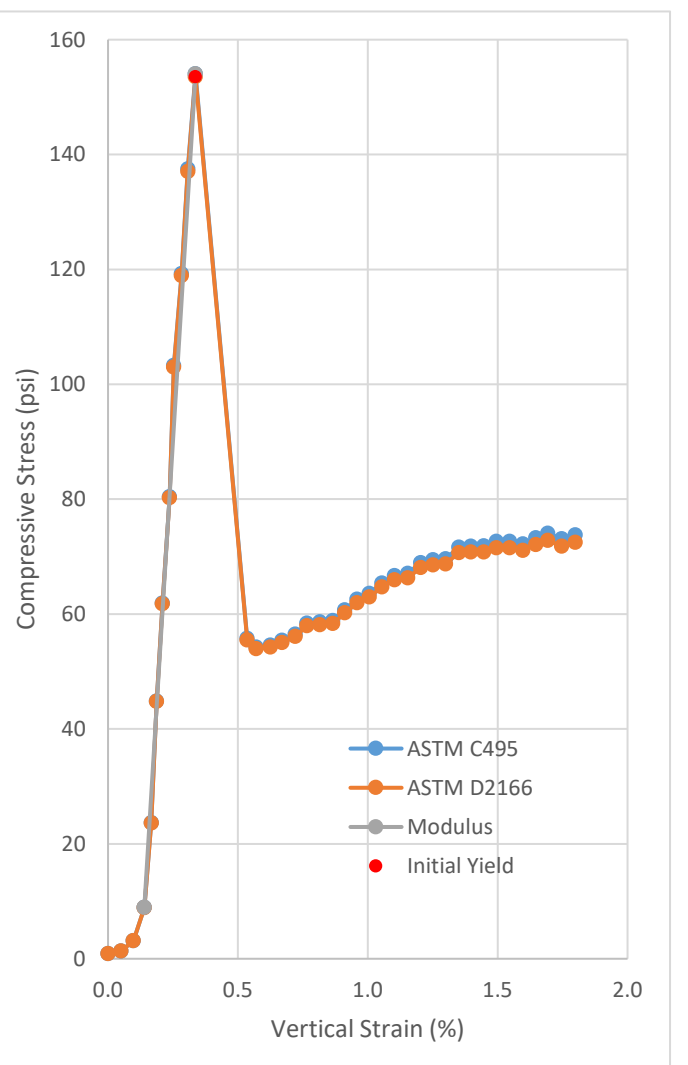

Uniaxial Compressive Strength of Lightweight Cellular Concrete

Sample ID:	**B3-06**
Height (in):	5.724
Height (mm):	145.4
Diameter (in):	2.981
Diameter (mm)	75.72
Area (in^2):	6.979
Area (mm^2):	4503
Mass (g):	252.18
Weight (lb):	0.5560
Weight (kN):	0.00247304
Volume (in^3):	39.95
Volume (mm^3):	654696
Density (g/mm^3):	0.0003852
Density (kg/m^3):	385.2
Unit Weight (pcf):	**24.05**
Unit Weight (kN/m^3):	3.777
Wet mass + tare (g):	567.30
Dry mass + tare (g):	516.78
Tare (g):	315.79
Water Content (%)	**25.14**
H:D ratio:	1.920
H:D correction:	0.9931

Age (days):	14
Cap:	None, surface ground
Maximum load (lb):	1080.9
Maximum load (kN):	4.808
Strain Rate (%/min):	1
Time to Failure (min):	0.76
Strain at Failure (%):	0.652
Initial yield (psi):	154.20
Modulus (psi):	60941
ASTM C495	
Comp. Strength (MPa):	1.0678
Comp. Strength (psi):	154.87
Corr. Comp. Strength (psi):	**153.80**
ASTM D2166	
Comp. Strength (kPa):	1063.1
Comp. Strength (psi):	154.20
Corr. Comp. Strength (psi):	**153.13**
Treatment:	AD

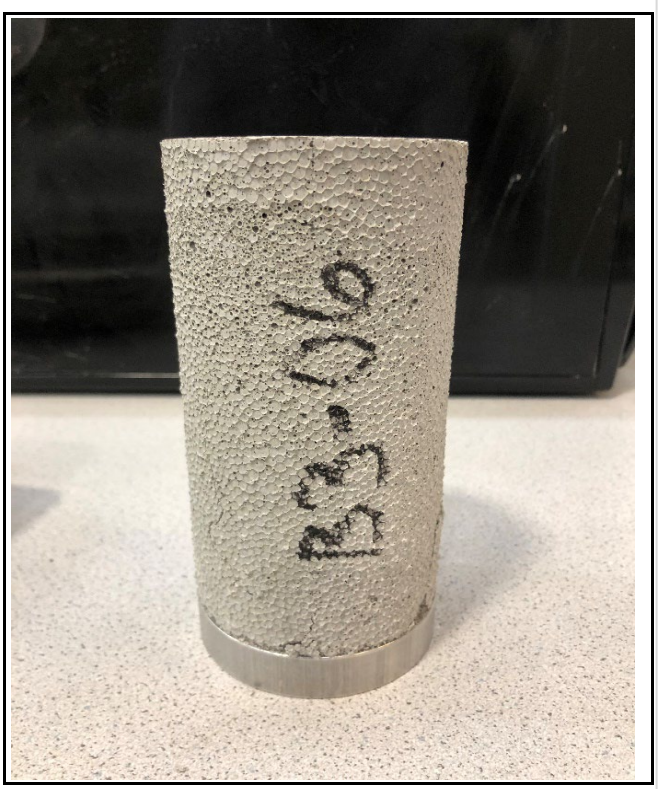

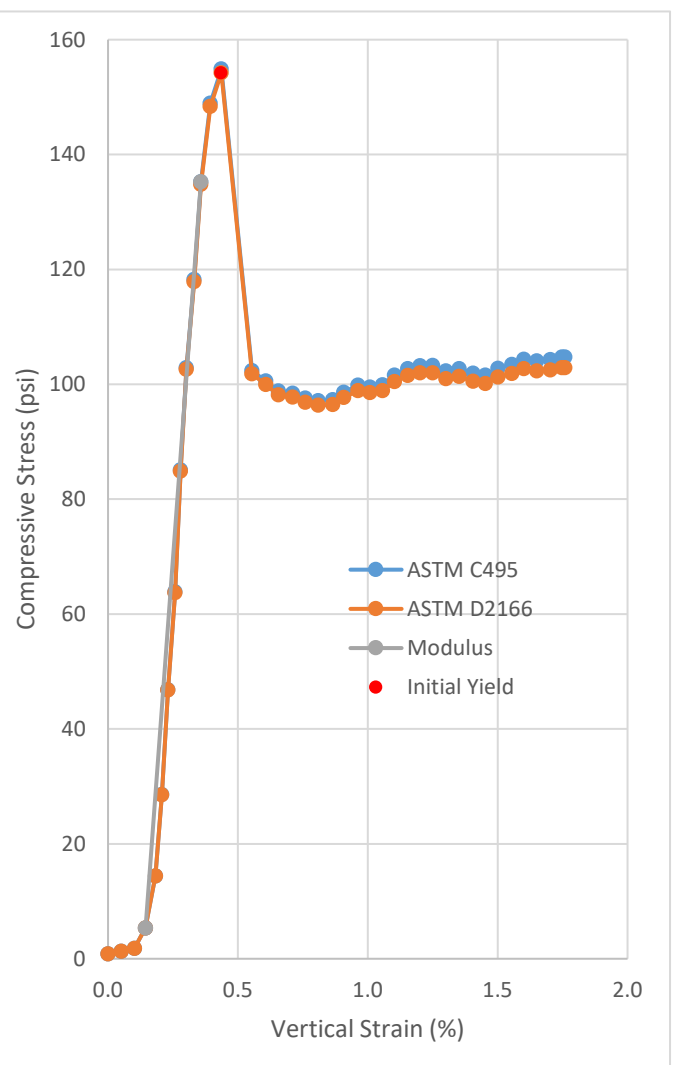

Uniaxial Compressive Strength of Lightweight Cellular Concrete

Sample ID:	**B1-07**
Height (in):	5.687
Height (mm):	144.4
Diameter (in):	2.958
Diameter (mm)	75.14
Area (in^2):	6.874
Area (mm^2):	4435
Mass (g):	227.92
Weight (lb):	0.5025
Weight (kN):	0.00223513
Volume (in^3):	39.09
Volume (mm^3):	640573
Density (g/mm^3):	0.0003558
Density (kg/m^3):	355.8
Unit Weight (pcf):	**22.21**
Unit Weight (kN/m^3):	3.489
Wet mass + tare (g):	692.39
Dry mass + tare (g):	656.32
Tare (g):	465.83
Water Content (%)	**18.94**
H:D ratio:	1.922
H:D correction:	0.9933

Age (days):	28
Cap:	None, surface ground
Maximum load (lb):	495.08
Maximum load (kN):	2.202
Strain Rate (%/min):	1
Time to Failure (min):	1.63
Strain at Failure (%):	1.545
Initial yield (psi):	62.29
Modulus (psi):	11044
ASTM C495	
Comp. Strength (MPa):	0.4966
Comp. Strength (psi):	72.03
Corr. Comp. Strength (psi):	**71.54**
ASTM D2166	
Comp. Strength (kPa):	489.5
Comp. Strength (psi):	70.99
Corr. Comp. Strength (psi):	**70.51**
Treatment:	AD

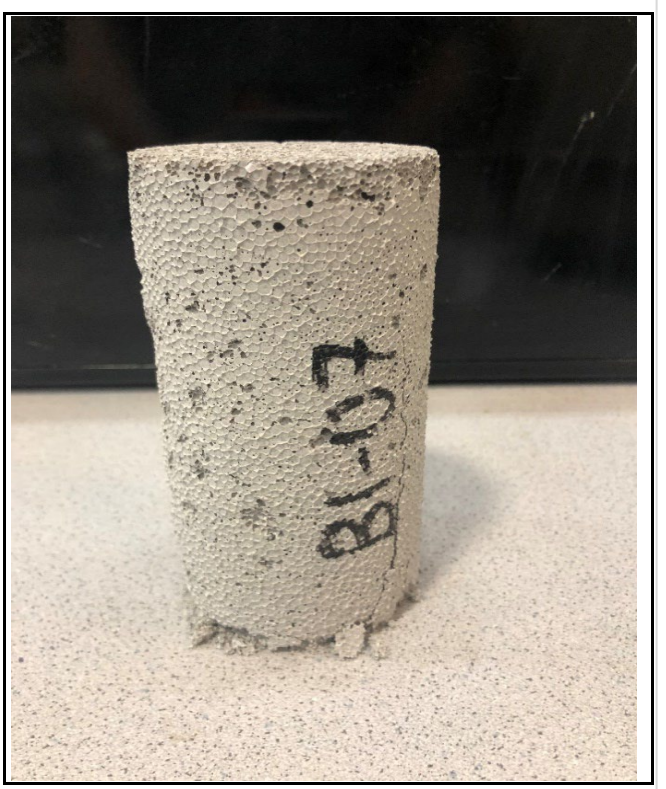

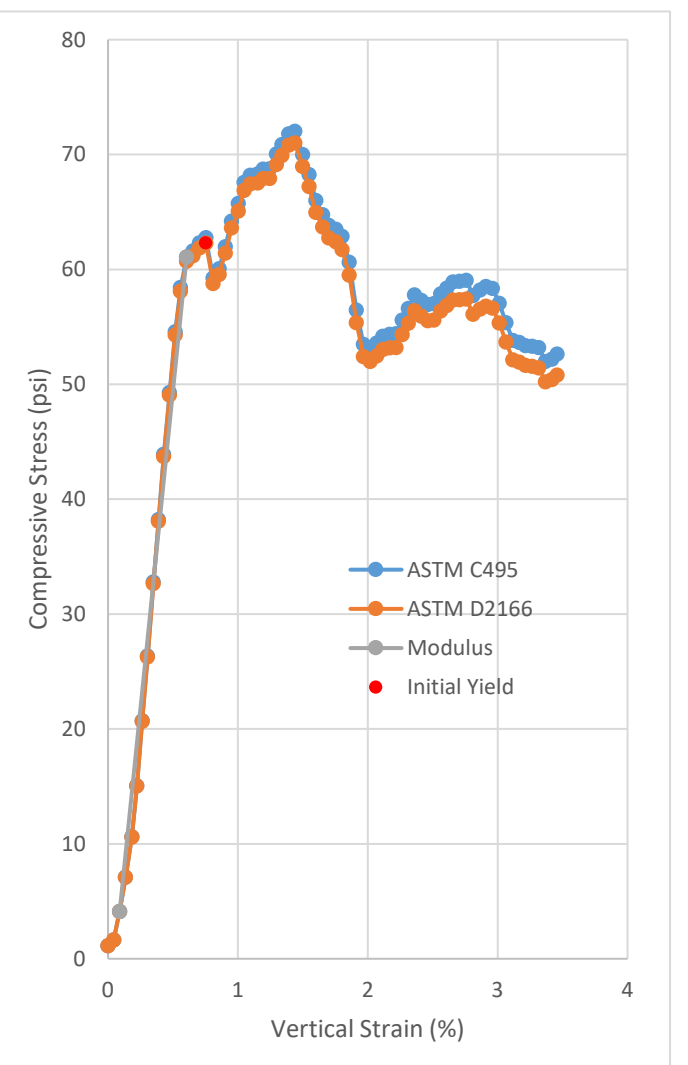

Uniaxial Compressive Strength of Lightweight Cellular Concrete

Sample ID:	**B1-08**
Height (in):	5.685
Height (mm):	144.4
Diameter (in):	2.977
Diameter (mm)	75.61
Area (in^2):	6.959
Area (mm^2):	4490
Mass (g):	231.3
Weight (lb):	0.5099
Weight (kN):	0.00226828
Volume (in^3):	39.56
Volume (mm^3):	648309
Density (g/mm^3):	0.0003568
Density (kg/m^3):	356.8
Unit Weight (pcf):	**22.27**
Unit Weight (kN/m^3):	3.499
Wet mass + tare (g):	560.91
Dry mass + tare (g):	524.97
Tare (g):	330.79
Water Content (%)	**18.51**
H:D ratio:	1.910
H:D correction:	0.9923

Age (days):	28
Cap:	None, surface ground
Maximum load (lb):	791.23
Maximum load (kN):	3.520
Strain Rate (%/min):	1
Time to Failure (min):	1.88
Strain at Failure (%):	1.798
Initial yield (psi):	80.80
Modulus (psi):	25192
ASTM C495	
Comp. Strength (MPa):	0.7839
Comp. Strength (psi):	113.70
Corr. Comp. Strength (psi):	**112.82**
ASTM D2166	
Comp. Strength (kPa):	771.4
Comp. Strength (psi):	111.88
Corr. Comp. Strength (psi):	**111.01**
Treatment:	AD

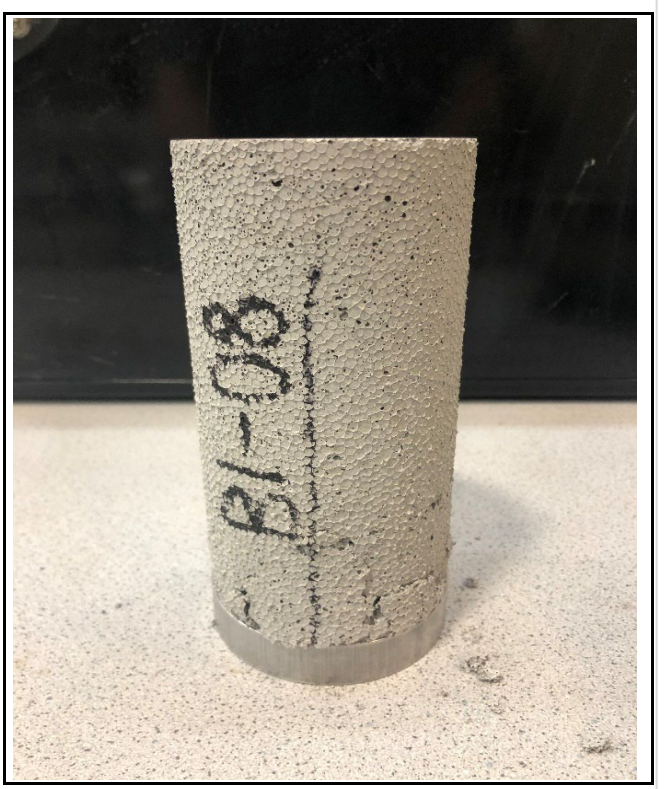

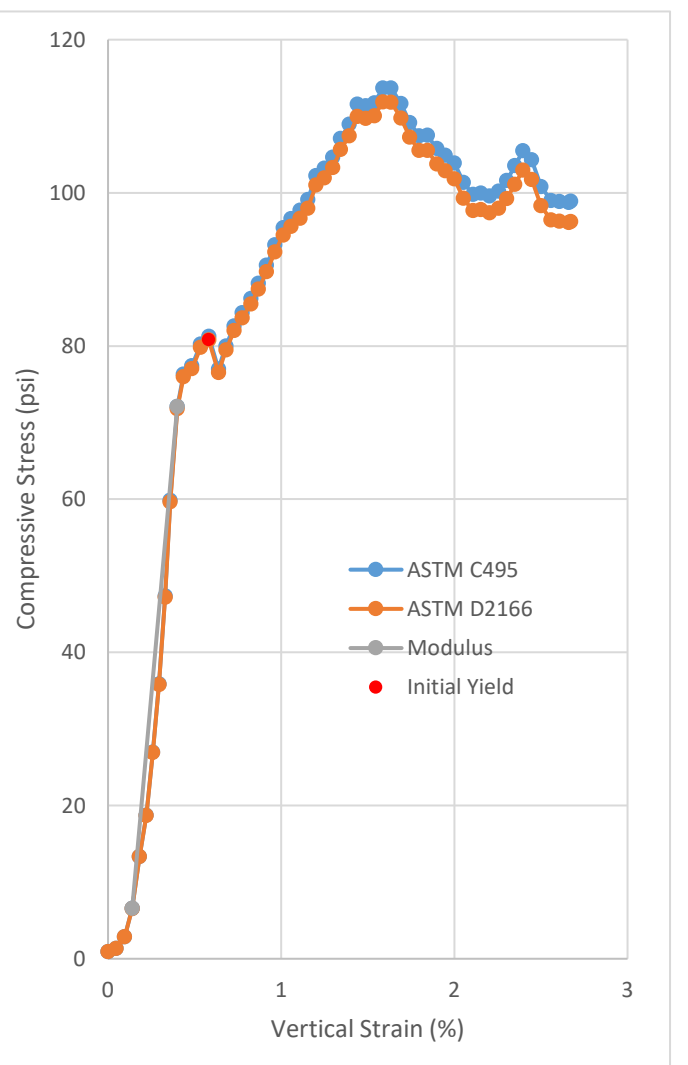

Uniaxial Compressive Strength of Lightweight Cellular Concrete

Sample ID:	**B1-09**
Height (in):	5.750
Height (mm):	146.1
Diameter (in):	2.979
Diameter (mm)	75.67
Area (in^2):	6.970
Area (mm^2):	4497
Mass (g):	234.15
Weight (lb):	0.5162
Weight (kN):	0.00229623
Volume (in^3):	40.08
Volume (mm^3):	656788
Density (g/mm^3):	0.0003565
Density (kg/m^3):	356.5
Unit Weight (pcf):	**22.26**
Unit Weight (kN/m^3):	3.496
Wet mass + tare (g):	558.92
Dry mass + tare (g):	521.35
Tare (g):	326.33
Water Content (%)	**19.26**
H:D ratio:	1.930
H:D correction:	0.9939

Age (days):	28
Cap:	None, surface ground
Maximum load (lb):	763.34
Maximum load (kN):	3.396
Strain Rate (%/min):	1
Time to Failure (min):	1.38
Strain at Failure (%):	1.305
Initial yield (psi):	101.40
Modulus (psi):	45046
ASTM C495	
Comp. Strength (MPa):	0.7551
Comp. Strength (psi):	109.52
Corr. Comp. Strength (psi):	**108.85**
ASTM D2166	
Comp. Strength (kPa):	746.4
Comp. Strength (psi):	108.26
Corr. Comp. Strength (psi):	**107.60**
Treatment:	AD

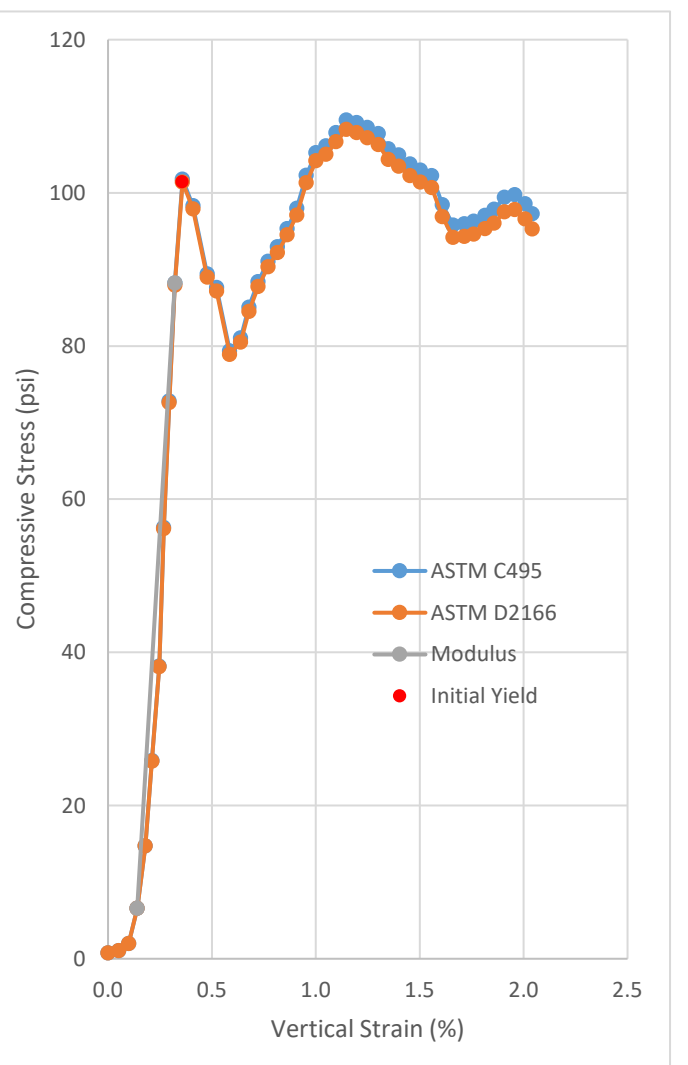

Uniaxial Compressive Strength of Lightweight Cellular Concrete

Sample ID:	**B2-07**
Height (in):	5.732
Height (mm):	145.6
Diameter (in):	2.974
Diameter (mm)	75.54
Area (in^2):	6.947
Area (mm^2):	4482
Mass (g):	243.06
Weight (lb):	0.5359
Weight (kN):	0.0023836
Volume (in^3):	39.82
Volume (mm^3):	652536
Density (g/mm^3):	0.0003725
Density (kg/m^3):	372.5
Unit Weight (pcf):	**23.25**
Unit Weight (kN/m^3):	3.653
Wet mass + tare (g):	688.13
Dry mass + tare (g):	648.46
Tare (g):	446.50
Water Content (%)	**19.64**
H:D ratio:	1.927
H:D correction:	0.9937

Age (days):	28
Cap:	None, surface ground
Maximum load (lb):	971.34
Maximum load (kN):	4.321
Strain Rate (%/min):	1
Time to Failure (min):	1.97
Strain at Failure (%):	1.855
Initial yield (psi):	136.09
Modulus (psi):	73536
ASTM C495	
Comp. Strength (MPa):	0.9641
Comp. Strength (psi):	139.83
Corr. Comp. Strength (psi):	**138.95**
ASTM D2166	
Comp. Strength (kPa):	948.9
Comp. Strength (psi):	137.63
Corr. Comp. Strength (psi):	**136.76**
Treatment:	AD

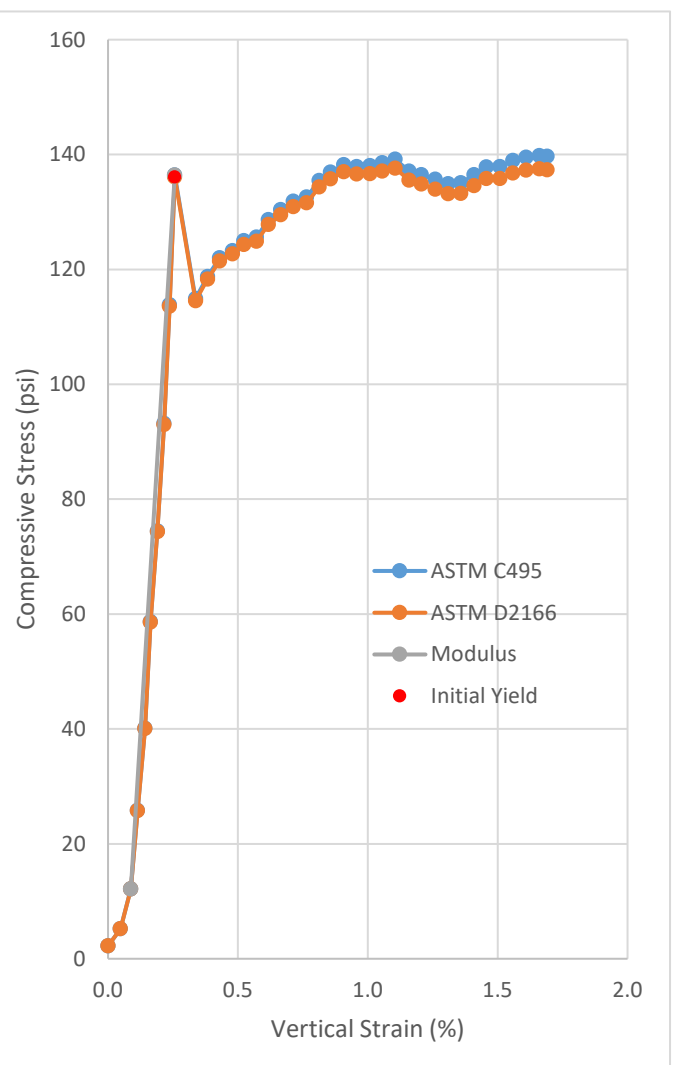

Uniaxial Compressive Strength of Lightweight Cellular Concrete

Sample ID:	**B2-08**
Height (in):	5.769
Height (mm):	146.5
Diameter (in):	2.981
Diameter (mm)	75.71
Area (in^2):	6.978
Area (mm^2):	4502
Mass (g):	236.04
Weight (lb):	0.5204
Weight (kN):	0.00231476
Volume (in^3):	40.25
Volume (mm^3):	659619
Density (g/mm^3):	0.0003578
Density (kg/m^3):	357.8
Unit Weight (pcf):	**22.34**
Unit Weight (kN/m^3):	3.509
Wet mass + tare (g):	643.46
Dry mass + tare (g):	606.18
Tare (g):	408.70
Water Content (%)	**18.88**
H:D ratio:	1.935
H:D correction:	0.9943

Age (days):	28
Cap:	None, surface ground
Maximum load (lb):	647.95
Maximum load (kN):	2.882
Strain Rate (%/min):	1
Time to Failure (min):	1.88
Strain at Failure (%):	1.803
Initial yield (psi):	76.54
Modulus (psi):	37443
ASTM C495	
Comp. Strength (MPa):	0.6402
Comp. Strength (psi):	92.86
Corr. Comp. Strength (psi):	**92.33**
ASTM D2166	
Comp. Strength (kPa):	629.5
Comp. Strength (psi):	91.31
Corr. Comp. Strength (psi):	**90.79**
Treatment:	AD

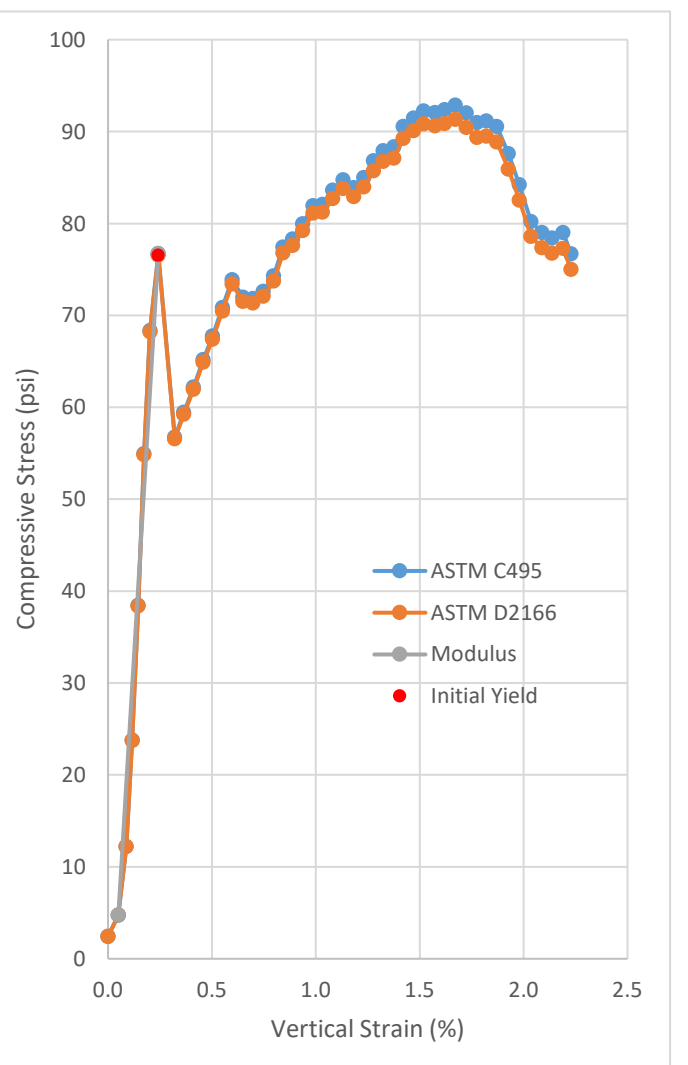

Uniaxial Compressive Strength of Lightweight Cellular Concrete

Sample ID:	**B2-09**
Height (in):	5.834
Height (mm):	148.2
Diameter (in):	2.973
Diameter (mm)	75.51
Area (in^2):	6.940
Area (mm^2):	4478
Mass (g):	235.99
Weight (lb):	0.5203
Weight (kN):	0.00231427
Volume (in^3):	40.49
Volume (mm^3):	663476
Density (g/mm^3):	0.0003557
Density (kg/m^3):	355.7
Unit Weight (pcf):	**22.20**
Unit Weight (kN/m^3):	3.488
Wet mass + tare (g):	563.63
Dry mass + tare (g):	527.08
Tare (g):	328.90
Water Content (%)	**18.44**
H:D ratio:	1.962
H:D correction:	0.9965

Age (days):	28
Cap:	None, surface ground
Maximum load (lb):	631.51
Maximum load (kN):	2.809
Strain Rate (%/min):	1
Time to Failure (min):	1.71
Strain at Failure (%):	1.601
Initial yield (psi):	69.58
Modulus (psi):	50510
ASTM C495	
Comp. Strength (MPa):	0.6274
Comp. Strength (psi):	90.99
Corr. Comp. Strength (psi):	**90.67**
ASTM D2166	
Comp. Strength (kPa):	618.1
Comp. Strength (psi):	89.65
Corr. Comp. Strength (psi):	**89.34**
Treatment:	AD

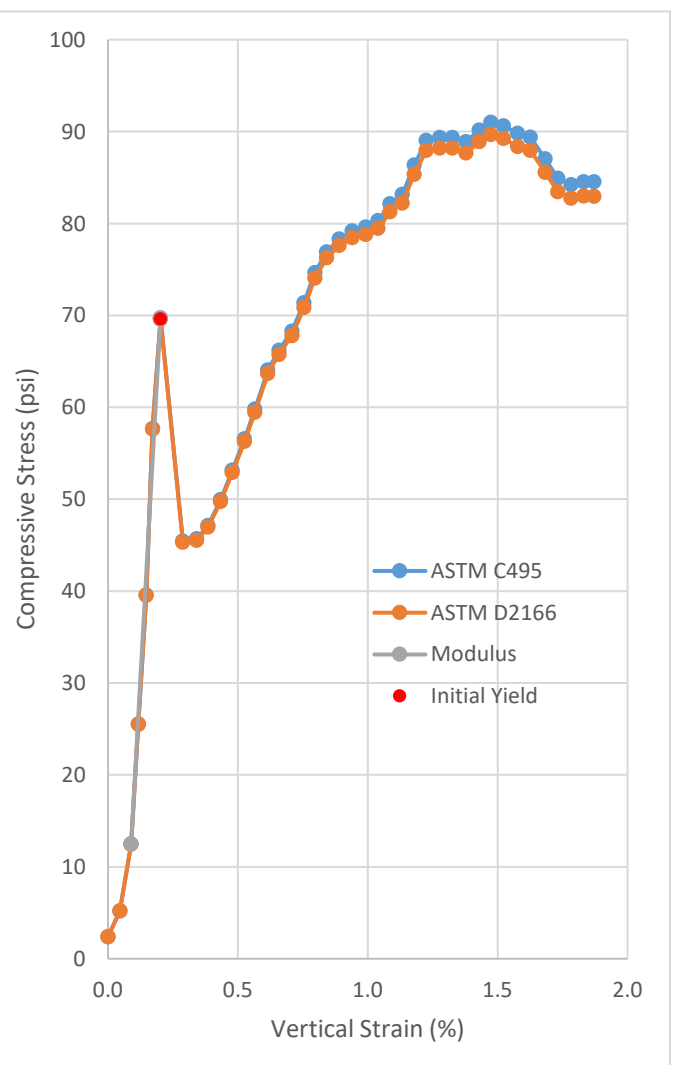

Uniaxial Compressive Strength of Lightweight Cellular Concrete

Sample ID:	**B3-07**
Height (in):	5.724
Height (mm):	145.4
Diameter (in):	2.963
Diameter (mm)	75.25
Area (in^2):	6.894
Area (mm^2):	4448
Mass (g):	243.17
Weight (lb):	0.5361
Weight (kN):	0.00238468
Volume (in^3):	39.46
Volume (mm^3):	646631
Density (g/mm^3):	0.0003761
Density (kg/m^3):	376.1
Unit Weight (pcf):	**23.48**
Unit Weight (kN/m^3):	3.688
Wet mass + tare (g):	573.97
Dry mass + tare (g):	534.54
Tare (g):	332.26
Water Content (%)	**19.49**
H:D ratio:	1.932
H:D correction:	0.9940

Age (days):	28
Cap:	None, surface ground
Maximum load (lb):	899.64
Maximum load (kN):	4.002
Strain Rate (%/min):	1
Time to Failure (min):	1.33
Strain at Failure (%):	1.247
Initial yield (psi):	107.87
Modulus (psi):	58942
ASTM C495	
Comp. Strength (MPa):	0.8998
Comp. Strength (psi):	130.50
Corr. Comp. Strength (psi):	**129.72**
ASTM D2166	
Comp. Strength (kPa):	890.2
Comp. Strength (psi):	129.11
Corr. Comp. Strength (psi):	**128.34**
Treatment:	AD

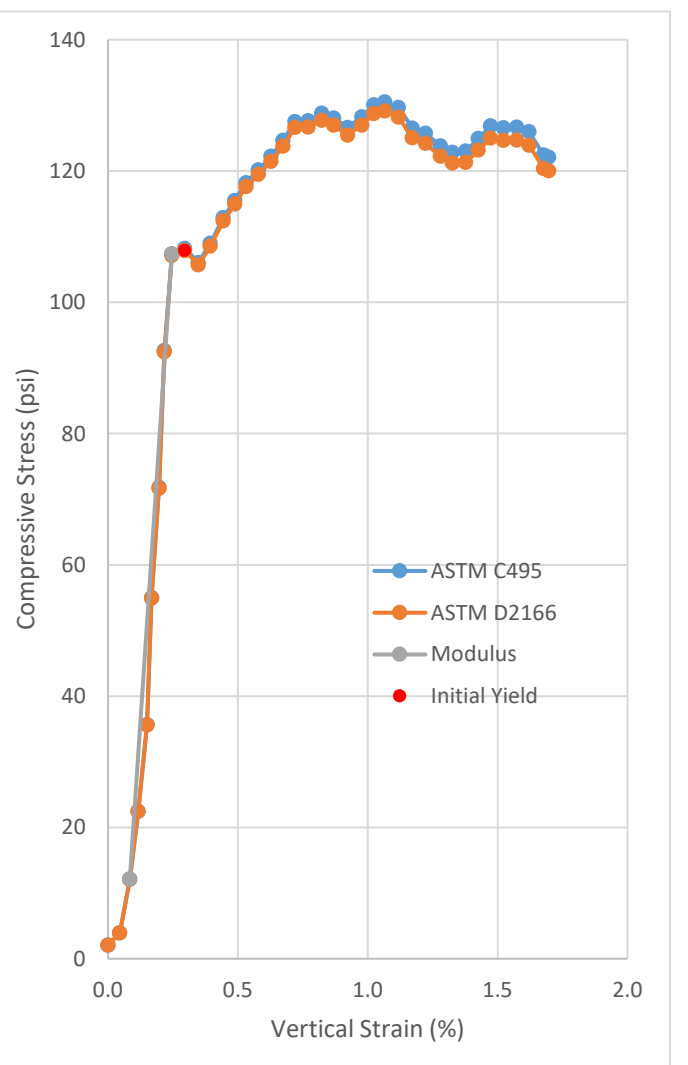

Uniaxial Compressive Strength of Lightweight Cellular Concrete

Sample ID:	**B3-08**
Height (in):	5.804
Height (mm):	147.4
Diameter (in):	2.972
Diameter (mm)	75.48
Area (in^2):	6.936
Area (mm^2):	4475
Mass (g):	246.54
Weight (lb):	0.5435
Weight (kN):	0.00241773
Volume (in^3):	40.25
Volume (mm^3):	659620
Density (g/mm^3):	0.0003738
Density (kg/m^3):	373.8
Unit Weight (pcf):	**23.33**
Unit Weight (kN/m^3):	3.665
Wet mass + tare (g):	709.98
Dry mass + tare (g):	668.68
Tare (g):	465.05
Water Content (%)	**20.28**
H:D ratio:	1.953
H:D correction:	0.9957

Age (days):	28
Cap:	None, surface ground
Maximum load (lb):	1050.1
Maximum load (kN):	4.671
Strain Rate (%/min):	1
Time to Failure (min):	1.57
Strain at Failure (%):	1.449
Initial yield (psi):	114.65
Modulus (psi):	65144
ASTM C495	
Comp. Strength (MPa):	1.0439
Comp. Strength (psi):	151.41
Corr. Comp. Strength (psi):	**150.76**
ASTM D2166	
Comp. Strength (kPa):	1030.9
Comp. Strength (psi):	149.52
Corr. Comp. Strength (psi):	**148.88**
Treatment:	AD

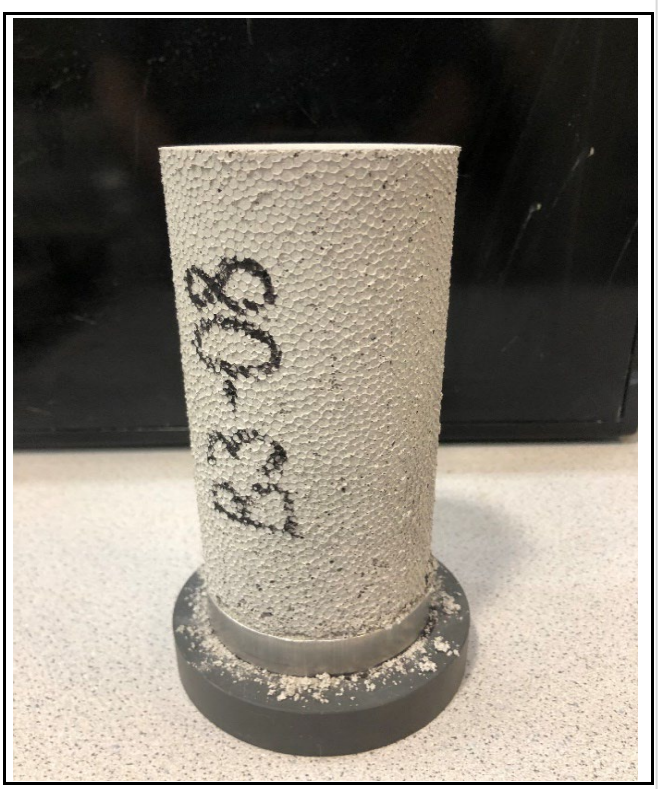

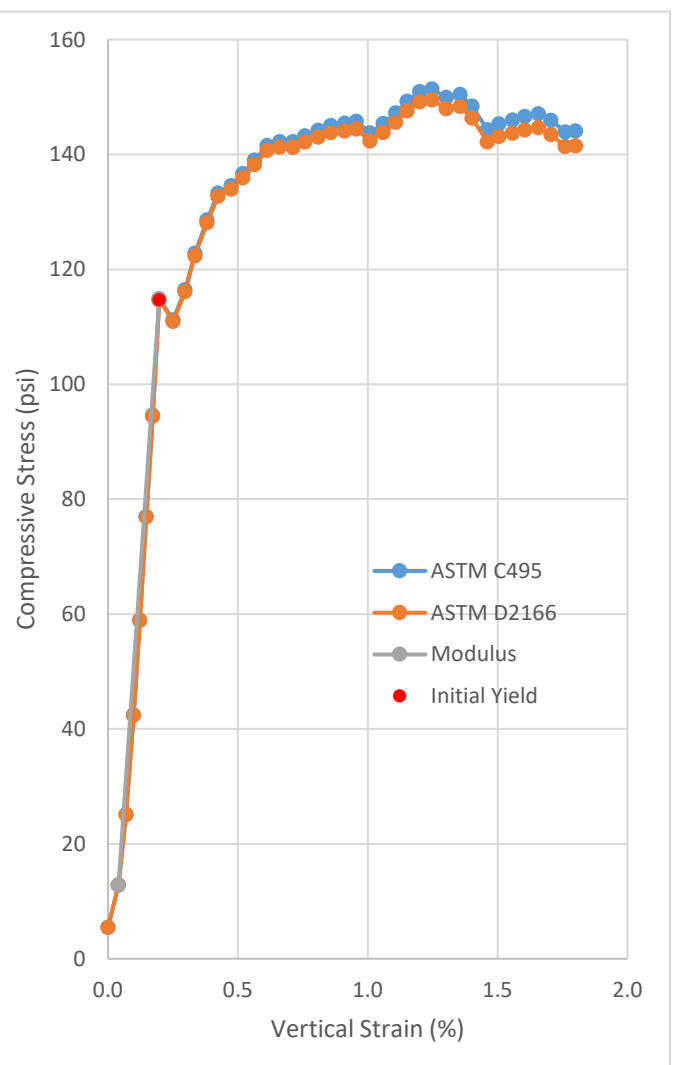

Uniaxial Compressive Strength of Lightweight Cellular Concrete

Sample ID:	**B3-09**
Height (in):	5.770
Height (mm):	146.6
Diameter (in):	2.984
Diameter (mm)	75.79
Area (in^2):	6.993
Area (mm^2):	4512
Mass (g):	245.59
Weight (lb):	0.5414
Weight (kN):	0.00240842
Volume (in^3):	40.35
Volume (mm^3):	661286
Density (g/mm^3):	0.0003714
Density (kg/m^3):	371.4
Unit Weight (pcf):	**23.18**
Unit Weight (kN/m^3):	3.642
Wet mass + tare (g):	553.49
Dry mass + tare (g):	512.99
Tare (g):	309.43
Water Content (%)	**19.90**
H:D ratio:	1.934
H:D correction:	0.9942

Age (days):	28
Cap:	None, surface ground
Maximum load (lb):	1042.3
Maximum load (kN):	4.636
Strain Rate (%/min):	1
Time to Failure (min):	1.70
Strain at Failure (%):	1.601
Initial yield (psi):	136.05
Modulus (psi):	67460
ASTM C495	
Comp. Strength (MPa):	1.0276
Comp. Strength (psi):	149.04
Corr. Comp. Strength (psi):	**148.17**
ASTM D2166	
Comp. Strength (kPa):	1013.3
Comp. Strength (psi):	146.96
Corr. Comp. Strength (psi):	**146.11**
Treatment:	AD

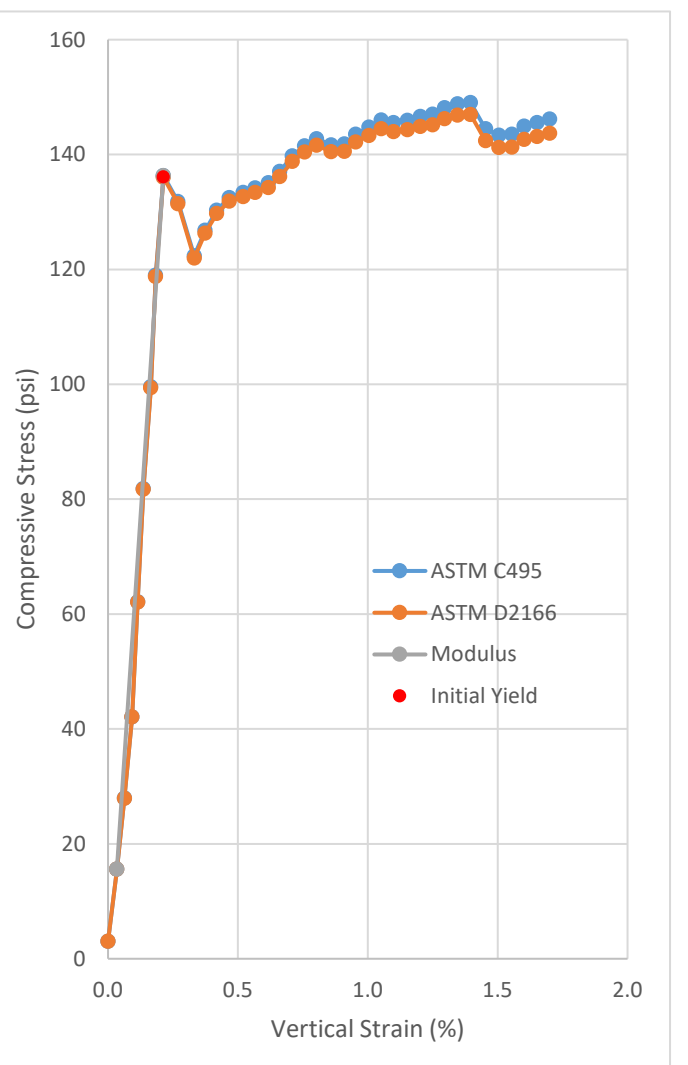

Uniaxial Compressive Strength of Lightweight Cellular Concrete

Sample ID:	**B1-10**
Height (in):	5.483
Height (mm):	139.3
Diameter (in):	2.978
Diameter (mm)	75.65
Area (in^2):	6.967
Area (mm^2):	4495
Mass (g):	226.53
Weight (lb):	0.4994
Weight (kN):	0.0022215
Volume (in^3):	38.20
Volume (mm^3):	625935
Density (g/mm^3):	0.0003619
Density (kg/m^3):	361.9
Unit Weight (pcf):	**22.59**
Unit Weight (kN/m^3):	3.549
Wet mass + tare (g):	550.79
Dry mass + tare (g):	509.53
Tare (g):	327.87
Water Content (%)	**22.71**
H:D ratio:	1.841
H:D correction:	0.9868

Age (days):	52
Cap:	Surface ground, 50 durometer end cap
Maximum load (lb):	640.19
Maximum load (kN):	2.848
Strain Rate (%/min):	1
Time to Failure (min):	1.00
Strain at Failure (%):	1.400
Initial yield (psi):	77.14
Modulus (psi):	13121
ASTM C495	
Comp. Strength (MPa):	0.6336
Comp. Strength (psi):	91.89
Corr. Comp. Strength (psi):	**90.68**
ASTM D2166	
Comp. Strength (kPa):	626.6
Comp. Strength (psi):	90.88
Corr. Comp. Strength (psi):	**89.67**
Treatment:	AD

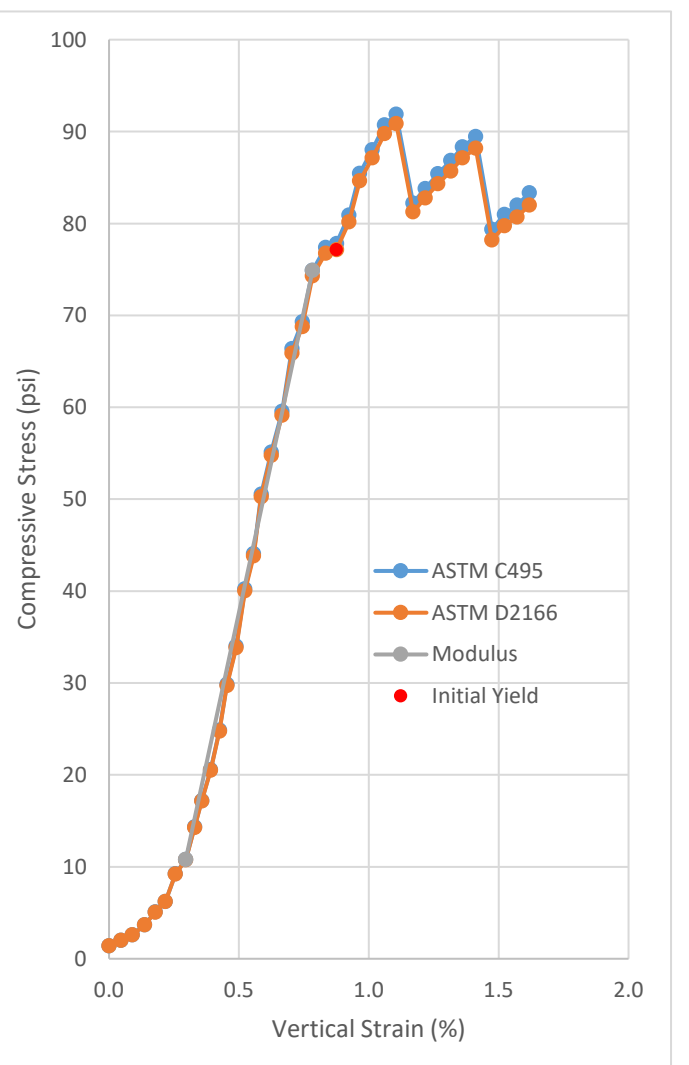

Uniaxial Compressive Strength of Lightweight Cellular Concrete

Sample ID:	**B2-10**
Height (in):	5.693
Height (mm):	144.6
Diameter (in):	2.974
Diameter (mm)	75.54
Area (in^2):	6.947
Area (mm^2):	4482
Mass (g):	246.87
Weight (lb):	0.5443
Weight (kN):	0.00242097
Volume (in^3):	39.54
Volume (mm^3):	648020
Density (g/mm^3):	0.0003810
Density (kg/m^3):	381.0
Unit Weight (pcf):	**23.78**
Unit Weight (kN/m^3):	3.736
Wet mass + tare (g):	579.99
Dry mass + tare (g):	533.56
Tare (g):	333.13
Water Content (%)	**23.17**
H:D ratio:	1.914
H:D correction:	0.9926

Age (days):	52
Cap:	Surface ground, 50 durometer end cap
Maximum load (lb):	1206.7
Maximum load (kN):	5.368
Strain Rate (%/min):	1
Time to Failure (min):	1.16
Strain at Failure (%):	2.896
Initial yield (psi):	148.78
Modulus (psi):	#N/A
ASTM C495	
Comp. Strength (MPa):	1.1977
Comp. Strength (psi):	173.71
Corr. Comp. Strength (psi):	**172.43**
ASTM D2166	
Comp. Strength (kPa):	1126.9
Comp. Strength (psi):	163.44
Corr. Comp. Strength (psi):	**162.23**
Treatment:	AD

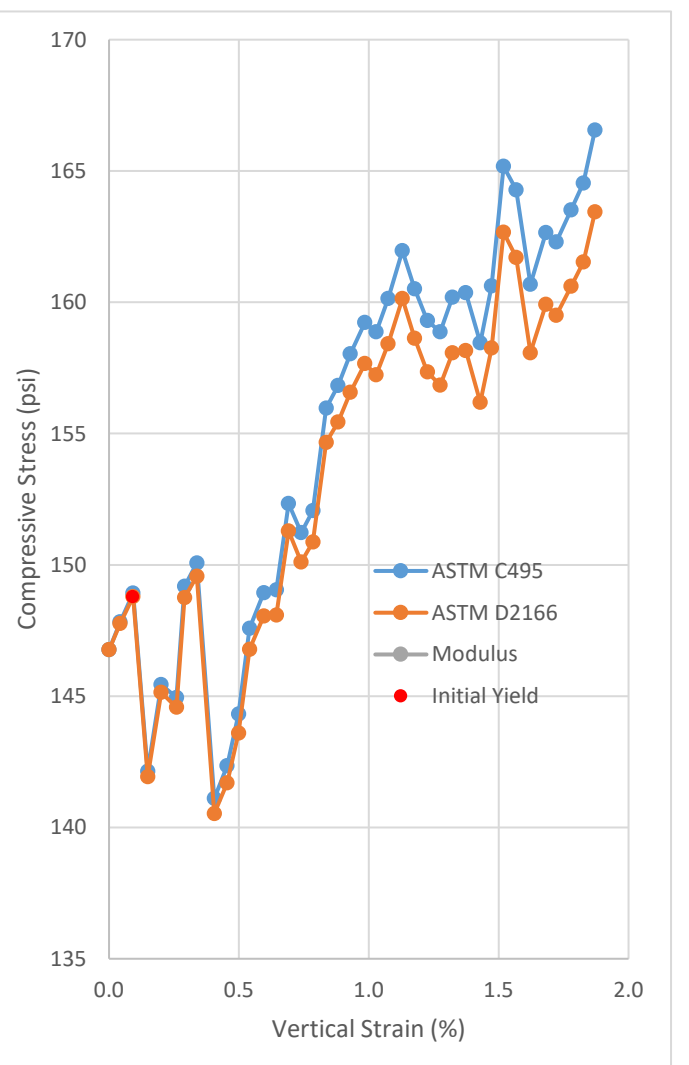

Note: Data acquisition error occurred during the initial portion of the test.

Uniaxial Compressive Strength of Lightweight Cellular Concrete

Sample ID:	**B3-10**
Height (in):	5.637
Height (mm):	143.2
Diameter (in):	2.972
Diameter (mm)	75.49
Area (in^2):	6.937
Area (mm^2):	4476
Mass (g):	240.87
Weight (lb):	0.5310
Weight (kN):	0.00236213
Volume (in^3):	39.10
Volume (mm^3):	640783
Density (g/mm^3):	0.0003759
Density (kg/m^3):	375.9
Unit Weight (pcf):	**23.47**
Unit Weight (kN/m^3):	3.686
Wet mass + tare (g):	648.53
Dry mass + tare (g):	606.41
Tare (g):	408.55
Water Content (%)	**21.29**
H:D ratio:	1.897
H:D correction:	0.9912

Age (days):	52
Cap:	Surface ground, 50 durometer end cap
Maximum load (lb):	1355
Maximum load (kN):	6.027
Strain Rate (%/min):	1
Time to Failure (min):	0.68
Strain at Failure (%):	1.294
Initial yield (psi):	164.21
Modulus (psi):	37570
ASTM C495	
Comp. Strength (MPa):	1.3467
Comp. Strength (psi):	195.32
Corr. Comp. Strength (psi):	**193.60**
ASTM D2166	
Comp. Strength (kPa):	1331.2
Comp. Strength (psi):	193.07
Corr. Comp. Strength (psi):	**191.37**
Treatment:	AD

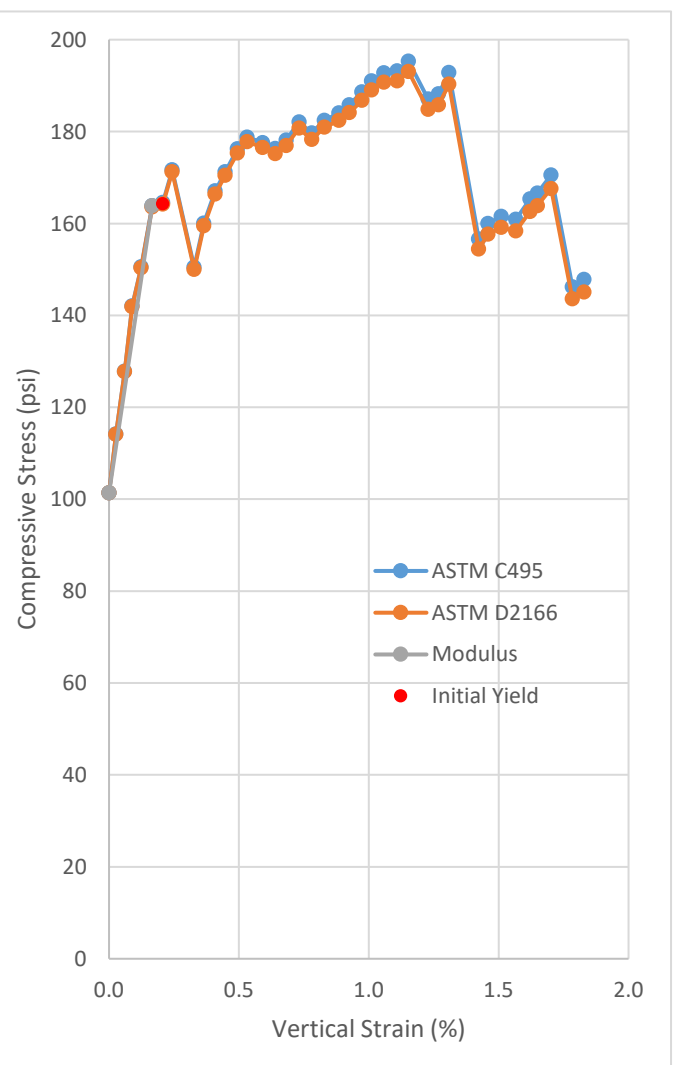

Note: Data acquisition error occurred during the initial portion of the test.

Uniaxial Compressive Strength of Lightweight Cellular Concrete

Sample ID:	**B1-11**
Height (in):	5.611
Height (mm):	142.5
Diameter (in):	2.976
Diameter (mm)	75.60
Area (in^2):	6.957
Area (mm^2):	4489
Mass (g):	237.89
Weight (lb):	0.5245
Weight (kN):	0.0023329
Volume (in^3):	39.04
Volume (mm^3):	639765
Density (g/mm^3):	0.0003718
Density (kg/m^3):	371.8
Unit Weight (pcf):	**23.21**
Unit Weight (kN/m^3):	3.647
Wet mass + tare (g):	553.83
Dry mass + tare (g):	507.29
Tare (g):	316.46
Water Content (%)	**24.39**
H:D ratio:	1.885
H:D correction:	0.9903

Age (days):	56
Cap:	Surface ground, 50 durometer end cap
Maximum load (lb):	758.73
Maximum load (kN):	3.375
Strain Rate (%/min):	2
Time to Failure (min):	0.53
Strain at Failure (%):	0.948
Initial yield (psi):	108.30
Modulus (psi):	17237
ASTM C495	
Comp. Strength (MPa):	0.7519
Comp. Strength (psi):	109.05
Corr. Comp. Strength (psi):	**107.99**
ASTM D2166	
Comp. Strength (kPa):	746.7
Comp. Strength (psi):	108.30
Corr. Comp. Strength (psi):	**107.25**
Treatment:	AD

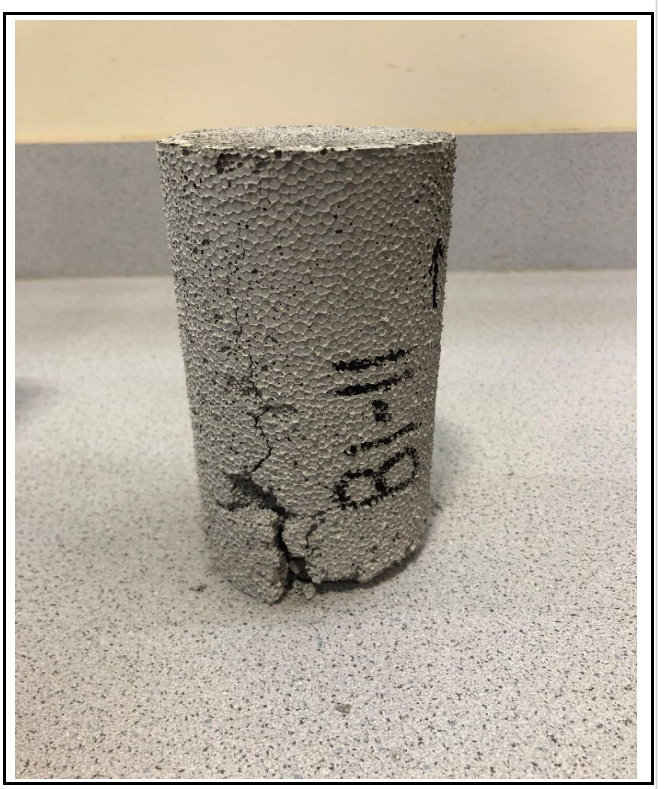

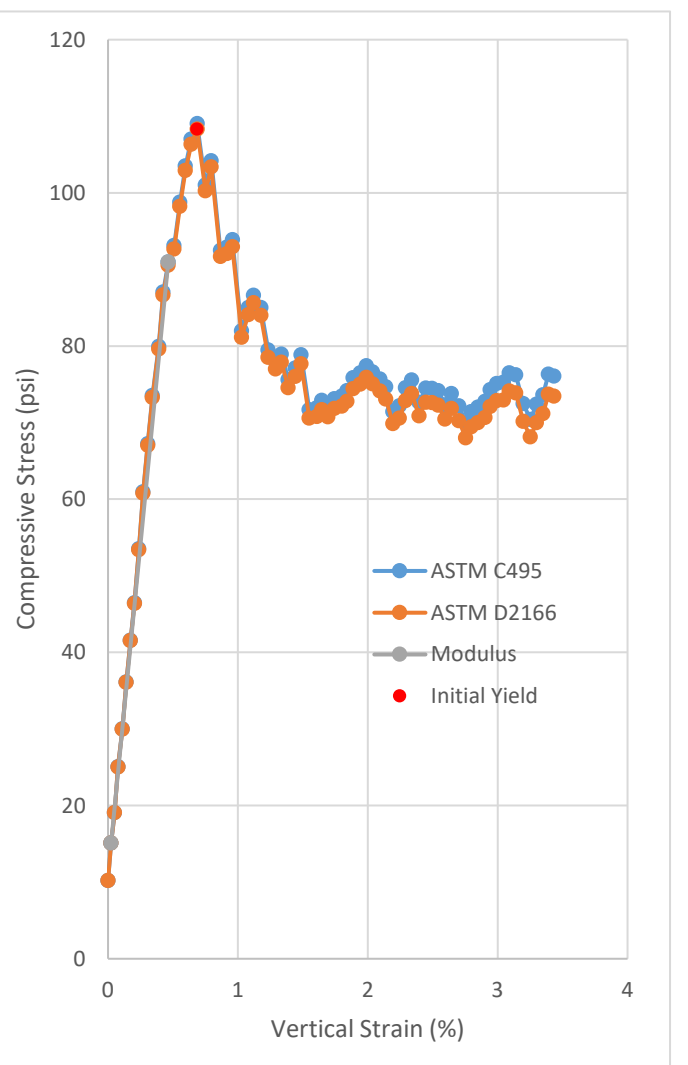

Uniaxial Compressive Strength of Lightweight Cellular Concrete

Sample ID:	**B1-12**
Height (in):	5.641
Height (mm):	143.3
Diameter (in):	2.980
Diameter (mm)	75.69
Area (in^2):	6.975
Area (mm^2):	4500
Mass (g):	235.58
Weight (lb):	0.5194
Weight (kN):	0.00231025
Volume (in^3):	39.35
Volume (mm^3):	644771
Density (g/mm^3):	0.0003654
Density (kg/m^3):	365.4
Unit Weight (pcf):	**22.81**
Unit Weight (kN/m^3):	3.583
Wet mass + tare (g):	565.75
Dry mass + tare (g):	521.37
Tare (g):	330.66
Water Content (%)	**23.27**
H:D ratio:	1.893
H:D correction:	0.9909

Age (days):	56
Cap:	Surface ground, 50 durometer end cap
Maximum load (lb):	690.71
Maximum load (kN):	3.072
Strain Rate (%/min):	2
Time to Failure (min):	0.29
Strain at Failure (%):	0.548
Initial yield (psi):	86.24
Modulus (psi):	18812
ASTM C495	
Comp. Strength (MPa):	0.6828
Comp. Strength (psi):	99.03
Corr. Comp. Strength (psi):	**98.13**
ASTM D2166	
Comp. Strength (kPa):	679.4
Comp. Strength (psi):	98.53
Corr. Comp. Strength (psi):	**97.64**
Treatment:	AD

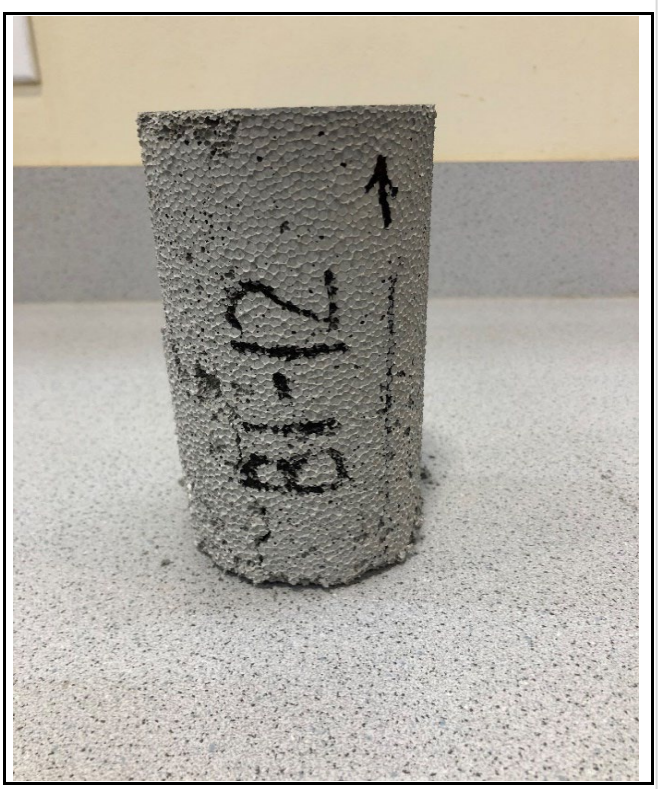

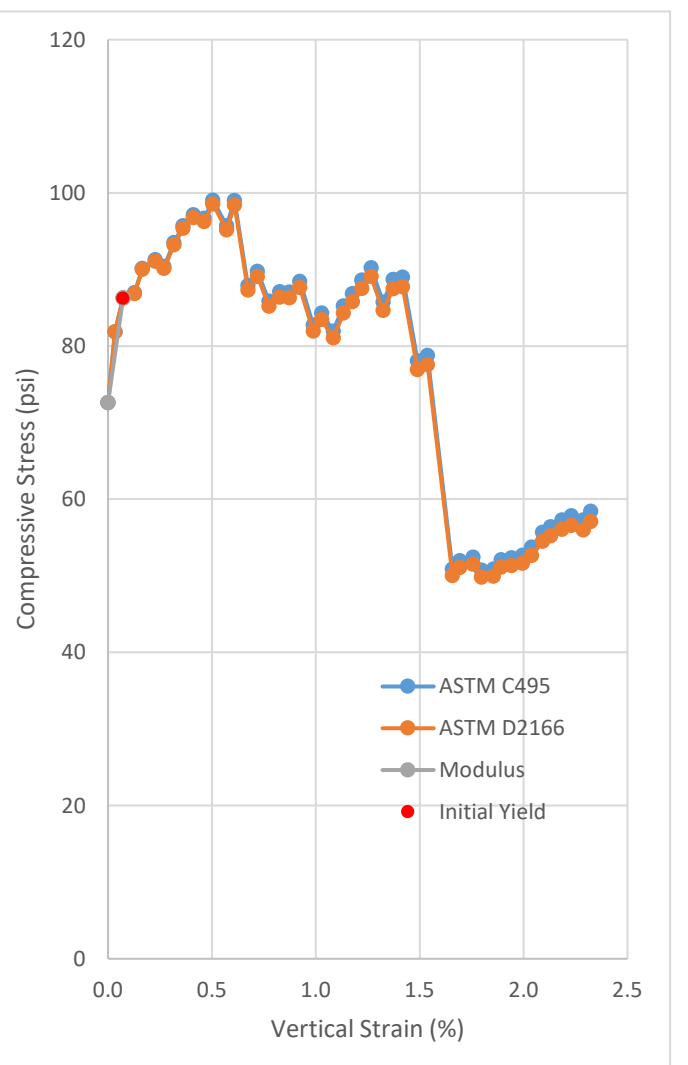

Note: Data acquisition error occurred during the initial portion of the test.

Uniaxial Compressive Strength of Lightweight Cellular Concrete

Sample ID:	**B1-13**
Height (in):	5.608
Height (mm):	142.4
Diameter (in):	2.977
Diameter (mm)	75.62
Area (in^2):	6.961
Area (mm^2):	4491
Mass (g):	234.18
Weight (lb):	0.5163
Weight (kN):	0.00229652
Volume (in^3):	39.03
Volume (mm^3):	639633
Density (g/mm^3):	0.0003661
Density (kg/m^3):	366.1
Unit Weight (pcf):	**22.86**
Unit Weight (kN/m^3):	3.590
Wet mass + tare (g):	697.77
Dry mass + tare (g):	653.55
Tare (g):	464.05
Water Content (%)	**23.34**
H:D ratio:	1.884
H:D correction:	0.9902

Age (days):	56
Cap:	Surface ground, 50 durometer end cap
Maximum load (lb):	601.64
Maximum load (kN):	2.676
Strain Rate (%/min):	2
Time to Failure (min):	0.57
Strain at Failure (%):	1.099
Initial yield (psi):	79.12
Modulus (psi):	16172
ASTM C495	
Comp. Strength (MPa):	0.5959
Comp. Strength (psi):	86.43
Corr. Comp. Strength (psi):	**85.58**
ASTM D2166	
Comp. Strength (kPa):	591.0
Comp. Strength (psi):	85.72
Corr. Comp. Strength (psi):	**84.88**
Treatment:	AD

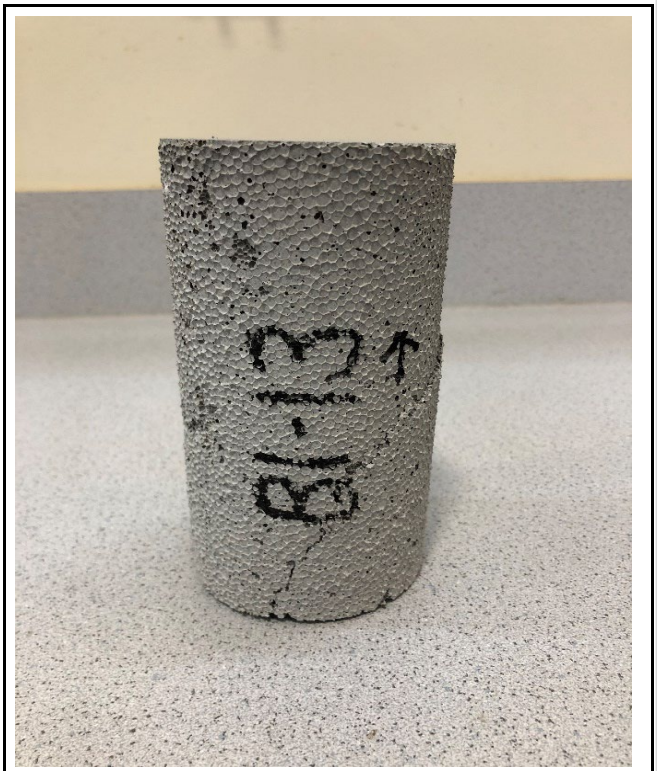

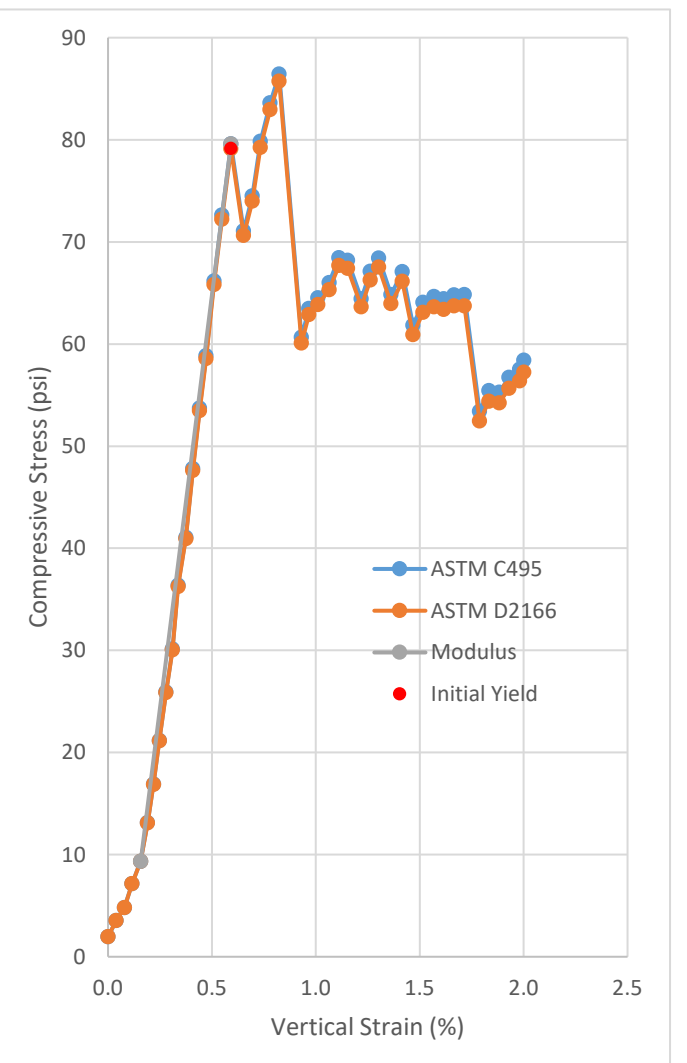

Uniaxial Compressive Strength of Lightweight Cellular Concrete

Sample ID:	**B2-11**
Height (in):	5.581
Height (mm):	141.8
Diameter (in):	2.973
Diameter (mm)	75.51
Area (in^2):	6.940
Area (mm^2):	4478
Mass (g):	234.81
Weight (lb):	0.5177
Weight (kN):	0.0023027
Volume (in^3):	38.74
Volume (mm^3):	634777
Density (g/mm^3):	0.0003699
Density (kg/m^3):	369.9
Unit Weight (pcf):	**23.09**
Unit Weight (kN/m^3):	3.628
Wet mass + tare (g):	680.77
Dry mass + tare (g):	638.23
Tare (g):	446.68
Water Content (%)	**22.21**
H:D ratio:	1.878
H:D correction:	0.9897

Age (days):	56
Cap:	Surface ground, 50 durometer end cap
Maximum load (lb):	729.26
Maximum load (kN):	3.244
Strain Rate (%/min):	2
Time to Failure (min):	0.56
Strain at Failure (%):	1.052
Initial yield (psi):	104.29
Modulus (psi):	19041
ASTM C495	
Comp. Strength (MPa):	0.7245
Comp. Strength (psi):	105.08
Corr. Comp. Strength (psi):	**103.99**
ASTM D2166	
Comp. Strength (kPa):	719.1
Comp. Strength (psi):	104.29
Corr. Comp. Strength (psi):	**103.21**
Treatment:	AD

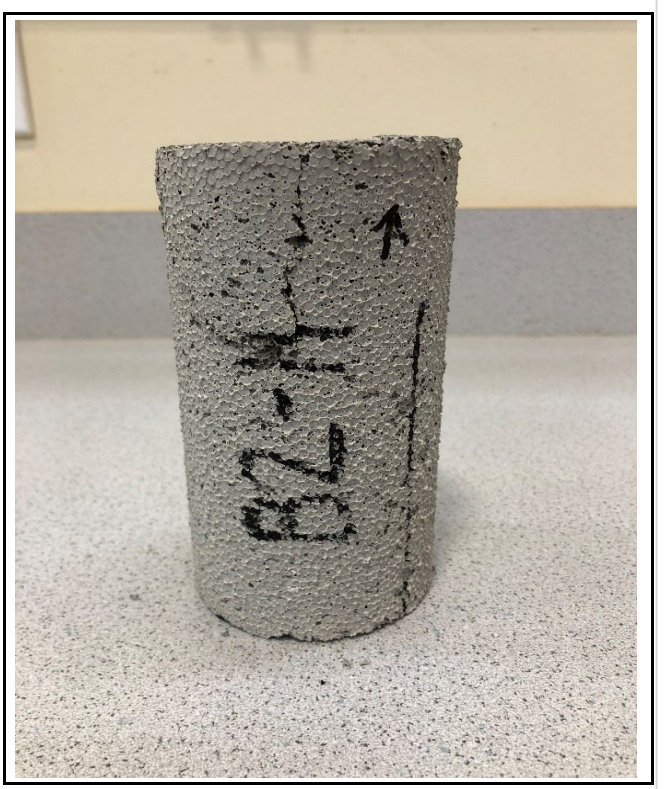

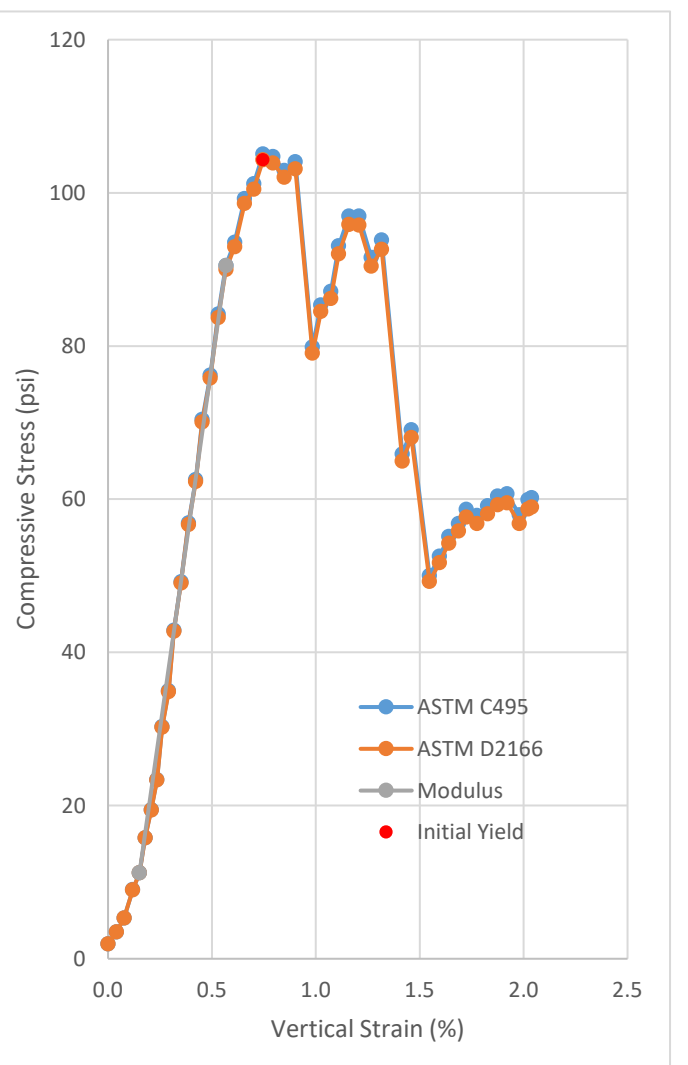

Uniaxial Compressive Strength of Lightweight Cellular Concrete

Sample ID:	**B2-12**
Height (in):	5.643
Height (mm):	143.3
Diameter (in):	2.973
Diameter (mm)	75.52
Area (in^2):	6.943
Area (mm^2):	4480
Mass (g):	234.81
Weight (lb):	0.5177
Weight (kN):	0.0023027
Volume (in^3):	39.18
Volume (mm^3):	642041
Density (g/mm^3):	0.0003657
Density (kg/m^3):	365.7
Unit Weight (pcf):	**22.83**
Unit Weight (kN/m^3):	3.587
Wet mass + tare (g):	543.93
Dry mass + tare (g):	500.78
Tare (g):	310.46
Water Content (%)	**22.67**
H:D ratio:	1.898
H:D correction:	0.9913

Age (days):	56
Cap:	Surface ground, 50 durometer end cap
Maximum load (lb):	703.74
Maximum load (kN):	3.130
Strain Rate (%/min):	2
Time to Failure (min):	0.32
Strain at Failure (%):	0.599
Initial yield (psi):	93.29
Modulus (psi):	31337
ASTM C495	
Comp. Strength (MPa):	0.6988
Comp. Strength (psi):	101.35
Corr. Comp. Strength (psi):	**100.47**
ASTM D2166	
Comp. Strength (kPa):	695.2
Comp. Strength (psi):	100.82
Corr. Comp. Strength (psi):	**99.94**
Treatment:	AD

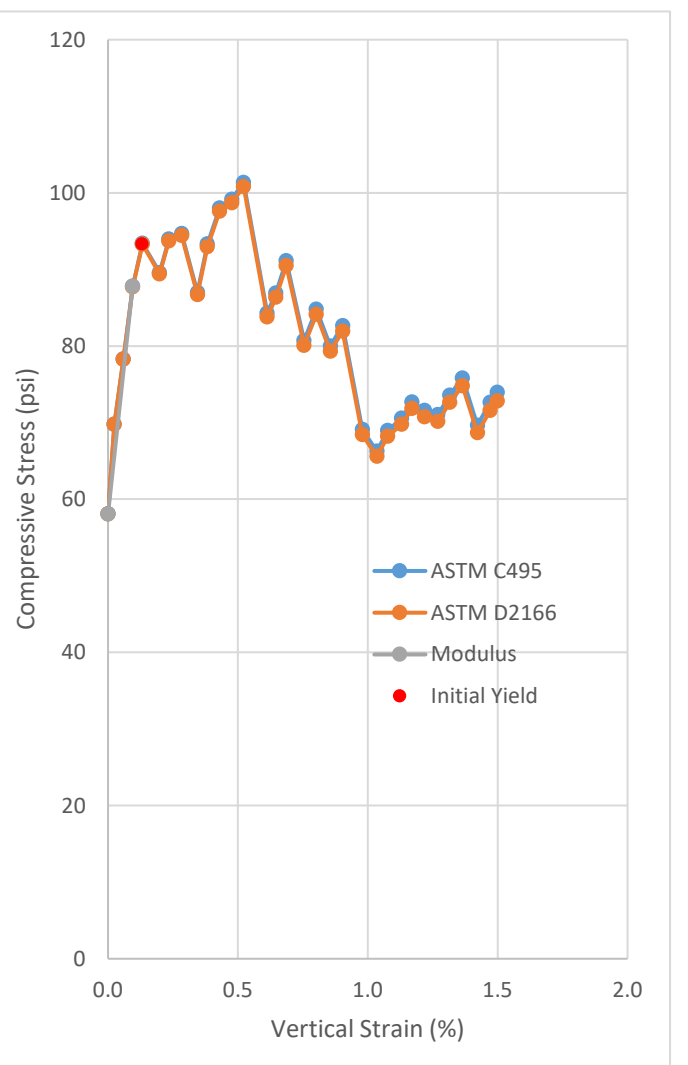

Uniaxial Compressive Strength of Lightweight Cellular Concrete

Sample ID:	**B2-13**
Height (in):	5.591
Height (mm):	142.0
Diameter (in):	2.976
Diameter (mm)	75.58
Area (in^2):	6.954
Area (mm^2):	4487
Mass (g):	236.11
Weight (lb):	0.5205
Weight (kN):	0.00231545
Volume (in^3):	38.88
Volume (mm^3):	637199
Density (g/mm^3):	0.0003705
Density (kg/m^3):	370.5
Unit Weight (pcf):	**23.13**
Unit Weight (kN/m^3):	3.634
Wet mass + tare (g):	550.64
Dry mass + tare (g):	506.43
Tare (g):	315.00
Water Content (%)	**23.09**
H:D ratio:	1.879
H:D correction:	0.9898

Age (days):	56
Cap:	Surface ground, 50 durometer end cap
Maximum load (lb):	745.05
Maximum load (kN):	3.314
Strain Rate (%/min):	2
Time to Failure (min):	0.50
Strain at Failure (%):	0.941
Initial yield (psi):	106.45
Modulus (psi):	19385
ASTM C495	
Comp. Strength (MPa):	0.7387
Comp. Strength (psi):	107.13
Corr. Comp. Strength (psi):	**106.04**
ASTM D2166	
Comp. Strength (kPa):	734.0
Comp. Strength (psi):	106.45
Corr. Comp. Strength (psi):	**105.36**
Treatment:	AD

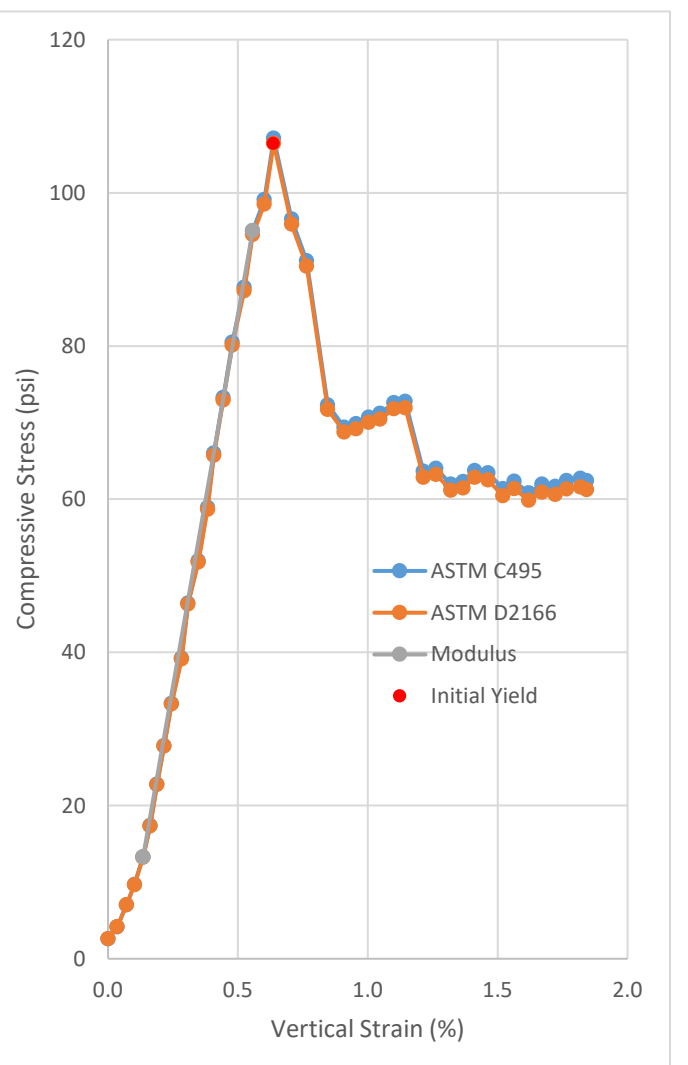

Uniaxial Compressive Strength of Lightweight Cellular Concrete

Sample ID:	**B3-11**
Height (in):	5.675
Height (mm):	144.1
Diameter (in):	2.965
Diameter (mm)	75.32
Area (in^2):	6.906
Area (mm^2):	4456
Mass (g):	245.72
Weight (lb):	0.5417
Weight (kN):	0.00240969
Volume (in^3):	39.19
Volume (mm^3):	642250
Density (g/mm^3):	0.0003826
Density (kg/m^3):	382.6
Unit Weight (pcf):	**23.88**
Unit Weight (kN/m^3):	3.752
Wet mass + tare (g):	555.52
Dry mass + tare (g):	511.09
Tare (g):	310.35
Water Content (%)	**22.13**
H:D ratio:	1.914
H:D correction:	0.9926

Age (days):	56
Cap:	Surface ground, 50 durometer end cap
Maximum load (lb):	1258.3
Maximum load (kN):	5.597
Strain Rate (%/min):	2
Time to Failure (min):	0.81
Strain at Failure (%):	1.607
Initial yield (psi):	169.66
Modulus (psi):	#N/A
ASTM C495	
Comp. Strength (MPa):	1.2562
Comp. Strength (psi):	182.20
Corr. Comp. Strength (psi):	**180.85**
ASTM D2166	
Comp. Strength (kPa):	1236.3
Comp. Strength (psi):	179.31
Corr. Comp. Strength (psi):	**177.98**
Treatment:	AD

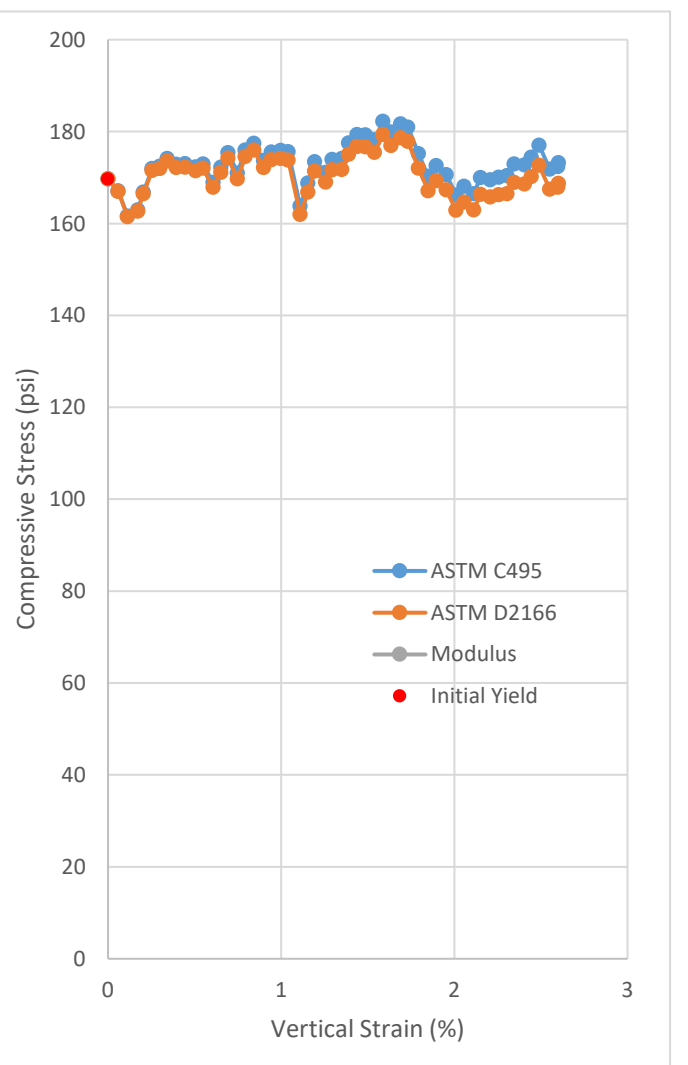

Note: Data acquisition error occurred during the initial portion of the test.

Uniaxial Compressive Strength of Lightweight Cellular Concrete

Sample ID:	**B3-12**
Height (in):	5.682
Height (mm):	144.3
Diameter (in):	2.962
Diameter (mm)	75.23
Area (in^2):	6.891
Area (mm^2):	4446
Mass (g):	246.97
Weight (lb):	0.5445
Weight (kN):	0.00242195
Volume (in^3):	39.15
Volume (mm^3):	641597
Density (g/mm^3):	0.0003849
Density (kg/m^3):	384.9
Unit Weight (pcf):	**24.03**
Unit Weight (kN/m^3):	3.775
Wet mass + tare (g):	710.98
Dry mass + tare (g):	666.42
Tare (g):	464.54
Water Content (%)	**22.07**
H:D ratio:	1.918
H:D correction:	0.9929

Age (days):	56
Cap:	Surface ground, 50 durometer end cap
Maximum load (lb):	1202.4
Maximum load (kN):	5.349
Strain Rate (%/min):	2
Time to Failure (min):	0.00
Strain at Failure (%):	0.000
Initial yield (psi):	174.50
Modulus (psi):	#N/A
ASTM C495	
Comp. Strength (MPa):	1.2031
Comp. Strength (psi):	174.50
Corr. Comp. Strength (psi):	**173.26**
ASTM D2166	
Comp. Strength (kPa):	1203.1
Comp. Strength (psi):	174.50
Corr. Comp. Strength (psi):	**173.26**
Treatment:	AD

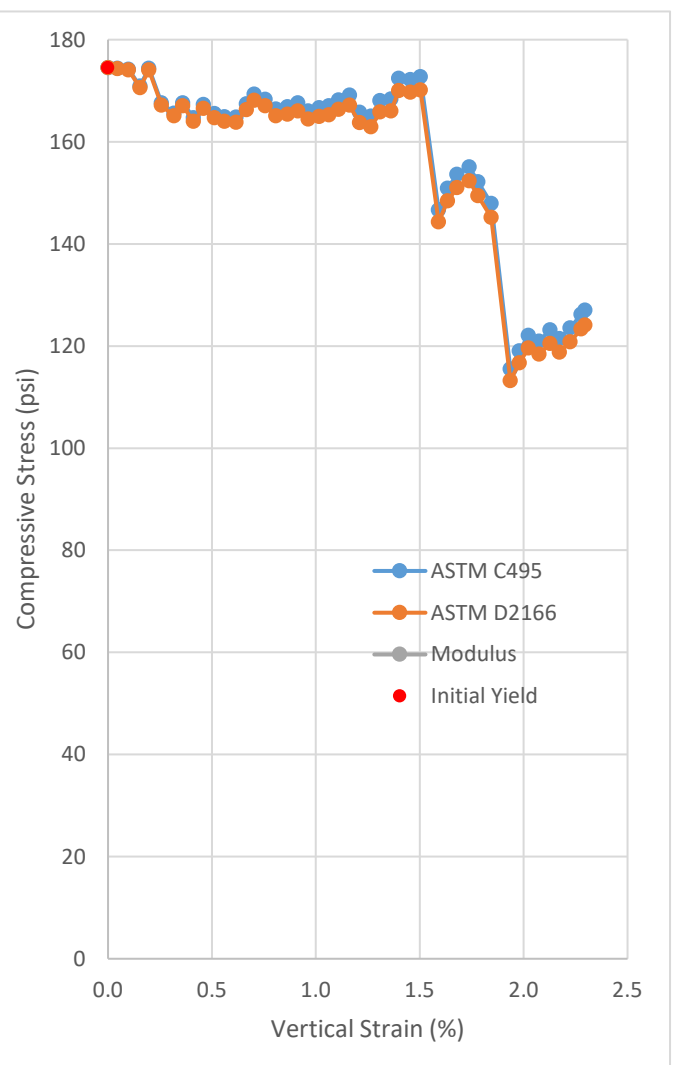

Note: Data acquisition error occurred during the initial portion of the test.

Uniaxial Compressive Strength of Lightweight Cellular Concrete

Sample ID:	**B3-13**
Height (in):	5.658
Height (mm):	143.7
Diameter (in):	2.972
Diameter (mm)	75.50
Area (in^2):	6.939
Area (mm^2):	4477
Mass (g):	246.39
Weight (lb):	0.5432
Weight (kN):	0.00241626
Volume (in^3):	39.26
Volume (mm^3):	643353
Density (g/mm^3):	0.0003830
Density (kg/m^3):	383.0
Unit Weight (pcf):	**23.91**
Unit Weight (kN/m^3):	3.756
Wet mass + tare (g):	654.06
Dry mass + tare (g):	607.86
Tare (g):	408.19
Water Content (%)	**23.14**
H:D ratio:	1.904
H:D correction:	0.9917

Age (days):	56
Cap:	Surface ground, 50 durometer end cap
Maximum load (lb):	1168.3
Maximum load (kN):	5.197
Strain Rate (%/min):	2
Time to Failure (min):	0.15
Strain at Failure (%):	0.253
Initial yield (psi):	163.34
Modulus (psi):	#N/A
ASTM C495	
Comp. Strength (MPa):	1.1609
Comp. Strength (psi):	168.37
Corr. Comp. Strength (psi):	**166.98**
ASTM D2166	
Comp. Strength (kPa):	1158.3
Comp. Strength (psi):	167.99
Corr. Comp. Strength (psi):	**166.60**
Treatment:	AD

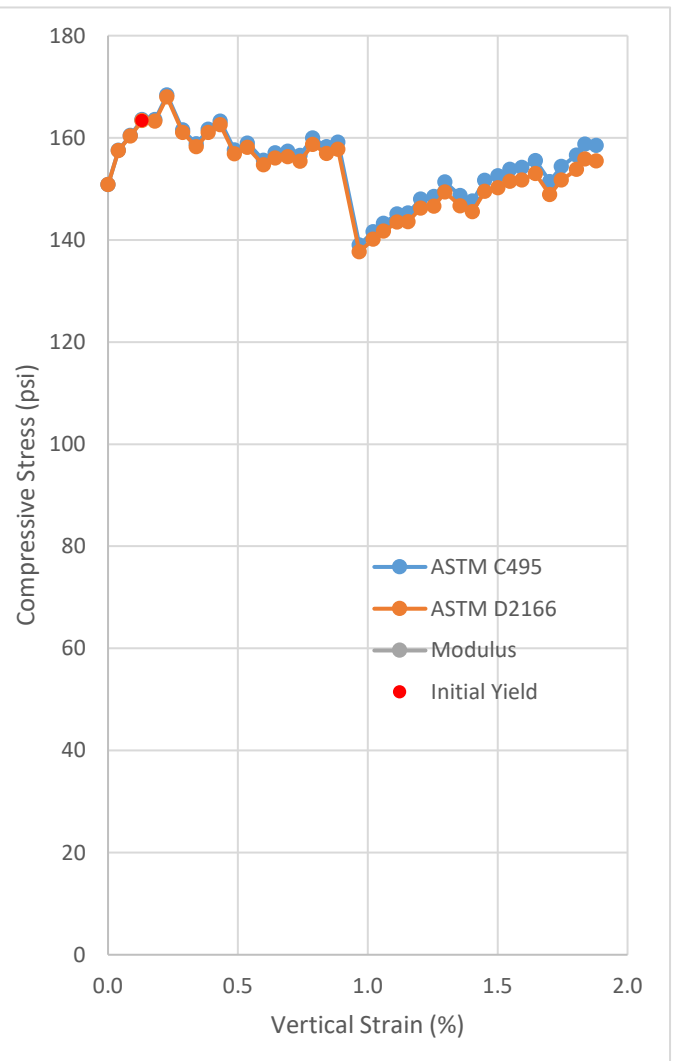

Note: Data acquisition error occurred during the initial portion of the test.

Uniaxial Compressive Strength of Lightweight Cellular Concrete

Sample ID:	**B1-14**
Height (in):	5.530
Height (mm):	140.5
Diameter (in):	2.973
Diameter (mm)	75.51
Area (in^2):	6.942
Area (mm^2):	4479
Mass (g):	229.41
Weight (lb):	0.5058
Weight (kN):	0.00224974
Volume (in^3):	38.39
Volume (mm^3):	629042
Density (g/mm^3):	0.0003647
Density (kg/m^3):	364.7
Unit Weight (pcf):	**22.77**
Unit Weight (kN/m^3):	3.576
Wet mass + tare (g):	620.11
Dry mass + tare (g):	579.22
Tare (g):	391.03
Water Content (%)	**21.73**
H:D ratio:	1.860
H:D correction:	0.9883

Age (days):	70
Cap:	Surface ground, 50 durometer end cap
Maximum load (lb):	666.37
Maximum load (kN):	2.964
Strain Rate (%/min):	2.5
Time to Failure (min):	0.56
Strain at Failure (%):	1.310
Initial yield (psi):	95.02
Modulus (psi):	14275
ASTM C495	
Comp. Strength (MPa):	0.6618
Comp. Strength (psi):	95.99
Corr. Comp. Strength (psi):	**94.87**
ASTM D2166	
Comp. Strength (kPa):	655.1
Comp. Strength (psi):	95.02
Corr. Comp. Strength (psi):	**93.90**
Treatment:	AD

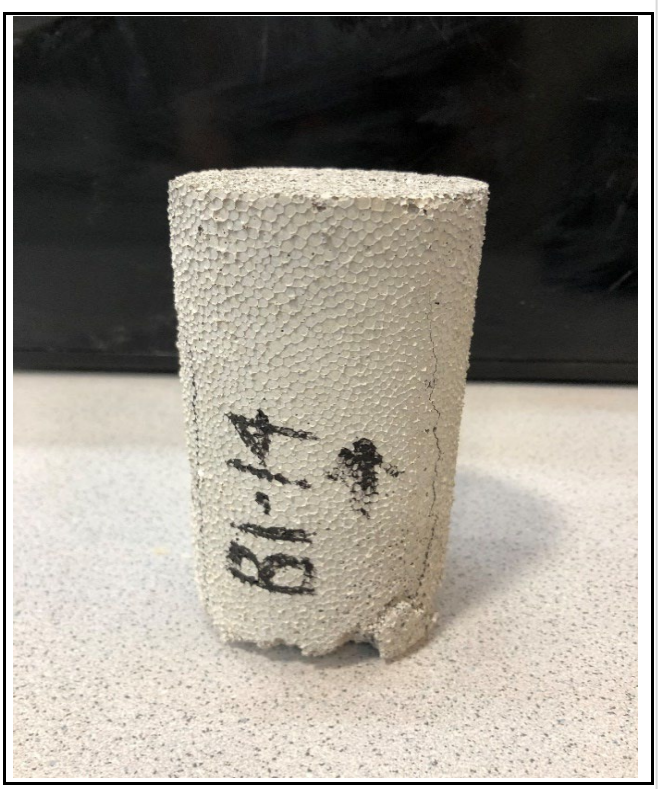

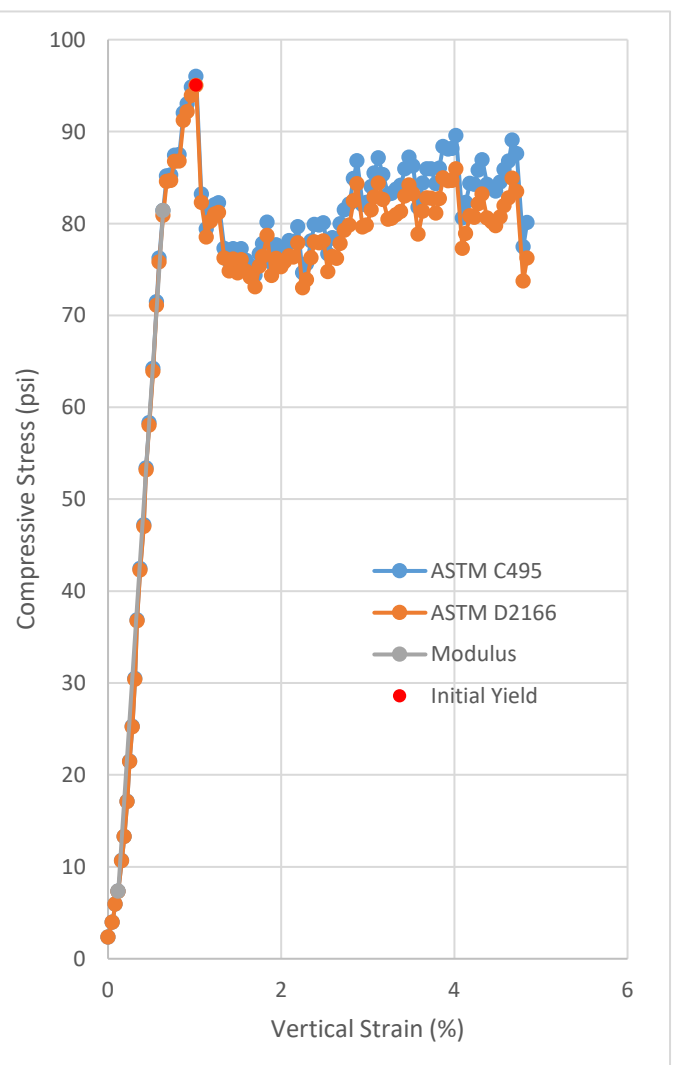

Uniaxial Compressive Strength of Lightweight Cellular Concrete

Sample ID:	**B1-15**
Height (in):	5.565
Height (mm):	141.3
Diameter (in):	2.968
Diameter (mm)	75.38
Area (in^2):	6.917
Area (mm^2):	4463
Mass (g):	225.17
Weight (lb):	0.4964
Weight (kN):	0.00220816
Volume (in^3):	38.49
Volume (mm^3):	630755
Density (g/mm^3):	0.0003570
Density (kg/m^3):	357.0
Unit Weight (pcf):	**22.29**
Unit Weight (kN/m^3):	3.501
Wet mass + tare (g):	633.26
Dry mass + tare (g):	594.76
Tare (g):	408.41
Water Content (%)	**20.66**
H:D ratio:	1.875
H:D correction:	0.9895

Age (days):	70
Cap:	Surface ground, 50 durometer end cap
Maximum load (lb):	573.36
Maximum load (kN):	2.550
Strain Rate (%/min):	2.5
Time to Failure (min):	0.38
Strain at Failure (%):	0.898
Initial yield (psi):	82.37
Modulus (psi):	14372
ASTM C495	
Comp. Strength (MPa):	0.5715
Comp. Strength (psi):	82.89
Corr. Comp. Strength (psi):	**82.02**
ASTM D2166	
Comp. Strength (kPa):	567.9
Comp. Strength (psi):	82.37
Corr. Comp. Strength (psi):	**81.50**
Treatment:	AD

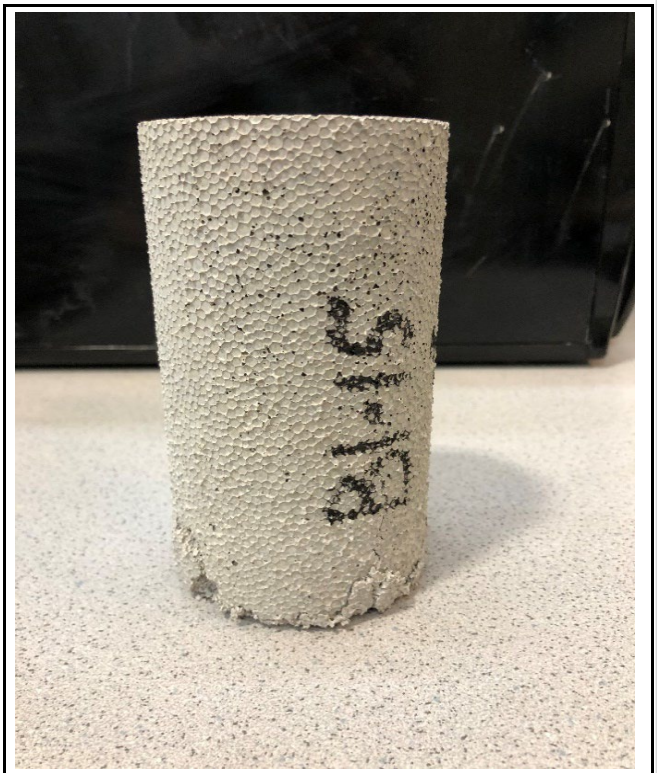

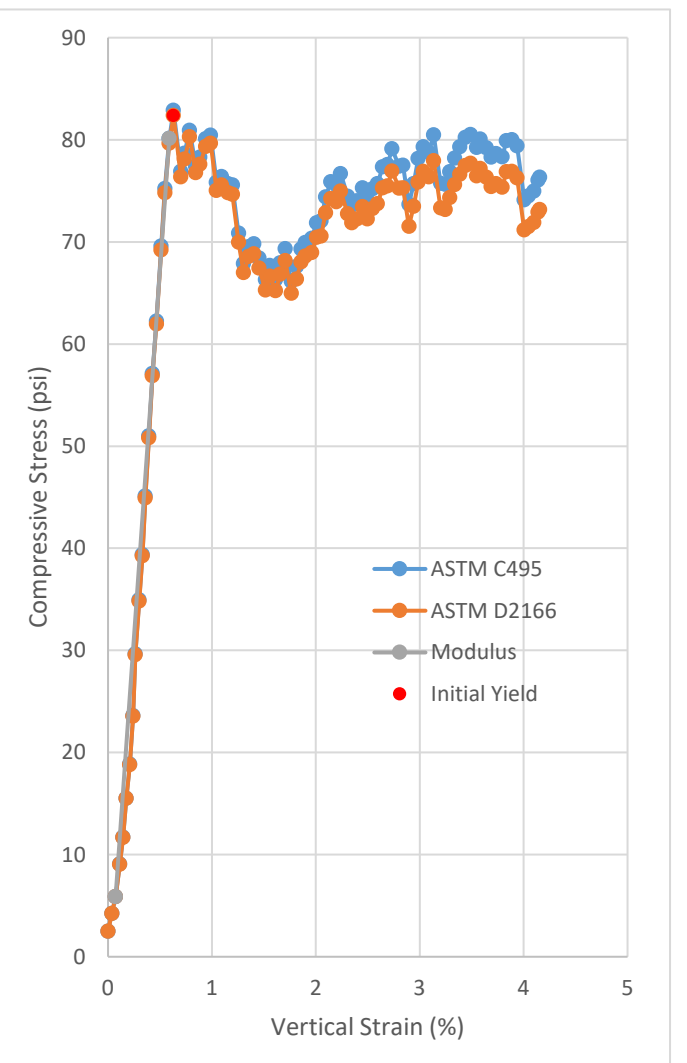

Uniaxial Compressive Strength of Lightweight Cellular Concrete

Sample ID:	**B1-16**
Height (in):	5.642
Height (mm):	143.3
Diameter (in):	2.984
Diameter (mm)	75.79
Area (in^2):	6.993
Area (mm^2):	4512
Mass (g):	235.89
Weight (lb):	0.5200
Weight (kN):	0.00231329
Volume (in^3):	39.46
Volume (mm^3):	646579
Density (g/mm^3):	0.0003648
Density (kg/m^3):	364.8
Unit Weight (pcf):	**22.78**
Unit Weight (kN/m^3):	3.578
Wet mass + tare (g):	643.22
Dry mass + tare (g):	601.80
Tare (g):	407.89
Water Content (%)	**21.36**
H:D ratio:	1.891
H:D correction:	0.9907

Age (days):	70
Cap:	Surface ground, 50 durometer end cap
Maximum load (lb):	854.91
Maximum load (kN):	3.803
Strain Rate (%/min):	2.5
Time to Failure (min):	0.53
Strain at Failure (%):	1.203
Initial yield (psi):	120.67
Modulus (psi):	21655
ASTM C495	
Comp. Strength (MPa):	0.8429
Comp. Strength (psi):	122.25
Corr. Comp. Strength (psi):	**121.11**
ASTM D2166	
Comp. Strength (kPa):	836.5
Comp. Strength (psi):	121.33
Corr. Comp. Strength (psi):	**120.20**
Treatment:	AD

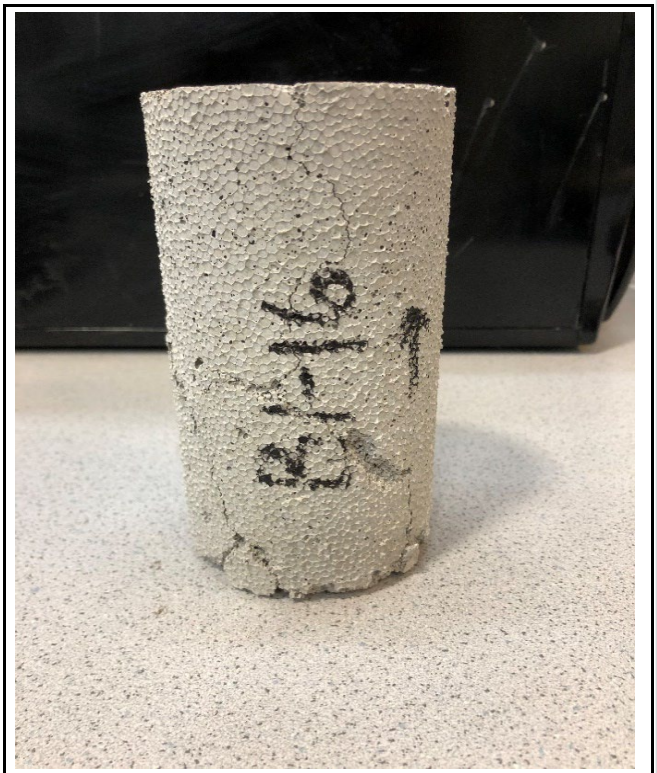

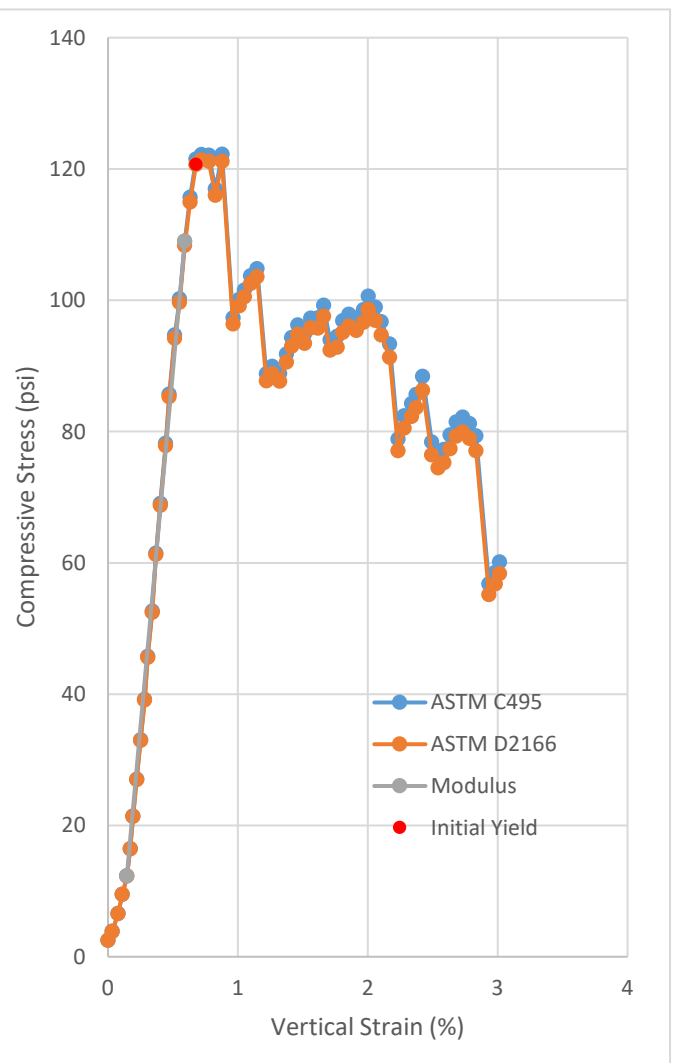

Uniaxial Compressive Strength of Lightweight Cellular Concrete

Sample ID:	**B2-14**
Height (in):	5.642
Height (mm):	143.3
Diameter (in):	2.981
Diameter (mm)	75.72
Area (in^2):	6.979
Area (mm^2):	4503
Mass (g):	245.02
Weight (lb):	0.5402
Weight (kN):	0.00240283
Volume (in^3):	39.38
Volume (mm^3):	645318
Density (g/mm^3):	0.0003797
Density (kg/m^3):	379.7
Unit Weight (pcf):	**23.70**
Unit Weight (kN/m^3):	3.723
Wet mass + tare (g):	654.32
Dry mass + tare (g):	611.76
Tare (g):	409.70
Water Content (%)	**21.06**
H:D ratio:	1.893
H:D correction:	0.9909

Age (days):	70
Cap:	Surface ground, 50 durometer end cap
Maximum load (lb):	1221.3
Maximum load (kN):	5.433
Strain Rate (%/min):	2.5
Time to Failure (min):	0.50
Strain at Failure (%):	1.098
Initial yield (psi):	173.77
Modulus (psi):	31666
ASTM C495	
Comp. Strength (MPa):	1.2065
Comp. Strength (psi):	174.99
Corr. Comp. Strength (psi):	**173.39**
ASTM D2166	
Comp. Strength (kPa):	1198.1
Comp. Strength (psi):	173.77
Corr. Comp. Strength (psi):	**172.18**
Treatment:	AD

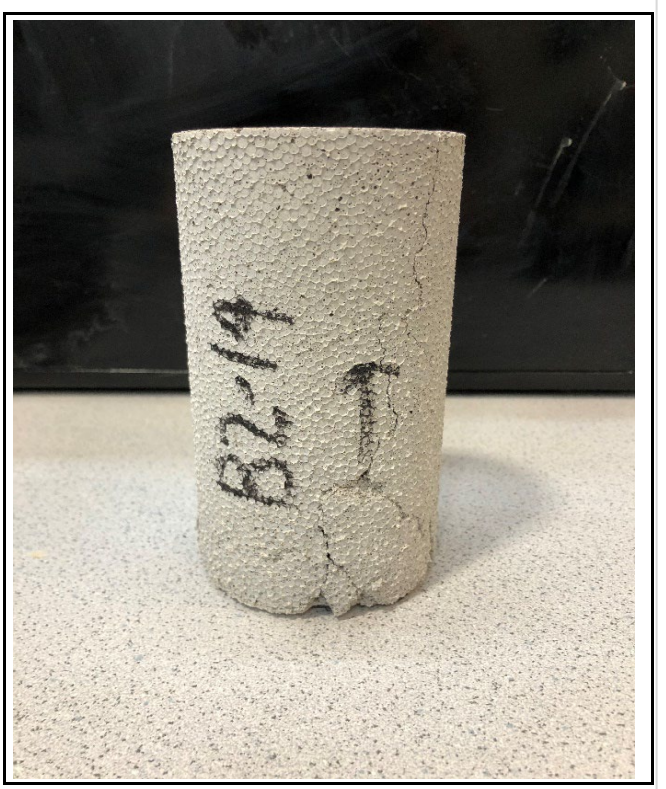

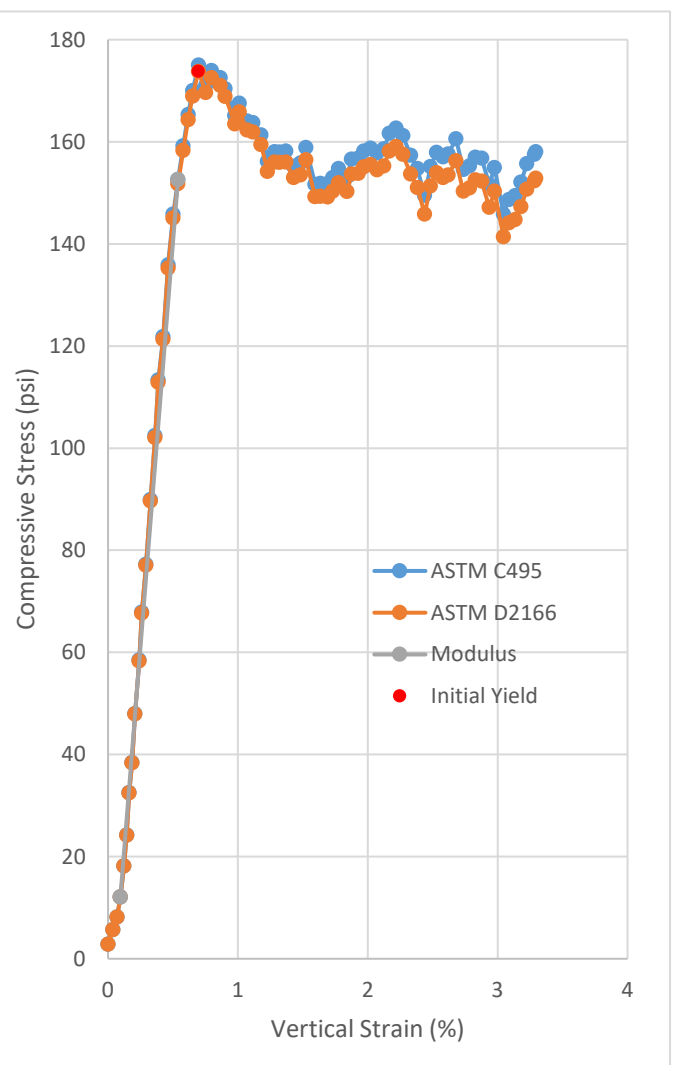

Uniaxial Compressive Strength of Lightweight Cellular Concrete

Sample ID:	**B2-15**
Height (in):	5.657
Height (mm):	143.7
Diameter (in):	2.976
Diameter (mm)	75.58
Area (in^2):	6.954
Area (mm^2):	4487
Mass (g):	234.25
Weight (lb):	0.5164
Weight (kN):	0.00229721
Volume (in^3):	39.34
Volume (mm^3):	644644
Density (g/mm^3):	0.0003634
Density (kg/m^3):	363.4
Unit Weight (pcf):	**22.68**
Unit Weight (kN/m^3):	3.564
Wet mass + tare (g):	642.57
Dry mass + tare (g):	604.22
Tare (g):	408.75
Water Content (%)	**19.62**
H:D ratio:	1.901
H:D correction:	0.9915

Age (days):	70
Cap:	Surface ground, 50 durometer end cap
Maximum load (lb):	887.67
Maximum load (kN):	3.949
Strain Rate (%/min):	2.5
Time to Failure (min):	1.96
Strain at Failure (%):	4.755
Initial yield (psi):	123.35
Modulus (psi):	23655
ASTM C495	
Comp. Strength (MPa):	0.8801
Comp. Strength (psi):	127.64
Corr. Comp. Strength (psi):	**126.56**
ASTM D2166	
Comp. Strength (kPa):	850.5
Comp. Strength (psi):	123.35
Corr. Comp. Strength (psi):	**122.31**
Treatment:	AD

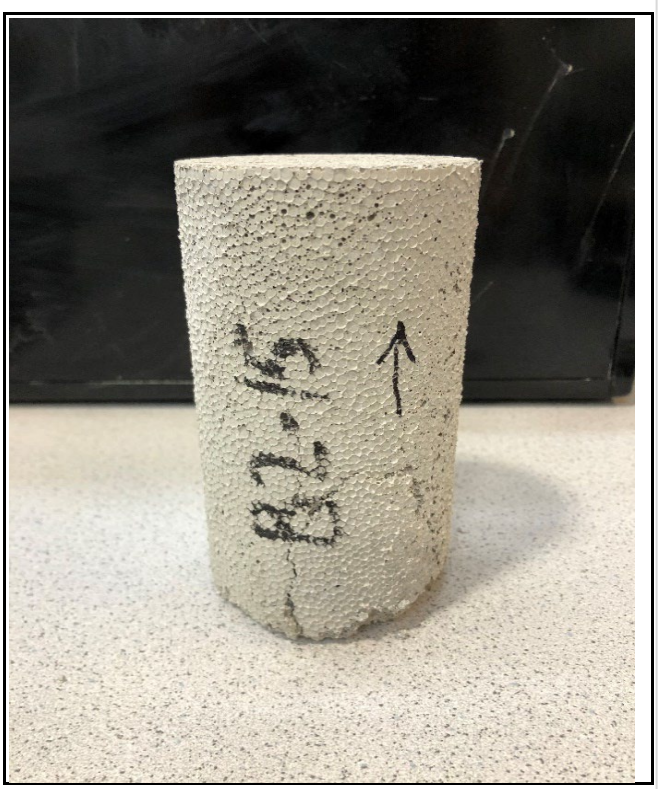

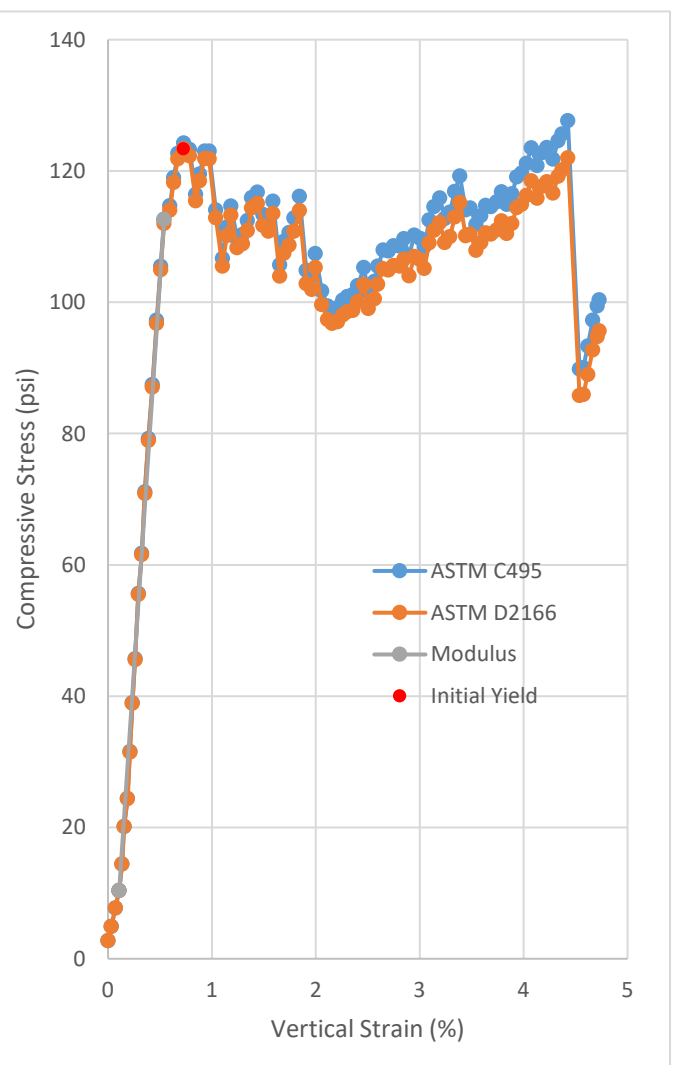

Uniaxial Compressive Strength of Lightweight Cellular Concrete

Sample ID:	**B2-16**
Height (in):	5.639
Height (mm):	143.2
Diameter (in):	2.970
Diameter (mm)	75.43
Area (in^2):	6.926
Area (mm^2):	4469
Mass (g):	242.87
Weight (lb):	0.5354
Weight (kN):	0.00238174
Volume (in^3):	39.06
Volume (mm^3):	640042
Density (g/mm^3):	0.0003795
Density (kg/m^3):	379.5
Unit Weight (pcf):	**23.69**
Unit Weight (kN/m^3):	3.721
Wet mass + tare (g):	570.36
Dry mass + tare (g):	527.23
Tare (g):	328.06
Water Content (%)	**21.65**
H:D ratio:	1.899
H:D correction:	0.9914

Age (days):	70
Cap:	Surface ground, 50 durometer end cap
Maximum load (lb):	1174.9
Maximum load (kN):	5.226
Strain Rate (%/min):	2.5
Time to Failure (min):	0.56
Strain at Failure (%):	1.302
Initial yield (psi):	144.88
Modulus (psi):	27565
ASTM C495	
Comp. Strength (MPa):	1.1695
Comp. Strength (psi):	169.63
Corr. Comp. Strength (psi):	**168.16**
ASTM D2166	
Comp. Strength (kPa):	1158.9
Comp. Strength (psi):	168.08
Corr. Comp. Strength (psi):	**166.63**
Treatment:	AD

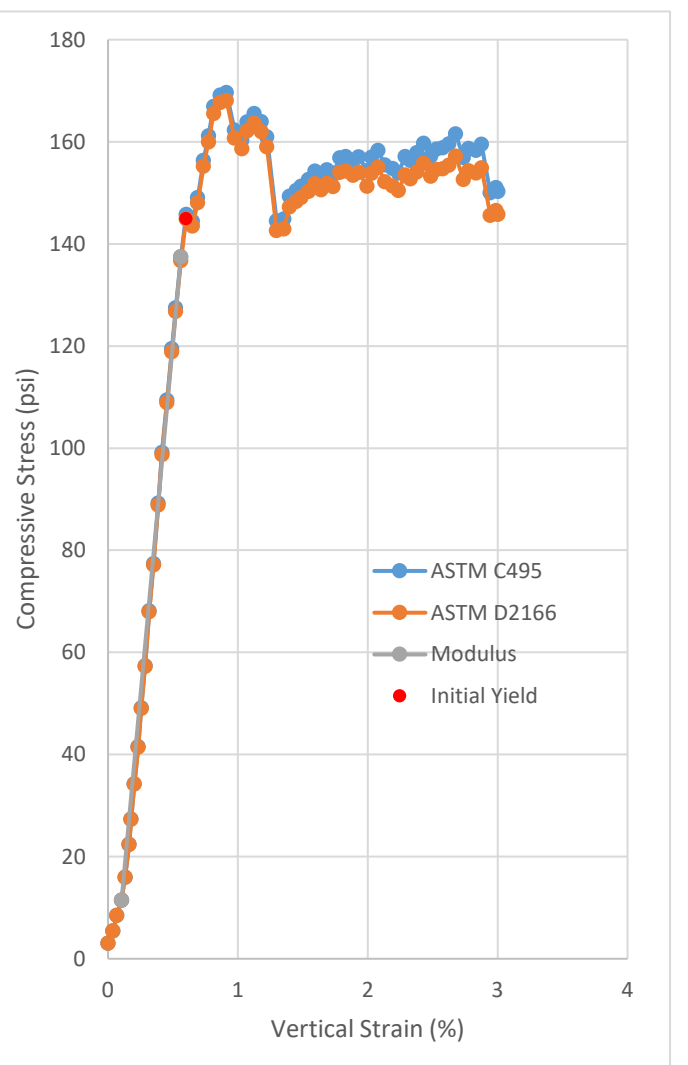

Uniaxial Compressive Strength of Lightweight Cellular Concrete

Sample ID:	**B3-14**
Height (in):	5.687
Height (mm):	144.4
Diameter (in):	2.970
Diameter (mm)	75.44
Area (in^2):	6.928
Area (mm^2):	4470
Mass (g):	241.48
Weight (lb):	0.5324
Weight (kN):	0.00236811
Volume (in^3):	39.40
Volume (mm^3):	645635
Density (g/mm^3):	0.0003740
Density (kg/m^3):	374.0
Unit Weight (pcf):	**23.35**
Unit Weight (kN/m^3):	3.668
Wet mass + tare (g):	551.17
Dry mass + tare (g):	510.37
Tare (g):	310.19
Water Content (%)	**20.38**
H:D ratio:	1.915
H:D correction:	0.9927

Age (days):	70
Cap:	Surface ground, 50 durometer end cap
Maximum load (lb):	1386.4
Maximum load (kN):	6.167
Strain Rate (%/min):	2.5
Time to Failure (min):	0.84
Strain at Failure (%):	1.958
Initial yield (psi):	188.53
Modulus (psi):	29322
ASTM C495	
Comp. Strength (MPa):	1.3798
Comp. Strength (psi):	200.12
Corr. Comp. Strength (psi):	**198.65**
ASTM D2166	
Comp. Strength (kPa):	1358.8
Comp. Strength (psi):	197.07
Corr. Comp. Strength (psi):	**195.62**
Treatment:	AD

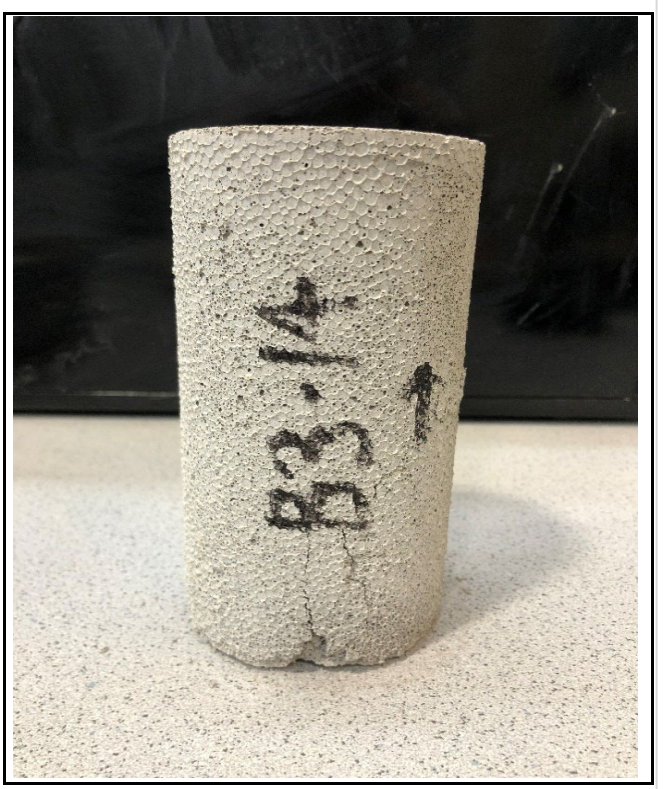

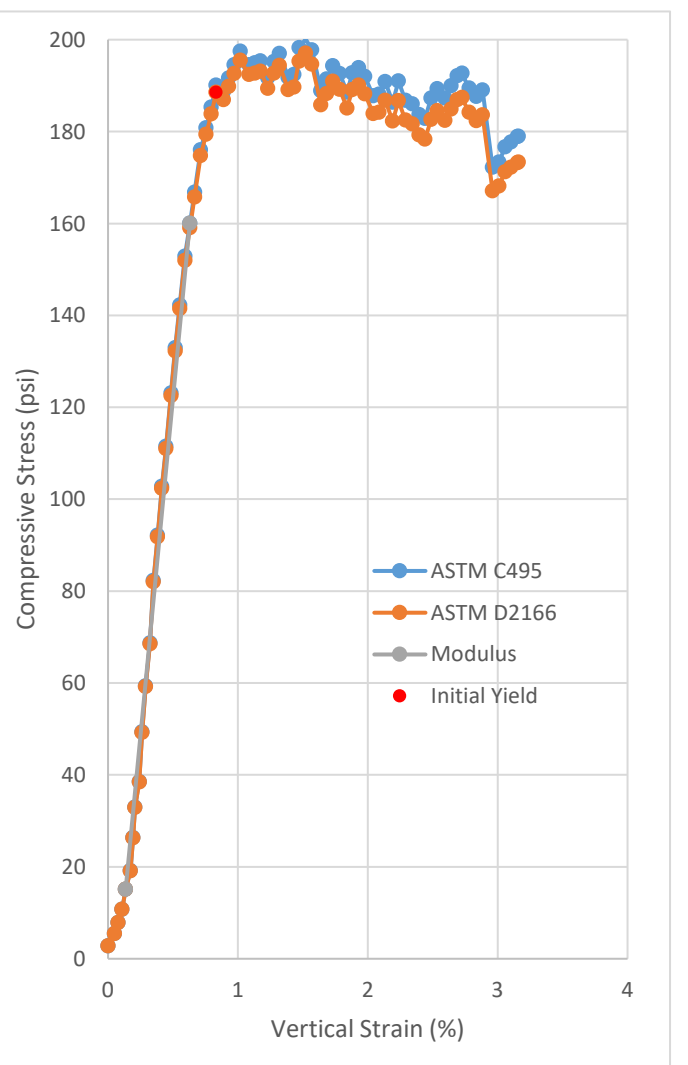

Uniaxial Compressive Strength of Lightweight Cellular Concrete

Sample ID:	**B3-15**
Height (in):	5.556
Height (mm):	141.1
Diameter (in):	2.966
Diameter (mm)	75.34
Area (in^2):	6.911
Area (mm^2):	4459
Mass (g):	234.15
Weight (lb):	0.5162
Weight (kN):	0.00229623
Volume (in^3):	38.39
Volume (mm^3):	629169
Density (g/mm^3):	0.0003722
Density (kg/m^3):	372.2
Unit Weight (pcf):	**23.23**
Unit Weight (kN/m^3):	3.650
Wet mass + tare (g):	545.19
Dry mass + tare (g):	505.94
Tare (g):	310.45
Water Content (%)	**20.08**
H:D ratio:	1.873
H:D correction:	0.9893

Age (days):	70
Cap:	Surface ground, 50 durometer end cap
Maximum load (lb):	1265.1
Maximum load (kN):	5.627
Strain Rate (%/min):	2.5
Time to Failure (min):	1.94
Strain at Failure (%):	4.690
Initial yield (psi):	160.85
Modulus (psi):	28667
ASTM C495	
Comp. Strength (MPa):	1.2622
Comp. Strength (psi):	183.06
Corr. Comp. Strength (psi):	**181.10**
ASTM D2166	
Comp. Strength (kPa):	1208.2
Comp. Strength (psi):	175.24
Corr. Comp. Strength (psi):	**173.37**
Treatment:	AD

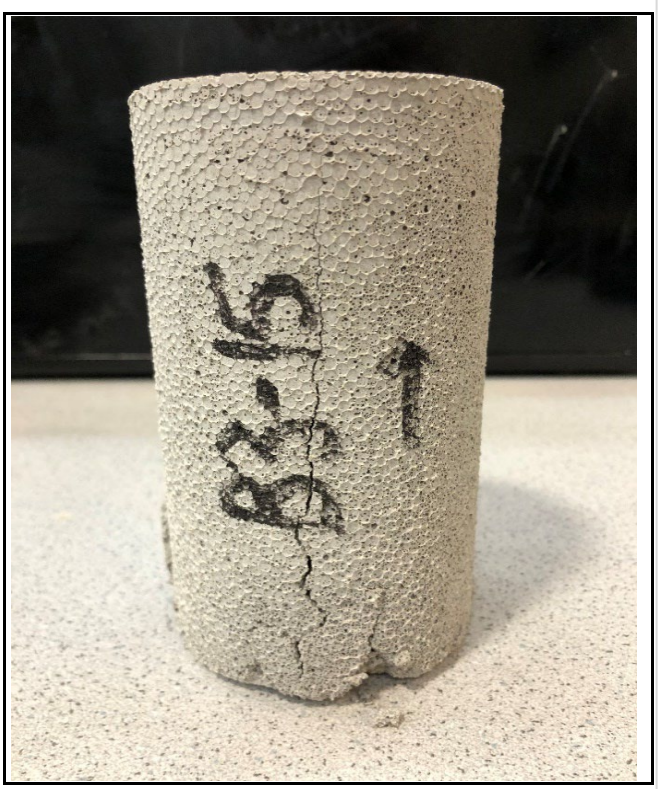

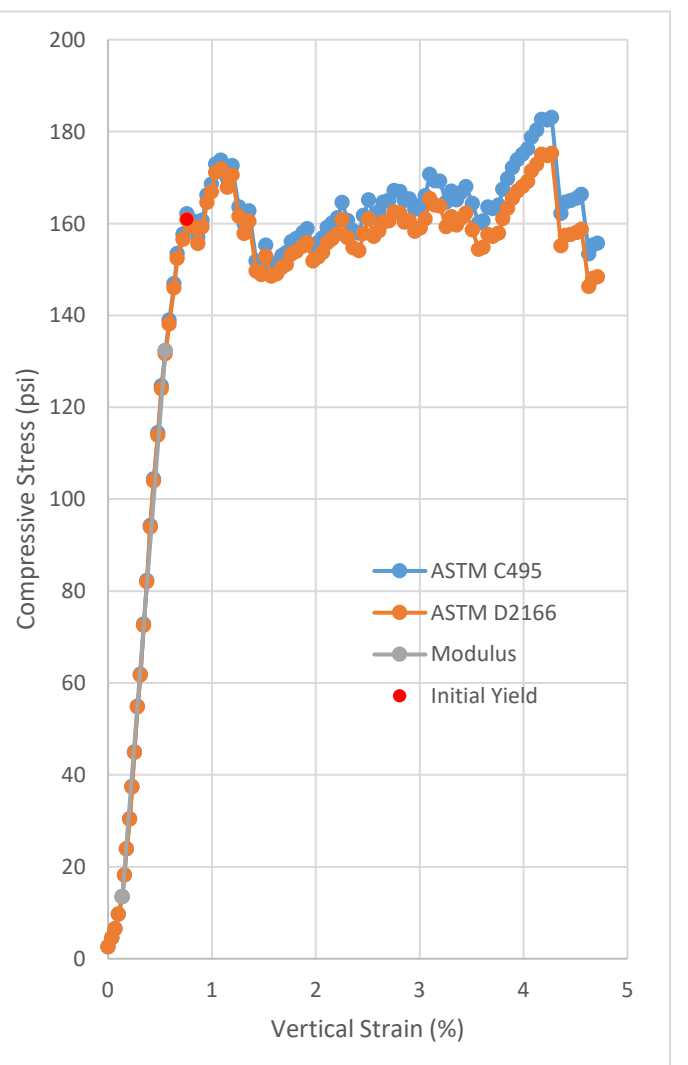

Uniaxial Compressive Strength of Lightweight Cellular Concrete

Sample ID:	**B3-16**
Height (in):	5.663
Height (mm):	143.8
Diameter (in):	2.976
Diameter (mm)	75.58
Area (in^2):	6.954
Area (mm^2):	4487
Mass (g):	241.29
Weight (lb):	0.5320
Weight (kN):	0.00236625
Volume (in^3):	39.38
Volume (mm^3):	645404
Density (g/mm^3):	0.0003739
Density (kg/m^3):	373.9
Unit Weight (pcf):	**23.34**
Unit Weight (kN/m^3):	3.666
Wet mass + tare (g):	551.20
Dry mass + tare (g):	512.46
Tare (g):	310.46
Water Content (%)	**19.18**
H:D ratio:	1.903
H:D correction:	0.9917

Age (days):	70
Cap:	Surface ground, 50 durometer end cap
Maximum load (lb):	1466.8
Maximum load (kN):	6.525
Strain Rate (%/min):	2.5
Time to Failure (min):	0.75
Strain at Failure (%):	1.703
Initial yield (psi):	190.82
Modulus (psi):	33382
ASTM C495	
Comp. Strength (MPa):	1.4542
Comp. Strength (psi):	210.92
Corr. Comp. Strength (psi):	**209.17**
ASTM D2166	
Comp. Strength (kPa):	1438.5
Comp. Strength (psi):	208.64
Corr. Comp. Strength (psi):	**206.91**
Treatment:	AD

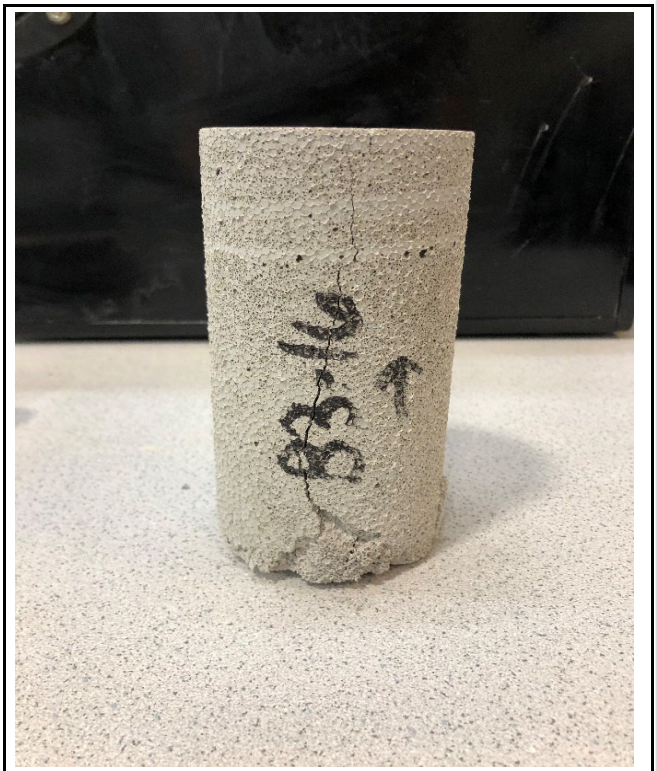

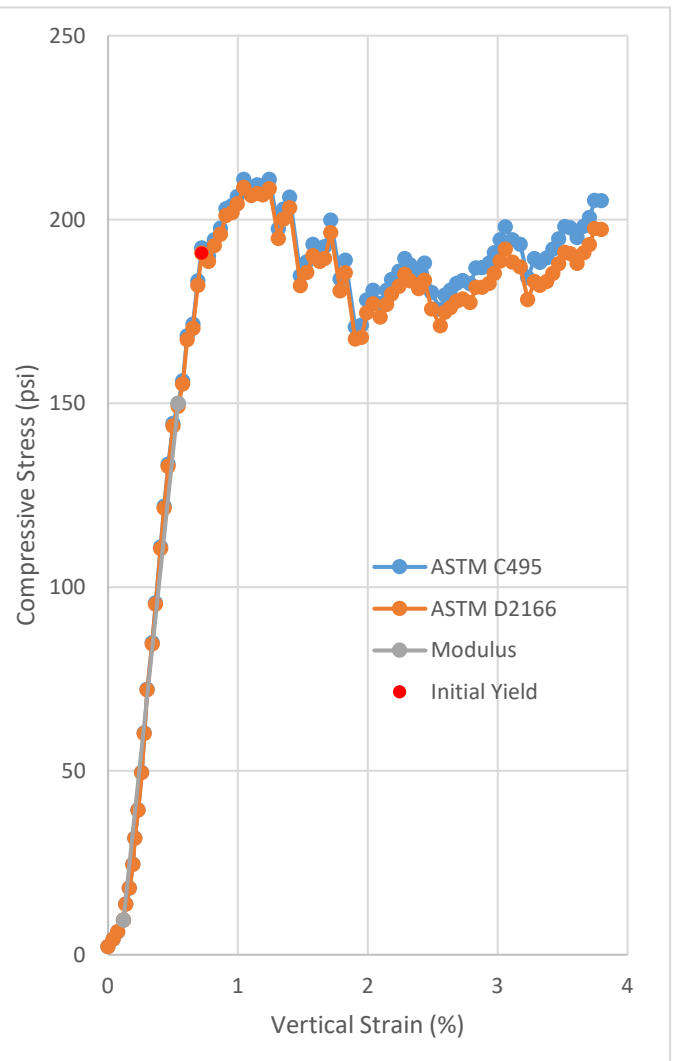

Uniaxial Compressive Strength of Lightweight Cellular Concrete

Sample ID:	**B1-17**
Height (in):	5.616
Height (mm):	142.6
Diameter (in):	2.963
Diameter (mm)	75.26
Area (in^2):	6.895
Area (mm^2):	4449
Mass (g):	234.02
Weight (lb):	0.5159
Weight (kN):	0.00229495
Volume (in^3):	38.72
Volume (mm^3):	634573
Density (g/mm^3):	0.0003688
Density (kg/m^3):	368.8
Unit Weight (pcf):	**23.02**
Unit Weight (kN/m^3):	3.617
Wet mass + tare (g):	544.22
Dry mass + tare (g):	504.83
Tare (g):	310.49
Water Content (%)	**20.27**
H:D ratio:	1.895
H:D correction:	0.9911

Age (days):	99
Cap:	Surface ground, 50 durometer end cap
Maximum load (lb):	1058.4
Maximum load (kN):	4.708
Strain Rate (%/min):	2.5
Time to Failure (min):	0.53
Strain at Failure (%):	1.190
Initial yield (psi):	150.55
Modulus (psi):	26647
ASTM C495	
Comp. Strength (MPa):	1.0583
Comp. Strength (psi):	153.50
Corr. Comp. Strength (psi):	**152.13**
ASTM D2166	
Comp. Strength (kPa):	1049.6
Comp. Strength (psi):	152.23
Corr. Comp. Strength (psi):	**150.88**
Treatment:	AD

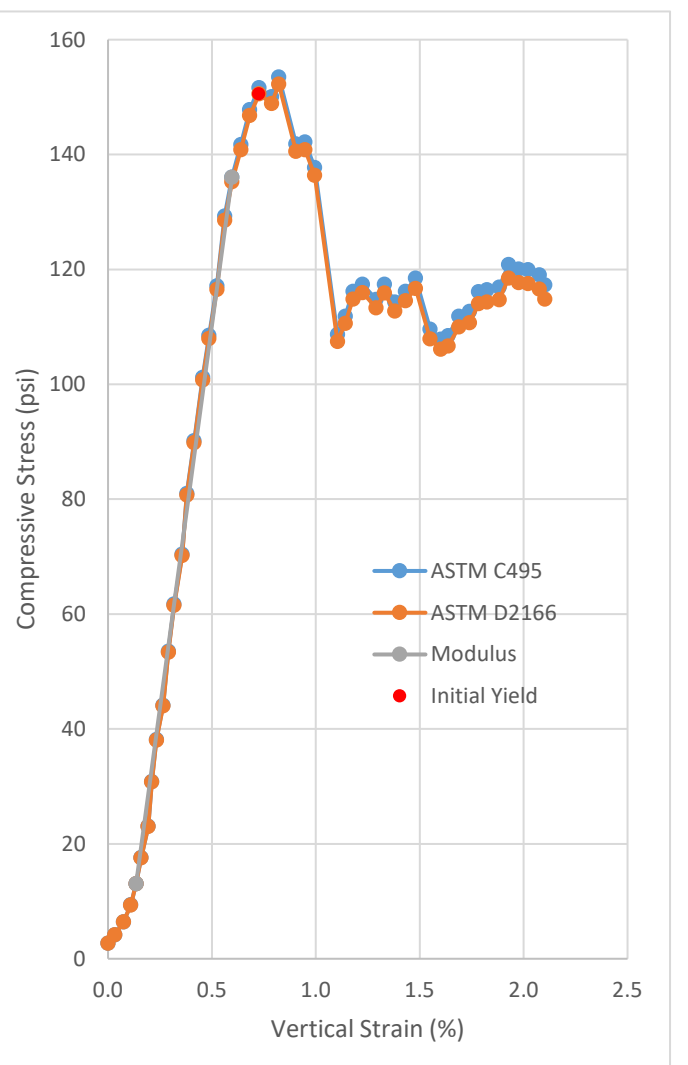

Uniaxial Compressive Strength of Lightweight Cellular Concrete

Sample ID:	**B1-18**
Height (in):	5.556
Height (mm):	141.1
Diameter (in):	2.958
Diameter (mm)	75.12
Area (in^2):	6.870
Area (mm^2):	4433
Mass (g):	229.71
Weight (lb):	0.5064
Weight (kN):	0.00225269
Volume (in^3):	38.17
Volume (mm^3):	625498
Density (g/mm^3):	0.0003672
Density (kg/m^3):	367.2
Unit Weight (pcf):	**22.93**
Unit Weight (kN/m^3):	3.601
Wet mass + tare (g):	539.81
Dry mass + tare (g):	500.33
Tare (g):	310.36
Water Content (%)	**20.78**
H:D ratio:	1.878
H:D correction:	0.9897

Age (days):	99
Cap:	Surface ground, 50 durometer end cap
Maximum load (lb):	1068.7
Maximum load (kN):	4.754
Strain Rate (%/min):	2.5
Time to Failure (min):	0.57
Strain at Failure (%):	1.343
Initial yield (psi):	147.43
Modulus (psi):	26251
ASTM C495	
Comp. Strength (MPa):	1.0725
Comp. Strength (psi):	155.55
Corr. Comp. Strength (psi):	**153.95**
ASTM D2166	
Comp. Strength (kPa):	1062.1
Comp. Strength (psi):	154.04
Corr. Comp. Strength (psi):	**152.46**
Treatment:	AD

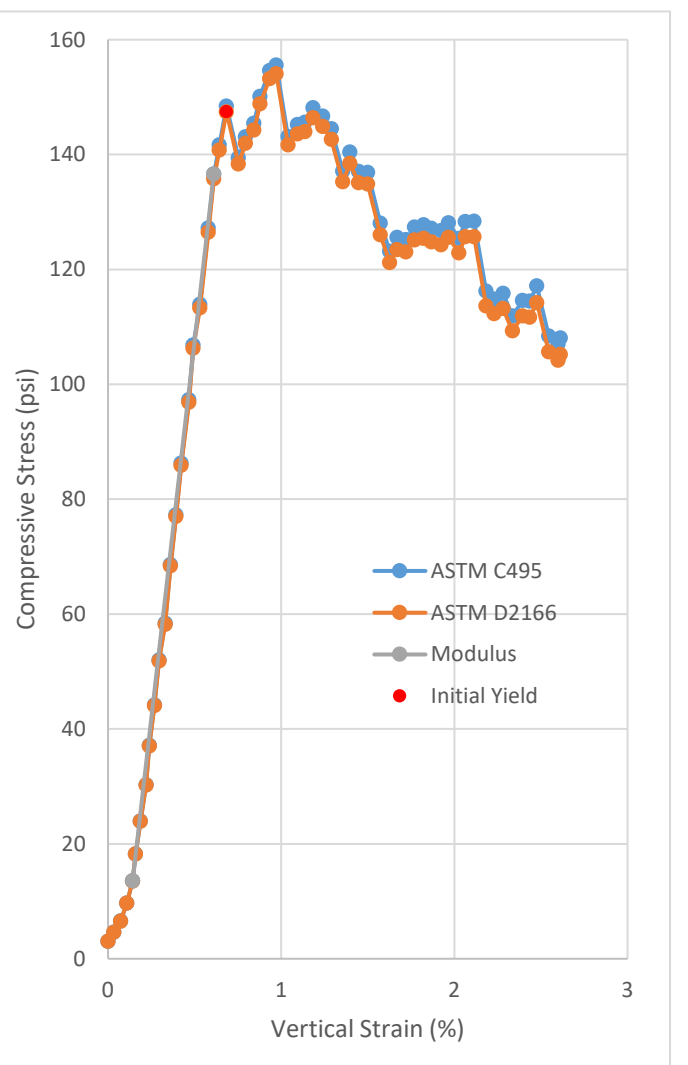

Uniaxial Compressive Strength of Lightweight Cellular Concrete

Sample ID:	**B1-19**
Height (in):	5.601
Height (mm):	142.3
Diameter (in):	2.968
Diameter (mm)	75.39
Area (in^2):	6.919
Area (mm^2):	4464
Mass (g):	231.59
Weight (lb):	0.5106
Weight (kN):	0.00227112
Volume (in^3):	38.75
Volume (mm^3):	635053
Density (g/mm^3):	0.0003647
Density (kg/m^3):	364.7
Unit Weight (pcf):	**22.77**
Unit Weight (kN/m^3):	3.576
Wet mass + tare (g):	563.52
Dry mass + tare (g):	523.57
Tare (g):	332.26
Water Content (%)	**20.88**
H:D ratio:	1.887
H:D correction:	0.9904

Age (days):	99
Cap:	Surface ground, 50 durometer end cap
Maximum load (lb):	1058.3
Maximum load (kN):	4.708
Strain Rate (%/min):	2.5
Time to Failure (min):	0.52
Strain at Failure (%):	1.206
Initial yield (psi):	141.68
Modulus (psi):	24512
ASTM C495	
Comp. Strength (MPa):	1.0547
Comp. Strength (psi):	152.96
Corr. Comp. Strength (psi):	**151.50**
ASTM D2166	
Comp. Strength (kPa):	1045.8
Comp. Strength (psi):	151.68
Corr. Comp. Strength (psi):	**150.23**
Treatment:	AD

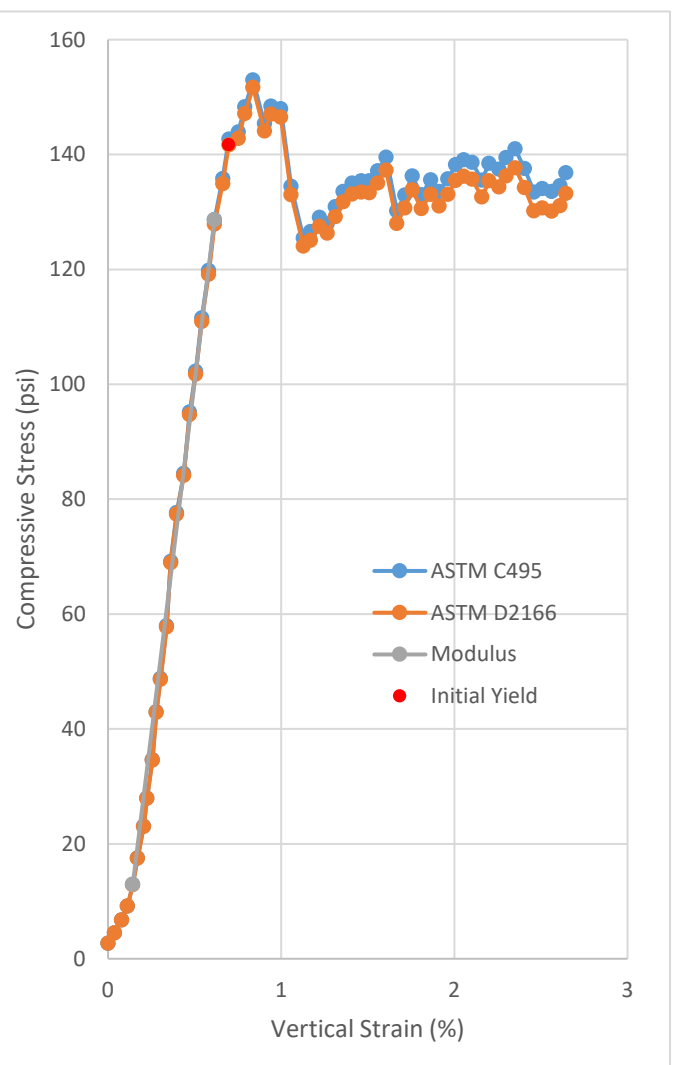

Uniaxial Compressive Strength of Lightweight Cellular Concrete

Sample ID:	**B2-17**
Height (in):	5.588
Height (mm):	141.9
Diameter (in):	2.974
Diameter (mm)	75.54
Area (in^2):	6.947
Area (mm^2):	4482
Mass (g):	226.79
Weight (lb):	0.5000
Weight (kN):	0.00222405
Volume (in^3):	38.82
Volume (mm^3):	636106
Density (g/mm^3):	0.0003565
Density (kg/m^3):	356.5
Unit Weight (pcf):	**22.26**
Unit Weight (kN/m^3):	3.496
Wet mass + tare (g):	634.43
Dry mass + tare (g):	598.77
Tare (g):	407.89
Water Content (%)	**18.68**
H:D ratio:	1.879
H:D correction:	0.9898

Age (days):	99
Cap:	Surface ground, 50 durometer end cap
Maximum load (lb):	853.85
Maximum load (kN):	3.798
Strain Rate (%/min):	2.5
Time to Failure (min):	0.50
Strain at Failure (%):	1.155
Initial yield (psi):	121.90
Modulus (psi):	22106
ASTM C495	
Comp. Strength (MPa):	0.8475
Comp. Strength (psi):	122.92
Corr. Comp. Strength (psi):	**121.66**
ASTM D2166	
Comp. Strength (kPa):	840.5
Comp. Strength (psi):	121.90
Corr. Comp. Strength (psi):	**120.65**
Treatment:	AD

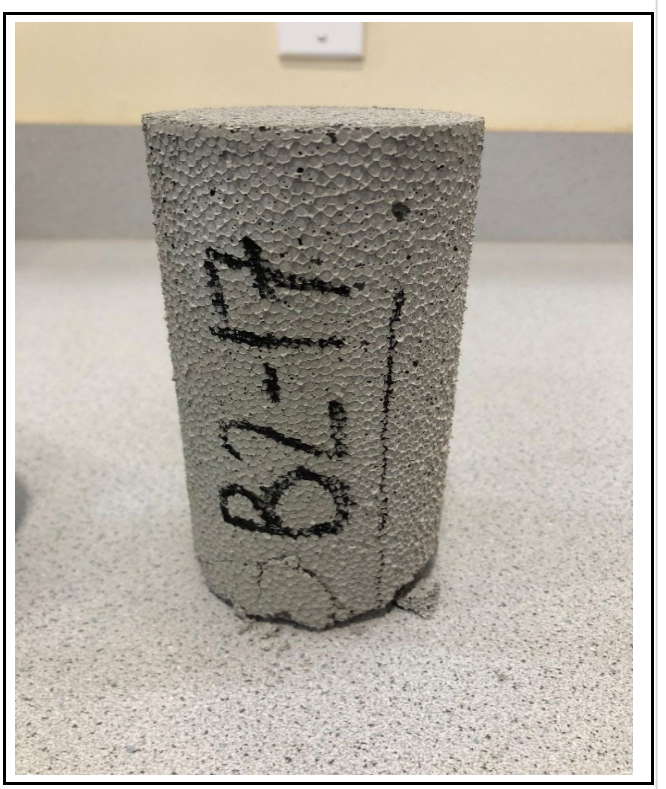

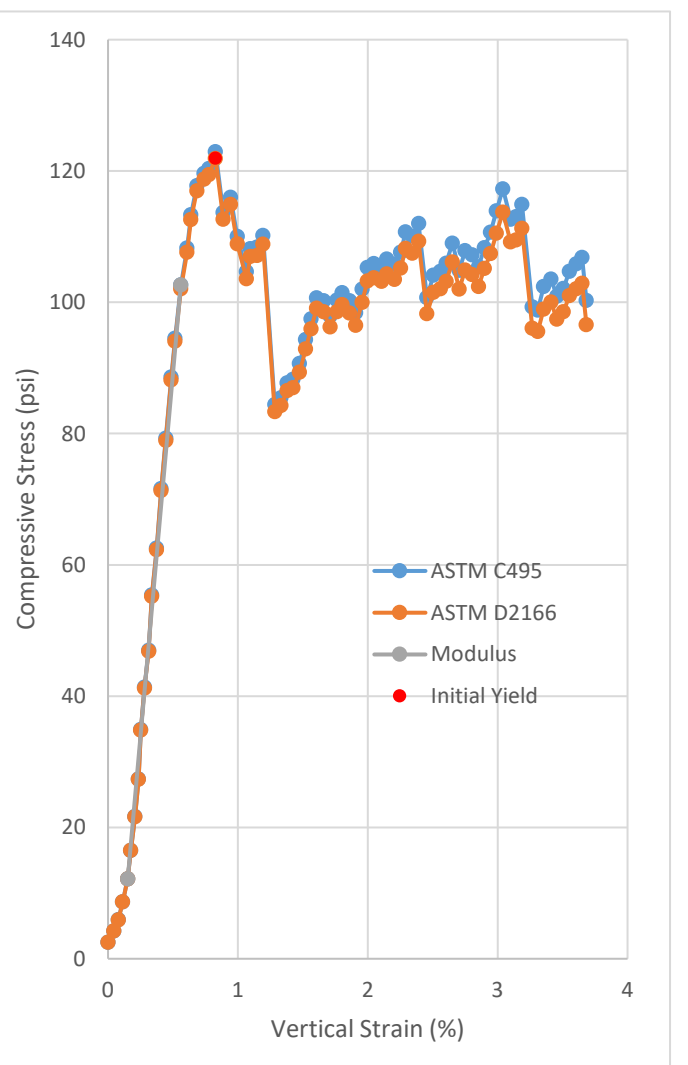

Uniaxial Compressive Strength of Lightweight Cellular Concrete

Sample ID:	**B2-18**
Height (in):	5.598
Height (mm):	142.2
Diameter (in):	2.968
Diameter (mm)	75.38
Area (in^2):	6.917
Area (mm^2):	4463
Mass (g):	229.05
Weight (lb):	0.5050
Weight (kN):	0.00224621
Volume (in^3):	38.72
Volume (mm^3):	634495
Density (g/mm^3):	0.0003610
Density (kg/m^3):	361.0
Unit Weight (pcf):	**22.54**
Unit Weight (kN/m^3):	3.540
Wet mass + tare (g):	638.53
Dry mass + tare (g):	601.83
Tare (g):	409.77
Water Content (%)	**19.11**
H:D ratio:	1.886
H:D correction:	0.9904

Age (days):	99
Cap:	Surface ground, 50 durometer end cap
Maximum load (lb):	790.57
Maximum load (kN):	3.517
Strain Rate (%/min):	2.5
Time to Failure (min):	0.47
Strain at Failure (%):	1.098
Initial yield (psi):	108.99
Modulus (psi):	23681
ASTM C495	
Comp. Strength (MPa):	0.7880
Comp. Strength (psi):	114.29
Corr. Comp. Strength (psi):	**113.19**
ASTM D2166	
Comp. Strength (kPa):	781.8
Comp. Strength (psi):	113.39
Corr. Comp. Strength (psi):	**112.30**
Treatment:	AD

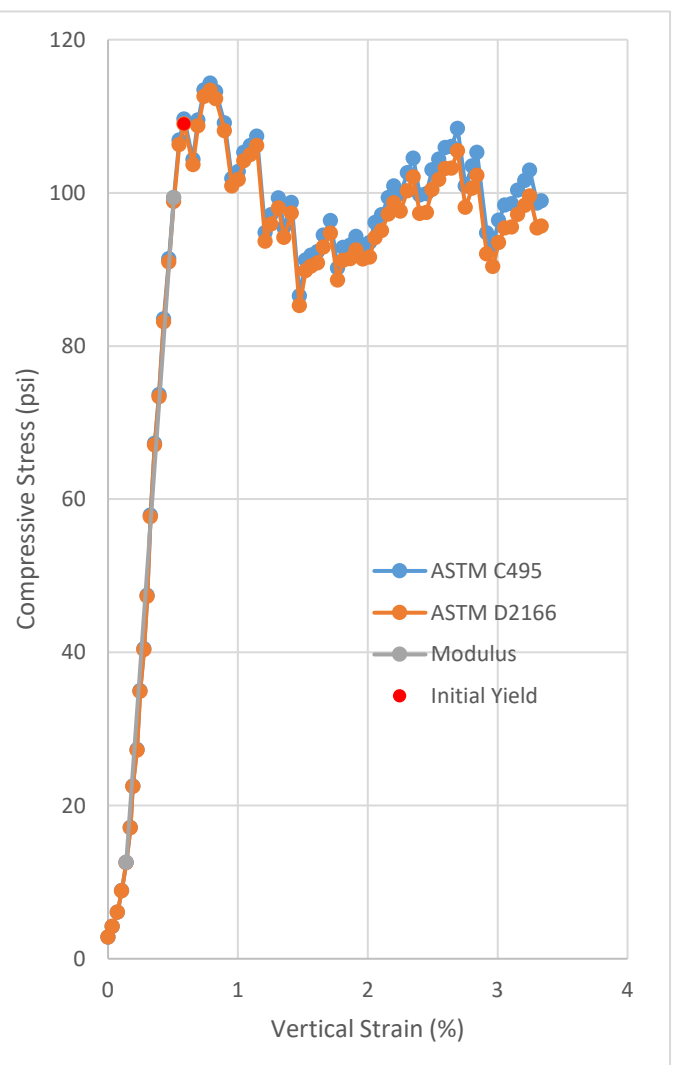

Uniaxial Compressive Strength of Lightweight Cellular Concrete

Sample ID:	**B2-19**
Height (in):	5.576
Height (mm):	141.6
Diameter (in):	2.975
Diameter (mm)	75.56
Area (in^2):	6.950
Area (mm^2):	4484
Mass (g):	228.72
Weight (lb):	0.5042
Weight (kN):	0.00224298
Volume (in^3):	38.75
Volume (mm^3):	634986
Density (g/mm^3):	0.0003602
Density (kg/m^3):	360.2
Unit Weight (pcf):	**22.49**
Unit Weight (kN/m^3):	3.532
Wet mass + tare (g):	636.86
Dry mass + tare (g):	599.68
Tare (g):	408.44
Water Content (%)	**19.44**
H:D ratio:	1.874
H:D correction:	0.9894

Age (days):	99
Cap:	Surface ground, 50 durometer end cap
Maximum load (lb):	838.07
Maximum load (kN):	3.728
Strain Rate (%/min):	2.5
Time to Failure (min):	0.46
Strain at Failure (%):	1.042
Initial yield (psi):	119.71
Modulus (psi):	19479
ASTM C495	
Comp. Strength (MPa):	0.8314
Comp. Strength (psi):	120.59
Corr. Comp. Strength (psi):	**119.32**
ASTM D2166	
Comp. Strength (kPa):	825.4
Comp. Strength (psi):	119.71
Corr. Comp. Strength (psi):	**118.44**
Treatment:	AD

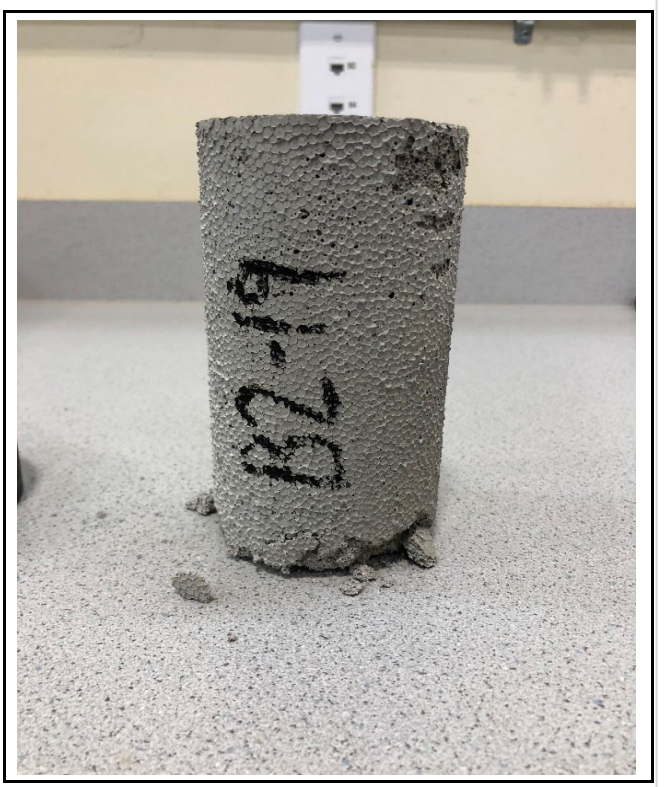

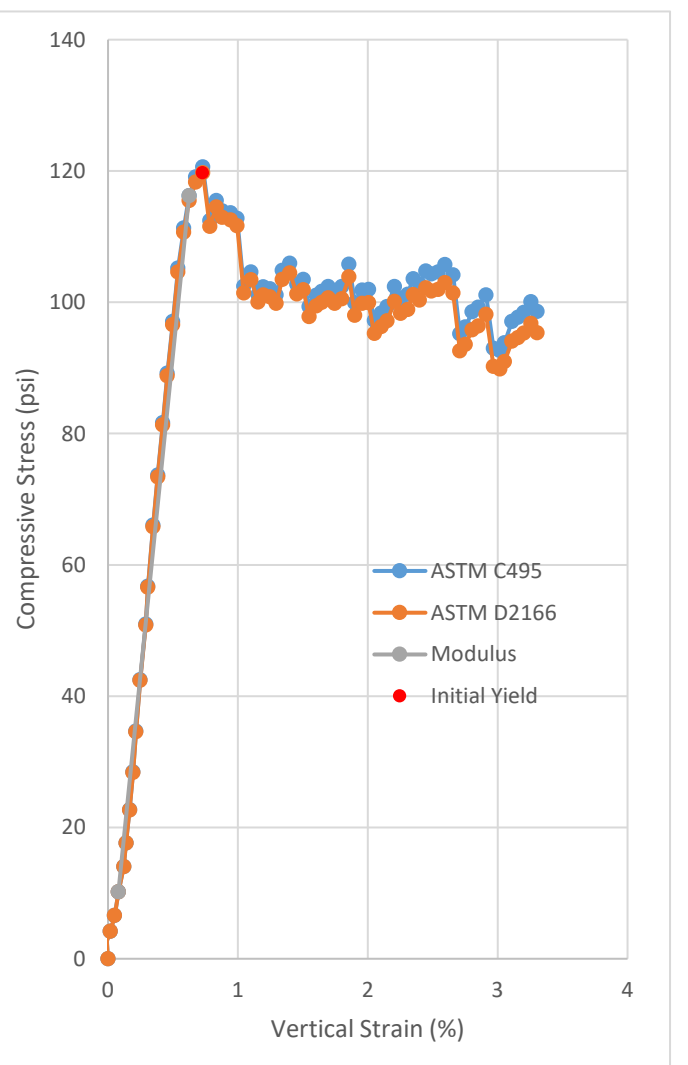

Uniaxial Compressive Strength of Lightweight Cellular Concrete

Sample ID:	**B3-17**
Height (in):	5.671
Height (mm):	144.0
Diameter (in):	2.977
Diameter (mm)	75.61
Area (in^2):	6.959
Area (mm^2):	4490
Mass (g):	241.35
Weight (lb):	0.5321
Weight (kN):	0.00236683
Volume (in^3):	39.46
Volume (mm^3):	646712
Density (g/mm^3):	0.0003732
Density (kg/m^3):	373.2
Unit Weight (pcf):	**23.30**
Unit Weight (kN/m^3):	3.660
Wet mass + tare (g):	551.21
Dry mass + tare (g):	509.99
Tare (g):	310.18
Water Content (%)	**20.63**
H:D ratio:	1.905
H:D correction:	0.9919

Age (days):	99
Cap:	Surface ground, 50 durometer end cap
Maximum load (lb):	1291.6
Maximum load (kN):	5.745
Strain Rate (%/min):	2.5
Time to Failure (min):	0.57
Strain at Failure (%):	1.287
Initial yield (psi):	176.56
Modulus (psi):	32817
ASTM C495	
Comp. Strength (MPa):	1.2797
Comp. Strength (psi):	185.60
Corr. Comp. Strength (psi):	**184.09**
ASTM D2166	
Comp. Strength (kPa):	1268.5
Comp. Strength (psi):	183.98
Corr. Comp. Strength (psi):	**182.48**
Treatment:	AD

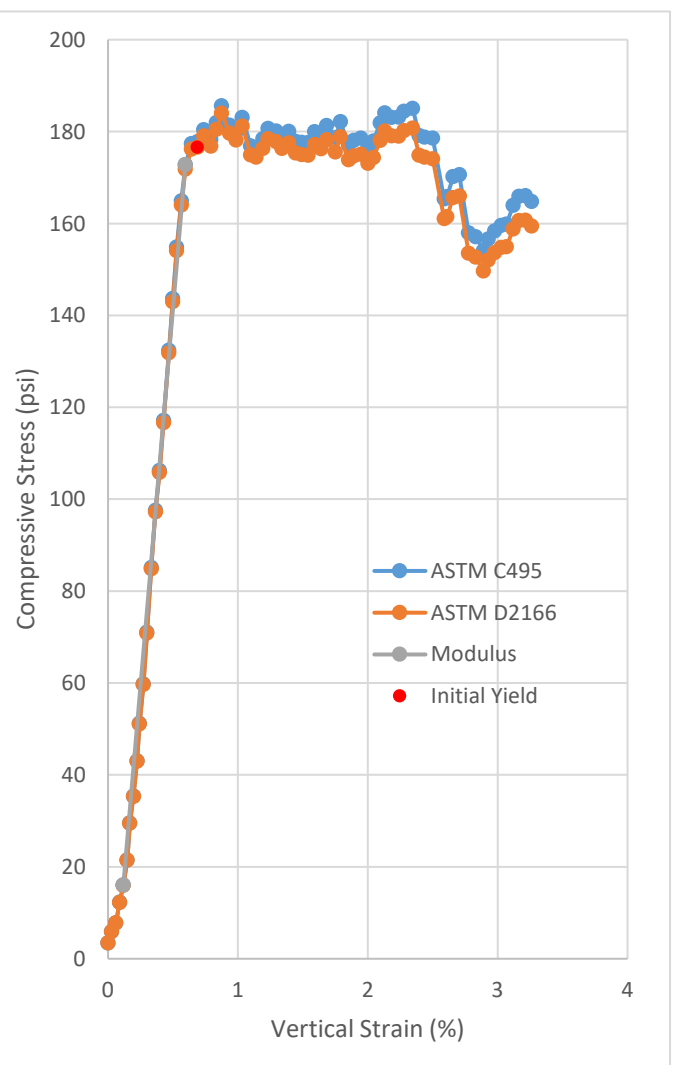

Uniaxial Compressive Strength of Lightweight Cellular Concrete

Sample ID:	**B3-18**
Height (in):	5.598
Height (mm):	142.2
Diameter (in):	2.971
Diameter (mm)	75.47
Area (in^2):	6.934
Area (mm^2):	4474
Mass (g):	237.6
Weight (lb):	0.5238
Weight (kN):	0.00233006
Volume (in^3):	38.82
Volume (mm^3):	636064
Density (g/mm^3):	0.0003735
Density (kg/m^3):	373.5
Unit Weight (pcf):	**23.32**
Unit Weight (kN/m^3):	3.663
Wet mass + tare (g):	646.01
Dry mass + tare (g):	604.43
Tare (g):	408.81
Water Content (%)	**21.26**
H:D ratio:	1.884
H:D correction:	0.9902

Age (days):	99
Cap:	Surface ground, 50 durometer end cap
Maximum load (lb):	1313
Maximum load (kN):	5.841
Strain Rate (%/min):	2.5
Time to Failure (min):	0.68
Strain at Failure (%):	1.591
Initial yield (psi):	184.74
Modulus (psi):	31302
ASTM C495	
Comp. Strength (MPa):	1.3055
Comp. Strength (psi):	189.35
Corr. Comp. Strength (psi):	**187.49**
ASTM D2166	
Comp. Strength (kPa):	1290.3
Comp. Strength (psi):	187.14
Corr. Comp. Strength (psi):	**185.30**
Treatment:	AD

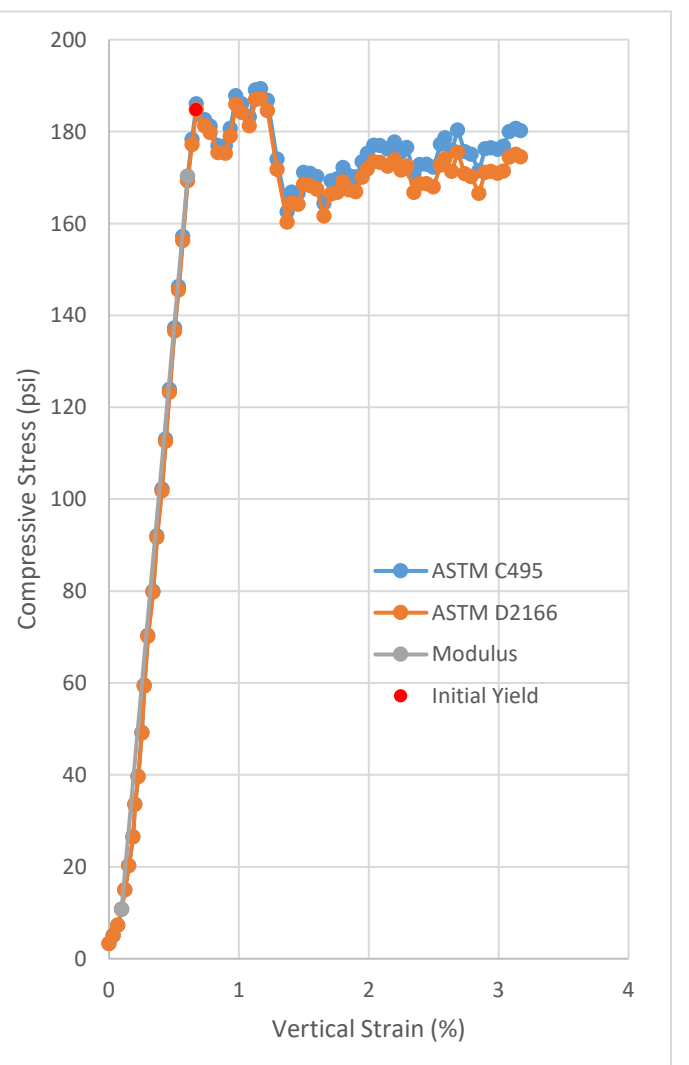

Uniaxial Compressive Strength of Lightweight Cellular Concrete

Sample ID:	**B3-19**
Height (in):	5.597
Height (mm):	142.2
Diameter (in):	2.974
Diameter (mm)	75.53
Area (in^2):	6.945
Area (mm^2):	4481
Mass (g):	238.72
Weight (lb):	0.5263
Weight (kN):	0.00234104
Volume (in^3):	38.87
Volume (mm^3):	637025
Density (g/mm^3):	0.0003747
Density (kg/m^3):	374.7
Unit Weight (pcf):	**23.39**
Unit Weight (kN/m^3):	3.675
Wet mass + tare (g):	702.93
Dry mass + tare (g):	662.35
Tare (g):	464.55
Water Content (%)	**20.52**
H:D ratio:	1.882
H:D correction:	0.9901

Age (days):	99
Cap:	Surface ground, 50 durometer end cap
Maximum load (lb):	1362.7
Maximum load (kN):	6.062
Strain Rate (%/min):	2.5
Time to Failure (min):	0.53
Strain at Failure (%):	1.194
Initial yield (psi):	194.72
Modulus (psi):	32857
ASTM C495	
Comp. Strength (MPa):	1.3528
Comp. Strength (psi):	196.21
Corr. Comp. Strength (psi):	**194.26**
ASTM D2166	
Comp. Strength (kPa):	1342.6
Comp. Strength (psi):	194.72
Corr. Comp. Strength (psi):	**192.79**
Treatment:	AD

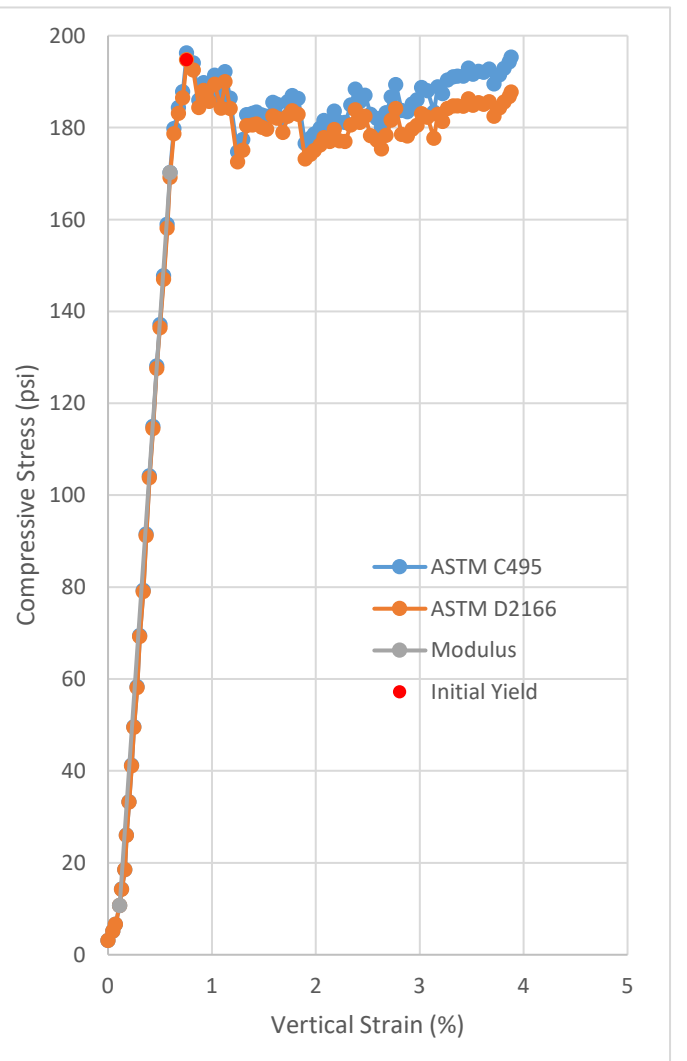

Uniaxial Compressive Strength of Lightweight Cellular Concrete

Sample ID:	**B2-24**
Height (in):	5.617
Height (mm):	142.7
Diameter (in):	2.962
Diameter (mm)	75.24
Area (in^2):	6.891
Area (mm^2):	4446
Mass (g):	214.07
Weight (lb):	0.4719
Weight (kN):	0.00209931
Volume (in^3):	38.71
Volume (mm^3):	634305
Density (g/mm^3):	0.0003375
Density (kg/m^3):	337.5
Unit Weight (pcf):	**21.07**
Unit Weight (kN/m^3):	3.310
Wet mass + tare (g):	341.30
Dry mass + tare (g):	324.17
Tare (g):	128.06
Water Content (%)	**8.73**
H:D ratio:	1.896
H:D correction:	0.9912
Saturation (%):	3.07

Age (days):	1051
Cap:	Surface ground, 50 durometer end cap
Maximum load (lb):	828.22
Maximum load (kN):	3.684
Strain Rate (%/min):	2.5
Time to Failure (min):	2.70
Strain at Failure (%):	6.891
Initial yield (psi):	113.35
Modulus (psi):	22413
ASTM C495	
Comp. Strength (MPa):	0.8287
Comp. Strength (psi):	120.19
Corr. Comp. Strength (psi):	**119.12**
ASTM D2166	
Comp. Strength (kPa):	781.5
Comp. Strength (psi):	113.35
Corr. Comp. Strength (psi):	**112.35**
Treatment:	AD

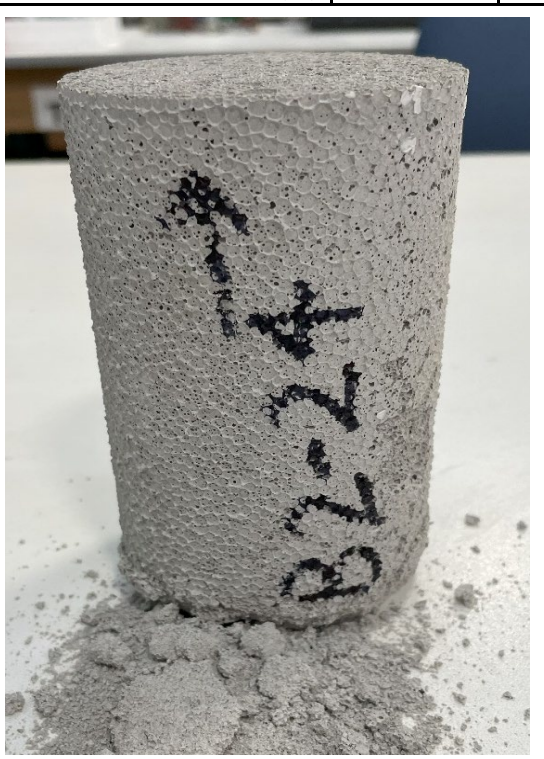

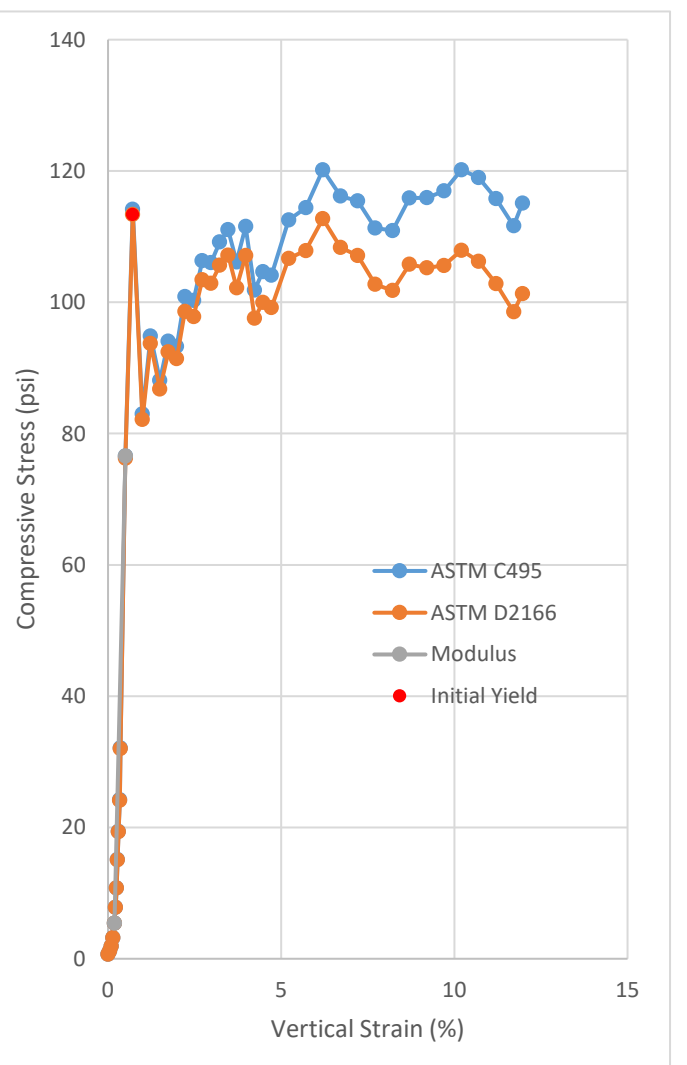

Uniaxial Compressive Strength of Lightweight Cellular Concrete

Sample ID:	**B2-25**
Height (in):	5.692
Height (mm):	144.6
Diameter (in):	2.933
Diameter (mm)	74.49
Area (in^2):	6.755
Area (mm^2):	4358
Mass (g):	217.57
Weight (lb):	0.4797
Weight (kN):	0.00213363
Volume (in^3):	38.45
Volume (mm^3):	630096
Density (g/mm^3):	0.0003453
Density (kg/m^3):	345.3
Unit Weight (pcf):	**21.56**
Unit Weight (kN/m^3):	3.386
Wet mass + tare (g):	345.76
Dry mass + tare (g):	328.44
Tare (g):	128.37
Water Content (%)	**8.66**
H:D ratio:	1.941
H:D correction:	0.9948
Saturation (%):	3.12

Age (days):	1052
Cap:	Surface ground, 50 durometer end cap
Maximum load (lb):	873.57
Maximum load (kN):	3.886
Strain Rate (%/min):	2.5
Time to Failure (min):	4.68
Strain at Failure (%):	6.756
Initial yield (psi):	109.66
Modulus (psi):	18127
ASTM C495	
Comp. Strength (MPa):	0.8917
Comp. Strength (psi):	129.32
Corr. Comp. Strength (psi):	**128.65**
ASTM D2166	
Comp. Strength (kPa):	834.8
Comp. Strength (psi):	121.08
Corr. Comp. Strength (psi):	**120.44**
Treatment:	AD

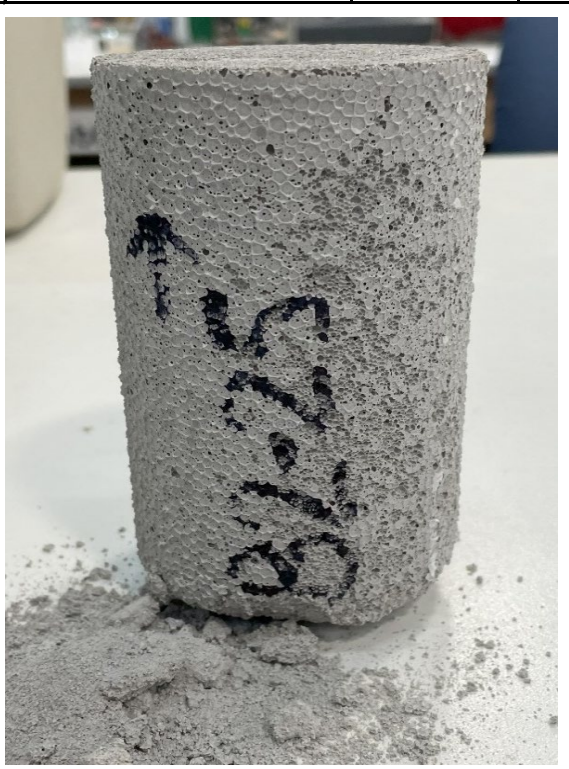

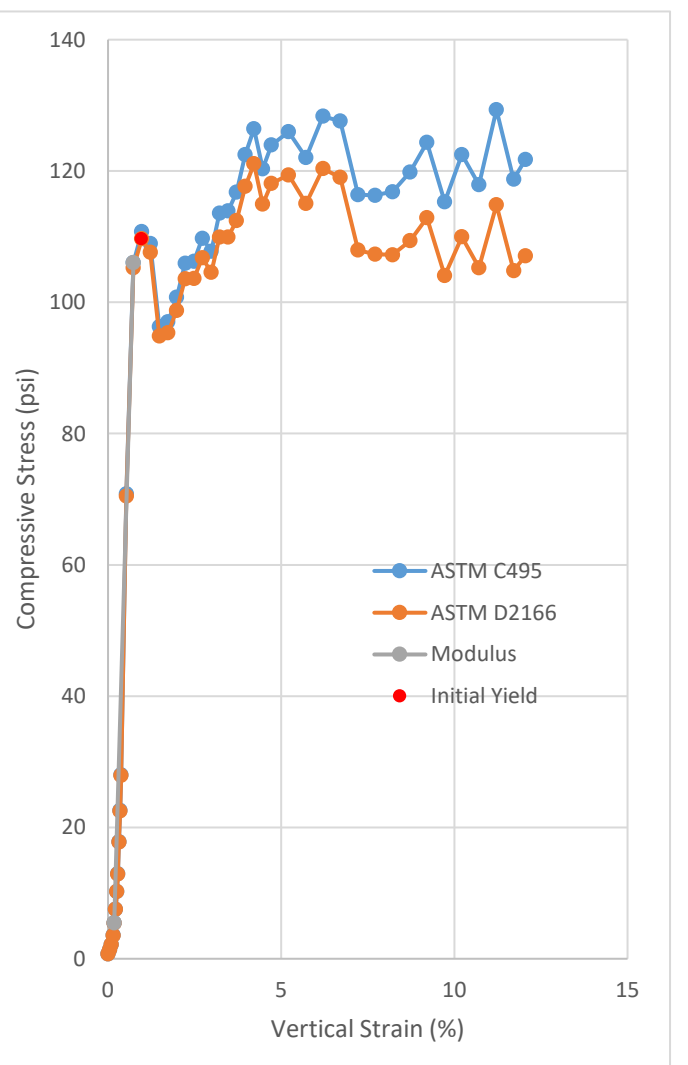

Uniaxial Compressive Strength of Lightweight Cellular Concrete

Sample ID:	**B2-26**
Height (in):	5.613
Height (mm):	142.6
Diameter (in):	2.966
Diameter (mm)	75.35
Area (in^2):	6.911
Area (mm^2):	4459
Mass (g):	222.43
Weight (lb):	0.4904
Weight (kN):	0.00218129
Volume (in^3):	38.79
Volume (mm^3):	635709
Density (g/mm^3):	0.0003499
Density (kg/m^3):	349.9
Unit Weight (pcf):	**21.84**
Unit Weight (kN/m^3):	3.431
Wet mass + tare (g):	344.71
Dry mass + tare (g):	324.63
Tare (g):	124.39
Water Content (%)	**10.03**
H:D ratio:	1.892
H:D correction:	0.9908
Saturation (%):	3.62

Age (days):	1052
Cap:	Surface ground, 50 durometer end cap
Maximum load (lb):	1719.5
Maximum load (kN):	7.649
Strain Rate (%/min):	2.5
Time to Failure (min):	4.12
Strain at Failure (%):	6.909
Initial yield (psi):	201.98
Modulus (psi):	29097
ASTM C495	
Comp. Strength (MPa):	1.7154
Comp. Strength (psi):	248.79
Corr. Comp. Strength (psi):	**246.51**
ASTM D2166	
Comp. Strength (kPa):	1551.7
Comp. Strength (psi):	225.06
Corr. Comp. Strength (psi):	**222.99**
Treatment:	AD

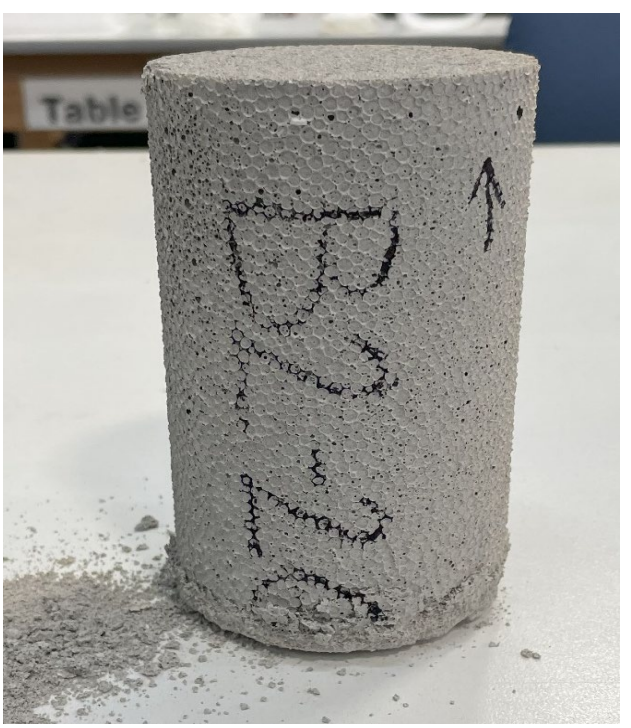

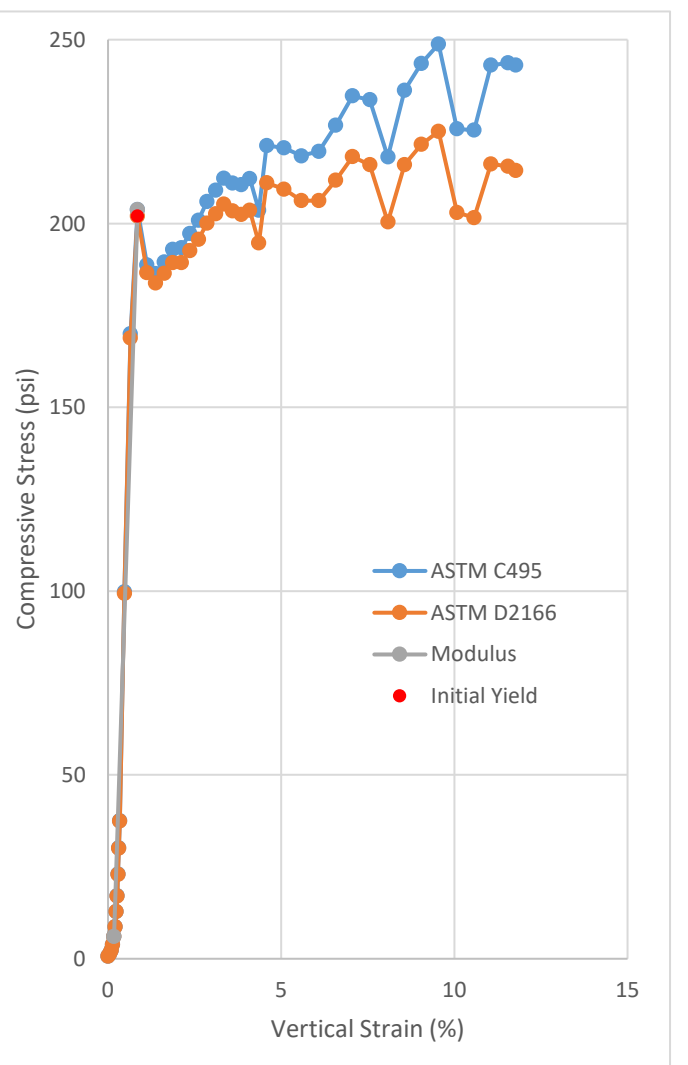

Uniaxial Compressive Strength of Lightweight Cellular Concrete

Sample ID:	**B3-23**
Height (in):	5.628
Height (mm):	142.9
Diameter (in):	2.948
Diameter (mm)	74.88
Area (in^2):	6.826
Area (mm^2):	4404
Mass (g):	221.35
Weight (lb):	0.4880
Weight (kN):	0.0021707
Volume (in^3):	38.41
Volume (mm^3):	629469
Density (g/mm^3):	0.0003516
Density (kg/m^3):	351.6
Unit Weight (pcf):	**21.95**
Unit Weight (kN/m^3):	3.448
Wet mass + tare (g):	344.47
Dry mass + tare (g):	328.17
Tare (g):	123.56
Water Content (%)	**7.97**
H:D ratio:	1.909
H:D correction:	0.9922
Saturation (%):	2.95

Age (days):	1051
Cap:	Surface ground, 50 durometer end cap
Maximum load (lb):	1213.1
Maximum load (kN):	5.396
Strain Rate (%/min):	2.5
Time to Failure (min):	4.73
Strain at Failure (%):	6.826
Initial yield (psi):	129.07
Modulus (psi):	21403
ASTM C495	
Comp. Strength (MPa):	1.2254
Comp. Strength (psi):	177.73
Corr. Comp. Strength (psi):	**176.34**
ASTM D2166	
Comp. Strength (kPa):	1088.7
Comp. Strength (psi):	157.91
Corr. Comp. Strength (psi):	**156.67**
Treatment:	AD

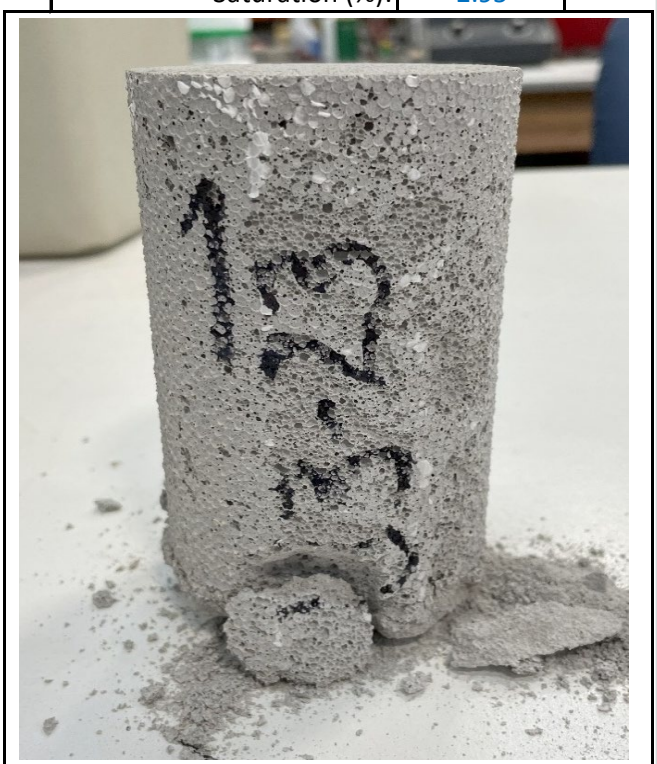

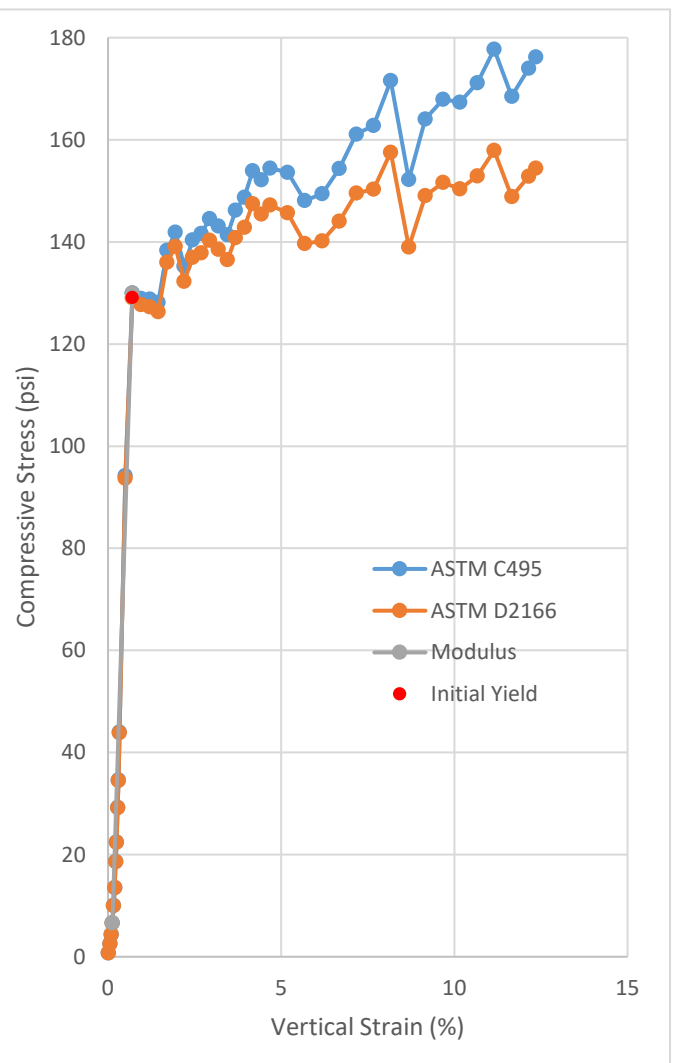

Uniaxial Compressive Strength of Lightweight Cellular Concrete

Sample ID:	**B3-25**
Height (in):	5.669
Height (mm):	144.0
Diameter (in):	2.947
Diameter (mm)	74.86
Area (in^2):	6.822
Area (mm^2):	4401
Mass (g):	219.14
Weight (lb):	0.4831
Weight (kN):	0.00214903
Volume (in^3):	38.67
Volume (mm^3):	633747
Density (g/mm^3):	0.0003458
Density (kg/m^3):	345.8
Unit Weight (pcf):	**21.59**
Unit Weight (kN/m^3):	3.391
Wet mass + tare (g):	358.87
Dry mass + tare (g):	341.66
Tare (g):	140.32
Water Content (%)	**8.55**
H:D ratio:	1.924
H:D correction:	0.9934
Saturation (%):	3.09

Age (days):	1051
Cap:	Surface ground, 50 durometer end cap
Maximum load (lb):	1177.8
Maximum load (kN):	5.239
Strain Rate (%/min):	2.5
Time to Failure (min):	4.50
Strain at Failure (%):	6.821
Initial yield (psi):	138.80
Modulus (psi):	23981
ASTM C495	
Comp. Strength (MPa):	1.1904
Comp. Strength (psi):	172.66
Corr. Comp. Strength (psi):	**171.51**
ASTM D2166	
Comp. Strength (kPa):	1063.6
Comp. Strength (psi):	154.27
Corr. Comp. Strength (psi):	**153.24**
Treatment:	AD

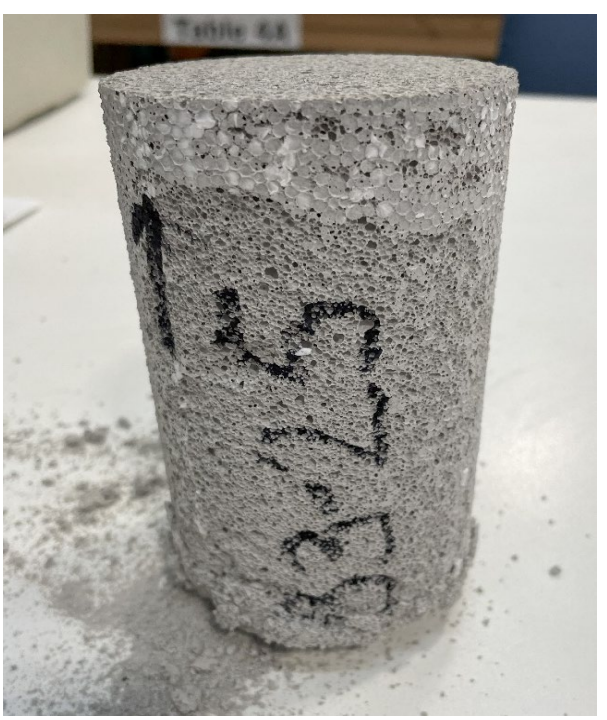

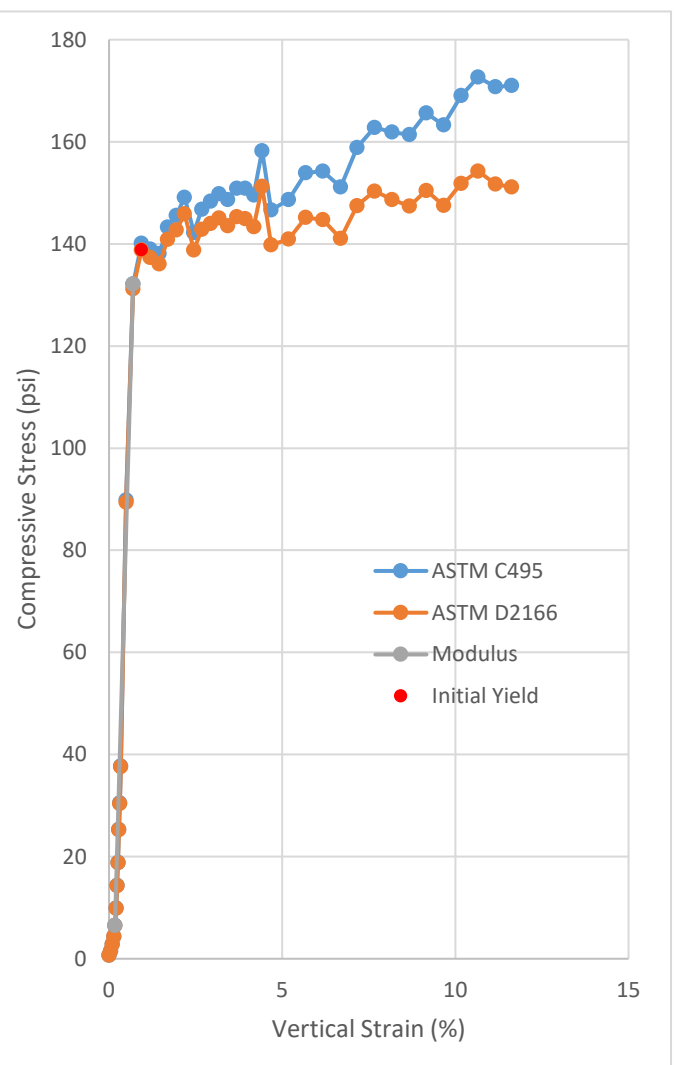

Uniaxial Compressive Strength of Lightweight Cellular Concrete

Sample ID:	**B2-27**
Height (in):	5.618
Height (mm):	142.7
Diameter (in):	2.971
Diameter (mm)	75.46
Area (in^2):	6.932
Area (mm^2):	4472
Mass (g):	226.02
Weight (lb):	0.4983
Weight (kN):	0.0022165
Volume (in^3):	38.94
Volume (mm^3):	638174
Density (g/mm^3):	0.0003542
Density (kg/m^3):	354.2
Unit Weight (pcf):	**22.11**
Unit Weight (kN/m^3):	3.473
Wet mass + tare (g):	438.77
Dry mass + tare (g):	414.36
Tare (g):	218.51
Water Content (%)	**12.46**
H:D ratio:	1.891
H:D correction:	0.9908
Saturation (%):	4.45

Age (days):	1058
Cap:	Surface ground, 50 durometer end cap
Maximum load (lb):	1546.5
Maximum load (kN):	6.879
Strain Rate (%/min):	2.5
Time to Failure (min):	5.01
Strain at Failure (%):	6.933
Initial yield (psi):	185.20
Modulus (psi):	30654
ASTM C495	
Comp. Strength (MPa):	1.5383
Comp. Strength (psi):	223.11
Corr. Comp. Strength (psi):	**221.05**
ASTM D2166	
Comp. Strength (kPa):	1357.4
Comp. Strength (psi):	196.87
Corr. Comp. Strength (psi):	**195.05**
Treatment:	H100

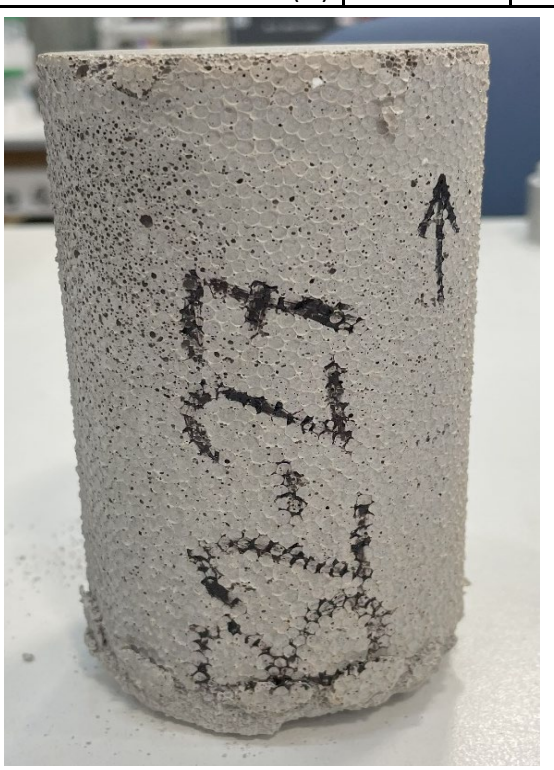

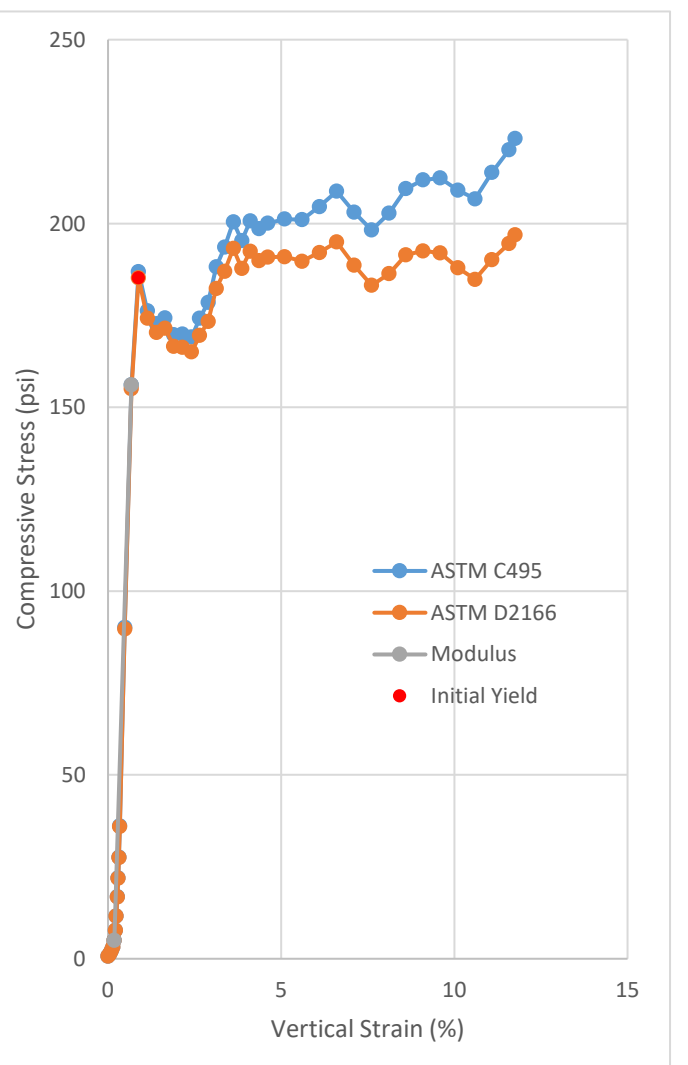

Uniaxial Compressive Strength of Lightweight Cellular Concrete

Sample ID:	**B2-28**
Height (in):	5.605
Height (mm):	142.4
Diameter (in):	2.961
Diameter (mm)	75.22
Area (in^2):	6.887
Area (mm^2):	4443
Mass (g):	228.57
Weight (lb):	0.5039
Weight (kN):	0.00224151
Volume (in^3):	38.60
Volume (mm^3):	632608
Density (g/mm^3):	0.0003613
Density (kg/m^3):	361.3
Unit Weight (pcf):	**22.56**
Unit Weight (kN/m^3):	3.543
Wet mass + tare (g):	348.75
Dry mass + tare (g):	324.92
Tare (g):	128.28
Water Content (%)	**12.12**
H:D ratio:	1.893
H:D correction:	0.9909
Saturation (%):	4.44

Age (days):	1058
Cap:	Surface ground, 50 durometer end cap
Maximum load (lb):	1592
Maximum load (kN):	7.082
Strain Rate (%/min):	2.5
Time to Failure (min):	4.51
Strain at Failure (%):	6.886
Initial yield (psi):	195.77
Modulus (psi):	31519
ASTM C495	
Comp. Strength (MPa):	1.5938
Comp. Strength (psi):	231.16
Corr. Comp. Strength (psi):	**229.05**
ASTM D2166	
Comp. Strength (kPa):	1425.4
Comp. Strength (psi):	206.74
Corr. Comp. Strength (psi):	**204.85**
Treatment:	H100

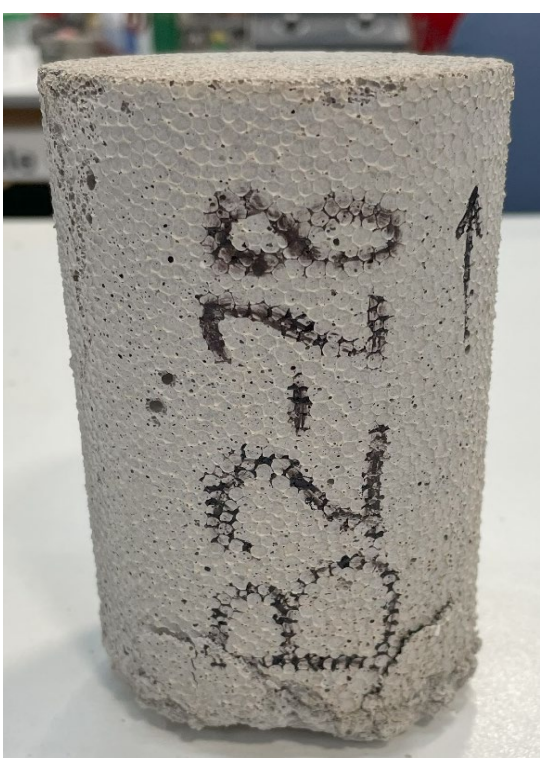

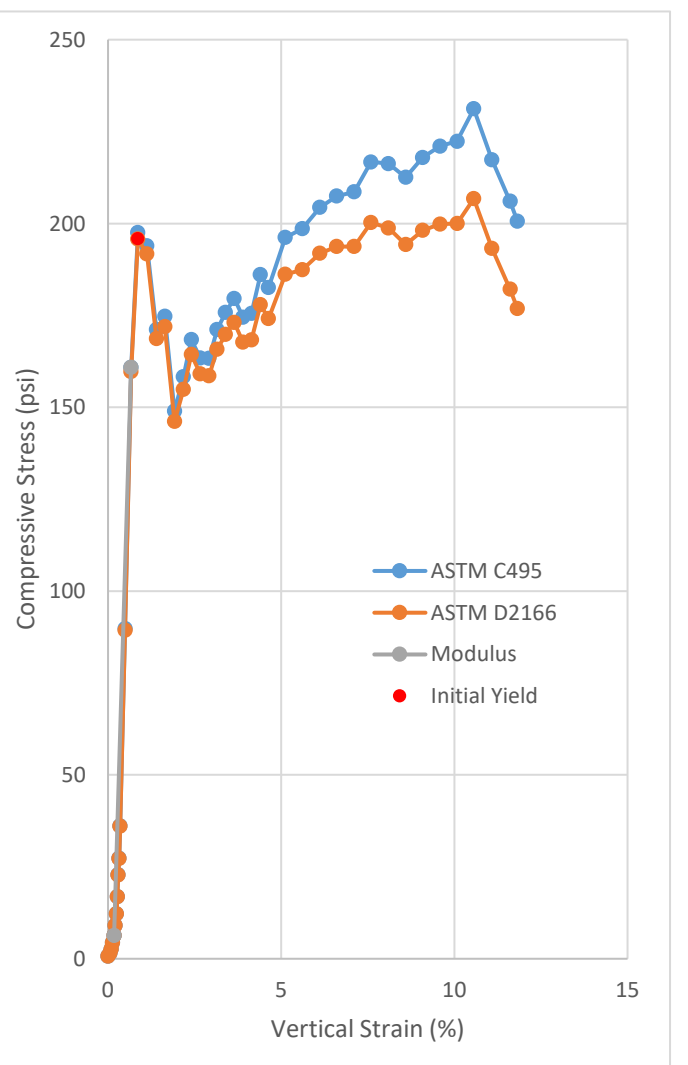

Uniaxial Compressive Strength of Lightweight Cellular Concrete

Sample ID:	**B2-29**
Height (in):	5.638
Height (mm):	143.2
Diameter (in):	2.962
Diameter (mm)	75.23
Area (in^2):	6.889
Area (mm^2):	4445
Mass (g):	226.3
Weight (lb):	0.4989
Weight (kN):	0.00221924
Volume (in^3):	38.84
Volume (mm^3):	636448
Density (g/mm^3):	0.0003556
Density (kg/m^3):	355.6
Unit Weight (pcf):	**22.20**
Unit Weight (kN/m^3):	3.487
Wet mass + tare (g):	348.28
Dry mass + tare (g):	325.00
Tare (g):	128.49
Water Content (%)	**11.85**
H:D ratio:	1.904
H:D correction:	0.9917
Saturation (%):	4.27

Age (days):	1058
Cap:	Surface ground, 50 durometer end cap
Maximum load (lb):	1264.1
Maximum load (kN):	5.623
Strain Rate (%/min):	2.5
Time to Failure (min):	3.30
Strain at Failure (%):	6.891
Initial yield (psi):	161.63
Modulus (psi):	28078
ASTM C495	
Comp. Strength (MPa):	1.2651
Comp. Strength (psi):	183.49
Corr. Comp. Strength (psi):	**181.98**
ASTM D2166	
Comp. Strength (kPa):	1172.8
Comp. Strength (psi):	170.10
Corr. Comp. Strength (psi):	**168.69**
Treatment:	H100

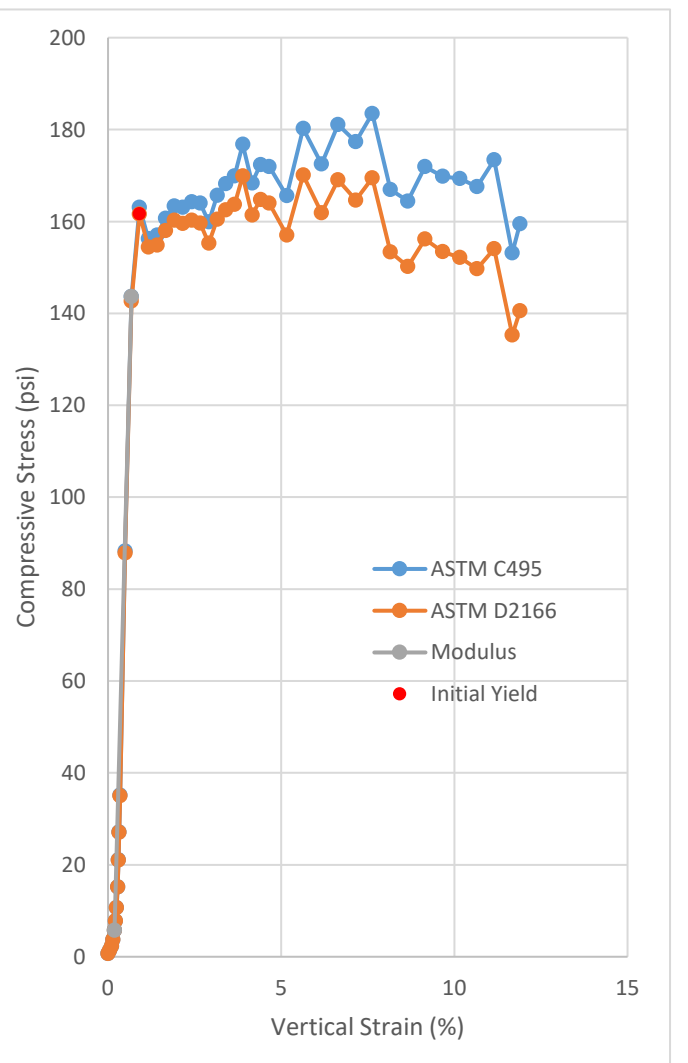

Uniaxial Compressive Strength of Lightweight Cellular Concrete

Sample ID:	**B2-30**
Height (in):	5.656
Height (mm):	143.7
Diameter (in):	2.962
Diameter (mm)	75.23
Area (in^2):	6.891
Area (mm^2):	4446
Mass (g):	224.33
Weight (lb):	0.4946
Weight (kN):	0.00219993
Volume (in^3):	38.97
Volume (mm^3):	638661
Density (g/mm^3):	0.0003513
Density (kg/m^3):	351.3
Unit Weight (pcf):	**21.93**
Unit Weight (kN/m^3):	3.445
Wet mass + tare (g):	329.44
Dry mass + tare (g):	307.19
Tare (g):	119.91
Water Content (%)	**11.88**
H:D ratio:	1.910
H:D correction:	0.9922
Saturation (%):	4.23

Age (days):	1058
Cap:	Surface ground, 50 durometer end cap
Maximum load (lb):	686.97
Maximum load (kN):	3.056
Strain Rate (%/min):	2.5
Time to Failure (min):	3.09
Strain at Failure (%):	6.891
Initial yield (psi):	80.46
Modulus (psi):	12657
ASTM C495	
Comp. Strength (MPa):	0.6874
Comp. Strength (psi):	99.70
Corr. Comp. Strength (psi):	**98.92**
ASTM D2166	
Comp. Strength (kPa):	646.2
Comp. Strength (psi):	93.73
Corr. Comp. Strength (psi):	**93.00**
Treatment:	H100

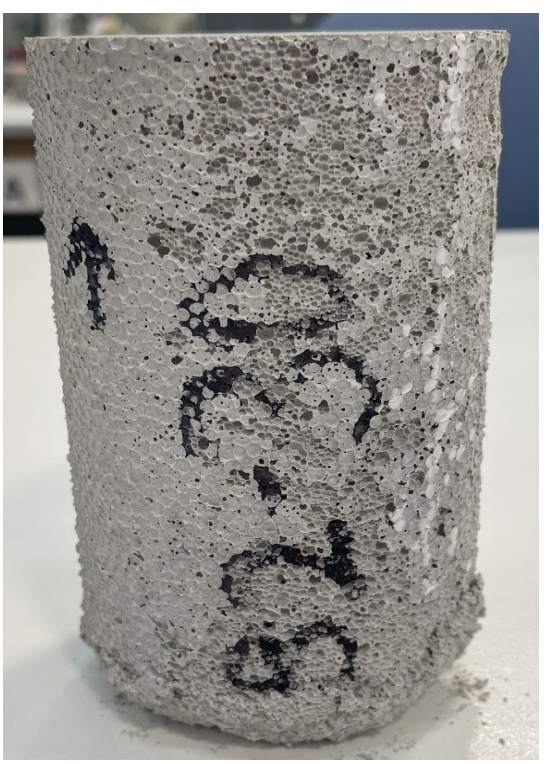

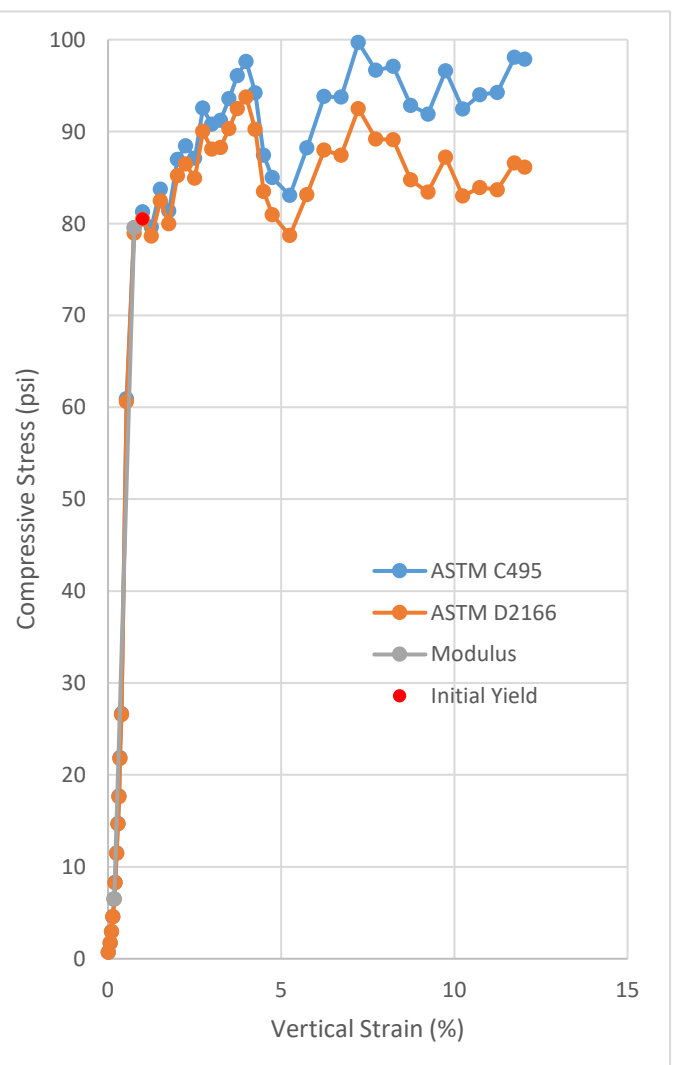

Uniaxial Compressive Strength of Lightweight Cellular Concrete

Sample ID:	**B2-31**
Height (in):	5.687
Height (mm):	144.5
Diameter (in):	2.978
Diameter (mm)	75.64
Area (in^2):	6.965
Area (mm^2):	4494
Mass (g):	228.96
Weight (lb):	0.5048
Weight (kN):	0.00224533
Volume (in^3):	39.61
Volume (mm^3):	649156
Density (g/mm^3):	0.0003527
Density (kg/m^3):	352.7
Unit Weight (pcf):	**22.02**
Unit Weight (kN/m^3):	3.459
Wet mass + tare (g):	311.70
Dry mass + tare (g):	288.06
Tare (g):	122.44
Water Content (%)	**14.27**
H:D ratio:	1.910
H:D correction:	0.9922
Saturation (%):	4.98

Age (days):	1059
Cap:	Surface ground, 50 durometer end cap
Maximum load (lb):	612.12
Maximum load (kN):	2.723
Strain Rate (%/min):	2.5
Time to Failure (min):	0.78
Strain at Failure (%):	6.965
Initial yield (psi):	86.29
Modulus (psi):	11942
ASTM C495	
Comp. Strength (MPa):	0.6059
Comp. Strength (psi):	87.88
Corr. Comp. Strength (psi):	**87.20**
ASTM D2166	
Comp. Strength (kPa):	598.3
Comp. Strength (psi):	86.77
Corr. Comp. Strength (psi):	**86.10**
Treatment:	H100

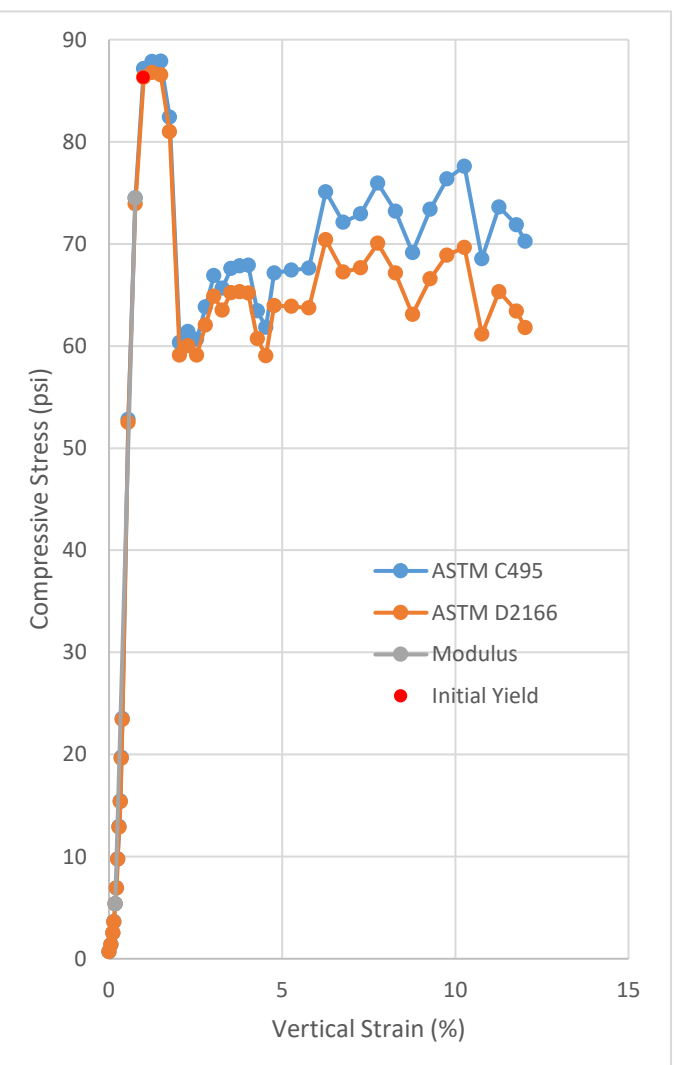

Uniaxial Compressive Strength of Lightweight Cellular Concrete

Sample ID:	**B2-70**
Height (in):	5.452
Height (mm):	138.5
Diameter (in):	2.964
Diameter (mm)	75.28
Area (in^2):	6.899
Area (mm^2):	4451
Mass (g):	257.96
Weight (lb):	0.5687
Weight (kN):	0.00252972
Volume (in^3):	37.62
Volume (mm^3):	616411
Density (g/mm^3):	0.0004185
Density (kg/m^3):	418.5
Unit Weight (pcf):	**26.13**
Unit Weight (kN/m^3):	4.104
Wet mass + tare (g):	377.21
Dry mass + tare (g):	313.47
Tare (g):	123.43
Water Content (%)	**33.54**
H:D ratio:	1.839
H:D correction:	0.9867
Saturation (%):	11.91

Age (days):	1075
Cap:	Surface ground, 50 durometer end cap
Maximum load (lb):	594.75
Maximum load (kN):	2.646
Strain Rate (%/min):	2.5
Time to Failure (min):	0.47
Strain at Failure (%):	6.900
Initial yield (psi):	85.57
Modulus (psi):	14713
ASTM C495	
Comp. Strength (MPa):	0.5943
Comp. Strength (psi):	86.20
Corr. Comp. Strength (psi):	**85.05**
ASTM D2166	
Comp. Strength (kPa):	590.0
Comp. Strength (psi):	85.57
Corr. Comp. Strength (psi):	**84.43**
Treatment:	M5

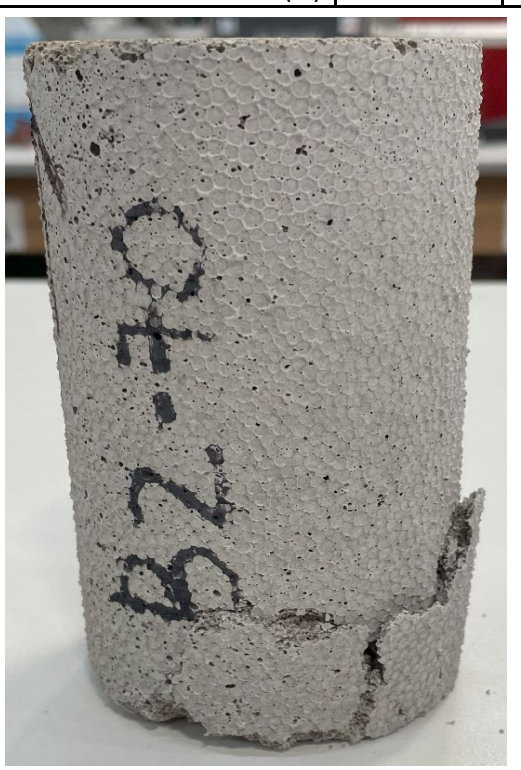

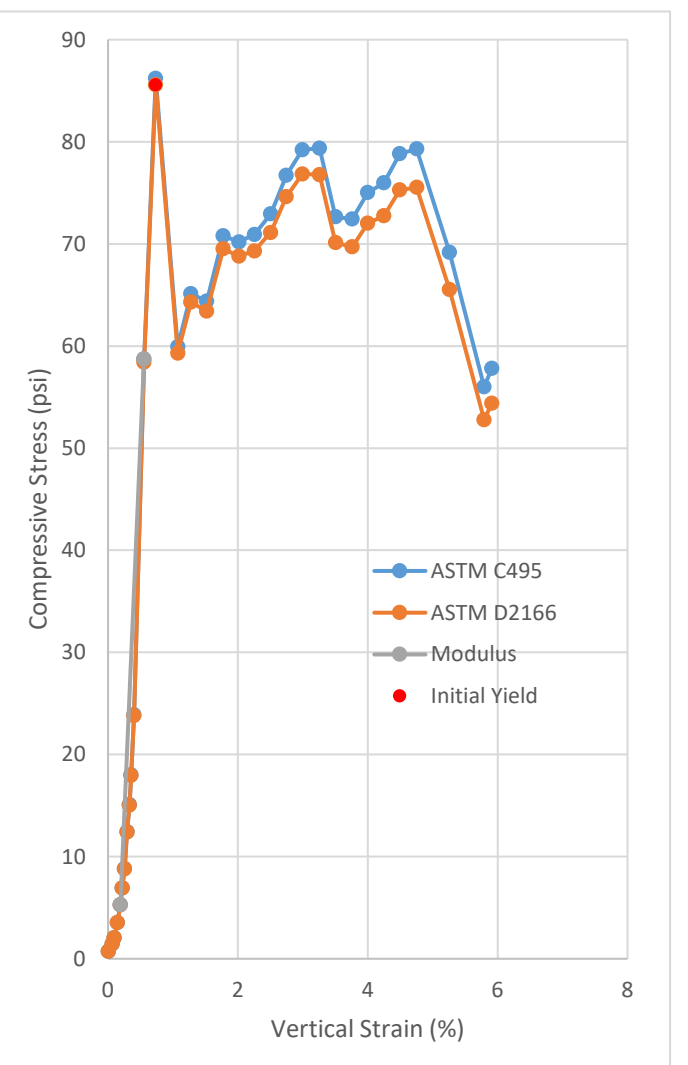

Uniaxial Compressive Strength of Lightweight Cellular Concrete

Sample ID:	**B2-71**
Height (in):	5.414
Height (mm):	137.5
Diameter (in):	2.965
Diameter (mm)	75.30
Area (in^2):	6.903
Area (mm^2):	4453
Mass (g):	244.65
Weight (lb):	0.5394
Weight (kN):	0.0023992
Volume (in^3):	37.37
Volume (mm^3):	612391
Density (g/mm^3):	0.0003995
Density (kg/m^3):	399.5
Unit Weight (pcf):	**24.94**
Unit Weight (kN/m^3):	3.918
Wet mass + tare (g):	352.14
Dry mass + tare (g):	302.93
Tare (g):	124.52
Water Content (%)	**27.58**
H:D ratio:	1.826
H:D correction:	0.9856
Saturation (%):	9.78

Age (days):	1075
Cap:	Surface ground, 50 durometer end cap
Maximum load (lb):	800.17
Maximum load (kN):	3.559
Strain Rate (%/min):	2.5
Time to Failure (min):	4.91
Strain at Failure (%):	6.905
Initial yield (psi):	112.26
Modulus (psi):	18352
ASTM C495	
Comp. Strength (MPa):	0.7993
Comp. Strength (psi):	115.92
Corr. Comp. Strength (psi):	**114.26**
ASTM D2166	
Comp. Strength (kPa):	774.0
Comp. Strength (psi):	112.26
Corr. Comp. Strength (psi):	**110.65**
Treatment:	M5

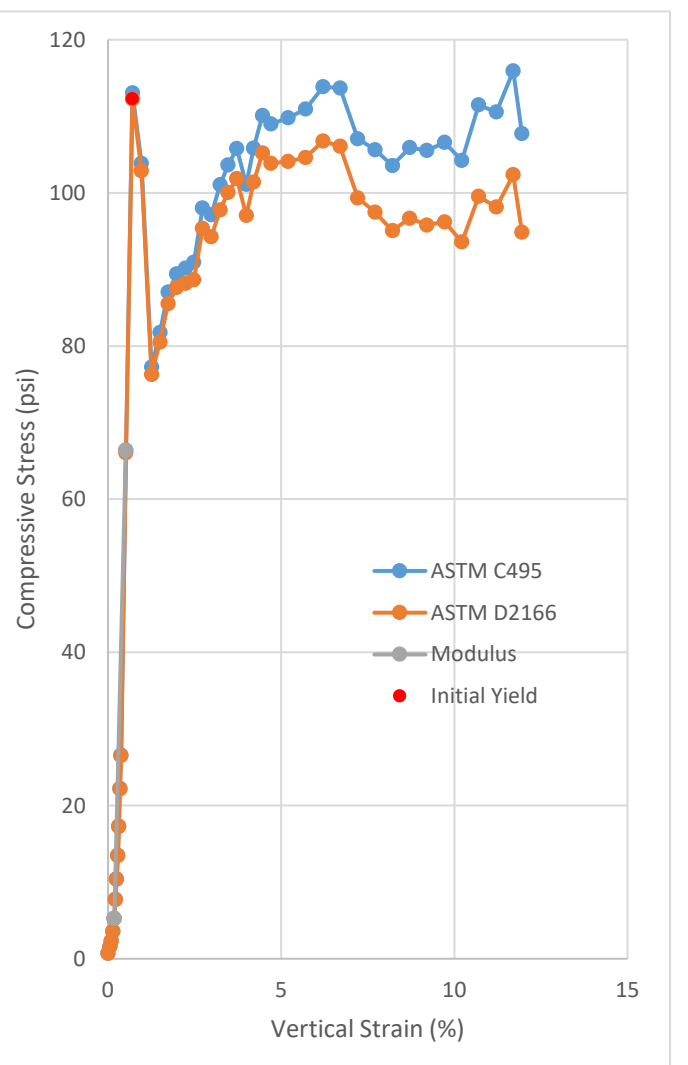

Uniaxial Compressive Strength of Lightweight Cellular Concrete

Sample ID:	**B2-72**
Height (in):	5.472
Height (mm):	139.0
Diameter (in):	2.955
Diameter (mm)	75.07
Area (in^2):	6.860
Area (mm^2):	4426
Mass (g):	249.69
Weight (lb):	0.5505
Weight (kN):	0.00244862
Volume (in^3):	37.54
Volume (mm^3):	615144
Density (g/mm^3):	0.0004059
Density (kg/m^3):	405.9
Unit Weight (pcf):	**25.34**
Unit Weight (kN/m^3):	3.981
Wet mass + tare (g):	355.32
Dry mass + tare (g):	304.28
Tare (g):	126.86
Water Content (%)	**28.77**
H:D ratio:	1.852
H:D correction:	0.9876
Saturation (%):	10.28

Age (days):	1075
Cap:	Surface ground, 50 durometer end cap
Maximum load (lb):	628.79
Maximum load (kN):	2.797
Strain Rate (%/min):	2.5
Time to Failure (min):	1.08
Strain at Failure (%):	6.858
Initial yield (psi):	85.57
Modulus (psi):	12906
ASTM C495	
Comp. Strength (MPa):	0.6320
Comp. Strength (psi):	91.66
Corr. Comp. Strength (psi):	**90.53**
ASTM D2166	
Comp. Strength (kPa):	617.9
Comp. Strength (psi):	89.61
Corr. Comp. Strength (psi):	**88.51**
Treatment:	M5

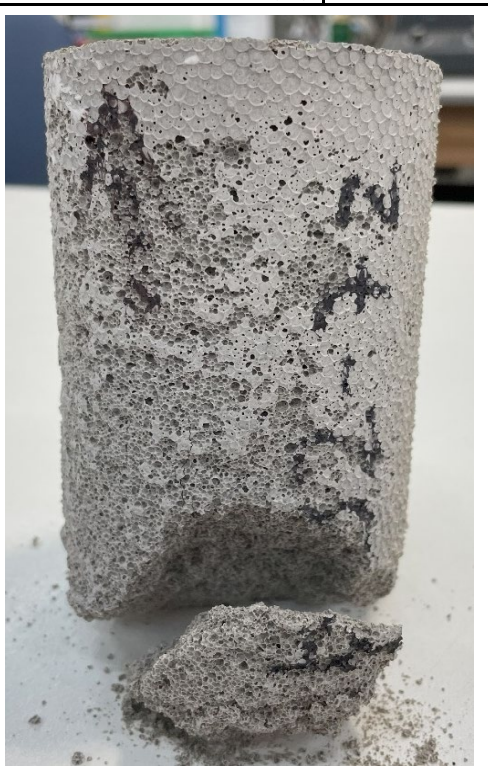

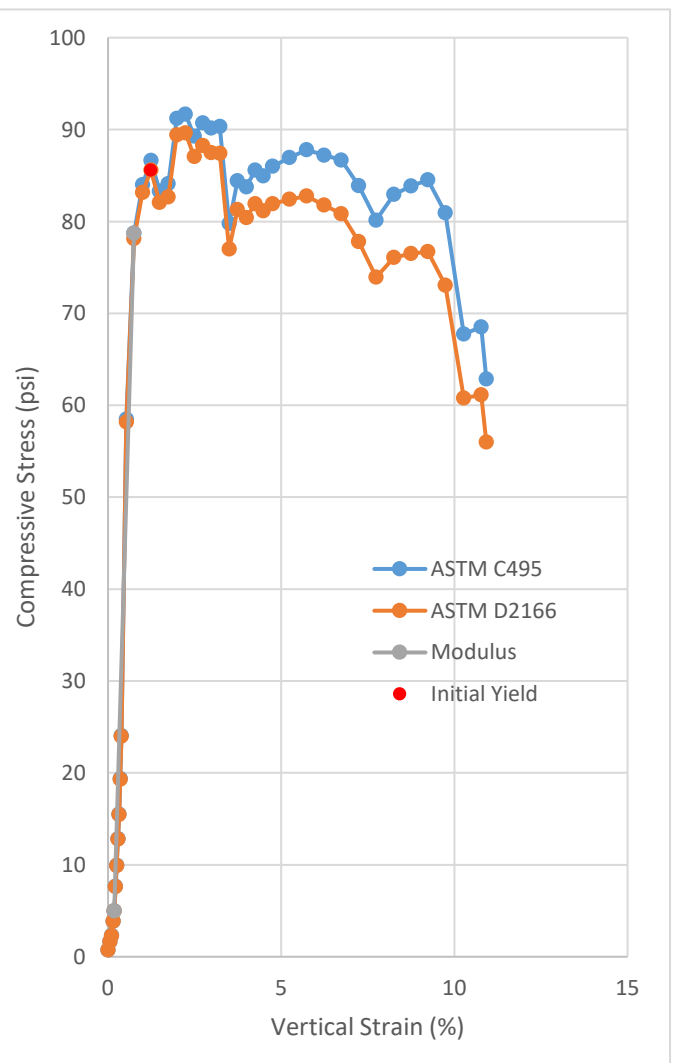

Uniaxial Compressive Strength of Lightweight Cellular Concrete

Sample ID:	**B2-73**
Height (in):	5.457
Height (mm):	138.6
Diameter (in):	2.964
Diameter (mm)	75.27
Area (in^2):	6.898
Area (mm^2):	4450
Mass (g):	245.47
Weight (lb):	0.5412
Weight (kN):	0.00240724
Volume (in^3):	37.64
Volume (mm^3):	616876
Density (g/mm^3):	0.0003979
Density (kg/m^3):	397.9
Unit Weight (pcf):	**24.84**
Unit Weight (kN/m^3):	3.902
Wet mass + tare (g):	345.72
Dry mass + tare (g):	298.89
Tare (g):	127.70
Water Content (%)	**27.36**
H:D ratio:	1.841
H:D correction:	0.9868
Saturation (%):	9.68

Age (days):	1075
Cap:	Surface ground, 50 durometer end cap
Maximum load (lb):	629.1
Maximum load (kN):	2.798
Strain Rate (%/min):	2.5
Time to Failure (min):	4.07
Strain at Failure (%):	6.900
Initial yield (psi):	84.41
Modulus (psi):	16264
ASTM C495	
Comp. Strength (MPa):	0.6288
Comp. Strength (psi):	91.20
Corr. Comp. Strength (psi):	**90.00**
ASTM D2166	
Comp. Strength (kPa):	606.7
Comp. Strength (psi):	87.99
Corr. Comp. Strength (psi):	**86.84**
Treatment:	M5

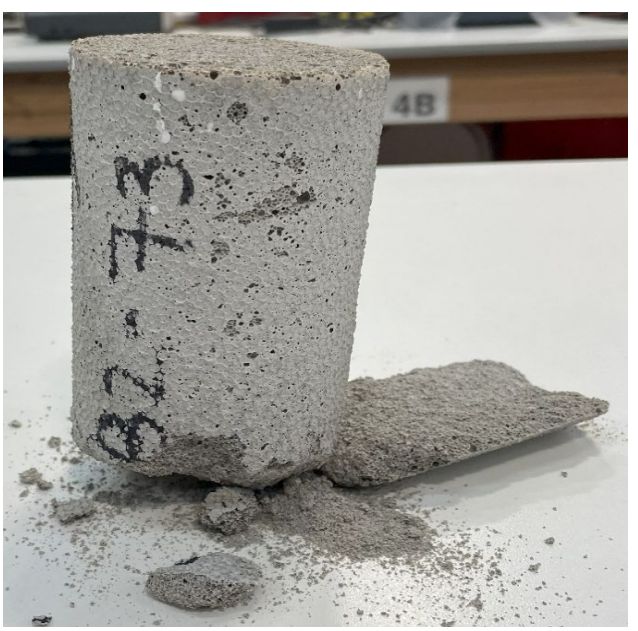

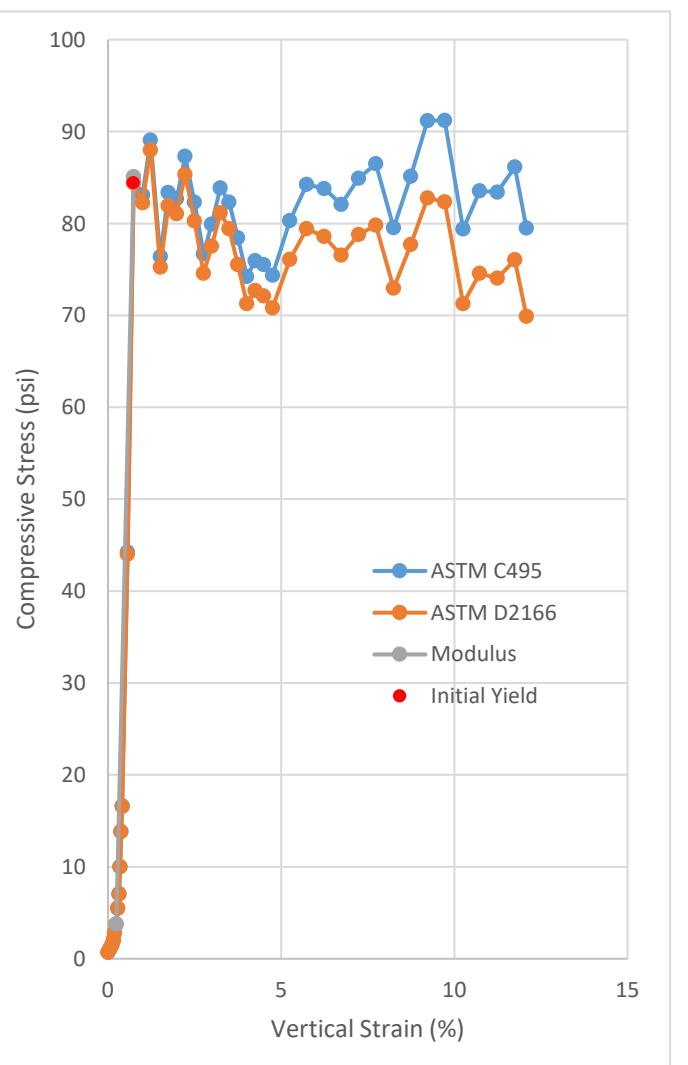

Uniaxial Compressive Strength of Lightweight Cellular Concrete

Sample ID:	**B2-74**
Height (in):	5.491
Height (mm):	139.5
Diameter (in):	2.961
Diameter (mm)	75.21
Area (in^2):	6.886
Area (mm^2):	4443
Mass (g):	249.6
Weight (lb):	0.5503
Weight (kN):	0.00244774
Volume (in^3):	37.81
Volume (mm^3):	619649
Density (g/mm^3):	0.0004028
Density (kg/m^3):	402.8
Unit Weight (pcf):	**25.15**
Unit Weight (kN/m^3):	3.950
Wet mass + tare (g):	367.52
Dry mass + tare (g):	312.57
Tare (g):	127.72
Water Content (%)	**29.73**
H:D ratio:	1.855
H:D correction:	0.9879
Saturation (%):	10.44

Age (days):	1075
Cap:	Surface ground, 50 durometer end cap
Maximum load (lb):	566.78
Maximum load (kN):	2.521
Strain Rate (%/min):	2.5
Time to Failure (min):	0.45
Strain at Failure (%):	6.886
Initial yield (psi):	81.70
Modulus (psi):	12445
ASTM C495	
Comp. Strength (MPa):	0.5675
Comp. Strength (psi):	82.31
Corr. Comp. Strength (psi):	**81.31**
ASTM D2166	
Comp. Strength (kPa):	563.3
Comp. Strength (psi):	81.70
Corr. Comp. Strength (psi):	**80.71**
Treatment:	M5

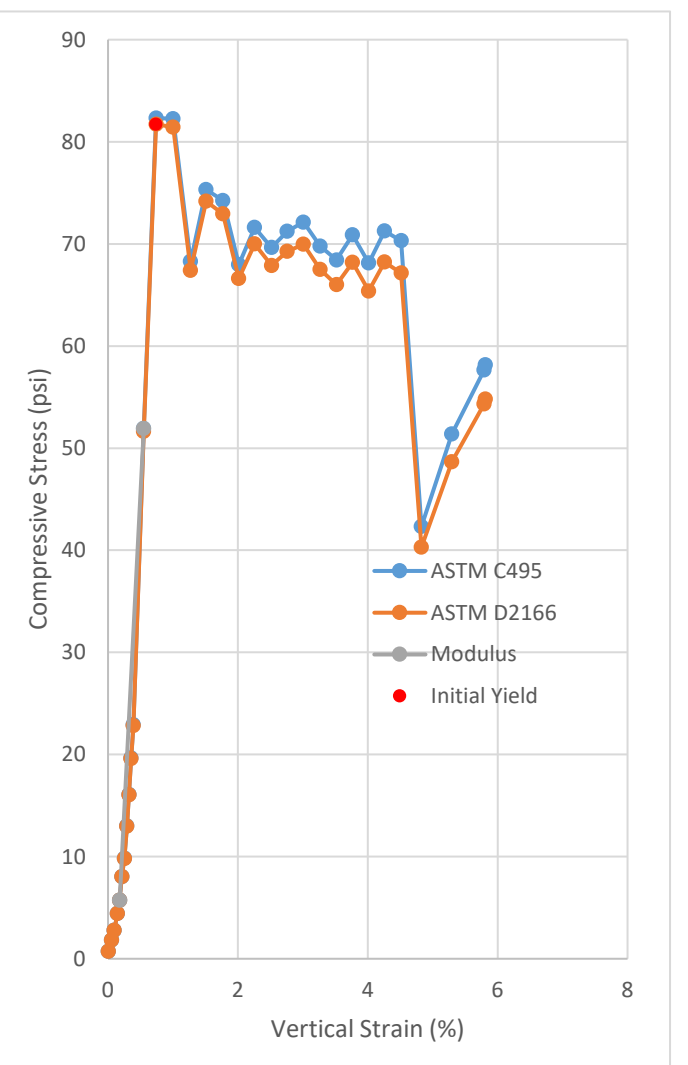

Uniaxial Compressive Strength of Lightweight Cellular Concrete

Sample ID:	**B2-32**
Height (in):	5.505
Height (mm):	139.8
Diameter (in):	2.959
Diameter (mm)	75.16
Area (in^2):	6.877
Area (mm^2):	4437
Mass (g):	284.74
Weight (lb):	0.6277
Weight (kN):	0.00279235
Volume (in^3):	37.86
Volume (mm^3):	620436
Density (g/mm^3):	0.0004589
Density (kg/m^3):	458.9
Unit Weight (pcf):	**28.65**
Unit Weight (kN/m^3):	4.501
Wet mass + tare (g):	381.49
Dry mass + tare (g):	302.33
Tare (g):	123.52
Water Content (%)	**44.27**
H:D ratio:	1.860
H:D correction:	0.9883
Saturation (%):	15.99

Age (days):	1063
Cap:	Surface ground, 50 durometer end cap
Maximum load (lb):	638.4
Maximum load (kN):	2.840
Strain Rate (%/min):	2.5
Time to Failure (min):	2.07
Strain at Failure (%):	6.877
Initial yield (psi):	83.57
Modulus (psi):	13770
ASTM C495	
Comp. Strength (MPa):	0.6400
Comp. Strength (psi):	92.83
Corr. Comp. Strength (psi):	**91.74**
ASTM D2166	
Comp. Strength (kPa):	617.8
Comp. Strength (psi):	89.60
Corr. Comp. Strength (psi):	**88.56**
Treatment:	D1

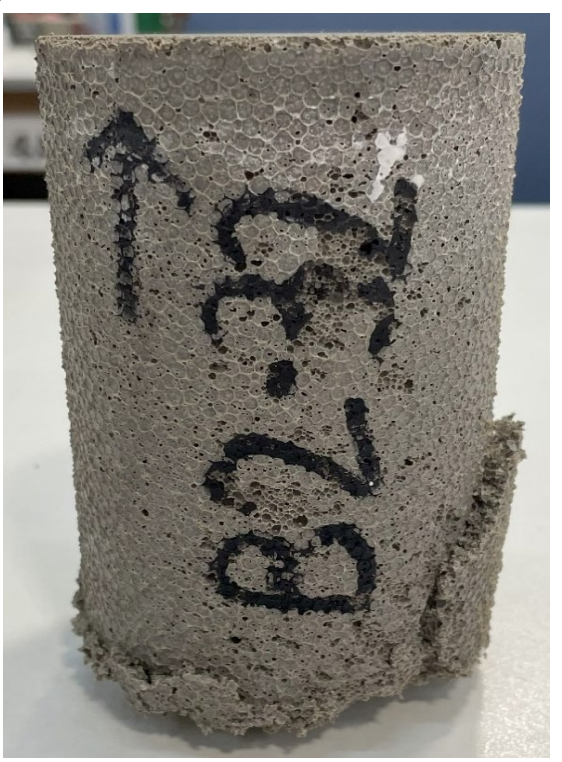

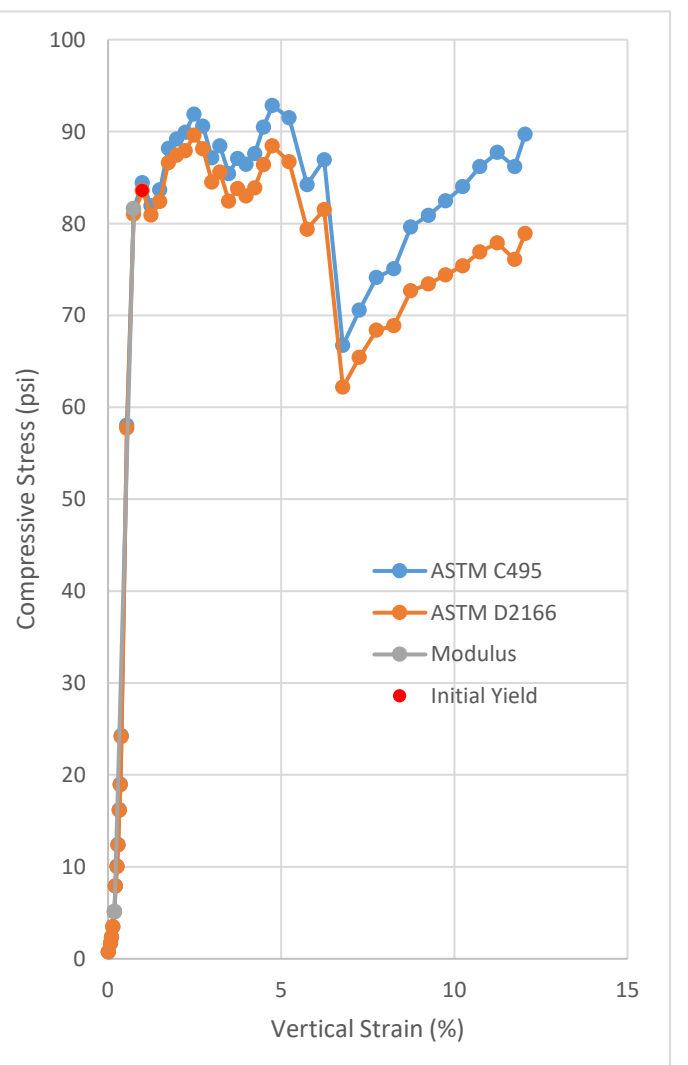

Uniaxial Compressive Strength of Lightweight Cellular Concrete

Sample ID:	**B2-33**
Height (in):	5.468
Height (mm):	138.9
Diameter (in):	2.954
Diameter (mm)	75.02
Area (in^2):	6.852
Area (mm^2):	4421
Mass (g):	276.1
Weight (lb):	0.6087
Weight (kN):	0.00270762
Volume (in^3):	37.47
Volume (mm^3):	614001
Density (g/mm^3):	0.0004497
Density (kg/m^3):	449.7
Unit Weight (pcf):	**28.07**
Unit Weight (kN/m^3):	4.410
Wet mass + tare (g):	345.11
Dry mass + tare (g):	275.29
Tare (g):	115.76
Water Content (%)	**43.77**
H:D ratio:	1.851
H:D correction:	0.9876
Saturation (%):	15.50

Age (days):	1063
Cap:	Surface ground, 50 durometer end cap
Maximum load (lb):	668.83
Maximum load (kN):	2.975
Strain Rate (%/min):	2.5
Time to Failure (min):	4.89
Strain at Failure (%):	6.854
Initial yield (psi):	84.77
Modulus (psi):	14675
ASTM C495	
Comp. Strength (MPa):	0.6730
Comp. Strength (psi):	97.61
Corr. Comp. Strength (psi):	**96.40**
ASTM D2166	
Comp. Strength (kPa):	623.7
Comp. Strength (psi):	90.46
Corr. Comp. Strength (psi):	**89.34**
Treatment:	D1

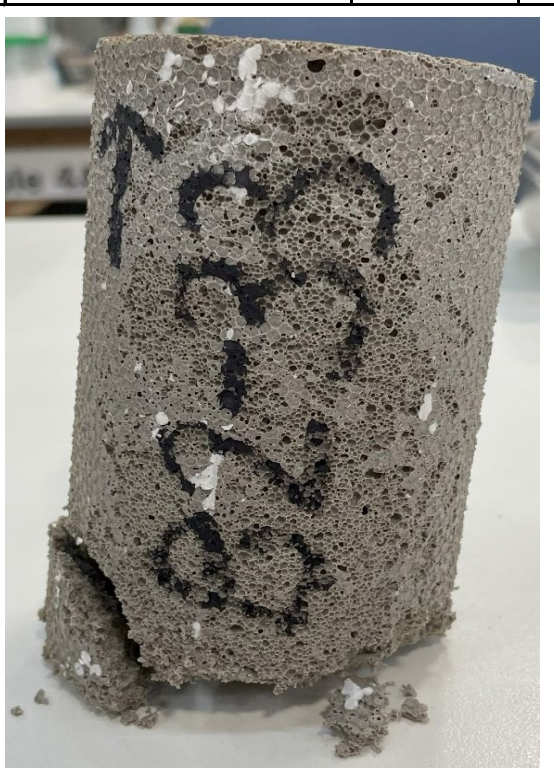

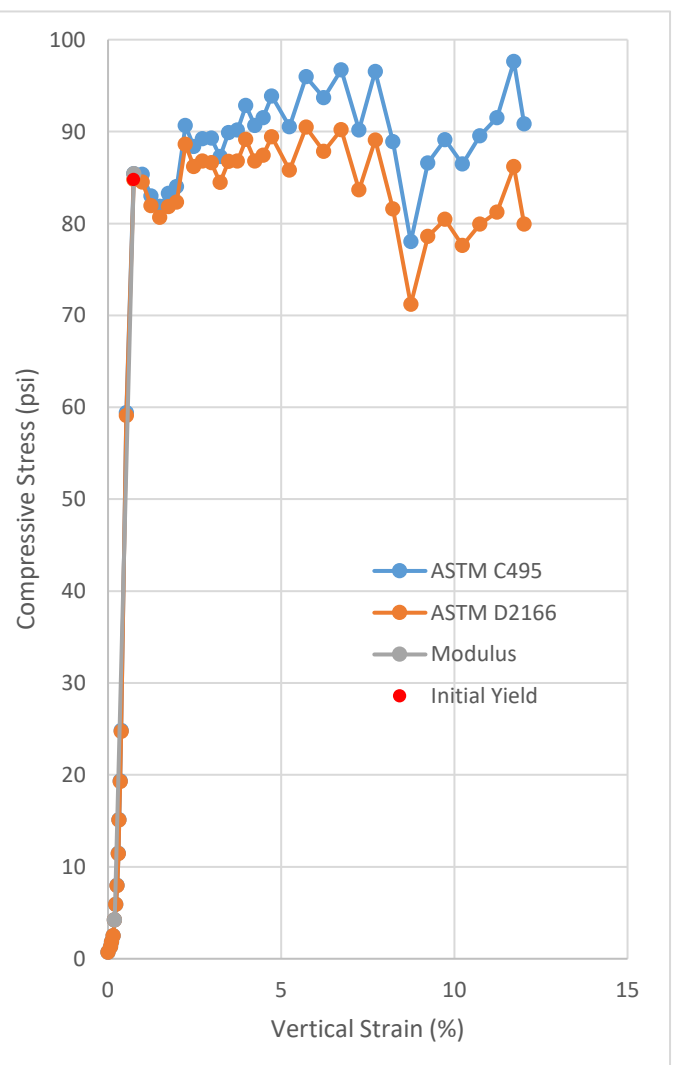

Uniaxial Compressive Strength of Lightweight Cellular Concrete

Sample ID:	**B2-34**
Height (in):	5.499
Height (mm):	139.7
Diameter (in):	2.957
Diameter (mm)	75.10
Area (in^2):	6.867
Area (mm^2):	4430
Mass (g):	276.35
Weight (lb):	0.6092
Weight (kN):	0.00271007
Volume (in^3):	37.76
Volume (mm^3):	618830
Density (g/mm^3):	0.0004466
Density (kg/m^3):	446.6
Unit Weight (pcf):	**27.88**
Unit Weight (kN/m^3):	4.379
Wet mass + tare (g):	355.27
Dry mass + tare (g):	283.84
Tare (g):	122.20
Water Content (%)	**44.19**
H:D ratio:	1.860
H:D correction:	0.9883
Saturation (%):	15.48

Age (days):	1063
Cap:	Surface ground, 50 durometer end cap
Maximum load (lb):	679.52
Maximum load (kN):	3.023
Strain Rate (%/min):	2.5
Time to Failure (min):	3.88
Strain at Failure (%):	6.867
Initial yield (psi):	95.95
Modulus (psi):	17277
ASTM C495	
Comp. Strength (MPa):	0.6823
Comp. Strength (psi):	98.96
Corr. Comp. Strength (psi):	**97.80**
ASTM D2166	
Comp. Strength (kPa):	661.6
Comp. Strength (psi):	95.95
Corr. Comp. Strength (psi):	**94.83**
Treatment:	D1

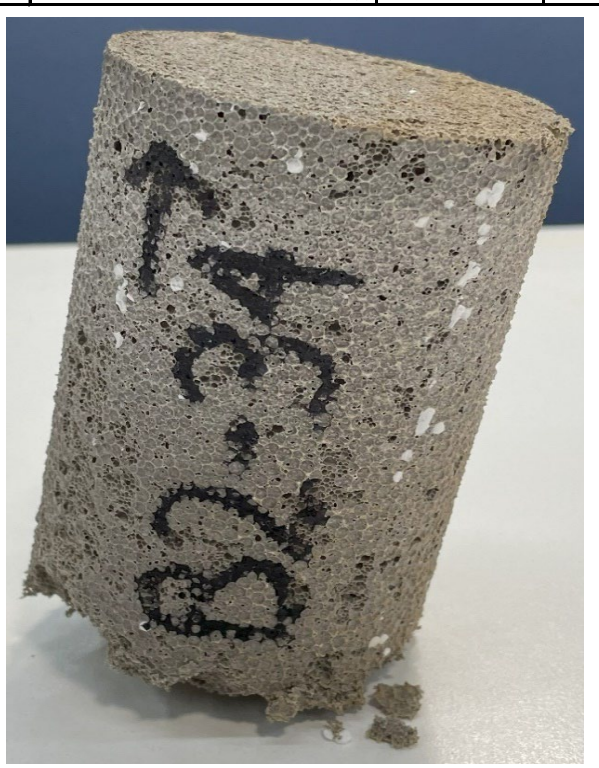

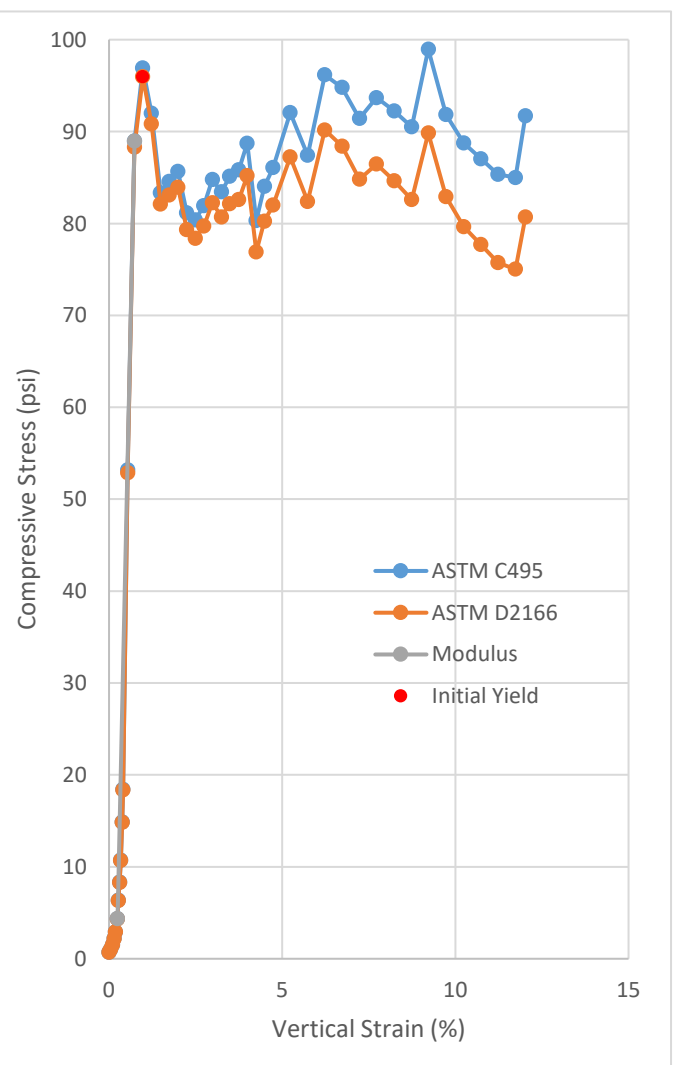

Uniaxial Compressive Strength of Lightweight Cellular Concrete

Sample ID:	**B2-35**
Height (in):	5.570
Height (mm):	141.5
Diameter (in):	2.959
Diameter (mm)	75.17
Area (in^2):	6.878
Area (mm^2):	4438
Mass (g):	287.82
Weight (lb):	0.6345
Weight (kN):	0.00282255
Volume (in^3):	38.31
Volume (mm^3):	627856
Density (g/mm^3):	0.0004584
Density (kg/m^3):	458.4
Unit Weight (pcf):	**28.62**
Unit Weight (kN/m^3):	4.496
Wet mass + tare (g):	376.64
Dry mass + tare (g):	301.11
Tare (g):	127.79
Water Content (%)	**43.58**
H:D ratio:	1.882
H:D correction:	0.9900
Saturation (%):	15.80

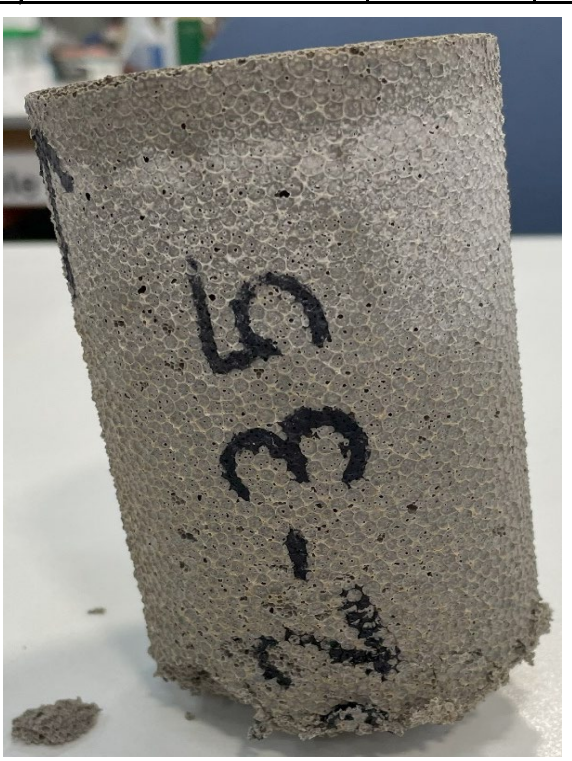

Age (days):	1063
Cap:	Surface ground, 50 durometer end cap
Maximum load (lb):	633.71
Maximum load (kN):	2.819
Strain Rate (%/min):	2.5
Time to Failure (min):	3.50
Strain at Failure (%):	6.877
Initial yield (psi):	76.41
Modulus (psi):	13047
ASTM C495	
Comp. Strength (MPa):	0.6352
Comp. Strength (psi):	92.13
Corr. Comp. Strength (psi):	**91.22**
ASTM D2166	
Comp. Strength (kPa):	582.9
Comp. Strength (psi):	84.55
Corr. Comp. Strength (psi):	**83.71**
Treatment:	D1

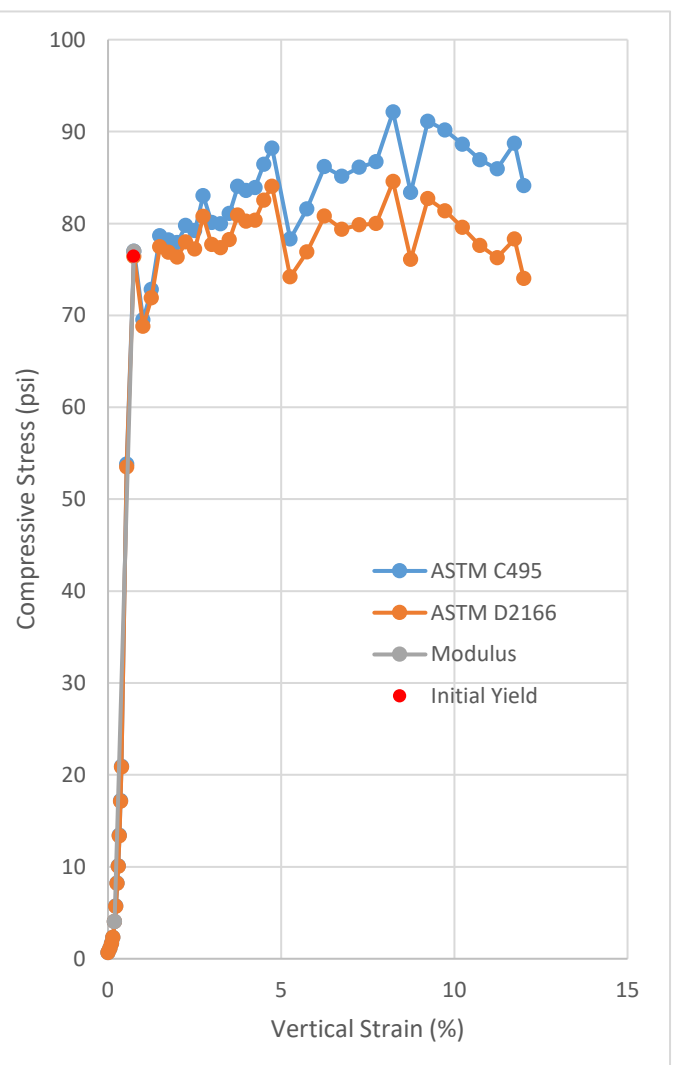

Uniaxial Compressive Strength of Lightweight Cellular Concrete

Sample ID:	**B2-36**
Height (in):	5.540
Height (mm):	140.7
Diameter (in):	2.963
Diameter (mm)	75.25
Area (in^2):	6.894
Area (mm^2):	4448
Mass (g):	289.86
Weight (lb):	0.6390
Weight (kN):	0.00284256
Volume (in^3):	38.19
Volume (mm^3):	625882
Density (g/mm^3):	0.0004631
Density (kg/m^3):	463.1
Unit Weight (pcf):	**28.91**
Unit Weight (kN/m^3):	4.542
Wet mass + tare (g):	396.81
Dry mass + tare (g):	309.22
Tare (g):	128.60
Water Content (%)	**48.49**
H:D ratio:	1.870
H:D correction:	0.9891
Saturation (%):	17.12

Age (days):	1064
Cap:	Surface ground, 50 durometer end cap
Maximum load (lb):	532.81
Maximum load (kN):	2.370
Strain Rate (%/min):	2.5
Time to Failure (min):	0.47
Strain at Failure (%):	6.895
Initial yield (psi):	76.71
Modulus (psi):	14885
ASTM C495	
Comp. Strength (MPa):	0.5329
Comp. Strength (psi):	77.29
Corr. Comp. Strength (psi):	**76.44**
ASTM D2166	
Comp. Strength (kPa):	528.9
Comp. Strength (psi):	76.71
Corr. Comp. Strength (psi):	**75.87**
Treatment:	D1

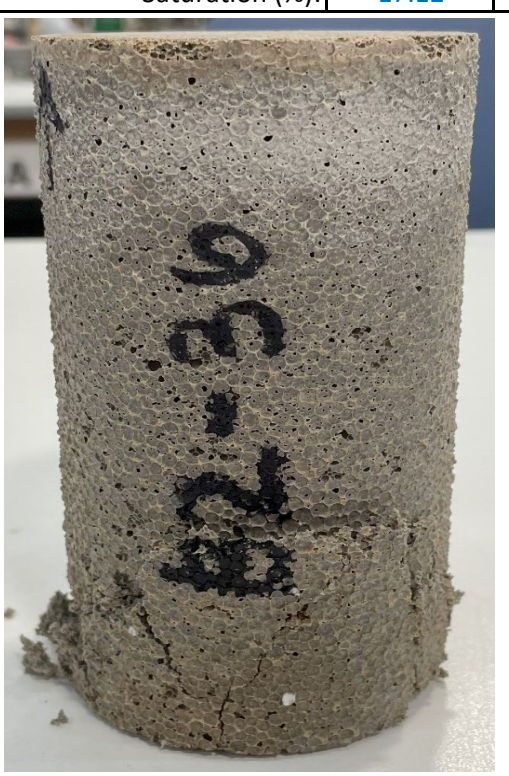

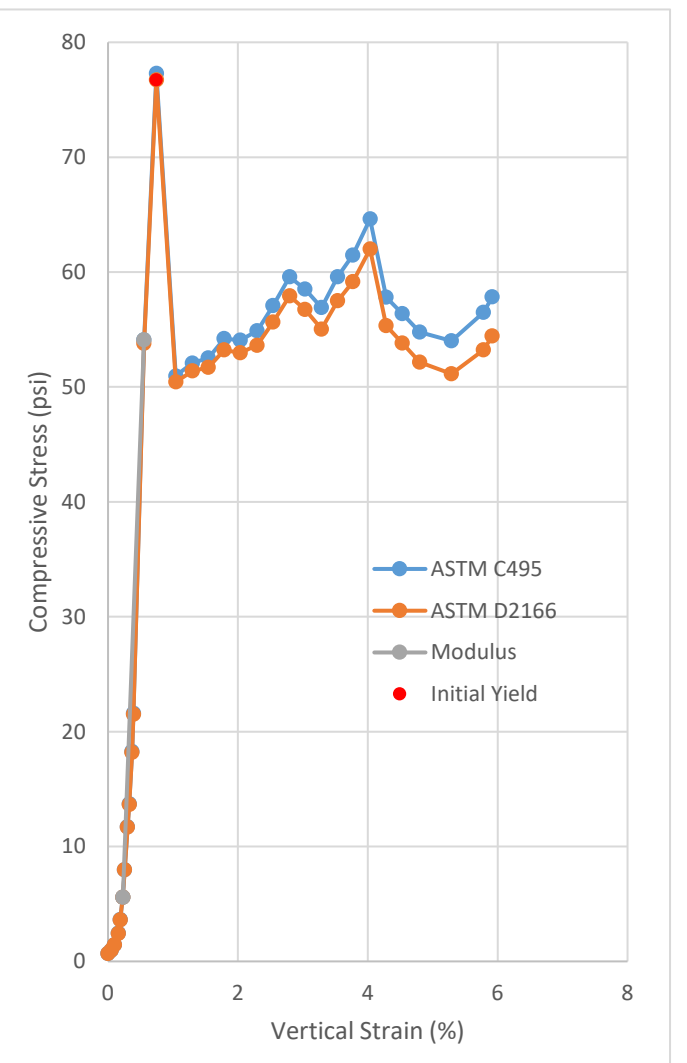

Uniaxial Compressive Strength of Lightweight Cellular Concrete

Sample ID:	**B2-37**
Height (in):	5.469
Height (mm):	138.9
Diameter (in):	2.957
Diameter (mm)	75.12
Area (in^2):	6.869
Area (mm^2):	4432
Mass (g):	289.1
Weight (lb):	0.6374
Weight (kN):	0.0028351
Volume (in^3):	37.57
Volume (mm^3):	615648
Density (g/mm^3):	0.0004696
Density (kg/m^3):	469.6
Unit Weight (pcf):	**29.32**
Unit Weight (kN/m^3):	4.605
Wet mass + tare (g):	420.91
Dry mass + tare (g):	335.27
Tare (g):	160.86
Water Content (%)	**49.10**
H:D ratio:	1.849
H:D correction:	0.9874
Saturation (%):	17.53

Age (days):	1066
Cap:	Surface ground, 50 durometer end cap
Maximum load (lb):	843.13
Maximum load (kN):	3.750
Strain Rate (%/min):	2.5
Time to Failure (min):	5.01
Strain at Failure (%):	6.867
Initial yield (psi):	103.79
Modulus (psi):	17924
ASTM C495	
Comp. Strength (MPa):	0.8462
Comp. Strength (psi):	122.74
Corr. Comp. Strength (psi):	**121.19**
ASTM D2166	
Comp. Strength (kPa):	771.8
Comp. Strength (psi):	111.94
Corr. Comp. Strength (psi):	**110.54**
Treatment:	W1

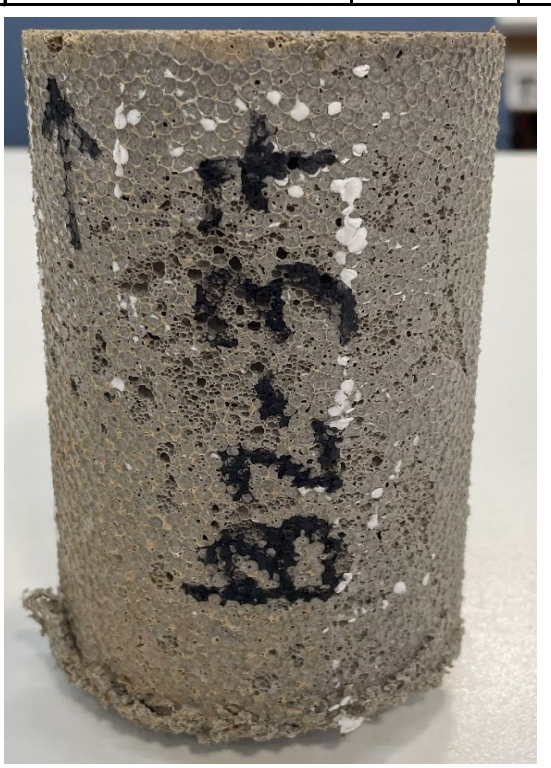

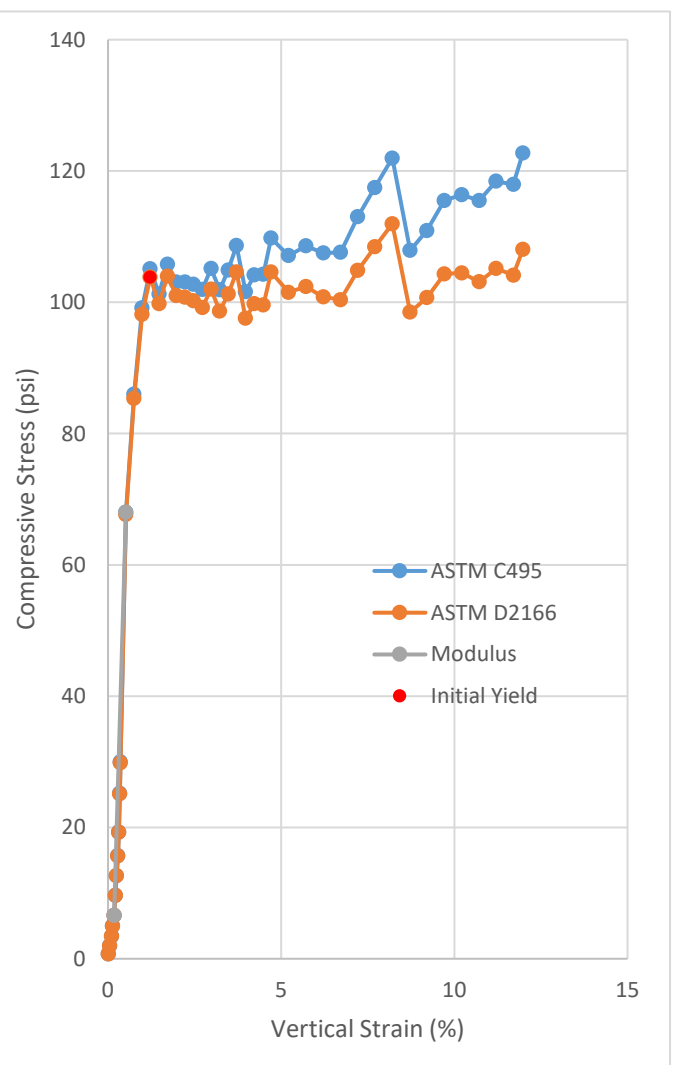

Uniaxial Compressive Strength of Lightweight Cellular Concrete

Sample ID:	**B2-38**
Height (in):	5.508
Height (mm):	139.9
Diameter (in):	2.954
Diameter (mm)	75.03
Area (in^2):	6.853
Area (mm^2):	4421
Mass (g):	293.58
Weight (lb):	0.6472
Weight (kN):	0.00287904
Volume (in^3):	37.74
Volume (mm^3):	618510
Density (g/mm^3):	0.0004747
Density (kg/m^3):	474.7
Unit Weight (pcf):	**29.63**
Unit Weight (kN/m^3):	4.655
Wet mass + tare (g):	384.15
Dry mass + tare (g):	296.64
Tare (g):	128.16
Water Content (%)	**51.94**
H:D ratio:	1.865
H:D correction:	0.9886
Saturation (%):	18.37

Age (days):	1066
Cap:	Surface ground, 50 durometer end cap
Maximum load (lb):	720.09
Maximum load (kN):	3.203
Strain Rate (%/min):	2.5
Time to Failure (min):	3.90
Strain at Failure (%):	6.854
Initial yield (psi):	94.61
Modulus (psi):	17057
ASTM C495	
Comp. Strength (MPa):	0.7245
Comp. Strength (psi):	105.08
Corr. Comp. Strength (psi):	**103.88**
ASTM D2166	
Comp. Strength (kPa):	665.3
Comp. Strength (psi):	96.49
Corr. Comp. Strength (psi):	**95.40**
Treatment:	W1

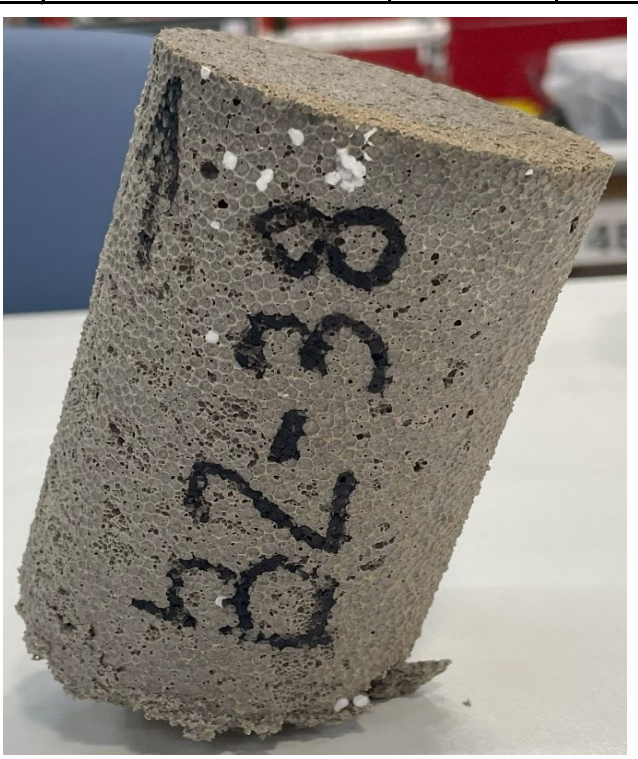

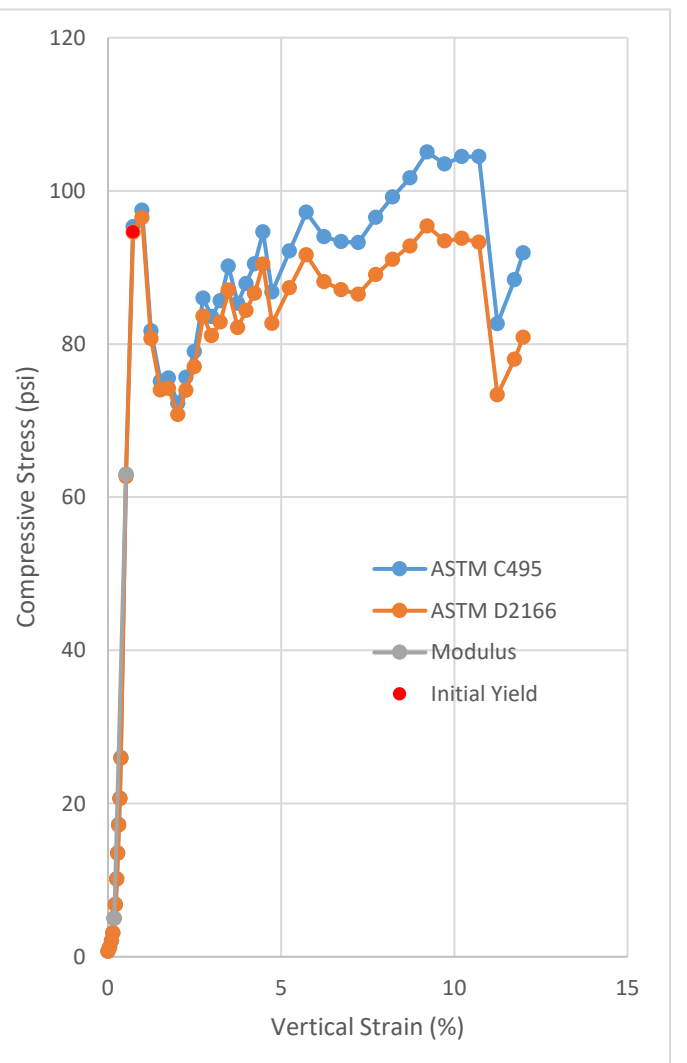

Uniaxial Compressive Strength of Lightweight Cellular Concrete

Sample ID:	**B2-39**
Height (in):	5.491
Height (mm):	139.5
Diameter (in):	2.964
Diameter (mm)	75.29
Area (in^2):	6.902
Area (mm^2):	4453
Mass (g):	306.17
Weight (lb):	0.6750
Weight (kN):	0.0030025
Volume (in^3):	37.89
Volume (mm^3):	620969
Density (g/mm^3):	0.0004931
Density (kg/m^3):	493.1
Unit Weight (pcf):	**30.78**
Unit Weight (kN/m^3):	4.835
Wet mass + tare (g):	395.65
Dry mass + tare (g):	297.55
Tare (g):	126.64
Water Content (%)	**57.40**
H:D ratio:	1.852
H:D correction:	0.9877
Saturation (%):	20.37

Age (days):	1066
Cap:	Surface ground, 50 durometer end cap
Maximum load (lb):	612.35
Maximum load (kN):	2.724
Strain Rate (%/min):	2.5
Time to Failure (min):	0.65
Strain at Failure (%):	6.900
Initial yield (psi):	87.63
Modulus (psi):	13667
ASTM C495	
Comp. Strength (MPa):	0.6118
Comp. Strength (psi):	88.73
Corr. Comp. Strength (psi):	**87.63**
ASTM D2166	
Comp. Strength (kPa):	604.2
Comp. Strength (psi):	87.63
Corr. Comp. Strength (psi):	**86.55**
Treatment:	W1

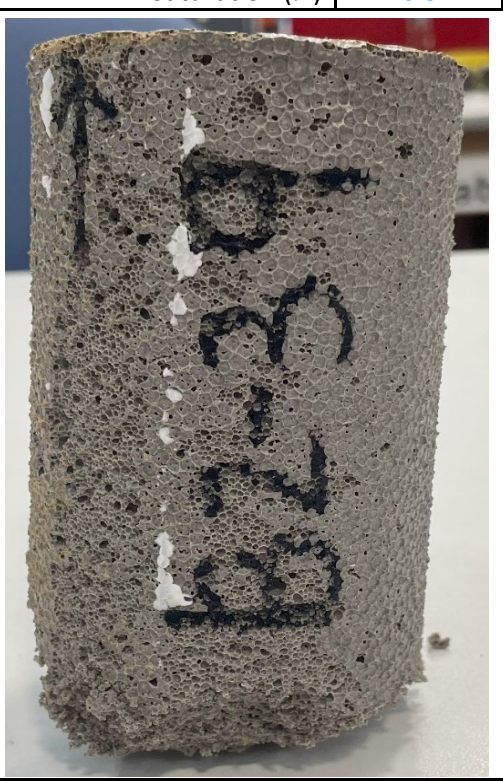

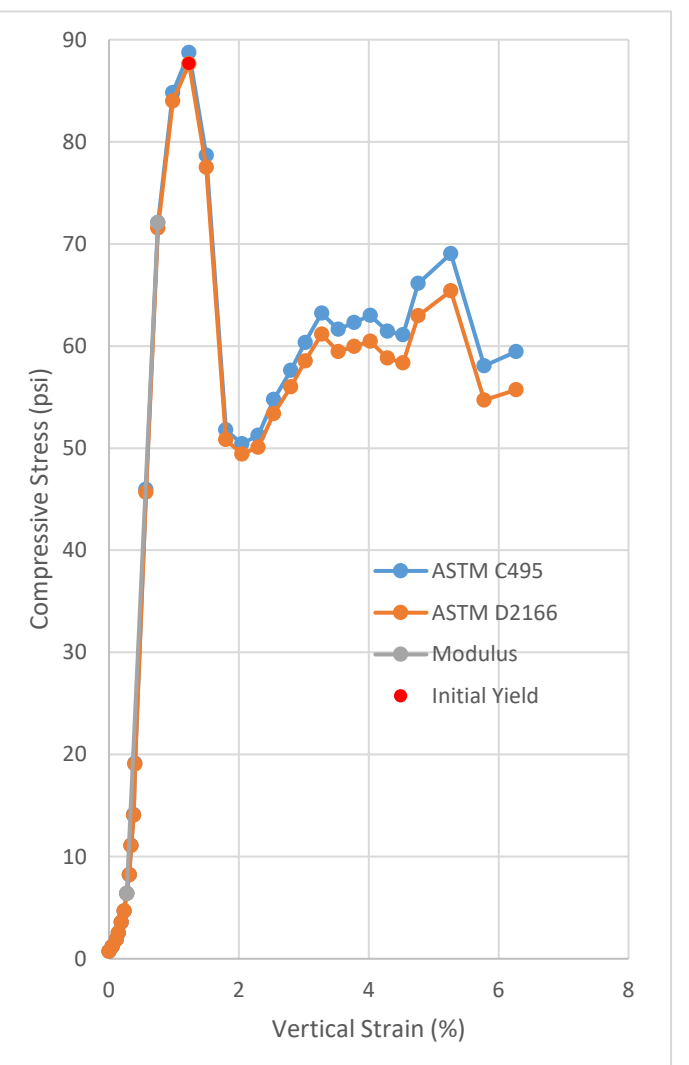

Uniaxial Compressive Strength of Lightweight Cellular Concrete

Sample ID:	**B2-40**
Height (in):	5.512
Height (mm):	140.0
Diameter (in):	2.950
Diameter (mm)	74.94
Area (in^2):	6.836
Area (mm^2):	4411
Mass (g):	299.55
Weight (lb):	0.6604
Weight (kN):	0.00293758
Volume (in^3):	37.68
Volume (mm^3):	617470
Density (g/mm^3):	0.0004851
Density (kg/m^3):	485.1
Unit Weight (pcf):	**30.29**
Unit Weight (kN/m^3):	4.757
Wet mass + tare (g):	382.46
Dry mass + tare (g):	292.20
Tare (g):	127.25
Water Content (%)	**54.72**
H:D ratio:	1.868
H:D correction:	0.9889
Saturation (%):	19.44

Age (days):	1066
Cap:	Surface ground, 50 durometer end cap
Maximum load (lb):	612.66
Maximum load (kN):	2.725
Strain Rate (%/min):	2.5
Time to Failure (min):	4.68
Strain at Failure (%):	6.835
Initial yield (psi):	83.50
Modulus (psi):	12444
ASTM C495	
Comp. Strength (MPa):	0.6179
Comp. Strength (psi):	89.62
Corr. Comp. Strength (psi):	**88.62**
ASTM D2166	
Comp. Strength (kPa):	575.7
Comp. Strength (psi):	83.50
Corr. Comp. Strength (psi):	**82.57**
Treatment:	W1

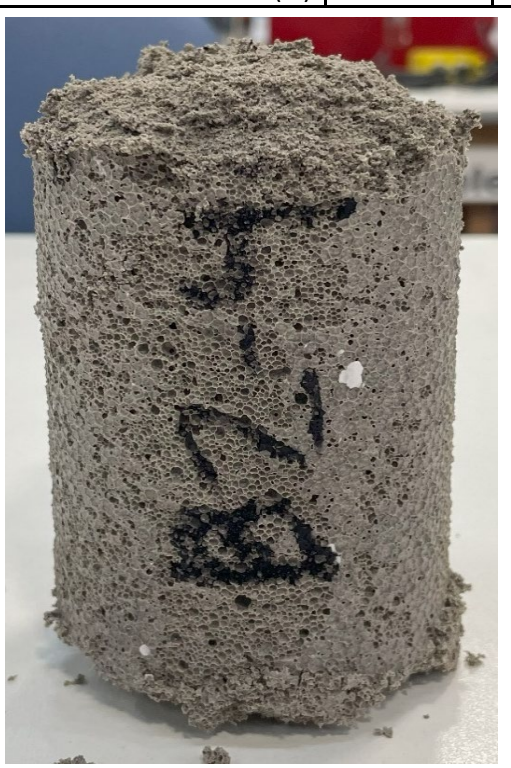

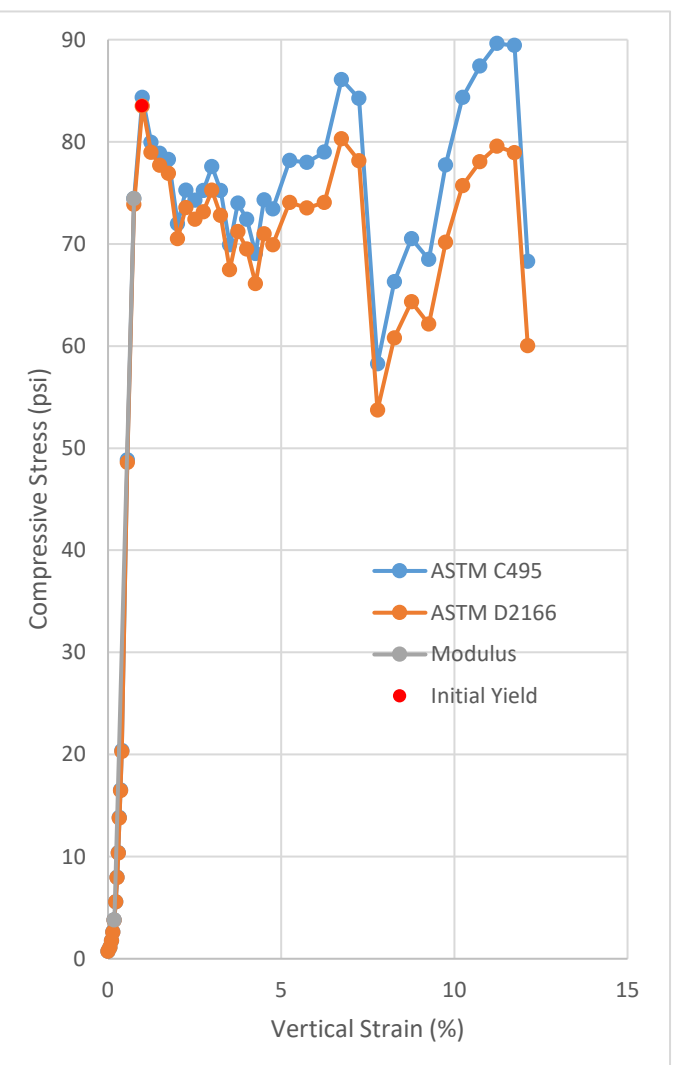

Uniaxial Compressive Strength of Lightweight Cellular Concrete

Sample ID:	**B2-41**
Height (in):	5.537
Height (mm):	140.6
Diameter (in):	2.967
Diameter (mm)	75.35
Area (in^2):	6.912
Area (mm^2):	4459
Mass (g):	302.32
Weight (lb):	0.6665
Weight (kN):	0.00296475
Volume (in^3):	38.27
Volume (mm^3):	627111
Density (g/mm^3):	0.0004821
Density (kg/m^3):	482.1
Unit Weight (pcf):	**30.10**
Unit Weight (kN/m^3):	4.728
Wet mass + tare (g):	370.67
Dry mass + tare (g):	287.79
Tare (g):	127.55
Water Content (%)	**51.72**
H:D ratio:	1.866
H:D correction:	0.9888
Saturation (%):	18.65

Age (days):	1070
Cap:	Surface ground, 50 durometer end cap
Maximum load (lb):	590.98
Maximum load (kN):	2.629
Strain Rate (%/min):	2.5
Time to Failure (min):	2.68
Strain at Failure (%):	6.914
Initial yield (psi):	83.34
Modulus (psi):	12981
ASTM C495	
Comp. Strength (MPa):	0.5895
Comp. Strength (psi):	85.50
Corr. Comp. Strength (psi):	**84.54**
ASTM D2166	
Comp. Strength (kPa):	574.6
Comp. Strength (psi):	83.34
Corr. Comp. Strength (psi):	**82.41**
Treatment:	W1

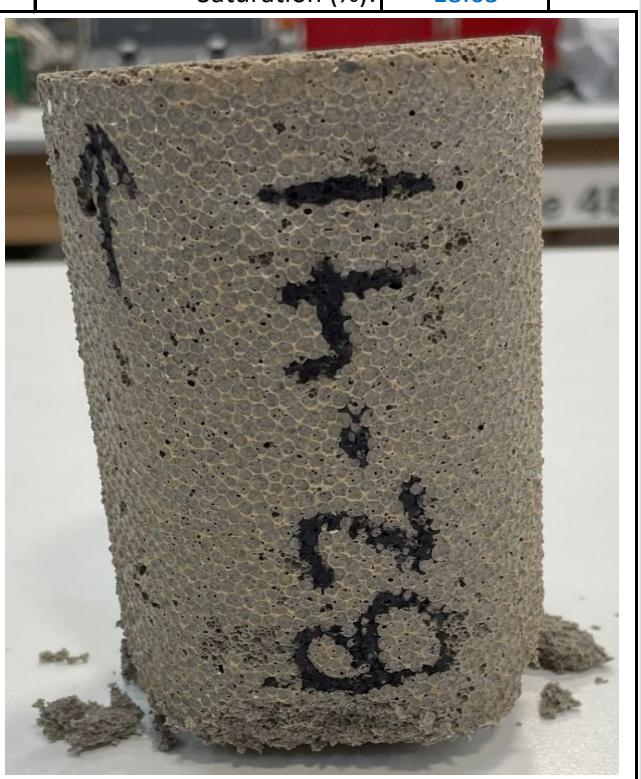

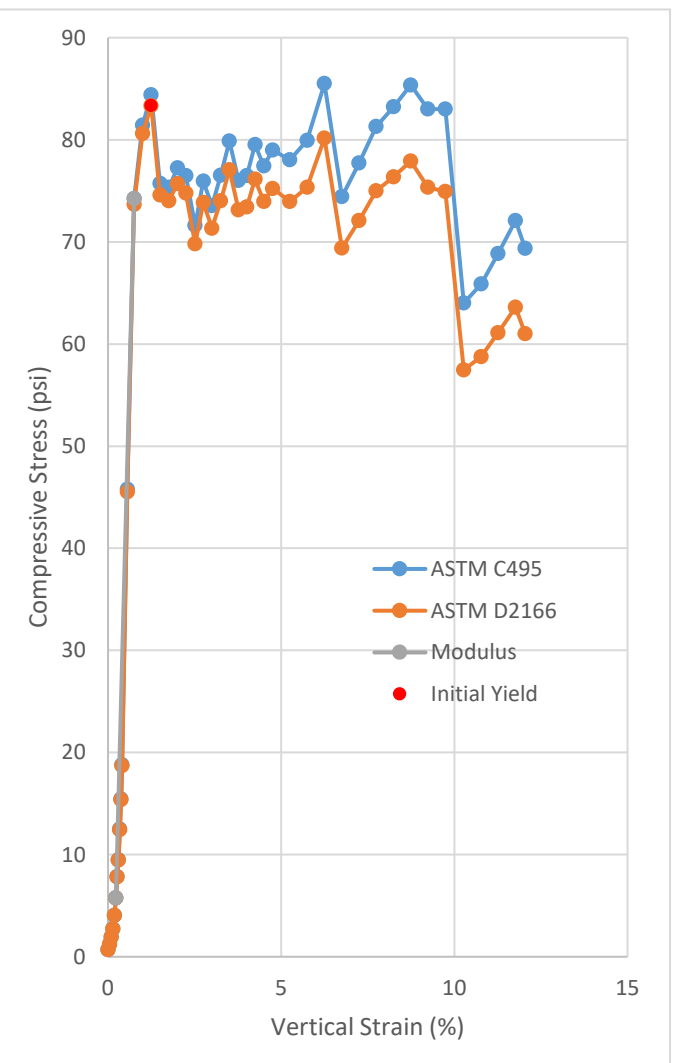

APPENDIX E

TRIAXIAL COMPRESSION STRENGTH TEST RESULTS

Consolidated-Drained Triaxial Shear, Lightweight Cellular Concrete

Sample ID:	**B2-42**
Height (in):	5.663
Height (mm):	143.8
Diameter (in):	2.962
Diameter (mm)	75.23
Area (in^2):	6.890
Area (mm^2):	4445
Mass (g):	216.40
Weight (lb):	0.4771
Weight (kN):	0.002122
Volume (in^3):	39.01
Volume (mm^3):	639318
Density (g/mm^3):	0.0003385
Density (kg/m^3):	338.5
Unit weight (pcf):	**21.13**
Dry unit weight (pcf);	**19.08**
Unit Weight (kN/m^3):	3.319
Wet mass + tare (g):	316.06
Dry mass + tare (g):	297.12
Tare (g):	121.28
Water content (%)	**10.77**
Saturation (%):	**3.72**
H:D ratio:	1.912
Age (days):	1052
Treatment:	AD

Strain rate (%/min):	0.2
Mean σ'_3 (psi):	3.7
Initial modulus (psi):	36132
Initial yield	
Time to failure (min):	1.3
Axial strain at failure (%):	0.266
σ'_1 (psi):	99.82
σ'_3 (psi):	3.58
$\sigma'_1 - \sigma'_3$ (psi):	96.24
σ'_1 / σ'_3:	27.87
p' (psi):	51.70
q (psi):	48.12
Volumetric strain (%):	0.147
Poisson's ratio:	0.223
Peak stress	
Time to failure (min):	25.6
Axial strain at failure (%):	5.115
σ'_1 (psi):	142.73
σ'_3 (psi):	3.75
$\sigma'_1 - \sigma'_3$ (psi):	138.98
σ'_1 / σ'_3:	38.06
p' (psi):	73.24
q (psi):	69.49
Volumetric strain (%):	4.424
Poisson's ratio:	0.068

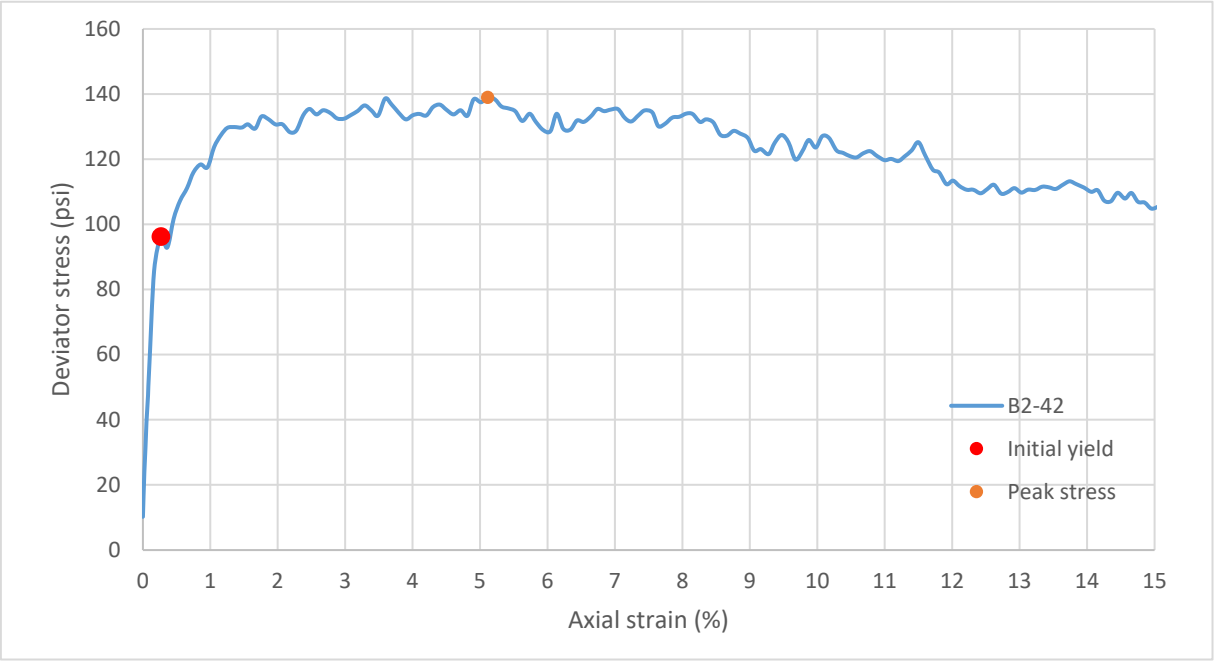

Sample ID:	B2-42

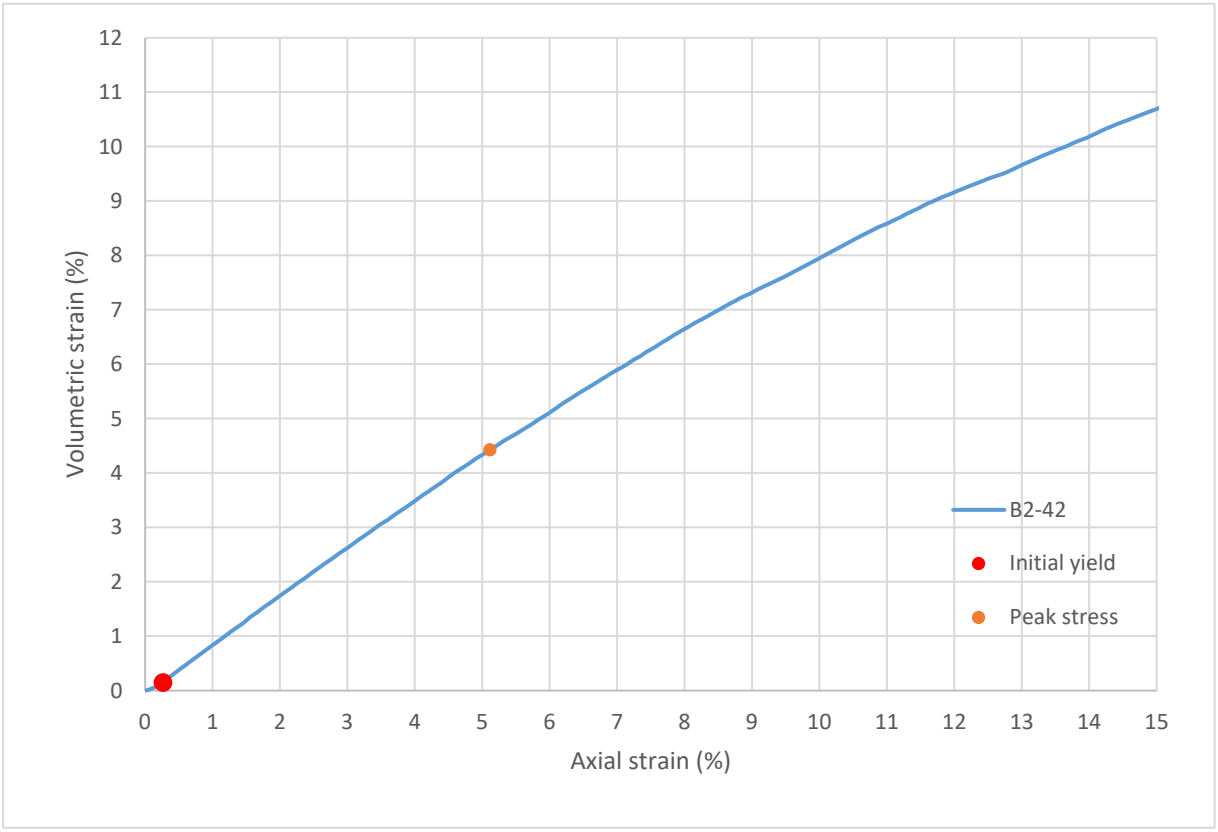

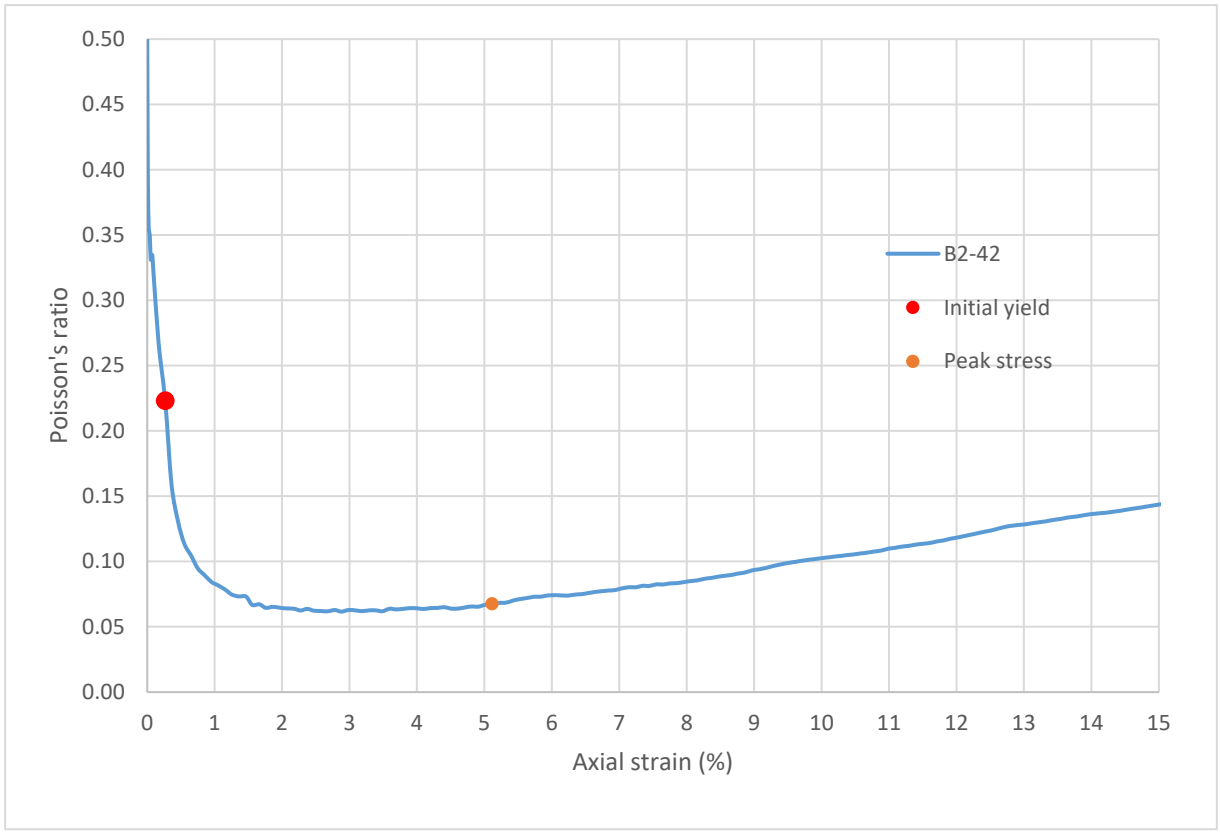

Sample ID:	B2-42

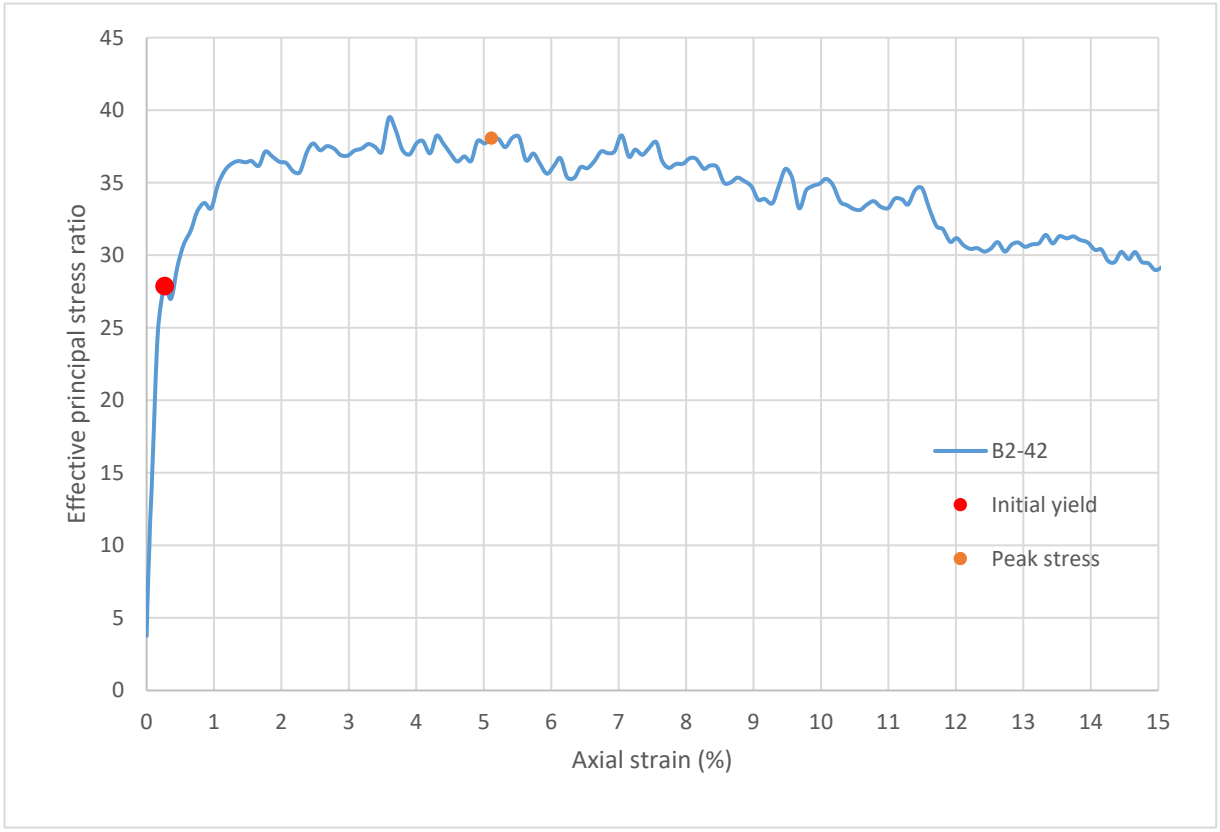

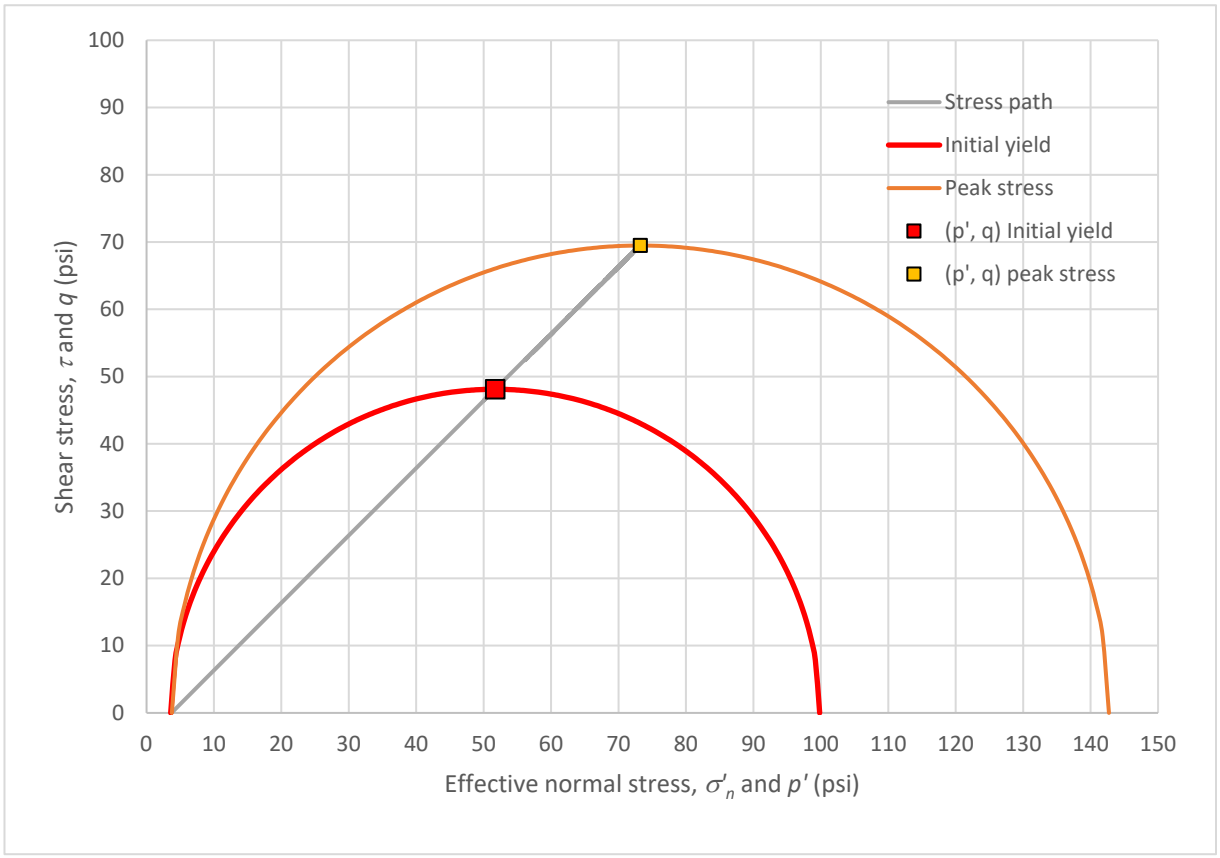

Consolidated-Drained Triaxial Shear, Lightweight Cellular Concrete

Sample ID:	**B2-43**
Height (in):	5.637
Height (mm):	143.2
Diameter (in):	2.952
Diameter (mm)	74.98
Area (in^2):	6.844
Area (mm^2):	4415
Mass (g):	215.17
Weight (lb):	0.4744
Weight (kN):	0.002110
Volume (in^3):	38.58
Volume (mm^3):	632140
Density (g/mm^3):	0.0003404
Density (kg/m^3):	340.4
Unit weight (pcf):	**21.25**
Dry unit weight (pcf);	**19.29**
Unit Weight (kN/m^3):	3.338
Wet mass + tare (g):	324.56
Dry mass + tare (g):	306.31
Tare (g):	126.20
Water content (%)	**10.13**
Saturation (%):	**3.54**
H:D ratio:	1.910
Age (days):	1052
Treatment:	AD

Strain rate (%/min):	0.2
Mean σ'_3 (psi):	3.0
Initial modulus (psi):	40616
Initial yield	
Time to failure (min):	1.2
Axial strain at failure (%):	0.244
σ'_1 (psi):	101.99
σ'_3 (psi):	2.92
σ'_1 -σ'_3 (psi):	99.07
σ'_1 / σ'_3:	34.91
p' (psi):	52.46
q (psi):	49.54
Volumetric strain (%):	0.124
Poisson's ratio:	0.246
Peak stress	
Time to failure (min):	18.3
Axial strain at failure (%):	3.667
σ'_1 (psi):	145.97
σ'_3 (psi):	2.88
σ'_1 -σ'_3 (psi):	143.09
σ'_1 / σ'_3:	50.61
p' (psi):	74.43
q (psi):	71.54
Volumetric strain (%):	3.200
Poisson's ratio:	0.064

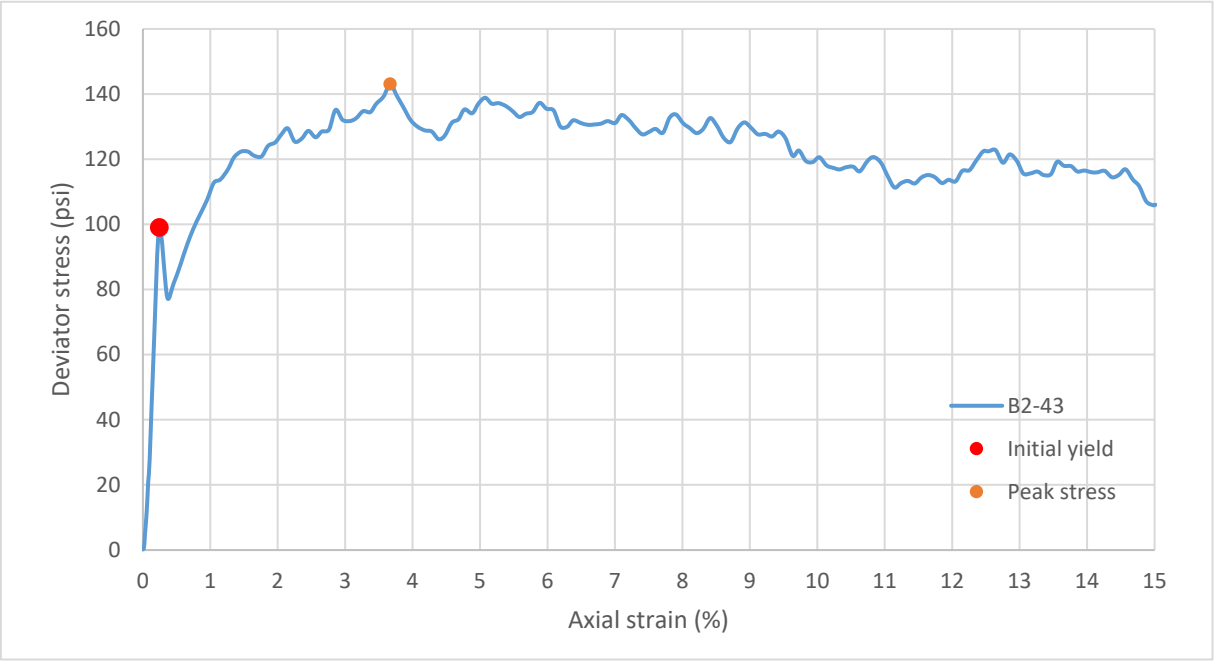

Sample ID:	B2-43

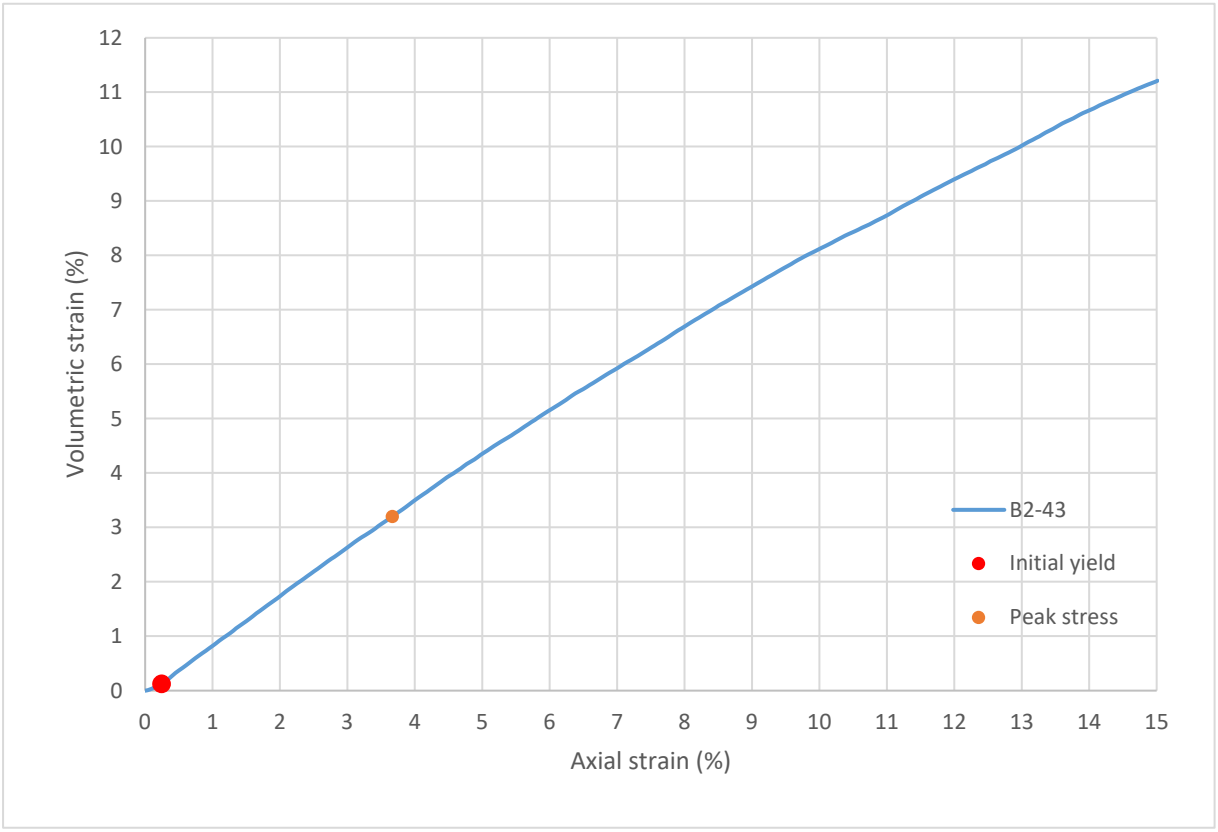

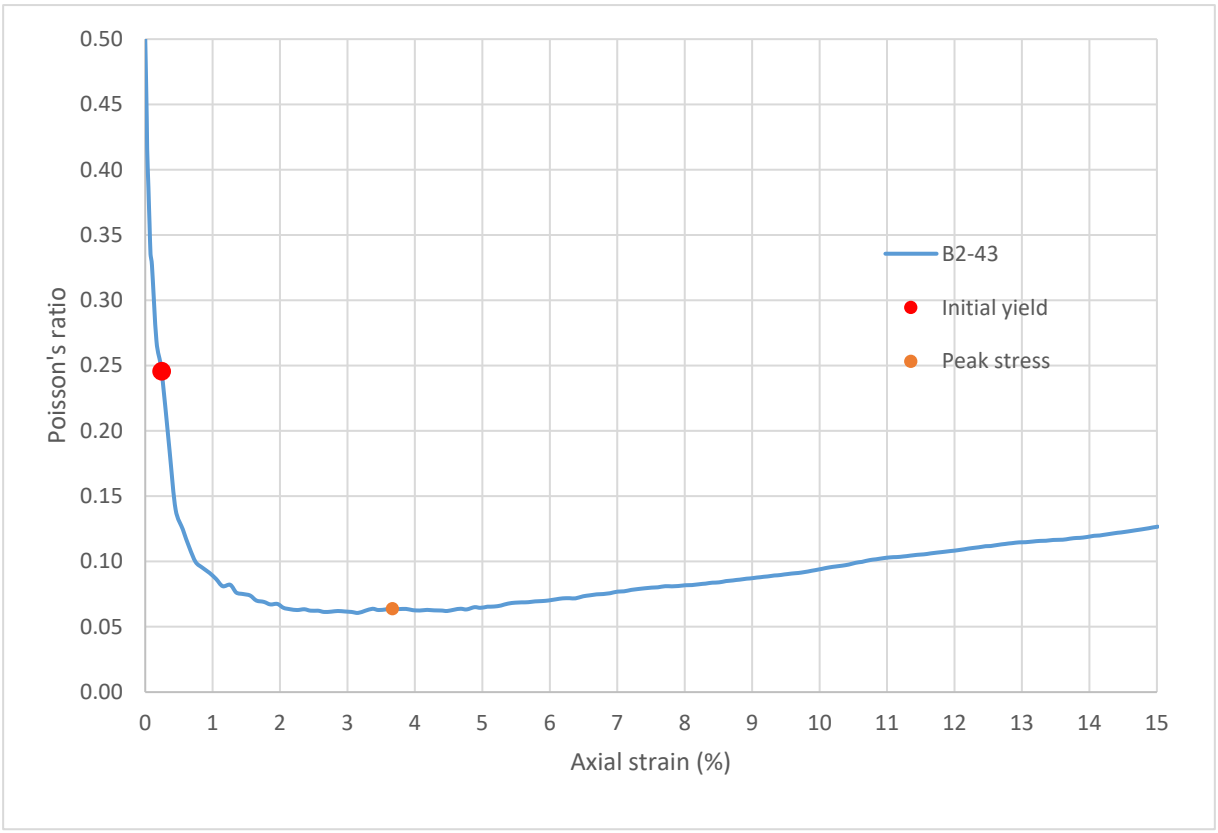

Sample ID:	B2-43

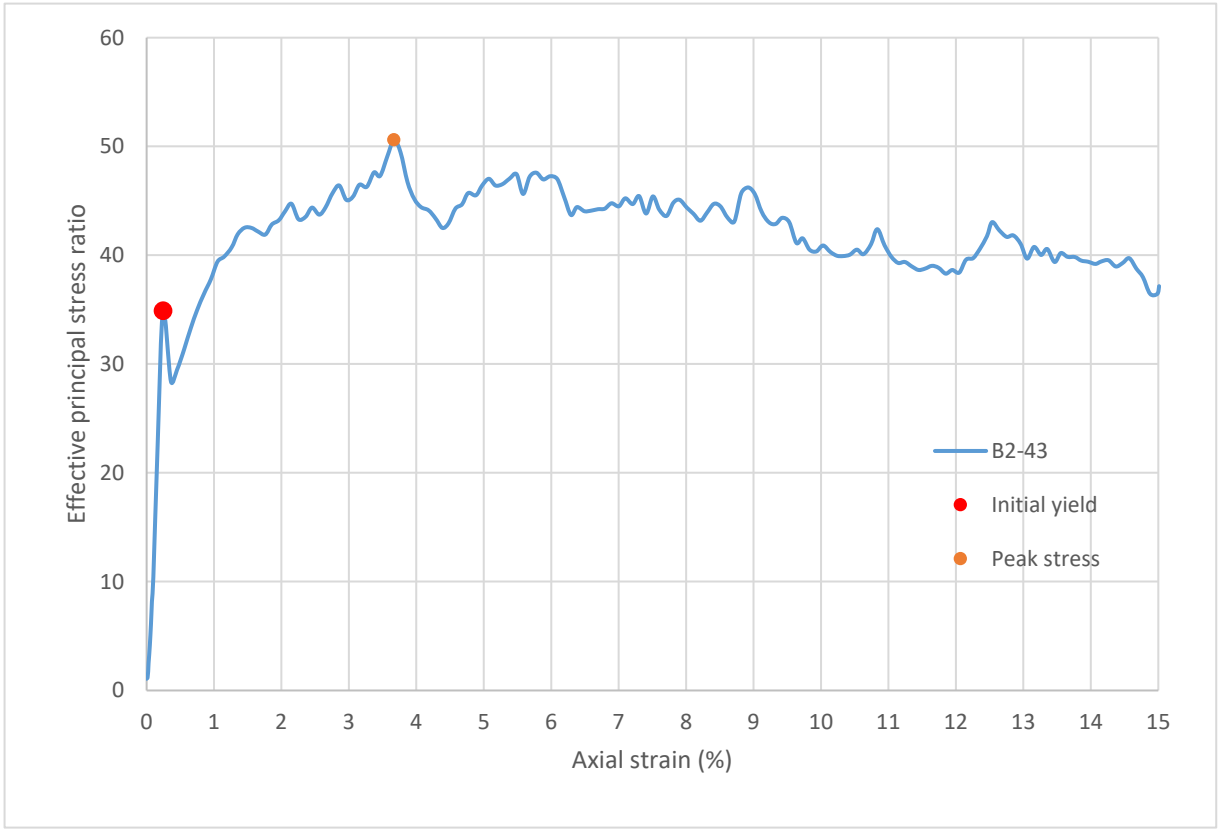

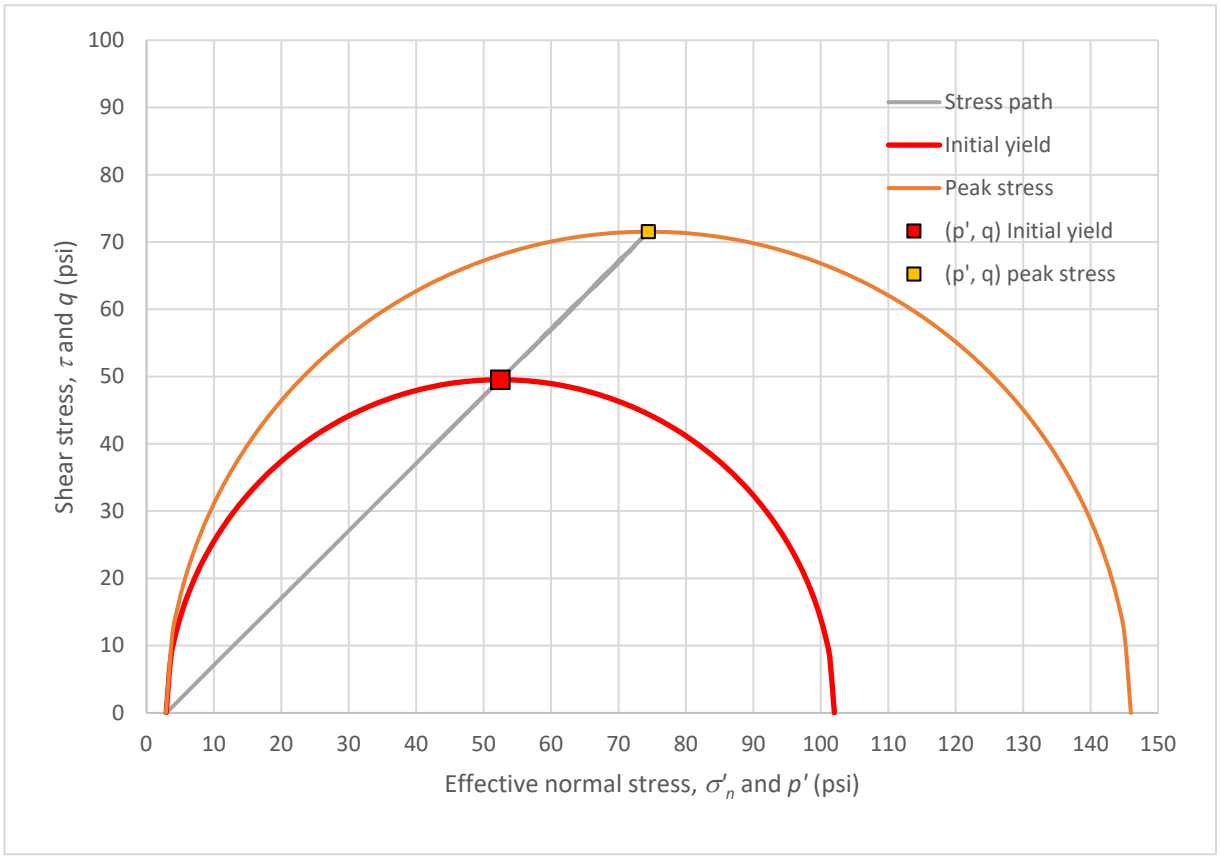

Consolidated-Drained Triaxial Shear, Lightweight Cellular Concrete

Sample ID:	**B2-44**
Height (in):	5.538
Height (mm):	140.7
Diameter (in):	2.959
Diameter (mm)	75.17
Area (in^2):	6.879
Area (mm^2):	4438
Mass (g):	209.38
Weight (lb):	0.4616
Weight (kN):	0.002053
Volume (in^3):	38.09
Volume (mm^3):	624221
Density (g/mm^3):	0.0003354
Density (kg/m^3):	335.4
Unit weight (pcf):	**20.94**
Dry unit weight (pcf);	**19.03**
Unit Weight (kN/m^3):	3.289
Wet mass + tare (g):	326.68
Dry mass + tare (g):	308.23
Tare (g):	124.51
Water content (%)	**10.04**
Saturation (%):	**3.46**
H:D ratio:	1.871
Age (days):	1053
Treatment:	AD

Strain rate (%/min):	0.2
Mean σ'_3 (psi):	4.0
Initial modulus (psi):	42805
Initial yield	
Time to failure (min):	1.3
Axial strain at failure (%):	0.251
σ'_1 (psi):	111.24
σ'_3 (psi):	3.92
σ'_1 -σ'_3 (psi):	107.32
σ'_1 / σ'_3:	28.39
p' (psi):	57.58
q (psi):	53.66
Volumetric strain (%):	0.122
Poisson's ratio:	0.258
Peak stress	
Time to failure (min):	28.0
Axial strain at failure (%):	5.593
σ'_1 (psi):	148.72
σ'_3 (psi):	4.02
σ'_1 -σ'_3 (psi):	144.70
σ'_1 / σ'_3:	37.00
p' (psi):	76.37
q (psi):	72.35
Volumetric strain (%):	4.887
Poisson's ratio:	0.063

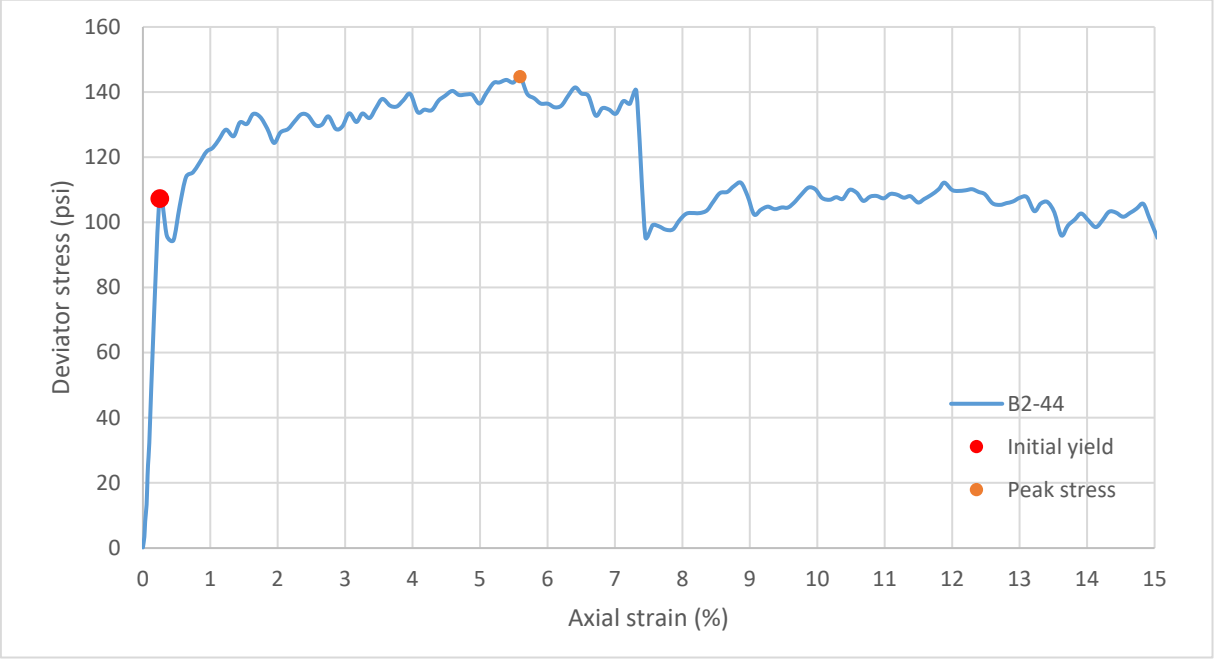

Sample ID:	B2-44

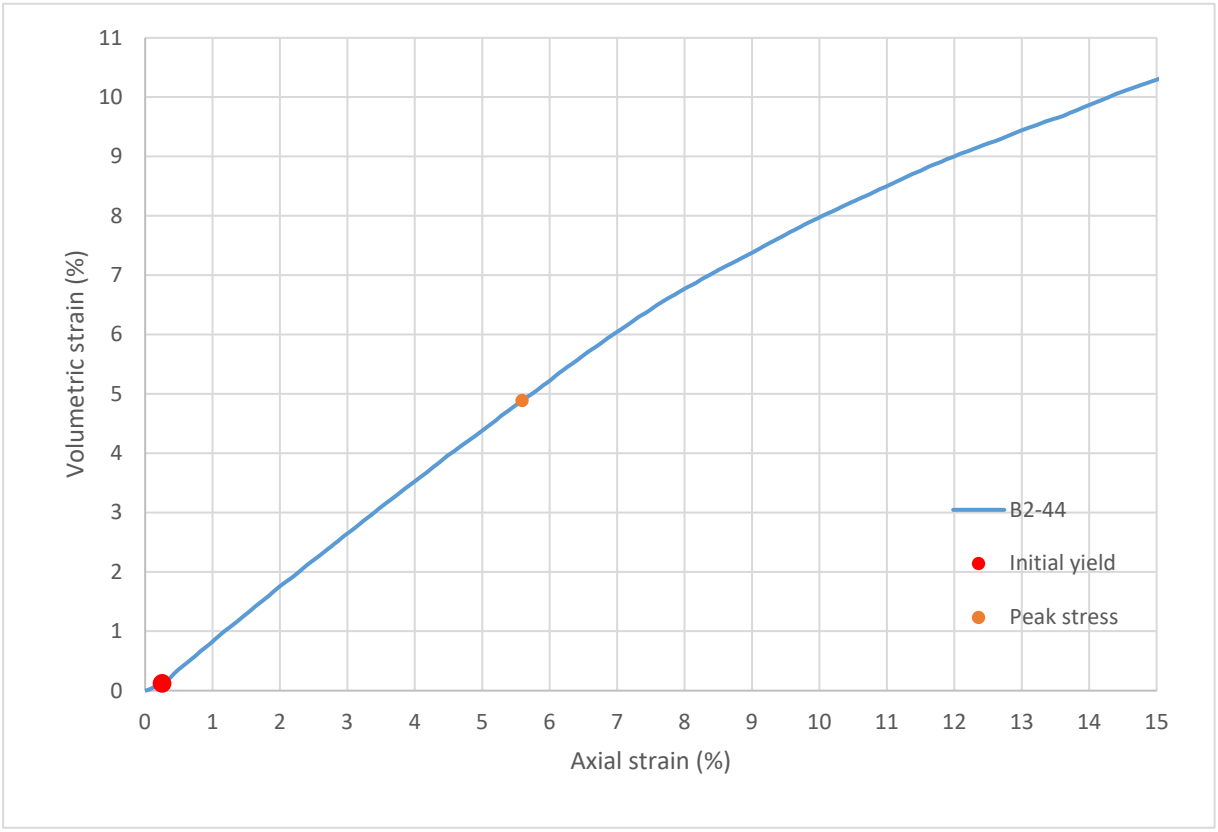

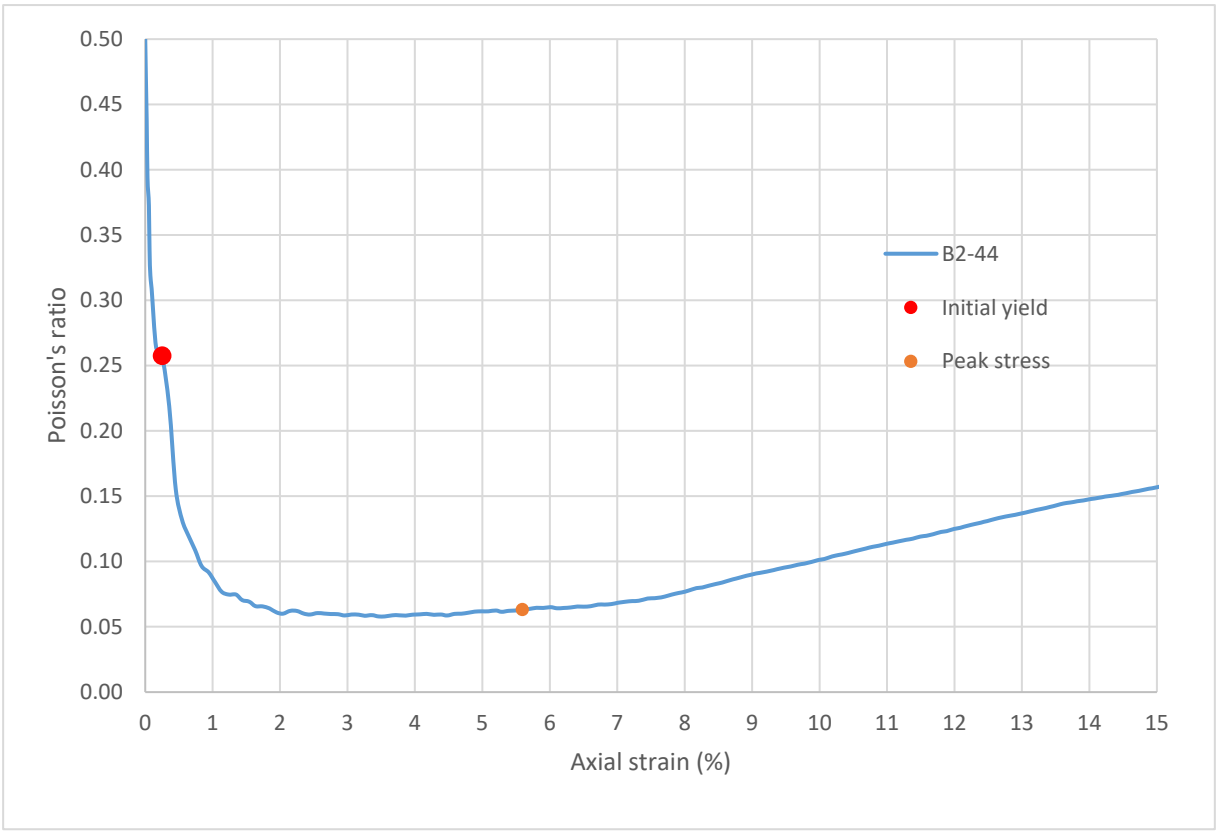

Sample ID:	B2-44

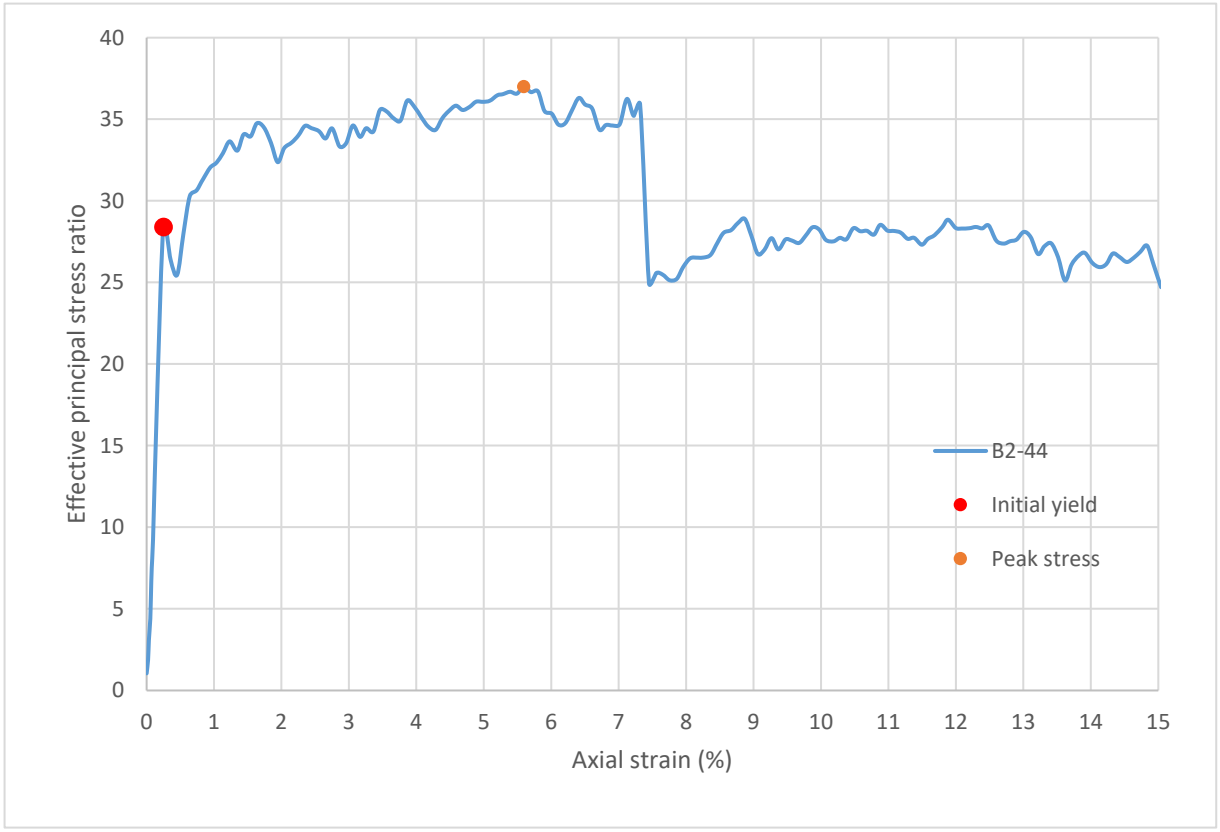

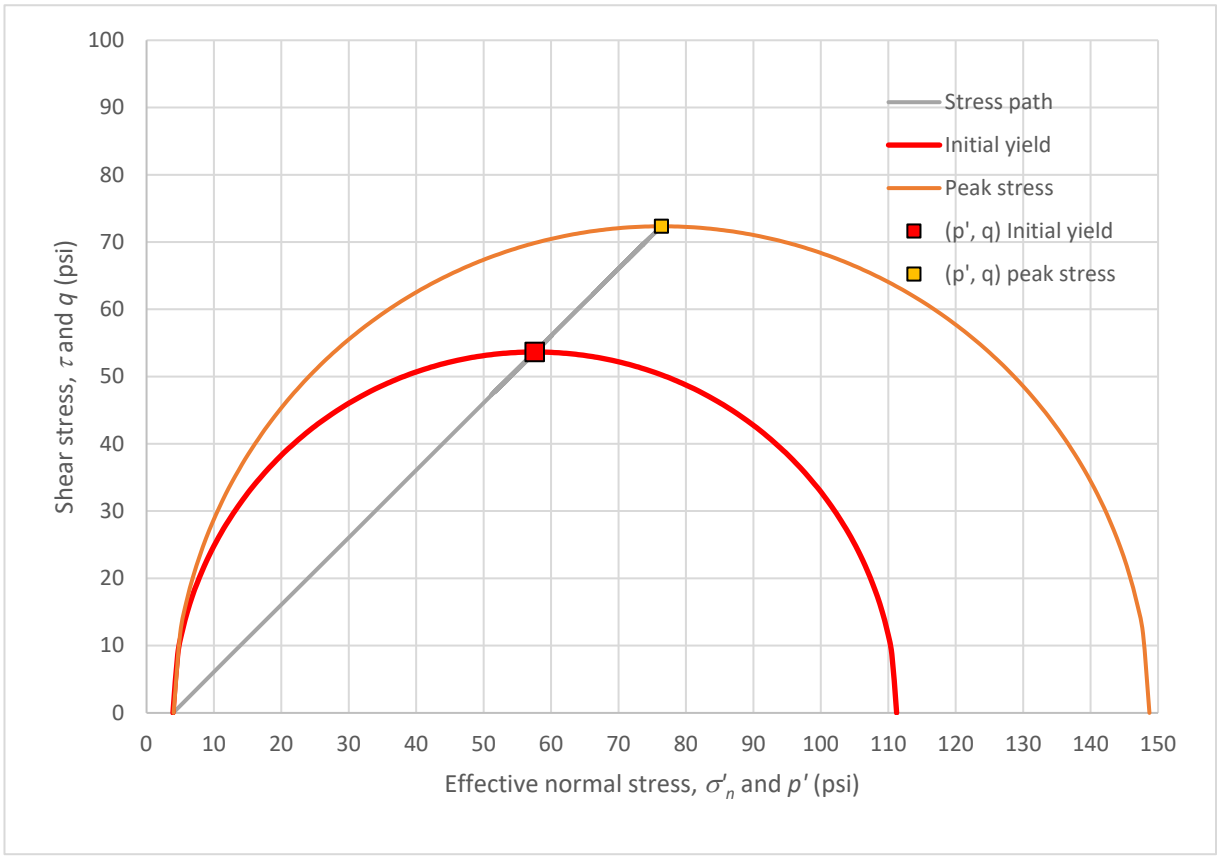

Consolidated-Drained Triaxial Shear, Lightweight Cellular Concrete

Sample ID:	**B2-45**
Height (in):	5.525
Height (mm):	140.3
Diameter (in):	2.962
Diameter (mm)	75.22
Area (in^2):	6.889
Area (mm^2):	4444
Mass (g):	209.68
Weight (lb):	0.4623
Weight (kN):	0.002056
Volume (in^3):	38.06
Volume (mm^3):	623644
Density (g/mm^3):	0.0003362
Density (kg/m^3):	336.2
Unit weight (pcf):	**20.99**
Dry unit weight (pcf);	**19.08**
Unit Weight (kN/m^3):	3.297
Wet mass + tare (g):	320.38
Dry mass + tare (g):	302.38
Tare (g):	122.22
Water content (%)	**9.99**
Saturation (%):	**3.45**
H:D ratio:	1.865
Age (days):	1053
Treatment:	AD

Strain rate (%/min):	0.2
Mean σ'_3 (psi):	3.0
Initial modulus (psi):	51660
Initial yield	
Time to failure (min):	1.5
Axial strain at failure (%):	0.297
σ'_1 (psi):	156.22
σ'_3 (psi):	3.01
σ'_1 -σ'_3 (psi):	153.21
σ'_1 / σ'_3:	51.93
p' (psi):	79.62
q (psi):	76.61
Volumetric strain (%):	0.149
Poisson's ratio:	0.249
Peak stress	
Time to failure (min):	16.1
Axial strain at failure (%):	3.217
σ'_1 (psi):	158.42
σ'_3 (psi):	3.05
σ'_1 -σ'_3 (psi):	155.38
σ'_1 / σ'_3:	52.01
p' (psi):	80.73
q (psi):	77.69
Volumetric strain (%):	2.821
Poisson's ratio:	0.062

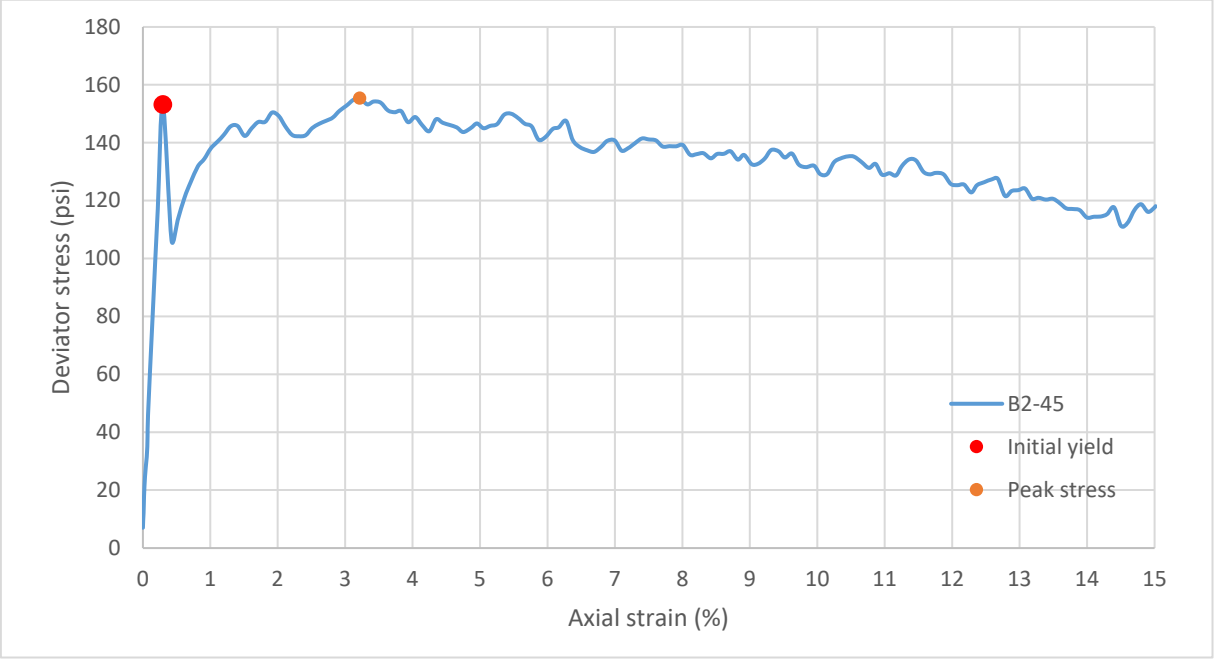

Sample ID:	B2-45

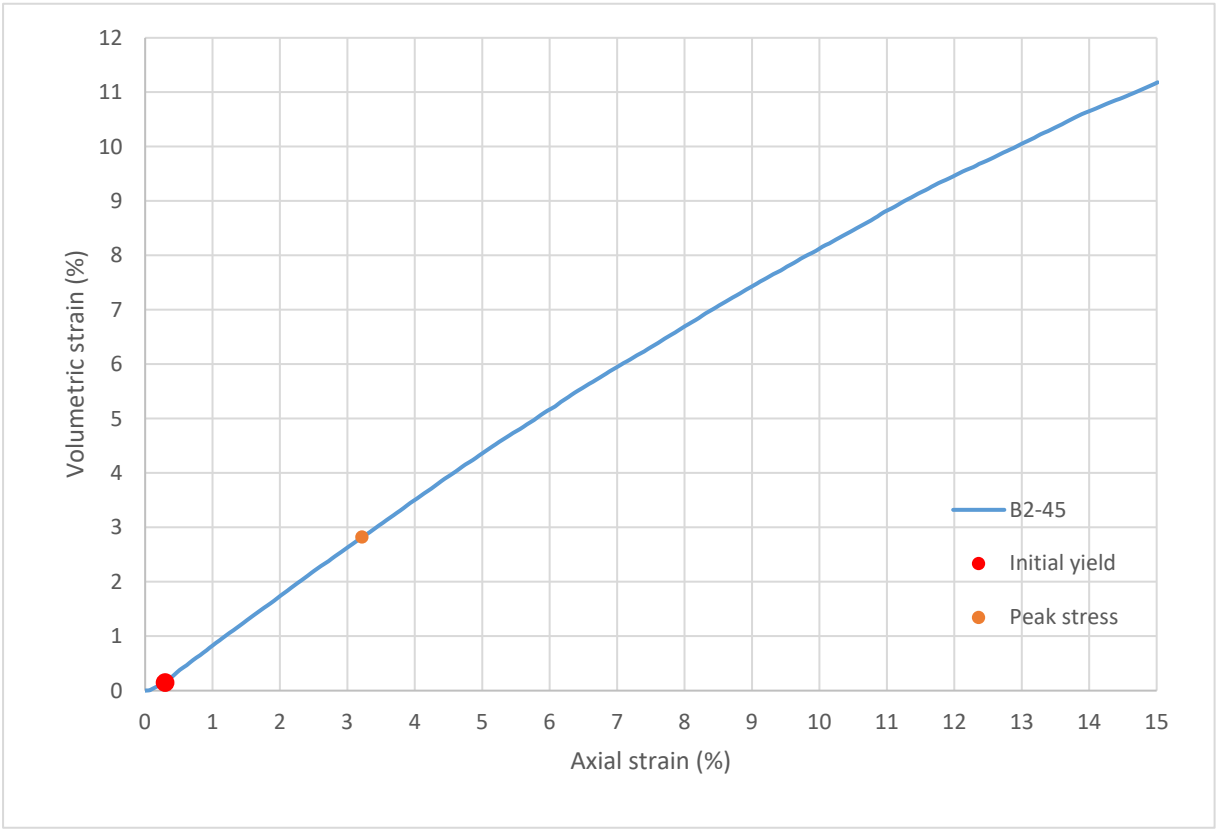

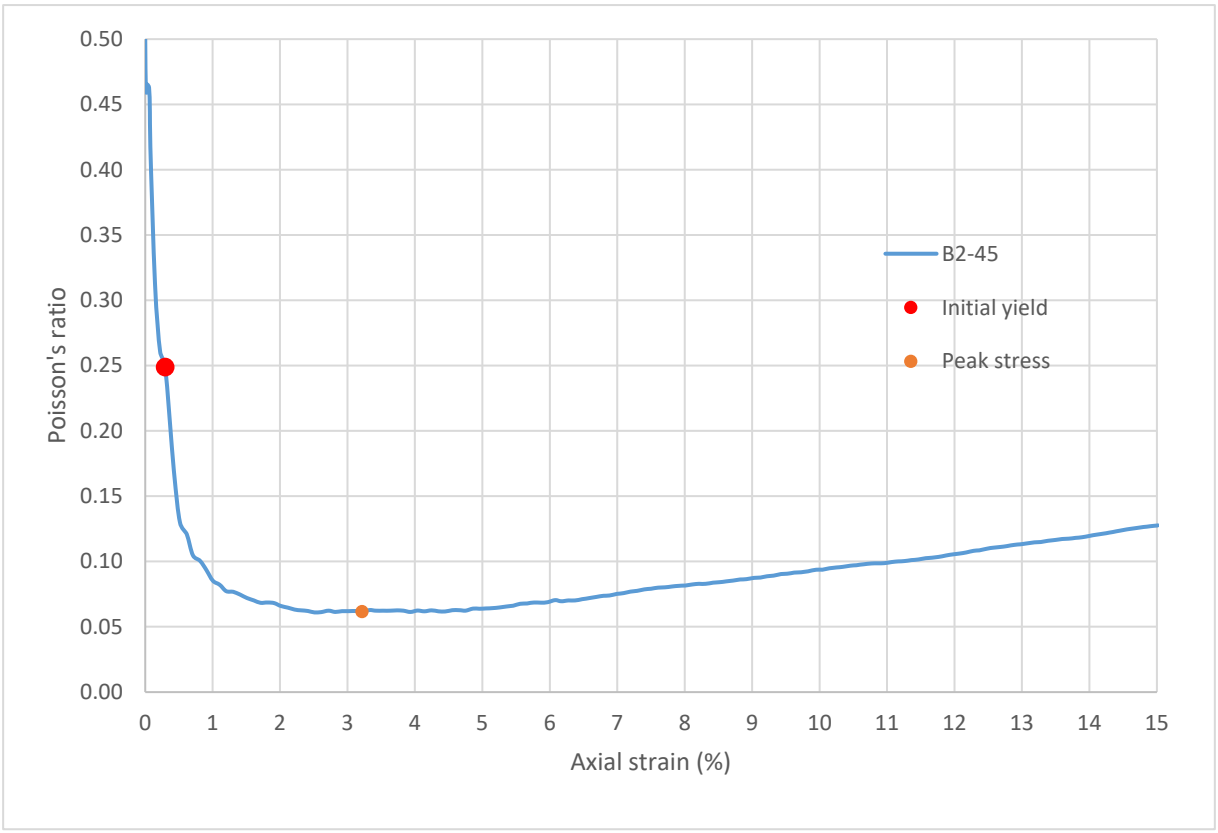

Sample ID:	B2-45

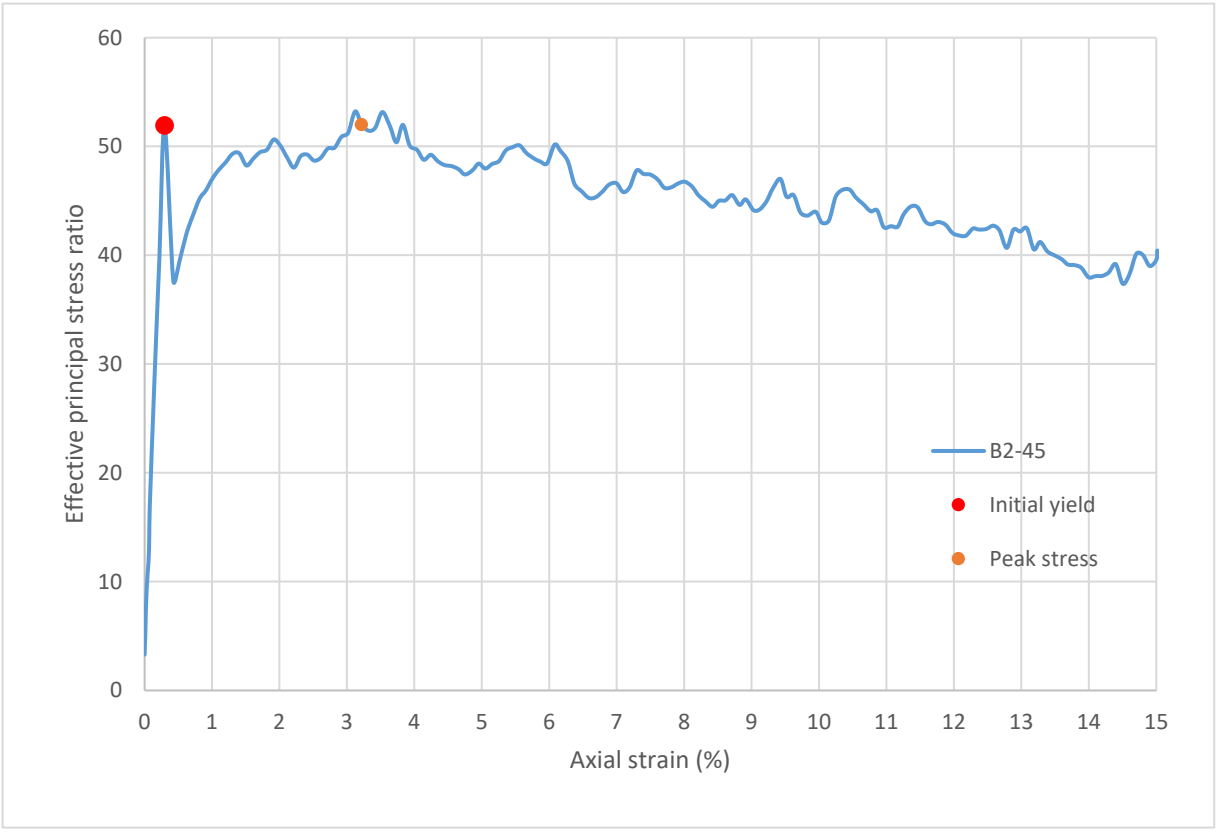

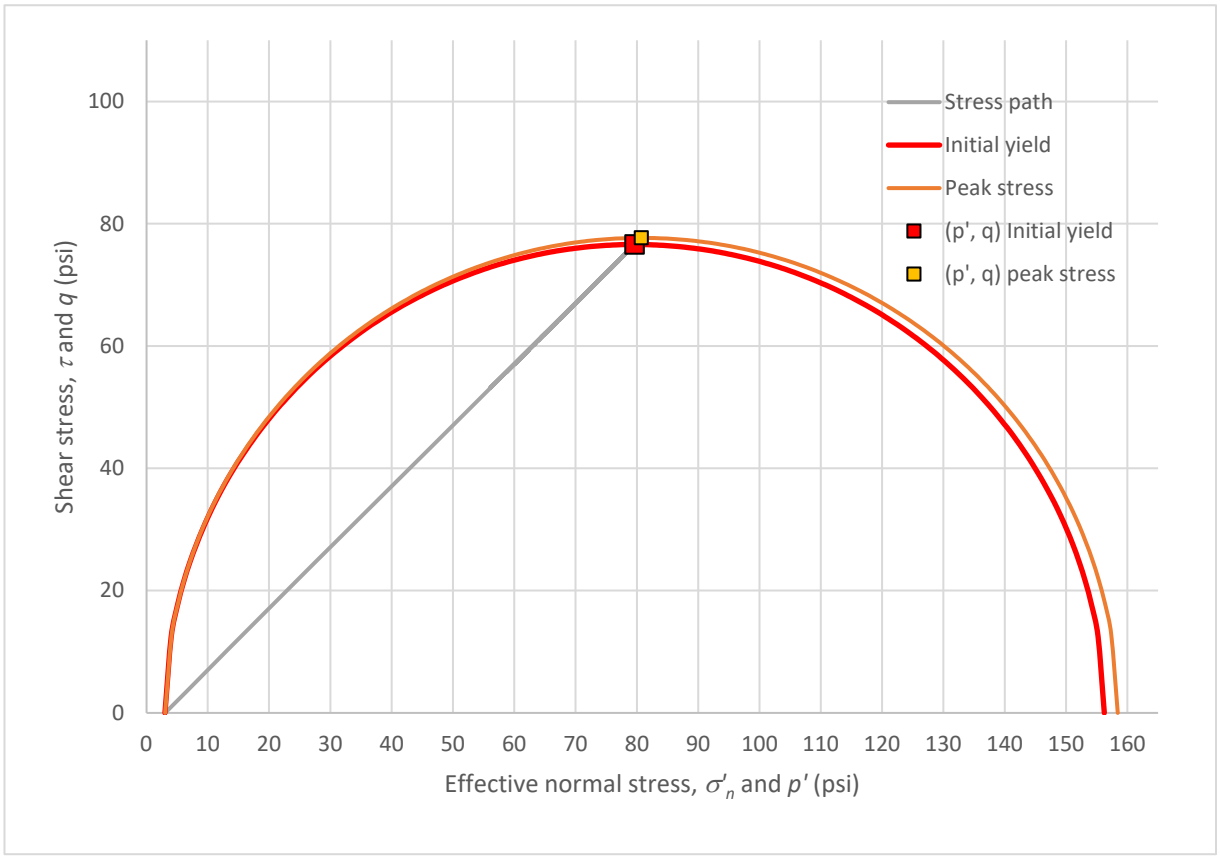

Consolidated-Drained Triaxial Shear, Lightweight Cellular Concrete

Sample ID:	**B2-46**
Height (in):	5.461
Height (mm):	138.7
Diameter (in):	2.944
Diameter (mm)	74.79
Area (in^2):	6.809
Area (mm^2):	4393
Mass (g):	208.27
Weight (lb):	0.4592
Weight (kN):	0.002042
Volume (in^3):	37.18
Volume (mm^3):	609308
Density (g/mm^3):	0.0003418
Density (kg/m^3):	341.8
Unit weight (pcf):	**21.34**
Dry unit weight (pcf);	**19.50**
Unit Weight (kN/m^3):	3.352
Wet mass + tare (g):	298.70
Dry mass + tare (g):	283.30
Tare (g):	119.62
Water content (%)	**9.41**
Saturation (%):	**3.33**
H:D ratio:	1.855
Age (days):	1053
Treatment:	AD

Strain rate (%/min):	0.2
Mean σ'_3 (psi):	3.1
Initial modulus (psi):	40619
Initial yield	
Time to failure (min):	1.6
Axial strain at failure (%):	0.321
σ'_1 (psi):	133.35
σ'_3 (psi):	3.02
σ'_1 -σ'_3 (psi):	130.33
σ'_1 / σ'_3:	44.16
p' (psi):	68.19
q (psi):	65.17
Volumetric strain (%):	0.180
Poisson's ratio:	0.219
Peak stress	
Time to failure (min):	1.6
Axial strain at failure (%):	0.321
σ'_1 (psi):	133.35
σ'_3 (psi):	3.02
σ'_1 -σ'_3 (psi):	130.33
σ'_1 / σ'_3:	44.16
p' (psi):	68.19
q (psi):	65.17
Volumetric strain (%):	0.180
Poisson's ratio:	0.219

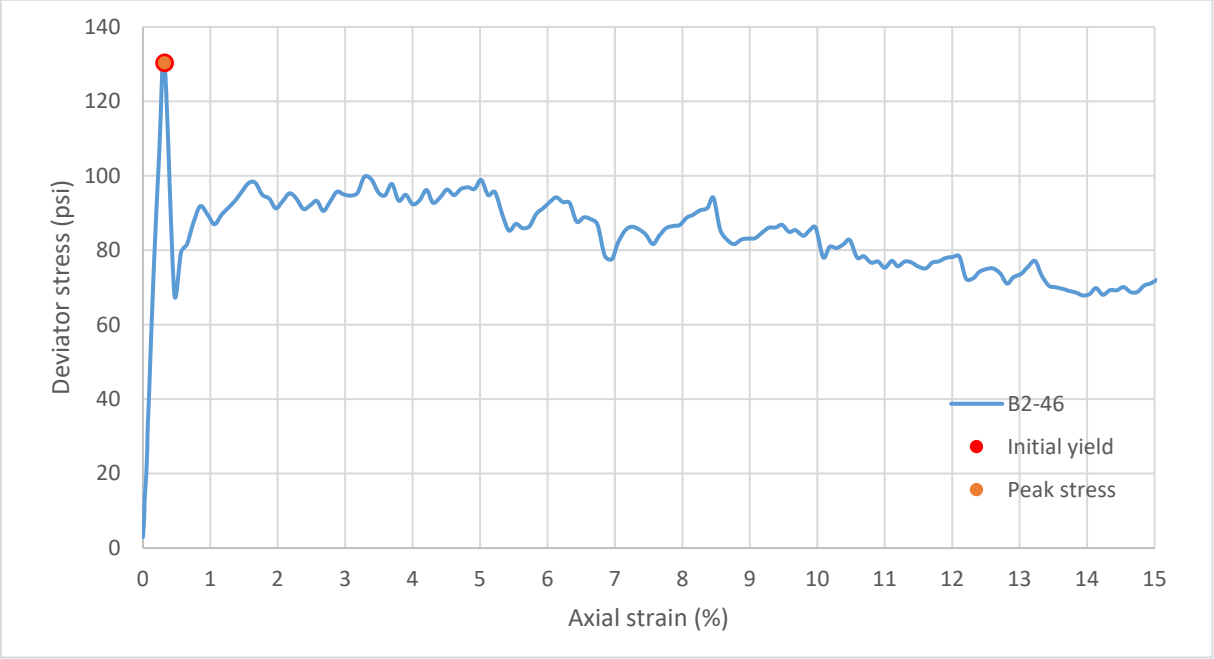

Sample ID:	B2-46

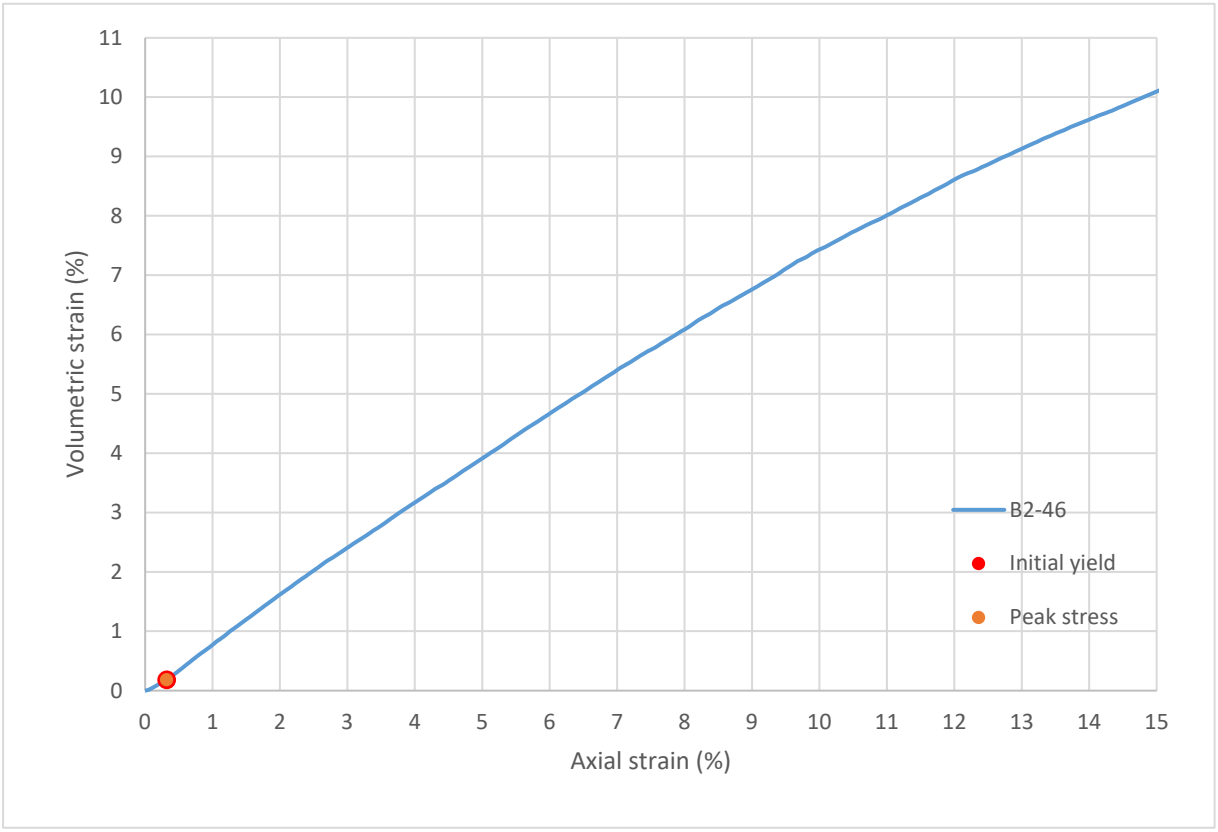

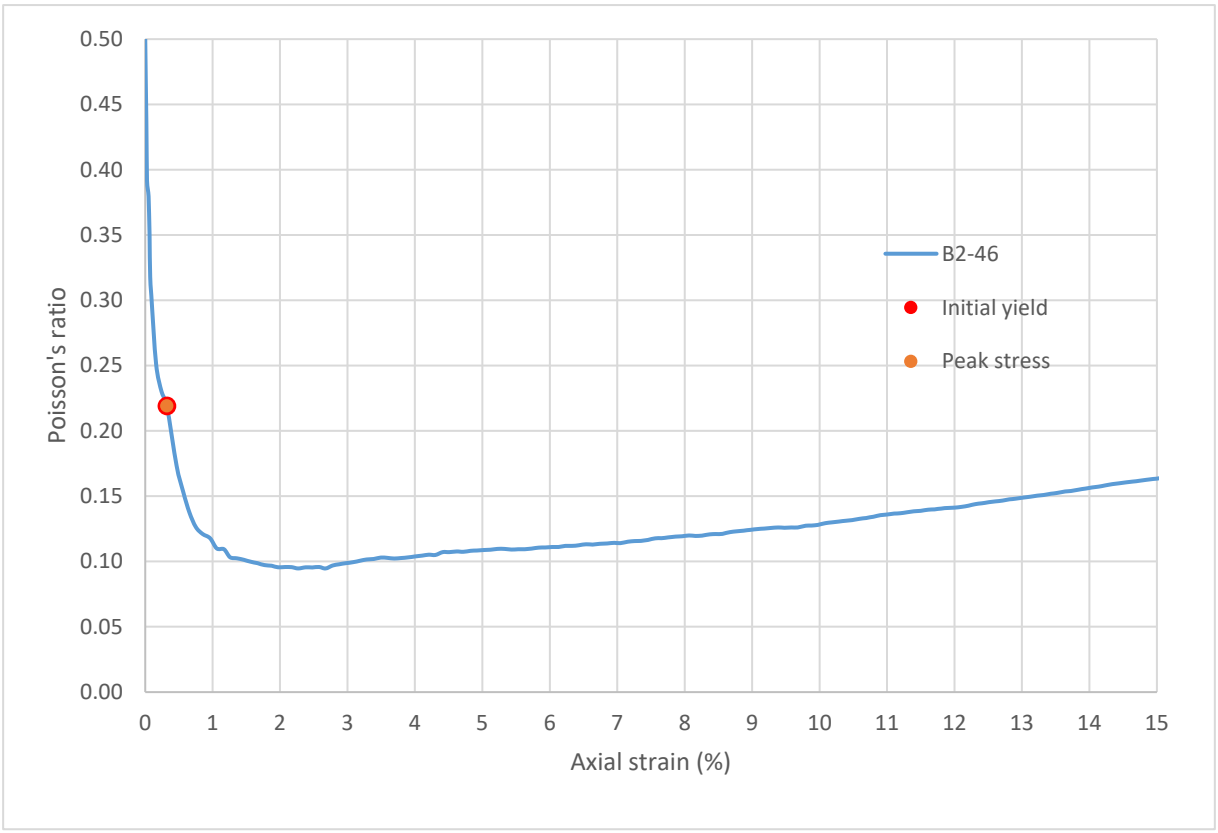

Sample ID:	B2-46

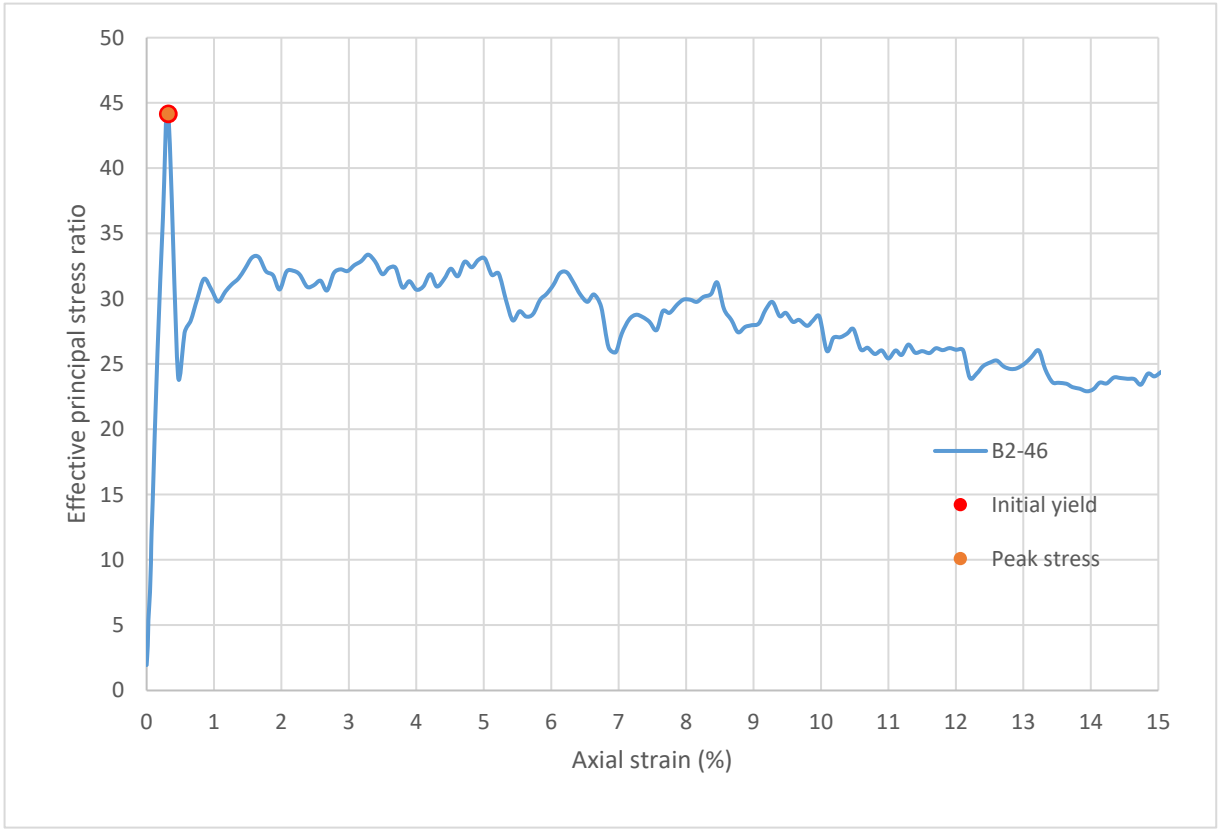

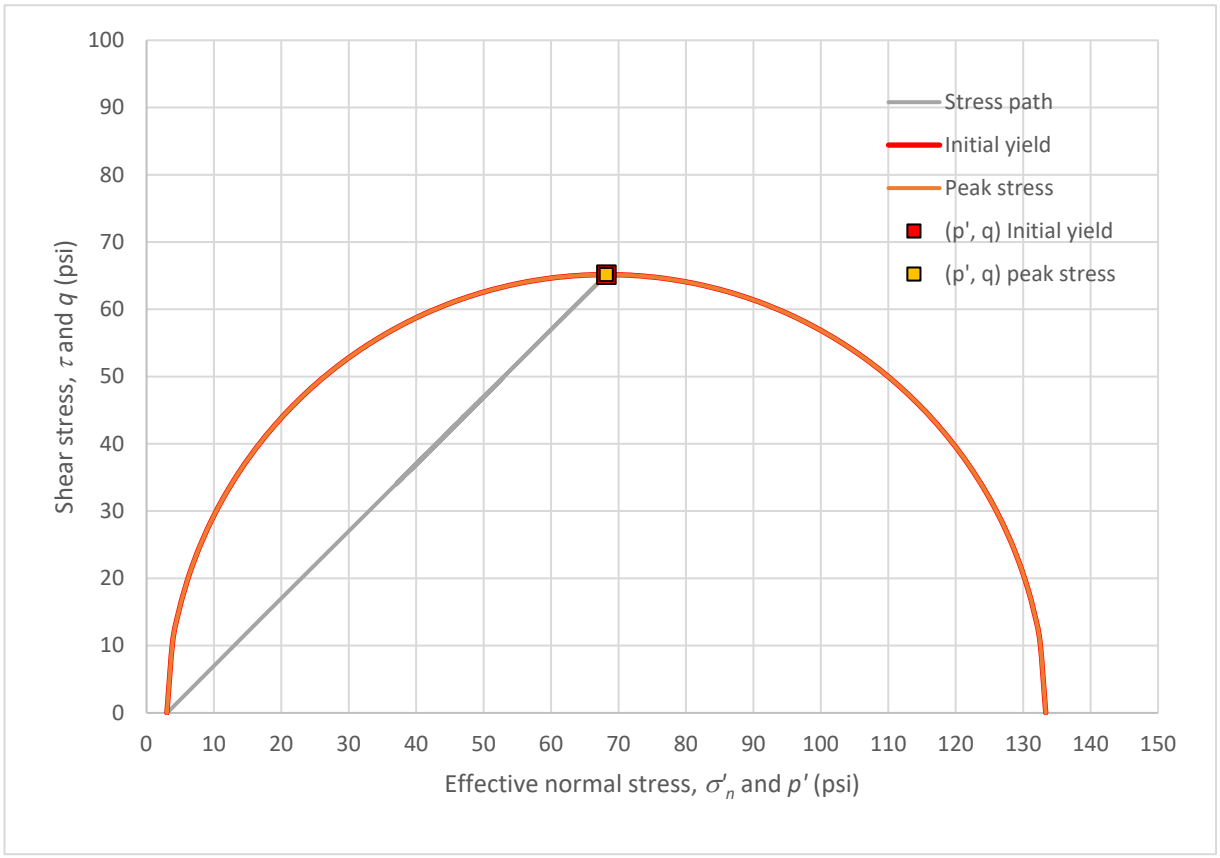

Consolidated-Drained Triaxial Shear, Lightweight Cellular Concrete

Sample ID:	**B2-47**
Height (in):	5.619
Height (mm):	142.7
Diameter (in):	2.957
Diameter (mm)	75.10
Area (in^2):	6.866
Area (mm^2):	4430
Mass (g):	220.18
Weight (lb):	0.4854
Weight (kN):	0.002159
Volume (in^3):	38.58
Volume (mm^3):	632163
Density (g/mm^3):	0.0003483
Density (kg/m^3):	348.3
Unit weight (pcf):	**21.74**
Dry unit weight (pcf);	**19.18**
Unit Weight (kN/m^3):	3.416
Wet mass + tare (g):	336.87
Dry mass + tare (g):	314.89
Tare (g):	150.74
Water content (%)	**13.39**
Saturation (%):	**4.65**
H:D ratio:	1.900
Age (days):	1059
Treatment:	H100

Strain rate (%/min):	0.2
Mean σ'_3 (psi):	3.2
Initial modulus (psi):	45264
Initial yield	
Time to failure (min):	0.8
Axial strain at failure (%):	0.165
σ'_1 (psi):	77.84
σ'_3 (psi):	3.07
σ'_1 -σ'_3 (psi):	74.77
σ'_1 / σ'_3:	25.34
p' (psi):	40.46
q (psi):	37.39
Volumetric strain (%):	0.074
Poisson's ratio:	0.275
Peak stress	
Time to failure (min):	74.8
Axial strain at failure (%):	14.966
σ'_1 (psi):	200.07
σ'_3 (psi):	3.12
σ'_1 -σ'_3 (psi):	196.96
σ'_1 / σ'_3:	64.21
p' (psi):	101.59
q (psi):	98.48
Volumetric strain (%):	10.792
Poisson's ratio:	0.139

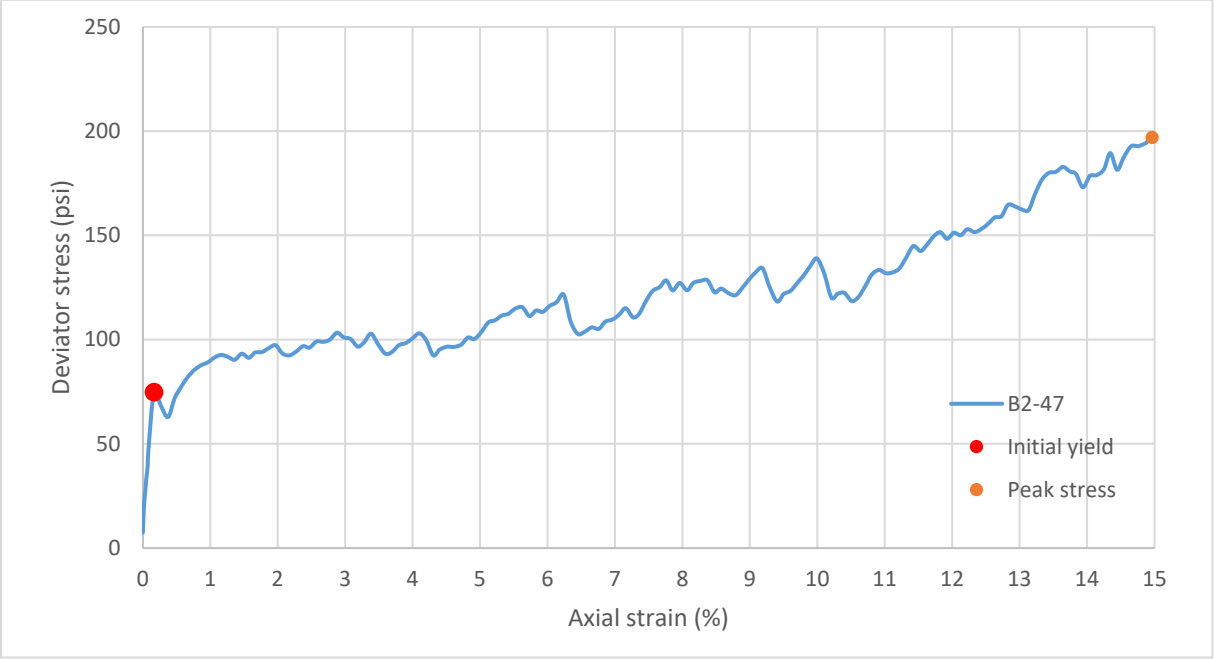

Sample ID:	B2-47

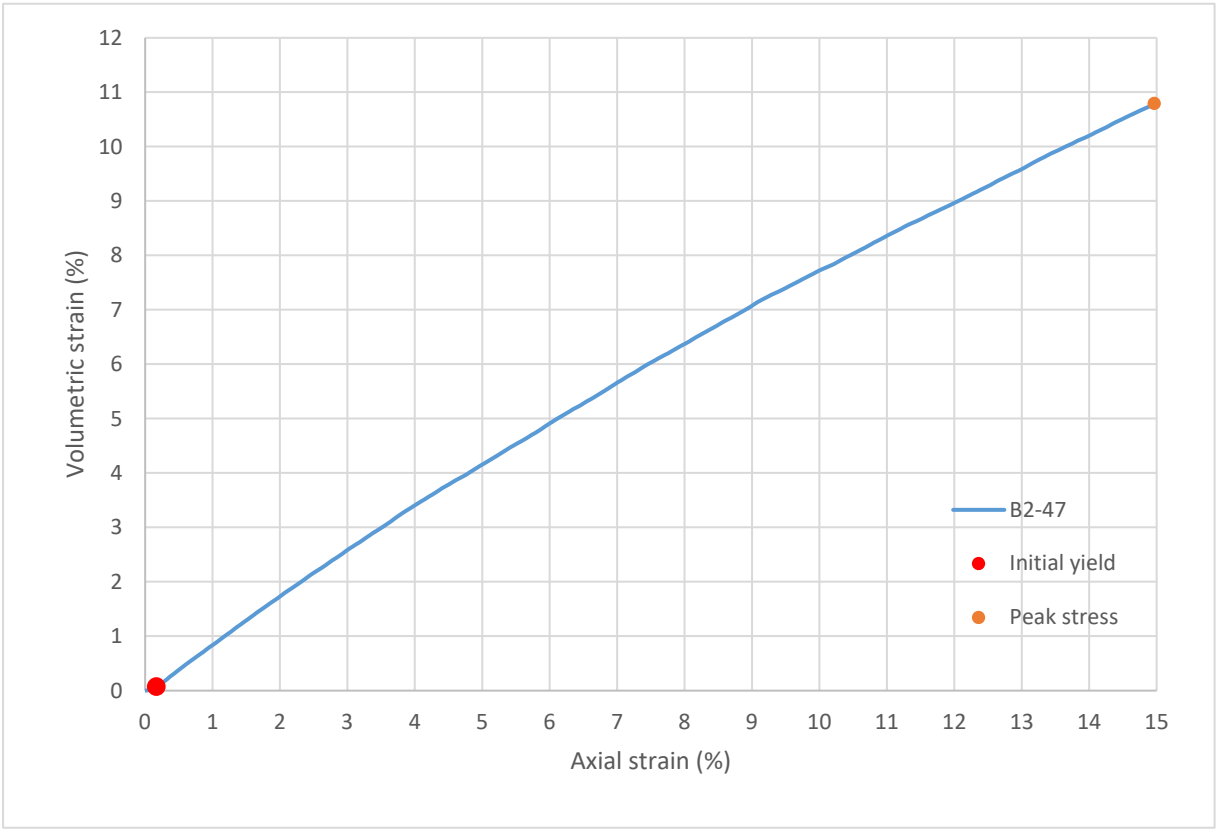

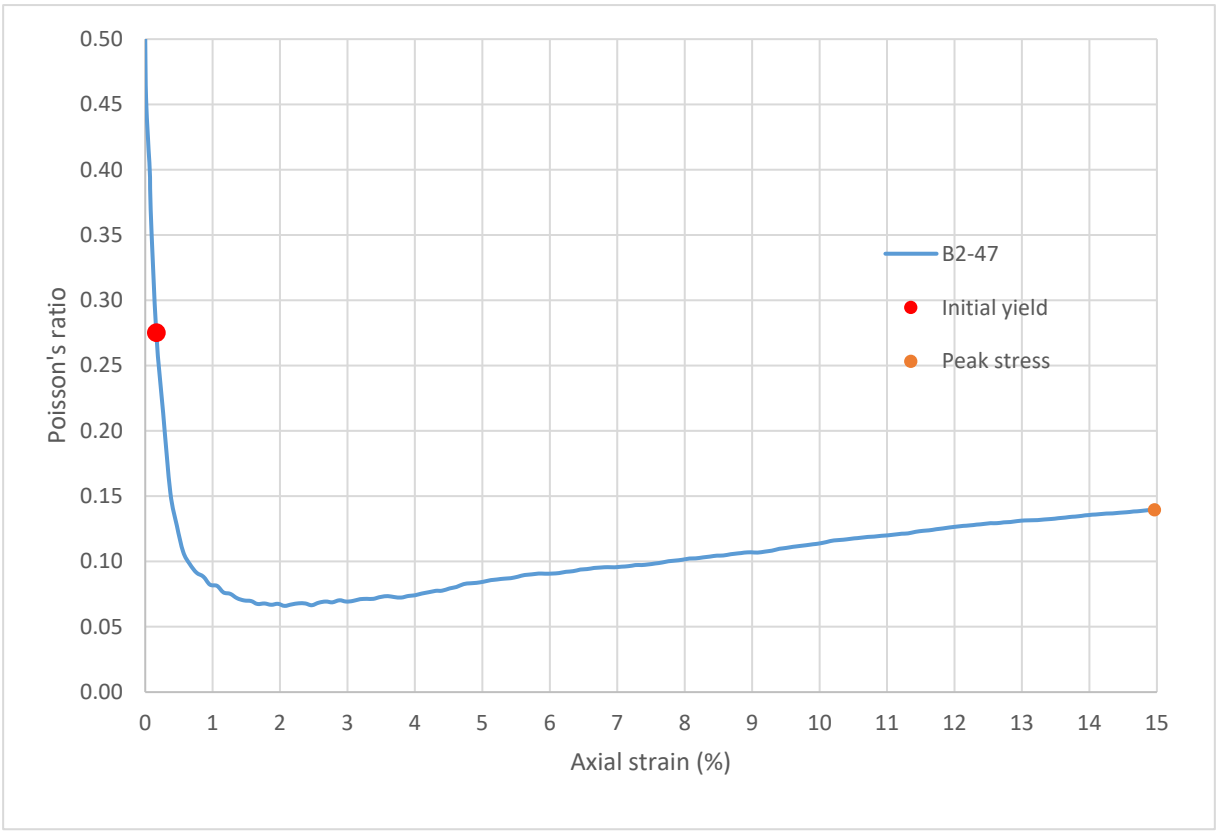

Sample ID:	B2-47

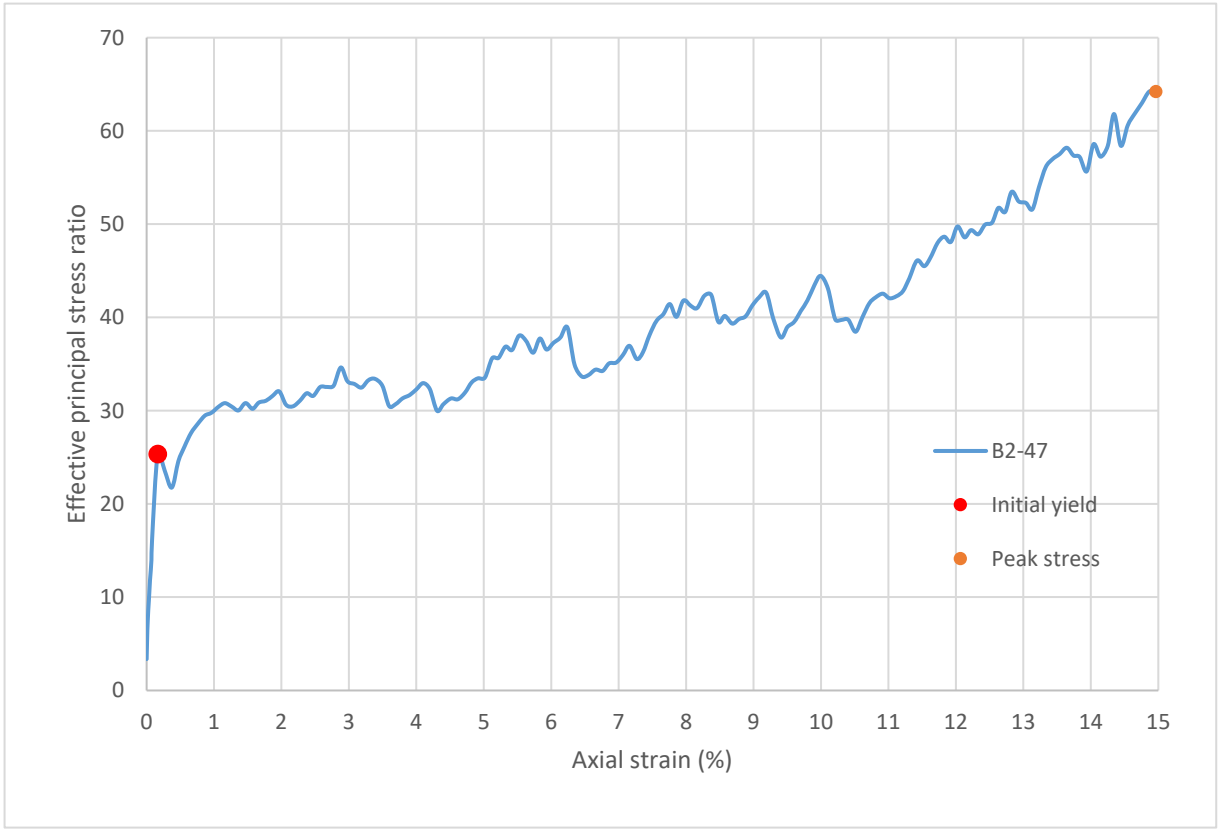

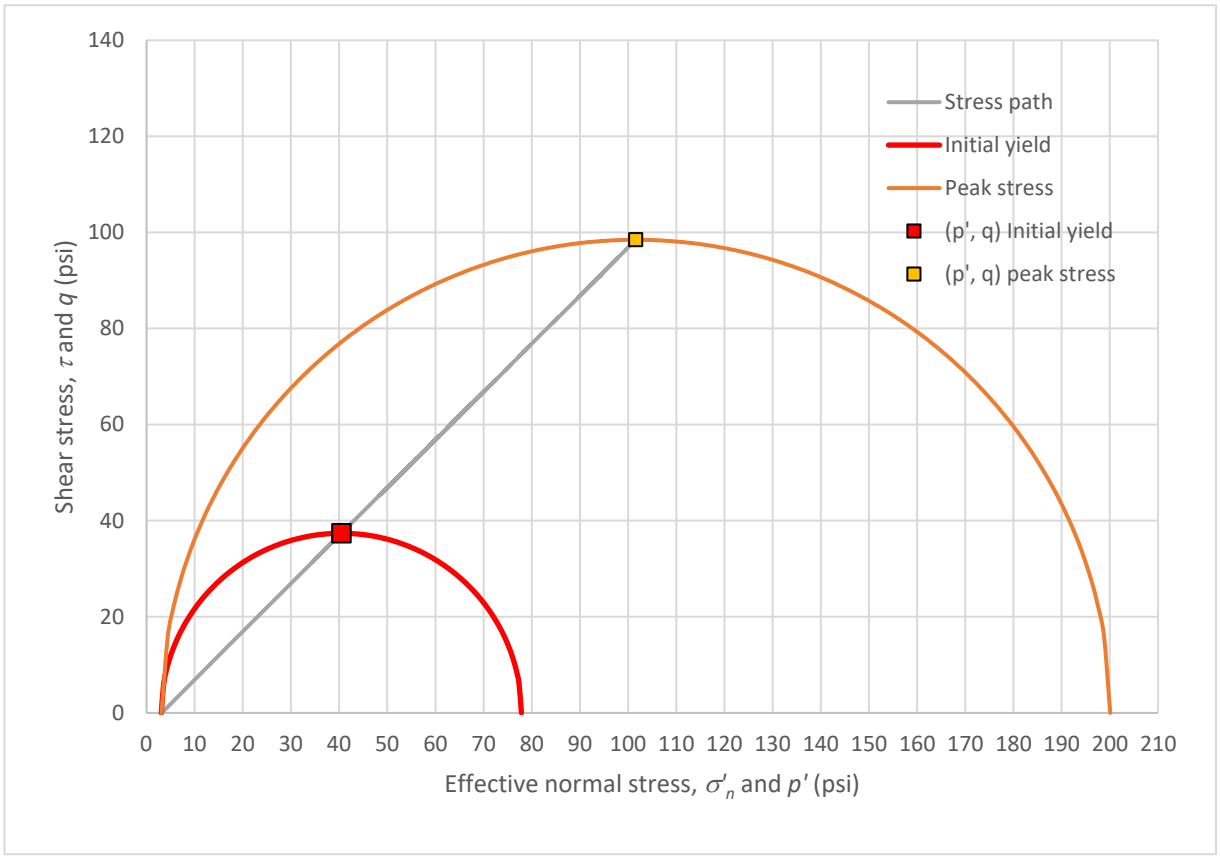

Consolidated-Drained Triaxial Shear, Lightweight Cellular Concrete

Sample ID:	**B2-48**
Height (in):	5.644
Height (mm):	143.4
Diameter (in):	2.953
Diameter (mm)	75.01
Area (in^2):	6.850
Area (mm^2):	4420
Mass (g):	222.92
Weight (lb):	0.4915
Weight (kN):	0.002186
Volume (in^3):	38.66
Volume (mm^3):	633582
Density (g/mm^3):	0.0003518
Density (kg/m^3):	351.8
Unit weight (pcf):	**21.96**
Dry unit weight (pcf);	**19.22**
Unit Weight (kN/m^3):	3.450
Wet mass + tare (g):	289.88
Dry mass + tare (g):	269.59
Tare (g):	127.45
Water content (%)	**14.27**
Saturation (%):	**4.97**
H:D ratio:	1.911
Age (days):	1059
Treatment:	H100

Strain rate (%/min):	0.2
Mean σ'_3 (psi):	3.1
Initial modulus (psi):	35673
Initial yield	
Time to failure (min):	1.3
Axial strain at failure (%):	0.251
σ'_1 (psi):	92.46
σ'_3 (psi):	3.03
σ'_1 -σ'_3 (psi):	89.43
σ'_1 / σ'_3:	30.55
p' (psi):	47.74
q (psi):	44.72
Volumetric strain (%):	0.131
Poisson's ratio:	0.238
Peak stress	
Time to failure (min):	1.3
Axial strain at failure (%):	0.251
σ'_1 (psi):	92.46
σ'_3 (psi):	3.03
σ'_1 -σ'_3 (psi):	89.43
σ'_1 / σ'_3:	30.55
p' (psi):	47.74
q (psi):	44.72
Volumetric strain (%):	0.131
Poisson's ratio:	0.238

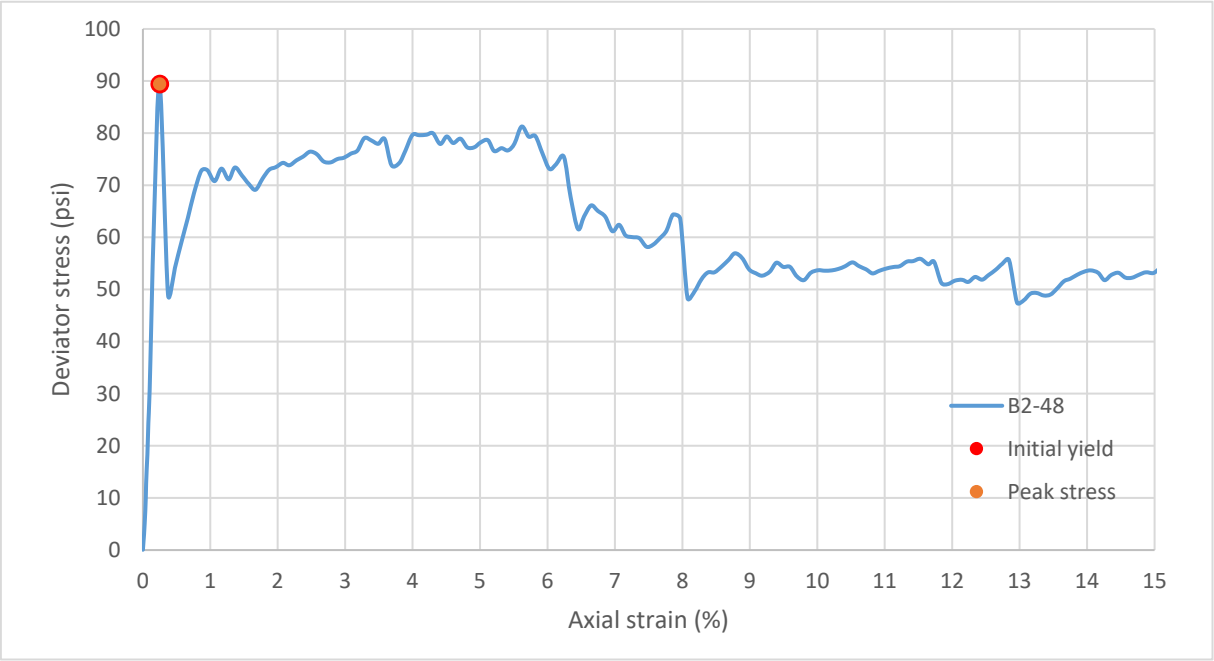

Sample ID:	B2-48

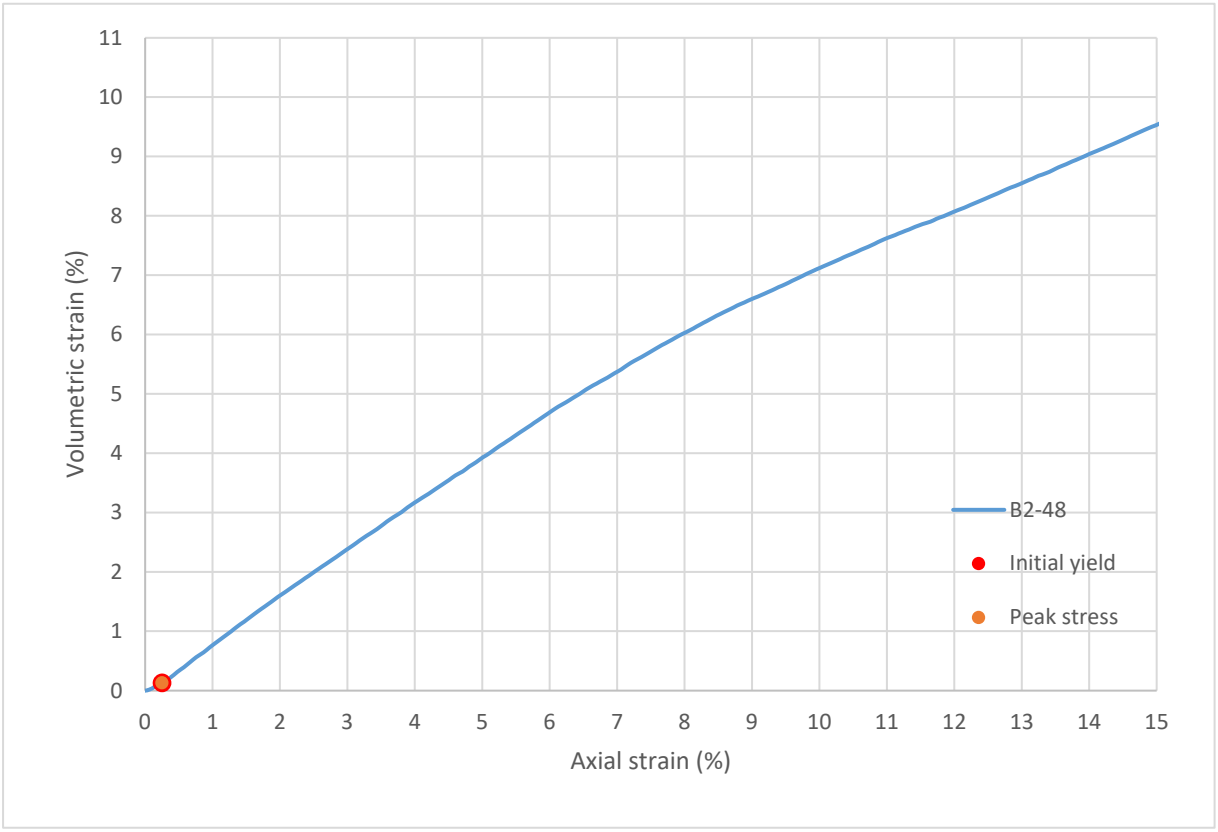

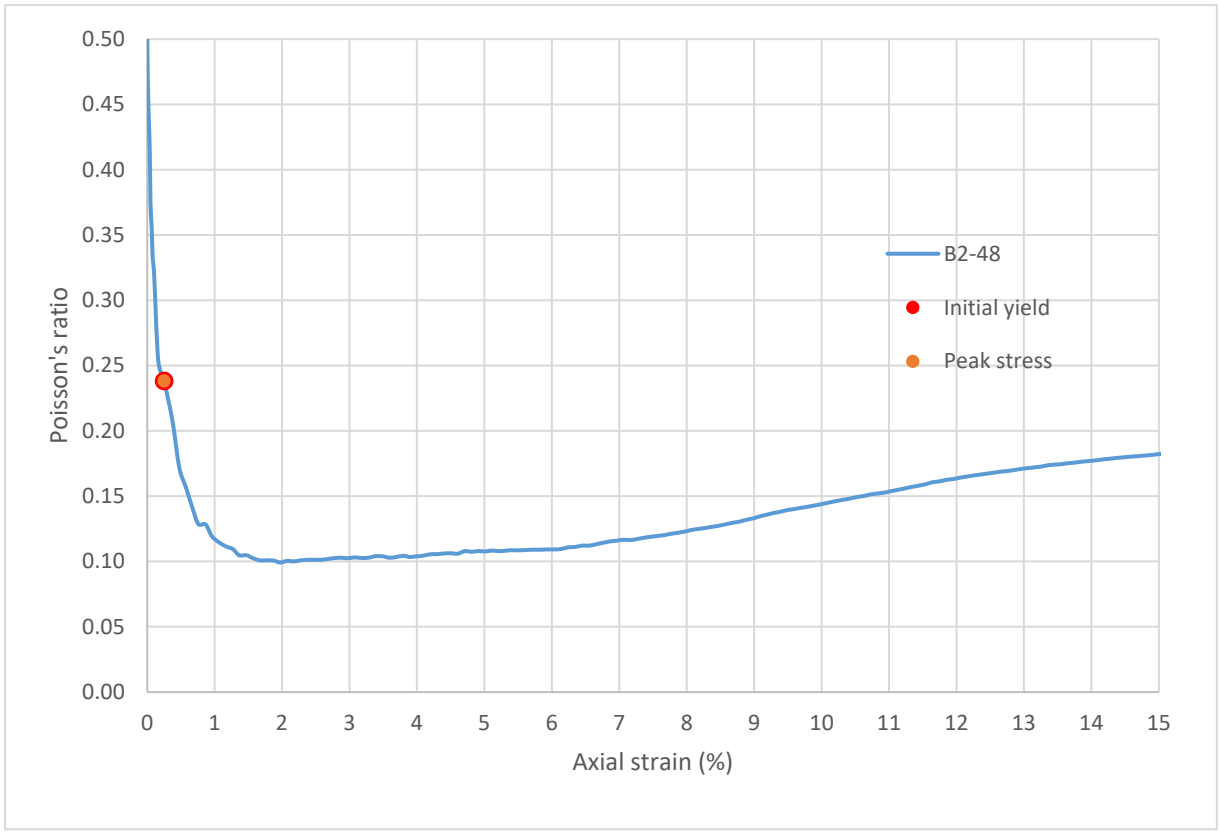

Sample ID:	B2-48

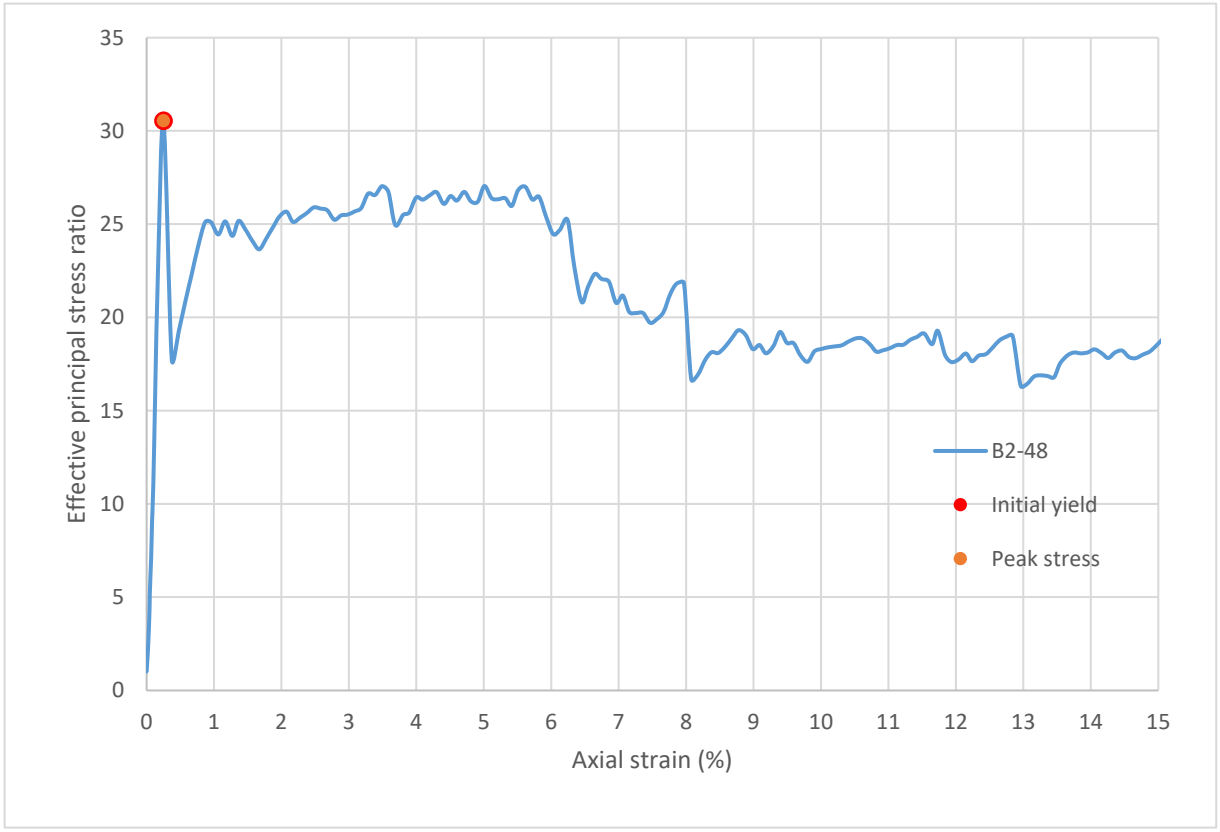

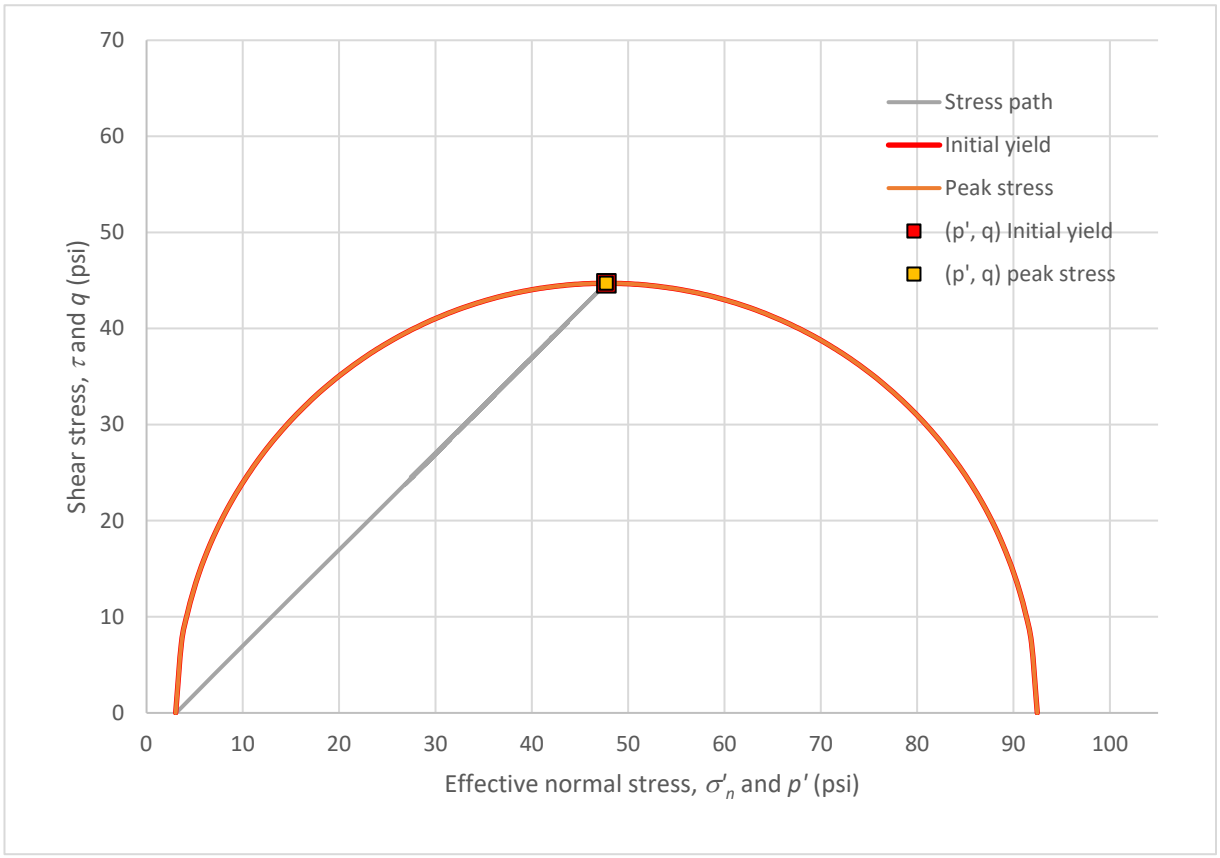

Consolidated-Drained Triaxial Shear, Lightweight Cellular Concrete

Sample ID:	**B2-49**
Height (in):	5.471
Height (mm):	139.0
Diameter (in):	2.945
Diameter (mm)	74.79
Area (in^2):	6.810
Area (mm^2):	4393
Mass (g):	214.39
Weight (lb):	0.4726
Weight (kN):	0.002102
Volume (in^3):	37.26
Volume (mm^3):	610516
Density (g/mm^3):	0.0003512
Density (kg/m^3):	351.2
Unit weight (pcf):	**21.92**
Dry unit weight (pcf);	**19.16**
Unit Weight (kN/m^3):	3.444
Wet mass + tare (g):	310.73
Dry mass + tare (g):	287.73
Tare (g):	128.10
Water content (%)	**14.41**
Saturation (%):	**5.00**
H:D ratio:	1.858
Age (days):	1060
Treatment:	H100

Strain rate (%/min):	0.2
Mean σ'_3 (psi):	3.9
Initial modulus (psi):	37882
Initial yield	
Time to failure (min):	1.3
Axial strain at failure (%):	0.254
σ'_1 (psi):	100.10
σ'_3 (psi):	3.87
σ'_1 -σ'_3 (psi):	96.22
σ'_1 / σ'_3:	25.83
p' (psi):	51.99
q (psi):	48.11
Volumetric strain (%):	0.132
Poisson's ratio:	0.239
Peak stress	
Time to failure (min):	1.3
Axial strain at failure (%):	0.254
σ'_1 (psi):	100.10
σ'_3 (psi):	3.87
σ'_1 -σ'_3 (psi):	96.22
σ'_1 / σ'_3:	25.83
p' (psi):	51.99
q (psi):	48.11
Volumetric strain (%):	0.132
Poisson's ratio:	0.239

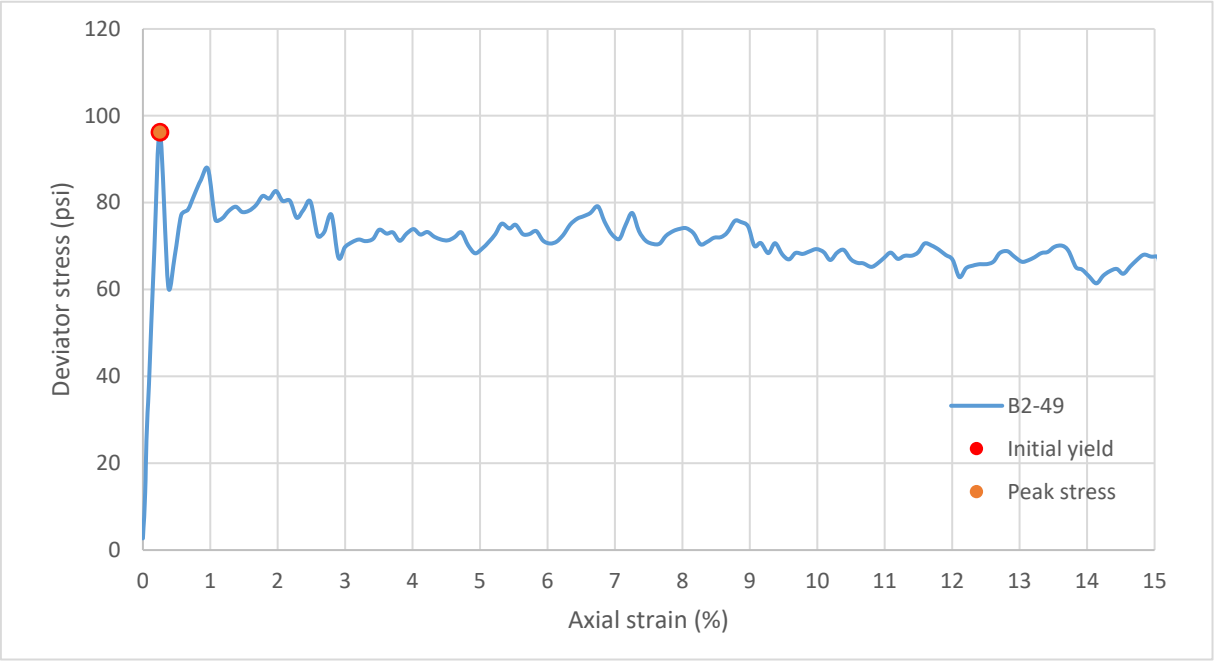

Sample ID:	B2-49

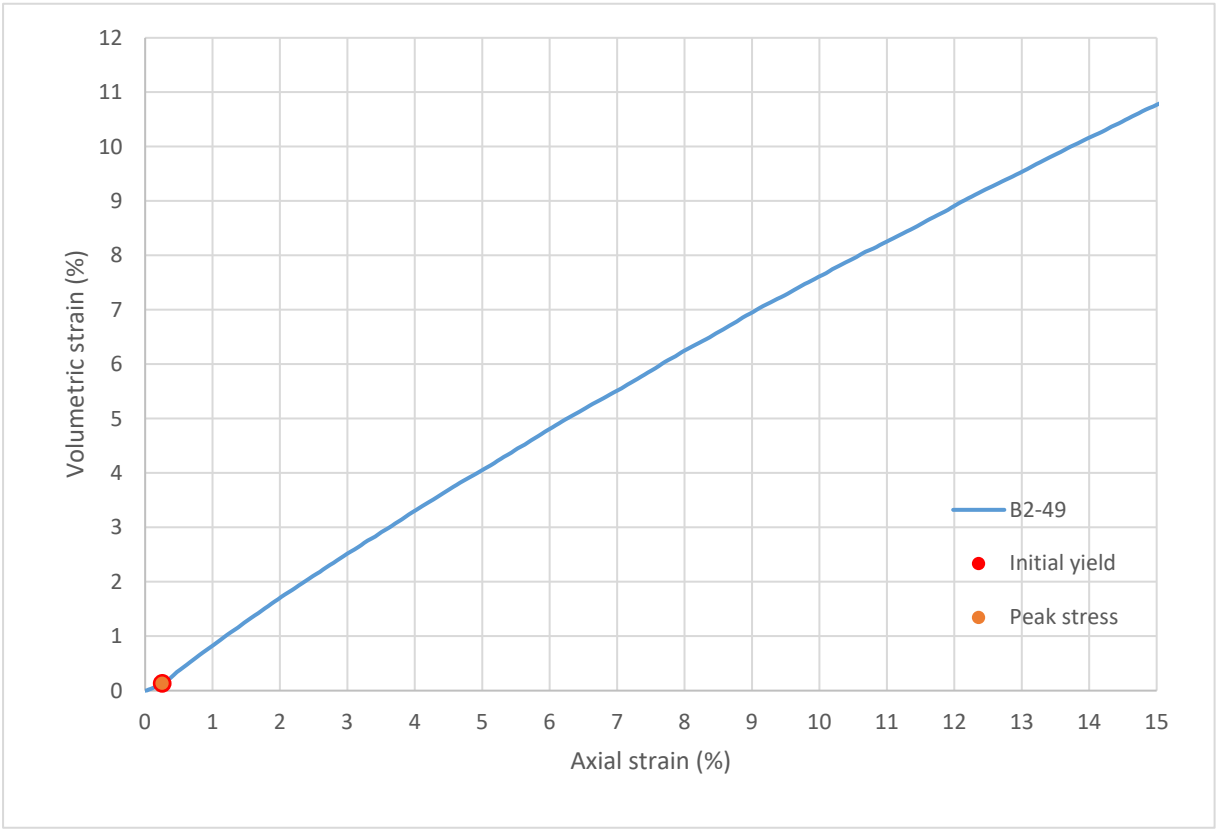

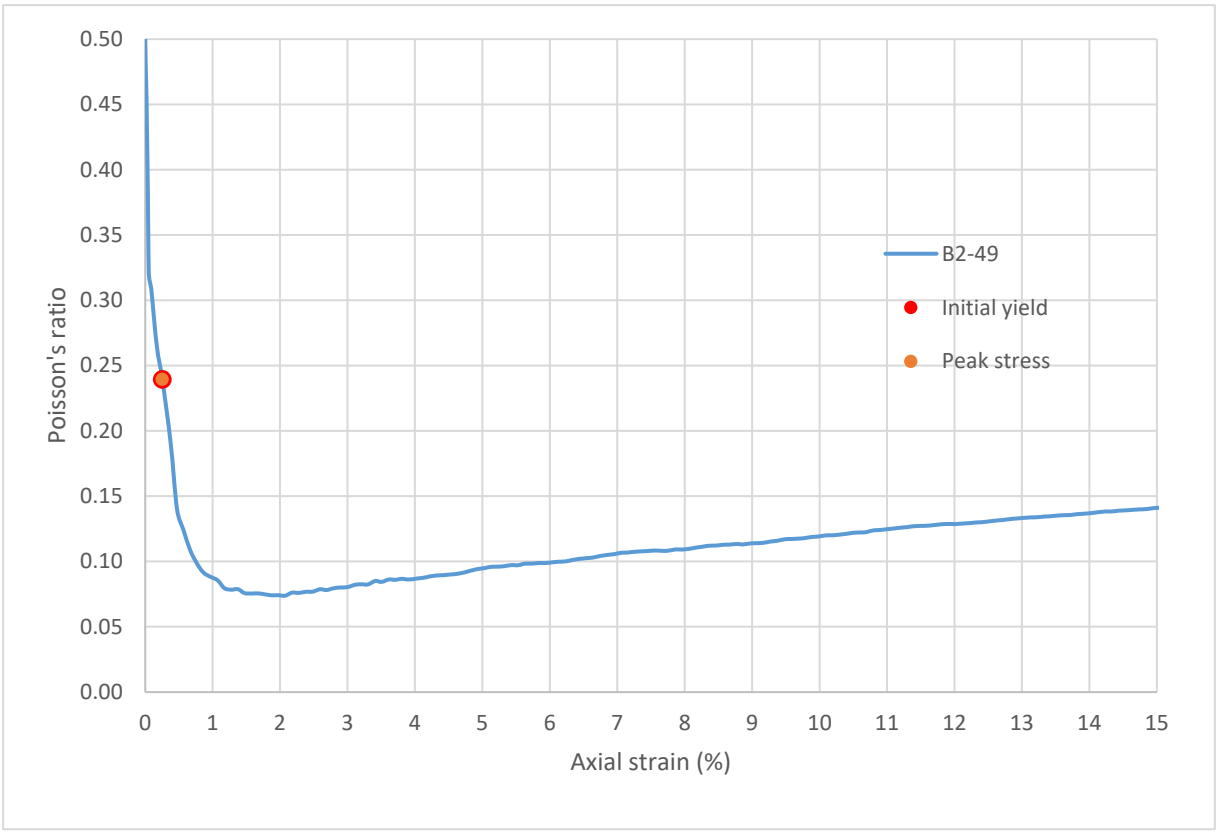

Sample ID:	B2-49

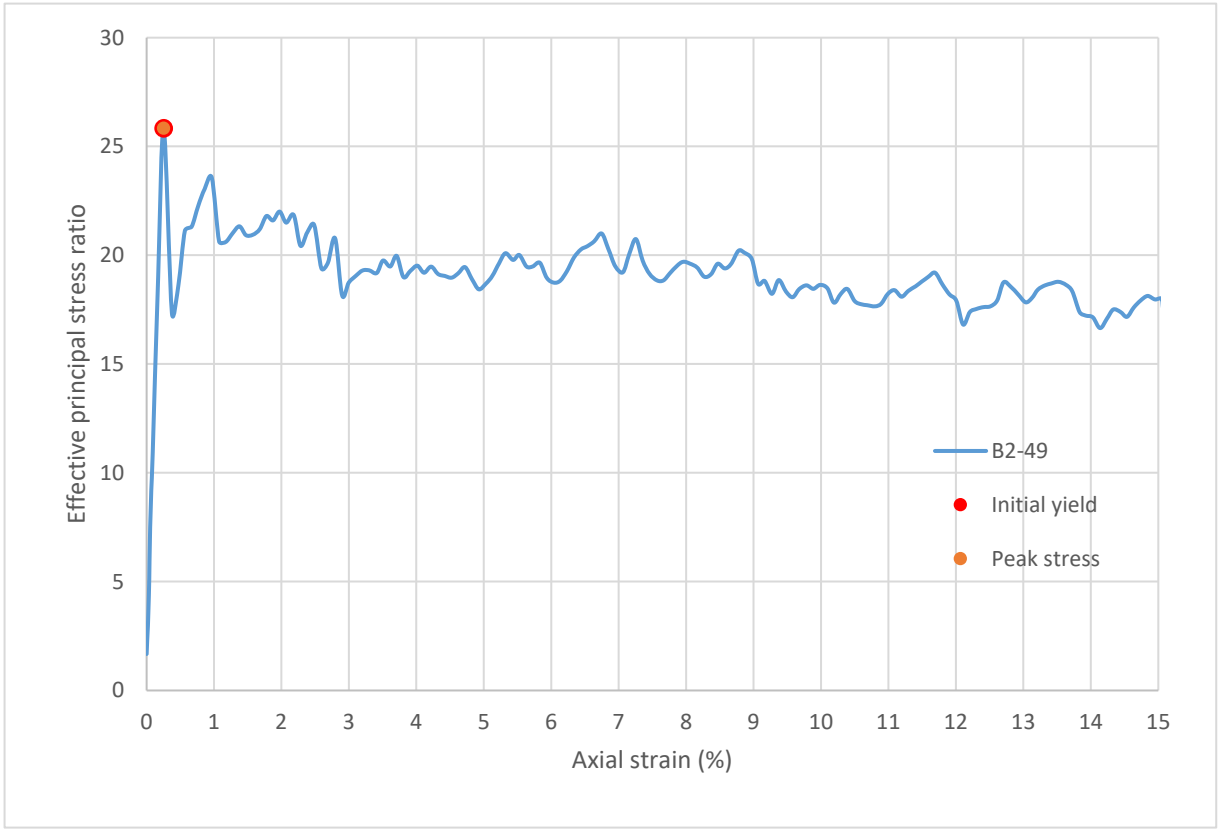

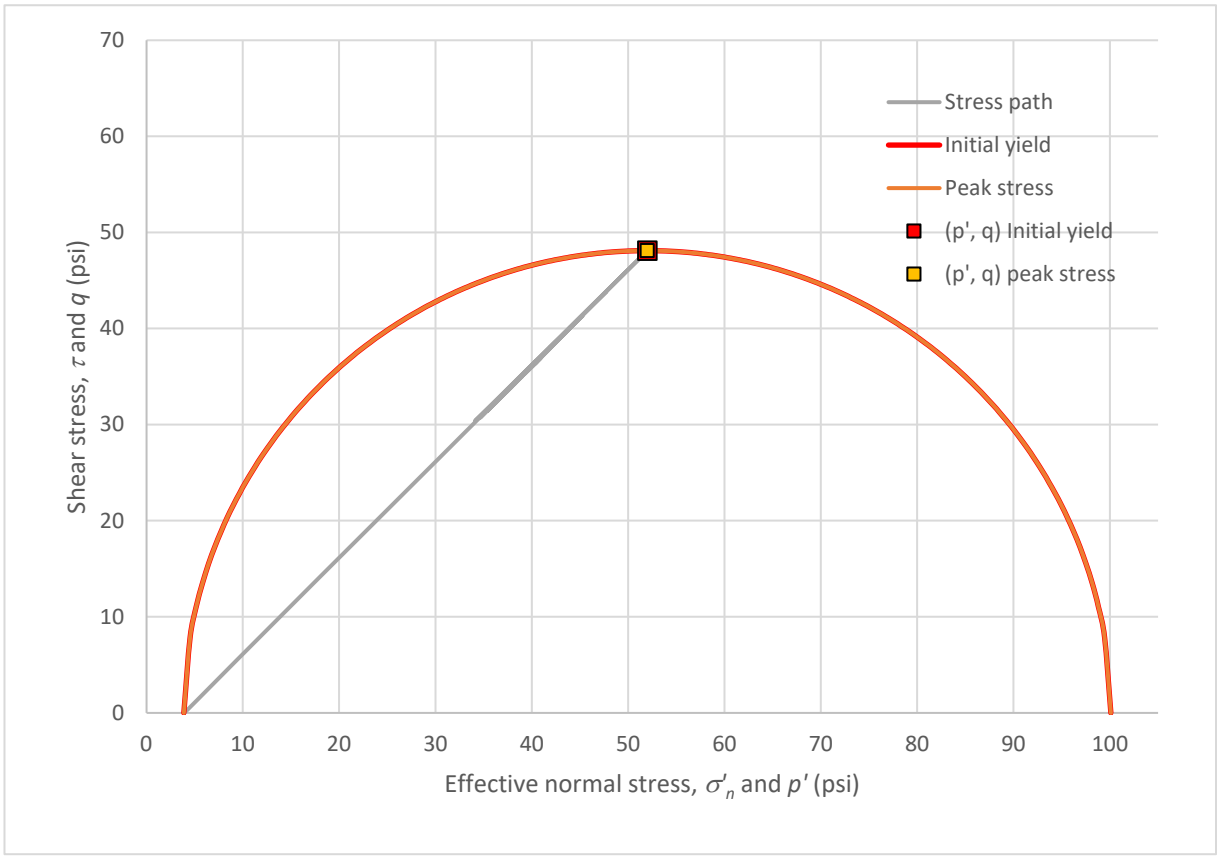

Consolidated-Drained Triaxial Shear, Lightweight Cellular Concrete

Sample ID:	**B2-50**
Height (in):	5.516
Height (mm):	140.1
Diameter (in):	2.967
Diameter (mm)	75.36
Area (in^2):	6.914
Area (mm^2):	4461
Mass (g):	218.28
Weight (lb):	0.4812
Weight (kN):	0.002141
Volume (in^3):	38.14
Volume (mm^3):	625042
Density (g/mm^3):	0.0003492
Density (kg/m^3):	349.2
Unit weight (pcf):	**21.80**
Dry unit weight (pcf);	**19.02**
Unit Weight (kN/m^3):	3.425
Wet mass + tare (g):	326.11
Dry mass + tare (g):	300.82
Tare (g):	128.06
Water content (%)	**14.64**
Saturation (%):	**5.03**
H:D ratio:	1.859
Age (days):	1060
Treatment:	H100

Strain rate (%/min):	0.2
Mean σ'_3 (psi):	3.1
Initial modulus (psi):	46223
Initial yield	
Time to failure (min):	1.2
Axial strain at failure (%):	0.242
σ'_1 (psi):	114.92
σ'_3 (psi):	3.02
σ'_1 -σ'_3 (psi):	111.89
σ'_1 / σ'_3:	38.03
p' (psi):	58.97
q (psi):	55.95
Volumetric strain (%):	0.112
Poisson's ratio:	0.269
Peak stress	
Time to failure (min):	25.6
Axial strain at failure (%):	5.112
σ'_1 (psi):	122.32
σ'_3 (psi):	3.07
σ'_1 -σ'_3 (psi):	119.24
σ'_1 / σ'_3:	39.78
p' (psi):	62.69
q (psi):	59.62
Volumetric strain (%):	4.279
Poisson's ratio:	0.081

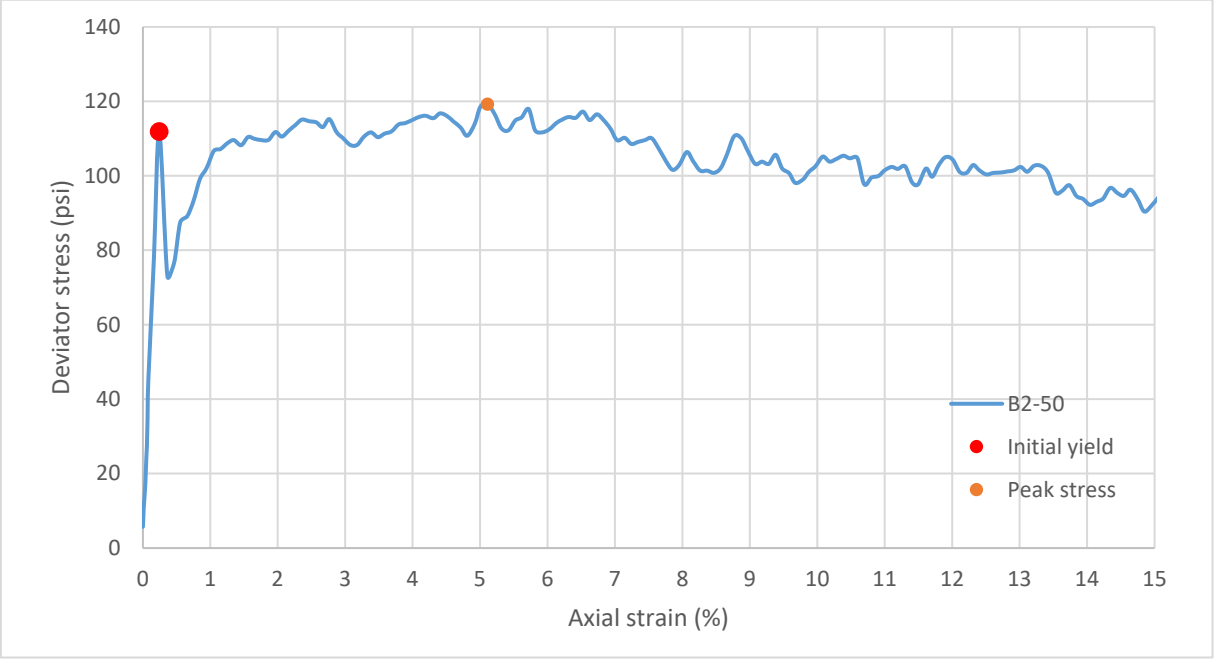

Sample ID:	B2-50

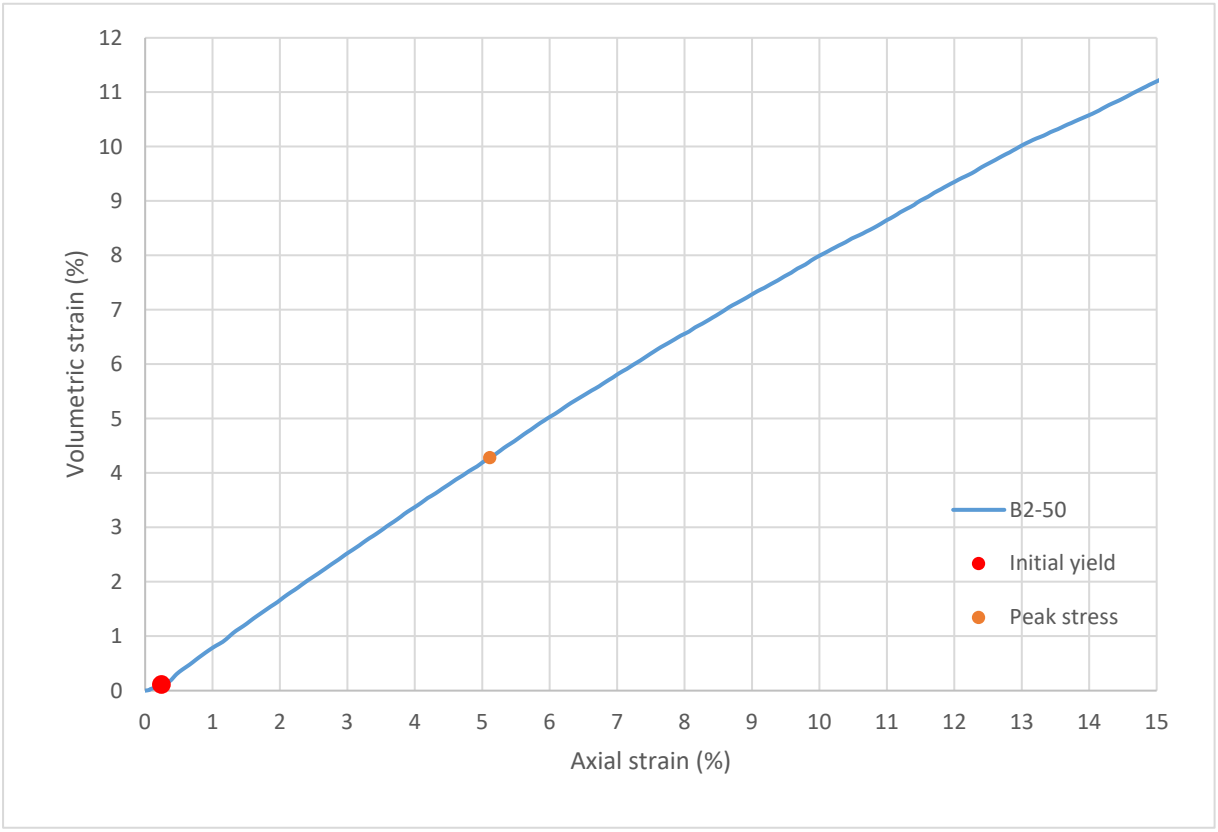

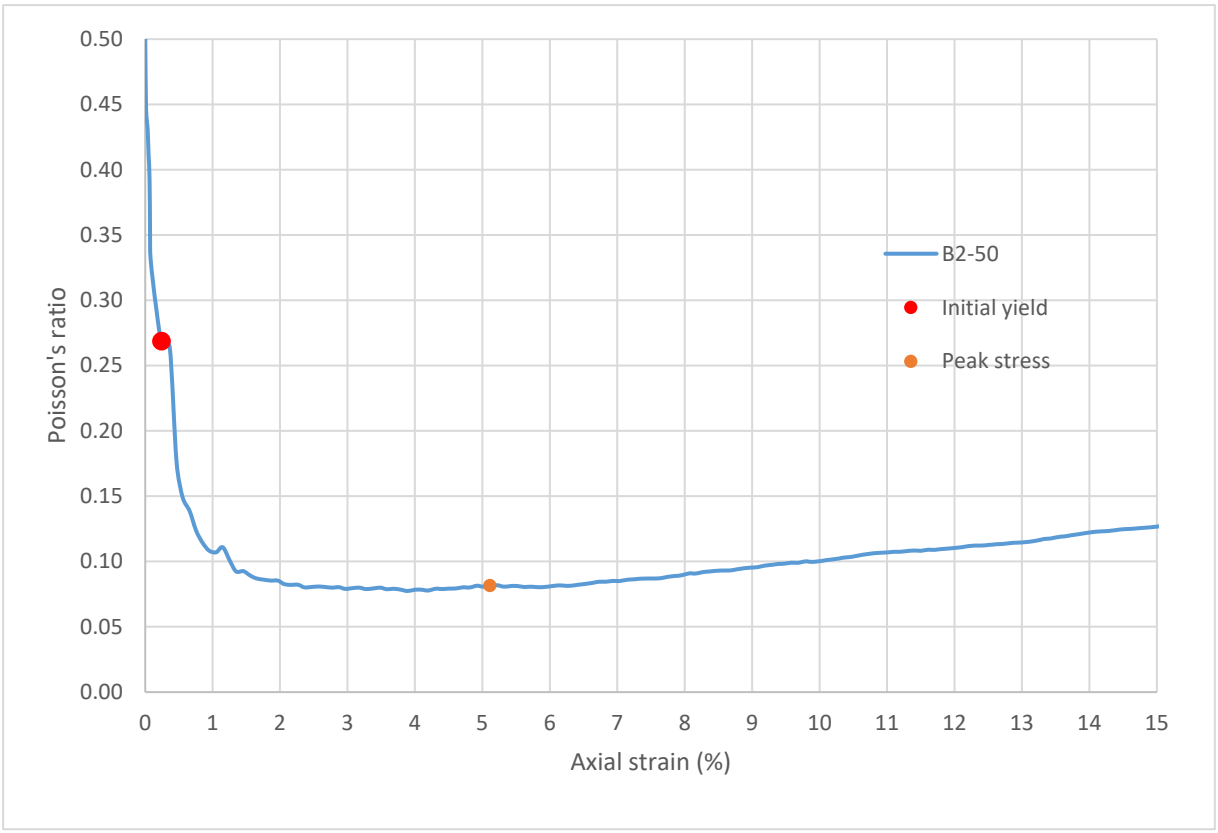

Sample ID:	B2-50

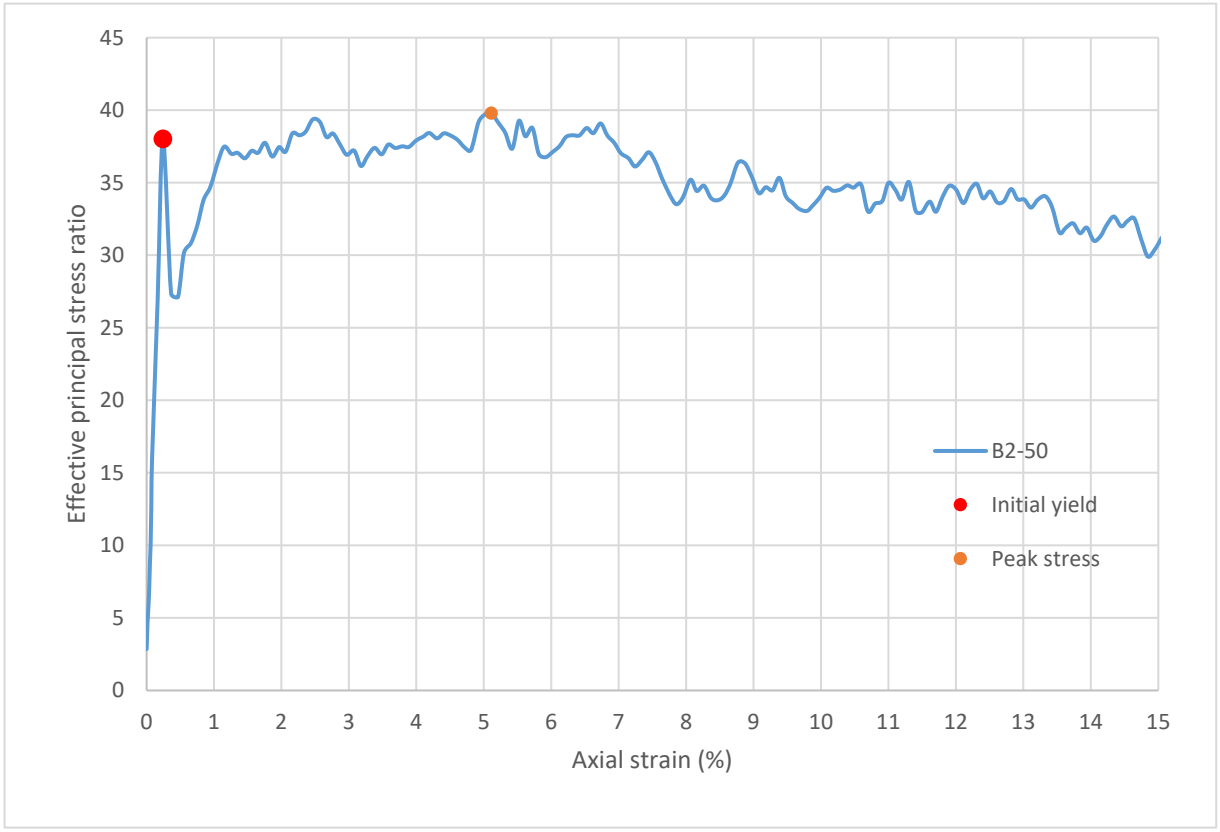

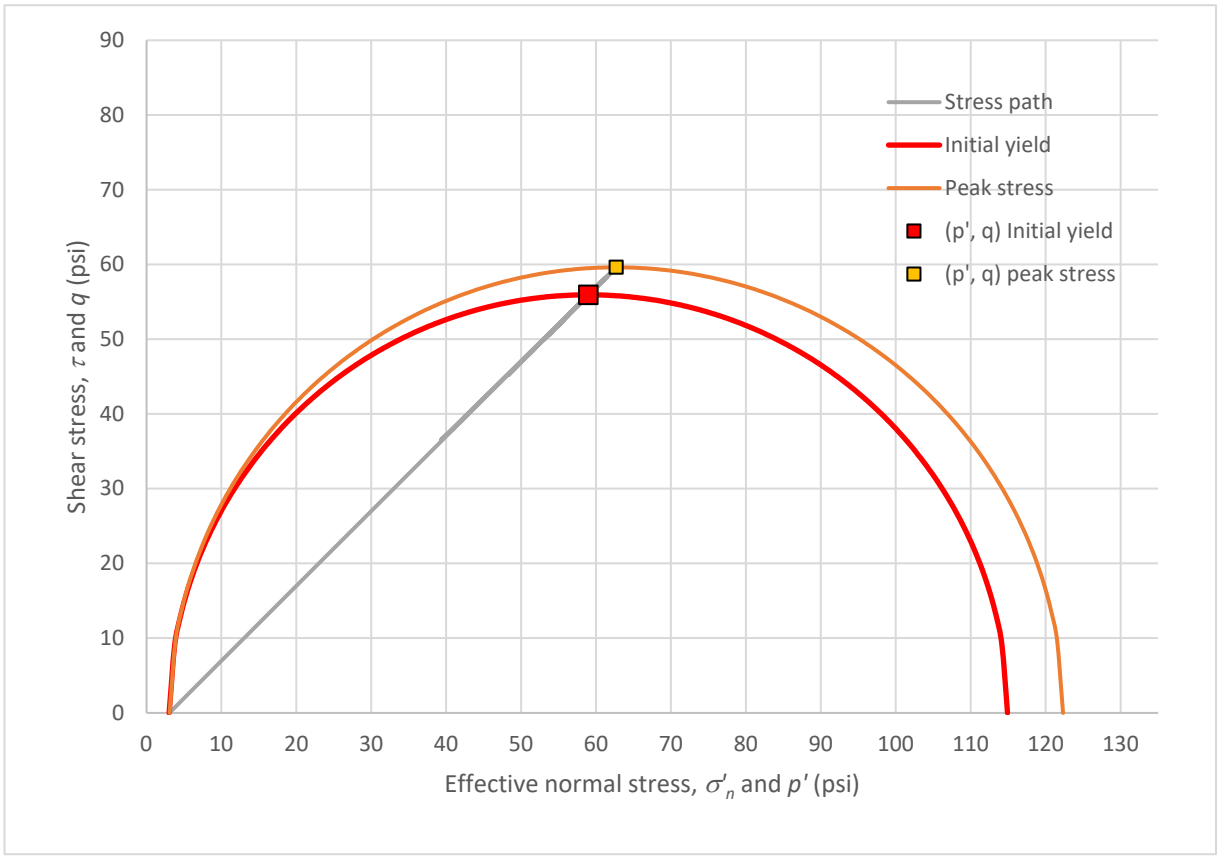

Consolidated-Drained Triaxial Shear, Lightweight Cellular Concrete

Sample ID:	**B2-51**
Height (in):	5.512
Height (mm):	140.0
Diameter (in):	2.964
Diameter (mm)	75.29
Area (in^2):	6.900
Area (mm^2):	4452
Mass (g):	221.42
Weight (lb):	0.4881
Weight (kN):	0.002171
Volume (in^3):	38.03
Volume (mm^3):	623242
Density (g/mm^3):	0.0003553
Density (kg/m^3):	355.3
Unit weight (pcf):	**22.18**
Dry unit weight (pcf);	**19.36**
Unit Weight (kN/m^3):	3.484
Wet mass + tare (g):	329.02
Dry mass + tare (g):	302.95
Tare (g):	123.55
Water content (%)	**14.53**
Saturation (%):	**5.10**
H:D ratio:	1.860
Age (days):	1060
Treatment:	H100

Strain rate (%/min):	0.2
Mean σ'_3 (psi):	3.1
Initial modulus (psi):	37358
Initial yield	
Time to failure (min):	1.6
Axial strain at failure (%):	0.316
σ'_1 (psi):	121.19
σ'_3 (psi):	3.01
σ'_1 -σ'_3 (psi):	118.18
σ'_1 / σ'_3:	40.32
p' (psi):	62.10
q (psi):	59.09
Volumetric strain (%):	0.150
Poisson's ratio:	0.263
Peak stress	
Time to failure (min):	18.3
Axial strain at failure (%):	3.658
σ'_1 (psi):	124.24
σ'_3 (psi):	3.05
σ'_1 -σ'_3 (psi):	121.18
σ'_1 / σ'_3:	40.68
p' (psi):	63.65
q (psi):	60.59
Volumetric strain (%):	3.026
Poisson's ratio:	0.086

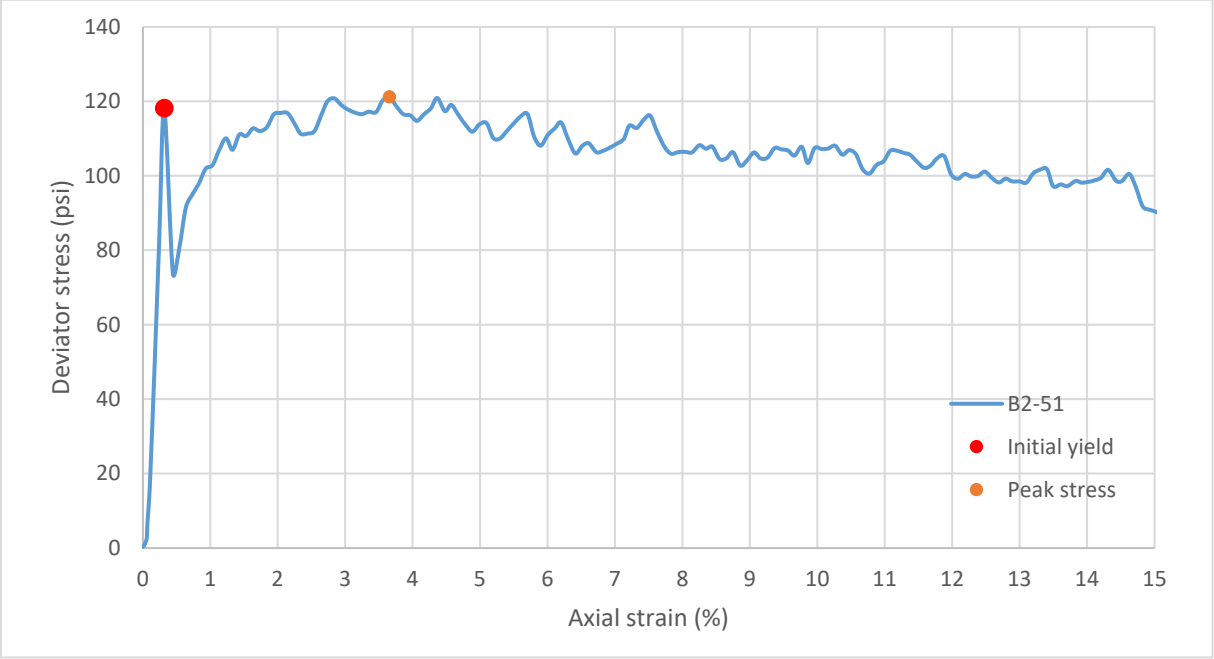

Sample ID:	B2-51

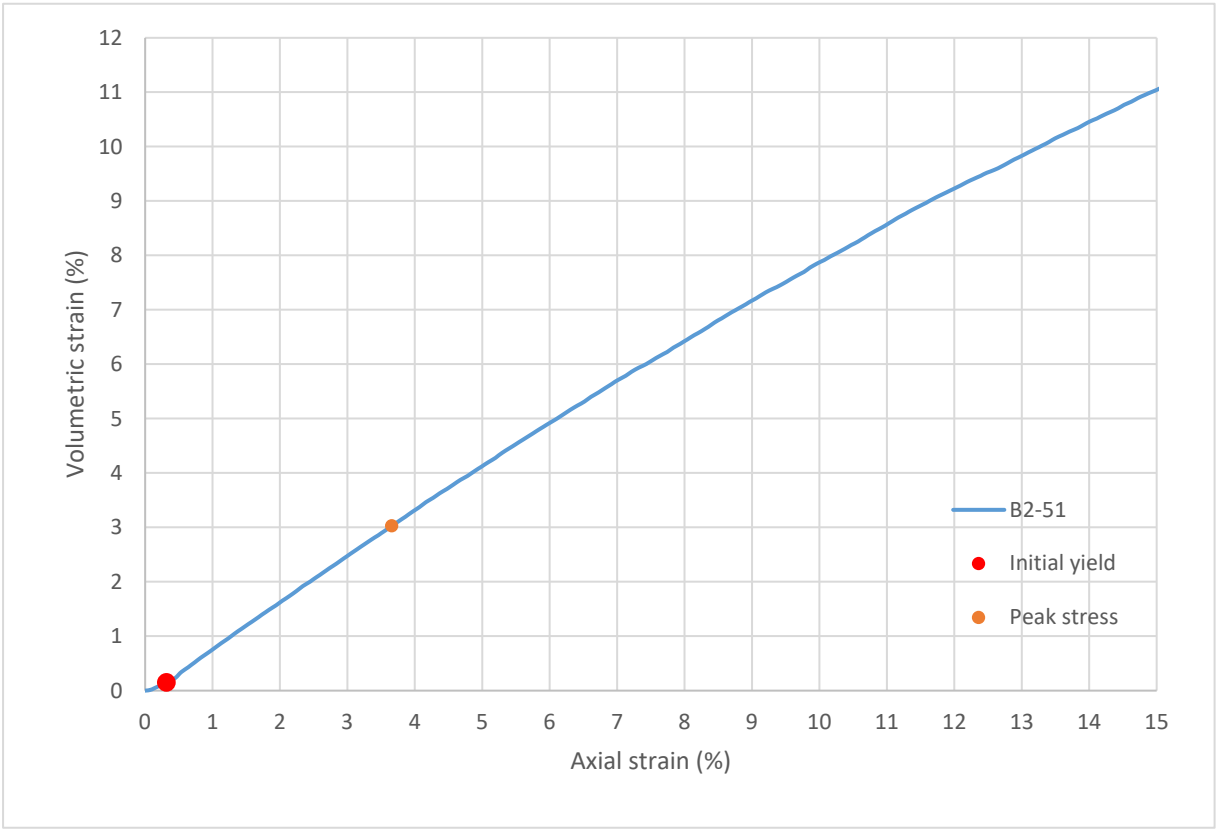

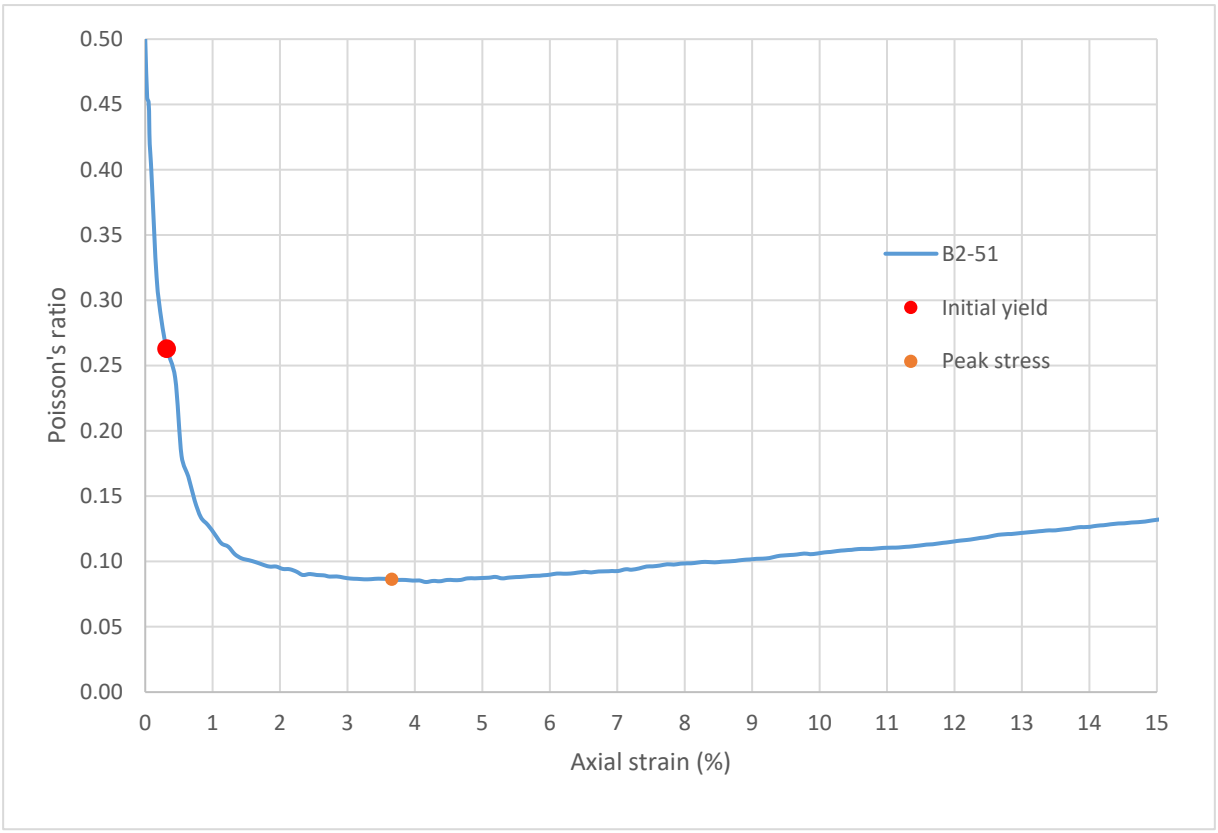

Sample ID:	B2-51

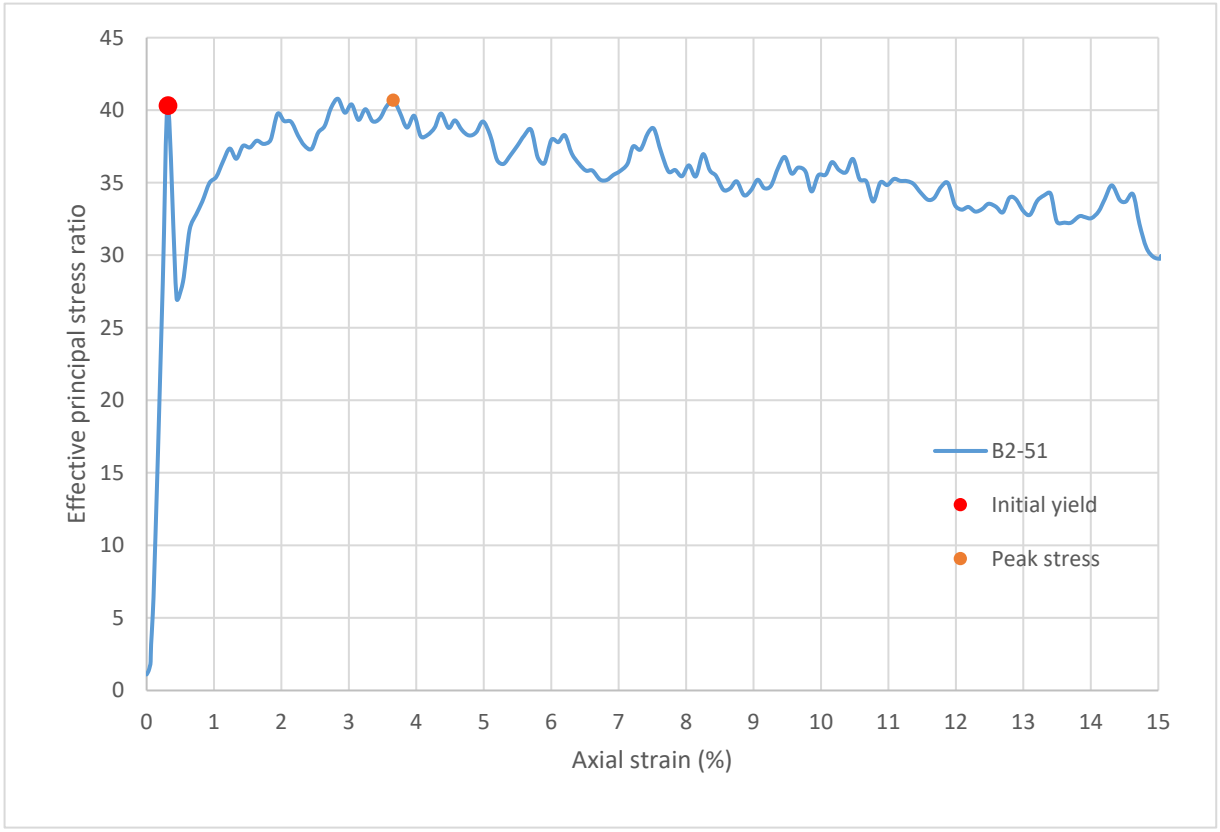

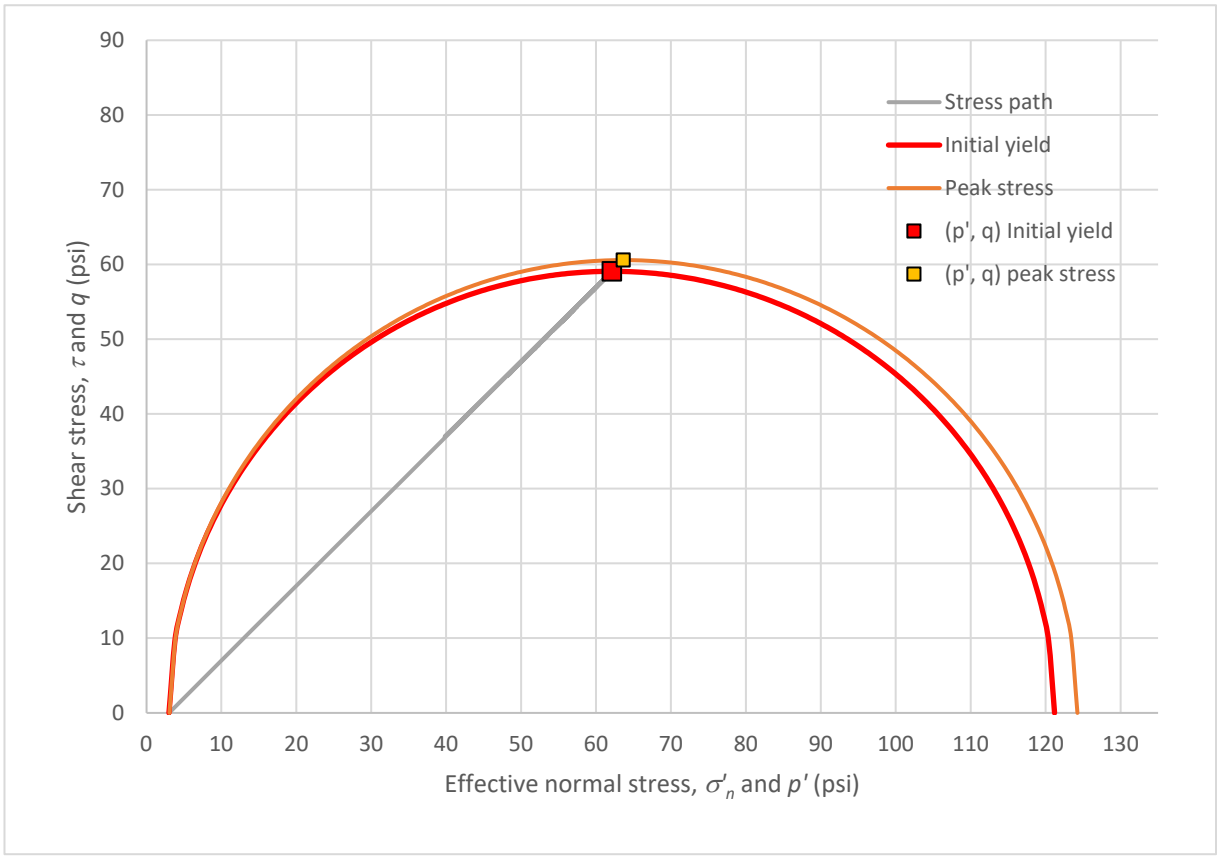

Consolidated-Drained Triaxial Shear, Lightweight Cellular Concrete

Sample ID:	**B2-52**
Height (in):	5.587
Height (mm):	141.9
Diameter (in):	2.963
Diameter (mm)	75.27
Area (in^2):	6.896
Area (mm^2):	4449
Mass (g):	289.64
Weight (lb):	0.6385
Weight (kN):	0.002840
Volume (in^3):	38.53
Volume (mm^3):	631391
Density (g/mm^3):	0.0004587
Density (kg/m^3):	458.7
Unit weight (pcf):	**28.64**
Dry unit weight (pcf);	**18.93**
Unit Weight (kN/m^3):	4.499
Wet mass + tare (g):	409.70
Dry mass + tare (g):	325.16
Tare (g):	160.19
Water content (%)	**51.25**
Saturation (%):	**17.53**
H:D ratio:	1.885
Age (days):	1064
Treatment:	D1

Strain rate (%/min):	0.2
Mean σ'_3 (psi):	3.0
Initial modulus (psi):	23093
Initial yield	
Time to failure (min):	1.3
Axial strain at failure (%):	0.265
σ'_1 (psi):	64.09
σ'_3 (psi):	2.87
σ'_1 -σ'_3 (psi):	61.22
σ'_1 / σ'_3:	22.33
p' (psi):	33.48
q (psi):	30.61
Volumetric strain (%):	0.173
Poisson's ratio:	0.174
Peak stress	
Time to failure (min):	18.0
Axial strain at failure (%):	3.607
σ'_1 (psi):	87.11
σ'_3 (psi):	2.98
σ'_1 -σ'_3 (psi):	84.13
σ'_1 / σ'_3:	29.19
p' (psi):	45.05
q (psi):	42.06
Volumetric strain (%):	3.175
Poisson's ratio:	0.060

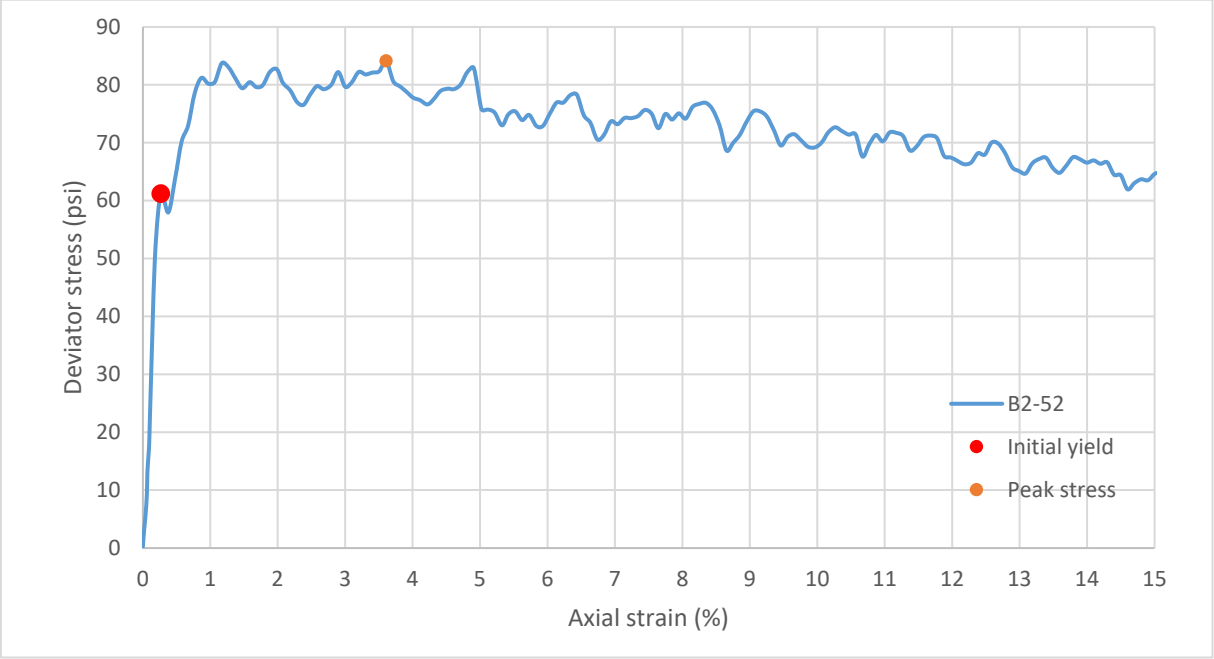

Sample ID:	B2-52

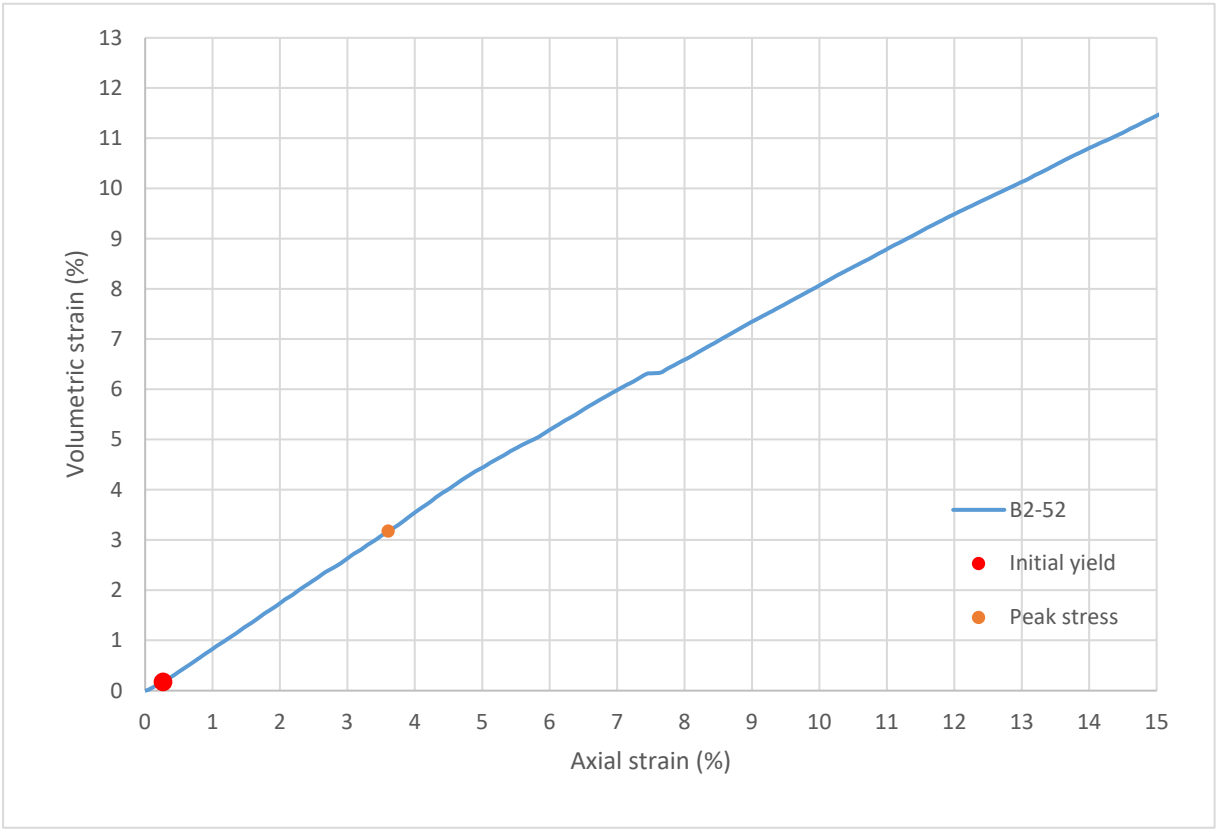

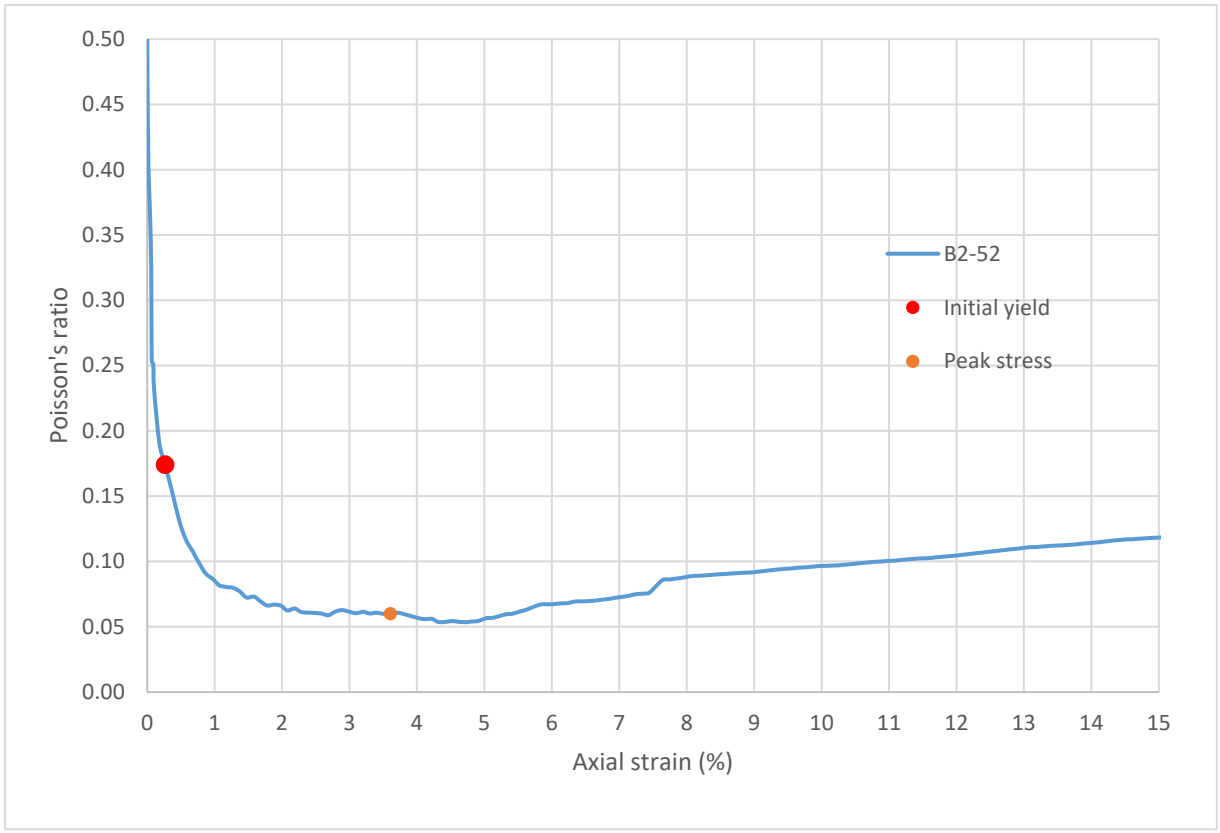

Sample ID:	B2-52

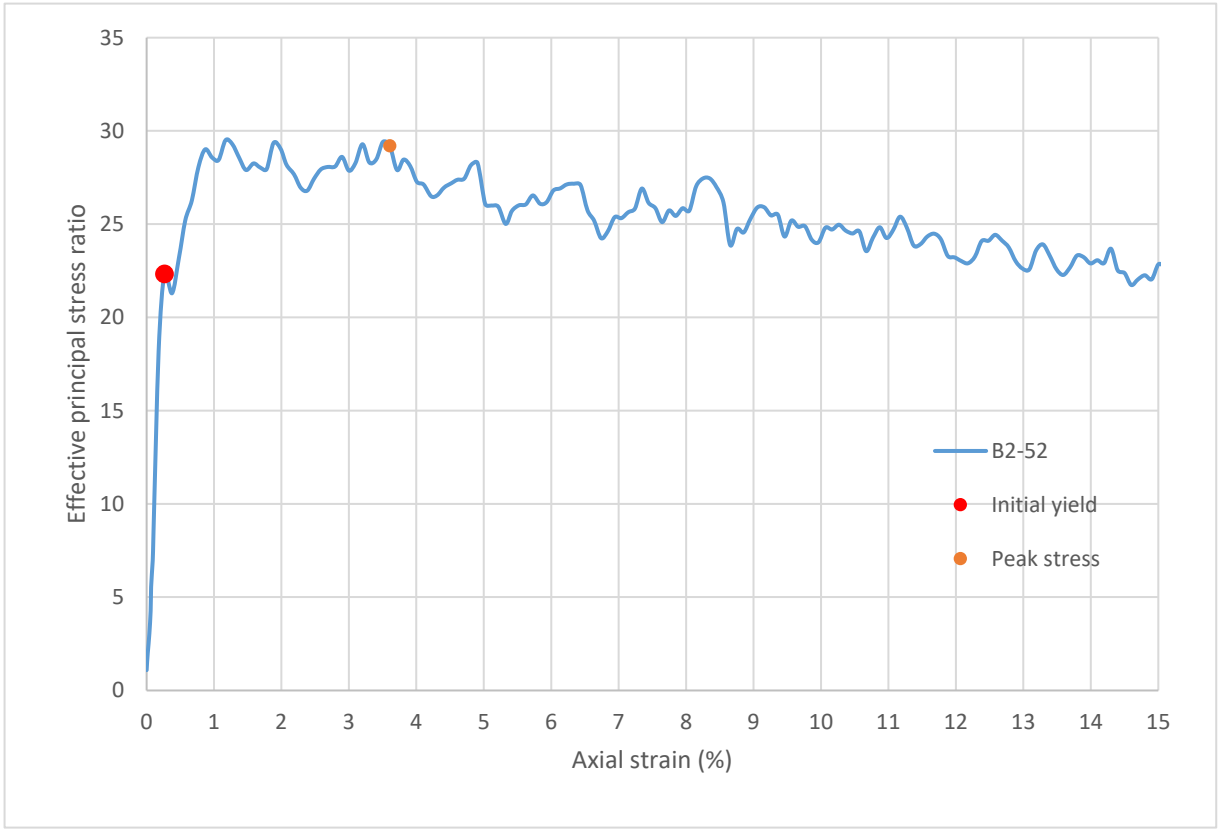

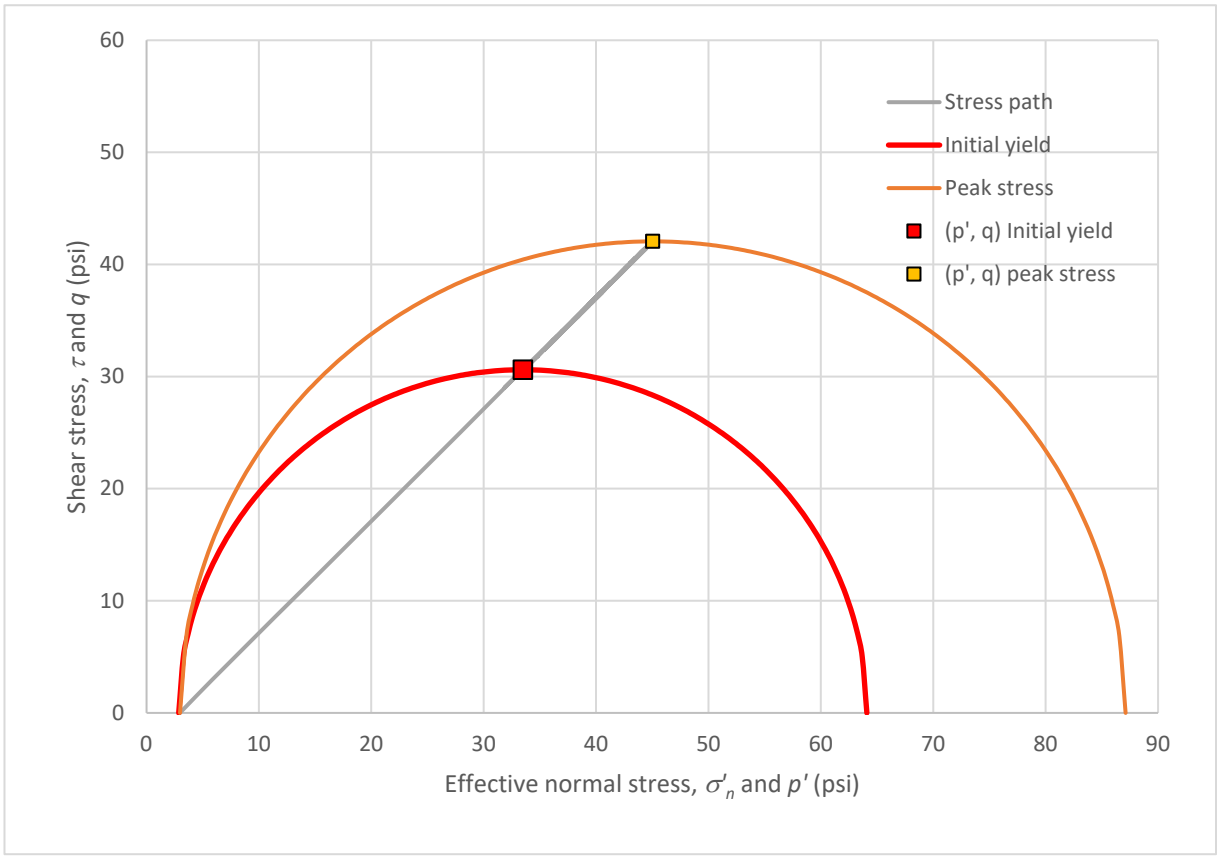

Consolidated-Drained Triaxial Shear, Lightweight Cellular Concrete

Sample ID:	**B2-53**
Height (in):	5.439
Height (mm):	138.1
Diameter (in):	2.953
Diameter (mm)	75.01
Area (in^2):	6.849
Area (mm^2):	4419
Mass (g):	274.34
Weight (lb):	0.6048
Weight (kN):	0.002690
Volume (in^3):	37.25
Volume (mm^3):	610394
Density (g/mm^3):	0.0004494
Density (kg/m^3):	449.4
Unit weight (pcf):	**28.06**
Dry unit weight (pcf);	**19.52**
Unit Weight (kN/m^3):	4.408
Wet mass + tare (g):	375.59
Dry mass + tare (g):	296.18
Tare (g):	114.70
Water content (%)	**43.76**
Saturation (%):	**15.49**
H:D ratio:	1.842
Age (days):	1064
Treatment:	D1

Strain rate (%/min):	0.2
Mean σ'_3 (psi):	3.0
Initial modulus (psi):	47250
Initial yield	
Time to failure (min):	0.8
Axial strain at failure (%):	0.155
σ'_1 (psi):	76.27
σ'_3 (psi):	2.96
σ'_1 -σ'_3 (psi):	73.31
σ'_1 / σ'_3:	25.76
p' (psi):	39.61
q (psi):	36.65
Volumetric strain (%):	0.077
Poisson's ratio:	0.252
Peak stress	
Time to failure (min):	24.0
Axial strain at failure (%):	4.802
σ'_1 (psi):	93.39
σ'_3 (psi):	3.05
σ'_1 -σ'_3 (psi):	90.34
σ'_1 / σ'_3:	30.58
p' (psi):	48.22
q (psi):	45.17
Volumetric strain (%):	4.312
Poisson's ratio:	0.051

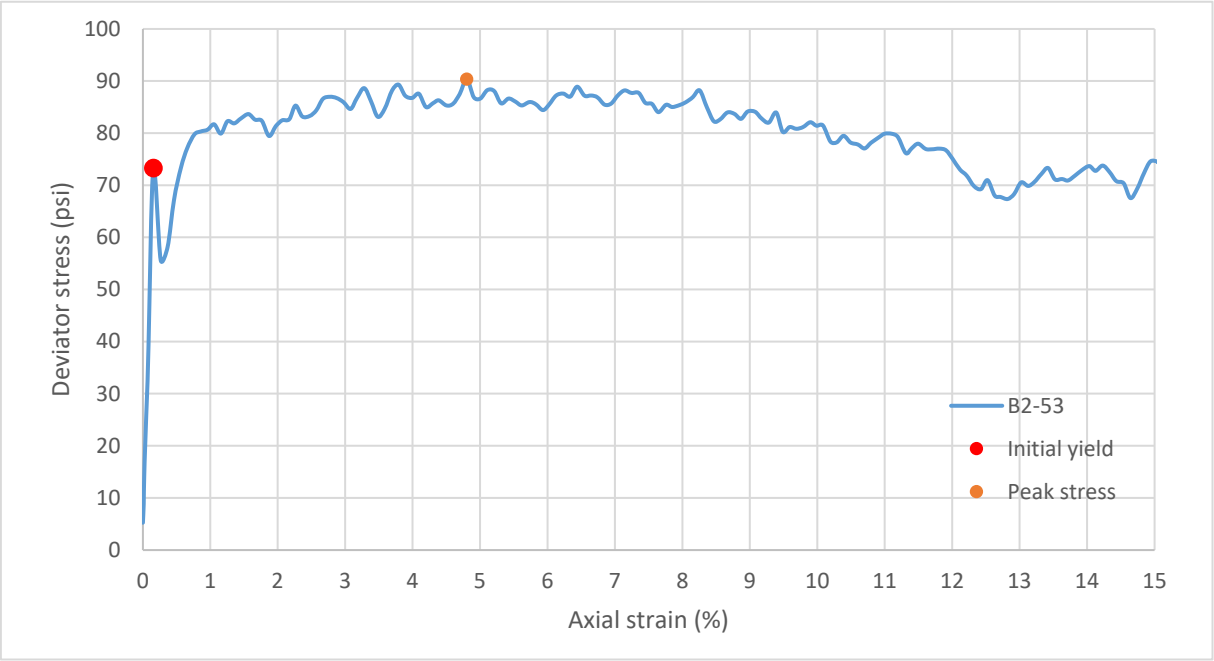

Sample ID:	B2-53

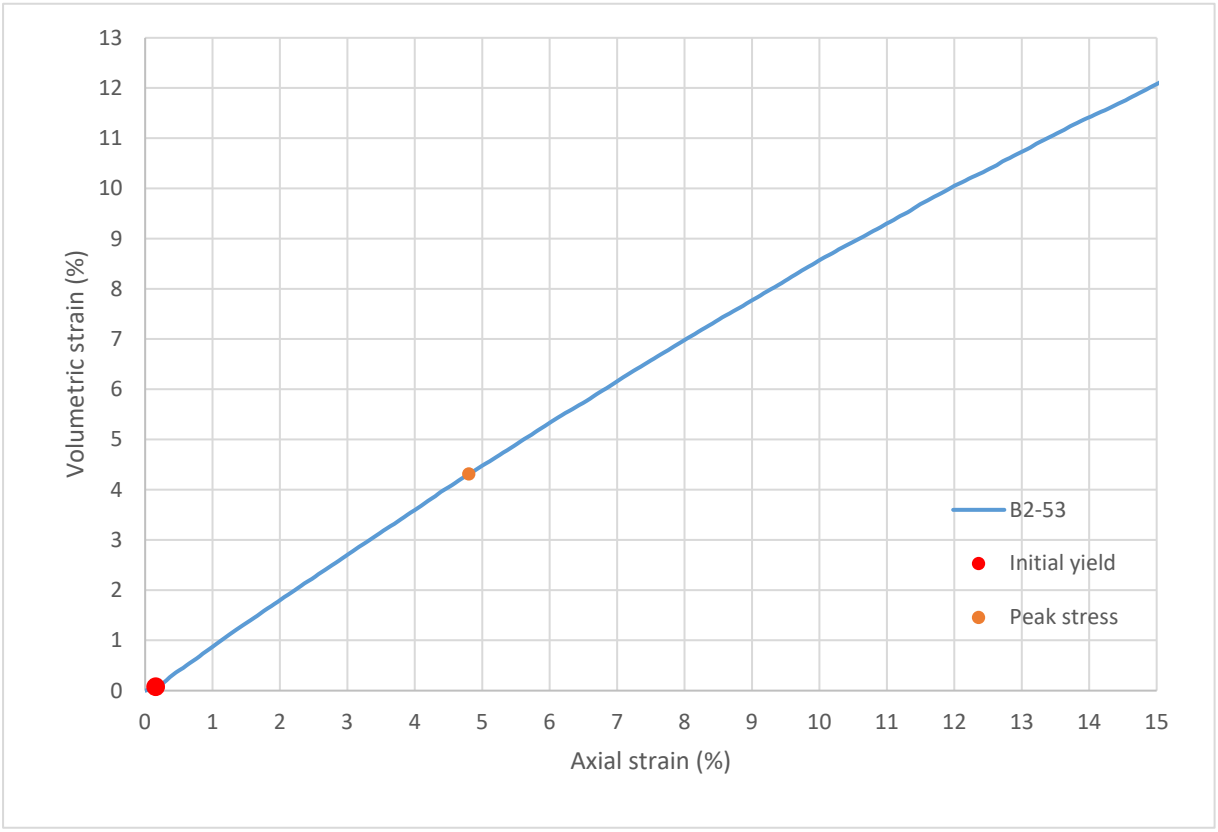

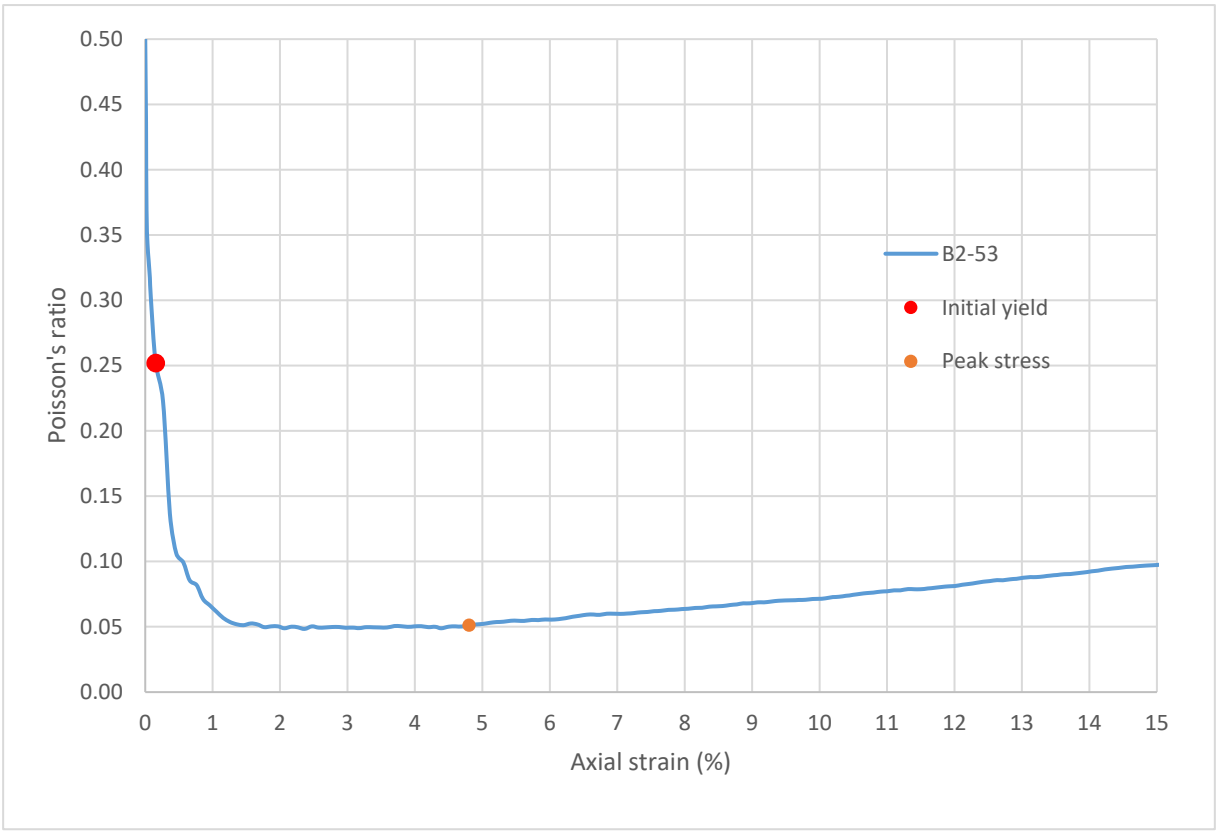

Sample ID:	B2-53

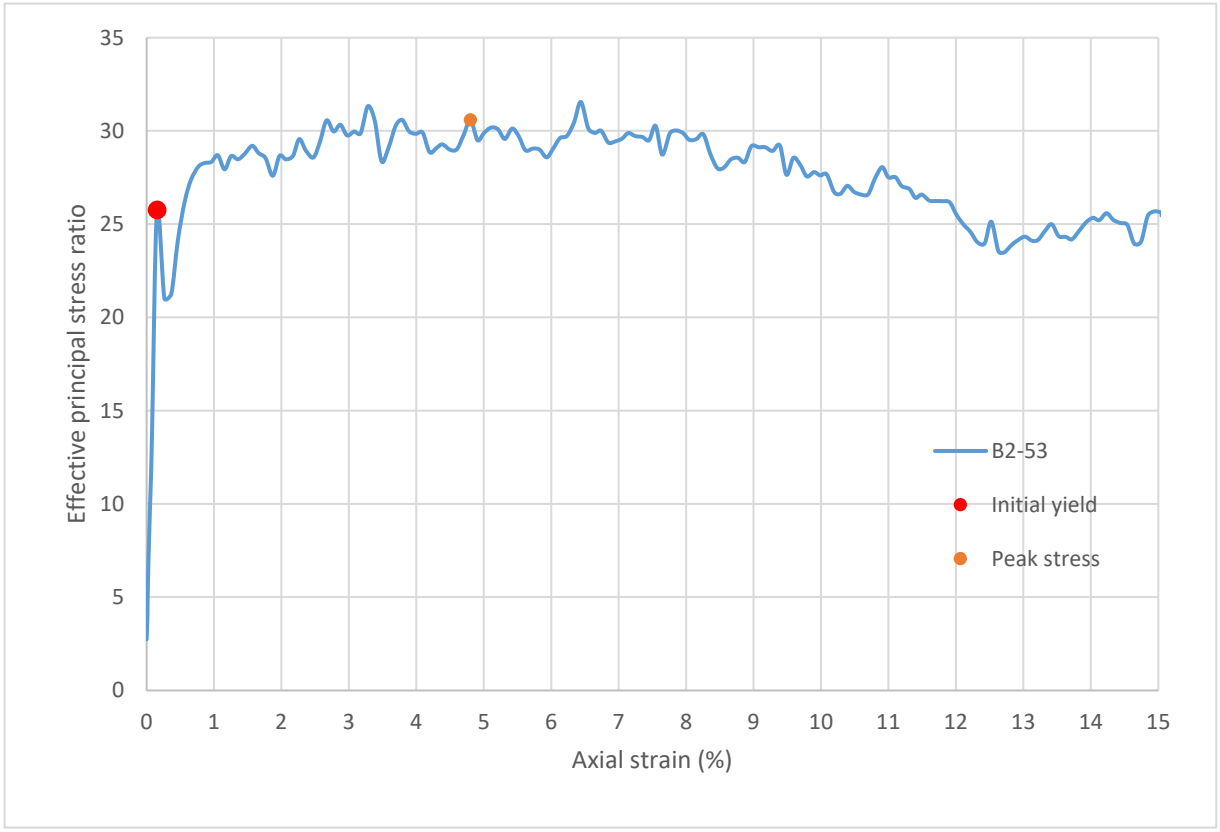

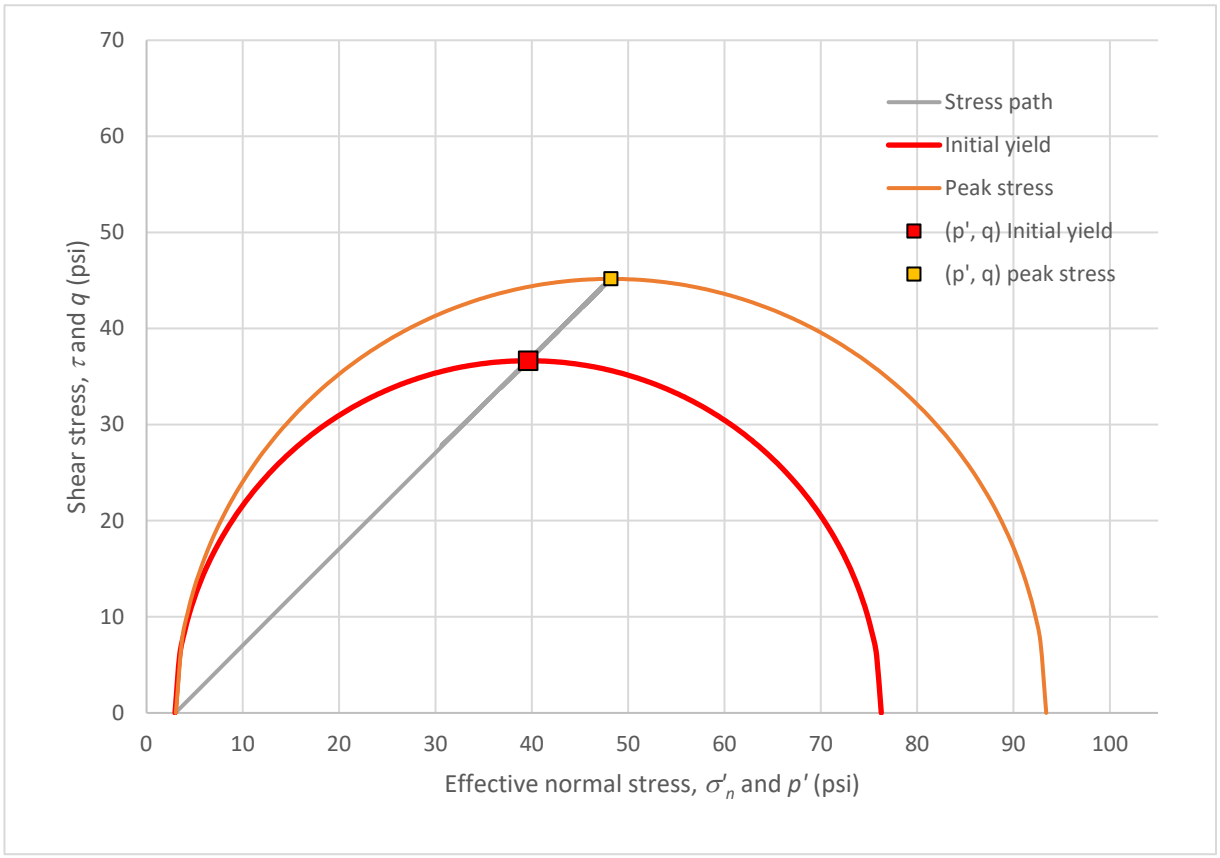

Consolidated-Drained Triaxial Shear, Lightweight Cellular Concrete

Sample ID:	**B2-54**
Height (in):	5.472
Height (mm):	139.0
Diameter (in):	2.970
Diameter (mm)	75.43
Area (in^2):	6.926
Area (mm^2):	4468
Mass (g):	281.76
Weight (lb):	0.6212
Weight (kN):	0.002763
Volume (in^3):	37.90
Volume (mm^3):	621078
Density (g/mm^3):	0.0004537
Density (kg/m^3):	453.7
Unit weight (pcf):	**28.32**
Dry unit weight (pcf);	**19.64**
Unit Weight (kN/m^3):	4.449
Wet mass + tare (g):	388.66
Dry mass + tare (g):	307.29
Tare (g):	123.25
Water content (%)	**44.21**
Saturation (%):	**15.76**
H:D ratio:	1.843
Age (days):	1065
Treatment:	D1

Strain rate (%/min):	0.2
Mean σ'_3 (psi):	3.7
Initial modulus (psi):	22244
Initial yield	
Time to failure (min):	1.3
Axial strain at failure (%):	0.269
σ'_1 (psi):	63.31
σ'_3 (psi):	3.55
σ'_1 -σ'_3 (psi):	59.76
σ'_1 / σ'_3:	17.86
p' (psi):	33.43
q (psi):	29.88
Volumetric strain (%):	0.170
Poisson's ratio:	0.184
Peak stress	
Time to failure (min):	11.9
Axial strain at failure (%):	2.380
σ'_1 (psi):	82.60
σ'_3 (psi):	3.64
σ'_1 -σ'_3 (psi):	78.96
σ'_1 / σ'_3:	22.69
p' (psi):	43.12
q (psi):	39.48
Volumetric strain (%):	2.135
Poisson's ratio:	0.051

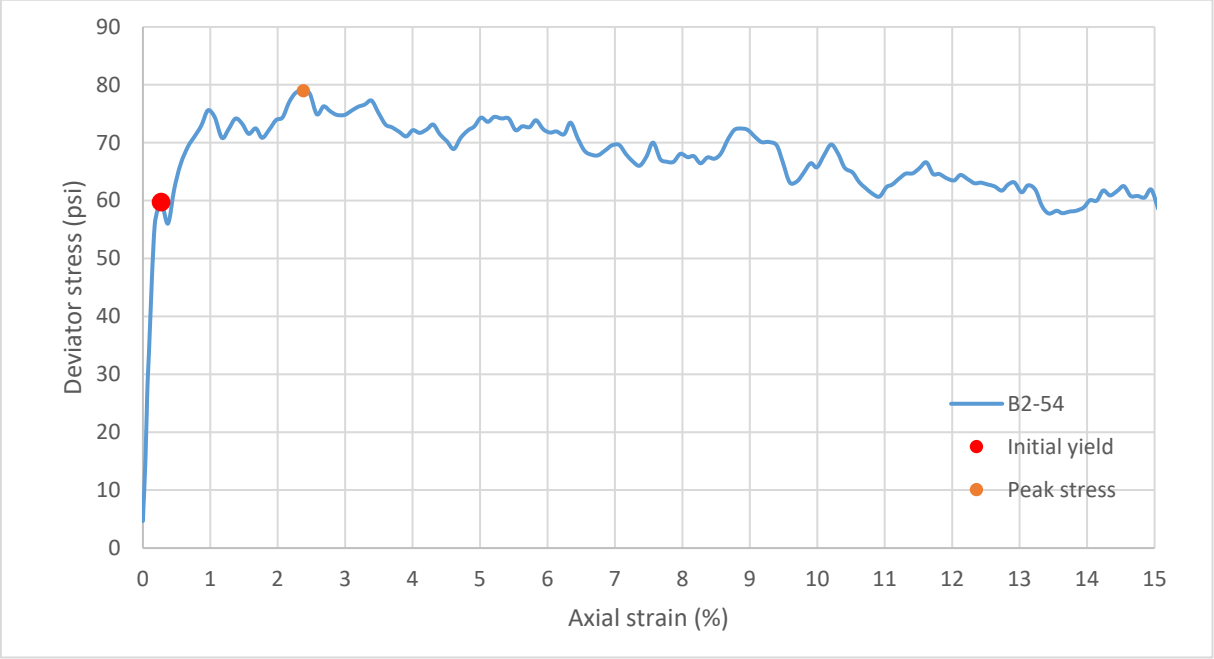

Sample ID:	B2-54

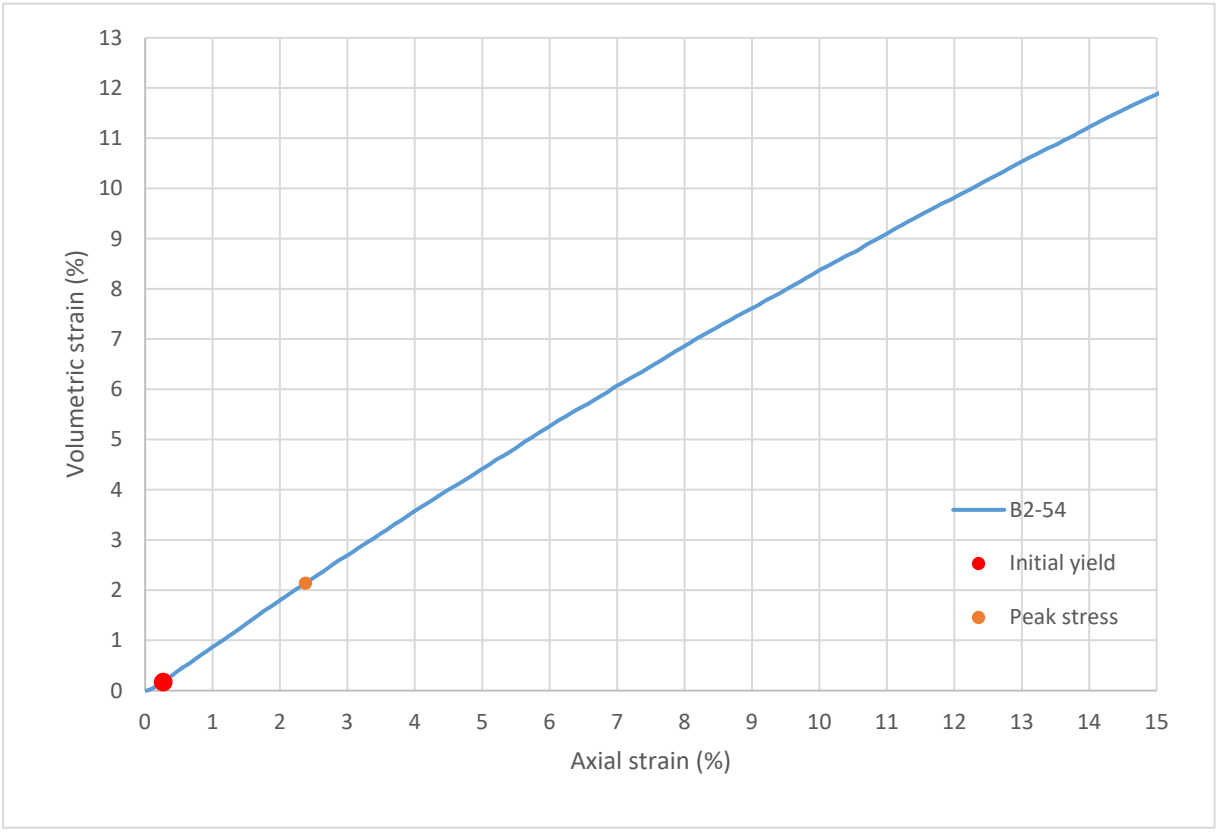

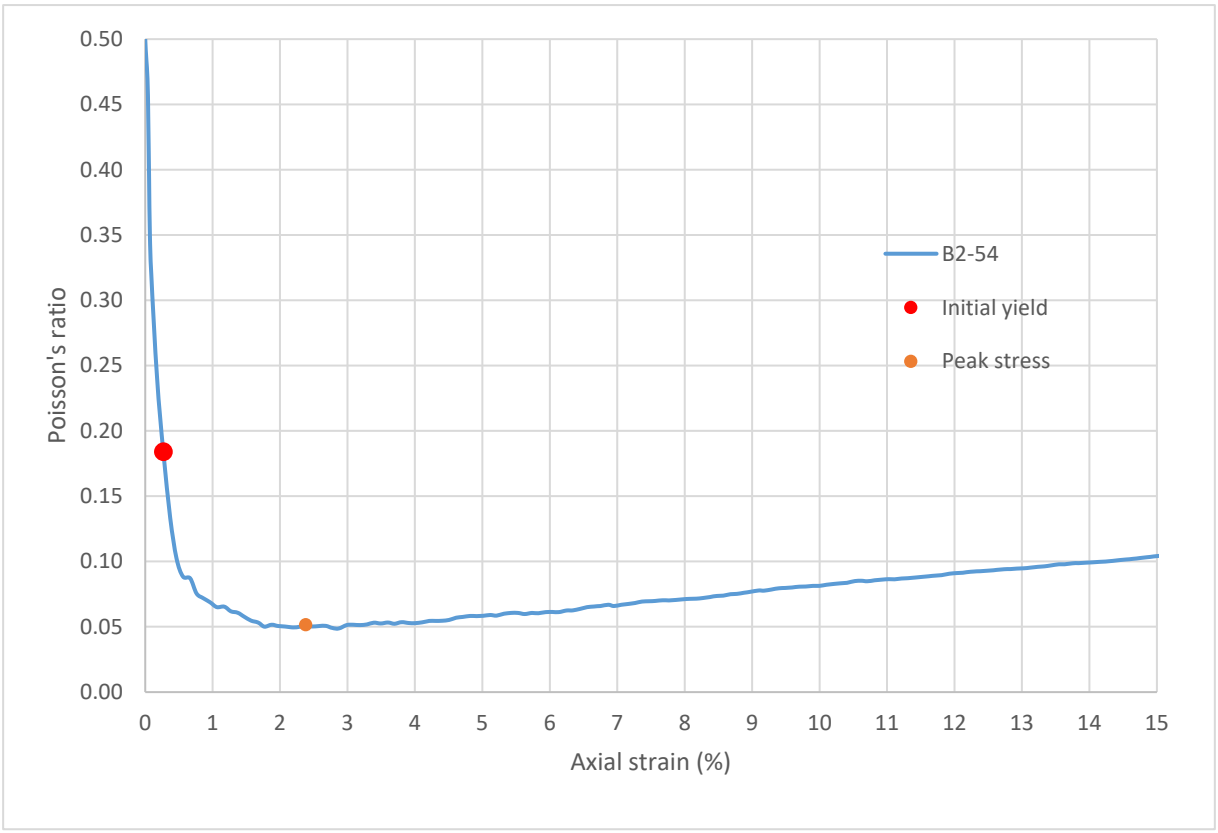

Sample ID:	B2-54

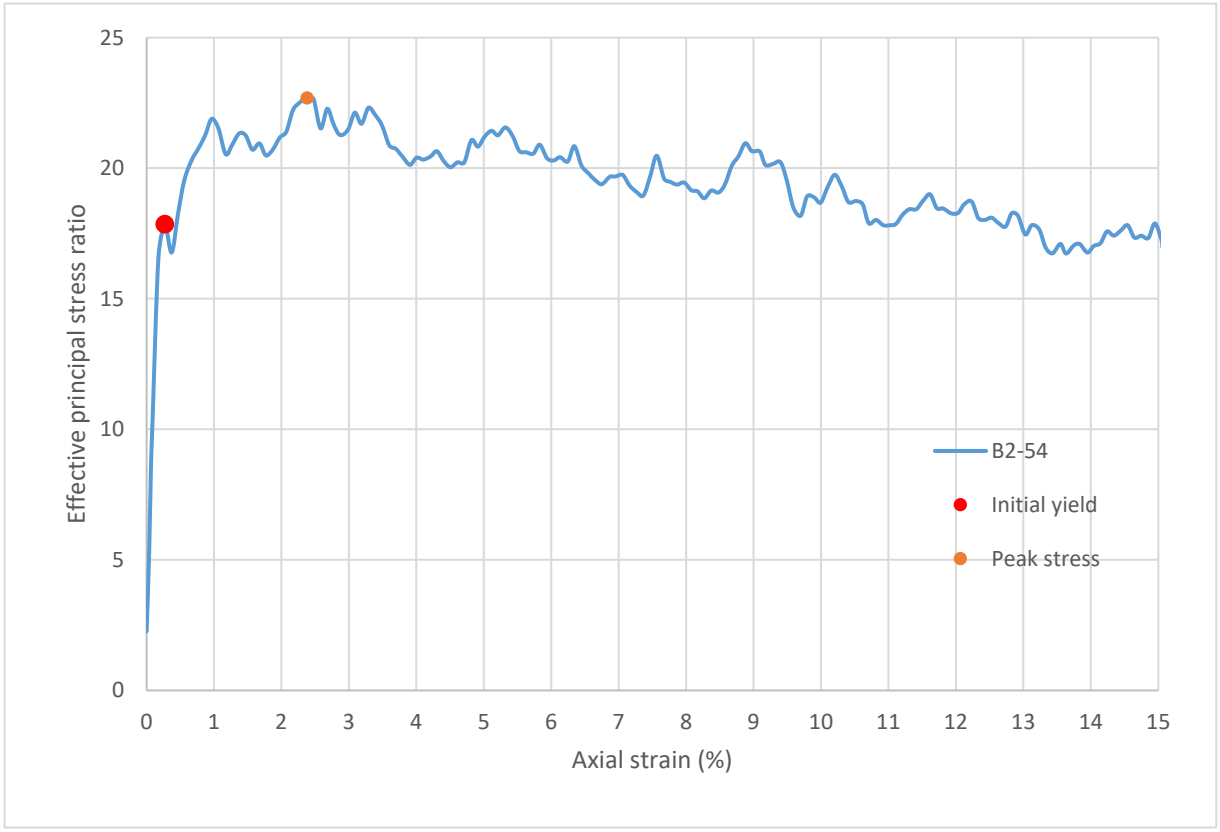

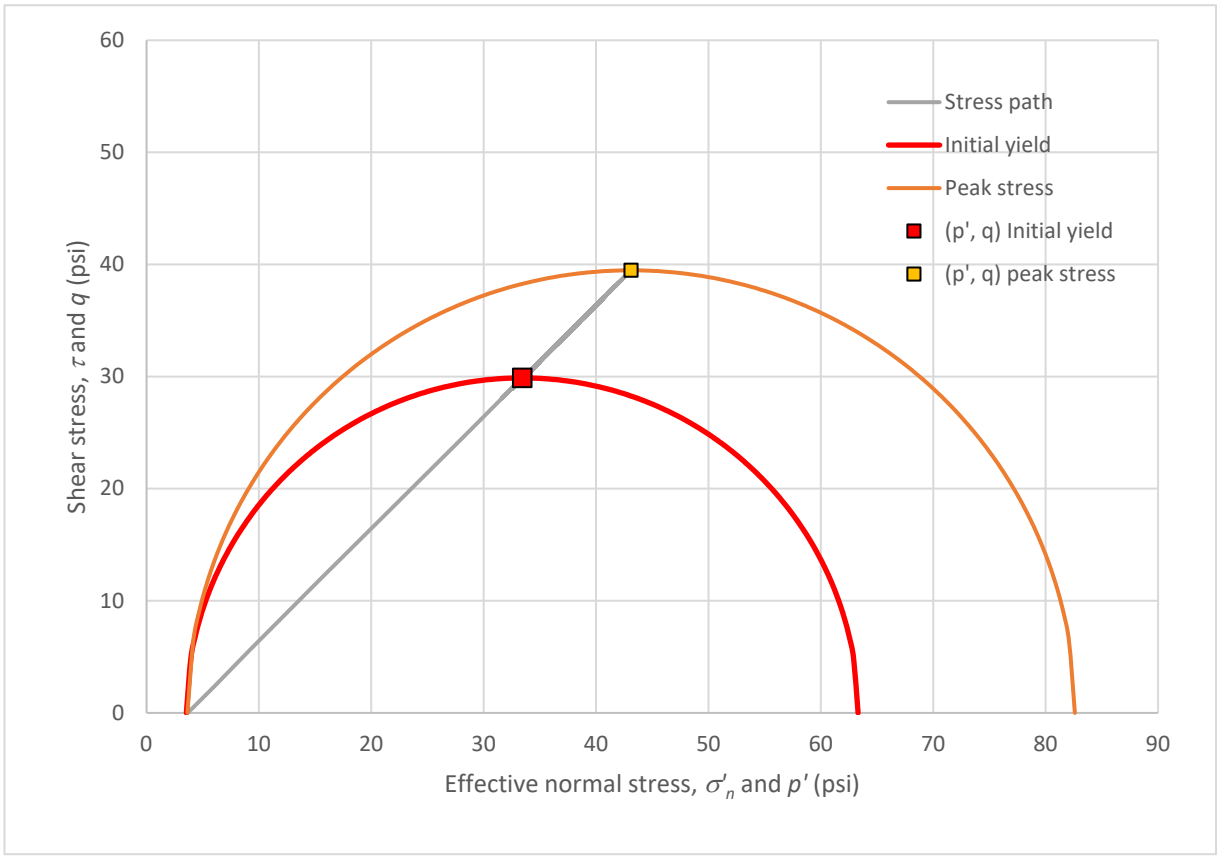

Consolidated-Drained Triaxial Shear, Lightweight Cellular Concrete

Sample ID:	**B2-55**
Height (in):	5.512
Height (mm):	140.0
Diameter (in):	2.961
Diameter (mm)	75.20
Area (in^2):	6.885
Area (mm^2):	4442
Mass (g):	297.01
Weight (lb):	0.6548
Weight (kN):	0.002913
Volume (in^3):	37.95
Volume (mm^3):	621888
Density (g/mm^3):	0.0004776
Density (kg/m^3):	477.6
Unit weight (pcf):	**29.82**
Dry unit weight (pcf);	**19.94**
Unit Weight (kN/m^3):	4.684
Wet mass + tare (g):	391.48
Dry mass + tare (g):	304.19
Tare (g):	128.04
Water content (%)	**49.55**
Saturation (%):	**17.97**
H:D ratio:	1.862
Age (days):	1065
Treatment:	D1

Strain rate (%/min):	0.2
Mean σ'_3 (psi):	3.1
Initial modulus (psi):	36381
Initial yield	
Time to failure (min):	1.2
Axial strain at failure (%):	0.247
σ'_1 (psi):	92.85
σ'_3 (psi):	3.04
$\sigma'_1 - \sigma'_3$ (psi):	89.82
σ'_1 / σ'_3:	30.58
p' (psi):	47.94
q (psi):	44.91
Volumetric strain (%):	0.129
Poisson's ratio:	0.238
Peak stress	
Time to failure (min):	1.2
Axial strain at failure (%):	0.247
σ'_1 (psi):	92.85
σ'_3 (psi):	3.04
$\sigma'_1 - \sigma'_3$ (psi):	89.82
σ'_1 / σ'_3:	30.58
p' (psi):	47.94
q (psi):	44.91
Volumetric strain (%):	0.129
Poisson's ratio:	0.238

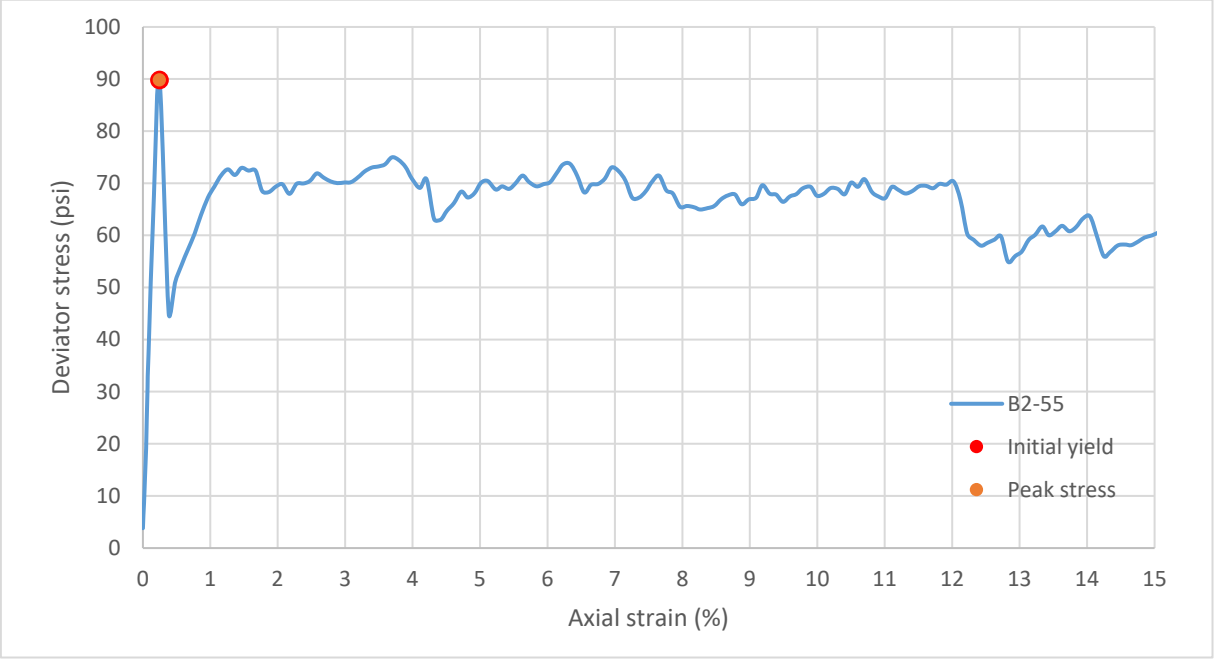

Sample ID:	B2-55

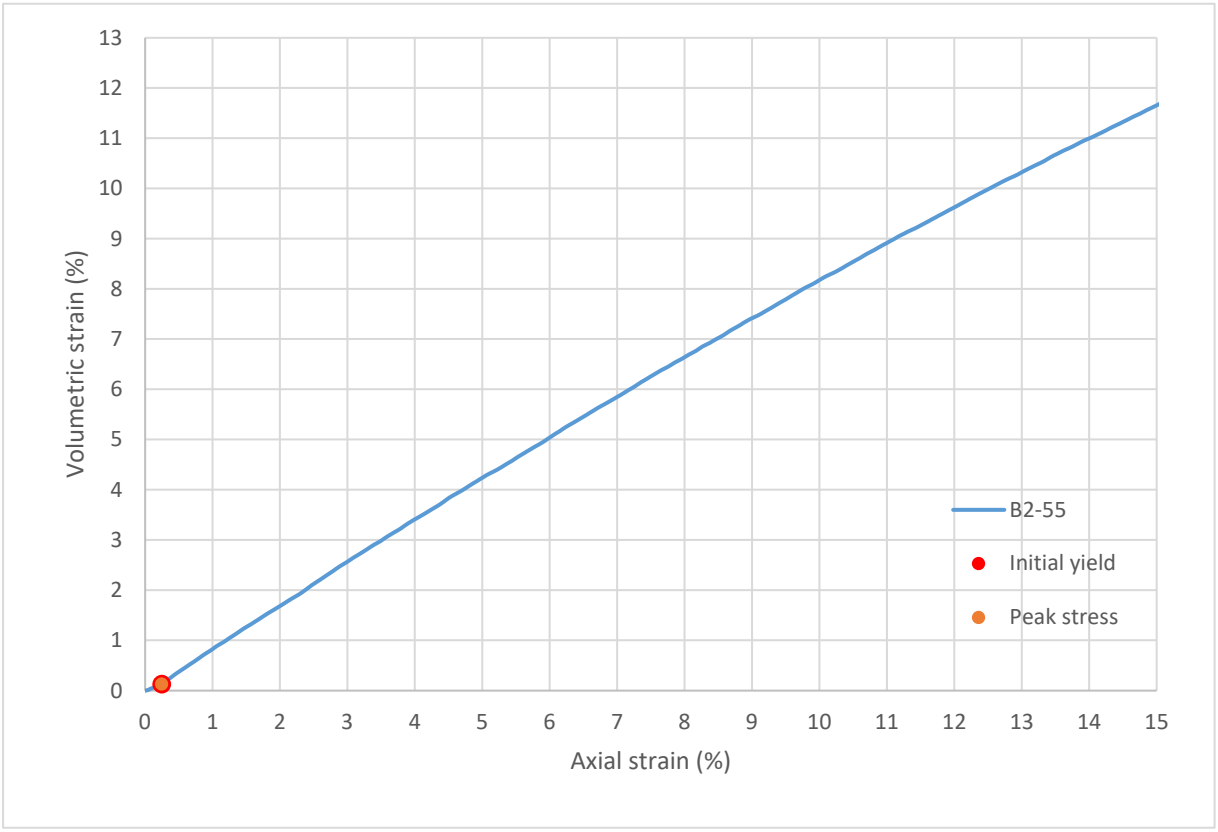

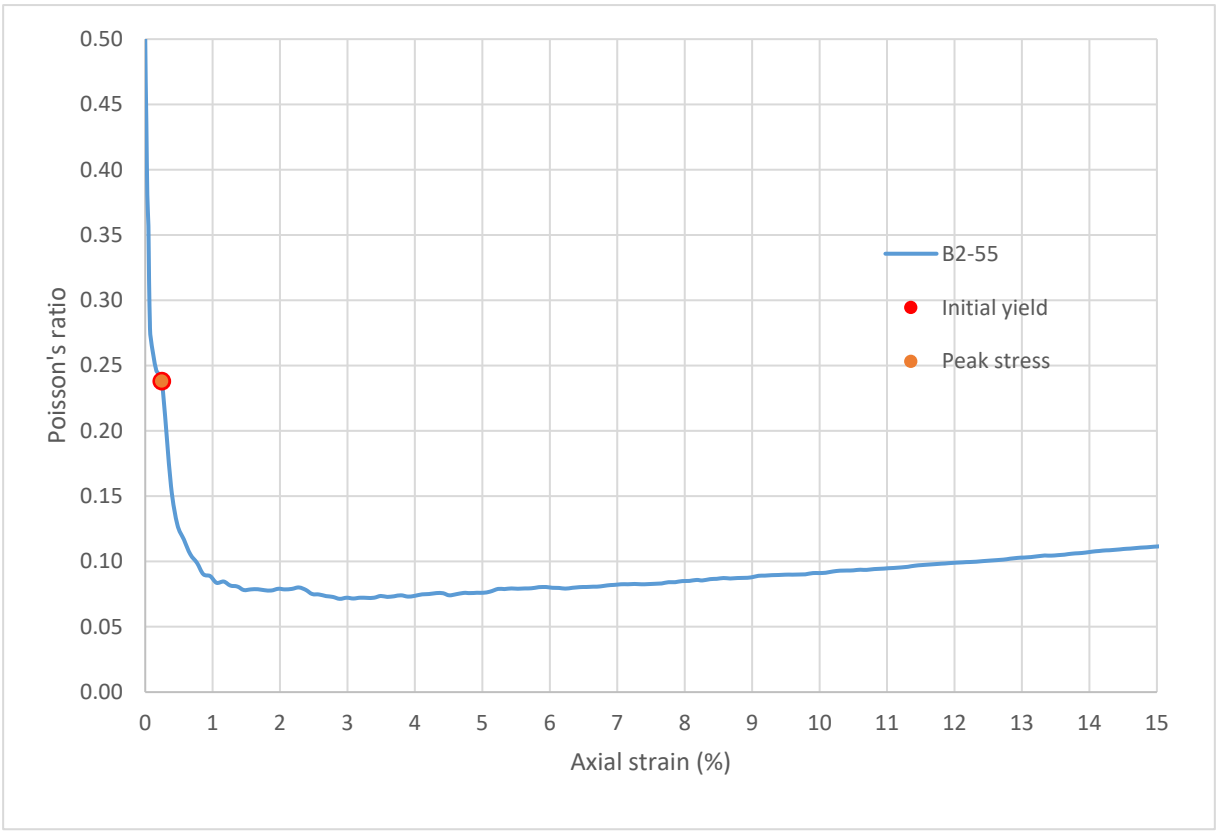

Sample ID:	B2-55

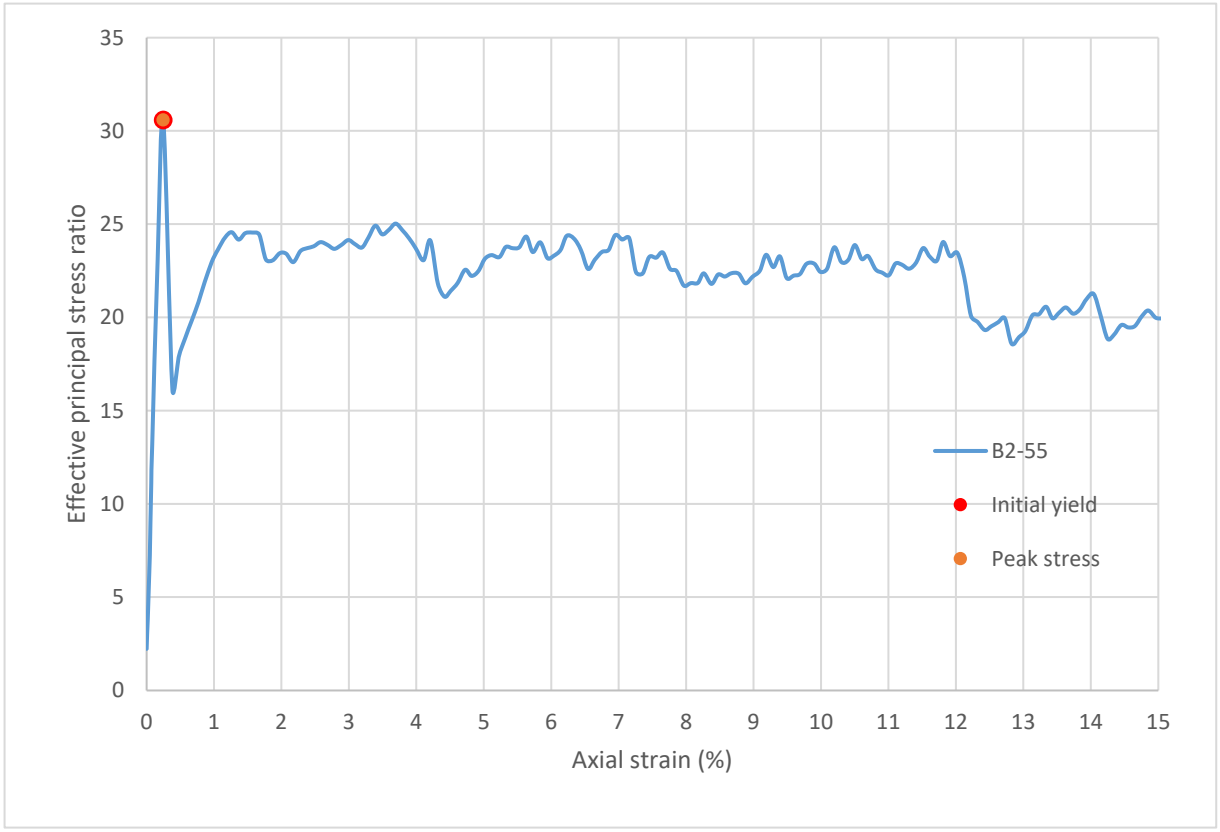

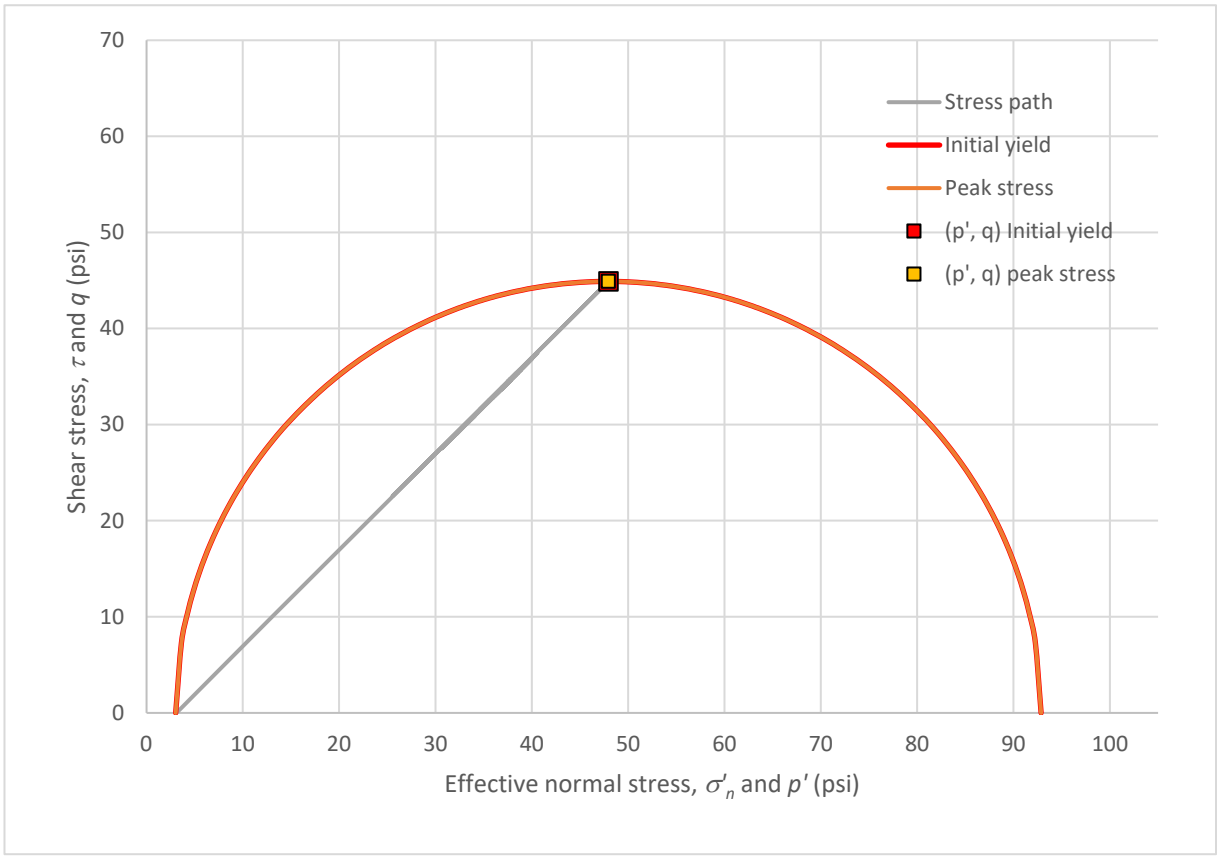

Consolidated-Drained Triaxial Shear, Lightweight Cellular Concrete

Sample ID:	**B2-56**
Height (in):	5.433
Height (mm):	138.0
Diameter (in):	2.965
Diameter (mm)	75.31
Area (in^2):	6.904
Area (mm^2):	4454
Mass (g):	284.44
Weight (lb):	0.6271
Weight (kN):	0.002789
Volume (in^3):	37.51
Volume (mm^3):	614670
Density (g/mm^3):	0.0004628
Density (kg/m^3):	462.8
Unit weight (pcf):	**28.89**
Dry unit weight (pcf);	**20.27**
Unit Weight (kN/m^3):	4.538
Wet mass + tare (g):	344.67
Dry mass + tare (g):	280.32
Tare (g):	128.87
Water content (%)	**42.49**
Saturation (%):	**15.71**
H:D ratio:	1.833
Age (days):	1065
Treatment:	D1

Strain rate (%/min):	0.2
Mean σ'_3 (psi):	3.1
Initial modulus (psi):	39325
Initial yield	
Time to failure (min):	0.9
Axial strain at failure (%):	0.172
σ'_1 (psi):	70.69
σ'_3 (psi):	3.00
σ'_1 -σ'_3 (psi):	67.69
σ'_1 / σ'_3:	23.55
p' (psi):	36.85
q (psi):	33.84
Volumetric strain (%):	0.081
Poisson's ratio:	0.263
Peak stress	
Time to failure (min):	14.5
Axial strain at failure (%):	2.904
σ'_1 (psi):	71.83
σ'_3 (psi):	3.00
σ'_1 -σ'_3 (psi):	68.82
σ'_1 / σ'_3:	23.92
p' (psi):	37.41
q (psi):	34.41
Volumetric strain (%):	2.603
Poisson's ratio:	0.052

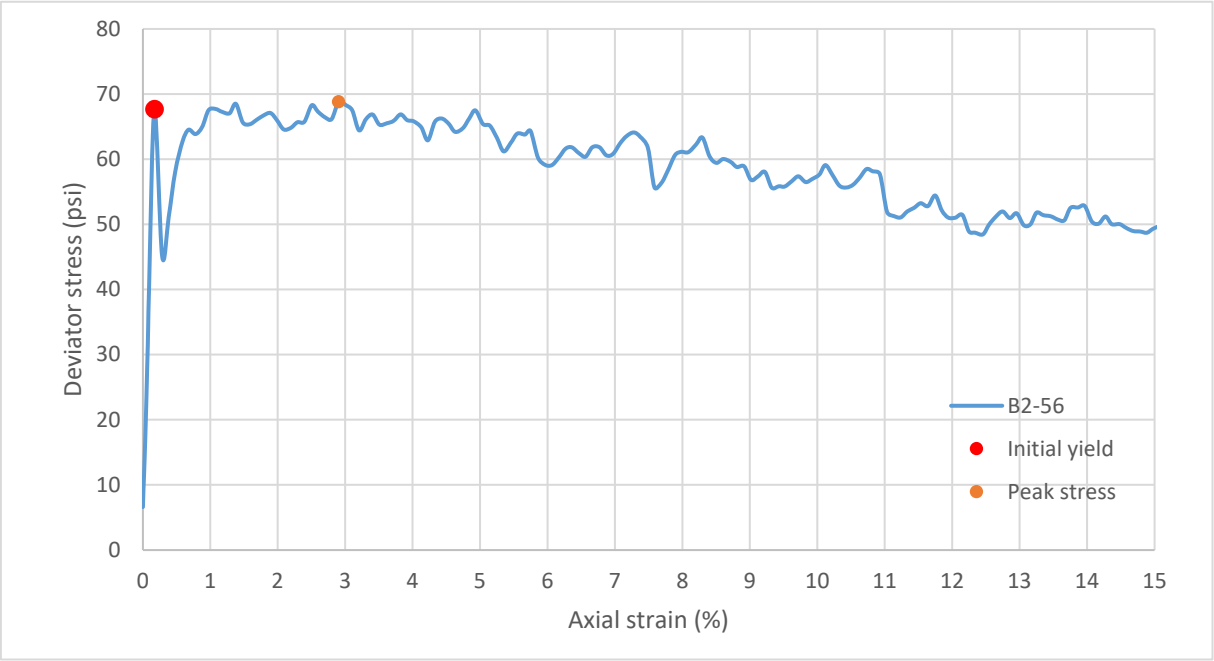

Sample ID:	B2-56

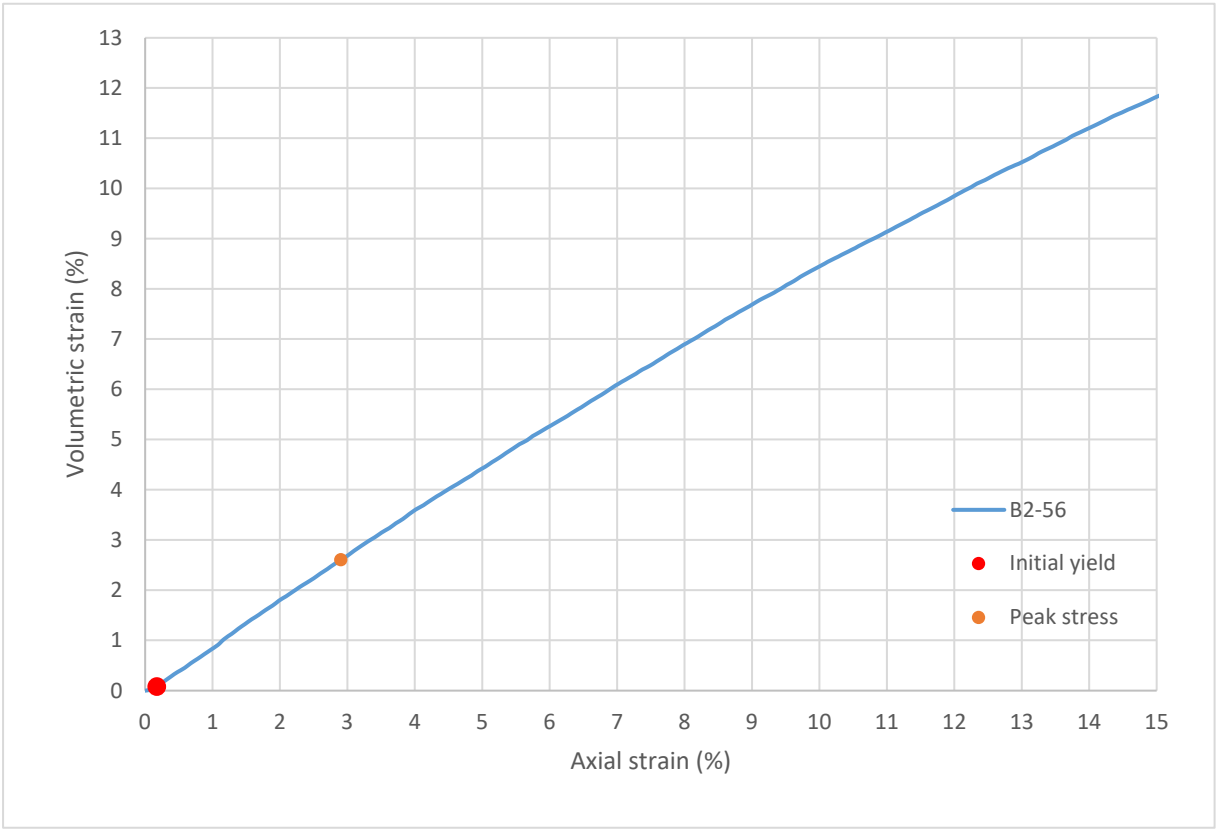

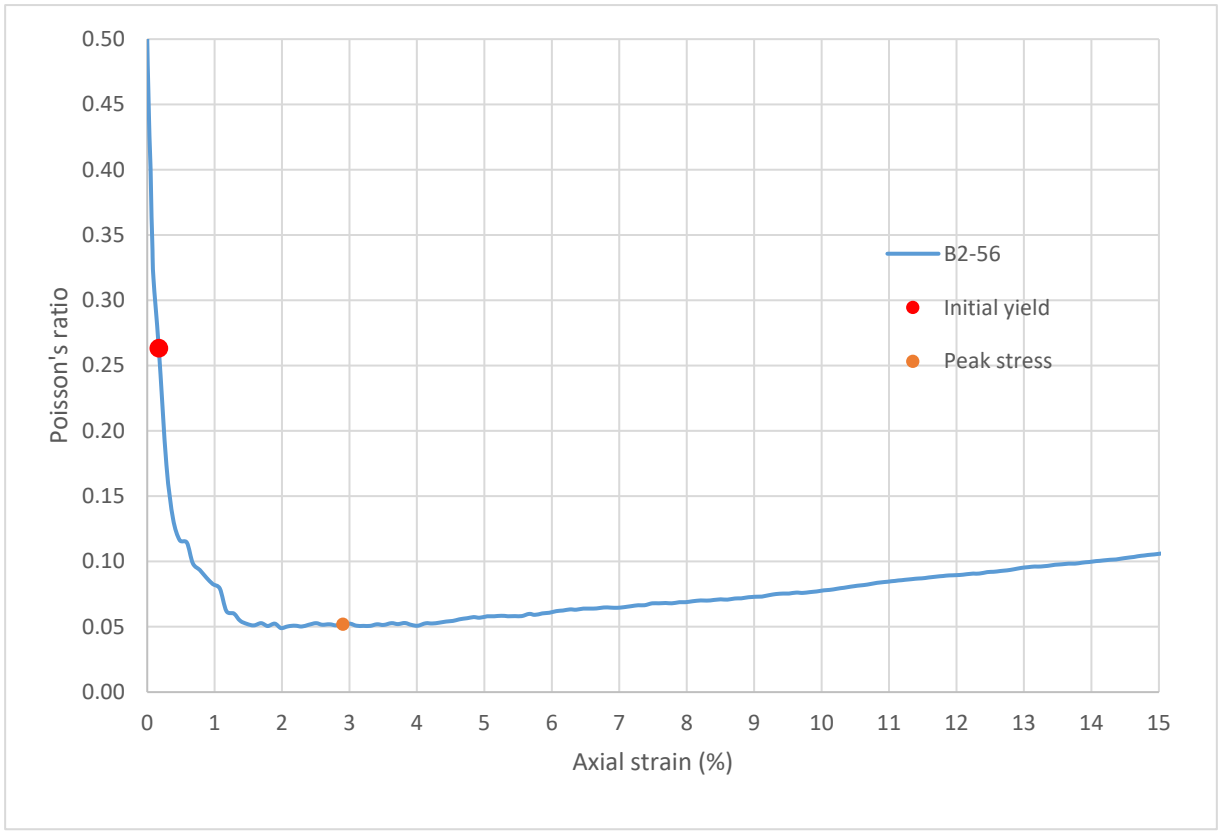

Sample ID:	B2-56

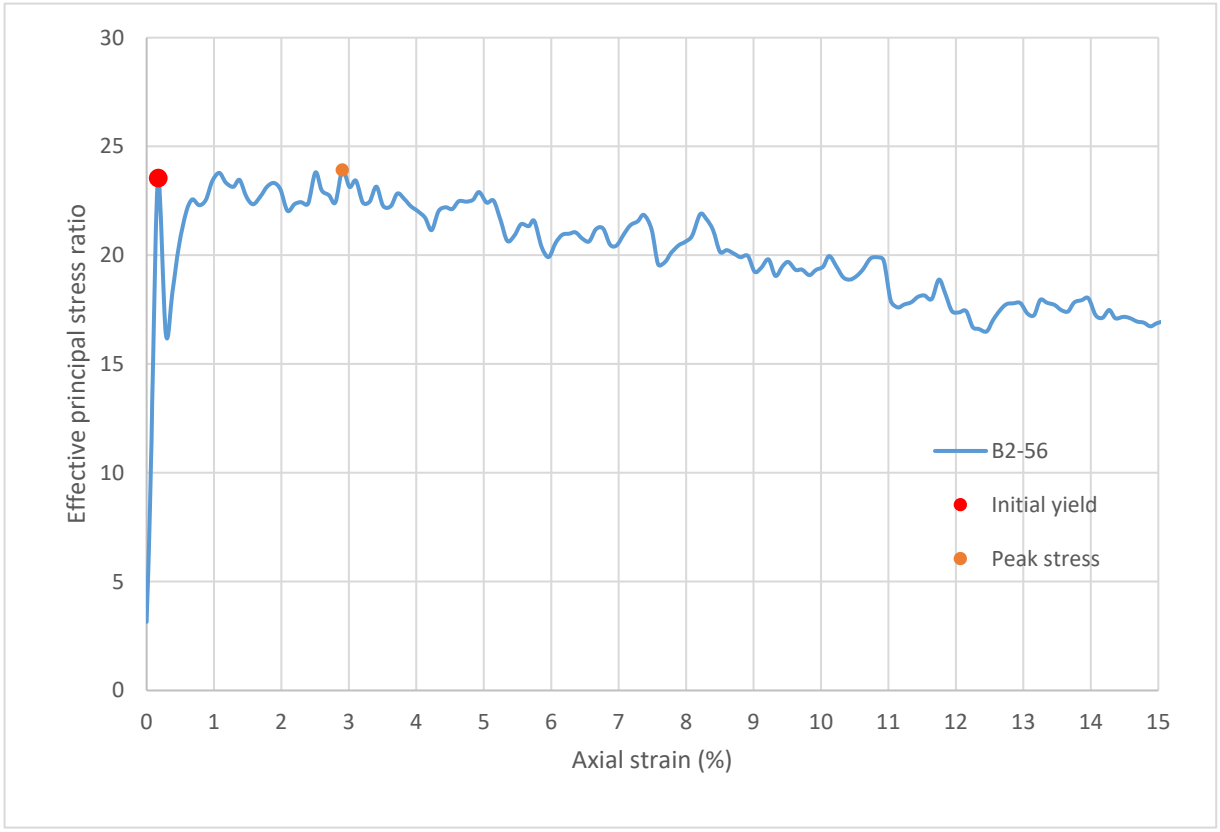

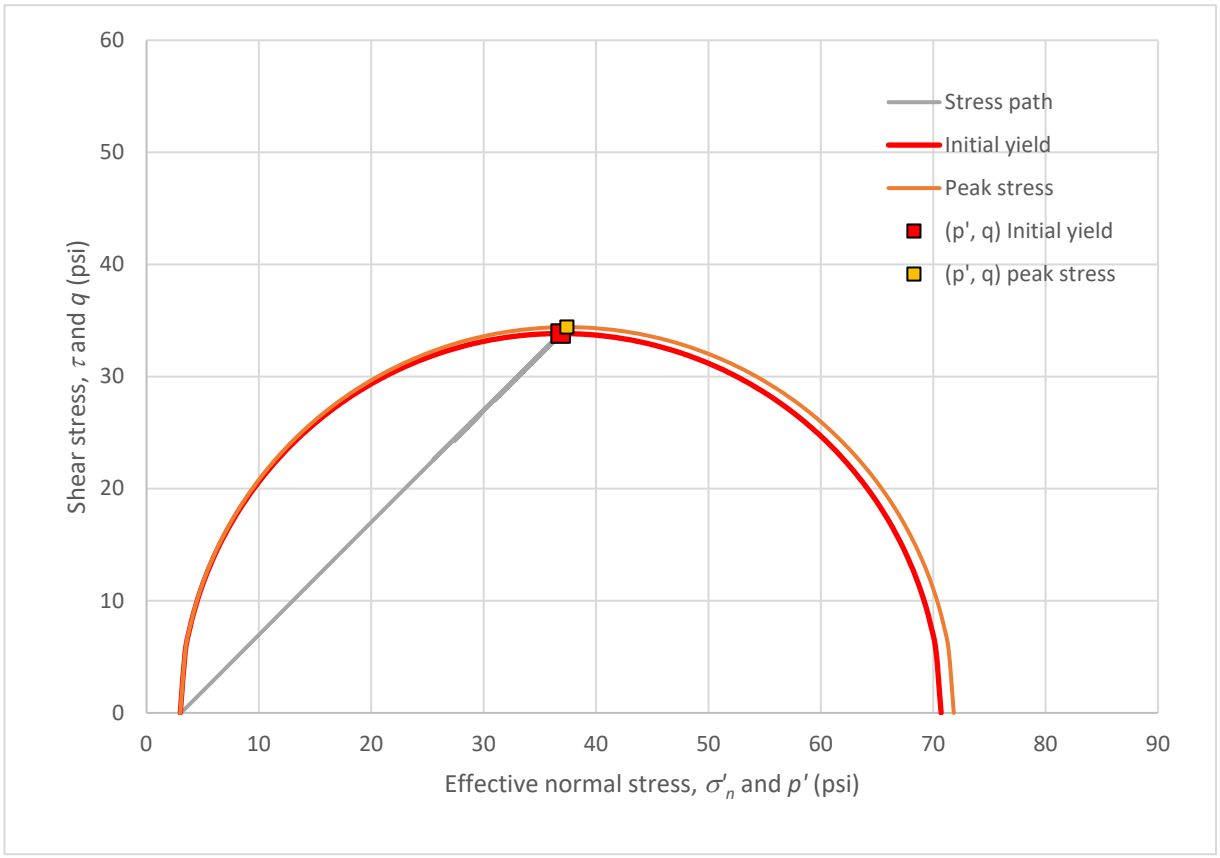

Consolidated-Drained Triaxial Shear, Lightweight Cellular Concrete

Sample ID:	**B2-57**
Height (in):	5.531
Height (mm):	140.5
Diameter (in):	2.955
Diameter (mm)	75.07
Area (in^2):	6.860
Area (mm^2):	4426
Mass (g):	285.34
Weight (lb):	0.6291
Weight (kN):	0.002798
Volume (in^3):	37.94
Volume (mm^3):	621785
Density (g/mm^3):	0.0004589
Density (kg/m^3):	458.9
Unit weight (pcf):	**28.65**
Dry unit weight (pcf);	**19.80**
Unit Weight (kN/m^3):	4.500
Wet mass + tare (g):	387.02
Dry mass + tare (g):	307.13
Tare (g):	128.28
Water content (%)	**44.67**
Saturation (%):	**16.08**
H:D ratio:	1.871
Age (days):	1070
Treatment:	W1

Strain rate (%/min):	0.2
Mean σ'_3 (psi):	3.0
Initial modulus (psi):	26842
Initial yield	
Time to failure (min):	1.3
Axial strain at failure (%):	0.268
σ'_1 (psi):	74.75
σ'_3 (psi):	2.94
σ'_1 -σ'_3 (psi):	71.81
σ'_1 / σ'_3:	25.39
p' (psi):	38.85
q (psi):	35.90
Volumetric strain (%):	0.141
Poisson's ratio:	0.236
Peak stress	
Time to failure (min):	18.9
Axial strain at failure (%):	3.779
σ'_1 (psi):	115.27
σ'_3 (psi):	3.08
σ'_1 -σ'_3 (psi):	112.19
σ'_1 / σ'_3:	37.46
p' (psi):	59.17
q (psi):	56.09
Volumetric strain (%):	3.513
Poisson's ratio:	0.035

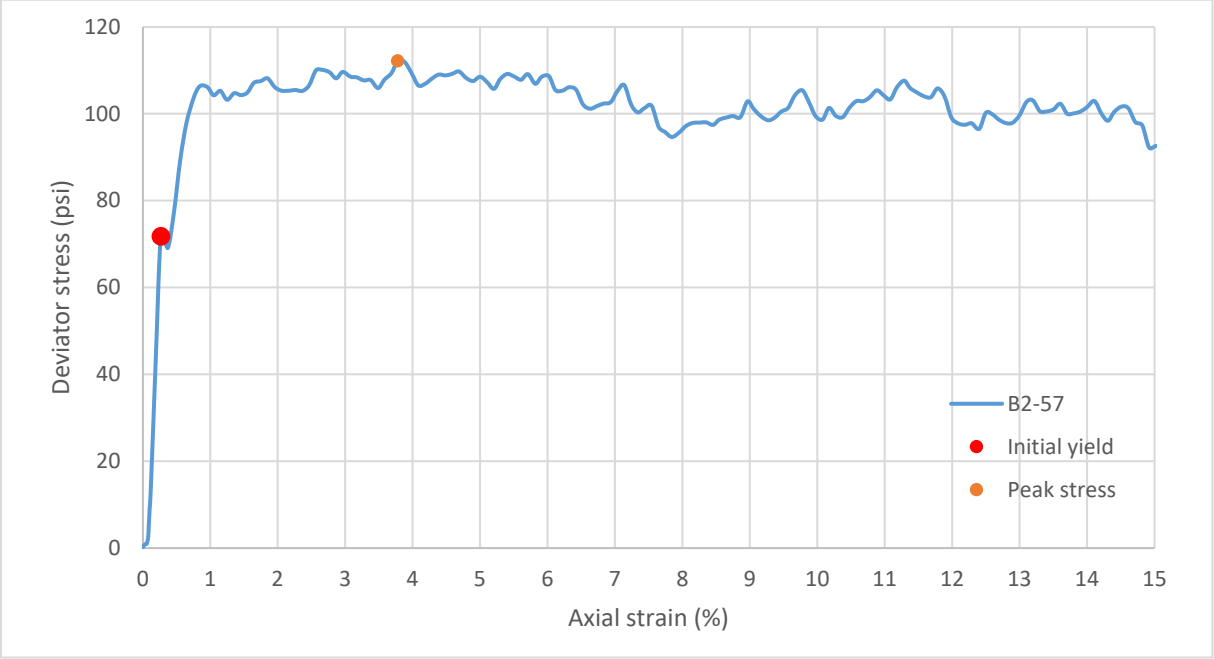

Sample ID:	B2-57

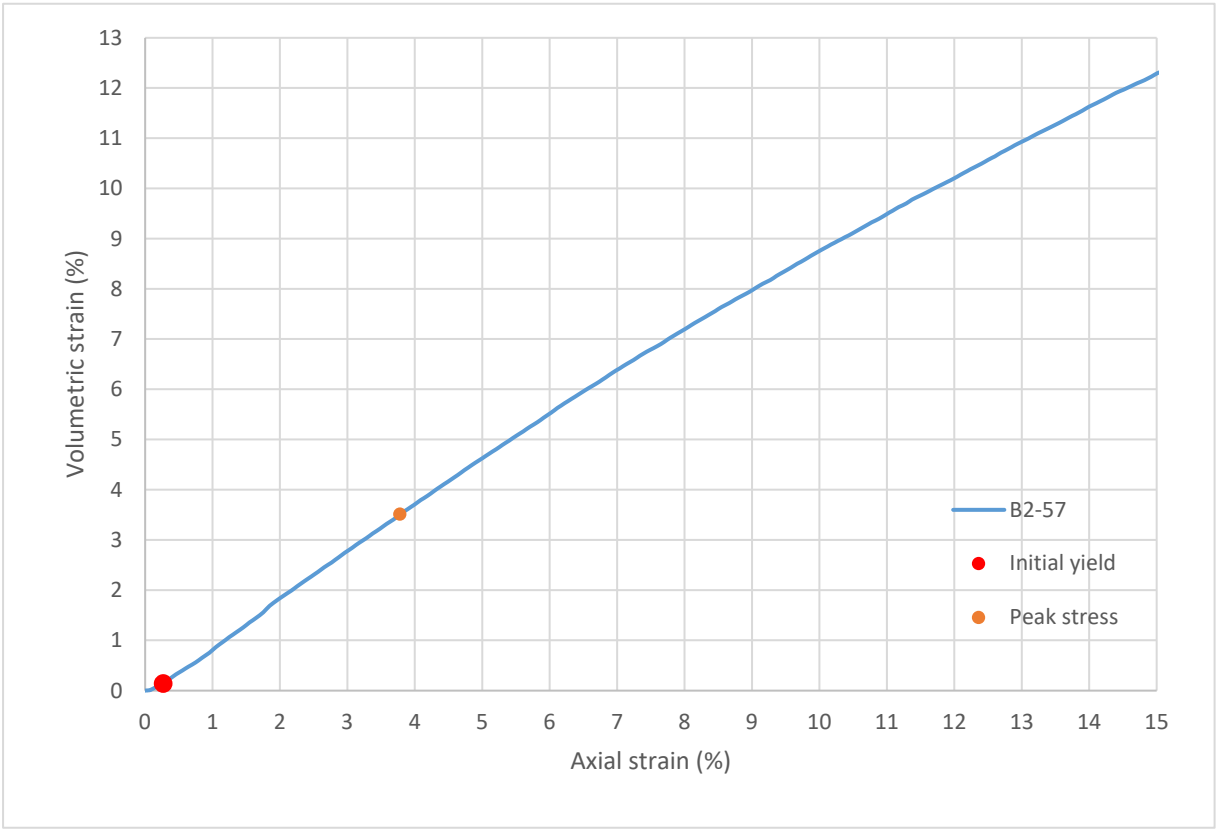

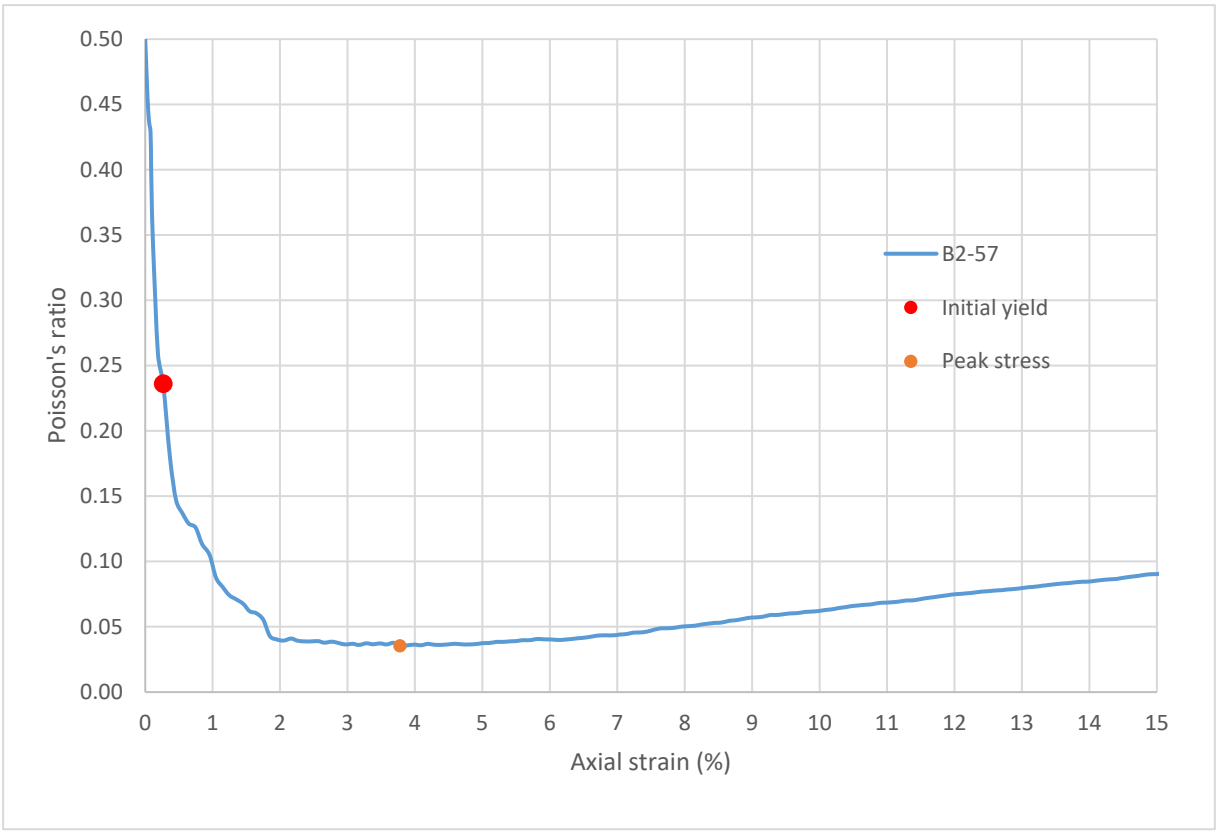

Sample ID:	B2-57

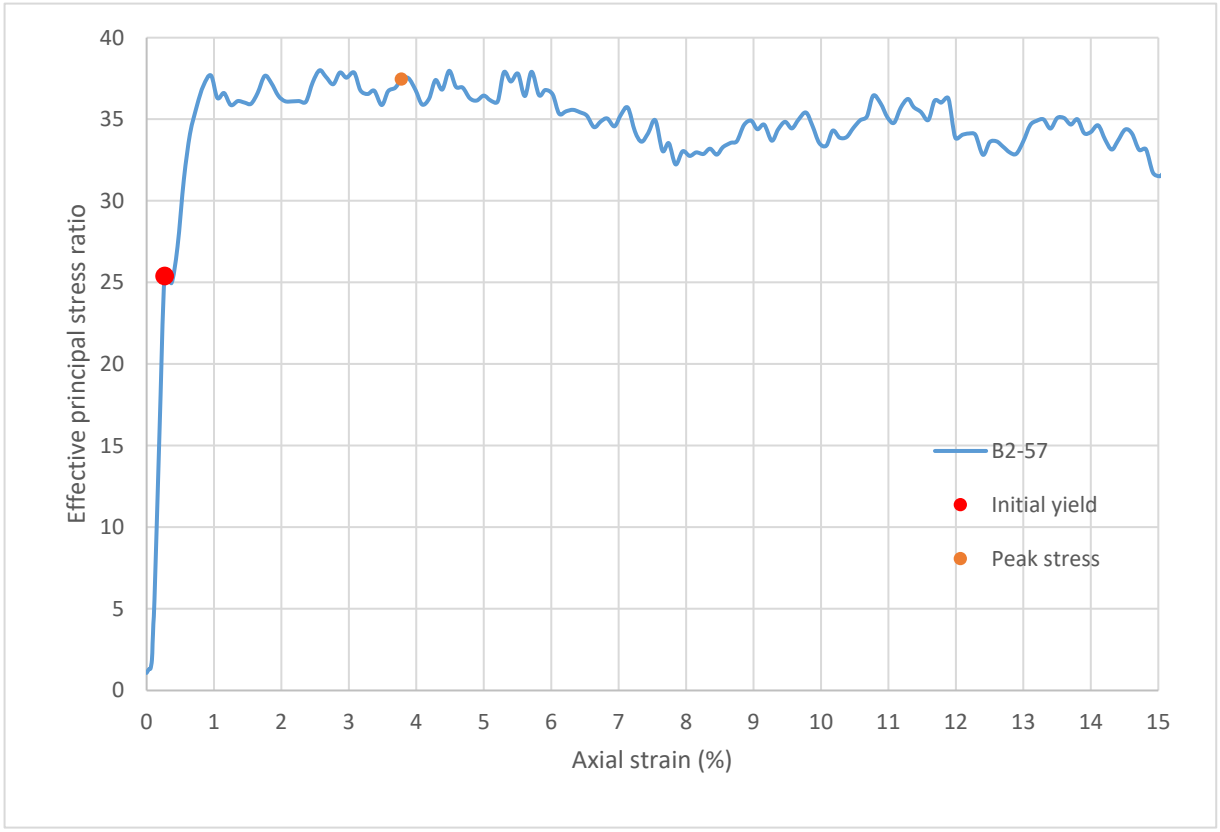

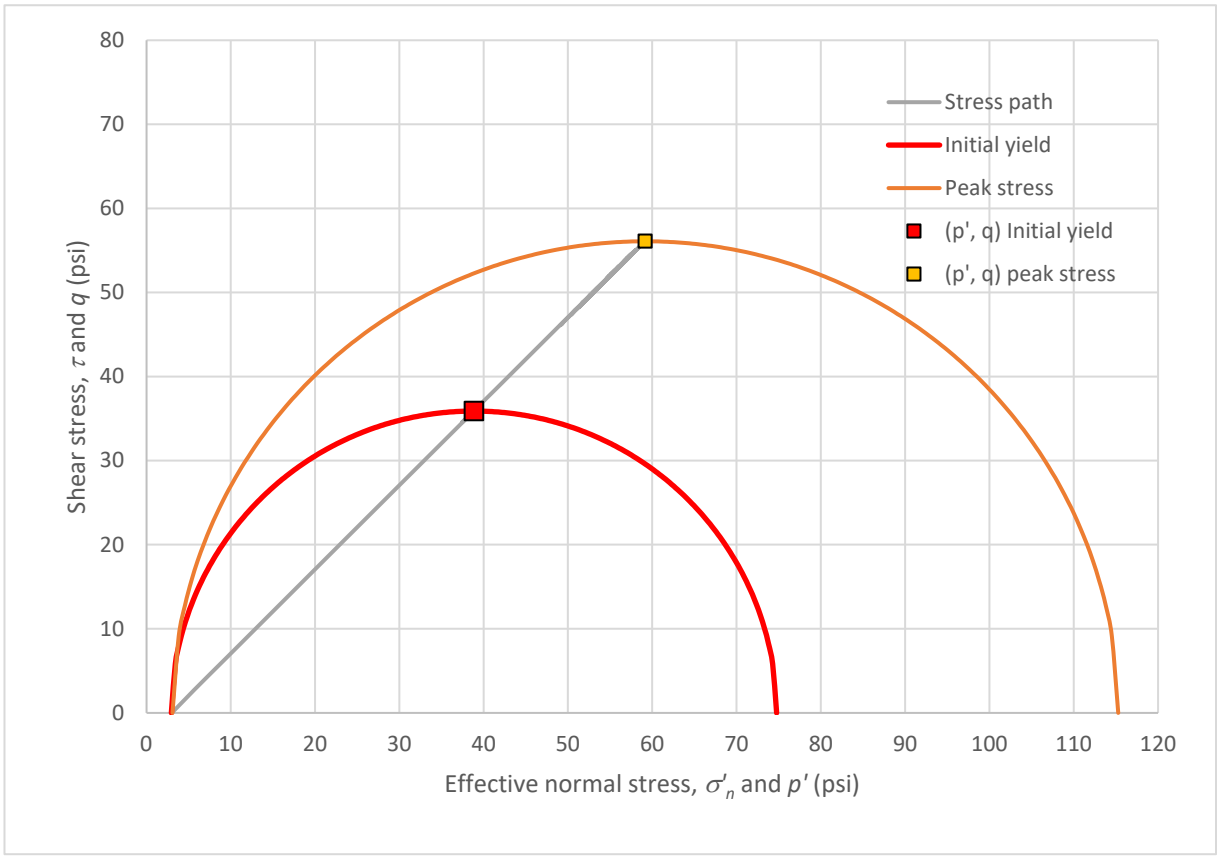

Consolidated-Drained Triaxial Shear, Lightweight Cellular Concrete

Sample ID:	**B2-58**
Height (in):	5.522
Height (mm):	140.3
Diameter (in):	2.959
Diameter (mm)	75.16
Area (in^2):	6.876
Area (mm^2):	4436
Mass (g):	283.26
Weight (lb):	0.6245
Weight (kN):	0.002778
Volume (in^3):	37.97
Volume (mm^3):	622184
Density (g/mm^3):	0.0004553
Density (kg/m^3):	455.3
Unit weight (pcf):	**28.42**
Dry unit weight (pcf);	**19.70**
Unit Weight (kN/m^3):	4.465
Wet mass + tare (g):	384.40
Dry mass + tare (g):	305.80
Tare (g):	128.28
Water content (%)	**44.28**
Saturation (%):	**15.84**
H:D ratio:	1.866
Age (days):	1070
Treatment:	W1

Strain rate (%/min):	0.2
Mean σ'_3 (psi):	3.0
Initial modulus (psi):	40834
Initial yield	
Time to failure (min):	0.8
Axial strain at failure (%):	0.163
σ'_1 (psi):	69.66
σ'_3 (psi):	2.93
σ'_1 -σ'_3 (psi):	66.73
σ'_1 / σ'_3:	23.77
p' (psi):	36.30
q (psi):	33.37
Volumetric strain (%):	0.090
Poisson's ratio:	0.225
Peak stress	
Time to failure (min):	22.9
Axial strain at failure (%):	4.582
σ'_1 (psi):	110.44
σ'_3 (psi):	3.08
σ'_1 -σ'_3 (psi):	107.36
σ'_1 / σ'_3:	35.88
p' (psi):	56.76
q (psi):	53.68
Volumetric strain (%):	4.315
Poisson's ratio:	0.029

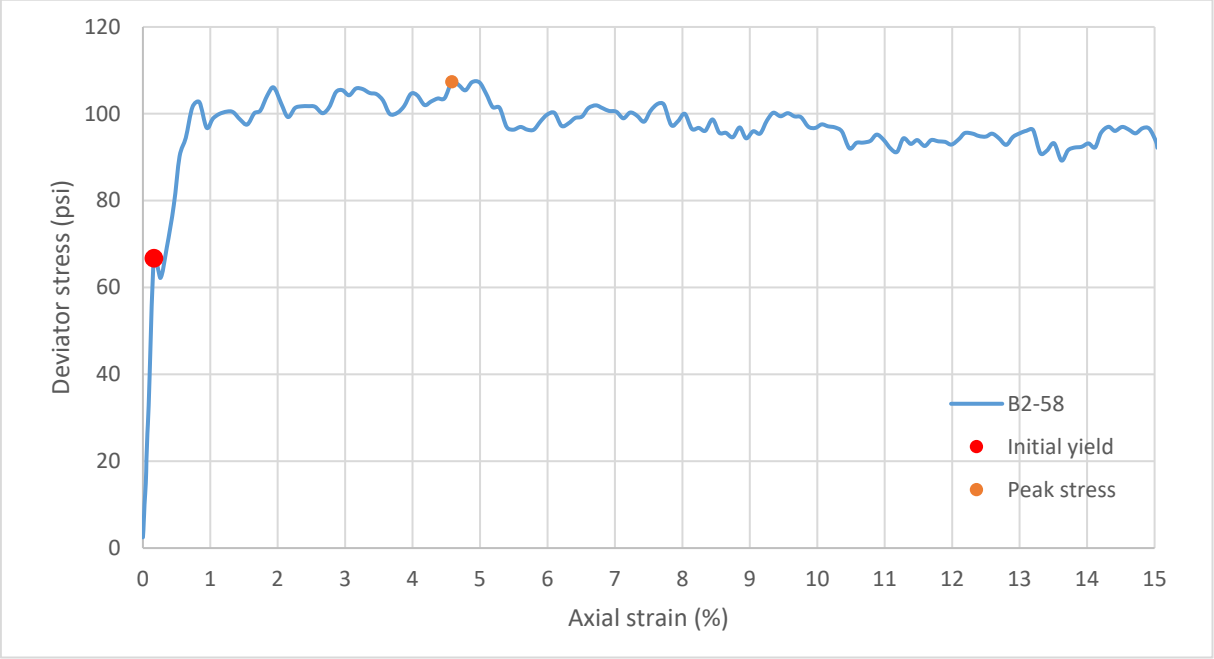

Sample ID:	B2-58

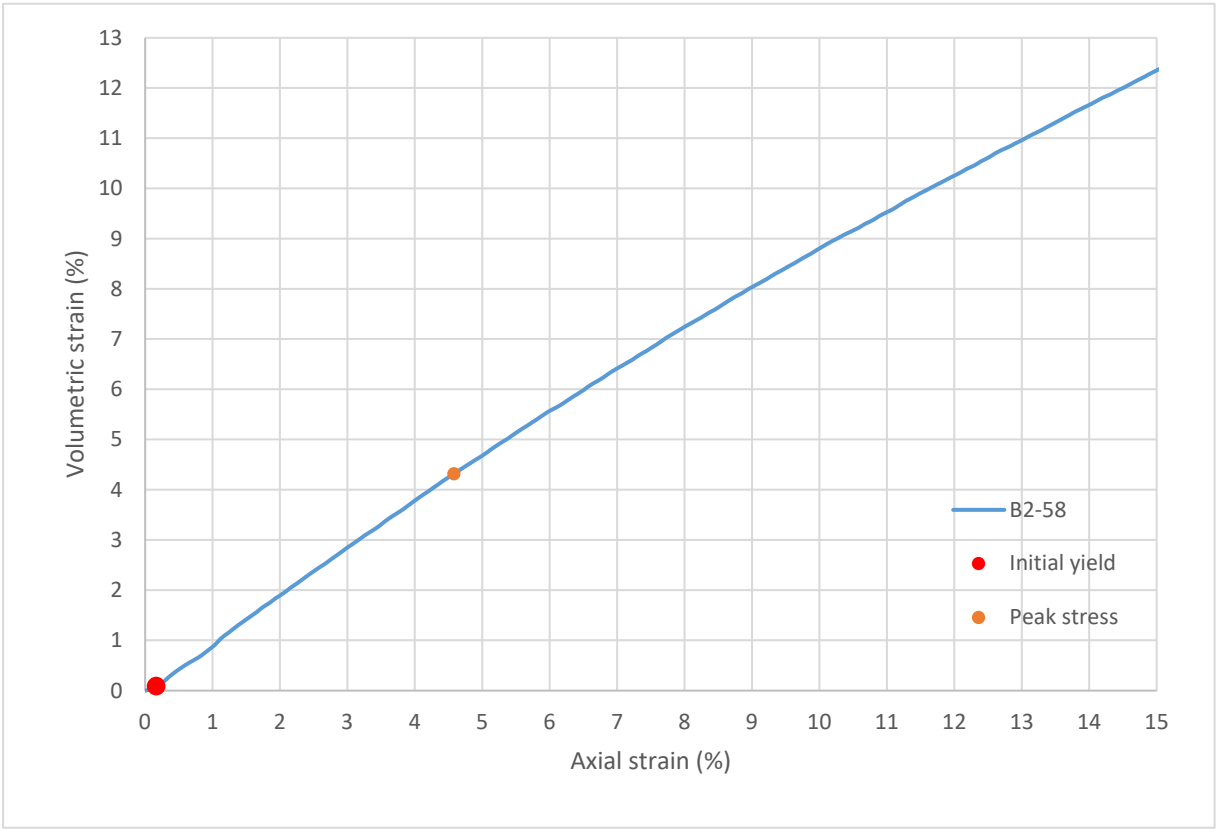

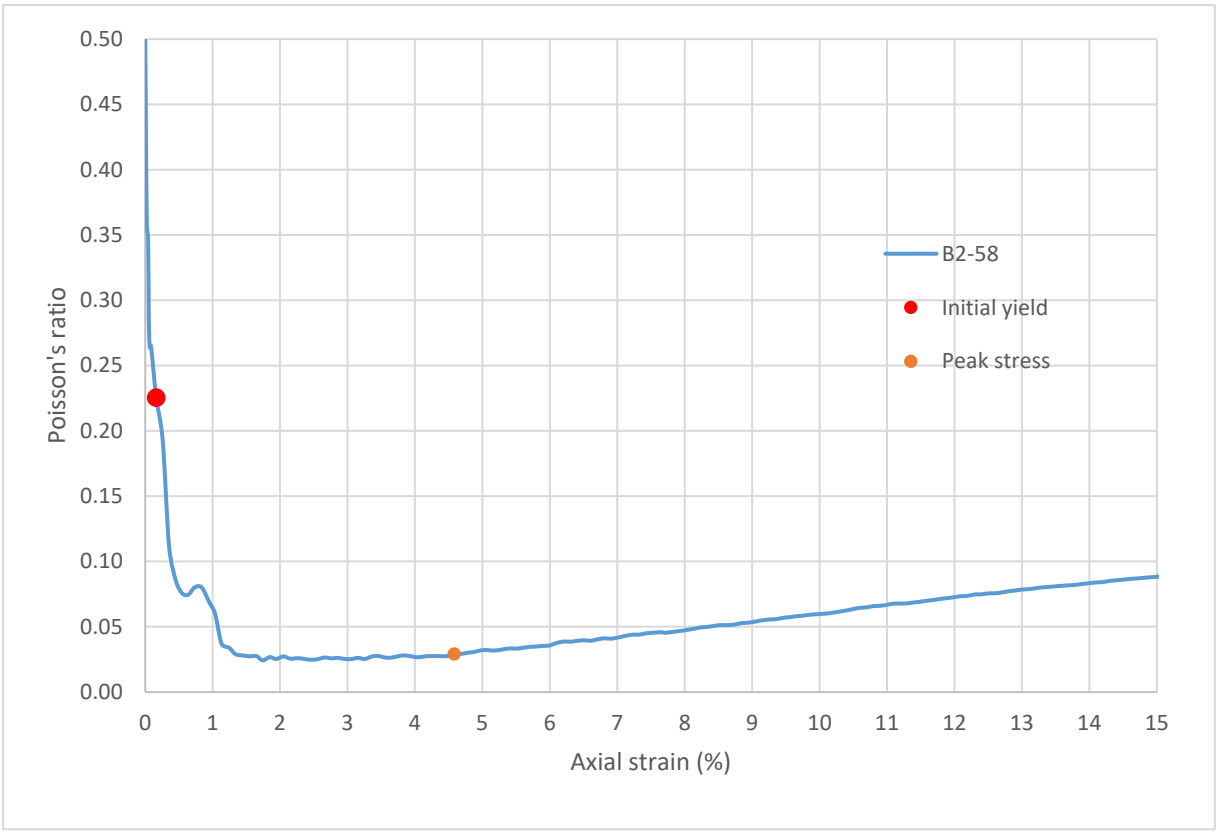

Sample ID:	B2-58

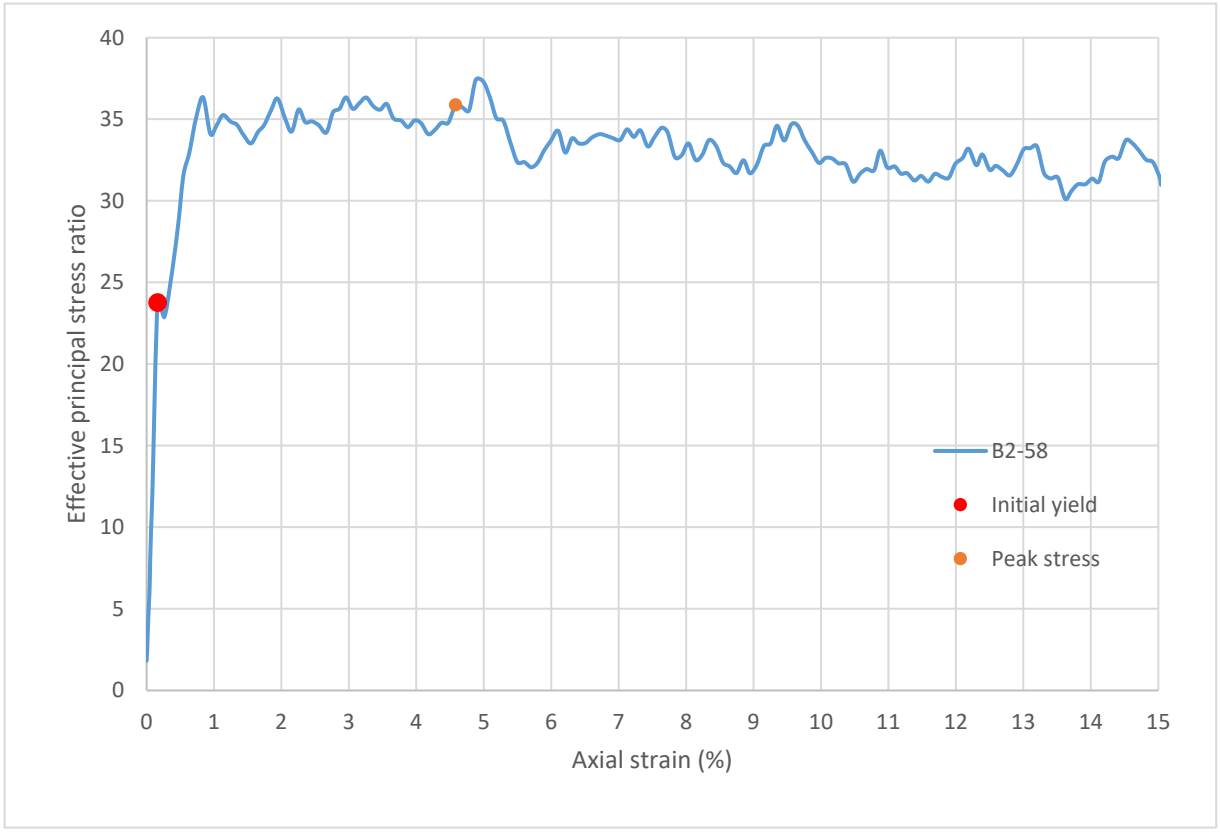

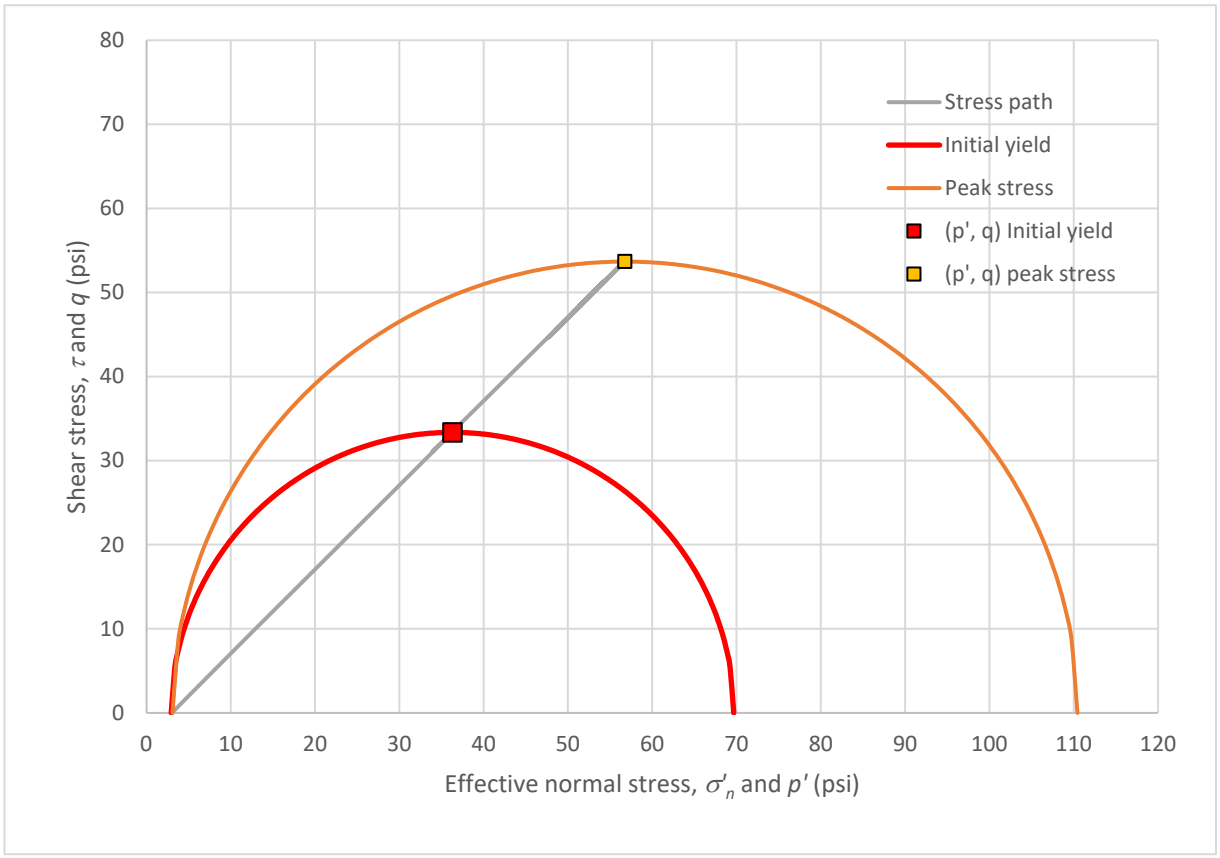

Consolidated-Drained Triaxial Shear, Lightweight Cellular Concrete

Sample ID:	**B2-59**
Height (in):	5.532
Height (mm):	140.5
Diameter (in):	2.964
Diameter (mm)	75.29
Area (in^2):	6.900
Area (mm^2):	4452
Mass (g):	288.05
Weight (lb):	0.6350
Weight (kN):	0.002825
Volume (in^3):	38.17
Volume (mm^3):	625512
Density (g/mm^3):	0.0004605
Density (kg/m^3):	460.5
Unit weight (pcf):	**28.75**
Dry unit weight (pcf);	**19.32**
Unit Weight (kN/m^3):	4.516
Wet mass + tare (g):	392.51
Dry mass + tare (g):	305.78
Tare (g):	128.10
Water content (%)	**48.81**
Saturation (%):	**17.08**
H:D ratio:	1.866
Age (days):	1073
Treatment:	W1

Strain rate (%/min):	0.2
Mean σ'_3 (psi):	3.1
Initial modulus (psi):	22398
Initial yield	
Time to failure (min):	2.1
Axial strain at failure (%):	0.420
σ'_1 (psi):	96.99
σ'_3 (psi):	2.98
σ'_1 -σ'_3 (psi):	94.01
σ'_1 / σ'_3:	32.55
p' (psi):	49.98
q (psi):	47.00
Volumetric strain (%):	0.189
Poisson's ratio:	0.274
Peak stress	
Time to failure (min):	14.1
Axial strain at failure (%):	2.829
σ'_1 (psi):	112.94
σ'_3 (psi):	3.16
σ'_1 -σ'_3 (psi):	109.78
σ'_1 / σ'_3:	35.74
p' (psi):	58.05
q (psi):	54.89
Volumetric strain (%):	2.530
Poisson's ratio:	0.053

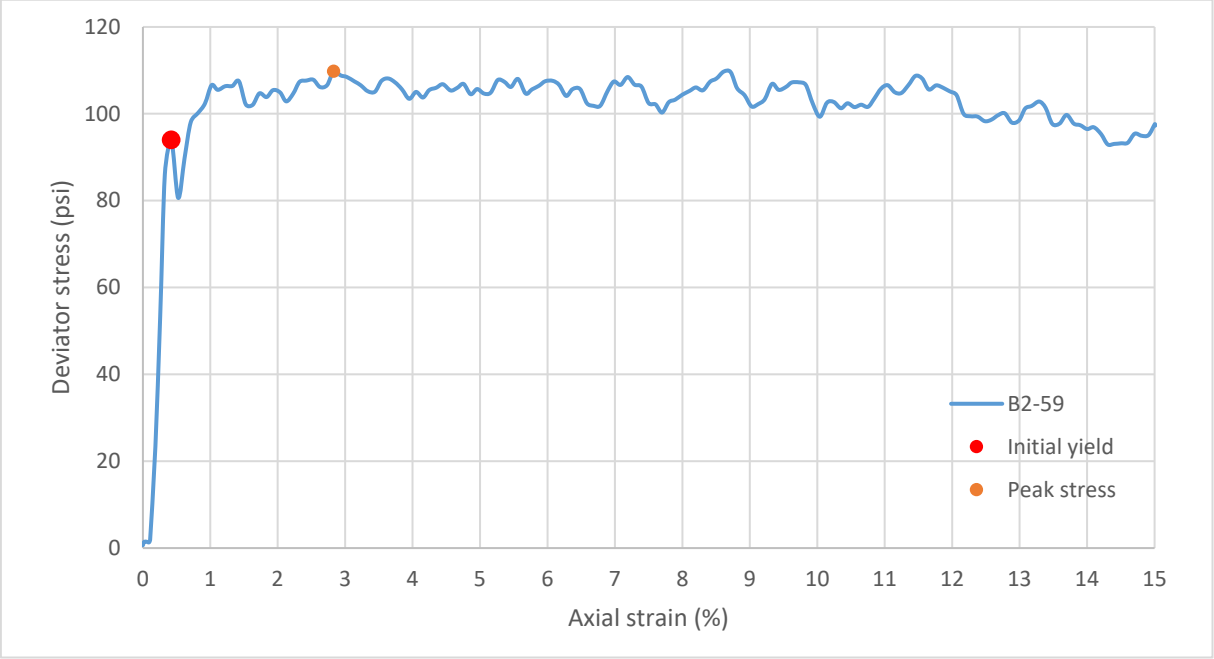

Sample ID:	B2-59

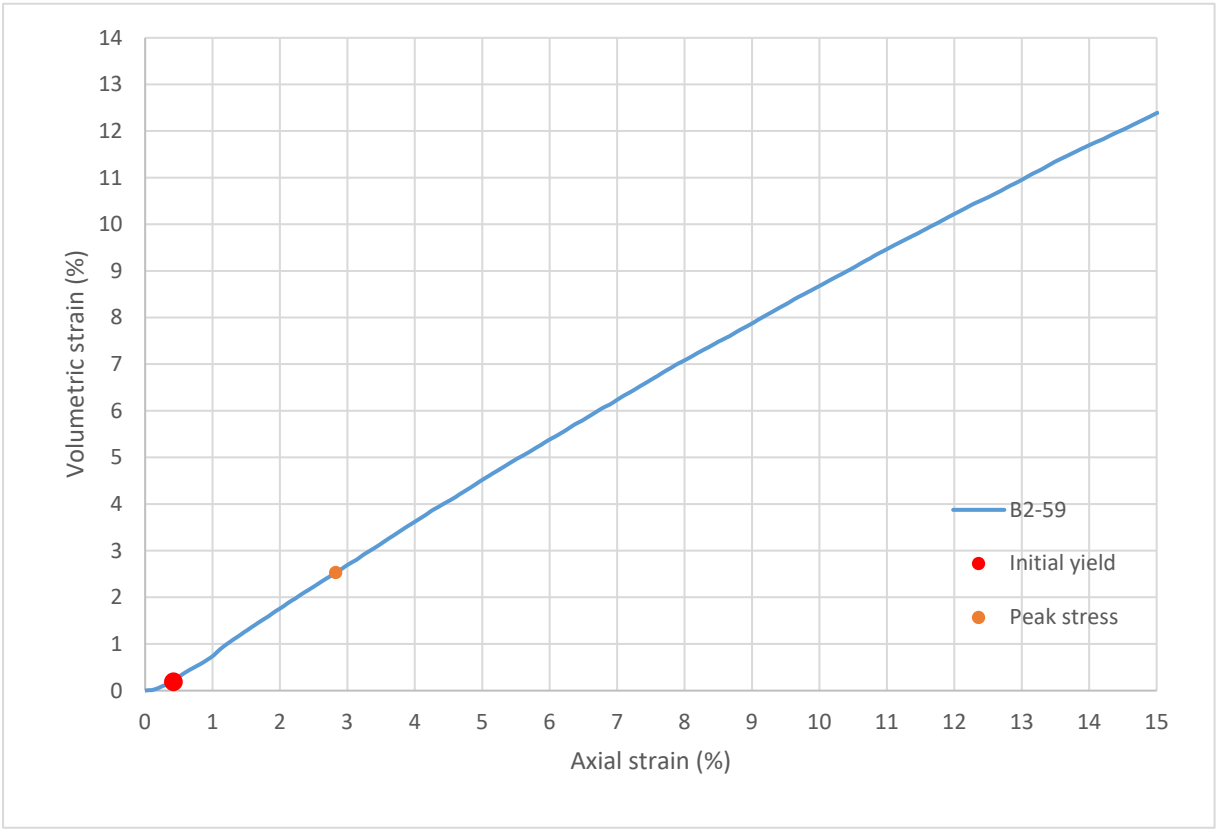

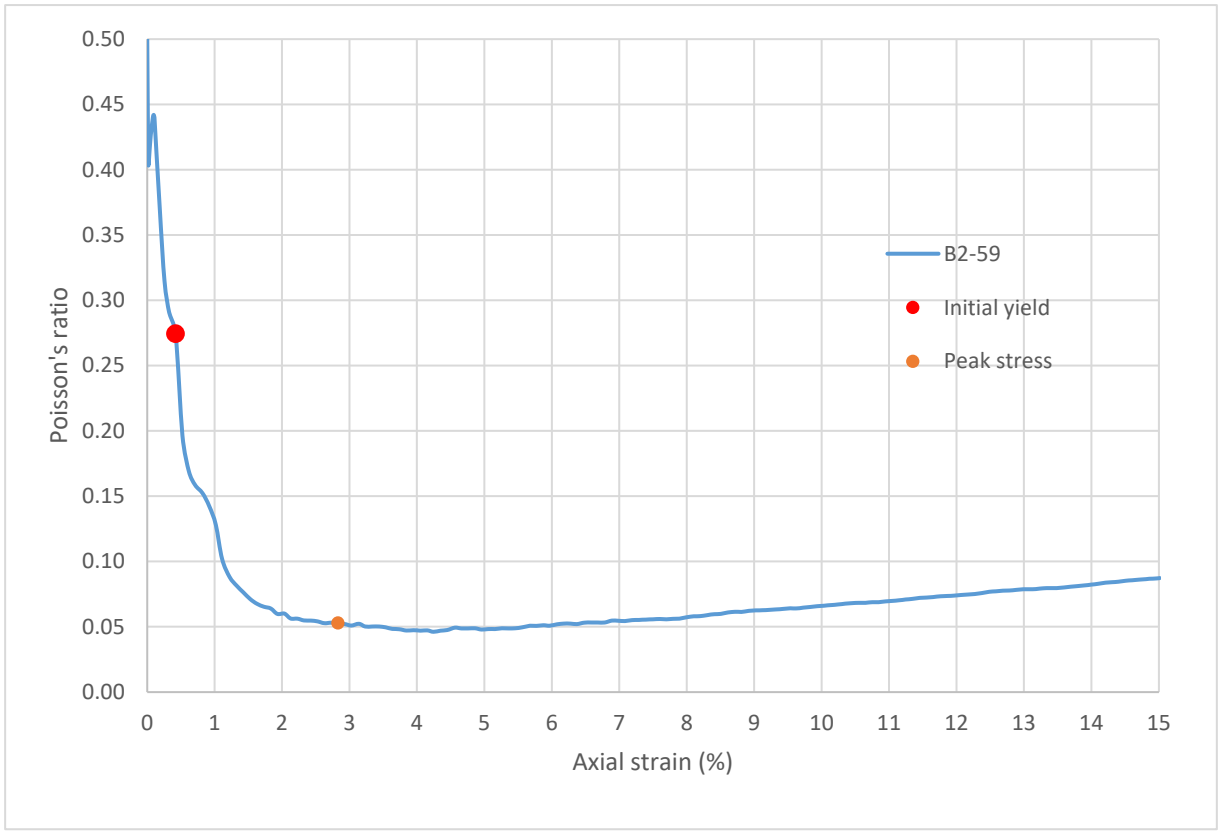

Sample ID:	B2-59

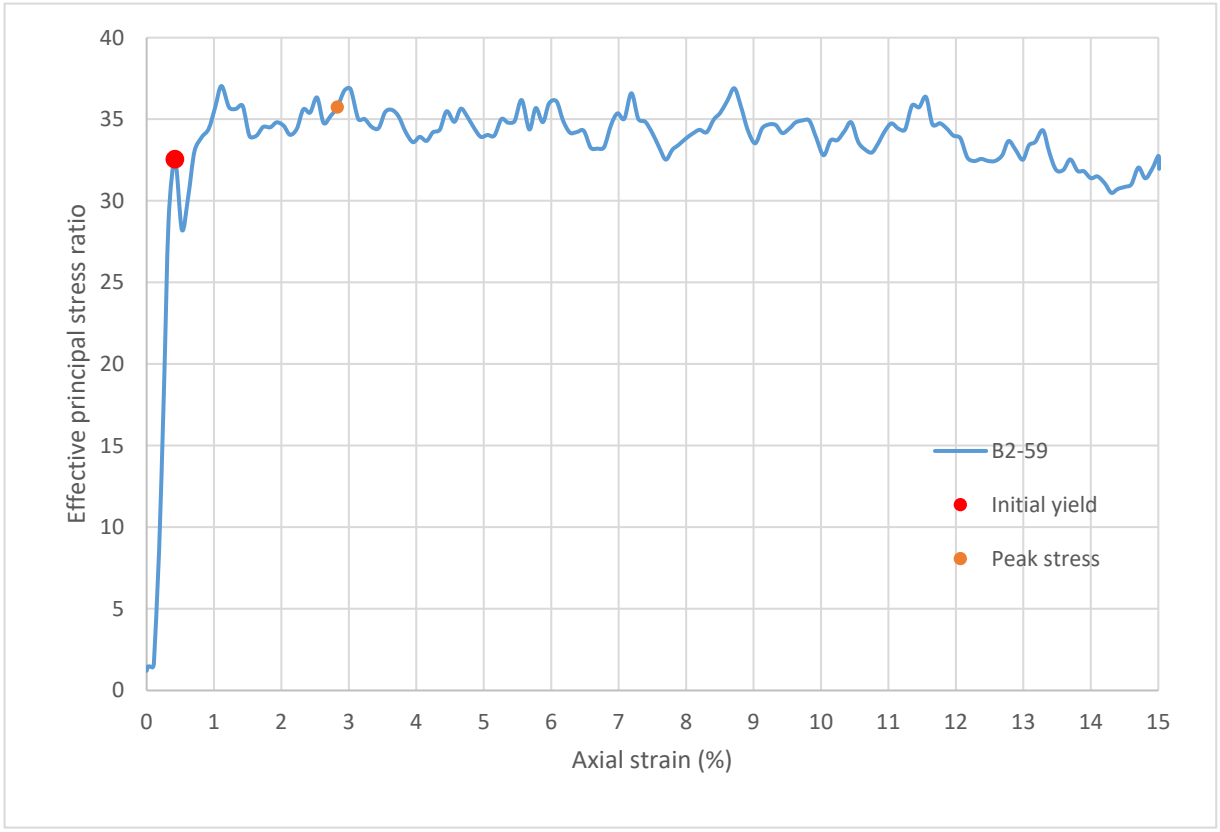

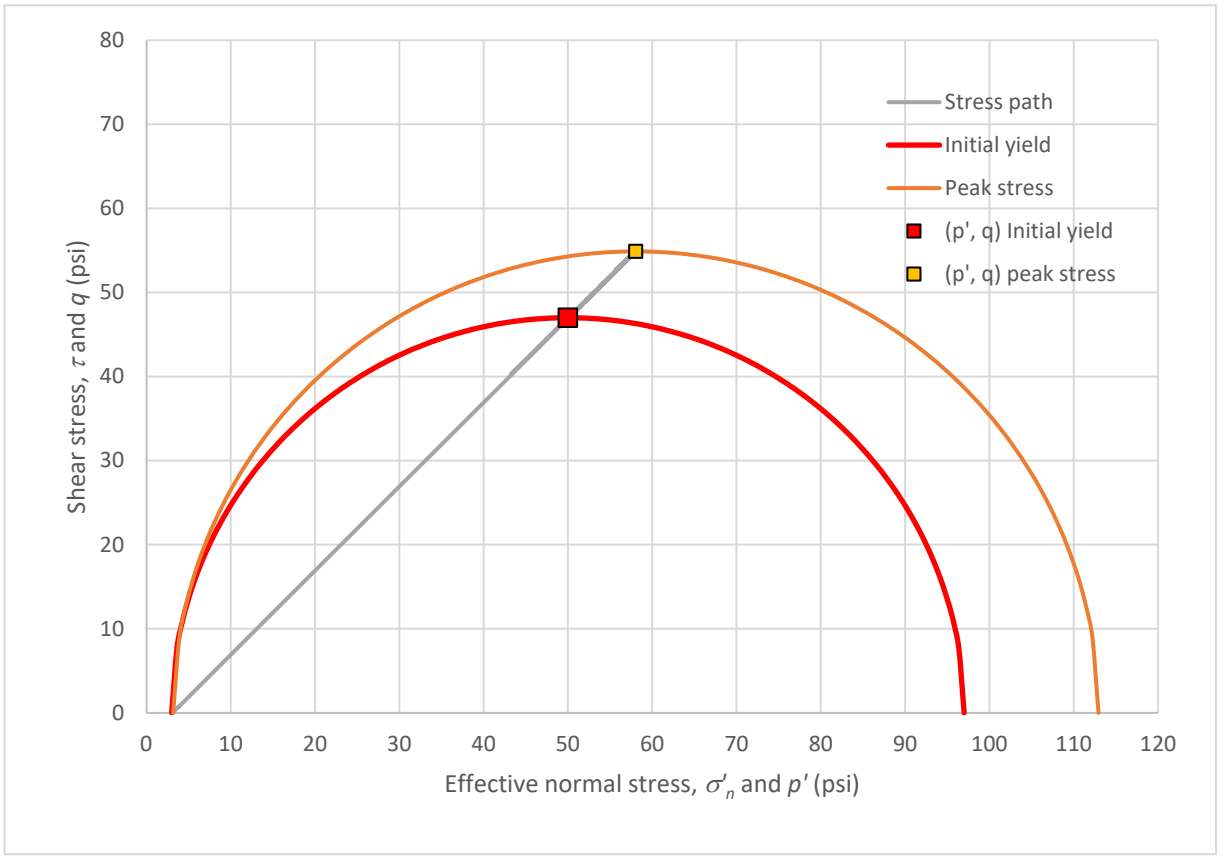

Consolidated-Drained Triaxial Shear, Lightweight Cellular Concrete

Sample ID:	**B2-60**
Height (in):	5.499
Height (mm):	139.7
Diameter (in):	2.963
Diameter (mm)	75.26
Area (in^2):	6.895
Area (mm^2):	4448
Mass (g):	297.98
Weight (lb):	0.6569
Weight (kN):	0.002922
Volume (in^3):	37.92
Volume (mm^3):	621344
Density (g/mm^3):	0.0004796
Density (kg/m^3):	479.6
Unit weight (pcf):	**29.94**
Dry unit weight (pcf);	**19.74**
Unit Weight (kN/m^3):	4.703
Wet mass + tare (g):	404.55
Dry mass + tare (g):	309.87
Tare (g):	126.71
Water content (%)	**51.69**
Saturation (%):	**18.54**
H:D ratio:	1.856
Age (days):	1073
Treatment:	W1

Strain rate (%/min):	0.2
Mean σ'_3 (psi):	3.0
Initial modulus (psi):	41398
Initial yield	
Time to failure (min):	0.8
Axial strain at failure (%):	0.164
σ'_1 (psi):	70.82
σ'_3 (psi):	2.94
σ'_1 -σ'_3 (psi):	67.88
σ'_1 / σ'_3:	24.10
p' (psi):	36.88
q (psi):	33.94
Volumetric strain (%):	0.086
Poisson's ratio:	0.237
Peak stress	
Time to failure (min):	26.5
Axial strain at failure (%):	5.308
σ'_1 (psi):	87.85
σ'_3 (psi):	3.04
σ'_1 -σ'_3 (psi):	84.81
σ'_1 / σ'_3:	28.90
p' (psi):	45.45
q (psi):	42.41
Volumetric strain (%):	4.750
Poisson's ratio:	0.053

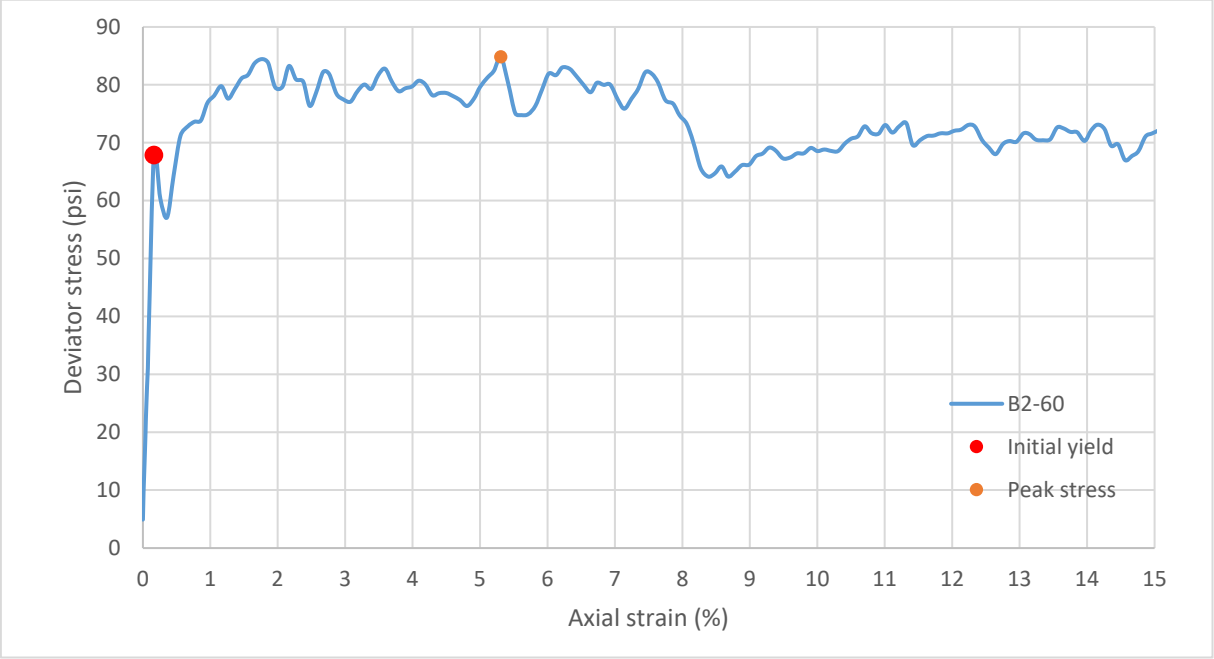

Sample ID:	B2-60

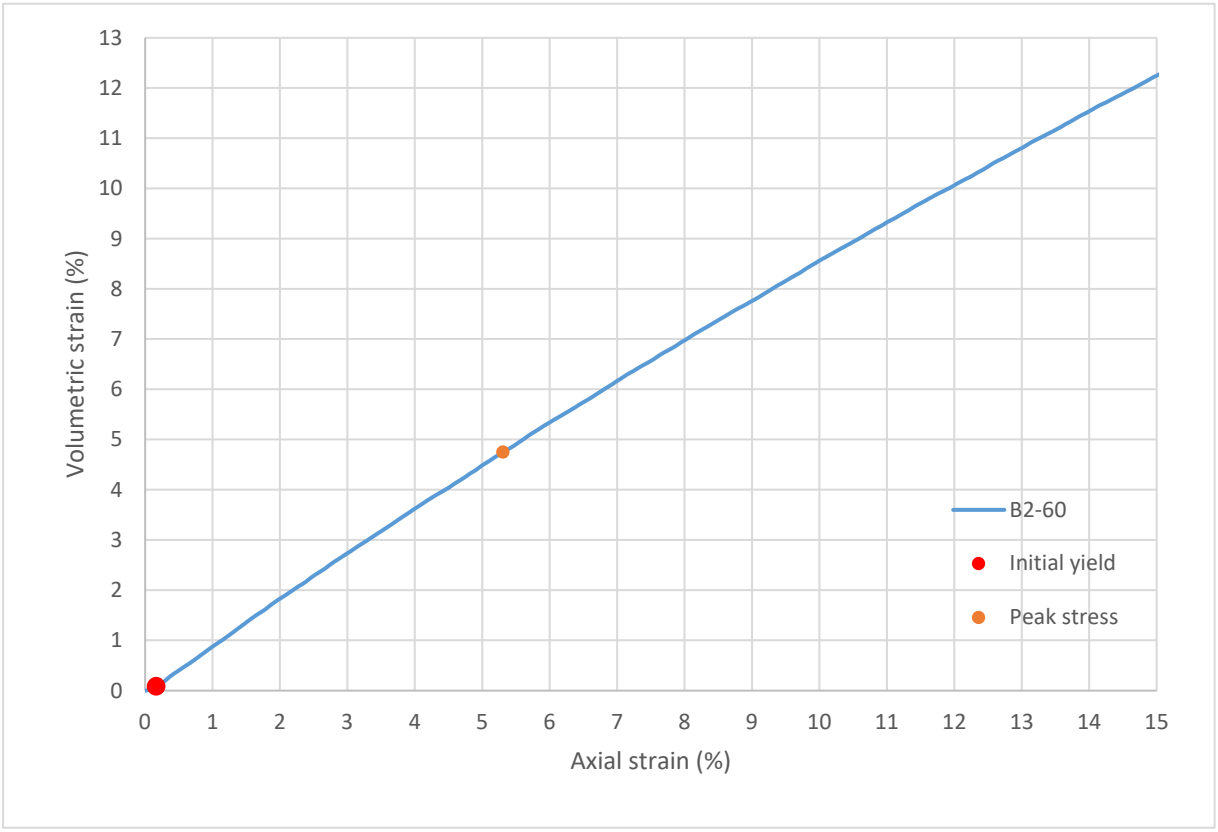

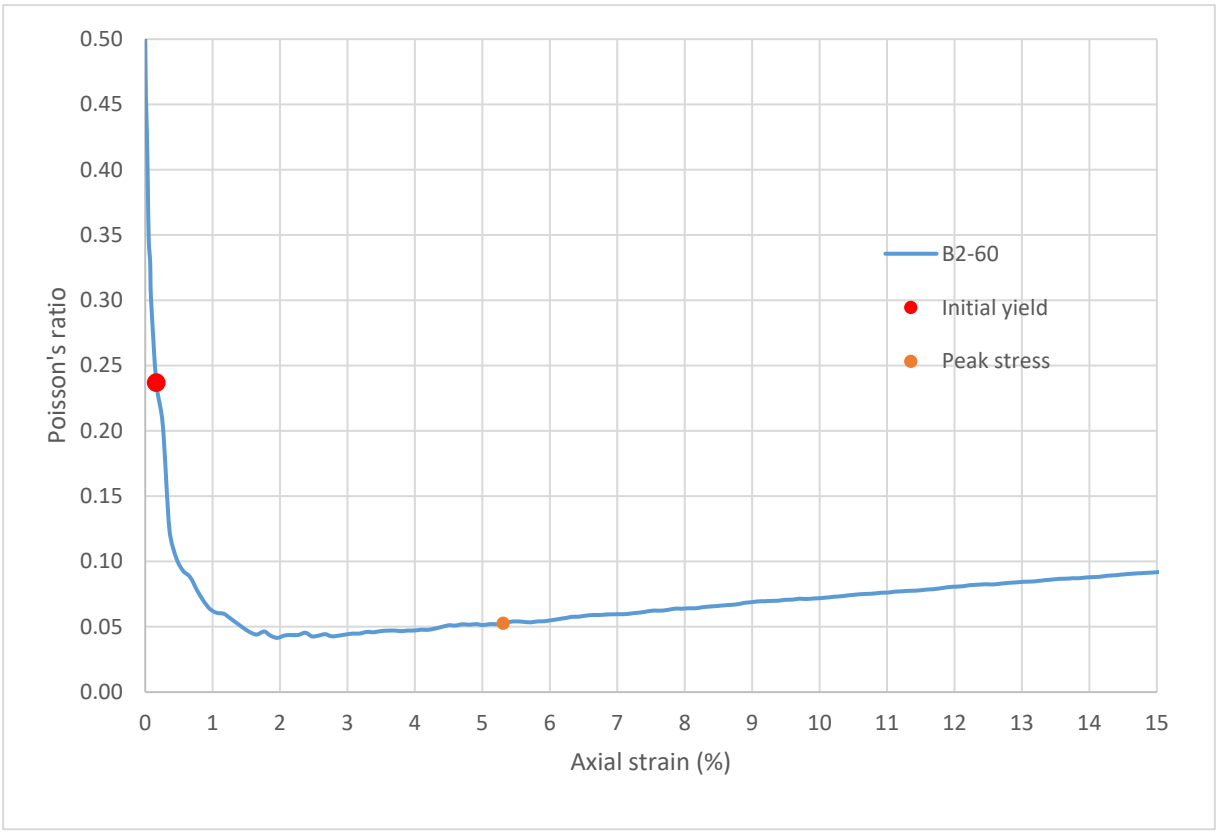

Sample ID:	B2-60

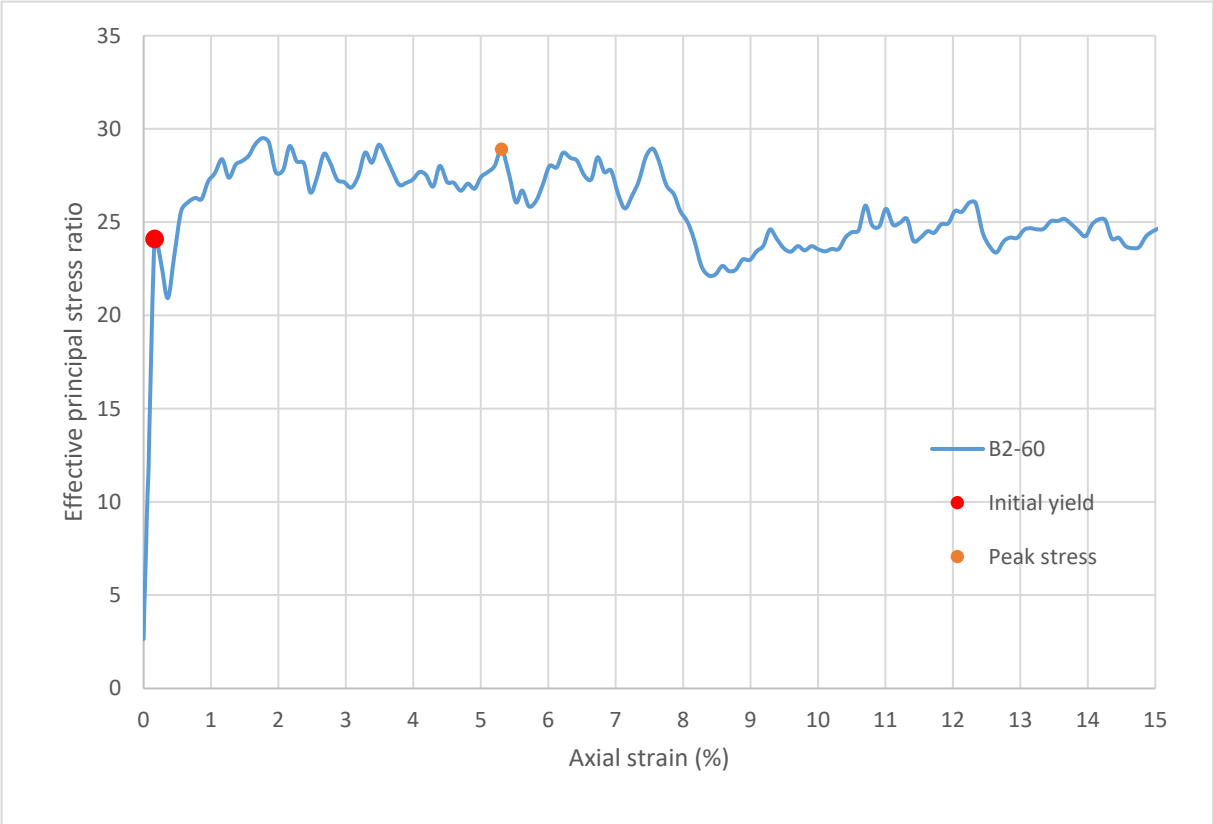

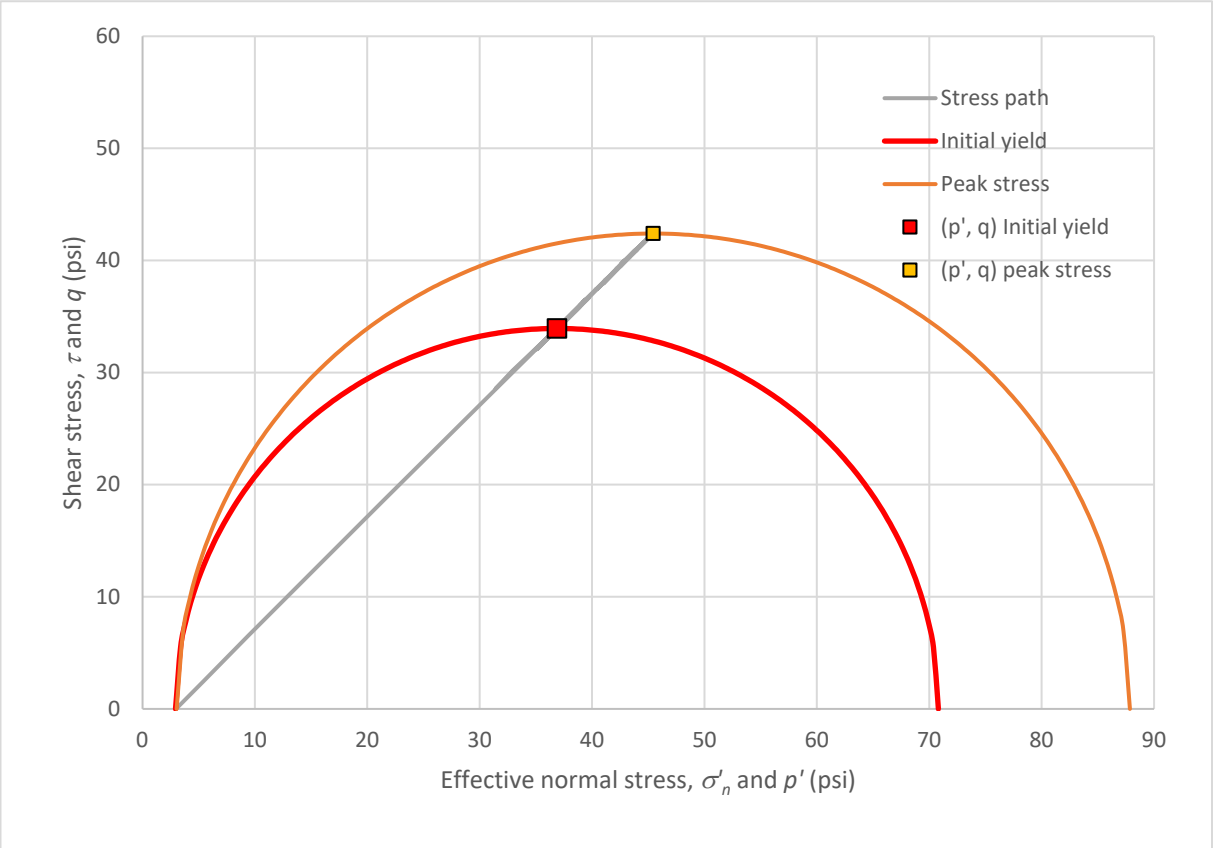

Consolidated-Drained Triaxial Shear, Lightweight Cellular Concrete

Sample ID:	**B2-61**
Height (in):	5.507
Height (mm):	139.9
Diameter (in):	2.971
Diameter (mm)	75.47
Area (in^2):	6.935
Area (mm^2):	4474
Mass (g):	304.81
Weight (lb):	0.6720
Weight (kN):	0.002989
Volume (in^3):	38.19
Volume (mm^3):	625808
Density (g/mm^3):	0.0004871
Density (kg/m^3):	487.1
Unit weight (pcf):	**30.41**
Dry unit weight (pcf);	**20.39**
Unit Weight (kN/m^3):	4.776
Wet mass + tare (g):	339.84
Dry mass + tare (g):	268.85
Tare (g):	124.39
Water content (%)	**49.14**
Saturation (%):	**18.28**
H:D ratio:	1.853
Age (days):	1072
Treatment:	W1

Strain rate (%/min):	0.2
Mean σ'_3 (psi):	3.0
Initial modulus (psi):	41311
Initial yield	
Time to failure (min):	0.8
Axial strain at failure (%):	0.164
σ'_1 (psi):	70.82
σ'_3 (psi):	2.89
σ'_1 -σ'_3 (psi):	67.93
σ'_1 / σ'_3:	24.51
p' (psi):	36.85
q (psi):	33.96
Volumetric strain (%):	0.083
Poisson's ratio:	0.248
Peak stress	
Time to failure (min):	14.4
Axial strain at failure (%):	2.881
σ'_1 (psi):	74.00
σ'_3 (psi):	2.97
σ'_1 -σ'_3 (psi):	71.03
σ'_1 / σ'_3:	24.94
p' (psi):	38.48
q (psi):	35.52
Volumetric strain (%):	2.601
Poisson's ratio:	0.049

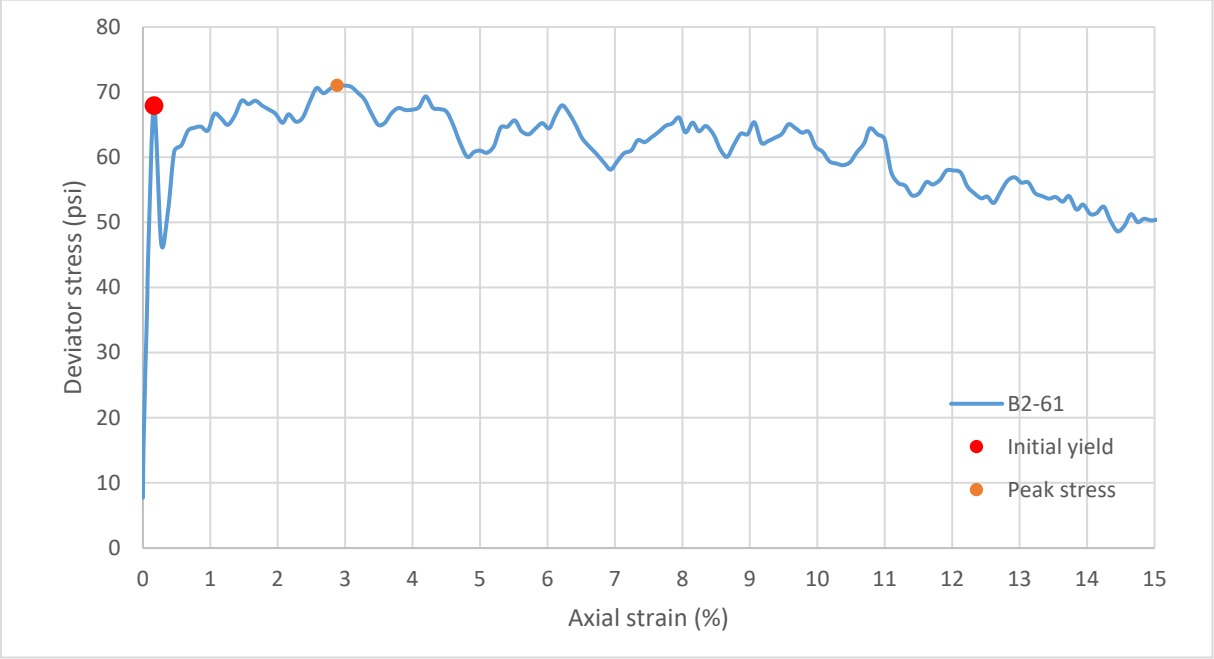

Sample ID:	B2-61

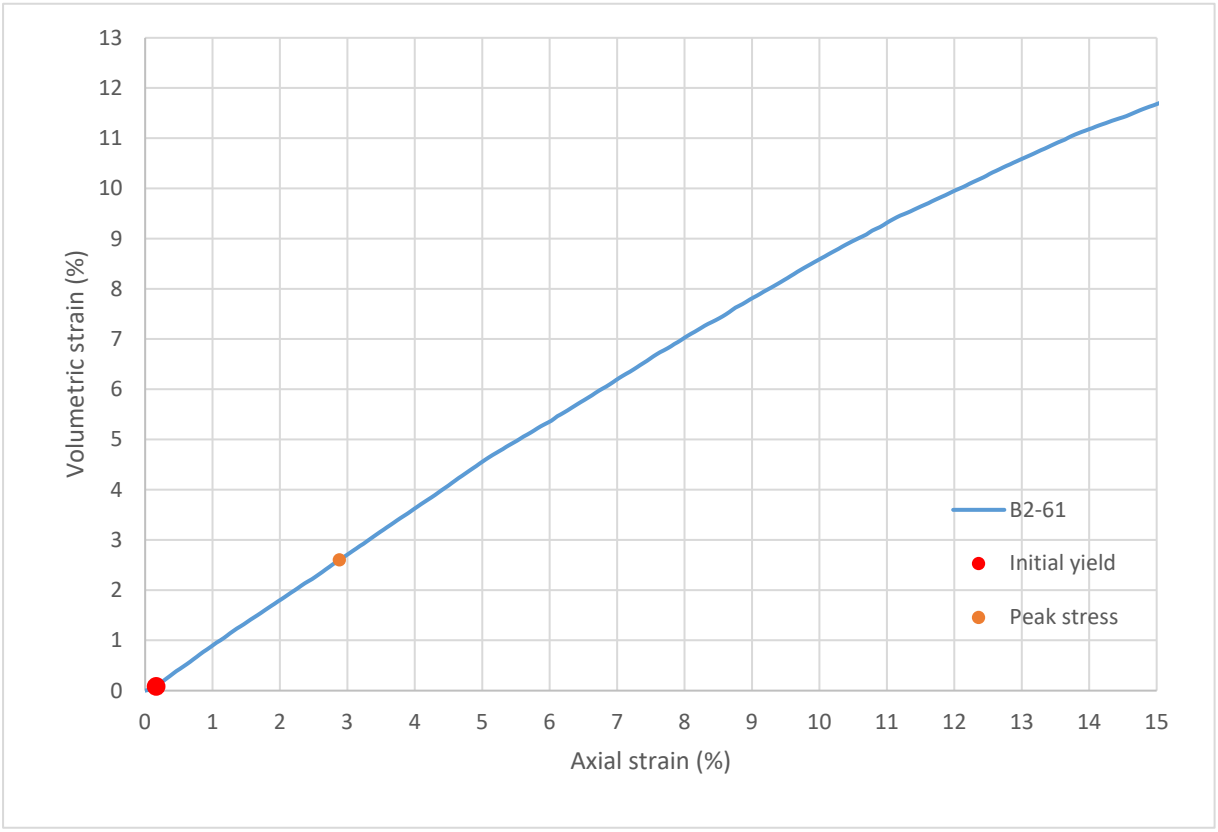

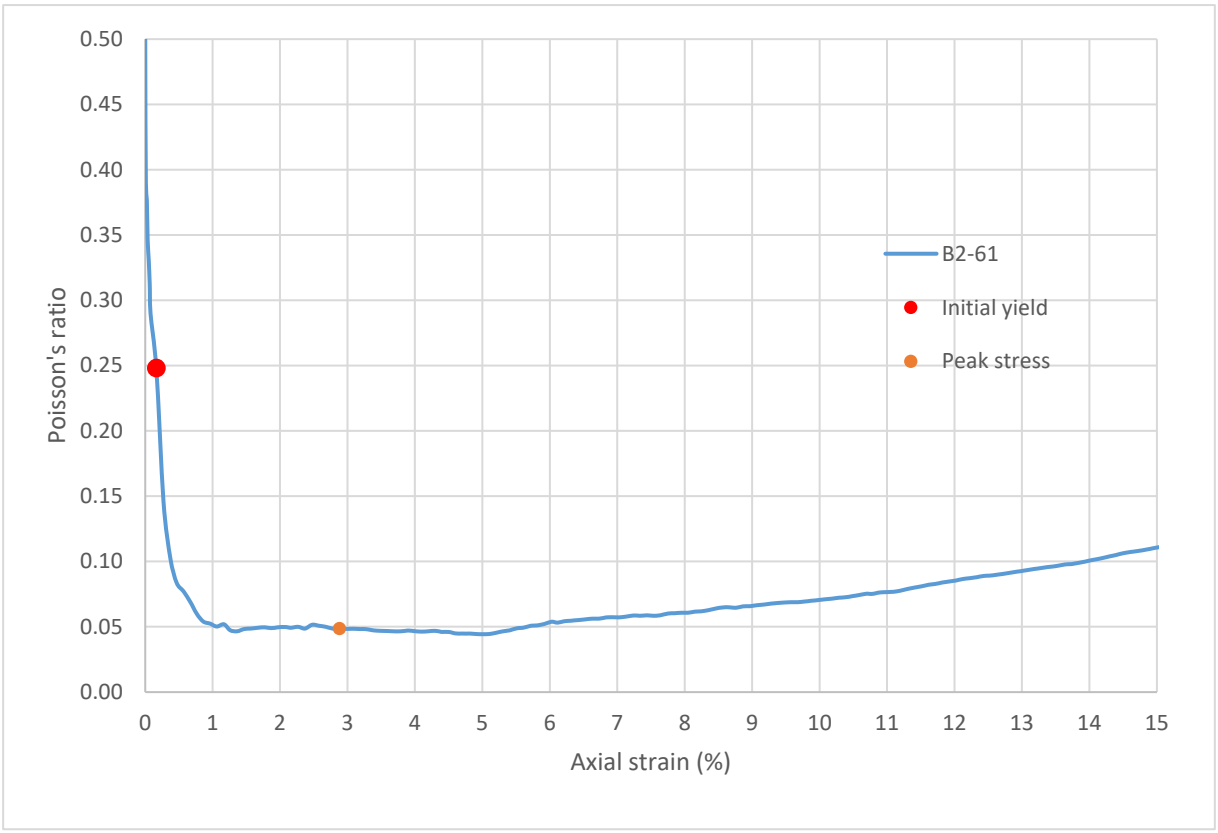

Sample ID:	B2-61

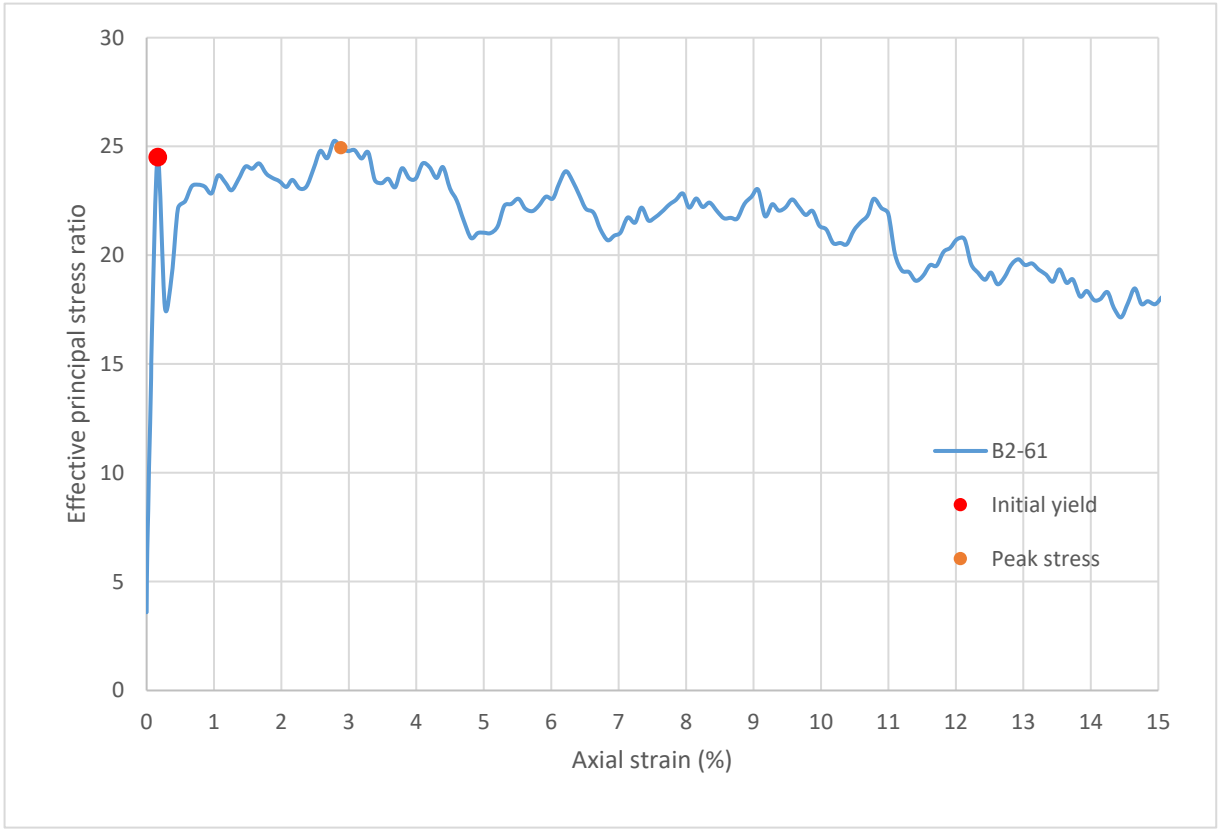

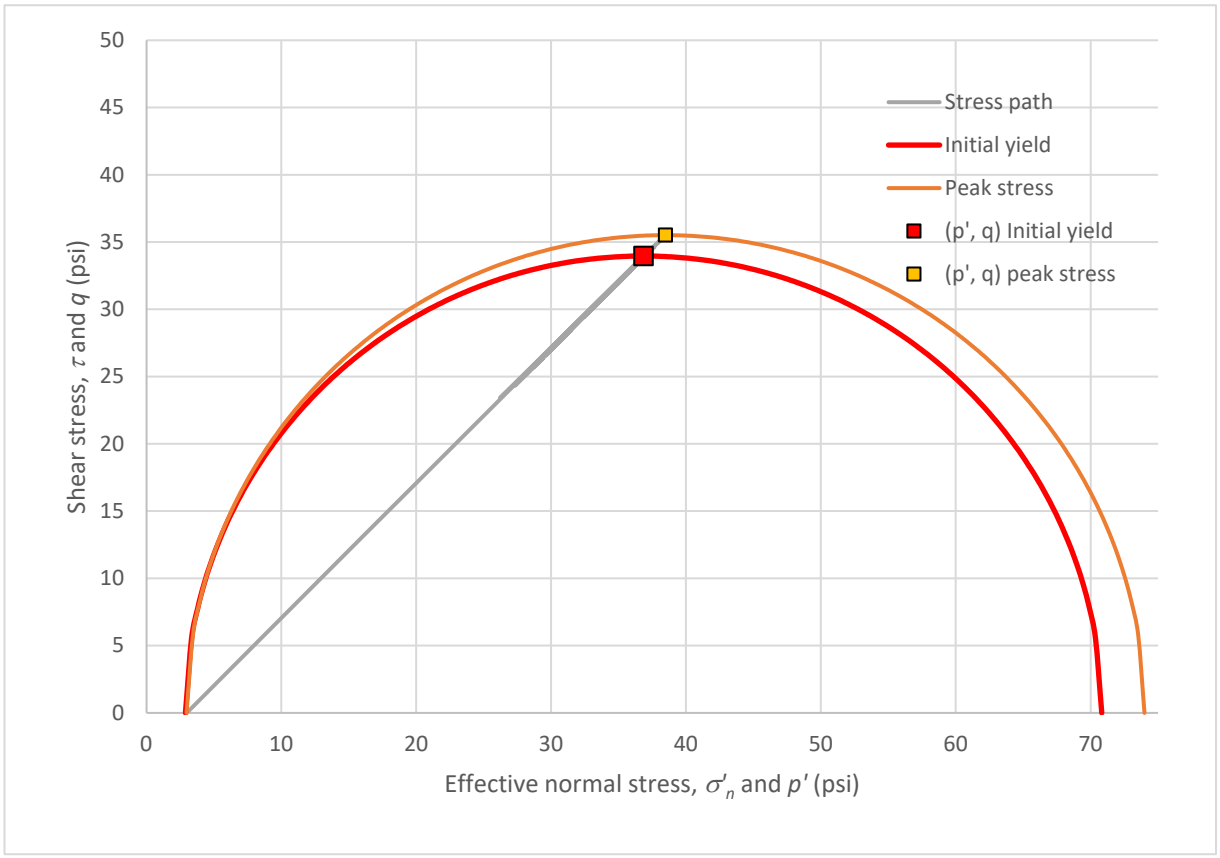

Consolidated-Drained Triaxial Shear, Lightweight Cellular Concrete

Sample ID:	**B2-62**
Height (in):	5.596
Height (mm):	142.1
Diameter (in):	2.971
Diameter (mm)	75.46
Area (in^2):	6.932
Area (mm^2):	4472
Mass (g):	218.32
Weight (lb):	0.4813
Weight (kN):	0.002141
Volume (in^3):	38.79
Volume (mm^3):	635722
Density (g/mm^3):	0.0003434
Density (kg/m^3):	343.4
Unit weight (pcf):	**21.44**
Dry unit weight (pcf);	**19.22**
Unit Weight (kN/m^3):	3.368
Wet mass + tare (g):	331.72
Dry mass + tare (g):	310.31
Tare (g):	124.70
Water content (%)	**11.53**
Saturation (%):	**4.01**
H:D ratio:	1.884
Age (days):	1057
Treatment:	AD

Strain rate (%/min):	0.2
Mean σ'_3 (psi):	6.1
Initial modulus (psi):	42322
Initial yield	
Time to failure (min):	1.3
Axial strain at failure (%):	0.254
σ'_1 (psi):	113.59
σ'_3 (psi):	6.04
σ'_1 -σ'_3 (psi):	107.56
σ'_1 / σ'_3:	18.81
p' (psi):	59.82
q (psi):	53.78
Volumetric strain (%):	0.138
Poisson's ratio:	0.228
Peak stress	
Time to failure (min):	20.9
Axial strain at failure (%):	4.183
σ'_1 (psi):	119.77
σ'_3 (psi):	6.14
σ'_1 -σ'_3 (psi):	113.62
σ'_1 / σ'_3:	19.50
p' (psi):	62.95
q (psi):	56.81
Volumetric strain (%):	3.688
Poisson's ratio:	0.059

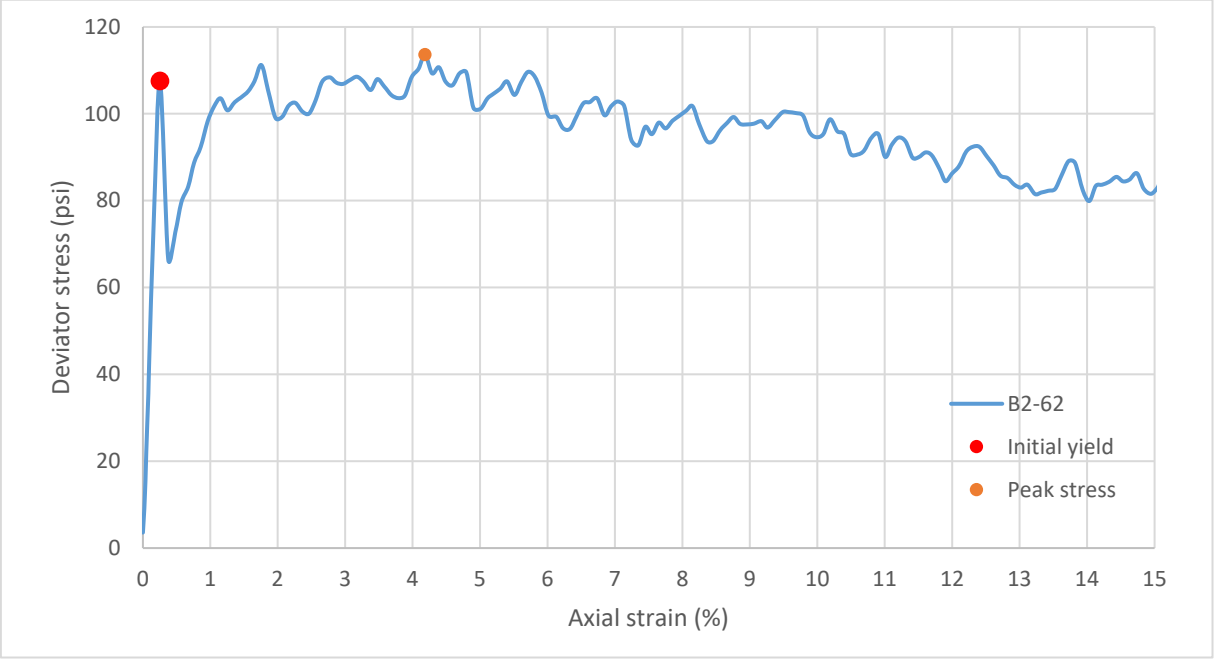

Sample ID:	B2-62

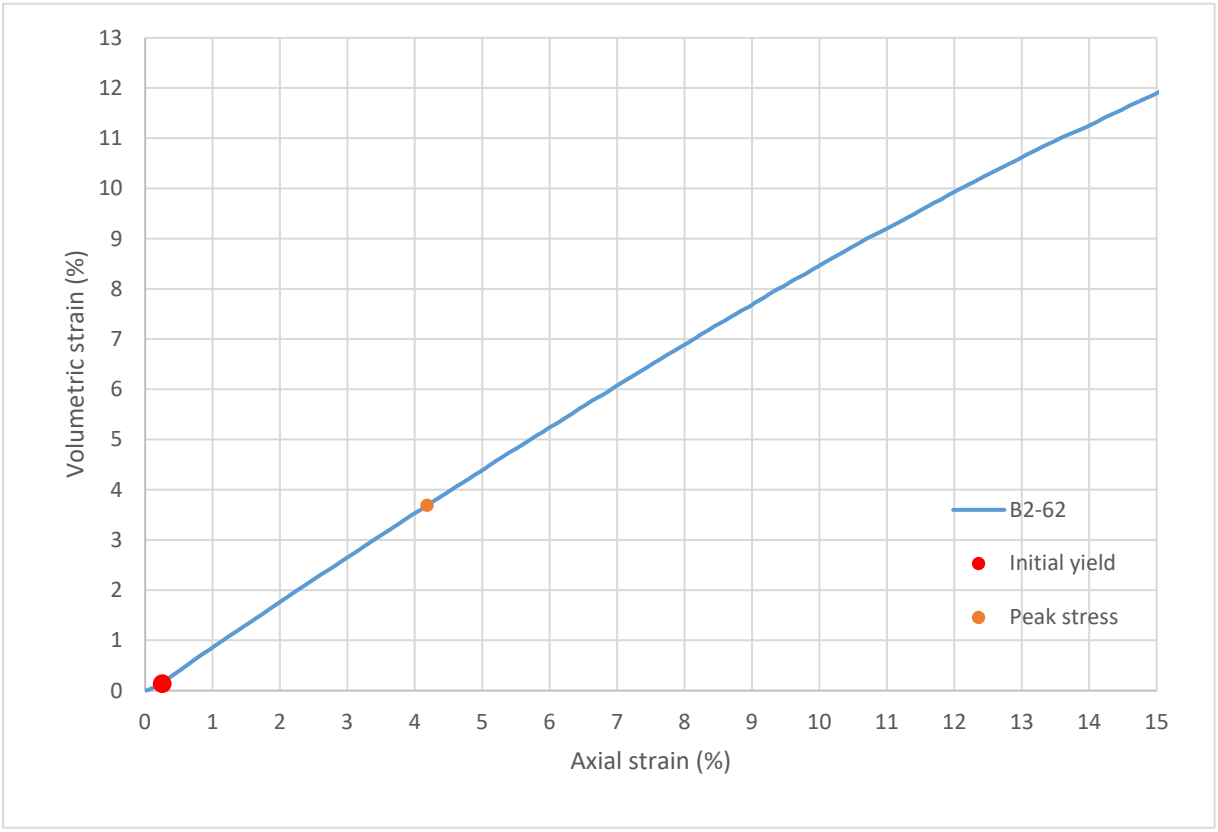

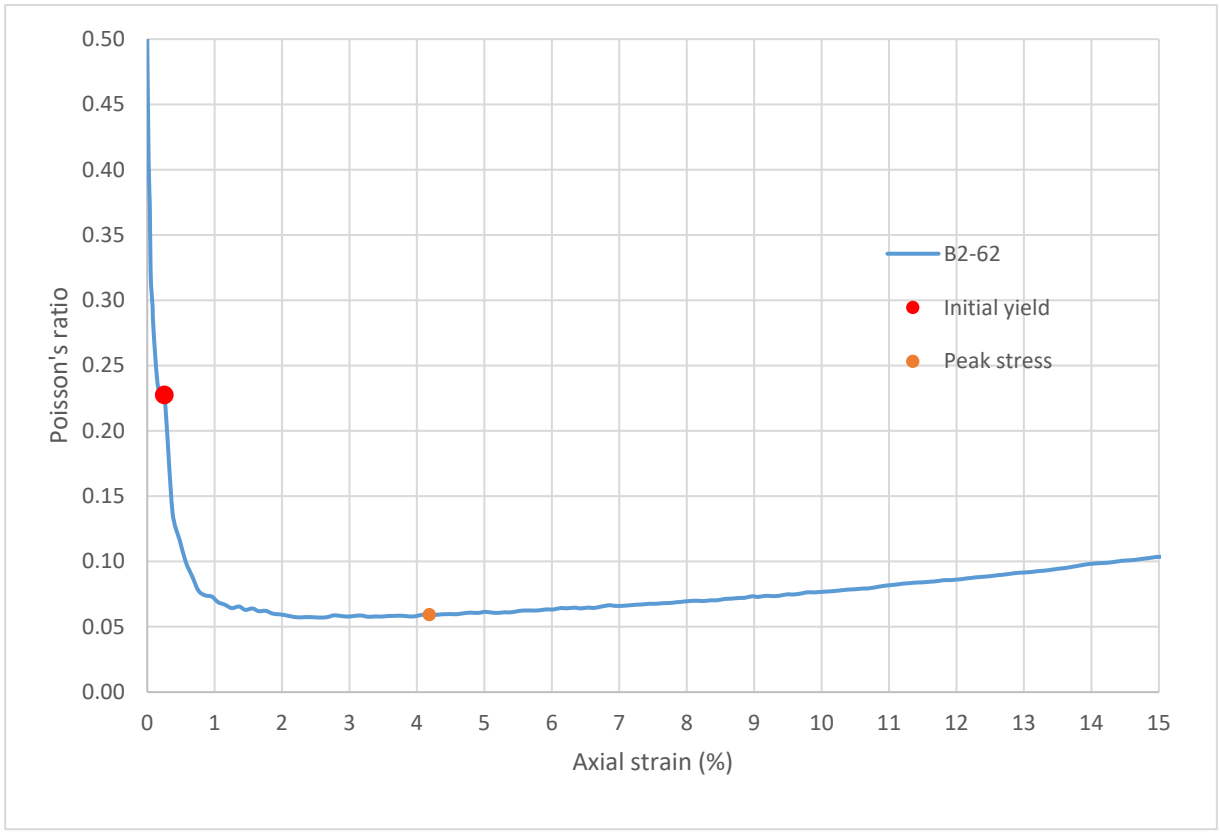

Sample ID:	B2-62

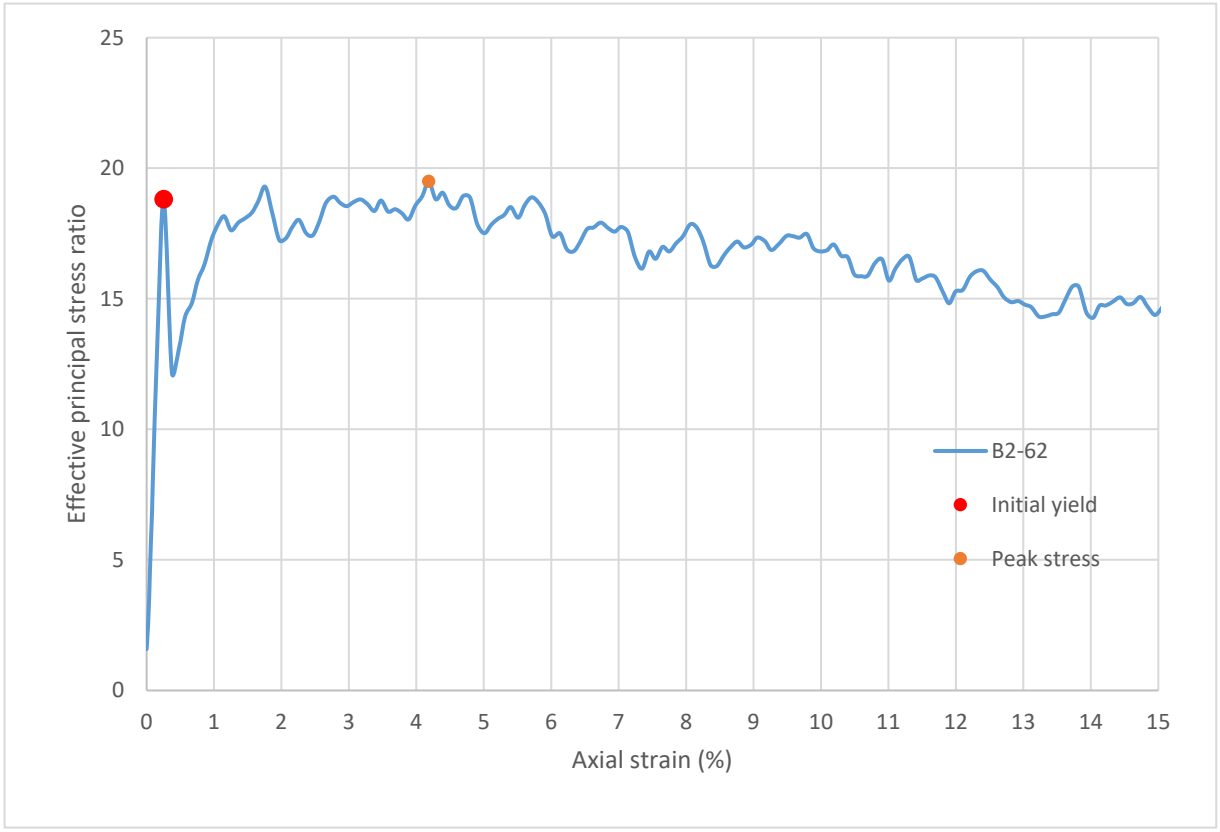

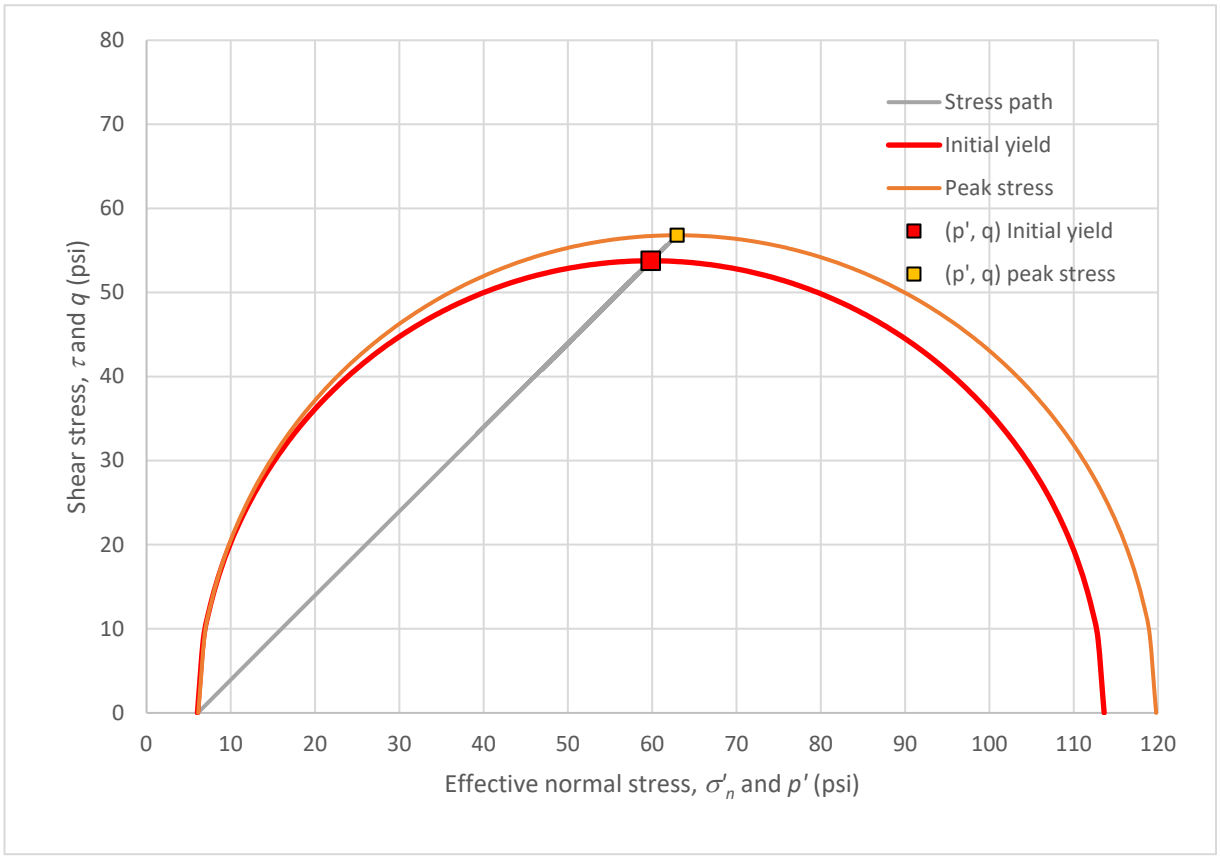

Consolidated-Drained Triaxial Shear, Lightweight Cellular Concrete

Sample ID:	**B2-63**
Height (in):	5.509
Height (mm):	139.9
Diameter (in):	2.964
Diameter (mm)	75.28
Area (in^2):	6.898
Area (mm^2):	4451
Mass (g):	210.83
Weight (lb):	0.4648
Weight (kN):	0.002068
Volume (in^3):	38.00
Volume (mm^3):	622763
Density (g/mm^3):	0.0003385
Density (kg/m^3):	338.5
Unit weight (pcf):	**21.13**
Dry unit weight (pcf);	**19.02**
Unit Weight (kN/m^3):	3.320
Wet mass + tare (g):	324.78
Dry mass + tare (g):	305.02
Tare (g):	127.36
Water content (%)	**11.12**
Saturation (%):	**3.82**
H:D ratio:	1.859
Age (days):	1057
Treatment:	AD

Strain rate (%/min):	0.2
Mean σ'_3 (psi):	12.0
Initial modulus (psi):	46807
Initial yield	
Time to failure (min):	1.1
Axial strain at failure (%):	0.226
σ'_1 (psi):	117.78
σ'_3 (psi):	11.97
σ'_1 -σ'_3 (psi):	105.82
σ'_1 / σ'_3:	9.84
p' (psi):	64.87
q (psi):	52.91
Volumetric strain (%):	0.127
Poisson's ratio:	0.218
Peak stress	
Time to failure (min):	24.4
Axial strain at failure (%):	4.873
σ'_1 (psi):	130.43
σ'_3 (psi):	12.09
σ'_1 -σ'_3 (psi):	118.34
σ'_1 / σ'_3:	10.79
p' (psi):	71.26
q (psi):	59.17
Volumetric strain (%):	4.442
Poisson's ratio:	0.044

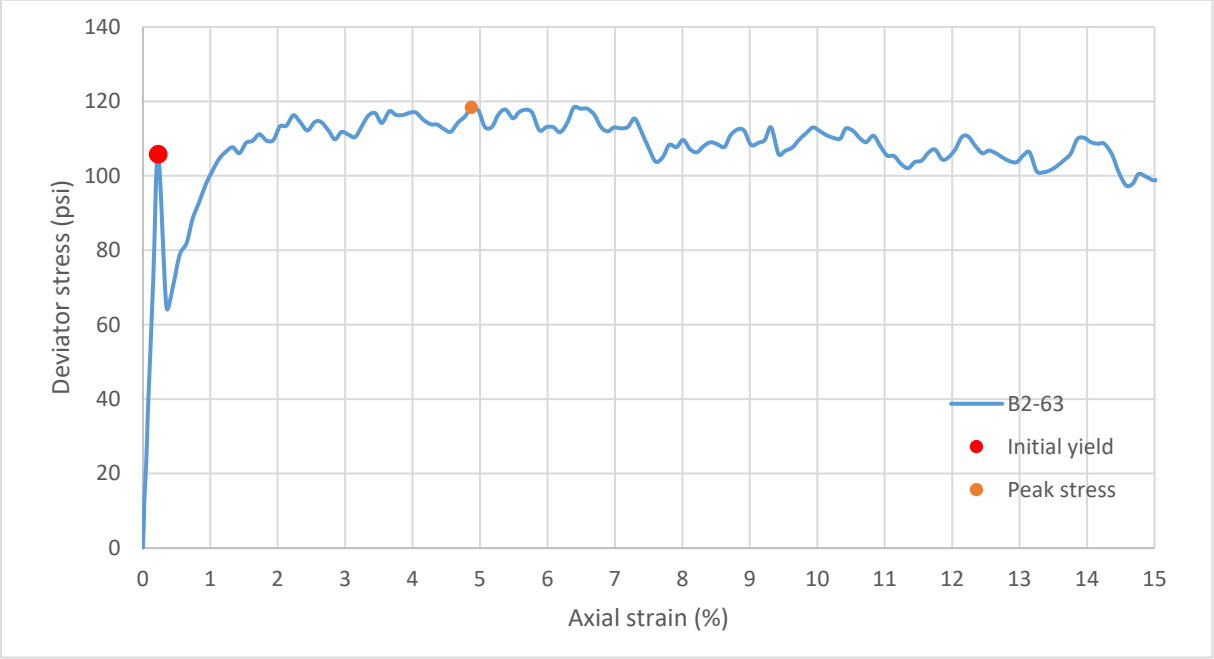

Sample ID:	B2-63

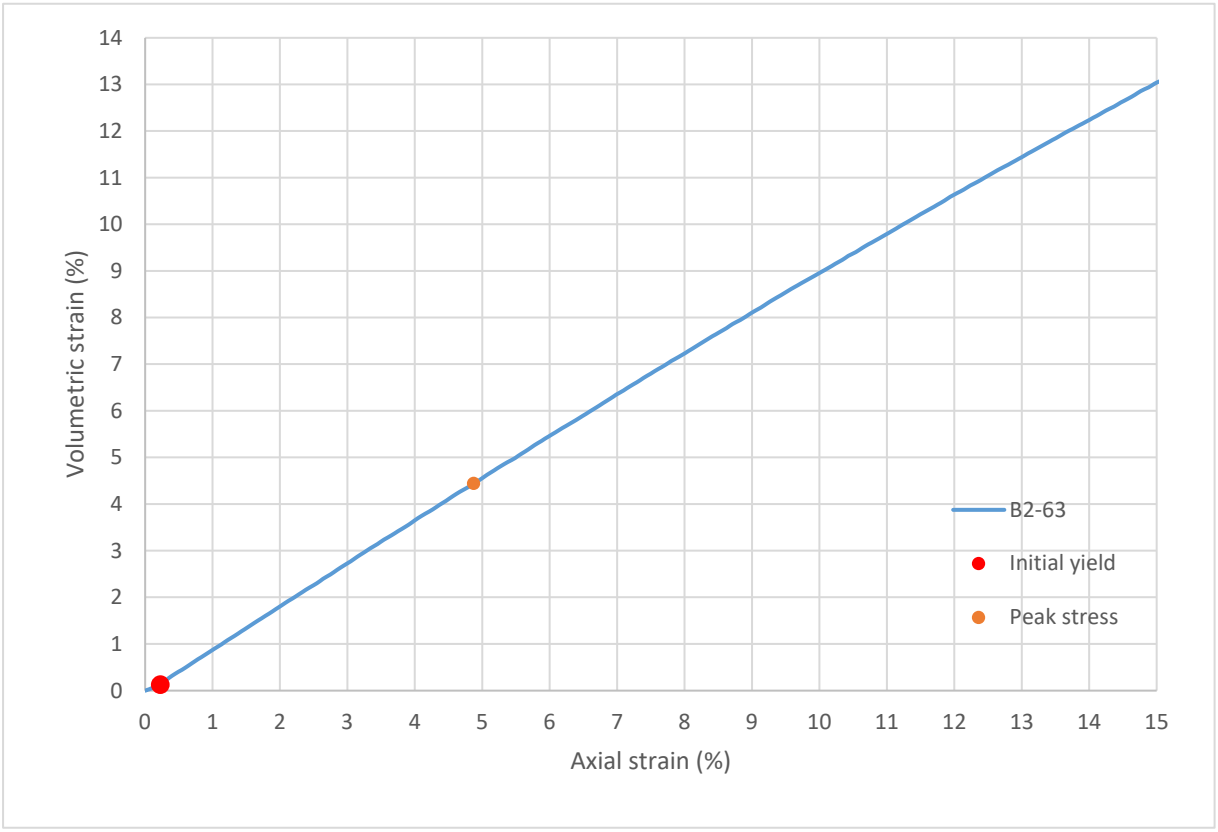

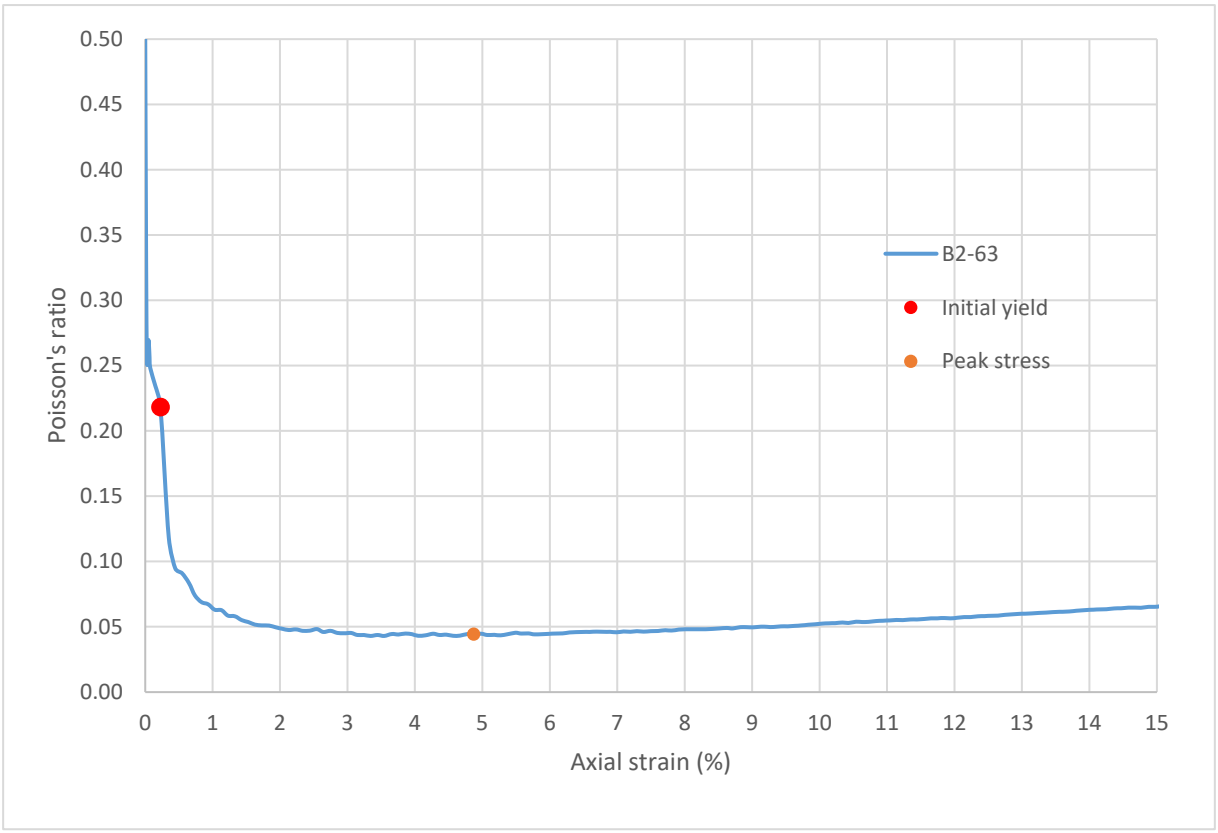

Sample ID:	B2-63

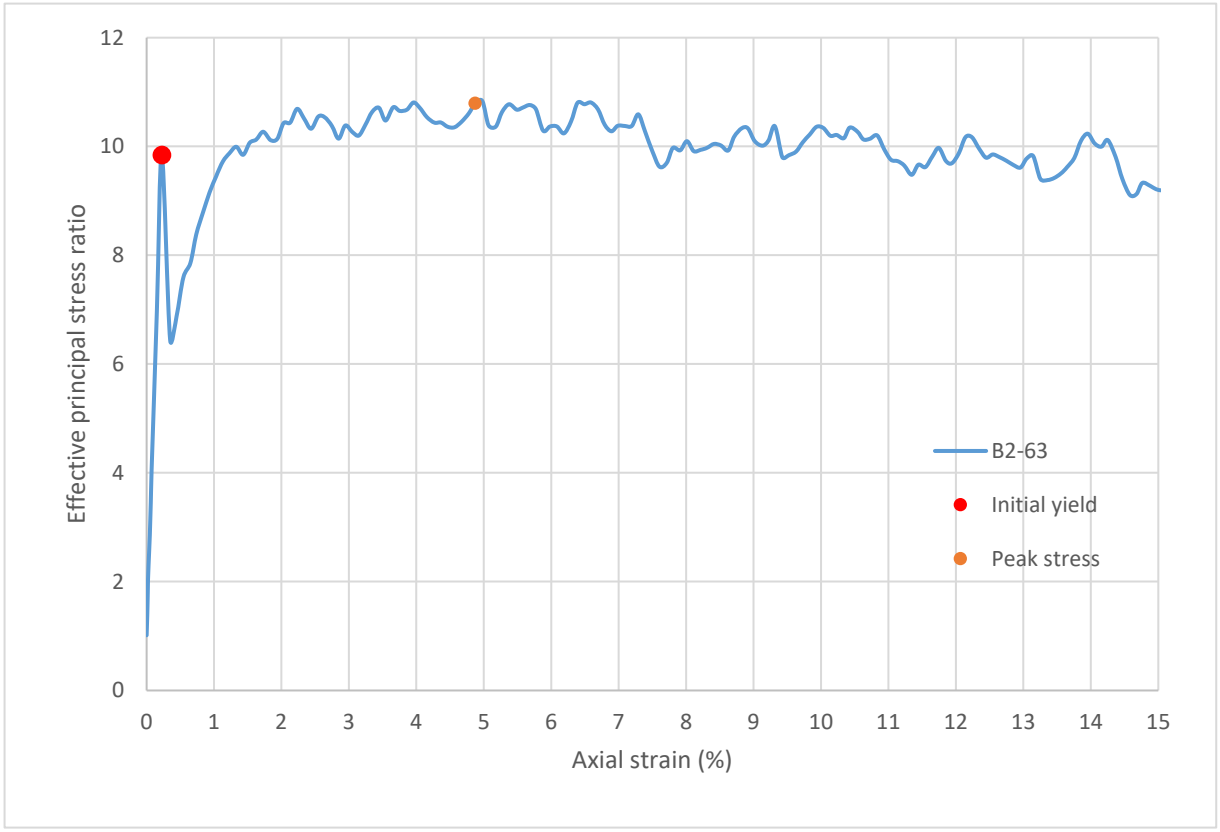

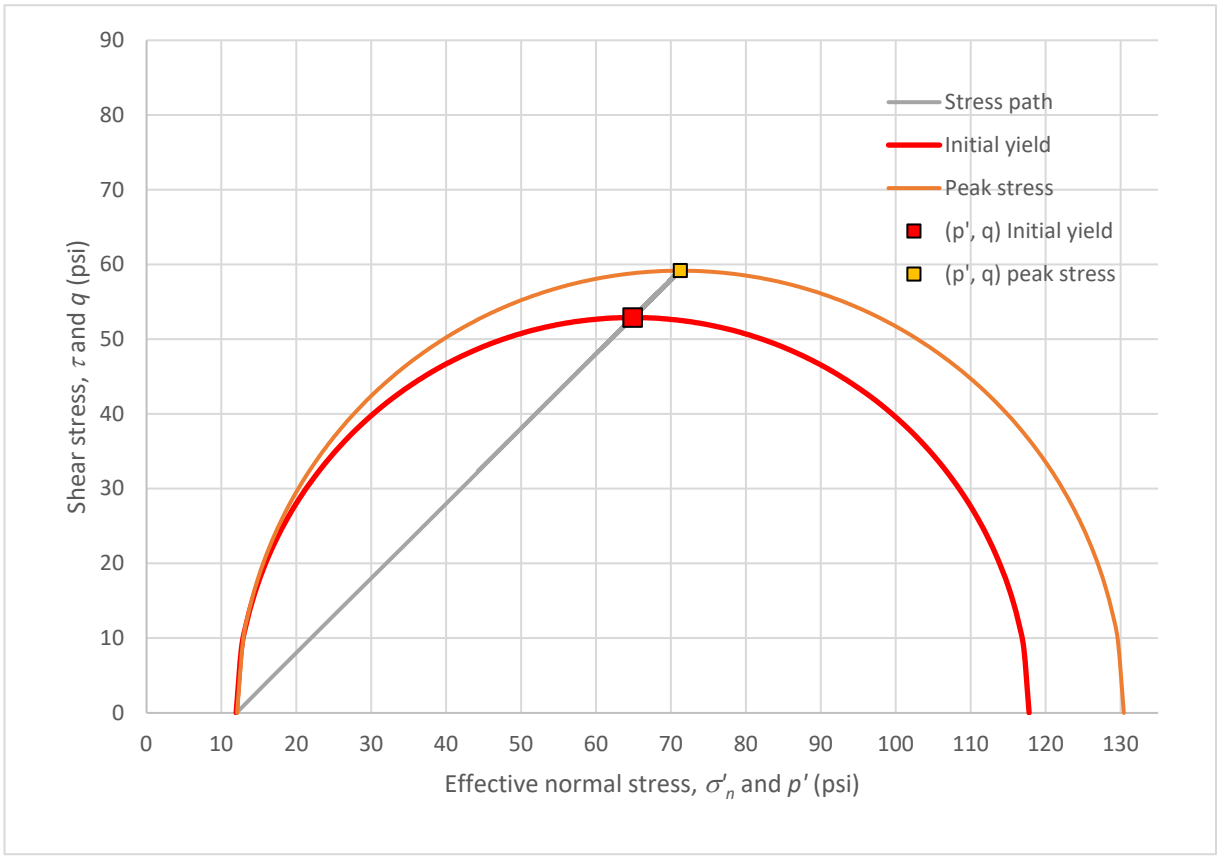

Consolidated-Drained Triaxial Shear, Lightweight Cellular Concrete

Sample ID:	**B2-64**
Height (in):	5.536
Height (mm):	140.6
Diameter (in):	2.957
Diameter (mm)	75.10
Area (in^2):	6.866
Area (mm^2):	4430
Mass (g):	219.62
Weight (lb):	0.4842
Weight (kN):	0.002154
Volume (in^3):	38.01
Volume (mm^3):	622909
Density (g/mm^3):	0.0003526
Density (kg/m^3):	352.6
Unit weight (pcf):	**22.01**
Dry unit weight (pcf);	**19.09**
Unit Weight (kN/m^3):	3.458
Wet mass + tare (g):	325.46
Dry mass + tare (g):	299.19
Tare (g):	127.69
Water content (%)	**15.32**
Saturation (%):	**5.29**
H:D ratio:	1.872
Age (days):	1067
Treatment:	H100

Strain rate (%/min):	0.2
Mean σ'_3 (psi):	6.7
Initial modulus (psi):	15409
Initial yield	
Time to failure (min):	2.3
Axial strain at failure (%):	0.456
σ'_1 (psi):	76.91
σ'_3 (psi):	6.61
σ'_1 -σ'_3 (psi):	70.30
σ'_1 / σ'_3:	11.64
p' (psi):	41.76
q (psi):	35.15
Volumetric strain (%):	0.328
Poisson's ratio:	0.141
Peak stress	
Time to failure (min):	6.2
Axial strain at failure (%):	1.243
σ'_1 (psi):	101.14
σ'_3 (psi):	6.68
σ'_1 -σ'_3 (psi):	94.46
σ'_1 / σ'_3:	15.14
p' (psi):	53.91
q (psi):	47.23
Volumetric strain (%):	1.099
Poisson's ratio:	0.058

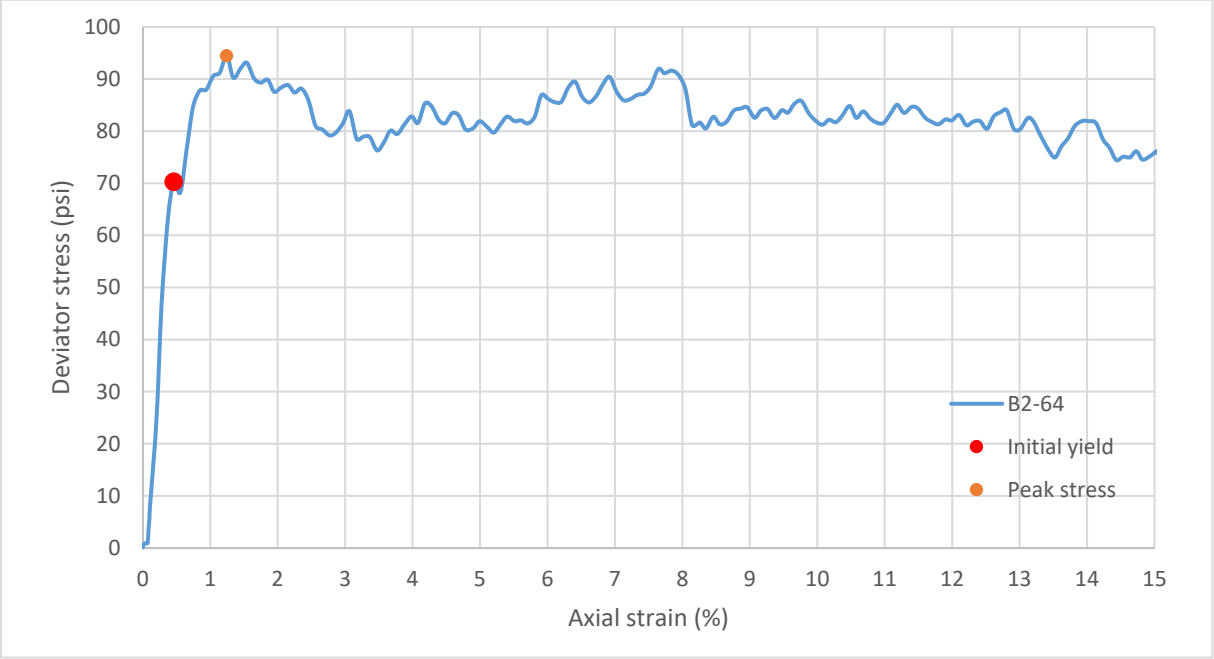

Sample ID:	B2-64

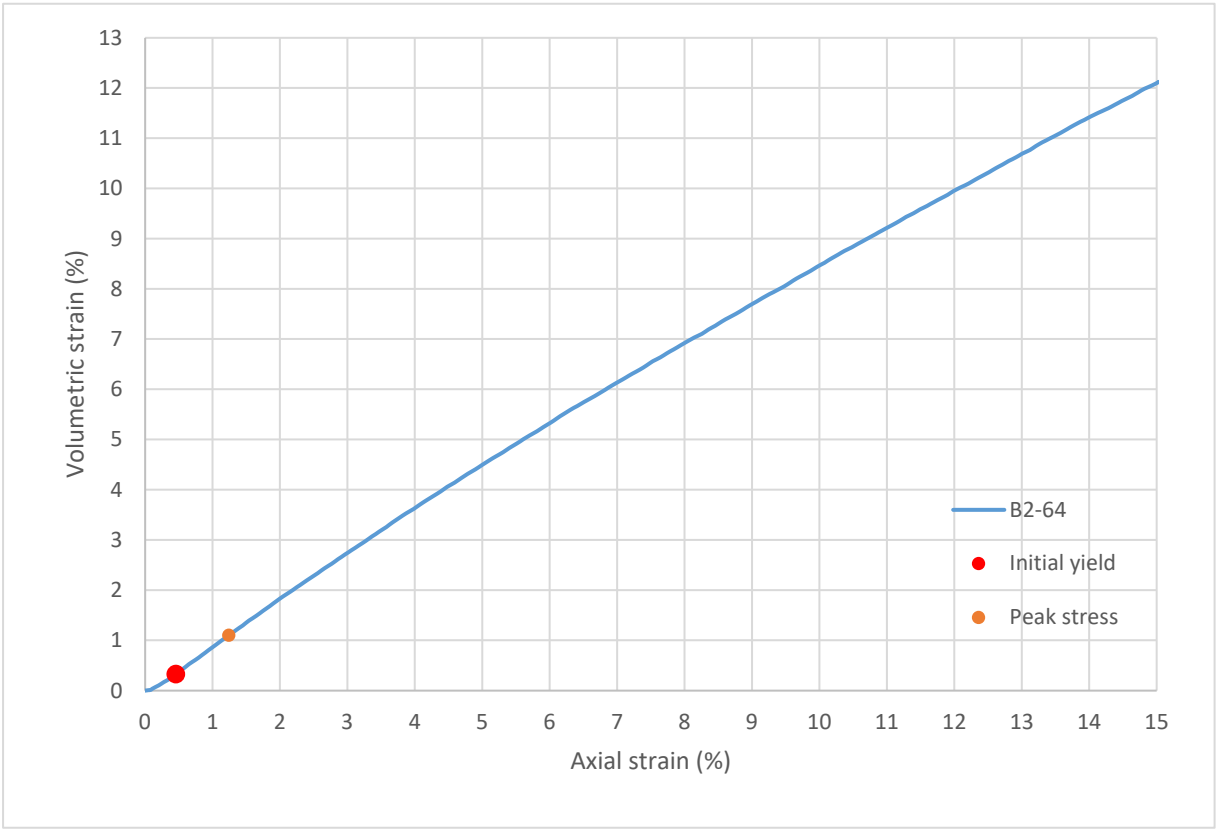

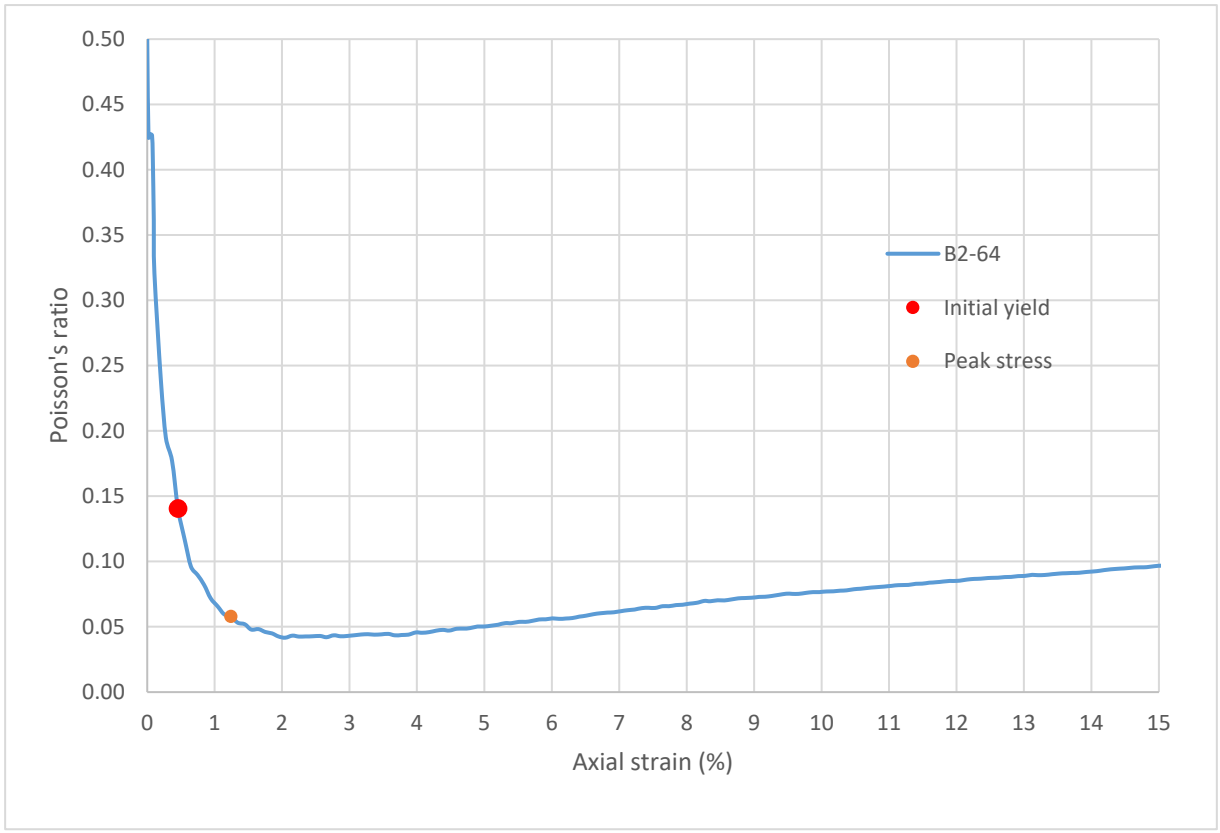

Sample ID:	B2-64

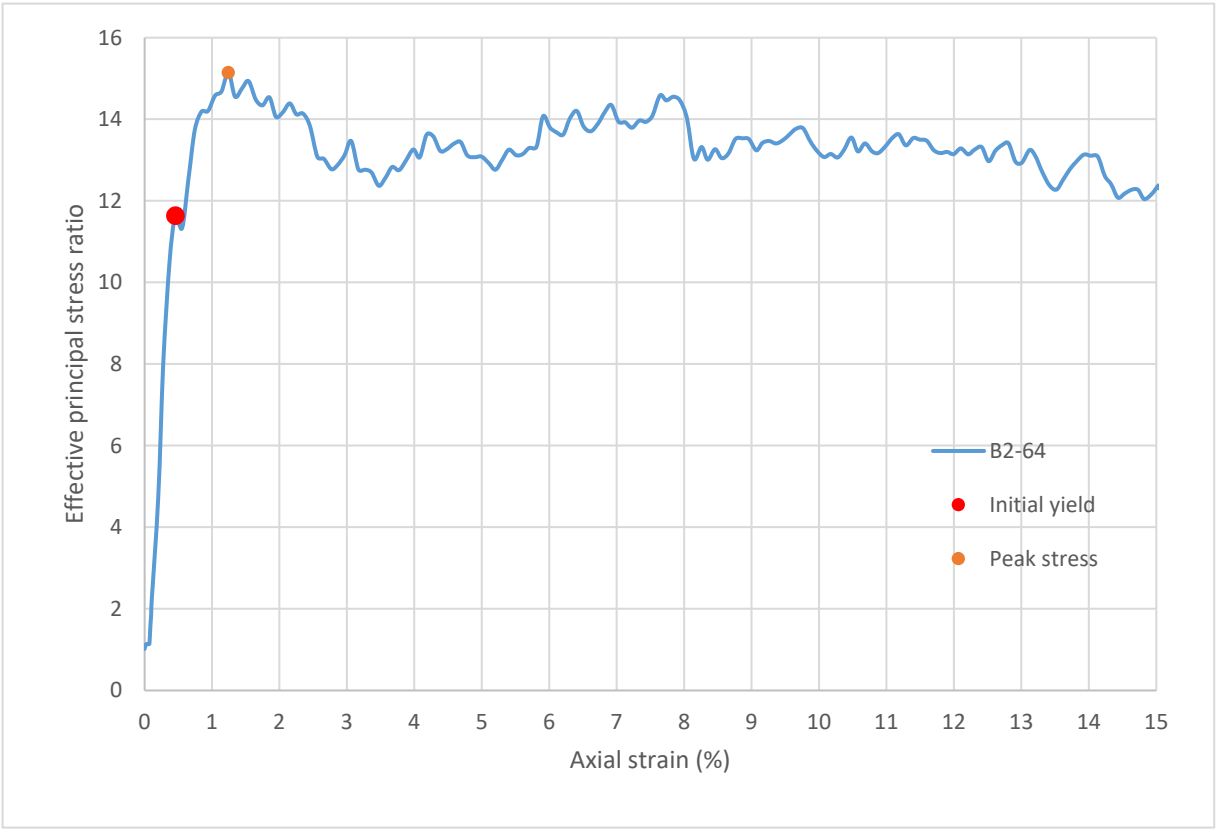

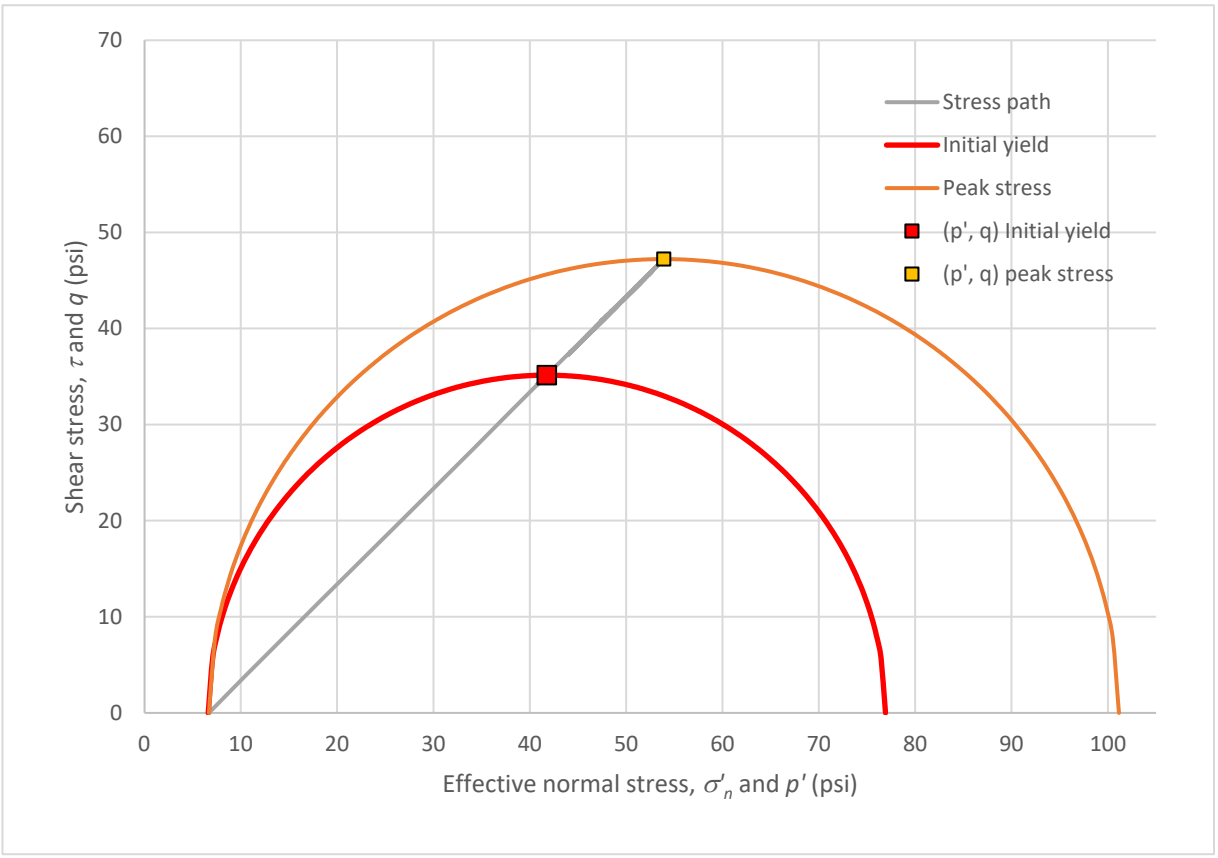

Consolidated-Drained Triaxial Shear, Lightweight Cellular Concrete

Sample ID:	**B2-65**
Height (in):	5.465
Height (mm):	138.8
Diameter (in):	2.953
Diameter (mm)	75.00
Area (in^2):	6.847
Area (mm^2):	4418
Mass (g):	215.73
Weight (lb):	0.4756
Weight (kN):	0.002116
Volume (in^3):	37.42
Volume (mm^3):	613174
Density (g/mm^3):	0.0003518
Density (kg/m^3):	351.8
Unit weight (pcf):	**21.96**
Dry unit weight (pcf);	**19.14**
Unit Weight (kN/m^3):	3.450
Wet mass + tare (g):	331.98
Dry mass + tare (g):	305.80
Tare (g):	128.45
Water content (%)	**14.76**
Saturation (%):	**5.11**
H:D ratio:	1.851
Age (days):	1067
Treatment:	H100

Strain rate (%/min):	0.2
Mean σ'_3 (psi):	12.0
Initial modulus (psi):	27310
Initial yield	
Time to failure (min):	1.7
Axial strain at failure (%):	0.341
σ'_1 (psi):	105.16
σ'_3 (psi):	11.93
σ'_1 -σ'_3 (psi):	93.23
σ'_1 / σ'_3:	8.82
p' (psi):	58.55
q (psi):	46.62
Volumetric strain (%):	0.161
Poisson's ratio:	0.264
Peak stress	
Time to failure (min):	43.7
Axial strain at failure (%):	8.733
σ'_1 (psi):	124.63
σ'_3 (psi):	12.01
σ'_1 -σ'_3 (psi):	112.61
σ'_1 / σ'_3:	10.37
p' (psi):	68.32
q (psi):	56.31
Volumetric strain (%):	7.914
Poisson's ratio:	0.047

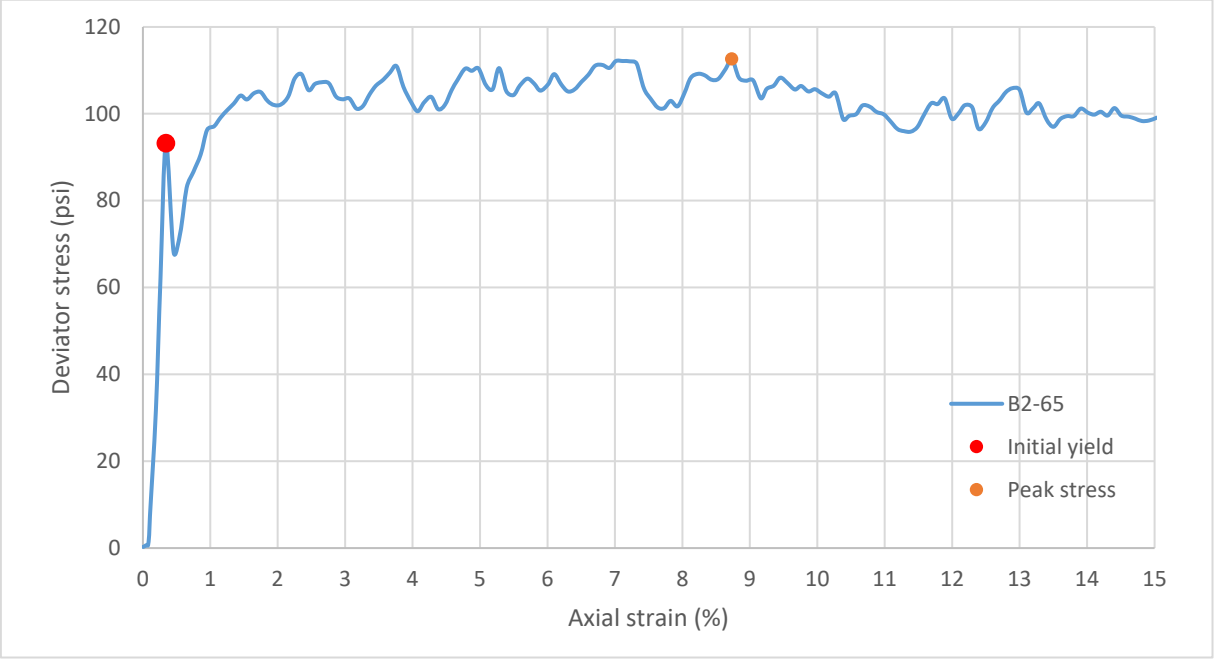

Sample ID:	B2-65

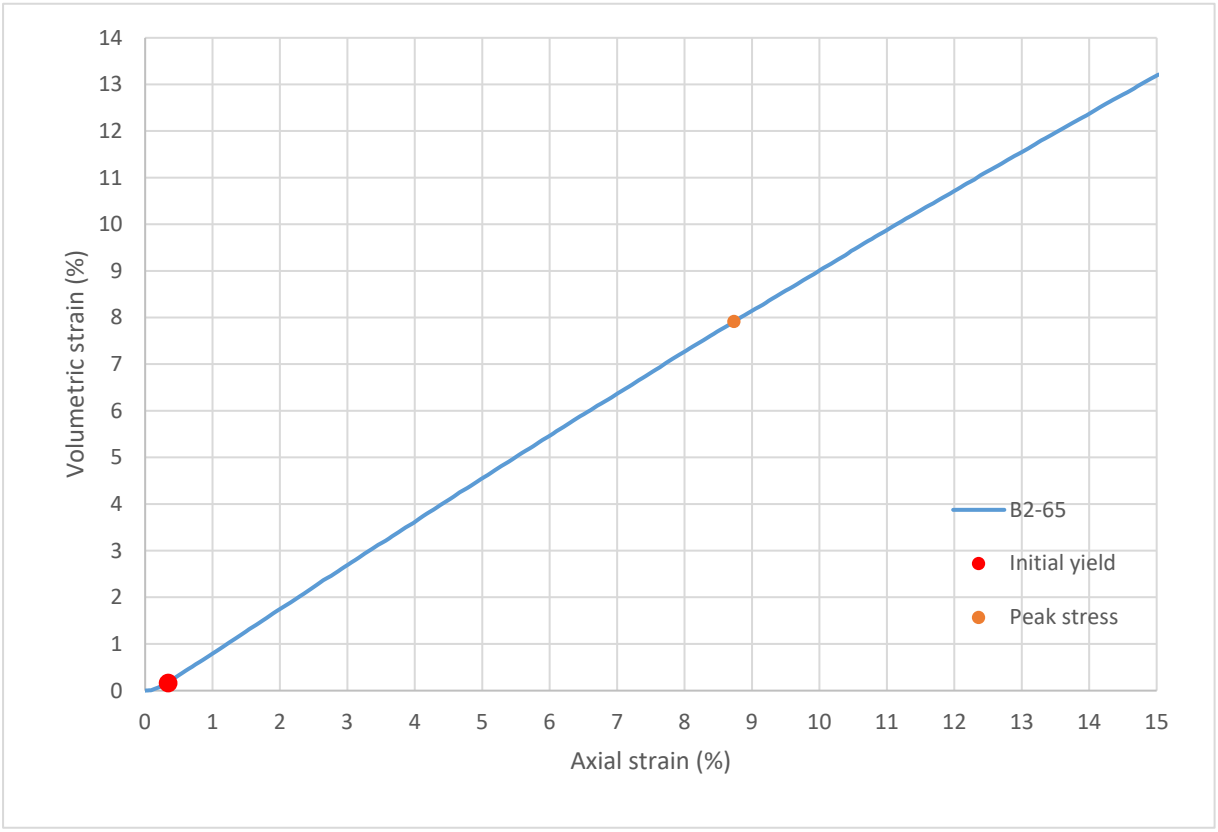

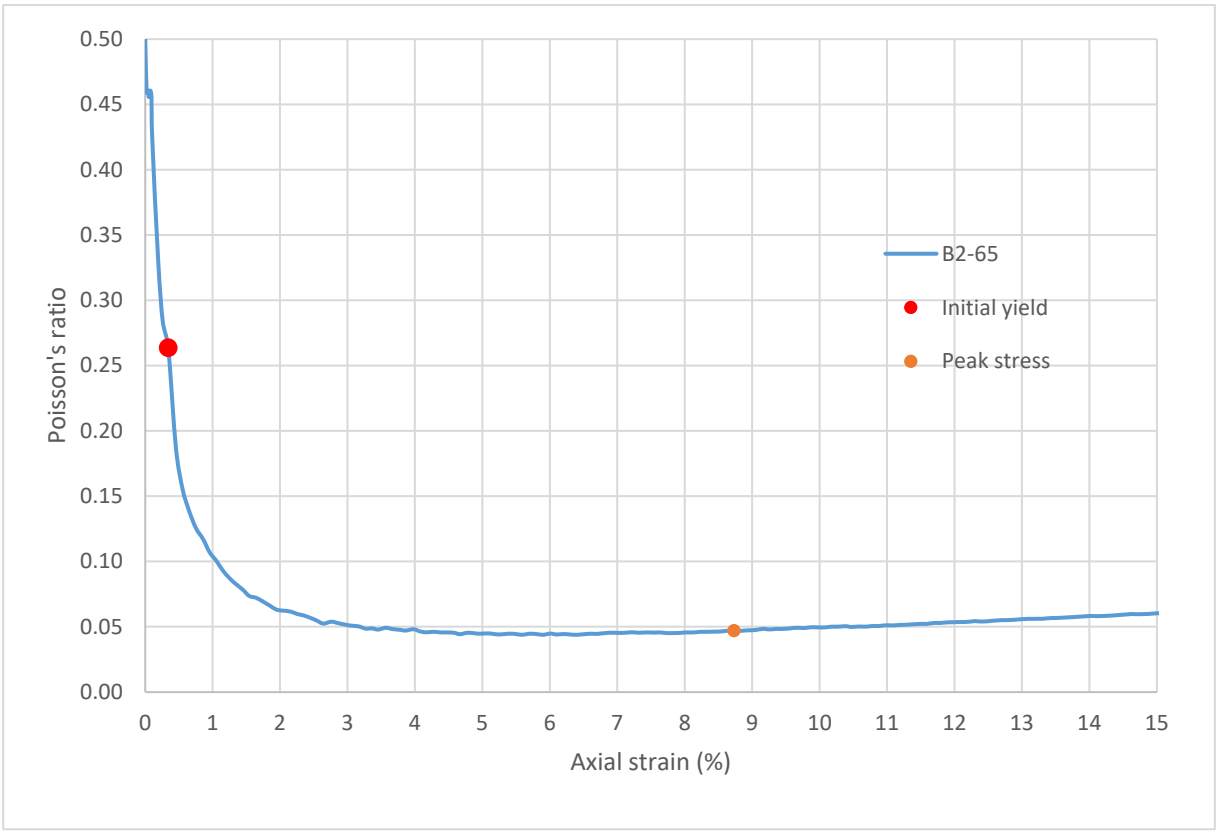

Sample ID:	B2-65

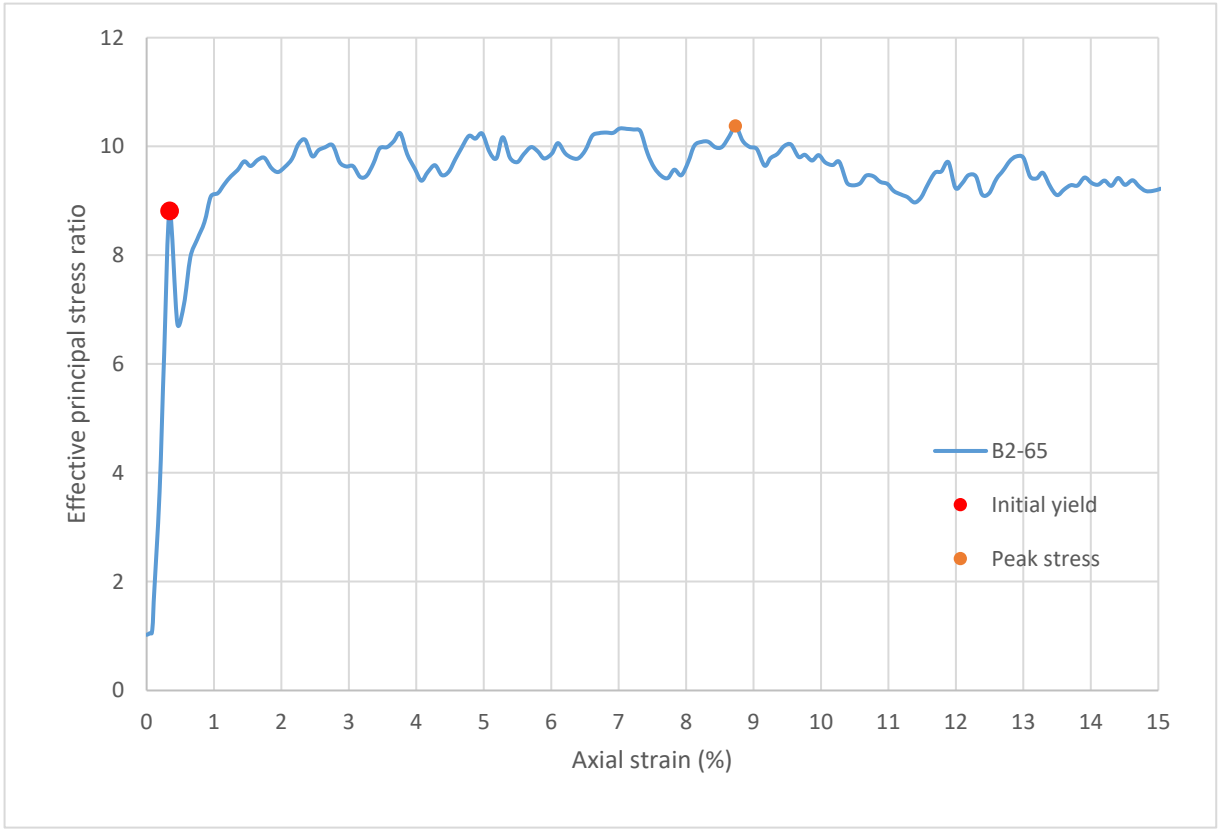

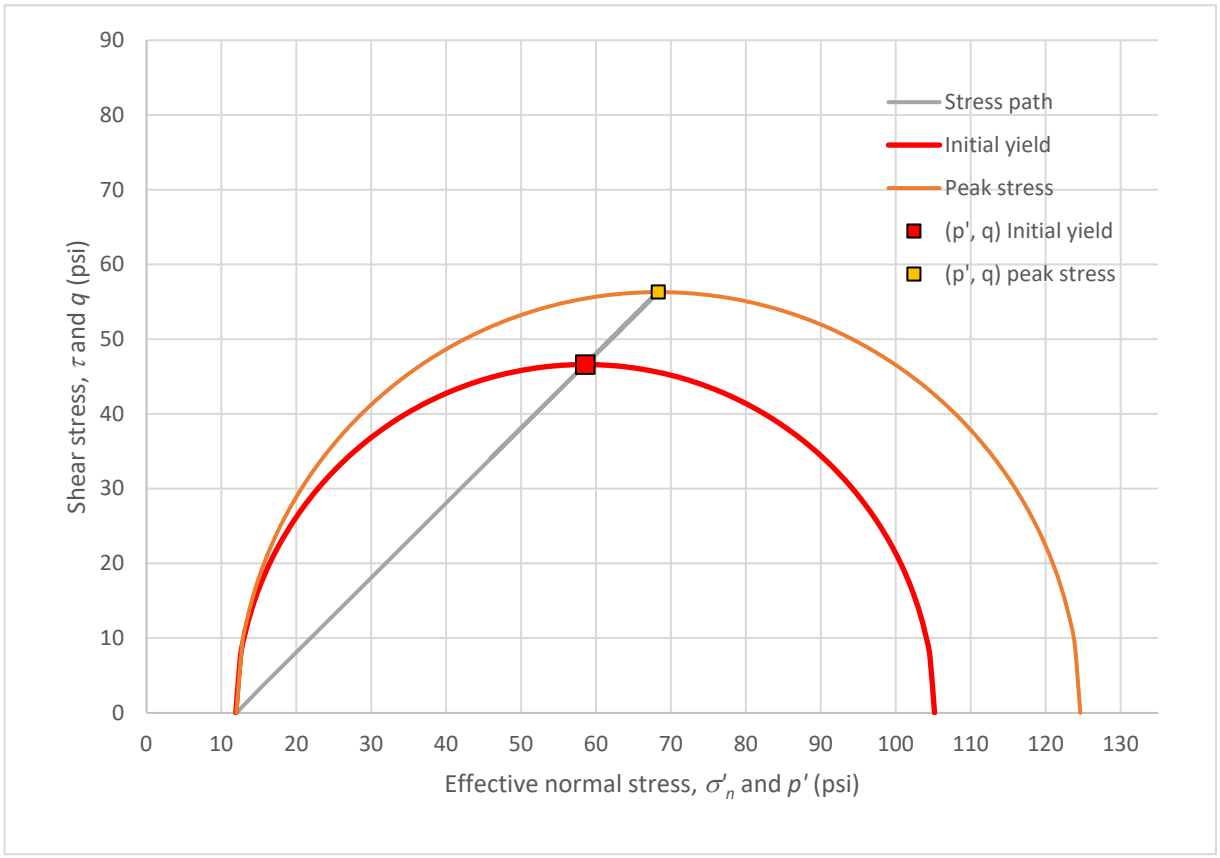

Consolidated-Drained Triaxial Shear, Lightweight Cellular Concrete

Sample ID:	**B2-66**
Height (in):	5.537
Height (mm):	140.6
Diameter (in):	2.948
Diameter (mm)	74.89
Area (in^2):	6.828
Area (mm^2):	4405
Mass (g):	280.93
Weight (lb):	0.6193
Weight (kN):	0.002755
Volume (in^3):	37.81
Volume (mm^3):	619514
Density (g/mm^3):	0.0004535
Density (kg/m^3):	453.5
Unit weight (pcf):	**28.31**
Dry unit weight (pcf);	**19.59**
Unit Weight (kN/m^3):	4.447
Wet mass + tare (g):	455.63
Dry mass + tare (g):	374.89
Tare (g):	193.60
Water content (%)	**44.54**
Saturation (%):	**15.83**
H:D ratio:	1.878
Age (days):	1067
Treatment:	D1

Strain rate (%/min):	0.2
Mean σ'_3 (psi):	6.0
Initial modulus (psi):	30273
Initial yield	
Time to failure (min):	1.3
Axial strain at failure (%):	0.250
σ'_1 (psi):	81.59
σ'_3 (psi):	5.80
σ'_1 -σ'_3 (psi):	75.79
σ'_1 / σ'_3:	14.07
p' (psi):	43.69
q (psi):	37.89
Volumetric strain (%):	0.162
Poisson's ratio:	0.176
Peak stress	
Time to failure (min):	20.8
Axial strain at failure (%):	4.163
σ'_1 (psi):	99.59
σ'_3 (psi):	6.00
σ'_1 -σ'_3 (psi):	93.59
σ'_1 / σ'_3:	16.60
p' (psi):	52.79
q (psi):	46.80
Volumetric strain (%):	3.873
Poisson's ratio:	0.035

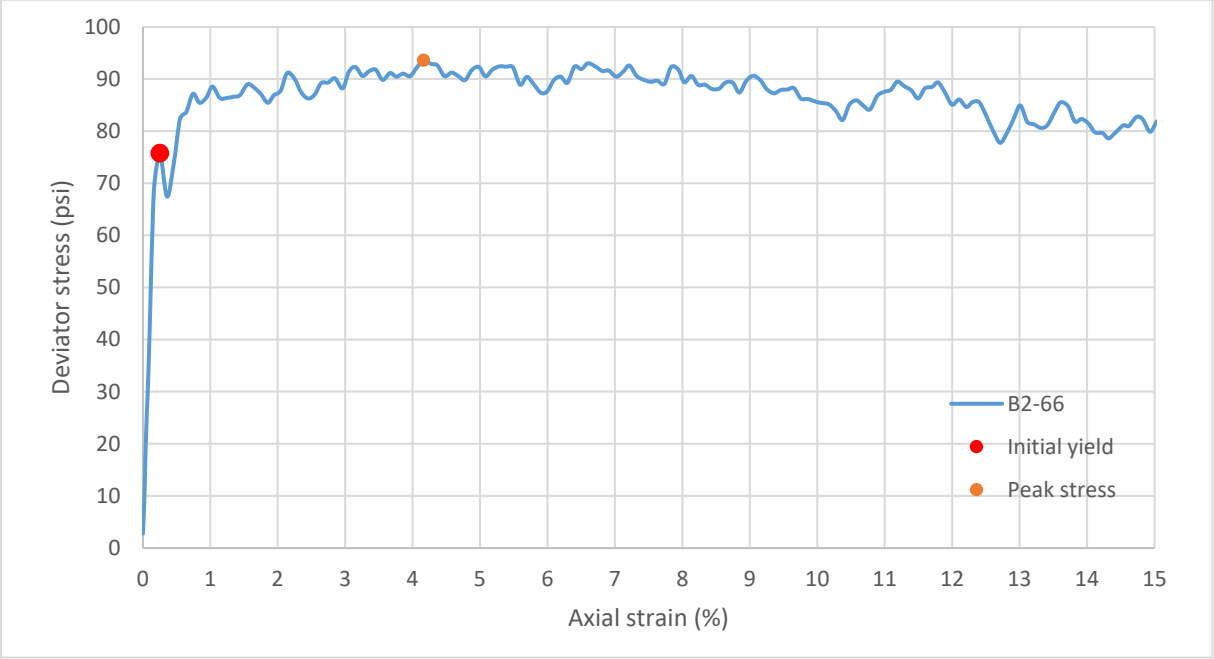

Sample ID:	B2-66

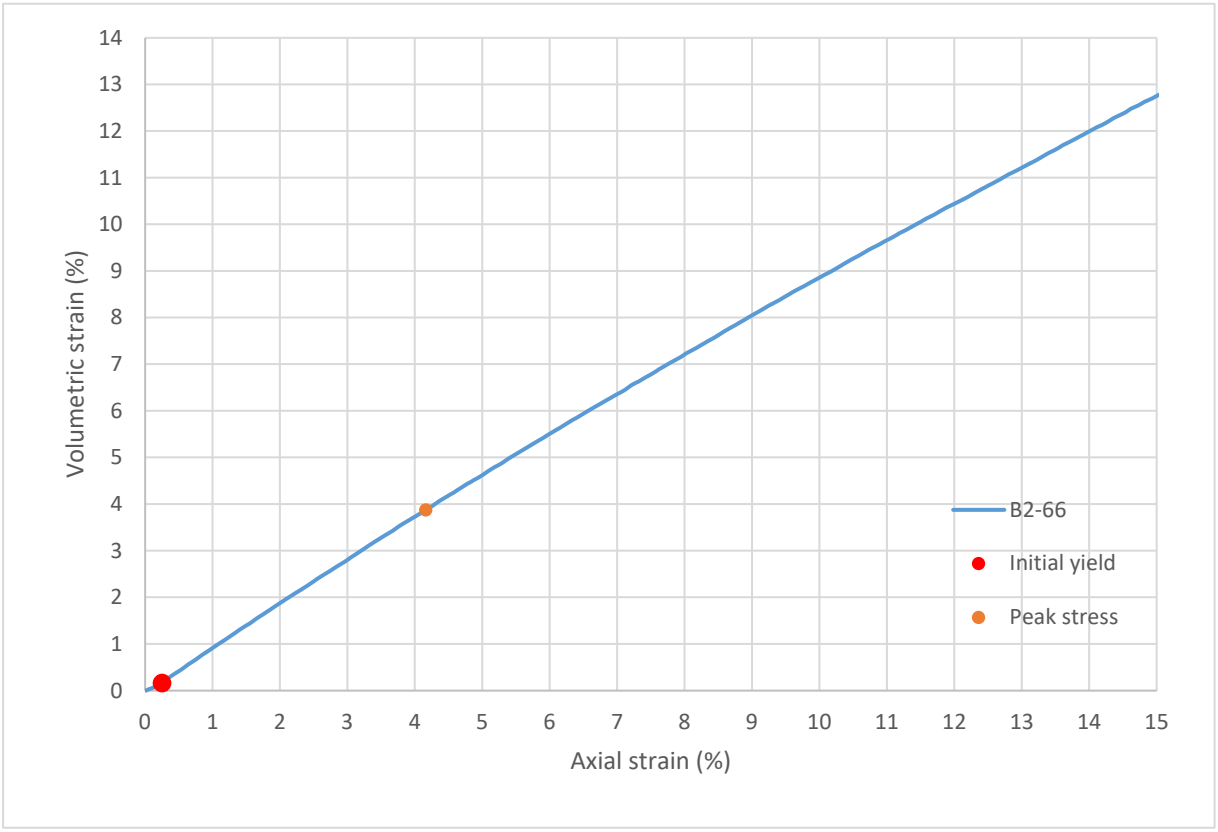

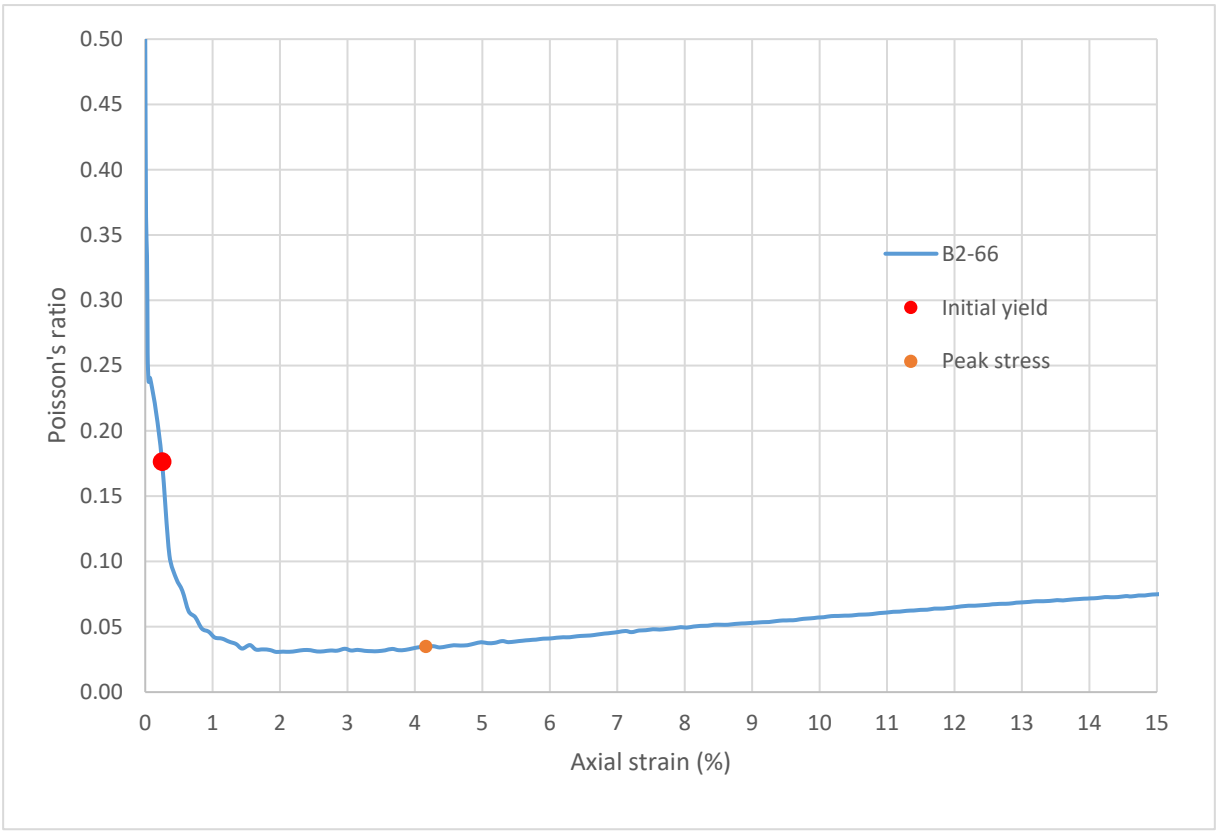

Sample ID:	B2-66

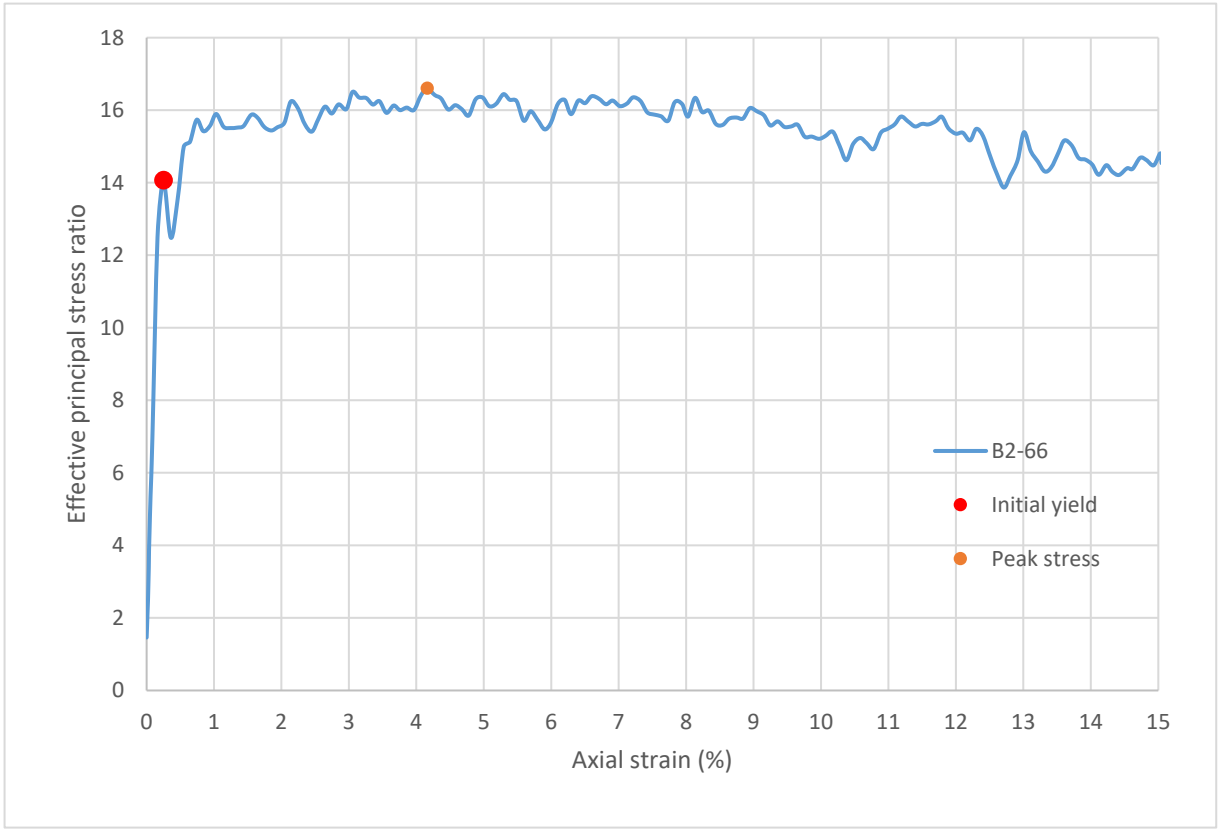

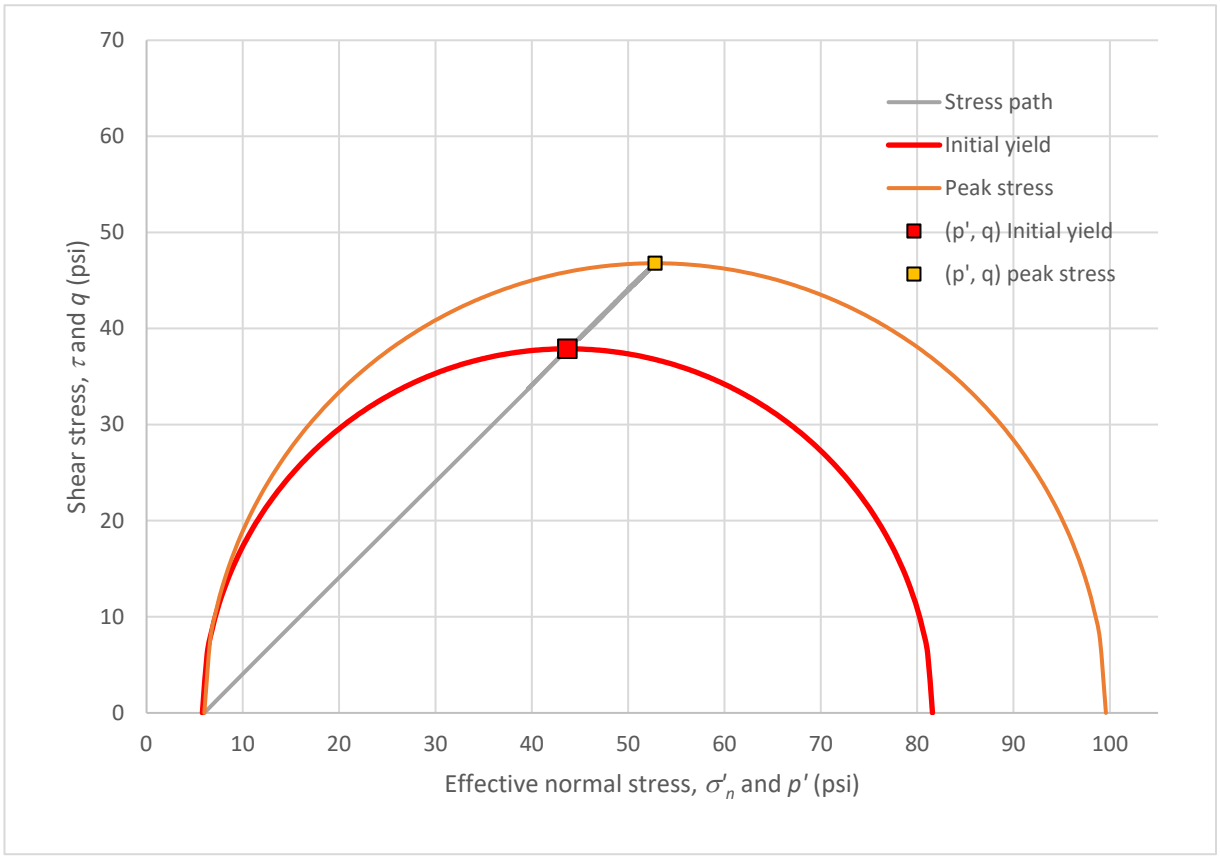

Consolidated-Drained Triaxial Shear, Lightweight Cellular Concrete

Sample ID:	**B2-67**
Height (in):	5.482
Height (mm):	139.3
Diameter (in):	2.964
Diameter (mm)	75.28
Area (in^2):	6.899
Area (mm^2):	4451
Mass (g):	293.46
Weight (lb):	0.6470
Weight (kN):	0.002878
Volume (in^3):	37.82
Volume (mm^3):	619795
Density (g/mm^3):	0.0004735
Density (kg/m^3):	473.5
Unit weight (pcf):	**29.56**
Dry unit weight (pcf);	**19.91**
Unit Weight (kN/m^3):	4.643
Wet mass + tare (g):	403.19
Dry mass + tare (g):	312.10
Tare (g):	124.08
Water content (%)	**48.45**
Saturation (%):	**17.55**
H:D ratio:	1.850
Age (days):	1073
Treatment:	D1

Strain rate (%/min):	0.2
Mean σ'_3 (psi):	11.9
Initial modulus (psi):	20949
Initial yield	
Time to failure (min):	2.4
Axial strain at failure (%):	0.470
σ'_1 (psi):	64.40
σ'_3 (psi):	11.78
σ'_1 -σ'_3 (psi):	52.62
σ'_1 / σ'_3:	5.47
p' (psi):	38.09
q (psi):	26.31
Volumetric strain (%):	0.152
Poisson's ratio:	0.338
Peak stress	
Time to failure (min):	46.5
Axial strain at failure (%):	9.301
σ'_1 (psi):	76.25
σ'_3 (psi):	11.98
σ'_1 -σ'_3 (psi):	64.27
σ'_1 / σ'_3:	6.37
p' (psi):	44.11
q (psi):	32.14
Volumetric strain (%):	8.309
Poisson's ratio:	0.053

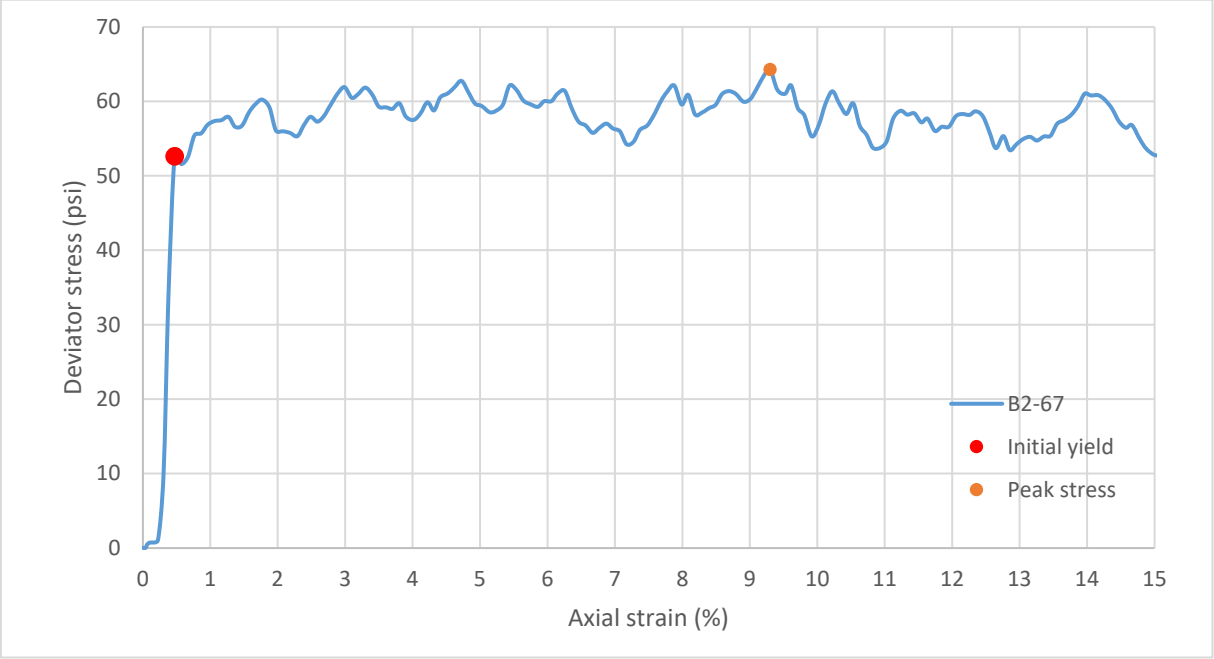

Sample ID:	B2-67

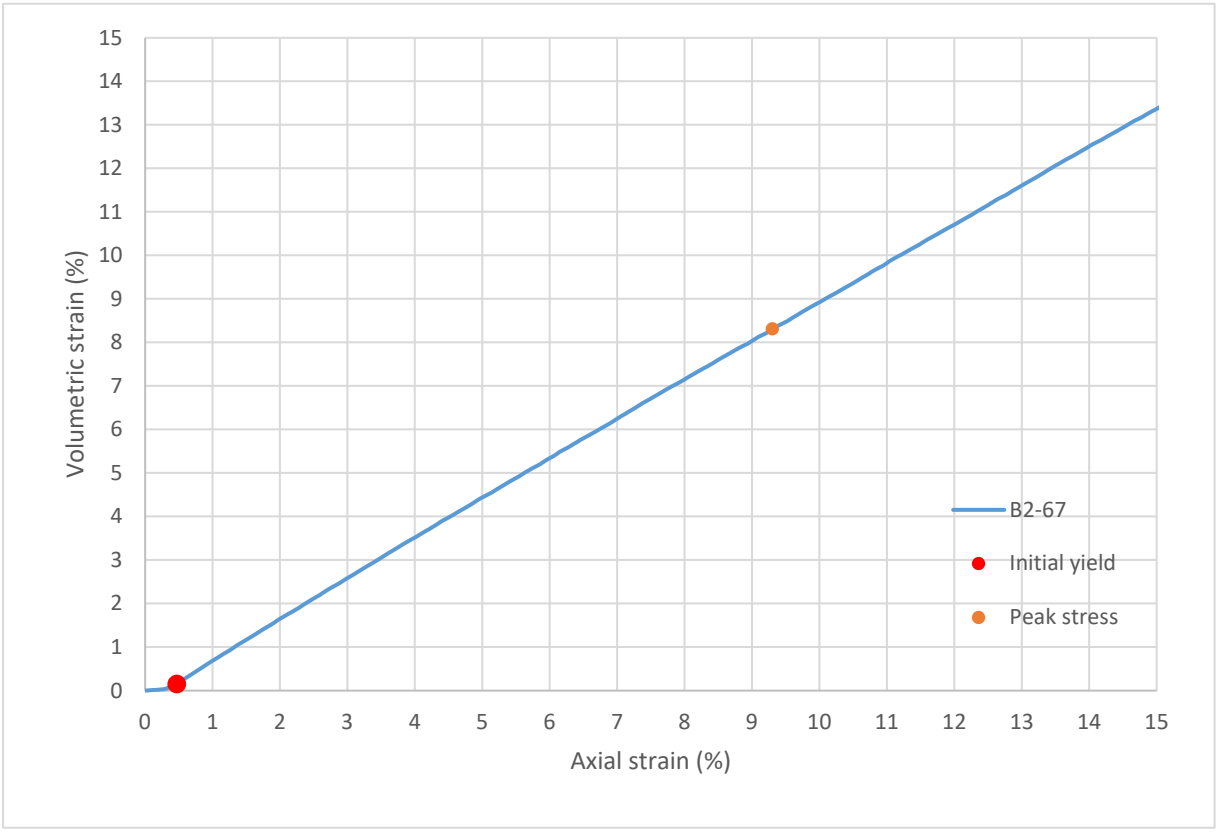

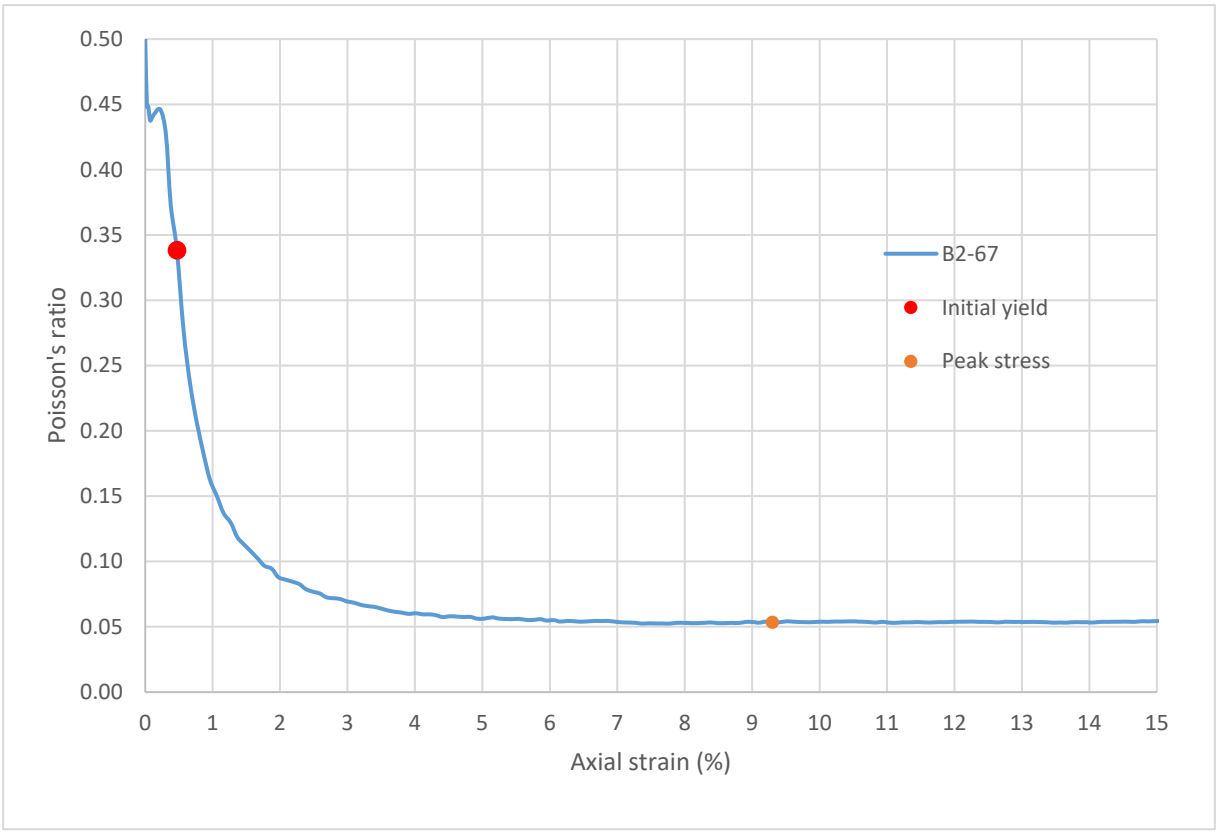

Sample ID:	B2-67

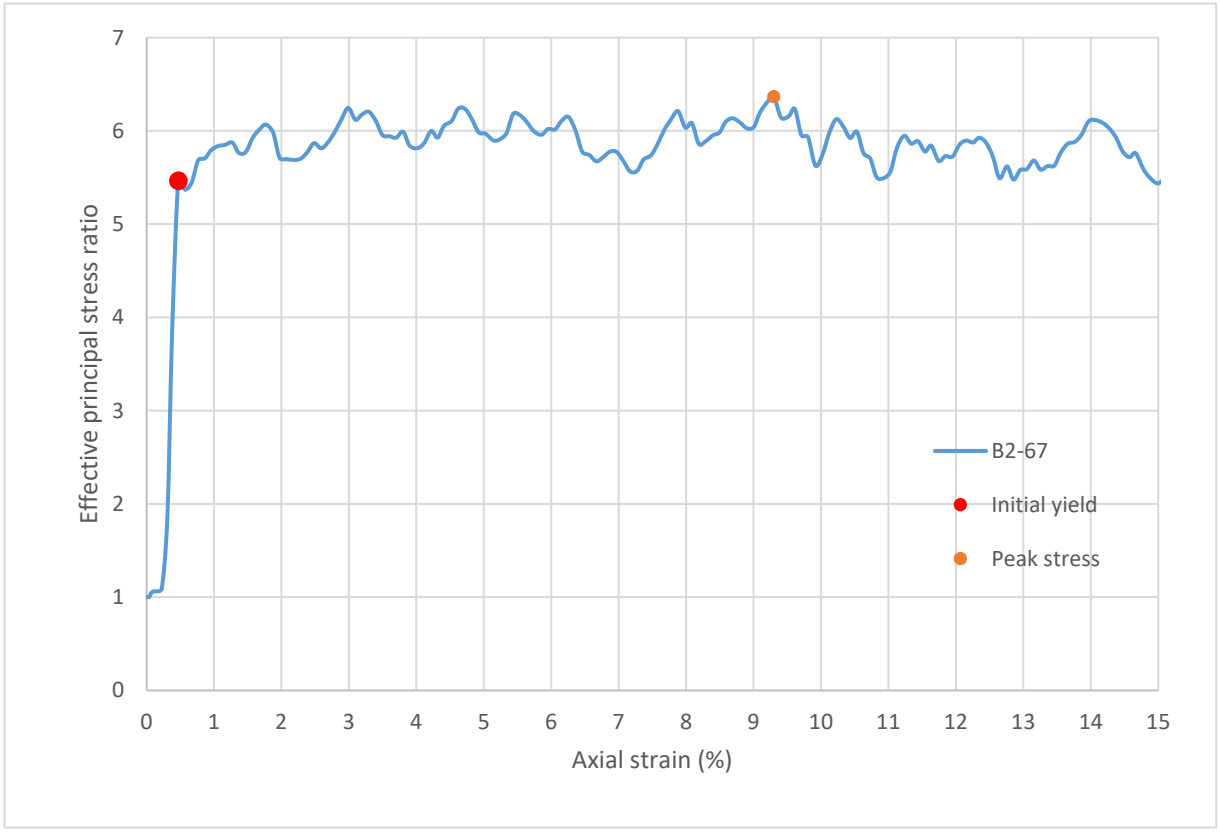

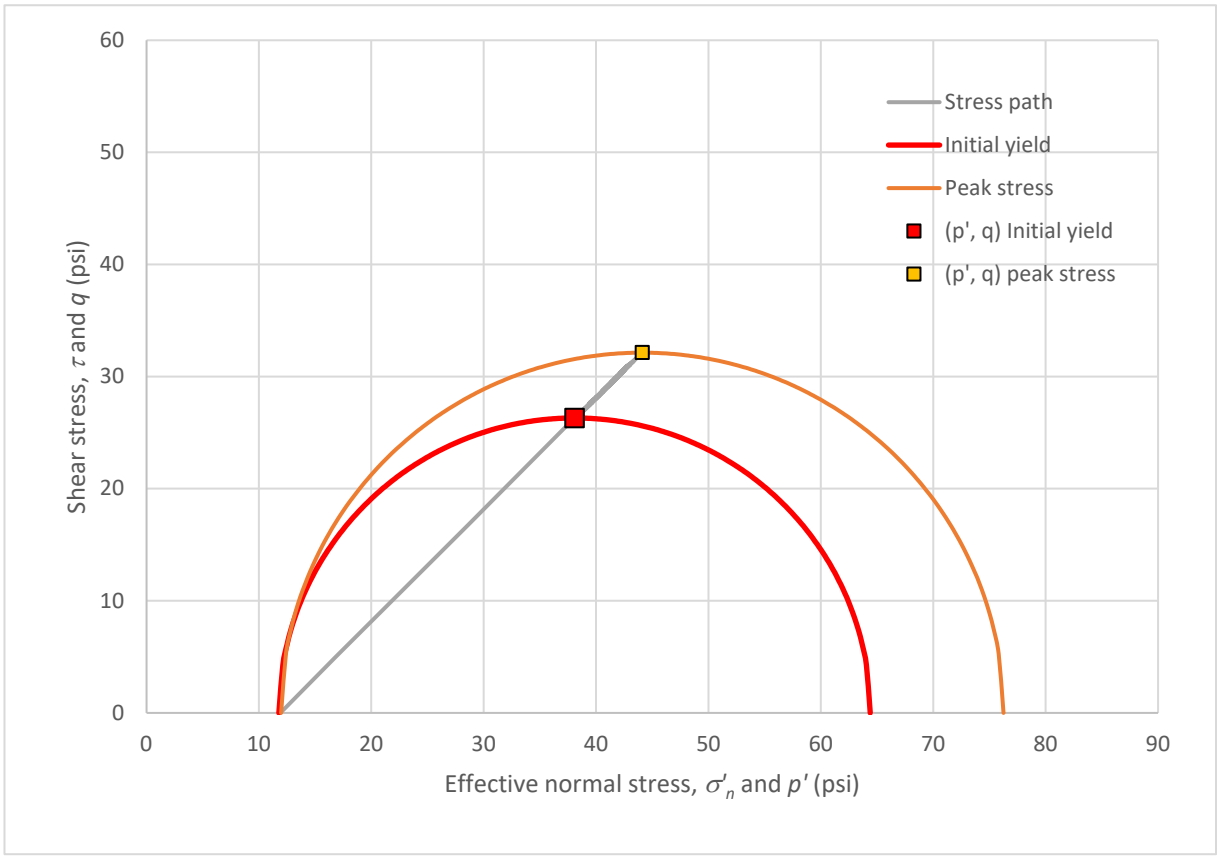

Consolidated-Drained Triaxial Shear, Lightweight Cellular Concrete

Sample ID:	**B2-68**
Height (in):	5.519
Height (mm):	140.2
Diameter (in):	2.962
Diameter (mm)	75.24
Area (in^2):	6.891
Area (mm^2):	4446
Mass (g):	295.76
Weight (lb):	0.6520
Weight (kN):	0.002900
Volume (in^3):	38.03
Volume (mm^3):	623276
Density (g/mm^3):	0.0004745
Density (kg/m^3):	474.5
Unit weight (pcf):	**29.62**
Dry unit weight (pcf);	**19.84**
Unit Weight (kN/m^3):	4.654
Wet mass + tare (g):	395.90
Dry mass + tare (g):	306.34
Tare (g):	124.62
Water content (%)	**49.28**
Saturation (%):	**17.78**
H:D ratio:	1.863
Age (days):	1072
Treatment:	W1

Strain rate (%/min):	0.2
Mean σ'_3 (psi):	6.0
Initial modulus (psi):	25796
Initial yield	
Time to failure (min):	0.9
Axial strain at failure (%):	0.173
σ'_1 (psi):	50.44
σ'_3 (psi):	5.90
σ'_1 -σ'_3 (psi):	44.54
σ'_1 / σ'_3:	8.55
p' (psi):	28.17
q (psi):	22.27
Volumetric strain (%):	0.097
Poisson's ratio:	0.220
Peak stress	
Time to failure (min):	44.8
Axial strain at failure (%):	8.959
σ'_1 (psi):	82.96
σ'_3 (psi):	6.01
σ'_1 -σ'_3 (psi):	76.95
σ'_1 / σ'_3:	13.79
p' (psi):	44.49
q (psi):	38.47
Volumetric strain (%):	8.094
Poisson's ratio:	0.048

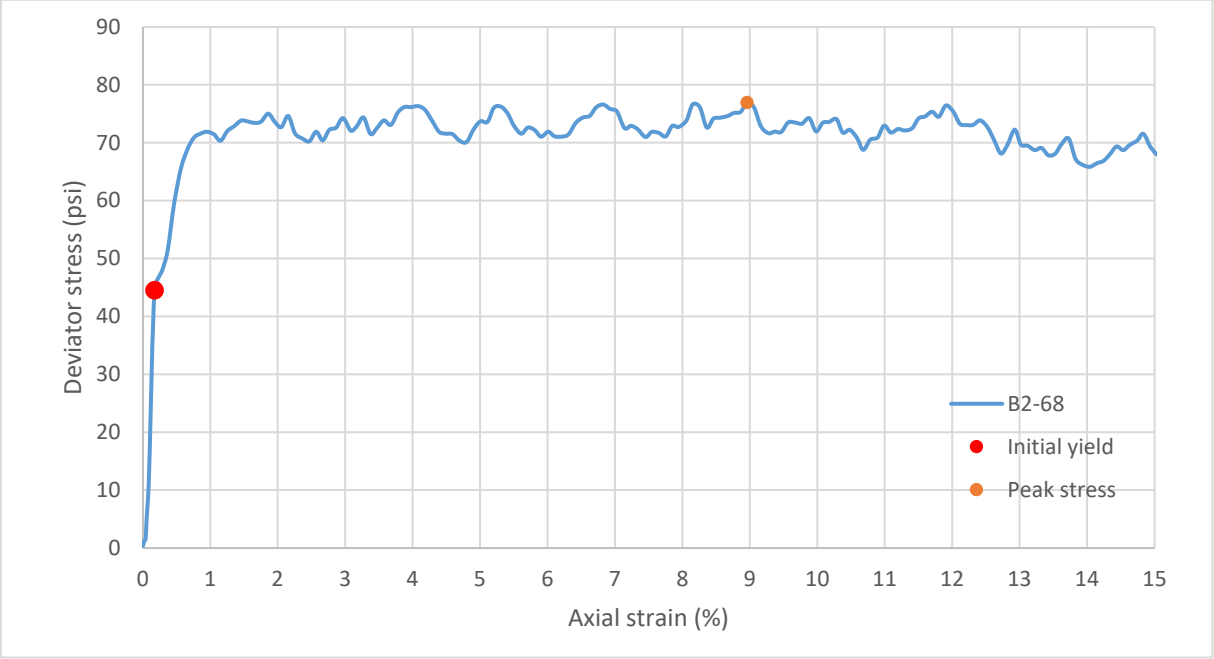

Sample ID:	B2-68

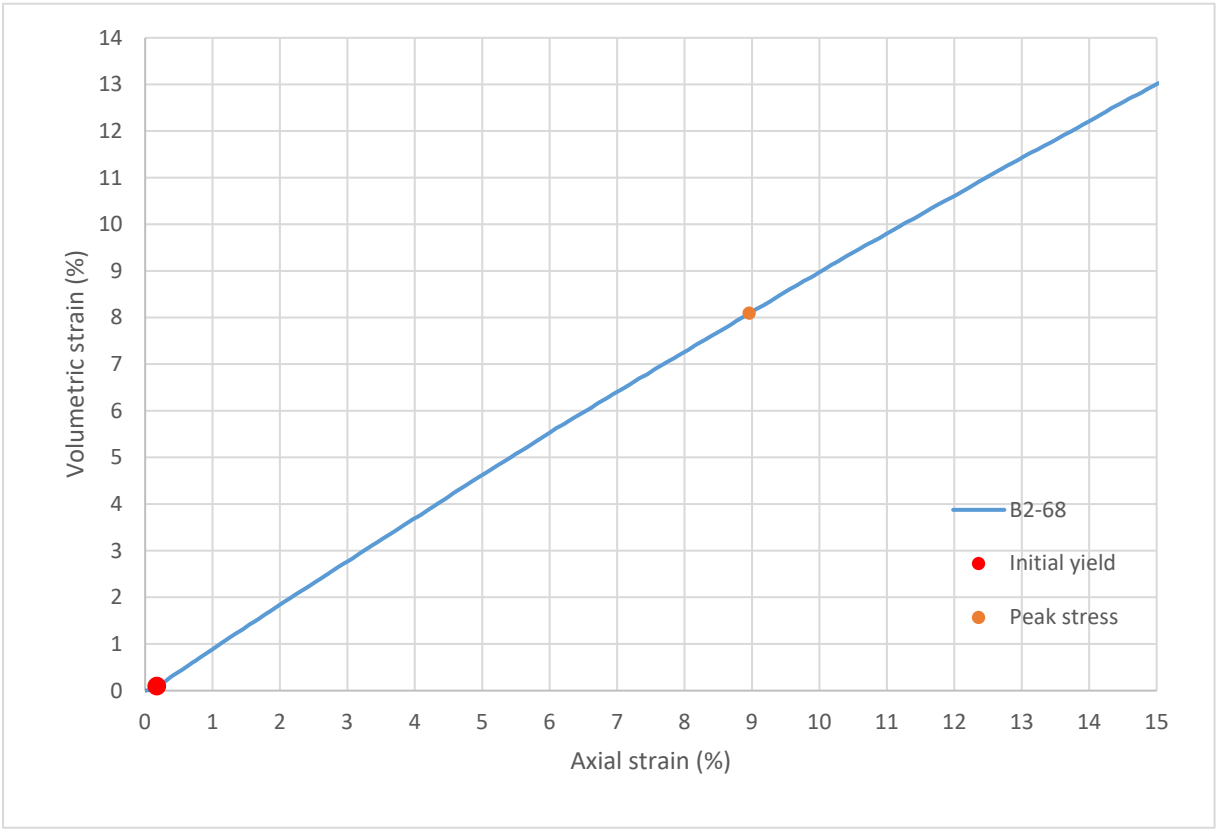

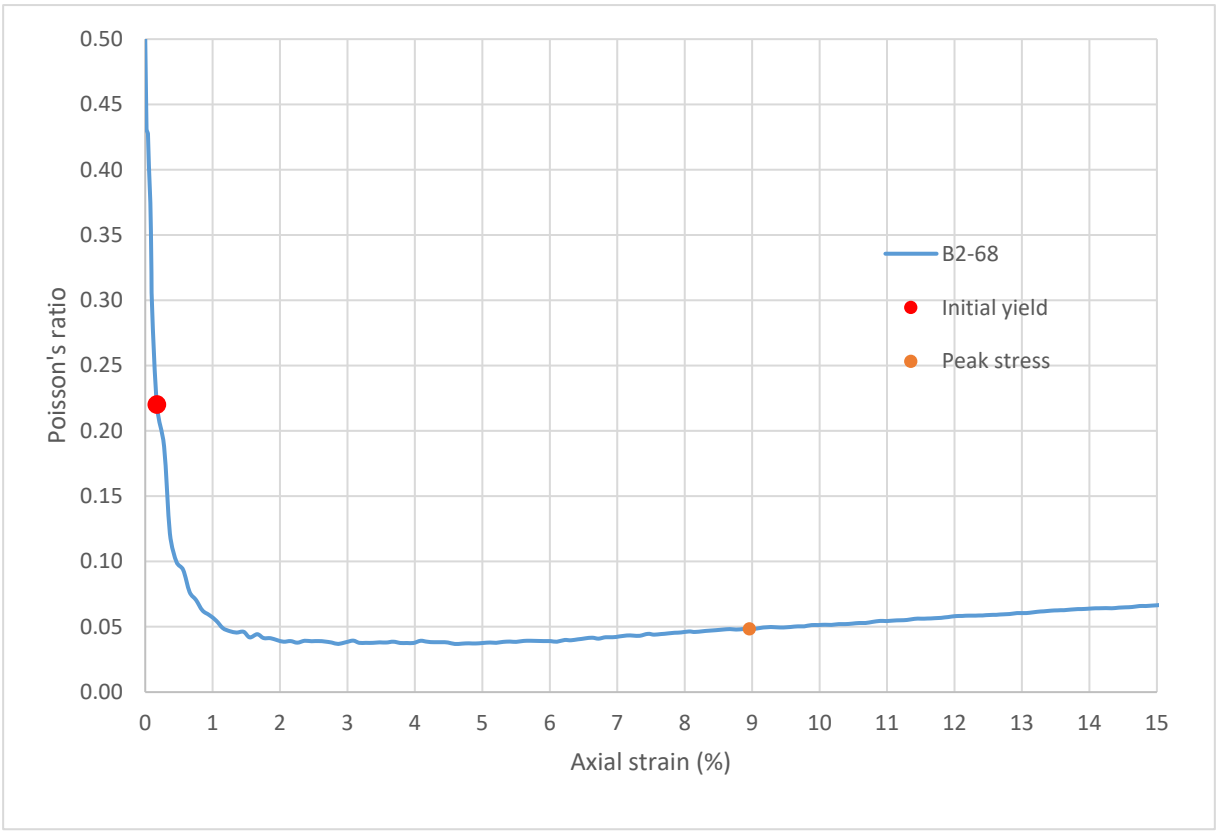

Sample ID:	B2-68

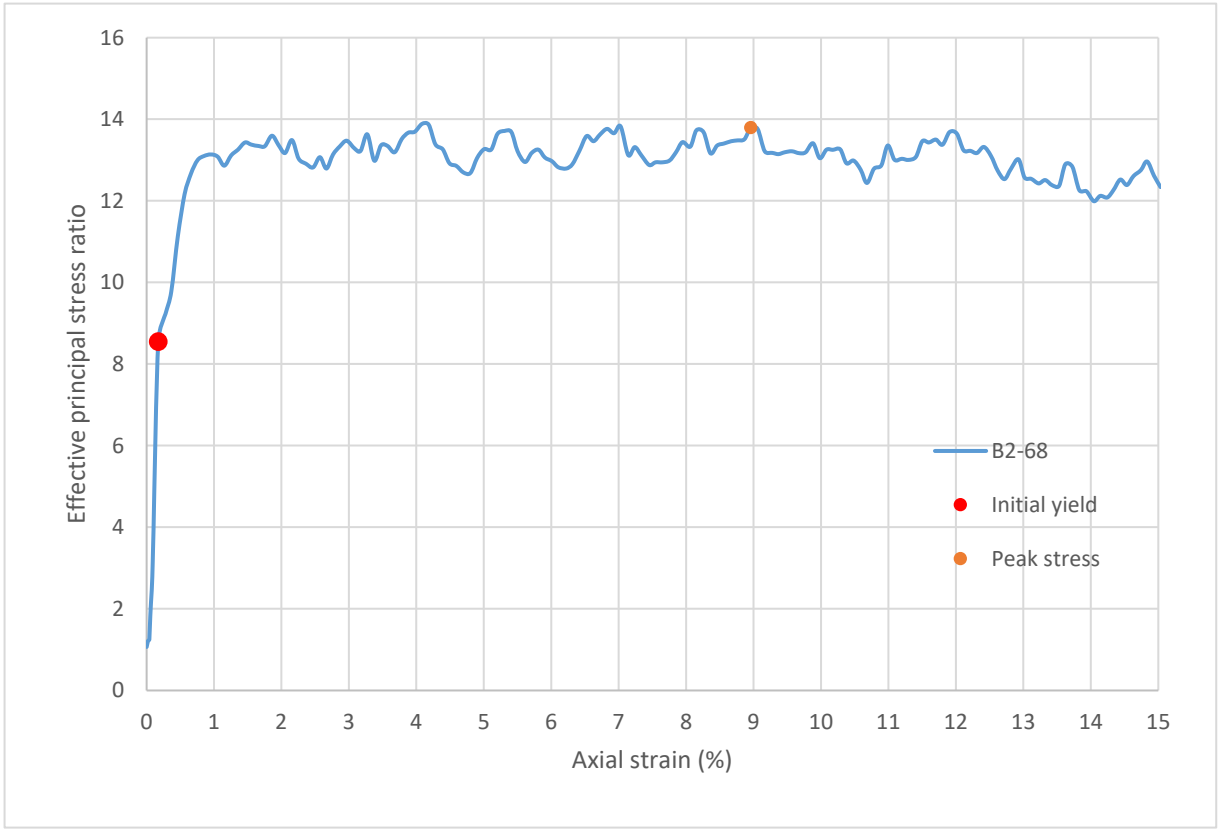

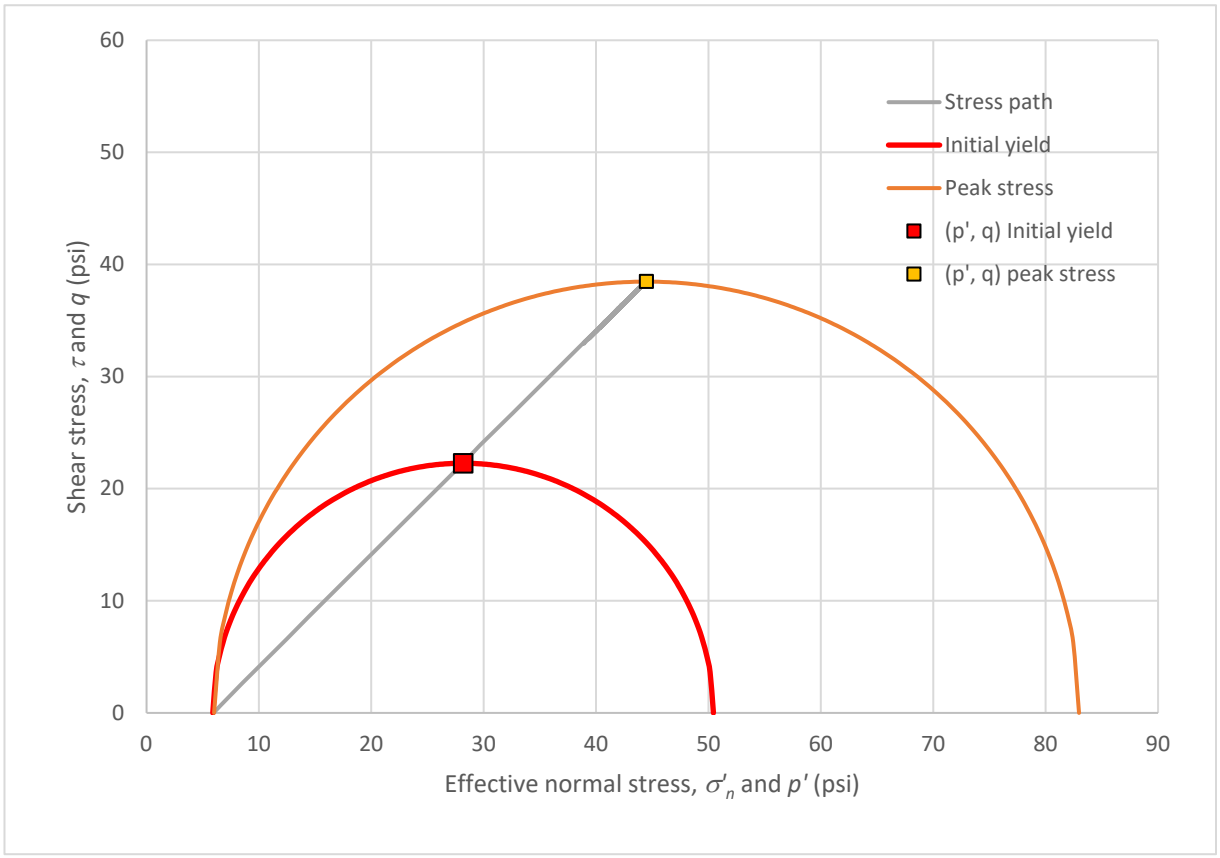

Consolidated-Drained Triaxial Shear, Lightweight Cellular Concrete

Sample ID:	**B2-69**
Height (in):	5.500
Height (mm):	139.7
Diameter (in):	2.941
Diameter (mm)	74.71
Area (in^2):	6.794
Area (mm^2):	4383
Mass (g):	302.71
Weight (lb):	0.6674
Weight (kN):	0.002969
Volume (in^3):	37.37
Volume (mm^3):	612364
Density (g/mm^3):	0.0004943
Density (kg/m^3):	494.3
Unit weight (pcf):	**30.86**
Dry unit weight (pcf);	**20.75**
Unit Weight (kN/m^3):	4.848
Wet mass + tare (g):	363.83
Dry mass + tare (g):	286.37
Tare (g):	127.49
Water content (%)	**48.75**
Saturation (%):	**18.50**
H:D ratio:	1.870
Age (days):	1072
Treatment:	W1

Strain rate (%/min):	0.2
Mean σ'_3 (psi):	11.9
Initial modulus (psi):	30946
Initial yield	
Time to failure (min):	0.8
Axial strain at failure (%):	0.169
σ'_1 (psi):	64.04
σ'_3 (psi):	11.83
σ'_1 -σ'_3 (psi):	52.20
σ'_1 / σ'_3:	5.41
p' (psi):	37.93
q (psi):	26.10
Volumetric strain (%):	0.094
Poisson's ratio:	0.221
Peak stress	
Time to failure (min):	60.2
Axial strain at failure (%):	12.034
σ'_1 (psi):	84.73
σ'_3 (psi):	12.01
σ'_1 -σ'_3 (psi):	72.72
σ'_1 / σ'_3:	7.06
p' (psi):	48.37
q (psi):	36.36
Volumetric strain (%):	11.113
Poisson's ratio:	0.038

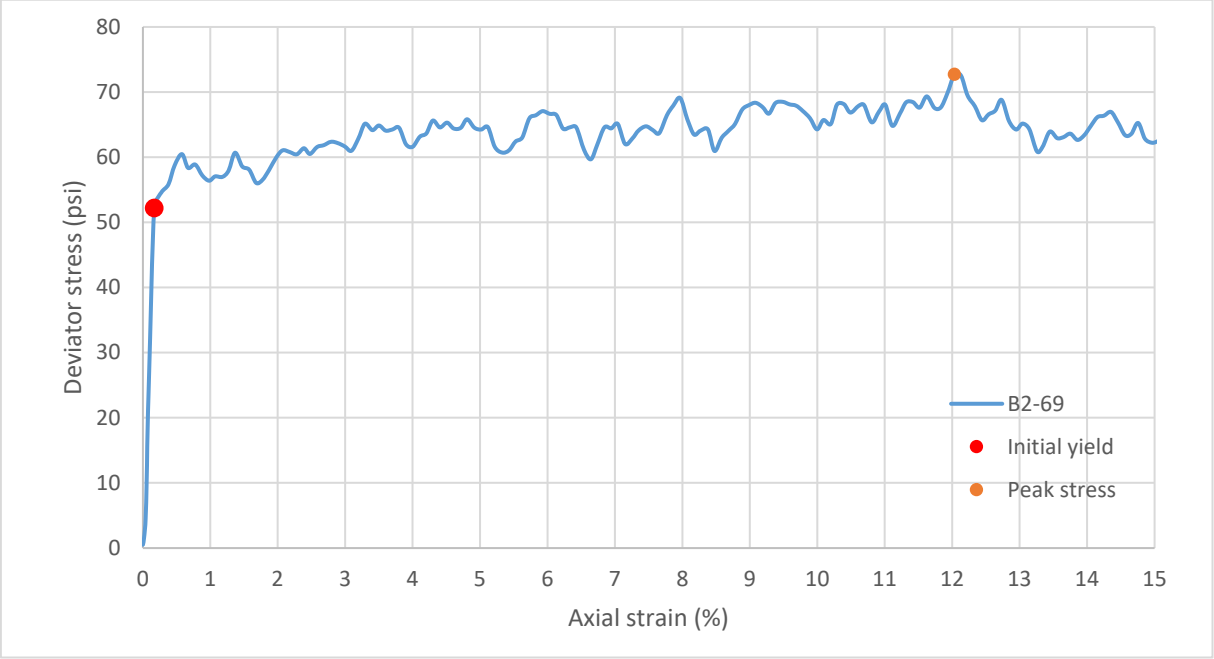

Sample ID:	B2-69

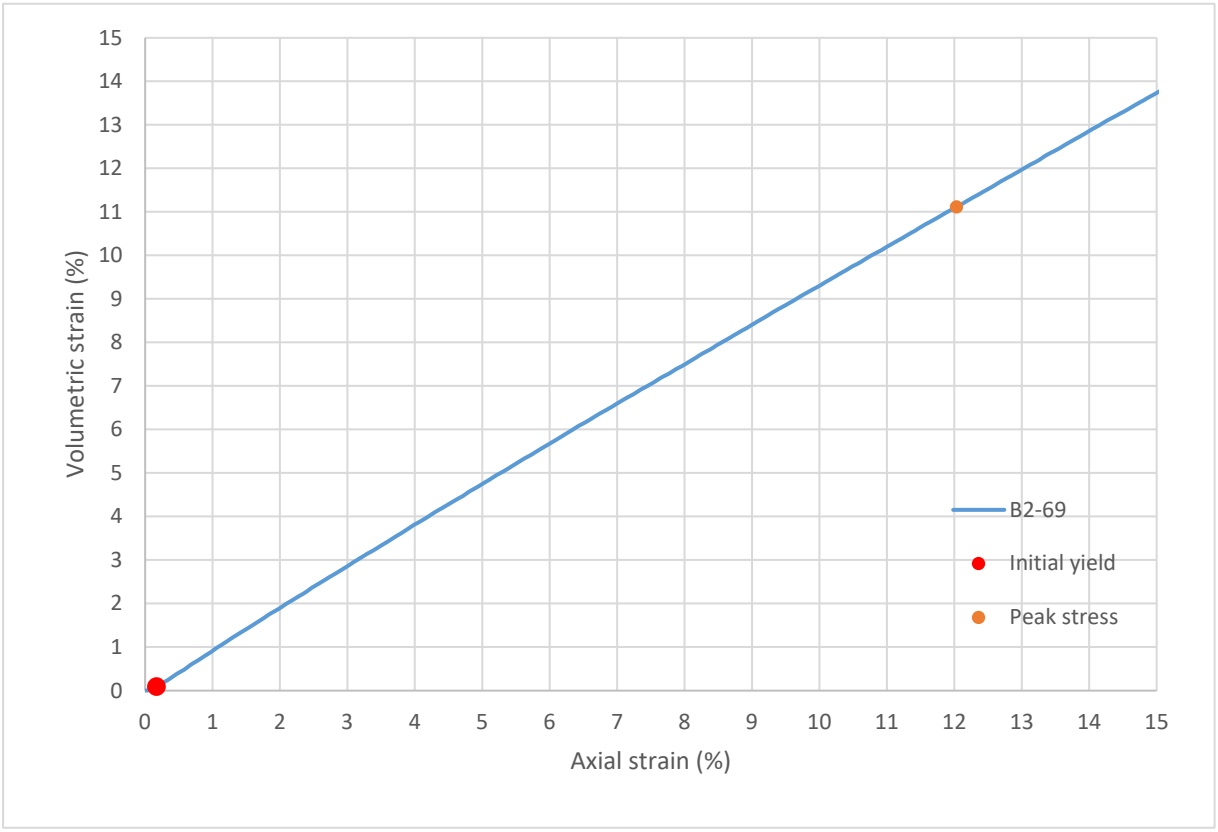

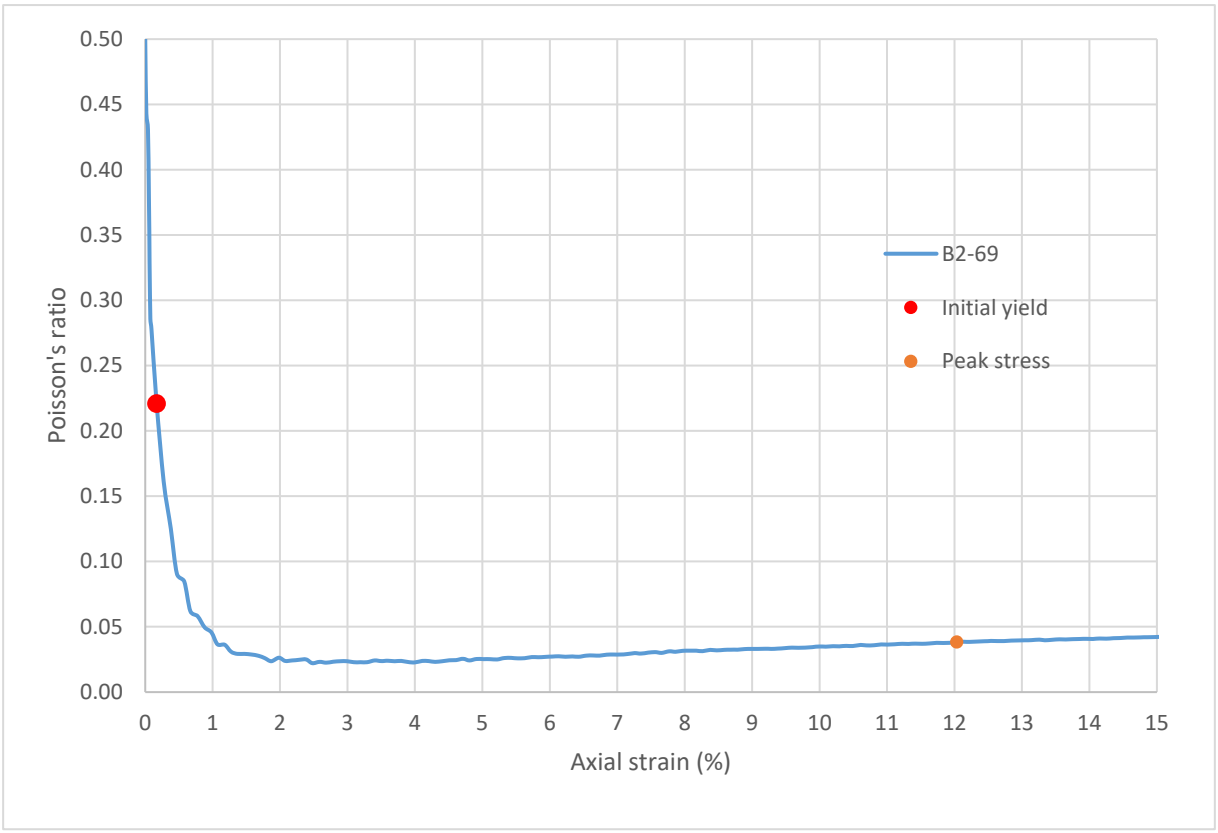

Sample ID:	B2-69

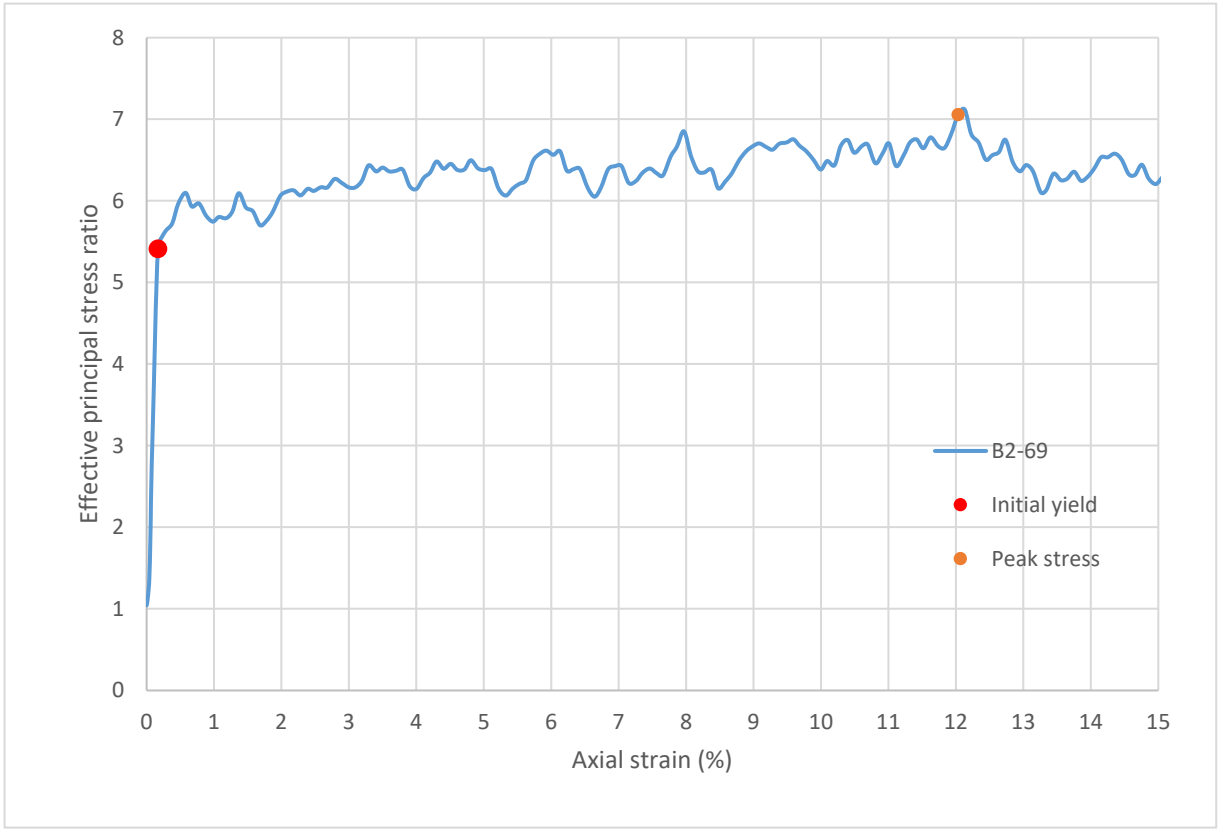

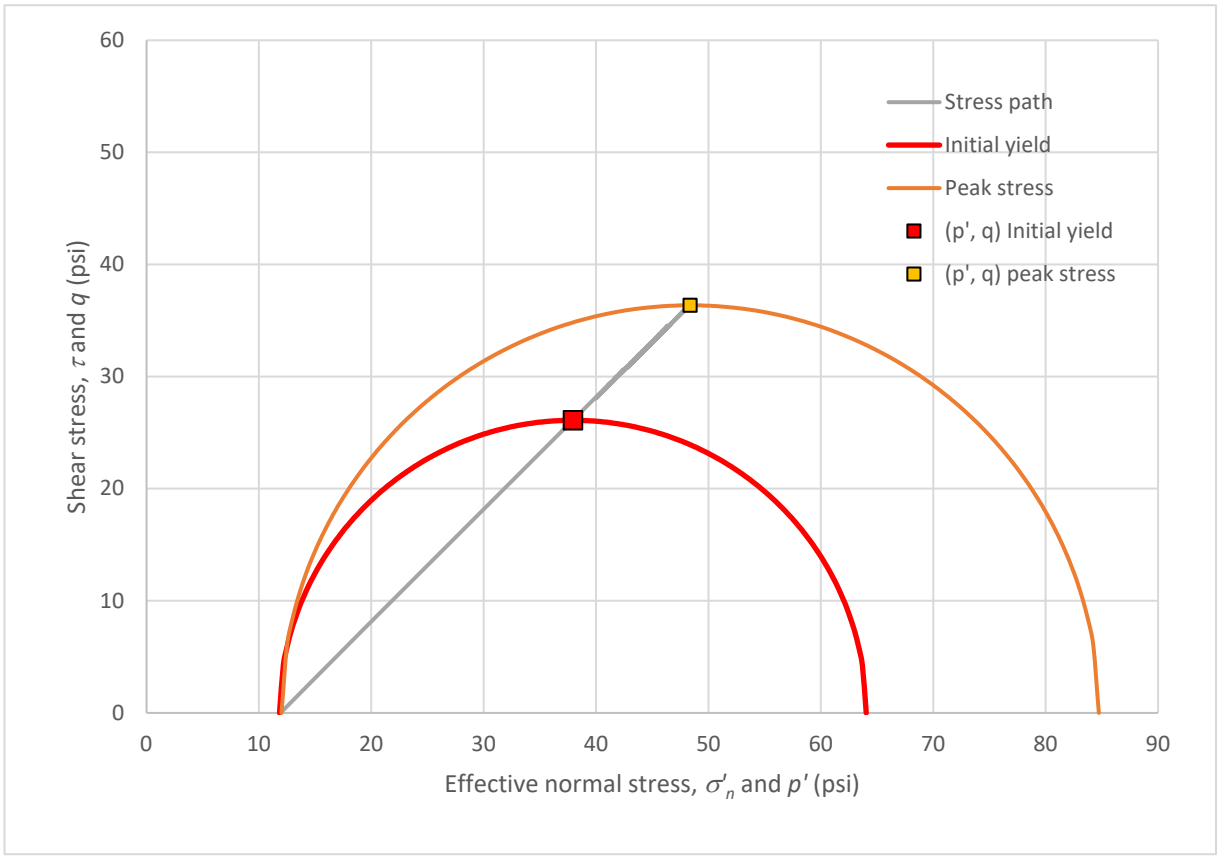

Consolidated-Drained Triaxial Shear, Lightweight Cellular Concrete

Sample ID:	**B2-75**
Height (in):	5.443
Height (mm):	138.3
Diameter (in):	2.953
Diameter (mm)	75.01
Area (in^2):	6.850
Area (mm^2):	4420
Mass (g):	245.42
Weight (lb):	0.5411
Weight (kN):	0.002407
Volume (in^3):	37.29
Volume (mm^3):	611056
Density (g/mm^3):	0.0004016
Density (kg/m^3):	401.6
Unit weight (pcf):	**25.07**
Dry unit weight (pcf);	**19.53**
Unit Weight (kN/m^3):	3.939
Wet mass + tare (g):	358.08
Dry mass + tare (g):	306.96
Tare (g):	126.81
Water content (%)	**28.38**
Saturation (%):	**10.05**
H:D ratio:	1.843
Age (days):	1076
Treatment:	M5

Strain rate (%/min):	0.2
Mean σ'_3 (psi):	3.0
Initial modulus (psi):	35072
Initial yield	
Time to failure (min):	1.7
Axial strain at failure (%):	0.335
σ'_1 (psi):	120.62
σ'_3 (psi):	2.97
σ'_1 -σ'_3 (psi):	117.65
σ'_1 / σ'_3:	40.64
p' (psi):	61.79
q (psi):	58.82
Volumetric strain (%):	0.201
Poisson's ratio:	0.201
Peak stress	
Time to failure (min):	1.7
Axial strain at failure (%):	0.335
σ'_1 (psi):	120.62
σ'_3 (psi):	2.97
σ'_1 -σ'_3 (psi):	117.65
σ'_1 / σ'_3:	40.64
p' (psi):	61.79
q (psi):	58.82
Volumetric strain (%):	0.201
Poisson's ratio:	0.201

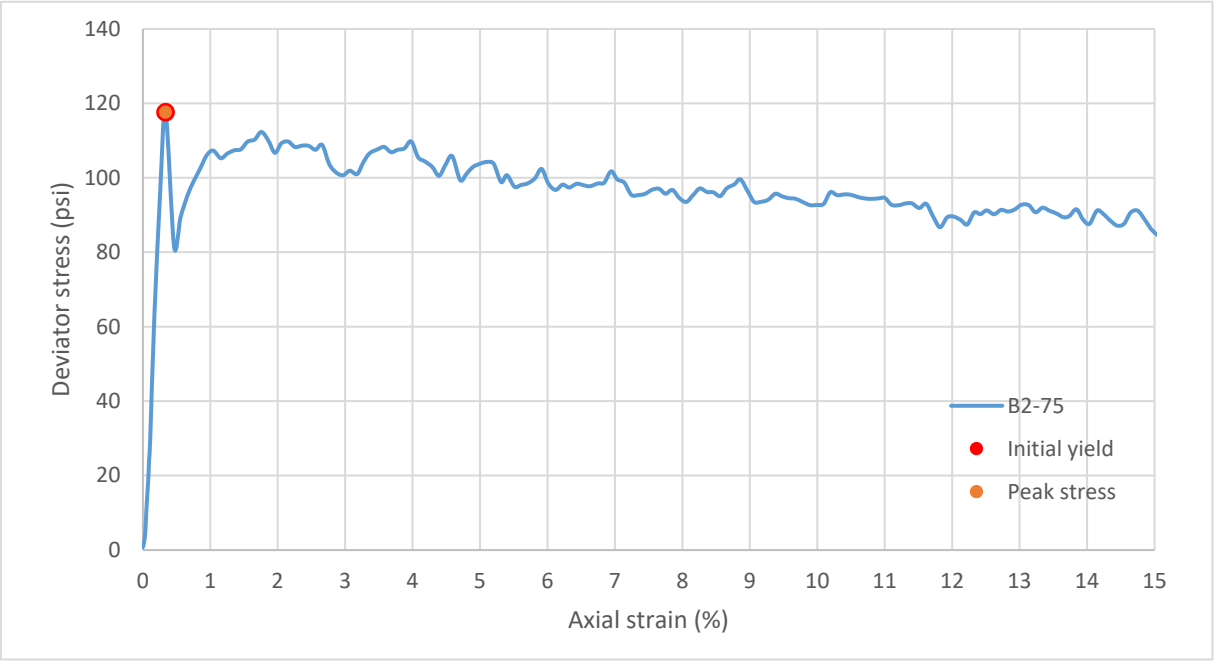

Sample ID:	B2-75

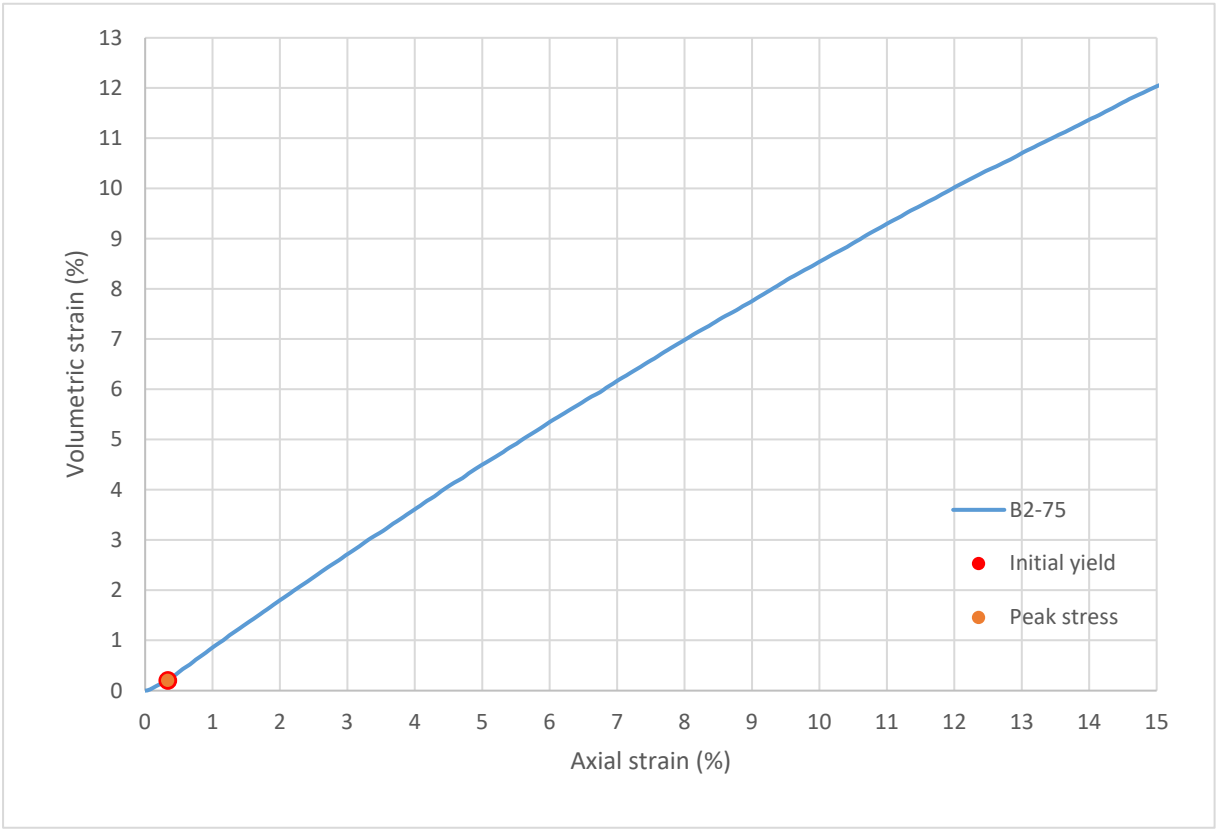

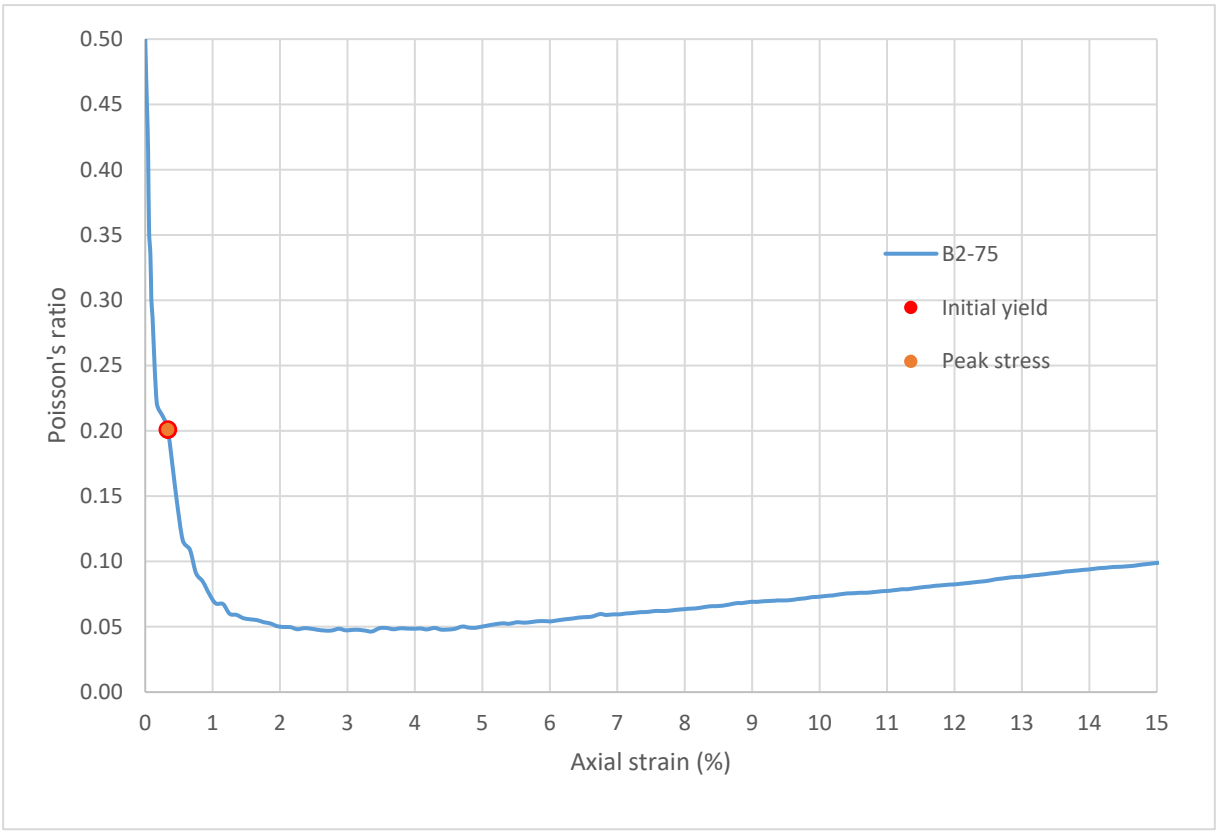

Sample ID:	B2-75

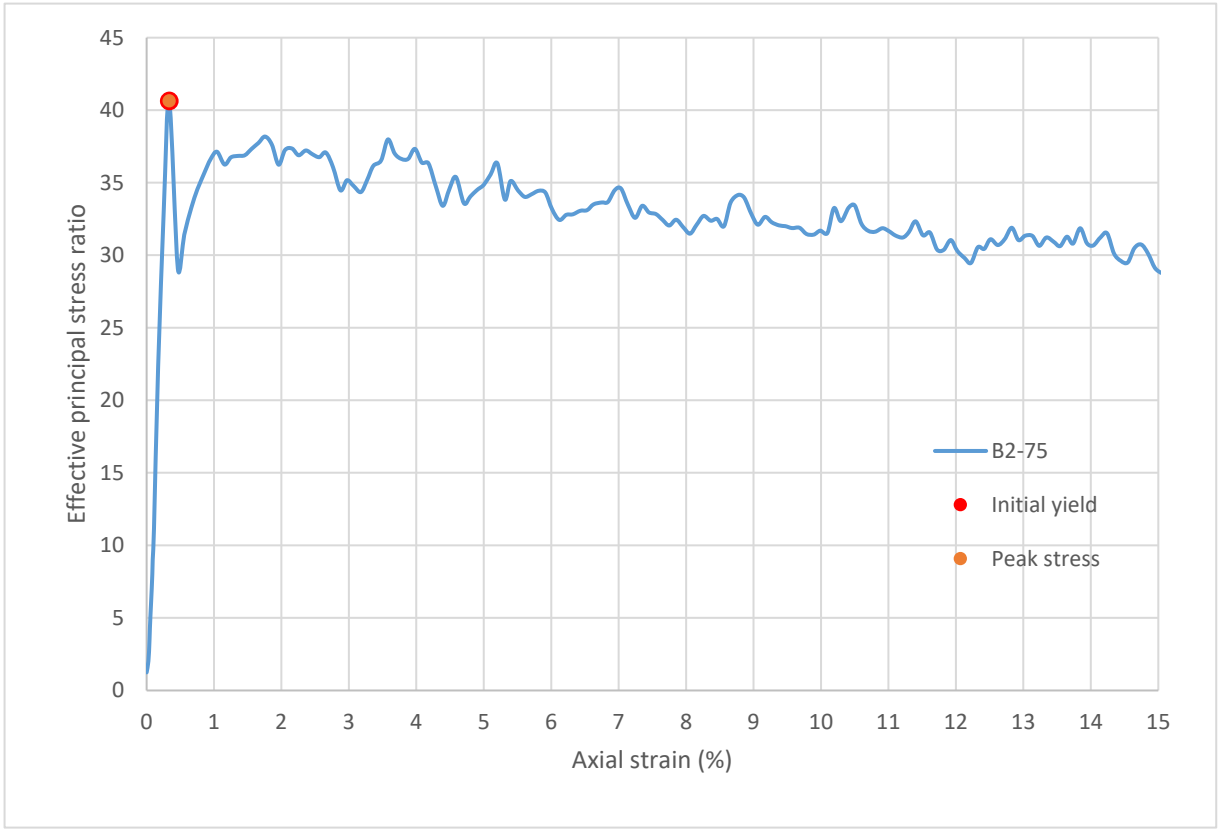

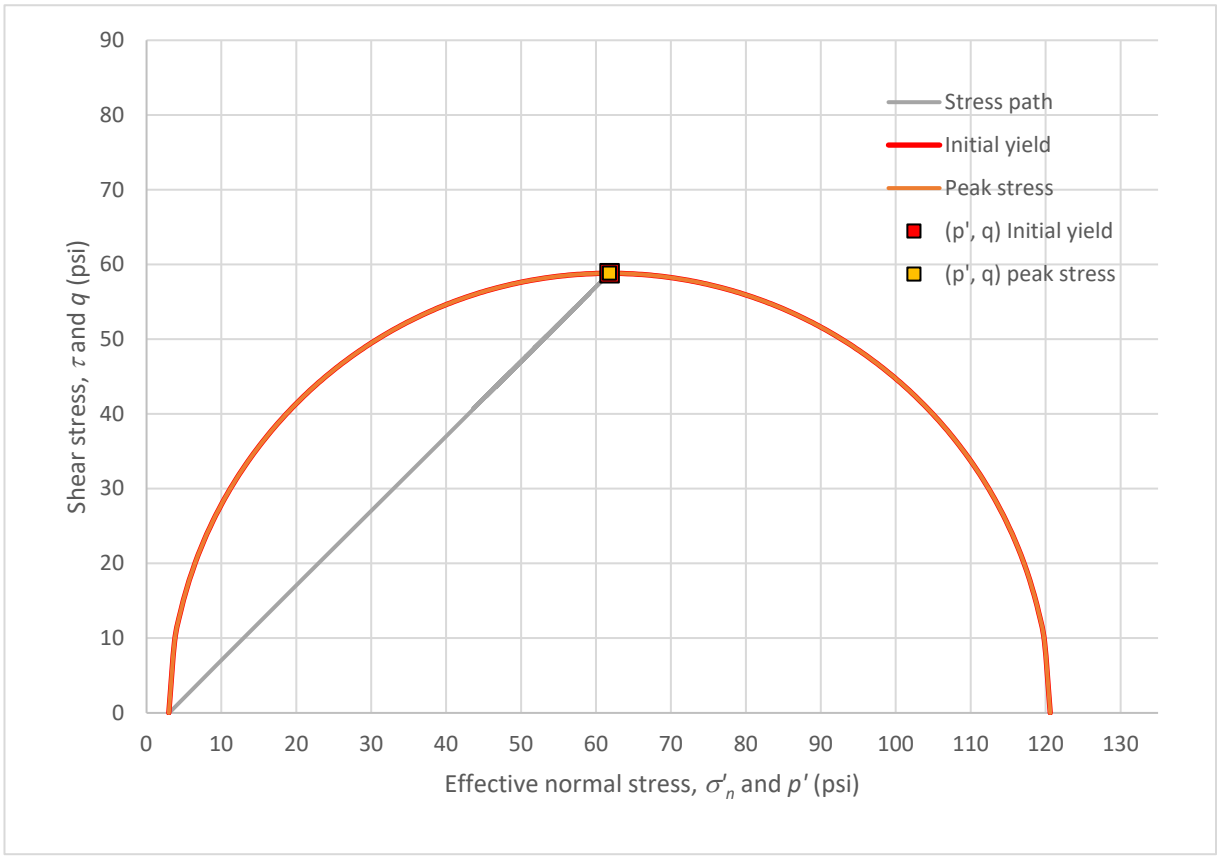

Consolidated-Drained Triaxial Shear, Lightweight Cellular Concrete

Sample ID:	**B2-76**
Height (in):	5.475
Height (mm):	139.1
Diameter (in):	2.955
Diameter (mm)	75.05
Area (in^2):	6.856
Area (mm^2):	4423
Mass (g):	248.27
Weight (lb):	0.5473
Weight (kN):	0.002435
Volume (in^3):	37.54
Volume (mm^3):	615157
Density (g/mm^3):	0.0004036
Density (kg/m^3):	403.6
Unit weight (pcf):	**25.20**
Dry unit weight (pcf);	**19.76**
Unit Weight (kN/m^3):	3.958
Wet mass + tare (g):	364.30
Dry mass + tare (g):	313.32
Tare (g):	128.16
Water content (%)	**27.53**
Saturation (%):	**9.88**
H:D ratio:	1.853
Age (days):	1076
Treatment:	M5

Strain rate (%/min):	0.2
Mean σ'_3 (psi):	3.0
Initial modulus (psi):	26062
Initial yield	
Time to failure (min):	1.8
Axial strain at failure (%):	0.352
σ'_1 (psi):	94.70
σ'_3 (psi):	2.90
σ'_1 -σ'_3 (psi):	91.81
σ'_1 / σ'_3:	32.71
p' (psi):	48.80
q (psi):	45.90
Volumetric strain (%):	0.249
Poisson's ratio:	0.146
Peak stress	
Time to failure (min):	13.8
Axial strain at failure (%):	2.757
σ'_1 (psi):	112.02
σ'_3 (psi):	2.99
σ'_1 -σ'_3 (psi):	109.03
σ'_1 / σ'_3:	37.48
p' (psi):	57.50
q (psi):	54.51
Volumetric strain (%):	2.469
Poisson's ratio:	0.052

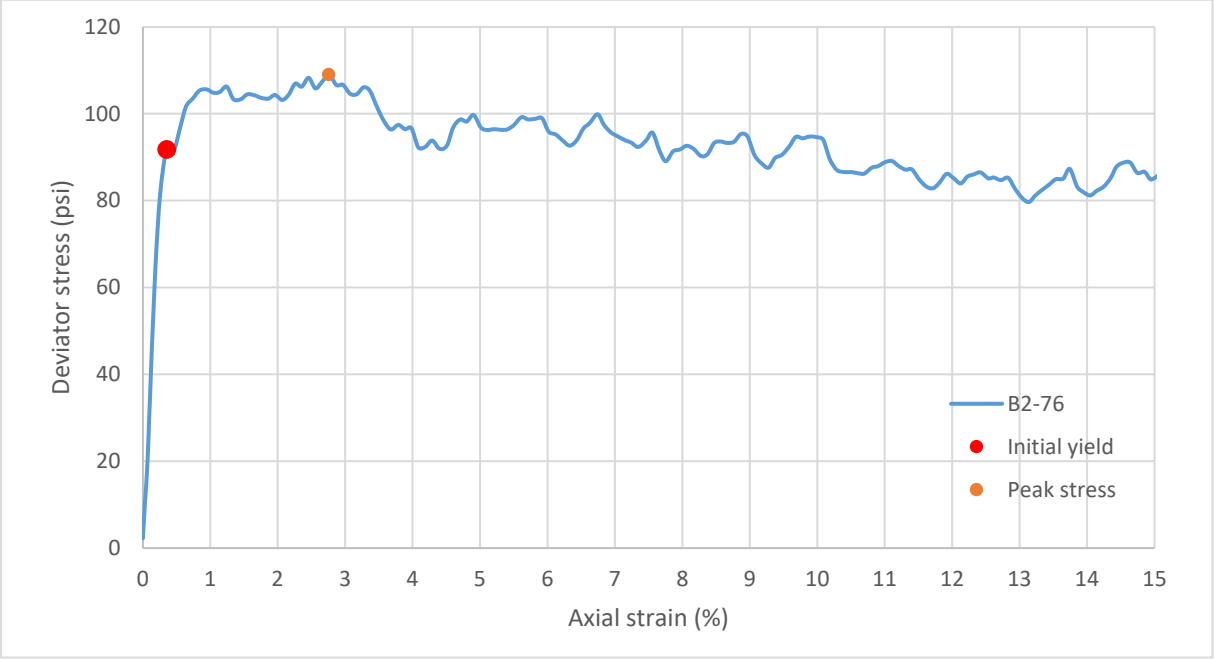

Sample ID:	B2-76

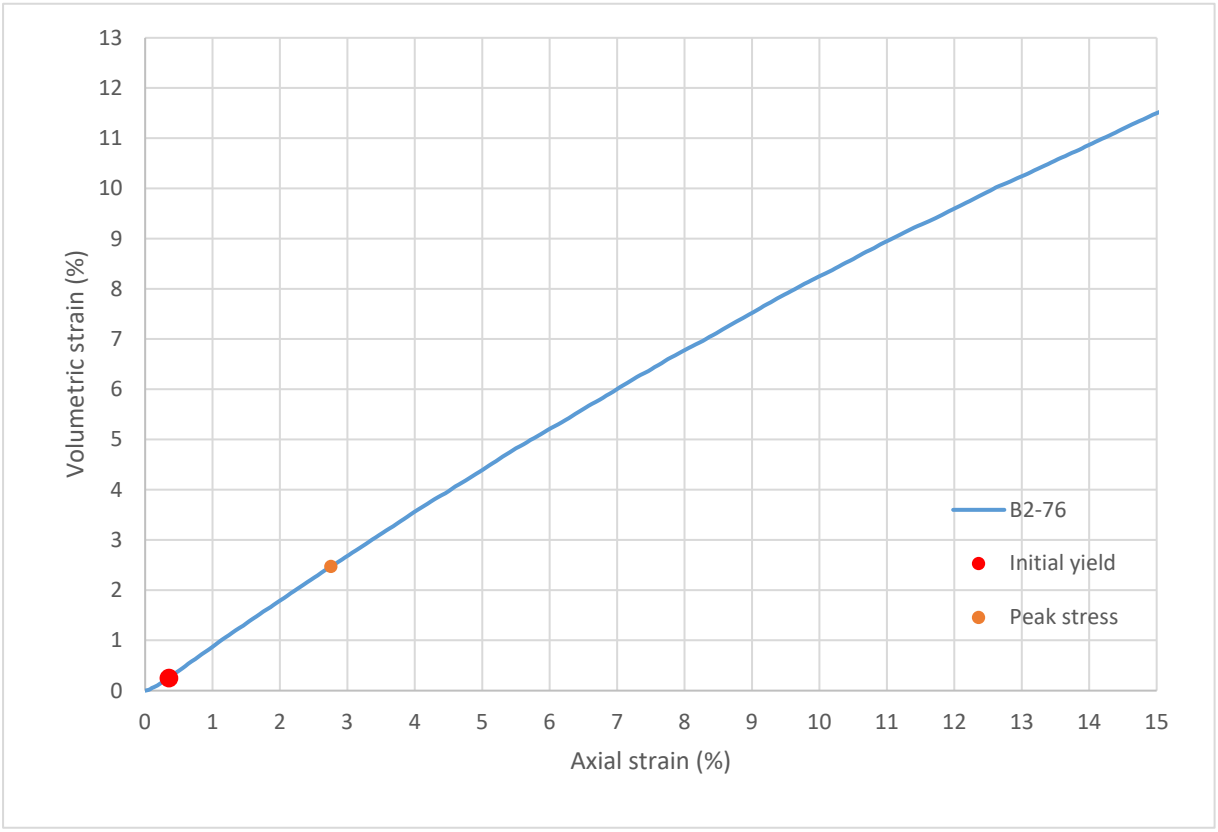

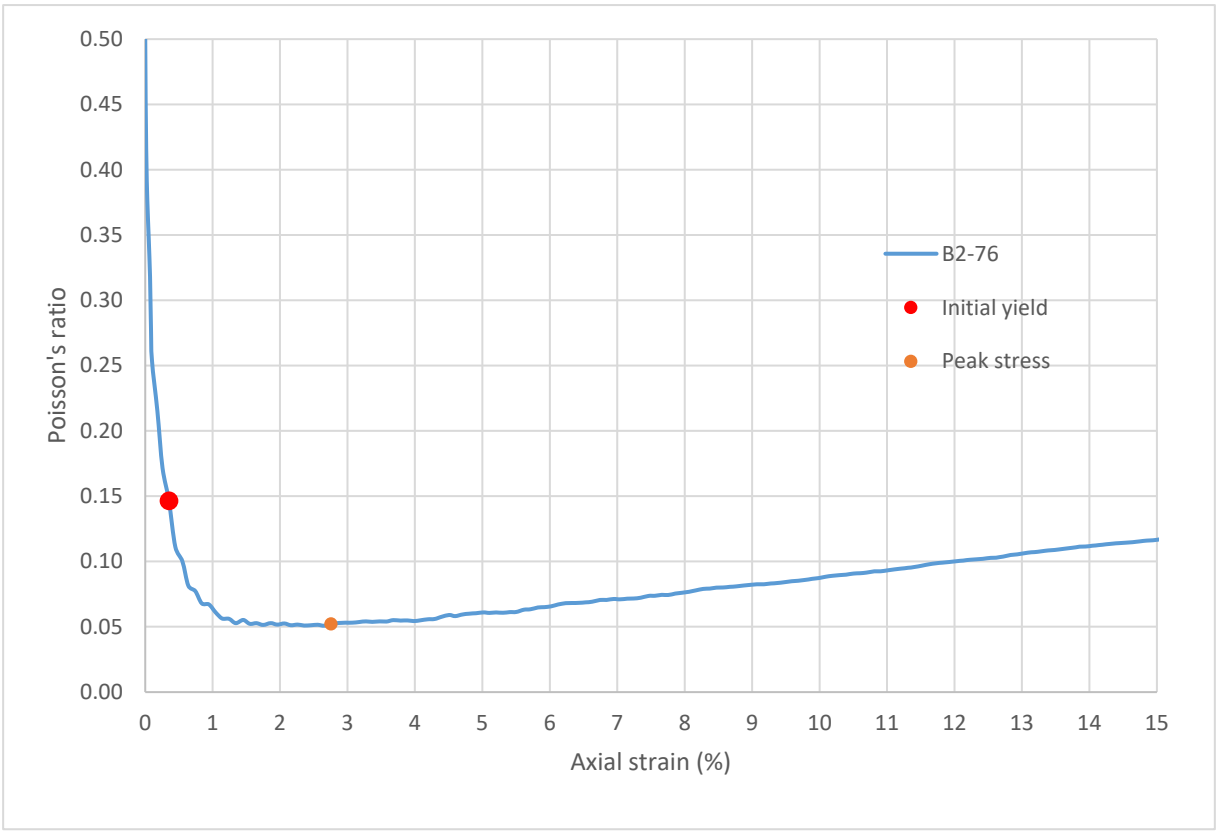

Sample ID:	B2-76

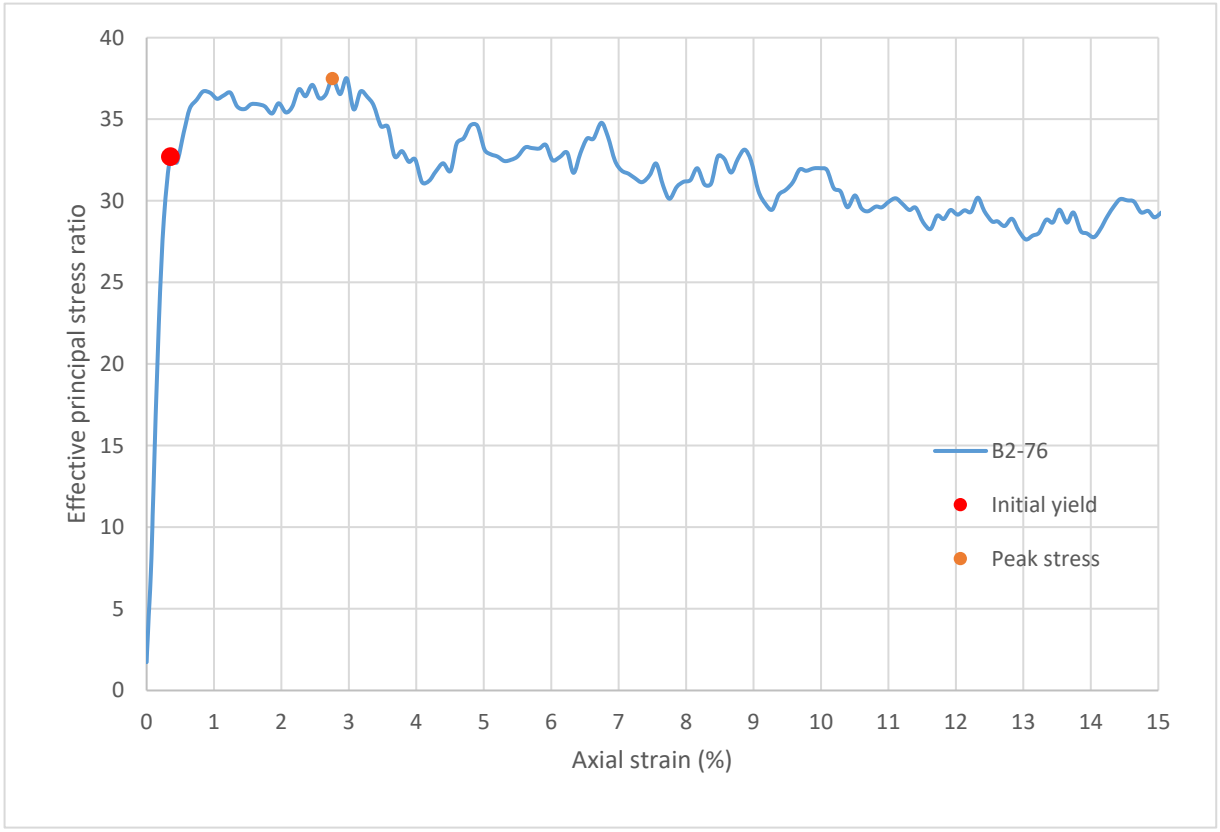

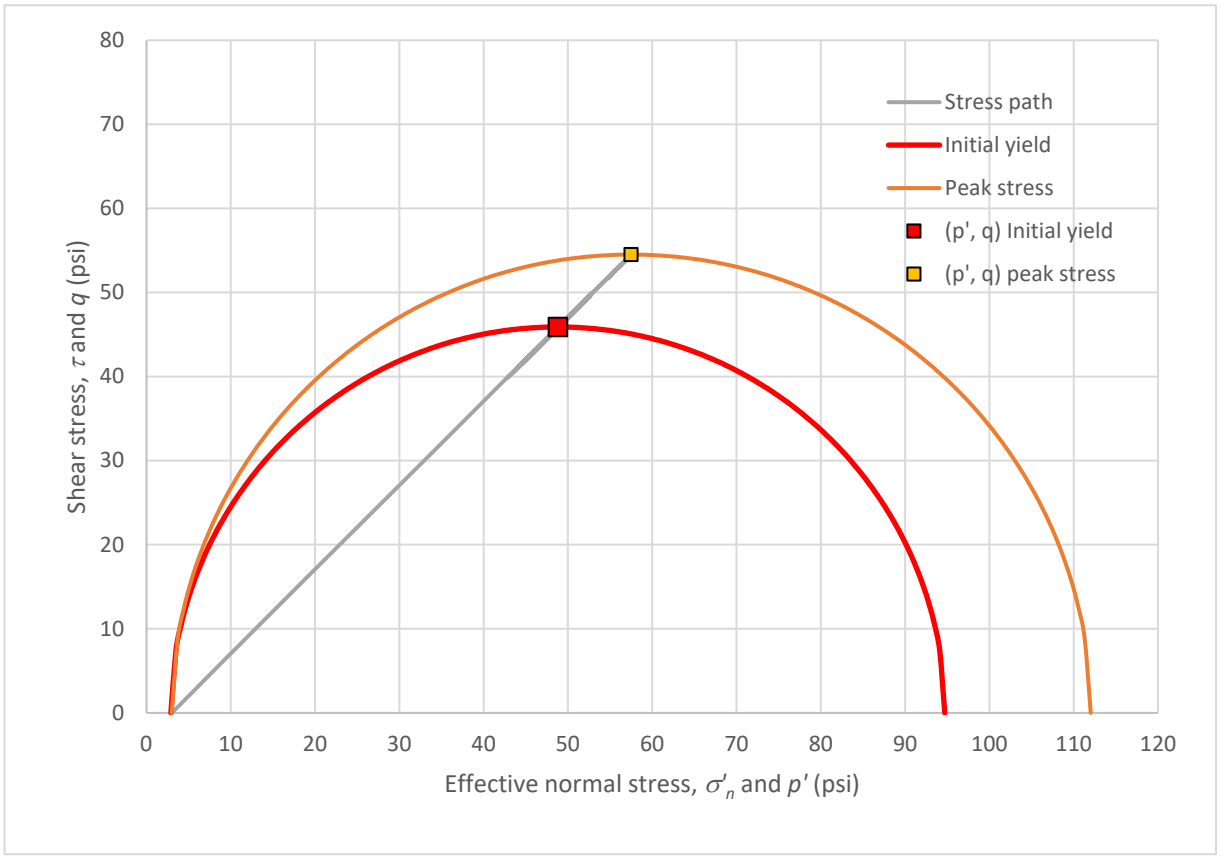

Consolidated-Drained Triaxial Shear, Lightweight Cellular Concrete

Sample ID:	**B2-77**
Height (in):	5.497
Height (mm):	139.6
Diameter (in):	2.958
Diameter (mm)	75.14
Area (in^2):	6.873
Area (mm^2):	4434
Mass (g):	253.60
Weight (lb):	0.5591
Weight (kN):	0.002487
Volume (in^3):	37.78
Volume (mm^3):	619079
Density (g/mm^3):	0.0004096
Density (kg/m^3):	409.6
Unit weight (pcf):	**25.57**
Dry unit weight (pcf);	**20.16**
Unit Weight (kN/m^3):	4.017
Wet mass + tare (g):	368.64
Dry mass + tare (g):	322.95
Tare (g):	152.71
Water content (%)	**26.84**
Saturation (%):	**9.86**
H:D ratio:	1.858
Age (days):	1076
Treatment:	M5

Strain rate (%/min):	0.2
Mean σ'_3 (psi):	3.0
Initial modulus (psi):	33817
Initial yield	
Time to failure (min):	1.3
Axial strain at failure (%):	0.261
σ'_1 (psi):	91.09
σ'_3 (psi):	2.97
σ'_1 -σ'_3 (psi):	88.12
σ'_1 / σ'_3:	30.65
p' (psi):	47.03
q (psi):	44.06
Volumetric strain (%):	0.165
Poisson's ratio:	0.184
Peak stress	
Time to failure (min):	5.2
Axial strain at failure (%):	1.048
σ'_1 (psi):	104.95
σ'_3 (psi):	2.97
σ'_1 -σ'_3 (psi):	101.99
σ'_1 / σ'_3:	35.37
p' (psi):	53.96
q (psi):	50.99
Volumetric strain (%):	0.920
Poisson's ratio:	0.061

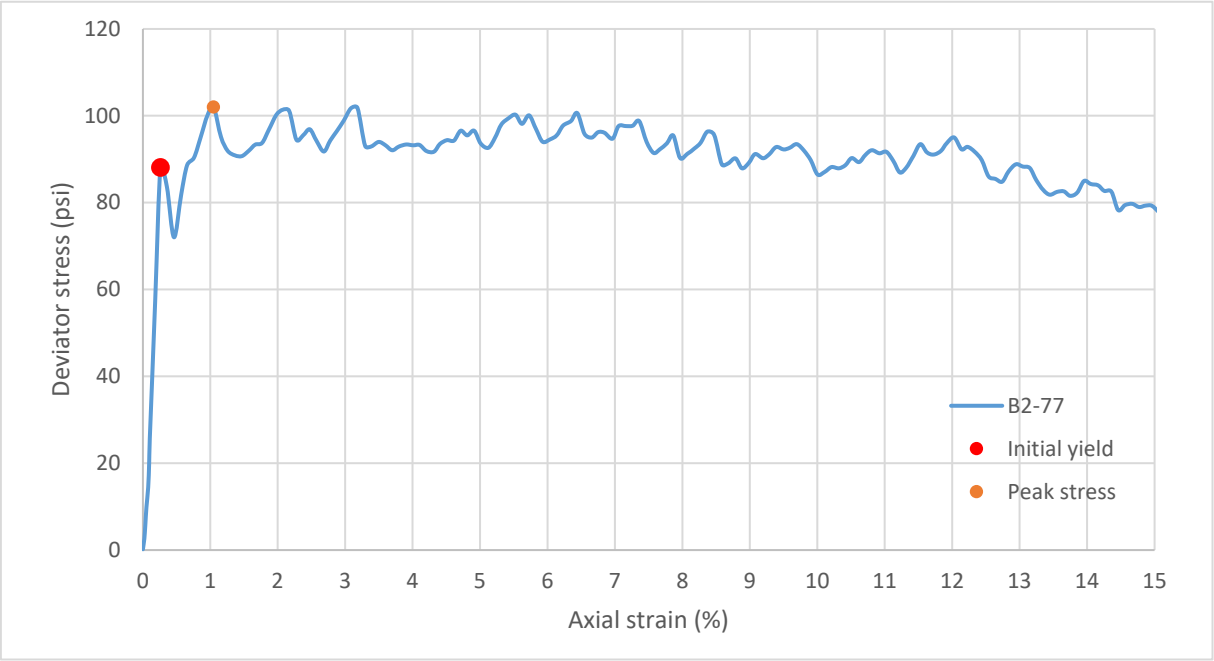

Sample ID:	B2-77

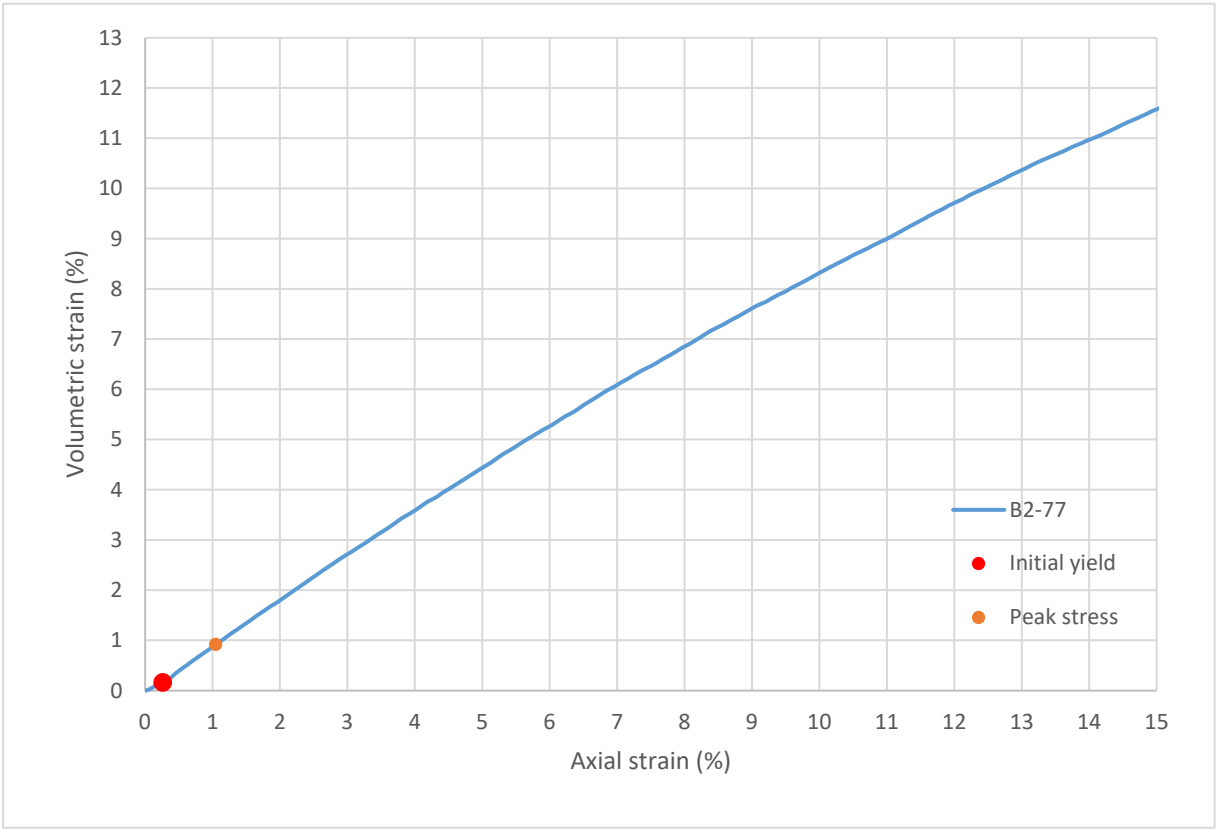

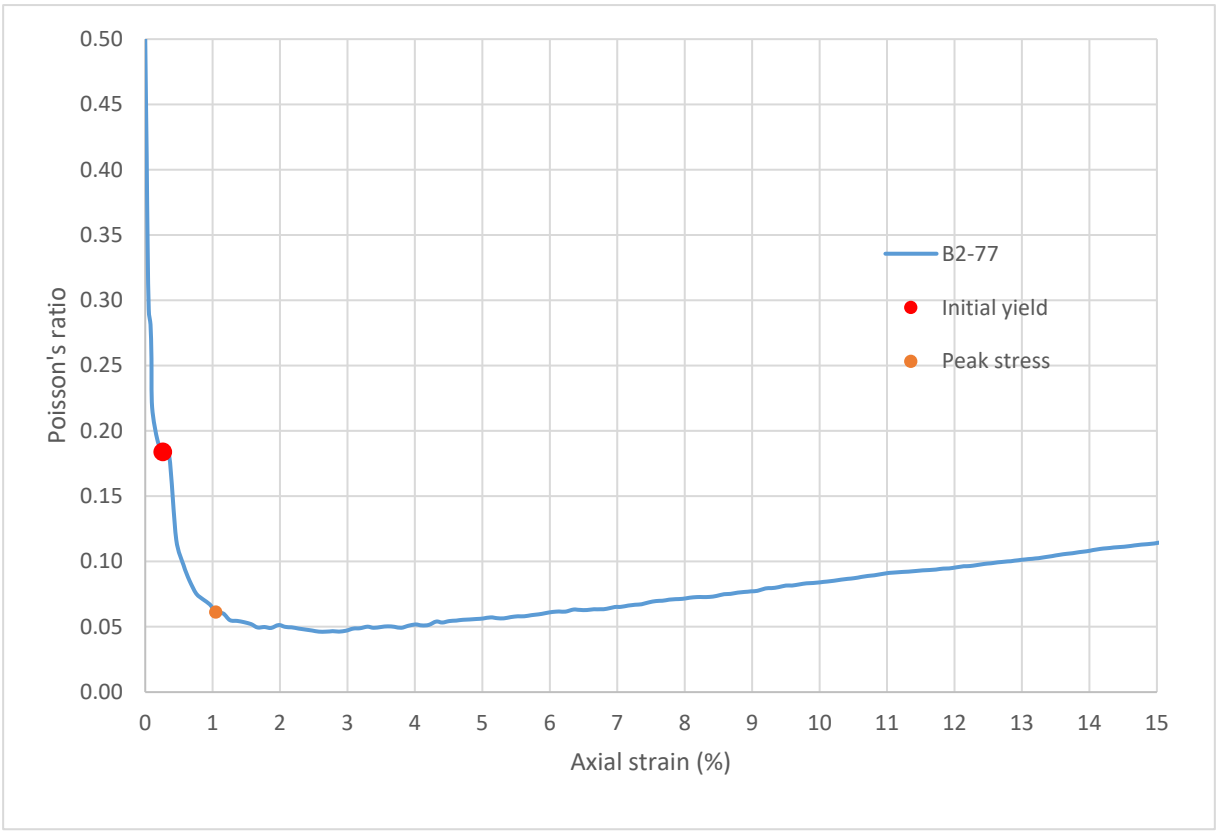

Sample ID:	B2-77

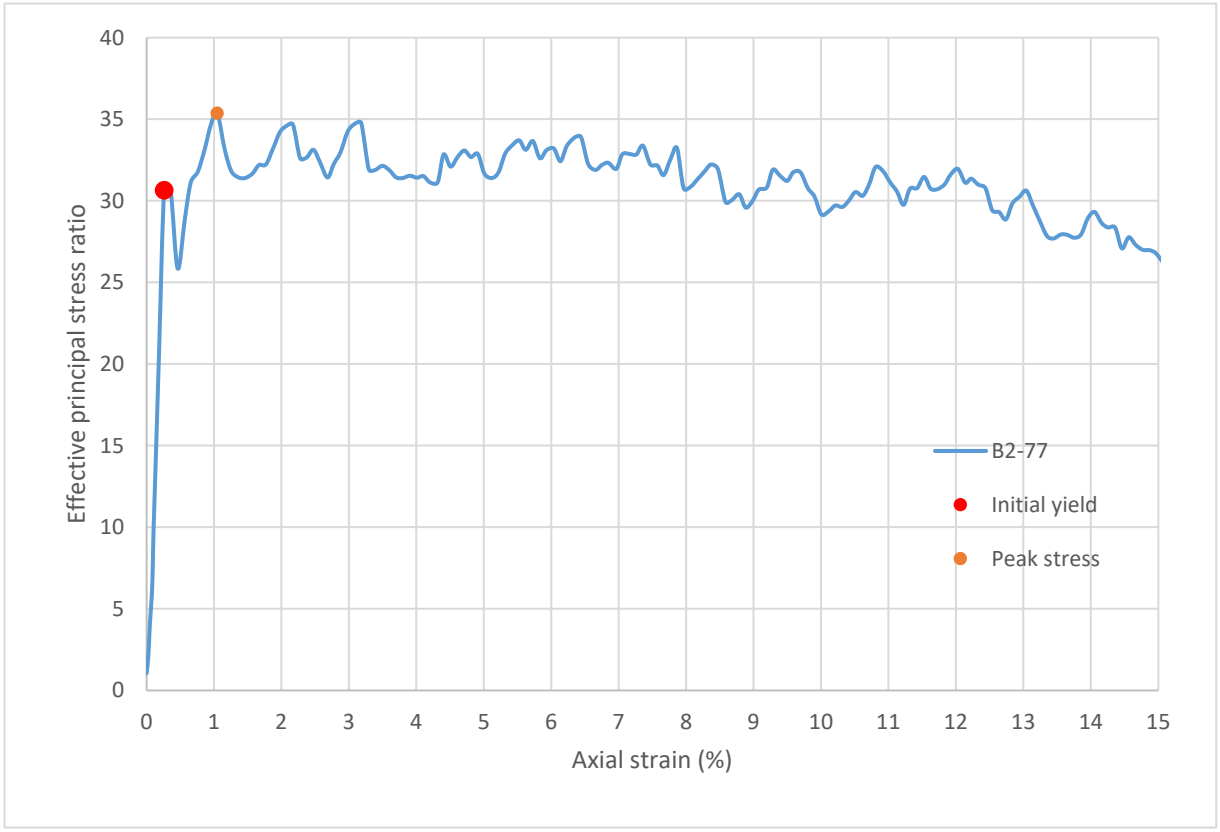

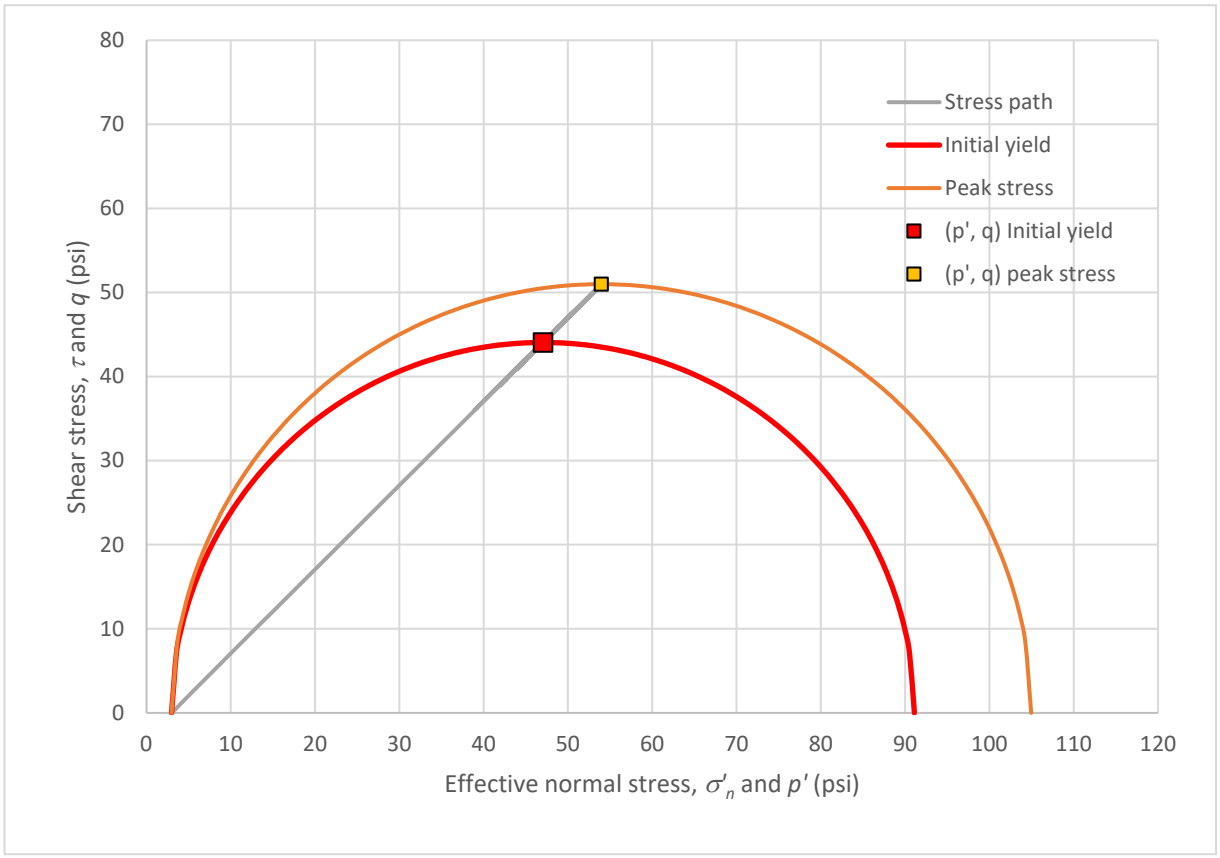

Consolidated-Drained Triaxial Shear, Lightweight Cellular Concrete

Sample ID:	**B3-26**
Height (in):	5.404
Height (mm):	137.3
Diameter (in):	2.959
Diameter (mm)	75.16
Area (in^2):	6.876
Area (mm^2):	4436
Mass (g):	245.40
Weight (lb):	0.5410
Weight (kN):	0.002407
Volume (in^3):	37.16
Volume (mm^3):	608887
Density (g/mm^3):	0.0004030
Density (kg/m^3):	403.0
Unit weight (pcf):	**25.16**
Dry unit weight (pcf);	**19.72**
Unit Weight (kN/m^3):	3.952
Wet mass + tare (g):	419.20
Dry mass + tare (g):	374.39
Tare (g):	212.10
Water content (%)	**27.61**
Saturation (%):	**9.89**
H:D ratio:	1.826
Age (days):	1077
Treatment:	M5

Strain rate (%/min):	0.2
Mean σ'_3 (psi):	3.0
Initial modulus (psi):	25130
Initial yield	
Time to failure (min):	1.3
Axial strain at failure (%):	0.253
σ'_1 (psi):	66.40
σ'_3 (psi):	2.93
σ'_1 -σ'_3 (psi):	63.47
σ'_1 / σ'_3:	22.68
p' (psi):	34.66
q (psi):	31.74
Volumetric strain (%):	0.132
Poisson's ratio:	0.239
Peak stress	
Time to failure (min):	17.5
Axial strain at failure (%):	3.503
σ'_1 (psi):	67.86
σ'_3 (psi):	2.93
σ'_1 -σ'_3 (psi):	64.92
σ'_1 / σ'_3:	23.14
p' (psi):	35.40
q (psi):	32.46
Volumetric strain (%):	3.002
Poisson's ratio:	0.072

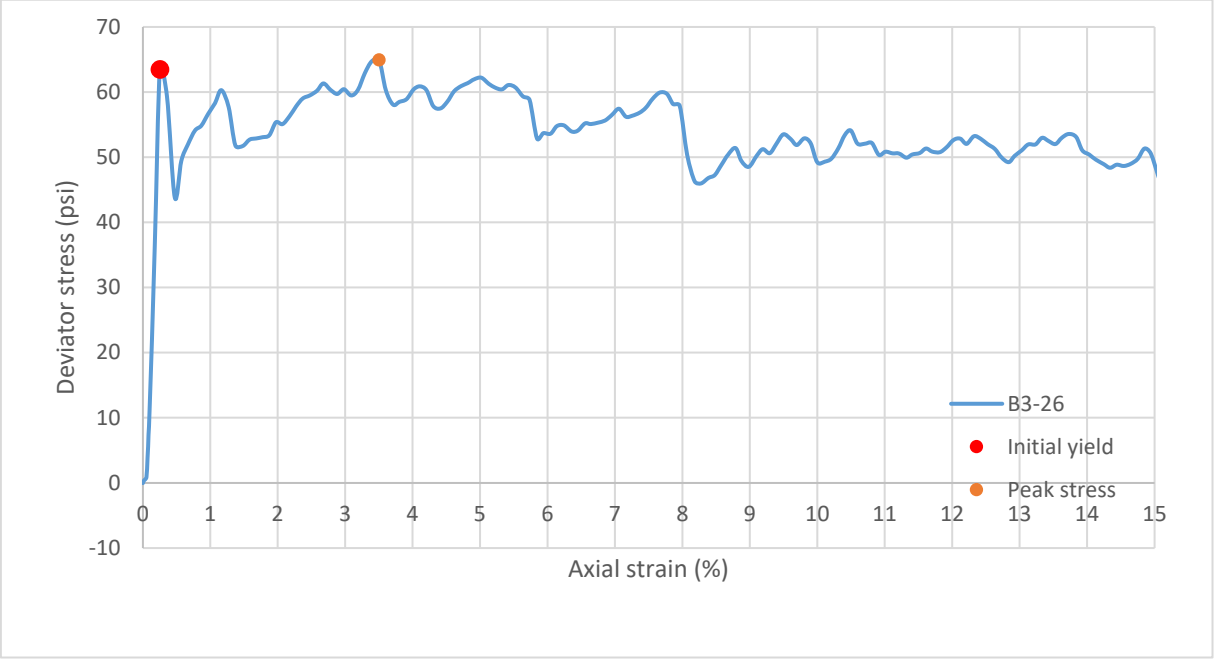

Sample ID:	B3-26

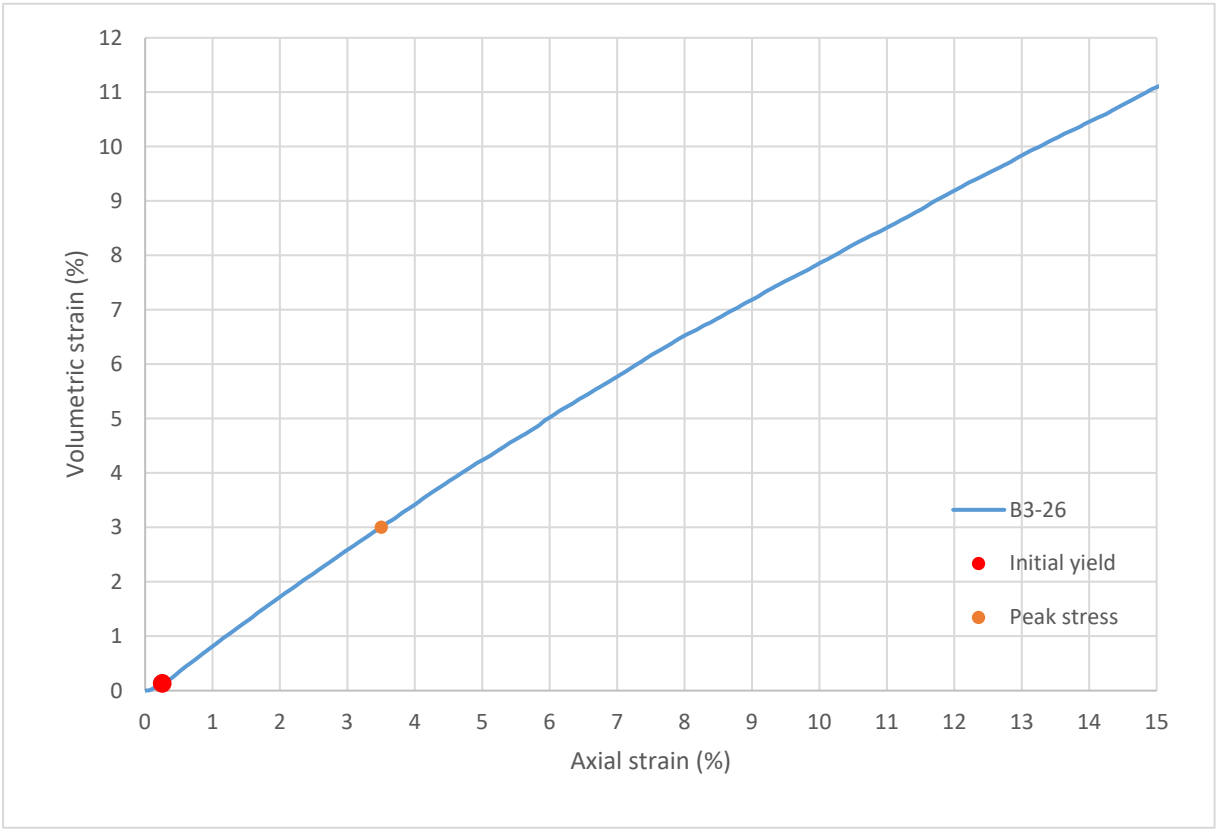

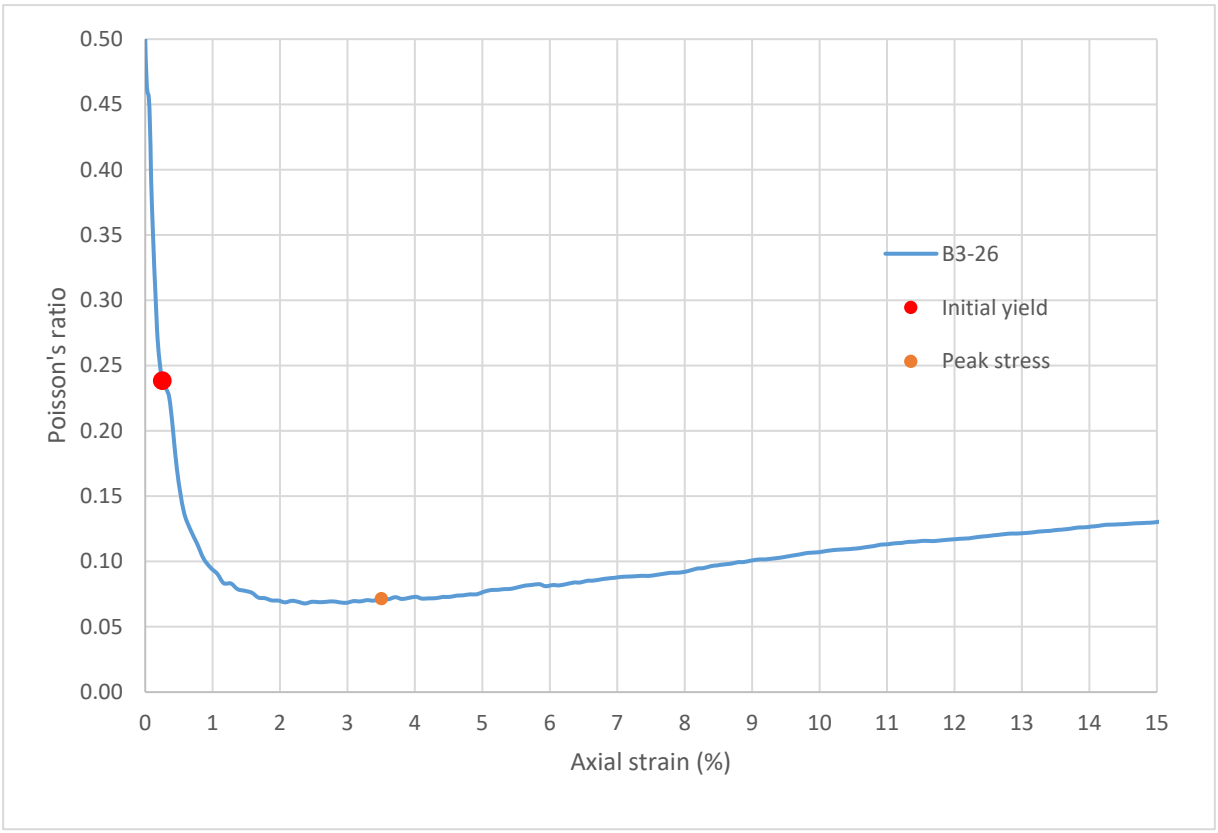

Sample ID:	B3-26

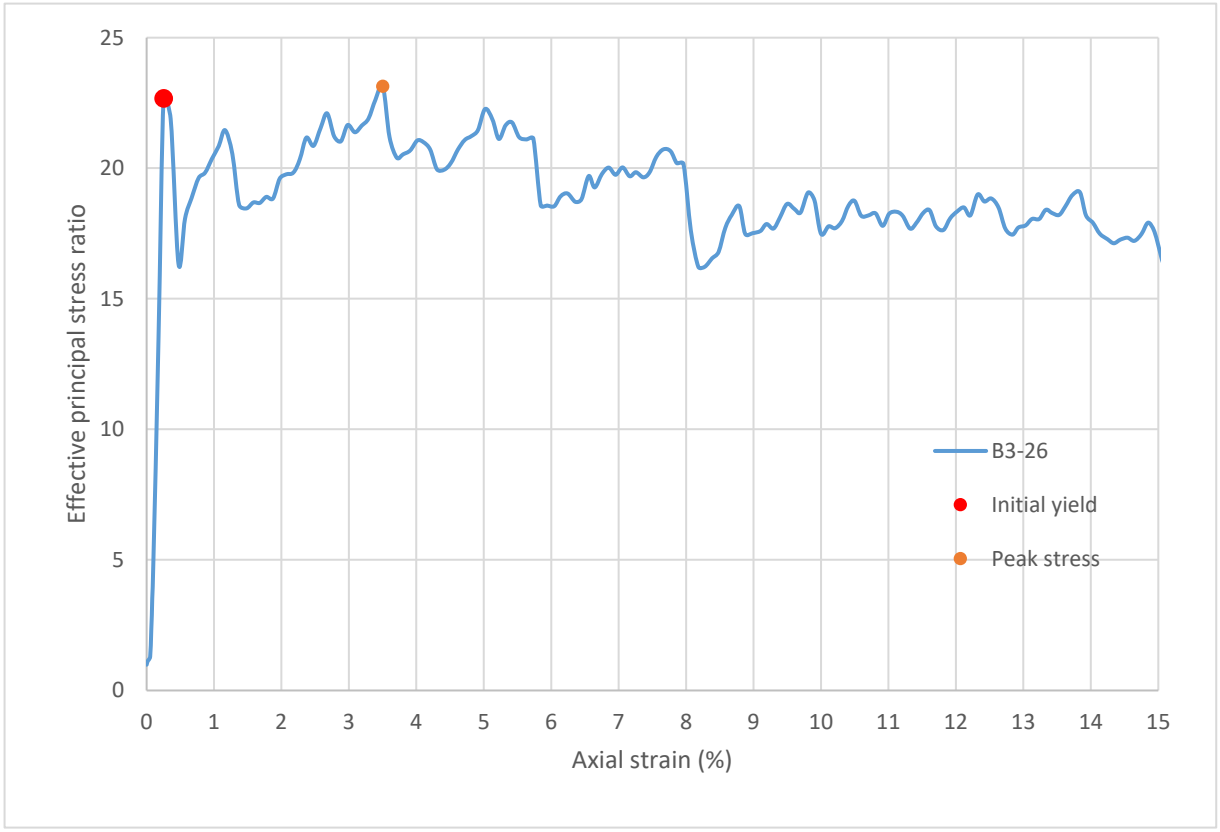

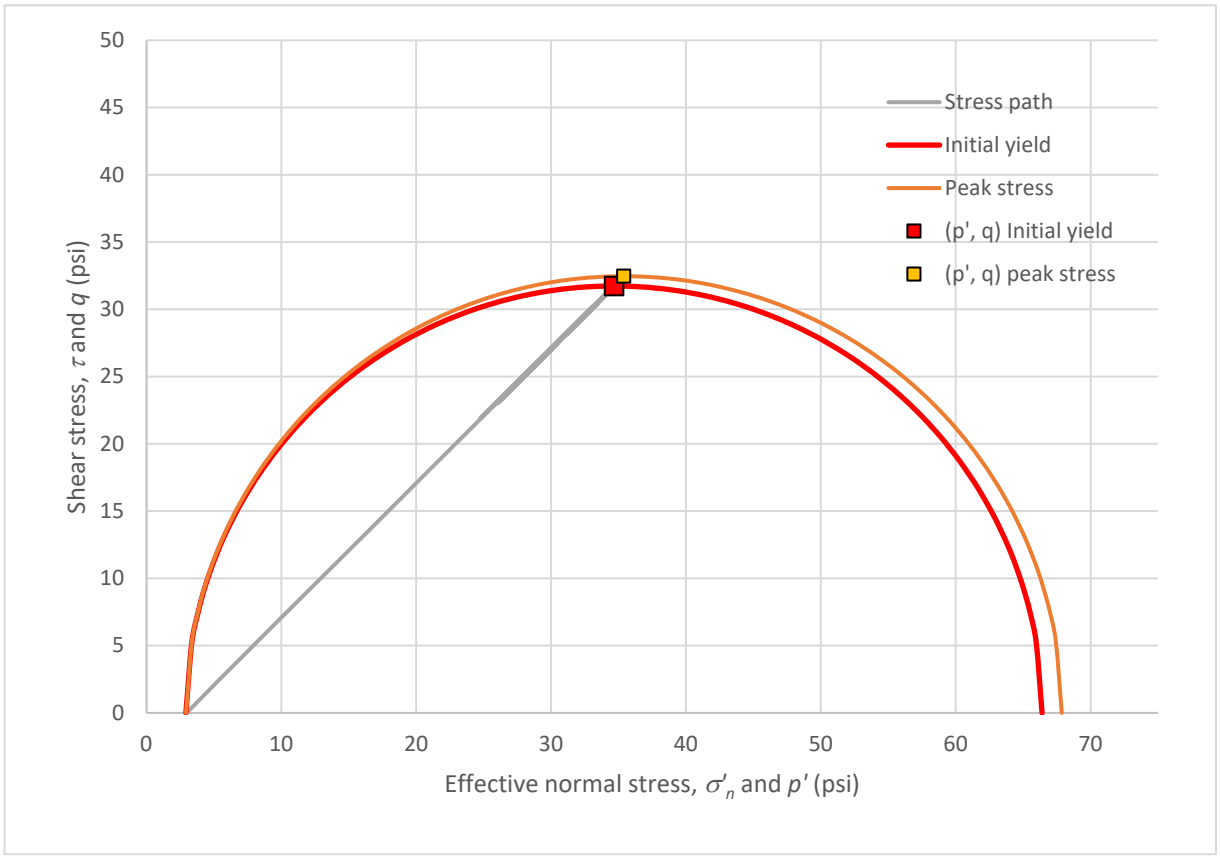

Consolidated-Drained Triaxial Shear, Lightweight Cellular Concrete

Sample ID:	**B3-27**
Height (in):	5.511
Height (mm):	140.0
Diameter (in):	2.951
Diameter (mm)	74.97
Area (in^2):	6.842
Area (mm^2):	4414
Mass (g):	248.06
Weight (lb):	0.5469
Weight (kN):	0.002433
Volume (in^3):	37.70
Volume (mm^3):	617823
Density (g/mm^3):	0.0004015
Density (kg/m^3):	401.5
Unit weight (pcf):	**25.07**
Dry unit weight (pcf);	**19.90**
Unit Weight (kN/m^3):	3.937
Wet mass + tare (g):	362.21
Dry mass + tare (g):	313.08
Tare (g):	123.66
Water content (%)	**25.94**
Saturation (%):	**9.39**
H:D ratio:	1.867
Age (days):	1077
Treatment:	M5

Strain rate (%/min):	0.2
Mean σ'_3 (psi):	3.1
Initial modulus (psi):	36485
Initial yield	
Time to failure (min):	2.2
Axial strain at failure (%):	0.447
σ'_1 (psi):	122.56
σ'_3 (psi):	2.99
σ'_1 -σ'_3 (psi):	119.58
σ'_1 / σ'_3:	41.05
p' (psi):	62.78
q (psi):	59.79
Volumetric strain (%):	0.174
Poisson's ratio:	0.305
Peak stress	
Time to failure (min):	16.3
Axial strain at failure (%):	3.255
σ'_1 (psi):	139.34
σ'_3 (psi):	3.01
σ'_1 -σ'_3 (psi):	136.33
σ'_1 / σ'_3:	46.29
p' (psi):	71.18
q (psi):	68.17
Volumetric strain (%):	2.820
Poisson's ratio:	0.067

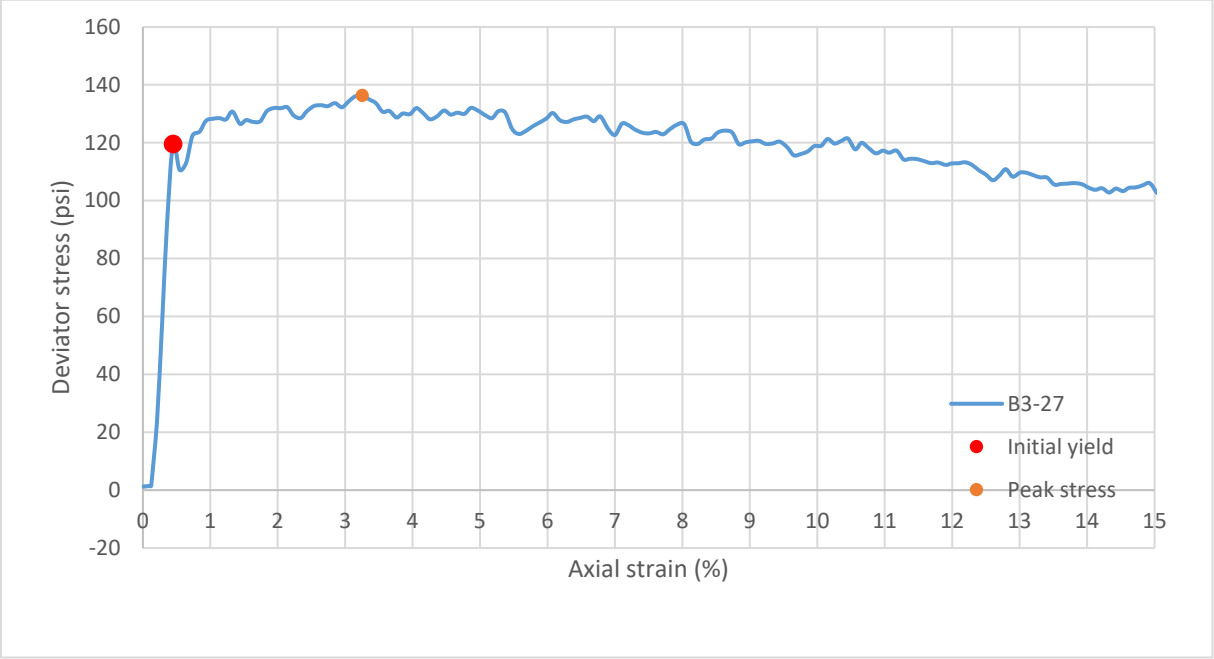

Sample ID:	B3-27

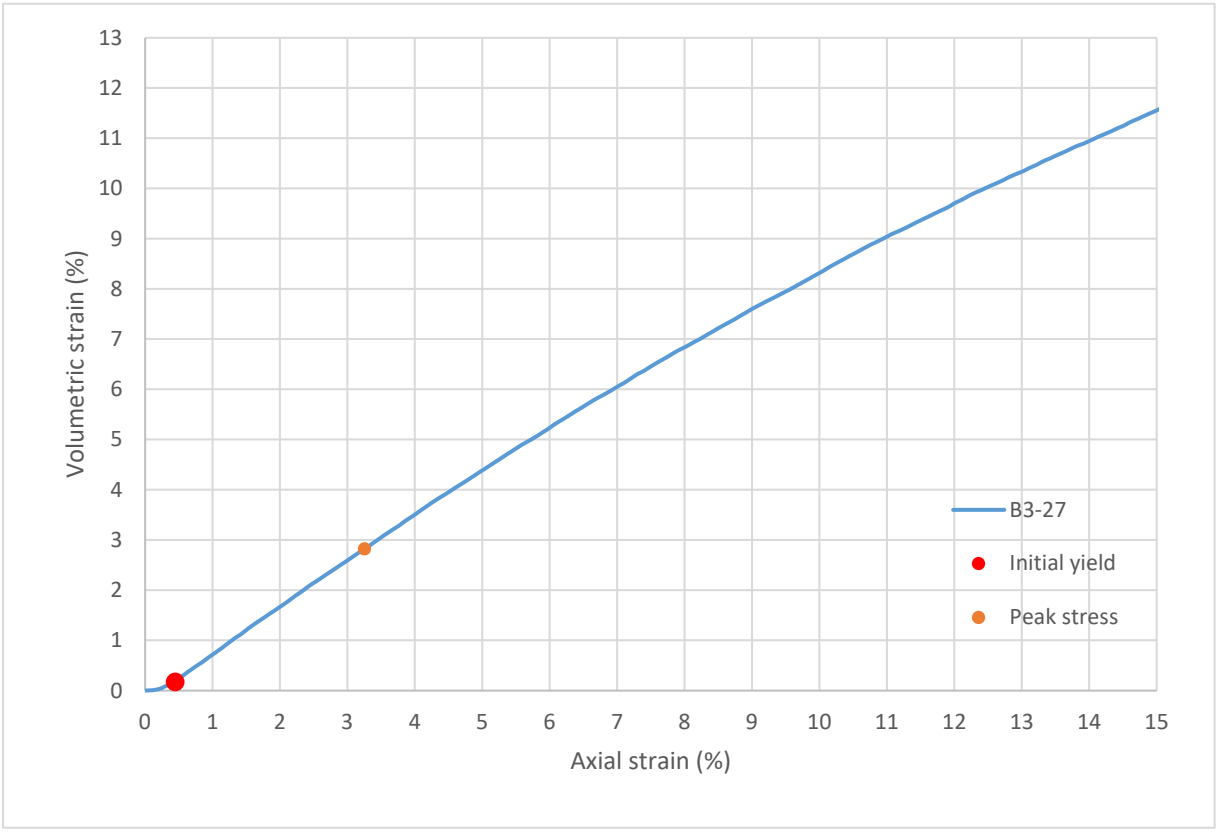

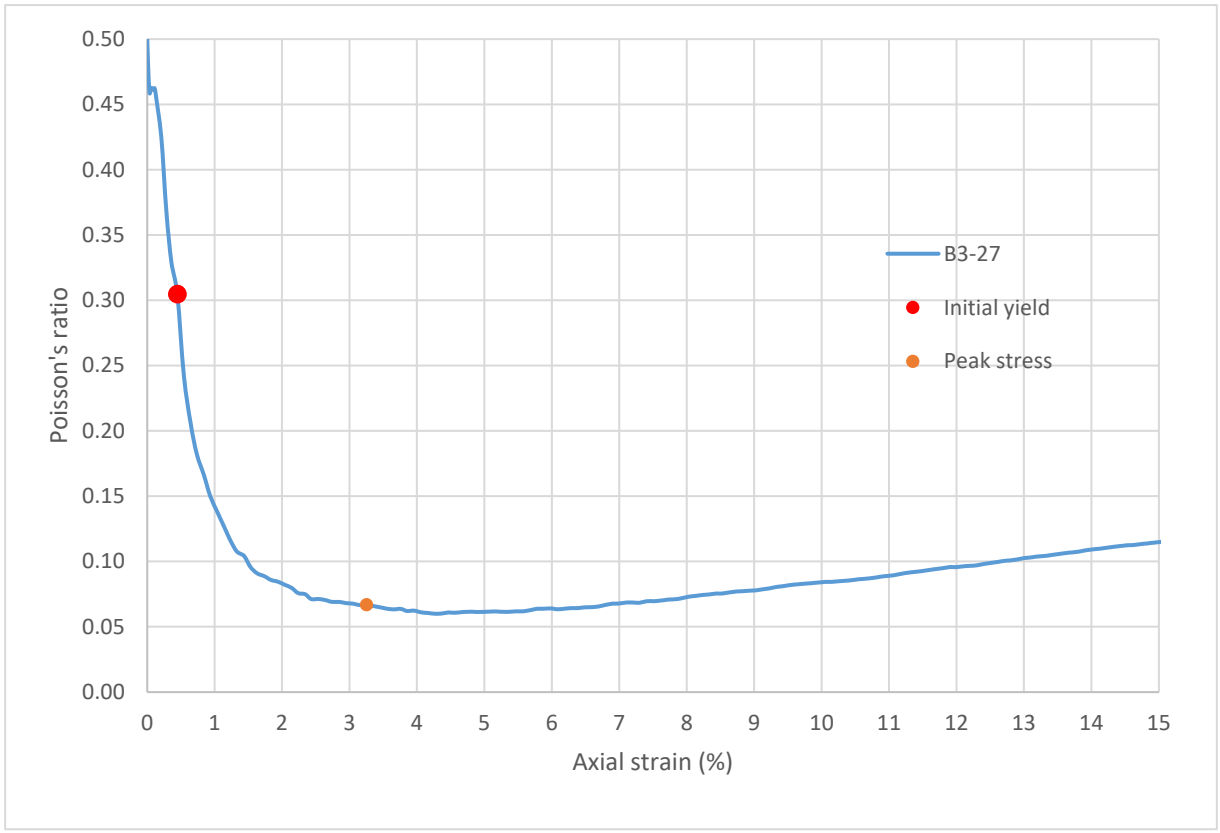

Sample ID:	B3-27

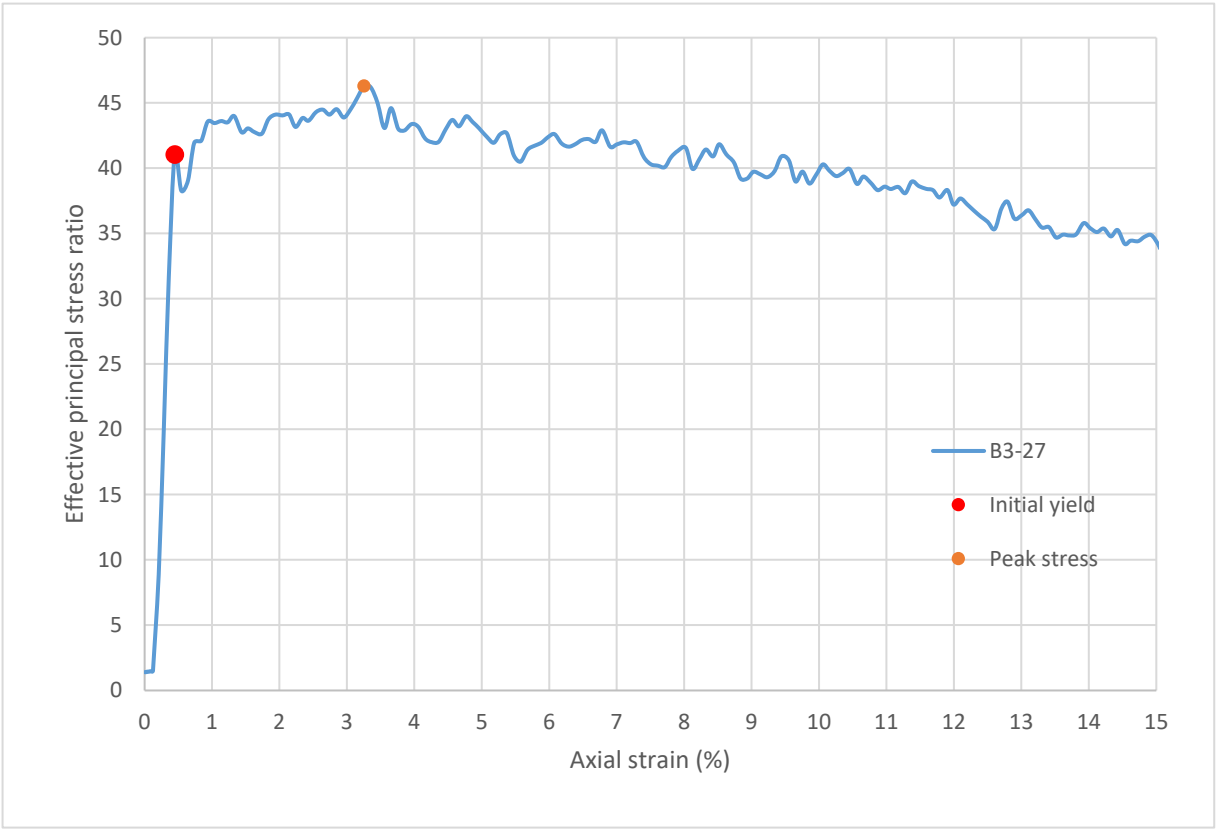

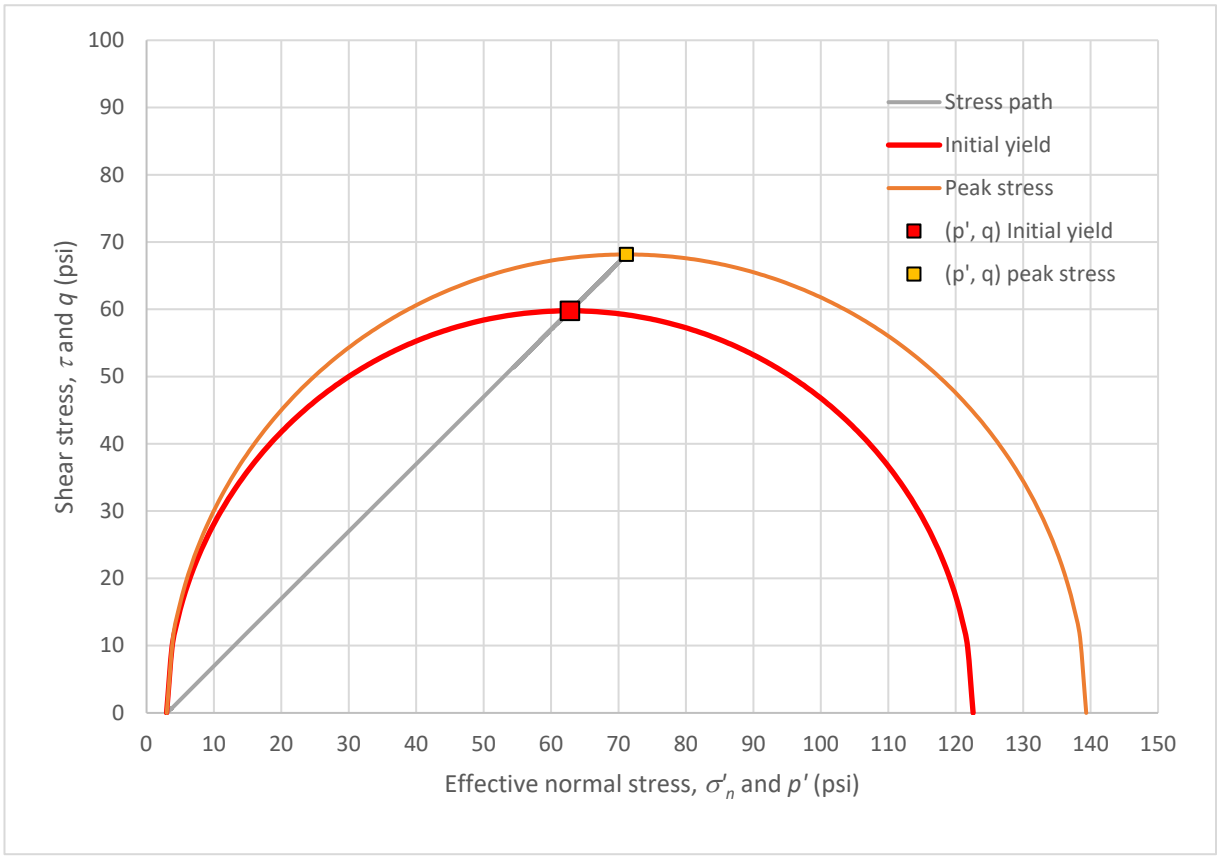

Consolidated-Drained Triaxial Shear, Lightweight Cellular Concrete

Sample ID:	**B3-28**
Height (in):	5.536
Height (mm):	140.6
Diameter (in):	2.952
Diameter (mm)	74.99
Area (in^2):	6.846
Area (mm^2):	4417
Mass (g):	256.79
Weight (lb):	0.5661
Weight (kN):	0.002518
Volume (in^3):	37.90
Volume (mm^3):	621122
Density (g/mm^3):	0.0004134
Density (kg/m^3):	413.4
Unit weight (pcf):	**25.81**
Dry unit weight (pcf);	**20.81**
Unit Weight (kN/m^3):	4.054
Wet mass + tare (g):	370.94
Dry mass + tare (g):	323.67
Tare (g):	126.70
Water content (%)	**24.00**
Saturation (%):	**9.14**
H:D ratio:	1.875
Age (days):	1077
Treatment:	M5

Strain rate (%/min):	0.2
Mean σ'_3 (psi):	6.0
Initial modulus (psi):	39554
Initial yield	
Time to failure (min):	1.3
Axial strain at failure (%):	0.251
σ'_1 (psi):	105.18
σ'_3 (psi):	5.85
σ'_1 -σ'_3 (psi):	99.33
σ'_1 / σ'_3:	17.97
p' (psi):	55.52
q (psi):	49.66
Volumetric strain (%):	0.158
Poisson's ratio:	0.186
Peak stress	
Time to failure (min):	22.9
Axial strain at failure (%):	4.579
σ'_1 (psi):	142.20
σ'_3 (psi):	6.03
σ'_1 -σ'_3 (psi):	136.17
σ'_1 / σ'_3:	23.59
p' (psi):	74.12
q (psi):	68.09
Volumetric strain (%):	4.178
Poisson's ratio:	0.044

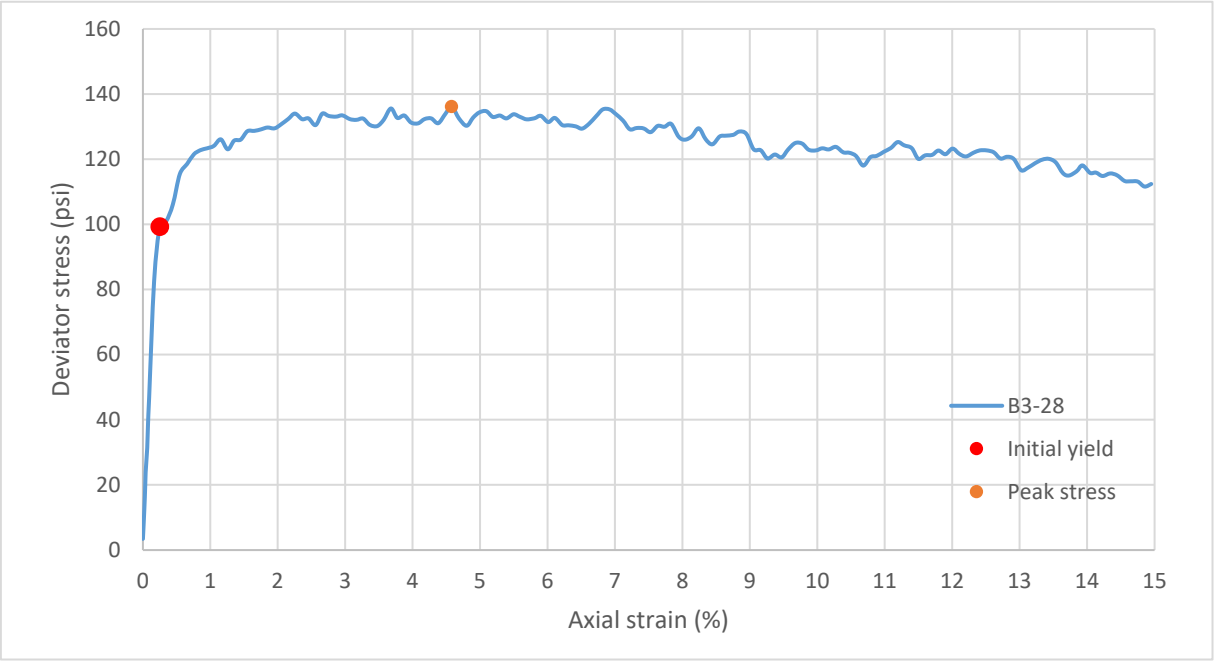

Sample ID:	B3-28

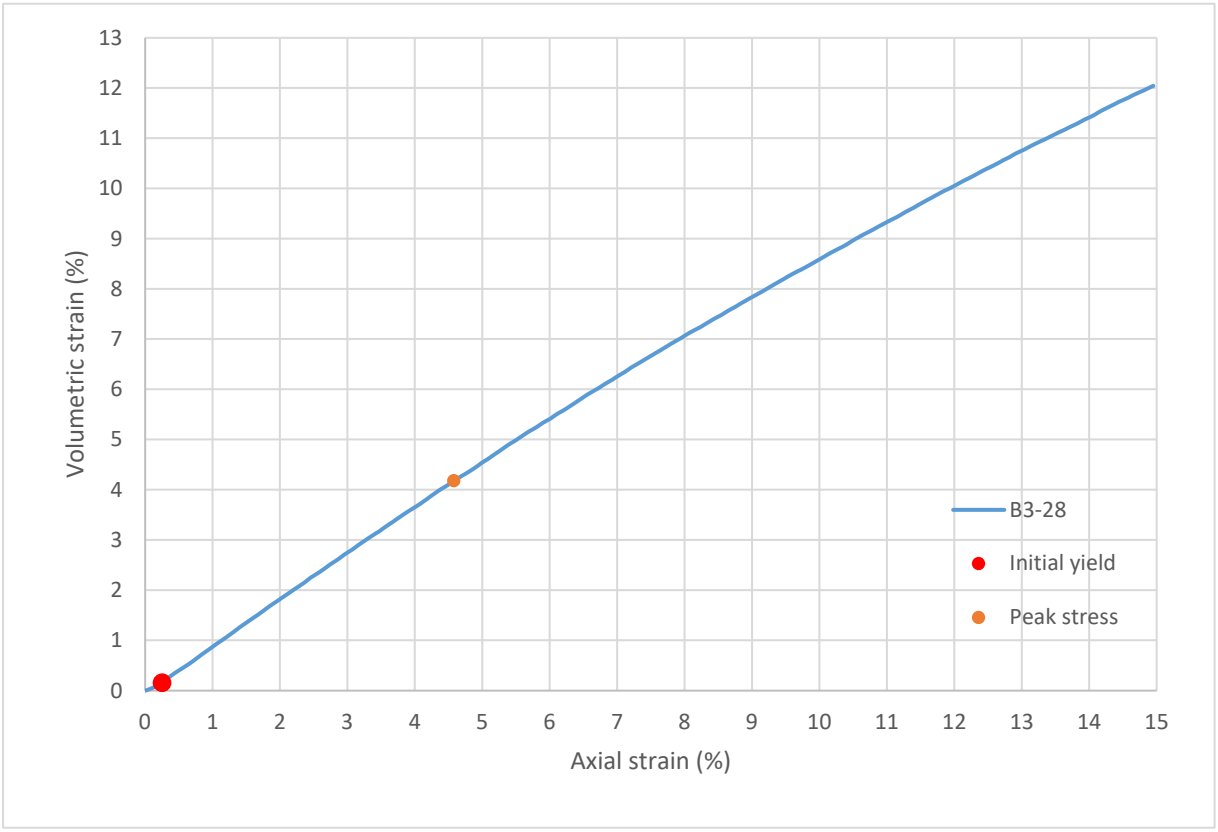

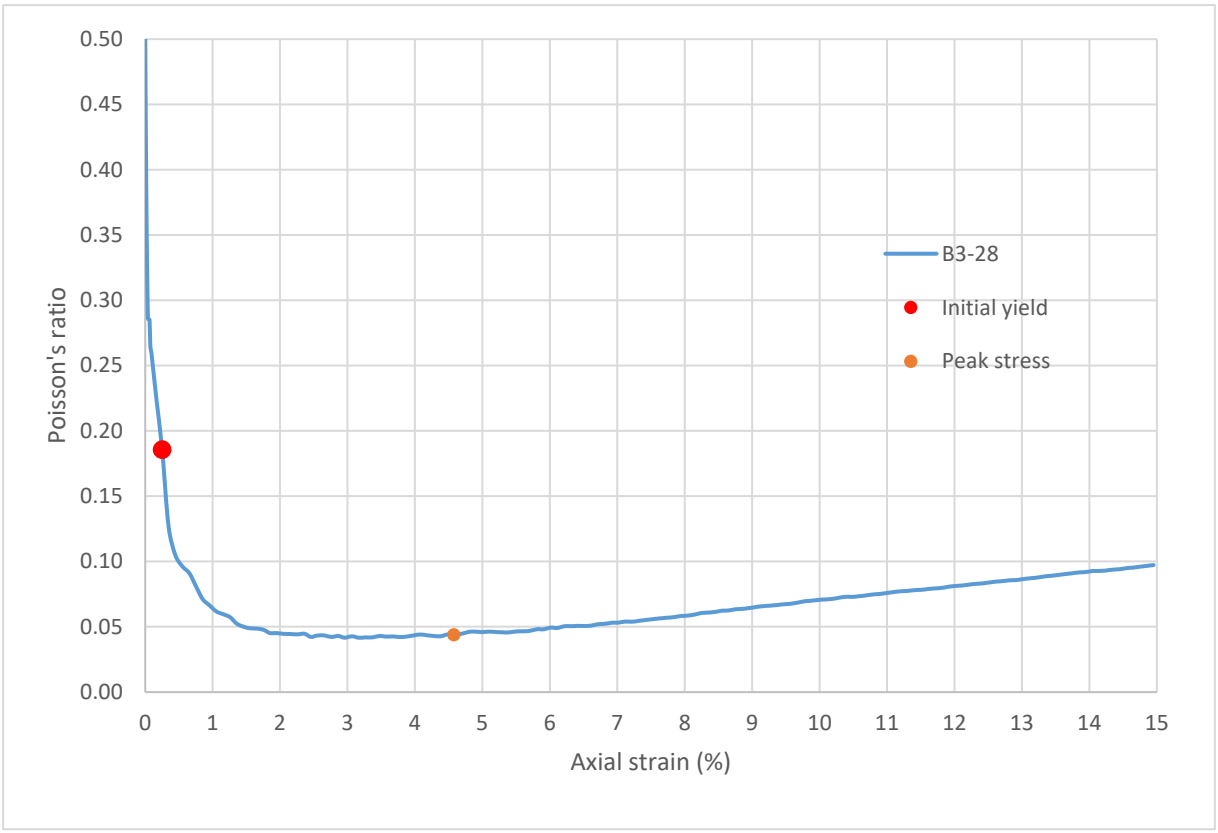

Sample ID:	B3-28

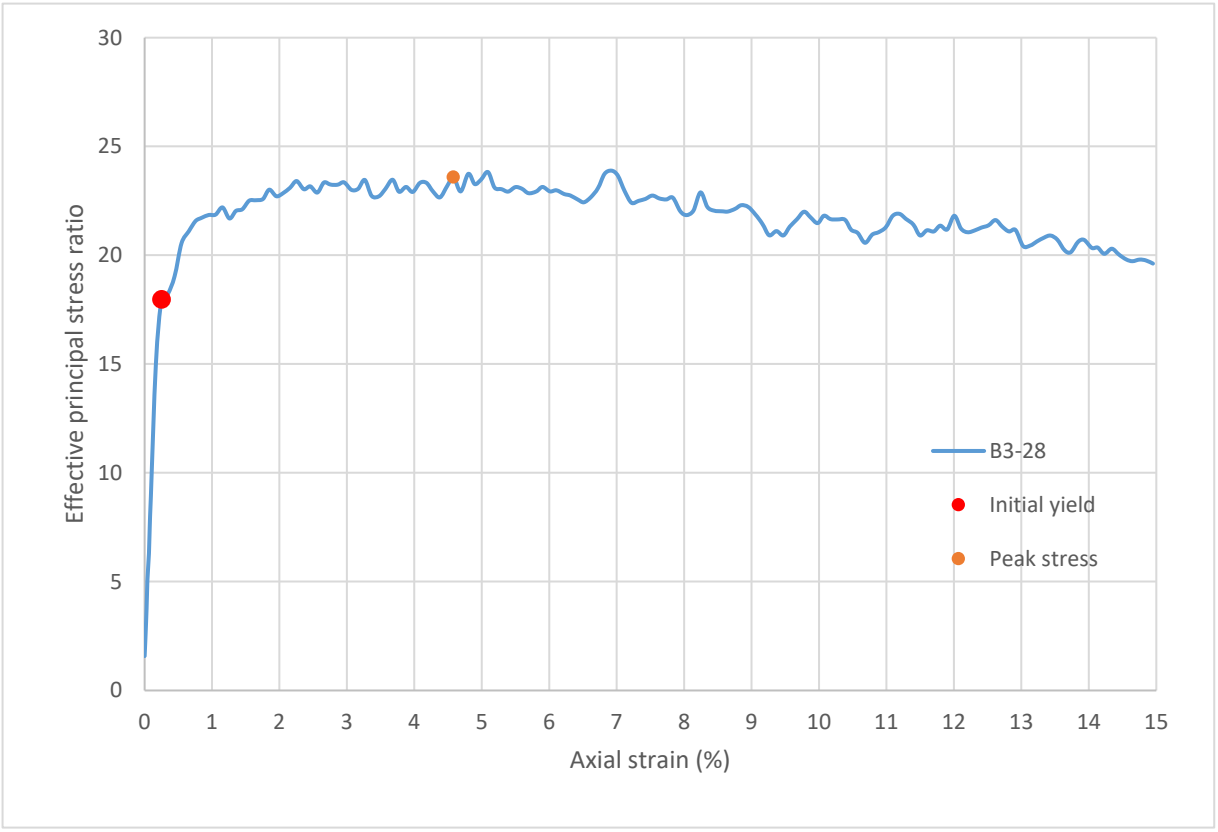

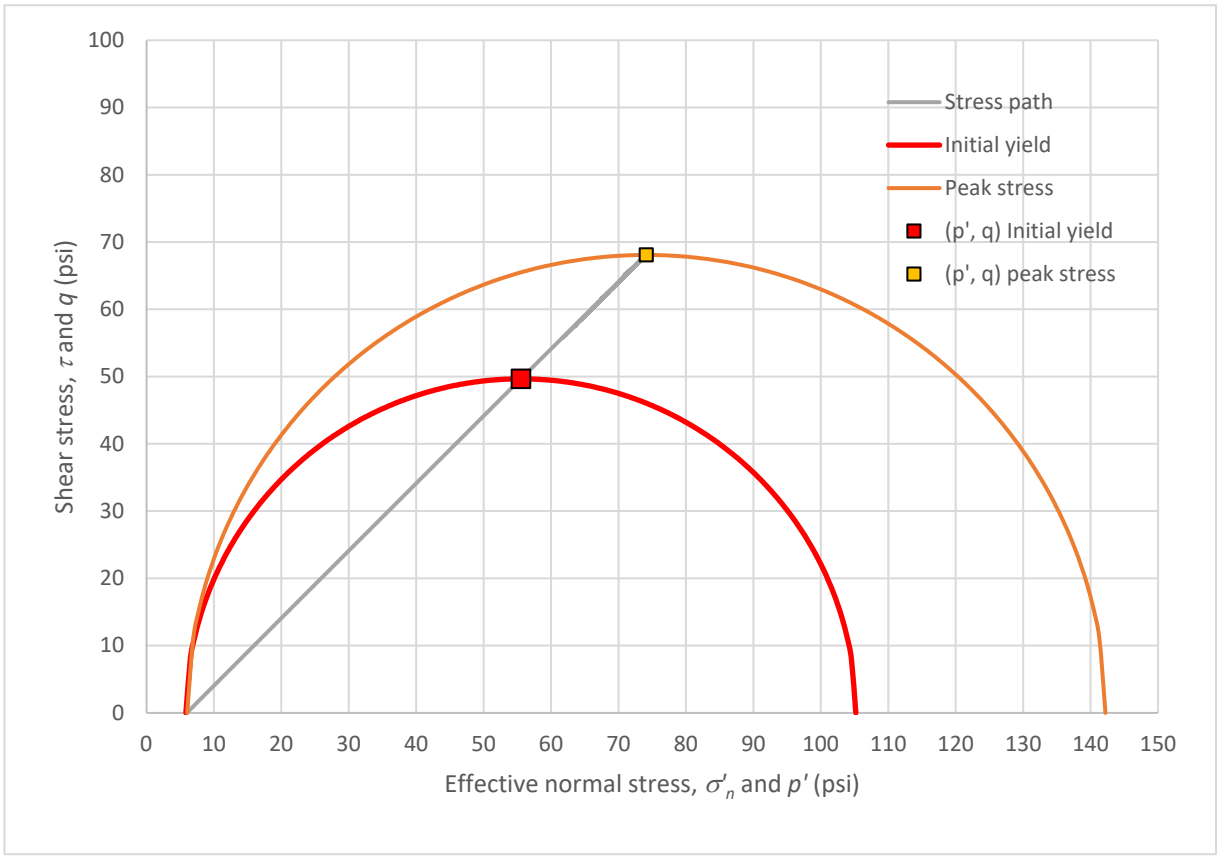

Consolidated-Drained Triaxial Shear, Lightweight Cellular Concrete

Sample ID:	**B3-29**
Height (in):	5.476
Height (mm):	139.1
Diameter (in):	2.958
Diameter (mm)	75.14
Area (in^2):	6.873
Area (mm^2):	4434
Mass (g):	247.94
Weight (lb):	0.5466
Weight (kN):	0.002431
Volume (in^3):	37.64
Volume (mm^3):	616751
Density (g/mm^3):	0.0004020
Density (kg/m^3):	402.0
Unit weight (pcf):	**25.10**
Dry unit weight (pcf);	**19.99**
Unit Weight (kN/m^3):	3.942
Wet mass + tare (g):	369.09
Dry mass + tare (g):	319.80
Tare (g):	126.84
Water content (%)	**25.54**
Saturation (%):	**9.29**
H:D ratio:	1.851
Age (days):	1077
Treatment:	M5

Strain rate (%/min):	0.2
Mean σ'_3 (psi):	12.0
Initial modulus (psi):	39578
Initial yield	
Time to failure (min):	1.2
Axial strain at failure (%):	0.244
σ'_1 (psi):	108.53
σ'_3 (psi):	11.86
σ'_1 -σ'_3 (psi):	96.66
σ'_1 / σ'_3:	9.15
p' (psi):	60.20
q (psi):	48.33
Volumetric strain (%):	0.142
Poisson's ratio:	0.210
Peak stress	
Time to failure (min):	25.4
Axial strain at failure (%):	5.077
σ'_1 (psi):	145.23
σ'_3 (psi):	12.02
σ'_1 -σ'_3 (psi):	133.21
σ'_1 / σ'_3:	12.08
p' (psi):	78.63
q (psi):	66.61
Volumetric strain (%):	4.672
Poisson's ratio:	0.040

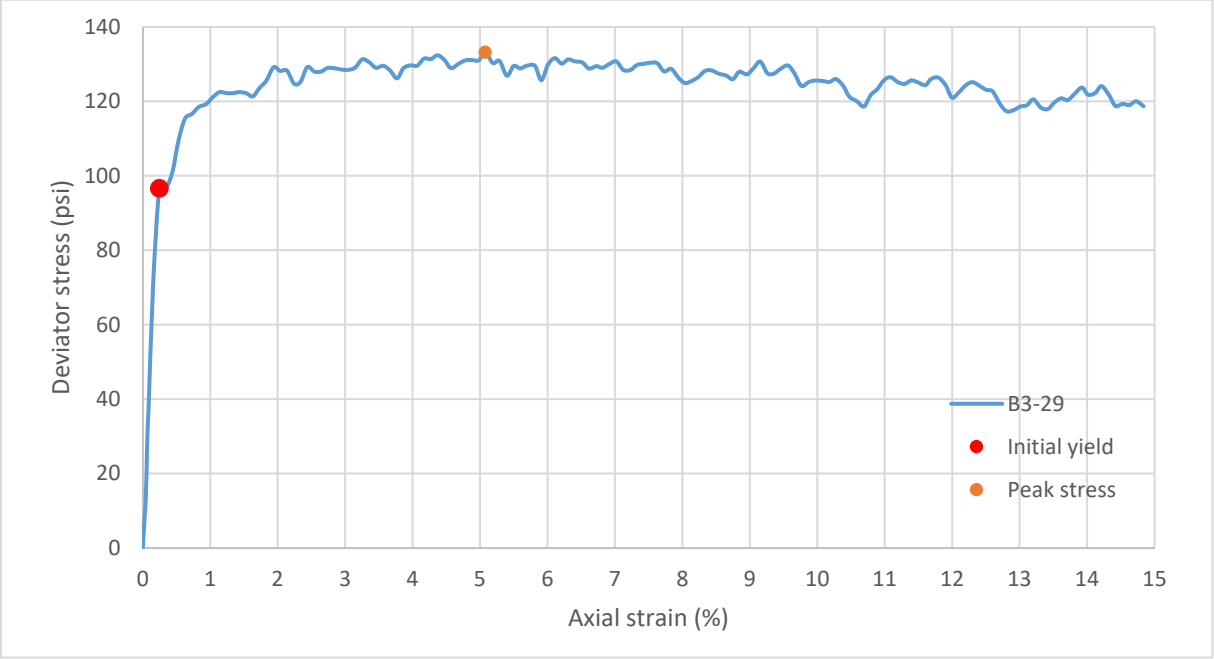

Sample ID:	B3-29

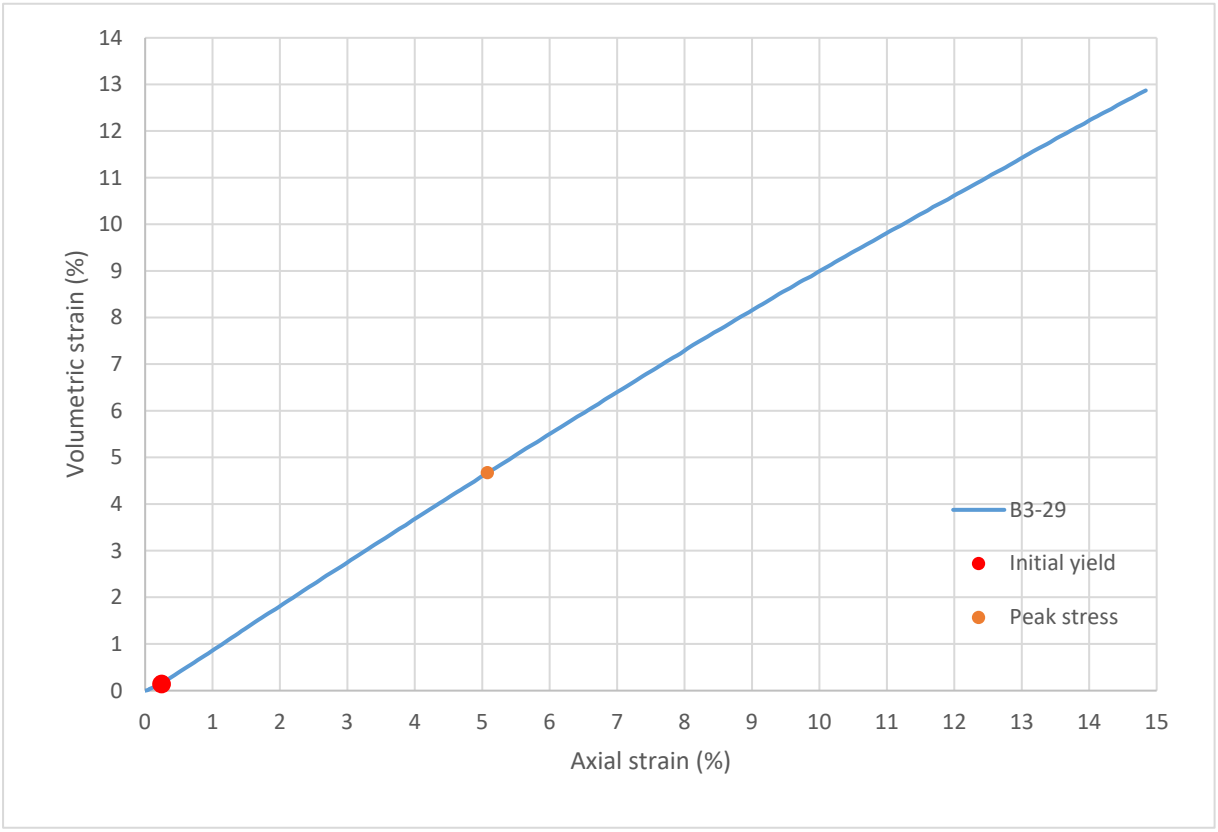

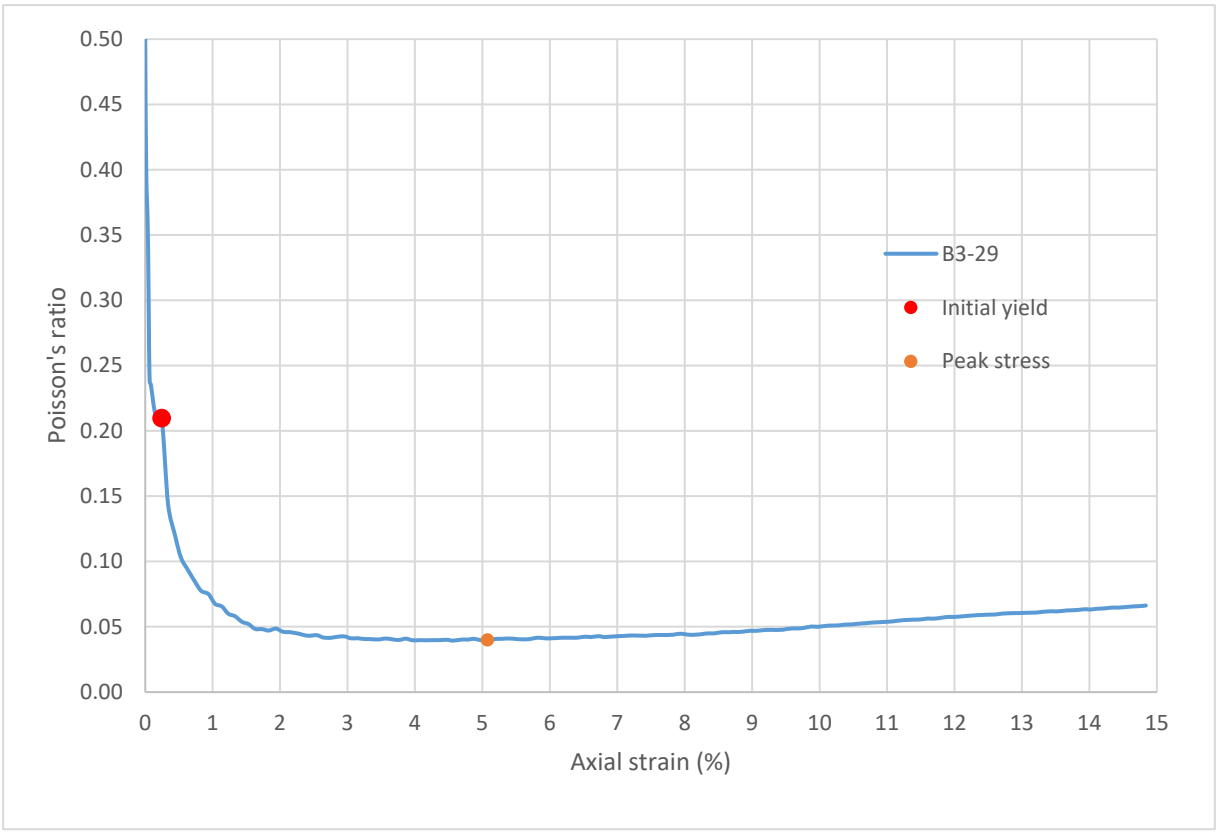

Sample ID:	B3-29

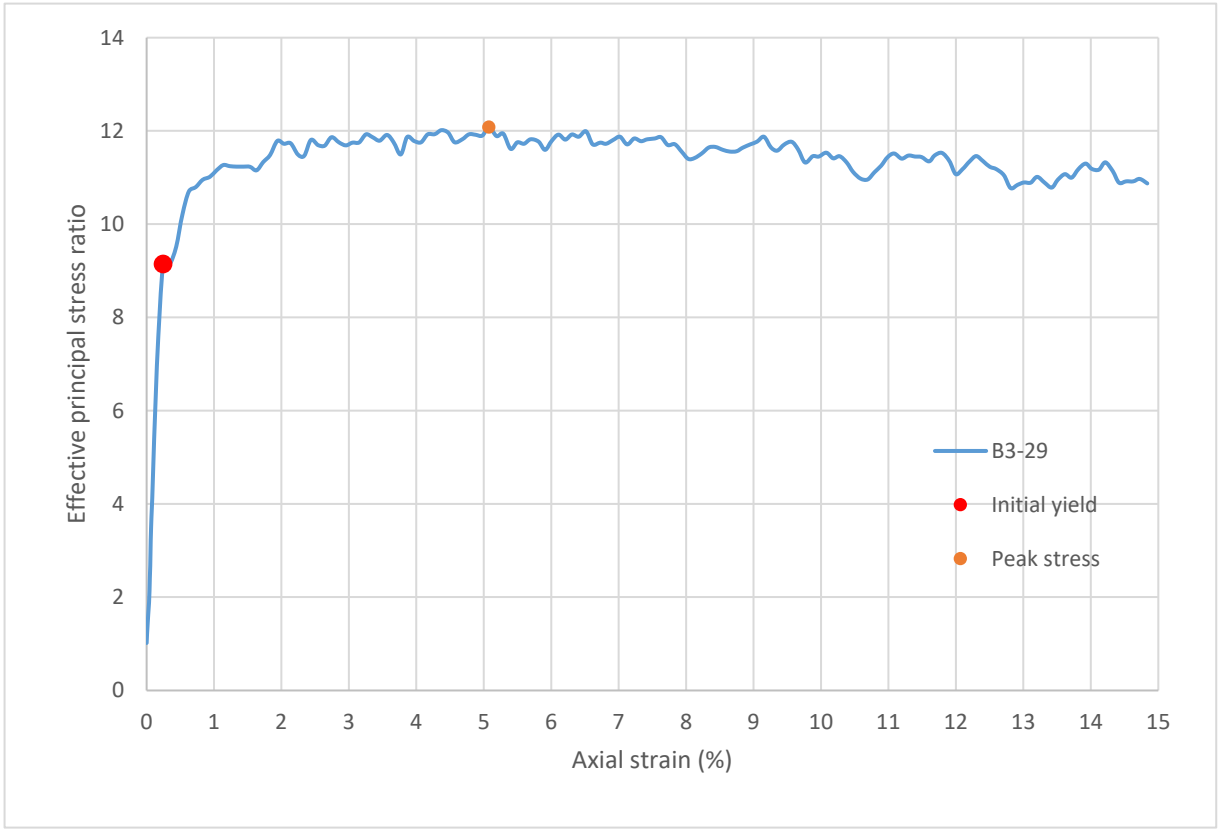

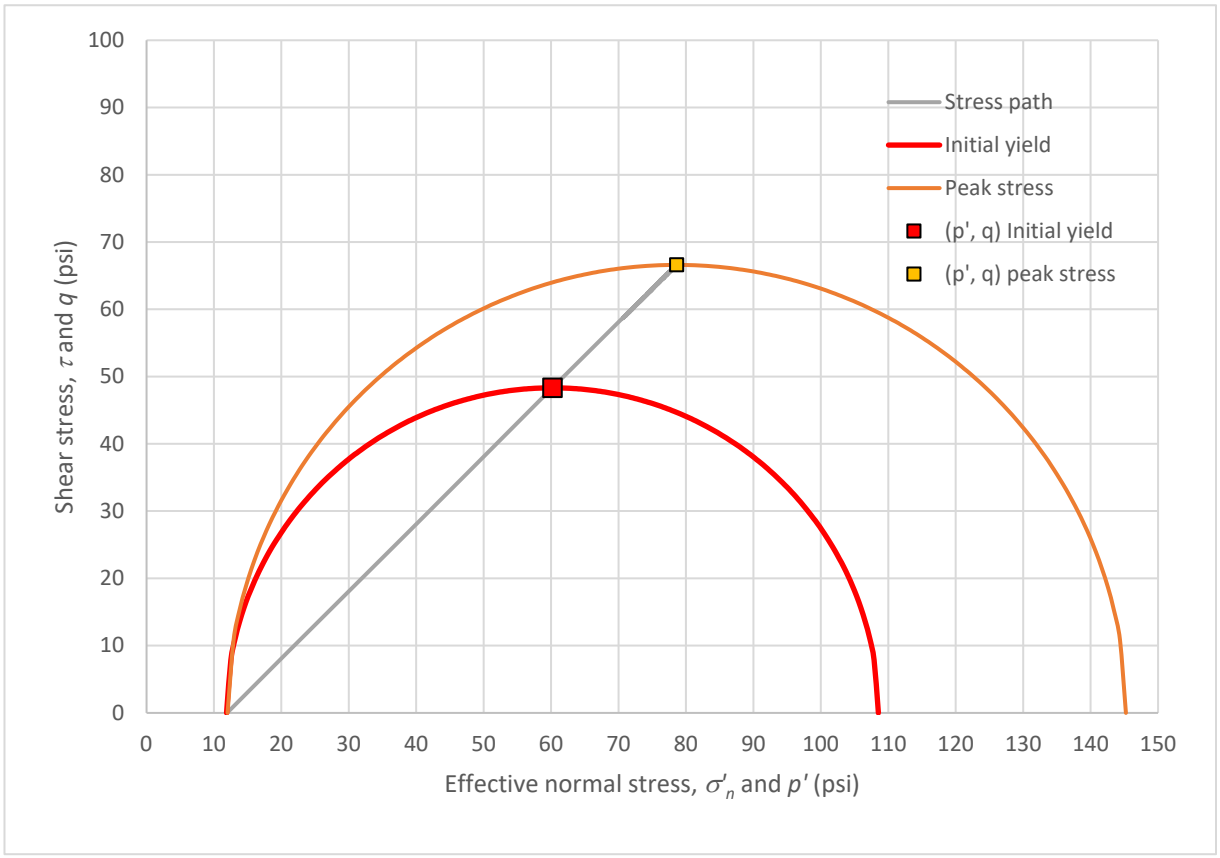

REFERENCES

AASHTO Technical Subcommittee: 1a, Soil and Unbound Recycled Materials. 2017. *T 307-99 Standard Method of Test for Determining the Resilient Modulus of Soils and Aggregate Materials*. Washington D.C.: AASHTO.

ACI Committee 523. 2006. *Guide for Cast-in-Place Low Density Cellular Concrete*. Cellular Concrete. American Concrete Institute.

Aerix Industries. n.d. "Clarification on Classes of LDCC." Aerix Industries.

Allen, D. L., and B. W. Meade. 1984. *An Evaluation of Elastizell Concrete as a Lightweight Fill Material*. Research Report. Kentucky Transportation Research Program, College of Engineering, University of Kentucky.

Amran, Y. H. M., N. Farzadnia, and A. A. Abang Ali. 2015. "Properties and applications of foamed concrete; a review." *Construction and Building Materials*, 101: 990–1005. https://doi.org/10.1016/j.conbuildmat.2015.10.112.

ASTM C09 Committee. 2011a. *C513/C513M-11 Test Method for Obtaining and Testing Specimens of Hardened Lightweight Insulating Concrete for Compressive Strength*. ASTM International.

ASTM C09 Committee. 2011b. *C869/C869M-11 Specification for Foaming Agents Used in Making Preformed Foam for Cellular Concrete*. ASTM International.

ASTM C09 Committee. 2012. *C495/C495M-12 Test Method for Compressive Strength of Lightweight Insulating Concrete*. ASTM International.

ASTM C09 Committee. 2015. *C666/C666M-15 Test Method for Resistance of Concrete to Rapid Freezing and Thawing*. ASTM International.

ASTM C09 Committee. 2019a. *C796/796M-19 Test Method for Foaming Agents for Use in Producing Cellular Concrete Using Preformed Foam*. ASTM International.

ASTM C09 Committee. 2019b. *C215-19 Test Method for Fundamental Transverse, Longitudinal, and Torsional Resonant Frequencies of Concrete Specimens*. ASTM International.

ASTM C09 Committee. 2019c. *C1138M-19 Test Method for Abrasion Resistance of Concrete (Underwater Method)*. ASTM International.

ASTM C16 Committee. 2019a. *C177-19 Test Method for Steady-State Heat Flux Measurements and Thermal Transmission Properties by Means of the Guarded-Hot-Plate Apparatus*. ASTM International.

ASTM C16 Committee. 2019b. *C1363-19 Test Method for Thermal Performance of Building Materials and Envelope Assemblies by Means of a Hot Box Apparatus*. ASTM International.

ASTM C16 Committee. 2021. *C518-21 Test Method for Steady-State Thermal Transmission Properties by Means of the Heat Flow Meter Apparatus*. ASTM International.

ASTM D18 Committee. 2014. *D854-14 Standard Test Methods for Specific Gravity of Solids by Water Pycnometer*. ASTM International.

ASTM D18 Committee. 2016a. *D5084-16a Test Methods for Measurement of Hydraulic Conductivity of Saturated Porous Materials Using a Flexible Wall Permeameter*. ASTM International.

ASTM D18 Committee. 2016b. *D2166/2166M-16 Standard Test Method for Unconfined Compressive Strength of Cohesive Soil*. ASTM International.

ASTM D18 Committee. 2019a. *D2434-19 Test Method for Permeability of Granular Soils (Constant Head)*. ASTM International.

ASTM D18 Committee. 2019b. *D2216-19 Standard Test Methods for Laboratory Determination of Water (Moisture) Content of Soil and Rock by Mass*. ASTM International.

ASTM D18 Committee. 2020. *D7181-20 Test Method for Consolidated Drained Triaxial Compression Test for Soils*. ASTM International.

ASTM E05 Committee. 2020. *E119-20 Test Methods for Fire Tests of Building Construction and Materials*. ASTM International.

Averyanov, S. 2018. “Analysis of construction experience of using lightweight cellular concrete as a subbase material.” Waterloo, Ontario, Canada: University Of Waterloo.

Bartlett, S. F. 2015. “Application of Caltrans mechanically stabliized earth wall design requirements to lightweight cellular concrete backfill.”

Bartlett, S. F., and E. C. Lawton. 2008. “Evaluating the Seismic Stability and Performance of Freestanding Geofoam Embankment.” *6th National Seismic Conference on Bridges and Highways*. Charleston, SC.

Bartlett, S. F., A. C. Trandafir, E. C. Lawton, and B. N. Lingwall. 2011. “Applications of EPS Geofoam in Design and Construction of Earthquake Resilient Infrastructure.” *EPS 2011*. Oslo Norway.

Cabrera, J. G., and C. J. Lynsdale. 1988. “A new gas permeameter for measuring the permeability of mortar and concrete.” *Magazine of Concrete Research*, 40 (11): 177–182.

Chica, L., and A. Alzate. 2019. “Cellular concrete review: New trends for application in construction.” *Construction and Building Materials*, 200: 637–647. https://doi.org/10.1016/j.conbuildmat.2018.12.136.

Davich, P., J. Labuz, B. Guzina, and A. Drescher. 2004. *Small Strain and Resilient Modulus Testing of Granular Soils*. 117. St. Paul, Minnesota: Minnesota Department of Transportation.

Decký, M., M. Drusa, K. Zgútová, M. Blaško, M. Hájek, and W. Scherfel. 2016. “Foam Concrete as New Material in Road Constructions.” *Procedia Engineering*, 161: 428–433. https://doi.org/10.1016/j.proeng.2016.08.585.

Galle, C. 2001. “Effect of drying on cement-based materials pore structure as identified by mercury intrusion porosimetry A comparative study between oven-, vacuum-, and freeze-drying.” *Cement and Concrete Research*, 11.

Hardy, R., M. Lee, and D. Bronowski. 2004. *Laboratory constitutive characterization of cellular concrete*.

Inti, S., T. W. Evans, M. Flores, J. S. Solanki, and C. V. Chandramouli. 2021. “Permeable low-density cellular concrete (PLDCC) as a replacement for aggregate layers in permeable parking lots.” *Developments in the Built Environment*, 8: 100060. https://doi.org/10.1016/j.dibe.2021.100060.

Jones, M. R., and A. McCarthy. 2005. “Preliminary views on the potential of foamed concrete as a structural material.” *Magazine of Concrete Research*, 57 (1): 21–31.

Kearsley, E. P., and P. J. Wainwright. 2001. “The effect of high fly ash content on the compressive strength of foamed concrete.” *Cement and Concrete Research*, 31 (1): 105–112. https://doi.org/10.1016/S0008-8846(00)00430-0.

Kearsley, E. P., and P. J. Wainwright. 2002. “The effect of porosity on the strength of foamed concrete.” *Cement and Concrete Research*, 32 (2): 233–239. https://doi.org/10.1016/S0008-8846(01)00665-2.

Kozłowski, M., and M. Kadela. 2018. “Mechanical Characterization of Lightweight Foamed Concrete.” *Advances in Materials Science and Engineering*, 2018: 1–8. https://doi.org/10.1155/2018/6801258.

Lannen, T., N. D. Skinner, and J. S. Keim. 2018. *Strength and Abrasion Testing of Cellular Grout*. 12. Great Plains Regional Office, Billings, MT: U.S Department of the Interior, Bureau of Reclamation, Research & Development Office.

Levine, D. M., P. P. Ramsey, and R. K. Smidt. 2001. *Applied Statistics for Engineers and Scientists*. Upper Saddle River, New Jersey 07458.

Liu, X., C. Ni, K. Meng, L. Zhang, D. Liu, and L. Sun. 2020. “Strengthening mechanism of lightweight cellular concrete filled with fly ash.” *Construction and Building Materials*, 251: 118954. https://doi.org/10.1016/j.conbuildmat.2020.118954.

Nambiar, E. K. K., and K. Ramamurthy. 2007. “Air-void characterisation of foam concrete.” *Cement and Concrete Research*, 37 (2): 221–230. https://doi.org/10.1016/j.cemconres.2006.10.009.

Namsone, E., G. Šahmenko, and A. Korjakins. 2017. “Durability Properties of High Performance Foamed Concrete.” *Procedia Engineering*, 172: 760–767. https://doi.org/10.1016/j.proeng.2017.02.120.

Narayanan, N., and K. Ramamurthy. 2000. “Structure and properties of aerated concrete: a review.” *Cement and Concrete Composites*, 22 (5): 321–329. https://doi.org/10.1016/S0958-9465(00)00016-0.

Ostle, B., and L. C. Malone. 1988. *Statistic in Research: Basic Concepts and Technicques for Research Workers*. Iowa State University, Ames, IA.

Pradel, D., and B. Tiwari. 2015. “The use of MSE walls backfilled with Lightweight Cellular Concrete in soft ground seismic areas.” *3rd International Conference on Deep Foundations*, 8. Mexico: Mexican Society for Geotechnical Engineering.

Ramamurthy, K., E. K. Kunhanandan Nambiar, and G. Indu Siva Ranjani. 2009. “A classification of studies on properties of foam concrete.” *Cement and Concrete Composites*, 31 (6): 388–396. https://doi.org/10.1016/j.cemconcomp.2009.04.006.

Sandler, I. S., and D. Rubin. 1979. “An algorithm and a modular subroutine for the CAP model.” *International Journal for Numerical and Analytical Methods in Geomechanics*, 3 (2): 173–186.

Schwartz, F. W., and H. Zhang. 2003. *Fundamentals of Groundwater*. John Wiley & Sons, Inc.

Seely, D., J. Bunger, J. Patten, J. Wiser, and S. Luthier. 2014. “Gas Containment and Water Exclusion Testing.” Colorado School of Mines.

Song, Y., and D. A. Lange. 2021. “Measuring dynamic Young’s modulus of low-density foam concrete using resonant frequency test.” *Journal of Testing and Evaluation*, 50 (1). https://doi.org/10.1520/JTE20200414.

Sutmoller, N. 2020. “An Introduction to Low-Density Cellular Concrete and Advanced Engineered Foam Technology.” *Geo-Congress 2020*, 630–640. Minneapolis, Minnesota: American Society of Civil Engineers.

Taylor, S. 2015. “Cellular Concrete: A Cushion Over A Fault Line - Tunnel Business Magazine.pdf.” *Tunnel Business Magazine*, 2015.

Taylor, S., and G. Halsted. 2021. *Guide to Lightweight Cellular Concrete for Geotechnical Applications*. 62. Iowa State University, Ames, IA: National Concrete Pavement Technology Center.

Teig, J., and J. Anderson. 2012. “Innovative Design for the Colton Flyover Grade Separation of UPRR and BNSF, Colton, CA.” *AREMA 2012 Annual Conference & Exposition*. Chicago, IL.

Tikalsky, P. J., J. Pospisil, and W. MacDonald. 2004. “A method for assessment of the freeze–thaw resistance of preformed foam cellular concrete.” *Cement and Concrete Research*, 34 (5): 889–893. https://doi.org/10.1016/j.cemconres.2003.11.005.

Tiwari, B., B. Ajmera, R. Maw, R. Cole, D. Villegas, and P. Palmerson. 2017. “Mechanical Properties of Lightweight Cellular Concrete for Geotechnical Applications.” *J. Mater. Civ. Eng.*, 29 (7): 06017007. https://doi.org/10.1061/(ASCE)MT.1943-5533.0001885.

Tiwari, B., B. Ajmera, and D. Villegas. 2018. “Dynamic Properties of Lightweight Cellular Concrete for Geotechnical Applications.” *J. Mater. Civ. Eng.*, 30 (2): 04017271. https://doi.org/10.1061/(ASCE)MT.1943-5533.0002155.

Von Quintus, H., and B. Killingsworth. 1998. *Analysis relating to pavement material characterizations and their effects on pavement performance*.

Wu, H., J. Liu, and X. Zhang. 2020. “Feasibility study on use of cellular concrete for air convection embankment on permafrost foundations in Fairbanks, Alaska.” *Transportation Geotechnics*, 22: 100317. https://doi.org/10.1016/j.trgeo.2020.100317.